MEDICAL RADIOLOGY

Diagnostic Imaging

A. L. Baert
M. Knauth
K. Sartor

Image Processing in Radiology

Current Applications

E. Neri
D. Caramella
C. Bartolozzi
Editors

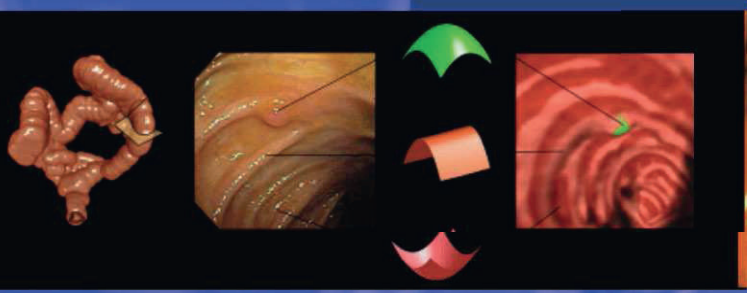

Springer

MEDICAL RADIOLOGY

Diagnostic Imaging

E. Neri · D. Caramella · C. Bartolozzi (Eds.)

Image Processing in Radiology

Current Applications

With Contributions by

A. J. Aschoff · E. Balogh · C. Bartolozzi · A. Bardine · V. Battaglia · C. R. Becker
R. Beichel · W. Birkfellner · A. Blum-Moyse · P. Boraschi · A. Bornik · E. Bozzi · C. Capelli
D. Caramella · C. Cecchi · F. Cerri · K. Cleary · A. Cotton · L. Crocetti · C. N. De Cecco
C. Della Pina · A. H. de Vries · F. Donati · R. Ferrari · G. Fichtinger · G. Galatola
T. M. Gallo · S. J. Golding · F. Iafrate · A. Jackson · N. W. John · S. Karampekios
J. Kettenbach · G. Kronreif · A. Laghi · L. Landini · C. Laudi · R. Lencioni · F. Lindbichler
M. Macari · P. Macheshi · S. Mazeo · B. Meyer · A. Melzer · E. Neri · L. Nyúl · K. Palágyi
V. Panebianco · P. Paolantonio · N. Papanikolaou · N. Popovic · V. Positano · D. Regge
B. Reitinger · M. Rieger · P. Rogalla · A. Ruppert · S. Salemi · M. F. Santarelli · B. Sauer
I. W. O. Serli · M. Sonka · E. Sorantin · S. M. Stivaros · D. Stoianovici · J. Stoker · V. Tartaglia
B. M. ter Haar Romeny · N. A. Thacker · F. Turini · P. Vagli · A. Vilanova i Bartrolí
T. W. Vomweg · F. M. Vos · S. R. Watt-Smith · G. Werkgartner · H. Yoshida

Foreword by

A. L. Baert

With 297 Figures in 544 Separate Illustrations, 224 in Color and 44 Tables

Springer

Emanuele Neri, MD
Diagnostic and Interventional Radiology
Department of Oncology, Transplants,
and Advanced Technologies in Medicine
University of Pisa
Via Roma 67
56100 Pisa
Italy

Davide Caramella, MD
Professor, Diagnostic and Interventional Radiology
Department of Oncology, Transplants,
and Advanced Technologies in Medicine
University of Pisa
Via Roma 67
56100 Pisa
Italy

Carlo Bartolozzi, MD
Professor, Division of Diagnostic
and Interventional Radiology
Department of Oncology, Transplants,
and New Technologies in Medicine
University of Pisa
Via Roma 67
56100 Pisa
Italy

Medical Radiology · Diagnostic Imaging and Radiation Oncology
Series Editors:
A. L. Baert · L. W. Brady · H.-P. Heilmann · M. Knauth · M. Molls · C. Nieder · K. Sartor

Continuation of Handbuch der medizinischen Radiologie
Encyclopedia of Medical Radiology

Library of Congress Control Number: 2006936011

ISBN 978-3-540-25915-2 Springer Berlin Heidelberg New York

Springer is part of Springer Science+Business Media

http//www.springer.com

Printed in Germany

Medical Editor: Dr. Ute Heilmann, Heidelberg
Desk Editor: Ursula N. Davis, Heidelberg
Production Editor: Kurt Teichmann, Mauer
Cover-Design and Typesetting: Verlagsservice Teichmann, Mauer

Printed on acid-free paper – 21/3180xq – 5 4 3 2 1 0

Foreword

Computer applications for image processing in radiological imaging have matured over the past decade and are now considered an indispensable tool for extracting maximal information from the enormous amount of data obtained with the new cross-sectional techniques such as ultrasound, computed tomography and magnetic resonance imaging. Indeed, the exquisite display of anatomy and pathology in all possible planes provided by these methods offers new and specific diagnostic information which will contribute to a better therapeutic management of the patient.

This volume not only covers very comprehensively the fundamental technical aspects of modern imaging processing, including the latest advances in this rapidly evolving field, but it also deals systematically and in depth with the numerous clinical applications in those specific body areas where these methods can be successfully applied. Special chapters are devoted to 3D image fusion and to image-guided robotic surgery. The well readable text is completed by numerous superb illustrations.

The editors, all from the department of diagnostic and interventional radiology of the University of Pisa, are internationally well known experts in the field and all share longstanding dedication and interest in radiological image processing, as demonstrated by their innovative research and publications. Other leading international experts have contributed outstanding individual chapters based on their specific expertise.

I would like to thank and congratulate most sincerely the editors and authors for their superb efforts which have resulted in this much needed and excellent book which will be of great assistance to all radiologists in their daily clinical work, as well as to surgeons and other medical specialists interested in enlarging their knowledge in this wonderful world of radiological computer processing.

I am confident that it will meet with the same success among readers as the previous volumes published in this series.

Leuven

Albert L. Baert

Preface

Two and three-dimensional image processing is an essential and integral part of the diagnostic workflow in the Radiology Department nowadays, significantly improving the quality of diagnosis and at the same time increasing reporting times. Thus, a precise knowledge of the technical aspects and clinical impact of image processing is mandatory for radiologists.

In this book, a group of well recognized experts in the field have sought to provide the radiologist with the information essential to optimizing the use of image processing tools in clinical workflow.

The initial section of the book is dedicated to the technical aspects of image processing, from image acquisition to image processing in the 2D and 3D domain. A larger part of the book is dedicated to clinical applications, where specific topics of Radiology subspecialties are comprehensively covered. A special topic section completes the book, highlighting new and advanced fields of research, such as computer-aided diagnosis and robotics.

We hope to have achieved our aim of providing our colleagues with a useful reference tool in their daily practice.

We would like to express our thanks to all the authors for their outstanding contribute.

We are also very grateful to Prof. Albert Baert for his valuable support in this project.

Pisa

Emanuele Neri
Davide Caramella
Carlo Bartolozzi

Contents

Technical Basis of Image Processing

Image Processing: Clinical Applications

Special Topics

Technical Basis of Image Processing

US Image Acquisition

1

Elena Bozzi, Laura Crocetti, and Riccardo Lencioni

CONTENTS

E. Bozzi, MD
Division of Diagnostic and Interventional Radiology, Department of Oncology, Transplants and New Technologies in Medicine, University of Pisa, Via Roma 67, 56125 Pisa, Italy
L. Crocetti, MD
Assistant Professor, Division of Diagnostic and Interventional Radiology, Department of Oncology, Transplants and New Technologies in Medicine, University of Pisa, Via Roma 67, 56125 Pisa, Italy
R. Lencioni, MD
Associate Professor, Division of Diagnostic and Interventional Radiology, Department of Oncology, Transplants and New Technologies in Medicine, University of Pisa, Via Roma 67, 56125 Pisa, Italy

1.1 Introduction

Three-dimensional (3D) ultrasonography, even if recently gaining large popularity, is a relatively new tool compared with 3D reconstructions obtained by CT and MR. Ultrasonography offers unique qualities including real-time imaging, physiologic measurements, use of non-ionizing radiations and invasiveness. Sonographic image quality has benefited from increasingly sophisticated computer technology: to date several systems, able to generate 3D ultrasound images, have been introduced.

Volume sonographic imaging has sparked interest in the academic community since the 1961. At that time Baum and Greenwood (1961) obtained serial parallel ultrasound images of the human orbit and created a 3D display by stacking sequential photographic plates with the ultrasound images. During the early 1970s also the commercial industry's interest for 3D ultrasound imaging grew up: in 1974 the Kretztechnik group, in order to achieve 3D images, developed a cylindrical-shaped transducer incorporating 25 elements mounted on a drum. This equipment performed a volume scan consisting of 25 parallel slices. The next step consisted of a more convenient end-fire transducer producing a fan scan. However, at that time the display and store technology was not suitable for 3D ultrasound imaging. In 1989 in Paris at the French Congress of Radiology, Kretztechnik presented the first commercially available ultrasound system featuring the 3D Voluson technique. It is only in the last few years that computer technology and visualization techniques have progressed sufficiently to make 3D ultrasound viable. Nowadays, 3D ultrasound imaging methods allow to present, in a few seconds, the entire volume in a single image (Brandal et al. 1999). The success of 3D ultrasound will depend on providing performance that equals or exceeds that of two-dimensional (2D) ultrasonography, including real time capability and interactivity. In addi-

tion, three-dimensional ultrasound is already being introduced alone or together with preoperational images for guidance of surgical applications.

US is a widely used tool for imaging guided procedures in the abdomen, especially in the liver. Its well-known advantages can be combined with those of computed tomography (CT) or magnetic resonance (MR) images by means of fusion imaging processes. Image fusion, the process of aligning and superimposing images obtained using two different imaging modalities, is in fact a rapidly evolving field of interest.

In this chapter, we review the various approaches that investigators have pursued in the development of 3D ultrasound imaging systems, with emphasis on the steps of the process of making 3D sonographic images. Moreover, an overview on US-CT/MR fusion imaging will be included.

1.2 Data Acquisition

Various techniques have been described until now for acquiring a sequence of sonograms and reconstructing them into a final 3D result. Acquiring the sequence is the critical step in the process for primarily two reasons. First, because the sequence of acquired tomographic images will be assembled into a 3D image, the acquisition geometry must be know exactly to avoid distortions, and the images must be acquired rapidly to avoid patient motion. Second, the mechanism that manipulates the transducer or localizes its position in the space must not interfere to the regular performance of the sonographic examination. In meeting these requirements, various solutions have been proposed. At present the main types of 3D data acquisition systems are: (1) mechanical scanning systems, (2) tracked freehand systems, and (3) untracked freehand systems, and (4) 2D transducer arrays.

1.2.1 Mechanical Scanning Systems

Mechanical scanning systems are based on commercially available linear or annular transducer array mounted on a mechanical assembly that allows precise movement of the transducer by a motor under computer control. At present, two different types of mechanical assemblies have been developed: external transducer fixation drive devices and, more recently, integrated volume transducers.

External transducer fixation drive devices represent the first implementation of mechanical scanning systems. In this approach the transducer is mounted on a special external device (mechanical arm) that holds the transducer firmly, offering precise movement during scanning. The device is then held in a fixed position, and a motor drive system on the device moves the transducer in a controlled and well-defined fashion to sweep out a volume. This system provides a high accuracy in locating the position of the transducer relative to the scanned planes. In the past it has been used for vascular (Downey and Fenster 1995a), prostate (Downey and Fenster 1995b) and obstetric (Steiner et al. 1994) imaging. Because of the constraints imposed by a rigid mechanical device that can result in being cumbersome for the operator and may interfere with the usual sonographic examination, to date these external devices are not in clinical use. In order to overcome these limitations, integrated volume transducers have been introduced.

The integrated volume transducer consisted of a conventional annular array transducer mounted on a hand-held assembly that allows the translation or rotation of the transducer by a motor drive computer system. Integrated volume transducers acquire a volume as a series of slices at slightly different orientations. After each slice the transducer plane is moved, by the stepping motor, to the next location. By this, the relative angle between slices is exactly known, eliminating distortion in the resultant scan. Integrated volume transducers tend to be relatively larger than standard transducers, but they eliminate most of the issues related to external position sensors with respect to calibration and accuracy. As a result the sonographer can use the transducer in the same manner as with conventional 2D ultrasonography systems by avoiding only immobilizing the probe during the image acquisition. It will require only a few seconds for obstetric studies, and a longer time, approximately 1 min, for cardiac-gated studies. Volumes can be acquired and reconstructed rapidly without registration artifacts. Such systems have a relatively small field of view that, although not posing problems for imaging small structures, may represent a significant limitation for large ones. Integrated volume

transducers have been produced for both transabdominal and intra-cavitary probes. This approach has been described for several applications: abdomen (Hamper et al. 1994), prostate (Hamper et al. 1999; Elliot et al. 1996; Tong et al. 1996), heart (De Castro et al. 1998) and obstetric (Johnson et al. 2000; Nelson et al. 1996). A particular application of this approach is represented by the use of a motorized rotating transducer mounted on the end of a catheter and introduced into the vasculature for intravascular imaging (Thrush et al. 1997; Klein et al. 1992). Withdrawal of the catheter and transducer through a vessel allows collection of a series of two dimensional images for forming a 3D volume.

The different types of mechanical assemblies used to produce 3D images can be divided into three basic types of motion: linear, tilting, and rotation (Fenster and Downey 2000).

The linear scanning requires that the transducer is moved by the stepping motor in a linear fashion along the surface of the patient's skin so that the 2D images obtained are parallel to each other. The 2D images are acquired at a regular spatial interval that is adjusted to ensure appropriate sampling of the anatomy. Because the 2D images are parallel and the spatial sampling interval is predetermined, the majority of the parameters required for the reconstruction can be precomputed, and the reconstruction time can be shortened. With this approach, a volume image can be obtained immediately after performance of a linear scan.

With tilt scanning the transducer is titled about its face, and images are digitized at a predetermined angular interval. The main advantage of this approach is that the scanning device is usually quite small, which allows easy handheld manipulations. On the contrary, the major problem related to the use of the tilt scanning approach is that the 2D images are acquired in a fanlike geometry; as a consequence the space between them increases and the resolution decreases with increasing depth.

In rotational scanning the transducer is rotated around an axis that is perpendicular to the transducer array. The 3D image data are then acquired by collecting a series of 2D B mode images as the probe is rotated at constant speed. As a result, the sampling distance increases and the resolution decreases as distance from the rotational axis increases. In addition, the digitized images intersect along the rotational axis, so that any motion creates artifacts at the center of the 3D image.

1.2.2 Tracked Freehand Systems

The freehand approach is very attractive: the transducer can be moved freely and without any restriction introduced by mechanics. The examination is performed in the same way as a standard ultrasound study. With tracked freehand systems, the operator holds an assembly composed of the transducer and a position-sensor device and manipulates it over the anatomic area being evaluated. During the acquisition of 2D images the tracking device attached to the probe monitors the spatial position and orientation of the ultrasound transducer. The tracking device has a limited size and weight and does not influence the movement of the transducer, the freedom or the usual working procedure of the physician. This system provides flexibility in selecting the best image plane sampling of the tissue volume from which data are acquired. In addition, it eliminates the need for more complex, dedicated 3D probes, which contain a mechanism to move the transducer through a pre-set field of acquisition. The principal types of tracking freehand systems are: acoustic tracking, optical tracking and magnetic field tracking.

Acoustic tracking makes use of sound emitters mounted on the transducer and small microphones for sound detection. The microphones must be positioned in different locations above the patient and must be sufficiently near the emitters to be able to detect the sound pulse. As the operator moves the probe, the sound emitters are energized in rapid sequence, producing sound waves that are detected by the microphones. The time of fly of the sound impulse from each emitter to each microphone is measured and corrected for environmental conditions, and then used to calculate the position of the transducer and the ultrasound image in a coordinate system defined by the microphone array. The trigger signal that is recorded by the ultrasound system allows coordination of the imaging and positional data. As a consequence, by activating the sound-emitting devices while the probe is moving freely, the position and orientation of the transducer can be continuously monitored, and real time acquisition of images and positional data are obtained (Ofili and Navin 1994; King et al. 1990). A disadvantage of the acoustic system is the requirement of a direct line of sight between the sensing equipment (microphones) and the ultrasound probe. The general idea with optical tracking is to use multiple cameras with

markers distributed on a rigid structure, where the geometry is specified beforehand. Up to three markers are necessary to determine the position and orientation of the rigid body in space. Additional markers allow a better camera visibility of the tracked object and improve the measurement accuracy. In addition, both the visibility of the tracked object and the accuracy of its 3D position and orientation are highly dependent on the position of the markers (West and Maurer 2004; Lindeseth et al. 2003; Treece et al. 2003).

The magnetic field tracking system, on the contrary, does not impose any restriction on transducer placement during scanning: magnetic tracking permits free transducer movement, allowing acquisition of arbitrarily oriented 2D images from one or more acoustic windows.

Magnetic field tracking is a relatively new tracked freehand technique that makes use of magnetic localizers to measure the transducer's position and angle in the space. At present it is considered the most successful tracked freehand technique. The system includes a magnetic field generator (transmitter), a miniature magnetic sensor (receiver) and a system control unit.

The receiver is small and mounted directly on the ultrasound scan head. Its size does not interfere with standard clinical ultrasound scanning methods. The transmitter, which is usually mounted on the examining table, emits three orthogonal magnetic fields. The control unit measures and compares the relative strengths of all three fields at the receiver. These measurements are used to compute the position and orientation of the receiver relative to the transmitter.

To achieve accurate 3D reconstruction, electromagnetic interference must be minimized, the transmitter must be close to the receiver, and there should be no ferrous or highly conductive metals in the vicinity (Downey et al. 2000; Kelly et al. 1994). Magnetic field tracking systems can be used with standard and endocavitary transducers. These systems have been used successfully for fetal (Kelly et al. 1994; Pretorius and Nelson 1994) and vascular (Hodges et al. 1994) 3D imaging. Recently, there has been some development with a miniature magnetic position sensor suitable for use with intra-vascular transducers.

Locating US images within a tracked coordinate system opens up a new world of possibilities: the images can be registered to a patient and to images from other modalities (Brendel et al. 2002; Comeau et al. 2000; Dey et al. 2002; Lindeseth et al. 2003).

All the tracking devices used for freehand systems work in a similar manner: the device tracks the position and orientation (pose) of the sensor on the probe, not the US image plane itself. So, an additional step must be added to compute the transformation (rotation, translation and scaling) between the origin of the sensor mounted on the probe and the image plane itself (Mercier et al. 2005; Hsu et al. 2006; Gee et al. 2005).

1.2.3 Untracked Freehand Systems

The sensorless techniques attempt to estimate the 3D position and orientation of a probe in space. Pennec et al. (2003), for example, proposed a system where a time sequence of 3D US volumes is registered to play the role of a tracking system. Sensorless tracking can be done by analyzing the speckle in the US images using decorrelation (Tuthill et al. 1998) or linear regression (Prager et al. 2003). This approach does not require any kinds of devices added to the probe. The operator has to move the transducer with a uniform and steady motion, in a constant linear or angular velocity. As a result the 2D images are acquired at a regular spatial interval that is adjusted to ensure appropriate sampling of the anatomy. However, Li et al. (2002) found that it was impossible to accomplish real freehand scanning using only speckle correlation analysis. Although this approach can result in being very attractive for the user, image quality is extremely variable, depending on the regularity of the transducer's movement. Moreover, geometric measurements (distance, volume, area) may be inaccurate. These drawbacks make the tool useless, or in any case unsuitable for accurate clinical applications.

1.2.4 2D Transducer Arrays

This system represents the ultimate approach to 3D sonographic acquisition. 2D arrays are matrix with a large number of elements arranged in rows and columns that are able, in principle, to have unrestricted scanning in 3D. A volumetric image is produced without moving the transducer: such an array generates pyramidal or conical ultrasound pulse

and processes the echoes to obtain 3D information in real time. These probes are relatively large and expensive in comparison with 2D probes, and their image resolution is not as good as their 2D counterparts. Although the ultimate expectation is that 2D transducer arrays will replace integrated mechanical scanning transducers or other position-sensing transducers, they are still in the research phase. Investigators have described several 2D arrays systems (Turnbull and Foster 1992; Turnbull et al. 1992); the one developed at Duke University for real time 3D echocardiography is the most advanced and has been used for clinical imaging (Light et al. 1998; Smith et al. 1992; Von Ramm and Smith 1990). At present the major problem related to the use of 2D transducer arrays consists of the complexity of the system, which requires sophisticated software and huge computer capabilities. In order to reduce system cost and complexity, sparse 2D arrays have been developed (Davidsen and Smith 1997; Davidsen et al. 1994). Moreover, 2D array transducers are relatively small, and, as a result, their field of view also is relatively small: it may be a limitation for large organ imaging (Nelson and Pretorius 1998). Other 3D probes can be either mechanically or electronically steered within the probe housing. An annular array producing a thin US beam can be accurately controlled by an internal mechanical motor in 2D to obtain a 3D volume with high resolution. 2D probes can also be electronically steered within the image plane to increase the field of view (FOV), as in Rohling et al. (2003).

1.3 Data Processing and Reconstruction

The 3D reconstruction process involves the generation of a 3D image from a digitized set of 2D images. The 3D reconstruction and processing architecture for 3D ultrasound is critical since it must take advantage of frequent processor, accelerator, and software upgrades to keep up with rapidly changing computer technology.

Three different groups of reconstruction algorithms have been used. These groups have been differentiated on the basis of implementation in voxel-based methods (VBM), pixel-based methods (PBM) and function-based methods (FBM) by Solberg et al. (2007).

1.3.1 Voxel-Based Methods

The voxel-based volume model represents the most common approach to 3D reconstruction techniques. With this method a volume is generated by placing each 2D image at the proper location in the 3D volume. In the different algorithms, one or several pixels may contribute to the value of each voxel. This approach preserves all the original information during 3D reconstruction: it allows reviewing repeatedly the 3D image by a variety of rendering techniques. Using a voxel-based volume model, the operator can scan through the data and then chooses the most suitable rendering technique. Moreover, this approach allows the use of segmentation and classification algorithms to measure volume and segment boundaries or the performance of various volume-based rendering operations. The major limitation of the voxel-based volume model is that it generates very large data files, requiring amounts of computer memory and making the 3D reconstruction process slower.

1.3.2 Pixel-Based Methods

Pixel-based methods traverse each pixel in the input images and assign the pixel value to one or several voxels. A PBM may consist of two steps: a distribution step (DS) and a hole-filling step (HFS). In the DS, the input pixels are traversed and the pixel value applied to one or several voxels, often stored together with a weight value. In the HFS, the voxels are traversed and empty voxels are being filled. Most hole-filling methods have a limit on how far from away from known values the holes are filled, so if the input images are too far apart or the hole-filling limits are too small, there will still be holes in the constructed volume.

1.3.3 Function-Based Methods

Function-based methods choose a particular function (like a polynomial) and determine coefficients to make one or more functions pass through the input pixels. Afterwards, the functions are used to create a regular voxel array by evaluating the functions at regular intervals.

1.4 Data Visualization

Once the volume has been created, it can be viewed interactively by the use of any 3D visualization and rendering software. Visualization of 3D data plays an important part in the development and use of 3D ultrasound, with three predominant approaches being utilized thus far: surface rendering, multiplanar reconstructions, and volume rendering (Fig. 1.1).

1.4.1 Surface Rendering

At present surface rendering is the most common 3D display technique. In surface rendering the surfaces of structures or organs are portrayed in the rendition. The surface can be extracted manually or automatically. Manual segmentation methods give the most accurate surface, but are a lengthy and laborious task for the operator. Unfortunately, to date, automatic segmentation methods, requiring simple user assistance, cannot be guaranteed to always work correctly in large applications. With this approach the boundaries are represented by a wire frame or mesh, the surface is texture mapped with an appropriate color and texture to represent the anatomical structure (Fenster and Downey 2000; Downey et al. 2000). Echocardiographic (Wang et al. 1994; Rankin et al. 1993) and fetal (Lee et al. 1995; Kelly 1994; Nelson and Pretorius 1992) 3D studies represent the major clinical applications of this rendering technique.

1.4.2 Multiplanar Reconstruction

At present two different multiplanar reconstruction techniques have been developed: section display and texture mapping.

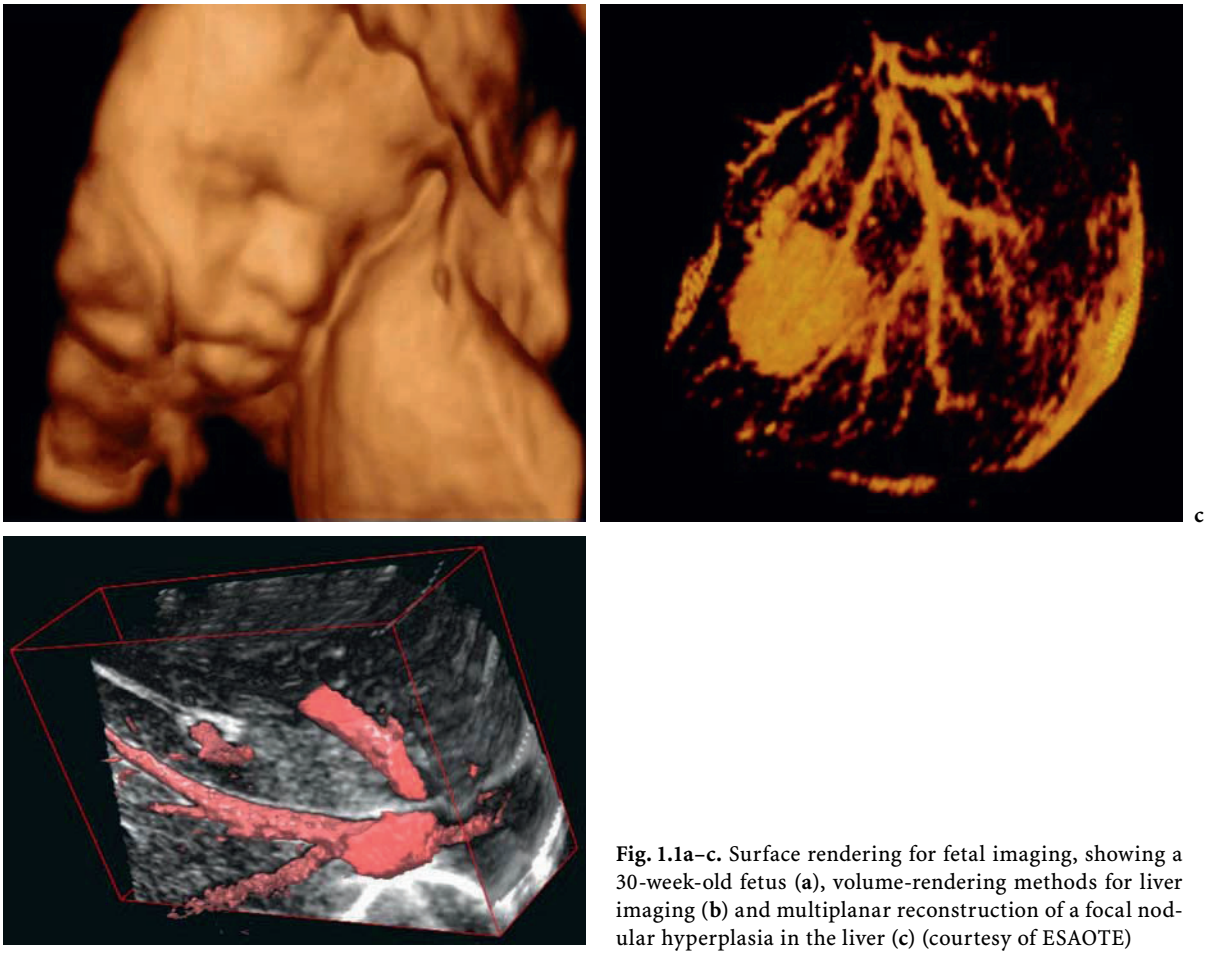

Fig. 1.1a–c. Surface rendering for fetal imaging, showing a 30-week-old fetus (**a**), volume-rendering methods for liver imaging (**b**) and multiplanar reconstruction of a focal nodular hyperplasia in the liver (**c**) (courtesy of ESAOTE)

Section display allows visualization of multiple sections of the acquired volume scan along three orthogonal planes: acquisition plane, transverse or sagittal reconstructed plane, and C-plane (parallel to the transducer surface). Computer-user interface tools allow the operator to rotate and reposition these planes so that the entire volume of data can be examined. Because this technique is easy to implement and allows short 3D reconstruction times, it has been largely used in clinical applications (Hamper et al. 1994).

The second technique, called texture mapping, displays the 3D image as a polyhedron with the appropriate anatomy texture mapped on each face. The reconstructed structure can be viewed by slicing into the volume, interactively, to form a cross-sectional image of the volume acquired in any orientation. As a result, this rendering approach provides a good means for visualizing spatial relationships for the entire volume in a readily comprehended manner (Tong et al. 1996; Fishman et al. 1991).

1.4.3 Volume Rendering

Volume-rendering methods map voxels directly onto the screen without using geometric primitives. They require that the entire data set be sampled each time an image is rendered or re-rendered. Volume rendering algorithms are attractive tools for displaying an image that synthesizes all the data contained in the numerical volume. The most popular volume visualization algorithm for the production of high-quality images is ray-casting. With the ray-casting approach a 2D array of rays is projected through the 3D image. Shading and transparency voxel values along each ray are then examined, multiplied by factors, and summed to achieve the desired rendering result. A wide spectrum of visual effects can be generated depending on how the algorithm interacts with each voxel encountered by a particular ray. Maximum and minimum intensity projection (MIP) methods are one form of ray casting where only the maximum (or minimum) voxel value is retained as the rays transverse the data volume. These techniques are quite simple to implement and provide good quality results for several applications (Fenster and Downey 2000; Nelson and Pretorius 1998; Pretorius and Nelson 1994). As a result the volume rendering displays the anatomy in a translucent manner, simulating light propagation in a semitransparent medium. Obviously if the image is complex, with soft tissue structures, interpretation is difficult, even with the addition of depth cues or stereo viewing. Thus, this rendering approach is best suited for simple anatomical structures in which image clutter has been removed or is not present. Thus far, volume rendering has been used, with great results, particularly in displaying fetal (Baba et al. 1999; Baba et al. 1997; Nelson et al. 1996; Pretorius and Nelson 1995) and cardiovascular anatomy (Kasprzak et al. 1998; Menzel 1997; Salustri et al. 1995).

1.5 Image Fusion

US is a widely used tool for imaging-guided procedures in the abdomen, especially in the liver. US is fast, easily available, allows real time imaging and is characterized by high natural contrast among parenchyma, lesions, and vessels. On the other hand, because of its high spatial resolution, good contrast, wide field of view, good reproducibility, and applicability to bony and air-filled structures, CT plays an important role especially in interventions that cannot be adequately guided by fluoroscopy or US (Haaga et al. 1977; Sheafor et al. 1998; Kliewer et al. 1999). However, in contrast to fluoroscopy and US, CT has been limited by the lack of real-time imaging so that many CT-guided abdominal interventions remain difficult or cumbersome in several locations (Kliewer et al. 1999). Moreover, the contrast resolution of baseline CT scan is low, and many liver lesions are visible only during the arterial and/or portal-venous phase of the dynamic study, and not uncommonly needle localization under the unenhanced phase of image guidance is based on nearby anatomical landmarks (Lencioni et al. 2005). The introduction of CT fluoroscopy allows real-time display of CT images with a markedly decreased patient radiation dose and total procedure time comparable with the use of conventional CT guidance (Daly et al. 1999; Carlson et al. 2001). Moreover, new systems of breath-hold monitoring have been implemented, and this could allow an easier access to mobile lesions (Carlson et al. 2005). However, despite marked improvements in procedure times compared with helical CT, CT

fluoroscopy may still require 40% longer procedure times than US (Sheafor et al. 2000).

Therefore, the ideal qualities of a targeting technique during image-guided liver procedures include clear delineation of the tumor(s) and the surrounding anatomy, coupled with real-time imaging and multiplanar and interactive capabilities. Given the advantage of US guidance, it would be ideal if the procedure can be performed with real-time US matched with supplementary information from contrast-enhanced CT or MR images. Numerous devices have been constructed to improve puncture accuracy for percutaneous radiological interventions, and the majority of these are based on CT (Magnusson and Akerfeldt 1991; Palestrant 1999; Ozdoba et al. 1991; Jacobi et al. 1999; Wood et al. 2003). Image fusion, the process of aligning and superimposing images obtained using two different imaging modalities, is a rapidly evolving field of interest, with its own specific operational conditions.

A multimodality fusion imaging system (Virtual Navigator System, Esaote SpA, Genoa, Italy) is included in a commercially available US platform (MyLab™GOLD Platform , Esaote SpA, Genoa, Italy). An electromagnetic tracking system, composed by a transmitter and a small receiver (mounted on the US probe) provides the position and orientation of the US probe in relation to the transmitter. This permits a correct representation in size and orientation of the second modality image. These data are provided by the US scanner by the network connection and automatically updated at every change on the screen of the ultrasound machine. The pre-procedural CT DICOM series is transferred to the Virtual Navigator, and the registration of the system, by means of superficial fiducial markers or internal anatomical markers, can be done. We tested the accuracy of targeting by using this image fusion system matching real-time US and CT. We used a target that was undetectable at US and that was very small in size (1.5 mm). This ideally represents the situation of a tiny lesion that is visible only at CT. The navigation system represented therefore the only guidance for the procedures. By deciding to insert the needle only once for each targeting/ablation procedure, we reproduced the need for minimal invasiveness. The study included two phases. The initial phase was to assess the accuracy of targeting using a 22 gauge (G) cytological needle. The second phase of the study was to validate such a technique using a 15 G RF multitined expandable needle (RITA Medical Systems, Mountain View, CA) and to examine the accuracy of the needle placement relative to the target. The tip of the trocar of the RF needle had to be placed 1 cm from the target and then the hooks had to be deployed to 3 cm. Unenhanced CT of the liver and multiplanar reconstructions were performed to calculate the accuracy of positioning. Excellent target accuracy was achieved in both phases of the study, with an acceptable mean needle to target distance of 1.9±0.7 mm (range 0.8–3 mm) in the first phase and a mean target-central tine distance of 3.9±0.7 mm (range 2.9–5.1 mm) in the second phase (Crocetti et al. 2008). The main limitation of the study is the absence of respiratory excursion and subject motion in this ex-vivo model. Either or both of these factors would introduce error, but were not evaluated in our feasibility study. To extrapolate the utility in routine clinical practice, precise registration of CT volume images into the patient requires proper synchronisation with respect to the respiratory phase and the arm's position during CT examination, and patient movement must be avoided. We appreciate that added procedure time may be required to achieve accurate patient registration in some cases, but this may be offset by the time taken to perform needle localization and RF ablation of a lesion invisible or poorly conspicuous on routine unenhanced US or CT (Fig. 1.2). Possible solutions for detection of patient movement would be the implementation of external electromagnetic position sensors to the patient's body. To target liver lesions that move during the breathing cycle, a breathing motion correction must be implemented. The solution could be based on methods used in radiation therapy, as well as on those used in positron emission tomography-CT image fusion (Giraud et al. 2003; Goerres et al. 2003).

Future advances include the automation of registration, which could further streamline clinical translation of such technologies. Miniaturization of internalized sensors for electromagnetic tracking of needles and ablation probes will have the ability to transform image-guided needle-based procedures by providing real-time multimodality feedback.

In conclusion, real-time registration and fusion of pre-procedure CT volume images with intra-procedure US are feasible and accurate in the experimental setting. Further studies are warranted to validate the system under clinical conditions. For simple biopsies, an experienced interventional radiologist will not ask for such a guidance tool and, given the cost and availability, US and CT guidance

a

b

c

Fig. 1.2a–c. A multimodality fusion imaging system (Virtual Navigator System, Esaote SpA, Genoa, Italy)–real-time registration and fusion of pre-procedure CT volume images with intra-procedure US–used for a percutaneous radiofrequency ablation of an hepatocellular carcinoma: targeting of the lesion (**a**), needle placement (**b**) and evaluation of the ablation zone

will remain the "workhorses" for biopsy procedures. For lesions hardly visible at US or CT or for more complex procedures, such as thermal tumor ablations that require positioning of multiple applicators and puncture of multiple lesions, fusion imaging systems might be of help to reduce puncture risk and procedure time and to allow for more complete and radical therapy.

References

Baba K, Okai T, Kozuma S (1997) Real-time processable three-dimensional US in obstetrics. Radiology 203:571–574

Baba K, Okai T, Kozuma S (1999) Fetal abnormalities: evaluation with real-time-processible three-dimensional US–preliminary report. Radiology 211:441–446

Baum G, Greenwood I (1961) Orbital lesion localization by three-dimensional ultrasonography. NY State J Med 61:4149–4157

Brandal H, Gritzky A, Haizinger M (1999) 3D ultrasound: a dedicated system. Eur Radiol 9:S331–S333

Brendel B, Winter S, Rick A et al (2002) Registration of 3D CT and ultrasound datasets of the spine using bone structures. Comput Aided Surg 7:146 –155

Carlson SK, Bender CE, Classic KL et al (2001) Benefits and safety of CT fluoroscopy in interventional radiologic procedures. Radiology 219:515–520

Carlson SK, Felmlee JP, Bender CE et al (2005) CT fluoroscopy-guided biopsy of the lung or upper abdomen with a breath-hold monitoring and feedback system: a prospective randomized controlled clinical trial. Radiology 237:701–708

Comeau RM, Sadikot AF, Fenster A et al (2000) Intraoperative ultrasound for guidance and tissue shift correction in image-guided neurosurgery. Med Phys 27:787–800

Crocetti L, Lencioni R, De Beni S, See TC, Della Pina C, Bartolozzi C (2008) Targeting liver lesions for radiofrequency ablation: an experimental feasibility study using a CT-US fusion imaging system. Invest Radiol, in press

Daly B, Templeton PA (1999) Real-time CT fluoroscopy: evolution of an interventional tool. Radiology 211:309–331

Davidsen RE, Jensen JA, Smith SW (1994) Two-dimensional random arrays for real time volumetric imaging. Ultrason Imaging 16:143–163

Davidsen RE, Smith SW (1997) A two-dimensional array for B-mode and volumetric imaging with multiplexed electrostrictive elements. Ultrason Imaging 19:235–250

De Castro S, Yao J, Pandian NG (1998) Three-dimensional echocardiography: clinical relevance and application. Am J Cardiol 18(81):96G–102G

Dey D, Gobbi DG, Slomka PJ et al (2002) Automatic fusion of freehand endoscopic brain images to three-dimensional surfaces: Creating stereoscopic panoramas. IEEE Trans Med Imaging 21:23–30

Downey DB, Fenster A (1995a) Vascular imaging with a three-dimensional power Doppler system. AJR 165:665–668

Downey DB, Fenster A (1995b) Three-dimensional power Doppler detection of prostatic cancer. AJR 165:741

Downey DB, Fenster A, Williams JC (2000) Clinical utility of three-dimensional US. Radiographics 20:559–571

Elliot TL, Downey DB, Tong S (1996) Accuracy of prostate volume measurements in vitro using three dimensional ultrasound. Acad Radiol 3:401–406

Fenster A, Downey DB (2000) Three-dimensional ultrasound imaging. Annu Rev Biomed Eng 2:457–475

Fishman EK, Magid D, Ney DR (1991) Three-dimensional imaging. Radiology 181:321–337

Gee AH, Houghton NE, Trece GM et al (2005) A mechanical instrument for 3D ultrasound probe calibration. Ultrasound Med Biol 31:505–18

Giraud P, Reboul F, Clippe S et al (2003) Respiration-gated radiotherapy: current techniques and potential benefits. Cancer Radiother 7:S15–S25

Goerres GW, Burger C, Schwitter MR et al (2003) PET/CT of the abdomen: optimizing the patient breathing pattern. Eur Radiol 13:734–739

Haaga JR, Reich NE, Havrilla TR et al (1977) Interventional CT scanning. Radiol Clin North Am 15:449–456

Hamper UM, Trapanotto V, Sheth S (1994) Three-dimensional US: preliminary clinical experience. Radiology 191:397–401

Hamper UM, Trapanotto V, DeJong MR (1999) Three-dimensional US of the prostate: early experience. Radiology 212:719–723

Hodges TC, Detmer PR, Burns PH (1994) Ultrasonic three-dimensional reconstruction: in vivo and in vitro volume and area measurement. Ultrasound Med Biol 20:719–729

Hsu PW, Prager RW, Gee AH et al (2006) Rapid, easy and reliable calibration for freehand 3D ultrasound. Ultrasound Med Biol Jun 32:823–35

Johnson DD, Pretorius DH, Budorick NE (2000) Fetal lip and primary palate: three-dimensional versus two-dimensional US. Radiology 217:236–239

Kasprzak JD, Salustri A, Roelandt JR (1998) Three-dimensional echocardiography of the aortic valve: feasibility, clinical potential, and limitations. Echocardiography 15:127–138

Kelly IG, Gardener JE, Brett AD (1994) Three-dimensional US of the fetus: work in progress. Radiology 192:253–259

King DL, King DL Jr, Shao MYC (1990) 3-D spatial registration and interactive display of position and orientation of real-time ultrasound images. J Ultrasound Med 9:525–532

Klein HM, Gunther RW, Verlande M (1992) 3D-surface reconstruction of intravascular ultrasound images using personal computer hardware and a motorised catheter control. Cardiovasc Intervent Radiol 15:97–100

Kliewer MA, Sheafor DS, Paulson EK et al (1999) Percutaneous liver biopsy: a cost benefit analysis comparing sonographic and CT guidance. AJR 173:1199–1202

Jacobi V, Thalhammer A, Kirchner J (1999) Value of a laser guidance system for CT interventions; a phantom study. Eur Radiol 9:137–140

Lee A, Kratochwil A, Deutinger J (1995) Three-dimensional ultrasound in diagnosing phocomelia. Ultrasound Obstet Gynecol 5:238–240

Lencioni R, Cioni D, Bartolozzi C (2005) Focal liver lesions. Springer, Berlin Heidelberg New York

Li PC, Li CY, Yeh WC (2002) Tissue motion and elevational speckle decorrelation in freehand 3D ultrasound. Ultrason Imaging 24:1–12
Light ED, Davidsen RE, Fiering JO (1998) Progress in two-dimensional arrays for real-time volumetric imaging. Ultrason Imaging 20:1–15
Lindseth F, Tangen GA, Langø T et al (2003) Probe calibration for freehand 3D ultrasound. Ultrasound Med Biol 29:1607–1623
Magnusson A, Akerfeldt D (1991) CT-guided core biopsies using a new guidance device. Acta Radiol 32:83–85
Menzel T, Mohr-Kahaly S, Kolsch B (1997) Quantitative assessment of aortic stenosis by three-dimensional echocardiography. J Am Soc Echocardiogr 10:215–223
Mercier L, Langø; T, Lindseth F, Collins LD (2005) A review of calibration techniques for freehand 3-D ultrasound systems. Ultrasound Med Biol 31:449–471
Nelson TR, Pretorius DH (1992) Three-dimensional ultrasound of fetal surface features. Ultrasound Obstet Gynecol 2:166–174
Nelson TR, Pretorius DH, Sklansky M (1996) Three dimensional echocardiographic evaluation of fetal heart anatomy and function: acquisition, analysis, and display. J Ultrasound Med 15:1–9
Nelson TR, Pretorius DH (1998) Three-dimensional ultrasound imaging. Ultrasound Med Biol 24:1243–1270
Ofili EO, Navin CN (1994) Three-dimensional and four-dimensional echocardiography. Ultrasound Med Biol 20:669–675
Ozdoba C, Voigt K, Nusslin F (1991) New device for CT-targeted percutaneous punctures. Radiology 180:576–578
Palestrant AM (1990) Comprehensive approach to CT-guided procedures with a hand-held guidance device. Radiology 174:270–272
Pennec X, Cachier P, Ayache N (2003) Tracking brain deformation in time sequences of 3D US images. Pattern Recog Lett 24:801–813
Prager RW, Gee AH, Treece GM et al (2003) Sensorless freehand 3-D ultrasound using regression of the echo intensity. Ultrasound Med Biol 29:437–446
Pretorius DH, Nelson TR (1994) Prenatal visualization of cranial sutures and fontanelles with three-dimensional ultrasonography. J Ultrasound Med 13:871–876
Pretorius DH, Nelson TR (1995) Fetal face visualization using three-dimensional ultrasonography. J Ultrasound Med 14:349–356
Rankin RN, Fenster A, Downey DB (1993) Three-dimensional sonographic reconstruction: techniques and diagnostic applications. AJR 161:695–702
Rohling R, Fung W, Lajevardi P. PUPIL (2003) Programmable ultrasound platform and interface library, MICCAI 2003. In: Lecture notes computer science, vol. 2879. Montreal, QUE, Canada Springer:424–431
Salustri A, Spitaels S, McGhie J (1995) Transthoracic three-dimensional echocardiography in adult patients with congenital heart disease. J Am Coll Cardiol 26:759–767
Sheafor DH, Paulson EK, Kliewer MA et al (2000) Comparison of sonographic and CT guidance techniques. Does CT fluoroscopy decrease procedure time? AJR 174:939–942
Sheafor DH, Paulson EK, Simmons CM et al (1998) Abdominal percutaneous interventional procedures: comparison of CT and US guidance. Radiology 207:705–710
Smith SW, Trahey GE, von Ramm OT (1992) Two-dimensional arrays for medical ultrasound. Ultrason Imaging 14:213–233
Solberg OV, Lindseth F, Torp H (2007) Freehand 3D ultrasound reconstruction algorithms – a review. Ultrasound Med Biol 33:991–1009
Steiner H, Staudach A, Spinzer D (1994) Three-dimensional ultrasound in obstetrics and gynaecology: technique, possibilities and limitations. Human Reprod 9:1773–1778
Thrush AJ, Bonnett DE, Elliott MR (1997) An evaluation of the potential and limitations of three-dimensional reconstructions from intravascular ultrasound images. Ultrasound Med Biol 23:437–445
Tong S, Downey DB, Cardinal HN (1996) A three-dimensional ultrasound prostate imaging system. Ultrasound Med Biol 22:735–746
Treece GM, Gee AH, Prager RW et al (2003) High-definition freehand 3-D ultrasound. Ultrasound Med Biol 29:529–546
Turnbull DH, Foster FS (1992) Simulation of B-scan images from two-dimensional transducer arrays: Part II–comparisons between linear and two-dimensional phased arrays. Ultrason Imaging 14:344–353
Turnbull DH, Lum PK, Kerr AT (1992) Simulation of B-scan images from two-dimensional transducer arrays: Part I–methods and quantitative contrast measurements. Ultrason Imaging 14:323–343
Tuthill TA, Krucker JF, Fowlkes JB et al (1998) Automated three-dimensional US frame positioning computed from elevational speckle decorrelation. Radiology 209:575–582
von Ramm OT, Smith SW (1990) Real time volumetric ultrasound imaging system. J Digit Imaging 3:261–266
Wang XF, Li ZA, Cheng TO (1994) Clinical application of three-dimensional trans-esophageal echocardiography. Am Heart J 128:380–388
West BJ, Maurer CR Jr (2004) Designing optically tracked instruments for image-guided surgery. IEEE Trans Med Imaging 23:533–545
Wood BJ, Banovac F, Friedman M et al (2003) CT-integrated programmable robot for image-guided procedures: comparison of free-hand and robot-assisted techniques. J Vasc Interv Radiol 14:S62

3D MRI Acquisition: Technique

2

Nickolas Papanikolaou and Spyros Karampekios

CONTENTS

2.1 Introduction

Magnetic resonance imaging (MRI) is one of the most important imaging modalities that have played a role in the development of three-dimensional (3D) representations of human organs. With its lack of radiation exposure and its rich soft-tissue contrast, MRI has inherent 3D imaging capabilities, providing images in all three orthogonal planes, as well as in oblique or even double oblique orientations.

Three-dimensional Fourier Transformation (3D FT) imaging can be considered the most efficient scanning method (Pykett et al. 1982), providing a significantly higher signal-to-noise ratio per unit of time compared to two-dimensional (2D) techniques, and contiguous thin slices that may be less than 0.5 mm. With 3D FT techniques it is possible to acquire truly isotropic data in clinically acceptable acquisition times no longer than 10 min.

According to 3D FT techniques, raw data are acquired by means of two phase-encoding gradients, not only encoding the phase but also the level of the slice in the respective imaging volume. The 3D nature of volumetric images, when isotropic, allows for simple and efficient computation of images that lie along the non-acquired orthogonal orientations of the volume (Robb 1994). Nowadays, multi-planar reformation of volumetric data sets is incorporated in the clinical routine, resulting in more efficient management of hundreds or even thousands of images.

In this chapter, the most important 3D MRI pulse sequences commonly used in the clinical routine will be reviewed.

2.2 Pulse Sequences

Spin echo (SE) sequences are considered the gold standard in terms of image contrast. A major limitation is the relatively long repetition time necessary for optimal contrast, especially in proton density and T2-weighted images. Since the acquisition time is directly proportional to the repetition time, spin echo sequences are inherently time-consuming. With the advent of gradient technology, fast or turbo spin echo (TSE) sequences were developed (Hennig 1986; Hennig 1988), significantly reducing the acquisition time while maintaining similar to spin echo contrast. On the other hand, sequences that utilised a pair of gradients (gradient echo sequences) instead of a refocusing 180° radiofrequency (RF) pulse for the echo generation, proved significantly faster (Frahm et al. 1986; Tkach and Haacke 1988). These techniques, with minor modifications, could be applied in volumetric

N. Papanikolaou, PhD
Biomedical Engineer, Department of Radiology, University Hospital of Heraklion, University of Crete, Faculty of Medicine, P.O. Box 2208, 71003 Iraklion Crete, Greece
S. Karampekios, MD
Department of Radiology, University Hospital of Heraklion, University of Crete, Faculty of Medicine, P.O. Box 2208, 71003 Iraklion Crete, Greece

acquisition mode, and the idea of real 3D imaging made clinically feasible. However, the contrast of 3D gradient echo techniques is considered unsatisfactory by many compared to that of SE images. The 3D gradient echo techniques are more sensitive to susceptibility artifacts, while true T2-weighting is difficult to generate.

In spin echo sequences, two RF pulses – a 90° excitation pulse and a 180° refocusing pulse – are needed to generate an echo. In gradient echo sequences the refocusing pulse is missing and the signal is generated through the application of a bipolar measurement gradient pulse. In general, multiple alpha RF pulses are applied. In case the repetition time (TR), which is defined as the time difference between two successive excitation RF pulses, is much smaller than the T2-relaxation time, two signals will be generated, namely: a free induction decay (FID) immediately following each RF pulse, and an echo-like signal from the preceding pair of RF pulses that reaches the maximum at the time of the subsequent RF pulse. After several excitations, a steady state is created in which both residual transverse and longitudinal magnetization remain relatively constant. This condition describes a dynamic equilibrium in which transverse and longitudinal magnetization persist at all times (Frahm et al. 1987). Steady-state free precession (SSFP) imaging falls into the broad category of fast MR imaging techniques, where a very short TR and flip angle of less than 90° are utilized in order to maximize signal-to-noise ratio (Ernst angle), while phase encoding is performed by means of incremental application of gradient pulses immediately before signal collection. These gradient pulses are applied again with the opposite polarity after signal collection (rewinder gradients) to maintain a zero net phase accumulation between successive RF pulses, so that steady state magnetization is maintained. This type of sequence can be described as a "balanced" sequence, since no net phase change is imparted to stationary spins by the various gradient and RF pulses.

2.2.1 Volumetric T1-Weighted Sequences

Two different variants of gradient echo sequences exist depending on whether the transverse magnetization is destroyed or maintained. In the so called steady state non-coherent gradient echo sequences, transverse magnetization is eliminated either by means of dedicated spoiler gradients or by phase cycling techniques (Zur et al. 1988; Zur et al. 1990). By doing so, T1-contrast can be generated, and these sequences used for dynamic contrast enhancement studies or in MR angiography. Acronyms of sequences belonging to the non-coherent steady state gradient echo techniques include FLASH, T1-FFE and SPGR.

One of the earliest clinical applications of volumetric T1-weighted sequences was MR angiography. Volumetric acquisitions are very useful since they can provide with increased spatial resolution both in- and through- plane, which is mandatory to visualize small calliper vessels. In both "time of flight" and "phase contrast" MR angiographic techniques, volumetric sequences are of great importance (Mills et al. 1984; Dumoulin et al. 1989). The 3D FT sequence comparing the 2D technique is able to visualize smaller vessels as long as the blood velocity is relatively high. Therefore, 3D FT is ideal for the demonstration of small intracranial arteries and the depiction of the circle of Willis (Fig. 2.1). On the other hand, 3D PCA, although time-consuming, can offer clear visualization of the entire head vasculature in three dimensions by combining it with maximum intensity projection (MIP) algorithms. However, the applications of volumetric techniques are limited only in areas without physiologic motion present since they are more sensitive than 2D techniques to motion-related blurring. During the 1990s significant technological improvements in gradient technology were responsible for the development of contrast-enhanced MR angiography (CE MRA). The most common sequence incorporated in CE MRA protocols is the spoiled gradient echo (FLASH) in volumetric acquisition mode (Hany et al. 1998). The selection of the latter sequence is based on its ability to provide heavily T1-weighted images with thin slices (< 1 mm) in less than 20 seconds covering a relatively large volume of tissues. The inherent high signal-to-noise ratio of volumetric techniques can be exploited in order to increase spatial resolution to get closer to that of competitive angiographic techniques. The combination of 3D spoiled gradient echo sequences with a bolus intravenous injection of paramagnetic gadolinium compounds can result in adequate contrast between the vessels presenting with high signal intensity and the rest of the tissues presenting with low signal intensity due to saturation effects (Prince et al. 1995; Krinsky et al. 1999) (Fig. 2.2).

Morphological imaging of the brain is also based on such 3D-spoiled gradient echo sequences that may

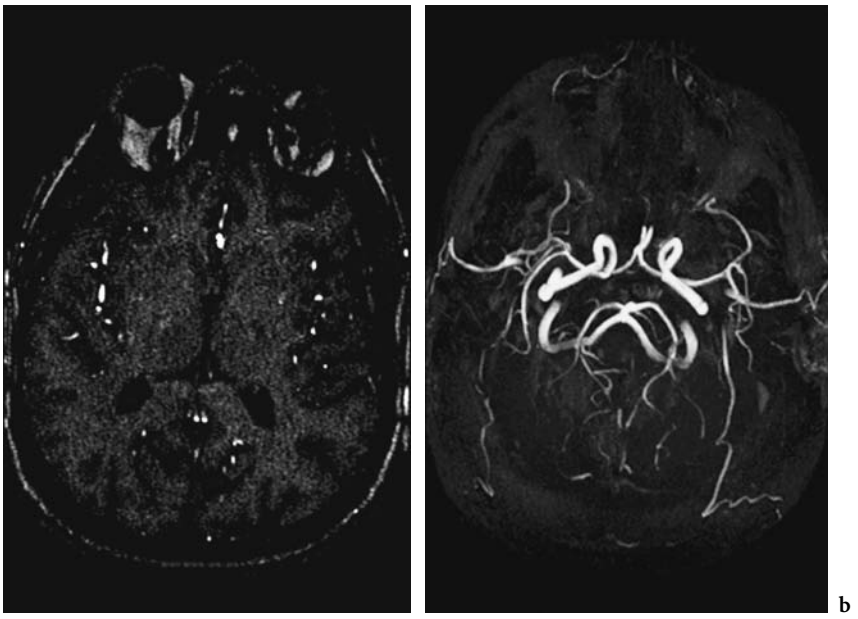

Fig. 2.1. a Axial source image of a 3D spoiled gradient echo sequence (FLASH). The combination of short repetition and echo time, as well as the flow compensation gradients applied, result in saturation effects of the tissues except for the blood moving inside the vessels, which appears bright due to the inflow effects. A complete volume of tissues can be acquired in order to generate 3D angiograms (**b**) by superimposing all the slices along any direction (MIP algorithm)

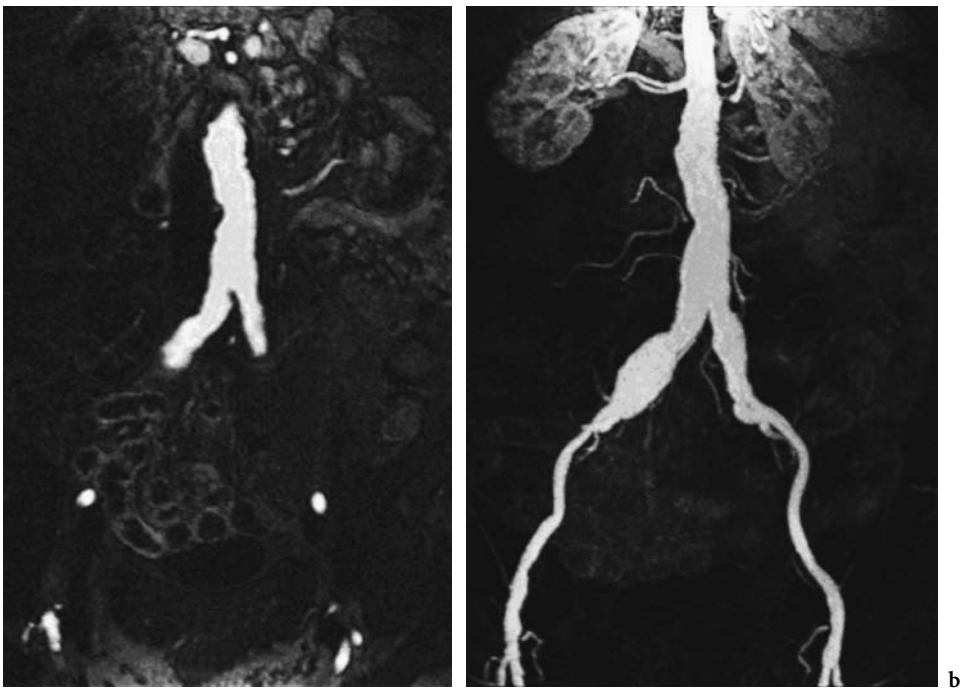

Fig. 2.2a,b. Gasolinium-enhanced magnetic resonance angiography of the abdomen. **a** Coronal source image of a 3D FLASH sequence with fat saturation prepulses acquired during the first pass of gadolinium. High contrast between the vessels containing gadolinium and the rest of nonvascular structures can be obtained, and 3D angiographic projections (**b**) are easily reconstructed by means of the MIP algorithm

offer superb contrast resolution and can be used to visualize the brain cortex (Runge et al. 1991). Voxel-based morphometry is a post-processing technique that involves a voxel-wise comparison of the local concentration of gray matter between two groups of subjects (Ashburner and Friston 2000). Volumetric T1-weighted gradient echo sequences are used to provide thin contiguous slices on which gray and white matter contrast is high enough to discriminate and segment these tissues (Fig. 2.3). This technique is a landmark method in modern neuroimaging studies of patients with dementia (Xie et al. 2006), amyotrophic lateral sclerosis (Kassubek et al. 2005), psychiatric disorders (Lochhead et al, 2004; Kubicki et al. 2002), epilepsy (Betting et al. 2006) and multiple sclerosis (Prinster et al. 2006).

In their initial implementation, the imaging protocols of MR mammography were based on 2D gradient echo sequences, but nowadays volumetric T1-weighted gradient echo sequences have replaced 2D techniques in state of the art MRI scanners. Again, volumetric acquisitions improve spatial resolution and smaller lesions are more clearly seen (Nakahara et al, 2001; Muller-Schimpfle et al. 1997). However, in the presence of gross motion, 2D techniques may be better, although recent advances in the field of in-line motion correction techniques may prove helpful to overcome motion artifacts in volumetric sequences. According to the MR mammography protocols, a volumetric T1-weighted gradient echo sequence is applied before and several times after a bolus intravenous injection of gadolinium in order to study the time-intensity enhancement curves of a potential lesion (Fig. 2.4).

One of the most popular pulse sequences, especially in abdominal imaging today, is the VIBE (volumetric interpolated breath hold examination) (Rofsky et al. 1999; Kim et al, 2001). This sequence is basically a FLASH sequence with 3D FT imaging, interpolation along the slice selection direction and fat saturation prepulses. With this sequence it is possible to acquire nearly isotropic resolution (on the order of 2 mm voxel size) in a breath-hold duration of less than 20 seconds. The combination of bolus contrast administration and the acquisition of a VIBE sequence given multiple times during injection have proved clinically useful. Characteristic enhancement patterns may be helpful in the characterization of various focal hepatic lesions. Most of the time these enhancement patterns are evaluated during arterial, portal and delayed phases. In addition, the contiguous thin slices offered by the VIBE sequence may increase sensitivity to the detection of small hepatic metastatic lesions (Fig. 2.5). Moreover, the VIBE sequence provides the possibility of evaluating the vasculature of a lesion since the MIP algorithm may be applied and angiographic projections can be generated.

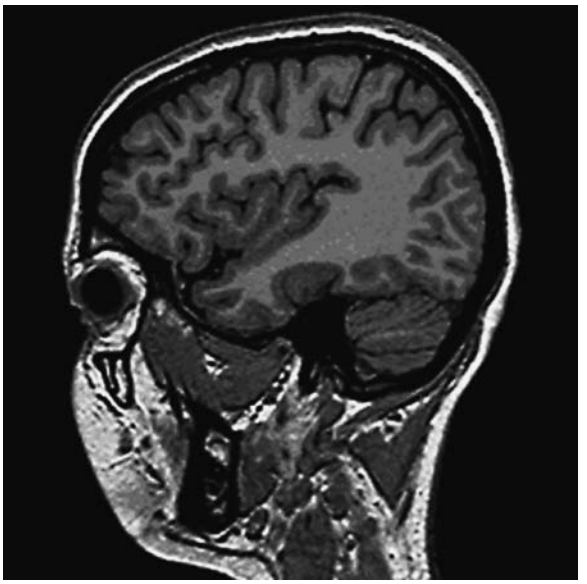

Fig. 2.3. Sagittal 3D spoiled gradient echo image offers superb contrast resolution to differentiate gray and white matter in combination with thin slices (less than 1 mm)

In small and large intestine MRI studies, volumetric T1-weighted FLASH sequences with fat saturation, in combination with oral or rectal administration of a paramagnetic solution (Fig. 2.6), provide high resolution images of the bowel lumen, which are appropriate for generation of virtual endoscopic views, by applying volume rendering algorithms (Papanikolaou et al. 2002). The acquisition of thin slices with high contrast-to-noise ratios between the bowel lumen and the surrounding tissues facilitates the segmentation process during virtual endoscopy post-processing and results in high quality virtual endoscopic views. When combining volumetric T1-weighted FLASH with a negative endoluminal contrast agent, such as an iso-osmotic water solution and intravenous administration of gadolinium, different enhancement patterns of involved segments with mural thickening can be demonstrated (Fig. 2.7). The previous technique leads to a “double contrast” type of appearance, rendering the intestinal lumen with low signal intensity and the intestinal wall with moderate to high signal intensity depending on the degree of contrast uptake (Gourtsoyiannis et al.

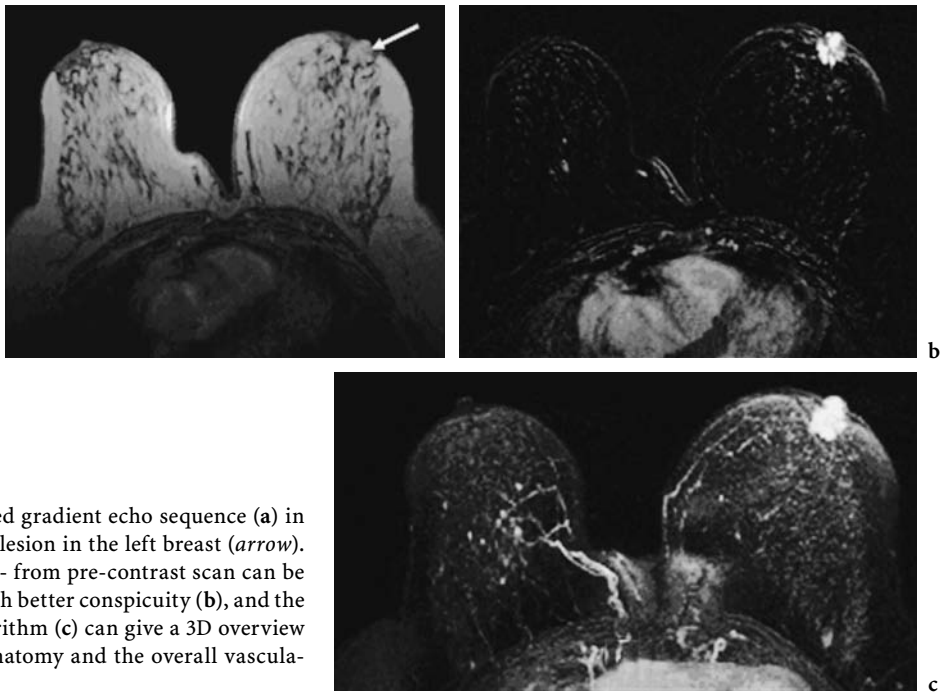

Fig. 2.4a–c. Axial 3D spoiled gradient echo sequence (**a**) in a patient with a malignant lesion in the left breast (*arrow*). The subtraction of the post- from pre-contrast scan can be used to detect the lesion with better conspicuity (**b**), and the application of an MIP algorithm (**c**) can give a 3D overview of the lesion, the nearby anatomy and the overall vasculature of both breasts

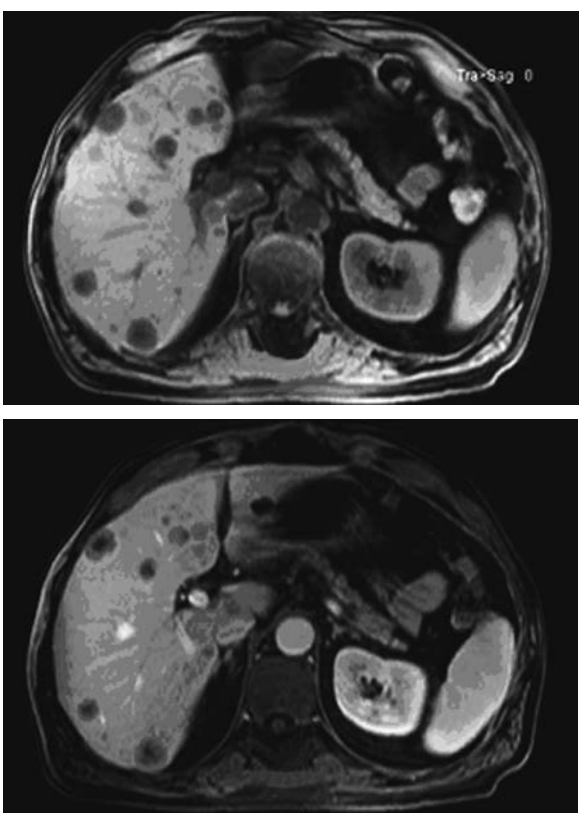

Fig. 2.5a,b. Axial VIBE images in a patient with colon carcinoma before (**a**) and after (**b**) the intravenous administration of gadolinium. Multiple metastatic lesions are recognized and characterized in the VIBE images

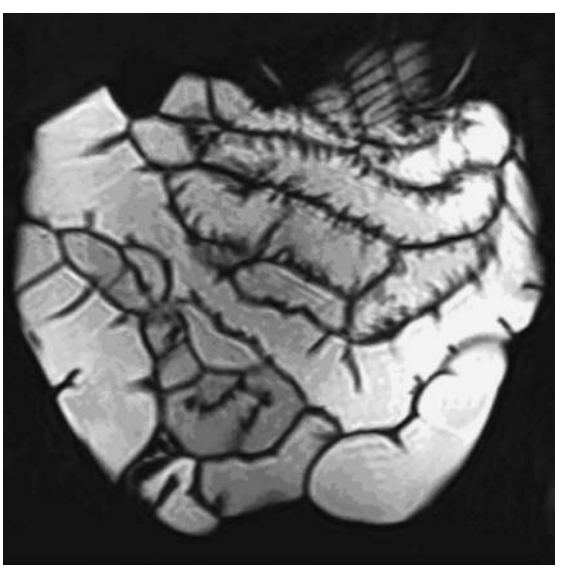

Fig. 2.6. Coronal 3D spoiled gradient echo with fat saturation image obtained after the administration of a gadolinium-spiked water solution (1:100 proportion). The presence of gadolinium as an intraluminal contrast agent results in bright luminal appearance of both small and large bowel

Fig. 2.7. Coronal VIBE sequence acquired 75 seconds after intravenous administration of gadolinium in a patient with Crohn's disease. Small bowel lumen was distended by means of an iso-osmotic water solution that resulted in low signal intensity of the lumen, while a multi-layered type of mural enhancement can be seen in involved loops (*arrow*), which is indicative of submucosal edema (*white arrow*)

2001; Gourtsoyiannis et al. 2004). This method can be used to detect colonic polyps and differentiate them from residual stool. Polyps present with variable degrees of enhancement, while residual stool do not exhibit any enhancement at all (Papanikolaou et al. 2003; Lauenstein et al. 2001).

Musculoskeletal applications of the VIBE sequence include the arthrographic evaluation of joints like the knee, wrist, ankle, hips and shoulder. Direct arthrography techniques utilize intra-articular injection of diluted gadolinium that can be nicely visualized and which reveal tears or other lesions in VIBE images (Nishii et al. 2005).

In case an inversion prepulse is added onto a volumetric FLASH sequence, the resulting sequence is called MP-RAGE (magnetization prepared rapid gradient echo. The MP-RAGE uses a 180° inversion pulse followed by a certain time delay (TI) to generate T1 contrast in the same manner as an inversion recovery (IR) sequence (Mugler and Brookeman 1991). As the longitudinal magnetization component evolves, the signal is acquired by a spoiled gradient echo sequence with a low flip angle and as short a repetition time as possible. Another variant of the MP-RAGE sequence involves water excitation. The

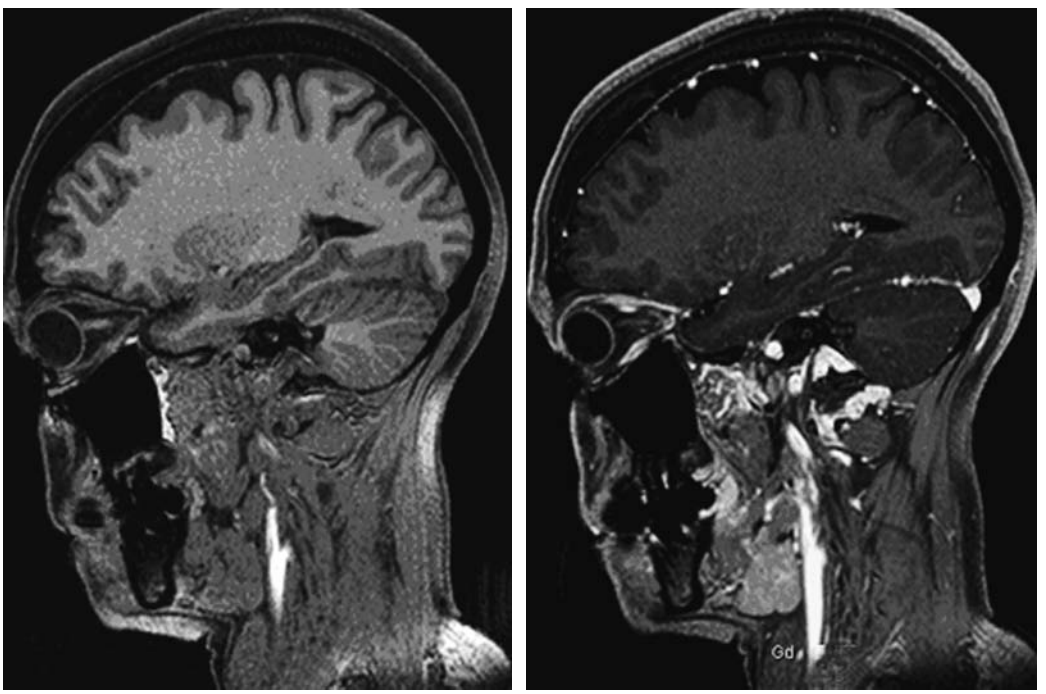

Fig. 2.8a,b. Sagittal MP-RAGE image with water excitation prepulses acquired before (**a**) and after (**b**) gadolinium injection. Homogeneous saturation of the orbital fat can be achieved, making this technique ideal for detecting small enhancing foci in the optical nerve

inversion and excitation pulses are frequency selective only for water protons; therefore the fat signal is destroyed. This sequence is a nice alternative to conventional 2D FT sequences for post-gadolinium evaluation, especially of small anatomic structures like the optical nerves (Fig. 2.8).

MP-RAGE is able to provide isotropic 1 mm resolution. The sequence exhibits strong T1-weighting and is routinely utilized in clinical protocols for visualising cranial nerves before and after gadolinium injection, for imaging with very thin slices the pituitary gland, and for detecting congenital brain abnormalities. Perhaps the most important clinical application of the MP-RAGE sequence is in patients with possible temporal medial sclerosis where, due to its high contrast resolution, MP-RAGE is of great help in making such a diagnosis. Due to its isotropic resolution capabilities, it is possible to generate high quality reformats in virtually any plane (Fig. 2.9).

2.2.2 Volumetric T2- and Mixed-Weighted Sequences

Steady-state coherent gradient echo techniques offer substantial advantages over spoiled gradient echo techniques for both SNR and contrast in tissues with long T2, such as CSF. As mentioned above, in case the steady state transverse magnetization component is maintained, there are coherent steady state sequences such as FISP, GRASS (Spritzer et al. 1988) and FFE (van der Meulen et al. 1988). According to these sequences, the development of residual transverse magnetization is due to rephasing the part of magnetization that has been dephased by the application of spatial encoding gradients. Since rephasing takes place in all three directions, the sequence is called true FISP (Oppelt et al. 1986) or balanced FFE. Although true FISP sequencing was invented at the late 1980s, only after the devel-

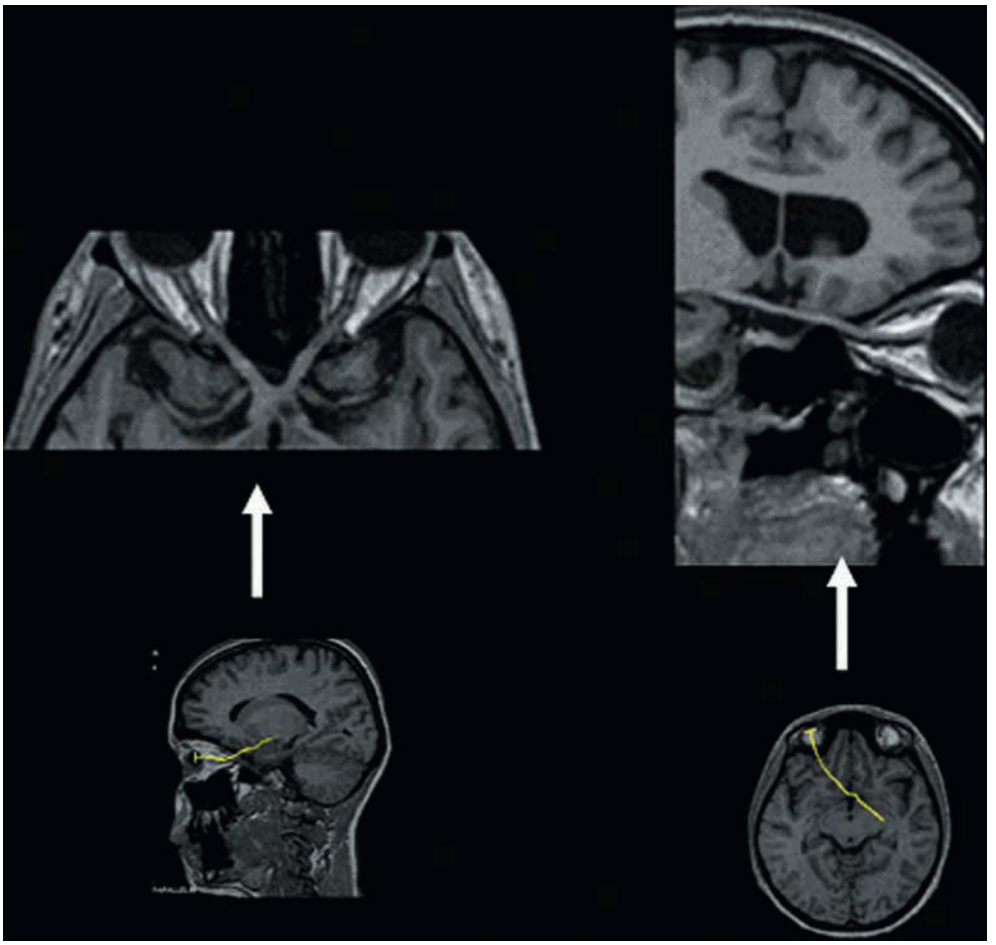

Fig. 2.9. Curved multi-planar reformats of the optical nerve and the chiasm obtained with an MP-RAGE sequence

opment of high performance gradient systems that offered short repetition times did the image quality become clinically acceptable. True FISP imaging uses balanced gradients in section-, read-, and phase-encoding directions, which, when combined with a short repetition time, assumes several desirable properties for imaging the heart and blood pool. True FISP sequencing is a mixed sequence in terms of contrast due to the fact that the steady-state signal is related to the ratio of T2 to T1; thus tissues with free moving protons such as fluids present with high signal intensity, whereas more solid tissues present with moderate to low signal intensity due to the lower T2 over T1 ratio they exhibit (Gourtsoyiannis et al. 2000). One of the most recent applications of true FISP sequence in 3D acquisition mode is in cardiac imaging. More specifically, high quality MR images of the coronary arteries can be obtained with this volumetric true FISP sequence with fat saturation and T2 preparation pulses. When using a true FISP pulse sequence for coronary artery imaging, the data have to be acquired in signal transience to steady-state to preserve the effectiveness of the fat saturation pulse. Therefore, due to the requirement of ECG-triggering, the signal has a relatively strong proton density weighting as opposed to the T2 and T1 weighting found in typical steady-state true FISP imaging. This reduces the blood-myocardial contrast. As the coronary arteries are in close proximity to fat and myocardial tissue, a higher blood background contrast is desirable to improve delineation of the vessels. For best contrast in coronary artery imaging, T2 preparation has been added to an ECG-triggered, navigator-gated, fatsat true FISP 3D pulse sequence (Deshpande et al. 2001). The basic pulse sequence structure is a segmented 3D approach with 'n' phase-encoded lines acquired per heartbeat. The partition gradient is incremented after 'm' heartbeats. Since true FISP sequencing is sensitive to magnetic field inhomogeneities and susceptibility artifacts it is mandatory to utilize short repetition times to minimize such negative effects.

Constructive interference steady state (CISS) is a strongly T2-weighted gradient echo sequence (Casselman et al. 1993). It consists of a pair of true FISP sequences acquired with differing regimes of alternating the phase of the excitation pulses. Individually these true FISP sequences display very strong T2 weighting, but are affected by dark phase dispersion bands caused by patient-induced local field inhomogeneities and made prominent by the relatively long TR used. The different excitation pulse regimes offset these bands in the two sequences. Combining the images results in a picture free of banding. The image combination is performed automatically after data collection, adding some time to the reconstruction process.

The overwhelming power of the 3D CISS sequence is its combination of high signal levels and extremely high spatial resolution (Fig. 2.10). CISS images yield the best detail available of the cisternal portions of cranial nerves. The sequence has inherent flow

a

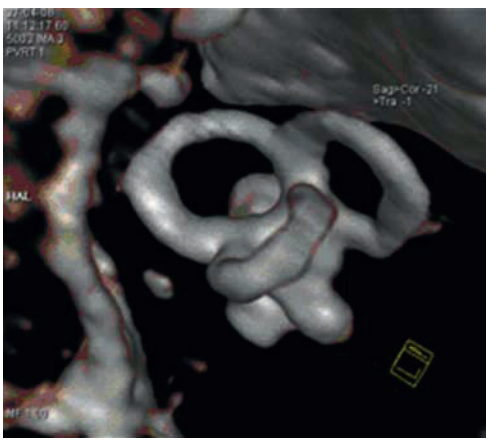

b

Fig. 2.10a,b. Axial 3D CISS image (**a**) demonstrating high contrast between the CSF and acoustic nerves. Due to the sub-millimeter isotropic resolution (0.7 mm) that CISS can provide it is possible to generate 3D representations of the cochlea (**b**) by applying volume-rendering algorithms

compensation because of its perfectly balanced gradients. Compared to conventional FISP or GRASS it is quite insensitive to CSF pulsations. True FISP and CISS sequences require a very high level of control over gradient switching and shaping. CISS requires very high local field homogeneity, so an excellent magnet homogeneity is required, and all sequences must be preceded with a patient-specific shim adjustment. Metal in the field will degrade the images substantially, so patient preparation should include the removal of all head and neck jewellery, as well as metal from clothing. CISS is available in 2D FT and 3D FT implementations.

Gradient echo-based sequences, such as constructive interference in steady state sequences, also are used for the imaging of the inner ear region (Casselman et al. 1996; Held et al. 1997). However, the specific absorption rate of these sequences may be higher than that of 3D fast spin echo-based sequences, and susceptibility artifacts may be more pronounced, especially at 3 T scanners.

The DESS (double echo steady state) sequence collects both signals acquired in FISP and PSIF (FISP sequence reversed in time) sequences and combines them (Dufour et al, 1993). This increases the signal-to-noise ratio, and isotropic resolution is therefore feasible with reasonable acquisition times. Phase rewinding takes place along the phase-encoding direction to maintain the transverse steady state magnetization. The frequency-encoding gradient is left on for the period of both echoes, and is incompletely balanced to avoid dark banding artifacts otherwise associated with long TR fully balanced steady state sequences.

The contrast of DESS is quite unique. There is a strong fluid signal, but fat is bright and other soft tissues appear similar to the short TR FISP image. The PSIF echo is very sensitive to motion but this is not a major problem in orthopedic applications (Hardy et al. 1996).

2.2.3 Volumetric T2-Weighted Sequences

Typically, 3D FT volume studies have been conducted with gradient echo sequences that could offer short acquisition time due to their short repetition time. Currently, 3D fast or turbo spin echo sequences can be applied clinically, and they offer pure T2-weighted volumetric images without susceptibility artifacts. Although fast or turbo spin echo sequences utilize a relatively long repetition time, their capability to acquire more than one k-space line during a repetition time interval makes them clinically acceptable, with scanning time less than 10 min. However, these sequences are not free of limitations that are mainly related to increased RF deposition and non-uniformity across the slice selection direction. As a result, 3D reformations generally are contaminated by artifacts at the junctions between slabs. In addition, because of slab profile effects, some of the outer sections in each slab typically are discarded, thus decreasing the efficiency. Power deposition is relatively high and may compromise the coverage attained per unit time, particularly at high field strengths such as 3 T. Each slab undergoes unwanted off-resonance magnetization-transfer effects from the large number of refocusing RF pulses applied to the other slabs during the acquisition (Oshio et al. 1991).

One application that has significantly benefit from the development of 3D TSE sequences is MR cholangiopancreatography (Chrysikopoulos et al. 1997; Papanikolaou et al. 1999; Textor et al. 2002). This can be explained in the basis of the superb T2 contrast that these sequences can offer. Usually in MR cholangiopancreatography the biliary and pancreatic ducts are presented as high signal intensity structures due to the presence of fluid, where all the other more solid types of tissues exhibit low signal intensity (Fig. 2.11). This happens because a relatively long echo time value to acquire heavily T2-weighted images was selected. Body fluids are described by long T2 relaxation times, as opposed to more solid tissues that express by moderate or short T2 relaxation times. In heavily T2-weighted images, solid tissue signals are attenuated significantly more than body fluids due to T2 relaxation effects. Special prepulses have been proposed to make this sequence more efficient in terms of acquisition time. One of these prepulses is the “restore” or “driven to equilibrium” pulse that is a -90° RF pulse that forces magnetization to come back to the longitudinal axis earlier (Lichy et al. 2005). In this way the repetition time could be significantly reduced while maintaining the same image contrast. The reduction of repetition time has a direct impact on acquisition time. Another way to speed up the sequence is to increase the number of refocusing RF pulses. Depending on the hardware capabilities, a relative increase in echo time will be forced to accommodate all the extra RF pulses. There is always a balance between the RF pulses.and the optimal echo time, so as to achieve fluid-weighted images in short acquisition times.

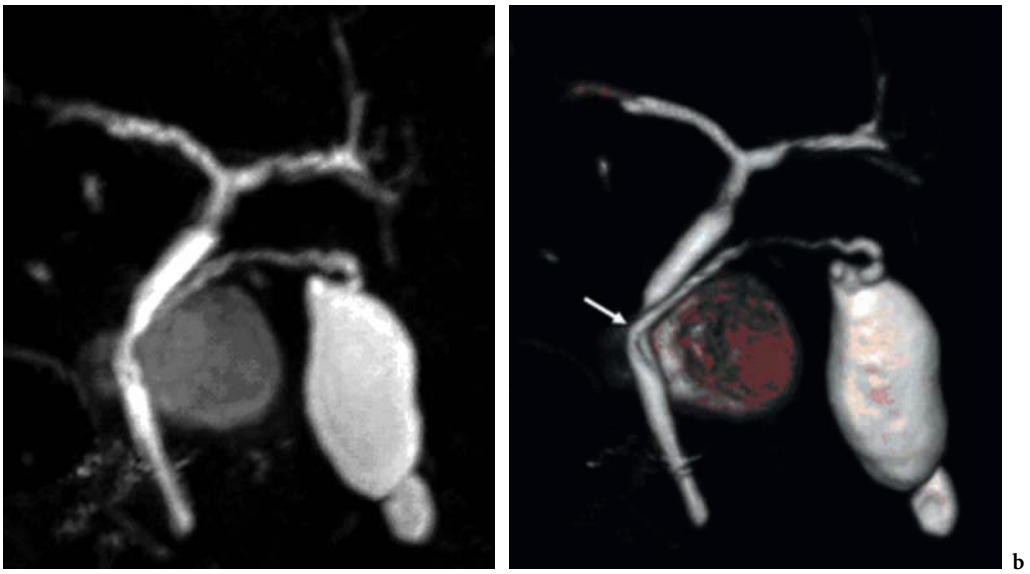

Fig. 2.11a,b. Oblique coronal MRCP MIP projection (**a**) and volume rendering view (**b**) based on a 3D turbo spin echo sequence, which was acquired with respiratory triggering to minimize respiratory-related motion artifacts. Note the superiority of the volume rendering view in revealing a low insertion point of the cystic duct (*arrow*)

2.3 Conclusion

3D imaging and visualization algorithms are emerging as the method of choice in many clinical examinations, replacing previously routine procedures and significantly complementing others. The continuing evolution of 3D imaging promises even greater capabilities for accurate noninvasive clinical diagnosis and treatment, as well as for quantitative biological investigations and scientific exploration.

References

Alley MT, Shifrin RY, Pelc NJ, Herfkens RJ (1998) Ultrafast contrast-enhanced three-dimensional MR angiography: state of the art. RadioGraphics 18:273–285

Ashburner J, Friston KJ (2000) Voxel-based morphometry–the methods. Neuroimage 11:805–821

Betting LE, Mory SB, Li LM, Lopes-Cendes I, Guerreiro MM, Guerreiro CA, Cendes F (2006) Voxel-based morphometry in patients with idiopathic generalized epilepsies. Neuroimage 15:498–502

Casselman JW, Kuhweide R, Ampe W, D'Hont G, Offeciers EF, Faes WK, Pattyn G (1996) Inner ear malformations in patients with sensorineural hearing loss: detection with gradient-echo (3DFT-CISS) MRI. Neuroradiology 38:278–286

Casselman JW, Kuhweide R, Deimling M, Ampe W, Dehaene I, Meeus L (1993) Constructive interference in steady state-3DFT MR imaging of the inner ear and cerebellopontine angle. AJNR 14:47–57

Chrysikopoulos H, Papanikolaou N, Pappas J, Roussakis A, Andreou J (1997) MR cholangiopancreatography at 0.5 T with a 3D inversion recovery turbo-spin-echo sequence. Eur Radiol 7:1318–1322

Deshpande VS, Shea SM, Laub G, Simonetti OP, Finn JP, Li D (2001) 3D magnetization-prepared true-FISP: a new technique for imaging coronary arteries. Magn Reson Med 46:494–502

Dufour I, Bittoun J, Idy-Peretti I, Jolivet O, Darrasse L, Di Paola R (1993) Implementation and optimization by the simplex method of a 3D double echo sequence in steady-state free precession. Magn Reson Imaging 11:87–93

Dumoulin CL, Souza SP, Walker MF, Wagle W (1989) Three-dimensional phase contrast angiography. Magn Reson Med 9:139–149

Frahm J, Haase A, Matthaei D (1986) Rapid NMR imaging of dynamic processes using the FLASH technique. Magn Reson Med 3:321–327

Frahm J, Hanicke W, Merboldt KD (1987) Transverse coherence in rapid FLASH NMR imaging. J Magn Reson 72:307–314

Gourtsoyiannis N, Papanikolaou N, Grammatikakis J, Maris T, Prassopoulos P (2001) MR enteroclysis protocol optimization: comparison between 3D FLASH with fat saturation after intravenous gadolinium injection and true FISP sequences. Eur Radiol 11:908–913

Gourtsoyiannis N, Papanikolaou N, Grammatikakis J, Maris T, Prassopoulos P (2000) MR imaging of the small

bowel with a true-FISP sequence after enteroclysis with water solution. Invest Radiol 35:707–711
Gourtsoyiannis N, Papanikolaou N, Grammatikakis J, Papamastorakis G, Prassopoulos P, Roussomoustakaki M (2004) Assessment of Crohn's disease activity in the small bowel with MR and conventional enteroclysis: preliminary results. Eur Radiol 14:1017–1024
Hany TF, Leung DA, Pfammatter T, Debatin JF (1998) Contrast-enhanced magnetic resonance angiography of the renal arteries: original investigation. Invest Radiol 33:653–659
Hardy PA, Recht MP, Piraino D, Thomasson D (1996) Optimization of a dual echo in the steady state (DESS) free-precession sequence for imaging cartilage. J Magn Reson Imaging 6:329–335
Held P, Fellner C, Fellner F, Seitz J, Strutz J (1997) MRI of inner ear anatomy using 3D MP-RAGE and 3D CISS sequences. Br J Radiol 70:465–472
Hennig J, Nauerth A, Friedburg H (1986) RARE imaging: a fast imaging method for clinical MR. Magn Reson Med 3:823–833
Hennig J (1988) Multiecho imaging sequences with low refocusing flip angles. Magn Reson Med 78:397–407
Kassubek J, Unrath A, Huppertz HJ, Lule D, Ethofer T, Sperfeld AD, Ludolph AC (2005) Global brain atrophy and corticospinal tract alterations in ALS, as investigatedby voxel-based morphometry of 3-D MRI. Amyotroph Lateral Scler Other Motor Neuron Disord 6:213–220
Kim MJ, Mitchell DG, Ito K et al (2001) Hepatic MR imaging: comparison of 2D and 3D gradient echo techniques. Abdom Imaging 26:269–276
Krinsky GA, Reuss PM, Lee VS, Carbognin G, Rofsky NM (1999) Thoracic aorta: comparison of single-dose breath-hold and double-dose non-breath-hold gadolinium-enhanced three-dimensional MR angiography. AJR (Am J Roentgenol) 173:145–150
Kubicki M, Shenton ME, Salisbury DF, Hirayasu Y, Kasai K, Kikinis R, Jolesz FA, McCarley RW (2002) Voxel-based morphometric analysis of gray matter in first episode schizophrenia. Neuroimage 17:1711–1719
Lauenstein TC, Herborn CU, Vogt FM, Gohde SC, Debatin JF, Ruehm SG (2001) Dark lumen MR-colonography: initial experience. Rofo 173:785–789
Lichy MP, Wietek BM, Mugler JP 3rd, Horger W, Menzel MI, Anastasiadis A, Siegmann K, Niemeyer T, Konigsrainer A, Kiefer B, Schick F, Claussen CD, Schlemmer HP (2005) Magnetic resonance imaging of the body trunk using a single-slab, 3-dimensional, T2-weighted turbo-spin-echo sequence with high sampling efficiency (SPACE) for high spatial resolution imaging: initial clinical experiences. Invest Radiol 40:754–760
Lochhead RA, Parsey RV, Oquendo MA, Mann JJ (2004) Regional brain gray matter volume differences in patients with bipolar disorder as assessed by optimized voxel-based morphometry. Biol Psychiatry 15:1154–1162
Mills CM, Brant-Zawadski M, Crooks LE et al (1984) Nuclear magnetic resonance – Principles of blood flow imaging. AJR (Am J Roentgenol) 142:165–170
Mugler JP 3rd, Brookeman JR (1991) Rapid three-dimensional T1-weighted MR imaging with the MP-RAGE sequence. J Magn Reson Imaging 1:561–567
Muller-Schimpfle M, Ohmenhauser K, Sand J, Stoll P, Claussen CD (1997) Dynamic 3D-MR mammography: is there a benefit of sophisticated evaluation of enhancement curves for clinical routine? J Magn Reson Imaging 7:236–240
Nakahara H, Namba K, Fukami A, Watanabe R, Maeda Y, Furusawa H, Matsu T, Akiyama F, Nakagawa H, Ifuku H, Nakahara M, Tamura S (2001) Three-dimensional MR imaging of mammographically detected suspicious microcalcifications. Breast Cancer 8:116–124
Nishii T, Tanaka H, Nakanishi K, Sugano N, Miki H, Yoshikawa H (2005) Fat-suppressed 3D spoiled gradient-echo MRI and MDCT arthrography of articular cartilage in patients with hip dysplasia. AJR (Am J Roentgenol) 185:379–385
Oppelt A, Graumann R, Barfuss H, Fischer H, Hertl W, Schajor W (1986) A new fast MRI sequence. Electromed 3:15–18
Oshio K, Jolesz FA, Melki PS, Mulkern RV (1991) T2-weighted thin-section imaging with the multislab three-dimensional RARE technique. J Magn Reson Imaging 1:695–700
Papanikolaou N, Grammatikakis J, Maris T, Lauenstein T, Prassopoulos P,Gourtsoyiannis N (2003) MR colonography with fecal tagging: comparison between 2D turbo FLASH and 3D FLASH sequences. Eur Radiol 13:448–452
Papanikolaou N, Karantanas AH, Heracleous E, Costa JC, Gourtsoyiannis N (1999) Magnetic resonance cholangiopancreatography: comparison between respiratory-triggered turbo spin echo and breath hold single-shot turbo spin echo sequences. Magn Reson Imaging 17:1255–1260
Papanikolaou N, Prassopoulos P, Grammatikakis J, Maris T, Kouroumalis E, Gourtsoyiannis N (2002) Optimization of a contrast medium suitable for conventional enteroclysis, MR enteroclysis, and virtual MR enteroscopy. Abdom Imaging 27:517–522
Prince MR, Narasimham DL, Stanley JC, Chenevert TL, Williams DM, Marx MV, Cho KJ (1995) Breath-hold gadolinium-enhanced MR angiography of the abdominal aorta and its major branches. Radiology 197:785–792
Prinster A, Quarantelli M, Orefice G, Lanzillo R, Brunetti A, Mollica C, Salvatore E, Morra VB, Coppola G, Vacca G, Alfano B, Salvatore M (2006) Grey matter loss in relapsing-remitting multiple sclerosis: a voxel-based morphometry study. Neuroimage 29:859–867
Pykett IL, Newhouse JH, Buonanno FS et al (1982) Principles of nuclear magnetic resonance imaging. Radiology 143:157–168
Robb RA (1994) Three-Dimensional Biomedical Imaging – Principles and Practice. New York: VCH. 282 pp
Rofsky NM, Lee VS, Laub G et al (1999) Abdominal MR imaging with a volumetric interpolated breath-hold examination. Radiology 212:876–884
Runge VM, Kirsch JE, Thomas GS, Mugler JP 3rd (1991) Clinical comparison of three-dimensional MP-RAGE and FLASH techniques for MR imaging of the head. J Magn Reson Imaging 1:493–500
Spritzer CE, Vogler JB, Martinez S, Garrett WE Jr, Johnson GA, McNamara MJ,Lohnes J, Herfkens RJ (1988) MR imaging of the knee: preliminary results with a 3DFT GRASS pulse sequence. AJR (Am J Roentgenol) 150:597–603

Textor HJ, Flacke S, Pauleit D, Keller E, Neubrand M, Terjung B, Gieseke J, Scheurlen C, Sauerbruch T, Schild HH (2002) Three-dimensional magnetic resonance cholangiopancreatography with respiratory triggering in the diagnosis of primary sclerosing cholangitis: comparison with endoscopic retrograde cholangiography. Endoscopy 34:984–990

Tkach J, Haacke E (1988) A comparison of fast spin echo and gradient field echo sequences. Magn Reson Imaging 6:373–389

van der Meulen P, Groen JP, Tinus AM, Bruntink G (1988) Fast Field Echo imaging: an overview and contrast calculations. Magn Reson Imaging 6:355–368

Xie S, Xiao JX, Gong GL, Zang YF, Wang YH, Wu HK, Jiang XX (2006) Voxel-based detection of white matter abnormalities in mild Alzheimer disease.Neurology 66:1845–1849

Zur Y, Wood ML, Neuringer LJ (1990) Spoiling of transverse coherences without spoiler gradients. Presented at Society of Magnetic Resonance in Medicine. New York; 1990

Zur Y, Wood ML, Neuringer LJ (1988) Spoiling of transverse magnetization in steady-state sequences. Magn Reson Med 21:251–263

MDCT Image Acquisition to Enable Optimal 3D Data Evaluation

3

Michael Macari

CONTENTS

3.1 Introduction

When considering an abdominal multi-detector-row CT (MDCT) protocol to enable optimal diagnostic capability, there are several important factors that need to be considered. Most importantly, what is the clinical indication for the study? This will enable the radiologist to tailor the CT protocol appropriately to obtain the diagnostic information requested. Appropriate tailoring of the protocol requires consideration of:

- The kind of oral contrast that should be administered (none, neutral, or positive) and over what period of time.
- What kind of IV contrast should be administered and at what rate?
- What slice collimation and dose that should be employed to enable a confident diagnosis to be made at axial imaging and how that data can be utilized for 3D rendering?

This chapter will review those aspects of the abdominal examination that will enable optimal acquisition of CT data to facilitate both axial and 3D data interpretation.

M. Macari, MD
Associate Professor, Department of Radiology, Section Chief, Abdominal Imaging, New York University School of Medicine, Tisch Hospital, 560 First Avenue, Suite HW 202, New York, NY 10016, USA

3.2 MDCT: Recent History

Until the late 1990s, helical single slice CT scanners were the "state of the art" in terms of CT technology. These scanners allowed a single CT slice to be obtained with each gantry rotation. The exception to this was the dual slice CT scanner from Elscinct. Most scanners had a gantry rotation time of one second while others decreased the rotation time to 0.8 s. When scanning the abdomen and pelvis, thin slices meant 3–5 mm collimation with long breatholds of up to 30–45 s to obtain a complete data set. Obvious problems were loss of the IV contrast bolus as well as breathing and motion artifacts. With the introduction of MDCT technology in 1998, two important aspects of data acquisition changed. First, data could now be acquired faster and second, thinner sections (down to 1 mm) could be obtained.

The first MDCT scanners were four row scanners allowing four CT slices to be obtained in a single gantry rotation. The gantry rotation times decreased as well (to 0.5 s) and now it was possible to obtain CT data of the entire abdomen and pelvis with slices slightly greater then 1mm in a 30 second breathold (Macari et al. 2002a).

Now in 2006, 64 row CT scanners are being installed which allow 64 × 0.6 mm slices to be obtained in a single gantry rotation with gantry rotation times decreasing to 0.33 s. The progression of data acquisition can be depicted by displaying the

evolution of CT colonography from single slice to 64 slice CT technology (Fig. 3.1).

By allowing thin section CT data to be obtained, the radiologist no longer needs to rely on axial data but can now visualize the volume of CT data using a 3D rendering, MIP projection, or with thin section coronal, sagittal, or off axis multi-planar reformations (MPR) (Fig. 3.2) (Sahani et al. 2006). Moreover, the routine use of coronal reformatted images sent directly by the CT technologist to a PACS workstation is extremely helpful and can, in many instances, improve the diagnostic capabilities of the examination (Fig. 3.3) (Rastogi et al. 2006). Numerous recent presentations at the 2005 and 2006 annual meetings of the RSNA and ARRS have pointed out the benefits of sending coronal reformatted images as well, as axial images, to the PACS for data interpretation.

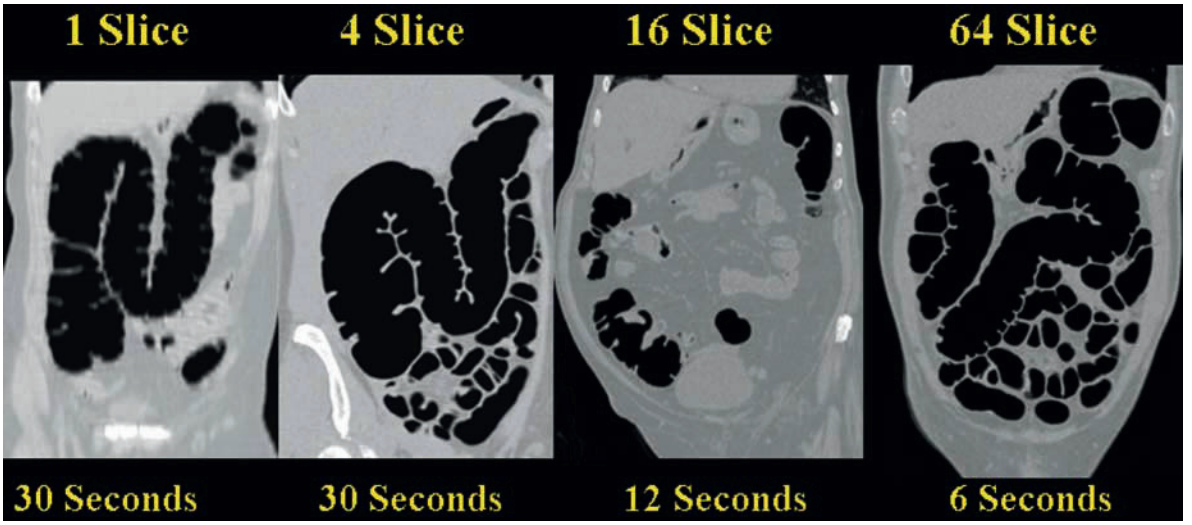

Fig. 3.1. Coronal CT images reconstructed from axial data. The single slice acquisition utilized 5 mm thick sections. The resulting Z-axis resolution is poor. The 4, 16 and 64 row scanners utilized 1.25, 1, and 0.75 mm thick axial sections respectively. Note improvement in time of acquisition

Fig. 3.2. Axial image (*left*) shows hypo-vascular pancreatic cancer (*arrow*) in continuity with peripancreatic artery (*arrowhead*). Volume rendered angiogram from same data set shows the vessel is a replaced common hepatic artery arising from the superior mesenteric artery (*arrow*)

a

b

Fig. 3.3a,b. Use of coronal reformatted images to aid in diagnosis. **a** Axial image shows edematous recently transplanted kidney (*arrow*). Renal vasculature was difficult to assess. **b** Coronal reformatted image shows renal artery (*arrow*) (*left*) and diminutive but patent renal vein (*arrow*) (*right*)

Coronal reformatted images should be reconstructed from the thinnest raw data available, generally every 1mm or less on CT scanners using 16 rows or greater, and made as 3 mm thick slices every 3 mm. We have found these to be extremely helpful for problem solving and sometimes for primary diagnosis. These routine coronal images generated generally mean another 60–90 images are sent to the PACS depending on the thickness of the patient. This does slow the workflow a little, but the advantage of having a permanent record of coronal slices, coronal presentation for the referring clinician, and improved diagnostic capabilities, outweigh the drawbacks of the extra images generated. At New York University we currently utilize 16, 40 and 64 row Siemens CT scanners. When considering a protocol to obtain CT data, one can think of all of these scanners as operating in one of two different modes. They can either acquire data with thick sections or thin sections. For example on the Siemens systems the two options are shown in Table 3.1.

The obvious advantage of scanning with the thinnest slice collimation possible is that the data can then be reconstructed using that slice thickness. Using a 40 or 64 row detector with the 0.6 mm detector configuration the typical CT voxel dimension is essentially isotropic in the X, Y and Z dimension. If one utilizes a thicker CT detector configuration to acquire data, a thinner slice can never be reconstructed.

Table 3.1. Siemens systems – the two options for acquiring data (with thick sections or thin sections)

CT scanner	Thick sections (mm)	Thin sections (mm)
16	16 × 1.5	16 × 0.75
40	24 × 1.2	40 × 0.6
64	24 × 1.2	64 × 0.6

However, there are two penalties to scanning with the thinnest slice collimation possible. The first is that it takes longer to cover the area. In general, this in not a problem when scanning the abdomen and pelvis given the high number of rows and fast gantry rotation times available. The second is of greater concern and is the increased radiation dose to the patient when scanning with the thinner detector configuration. In fact, for a similar amount of noise on a 64 row scanner using the 0.6 mm detector configuration when compared to the 1.2 mm detector configuration, there is approximately 14% and 21% increased absorbed dose to the male and female patient respectively (Figs. 3.4 and 3.5). When considering an imaging protocol to evaluate a clinical indication, one should always consider the possibility of a technique such as US or MR imaging which do not require ionizing radiation (Fig. 3.6).

The remainder of this chapter will focus on the current NYU protocols for acquiring CT data for 3D data interpretation for three specific indications in the abdomen and pelvis, CT enterography, pancreatic and upper abdominal pain evaluation, and in those patients with lower abdominal pain. At the end of the chapter I have attached a list of the common CT protocols that we use for various clinical indications in abdomen and pelvis.

The protocols show:

- The phase (timing) of data acquisition and whether we use the thin or thick detector configuration. Thin or thick detector configuration can be applied to any MDCT scanner.
- The type, rate, and timing of IV contrast administration.
- They type and amount of oral contrast used.
- The kind of axial and coronal data sets that are sent to the PACS.

It should be noted that, in all cases, thin section data is sent directly to a 3D workstation where the radiologist can perform dedicated angiography, volume rendering, colonography, and other interactive 3D processes that are required to facilitate the diagnosis.

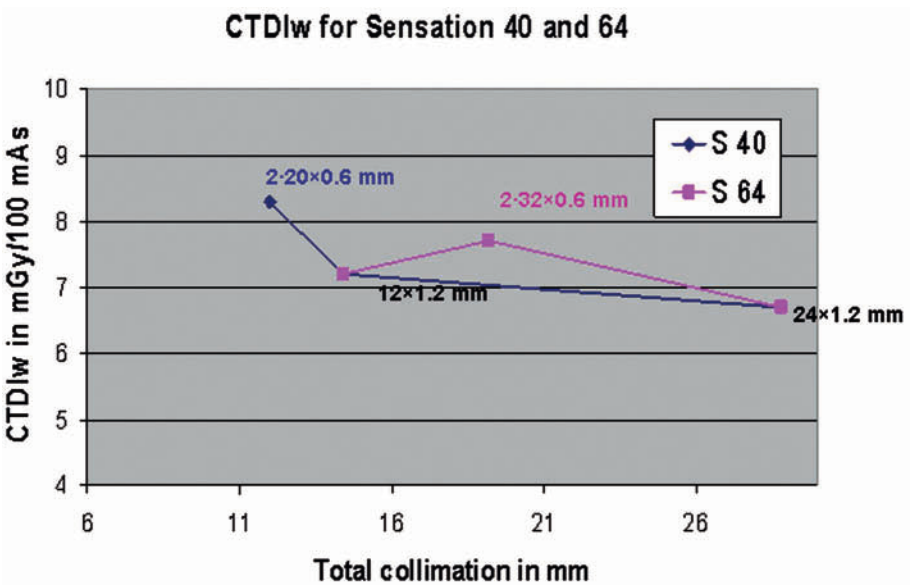

Fig. 3.4. Chart shows approximate CTDIw for given protocols using the 40 slice and 64 slice CT scanner. Image provided by Siemens Medical Solutions

Fig. 3.5. Coronal reformatted image from CT colonography data sets shows supine acquisition (*left*) and prone acquisition (*right*) in same patient. CTC data obtained in supine positions was obtained with 16 × 75 mm slices and the prone acquisition with 16 × 1.5 mm slices. Obviously there is better Z-axis resolution on the supine data set. The CTDI was 14% higher for the supine acquisition

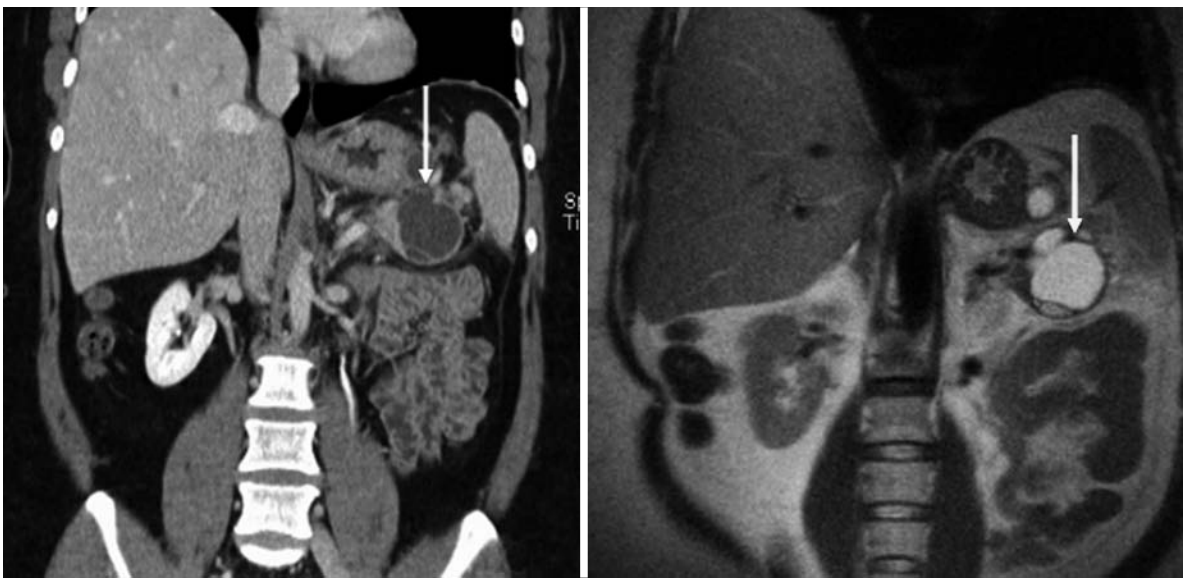

Fig. 3.6. Coronal reformatted image of endoscopically proven pseudocyst based on analysis of cyst fluid at aspiration. Coronal reformatted CT image (*left*) and coronal single shot fast spin echo MR image (*right*) shows pseudocyst (*arrow*) in the tail of the pancreas. Similar information is obtained without the use of radiation at MR imaging

3.3 CT Enterography

The application of CT to detect small bowel and gastric pathology has been with us a very long time. More recently, with the use of MDCT scanners, neutral oral contrast and IV contrast, coupled with 3D data evaluation, a technique known as CT enterography has emerged which may markedly improve our ability to evaluate the small bowel (Fig. 3.7). This technique may improve the ability of CT to detect various pathologies in the small bowel including the cause of obscure GI bleeding, inflammation, and neoplasms.

Confident detection and optimal evaluation of an abnormal segment or loop of small bowel is achieved when the small bowel is well distended, IV contrast has been administered, and thin section (≤1 mm) CT is utilized. Traditionally, positive contrast materials such as dilute barium or water soluble iodinated solutions have been used to mark and sometimes distend the small bowel at CT (Macari and Balthazar 2001; Maglinte 2005; Gourtsoyiannis et al. 2004; Bodily et al. 2006; Hara et al. 2005). These contrast agents work well in delineating the small bowel; the degree of distension being proportionate to the amount of contrast consumed, the rate at which it is consumed and the time delay of the examination itself. When the small bowel is distended with positive contrast, wall thickness ranges from imperceptible to no greater than 2 mm (Macari and Balthazar 2001). However, unless care is taken in administering these agents, any portion of the bowel may be either under-distended or even unfilled with contrast leading to possible false positive diagnosis. In general, adequate luminal distension is present if the diameter of the small bowel is ≥ 2 cm.

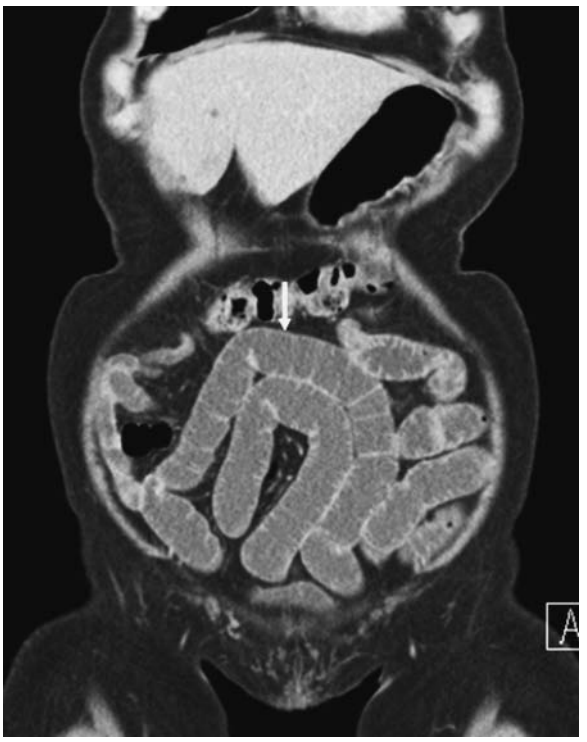

Fig. 3.7. CT Enterography. Coronal reformatted image from CT enterography data set performed after the use of VoLumen to distend the small bowel and IV contrast administration. Note excellent depiction of the wall of the small bowel (*arrow*)

When the small bowel is distended with positive contrast, the wall is thin, and may be imperceptible but should not measure more that 1–2 mm (Macari and Balthazar 2001). The use of dilute barium and iodinated positive oral contrast agents are particularly well suited in evaluating thin patients without a lot of intraperitoneal adipose tissues and in oncology patients where implants and lymph-nodes will stand out from the small bowel. A potential limitation of positive oral contrast agents in the evaluation of the small bowel is that mucosal enhancement may be obscured by the luminal contrast and thus the pattern of enhancement, which serves as a primary aid in the differential diagnosis of an abnormal stomach or small bowel segment, may be impaired (Fig. 3.8).

Neutral oral contrast agents allow full visualization of the normal intestinal wall thereby allowing analysis of the degree and pattern of small bowel enhancement (Hara et al. 2005; Megibow et al. 2006; Arslan et al. 2005; Raptopoulos et al. 1997; Boudiaf et al. 2004; Reitner et al. 2002; Wold et al. 2003; Paulsen et al. 2006). Neutral contrast refers to agents that have an attenuation value similar to water (10–30 H). For neutral contrast agents to be effective they need to be used with IV contrast and there needs to be optimal small bowel distension.

Several neutral contrast agents have been evaluated for small bowel distension including water, water in combination with a bulking agent such as methylcellulose or locust bean gum, polyethylene glycol solutions, and a commercially available low density barium solution (VoLumen, EZ-EM, Westbury, NY) (Hara et al. 2005; Megibow et al. 2006). A limitation of using water is that it is rapidly absorbed across the small intestinal mucosa resulting in suboptimal small bowel distension. VoLumen and polyethylene glycol solutions are less rapidly absorbed; studies have

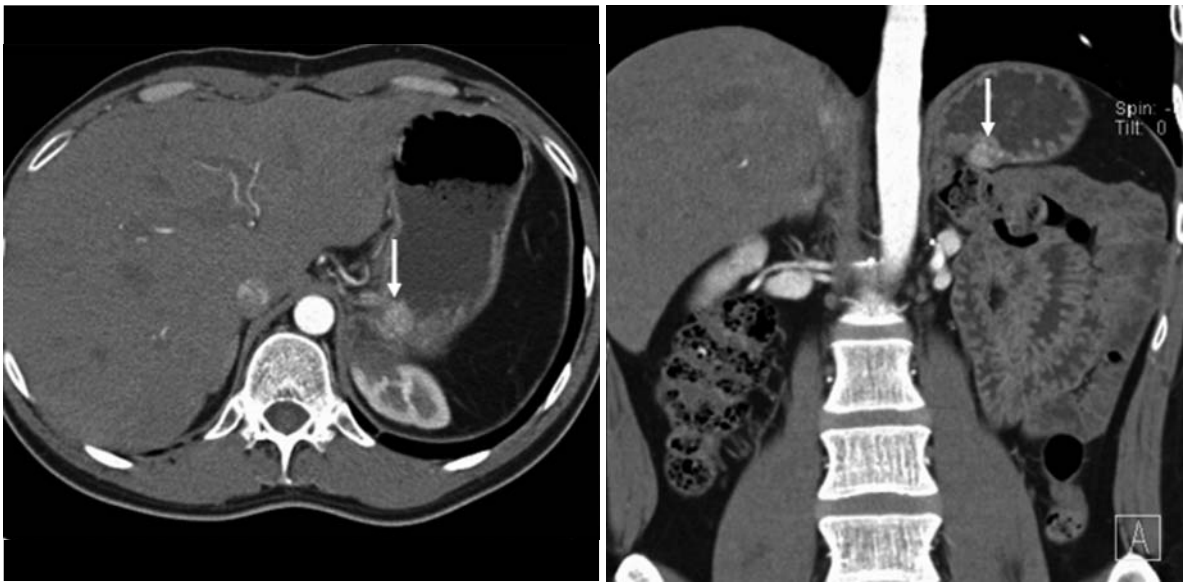

Fig. 3.8. Enhanced visualization of GI pathology at CT enterography. Axial (*left*) and coronal reformatted image (*right*) shows enhancing hyper vascular neuroendocrine tumor (*arrows*) in stomach

shown that they are superior to either water or methylcellulose in achieving small bowel distension (Hara et al. 2005; Megibow et al. 2006; Arslan et al. 2005; Paulsen et al. 2006). The initial studies evaluating the potential use of CT enterography were performed with positive oral contrast agents (Raptopoulos et al. 1997). However, since that time most studies and reports of CTE have been performed with a neutral oral contrast agent (Hara et al. 2005; Megibow et al. 2006; Arslan et al. 2005; Boudiaf et al. 2004; Reitner et al. 2002; Wold et al. 2003; Paulsen et al. 2006). Peroral CT enterography differs from CT enteroclysis in that the latter technique is performed after placement of a naso-jejunal tube in conjunction with active small bowel distension. It should be noted that CT enterography performed with VoLumen is inferior to CT enteroclysis in achieving small bowel distension (Megibow et al. 2006). However, the non-invasive nature and speed of CT enterography make it well suited as a fist line technique for the evaluation of suspected bowel small disease (Bodily et al. 2006; Hara et al. 2005; Paulsen et al. 2006).

Our specific protocol (Protocol 3.1) for performing CTE requires fasting for at least 3 h prior to the examination. This will decrease the possibility of misinterpreting a foreign body as a polyp or tumor. Upon arrival to the imaging center, patients ingest two 450 ml bottles of VoLumen over a 30 min period. The first bottle is ingested 30 min prior to the procedure, the second 20 min prior to the procedure. Immediately before the patient changes for the examination, the patient consumes 225 mL of water and finally upon entering the scanning room, the patient drinks a final 225 mL of water. The total volume of fluid is therefore 1350 mL. Water is adequate for the final contrast because it is designed to primarily distend the stomach and duodenum. Other centers deliver a similar volume of contrast material over a 1 h period (450 mL 60 min and 40 min before scanning; 225 mL 20 min and 10 min before scanning) (Paulsen et al. 2006).

The optimal timing of the administration of oral contrast material will continue to be investigated. It is likely easier for the patient to ingest the oral volume over a longer period of time. However, if ingested over too long a period, the contrast material may be in the colon. Whether the contrast is administered over 30 or 60 min, if insufficient volume is ingested, suboptimal small bowel distension will limit the CTE examination. Therefore, it is important to explain the importance of the oral contrast to the patient. This is facilitated by having the CT technologist or nurse instruct and monitor the patient while they are ingesting the oral contrast material. If patients are left on their own suboptimal distension may occur.

Intravenous contrast enhancement is essential when performing CTE. A 20 gauge catheter is inserted into an arm vein and 1.5 mL/kg of iodinated contrast (Iopramide, 300 mg I/mL, Berlex Laborato-

ries, Wayne, NJ) is injected at a rate of at least 4 mL/s. Without intravenous contrast, the bowel wall is not seen and intestinal marking is compromised. If there is a possibility of compromised venous access or the patient cannot receive IV contrast, we perform the study with positive contrast. The optimal timing of data acquisition for CTE is somewhat controversial. We begin the acquisition 60 s after the initiation of the bolus. Others have suggested that an enterography phase (approximately 45 s after the injection), or even a dual phase acquisition may be helpful in patients with obscure gastrointestinal bleeding (Reitner et al. 2002; Wold et al. 2003; Paulsen et al. 2006). Glucagon in a dose of 0.1 mg is administered intravenously and given a few minutes prior to data to diminish peristalsis.

MDCTE should be performed on a 16 detector row or higher scanner. These scanners can acquire sub millimeter isotropic data necessary for 3D displays in a short enough time to minimize motion artifacts. At our institution we utilize either a 16 × .75 mm or 64 × .6 mm detector configuration depending on whether a 16 or 64 row detector scanner is used reconstructing either 1 mm or 0.8 mm slices. From this data set, the technologist will generate a set of axial 4-mm sections and a set of 3 mm thick coronal MPR images at 3 mm intervals encompassing the entire bowel. These are sent to the PACS for review.

Additionally, the thin slices are sent to a workstation where they are available for the radiologist to view the data in 3D volume rendering or MIP displays (Paulsen et al. 2006; Caoli and Paulson 2000). Images are acquired at 120 kVp, 0.4 s gantry rotation, and effective 180 mAs. A dose modulator, available on all MDCT scanners, which automatically decreases the radiation exposure to thinner areas of the patient, is employed and can reduce the dose up to 30%.

The basic principles of the CT enterography protocol can be applied to other abdominal indications. If there is a clinical concern for mesenteric ischemia or obscure GI bleeding, a dual phase acquisitions may be helpful not only to evaluate the vasculature, but also to assess for a possible source of GI bleeding. In these cases, we usually modify the protocol to include an early and delayed phase (Protocol 3.2).

3.4 CT of the Pancreas / Biliary Tree / Upper Abdominal Pain

The principles of intestinal enhancement and distension are important when dealing with all upper abdominal processes. By having neutral oral contrast in the small bowel vascular imaging in not compromised. By using thin section MDCT data acquisition, exquisite anatomic information can be

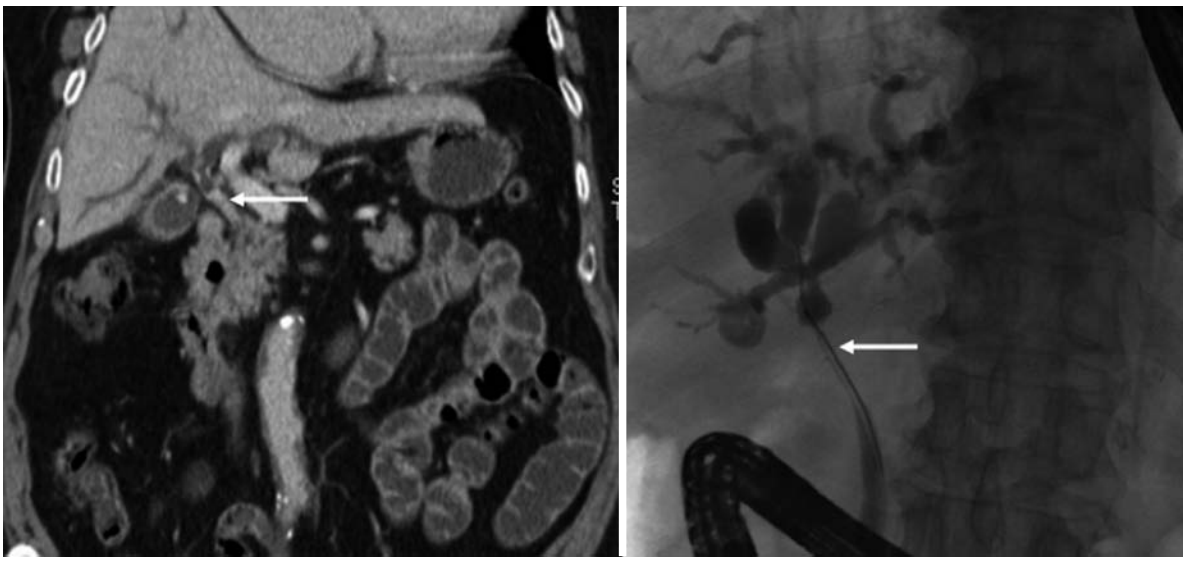

Fig. 3.9. Coronal reformatted CT image (*left*) shows enhancing mass (*arrow*) in common hepatic duct obstructing the duct and causing jaundice. Findings are most consistent with cholangiocarcinoma. ERCP image (*right*) confirms stricture which was proven to be a cholangiocarcinoma at surgery

generated (Fig. 3.9). Dual phase acquisition after administration of IV contrast has been shown to be particularly helpful in evaluating the pancreas. When deciding how to evaluate the pancreas, and pancreatic neoplasms in particular at MDCT, we need to ask ourselves what we need to know:

1. We want to be able to differentiate normal pancreas from neoplasm.
2. Can we further characterize the pancreatic neoplasm as solid or cystic, and as being hypo-vascular or hyper-vascular?
3. Can we differentiate normal peri-pancreatic vessels from tumor encasement and encroachment?
4. Is there adjacent organ invasion?
5. Are there peri-pancreatic lymph-nodes present?
6. Are there distant metastases to the liver or omentum?

In order to evaluate these features best , it has been shown that a dual-phase MDCT protocol should be used (Goshima et al. 2006; Kim et al. 1999; Lu et al. 1997; Vargas et al. 2004; Prokesch et al. 2002; McNulty et al. 2001; Schueller et al. 2006) (Protocol 3.3). This protocol can be used for the following indications: pancreatic mass, pancreatitis (initial study), jaundice, cholecystitis, gallbladder disease, biliary disease, severe epigastric pain, weight loss, gastric cancer evaluation.

The pancreas is best evaluated during the combined "pancreatic phase" of contrast enhancement and during the "portal venous phase" of contrast enhancement with MDCT (Goshima et al. 2006; Lu et al. 1997; Vargas et al. 2004; Prokesch et al. 2002; McNulty et al. 2001; Schueller et al. 2006). By evaluating the gland during both phases, we optimize the ability to detect the important features (listed above) in patients with pancreatic cancer (Fig. 3.10). This will allow better triage of those patients who are candidates for resection versus those that would not benefit from surgery.

The "pancreatic phase" of contrast enhancement is performed through the pancreas 40–45 s after a bolus of iodinated contrast is power injected through an antecubital vein at a rate 4 mL/s. For the pancreatic phase of contrast enhancement, the scan is performed from the diaphragm to the iliac crests. This should be performed with the thinnest slice collimator available on the CT scanner, so for a 16 row scanner 16 × 75.

The pancreatic phase of contrast enhancement optimizes our ability to detect pancreatic adenocarcinoma and differentiate it from normal pancreatic tissue. Studies have shown that because pancreatic ductal adenocarcinoma often has a marked desmoplastic response associated with it, it will be hypo-attenuating relative to the normal pancreas after contrast enhancement during the pancreatic phase (Lu et al. 1997). The degree of tumor conspicuity is enhanced during the "pancreatic phase" and decreases during the portal venous phase. This

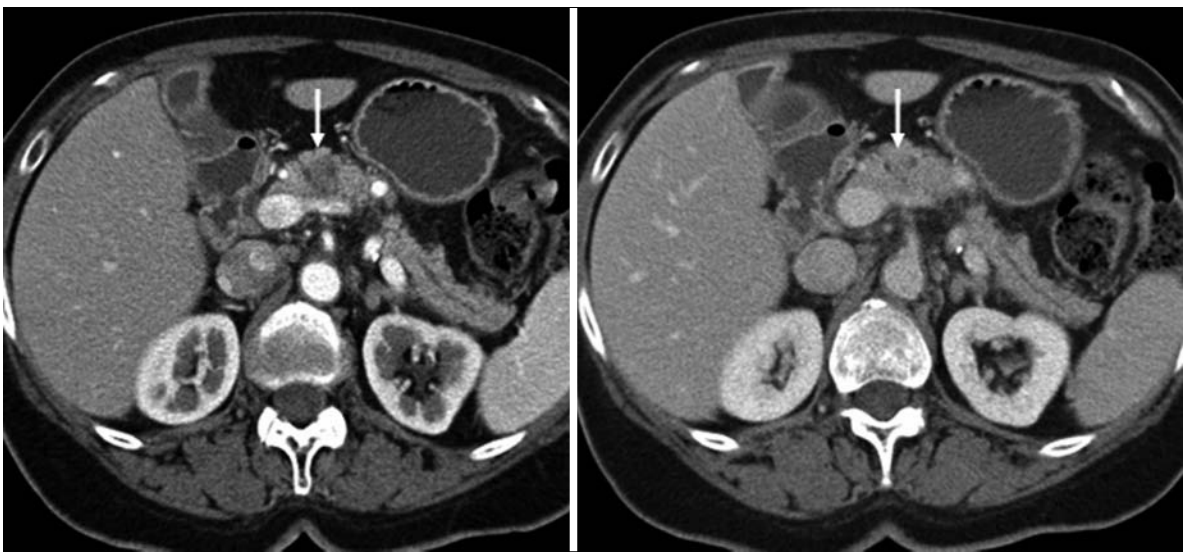

Fig. 3.10. Dual phase MDCT of pancreatic cancer. Axial CT obtained during the pancreatic phase of enhancement (*left*) shows 2 cm hypo-vascular pancreatic adenocarcinoma (*arrow*). During the portal venous phase (*right*) the tumor is iso-attenuating (*arrow*)

is related to the fact that over time the pancreatic neoplasm will continue to increase in attenuation, while the normal vascular pancreas will begin to de-enhance over time. It should be remembered that about 11% of pancreatic carcinomas will be iso-attenuating with the pancreatic parenchyma (Vargas et al. 2004; Prokesch et al. 2002). In these cases, secondary signs of pancreatic carcinoma including ductal dilatation and biliary dilatation or morphologic changes in the contour or texture of the pancreas can aid in diagnosis. We have also found that in some cases MR imaging is better able to delineate the tumor because of the inherently higher soft tissue contrast of MR imaging.

Hyper-vascular tumors such as islet cell tumors and certain hyper-vascular (renal cell carcinoma) metastases will often appear hyper-attenuating on the pancreatic phase which allows for better characterization of these tumors (Fig. 3.11).

By performing the pancreatic phase of contrast enhancement 40 s after the bolus of contrast injection and not during an "arterial phase" (20–25 s) of contrast enhancement, excellent arterial enhancement and adequate venous enhancement are usually obtained. This allows us to evaluate the peri-pancreatic vessels optimally (see Fig. 3.2).

When a true angiogram is needed we use a bolus tracking technique. Our protocol is to do serial low mAs scans on the vessel of interest (in the case of the pancreas, we bolus track at the level of the aortic hiatus) and when the attenuation reaches 150 HU, scanning in initiated 6 s later. This provides excellent vascular enhancement. When evaluating a liver lesion, arterial phase imaging is performed 15 s after the vessel reaches 150 HU to allow for optimal arterial enhancement of a liver lesion (see Protocol 3.9).

Vessel evaluation is facilitated by reviewing the data set at a workstation equipped with software that allows 2D multi-planar reconstructions as well as 3D angiographic images to be obtained (Fig. 3.12). This information is helpful in delineating the anatomy and in providing useful information to the surgeon. Moreover, it has been shown that thin section MDCT can be used to generate curved MPR images of the pancreatic duct which is very helpful in looking at a tumor and its relationship to the duct and vessels, as well as for evaluating intraductal papillary mucinous neoplasms (Vargas et al. 2004). In order to maximize the diagnostic capability of MDCT, access and knowledge of how to use a 3D workstation is essential.

The portal venous phase of contrast enhancement is performed approximately 80–90 s after the bolus of contrast enhancement using state of the art MDCT scanners. For the portal venous phase of contrast enhancement, scanning is initiated from the dome of the liver through the abdomen and pelvis. The portal venous phase of enhancement is criti-

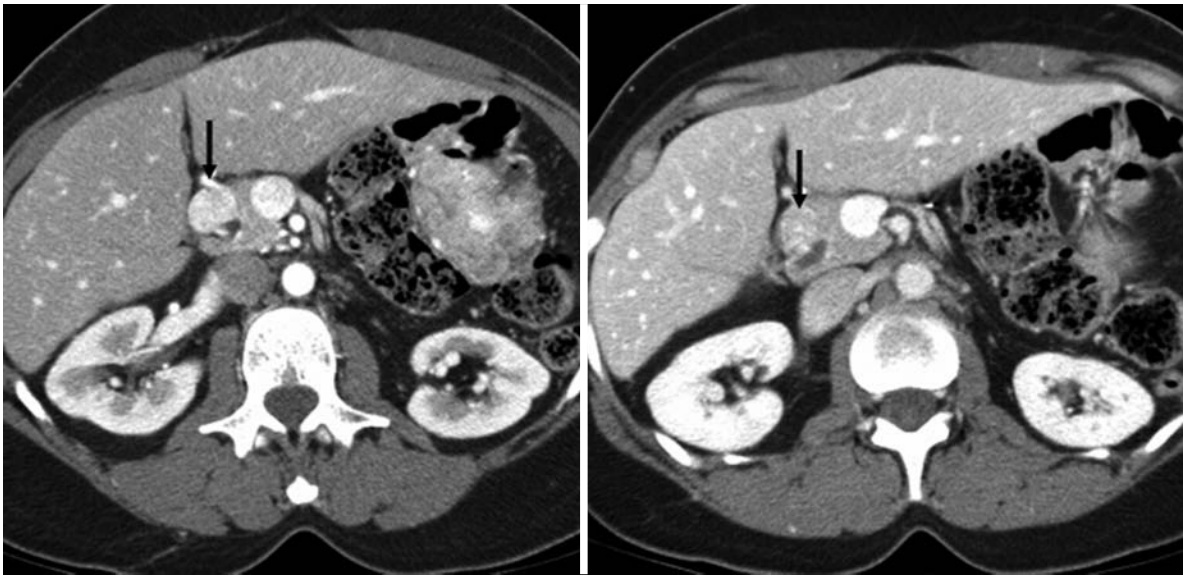

Fig. 3.11. Dual phase MDCT of gastrinoma. Axial CT obtained during the pancreatic phase of enhancement (*left*) shows 1.5 cm hyper-vascular pancreatic isulinoma (*arrow*). During the portal venous phase (*right*) the tumor is iso-attenuating (*arrow*)

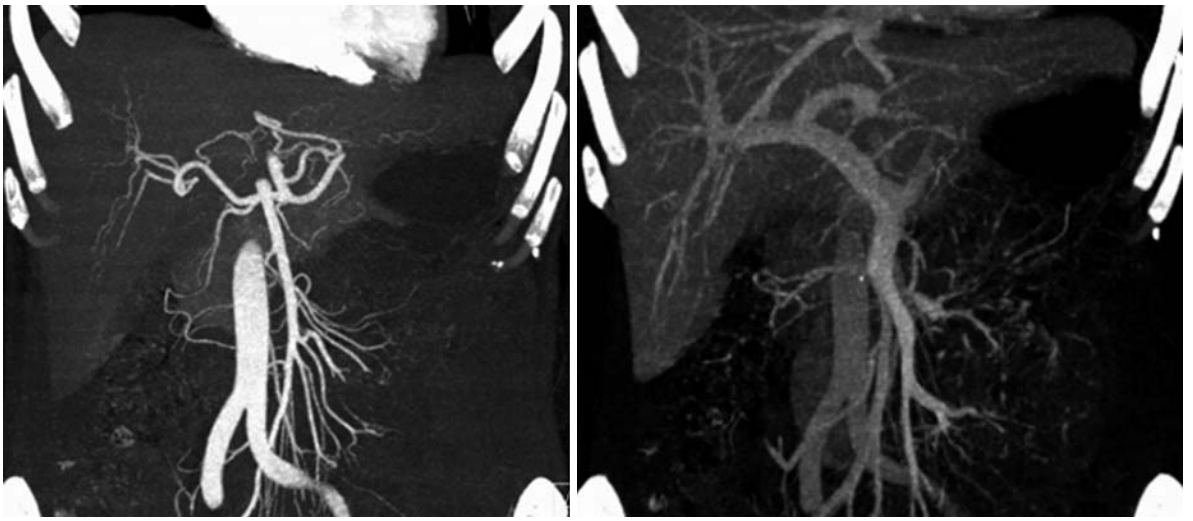

Fig. 3.12. Coronal MIP image of the mesenteric vasculature (*left*) and the portal venous system (*right*) obtained on a 64 row CT scanner

cal in evaluating the liver for potential metastatic disease. During the pancreatic phase of contrast enhancement the liver is sub-optimally enhanced. Therefore, small hepatic metastases may appear isoattenuating to the liver or unopacified vessels. During the "portal venous phase" there is maximal enhancement of the liver and hepatic metastases from hypo-vascular tumors will appear hypoattenuating relative to the liver, allowing maximal conspicuity and detection. It should be noted that tumors such as islet cell carcinomas, carcinoids, renal cell carcinoma, choriocarcinoma, and thryroid carcinoma are often hyper-vascular and in the cases we acquire MDCT data during the hepatic arterial phase (early portal venous in flow phase) as well as during the portal venous phase to maximize tumor conspicuity.

3.5 CT Data Acquisition in Lower Abdominal Pain

A variety of acute inflammatory conditions may affect the lower abdomen and right lower quadrant in particular prompting the patient to seek medical evaluation (de Dombal 1991). The work-up of a patient with right lower quadrant pain is based on the clinical history and physical examination, laboratory evaluation and classically "plain-film radiography". However, in patients with acute right lower quadrant pain (and abdominal pain in general), plain-film radiography is often non-contributory (Ahn et al. 2002). A study evaluating patients with abdominal pain showed that plain-film radiography was interpreted as nonspecific in 588 (68%) of 871 patients, normal in 200 (23%), and abnormal in 83 (10%). In this study, abdominal radiography had 0% sensitivity for appendicitis, pyelonephritis, pancreatitis, and diverticulitis. Moreover, the clinical history and physical examination in patients with right lower quadrant pain are often nonspecific. Therefore abdominal and pelvic MDCT is often performed to confirm if an inflammatory condition is present and to further characterize it (Balthazar et al. 1994).

With the widespread use of MDCT scanners in emergency departments throughout the country, this trend will likely continue (Novelline et al. 1999). In most patients with acute right lower quadrant pain, a specific diagnosis of appendicitis can be made with CT leading to prompt surgical intervention (Birnbaum and Wilson 2000). Moreover, MDCT has been shown to be highly accurate in assessing patients with a variety of etiologies for abdominal pain including determining the site of GI perforation in patients with extra-luminal intraperitoneal gas (Hainaux et al. 2006).

Appendicitis is likely the most common cause of the acute abdomen particularly in young individuals. However, it is important for the clinician and radiologist to remember that abdominal symptoms

and physical signs located in the right lower quadrant may be caused by a variety of other conditions (de Dombal 1991; Birnbaum and Wilson 2000). In a review of 10,682 patients with acute abdominal pain, de Dombal (Macari et al. 2002a) found that 28% had appendicitis, 9.7% had cholecystitis, 4.1% had small bowel obstruction, 4.0% had gynecologic disorders, 2.9% had pancreatitis, 2.9% had renal colic, 2.5% had peptic ulcer disease, 1.5% had cancer, and 1.5% had diverticular disease, and 9% a variety of less common conditions. In this review, a specific diagnosis was not established in 34% of cases. It is likely that, in many cases where a clinical diagnosis could not be made, MDCT imaging would have been helpful in establishing a specific etiology (Figs. 3.13 and 3.14).

Furthermore, among the more common acute abdominal conditions enumerated in de Dombal's series, Crohn's disease, epiploic appendagitis, infectious ileitis, mesenteric adenitis, omental infarc-

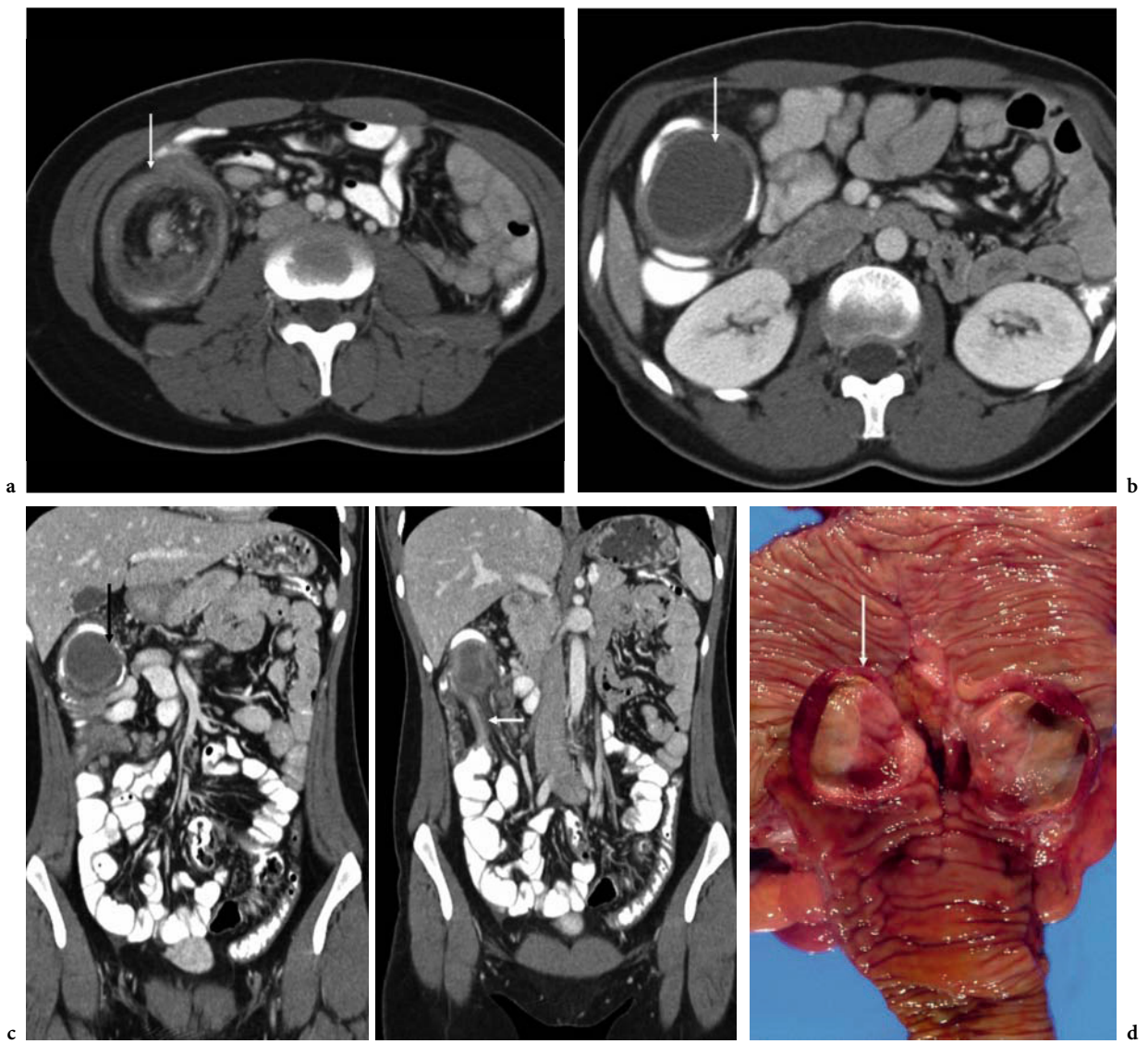

Fig. 3.13a–d. Use of coronal reformatted images to assist in diagnosis. **a** Axial CT image shows large intussusception in the right lower quadrant (*arrow*). **b** Axial CT slice obtained cephalad to a shows well circumscribed low attenuated mass as lead point (*arrow*). **c** Coronal reformatted image (*left*) show that the mass is spherical (*arrow*) and at the level of the ileo-cecal valve (*right*). Note terminal ileum (*arrow*). The spherical nature of the lesion excluded mucocele and therefore the most likely diagnosis is duplication cyst. **d** Duplication cyst was confirmed at surgery (*arrow*)

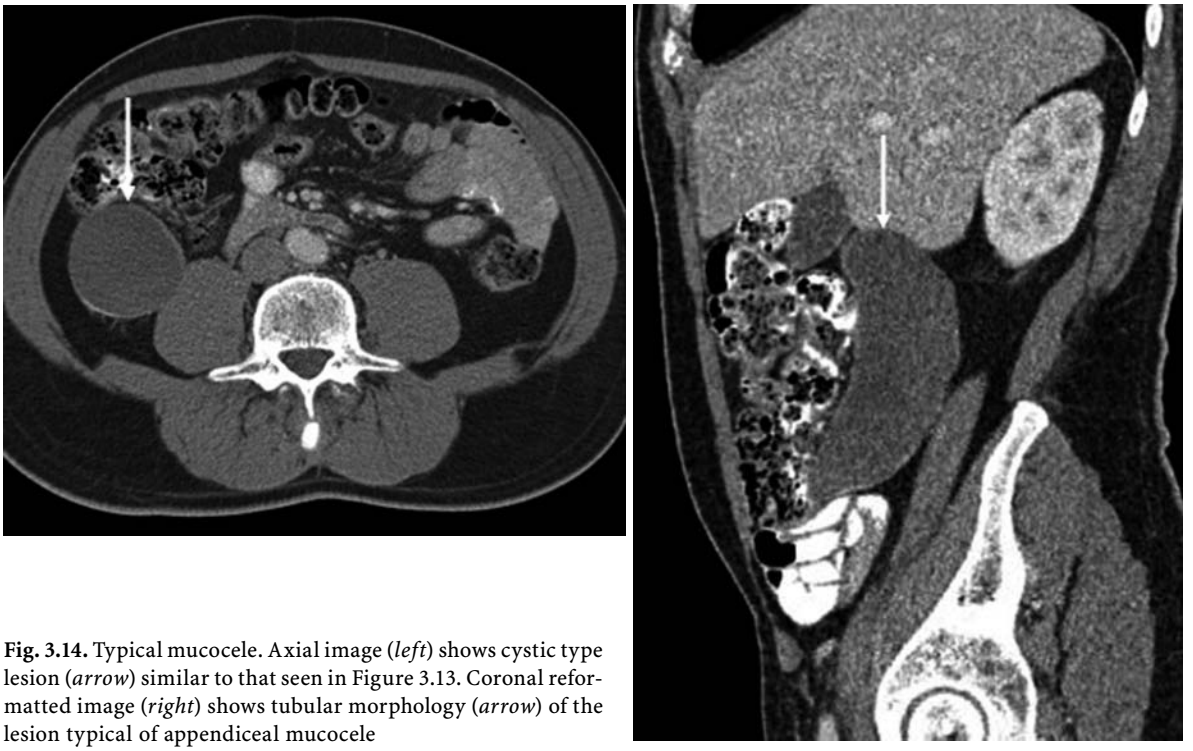

Fig. 3.14. Typical mucocele. Axial image (*left*) shows cystic type lesion (*arrow*) similar to that seen in Figure 3.13. Coronal reformatted image (*right*) shows tubular morphology (*arrow*) of the lesion typical of appendiceal mucocele

tion, ileal, cecal, and right-sided colonic diverticulitis, Meckel's diverticulitis, typhlitis, and intestinal ischemia are not listed. While some of these conditions are relatively uncommon, taken as a whole, they make up a substantial number of patients that present with acute right lower abdominal pain (Birnbaum and Wilson 2000; Hainaux et al. 2006; Rao et al. 1997b; Macari et al. 1998, 2002b; Gore et al. 1996; Bennett et al. 2002; Balthazar et al. 1998; Bendeck et al. 2002; Lim et al. 1996; Jeffrey et al. 1994; Puylaert 1986; Sivit et al. 2000; Lane et al. 1997, 1999; Ege et al. 2002; Grayson et al. 2001; Jacobs et al. 2001; Fefferman et al. 2001; Kamel et al. 2000; Oto et al. 2006; O'Malley et al. 2000; Weltman et al. 2000). All of these conditions may be diagnosed with MDCT.

Our MDCT protocol for evaluating patients with lower abdominal pain uses positive oral and IV contrast (Protocol 3.3). There is some controversy about which oral contrast to use, positive (barium or gastrograffin), neutral (water or VoLumen) or no oral contrast. A number of techniques have been advocated to evaluate the patient with right lower abdominal pain including CT without any contrast, CT performed with contrast instilled through the rectum, CT with oral contrast only, and CT with both oral and IV contrast (Lane et al. 1997, 1999; Ege et al. 2002; Grayson et al. 2001; Jacobs et al. 2001; Fefferman et al. 2001; Rao et al. 1997a; Kamel et al. 2000; Oto et al. 2006; O'Malley et al. 2000; Weltman et al. 2000).

In the setting of suspected appendicitis, Balthazar et al. (1994) documented sensitivity of 98%, specificity of 88%, and overall accuracy of 95% when performing CT with oral and IV contrast material. A survey of academic institutions regarding imaging protocols used in patients with suspected appendicitis showed that IV, oral, and rectal contrast material are routinely given at 79%, 82%, and 32% of institutions, respectively (O'Malley et al. 2000). Of the institutions, 21% routinely use IV, oral, and rectal contrast material simultaneously. Therefore, among the numerous options available to scan the patient, CT with oral and IV contrast material continues to be the most commonly employed technique. We continue to rely on oral and IV contrast enhanced MDCT of the abdomen and pelvis to evaluate for suspected acute appendicitis and in patients with lower abdominal pain to diagnose alternative acute abdominal conditions that can masquerade as appendicitis. Regarding our CT technique, it is important to opacify the cecum using oral contrast material.

We administer 800–1000 mL of oral contrast (dilute Gastrografin) in small increments over 1.5 h before the examination is to be performed. The patient is then placed on the CT table and a scout topogram is obtained to document filling of the cecum. If it is uncertain whether there is filling of the cecum, a single CT slice at the level of the sacroiliac joints can be obtained. If the cecum is opacified, we begin the examination, otherwise, the patient is taken off the CT scanner and waits an additional 30 min and then placed back on the CT scanner.

Once the cecum is opacified, MDCT of the abdomen and pelvis are performed using the thinnest detector configuration available to maximize the potential of the data set. A recent study has shown that MDCT can be of great value in localizing the origin of the appendix relative to McBurneys's point (Oto et al. 2006). This was facilitated by using 3D data sets for appendiceal localization. We have found that coronal and volume rendered data sets are extremely helpful when evaluating patients with right lower quadrant pain. Coronal data should be sent directly to the PACS station so that a permanent record is kept as thin section data are often not archived for future use.

3.6 Conclusions

Optimal abdominal MDCT data acquisition for 3D evaluation is determined by the scanner available, clinical indication, choice of oral and IV contrast material, and knowledge of the risks of radiation. A list of the current NYU MDCT protocols for specific indications are listed at the end of this chapter. These protocols were developed to allow optimal CT data acquisition for both 2D and 3D data interpretation while trying to limit radiation dose to the patient. By obtaining thin section MDCT data, 3D data interpretation is facilitated by the use of isotropic voxels which enable both MPR and volume rendering to be performed.

Protocol 1. CT Enterography

Phase 1	CT enterography phase (60 s) – diaphragm to symphysis (thin)
KV/mAs/rotation	Care dose or 120/180/0.5
Oral contrast	2 bottles of Volumen and then 2 cups of H_2O just before being placed on CT table
IV contrast rate	4 mL/s
IV Contrast dose	1.5 mL/kg followed by 20 mL saline
Archive to PACS	Axial 4 mm, coronal 3 mm

Protocol 2. Mesenteric ischemia

Phase 1	CTA phase (bolus track aorta – 150 HU) – diaphragm to symphisis (thin)
Phase 2	Venous (90 s) diaphragm to symphisis (thin)
KV/mAs/rotation	Care dose or 120/180/0.42
Oral contrast	Volumen (2 bottles over 30–45 min) at FPO
IV contrast rate	4 mL/s
IV Contrast dose	1.5 mL/kg followed by 20 ml saline
Archive to Pacs	Axial 4 mm, coronal phase 1 and 2

Protocol 3. Lower abdominal pain

Indications: appendicitis, diverticulitis, pelvic pain, acute abdomen	
Phase 1	Venous (90 s) diaphragm to symphisis (thin)
KV/mAs/totation	Care dose or 120/180/0.42
Oral contrast	Dilute Gastrograffin 1 L (unless allergy, then consider barium)
IV contrast rate	3–4 mL/s
IV contrast dose	1.5 mL/kg followed by 20 mL saline
Archive to Pacs	Axial 4 mm, coronal 3 mm

Protocol 4. CT colonography

Phase 1	Supine – diaphragm to symphisis (thin)
Phase 2	Prone – diaphragm to symphisis (thick)
KV/mAs/rotation	120 kVP, care dose set at 50 mAs, 0.42–0.5 s
Slice thickness	4 mm axial to PACS
Oral contrast	None
Rectal contrast	Use CO_2 and automated insufflation
IV contrast dose	None
Archive to Pacs	4 mm
Recon	1/1-supine and 2/1 prone, send thin section data to workstation for data interpretation with dedicated CTC software

Protocol 5. Renal calculi / obstruction

Indications: renal stone	
Phase 1	NCCT – diaphragm-symphysis (thick) scan prone
KV/mAs/rotation	Care dose or 120/180/0.5
Oral contrast	None
IV contrast	None
Archive to Pacs	Axial 4 mm, coronal 3q3

Protocol 6. Hematuria

Phase 1	NCCT – kidneys (thick)
Phase 2	Nephrogram (90 s) – diaphragm-pymphisis kidneys (thin)
Phase 3	Urogram – (7 min) – kidneys through bladder (thin)
Lasix	10 mg before scout
KV/mAs/rotation	Care dose or 120/180/0.42
Oral contrast	500 mL H_2O–15 min prior to scan
IV contrast rate	200 mL of 240 mgI/mL @ 4 mL/s
Archive to Pacs	Axial 4 mm, coronal 3 mm phase 2

Protocol 6. Renal mass (CTA)

Indication – known renal mass evaluation. NOT for follow-up of kidney cancer	
Phase 1	NCCT - kidneys (thick)
Phase 2	(CTA) - kidneys bolus track (thin)
At the level of T12	
	
	
Phase 3	Nephrogram (120 s) diaphragm-symphisis kidneys (thin)
Phase 4	Urogram (7 min) kidneys only (thin)
KV/mAs/rotation	Care dose or 120/180/0.42
Oral contrast	Water + fizzies
IV contrast rate	3–4 mL/s
IV contrast dose	1.5 mL/kg (min 100)
Archive to Pacs	Axial 4 mm, coronals phase 3 (nephrograms)

Protocol 7. Bladder cancer (pre-operative evaluation NOT follow-up)

Phase 1	NCCT – abdomen (thick)
Phase 2	90 s – diaphragm-symphisis (thin)
Phase 3 (7 min)	Kidneys to bladder (thin)
KV/mAs/rotation	Care dose or 120/180/0.42
Oral contrast	500 mL H_2O +fizzies – 15 min prior to scan
IV contrast rate	3 mL/s
IV contrast dose	1.5 mL/kg followed by 20 mL saline
Archive to Pacs	Axial 4 mm, coronal phase 2

Protocol 8. UPJ

Phase 1	NCCT – kidneys (thick)
Phase 2	(CTA) – kidneys bolus track (thin) trigger at celiac artery at 150 HU (start 6 s later)
	
	
Phase 3	Nephrogram (120 s) diaphragm-symphisis (thin)
KV/mAs/rotation	Care dose or 120/180/0.42
Oral contrast	None
IV contrast rate	3–4 mL/s
IV contrast dose	1.5 mL/kg (min 100)
Archive to Pacs	Axial 4 mm, coronals phase 2

Protocol 9. Three phase liver

Indications: HCC, pre-transplant evaluation, abnormal LFTs (NOT jaundice), cirrhosis, known liver mass evaluation	
Phase 1	NCCT – liver (thick)
Phase 2	Arterial (bolus track/add 15 s) - abdomen (thin)
	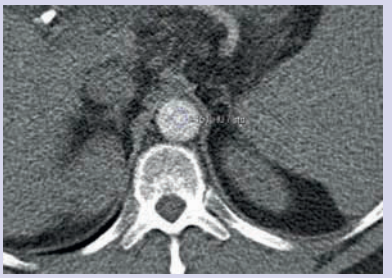
	
Phase 3	Venous (90 s) diaphragm to symphisis (thin)
KV/mAs/rotation	Care dose or 120/180/0.42
Oral contrast	500 mL H_2O +fizzies
IV contrast rate	5 mL/s
IV contrast dose	150 mL of contrast
Archive to Pacs	4 mm all axial acquisitions, coronal 3q3 phase 3

* Bolus track the aorta at 150 HU and add 15 s prior to start of scan

Protocol 10. Oncology survey

Phase 1	Venous (90 s) diaphragm to symphisis (thick)
KV/mAs/rotation	Care dose or 120/180/0.42
Oral contrast	Dilute barium (1 L)
IV contrast rate	3 mL/s
IV contrast dose	1.5 mL/kg followed by 20 mL saline
Archive to Pacs	4 mm, coronal 3 mm

References

Ahn SH, Mayo-Smith WM, Murphy BL, Reinert SE, Cronan JJ (2002) Acute nontraumatic abdominal pain in adult patients: abdominal radiography compared with CT evaluation. Radiology 225:159–164

Arslan H, Etlik O, Kayan M et al (2005) Peroral CT enterography with lactulose solution: preliminary observations. AJR Am J Roentgenol 185:1173–1179

Balthazar EJ, Birnbaum BA, Yee J et al (1994) Acute appendicitis: CT and US correlation in 100 patients. Radiology 190:31–35

Balthazar EJ, Rofsky NM, Zucker R (1998) Appendicitis: the impact of computed tomography imaging on negative appendectomy and perforation rates. Am J Gastroenterol 93:768–771

Bendeck SE, Nino-Murcia M, Berry GJ, Jeffrey RB Jr (2002) Imaging for suspected appendicitis: negative appendectomy and perforation rates. Radiology 225:131–136

Bennett GL, Slywotzky CM, Giovanniello G (2002) Gynecologic causes of acute pelvic pain: spectrum of CT findings. RadioGraphics 22:785–801

Birnbaum BA, Wilson SR (2000) Appendicitis at the millennium. Radiology 215:337–348

Bodily KD, Fletcher JG, Solem CA et al (2006) Crohn disease: mural attenuation and thickness at contrast-enhanced CT enterography-correlation with endoscopic and histologic findings of inflammation. Radiology 238:505–516

Boudiaf M, Jaff A, Soyer P et al (2004) Small-bowel diseases: prospective evaluation of multidetector helical CT enteroclysis in 107 consecutive patients. Radiology 233:338–344

Caoli EM, Paulson EK (2000) CT of small bowel obstruction: another perspective using multiplanar reformations. AJR Am J Roentgenol 174:993–998

de Dombal FT (1991) Diagnosis of acute abdominal pain, 2nd edn. Churchill Livingstone, New York, NY

Ege G, Akman H, Sahin A, Bugra D, Kuzucu K (2002) Diagnostic value of unenhanced helical CT in adult patients with suspected acute appendicitis. Br J Radiol 75:721–725

Fefferman NR, Roche KJ, Pinkney LP, Ambrosino MM, Genieser NB (2001) Suspected appendicitis in children: focused CT technique for evaluation. Radiology 220:691–695

Gore RM, Balthazar EJ, Ghahremani GG, Miller FH (1996) CT features of ulcerative colitis and Crohn's disease. AJR Am J Roentgenol 167:3–15

Goshima S, Kanematsu M, Kondo H et al (2006) Pancreas: optimal scan delay for contrast-enhanced multi-detector row CT. Radiology 241:165–174

Gourtsoyiannis N, Papanikolaou N, Grammatikakis J et al (2004) Assessment of Crohn's disease activity in the small bowel with MR and conventional enteroclysis: preliminary results. Eur Radiol 14:1017–1024

Grayson DE, Wettlaufer JR, Dalrymple NC, Keesling CA (2001) Appendiceal CT in pediatric patients: relationship of visualization to amount of peritoneal fat. AJR Am J Roentgenol 17:497–500

Hainaux B, Agneessens E, Bertinotti R et al (2006) Accuracy of MDCT in predicting site of gastrointestinal tract perforation. AJR Am J Roentgenol 187:1179–1183

Hara AK, Leighton JA, Virender K et al (2005) Imaging of small bowel disease: comparison of capsule endoscopy, standard endoscopy, barium examination, and CT. Radiographics 25:697–718

Jacobs JE, Birnbaum BA, Macari M, Megibow AJ, Israel G, Maki DD, Aguiar AM, Langlotz CP (2001) Helical CT diagnosis of acute appendicitis: comparison of focused appendiceal technique using oral contrast and non focused technique using oral and intravenous contrast. Radiology 220:683–690

Jeffrey RB Jr, Jain KA, Nghiem HV (1994) Sonographic diagnosis of acute appendicitis: interpretive pitfalls. AJR Am J Roentgenol 162:55–59

Kamel IR, Goldberg SN, Keogan MT, Rosen MP, Raptopoulos V (2000) Right lower quadrant pain and suspected appendicitis: nonfocused appendiceal CT-review of 100 cases. Radiology 217:159–163

Kim T, Murakami T, Takahashi S et al (1999) Pancreatic CT imaging: effects of different injection rates and doses of contrast material. Radiology 212:219–225

Lane MJ, Katz DS, Ross BA et al (1997) Unenhanced helical CT for suspected acute appendicitis. AJR Am J Roentgenol 168:405–409

Lane MJ, Liu DM, Huynh MD, Jeffrey RB Jr, Mindelzun RE, Katz DS (1999) Suspected acute appendicitis: nonenhanced helical CT in 300 consecutive patients. Radiology 213:341–346

Lim HK, Lee WG, Lee SJ, Namgung S, Lim JH (1996) Focal appendicitis confined to the tip: diagnosis at US. Radiology 200:799–801

Lu DS, Reber HA, Krasny RM, Kadell BM, Sayre J (1997) Local staging of pancreatic cancer: criteria for unresectability of major vesses as revealed by pancreatic phase, thin section helical CT. AJR Am J Roentgenol 168:1439–1443

Macari M, Balthazar EJ (2001) Review: computed tomography of bowel wall thickening: significance and pitfalls of interpretation. AJR Am J Roentgenol 176:1105–1116

Macari M, Balthazar EJ, Krinsky G, Cao H (1998) CT diagnosis of ileal diverticulitis. Clinical Imaging 22:243–245

Macari M, Bini EJ, Xue X et al (2002a) Prospective comparison of thin-section low-dose multislice CT colonography to conventional colonoscopy in detecting colorectal polyps and cancers. Radiology 224:383–392

Macari M, Hines J, Balthazar EJ, Megibow AJ (2002b) Mesenteric adenitis: CT diagnosis of primary vs. secondary causes, incidence, and clinical significance. AJR Am J Roentgenol 178:853–858

Maglinte DT (2005) Capsule imaging and the role of radiology in the investigation of diseases of the small bowel. Radiology 236:763–767

McNulty NJ, Francis IR, Platt JF, Cohan RH, Korobkin M, Gebremariam A (2001) Multi-detector row helical CT of the pancreas: effect of contrast-enhanced multiphasic imaging on enhancement of the pancreas, peripancreatic vasculature, and pancreatic adenocarcinoma. Radiology 220:97–102

Megibow AJ, Babb JS, Hecht EM, Cho JJ, Houston C, Boruch MM, Williams AB (2006) Evaluation of bowel distention and bowel wall appearance by using neutral oral contrast agent for multi-detector row CT. Radiology 238:87–95

Novelline RA, Rhea JT, Rao PM, Stuk JL (1999) Helical CT in emergency radiology. Radiology 213:321–339

O'Malley ME, Halpern E, Mueller PR, Gazelle GS (2000) Helical CT protocols for the abdomen and pelvis: a survey. AJR Am J Roentgenol 175:109–113

Oto A, Ernst RD, Mileski WJ et al (2006) Localization of the appendix with MDCT and influence of findings on choice of appendectomy incision. AJR Am J Roentgenol 187:987–990

Paulsen SR, Huprich JE, Fletcher JC et al (2006) CT enterography as a diagnostic tool in evaluating small bowel disorders: review of clinical experience with over 700 cases. Radiographics 26:641–662

Prokesch RW, Chow LC, Beaulieu CF, Bammer R, Jeffrey RB Jr (2002) Isoattenuating pancreatic adenocarcinoma at multi-detector row CT: secondary signs. Radiology 224:764–768

Puylaert JB (1986) Acute appendicitis: US evaluation using graded compression. Radiology 158:355–360

Rao PM, Rhea JT, Noveline RA et al (1997a) Helical CT technique for the diagnosis of appendicitis: prospective evaluation of focused appendix technique. Radiology 202:139–144

Rao PM, Rhea JT, Novelline RA (1997b) CT diagnosis of mesenteric adenitis. Radiology 202:145

Raptopoulos V, Schwartz RK, McNicholas MMJ et al (1997) Multiplanar helical CT enterography in patients with Crohn's disease. AJR Am J Roentgenol 169:1545–1550

Rastogi N, Sahani DV, Blake MA, Ko DC, Mueller PR (2006) Evaluation of living renal donors: accuracy of three-dimensional 16-section CT. Radiology 240(1):136–144

Reitner P, Goritschnig T, Petritisch W et al (2002) Multiplanar spiral CT enterography in patients with Crohn's disease using a negative oral contrast material: initial results of a noninvasive imaging approach. Eur Radiol 9:2253–2257

Sahani D, Kadaviegere R, Blake M, Fernandez C, Lauwers G, Hahn P (2006) Characterization of IPMN of the pancreas with MDCT: correlation of 2D curved reformations with MRCP and pathology. Radiology 238:560–569

Schueller G, Schima W, Schueller-Weidekamm C et al (2006) Multidetector CT of the pancreas: effects of contrast material flow rate and individualized scan delay on enhancement of pancreas and tumor contrast. Radiology 241:441–448

Sivit CJ, Applegate KE, Stallion A et al (2000) Imaging evaluation of suspected appendicitis in a pediatric population: effectiveness of sonography versus CT. AJR Am J Roentgenol 175:977–980

Vargas R, Nino-Murcia M, Trueblood W, Jeffrey RB Jr (2004) MDCT in pancreatic adenocarcinom: prediction of vascular invasion and resectability using a multiphasic technique with curved planar reformations. AJR Am J Roentgenol 182:419–425

Weltman DI, Yu J, Krumenacker J Jr, Huang S, Moh P (2000) Diagnosis of acute appendicitis: comparison of 5- and 10 mm CT sections n the same patient. Radiology 216:172–177

Wold PB, Fletcher JG, Johnson CS, Sandborn WJ (2003) Assessment of small bowel Crohn disease: noninvasive peroral CT enterography compared with other imaging methods and endoscopy-feasibility study. Radiology 229:275–281

Segmentation of Radiological Images

4

Nigel W. John

CONTENTS

4.1 Introduction

Today's typical hospital environment is well-equipped with medical scanners that routinely provide valuable information to aid with the diagnosis or treatment planning for a particular patient. Computerised tomography (CT), magnetic resonance imaging (MRI), ultrasound, and positron emission tomography (PET) are examples of imaging modalities that are frequently used. An experienced radiologist can gain much insight by viewing the individual images that a scanner produces. However, segmentation of the radiological images to extract or classify a specific region or volume of interest is often required to partition the image data into its constituent components. Image segmentation provides quantitative information about relevant anatomy, for example to determine the size or volume. It also enables an accurate three-dimensional (3D) visualisation of a particular structure using surface triangulation, isosurfacing or volume rendering. There is no single approach that can generally solve the problem of segmentation, and different methods will be more effective depending on the image modality being processed. Pham et al. (2000) and Preim and Bartz (2007) provide detailed reviews of the classic segmentation algorithms, many of which are now implemented within the radiological software supplied by the scanner manufacturer. There are also many excellent software packages freely available in the public domain; however, a software review is outside the scope of this chapter. The interested reader should refer to the Insight Toolkit (ITK), which is an open-source software system that supports a comprehensive collection of the latest segmentation techniques (Yoo 2004). Most of the figures in this chapter have been generated using either the ImageJ (Abramoff et al. 2004) or ITK-SNAP (Yushkevich et al. 2006) software applications.

The remainder of this chapter provides an overview of the most common segmentation techniques currently in use, and highlights their specific advantages and disadvantages.

4.2 Manual Segmentation

The simplest approach for implementing a segmentation tool is to allow for manual tracing or drawing onto the radiological images. Geometric shapes can be used for boundaries, but most approaches record vertices at each mouse click and then draw a line seg-

N. W. John, PhD
Professor of Computing, School of Computer Science, Bangor University, Dean Street, Bangor LL57 1UT, UK

ment or spline curve between consecutive vertices. Alternatively, the mouse position can be sampled continuously, following the arc of the mouse movements across the screen. The mouse click method is demonstrated in Figure 4.1, which has been created using the open source ITK-SNAP software tool. Each slice on which the structure of interest occurs has to be processed in turn, resulting in a stack of contours. Typically, editing functions are also provided to adjust the position of the contour on a slice. Points on the boundary and inside the contour are considered as belonging to the target structure. Points outside of the contour do not belong to the structure. A surface triangulation algorithm can then be applied to convert the contour stack into a surface mesh that can be visualized in 3D. There are several well-known algorithms in computer graphics that can achieve this task; typically they are based on Delaunay triangulation (Delaunay 1934)[1]. Boissonnat (1988), for example, showed how to efficiently compute the Delaunay triangulation between two adjacent contours, two by two, and using only 2D operations. Other segmentation methods described below also produce a contour stack and will require such a surface triangulation technique (see Fig. 4.5d).

[1] Delaunay triangulation for a set P of points in the plane is the triangulation DT(P) of P such that no point in P is inside the circumcircle of any triangle in DT(P). Delaunay triangulations maximise the minimum angle of all the angles of the triangles in the triangulation.

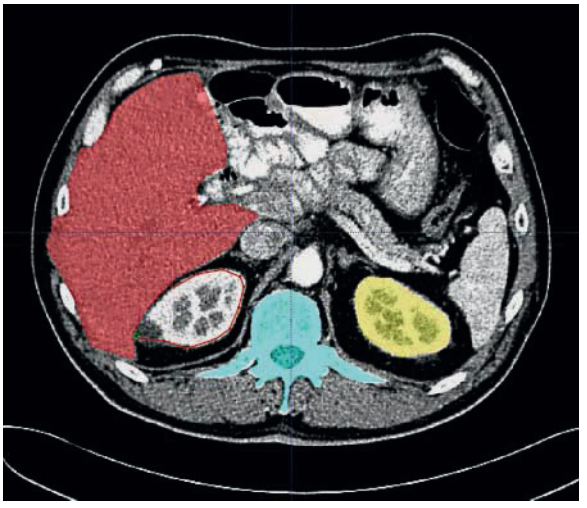

Fig. 4.1. Manual segmentation on a single CT axial image. Liver, left kidney and spine have already been traced. Segmentation of the right kidney is in mid process. Original CT data set (512 × 512 pixels, 246 slices) courtesy of Derek Gould, Royal Liverpool University Hospitals, UK

Manual segmentation is time-consuming and prone to the inaccuracies introduced by the end user's skill with the mouse. Care must also be taken when there are contours within contours, defining "holes" in the target structure.

4.3 Thresholding

Another straightforward but fast image segmentation method is thresholding. Individual pixels in the image are marked as target pixels if their value is greater than some threshold value; otherwise they are marked as background pixels. A tolerance value is typically used so that values close to the selected threshold will also be selected. The resulting segmentation is a binary image with all target pixels given a value of 1, and all other (background) pixels given a value of 0.

A common technique for choosing a threshold value is to select a local minimum from a histogram of the image pixel intensities. Figure 4.2 is an example of the results that can be obtained; in this case the isodata algorithm (Ridler and Calvard 1978) has been used to determine a threshold. The problem is that the boundary between two tissue types often overlaps, and is often referred to as the partial volume effect. In such cases a local minimum may not be detectable in the histogram. More sophisticated techniques have been developed; for example, Otsu (1979) maximizes the separation between different threshold classes in the data, based on an initial guess of the thresholds.

Thresholding is often combined with a connected component analysis (CCA) step. The binary image is scanned pixel-by-pixel from top to bottom and left to right to identify and label connected pixel regions. Once a tissue type has been labelled, the process can be repeated by generating a new binary image using a threshold value for another tissue type.

In 3D, an isosurface algorithm can be applied to the raw image data, or preferably to segmented data. Using a particular threshold value, a surface can be extracted using, for example, the well-known marching cubes algorithm (Lorensen and Cline 1987). Isosurfacing is usually carried out after one of the more sophisticated segmentation techniques described below has been applied.

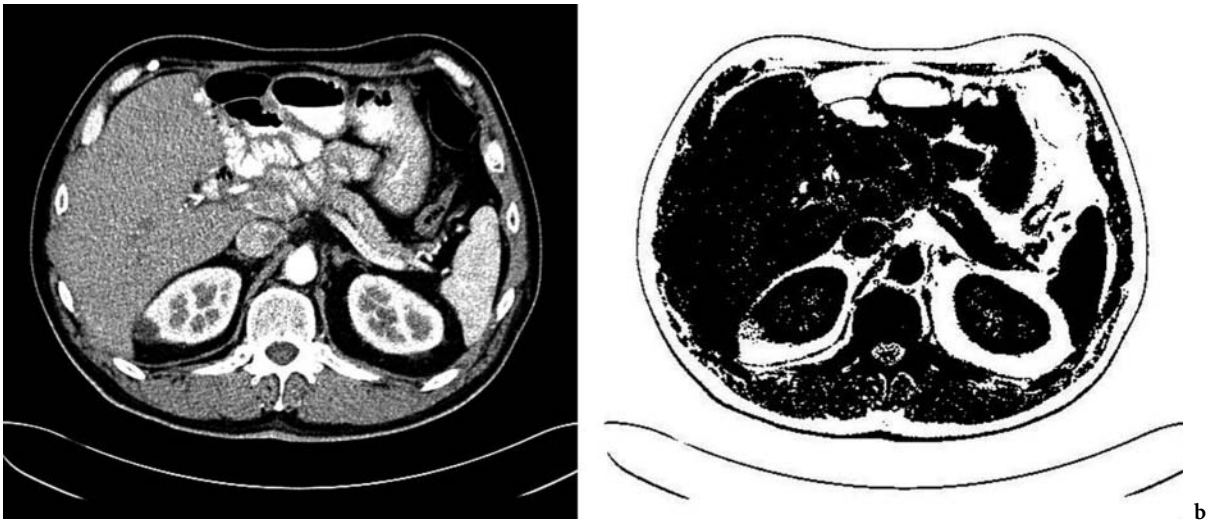

a b

Fig. 4.2. a Original CT image. **b** Threshold-based segmentation applied to the whole image. Produced using the ImageJ image processing and analysis software

4.4 Edge-Based Segmentation

Edge-based segmentation techniques rely on discontinuities in the image data at the border of the target structure, as typically the pixel values change rapidly at the boundary between two regions. The basic method here is to apply a gradient operator such as the Sobel (see Fig. 4.3) or the Roberts filter to detect edges in the image. High values of the filter provide candidates for region boundaries, which must then be modified to produce closed curves representing the boundaries between regions. Converting the edge pixel candidates to boundaries of the regions of interest is a difficult task, however.

As with previous methods, an edge-based segmentation is applicable to a 2D image. For the segmentation of 3D volume data sets, the interactive generation of the target structure has to be applied to each slice of the volume. Note also that some techniques have been extended to operate in 3D (see Section 4.4.1, for example).

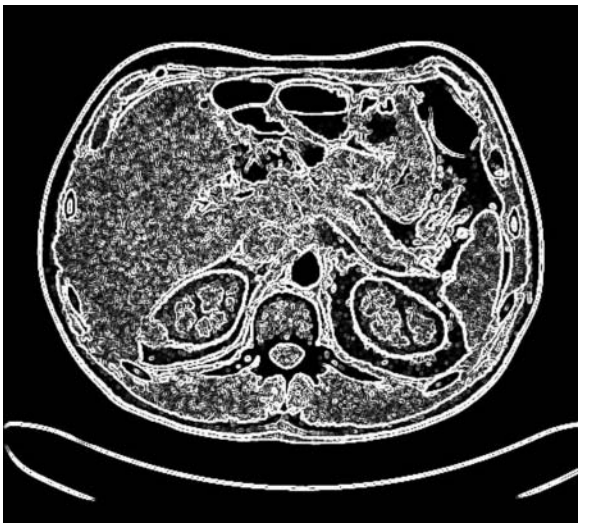

Fig. 4.3. Applying the Sobel filter to the CT image in Figure 4.2a. Two 3×3 convolution kernels have been used to generate vertical and horizontal derivatives. These are combined using the square root of the sum of the squares to produce the final image. Image produced using ImageJ

4.4.1 Live-wire

Live-wire (Barret and Mortensen 1997), also called intelligent scissors (Mortensen and Barret 1995), is an edge-based segmentation technique based on the concept of intelligent contour generation. The 2D image is transferred into a weighted graph, whose vertices correspond to image pixels and whose edges connect neighbouring pixels. Edge weights are defined in terms of local cost functions. Contour extraction is achieved by the user first by selecting a seed point on the boundary of the target structure. A second boundary point on the target is then selected and a minimal cost path from the

seed to this point is computed using Dijkistra's graph search algorithms. Ideally, the path will wrap around the object boundary. If the generated path deviates from the desired boundary, then a new target point is selected nearer the seed point. Once the first path segment has been generated, the target point becomes the new seed point and the next path segment is generated. The process is repeated until the whole boundary is outlined. The resulting contour is composed of multiple minimal-cost path segments.

A 3D version of the live-wire approach using adaptive propagation has been proposed by Salah et al. (2005). The goal is to avoid repeating the interactive generation of contours for all slices, and so the target points from the initial live-wire contour are propagated to the next slice. This is a reasonable strategy, as an anatomical structure does not tend to change shape too much between slices. The propagated points will not necessarily lie exactly on the target structure's boundary, but can be assumed to be close to it. In the next step the positions of propagated points are corrected by moving each target point towards the actual boundary of the object on this slice by selecting the pixel in the neighbourhood with the largest gradient magnitude.

4.5 Region-Based Segmentation

Region-based segmentation algorithms regard the target structure as a homogeneous region that can be determined by a search process. For example, region-growing (see below) is often used for the segmentation of contrast-enhanced vascular structures from CT or MR angiography data (Selle et al. 2002).

The first region-based method devised was the split and merge algorithm (Horowitz and Pavlidis 1974), which starts from the initial assumption that the entire image is a single region, and then determines if the homogeneity criterion is satisfied. If not, then the square region is divided into four smaller regions and the process is repeated on each of the subregions until no further subdivision is necessary. The resulting small regions are then compared and merged if they are similar to give larger irregular regions.

4.5.1 Region Growing from Seed Points

The use of seed points has been suggested by Adams and Bischof (1994) and others. The clinician identifies one or more seed points within the target structure, often by using a mouse click. A homogeneous region is then grown around the seed point(s) with neighbouring pixels (or voxels in 3D) with similar intensities being iteratively added to the region. Region-growing algorithms vary depending on the criteria used to decide whether a pixel should be included in the region or not, the connectivity used to determine neighbours and the strategy used to visit neighbours. The criterion of homogeneity is often based on a connected threshold, i.e. collect all neighbours with intensity lower than or equal to the seed point's intensity and above a threshold. The threshold selection is usually a trial-and-error process: the segmentation is started with a certain threshold and then modified until the desired result is achieved. An alternative is to use confidence connectivity, in which the mean and standard deviation of the pixels currently in the region are calculated. The standard deviation is multiplied by a user-provided scale factor that defines a range around the mean. All neighbouring pixels whose intensity values fall inside this range are then included in the region. The mean and standard deviation of the intensity levels of the new region are then computed and the process repeated until the maximum number of iterations is reached.

For certain image modalities, automated seed selection is also possible. For example, Adams and Bischof (1994) discuss the use of the converging squares algorithm (O'Gorman and Sanderson 1984) to identify the seed points in human chest X-ray images. Another approach is discussed in section 4.8. Note that there are also situations where region-growing cannot reliably discriminate between adjacent structures. In such cases it is necessary to provide additional interaction facilities. For example, the user may specify a direction of the growing process or specify barriers that should stop the region growing into a particular area.

4.5.2 Watershed

Watershed segmentation (Digabel and Lantuejoul 1978) is also a region-based method. The analogy for

this algorithm is to imagine a stream of water running into a landscape topology and flowing with gravity to collect in low basins. The water level in the basins will grow until they spill into one another, causing small basins to merge together into larger basins. In the image domain, data may be interpreted as a topographic surface where the intensity levels represent altitudes. Regions (called catchment basins) are formed by using local geometric structure to associate points in the image domain with local extrema in some feature measurement such as curvature or gradient magnitude. The catchment basins correspond to the homogeneous grey level regions of the image, i.e. all pixels belonging to the same catchment basin are connected with the basin's region of minimum altitude (grey level) by a simple path of pixels that have monotonically decreasing altitude (grey level) along the path. In 3D data sets the voxel values are regarded as height. Watershed lines divide individual catchment basins. Vincent and Soille (1991) were the first to implement a practical version of watershed segmentation. Their algorithm is based on sorting the pixels in increasing order of their grey values, followed by a flooding step consisting of a fast breadth-first scanning of all pixels in the order of their grey levels.

The watershed technique is less sensitive to user-defined thresholds than classic region-growing methods, and can be suitable if the clinician wants to register together segmented features from different data sets. It also offers more flexibility as it produces a hierarchy of segmentations from which a single region or set of regions can be extracted *a priori* using a threshold, or interactively with the help of a graphical user interface. In practice, however, the watershed algorithm often produces over-segmentation due to noise or local irregularities in the gradient image. Applying image blur as a pre-processing step to smooth the image (e.g. replace each pixel with the average of its neighbourhood) can help (see Fig. 4.4). A better method is to allow the user to place markers to specify locations that belong to the target structure (include points), or do not belong the target structure (exclude points). An additional watershed is constructed at the maximum level between these include and exclude regions, thus preventing them from being merged.

4.6 Deformable Models

Deformable models apply prior knowledge of geometry, physics, and approximation theory to solving the segmentation problem. They are capable of accommodating the variability of biologi-

a b

Fig. 4.4a,b. Applying watershed segmentation to the CT image from Figure 4.2a. **a** Shows catchment basins. **b** A smoothing filter (averaging the 3 × 3 neighbourhood of each pixel) is applied before the watershed. Images produced using the watershed plug-in for ImageJ (Sage 2005)

cal structures over time and across different individuals. This section focuses on two approaches – level sets and active contours. McInerney and Terzopulos (2000) provide a wider discussion of deformable model methods used in medical imaging.

4.6.1 Level Sets

The level set is a numerical method for tracking the evolution of contours and surfaces introduced by Osher and Sethian (1988). Instead of manipulating the contour directly, it is embedded as the zero level set of a higher dimensional function called the level set function. The level set function is then evolved under the control of a differential equation. At any time, the evolving contour can be obtained by extracting the zero level set from the output. The level set method makes it very easy to follow shapes that change topology, for example when a shape splits in two, or develops holes. Level sets can be used for image segmentation by using image-based features such as mean intensity, gradient and edges in the governing differential equation. In a typical approach, a contour is initialised by a user and is then evolved until it fits the form of an anatomical structure in the image.

The related fast marching methods (Sethian 1999) have also been applied to image segmentation. These methods are faster, but are designed for problems in which the speed function never changes sign, so that the front is always moving forward or backward.

4.6.2 Active Contours

Active contours (or snakes) is a popular segmentation method that uses the idea of energy minimizing splines (Kass et al. 1988). An initial contour is defined by a set of control points supplied either by the user, or derived from prior knowledge of the data or geometric constraints. The active contouring algorithm then attempts to minimise the snake's energy by weighting several internal and external energies. For example, starting with a contour around the target object, the contour moves toward its interior normal and has to stop on the boundary of the target. Snake evolution is determined by the sum of different types of velocities that act on each point of the snake in the direction perpendicular to the snake. Some of these velocities are image-dependent, while others depend on the shape of the snake. The image-dependent velocities are defined in terms of the image feature, to which they are proportional. This is typically based either on edges in the input image, or on regions of uniform intensity. Methods have also been described that use level sets in determining the snake evolution (Malladi et al. 1993; Chan and Vese 2001). Three types of velocities calculated are:

1. Image-dependent propagation velocity. In a homogeneous region of the image, the propagation velocity is constant and causes the snake to expand (or contract) at a uniform speed.
2. Shape-dependent curvature velocity. The effect of curvature velocity is to slow down the snake evolution at places of high curvature, effectively smoothing out the sharp corners that may otherwise be formed.
3. Image-dependent advection velocity (only used with the edge features). This is defined by the dot product of the unit vector perpendicular to the snake and the gradient vector of the image feature. It causes the snake to slow down or stop as it approaches edges.

These velocity types can be weighted according to the segmentation problem. The movement of a point on the snake is determined by the sum of the velocities at that point. The process iterates until the energy minimisation criterion in the image is reached, and segmentation is complete.

For 3D segmentation, active contour models are applied slice by slice. As with live-wire segmentation, adaptive progression takes the fitted contour in one slice as the initial contour in neighbouring slices (Lin and Chen 1989). This approach has been applied in Figure 4.5, which depicts segmentation of the right kidney (from the CT data set used previously) using the snake evolution support in ITK-SNAP. Active contour models have also been extended to 3D by deforming surfaces instead of contours, which is known as balloon segmentation (Terzopoulos et al. 1988). A polygonal representation of the initial shape is fitted to the target structure. The user can either select small volumes that are iteratively inflated until the forces converge, or enclosing volumes are specified by the user and iteratively deflated.

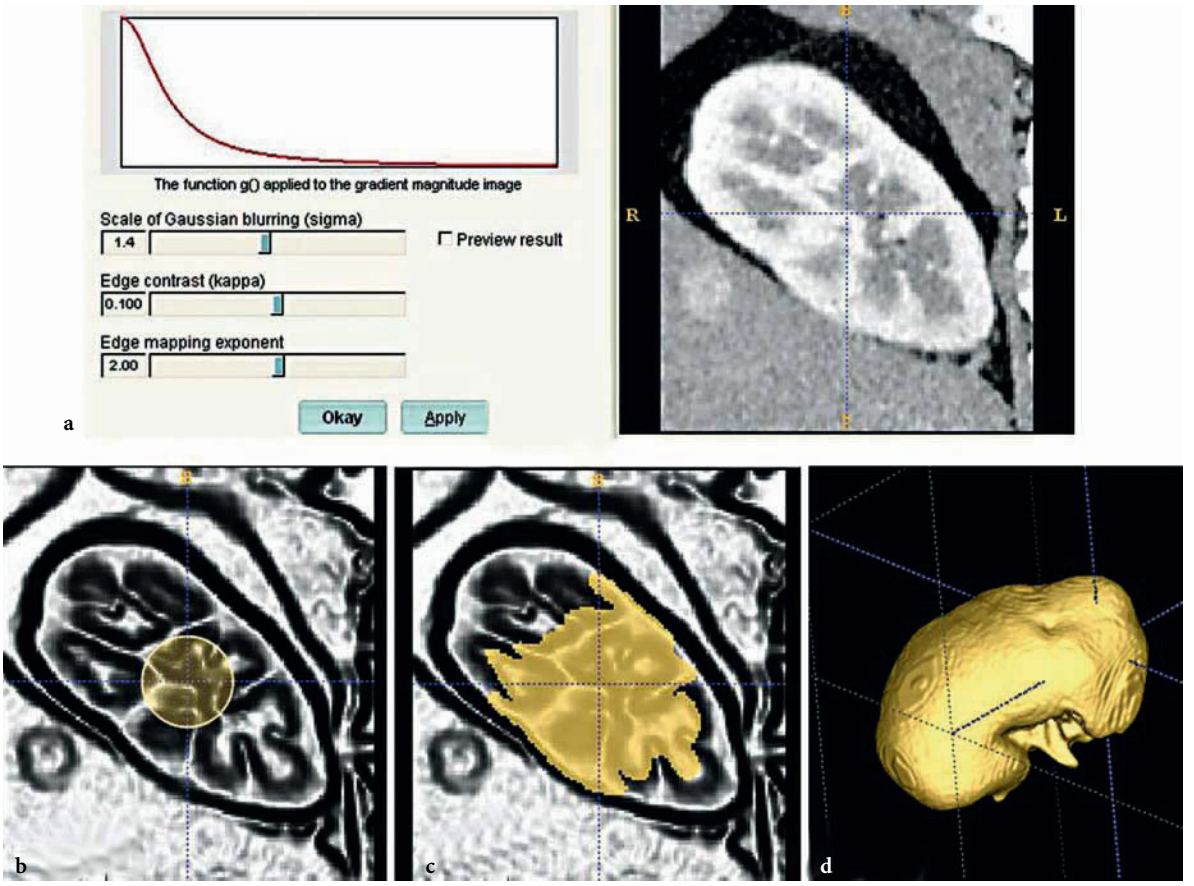

Fig. 4.5a–d. Using snakes to segment the right kidney from a region of the full 3D CT data set described in Figure 4.2.**a** The gradient magnitude of each pixel on every slice is computed in the range [0,1]. **b** Initial snake contour is defined on starting slice. In this case it is within the target structure. **c** The contour grows outwards towards the target boundary. Shown here after 280 iterations. **d** Final 3D surface of segmented kidney generated from the stack of snake contours. Images produced using ITK-SNAP

4.7 Statistical Analysis

Statistical analysis can also provide the basis for solving the segmentation problem. The topic of how statistics can be used to control region growing (Section 4.5.1) has already been discussed. This section describes three other useful approaches that have been applied to medical image segmentation.

4.7.1 Active Shape Models

Active shape models (ASMs) are statistical models of the shape of objects (represented by a set of points) that iteratively deform to fit the target structure in a new image (Cootes et al. 1993). The shapes are constrained by a statistical model to vary only in ways seen in a training set of labelled examples. ASM works by alternating the following steps:

- Look in the image around each point for a better position for that point.
- Update the model parameters for the best match to these new found positions.

To locate a better position for each point, one can either look for strong edges, or a match to a statistical model of what is expected at the point. ASMs are time-consuming to set up, and the quality of the segmentation is strongly dependent on the quality of the acquired model. For 3D segmentation, establishing correspondences between landmarks can also be challenging. Nevertheless, there are many

examples of the successful use of ASMs for medical image segmentation.

Related to the ASM is the active appearance model (AAM) (Cootes et al. 2001). This algorithm uses the difference between the current estimate of appearance and the target image to drive an optimization process. By taking advantage of least squares techniques, it can quickly match to new images. AAMs are more specialised; for example they cannot be applied to CT and MRI data simultaneously.

4.7.2 Classifiers

Classifier methods partition a feature space (in this case the image intensities) using pattern recognition techniques. A histogram is an example of a 1D feature space – all pixels at a particular intensity level are grouped into one class.

Classifiers are also known as supervised methods because they require labelled training data, e.g. collected from manual segmentation. A simple classifier is nearest-neighbour, which places each pixel in the same class as the training datum with the closest intensity. The k-nearest-neighbour classifier generalizes this approach and classifies pixels into the same class as the majority of the k-closest training data. A popular parametric classifier is the naive Bayes classifier, which is based on a probability model that incorporates strong independence assumptions that often have no bearing in reality, and hence are (deliberately) naive. In this case, the classifier assumes that the pixel intensities are independent samples from a mixture of probability distributions, usually Gaussian. Training data are collected by obtaining representative samples from each component of the mixture model and then estimating K-means[2], covariance and mixing coefficients. Classification of new data is obtained by assigning each pixel to the class with the highest posterior probability. Classifiers are relatively computationally efficient to apply, and, unlike thresholding methods, they can be applied to multi-channel images. However, in general they do not perform any spatial modelling.

[2] K-means is an algorithm to cluster objects based on attributes into k partitions. It is a variant of the expectation-maximisation algorithm in which the goal is to determine the k means of data generated from Gaussian distributions.

4.7.3 Expectation-Maximisation

Clustering algorithms are similar to classifiers, but they are unsupervised methods that perform data classification without the use of training data. In a sense, clustering methods train themselves using the available data by alternating between segmenting the image and characterizing the properties of each class. The expectation-maximization (EM) algorithm is a good example often used for data clustering. It alternates between performing an expectation (E) step, which computes an expectation of the likelihood by including the latent variables as if they were observed, and a maximization (M) step, which computes the maximum likelihood estimates of the parameters by maximising the expected likelihood found on the E step. Pokric et al. (2001) use EM in their multi-dimensional segmentation technique that takes into account the partial volumes effect at tissue boundaries. Multiple images of different modalities are used to improve segmentation, as better tissue separation can be achieved in a higher dimensional space. The parameters of the multi-dimensional model of pure tissues and their mixtures are iteratively adjusted using EM. Bayes theory is then used to generate probability maps for each segmented tissue, which estimates the most likely tissue volume fraction within each voxel. Other approaches just attempt to compute how likely a certain grey level would be generated by a particular tissue class. The values in the probability maps range from 0 to 1, and can be used for boundary location extraction (e.g. 0.5 probability point represents the boundary location between two tissues) or volume rendering.

4.8 Automatic Segmentation

All of the segmentation methods described above involve interaction from an end user. In some cases, segmentation can be a time-consuming process. A general goal is to produce accurate segmentation of medical images automatically. However, this is a challenging task and is still to be fully achieved. Some of the current approaches to this goal are discussed below.

Consider an input image and blurred versions of this image at various degrees. If these images are convolved together, it can be mathematically proven that an unambiguous hierarchy of the critical points (i.e. those of local minimum or maximum image intensities) and regions of their influence describing the image can be obtained. This allows one to automatically segment the image in a hierarchical manner without any a priori knowledge (Kuijper et al. 2003). At Bangor, technical problems encountered when applying this theory to the practical segmentation of medical images, including 3D volume data, are being resolved. For instance, a guaranteed method of finding all the critical points in an image, which is a vital component in this automatic segmentation, was recently devised. Figure 4.6 gives an example of the automatic segmentation results based on this method.

The use of artificial intelligence techniques has also been investigated for automatic segmentation. Tzeng et al. (2005) couple machine learning and a painting metaphor to allow more sophisticated classification in an intuitive (initially semi-automatic) manner. The user works in the volume data space by directly painting on sample slices of the volume, and the painted voxels are used in an iterative training process. The trained system can then classify the entire volume, and the trained system for one data set may be reused to automatically classify other data sets with similar characteristics.

Fig. 4.6. CT Image from Figure 4.2a after automatic region-growing segmentation using critical point detection to select seed points. Image courtesy of Jin Zheng, University of Wales, Bangor

4.9 Conclusions

Many approaches have been suggested for medical image segmentation. An overview of some of the more common techniques has been presented above, but there are many other variations and methods that could not be covered in the space available here. The final choice for the radiologist largely depends on the image modality being used, and often a hybrid of two or more segmentation methods will be the most effective. The ITK software even supports a hybrid segmentation engine that facilitates the combining of different boundary-based and region-based algorithms.

Other factors will also influence the future of segmentation of radiological images. The user interface, for example, will have an impact as alternatives to the keyboard and mouse become more readily available. Vidholm and Nystrom (2005) have already demonstrated how a haptic joystick can aid with the placement of seed points for 3D segmentation. Their technique is based on gradient vector flow (GVF) and allows a user to stay centred inside the target object whilst feeling the object boundaries. Preim and Bartz (2007) provide an excellent review of advanced interaction techniques for segmentation. The processing time required will also drop significantly. For example, fast segmentation using programmable graphics hardware is now becoming possible (Sherbondy et al. 2003).

Throughout this book, further examples will be given of segmentations that have been applied effectively in different imaging scenarios. The goal of this chapter has been to introduce the reader to a core set of segmentation techniques and to provide reference material for further in-depth information.

Acknowledgements

The author would like to thank Ik Soo Lim and Jin Zheng at Bangor University, for their contribution and suggestions in writing this chapter. Also to Derek Gould, Royal Liverpool University Hospitals, who supplied the data set used in the figures.

References

Abramoff MD, Magelhaesv PJ, Ram SJ (2004) Image processing with ImageJ. Biophotonics International 11:36–42

Adams R, Bischof L (1994) Seeded region growing. IEEE Trans. on Pattern Analysis and Machine Intelligence 16:641–647

Barret W, Mortensen E (1997) Interactive live-wire boundary extraction. Medical Image Analysis 1:331–341

Boissonnat JD (1988) Shape reconstruction from planar cross sections. Computer Vision, Graphics, and Image Processing 44:1–29

Chan TF, Vese LA (2001) Active contours without edges. IEEE Trans. Image Processing 10:266–277

Cootes TF, Taylor CJ, Hill A, Haslam J (1993) The use of active shape models for locating structures. In Proc. 13th International Conference on Information Processing in Medical Imaging, (Eds. H.H.Barrett, A.F.Gmitro) Springer-Verlag, pp 33–47

Cootes TF, Edwards GJ, Taylor CJ (2001) Active appearance models. IEEE Trans. on Pattern Analysis and Machine Intelligence 23:681–685

Delaunay B (1934) Sur la sphère vide, Izvestia Akademii Nauk SSSR, Otdelenie Matematicheskikh i Estestvennykh Nauk, 7:793–800

Digabel H, Lantuejoul C (1978) Iterative algorithms. In Proc. of 2nd European Symposium on Quantitative Analysis of Microstructures in Material Science, pp 85–99, Stuttgart, Riederer

Horowitz SL, Pavlidis T (1974) Picture segmentation by a directed split-and-merge procedure, Proc. 2nd Int. Joint Conf Pattern Recognit. pp 424–433

Kass M, Witkin A, Terzopoulos D (1988) Snakes: active contour models. International Journal of Computer Vision 1:321–331

Kuijper A, Florack LMJ, Viergever MA (2003) Scale space hierarchy. Journal of Mathematical Imaging and Vision 18:169–189

Lin WC, Chen SY (1989) A new surface interpolation technique for reconstructing 3D objects from serial cross-sections. Computer Vision, Graphics, and Image Processing 48:124–143

Lorensen W, Cline HE (1987) Marching cubes: a high resolution 3D surface construction algorithm. Computer Graphics (SIGGRAPH 87 Proceedings) 21:163–170

Malladi R, Sethian JA, Vemuri BC (1993) A topology independent shape modelling scheme. In Proc. SPIE Conf. Geometric Methods Computer Vision II, vol. 2031, pp 246–258

McInerney T, Terzopoulos D (2000) Deformable Models. In Handbook of Medical Imaging, Processing and Analysis, I. Bankman (ed.), Academic Press, San Diego, Ch. 8, pp 127–145

Mortensen E, Barret W (1995) Intelligent Scissors for Image Composition. In: Proc. of ACM SIGGRAPH 1995, pp 191–198

O'Gorman L, Sanderson AC (1984) The converging squares algorithm: An efficient method for locating peaks in multidimensions. IEEE Trans. Pattern Anal. Machine Intell., vol. PAMI-6, pp 280–288

Osher S, Sethian JA (1988) Fronts propagating with curvature dependent speed: algorithms based on Hamilton-Jacobi formulations. Journal of Computational Physics 79:12–49

Otsu NA (1979) A threshold selection method from gray-level histograms. IEEE Transactions on Systems, Man, and Cybernetics 9:62–66

Pham DL, Xu C, Prince JL (2000) Current methods in medical image segmentation. Annual Review of Biomedical Engineering, Annual Reviews 2:315–337

Pokric M, Thacker NA, Scott MLJ, Jackson A (2001) The Importance of Partial Voluming in Multi-dimensional Medical Image Segmentation. In Proc. of the 4th International Conference on Medical Image Computing and Computer-Assisted Intervention, pp 1293–1294

Ridler TW, Calvard S (1978) Picture thresholding using an iterative selection method. IEEE Trans. on Systems, Man, and Cybernetics SMC-8: pp 630–632

Preim B, Bartz D (2007) Visualization in Medicine: Theory, Algorithms, and Applications, Morgan-Kaufmann

Sage D (2005) Watershed Segmentation Demonstration Web Page. Last visited August 2007. http://bigwww.epfl.ch/sage/soft/watershed/

Salah Z, Orman J, Bartz D (2005) Live-Wire Revisited. In Workshop Bildverarbeitung für die Medizin, Berlin

Selle D, Preim B, Schenk A, Peitgen H-O (2002) Analysis of vasculature for liver surgery planning. IEEE Trans. on Medical Imaging, 21:1344–1357

Sethian JA (1999) Level Set Methods and Fast Marching Methods: Evolving Interfaces in Computational Geometry, Fluid Mechanics, Computer Vision, and Materials Science (2nd ed.). Cambridge University Press

Sherbondy A, Houston M, Napel S (2003) Fast Volume Segmentation With Simultaneous Visualization Using Programmable Graphics Hardware. In Proc. IEEE Visualization 2003 (VIS'03), pp 23–30

Terzopoulos D, Witkin A, Kass M (1988) Constraints on deformable models: Recovering 3D shape and nonrigid motion. Artificial Intelligence 36:91–123

Tzeng F-Y, Lum EB, Ma K-L (2005) An intelligent system approach to higher-dimensional classification of volume data. IEEE Trans. on Visualization and Computer Graphics 11:273–284

Vidholm E, Nystrom I (2005) A haptic interaction technique for volume images based on gradient diffusion. In Proc. First Joint Eurohaptics Conference and Symposium on Haptic Interfaces for Virtual Environment and Teleoperator Systems, pp 336–341

Vincent L, Soille P (1991) Watersheds in digital spaces: an efficient algorithm based on immersion simulations. IEEE Trans. on Pattern Analysis and Machine Intelligence 13:583–598

Yoo T (ed) (2004) Insight into Images: Principles and Practice for Segmentation, Registration, and Image Analysis., A K Peters, Massachusetts

Yushkevich PA, Piven J, Hazlett HC et al (2006) User-guided 3D active contour segmentation of anatomical structures: significantly improved efficiency and reliability. Neuroimage 31:1116–28

Elaboration of the Images in the Spatial Domain. 2D Graphics

5

Paolo Marcheschi

CONTENTS

5.1 Introduction

Digital images assume a fundamental importance in the practice of radiologists or technicians. The understanding of the processes that are at the root of the digital processing allow a more acute and responsible management of the processing stream of the radiology laboratory.

P. Marcheschi, MSc
Istituto di Fisiologia Clinica, CNR, Via Moruzzi 1,
56124 Pisa, Italy

5.1.1 Digital Images and the Color Depth

A digital image can be represented by a matrix of points, called pixels or pels (acronym of Picture ElementS); this matrix is in general rectangular, but square matrices are often used in medicine. The preferred dimensions are, for instance, 256 × 256, 512 × 512, 1,024 × 1,024, and so on. Every pixel or element of this matrix is represented by a number that expresses its brightness. According to the number of bits with which such a value is represented, we can have a smaller or greater value of brightness. The number of bits with which the color of the pixel is expressed is called "color depth", and its unity of measure is the bpp (bits per pixel).

For instance, if we want to represent a maximum number of 256 (2^8) colors, the color depth will be 8 bits, and the representable values will be included among 0 and 255, or rather among 0 and (2^8–1). If we want to represent a maximum number of 65,536 gray tones (2^{16}), the color depth will be 16 bits. And the representable values will be included among 0 and 65,535, or rather among 0 and (2^{16}–1).

The radiological images produced by modern diagnostic modalities, such as CT scan or magnetic resonance imaging, have the characteristic to get an elevated color depth, in that case we have no color on, but we speak of gray levels, and the value of the pixel is related to the value of brightness of the pixel. In this case: 0 is black, or absence of brightness; 2^n–1 is the white or the maximum brightness.

5.1.2 Spatial Domain

Operations of digital elaboration and analysis that occur in the spatial domain are those operations that are being made in the domain belonging to pixels of the matrix that constitutes the image. These operate directly on the pixels and therefore on their value.

A way of representing an image matrix is to characterize it through a function f of the coordinates x and y in such a way that $f(x, y)$ is the value of gray levels at the point of the coordinates (x, y).

The coordinates system used in the field of the digital image processing (Jahne 1995) is represented in Figure 5.1. This particular coordinate system is inverted in comparison with the usual Cartesian coordinate system we are used to working with. The origin of the axis is situated in the upper left corner.

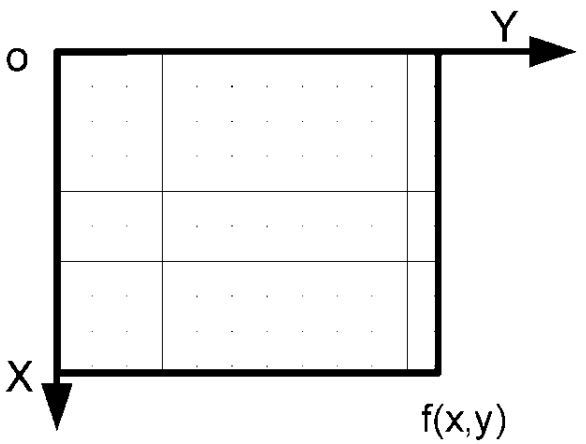

Fig. 5.1. Image coordinate system

In general any operation applied to a digital image $f(x, y)$ produces in turn a resulting digital image $g(x, y)$. If we denote with T the operator applied to first digital image, we can write:

$$g(x, y) = T[f(x, y)]$$

In most cases, T is an operator defined in the neighborhood of the point defined by (x, y), and it can operate also on more than one image, as in the case of the subtraction operator known in radiology as DSA (digital subtraction angiography) (Kirbas and Quek 2004). In this particular case we have:

$$T[f(x\,y), g(x, y)]=f(x, y)-g(x, y)$$

5.2 Image Operation Classification

Image operation and elaboration can be divided into three main classes:

- Punctual
  We define as punctual an operation that is applied to a single pixel via a mathematical function $g(v)$ where v is the brightness value of the pixel. Examples of such operations are the inverter or negative image, the windowing, and the LUT (Look Up Table) operation.
- Local
  A local operation computes a pixel value on behalf of the value of the same pixel and its neighborhood; an example is the convolution operation, or the mask filtering.
- Global
  Global is an operation applied to the whole image. Examples are histogram based operations.

5.2.1 Punctual Operations

5.2.1.1 Negative Image or Inverter

Among the punctual operations used in radiological field, one of the simplest and most used is the negative image or inverter. It allows us to underline particular white or gray details in very dark zones. This simple operation can be applied using a simple formula to every single pixel in the image. For an image with a color depth of 8 bits, the negative image can be applied subtracting from 255 the value of the intensity of the shade of gray of the pixel. It can be described by:

$$s=255-r$$

s is the value of the shade of gray in the negative image, and r is the value of the shade of gray of the pixel in the original image. This is the equation of a line with a slope of –45 degrees as shown in Figure 5.2. It is also possible to use the inverter on a small section of the brightness range giving the possibility to explore dark or saturated portion of the image.

5.2.2 Digital Subtraction of Images

The digital subtraction is a very important technique, among the image math techniques, especially in radiology where this technique is used for the

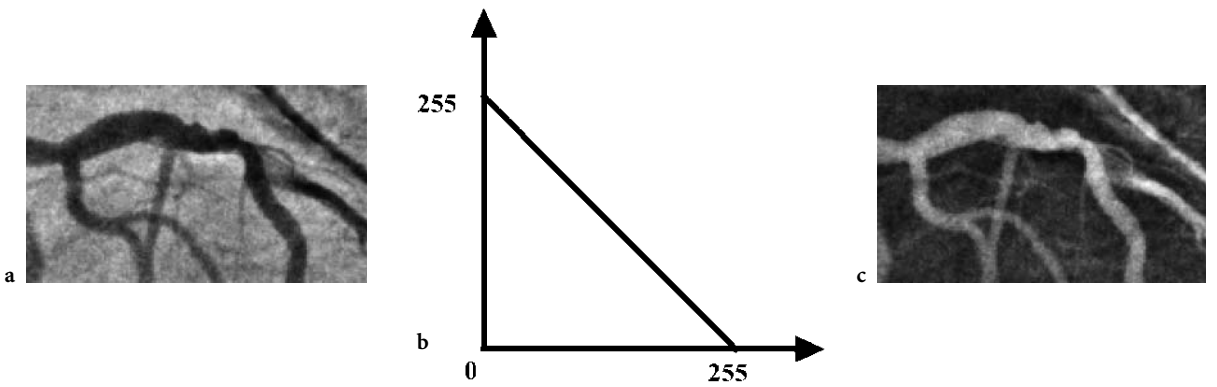

Fig. 5.2a–c. Example of inverter filter application: **a** original image, **b** inverter function, **c** result image

recognition of particular vascular structures. In this case, it is called DSA (Erik et al. 1999) (digital subtraction angiography).

Given two images, *f(x, y)* and *g(x, y)*, their difference can be expressed as:

$$e(x, y) = f(x, y) - g(x, y)$$

It is calculated associating to every pixel of *e(x, y)* the difference among the corresponding couples of *f(x, y)* and *g(x, y)*.

Such a method is used also to appraise the differences among two or more images and the errors we get after a lossy compression of an image.

A problem that arises in the execution of this transformation is the generation of negative values of brightness that cannot exist. To obviate this problem a simple algorithm can be used. If we indicate with L the maximum number of levels of shades of gray, and we add $L-1$ to every value of the pixel, and we divide it by 2:

$$\left[\frac{(x+L-1)}{2}\right],$$

the final range is guaranteed between 0 and $L-1$.

Another method involves the shifting of all values of the resulting image by the most negative value. This makes all values positive, but possibly out of range; to restrict the values to the right range we have to multiply each of them for

$$\frac{(L-1)}{Max},$$

indicating with *Max* the maximum value obtained by the first operation.

5.2.3 Window/Level

One of the most important characteristics, and at the same time little known, of radiological images is the elevated range of the gray levels that every pixel can assume. A CT or MR scan image has, for instance, a 16-bit color depth. The human eye has an important limitation on the ability to distinguish different levels of gray, while it can distinguish thousands of colors. A trained eye can distinguish from 50 to 100 tones of different gray levels. This observation allows us to understand how it is impossible for the human eye to be able to interpret correctly the full range gray levels present in a radiological image that potentially contains 65,536 levels of gray.

To obviate this problem there are various methods, one of which is to apply some LUTs (Look Up Table) so that it is possible to exploit the greatest range of distinguishable colors by the human eye. Another solution is to use a windowing transformation, which allows us to tighten the window of visualization in a more opportune range.

Windowing or Window/Level (W/L) transforms the original image with 16-bit color depth to an 8-bit color depth enhancing the contrast and at the same time redistributing the chosen window levels to the full 8-bit range.

This filter can be applied defining a window W and a level L centered in the middle of the window, as shown in Figure 5.3. In abscissa we put the shades of gray values belonging to the original image and in the ordinates the shades of gray values belonging to the resulting image, the one that will be represented on the output device, the monitor.

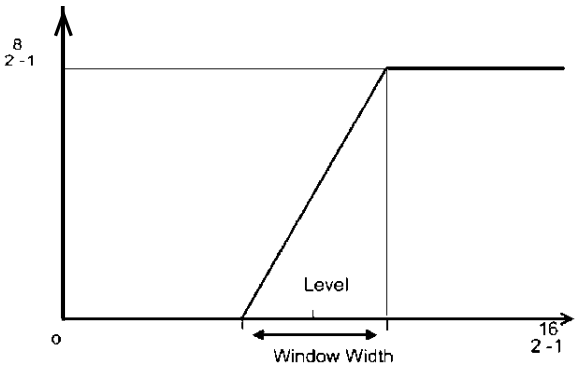

Fig. 5.3. Window/level filter

The window/level filter turns all the values fewer than

$$L-\frac{W}{2}$$

to black (0 value) and all the values greater than

$$L+\frac{W}{2}$$

to white (255 value). The values in the W range are projected on the ordinates following the filter. Thanks to the slope of the line we can increase the contrast in the resulting image; the narrowest window W is the better contrast we have in the resulting image.

CT image pixel values are often negative because they are in Hounsfield (1980) units or Hounsfield scale, which is a quantitative scale for describing radio density. The radio density of distilled water at standard pressure and temperature (STP) is defined as zero Hounsfield units (HU). The radio density of air at STP is defined as -1,000 HU. Other important HUs are fat: -50, soft tissue such as muscle: + 40, calculus: + 100 to + 400 and bone: + 1,000. The range of possible values is -1,000 to +1,000.

5.3 Threshold

The threshold operation allows us to identify structures of interest that reasonably have a uniform brightness level, in general in an interval also known as the threshold range.

This type of operation is the base of numerous elaboration techniques including three-dimensional surface reconstruction and volume rendering. The brightness therefore is a characteristic that helps to segment and to underline an object taking into account the complete image.

If, for instance, an object is white on a black background, it is simple to extract the object isolating all the white values, applying a simple threshold filter. Reality is more complex, and in radiological images, the object to be underlined is composed of a large number of different gray levels, so the background of objects is usually not uniform.

It is necessary in these cases to apply more sophisticated elaborations that allow us to see if a particular pixel belongs to the object of interest or not. This kind of operation therefore is called segmentation and produces a binary image often called the image mask. If a pixel has a value of 1, it belongs to the object of interest; otherwise the pixel assumes a value of 0.

5.3.1 Contrast Stretching

This one is another simple linear transformation that is useful to improve the dynamic range of images having low contrast. Every time the desired result is to enhance the contrast between two adjacent pixels, it is possible to use this technique. This operation is known also as normalization. It applies a scaling function to all the pixels present in the image.

If we consider an 8-bit image, we have the lowest value of 0 and the maximum value of 255; these are the values to which we want to stretch the pixel intensity. In general we have I_{min} and I_{max} (0 and 255, respectively, in this example). After that, we have to scan all pixels in the image and compute the lowest and the highest assumed value of the pixel; we call them V_{min} and V_{min}. In order to apply the contrast stretching operation, we apply the following formula to each pixel P_i obtaining P_o:

$$P_o=(P_i-V_{min})\left(\frac{I_{max}-I_{min}}{V_{max}-V_{min}}\right)+I_{min}$$

P_o is the resulting scaled pixel.

5.3.2 Logarithm Operator

The logarithm operator is used to compress the dynamic range of the image. It simply replaces the

value of each pixel with its logarithm. The formula most in use is:

$$P_o = \frac{I_{max}}{\log(1+V_{\max})} \log(1+P_i) I_{min}$$

where I_{max}, V_{max}, P_o and P_i have the same meaning as in the contrast stretching operator. We can use different bases for the logarithm operator.

5.3.3 Exponential Operator

The exponential operator is complementary to the logarithmic operator and is used to enhance the dynamic range of the image. It replaces the value of each pixel with its exponential value:

$$P_o = k b^{P_i}$$

where k is a constant and b is the exponential base.

There are several variations on this kind of operation, for example, the "raise to power" operation:

$$P_o = k P_i^n$$

where n is the power and k is a multiplicative constant.

This kind of operator is useful in all those applications where we want to manipulate the contrast of an image in a full automatic way, choosing only the values of some constants.

5.4 Local Operations

5.4.1 Convolution

The basis for the filtering operation is the convolution operator; to introduce this operation we have to define a $K \times K$ matrix known as the kernel or mask:

$$w_{i,j} = \begin{bmatrix} w_{11} & w_{12} & \cdots & w_{1k} \\ w_{21} & & & w_{2k} \\ \vdots & & & \vdots \\ w_{k1} & w_{k2} & \cdots & w_{kk} \end{bmatrix}$$

$$f_{i,j} = \begin{bmatrix} f_{11} & f_{12} & \cdots & f_{1k} \\ f_{21} & & & f_{2k} \\ \vdots & & & \vdots \\ f_{k1} & f_{k2} & \cdots & f_{kk} \end{bmatrix}$$

$w_{i,j}$ are the elements of the kernel and f_{mn} the values of the image with $M \times N$ dimension.

$$g_{m,n} = f_{m,n} \times w_{i,j}$$

The result of this operation of spatial convolution is another image whose dimension is equal to the sum of the dimensions of the kernel and the original image, but only the central part of the resulting image is considered in order to obtain an image of the original dimension.

Usually the kernel is normalized; hence the sum of the kernel's elements is unitary. The convolution filter is the basis for numerous image processing filters and gives the way to multiply pixel values from an image with a kernel matrix that represents our filter. With a 3×3 kernel matrix, this complex operation reduces to a much simpler one, and this is the one that it is used for general purpose image processing.

5.4.2 Smoothing Filter or Low-Pass Filter

The smoothing filter can decrease image noise, and thanks to this characteristic it is usually employed in radiology. It is defined by:

$$w_{i,j} = \frac{1}{K^2} \forall_{i,j}$$

For example, a smoothing filter with a 3×3 kernel ($k=3$) is:

$$\frac{1}{9} \begin{bmatrix} 1 & 1 & 1 \\ 1 & 1 & 1 \\ 1 & 1 & 1 \end{bmatrix}$$

This is the classic operation of the moving average. It replaces the pixel of the image with the average of the pixel in the neighborhood. This kind of filter is used to remove noise from an image; the name indicates that the high spatial frequencies in the image are removed, and only low frequencies remain.

The high frequencies in an image correspond to well-defined edges and to noise; in fact high fre-

quency in the spatial domain is equivalent to a rapid change in the brightness of two or more adjacent pixels. This rapid change is a big difference in the value of the shade of gray associated with the pixel.

These rapid changes not only are noise, but also edges. Edges are very important in medical images, because they correspond to contours. Hence the application of a low-pass is useful for removing noise, but the drawback is that it blurs the image as shown in Figure 5.4.

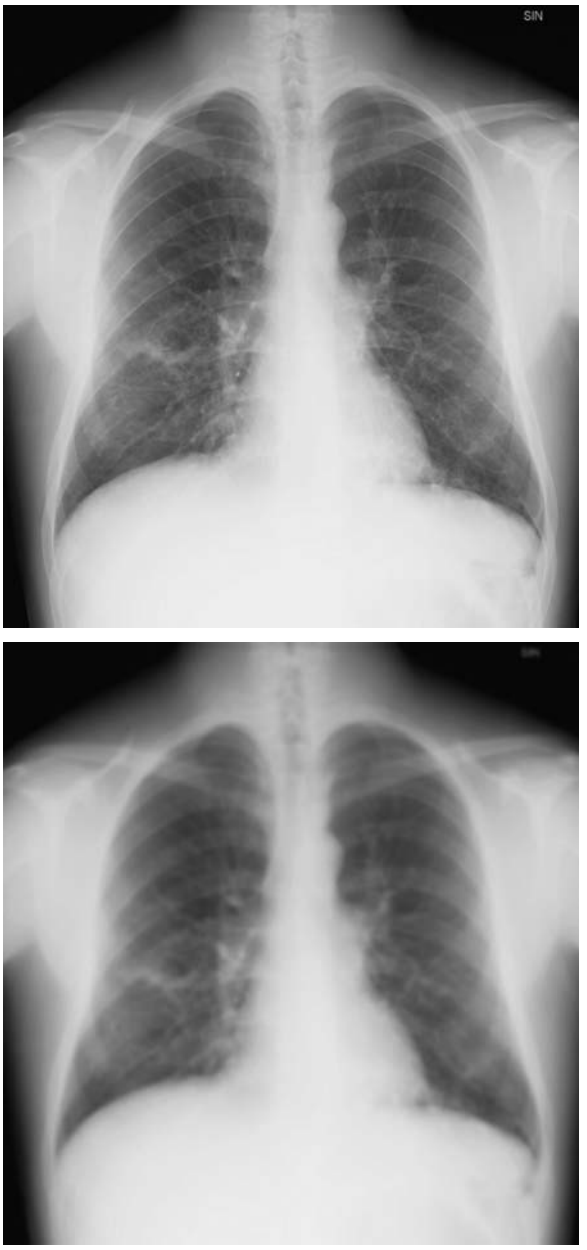

a

b

Fig. 5.4a,b. Low-pass filter application: **a** original image, **b** filtered image

The low-pass filter can be seen in highly lossy compressed images; these kinds of images are used often in radiology tele-consultation where they can be transmitted between a remote workstation and a central reviewing hospital or facility. In these occasions it must be noticed that high compression techniques can interfere with correct interpretation of pathologies because of the blurring effect of lossy compression.

5.4.3 Gaussian Filter

Another kind of filter dedicated especially to noise removal is the Gaussian filter (Bovik 2000), where the kernel is a discrete bi-dimensional Gaussian. For example:

$$\frac{1}{16}\begin{bmatrix} 1 & 2 & 1 \\ 1 & 4 & 2 \\ 1 & 2 & 1 \end{bmatrix}$$

For the Gaussian filter, the central value of the kernel is the biggest, and the weights of the other elements are inversely proportional to the distance from the center of the matrix. Matrices whose values are fractional are not used, since their computation is inefficient; for this reason it is preferred to put the fractional term in evidence. Another and more complex example of the Gaussian filter is the following:

$$\frac{1}{256}\begin{bmatrix} 0 & 0 & 1 & 1 & 1 & 1 & 1 & 0 & 0 \\ 0 & 1 & 2 & 3 & 3 & 3 & 2 & 1 & 0 \\ 1 & 2 & 3 & 6 & 7 & 6 & 3 & 2 & 1 \\ 1 & 3 & 6 & 9 & 11 & 9 & 6 & 3 & 1 \\ 1 & 3 & 7 & 11 & 12 & 11 & 7 & 3 & 1 \\ 1 & 3 & 6 & 9 & 11 & 9 & 6 & 3 & 1 \\ 1 & 2 & 3 & 6 & 7 & 6 & 3 & 2 & 1 \\ 0 & 1 & 2 & 3 & 3 & 3 & 2 & 1 & 0 \\ 0 & 0 & 1 & 1 & 1 & 1 & 1 & 0 & 0 \end{bmatrix}$$

A strategy used for the creation of this kind of mask is to give a greater weight to the central point of the mask, giving, in this way, a greater importance to the central point in comparison with the others. In the operation of the average, such a stratagem is used to reduce the blurring feeling of the image. It should be noticed that the denominator of the multiplicative factor is equal to the sum of the coefficients of the matrix so the matrix is normalized.

5.4.4 Gradient Operator

The convolution filter with the mask can also be used to find contours inside an image; this operator is widely used in radiological imaging due to the subsequent elaboration it supports, such as volumetric and surface post processing. It is the first step to contours detection; in simple words, it helps the detection of contours by isolating the part of the image that represents an edge, a part of the image where luminosity changes rapidly. In digital images these parts are effectively detected by subtracting each pixel value with the one next to it along the x or y directions. A map of these differences is the output of a gradient operator.

This kind of operator is in general dependent on the viewpoint, and multiple operations from different viewpoints are often merged in order to achieve better effectiveness.

Practically, we can use Roberts (1965) cross convolution masks:

$$G_x = \begin{bmatrix} +1 & 0 \\ 0 & -1 \end{bmatrix}$$

$$G_y = \begin{bmatrix} -1 & 0 \\ 0 & +1 \end{bmatrix}$$

Or the Sobel (Pingle 1969), convolution masks:

$$G_x = \begin{bmatrix} -1 & 0 & +1 \\ -2 & 0 & +2 \\ -1 & 0 & +1 \end{bmatrix}$$

$$G_y = \begin{bmatrix} +1 & +2 & +1 \\ 0 & 0 & 0 \\ -1 & -2 & -1 \end{bmatrix}$$

In most cases all these operations are computed with analysis in the frequency space (Pratt 2001). This subject is frequently skipped because of the difficulties in math formulas or in math in general. But spatial domain and frequency domain are linked, and every operation that can be made in spatial domain with an augmented difficulty and with more computational resources can be made easily in the frequency domain. The word "filter" comes from the frequency world and is one of the common operations done in image or signal analysis. One of the common operations done in the frequency domain is the compression of images; this aspect has lately returned to the footlight thanks to the need of radiologic tele-consultation and tele-medicine. One of the most common algorithms for lossy compression of images, JPEG, is based on removal of the high spatial frequency area in image. This is done with the aid of another frequency transformation derived from Fourier, the DCT (discrete cosine transform) preferred for the ability to better approximate a linear signal with a low number of coefficients. In Figure 5.5 we can see the result of a gradient filter.

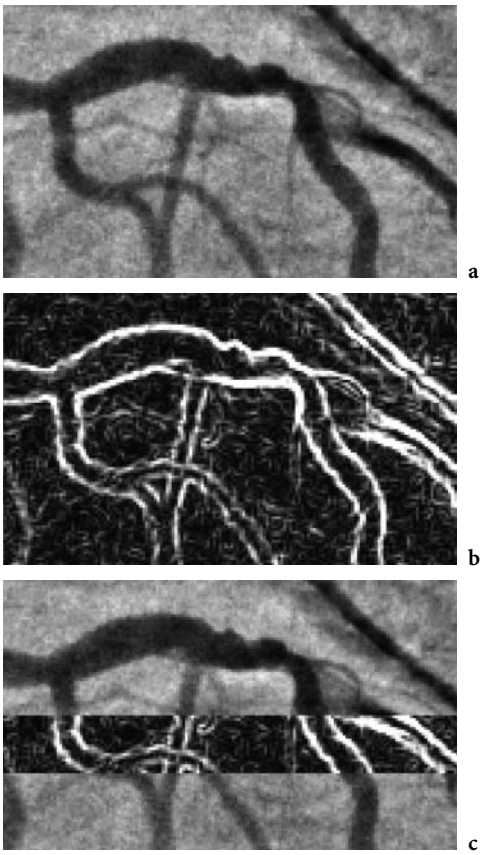

Fig. 5.5a–c. Example of application of gradient filter. **a** Original image, **b** filtered image, **c** gradient applied to a portion of image

5.5 Global Operations

5.5.1 Histogram

With this operation we denote the distribution of gray levels in an image. It can be applied to every

digital image, and it shows in a graphic plot the distribution of the number of pixels with a certain shade of gray by the levels of gray present in the gray scale of the image.

The histogram of a digital image is a discreet function $h(r_k) = n_k$ of the shades of gray r_k. r_k is the shade of gray, and n_k is the total number of pixels that in the image assumes that particular shade of gray. Commonly this function is being normalized in comparison to the total number n of the pixels present in the image. In this case the normalized histogram

$$p(r_k) = \frac{n_k}{n}$$

gives the probability to have that level r_k of gray inside the image.

Hence, in order to visualize this function, we put the values of shades of gray r_k on the horizontal axis, and the probability to have that level r_k of gray inside the image on the vertical axis as represented in Figure 5.6.

5.5.2 Histogram Equalization

One of the most common operations done with the histogram is the histogram equalization; it consists in the spreading of the various gray levels inside the full range of values in order to show more details. We can notice from Figure 5.6 that not all the possible values are used; only a restricted range of levels are present with positive probability. Hence histogram equalization permits to distribute the probability to have the level r_k of gray across all possible gray levels. In Figure 5.7 we show the original image with its histogram and the result image after the equalization process, with its correspondent histogram. This is a lossy transformation; in fact pixels that had different values had the same value in the transformed image, while levels are spread and the histogram presents several gaps in its structure.

5.5.3 A More Complex Example

Figure 5.8 shows a digital angiography image and the correspondent histogram in Figure 5.9. This kind of image has a high contrast due to the radio-opaque contrast media injected in the coronary artery tree of the human heart. To be able to perform elaborations on this sort of images the digital subtraction angiography (DSA) filter should be used in order to remove the presence of background artifacts (see Figure 5.10).

We can see that after the DSA operation the background has a better uniformity, and the coronary tree has a better contrast relative to the original image. The application of DSA to cardiac angiography imaging is rarely used because it needs a heart beat synchronization. In fact the heart is moving and twisting during the heart beat, and this motion

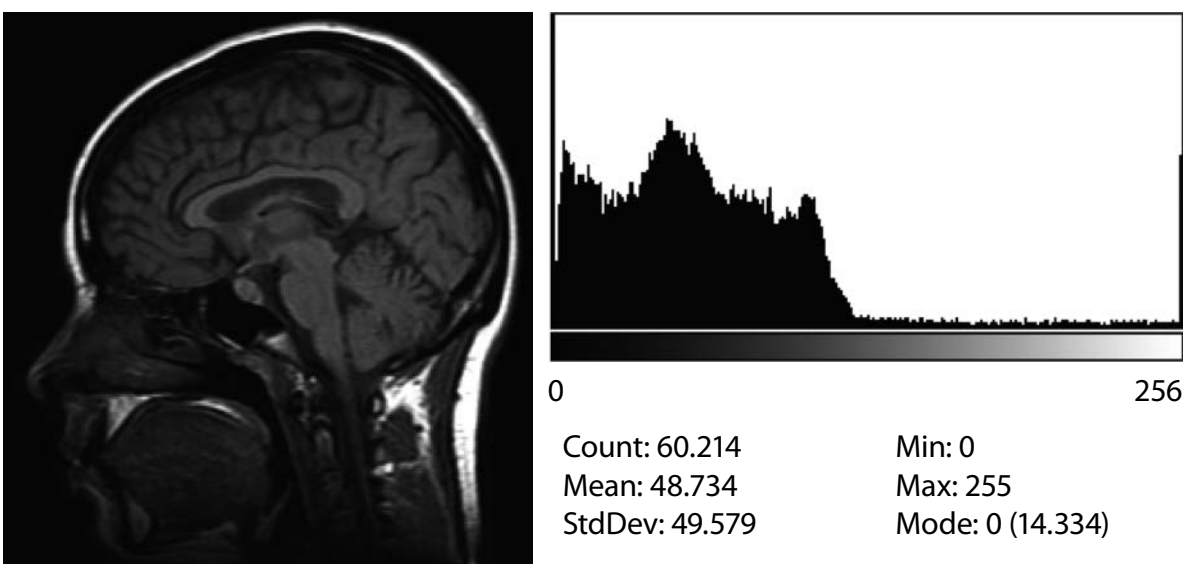

Fig. 5.6. Histogram of MR scan calculated with Image J Program (Abramoff et al. 2004)

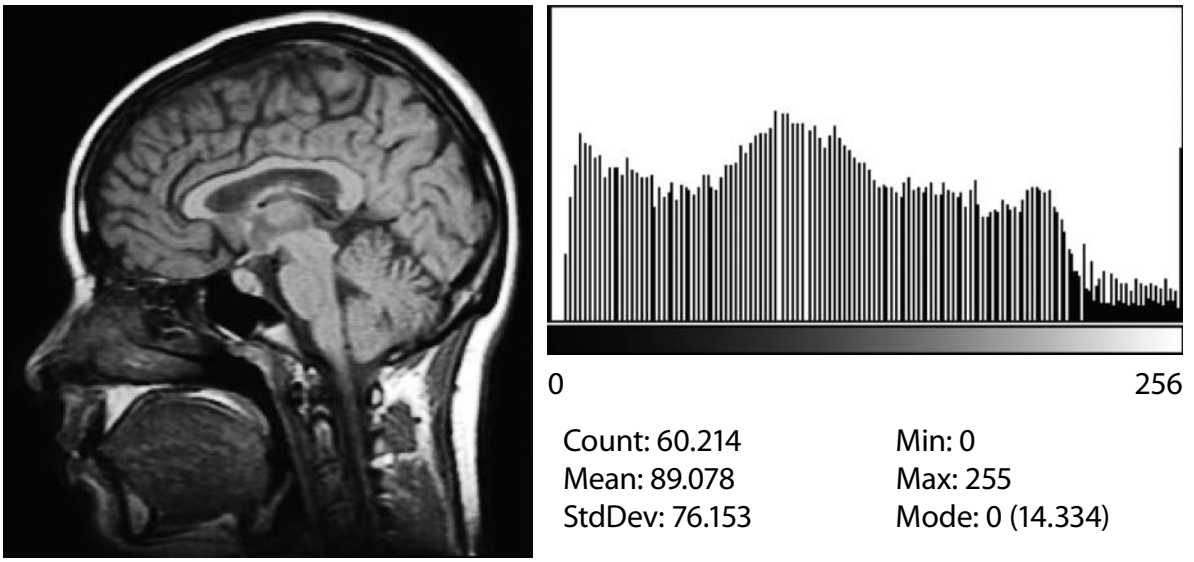

Fig. 5.7. Histogram equalization of MR image

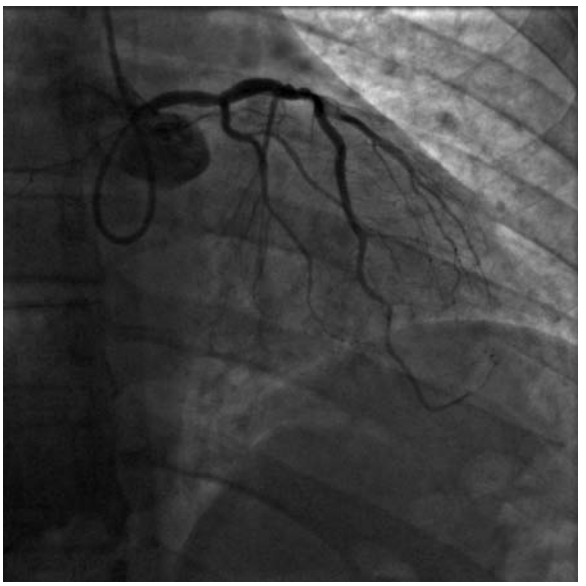

Fig. 5.8. Digital cardiac angiography image

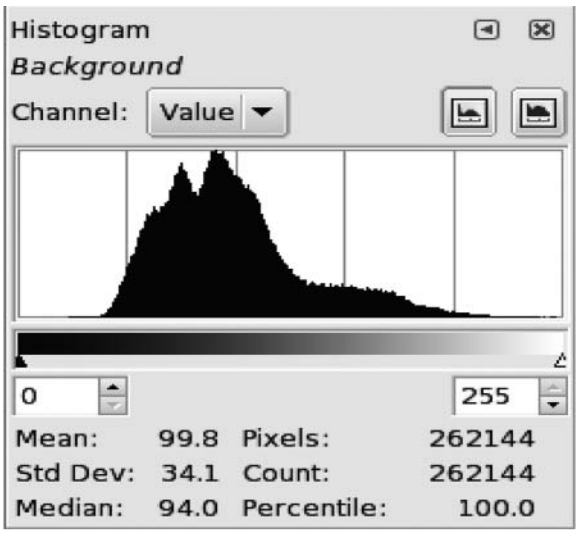

Fig. 5.9. Histogram created with GIMP (Bunks 2000)

creates a lot of artifacts. To correct this behavior, it is possible to record images belonging to an entire cycle of heart beat, without any contrast injection. After that, these images are subtracted one by one from the corresponding images of the loop following the ECG synchronization. This procedure assures a fine subtraction of images in the case of patient immobilization or steadiness. If a patient moves during the acquisition, there are several registration techniques (Erik 1999; Meijering et al. 1999) to correct the misalignment of successive images in the sequence.

A threshold filter can now be applied to extract the coronary artery tree. The threshold can be applied with the aid of the histogram plot, and the result is shown in Figure 5.11.

The threshold operation is chosen in an interval with a heuristic method; all the points inside this range assume the value of "1" (white) and the others the value "0" (black).

Fig. 5.10. DSA applied to cardiac angiography

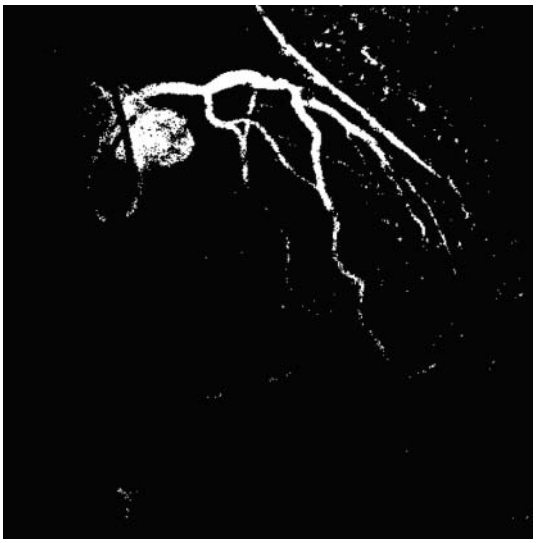

Fig. 5.11. Threshold operation on DSA image

5.5.4 Region-Based Methods

These methods can be subdivided into two classes of operators: "region growing" and "split and merge."

5.5.5 Region Growing

The technique of region growing relies on the automatic grouping of pixel regions that have a common property, for instance, groups of pixels that have the same brightness or pixels that are "similar" due to a particular property (Fig. 5.12).

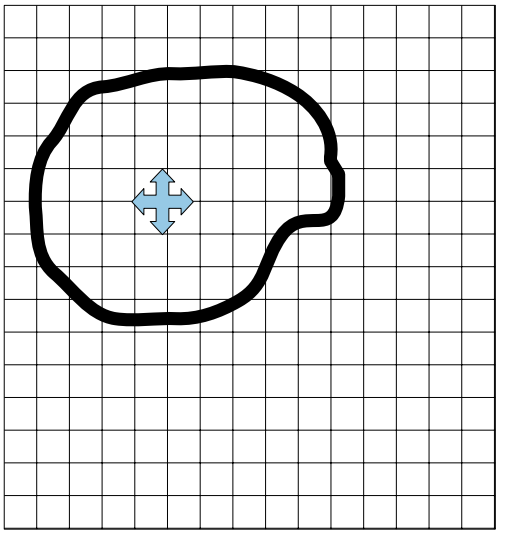

Fig. 5.12. Region growing: the seed grow from pixel to region

The first step is to choose an arbitrary "seed pixel" that is compared with adjacent pixels; after that all adjacent pixels are analyzed with a recursive pattern, and clusters regions with the same similarity property are found; when the growth of these regions cease the algorithm is stopped. This is a so-called "bottom up" method because it starts from a region inside the image and grows to the whole image.

5.6 Region Splitting

This method is the opposite of region growing and is also called "split and merge," and the approach is based on similarity as to a certain property. Here we do not use the seed, but we consider the whole image to be divided into pieces with a similar property. The algorithm starts from the image and checks if the area under observation behaves according to the property we have fixed; if not, the area is split into equal regions, generally four. In every region the same algorithm is applied until all regions are found. The merging is applied when all regions are found in order to group adjacent similar regions. This is a so-called "top down" method because it starts from the whole image and finds regions inside.

Reference

Abramoff MD, Magelhaes PJ, Ram SJ (2004) Image processing with Image J. Biophotonics Int 11:36–42

Bunks C (2000) Grokking the GIMP. New Riders Publishing, Thousand Oaks, CA

Bovik AC (2000) Handbook of image and video processing. Bovik AC, Gibson JD, Bovik AI (eds) Academic Press, New York

Hounsfield GN (1980) Nobel award address. Computed medical imaging. Med Phys 7:283–290

Jahne B (1995) Digital image processing: concepts, algorithms, and scientific applications, 3rd edn. Springer, Berlin Heidelberg New York

Kirbas C, Quek F (2004) A review of vessel extraction techniques and algorithms. ACM Comput Surv 36:81–121

Meijering EHW, Niesssen WJ, Viergever MA (1999) Retrospective motion correction in digital subtraction angiography: a review. IEEE Trans Med Imaging 18:2–21

Meijering EHW, Zuiderveld KJ, Viergever MA (1999) Image registration for digital subtraction angiography. Int J Computer Vision 31:227–246

Pingle K (1969) Visual perception by a computer, automatic interpretation and classification of images. New York, Academic Press, pp 277–284

Pratt WK (2001) Digital image processing: piks inside. John Wiley & Sons, New York

Roberts L (1965) Machine perception of 3D solids. Optical and electro-optical information processing. MIT Press, Cambridge, MA

3D Medical Image Processing

6

Luigi Landini, Vincenzo Positano, and Maria Filomena Santarelli

CONTENTS

6.1 Introduction

Three-dimensional (3D) medical image processing is a large field that has evolved in recent years, leading to a major improvement in patient care. The revolutionary capabilities of new 3D and 4D medical imaging modalities, along with computer reconstruction, visualization, and analysis of multi-dimensional medical volume image data, provide powerful new opportunities for medical diagnosis and treatment. 3D image processing provides an extensive set of tools for 3D volume calculation, measurement, and quantitative analysis. Starting from 3D models of the patient, automatically identified and extracted from anatomical structures, diagnosis and surgical simulation can be supported. Moreover, using augmented reality capabilities, it is possible to merge pre-operative or intra-operative data with reality, which is a valuable tool in the field of image guided surgery.

The basic tasks in 3D image processing can be classified into three parts following the traditional computer vision approach. Early vision includes image restoration and basic image segmentation, as well as the image formation problem. Mid-level vision is about advanced image segmentation, image registration and volumetric image visualization. Finally, high-level vision covers image recognition and understanding, linking the image processing field with the machine intelligence field.

In applying image processing to the field of medicine, just about all aspects of computer vision are important, but the fundamental aspects are image segmentation, image registration and image visualization.

Image segmentation is the task of partitioning the data into contiguous regions representing individual anatomical objects. In fact, image segmentation associates different tissues imaged by an acquisition device to different logical classes. It is a prerequisite for further investigations in many computer-assisted medical applications, e.g. individual therapy planning and evaluation, diagnosis, simulation and image guided surgery. A central problem in 3D image segmentation is distinguishing objects from background or different objects in a complex scene. This is due to the characteristics of the imaging process, as well as the gray-value mappings of the objects themselves.

L. Landini, MD
Professor, Department of Information Engineering, University of Pisa, Via Diotisalvi 2, 56126 Pisa, Italy
V. Positano
M. F. Santarelli
CNR – Institute of Clinical Physiology, Via Moruzzi 1, 56124 Pisa, Italy

Medical image data come from different sources that can be combined (or fused together) in the same 3D data volume. This is extremely useful in understanding how different aspects of anatomy and function relate to each other. Image fusion operation requires that images must first be geometrically and/or temporally aligned. This alignment process is known as registration. The registration procedure usually involves images coming from different modalities, and is defined as multimodal registration.

Image visualization represents perhaps the most important connection between the image data and the user. Volume rendering works directly on image data, but requires more computational power. Surface rendering is used in many medical applications when 3D visualization must be performed in real time or in near real time. The surface rendering approach uses image segmentation to extract the relevant regions to visualize.

In this chapter, image segmentation, image visualization, and image registration will be examined. It is impossible here to examine all algorithms related to these three main aspects of image processing. However, for each section some representative approaches will be described in detail.

6.2 3D Data Volume

3D image processing algorithms operate on volumetric data, i.e. a 3D region in the space. This data type may be directly available from the scanner, as in 3D acquisition modality, or it may be reconstructed using computer algorithms. Nowadays, 3D image data are almost always digitized. This means that image data are stored in numerical form in a computer station, and codified in specific image format as DICOM. Generally, a 3D volume will be consistent in a series of parallel slices covering the region of interest. Most of the 3D medical images are sampled anisotropically, with the distance between consecutive slices greater than in-plane pixel size. So, the spatial resolution – that is the size of the image voxels – may be different in the three different directions. In such a case the data volume is made of voxels, with a base corresponding to the pixel dimension dictated by the in-plane resolution of the scanner, and a height corresponding to the distance between consecutive slices. Usually pixels have a square shape because the in-plane resolution along the two axes is the same.

In Figure 6.1 three data volumes are depicted with different voxel size: a) isotropically sampled image at low resolution; b) anisotropically sampled image with in-plane resolution higher than resolution between consecutive slices; and c) isotropically sampled image at high resolution.

From the image processing point of view, the best situation is represented by cubic voxels. In fact, 3D image processing algorithms are sensitive to the anisotropy in the data volume, and the quality of the process is degraded for non-cubic data volume. When the voxel size is provided isotropically, 3D rendering will have the correct scale in all three dimensions. This permits it to perform measurements at any plane and to reslice the image along an arbitrary axis in 3D space. Simply define the 3D angle and a new image is created. When cubic shape is not available, an interpolation phase is required that introduces errors directly related to the anisotropy strength in the data volume.

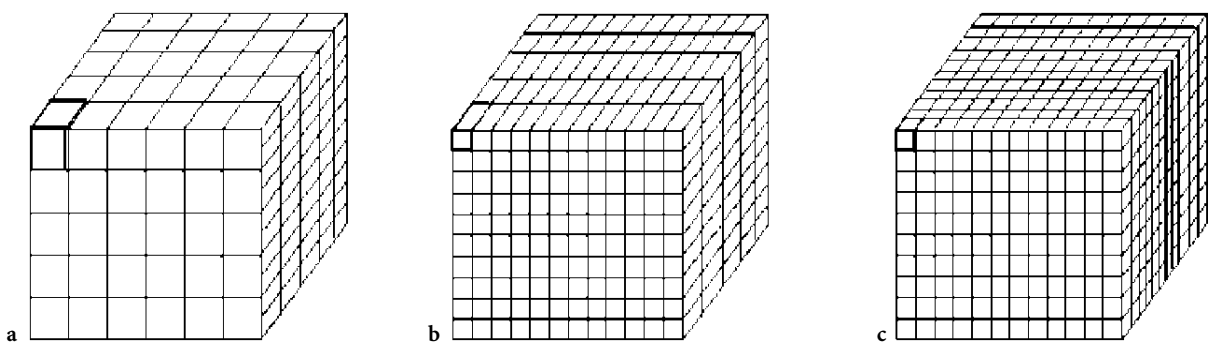

Fig. 6.1a–c. Voxels size: **a** isotropically sampled data at low resolution; **b** anisotropically sampled data; **c** isotropically sampled data at high resolution

6.3 3D Image Segmentation

The aim of the segmentation process is to extract a three-dimensional surface for each anatomic object from volumetric data. Because of the importance of identifying objects from an image, there have been extensive research efforts on image segmentation in recent decades. A number of image segmentation methods have been developed using fully automatic or semi-automatic approaches for medical imaging and other applications.

The key difficulty with segmentation of medical images is the presence of gray scale inhomogeneities. In magnetic resonance images (MRI), for instance, these are caused by radiofrequency (RF) wave attenuation by tissue, inhomogeneities in the static magnetic field, non-uniform RF coil transmission or sensitivity, and magnetic susceptibility of tissue. These gray scale inhomogeneities change over time and with different acquisition parameters, and appear in images as local changes in tissue mean and variance. This means that the same tissue can assume different signal levels in different space locations. Such intensity variations can be smoothed out using special filters such as anisotropic filters.

An impressive number of 3D segmentation algorithms were developed in the past few years. Perhaps the most used method in object-specific segmentation is based on deformable models (Ducan and Ayace 2000; Singh et al. 1998; Kass et al.1987; Ayache et al. 1992; Bardinet et al. 1996; Cohen 1991; Cohen and Cohen 1993). Such deformable models or snakes were improved by the introduction of a new class of external force, called the gradient vector flow (GVF) field, which are vector fields derived from images by minimizing an energy functional in a variational framework (Xu and Prince 1998). Another common method is clustering, which is based on the analysis of gray level distribution in the volume. Alternatively, region-growing methods can be used that utilize multiparametric data coming from different data sources, such as MRI acquired with different pulse sequences (O'Donnell et al. 1986). Basic decision trees (minimum spanning trees) and statistical clustering strategies are employed to combine the information coming from different channels.

In the following sections the anisotropic filtering approach, often used as a pre-processing step in medical image processing, will be described first. Next, the GVF-based deformable model, one of the most well known approaches to contour-based segmentation, will be described. Finally, a gray level-based segmentation, in particular the fuzzy C-mean algorithm, will be introduced.

6.3.1 Anisotropic Filtering

Smoothing (isotropic) is often used as a pre-processing step in medical image analysis in order to reduce image noise. However, the smoothing operation has a blurring effect on image region boundaries, reducing the effectiveness of the following segmentation procedure. A possible solution is the use of an anisotropic filter – that is, a filter that works in a different way on different regions of the image.

Perona and Malik (1990) formulated smoothing as a diffusive process that is suppressed or stopped at boundaries by selecting proper spatial diffusion strengths. In particular, depending on the values assumed by diffusion strength, the filter is able to realize intra-region smoothing without smoothing across boundaries. Theoretically, the nonlinear anisotropic diffusion equation is:

$$\frac{\partial}{\partial t} I(\mathbf{x},t) = c(\mathrm{x},t)\Delta I(\mathrm{x},t) + \nabla c(\mathrm{x},t)\cdot\nabla I(\mathrm{x},t) \qquad (6.1)$$

Where ∇ and Δ are, respectively, the gradient and the laplacian operators. The diffusion strength is controlled by $c(\mathbf{x},t)$. The vector $\mathbf{x}$ represents the spatial coordinates, while the variable t in discrete implementation corresponds to iteration step n. The function $I(\mathbf{x},t)$ is the image intensity. The diffusion function $c(\mathbf{x},t)$ assumes a constant value for linear isotropic diffusion. In that case the diffused image derives from application of the Laplacian operator to the image isotropically. Alvarez et al. (1992) showed that the price for eliminating the noise with linear diffusion is the blurring of edges, which makes detecting and localizing them difficult.

In order to preserve edges, the diffusion must be reduced or even blocked when close to a discontinuity. The diffusion function $c(\mathbf{x},t)$ was chosen as a nonlinear function of gradient image intensity $\nabla I(\mathbf{x},t)$, as follows:

$$c(\mathrm{x},t) = g(\left|\nabla I(\mathrm{x},t)\right| = e^{-\frac{\left|\nabla I(\mathrm{x},t)\right|^2}{2K^2}} \qquad (6.2)$$

The diffusion coefficient $c(\mathbf{x},t)$ monotonical decreases with increasing gradient ∇I. The parame-

ter K is the diffusion constant, and is chosen in order to preserve edge strength at the object's boundary and to reduce noise contribution. The flow strength is dependent on the relationship between K and ∇I. The maximum flow is produced at image location with ∇I = K. When ∇I is below K, the flow function reduces to zero because in most homogeneous regions the flow is minimal. For ∇I larger than K, the flow function again decreases to zero, halting diffusion at locations of high gradients. Therefore, a proper choice of diffusion function not only preserves, but also enhances, object edges usually situated at high gradient values.

Figure 6.2 shows the effect of different levels of anisotropic filter on a MRI cardiac image. It should be noted that the noise in the image is reduced proportionally to the filtering level, but the transitions between different tissues remains sharp.

6.3.2 GVF Snake Model

A deformable model (also known as snake) is a surface (a curve in the 2D space) that moves through the spatial domain of the image itself. Snakes or active contours can move under the influence of internal forces coming from within the curve itself, as well as external forces computed from the image data. The internal and external forces are defined so that the snake will conform to an object boundary or other desired features within an image. In general, the standard snake algorithm suffers two limitations: first, it is very sensitive to the initialization curve that must be as near as possible to the detecting contour; second, active contours have difficulty progressing into boundary concavities. The introduction of a new external force in the active contour model, as described by Xu and Prince (1998), overcomes previous drawbacks. It has been defined as gradient vector flow snake (GVF snake) and is computed starting from the gradient vectors of a gray level or binary edge (gradient) map derived from the image. The use of GVF snake brings a more stable and accurate solution to contour detection and rough curve initialization.

Given the gradient map $\nabla \mathrm{I}(\mathbf{x},\mathrm{t})$ evaluated on an image, the GVF can be defined as a vector field $\mathbf{v}(\mathbf{x},\mathrm{t})$ that minimises the following functional:

$$\mathcal{E} = \iiint \mu \left|\nabla \mathrm{v}(\mathrm{x},t)\right|^2 + \left|\nabla I(\mathrm{x},t)\right|^2 \left|\mathrm{v}(\mathrm{x},t) - \nabla I(\mathrm{x},t)\right|^2 d\mathrm{x} \qquad (6.3)$$

where $\nabla \mathbf{v}(\mathbf{x},\mathrm{t})$ is the gradient of the vector field $\mathbf{v}(\mathbf{x},\mathrm{t})$.

This formulation forces the field to vary slowly in homogeneous regions and to keep $\mathbf{v}$ nearly equal to the gradient map where high spatial variations are present. In fact, the first term in Equation 6.3 becomes dominant where $\nabla \mathrm{I}(\mathbf{x},\mathrm{t})$ is small, yielding a slowly varying field in homogeneous regions. On the other hand, the second term becomes dominant where $\nabla \mathrm{I}(\mathbf{x},\mathrm{t})$ is large, and is minimized by setting $\nabla \mathbf{v}(\mathbf{x},\mathrm{t}) = \nabla \mathrm{I}(\mathbf{x},\mathrm{t})$. The μ parameter governs the trade-off between the first and second term in the integral, and depends on the amount of image noise: high noise requires a high μ value. In fact, the slowly varying field produced by the first term must exceed the noise value in homogeneous regions.

In Equation 6.3 $\mathbf{v}(\mathbf{x},\mathrm{t})$ is treated as function of t (i.e. the number of iteration steps in our discrete implementation) as follows:

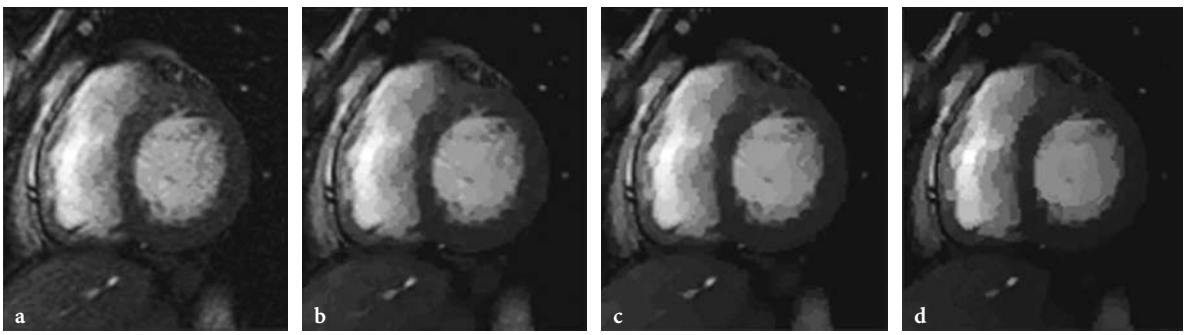

Fig. 6.2a–d. Anisotropic filtering of MRI cardiac images. Images from left to right show the effects of different (different K-values) strengths of the filtering operation

$$v_t(x,t) = \mu\nabla^2 v(x,t) - (v(x,t) - \nabla I(x,t))\left|\nabla I(x,t)\right|^2 \quad (6.4)$$

where $\mathbf{v}_t(\mathbf{x},t)$ is the first derivative of $\mathbf{v}(\mathbf{x},t)$ with respect to t. The steady-state solution of the linear parabolic Equation 6.4 is the solution of Equation 6.3. Equation 6.3 can be solved in the iterative manner using standard numerical methods.

The energy functional is defined as follows:

$$E = \int_0^1 \frac{1}{2}[\alpha\left|\mathbf{x}'(s)\right|^2 + \beta\left|\mathbf{x}''(s)\right|^2 + E_{ext}(\mathbf{x}(s))]ds \quad (6.5)$$

where: $\mathbf{x}(s) = [x(s), y(s), z(s)]$ is the deformable model, $s \in [0,1]$, αa and βb are weights that control the mechanical properties of the deformable model, i.e. tension and rigidity respectively; $\mathbf{x}'(s)$ and $\mathbf{x}''(s)$ denote the first and the second derivatives of $\mathbf{x}(s)$ with respect to s; and $E_{ext}(\mathbf{x})$ is the potential force associated to the external field $\mathbf{v}(\mathbf{x},t)$. According to Equation 6.5 the deformable model can be computed as follows:

$$\mathbf{x}_t(s,t) = \alpha\mathbf{x}''(s) - \beta\mathbf{x}''''(s) + \mathbf{v}(\mathbf{x},t) \quad (6.6)$$

where $\mathbf{x}_t(s,t)$ is the first derivate of $\mathbf{x}(s,t)$ with respect to t, the external field $\mathbf{v}(\mathbf{x},t)$ is the potential force derived by Equation 6.4, and $\mathbf{x}''(s)$ and $\mathbf{x}''''(s)$ are, respectively, the second and the fourth derivatives of $\mathbf{x}(s)$ with respect to s. The parametric deformable surface that represents the steady-state solution of Equation 6 is called the GVF snake. From the numerical point of view, this solution can be found by using an iterative algorithm, as described in Xu and Prince (1998).

In Figure 6.3b, a GVF field representation of the MR image in Figure 6.3a is shown. As expected, the GVF vectors are pointing out into the boundary cavity, thus confirming the peculiarity of this operator to enter into boundary concavities.

As an example, in Figure 6.4 the GVF snake is applied to the detection of the endocardial border in a MRI image of the human heart (Santarelli et al. 2003). In (a), the original MRI image and the corresponding GVF field are shown. In (b), the original placement of the snake is depicted on both the MRI image and the GVF map. In (c), the snake converges to a maximum of the GVF field, which corresponds to the endocardial border in the MRI image.

6.3.3 Fuzzy C-Mean Cluster Segmentation

The fuzzy C-mean (FCM) approach (Udupa and Samarasekera 1996; Bezdek 1948) is able to make unsupervised classification of data in a number of clusters by identifying different tissues in an image without the use of an explicit threshold. The FCM algorithm performs a classification of image data by computing a measure of membership, called fuzzy membership, at each pixel for a specified number of classes. The fuzzy membership function, con-

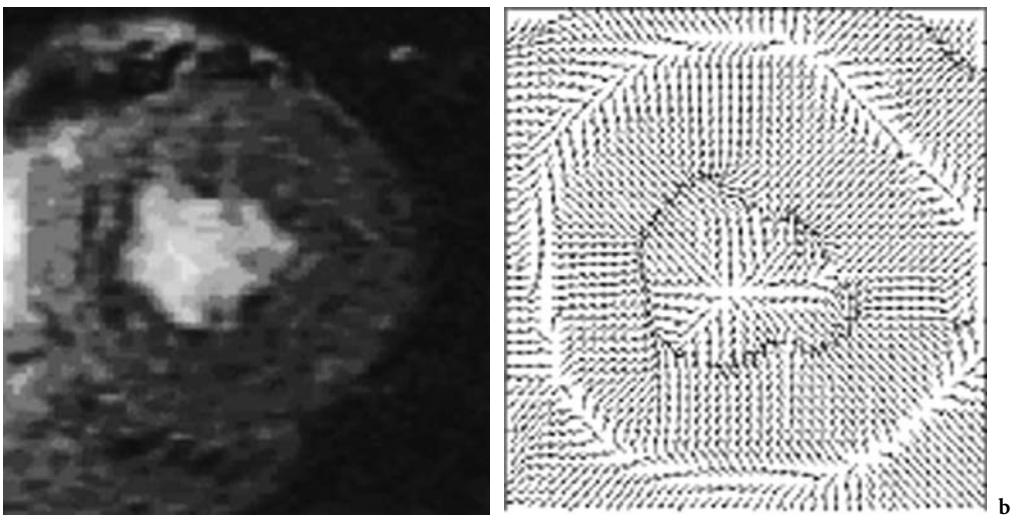

a b

Fig. 6.3a,b. GVF field extracted from a MRI image of the left heart ventricle

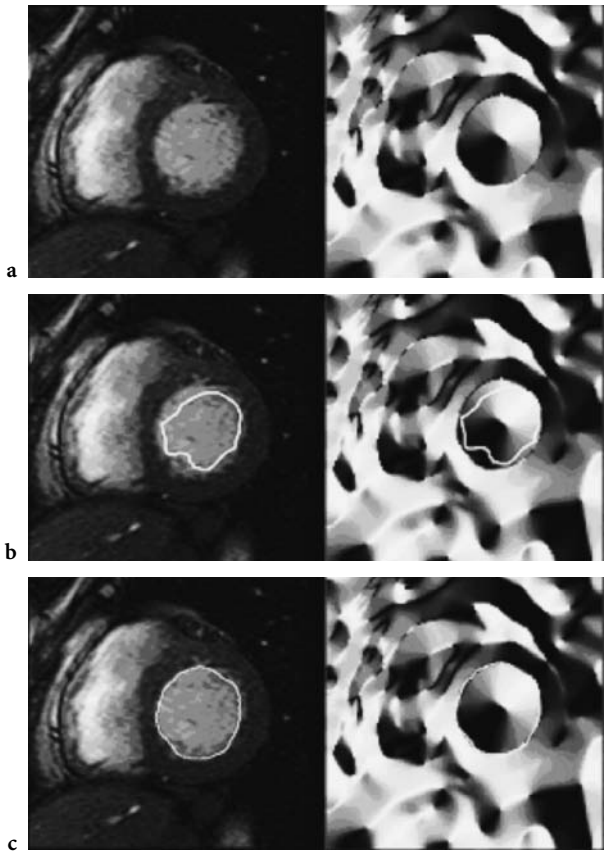

Fig. 6.4a–c. Detection of the endocardial wall in MRI heart images by application of the GVF-snake approach

strained to be between 0 and 1, reflects the level of similarity between the image pixel at that location and the prototypical data value or centroid of its class. Thus, a membership value near unity means that the image pixel is close to the centroid for that particular class. FCM is formulated as the minimization of the following objective function with respect to the membership function u and centroids v:

$$J_{FCM} = \sum_{j\in\Omega}\sum_{k=1}^{C} u_{jk}^{q} \left\| y_j - v_k \right\|^2 \tag{6.7}$$

where Ω represents the pixel location in image domain, q is a parameter greater than the one that determines the amount of fuzziness of the classification (typically q = 2 is used), u_{jk} is the membership value at location j for class k, y_i is the intensity value at j-th location, v_k is the centroid of class k, and C is the number of classes.

When the above objective function is minimized, the value of u_{jk} approaches 1 only if the pixel intensity at j-th location is close to the centroids of class k. Similarly, the value of u_{jk} approaches 0 only if the pixel intensity at j-th location is far from the centroids of class k. Also, the pixels with the same intensity value are grouped into the same groups with the same probability.

The minimization of J_{FCM} is based on suitably selecting u and v by using an iterative process through the following equations:

$$u_{jk} = \left(\sum_{i=1}^{C} \left(\frac{\left\| y_j - v_k \right\|^2}{\left\| y_i - v_k \right\|^2} \right)^{\frac{2}{q-1}} \right)^{-1} \tag{6.8}$$

$$v_i = \frac{\sum_{j\in\Omega} u_{jk}^{q} y_j}{\sum_{j\in\Omega} u_{jk}^{q}} \tag{6.9}$$

The algorithm stops when the value of u_{jk} converges.

The results of the algorithm are the intensity values that characterize the tissue classes (v_k) and the u_k masks that describe the distribution of the classified tissues along the processed image.

Figure 6.5 shows an example of the use of the FCM method on MRI abdominal images (Positano et al. 2004). In this kind of problem, three tissue classes can be identified: background/air signal, fat signal and signal related to other tissues such as muscle, blood, etc. Consequently, C = 3 in the FCM algorithm. Three masks were extracted from each image, each related to a tissue distribution and to a representative value v_k for the extracted tissues. In each mask, white pixels represent pixels with a high value of u_k (i.e. values near 1.0), dark pixels are related to low values of u_k (i.e. values near 0.0). In other words, white pixels represent the background/air area in Figure 6.5b, the no-fat tissues in Figure 6.5c, and the fat tissues in Figure 6.5d. The representative intensity values are v_1 (air), v_2 (no-fat tissue) and v_3 (fat tissue).

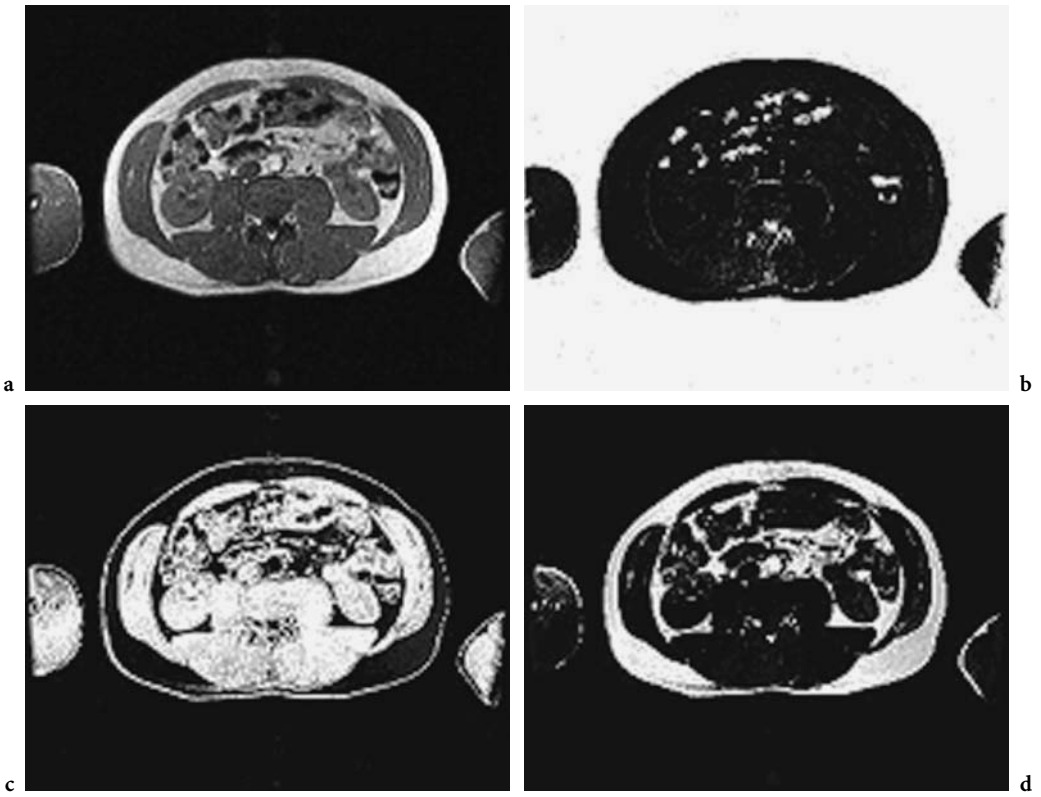

Fig. 6.5a–d. Segmentation of MRI abdominal images by the fuzzy C-mean clustering algorithm. Original image (**a**), background signal map (**b**), muscle tissue map (**c**) and fat map (**d**)

6.4 3D Image Visualization

6.4.1 Surface Rendering

Surface rendering is a process in which apparent surfaces are produced from the data volume and an image of the extracted surfaces is suitably visualized. Surface contours are modelled with bi-dimensional primitives, as triangles or polygons, in order to represent a 3D object. The basic idea is to extract a surface from the 3D data volume as a collection of adjacent polygons and to visualize the extracted surface by appropriate algorithms. Diffusion and shading of light are exploited as well, increasing the 3D illusion.

Figure 6.6 shows a wire-frame representation of the heart (right) and the resulting 3D visualization (left). Original data were acquired by cardiovascular MRI.

Most of the research in this field is focused on how the surface is determined with a high degree of fidelity. This represents a segmentation problem that can be solved in several ways, including those described in the previous sections. The segmentation process of 3D data may produce a series of contours (as in the GVF snake algorithm) defined on each slice, or a 3D mask (as in clustering algorithms) that defines the object of interest. In the first case, the 3D surface is reconstructed by a triangulation algorithm. In the second case, the marching-cube algorithm will be exploited.

The triangulation approach is described in Figure 6.7. Contours defined on two adjacent slices are divided into the same number of equiangular sectors. The points corresponding to sector neighbors are connected by obtaining a series of triangles that will define the surface.

The marching-cube algorithm works on a 3D mask that defines the object of interest obtained by a threshold-based or a more complex segmen-

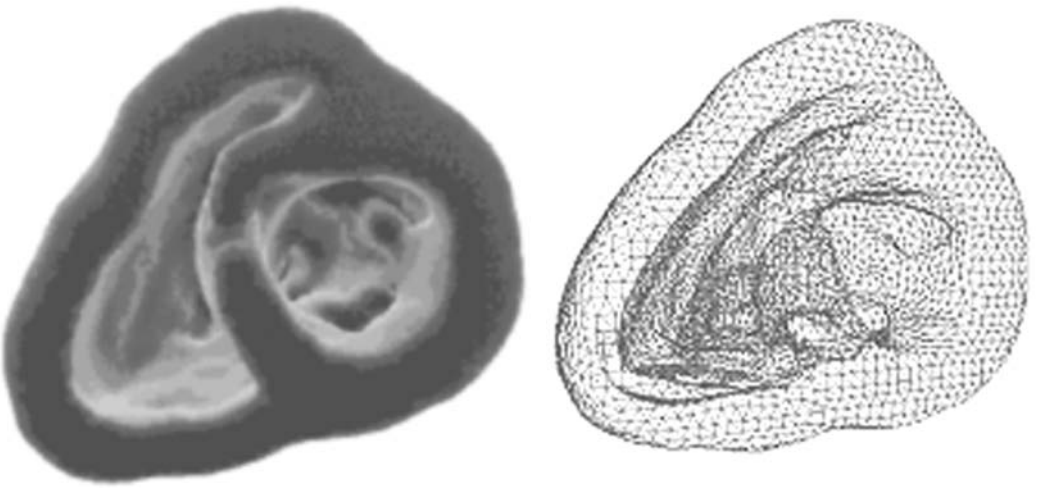

Fig. 6.6. Surface rendering of human heart

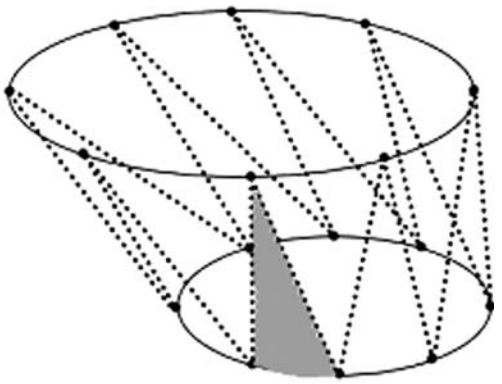

Fig. 6.7. Triangulation method

tation algorithm. For sake of simplicity, the algorithm is described in Figure 6.8 using a 2D example. Gray pixels mean object mask; white pixels define the region outside the object to be visualized. The algorithm proceeds moving a square (A) with the four edges that point to four image pixels. For each square position, the configuration of the four image pixels is searched in the table in the lower part of the figure that represents all 16 possible combinations. For instance, the square A corresponds to position 3 in the table, so that a segment will be drawn accordingly. Square B corresponds to position 7 in the table, so that a vertical segment will be drawn, and so on. Moving the marching square over the entire image, a 2D smooth contour will be obtained that describes the segmented object.

When the marching cube algorithm is used on 3D data, a cube will move across the 3D data set, and the table will contain 256 possible configurations. The result of the marching cube algorithm will be a smoothed surface that will be visualized.

When the surface is defined by triangulation or marching-cube algorithms, the following step serves to remove hidden surfaces. This means that, for the chosen point-of-view, the background triangles must be removed. This task is accomplished by a depth-sort algorithm.

Another important aspect in the surface rendering algorithm is the exploitation of the shading and diffusion effects. Virtual light sources are inserted in the scene, and the diffusion and reflection of light is simulated to increase the quality of the visualization. Figure 6.9 shows the difference between a 3D reconstruction of a cube with poor shading effect (left) and a more accurate lighting simulation (right). This simple example shows the importance of an accurate light simulation in 3D surface rendering.

The main advantage of the surface rendering approach is the reduction of the data to be processed. In fact, 3D data are reduced to a 2D surface that can be represented by a simple list of polygons and the connections between them. Moreover, the surface rendering approach can exploit the hardware and software libraries developed for the video games market, with a dramatic reduction of the needed cost. The main drawback is the need of a pre-processing step that consists of a segmentation of the

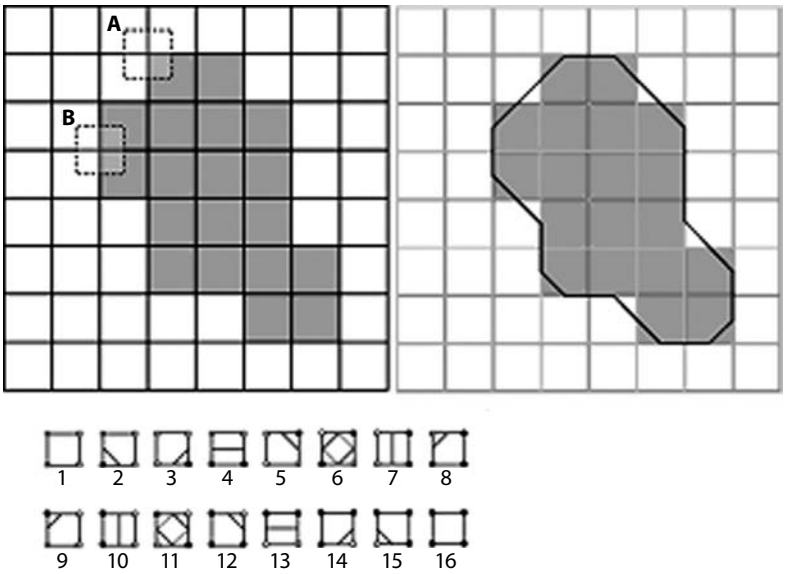

Fig. 6.8. "Marching square" algorithm

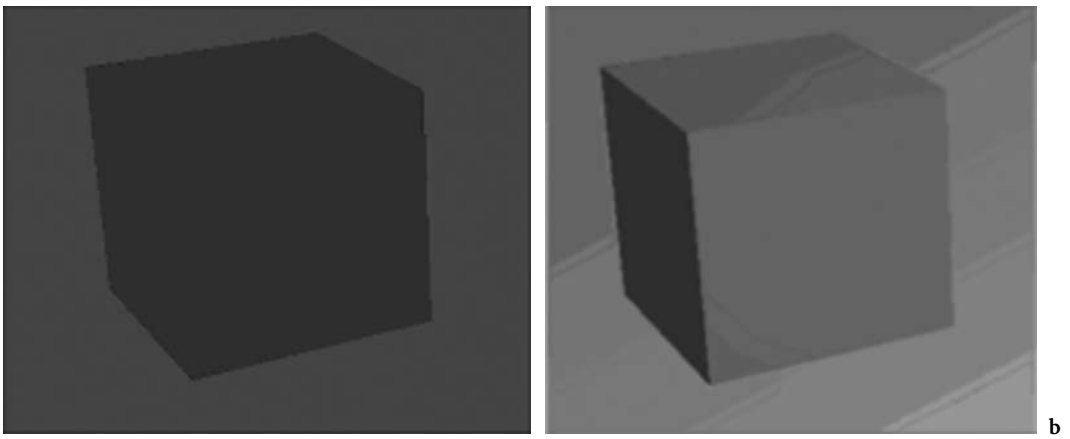

Fig. 6.9a,b. Lighting effect

object to be visualized from the 3D data volume. Segmentation may be difficult and tedious, and an error committed in the segmentation process will propagate in the visualization step.

6.4.2 Volume Rendering

Volume rendering is a process that visualises sampled functions of 3D data volume by computing 2D projections of a semi-transparent volume from a desired point of view without the use of any segmentation procedure; i.e. it preserves any information contained in the data volume. Typically, at each voxel in the data volume a color and a transparency is assigned, depending on look-up tables. Then rays are traced into the volume and are attenuated and colored depending on their route through the volume.

The main disadvantage of this method is the huge amount of data to be manipulated during the different phases of the algorithm, which requires a huge amount of computational power.

A few methods are used in computer graphics to render 3D data volumes into 2D screens by preserving information contained in the data volume. Among them is ray casting, which is a significantly

faster version of the ray tracing algorithm, and which will be described in below in more detail. In fact, ray tracing accounts for multiple reflections from virtual surfaces, but the quantity of data to deal with is of the order of the data volume dimension. For instance, a cubic volume of 256^3 voxels contains about 17 million voxels. A surface rendering operation applied to the same data volume requires only a few thousand geometric primitives.

In Figure 6.10 the basic principle of the ray tracing method is explained: the data volume is scanned by one or more light ray sources.

Rays emitted by the light sources (B) are reflected or diffused by each voxel in the data volume (C). The available information from a data volume is the gray level associated to each voxel, which reflects some tissue properties according to the type of energy used during image acquisition. Reflected rays travelling toward the observer (A) will produce an image (D) of the 3D data volume as seen by an observer from a particular point of view.

Usually, each voxel is characterized by two different values: an opacity value that defines the light quantity that crosses the voxel, and a shading value that represents the reflection or diffusion properties of the tissue.

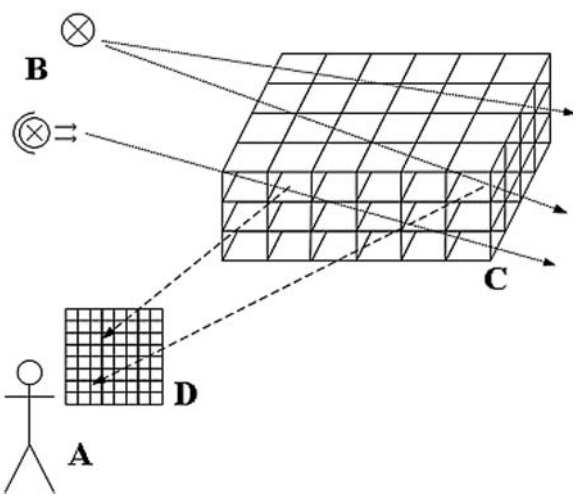

Fig. 6.10. Scheme of volume-rendering algorithm. (*A*) observer; (*B*) light sources; (*C*) data volume; (*D*) reconstructed image

The opacity value associated to each voxel is a quantity that varies from 0 (the voxel is completely transparent and all light crosses the voxel) to 1 (the voxel is completely non-transparent). The correspondence between voxel gray level intensity and degree of transparency is operator-dependent. For instance, dealing with TAC images of the brain, the opacity value can be set to 0 for soft tissues, so only the rendering of the bone tissue is available, or to 0.5, so both soft tissue and bone are visible. Usually the operator chooses the best opacity value trough a graphical user interface.

In Figure 6.11 the results obtained by modifying the opacity value on an object constituted by two cubic data volumes one inside the other are shown. The external cube is characterized by an opacity value of 0.5, while the inner one has an opacity value of 1. The two plots in the figure describe two possible choices of opacity value: the horizontal axis reports the intensity distribution relevant to the voxels, while the vertical axis reports the opacity value. In (A) a 0 opacity value is applied to voxels with an intensity value lower than 50, and an opacity value equal to 1 applied to voxels with intensity value equal to 100. In such situations, only the inner cube is visualized. In (B) the opacity value of the external cube is 0.2 (almost transparent), while the inner cube is completely non-transparent.

Shading function is used to improve the shape of an object in a data volume. To assign the shading function to a data volume, first a virtual surface inside the data volume is extracted. The simplest method consists of evaluating the gradient at each voxel as the difference between the current intensity value and the adjacent ones. The relevant gradient map delineates the surface of the border of the organ inside the data volume. A filtered version of the gradient map can be used as a virtual surface. Usually, the relationship between gradient values and shading parameters is automatically defined by the visualization algorithm.

Figure 6.12 shows the effect of the shading function: in (A) only the opacity function is accounted, so the cube shape is poorly defined; in (B) the introduction of the shading function improves the cube visualization.

As is the case with opacity function, the shading function can be modified by the user through a graphical user interface.

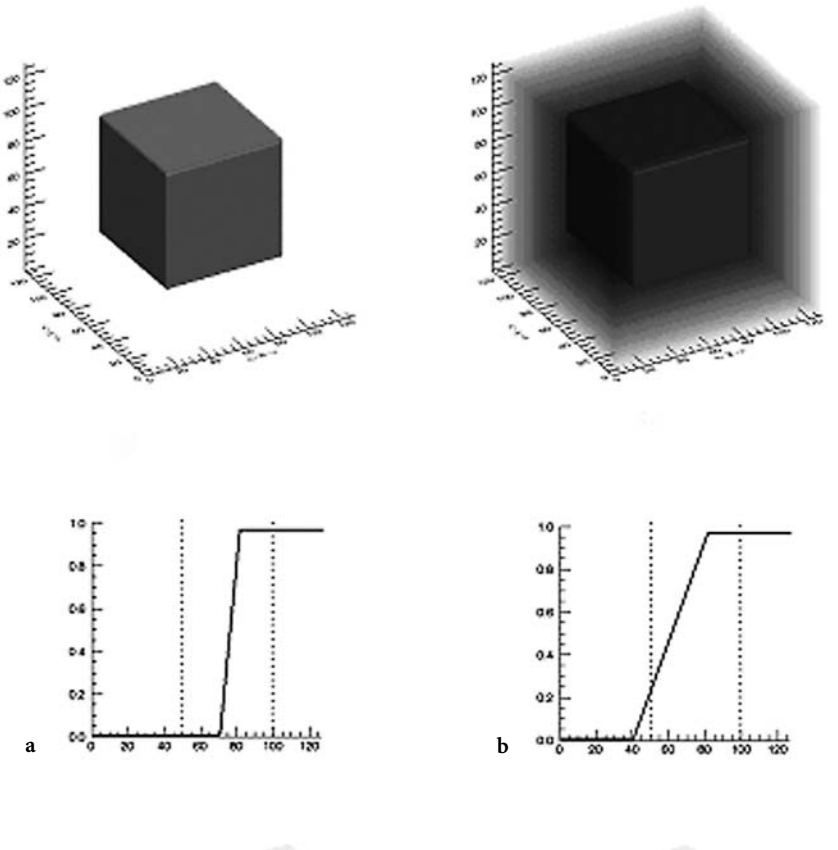

Fig. 6.11a,b. Opacity function effects on volume rendering

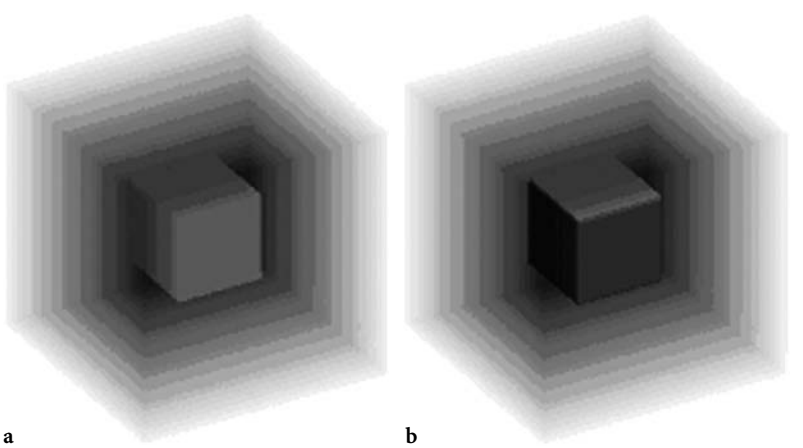

Fig. 6.12a,b. Shading function effect: **a** rendering without shading, **b** rendering with shading

6.4.3 Projection Algorithms

This family of algorithms mimics the physical phenomena behind the production of radiographic images. The 3D data set consists of a sequence of parallel slices (A in Fig. 6.13). A projection direction (B) is chosen, and projection rays are defined parallel to the projection direction. The projection rays intercept the volume slices in a series of points (C). Consequently, for any ray a series of gray level values are defined. In the MIP (maximum intensity projection) algorithm, the maximum value is chosen among all computer gray values and mapped on the projected image (D). The projected image represents the 3D MIP visualization of the 3D data volume. MIP algorithm is usually used when the object of interest is characterized by a high signal level (e.g. MR

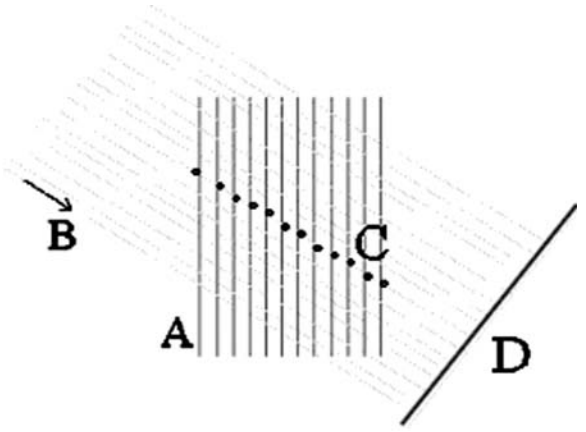

Fig. 6.13. Ray-sum algorithm

or CT angiography). The MIP (minimum intensity projection) algorithm is complementary in respect to the MIP and is used when the object of interest presents a low intensity value (e.g. X-angiography). In the RaySum algorithm, the projected value is computed by summing all pixel values collected by the projection ray.

The use of parallel projection rays implies that the virtual point of view is far from the reconstructed object. In some applications, such as virtual endoscopy, this simplified hypothesis does not hold, and a more complex perspective projection should be used.

6.4.4 3D Visualization Tools

Any 3D rendering algorithm is not able to fully exploit its potentialities when the support for visualization is a bi-dimensional screen. Thus, a number of tools are available, based on 3D glasses, for increasing the illusion of three-dimensionality. The basic principle consists of supplying the two eyes of the observer with two slightly different images, exploiting what happens in the real word. In fact, in the vision mechanism for an observer placed at a distance from an object, the two eyes receive two images seen from two different perspectives. The eye-brain system integrates the two images in order to derive the three-dimensionality (stereoscopy) of the object.

In glasses supplied with optical filters, each lens is constituted by an optical filter, i.e. red or green, in order to supply each eye with light of only one color. On the screen, two superimposed images are visualized, one in red and the other in green. Using optical filters it is now possible to observe different images with each eye, thus creating the illusion of 3D in the brain.

In shutter glasses each lens is constituted by a crystal liquid lens, which has the property to block the light when suitable polarized. The two images, right-eye image and left-eye image, used to produce the 3D illusion are alternatively projected on a screen. When the right image is projected, the shutter will switch off the left eye lens, and vice versa during left image projection.

In LCD glasses each lens consists of small liquid crystal screens, so each eye is able to visualize one of the two stereoscopic images. With LCD glasses the quality of the 3D illusion is superior, though this method is still expensive.

6.5 3D Image Registration

In the late 1980s, clinicians, physicists and image analysis researchers began to think seriously about integrating different forms of image-derived information. To permit this fusion, 3D datasets, often acquired with different image modalities, had to be registered.

The first widely known registration of 3D data involved matching surfaces manually extracted from either CT, MRI, SPECT or PET images (Pellizzari et al. 1989). This approach, know as feature-based registration, dominated the field of 3D images registration until mid-1990s due to computational complexity constraints. In fact, the main advantage of this approach is the dramatic reduction of required processing time, because the dimension of extracted features is usually at least an order of magnitude below the dimension of images (i.e. lines vs. 2D images, surfaces vs. 3D images). The main disadvantages of the feature-based approach are the arbitrary choice of the feature to extract and the drawbacks in the correct extraction of the features. In feature-based registration, an important step was the adoption of the iterative closest point (ICP) algorithm, as described by Besl and McKay (1992). The ICP algorithm allowed to effectively register features (i.e. lines or surfaces) extracted from 3D data sets.

In mid-1990s, voxel intensity-based methods became available due to the increase of computing power. Viola and Wells (1995) and Collignon et al. (1995) introduced the concept of mutual information, which in the years following became the most effective and widely used metric in the voxel-intensity registration methods (Pluim et al. 2003). An excellent review and categorization of registration strategies through 1998 is contained in the article by Maintz and Viergever (1998).

At present, work on 3D image registration mainly involves non-rigid mapping schemes, as described by Crum et al. (2004). Non-rigid registration is needed when information coming from two patients or from one patient and an atlas must be related. Moreover, when different image modalities are used, non-rigid registration algorithms are needed to take into account differences in acquisition protocols, resolution, etc.

With the development of image-guided intervention, imaging and image processing become key parts of a surgeon's procedure, and real-time or near real-time image registration become an important issue. Furthermore, the registration of different types of intra-operative information to pre-operative images and atlases present a variety of new challenges.

Many criteria can be used to classify registration methods. If the registration procedure involves images coming from different modalities, it is defined as multimodal registration. When the registration involves images produced by the same modality, the registration is called unimodal.

Criteria can be also related to the dimensionality of the images (2D, 3D or dynamic 3D images), the nature of registration basis, the nature of the transformation (rigid, affine, projective or curved), the interaction (manual, semi-automatic and automatic methods), the modalities involved and the subject (intra-subject, inter-subject or atlas).

About the nature of registration basis, image-based registration can be divided in two main classes:

1. extrinsic, i.e. based on foreign objects introduced into the imaged space designed to be well visible in the pertinent modalities. The main disadvantage of extrinsic methods is that they are invasive in nature.
2. intrinsic, i.e. based only on the image data. Intrinsic methods can be based on a limited set of salient points (landmarks), on alignment of segmented structures (segmentation of features-based) or on measures computed from the image gray values (voxel-based). Landmarks can be manually selected by the user (anatomical landmarks) or automatically extracted (geometrical landmarks). Geometrical landmarks correspond to the optimum of some geometrical proprieties, such as corners and local curvature . In the segmentation-based methods, two lines or surfaces sets (i.e. image features) are extracted from both images, and used as input for the alignment procedure. The voxel-based methods operate directly on the image gray values. In principle axes and moment-based methods, the image content is reduced to a representative set of vectors, and the registration is performed using the extracted vector set. The methods using the full image content attempt to perform the registration by maximising the cross-correlation, the mutual information or some other relationship between images. Voxel-based registration does not generally require extensive pre-processing, such as segmentation or feature extraction.

With regard to interaction, the registration methods can be categorized as:

- Automatic, which is when the user only supplies the algorithm with the image data.
- Semi-automatic, which is when the user has to initialize the algorithm performing the segmentation or accept or reject suggested registrations.
- Interactive, which is when the user does the registration himself, helped by the software.

In automatic or semi-automatic registration algorithms, there are generally three main aspects (Brown 1992).

1. The search space is in the class of potential transformations, such as rigid, affine and elastic, used to align the images. 3D rigid-body registration has six degrees of freedom: x, y and z translation, and rotation around the x, y and z axes. Affine transformations add shearing and scaling. The most general class of transformation, elastic or nonlinear registration, have (in theory) infinite degrees of freedom.
2. The similarity metric is an indicator of how well the features or intensity values of two images match.
3. The search strategy optimises the similarity metric. Examples include local or global searches, multi-resolution approaches and other optimization techniques.

Although nonlinear registration is more realistic in principle, because tissues are deformable in some manner, rigid registration is often used in unimodal registration, which is a field of particular interest in MRI and CT. Moreover, when a large set of data is involved, nonlinear registration requires exceptional computational power. With regard to similarity metrics, the current focus is on mutual information measures, which is the most often used technique in the registration field. Optimization techniques range from the classical (i.e. simplex and Powell methods) to the advanced (i.e. genetic algorithms).

6.5.1 The Registration Problem

In the following, it was assumed that an image has three dimensions. T denotes the spatial transformation that maps coordinates (spatial locations) from one image or coordinate space to another image or coordinate space. P_A and P_B denote coordinate points (pixel locations) in images A and B, respectively. The image registration problem is to determine T so that the mapping

$$T : p_A \rightarrow p_B \Leftrightarrow T(p_A) = p_B \tag{6.10}$$

results in the best alignment of A and B. The domain where T is defined is called the search space of the registration problem. The function that defines the quality factor for the alignment is called the similarity metric or registration metric. The algorithm used for the search of the function T that maximises the chosen metric is called the search strategy.

In the most general case, two medical images may differ from one another by any amount of rotation about an axis or by any amount of translation in any direction. They may differ in scale, and non-rigid transformation can be present. Moreover, these features may vary locally throughout the volumetric extent of the images. The nature of the T transformation characterises the search space of the registration problem, ranging from nonlinear transformation, with a virtually infinite degree of freedom, to rigid registration with six (for 3D volumes) degrees of freedom. Intermediate cases are affine transformations, meaning the images can be scaled and sheared.

It is important to note that biomedical images are usually coded in digital image format, typically the DICOM (digital imaging and communications in medicine) format. The DICOM format includes some information that can be useful for image registration, such as the position and orientation of the image with respect to the acquisition device and the patient, as well as to the voxel size, which means a preliminary registration can be performed using this geometrical data, thus reducing the image misalignment. In unimodal registration, the absence of image scaling can be assured by the use of the same acquisition device with the same acquisition parameters. Moreover, because the pixel dimension in both images is known from the acquisition parameters, the scaling factor can be easily computed, and image scaling easily applied. Main sources of non-rigid distortions in some biomedical images, such as MRI, are due to subject breath during acquisition. This kind of distortion affects cardiovascular and abdominal MRI, but is negligible in brain imaging. Moreover, because heart movement is not rigid in nature, some deformation of heart shape can occur due to poor EEG synchronization in cardiac MRI. In practice, one can often suppose that the images to be registered will differ only for a rigid transformation.

For 3D rigid body registration, the mapping of coordinates $p_A = [x\ y\ z]$ into $p_B = [x'\ y'\ z']$ can be formulated as a matrix multiplication in homogeneous coordinates:

$$\begin{bmatrix} x' \\ y' \\ z' \\ 1 \end{bmatrix} = \begin{bmatrix} \cos\beta\cos\gamma & \cos\alpha\sin\gamma + \sin\alpha\sin\beta\cos\gamma & \sin\alpha\sin\gamma - \cos\alpha\sin\beta\cos\gamma & t_x \\ -\cos\beta\sin\gamma & \cos\alpha\cos\gamma - \sin\alpha\sin\beta\sin\gamma & \sin\alpha\cos\gamma + \cos\alpha\sin\beta\sin\gamma & t_y \\ \sin\beta & -\sin\alpha\cos\beta & \cos\alpha\cos\beta & t_z \\ 0 & 0 & 0 & 1 \end{bmatrix} \begin{bmatrix} x \\ y \\ z \\ 1 \end{bmatrix} \tag{6.11}$$

Where (t_x, t_y, t_z) are the translation vectors and (α, β, γ) are the rotation values around the three axes.

Because digital images are sampled on a discrete grid, but T generally maps to continuous values, interpolation of intensities is required. The interpolation process can affect the effectiveness of the registration, so that the choice of an appropriate interpolation algorithm plays an important role in the development of the registration procedure.

In the registration process, one can define a reference image and a floating image, the latter of which

is the image to be registered with respect to the reference image. The similarity function between the reference image and the floating image is evaluated. An optimization algorithm is used to estimate the best transformation function (T) that maximises the similarity function; the estimate function is used to transform the floating image. An interpolation operation is also required. If the result is satisfactory, the procedure ends; if not, a new transformation function is evaluated and a new loop is executed. The key issues in the registration algorithm are the choice of the similarity metric and the choice of the optimization algorithm. These issues will be described in the following sections.

Sometimes, the images involved in registration can be pre-processed in order to improve the effectiveness of the registration algorithm. The most common pre-processing step is defining a region of interest in images to exclude structures that may negatively affect the registration process. Other pre-processing techniques consist of image filtering to remove noise, correction for intensity inhomogeneities and image resampling to achieve the same spatial resolution in both images.

6.5.2 Similarity Metrics

The similarity metric for image registration should satisfy some constraints. First, similarity metrics must be robust; that is, they should converge to a global maximum at the correct registration. In some cases, the best registration might be a local (not global) optimum. However, this problem can be overcome by selecting an initial orientation close to the correct registration, as described in the previous section. In the following example it is assumed that the global optimum is obtained at the correct registration transformation. Another important quality of the similarity metric is the computational complexity that affects the time required to perform the registration.

Generally, three types of similarity metrics have been proposed in image registration (Maintz and Viergever 1998). They are based on corresponding points, corresponding surfaces and corresponding image intensities. The first two methods can be grouped into one, and the two main approaches to registration can be summarized as follows:

1. Similarity measured by extraction of some geometrical features from the two images. The extracted features are compared, and a similarity index is extracted. The main advantage of this approach is the dramatic reduction of required processing time. In fact, the dimension of extracted features is usually at least an order of magnitude below the dimension of images (i.e. lines vs. 2D images, surfaces vs. 3D images). The main disadvantages are the arbitrary choice of the feature to extract and the drawbacks in the correct extraction of the features.
2. Similarity measured by direct comparing of images to be registered. The main disadvantage of this approach is about the required processing time. In fact, all image data are involved in the analysis. The main advantage is the independence from any user input. This kind of method is also known as a voxel-based (3D) or pixel-based (2D) method.

Both approaches were extensively used for medical image registration. An example of the first approach is the registration procedure for two MRI cardiac images. First, one must extract the same geometrical feature from both the reference and floating images. In the case of the cardiac MR image registration, the left ventricle contour is a natural choice and can be extracted from both images with an automatic algorithm such as the one described in Santarelli et al. (2003). If the left ventricle contours were correctly extracted from both images, the similarity between the two images could be defined as the difference between the two extracted contours, introducing a definition of the distance between two closed curves. An optimization process could then be used to minimize such a distance, performing the image registration. An example of this procedure is the ICP algorithm introduced by Besl and McKay (1992); it is a general purpose method for the registration of two generic point set representations, including line segments sets, implicit curves, parametric curves and generic surfaces. At the end of the optimization process is the rotation matrix and the translation vector that register the two curves. The convergence theorem guarantees the achievement of a local minimum. The roto-translation matrix can be now applied to the floating image to perform the registration. The example shows both the advantages and disadvantages of the feature-based approach: the registration operation involves 1D data (i.e. the extracted contour) and consequently it is very fast and accurate. On the other hand, the feature extraction (i.e. the localization of left ventricle contours) can be difficult and error prone. In conclusion, the

use of feature-based algorithms is suggested only when fast and effective segmentation algorithms are available on the images to be registered.

Voxel-based methods imply the comparison of image gray levels to be registered.

The simplest metric involves the use of difference or absolute difference between images (mean square difference):

$$MQ(A,B)=\sqrt{\sum_{i,j\in S}\left(a_i-b_j\right)^2} \tag{6.12}$$

where (i,j) denotes the couples of corresponding voxels in the two images, and S is the domain where both images are defined. The introduction of the S domain means that the metric must be computed only in the geometrical region where both images are defined. This approach applies to all voxel-based metrics. This simple metric can be effectively used when the images to be registered are similar enough to each other.

Much of the current work on biomedical image registration utilises voxel similarity measures; in particular, mutual information based on the Shannon definition of entropy. The mutual information (MI) concept comes from information theory, measuring the dependence between two variables or, in other words, the amount of information that one variable contains about the other. The mutual information measures the relationship between two random variables, i.e. intensity values in two images: if the two variables are independent, MI is equal to 0. If one variable provides some information about the second one, the MI becomes > 0. The MI is related to the image entropy by:

$$MI(X;Y)=H(X)+H(Y)-H(X,Y) \tag{6.13}$$

where: X and Y are the two images and H(.) is the entropy of a random variable, and is defined as:

$$H(X)=-\sum_{x_i\in\Omega_X}\log[P(X=x_i)]\cdot P(X=x_i) \tag{6.14}$$

The joint entropy of X and Y is:

$$H(X,Y)=-\sum_{x_i\in\Omega_X}\sum_{y_j\in\Omega_Y}\log[P(X=x_i,Y=y_j)]\cdot P(X=x_i,Y=y_i) \tag{6.15}$$

All entropies must be evaluated on the domain where both images are defined, usually overlapping areas. Normalized mutual information (NMI), given as:

$$I_N(X,Y)=\frac{H(X)+H(Y)}{2H(X,Y)} \tag{6.16}$$

is less sensitive to the size of the overlap and can be used instead of MI.

The probability distribution for the evaluation of MI and NMI can be estimated with Parzen windows, histograms or other probability density estimators. The most common method uses images histograms. Q and K are images with M pixels that can assume N gray levels $g_1,g_2,\ldots g_N$. The MI between Q and K can be defined as:

$$MI(Q,K)=H(Q)+H(K)-H(Q,K) \tag{6.17}$$

where $H(.)$ is the entropy of an image. $H(Q)$ can be written as:

$$H(Q)=-\sum_{i=1}^{N}\log[P(Q=g_i)]\cdot P(Q=g_i) \tag{6.18}$$

$P(Q=g_i)$

which is the probability that a pixel in Q image will assume the value g_i.

The image entropy can be written in terms of the image histogram His_Q:

$$H(Q)=-\frac{1}{M}\sum_{i=1}^{N}\log[\frac{His_Q(i)}{M}]\cdot His_Q(i) \tag{6.19}$$

Further, the joint entropy of images Q and K with the same number of pixels M and the same gray level range N can be written in terms of joint image histogram His_{QK}:

$$H(Q,K)=-\frac{1}{M^2}\sum_{i=1}^{N}\sum_{j=1}^{N}\log[\frac{His_{QK}(i,j)}{M^2}]\cdot His_{QK}(i,j) \tag{6.20}$$

where $His_{QK}(i,j)$ is equal to the number of simultaneous occurrences of $Q=i$ and $K=j$.

The MI registration criterion states that the MI of the image intensity values of the corresponding voxel pair is maximal if the images are geometrically aligned. Because no assumption is made about the nature of the relation between the image intensities, this criterion is very general and powerful. Mutual information has been shown to be robust for both multimodal and unimodal reg-

istration, and it does not depend on the specific dynamic range or intensity scaling of the images. The mutual information as previously defined is a not negative number. Because many optimization algorithms are formulated as minimization algorithms, the negative of MI (-MI) is often used as a similarity metric.

6.5.3 The Interpolation Effect in the Registration Problem

When sub-voxel translation or image rotation is involved, image interpolation (also defined as resampling) is also required to obtain the roto-translated image. In the interpolation operation, the coordinate grid is defined by the voxel locations in the reference image. The voxel values of the roto-translated floating image must be recomputed in the coordinate grid. Several methods have been proposed for interpolation of medical images; an extended review can be found in Lehmann et al. (1999). Main interpolation methods are: truncated and windowed sync, nearest neighbor, linear, quadratic, cubic B-spline, Lagrange and Gaussian interpolation. Because the interpolation operation has to be repeated for each computation of the similarity function, both interpolation accuracy and computational complexity are important in the choice of the interpolation method. Some methodologies, although more effective with respect to traditional methods, may be too slow to be adopted in the solution of the registration problem. Instead, the interpolation required to obtain the final registered image is performed only once, and the choice of an accurate interpolation method is appropriate.

The main trouble with interpolation operation is that it can modify the gray level values, affecting the evaluation of the similarity function. This effect can lead to incorrect registration results if a histogram-based metric, such as MI or NMI, is used. Often, the image dynamic is reduced to avoid this effect.

The simplest interpolation algorithm is the nearest neighbor interpolation, where the new voxel values are recomputed as the value of the closest neighboring voxel. This algorithm preserves the gray values of the original voxels, but makes the registration metric insensitive to intra-voxel misalignment, because image movements less than the half of pixel size do not modify the interpolated images.

A more effective interpolation algorithm is the trilinear interpolation (bilinear in 2D images) where the value of recomputed voxels is evaluated as the weighted sum of the neighboring voxels. This technique introduces new gray values in the interpolated image.

When the similarity function is based on joint histogram computation, as in mutual information, it should be preferable to use an interpolation technique that preserves the gray level distribution. This technique, introduced by Pluim et al (2003), named trilinear partial volume distribution (PV) interpolation, updates the joint histogram for each voxel pair in the two images. Instead of interpolating new intensity values, the contribution of the image intensity of each voxel to the joint histogram is distributed over the all intensity values of the neighboring voxels, using the same weights as for trilinear interpolation.

Figure 6.14 shows the previously described interpolation algorithms.

Nearest neighbor (NN) interpolation and trilinear (bilinear in the present 2D example) interpolation find the reference image intensity value at position p, and update the corresponding joint histogram entry at p, while partial volume (PV) interpolation distributes the contribution of this sample over multiple histogram entries defined by its NN intensities, using the same weights as for bilinear interpolation.

It can be demonstrated that PV interpolation performs better in the MI-based registration of data set, because spurious gray levels are not introduced.

6.5.4 Optimization Techniques in Image Registration

The problem of finding the parameters set that maximises a multi-variable function is called the optimization problem. In the rigid registration problem, the optimization algorithm should find the rotation and translation parameters that will maximize the similarity function. If the registration is elastic, the number of parameters is virtually infinite and should be reduced by introducing appropriate hypotheses. A common approach is to perform a rigid registration extended to the whole image, followed by a local elastic registration. The elastic registration is constrained to some mathematical model to limit the needed number of parameters.

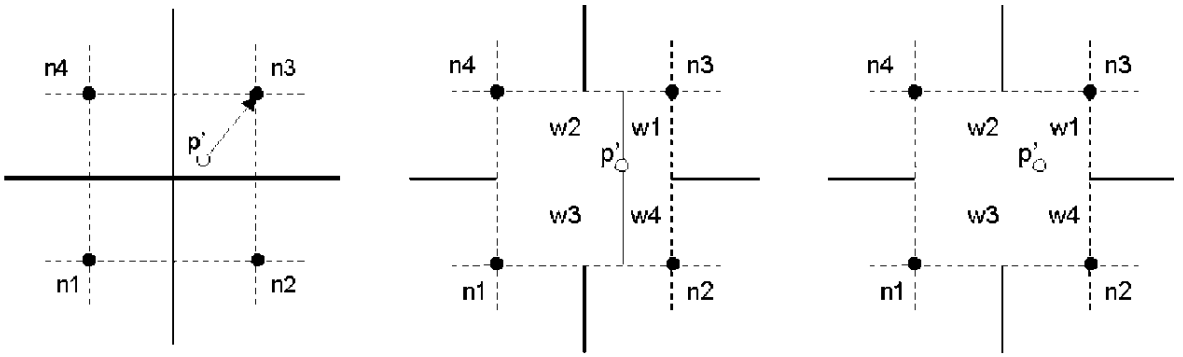

$\arg\min_{n_i} d(p', n_i) = n_3$
$B(p') = B(n_3)$
$h(A(p), B(p')) += 1$

$\sum_i w_i = 1$
$B(p') = \sum_i w_i B(n_i)$
$h(A(p), B(p')) += 1$

$\sum_i w_i = 1$
$\forall i: h(A(p), B(n_i)) += w_i$

Fig. 6.14. Three types of interpolation for the evaluation of the joint histogram

To reduce the required processing time, a multi-scale approach is often used. In the multi-scale approach, the registration is an iterative process. In the first step, low-resolution images are registered. The result of this step is used as an initial estimate for the next registration, which involves images at higher resolution. The process is iterated until the best available resolution is reached. The main trouble with the registration process is the presence of local maxima of the similarity metric. Many similarity metrics, such as mutual information, are irregular and rough and are often trapped in local optima. In particular, this problem affects the multi-resolution approach because the global optimum may not present in lower resolutions.

In conclusion, the choice of the appropriate optimization technique is a compromise between the effectiveness of the method (i.e. the ability to find the global optimum) and the processing time required for the optimization process. Local methods, such as the Powell method, conjugate gradient, Levenberg-Marquard or the simplex algorithm provide good performance but do not guarantee to reach the global optimum of the similarity function. On the other hand, global optimization methods such as simulated annealing, genetic algorithms, tabu search and particle swarm optimization are generally more expensive in terms of processing time while they assure, under some conditions, the convergence to a global optimum. An extensive description of the optimization is beyond the limit of this chapter.

6.6 Conclusion

Some conclusions can be inferred from the 3D image processing aspects discussed in this chapter, and some speculation can be made about the future of medical image processing. First, as discussed previously, image segmentation is the key issue in the whole 3D image processing field. In fact, segmentation is involved in both advanced 3D visualization and feature-based registration. 3D image segmentation use in explicit or explicit way some modelling of the images involved in the processing. Optimal parameter settings in the formulation of anisotropic filtering and GVF-snake depend on the nature of the image under examination. In the fuzzy C-mean algorithm, the number of tissue classes to be used depends on the image nature as well. The approach to image segmentation explicitly includes the algorithm dependence from data, and the so called model-based segmentation, which incorporates a model of the structure to be identified in the algorithm, is extensively used. Another popular approach is the Bayesian approach, where the prior knowledge of the object to be recognized is included as a priori hypothesis. It is likely that the use of a machine learning approach to learn the optimal algorithm setting from data will be used extensively in the coming years.

The second important point is that complex image processing approaches (such as volume rendering or image registration) require a lot of com-

putational power, and may require anywhere from several seconds to many hours to produce the final result. This means that these algorithms are difficult to use where real time constraints are introduced, as in virtual reality applications. Possible solutions are the reduction of the data size, image down-sampling in the space or time domain, and the use of peculiar computer architectures, such as parallel computers or dedicated hardware.

With regard to image registration, global and simultaneous registration of multiple data sets coming from different acquisition modalities will soon become an important issue in medical image processing due to the growing importance of 3D methodologies and 3D functional imaging. Although some research was carried out on this topic, the common current approach is quite heuristic. A major problem is the lack of an effective registration quality index to be used when assessing the quality of the registration process. The accuracy and robustness of a registration method depend on a number of factors, such as imaging modality, image content and image degrading effects, the class of spatial transformation used for registration, similarity measure, optimization, and numerous implementation details. The complex interdependence of these factors makes the assessment of the influence of a particular factor on registration difficult, although it is often desirable to have some estimate of such influences prior to registration. More thorough, optimization-independent, and systematic statistical evaluation of registration quality is needed to assess the effectiveness of the proposed registration algorithms.

Finally, it is important to note that the performance of image processing algorithms strongly depends on image quality. Consequently, the optimization of the acquisition procedure is the first and perhaps most important step to achieving an effective image processing procedure.

References

Alvarez L, Lions PL, Morel JM (1992) Image selective smoothing and edge detection by nonlinear diffusion. SIAM J Number Anal 29:845–866

Ayache N, Cohen I, Herlin I (1992) Medical image tracking. In: Blake A and Yuille A (eds) Active Vision. MIT-Press, Chap. 17

Bardinet E, Cohen L, Ayache N (1996) Tracking medical 3D data with a deformable parametric model Proc. Eur. Conf. of Computer Vision (ECCV'96) Cambridge, England

Besl PJ, McKay ND (1992) A method for Registration of 3D Shapes. IEEE Trans. on Pattern Analysis and Machine Intelligence 14:239–256

Bezdek J, Hall L, Clarke L (1993) Review of MR image segmentation using pattern recognition Med Phys 20:1033–1948

Brown L (1992). A survey of image registration techniques. ACM Comput Surv 24:325–376

Cohen LD (1991) On active contour models and ballons. Computer Vision, Graphics and Image Processing: Image Understanding 2:211–218

Cohen LD Cohen I (1993) Finite element methods for active contour models and balloons for 2D and 3D images. IEEE Trans on Pattern Analysis and Machine Intelligence 15:1131–1147

Collignon A, Maes F, Delaere D, Vandermeulen D, Suetens P, Marchal G (1995) Automated multi-modality image registration based on information theory. Information Processing in Medical Imaging 263–274

Crum WR, Hartkens T, Hill DLG (2004) Non-rigid image registration: theory and practice. Br J Radiol 77:S140–S153

Duncan JS, Ayace N (2000) Medical Image analysis: Progress over two decades and the challenges ahead. IEEE Transaction on Pattern analysis and Machine Intelligence 22:85–106

Lehmann TM, Gonner C, Spitzer K (1999). Survey: Interpolation Methods in medical image processing. IEEE Trans. on Medical Imaging 18:1049–1075

Kass M, Witkin A, Terzopoulos D (1987) Active contours models. Int J Comp Vision 1:321–331

Maintz JBA, Viergever MA (1998) A survey of Medical Image Registration. Med Image Anal. 2:1–16

O'Donnell M, Goie J, Adams W (1986) Towards an Automatic Algorithm for NMR imaging II: Initial Segmentation algorithm. Medical Physics. 13:293–247

Pellizzari CA, Chen GTY, Spelbring DR, Weichselbaum RR, Chen CT (1989) Accurate 3 -dimensional Registration of CT, PET and/or MR images of the Brain. J Comput Assist Tomogr. 13:20–26

Perona P, Malik J (1990) Scale space and edge detection using anisotropic diffusion. IEEE Trans. On Pattern Analysis and Machine Intelligence. 12:629–639

Pluim JPW, Maintz JBA, Viergever MA (2003) Mutual-information-based registration of medical images: a survey. IEEE Trans. on Medical Imaging 22:986–1004

Positano V, Gastaldelli A, Sironi AM, Santarelli MF, Lombardi M, Landini L (2004) An accurate and robust method for unsupervised assessment of abdominal fat by MRI. J Magn Reson Imaging 20:684–689

Santarelli MF, Positano V, Michelassi C, Lombardi M, Landini L (2003). Automated cardiac MR image segmentation: theory and measurement evaluation. Med Eng Phys, 25:149–159

Singh A, Goldgof D, Terzopoulos D (1998) Deformable Models in Medical Image Analysis. IEEE Press

Udupa JK, Samarasekera S (1996) Fuzzy connectedness and object definition: Theory, algorithm and application in image segmentation. Graphical Models and Image Processing 58:246–261

Viola P, Wells III WM (1995) Alignment by maximization of mutual information. Proc Int Conf Computer Vision 16–23

Xu C, Prince JL (1998) Snakes, Shapes, and Gradient Vector Flow. IEEE Trans. On Image Process. 7:359–369

Virtual Endoscopy

7

Paola Vagli, Emanuele Neri, Francesca Turini, Francesca Cerri, Claudia Cecchi, Alex Bardine, and Davide Caramella

CONTENTS

7.1 Introduction

Virtual endoscopy is a computer-generated simulation of the endoscopic perspective obtained by processing computed tomography (CT) or magnetic resonance (MR) datasets (Rubin et al 1996; Yuh et al. 1999) and is one of the applications of virtual reality in medicine (Geiger and Kikinis 1994).

The first presentations of virtual endoscopy in the radiological field were given by Vining in 1993 and 1994, who reported the application in the study of bronchi and colon, respectively. The idea to fly-through anatomical structures was followed by many investigators that had experienced the use of virtual endoscopy. Initial works were oriented to demonstrate the feasibility of the technique in the exploration of the entire human body (Lorensen 1995; Hara et al 1996; Rubin et al 1996), but soon focused experiences were carried out for specific clinical problems. Nowadays virtual endoscopy includes reports on the study of the colon, stomach, bronchial tree, larynx and trachea, middle and inner ear, paranasal sinuses, brain ventricles, vessels, biliary tract, urinary tract, and joints. The terminology used to describe the technique was adapted to the anatomical district in exams, i.e., virtual colonoscopy, bronchoscopy, cholangioscopy, ureterorenoscopy, angioscopy, etc.

P. Vagli, MD; E. Neri, MD; F. Turini, MD; F. Cerri, MD; C. Cecchi, MD; A. Bardine, MD; D. Caramella, MD
Diagnostic and Interventional Radiology, Department of Oncology, Transplants, and Advanced Technologies in Medicine, University of Pisa; Via Roma 67, 56100, Pisa, Italy

7.2 Technical Approach to Virtual Endoscopy

7.2.1 Image Acquisition

The unique difference between virtual endoscopy and other 3D (three-dimensional) imaging methods is the type of perspective. In virtual endoscopy the typical perspective of fiber-optic endoscopes is reproduced by a dedicated computer program; one can freely fly-through or around 3D objects that are produced by common 3D processing techniques based on surface or volume rendering. As a consequence, the properties of data that are used to generate virtual endoscopy are the same as any data used for other image processing techniques: volumes that respect the spatial relationships of the human body. However, it can be taken for granted that in virtual endoscopy there are specific requirements of image acquisition related to the purpose of the virtual endoscopic examination.

An obvious question regarding image acquisition is whether the acquisition should be focused specifi-

cally for virtual endoscopy or is independent, and if this technique can be used variably in any data set. In many situations virtual endoscopy is proposed as an additional tool of the standard examination, and imaging is performed using routine protocols, i.e., general survey of the abdomen. In such cases many parameters of the acquisition in CT or MR can influence the quality of virtual endoscopy.

7.2.1.1 Colon

Virtual endoscopy of the colon is a typical and probably the most important example of a dedicated study in the field of virtual endoscopy. The so-called "virtual colonoscopy" allows the evaluation of the internal surface of the colon in a minimally invasive manner, providing promising results for the diagnosis of cancer and clinically significant polyps (Fig. 7.1).

Many efforts have been made in the last years to improve the technique and patient's acceptance. Prior to examination the patient must perform an adequate colon cleansing in order to avoid the presence of fecal residue that can simulate polyps or block their visualization. The current standard is to obtain a colon as clean and dry as possible (Barish et al. 2005).

However bowel preparation should be tailored to the indication, with full or reduced cathartic preparation associated to tagging of fluids or stool. Adequate colonic distension (pneumocolon) is crucial for identification of colorectal polyps and differentiation between obstructive cancers and a collapsed segment. Distension is achieved by rectal air or carbon-dioxide insufflation, and standard scout view in lateral and anterior-posterior projections are acquired to verify the distension of the entire colon. The intravenous administration of a muscle relaxant, to reduce large bowel movement and

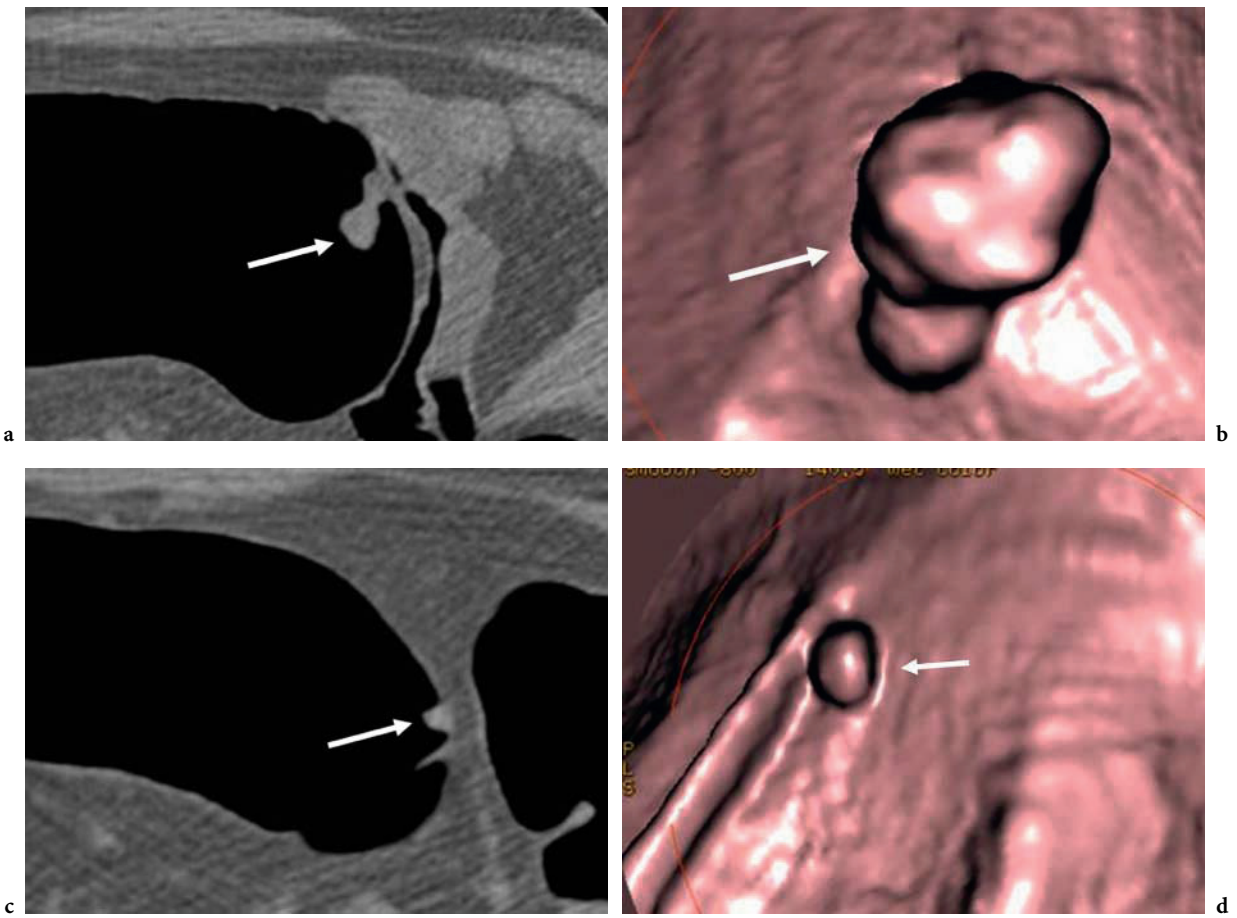

Fig. 7.1a–d. Multi-row CT colonography datasets showing a pedunculated (**a**, axial; **b**, endoluminal view) and sessile (**c**, axial; **d**, endoluminal view) polyp, located in the sigmoid colon

increase distension of the lumen, has been recently put aside because of frequent secondary effects and no significant improvement in colon distension and procedural discomfort (Yee et al. 1999; Luboldt et al. 2002). The scan protocol will depend on the equipment available. CT studies are performed in a single breath hold per position on a multi-row scanner, at least a four-slice scanner. However, 16-, 40- or 64-slice scanners are preferred combining small collimation and short breath hold, thus leading to improved patient comfort and reducing breathing artifacts. Currently a double scanning (prone and supine decubitus) is performed because distension of certain segments is influenced by position, and also the mobility may help to differentiate stools from lesions. Scans parameters should be optimized for detecting all relevant lesions (polyps larger than 5 mm), with tailored kV and mAs settings for the indications (symptomatic vs. screening). Using single-slice CT a collimation of 3–5 mm can be used to encompass the entire colon with pitch 2 and reconstruction spacing 1–2.5 mm; with a multi-row detector CT a 2–2.5 mm row thickness can be selected, but can be further reduced to 0.5–1 mm in 8 to 64 slice scanners, and even the scanning time can be shortened accordingly (Laghi et al. 2000; Rust et al. 2000; Rogalla et al. 2000; Hara et al. 2001). The use of intravenous contrast is not a prerequisite for endoluminal views (Morrin 2000) and will depend either on the indication for the examination and the bowel preparation that is used. In asymptomatic patients, there is no consensus on the use of intravenous contrast medium, but most prefer to not use it because of costs and risks. Disadvantage of this approach is the inferior evaluation of extracolonic findings and of submerged polyps in those patients not prepared with tagging.

The data for exploring the colon can also be produced by MR (Luboldt et al. 1999, 2000), but a final protocol has not been defined yet. First reports described breath hold 3D gradient echo (GRE) sequences in the coronal plane, with 5-mm partition thickness and the use of phased array coils at high field strength (1.5 T). Air and carbon dioxide have been used as colonic distension agents, but most reports address liquid enema techniques (Morrin et al. 2001; So et al. 2003). Currently three different liquid enema techniques are used: bright lumen, black lumen and fecal tagging. Both bright and black lumen methods are used after bowel cleansing. The bright lumen is based on a water-gadolinium enema completely filling the colonic lumen with thin-section 3D spoiled T1-weighted GRE sequence. Hereafter, a two-dimensional (2D) half-Fourier single-shot turbo spin echo sequence can be used for delineation of the colonic wall (Luboldt et al. 2000). The black lumen is based on a water enema for luminal distension and intravenous infusion of gadolinium for enhancement of the colonic wall depicted by a 3D spoiled T1-weighted GRE sequence. Also a 2D or 3D balanced GRE sequence to display a bright lumen can be added before gadolinium injection (Geenen et al. 2003). The fecal tagging technique is based on a diet that contains barium to give stools the same signal intensity as water on 3D spoiled T1-weighted GRE sequences obtained after a water enema and gadolinium injection (Lauenstein et al. 2002).

7.2.1.2 Vessels

Virtual vascular endoscopy "virtual angioscopy" uses 2D and 3D data sets from MR or CT angiography to create endoluminal views of blood vessels. This technique provides the view of the internal surface of vessels in a unique fashion and a corresponding clinical technique is not currently available. The study of vessels with virtual endoscopy requires the use of contrast in order to opacify the lumen and permit an adequate segmentation with surface or volume rendering. Dedicated angiographic protocols with a proper scan delay from contrast administration (generally performed with a bolus timing test) have developed according to the CT or MR equipment available. Initial studies regarding aortic diseases were aimed to facilitate both a qualitative and potentially a quantitative analysis to enhance diagnostic capabilities. Aortic dissection has represented one of the most exciting applications of virtual angioscopy in the era of single slice scanners, (collimation 3 mm, pitch 2 and reconstruction spacing 1 mm for the study of abdominal aorta and 5 mm collimation for the study of thoracic aorta), allowing to improve the assessment of the intimal flap origin, the extension of the true and false lumen and the relationship between the false lumen and supraortic vessels (Sbragia et al. 2001; Bartolozzi et al. 1998). The advent of multi-row CT angiographic protocols with faster scanning, thinner sections ($\leq$1 mm), greater scanning and contrast efficiency and reduced dose of contrast in respect to single-slice protocols (Neri et al. 1999b; Rubin et al. 2000), allow better resolution of images acquired, suggesting a subsequent better quality for virtual endoscopy and the possibility to

explore branching vessels such as renal, carotid and coronary arteries (Fig. 7.2). In these smaller vessels virtual angioscopy provides a better definition of anatomic details of the inner intimal surface (plaque morphology) or the internal stent lining, allowing a measurement of the luminal caliber of the vessels or the presence of intrastent stenosis (Carrascosa et al. 2005; Rilinger et al. 2003; Orbach et al. 2006).

The optimal MR angiography datasets for virtual endoscopy are those obtained with the contrast-enhanced technique. A bolus of i.v. gadolinium (0.1–0.2 ml/kg at 2–3 ml/s) is administered to the patient, and in the same fashion as CT angiography, the acquisition starts with the proper scan delay for the arterial phase (20–30 s). The imaging sequence is quite similar to the study of the colon and implies a SPGR sequence in the coronal plane with 3 mm partition thickness (Hany et al. 1998; Wildermuth and Debatin 1999). Previous and preliminary work reports the use of time of flight (TOF) sequences, but this technique is no longer proposed for such purposes (Davis et al. 1996).

The requirements for high quality virtual angioscopic images include homogeneous vascular enhancement, excellent definition of vessel boundaries, and high signal-to-noise ratio within the lumen. As a general rule, good source images generate high quality virtual angioscopic images. MR vir-

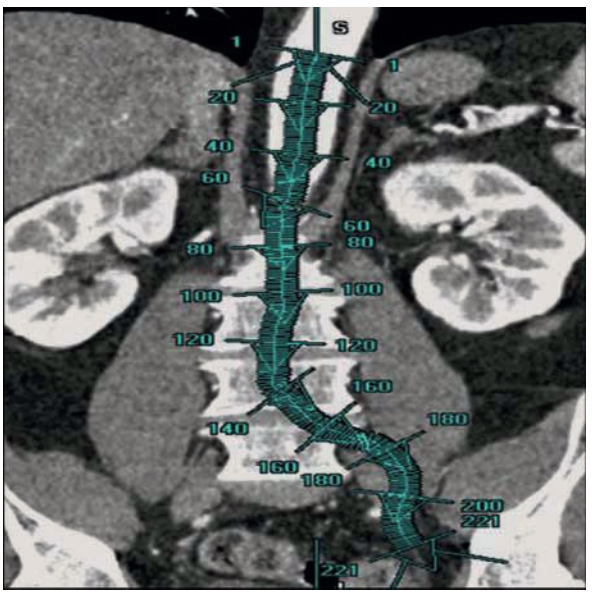

a

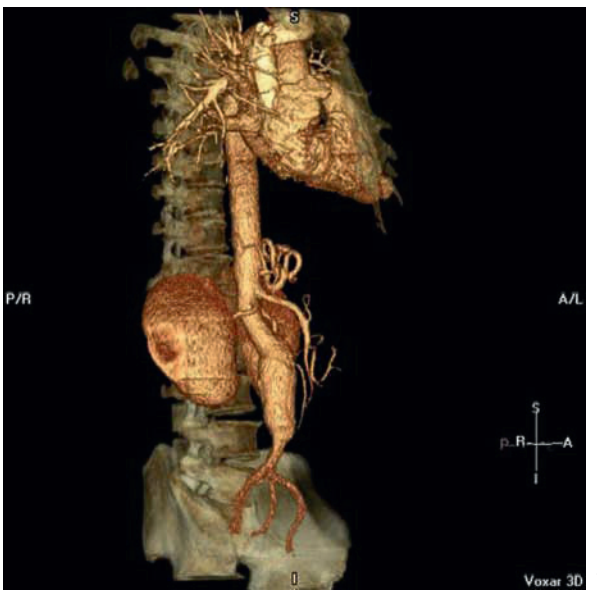

b

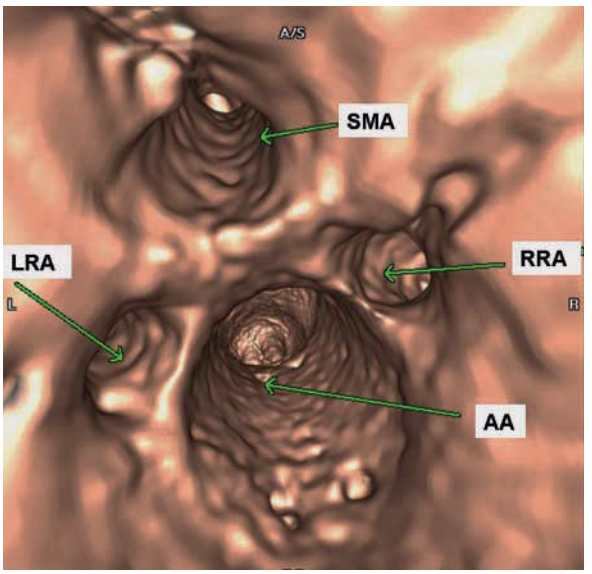

c

Fig. 7.2a–c. Multi-row CT angiography of the entire aorta. **a** MPR with cross sectional measurement of the vessel diameters, **b** 3D volume rendering and **c** endoluminal view obtained at the level of the renal arteries. In this latter view the orifi ces of the superior mesenteric artery (*SMA*), right (*RRA*) and left (*LRA*) renal arteries and the lumen of the abdominal aorta (*AA*) can be appreciated

tual angioscopy offers a unique perspective for visualizing 3D gadolinium-enhanced MR angiographic images. The clinical application of this technique is not completely defined, but may include preoperative planning for surgical and interventional procedures, detection of atherosclerotic plaques, and monitoring of disease progression or regression.

The current opinion is that the technology available is able to produce high quality virtual endoscopic images. Although axial and multiplanar (MPR) views are usually adequate for detecting a vascular disorder, virtual angioscopic views better define anatomic details, or this technique could be simply an alternative method for data presentation as 3D volumetric data sets continue to increase in size (Carrascosa et al. 2005; Glockner 2003).

7.2.1.3 Bronchi

Virtual endoscopy of the bronchial tree is done by processing spiral CT datasets (Ferretti et al. 1995; Vining et al. 1996; Summers et al. 1996; Aquino and Vining 1999). The study of this region is dependent on two main critical factors: the patients should hold the breath as long as possible in order to minimize movement artifacts and images should be acquired at a very high resolution to detect even segmental branches of the bronchi. Neumann et al. (2000) reported that the best results of virtual endoscopy were obtained using an examination protocol with a small beam collimation and a maximum pitch. The author concludes that the performance of virtual bronchoscopy strongly depends on the applied CT examination protocol and the observers experience with the software used for 3D imaging.

Lee et al. (1997) proposed the following single-slice spiral CT protocol for virtual endoscopy of the bronchial tree: thickness 3 mm, pitch 1, and reconstruction interval 1.5 mm. The technique has a limited scan distance of 9 cm, but the pitch can be increased to 2 for reaching 18 cm coverage (enough for the trachea and major airways). Fishman (2000) proposed the following protocol for virtual endoscopy with multi-row CT: collimation 1 mm, slice thickness 1.25 mm, reconstruction spacing 1 mm, and pitch 6 (time per rotation 0.5 s). In both cases no oral and intravenous contrast agents are needed for depicting the bronchial tree.

Multi-row CT protocols have improved the diagnostic value of virtual bronchoscopy allowing higher spatial resolution and therefore the visualization of the seventh or eight generations of airways or the bronchi below a closed obstruction. In addition the extraluminal location of a lesion can be visualized in transparency (usually enhanced mediastinal structures or pulmonary masses). Virtual bronchoscopy, initially referred to the simple depiction of the bronchial tree with poor clinical meaning, has became a powerful tool for thoracic interventions providing a road map for conventional bronchoscopy as a guide for transbronchial biopsy and for endobronchial treatment planning (Ferguson and McLennan 2005) (Fig. 7.3).

7.2.1.4 Biliary and Urinary Tract

At our institution, as well as for other authors, biliary and urinary tract imaging with MR was used to generate virtual endoscopy of this anatomical district (Dubno et al. 1998; Neri et al. 1999a; 2000a).

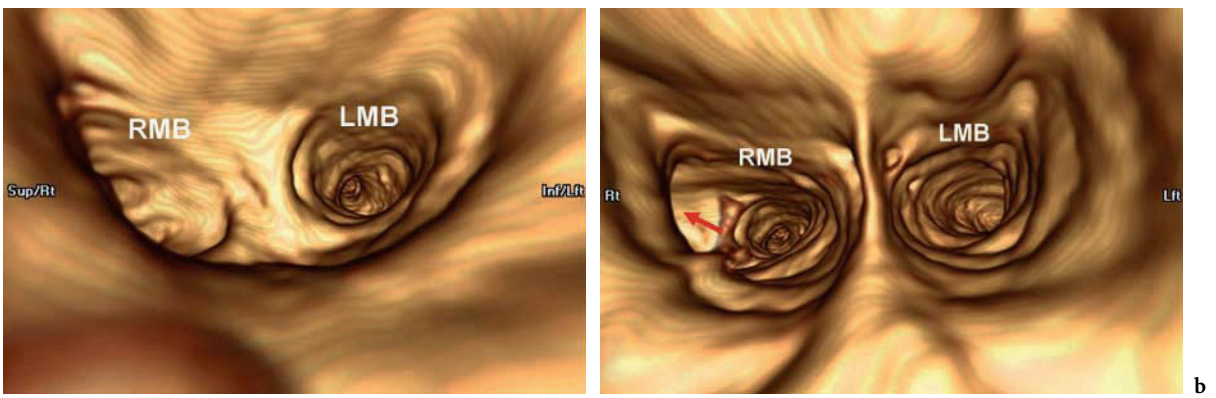

a b

Fig. 7.3a,b. Endoluminal views of the bronchial bifurcation. In **a** the right and left main bronchi are visible from the trachea. A more caudal view (**b**) shows even the orifice of the bronchus for the righ upper lobe (*red arrow*)

Datasets were obtained with MR cholangiopancreatography and MR urography techniques, producing the so-called "water images." These methods exploit the presence of stationary fluids within the biliary and urinary tracts that are therefore used as endoluminal contrast. Imaging sequences include heavily T2-weighted acquisitions in the axial, sagittal and coronal plane. To facilitate the generation of endoscopic views, the contrast between intraluminal fluid and extraluminal tissue can be improved by fat saturation and i. v. contrast administration (Prassopoulos et al. 2002; Simone et al. 2004).

As alternative method to MR in exploring the urinary tract, some experiences with CT pneumocystoscopy have been proposed for evaluating the urinary bladder after air or carbon-dioxide distension through a Foley catheter (Regine et al. 2003; Song et al. 2001).

7.2.1.5 Larynx

The study of the larynx is another important field of application of virtual endoscopy, and the use of high-resolution spiral CT images is recommended. Rodenwaldt (1997) evaluated the image quality of virtual endoscopy performed in a cadaver phantom, scanned with single slice spiral CT and varying the scanning collimation from 1 to 10 mm, and the pitch from 0.5 to 3. The best correlation between virtual endoscopy and anatomical findings in terms of diagnostic quality of the axial slices, and useful longitudinal coverage of the examination was observed with a collimation of 3 mm and a pitch of 1.5. In the larynx the complex anatomy requires the use of thin collimations (1–3 mm), but also the movement of the glottic plane in the course of phonation is a potential source of artifacts. This factor suggests the need of a fast scanning technique; Magli et al. (2001) report their experience with multi-row detector CT carried out in the evaluation of 22 patients (10 normal, 12 with pathology), by using slice thickness 1.3 mm, increment 0.6 mm, pitch 0.875, and rotation time 0.75.

To obtain virtual endoscopy of the larynx, the image acquisition is performed with the patient in the supine position on the CT table with moderate extension of the neck. The patient is asked to phonate the vocalic sounds "ee" or "ay;" this allows the true vocal cords to be parallel and more clearly visible since they are aligned in the middle line of the glottis (Fig. 7.4).

Virtual laryngoscopy can also be achieved from MR data and is particularly useful when the patient cannot tolerate clinical examination, when infection, neoplasms, or congenital defects compromise the lumen and for assessment the subglottic region (Byrne et al. 2005).

7.2.1.6 Nose and Paranasal Sinuses

The study of the nasal cavity and paranasal sinuses with virtual endoscopy can be performed by processing spiral CT data sets. Rogalla (1998) tried virtual endoscopy in 45 spiral CT examinations of the paranasal sinuses at low dose and compared virtual view with endoscopic images obtained during sinus surgery. De Nicola et al. (1997) applied virtual endoscopy with a surface reconstruction to spiral CT datasets in a wide range of paranasal sinus pathologies; Gilani et al. (1997) tried the same experience with a volume-rendered reconstruction. Spiral CT is addressed as the method of choice in 3D imaging of the paranasal sinuses. The spiral CT acquisition protocol includes axial thin section helical scan with 1–3 mm collimation, variable pitch and 1–2 mm reconstruction spacing, bone reconstruction algorithm, and 16 cm field of view. However, excellent results of virtual endoscopy of the nose and paranasal sinuses in defining anatomy were also obtained by Morra et al. (1998), who performed the study with a conventional CT scanner and proposed the following protocol: axial and coronal scan with 1.5–3 mm collimation, 1.5–3 mm table feed, 120 kV, 140 mAs, 2 s scan time, bone reconstruction algorithm and 14–16 cm field of view (Fig. 7.5).

MR offers some advantages in the study of the paranasal sinuses concerning the reduced artifacts caused by dental fillings and the ability of displaying the anatomical details in a multiplanar fashion by using slices of 4–5 mm or smaller. Recent sequences such as FLASH (fast low angle shot) or FISP (fast imaging with steady state processing) may provide a detailed representation by means of thin (1 mm) sections or with 3D volumetric acquisitions. A head coil is commonly used, although better details can be achieved with dedicated surface coils.

7.2.1.7 Middle and Inner Ear

Pozzi Mucelli et al. (1997), who first tried to generate virtual endoscopic images of the tympanic

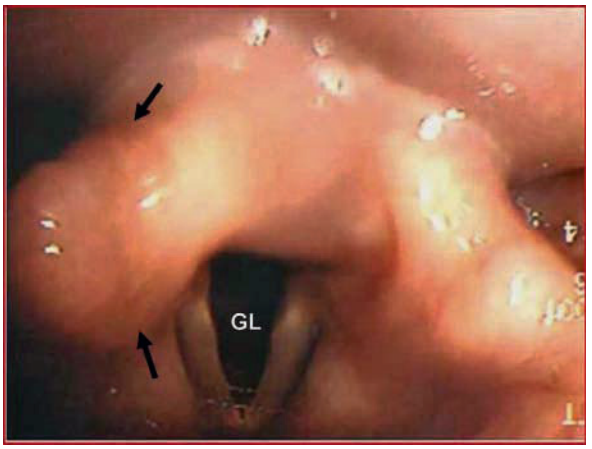

a

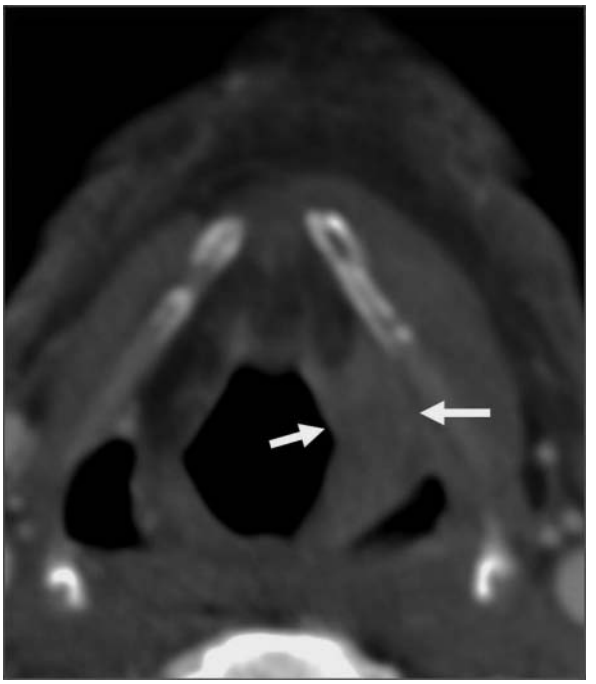

b

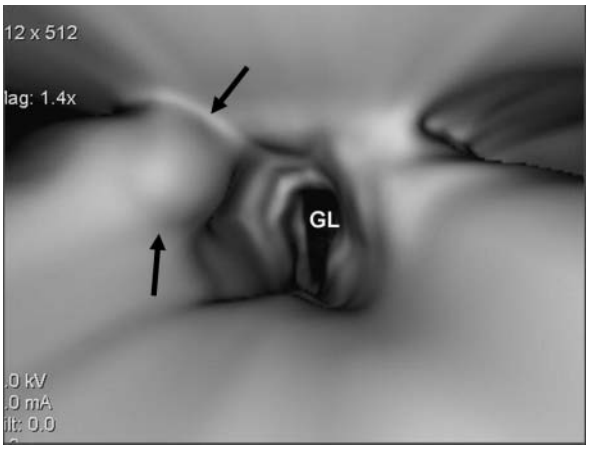

c

Fig. 7.4a–c. Laryngoscopy and multi-row CT of the larynx. At laryngoscopy a thickening of the left arithenoid and the corresponding glosso-epiglottic fold is demonstrated (**a**, *arrows*). Axial multi-row CT image (**b**) and 3D endoluminal view (**c**) confirm the presence of a larynx cancer (*arrows*)

a

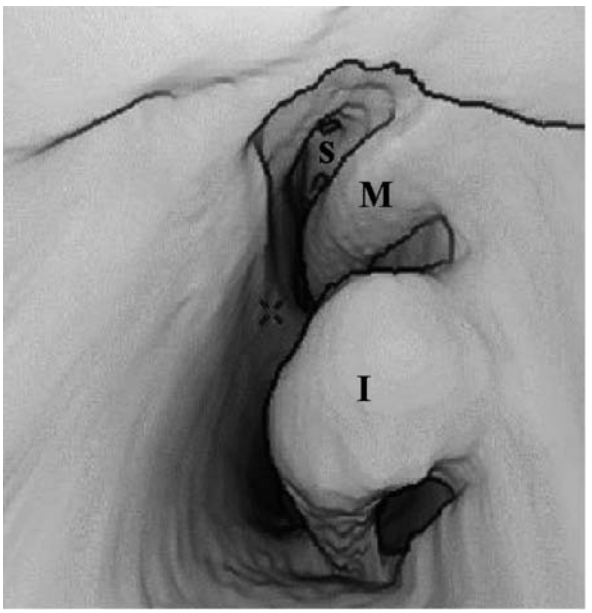

b

Fig. 7.5a,b. CT virtual endoscopy of the nasal cavity created with a perspective positioned in the rynopharynx (**a**). The *arrow* indicates the orientation of the virtual endoscope. The right superior (*s*), middle (*M*) and inferior (*I*) turbinates are shown (**b**)

cavity, used a conventional CT with high-resolution acquisitions (1 mm collimation) and obtained excellent results in visualizing the ossicular chain.

In the study of the middle and inner ear we have proposed the following single-slice spiral CT protocol: axial and coronal acquisitions; beam collimation, 1 mm; pitch 1 and 0.5 mm reconstructions spacing (see Chap. 10 on temporal bone for details) (Neri et al. 2000b). In this study all components of the middle ear could be visualized, but also endoluminal views of the bone labyrinth were created (Fig. 7.6).

Tomandl et al. (2000) applied the same acquisition protocol and used a volume-rendered technique to reconstruct the labyrinth with excellent results in terms of anatomical definition of labyrinthine components.

Actually no substantial difference between spiral CT and conventional CT in generating virtual endoscopy of the middle and inner ear is reported; however, the anatomical details of the middle ear seem to be better displayed using the multi-row detector CT (see Chap. 10 on temporal bone). Although clinical applications of the technique remain to be defined, it may play a role in presurgical diagnostic evaluation of the ossicular chain, epitympanum–retrotympanum, bone labyrinth and postoperatively for the assessment of the position of implants. High-resolution MR imaging with dedicated surface coils provides 3D data useful for the evaluation of the membranous labyrinth.

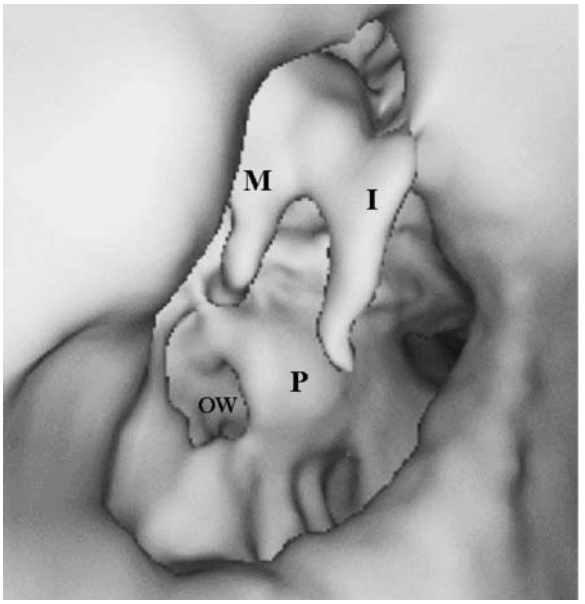

Fig. 7.6. CT virtual endoscopy of the middle ear generated from a point of view located in the external auditory canal, shows the incus (*I*), malleus (*M*), promontory (*P*) and oval window (*OW*)

7.2.2 Volume Generation

Each patient dataset is composed by a definite number of series corresponding to the different phase of acquisition, unenhanced or enhanced. Nowadays, the images format respects the DICOM standard, and all available workstations support it (Prior 1993; Ackerman 1994).

Once the CT or MR datasets have been acquired and transferred to dedicated workstations, these are processed by the software to generate volume. The volume is composed by stacking all the reconstructed slices along the centerline of each slice. The centerline corresponds to the longitudinal axis (Z axis) in spiral CT, but in case of MR can be oriented along any other plane (coronal, sagittal). One problem of MR arises when the acquisition plane is oblique; in this case some software does not accept the reslicing of such native images because they are not perpendicular to the centerline.

The volume is in general automatically created by each 3D software, and the radiologist is asked uniquely to select the desired imaging series to be reconstructed. To reduce the image overload a reduced volume can be reconstructed by selecting the images corresponding to a selected anatomical area. To do this the starting and ending points of the acquisition (on the Z axis) should be annotated and then this value can be changed by the operator at the image processing workstation.

Within the software architecture the volumetric dataset is organized in terms of voxels. These are near cubic elements that arise from each image pixel. This latter is the basic building block for the voxel to which a Hounsfield value (in case of CT) or an intensity value (in case of MR) is assigned; each voxel has also a defined spatial position and dimension in the volume.

The ideal volumetric dataset, which respect precisely the imaged structures, is obtained when all voxels are isotropic, and therefore their shape is cubic. Unfortunately conventional CT and spiral CT did not fulfill completely these acquisition requirements. Dedicated MR sequences and multi-row detector CT (over 16 slices) overcome this limitation generating isotropic voxels and reducing motion artifacts thanks to faster acquisition protocols.

7.2.3 Volume Segmentation

Surface and volume renderings are the methods used to virtually represent the human body in three dimensions. Each owns a specific principle of dataset segmentation in order to select the anatomical structure to display from the inside. For details on the technical basis of segmentation in surface and volume rendering, refer to dedicated chapter.

Most available software for virtual endoscopy allows the radiologist to interact with the volumetric sample and segment it in real time. By using surface rendering the change of visible structure is made by the selection of a threshold that defines the edge line of a surface to display and represents effectively the passage between two different density or intensity values (i.e., the colonic mucosa and the colonic lumen filled by air). Thus, before starting the inner visualizations with this method, the operator should be aware on the different threshold values used. For example, the colonic surface in a CT study with pneumocolon can be optimally represented with thresholds ranging from –800 to –700 HU (those value are modified in case of tagging, or tagged stool may be eliminated by dedicated algorithms such as "electronic cleansing"), the middle ear –500 HU, and the threshold for displaying aortic lumen depends on the degree of contrast enhancement (in both CT and MR angiography).

In volumerendering technique the generation of endoscopic view is quite flexible and interactive when the computer used is powerful enough. In fact, volume rendering requires high computational power and specific hardware capabilities (see Chap. 6). Almost all commercially available software has been implemented with pre-defined volume-rendering protocols that produce endoluminal views of specific organs. To simplify the concept, in volume rendering the use of a threshold is strongly smoothed by the use of transfer opacity functions; therefore, the passage between structures having different voxel properties is attenuated and progressively increased or decreased by a linear scale of values.

7.2.4 Perspective Generation

The typical endoscopic view is generated by a ray casting algorithm (Roth 1982). In ray casting, parallel rays are virtually generated by a source point (the eye of the observer or point in which the endoscope is positioned); the rays transverse the acquired volume along a divergent direction, and applying surface- or volume-rendering algorithms, the encountered voxels are classified by the attribution of opacity values. In surface rendering the voxels located above or below a specific threshold that are encountered by the rays cast are fixed and transformed in a mesh of polygons reflecting each ray. The algorithm used to perform the surface extraction is called "marching cube" (Lorensen and Cline 1987). It transforms the cubic shape of a voxel into a mesh of triangles (triangulation), and the final composition of the transformed voxels constitutes an isosurface.

In volume rendering the classification of voxels is given by linear opacity functions that attribute different opacity values to particular voxel intensities. The advantages of this approach are the optimization of the dynamic range and the ability to change tissue opacities to produce 3D renderings that maintain surface details and represent the entire data set.

The final image of surface- or volumerendered ray casting will have a conic field of view (as in endoscopy). As a result, parts of the examined organ close to the point of view appear larger than those of identical size at greater distance. The field of view can be changed by the viewing angle. Many softwares have a large viewing angle, but increasing this value a certain distortion of the surface morphology occurs and alters the possibility to recognize pathological findings. This approach seems to have other limitations that are also proper of the real endoscopy; i.e., exploring the colon from the rectum to cecum, even using the widest viewing angle, not all haustral folds are entirely visualized (Fig. 7.7). To reach a major diagnostic confidence a backward navigation is recommended, from cecum to rectum, in order to explore some hidden corners not visible with a single navigation. This is a time-consuming approach; therefore navigation is actually validated for problem solving when doubt persists after viewing of sources or multiplanar images. Many investigators are trying to set up different viewing perspectives that could display the entire colonic wall in a single navigation. Paik et al. (2000) proposed a map projection of the colon based on both Mercator and stereographic techniques and compared this approach with the conic view. The work showed that the percentage of mucosal surface visualized by map projection (98.8%) could only be reached by the conic view at a very high

viewing angle, an effect that causes a certain viewing distortion of mucosal details. Moreover, polyps >7 mm were analyzed, and map projection showed a significantly higher sensitivity (87.5%) than axial images (62.5%) and conic views (67.5%).

One similar and interesting approach to colon visualization, called "unfolding," has been proposed by Sorantin (2001) (Chaps. 18, 19). The technique is based on non-linear ray casting of polyps, and non-linear 2D scaling to compensate the distortions due to the unfolding (Vilanova Bartroli 2000). In substance the colon is completely unfolded, sliced open and projected on a bi-dimensional plane similar to a gross pathologic specimen. This technique has the potential to reduce evaluation time and may also improve accuracy by reducing blind spots present in 3D endoluminal displays (Fig. 7.8). A disadvantage of virtual dissection is the potential for distortion of colonic lesions and normal anatomy (Silva et al. 2006). A similar approach has been proposed by Wang et al. (1996 and 1998) in multiple applications.

Initial data using computer-aided detection (CAD) software for colon examination have suggested a CAD-assisted 2D read is as sensitive, but significantly more time efficient than primary 3D (endoscopic) analysis (Taylor et al. 2006), although the influence of CAD on those using a primary 3D analysis is also promising (Chap. 27).

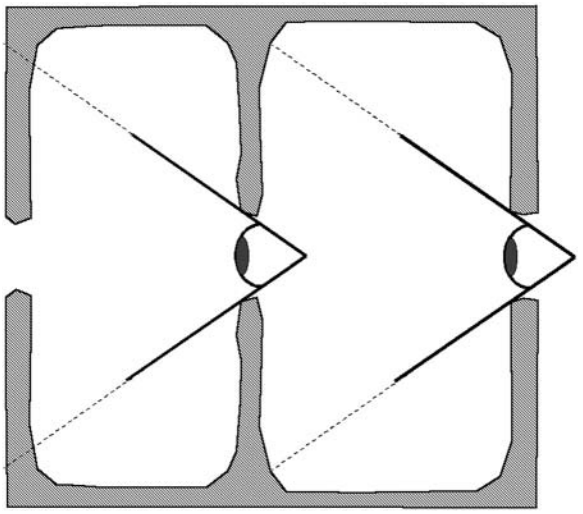

Fig. 7.7. Effects of conic view in virtual endoscopy of the colon. The exploration can be obscured by colonic folds; if a restricted viewing angle is used some hidden corners of the colonic wall are not visualized

7.2.5 Fly-Through Path

Fly-path planning is a critical issue in virtual endoscopy. The navigation through tubular structures is quite difficult, especially if these are tortuous and present sharp curves, caliber enlargement or strong reduction along their path. The calculation of the shorter and central navigation path is required to help the radiologist. The ideal assisted navigation should allow the radiologist to stay comfortably in front of the computer display and look at a movie of the complete fly-through of the structure in the exam. This is easy to perform in structures that are quite straight, such as the abdominal aorta or trachea, but become difficult in examining the colon.

The requirements of an assisted navigation are: automatic path planning, collision detection, and

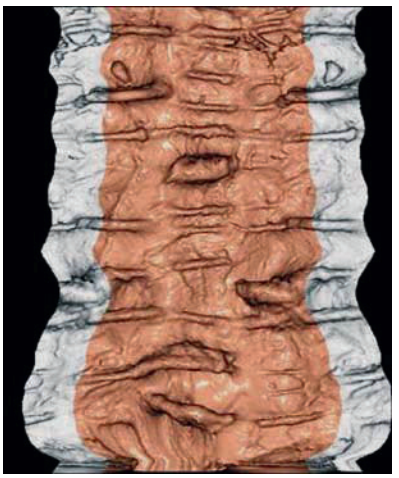

a

b

Fig. 7.8a,b. Dissected view tools of the colon generated with software from different vendors. Barco/Voxar Colonscreen (**a**) and GE Medical Systems Virtual dissection (**b**)

direct interaction with the objects displayed. The last point should consist of the following steps: stop the navigation, look the object, touch the object, cross correlation with other images (axial, MPR, and external 3D models). The line on which the virtual camera is traced can be determined either by automatic routes that follow anatomy or by manual or semiautomatic point placement. A curve fit to these points permits intermediate points to be calculated and can be saved for future playback of the fly-through. The viewing angle relative to the curve can also be varied along the line. The calculation of automatic path has been proposed by various authors. Joles (1997) proposed a method in which the endoscopic camera is considered as a robot and the walls of the organs as obstacles. The obstacles are identified as ranges of threshold values, or tissue labels and the path planner labeled all voxels within the 3D dataset with a distance to a goal. Then, given a starting point, the path planning algorithm finds the shortest path to the goal and the voxel coordinates for each point in the path are recorded.

Paik et al. (1998) proposed a method based on the medial axis transform. The method calculates the centerline of hollow organs by iterative thinning of the segmented structure and path correction. A similar method is the cylindrical approximation of tubular organs, proposed by Vilanova Bartroli (2000).

However, any given automatic path is not free of errors in calculation, and the collision with the organ's surface is possible. Collision detection algorithms work as in the case of the Joles et al. (1997) method. The surface is identified as a variation of threshold value, and therefore when the endoscope finds it, it performs a change or direction.

The collision detection algorithm is also used in VRML (virtual reality modeling language), where surface-rendered models represent different objects of a virtual world that can be explored through Internet browsers. We have made and are experienced in the use of VRML to fly-through abdominal aortic aneurysms. The fly-through path was created after segmentation of CT angiography datasets by calculating the centerline of consecutive sections of the aorta obtained along perpendicular planes to the main axis of the vessel (Neri 2000c).

The direct interaction with the objects displayed in the endoscopic views is an absolute requirement of virtual endoscopy. The main criticism of this technique is that it can wrongly represent objects of the real world. To overcome this problem most software allows the visualization of the target object, points on it with the computer mouse and obtains the corresponding axial or MPR image crossing through it. On the other hand, we must remind physicians that virtual endoscopy is not a stand-alone technique, but is one of the possible means through which volumetric datasets can be represented. Therefore, a constant correlation with native data and MPR should always be performed, especially to confirm endoscopic findings.

7.3 Conclusion

Virtual endoscopy is an emerging technique in radiology developed in the past decade. The last few years have seen the continued development of increasingly advanced 3D-rendering softwares, and sophisticated visualized displays have been developed, including flattened endoluminal perspective or "virtual pathology." Investigation of the impact of new technologies on data set analysis is in its infancy with data both for and against the new technology. There is some evidence that primary 3D analysis may be more sensitive than the analysis of the native images, especially for less experienced readers.

Virtual endoscopy can be used for visualizing CT, MR and US datasets, and even if in each case the technical approach is quite similar, the image acquisition strongly impacts on the final 3D image. In most cases the image acquisition is performed with specific protocols for characterizing pathologies that are not compliant with 3D reconstructions. On the other hand the developments in image acquisition are oriented to generate volumetric data much more compatible for this purpose. Thus, the future of virtual endoscopy in radiology seems to be less affected by image acquisition; the real issue is whether or not it will be clinically effective. Some applications of virtual endoscopy may be considered as pure iconographic means, although in some cases they may help to display a complex anatomy or can provide a more familiar perspective, especially for surgeons.

Most investigators agree that the colon exploration actually represents the main clinical impact of virtual endoscopy. In the last decade, this dedicated technique has been validated as a reliable tool for

the non-invasive diagnosis of colorectal polyps and cancer, and many efforts have been made to improve the technique and patient acceptance.

References

Ackerman LV (1994) DICOM: the answer for establishing a digital radiology department. Radiographics 14:151–152

Aquino SL, Vining DJ (1999) Virtual bronchoscopy. Clin Chest Med 20:725–730

Bartolozzi C, Neri E, Caramella D (1998) CT in vascular pathologies. Eur Radiol 8:679–684

Barish MA, Soto JA, Ferrucci JT (2005) Consensus on current clinical practise of virtual colonoscopy. AJR 184:786–792

Byrne AT, Walshe P, McShane D, Hamilton S (2005) Virtual laringoscopy–preliminary experience. Eur J Radiol 56:38–42

Carrascosa P, Capunay C, Vembar M, Ciancibello L, Carrascosa J (2005) Multislice CT virtual angioscopy of the abdomen. Abdom Imaging 30:249–258

Davis CP, Ladd ME, Romanowski BJ, Wildermuth S, Knoplioch JF, Debatin JF (1996) Human aorta: preliminary results with virtual endoscopy based on three-dimensional MR imaging data sets. Radiology 199:37–40

De Nicola M, Salvolini L, Salvolini U (1997) Virtual endoscopy of nasal cavity and paranasal sinuses. Eur J Radiol 24:175–180

Dubno B, Debatin JF, Luboldt W, Schmidt M, Hany TF, Bauerfeind P (1998) Virtual MR cholangiography. AJR 171:1547–1550

Ferguson JS, McLennan G (2005) Virtual bronchoscopy. Proc Am Thorac Soc 2:488–491

Ferretti G, Knoplioch J, Coulomb M, Brambilla C, Cinquin P (1995) Endoluminal 3D reconstruction of the tracheobronchial tree (virtual bronchoscopy). J Radiol 76:531–534

Fishman EK (2000) Spiral and multidetector CT of thoracic pathology: techniques and clinical applications. Radiology 217 (S1):618

Geenen RWF, Hussain SM, Cademartiri F, Poley JW, Siersema PD, Krestin GP (2003) CT and MR colonography: scanning techniques, postprocessing, and emphasis on polyp detection. Radiographics 24:e18

Geiger B, Kikinis R (1994) Simulation of endoscopy. AAAI Spring Symposium Series: Applications of Computer Vision in Medical Images Processing, Stanford University, pp 138–140

Gilani S, Norbash AM, Ringl H, Rubin GD, Napel S, Terris DJ (1997) Virtual endoscopy of the paranasal sinuses using perspective volume rendered helical sinus computed tomography. Laryngoscope 107:25–29

Glockner JF (2003) Navigating the aorta: MR virtual vascular endoscopy. Radiographics 23:e11 review

Hany TF (1998) Diagnostic impact of four postprocessing techniques in evaluating contrast-enhanced three-dimensional MR angiography. AJR 170:907–912

Hara AK, Johnson CD, Reed JE, Ahlquist DA, Nelson H, Ehman RL, McCollough CH, Ilstrup DM (1996) Detection of colorectal polyps by computed tomographic colography: feasibility of a novel technique. Gastroenterology 110:284–290

Hara AK, Johnson CD, MacCarty RL, Welch TJ, McCollough CH, Harmsen WS (2001) CT colonography: single- versus multi-detector row imaging. Radiology 219:461–465

Jolesz FA, Lorensen WE, Shinmoto H, Atsumi H, Nakajima S,Kavanaugh P, Silverman SG, Phillips M, Kikinis R (1997) Interactive virtual endoscopy. AJR 169:1229–1237

Lauenstein TC, Goehde SC, Ruehm SG, Holtmann G, Debatin JF (2002) MR colonography with barium-based fecal tagging: initial clinical experience. Radiology 223:248–254

Lorensen WE, Cline HE (1987) Marching cubes: a high resolution 3D surface reconstruction algorithm. Computer Graphics 21:163–169

Lorensen WE (1995) The exploration of cross-sectional data with a virtual endoscope. In: Interactive technology and the new paradigm for healthcare. Morgan K, Satava RM, Sieburg HB, Mattheus R, Christensen JP (eds). IOS Press and Ohmsha, Berlin, pp 221–230

Laghi A, Catalano C, Panebianco V, Iannaccone R, Iori S, Passariello R (2000) Optimization of the technique of virtual colonoscopy using a multislice spiral computerized tomography. Radiol Med 100:459–464

Lee KS, Yoon JH, Kim TK,Kim JS, Chung MP, Kwon OJ (1997) Evaluation of tracheobronchial disease with helical CT with multiplanar and three-dimensional reconstruction: correlation with bronchoscopy. Radiographics 17:555–567

Luboldt W, Frohlich JM, Schneider N, Weishaupt D,Landolt F, Debatin JF (1999) MR colonography: optimized enema composition. Radiology 212:265–269

Luboldt W, Wildermuth S, Marincek B, Fried M, Debatin JF (2000) Colonic masses: detection with MR colonography. Radiology 216:383–388

Luboldt W, Fletcher JG, Vogl TJ (2002) Colonography: current status, research directions and challenges: update 2002. Eur Radiol 12:502–524

Magli T, Fella R, Scialpi M, Lorenzini E (2001) Virtual laryngoscopy with multislice volumetric spiral CT: preliminary study. Eur Radiol 11(Suppl 1): 399–400

Morra A, Calgaro A, Cioffi V, Pravato M, Cova M, Pozzi Mucelli R (1998) Virtual endoscopy of the nasal cavity and the paranasal sinuses with computerized tomography. Anatomical study. Radiol Med 96:29–34

Morrin MM, Farrell RJ, Kruskal JB, Reynolds K, McGee JB, Raptopoulos V (2000) Utility of intravenously administerd contrast material at CT colonography. Radiology 217: 765–771

Morrin MM, Hochman MG, Farrell RJ, Marquesuzaa H, Rosemberg S, Edelman RR (2001) MR colonography using colonic distension with air as the contrast material: work in progress. AJR 176:144–146

Neri E, Boraschi P, Braccini G, Caramella D, Perri G, Bartolozzi C (1999a) MR virtual endoscopy of the pancreaticobiliary tract. Magn Reson Imaging 17:59–67

Neri E, Caramella D, Falaschi F, Sbragia P, Vignali C, Laiolo E, Viviani A, Bartolozzi C (1999b) Virtual CT intravascular endoscopy of the aorta: pierced surface and floating shape thresholding artifacts. Radiology 212:276–279

Neri E, Boraschi P, Caramella D, Battolla L, Gigoni R, Armillotta N, Braccini G, Bartolozzi C (2000a) MR virtual endoscopy of the upper urinary tract. AJR 175:1697–1702

Neri E, Caramella D, Battolla L, Cosottini M, Scasso CA, Bruschini P, Pingitore R, Bartolozzi C (2000b) Virtual endoscopy of the middle and inner ear with spiral computed tomography. Am. J Otol 21:799–803

Neri (2000c) Virtual reality modeling language: applications to the study of abdominal aortic aneurysms. Radiology 217 (S1):486–487

Neumann K, Winterer J, Kimmig M, Burger D, Einert A, Allmann KH, Hauer M, Langer M (2000) Real-time interactive virtual endoscopy of the tracheo-bronchial system: influence of CT imaging protocols and observer ability. Eur J Radiol 33:50–54

Orbach DB, Pramanik BK, Lee J, Maldonado TS, Riles T, Grossman RI (2006) Carotid artery stent implantation: evaluation with multi-detector row CT angiography and virtual angioscopy–initial experience. Radiology 238:309–320

Paik DS, Beaulieu CF, Jeffrey RB, Rubin GD, Napel S (1998) Automated flight path planning for virtual endoscopy. Med Phys 25:629–637

Paik DS, Beaulieu CF, Jeffrey RB Jr, Karadi CA, Napel S (2000) Visualization modes for CT colonography using cylindrical and planar map projections. J Comput Assist Tomogr 24:179–188

Pozzi Mucelli RS, Morra A, Calgaro A, Cova M, Cioffi V (1997) Virtual endoscopy of the middle ear with computed tomography. Radiol Med 94:440–446

Prassopoulos P, Papanikolaou N, Maris T, Gogas C, Mouzas J, Gourtsoyiannis N (2002) Development of contrast-enhanced virtual MR cholangioscopy. Eur Radiol 12:1438–1441

Prior FW (1993) Specifying DICOM compliance for modality interfaces. Radiographics 13:1381–1388

Regine G, Atzori M, Buffa V, Miele V, Ialongo P, Adami L (2003) Virtual CT pneumocystoscopy: indications, advantages and limitations. Our experience. Radiol Med 106:154–159

Rilinger N, Seifarth H, Sokiranski R, Kramer S, Liewald F, Goerich J, Tomzcak A, Nierhoff CEE (2003) Virtual intra-arterial angioscopy of the carotid artery based on helical CT data. Br J Radiol 76:792–797

Rogalla P, Nischwitz A, Gottschalk S, Huitema A, Kaschke O, Hamm B (1998) Virtual endoscopy of the nose and paranasal sinuses. Eur Radiol 8:946–950

Rogalla P, Meiri N, Ruckert JC (2000) Colonography using multislice CT. Eur J Radiol 36:81–85

Rodenwaldt J, Kopka L, Roedel R, Margas A, Grabbe E (1997) 3D virtual endoscopy of the upper airway: optimization of the scan parameters in a cadaver phantom and clinical assessment. J Comput Assist Tomogr 21:405–411

Roth SD (1982) Ray casting for solid modelling. Comput Graph Image Proc 18:109–144

Rubin GD, Beaulieu CF, Argiro V, Ringl H, Norbash AM, Feller JF, Dake MD, Jeffrey RB, Napel S (1996) Perspective volume rendering of CT and MR images: Applications for endoscopic imaging. Radiology 199:321–339

Rust GF,Eisele O, Hoffmann JN, Kopp R, Fürst H, Reiser M (2000) Aorta and iliac arteries: single versus multiple detector-row helical CT angiography. Radiology 215:670–676

Rust GF (2000) Virtual coloscopy with multi-slice computerized tomography. Preliminary results. Radiologe 40:274–282

Sbragia P, Neri E, Panconi M, Gianni C, Cappelli C, Bargellini I, Bartolozzi C (2001) CT virtual angioscopy in the study of thoracic aortic dissection. Radiol Med 102:245–249

Silva AC, Wellnitz CV, Hara AK (2006) Three-dimensional virtual dissection at CT colonography: unravelling the colon to search for lesions. Radiographics 26:1669–1686

Simone M, Mutter D, Rubino F, Dutson E, Roy C, Soler L, Marescaux J (2004) Three-dimensional virtual cholangioscopy. Ann Surg 240:82–88

So NM, Lam WW, Mann D, Leug KL, Metreweli C (2003) Feasibility study of using air as a contrast medium in MR colonography. Clin Radiol 58:555–559

Song JH, Francis IR, Platt JF, Cohan RH, Mohsin J, Kielb SJ, Korobkin M, Montie JE (2001) Bladder tumor detection at virtual cystoscopy. Radiology 218:95–100

Sorantin E (2001) Technique of virtual dissection of the colon based on spiral CT data. Bartolozzi C, Caramella D (eds) In: Medical radiology–diagnostic imaging. Springer, Berlin Heidelberg New York

Summers RM, Feng DH, Holland SM, Sneller MC, Shelhamer JH (1996) Virtual bronchoscopy: segmentation method for real-time display. Radiology 200:857–862

Taylor SA, Halligan S, Slater A (2006) Polyp detection with CT colonography: primary 3D endoluminal analysis versus primary 2D transverse analysis with computer-assisted reader software. Radiology 239:759–767

Tomandl BF, Hastreiter P, Eberhardt KE, Rezk-Salama C, Greess H, Nissen U, Huk WJ (2000) Virtual labyrinthoscopy: visualization of the inner ear with interactive direct volume rendering. Radiographics 20:547–558

Vining DJ (1993) Virtual bronchoscopy: a new perspective for viewing the tracheobronchial tree. Radiology 189:438

Vining DJ (1994) Virtual colonoscopy. Radiology 193:446

Vining DJ, Liu K, Choplin RH, Haponik EF (1996) Virtual bronchoscopy. Relationships of virtual reality endobronchial simulations to actual bronchoscopic findings. Chest 109:549–553

Vilanova Bartroli A (2000) Cylindrical approximation of tubular organs for virtual endoscopy. In: Hamza MH (ed) Proceedings of Computer Graphics and Imaging, 283–289. IASTED/ACTA

Wang G, Vannier MW, Skinner MW, Kalender WA, Polacin A, Ketten DR (1996) Unwrapping cochlear implants by spiral CT. IEEE Trans Biomed Engineer 43:891–900

Wang G, McFarland EG, Brown BP, Vannier MW (1998) GI tract unraveling with curved cross sections. IEEE Transaction on Medical Imaging 17:318–322

Wildermuth S, Debatin JF (1999) Virtual endoscopy in abdominal MR imaging. Magn Reson Imaging Clin N Am 7:349–364

Yee J, Hung RK, Akerkar GA, Wall SD (1999) The usefulness of glucagon hydrochloride for colonic distention in CT colonography. AJR 173:169–172

Yuh EL, Jeffrey RB Jr, Birdwell RL, Chen BH, Napel S (1999) Virtual endoscopy using perspective volume-rendered three-dimensional sonographic data: technique and clinical applications. AJR 172:1193–1197

3D Image Fusion

8

Alan Jackson, Neil A. Thacker, and Stavros M. Stivaros

CONTENTS

8.1 Introduction

The routine production of 3D imaging data from modern imaging systems has led to a rapid growth in image post-processing methods. As described in previous chapters, many of these can be applied to single 3D data sets to improve data interpretation by producing 3D visualizations of data content, or by allowing automatic identification of specific features using segmentation techniques. However, in many cases the data content of a single 3D image is inadequate to provide all the information required. Under these circumstances a combination of information from two or more separate data sets may be necessary. As practicing radiologists we subconsciously perform this type of data fusion when we use images from for example, CT and MRI sequences to attempt to better characterise an abnormality, or when we compare images from a single case taken at different times to allow monitoring of disease progression. For example, faced with a cystic mass at the base of the brain we would routinely request T1 and T2W MRI to determine the presence of free fluid in the cyst and the presence and extent of oedema, MR angiography to determine the spatial relationship of the lesion to the major vessels and CT scanning to determine the presence of any bony abnormality. When we perform this type of analysis we are instinctively increasing the information content of our data, using additional examinations to provide complementary information required for our analysis. When reporting this type of multimodality imaging we also instinctively register the anatomical locations of features from the various examinations.

The increased data content of such multiparametric data sets can also be used to support a range of sophisticated image analysis techniques with a wide range of both clinical and research applications. It has been shown that image coregistration of different imaging modalities and interrogation of the fused images is diagnostically superior to side-by-side analysis of non-fused images (Amthauer et al. 2005). Analysis of data from multiple 3D images inevitably assumes spatial coregistration between the data sets. In practice it is extremely unusual to acquire images with these characteristics. Simultaneous collection of two or more data sets will ensure accurate coregistration. This can be exploited by the use of multiple echoes on MRI examinations to produce matched proton density and T2W images from the same series of excitations, or new echo planar

A. Jackson, PhD, FRCR, FRCP
Professor, Imaging Science and Biomedical Engineering, The Medical School, University of Manchester, Stopford Building, Oxford Rd, Manchester M13 9PT, UK
N. A. Thacker, MD
S. M. Stivaros, MD
Imaging Science and Biomedical Engineering, The Medical School, University of Manchester, Oxford Rd, Stopford Building, Manchester M13 9PT

imaging techniques which allow the simultaneous acquisition of predominantly T1 weighted and T2* weighted images in dynamic contrast-enhanced perfusion studies (Zaitsev et al. 2005). This approach is extremely restrictive and in most cases 3D images will be collected at different times and often on different modalities. In these circumstances separate 3D images must be co-registered in some way to provide absolute spatial coregistration.

8.2 Basic Theory of Image Coregistration

The aim of image coregistration techniques is to ensure that:

"Each pixel in the various data sets represents exactly the same volume of tissue in the patient."

In practice there are many ways in which we can attempt to achieve this and the technique selection will depend on the imaging modalities involved, the reason for coregistering the images and the accuracy of coregistration required for the analysis technique to be employed.

The simplest approach to coregistration of data sets is to attempt to acquire subsequent images with a spatial geometry identical to that of the original base images. Image registration can be attempted by using a baseline set of images to guide the acquisition of the subsequent acquisitions. In practice this is relatively difficult except with MRI where the ability to produce rapid high-resolution anatomical survey images allows relatively accurate manual prescription of the slice positions. Using this approach allows matching of images with a typical accuracy of only 1–2 voxels, which is inadequate for the majority of applications (Hajnal and Bydder 1997).

An alternative and attractive solution has been applied to the problem of providing anatomical localization of isotope images from SPECT/PET and MRI scans. Besides the relatively low spatial resolution of these isotope modalities, they commonly aim to identify very specific physiological targets, such as inflammation, so that little or no anatomical information may be present in the image. This invalidates the use of most coregistration techniques except for the use of small spatial localization markers (fiducials) which can be seen on the isotope study and other imaging modalities such as fluoroscopy, CT or MRI. These fiducials may be used within the machine itself for calibration purposes as in the development of a hybrid X-ray/MRI system (XMR) where a calibration phase for coregistering the field of views of the MRI and fluoroscopy systems is performed using a 16 fiducial marker phantom. This enables the integration of both modalities and their use concurrent use during interventional procedures (Yu et al. 2005). Fiducial placement has also been applied to patient fixation devices, such as a novel moulded mattress, enabling coregistration of SPECT and CT images (Forster et al. 2003; Gabriel et al. 2005). Finally, the fiducials may be directly attached to the patient, although this is not entirely satisfactory since they may become dis-

a b

Fig. 8.1a,b. A schematic (**a**) and product (**b**) photograph of a combined CT and gamma camera system. (Courtesy of GE Medical Systems)

lodged or change their relative position to internal tissues as the patient moves (Wu et al. 2003).

Manufacturers have further tackled the specific problem of lack of anatomical data for image coregistration by constructing hybrid scanning systems that allow simultaneous acquisition of CT and SPECT or PET data (Fig. 8.1). The respective modalities are actually incorporated into one machine system served by one examination table. In PET/CT the CT is acquired first, followed by the PET; this means that the patient is in the same position on the table and both data sets can be better coregistered with more accurate anatomical identification of the site of isotope uptake even where a single focus of isolated uptake occurs in an image with no anatomical information (Figs. 8.2 and 8.3). These systems have the additional advantage that the CT attenuation data can be used to calibrate the tissue attenuation maps required for quantitative analysis of the isotope data and also for routine monitoring and quality assurance (Thomas et al. 2005). Imaging systems which allow the combination of data sets from MRI, CT, rotational angiography, fluoroscopy, mammography and ultrasound in varying combinations are also being developed to support interventional image guided procedures (Fig. 8.4).

However, there are inherent problems with these systems including scan times of 15–40 min, inevitably resulting in patient movement (which occurs even in single modality scanning as dis-

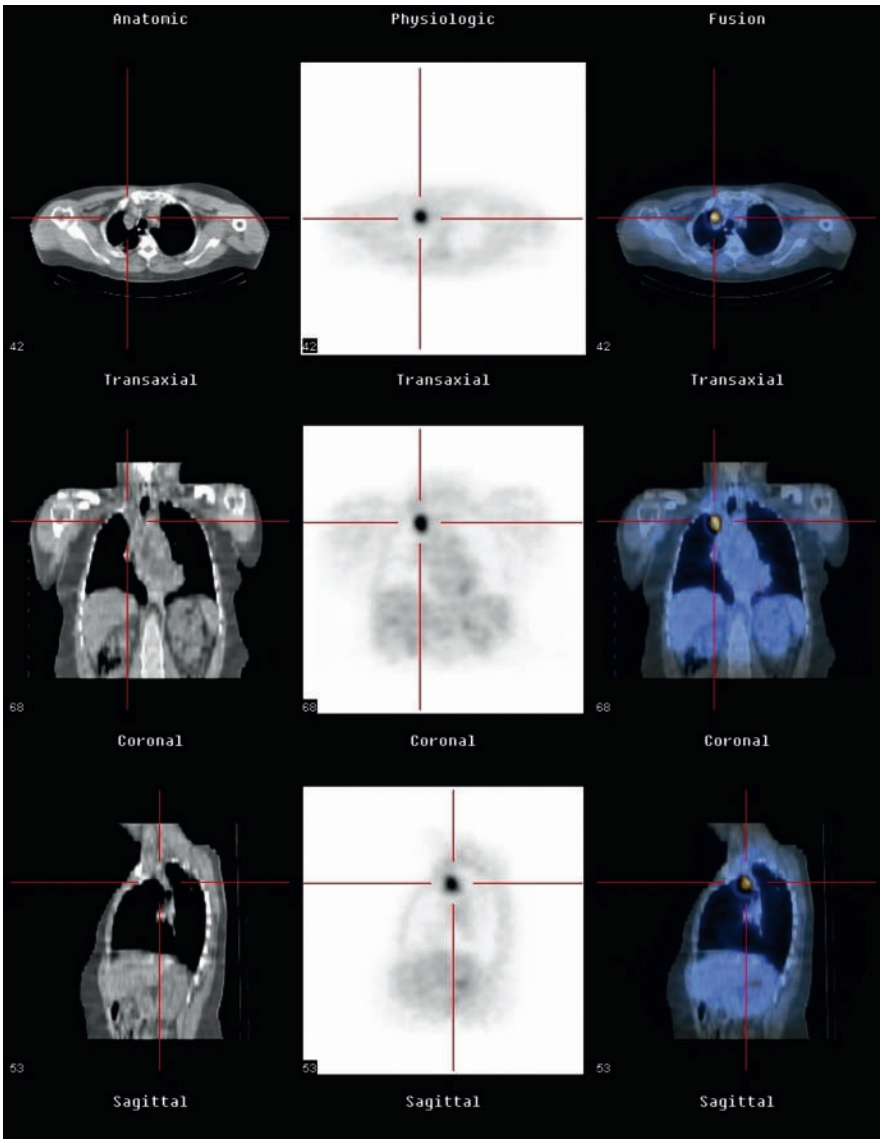

Fig. 8.2. Images of a patient with small cell lung carcinoma imaged using combined CT and FDG PET. The figure shows CT (*left*), PET (*centre*) and fused images (*right*). Images illustrate a tumour in the right upper lobe. (Courtesy of Duke University and GE Medical Systems)

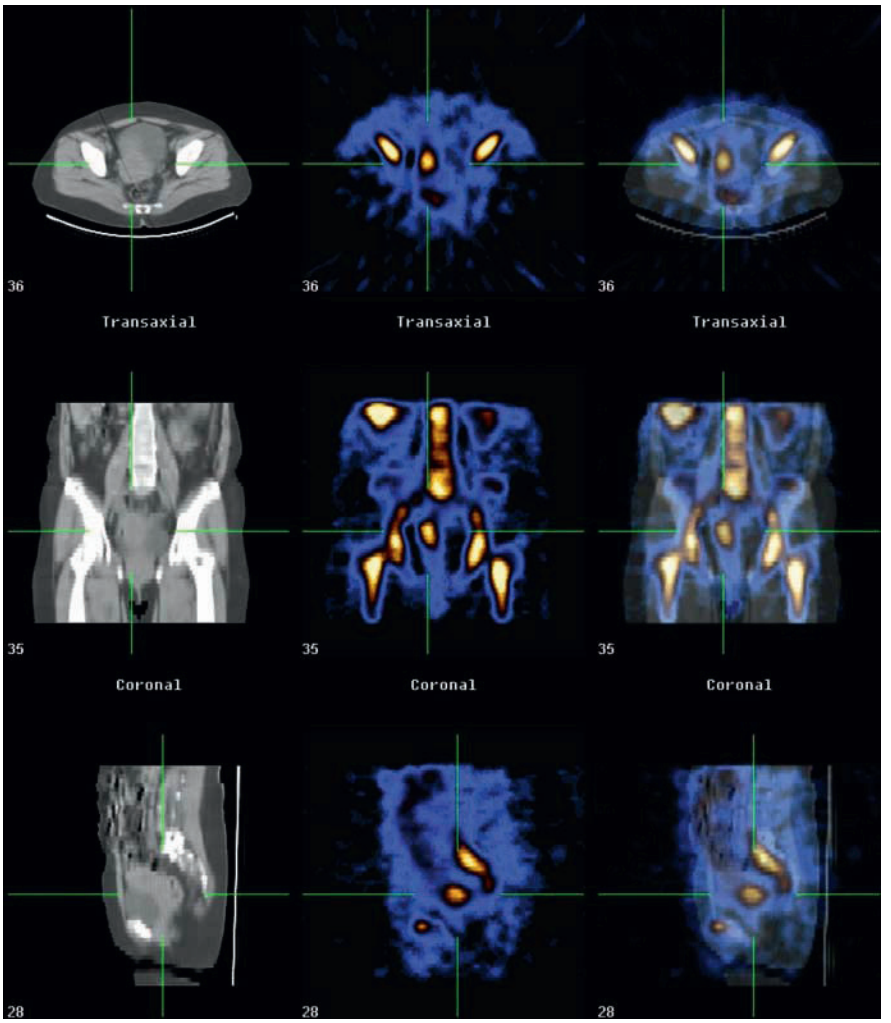

Fig. 8.3. Image acquired using combined CT and Ga^{67} SPECT. The figure shows CT (*left*), PET (*centre*) and fused images (*right*). Images illustrate an uptake of isotope in a recurrent cervical carcinoma. (Courtesy of Rambam Medical Centre and GE Medical Systems)

Fig. 8.4. Interventional MRI suite combining 1.5-T MRI and C-arm angiography systems. (Courtesy of Philips Medical Systems Ltd)

cussed below), and the problems of different breathing cycles during the respective scan acquisitions (Goerres et al. 2002, 2003; de Juan et al. 2004; Nehmeh et al. 2004). PET is currently acquired with the patient breathing shallowly and accurate image fusion would be best obtained with the CT acquired in expiration (Veit et al. 2006). As we move towards increasing the number of slices in the CT portion of these hybrid scanners (Beyer et al. 2005) and as PET acquisition with respiratory gating is used, this will become less of a problem, but at present dedicated breathing protocols are required to aid with image coregistration due to respiration artefact (Nehmeh et al. 2004; Larson et al. 2005; Veit et al. 2006).

In single modality imaging, such as CT scans acquired before and after contrast or MRI examinations with different sequences, the images are often acquired as part of a single examination and the patient is not moved between acquisitions. Despite this, small amounts of movement commonly occur. If a healthy volunteer is asked to keep absolutely still throughout a long examination sequence then movement of several millimetres can be expected in images of the head over a period of 5–10 min even if the head is supported and partially restrained (Fig. 8.5). In some areas of the body, such as the pelvis, this movement may be less marked and in others such as the limbs, it may be far worse. In addition to this unconscious movement there are also problems associated with physiological movements due to breathing, cardiac motion, vessel pulsation and peristalsis. These movements are also often associated with distortion of the tissues and loss of the spatial relationships between tissues from one image to the next. These physiological sources of movement and tissue deformation introduce special problems into the design of coregistration modalities for many areas of the body and have led most workers to concentrate on the design of coregistration techniques for use in the brain. The rationale for this is twofold. First, the brain is protected from movement related deformation by the skull and can, in many circumstances, be assumed to act as a rigid body, subject only to motion and not to deformation. Second, many of the major applications for coregistered data sets have been developed and clinically applied in the brain. In this chapter we will initially concentrate on techniques for coregistration of imaging data from the brain in order to illustrate the concepts and applications of the technique before discussing some further applications.

In view of the problems of spatially synchronising image acquisitions it is necessary in the majority of cases to coregister 3D images using post-processing techniques. In principle this is relatively simple to perform, requiring two basic steps: (1) image registration, (2) image reslicing. Image registration is the process of measuring the exact difference in spatial location between the two data sets. Data reslicing is the process of resampling one of the data sets so that it is perfectly spatially coregistered with the baseline image.

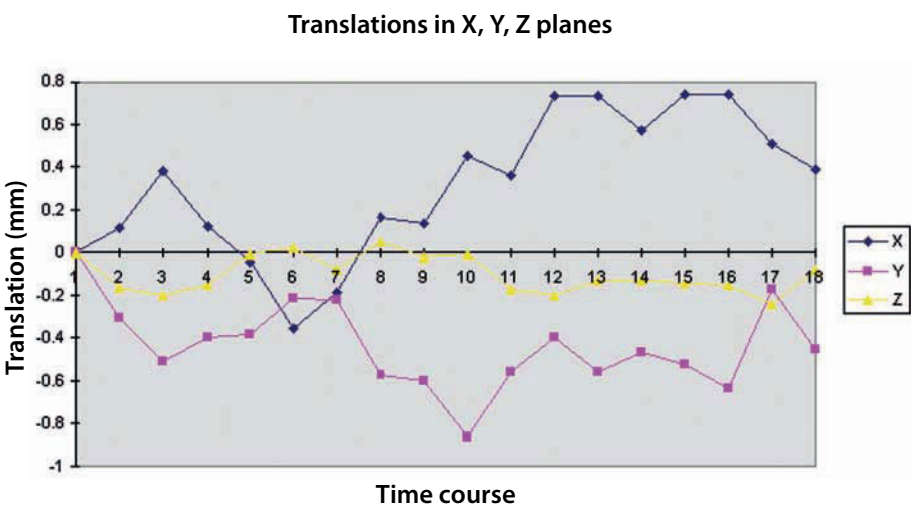

Fig. 8.5. Graph of head movement occurring during a functional MRI scan. The graph shows translations in the x, y and z planes during the collection of 18 dynamic images over a period of just under 2 min

8.3 Accuracy of Spatial Location Information in 3D Images

Medical 3D images consist of a matrix of image intensity values which makeup a "spreadsheet" of data describing the object. The dimensions of the individual data elements govern the spatial resolution of the images so that smaller voxels will provide a higher spatial resolution. However these 3D data sets commonly contain information that allows the spatial location of features within the image with accuracy far higher than the spatial resolution. This information is derived from the distribution of image intensities within the data space. The image intensity in each pixel reflects the tissue, or mixture of tissues within it. Variations in tissue content produce intensity gradients across several pixels or well defined edges where they occur over a small distance. If these gradients and edges are misaligned in two otherwise matched images then subtraction of the images will clearly identify areas of misregistration even where these are less than 1 pixel in magnitude. This occurs because the subtraction process is sensitive to the pixel intensity that can be affected even by a small spatial misregistration (Fig. 8.6). The magnitude of the pixel in the difference image will be affected by the degree of misregistration and by the relative intensities of the two tissues forming the tissue boundary. Within a large 3D image many of these edges and gradients will be present varying in extent, orientation and magnitude. The process of coregistration is designed to minimize these differences and accurate coregistration should eliminate them completely (Fig. 8.7). Conversely, automated coregistration algorithms work by minimizing these differences on the assumption that the minimum difference between the images will be seen where the images are perfectly coregistered.

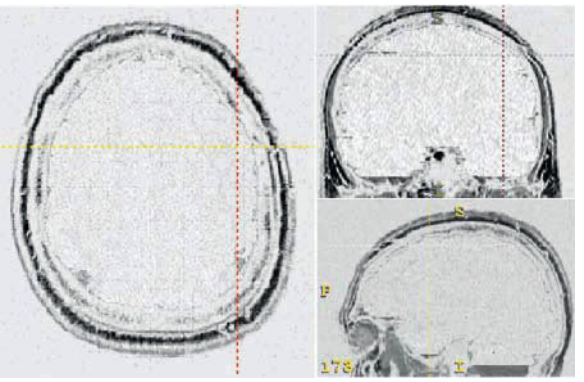

Fig. 8.7. Subtraction images of two 3D MRI brain scans performed in a healthy individual. The brains in the two scans have been coregistered and subtracted resulting in complete loss of structural information in the brain. Note that the peripheral tissues are clearly seen since these were removed from one data set prior to coregistration

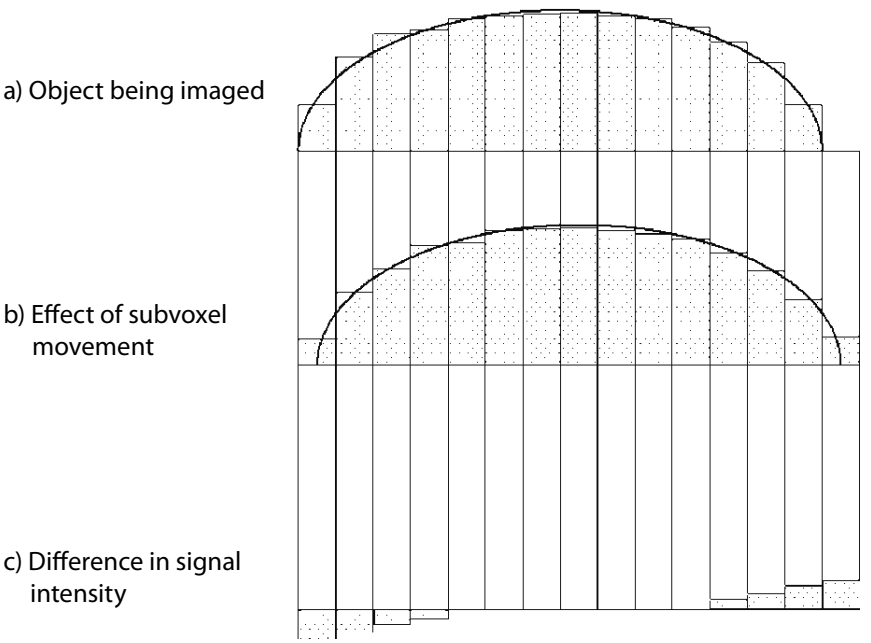

Fig. 8.6a–c. Shows changes in image intensity that are generated by subvoxel shifts. The top image (**a**) shows the intensity profile (histogram) produced by imaging a smooth curved object. In **b** the object has moved by a fraction of a pixel. The lower image (**c**) shows the difference in image intensities generated by the subtraction of **a** from **b**. (Adapted from Hajnal and Bydder 1997)

8.4 Image Registration

The image registration process produces a description of the difference in spatial location between the two images. In the simplest case this description will contain details of the movements (translations) required in the three ordinal directions (anterior-posterior, right left and superior-inferior) and of the rotations required in the same three planes (pitch, roll and yaw). This mathematical description is called the transformation matrix and can be used to guide resampling of the test data set so that it matches the base images.

Estimation of the appropriate transformation matrix can be performed in a number of ways. In theory the position of a 3D data set can be described by specifying the coordinates of three fixed points or of one fixed point and a plane. The simplest method to coregister two data sets is therefore to define a series of standard registration points or fiducials.

This technique is used in stereotaxic brain surgery where the brain is rotated into a standard plane by identification of two points, the centres of the anterior and posterior commissures, and of the horizontal midline plane. The two points are used to define a baseline horizontal plane, the sagittal midline plane forms a vertical baseline and a coronal plane passing through the anterior commissure forms the third. Using the intersection of the three planes as the zero point the location of any point in the brain can then be described using a set of x, y, z coordinates. In order to allow for variations in brain size the coordinate system is linearly scaled in all three axes. This stereotaxic coordinate system was described by Talairach and Tournoux (1988) and is commonly referred to as the Taliarach system. Assuming that brains have the same shape and differ only in size, then any anatomical area can theoretically be described in terms of its Taliarach coordinates. This assumption holds true for healthy brains, which show remarkably stable stereotactic locations for deep brain structures. The location of cortical areas within the coordinate system is more variable and distortion of brain shape due to pathology can also cause significant changes in the stereotactic locations of anatomical structures.

The use of anatomical fiducials relies on the ability of the images to accurately allow their identification, which is, in turn, directly related to the spatial resolution of the images. Even with high spatial resolution MRI this is unlikely to be greater than 1 mm in any direction, which could cause significant potential error in the location of the anatomical landmarks. With other imaging modalities such as SPECT and PET, the low spatial resolution and lack of anatomical information in many images may make the identification of anatomical fiducials impossible, or at best highly inaccurate. The effects of these errors on the spatial localization of the data set will be least if the fiducial points are well separated and greater if they lie close together. This has led many workers to develop artificial fiducial markers that can be seen on all the imaging modalities employed (Kremser et al. 1997; Maurer et al. 1997; Alp et al. 1998; West et al. 1999; Zylka and Sabczynski 1999). Small samples of radioactive isotope in a lipid solution will provide clear points for identification on both MR and isotope imaging and the design of the fiducial markers can be adjusted depending on the combination of imaging modalities to be employed (Fig. 8.8). The problem with external fiducials is rendering their position fixed with regard to the internal structures being studied. For imaging the brain fixation of fiducial markers to the skin is unsatisfactory since the scalp is highly mobile with respect to the skull. Markers can be fixed in a tooth bar which is designed to fit accurately into the bite and which considerably reduces the problems of fiducial movement whilst maintaining the fiducial positions at the periphery of the imaging volume. In some circumstances fiducials may be fixed by attaching them to bone screws fixed into the skull. This may be justified in cases where accurate image guided surgery is necessary but is inappropriately invasive in most cases. The use of fiducial markers is therefore limited to specific applications where automated coregistration algorithms are inappropriate due to inadequate information content in one of the images, or as discussed earlier during the calibration phase of a hybrid system for the coregistration of different imaging system fields of view (Yu et al. 2005). Using fiducial-based techniques the coordinates of each fiducial within the each image are measured and the corresponding transformation matrix can be calculated from these coordinate sets. This is a simple calculation which is undemanding of computer power and which can be easily performed by taking measurements on most image analysis workstations and calculating the transformation matrix using a simple program or spreadsheet application.

The most commonly applied technique for image coregistration is to estimate the transforma-

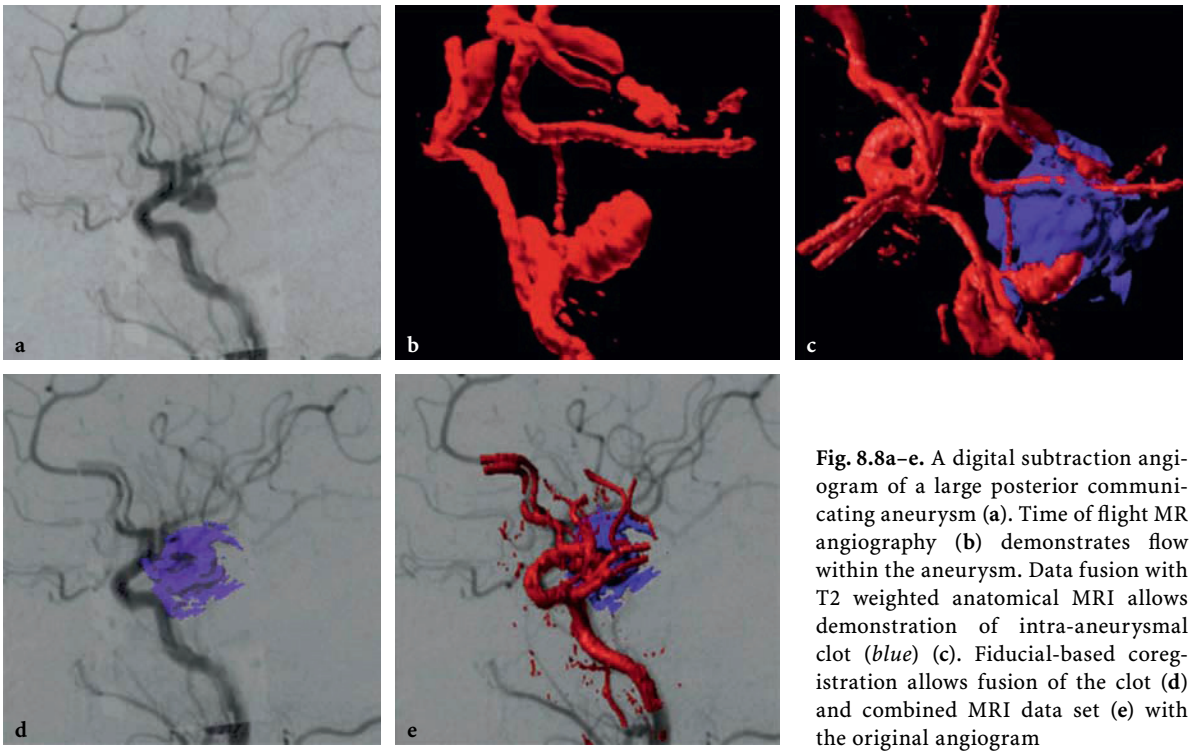

Fig. 8.8a–e. A digital subtraction angiogram of a large posterior communicating aneurysm (**a**). Time of flight MR angiography (**b**) demonstrates flow within the aneurysm. Data fusion with T2 weighted anatomical MRI allows demonstration of intra-aneurysmal clot (*blue*) (**c**). Fiducial-based coregistration allows fusion of the clot (**d**) and combined MRI data set (**e**) with the original angiogram

tion matrix by direct comparison of the two images (Woods et al. 1998). This approach has been used manually in 2D for many years to produce subtraction angiograms. Prior to digital imaging an exact but inverted copy of a plain skull film was used to mask the bony details from a matching angiogra=m image to produce a dense composite negative in which the bone details were cancelled out by superimposition of the positive and negative images. This process is still used today in digital subtraction angiogram systems. To optimise the quality of the subtraction the negative and positive images can be moved relative to each other until no edges are seen in the images. Automated coregistration techniques use the same approach by comparing various orientations of the two images and measuring the differences between them. The actual measurement of difference between the images may use one of several difference metrics. These range from relatively simple measures, such as the difference in intensity between the images (Hajnal and Bydder 1997), to more complex metrics, such as the standard deviation of the ratio of the voxel intensities (Woods et al. 1998a,b), designed to optimise the accuracy of the registration technique. Whatever the chosen metric may be, the aim of the program is to find the orientation of the two images that minimizes the cumulative difference between corresponding voxels. A simple example of this is given in Equation (1) using the chi squared statistic (χ^2):

$$\chi^2 = \sum_n \frac{(SI_a - SI_b)^2}{n} \tag{1}$$

where SI_a is the intensity of the voxel in image a, SI_b the intensity in image b, and n is the total number of voxels. The minimum value for χ^2 is calculated by moving image a relative to image b until the minimum value is found. This approach is extremely demanding of computing power and can be extremely time consuming, especially with large data sets. In order to reduce the computation time a number of strategies have been employed including using only voxels above a certain threshold, using only voxels with data in both images and performing the minimization iteratively using gradually increasing spatial resolution to allow the software to "home-in" on the correct solution. The exact approach used depends on the specific software package employed, and the time taken is also directly related to the image size. Many automated grey-level matching techniques have now been described and most seem capable of

estimating the transformation matrix to subpixel levels under ideal conditions.

In practice it is important to be aware that automated grey-scale matching algorithms of this type operate on the basis of a series of essential assumptions and can be expected to perform poorly where these assumptions are incorrect. These assumptions are:

1. That the relative grey scale values of structures are the same in both images.
2. That the relative spatial relationships of all structures in the imaging volume are identical in both images.

The first assumption is essential if direct comparison of the images is to be used as the difference metric but can be avoided by the selection of alternative appropriate metrics. Even in images where the relative grey scale values differ considerably, it is possible to obtain acceptable coregistration by choice of an appropriate metric such as an image of edge strength or some alternative derived value which will make the image sets more directly comparable.

The second assumption is intrinsic to the technique. We are attempting to coregister accurately two identical volumes which must therefore be identical. In practice we often wish to coregister volumes which actually differ significantly, often to improve the identification of these differences. We can assume that the difference between the images is minimal and will not affect the overall coregistration; however this is also an assumption and will not always be true. Once again the errors can be reduced by selection of an appropriate metric for minimization and by performing coregistration using only a part of the image set. A classic example of this is the coregistration of head scans where accurate coregistration is impossible in most cases due to variations in the facial structures which are highly variable and which dominate the matching process. Coregistration of head images is therefore conducted using one baseline image and a second image which has had the extracerebral tissues edited out to avoid errors. This technique of skull stripping is essential for the acquisition of accurate coregistrations (Fig. 8.7).

An alternative approach to coregistration is to identify a plane in one image and to coregister it to the same plane using a surface matching technique. This approach can be used to coregister the images of the cranial vault by extracting the CSF surface and using this "convex hull" to match to the same surface from another image. The technique tends to be less accurate than grey-scale matching methods but can be extremely useful where these approaches are not appropriate. This method is commonly used to coregister imaging data with an image of the body surface derived from stereo cameras or interferometry, which can allow image guidance of surgical, or radiotherapy techniques in theatre.

8.5 Data Reslicing

Once the transformation matrix has been calculated, one of the data sets must be resliced so that it matches the baseline image. The aim of the reslicing process is to calculate a value for every voxel that is identical to the value we would have obtained if the image had been acquired in that position. Reslicing is performed by calculating a new value for each voxel from the intensities of the voxels in the original image in which it now lies. This requires us to make an assumption about the relative contribution that each voxel would make to the new voxel value. Once we have decided on this assumption, we can use the data from surrounding voxels to synthesise a final value for the new voxel; this process is known as interpolation. The simplest approach to data interpolation is to assume that the contribution to signal intensity from the original voxels will be linearly related to the proportion of the voxel included in the final sample. This approach known as linear interpolation is simple to perform, uses linear algebra and requires data only from the voxels which contribute directly to the final pixel. The accuracy of the interpolation process can be improved by the selection of an appropriate non-linear function. The appropriate function will depend on the imaging modality and the image formation process. This is a particular problem with MRI data, which is acquired as a series of phase/frequency maps in the Fourier domain and reconstructed using an inverse Fourier transform. The result is a complex relationship between pixels and the surrounding image elements. This relationship, described by a sinc function, means that voxels nearest to the reference point will have the greatest effect on the intensity of the interpolated data but that even pixels at the extremes of the image will have some residual effect. To perform a sinc interpolation the contribution of each voxel in the image to the new

single voxel value is calculated as the product of the original voxel values and the sinc function (Fig. 8.9). Since the sinc function has significant negative components many voxels will make negative contributions to the final voxel value, which is calculated by summating all the individual voxel contributions.

It would be incorrect to believe that the images interpolated this way are identical to what would have been obtained if the subject had been translated in the spatial domain to the required position. That assumption would be true only if the original data were exactly defined by the truncated Fourier description in the original data set. However, provided that the sinc kernel has a size equal to the image, interpolation with a sinc function is at least consistent with the way the image has been acquired and no information which was available at the scanner is lost. Such interpolation would have to be considered optimal.

For computational reasons it is inappropriate to apply a large sinc kernel, but as the kernel itself is quite spatially compact it is possible to truncate it at some level. A common kernel size for medical image subtraction work is 13 × 13 × 13 (Hajnal et al. 1995; Freeborough et al. 1996). This is a direct result of the first order reciprocal scaling and a range of 6 pixels is required for the sinc function to reduce to a negligible level (i.e. less than 1% for a windowed kernel). The computational implications of using large-scale kernels are offset somewhat by the fact that the coefficients required for sinc interpolation can be decomposed (Freeborough et al. 1996) so that the computation is linearly proportional to the kernel size rather than its volume (a 'fast sinc'). In addition, it is re-normalised of the sinc function so that it has a constant integral improves interpolation accuracy and allows the use of smaller kernels which increases processing speed (Thacker et al. 1999). Thus despite its somewhat complicated form, sinc interpolation seems to offer as good a solution as the best techniques in terms of computational requirement on equivalent sized kernels.

8.6 Complex Coregistrations

The techniques we have described in the preceding sections make the assumption that the structure to be coregistered is a "rigid body" so that the relative spatial relationships of all structures in the imaging volume are identical in both images. This would be true for a solid phantom imaged in different positions where the differences between any corresponding structure can be described by the transformation matrix. Such movements of rigid bodies in a coordinate space are commonly called affine transforms.

In many applications attempts to coregister, data are confounded by deformation of the tissues which

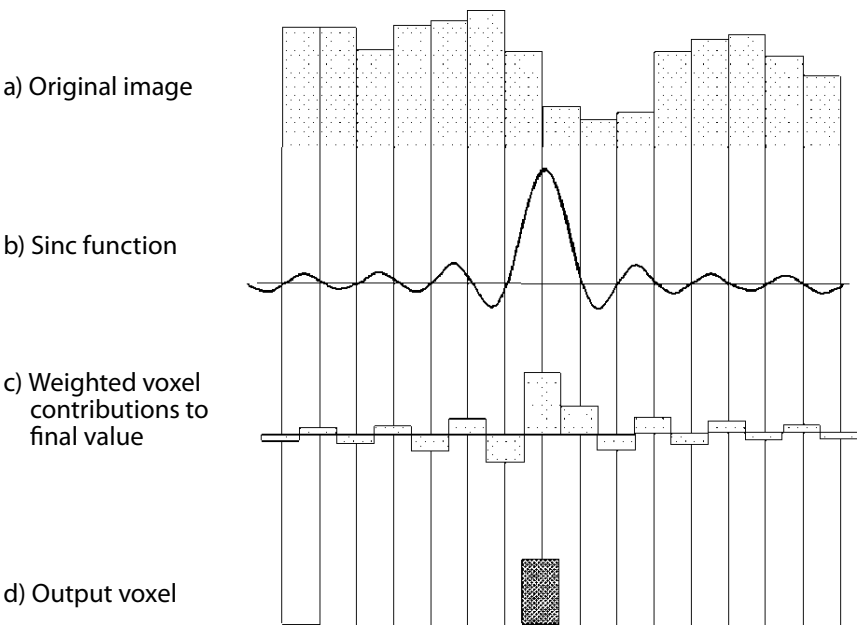

Fig. 8.9a–d. The calculation of a new voxel value following a subvoxel shift using sinc interpolation. The intensity profile (**a**) of the original image. A new image is to be generated 0.5 pixels to the left. The sinc function (**b**) aligned on the centre of the new pixel. The product (**c**) of the sinc function and the corresponding pixels in the original image and (**d**) the sum of these which is the final calculated voxel value. (Adapted from Hajnal and Bydder 1997)

has occurred between the data collections. In many cases this distortion will affect the tissues throughout the image. A good example would be an attempt to coregister the abdominal organs on abdominal CT scans obtained in the supine position with scans obtained prone. These images are not simply the same images inverted but will demonstrate a complete change in the spatial relationships of one organ to another and of the internal structures within the organs. An affine or rigid body transformation cannot describe the changes which have occurred in these situations and the coregistration process requires a far more complex "non-affine" transformation sometimes referred to as image warping. The problems with non-affine transformation techniques are considerable. Using the brain as an example, many groups have developed methods to improve coregistration results by application of non-affine transformations. These brain warping techniques have been employed to correct for variations between individuals when coregistering images to a computerised brain atlas or to improve spatial coregistration between different individuals to allow transformation of several studies into a standard data space. Unfortunately image warping techniques must be based on a theoretical physical model of the tissues. If such a model were perfect and were able to describe the interplay of physical properties such as flexibility, rigidity and tensile strength in every tissue component then it might be possible to constrain the solutions to the warp sufficiently to provide the correct solution. This approach, called finite element modelling, is widely used in engineering where the physical properties of materials are well documented. However it can easily be seen that the finite element modelling approach is extremely limited in medical applications due to the extreme complexity of the body and the variability in tissue properties.

An alternative approach to image warping is to assume that the elastic properties of the tissues are constant. This is clearly totally incorrect and no one would suggest that the skull and the brain display identical elastic properties if a force is applied to the head. However, many models assume that this approach is appropriate in a limited tissue such as the brain itself. In these circumstances a degree of distortion detected by noting displacement of specific structures can be "corrected" by application of a linear or other simple image warp. The problems with this approach are that it makes assumptions about the way in which structures will move relative to one another (Fig. 8.10). These models are based on the assumption that the structures in the two brains have the same spatial relationship which has become distorted by a process described by the warping technique. These assumptions can be confirmed only by observation of the displacements which occur to other structures when the warp field is applied. Several workers have looked at the standard deviation of the spatial coordinates of easily recognised structures following warping of brain images. If the assumptions of the warping process are correct then these should be smaller after warping than when a simple affine transform is applied. One example of such a study used the computerized brain atlas developed at the Karolinska Institute in Stockholm and showed an improvement in registration accuracy when a non-affine process was included in the registration method. Despite this the standard deviations of the coordinates of individual

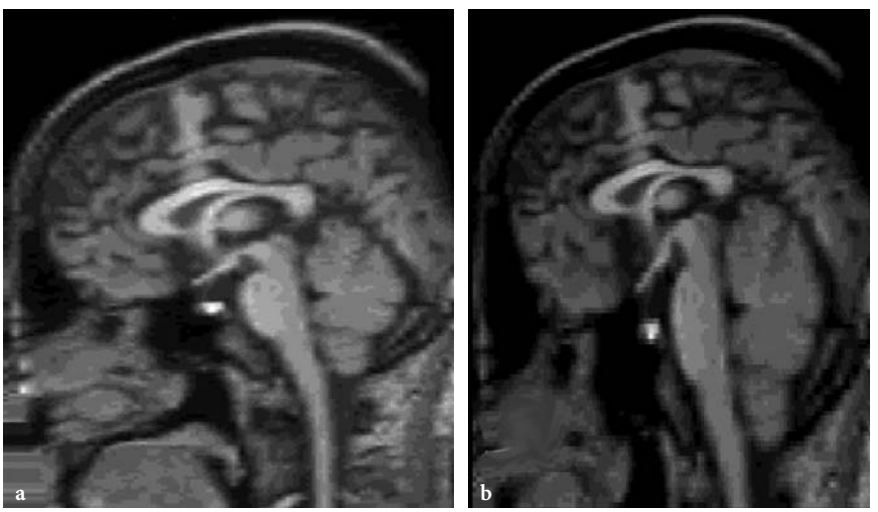

Fig. 8.10a,b. A sagittal MRI image of the head (**a**) and a warped image (**b**). The warp has assumed a linear elasticity in all tissues and has been used to stretch" the brain below the AC-PC line ventrally by 50%. Note the distortion of the anatomy and that equal degrees of distortion are seen in all tissues

structures varied from 0.9 to 4.5 mm (Ingvar et al. 1994). Interestingly, when this same atlas, developed on averaged data from Swedish subjects, was applied to a Japanese population the distribution of the same structures was worse than that obtained with a simple affine transform. This illustrates the problems of generalised image warping techniques which cannot contain sufficient constraints to accurately describe the behaviour of biological systems. Despite this, significant improvements may be seen in specific limited applications such as the coregistration of multiple healthy brains for functional MRI (Ashburner et al. 2000).

The problems of the image warping approach can be easily illustrated with a simple thought experiment. Imagine 3D MRI images of two brains are being coregistered into the Taliarach coordinate system. In each patient one cerebral hemisphere is smaller than the other so that an affine warp cannot be applied successfully. In one patient the smaller hemisphere demonstrates a diffuse lobar atrophy affecting all areas of the brain, in the other a focal disorder has caused loss of the central basal ganglia and the peripheral cortical mantle is relatively normal. If we hope to warp these images back into a standard healthy brain configuration, perhaps to apply a computerized brain atlas, we will need to include in our warping model specific information about the location and severity of tissue loss and the physical properties displayed in the tissues which have responded to it. The only hope for such an approach is to identify multiple anatomical landmarks which can be used to allow detailed comparison of the distortions between the two images and from which we can derive information about the nature of the distortion which has occurred in different areas. These landmarks may be identified manually. Alternatively, a grey-scale coregistration technique similar to the one applied for affine transformations may be used. The technique must be modified to allow non-affine distortions and will generate not a simple transformation matrix but a complex detailed distortion map describing the individual changes in voxel shape which must be applied to produce the minimum difference between the images. This approach can applied successfully if the aims of the experiment are appropriate and if the user realizes the inherent inaccuracies of the technique. Estimations of the warp field required to align healthy and pathological brains can be used to indicate the areas of the brain where the majority of tissue loss or gain has occurred (Fig. 8.11). Due to the limitations of the method, the spatial accuracy of the warp information will be lower, often far lower than the spatial resolution of the image and will be subject to errors where misregistrations have occurred between apparently similar structures.

An alternative approach to this type of image warping is to develop techniques to identify specific anatomical structures within the tissue (Rasser et al. 2005). These anatomical statistical trained models (STMs) are trained using a large sample of images on which specific features are manually identified. The statistical variability of these features is then calculated and the trained STM can then "search" similar images to find the best estimation of the structure.

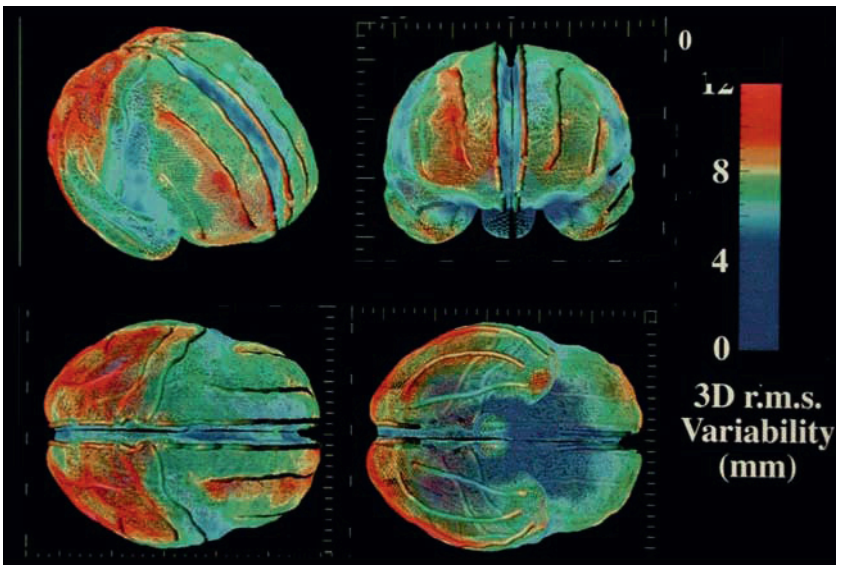

Fig. 8.11. Images showing the differences in the cortical structure between a group of healthy controls and a group of patients with Alzheimer's disease. The patients' brains have been warped into a standard coordinate system and these images show the differences in the amount of deformation needed to make the AD brains conform to the heathly controls. The colour coding therefore represents the average amount of tissue deformation required showing considerable atrophy has occurred in the frontal and posterior parietal lobes

This approach can be applied to the identification of structures like cerebral gyri, blood vessels or bone edges. The problems with STMs relate to the complexity of the models in 3D data sets and the reliance on the training set of images to accurately describe the variations which may occur in the sample. However, within the limits of their training set, STMs can be used to identify target features which could be used to drive an image warping technique.

8.7 Applications of Data Coregistration

The ability to coregister 3D data sets facilitates a wide variety of post-processing techniques. Some of these are described in brief below. The list is far from exhaustive and serves to illustrate the importance of data fusion in medical applications.

8.7.1 Analysis of Temporal Image Sequences

The techniques of automated image coregistration were first applied to medical data sets to improve the stability of data analysis in functional magnetic resonance imaging (fMRI). Functional MRI techniques for the measurement of brain activation, cerebral perfusion and capillary permeability rely on the analysis of multiple images collected over a period of 2–60 min. All of these analysis techniques perform calculations on a pixel by pixel basis that uses the signal intensity changes in the pixel which occur over time. The nature of the changes and of the analysis performed is presented in detail in the chapter on fMRI. In all cases the presence of movement in the data set means that the time course change may represent the movement of structures through the sample space rather than physiologically induced signal changes (Ashburner et al. 2000). This is of particular importance in blood oxygen level dependant (BOLD) fMRI where data collections tend to be long lasting and the subject is often performing cognitive or motor tasks that produce motion (Thacker et al. 1999). The latter motion may be greatest when the subject is performing the task so that the presence of motion correlates with the timing of the test paradigm. This stimulus correlated motion can produce spurious activations on fMRI which are eliminated by appropriate motion correction (Fig. 8.12).

The ability to coregister temporally spaced image acquisitions has also been applied in musculoskeletal imaging to assess tibial plateau cartilage changes in a coregistered region of interest of the knee taken over a period of two years (Jaremko et al. 2006) (Fig. 8.13).

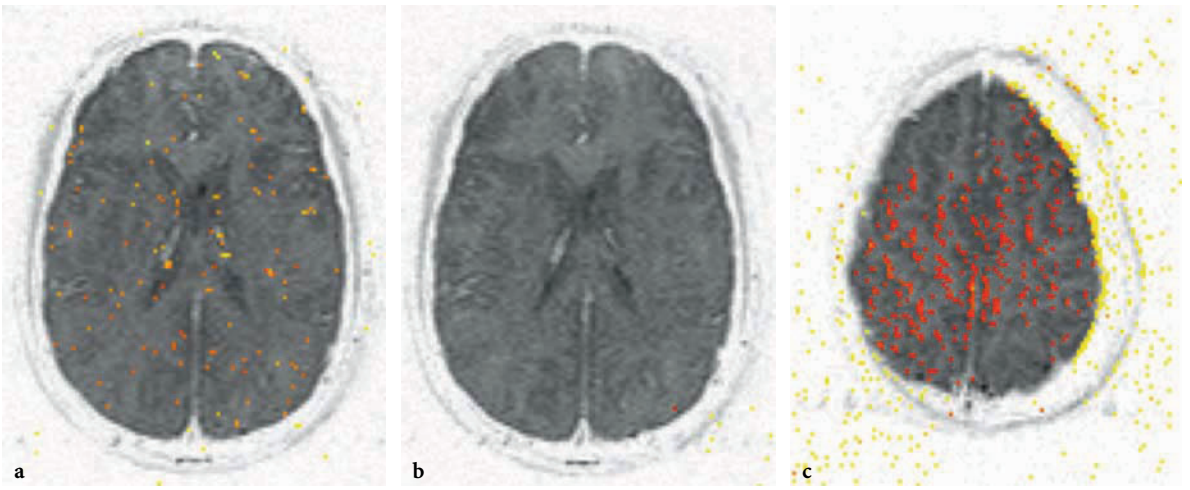

Fig. 8.12a–c. Functional MRI experiment using a block paradigm. In this case the subject is at rest throughout the experiment. Apparent areas of significant activation (**a**) which disappear after coregistration (**b**). Activations (**c**) in a synthetic data set constructed from multiple identical copies of the baseline image. These copies were then coregistered to mimic exactly the movements made by the subject during the actual experiment. These data appear to generate multiple areas of highly significant activation that are entirely due to coincidental stimulus correlated motion. The activations are far greater than seen in the real data only because the noise structure in the synthetic images is identical in each image

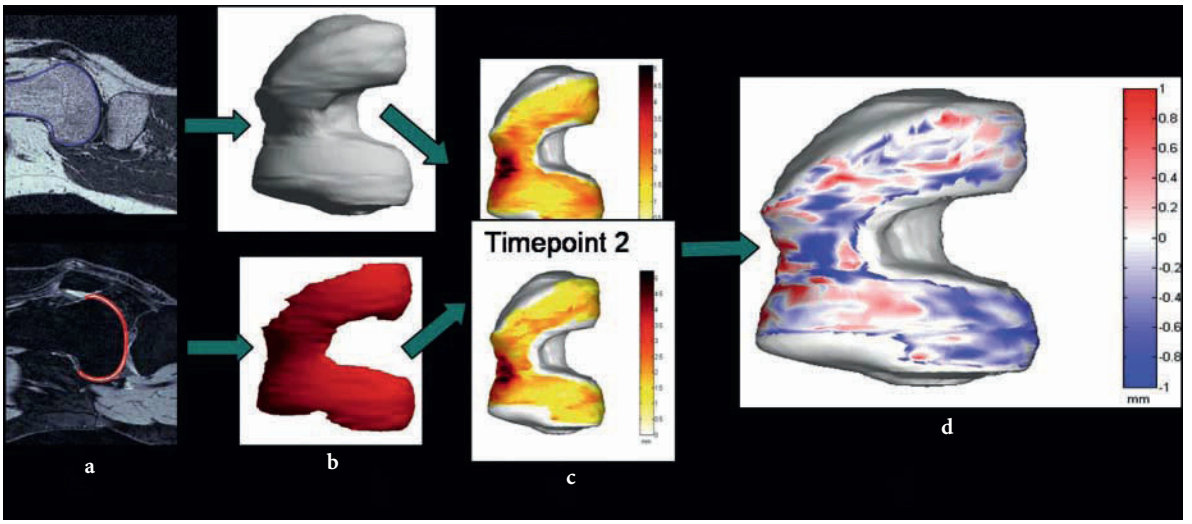

Fig. 8.13a–d. Measurement of knee cartilage loss in osteoarthritis. T1 FatSat is used to highlight bone and T2 the endosteal surface (**a**). Surface representations of the bone and cartilage are constructed (**b**). Following this, thickness maps (**c**) are produced by measuring cartilage at dense points on the bone surface resulting in a bone referenced cartilage thickness map. This is repeated for subsequent visits of the same patient. By comparing the cartilage over subsequent attendances a map of change in thickness can be constructed (**d**) with *blue* indicating regions of thinning and *red* thickening or swelling. (Courtesy of Dr. Tomos Williams Department of Imaging Science and Biomedical Engineering, School of Medicine, University of Manchester, UK)

8.7.2 Visualizations from Multiple Data Sets

The ability to coregister images from multiple modalities or from multiple examinations allows the development of true data fusion to support both 2D and 3D visualization techniques. We have already seen examples of coregistered CT and isotope images acquired simultaneously from dedicated systems (Figs. 8.2 and 8.3). Using post-processing coregistration we can produce similar fused images that allow identification of anatomy from CT or MRI with overlays of data from PET or SPECT (Fig. 8.14). Indeed such coregistration has become a matter of routine in the analysis of functional brain images where due to the minimal amount of anatomic alterations the value of hybrid PET or SPECT/CT machines is not as critical as in whole body imaging (Myers 2002; Yokoi et al. 2004; Otte and Halsband 2006). Since these data acquisitions are 3D in nature, we can visualize these fused data using standard 3D visualization techniques to demonstrate separate tissue components from different images. Figure 8.15 demonstrates the relationship between the skull (identified on CT), an acoustic neuroma (identified on contrast enhanced MRI) and the adjacent blood vessels (identified on time of flight angiography). Such combined images allow improved 3D image interpretation and are of particular use in surgical planning applications, (Chao et al. 2001; Murphy et al. 2001; Feichtinger et al. 2002; Mahvash et al. 2006) or for the assessment of post surgical outcomes of, for example, cochlea implant electrode positioning in post surgical CT scans coregistered to pre-surgical MRI (Neri et al. 2005).

In addition there is the further advantage of being able to fuse images over time which will become increasingly important with regard to PET and SPECT based molecular and metabolic imaging (Kartachova et al. 2006; Mayer-Kuckuk et al. 2006; Otte and Halsband 2006), enabling assessment of treatment responses as well as being an invaluable research tool.

In cardiac imaging this has been taken further with coregistration of cardiac-gated SPECT images of the heart to "cine" MRI and delayed enhancement MRI cardiac images helping to visualise perfusion, function and viability of myocardium (Klein and Thirion 2005; Misko et al. 2006). Furthermore, the fusion of CT and MRI images allows for more accurate assessment of atherosclerotic plaque lesions in vascular imaging (Dey et al. 2006). Work is also progressing on the application of the fusion of 3D rota-

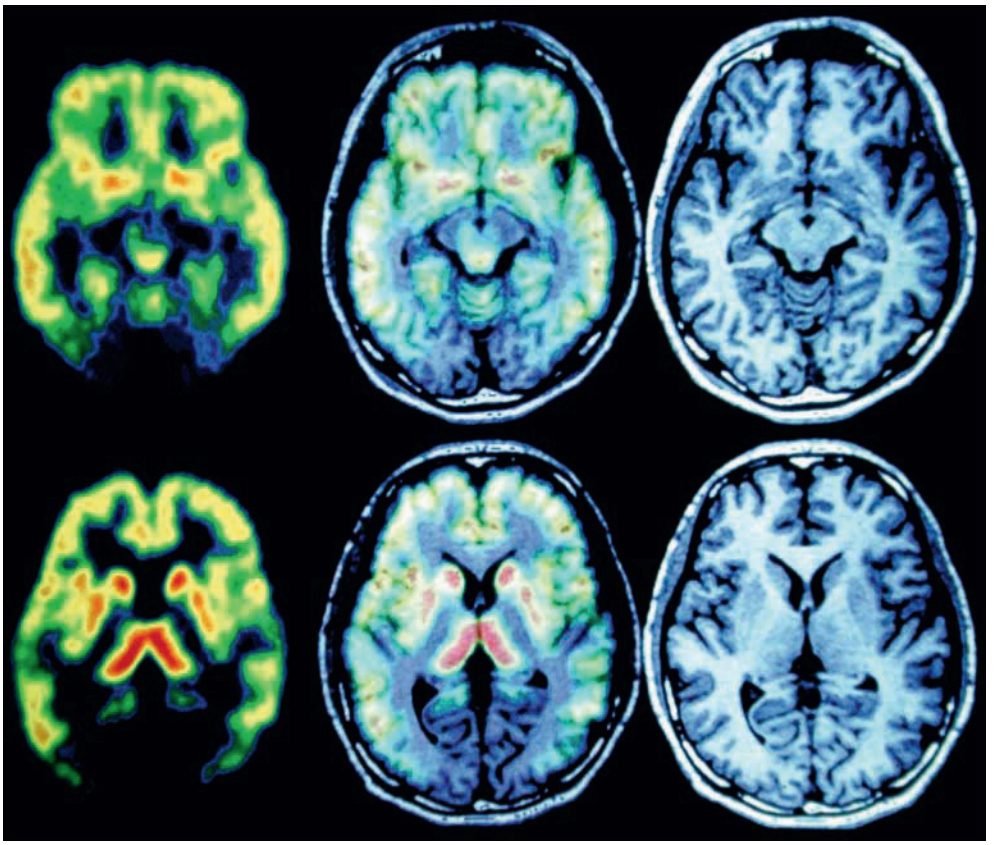

Fig. 8.14. Images of C^{11}Buprenorphine binding on PET (*left*) and MRI images of the same brain (*right*) with fused images shown in the *centre*. (Courtesy of Dr A Jones, Hope Hospital, Salford, UK)

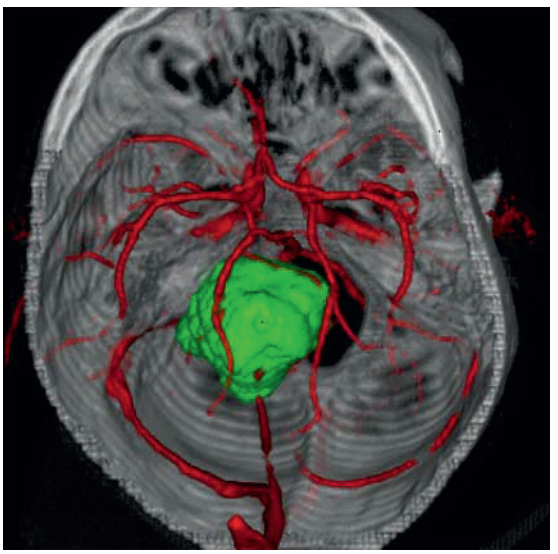

Fig. 8.15. A 3D visualization of an acoustic neuromas patient. The image demonstrates the relationship between the skull (identified on CT), an acoustic neuroma (identified on contrast enhanced MRI) and the adjacent blood vessels (identified on time of flight angiography)

tional angiographic images of cerebral aneurysms where the aneurysm is supplied by more than one artery, and the image acquisitions are from contrast injections into the corresponding arteries themselves. Following image fusion, it is then possible to visualise the intra-aneurysmal flow patterns from the inflow arterial streams (Castro et al. 2006).

Coregistration with accurate image fusion of SPECT ventilation/perfusion studies and CT pulmonary angiography has made possible the development of clinically useful techniques for respiratory assessment in patients who have non-diagnostic initial investigations or require further diagnostic confirmation (Suga et al. 2004a,b; Harris et al. 2007) (Fig. 8.16).

Fusion of complementary imaging modalities has also been applied in breast imaging to improve the sensitivity and specificity of breast lesion detection using novel approaches such as coregistration of diffuse optical spectroscopy and MRI as well as more traditional imaging techniques fusing ultrasound (US) to X-ray images (mammography) (Kapur et al.

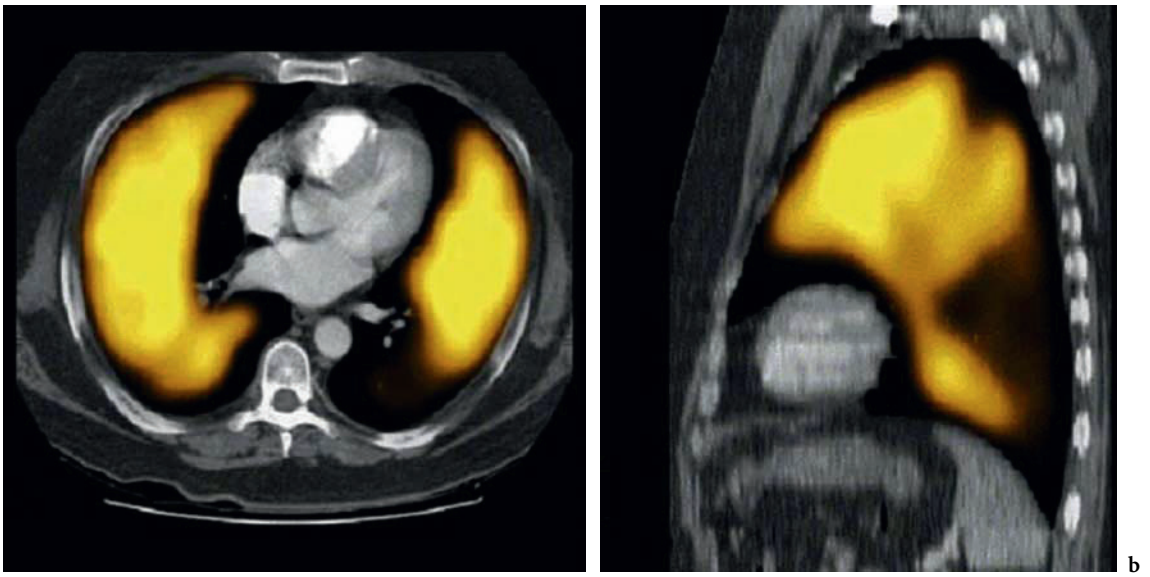

a b

Fig. 8.16a,b. Fused CTPA-perfusion SPECT of the transverse (**a**) and sagittal (**b**) views in a 48-year-old male demonstrating left lower lobe apical and posterobasal segmental defects. An additional perfusion defect is also seen in the apico-posterior segment of the upper lobe. The patient was diagnosed as having suffered pulmonary embolism despite no filling defects being seen on CTPA. (Courtesy of Harris et al. 2007)

2004; Hsiang et al. 2005; Suri et al. 2005) and PET/CT (Zangheri et al. 2004).

With regards to radiotherapy planning and tumour staging, image coregistration is used to combine real time US with CT, and SPECT with CT (for sentinel node location) in head and neck tumours. PET/CT and SPECT/CT is used in lung cancer, Hodgkin's lymphoma, neuroendocrine tumour and differentiated thyroid carcinoma staging as well as tumour recurrence (Chao et al. 2001; Yamamoto et al. 2003; Amthauer et al. 2004; Lopez et al. 2004; Brianzoni et al. 2005; Halpern et al. 2005; Messa et al. 2005; Wein et al. 2005). PET/CT is also used for determining repositioning errors during precision radiotherapy (Robar et al. 2005).

8.7.3 Computerised Atlases

Several groups have developed computerised atlases of the human brain that can be applied to images from individual patients to improve the identification of structures. This is particularly useful in educational applications and in the identification of structures, such as Brodmann's cortical areas, which are not anatomically defined on the images themselves (Greitz et al. 1991; Ingvar et al. 1994; Nowinski et al. 1997; Woods et al. 1999; Nowinski and Thirunavuukarasuu 2000; Rasser et al. 2005), allowing for further research into the relationship between function and anatomical structure (Nowinski and Thirunavuukarasuu 2000; Thottakara et al. 2006). These atlases vary from simple affine transformation systems which assume that the brain is a rigid structure to more sophisticated systems which apply a low order non-affine warp in order to improve fitting of the data to the atlas. In practice these atlases are extremely useful for the approximate identification of cortical areas in clinical patients and on images from modalities where anatomical content is poor, such as isotope investigations or fMRI (Figs. 8.17 and 8.18).

Atlases can also be used to guide the selection of brain regions for more complex analyses (Gardner and Yazdani 1998; Nowinski 2004). We have used a simple coordinate system based on the position and size of the CSF space to allow automatic measurements of the position and severity of cerebral atrophy in patients with dementia. In this case the atlas is deliberately extremely simple and of very low spatial resolution identifying only the front, middle, back, top and bottom and right and left of the CSF space. Despite this, the distribution of CSF in this standard space allows differential diagnosis between dementias of different types with accuracy

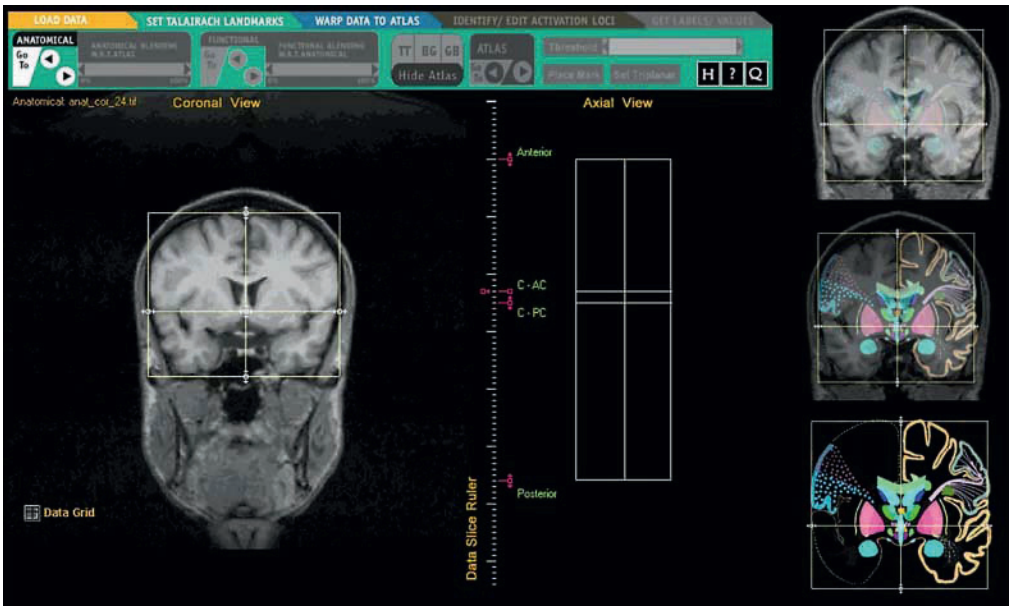

Fig. 8.17. Screenshot from the Brain Atlas for Functional Imaging (BAFI) (Nowinski and Thirunavuukarasuu 2000). Showing the application of a Taliarach coordinate system to a coronal image from a 3D brain MRI. After application of the coordinate space the images can be coregistered to the standard Taliarach map. The images on the *right* show the coregistered images with varying degrees of opacity to demonstrate the image (*top*), the pure atlas (*bottom*) and a fused version (*middle*)

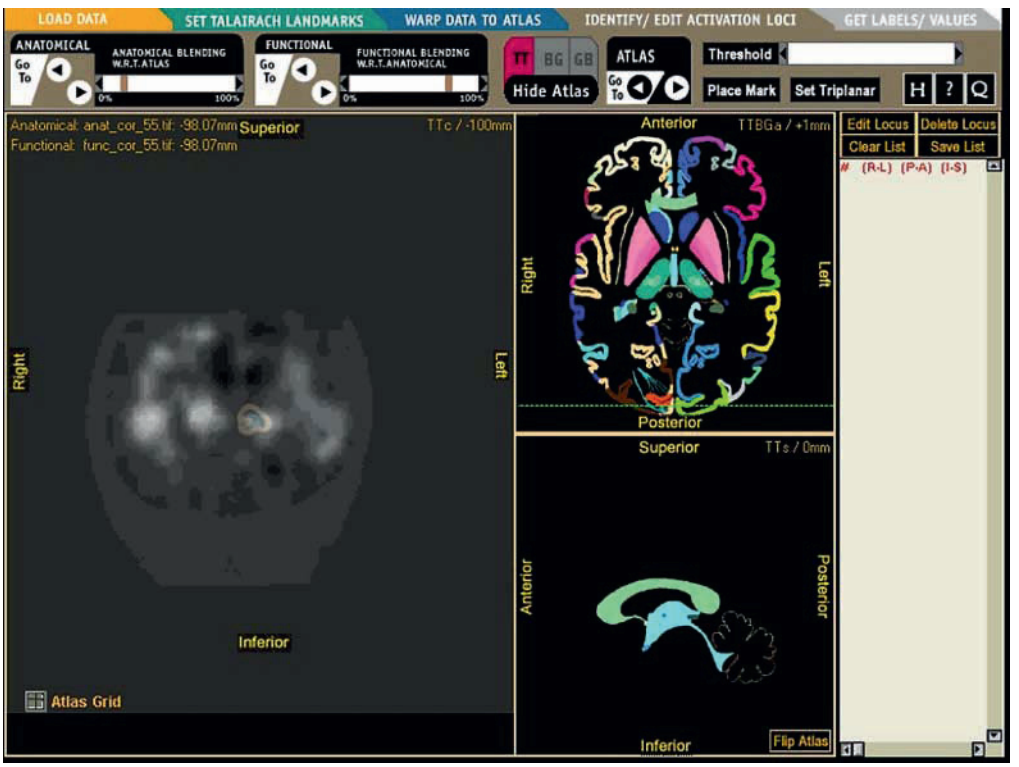

Fig. 8.18. Also taken from the Brain Atlas for Functional Imaging (BAFI) (Nowinski and Thirunavuukarasuu 2000). Image shows a coronal image from a functional MRI series which has been coregistered into the Taliarach coordinate system. The *right panels* indicate the position of the marker point on the atlas and the *far right panel* gives a coordinate description of the areas of activation

in excess of 80%. This is illustrated in Figure 8.19, which uses this technique to show the separation of patients with different dementing diseases (Thacker et al. 2000). Further atlas development has made use of image coregistration in developing population-based lymph node maps of the head and neck (Poon et al. 2004).

8.7.4 Subtraction Imaging

Another application of data coregistration is to allow comparison of apparently similar examinations to improve the detection of small structural changes. The use of an automated coregistration technique will allow generation of matching images with subvoxel accuracy, which can then be directly compared (Fig. 8.20). This process assumes that the differences between the images will not affect the accuracy of the coregistration process. Where changes are small, affecting only a small volume of the data and do not occur in areas of strong edge strength, this assumption appears to be true. The beauty of this approach is that is possible to visualize tiny changes in structure of the order of a fraction of a pixel in magnitude (Bydder 1995; Hajnal et al. 1995; Hajnal and Bydder 1997). This allows visualization of changes due to brain atrophy, tumour growth or other processes where the change between the images is too small to be appreciated by eye (Fig. 8.21).

A combination of subtraction imaging and multiple data set imaging is also being facilitated through the use of image coregistration where subtraction is

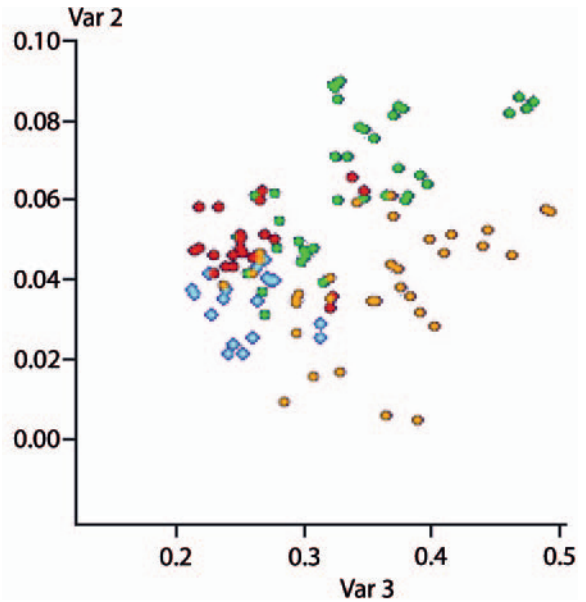

Fig. 8.19. Scattergram of the distribution of CSF within a simple stereotactic coordinate system. Each point represents a single patient with Alzheimer's disease (*green*), frontotemporal dementia (*orange*) or vascular dementia (*red*). *Blue* points are normal age matched controls. Note the excellent separability of the groups which provides useful support information for diagnosis

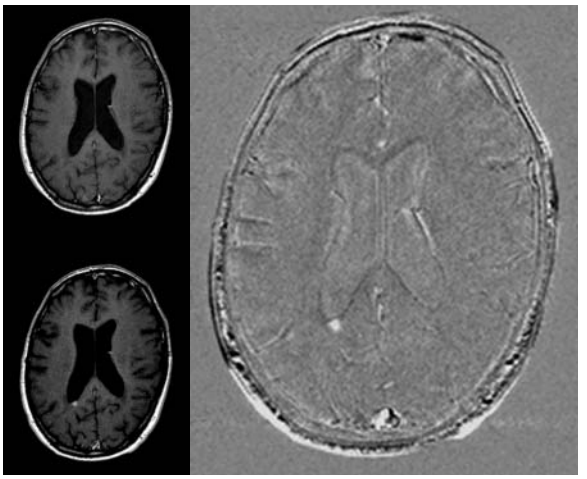

Fig. 8.20. MR images and subtraction image of an enhancing plaque in a patient with MS

Fig. 8.21. Subtraction image from two MRI examinations in a child with hydrocephalus. The white border around the ventricle indicates that the ventricle has shrunk between the examinations

performed of temporally spaced ictal and interictal SPECT images of the brain, the resultant subtraction SPECT image being coregistered with an MRI scan (Mumcuoglu et al. 2006).

The interpretation of subtraction images is quite difficult since changes may be caused either by changes in intensity or by movements of tissue boundaries (Bydder 1995). In addition, the magnitude of the differences in the subtraction images can be small making them difficult to identify. The use of statistical approaches to identify significant differences between the images improves the detection of difference and allows automated identification of the pixels that have changed. The use of statistical subtractive techniques also allows the comparison of images with different grey scale characteristics that would demonstrate residual signal on standard subtraction images (Fig. 8.22).

8.7.5 Measuring Changes in Brain Volume

The accuracy of automated coregistration algorithms has been utilised to allow measurement of the small volume changes that occur due to atrophic brain diseases. Using an accurate coregistration technique will produce images with no features in the brain except in areas where the brain edge has moved due to atrophy. These changes can be seen at the brain edge even when the movement is far less than 1 pixel in magnitude and form the basis of the subtraction technique described above. Where the signal intensities on each side of the boundary are known, the intensity of the voxel in the difference image can be used to calculate the movement of the edge within the voxel that must have occurred. The volume change can then be expressed as the appropriate fraction of the voxel volume. This technique has been applied to the brain in patients with Alzheimer's disease and allows detection of hippocampal atrophy in only 6 months (Freeborough et al. 1996). The technique can also be used to measure volume changes due to other pathological processes such as tumours.

8.7.6 Segmentation and Classification

One of the main advantages of coregistration is the ability to combine information about a single voxel from images acquired using different modalities. This generates a data rich multi-parametric data set for each voxel that can be used to characterise the voxel far more accurately than could be achieved with a single image (Alfano et al. 1997; Holden et al. 2000). This type of data set can be analysed using statistical clustering techniques, separating specific tissue types from the data with great accuracy (Fig. 8.23). The data content of these multiparametric images can be adjusted by selection of appropriate imaging modalities to add the missing information required for a particular analysis. This

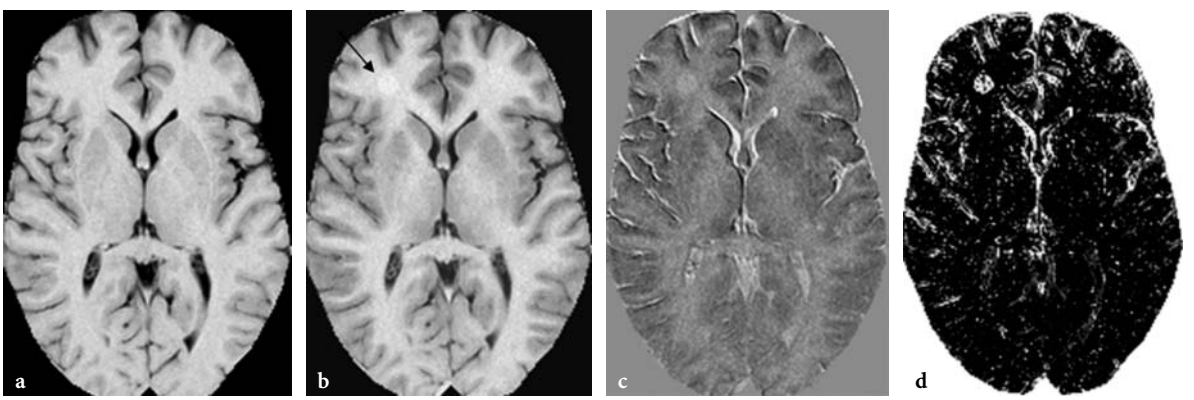

Fig. 8.22a–d. Demonstrates the principles of statistical non-parametric image subtraction in a healthy brain. **a,b** Two inversion recovery images which have been acquired with different inversion times to produce small but significant differences in grey scale structure. In **b** a small phantom area has been inserted (*arrow*). This circle is lighter than the background image by 2 × the standard deviation of the background noise and can hardly be detected by eye. **c** A subtraction image of **b** – a. The circle is slightly more visible but the major difference is the intensity of the grey matter due to the difference in image acquisition technique. **d** A statistical subtraction map where the intensity of the pixels indicates the probability that the image structure is different. The circular phantom is clearly seen

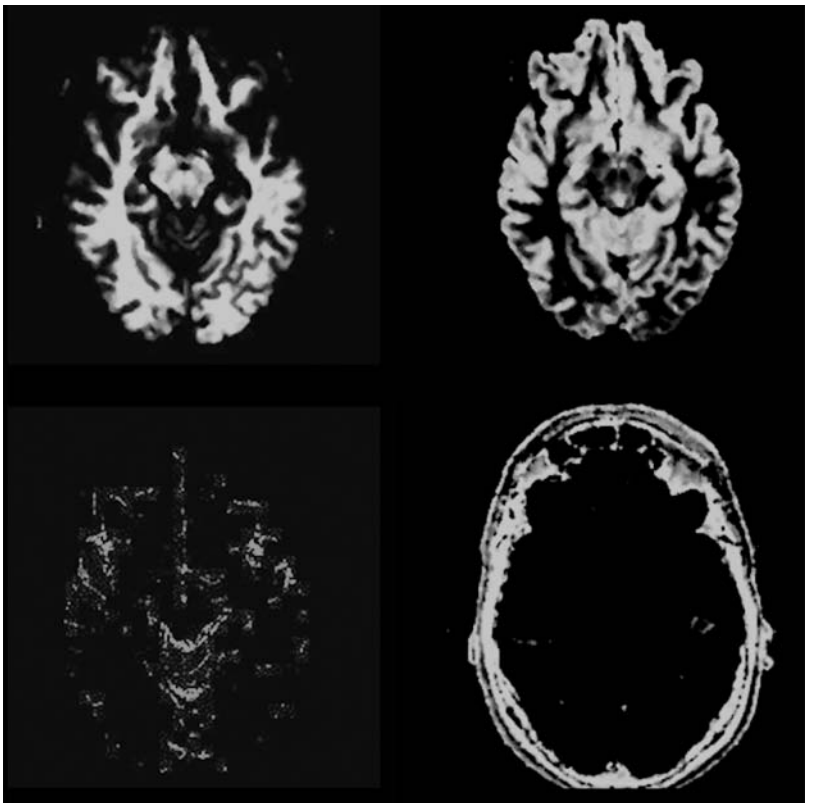

Fig. 8.23. Multispectral segmentation of healthy tissues from a coregistered series of MRI data sets. The images show the probability distribution (tissue maps) for white-matter, grey-matter, CSF and soft tissues (*top left clockwise*)

allows accurate identification not only of healthy tissues but also of pathological abnormalities within the data set.

8.7.7 MRI Prescription Guidance

Techniques for 3D image coregistration are becoming far faster as algorithmic improvements are developed. This has led several manufacturers to experiment with systems to allow automated prescription of the scanning geometry in MRI based on previous images. The concept is relatively simple. When a patient attends for a follow-up scan the system will perform a relatively detailed survey scan. This survey will be coregistered to the scan performed on the previous visit and the transformation matrix will be used to adjust the scanning parameters. In theory this should allow the follow-up scan to be acquired in a geometry already coregistered to the original examination. In practice there remain some logistical problems with this approach and it remains unclear how practical it will be to obtain sub-pixel coregistered examinations of large anatomical data sets. However, in fMRI experiments this technique is of considerable benefit allowing the image prescription to track the movements of the head as the experiment is performed. Although this does not remove the need to coregister the data, it does mean that the amount by which the images need to be transposed is minimized and is of similar magnitude for all images. This approach also allows the generation of acceptable fMRI images on the scanner console without further coregistration in clinical applications.

References

Alfano B, Brunetti A, Covelli EM et al. (1997) Unsupervised, automated segmentation of the normal brain using a multispectral relaxometric magnetic resonance approach. Magn Reson Med 37(1):84–93

Alp MS, Dujovny M, Misra M et al. (1998) Head registration techniques for image-guided surgery. Neurol Res 20(1):31–37

Amthauer H, Ruf J, Bohmig M et al. (2004) Diagnosis of neuroendocrine tumours by retrospective image fusion: is there a benefit? Eur J Nucl Med Mol Imaging 31(3):342–348

Amthauer H, Denecke T, Rohlfing T et al. (2005) Value of image fusion using single photon emission computed tomography with integrated low dose computed tomography in comparison with a retrospective voxel-based method in neuroendocrine tumours. Eur Radiol 15(7):1456–1462

Ashburner J, Andersson JL, Friston KJ (2000) Image registration using a symmetric prior – in three dimensions. Hum Brain Mapp 9(4):212–225

Beyer T, Rosenbaum S, Veit P et al. (2005) Respiration artifacts in whole-body (18)F-FDG PET/CT studies with combined PET/CT tomographs employing spiral CT technology with 1 to 16 detector rows. Eur J Nucl Med Mol Imaging 32(12):1429–1439

Brianzoni E, Rossi G, Ancidei S et al. (2005) Radiotherapy planning: PET/CT scanner performances in the definition of gross tumour volume and clinical target volume. Eur J Nucl Med Mol Imaging 32(12):1392–1399

Bydder G (1995) The MacKenzie Davidson Memorial Lecture: Detection of small changes in the brain with serial magnetic resonance imaging. BRJ 68:1271–1295

Castro MA, Putman CM, Cebral JR (2006) Patient-specific computational modeling of cerebral aneurysms with multiple avenues of flow from 3D rotational angiography images. Acad Radiol 13(7):811–821

Chao ST, Suh JH, Raja S et al. (2001) The sensitivity and specificity of FDG PET in distinguishing recurrent brain tumor from radionecrosis in patients treated with stereotactic radiosurgery. Int J Cancer 96(3):191–197

de Juan R, Seifert B, Berthold T et al. (2004) Clinical evaluation of a breathing protocol for PET/CT. Eur Radiol 14(6):1118–1123

Dey D, Slomka P, Chien D et al. (2006) Direct quantitative in vivo comparison of calcified atherosclerotic plaque on vascular MRI and CT by multimodality image registration. J Magn Reson Imaging 23(3):345–354

Feichtinger M, Holl A, Korner E et al. (2002) Future aspects of the presurgical evaluation in epilepsy. Acta Neurochir Suppl 84:17–26

Forster GJ, Laumann C, Nickel O et al. (2003) SPET/CT image co-registration in the abdomen with a simple and cost-effective tool. Eur J Nucl Med Mol Imaging 30(1):32–39

Freeborough P, Woods R, Fox NC. (1996) Accurate registration of serial 3D MR brain images and its application to visualising change in neurodegenerative disorders. J Comp Assist Tomogr 20(60):1012–1022

Gabriel M, Hausler F, Bale R et al. (2005) Image fusion analysis of (99m)Tc-HYNIC-Tyr(3)-octreotide SPECT and diagnostic CT using an immobilisation device with external markers in patients with endocrine tumours. Eur J Nucl Med Mol Imaging 32(12):1440–1451

Gardner JC, Yazdani F (1998) Correlating MR lesions and functional deficits in multiple sclerosis patients. Anatomical atlas registration. Phys Med Rehabil Clin N Am 9(3):569–586, vi

Goerres GW, Kamel E, Heidelberg TN et al. (2002) PET-CT image co-registration in the thorax: influence of respiration. Eur J Nucl Med Mol Imaging 29(3):351–360

Goerres GW, Burger C, Schwitter MR et al. (2003) PET/CT of the abdomen: optimizing the patient breathing pattern. Eur Radiol 13(4):734–739

Greitz T, Bohm C, Holte S et al. (1991) A computerized brain atlas: construction, anatomical content, and some applications. J Comput Assist Tomogr 15(1):26–38

Hajnal JV, Bydder GM (1997) Registration and subtraction of serial magnetic resonance images. Part 1: Technique. Advanced MR imaging techniques. Bradley WG, Bydder GM (eds) . Martin-Dunitz, London

Hajnal JV, Saeed N, Oatridge A et al. (1995) Detection of subtle brain changes using subvoxel registration and subtraction of serial MR images. J Comput Assist Tomogr 19(5):677–691

Halpern BS, Schiepers C, Weber WA et al. (2005) Presurgical staging of non-small cell lung cancer: positron emission tomography, integrated positron emission tomography/CT, and software image fusion. Chest 128(4):2289–2297

Harris B, Bailey D, Roach P et al. (2007) Fusion imaging of computed tomographic pulmonary angiography and SPECT ventilation/perfusion scintigraphy: initial experience and potential benefit. Eur J Nucl Med Mol Imaging 34(1): 135-42

Holden M, Hill DL, Denton ER et al. (2000) Voxel similarity measures for 3-D serial MR brain image registration. IEEE Trans Med Imaging 19(2):94–102

Hsiang D, Shah N, Yu H et al. (2005) Coregistration of dynamic contrast enhanced MRI and broadband diffuse optical spectroscopy for characterizing breast cancer. Technol Cancer Res Treat 4(5):549–558

Ingvar M, Bohm C, Thurfjell L et al. (1994) The role of a computerized adjustable brain atlas for merging of data from examinations using PET, SPECT, MEG, CT and MR images. Functional neuroimaging: technical foundations. Thatcher R, Hallet M, Zeffiro TA, John ER, Huerta M (eds) . Academic Press, San Diego

Jaremko JL, Cheng RW, Lambert RG et al. (2006) Reliability of an efficient MRI-based method for estimation of knee cartilage volume using surface registration. Osteoarthritis Cartilage 14(9):914–922

Kapur A, Carson PL, Eberhard J et al. (2004) Combination of digital mammography with semi-automated 3D breast ultrasound. Technol Cancer Res Treat 3(4):325–334

Kartachova MS, Valdes Olmos RA, Haas RL et al. (2006) Mapping of treatment-induced apoptosis in normal structures: (99m)Tc-Hynic-rh-annexin V SPECT and CT image fusion. Eur J Nucl Med Mol Imaging 33(8):893–899

Klein GJ, Thirion JP (2005) Cardiovascular imaging to quantify the evolution of cardiac diseases in clinical development. Biomarkers 10(Suppl 1):S1–9

Kremser C, Plangger C, Bosecke R et al. (1997) Image registration of MR and CT images using a frameless fiducial marker system. Magn Reson Imaging 15(5):579–585

Larson SM, Nehmeh SA, Erdi YE et al. (2005) PET/CT in non-small-cell lung cancer: value of respiratory-gated PET. Chang Gung Med J 28(5):306–314

Lopez R, Payoux P, Gantet P et al. (2004) Multimodal image registration for localization of sentinel nodes in head and neck squamous cell carcinoma. J Oral Maxillofac Surg 62(12):1497–1504

Mahvash M, Konig R, Urbach H et al. (2006) FLAIR-/T1-/T2-co-registration for image-guided diagnostic and resective epilepsy surgery. Neurosurgery 58(Suppl. 1):ONS69–75; discussion ONS69–75

Maurer CR Jr, Fitzpatrick JM, Wang MY et al. (1997) Registration of head volume images using implantable fiducial markers. IEEE Trans Med Imaging 16(4):447–462

Mayer-Kuckuk P, Doubrovin M, Bidaut L et al. (2006) Molecular imaging reveals skeletal engraftment sites of transplanted bone marrow cells. Cell Transplant 15(1):75–82

Messa C, Ceresoli GL, Rizzo G et al. (2005) Feasibility of [18F]FDG-PET and coregistered CT on clinical target volume definition of advanced non-small cell lung cancer. Q J Nucl Med Mol Imaging 49(3):259–266
Misko J, Dziuk M, Skrobowska E et al. (2006) Co-registration of cardiac MRI and rest gated SPECT in the assessment of myocardial perfusion, function and viability. J Cardiovasc Magn Reson 8(2):389–397
Mumcuoglu EU, Nar F, Yardimici Y et al. (2006) Simultaneous surface registration of ictal and interictal SPECT and magnetic resonance images for epilepsy studies. Nucl Med Commun 27(1):45–55
Murphy M, O'Brien TJ, Morris K et al. (2001) Multimodality image-guided epilepsy surgery. J Clin Neurosci 8(6):534–538
Myers R (2002) The application of PET-MR image registration in the brain. Br J Radiol 75 Spec No: S31–35
Nehmeh SA, Erdi YE, Pan T et al. (2004a) Four-dimensional (4D) PET/CT imaging of the thorax. Med Phys 31(12):3179–3186
Nehmeh SA, Erdi YE, Pan T et al. (2004b) Quantitation of respiratory motion during 4D-PET/CT acquisition. Med Phys 31(6):1333–1338
Neri E, Berrettini S, Salvatori L et al. (2005) 3-D CT and MRI co-registration in the assessment of cochlear implantation. Med Sci Monit 11(10):MT63–67
Nowinski WL (2004) Co-registration of the Schaltenbrand-Wahren microseries with the probabilistic functional atlas. Stereotact Funct Neurosurg 82(4):142–146
Nowinski W, Thirunavuukarasuu A (2000) Brain atlas for functional imaging. Thieme Verlag, Stuttgart
Nowinski W, Bryan R et al. (1997) The electronic clinical brain atlas multiplanar navigation of the human brain. Theime, New York Stuttgart
Otte A, Halsband U (2006) Brain imaging tools in neurosciences. J Physiol Paris 99(4/6):281–292
Poon I, Fischbein N, Lee N et al. (2004) A population-based atlas and clinical target volume for the head-and-neck lymph nodes. Int J Radiat Oncol Biol Phys 59(5):1301–1311
Rasser PE, Johnston P, Lagopoulos J et al. (2005) Functional MRI BOLD response to Tower of London performance of first-episode schizophrenia patients using cortical pattern matching. Neuroimage 26(3):941–951
Robar JL, Clark BG, Schella JW et al. (2005) Analysis of patient repositioning accuracy in precision radiation therapy using automated image fusion. J Appl Clin Med Phys 6(1):71–83
Suga K, Kawakami Y, Zaki M et al. (2004a) Clinical utility of co-registered respiratory-gated(99m)Tc-Technegas/MAA SPECT-CT images in the assessment of regional lung functional impairment in patients with lung cancer. Eur J Nucl Med Mol Imaging 31(9):1280–1290
Suga K, Yasuhiko K, Zaki et al. (2004b) Assessment of regional lung functional impairment with co-registered respiratory-gated ventilation/perfusion SPET-CT images: initial experiences. Eur J Nucl Med Mol Imaging 31(2):240–249
Suri JS, Danielson T, Guo Y et al. (2005) Fischer's Fused Full Field Digital Mammography and Ultrasound System (FFDMUS) " Stud Health Technol Inform 114:177–200
Talairach J, Tournoux P (1988) Co-planar stereotactic atlas of the human brain. Georg Thieme Verlag, Stuttgart New York
Thacker NA, Burton E, Lacey A et al. (1999) The effects of motion on parametric fMRI analysis techniques. Physiol Meas 20(3):251–263
Thacker N, Bathgate D, Varma A et al. (2000) Automated analysis of the distribution and severity of cerebral atrophy in dementing diseases: diagnostic power in Alzheimer's, frontotemporal and vascular dementia. Proceedings of the 8th Annual Meeting of the ISMRM, Denver, USA
Thomas MD, Bailey DL, Livieratos L (2005) A dual modality approach to quantitative quality control in emission tomography. Phys Med Biol 50(15):N187–194
Thottakara P, Lazar M, Johnson SC et al. (2006) Application of Brodmann's area templates for ROI selection in white matter tractography studies. Neuroimage 29(3):868–878
Veit P, Ruehm S, Kuehl H et al. (2006) Lymph node staging with dual-modality PET/CT: enhancing the diagnostic accuracy in oncology. Eur J Radiol 58(3):383–389
Wein W, Roper B, Navab N (2005) Automatic registration and fusion of ultrasound with CT for radiotherapy. Med Image Comput Comput Assist Interv Int Conf Med Image Comput Comput Assist Interv 8(2):303–311
West J, Fitzpatrick JM, Wang MY et al. (1999) Retrospective intermodality registration techniques for images of the head: surface-based versus volume-based. IEEE Trans Med Imaging 18(2):144–150
Woods RP, Grafton ST, Holmes CJ et al. (1998a) Automated image registration: I. General methods and intrasubject, intramodality validation. J Comput Assist Tomogr 22(1):139–152
Woods RP, Grafton ST, Watson JD et al. (1998b) Automated image registration: II. Intersubject validation of linear and nonlinear models. J Comput Assist Tomogr 22(1):153–165
Woods RP, Dapretto M, Sicotte NL et al. (1999) Creation and use of a Talairach-compatible atlas for accurate, automated, nonlinear intersubject registration, and analysis of functional imaging data. Hum Brain Mapp 8(2/3):73–79
Wu TH, Wang JK, Lee JJ et al. (2003) An imaging co-registration system using novel non-invasive and non-radioactive external markers. Eur J Nucl Med Mol Imaging 30(6):812–818
Yamamoto Y, Nishiyama Y, Monden T et al. (2003) Clinical usefulness of fusion of 131I SPECT and CT images in patients with differentiated thyroid carcinoma. J Nucl Med 44(12):1905–1910
Yokoi T, Soma T, Shinohara H et al. (2004) Accuracy and reproducibility of co-registration techniques based on mutual information and normalized mutual information for MRI and SPECT brain images. Ann Nucl Med 18(8):659–667
Yu H, Fahrig R, Pelc NJ (2005) Co-registration of X-ray and MR fields of view in a hybrid XMR system. J Magn Reson Imaging 22(2):291–301
Zaitsev M, D'Arcy J, Collins DJ et al. (2005) Dual-contrast echo planar imaging with keyhole: application to dynamic contrast-enhanced perfusion studies. Phys Med Biol 50(19):4491–4505
Zangheri B, Messa C, Picchio M et al. (2004) PET/CT and breast cancer. Eur J Nucl Med Mol Imaging 31(Suppl 1): S135–142
Zylka W, Sabczynski J (1999) Effect of localization devices and registration methods on the accuracy of stereotactic frame systems predicted by the Gaussian approach. Comput Aided Surg 4(2):77–86

Image Processing on Diagnostic Workstations

9

Bart M. ter Haar Romeny

CONTENTS

9.1 Introduction

Medical workstations have developed into the super-assistants of radiologists. The overwhelming production of images, hardware that rapidly became cheaper and powerful 3D visualization and quantitative analysis software have all pushed the developments from simple PACS viewing into a really versatile viewing environment. This chapter gives an overview of these developments, aimed at radiologists' readership. Many references and internet links are given which discuss the topics in more depth than is possible in this short paper. This paper is necessarily incomplete.

Viewing stations are core business in a radiologist's daily work. All big medical imaging industries supply professional and integrated environments (such as Philips ViewForum, Siemens Syngo X, GE Advantage, etc.). There are dedicated companies for viewing software (a.o. Merge eFilm) or OEM solutions (a.o. Mercury Visage, Barco). The application domain of workstations is increasing. We now see them regularly employed in PACS and teleradiology diagnostic review, 3D/3D-time (4D) visualization, computer-aided detection (CAD), quantitative image analysis, computer-assisted surgery (CAS), radiotherapy treatment planning, and pathology. Also the applications for medical image analysis in the life-sciences research are increasing, due to the increased attention to small-animal scanning systems for molecular imaging, and the many types of advanced microscopes (such as confocal microscopy and two-photon laser scanning microscopes), all giving huge 3D datasets. The focus of this chapter is on image processing (also termed image analysis or computer vision) applications.

9.2 Hardware

Early systems were based on expensive hardware platforms, called workstations, often based on the UNIX operating system. Today, most systems are

B. M. ter Haar Romeny, PhD
Professor, Eindhoven University of Technology, Dept. of Biomedical Engineering, Image Analysis and Interpretation, PO Box 513, WH 2.106, 5600 MB Eindhoven, The Netherlands

Scientific terms marked with are explained in Wikipedia: www.wikipedia.org

based on readily available and affordable PC and Mac hardware platforms (running MS-Windows or Mac-OS respectively), which are still following Moore's law of increasing performance (a doubling every 24 months) at a stable price level.

The central processor unit (CPU) is the core of the system, running today at several Gigahertz, and performance is expressed in Giga-FLOPS (10^9 floating point operations per second). Famous CPUs are the Intel Pentium chip, and the AMD Athlon processor. Today, we see the current 32 bit processors being replaced by 64 bit processors, which are capable of processing more instructions simultaneously and addressing a larger number of memory elements ($2^{32} = 4.2 \times 10^9$, so a 32 bit system cannot have more than 4.2 GB of memory (10^9 = Giga)). There is also a trend to have more CPUs ('dualcore') on the motherboard, paving the way to parallel processing, which is currently still in its infancy.

The memory in the diagnostic workstation is organized in a hierarchical fashion. From small to large: the CPU has a so-called cache on its chip, as a local memory scratchpad for super-fast access, and communicates with the main RAM (random access memory, today typically 1–4 GB) through the data bus, a data highway in the computer. As the RAM is fully electronic, access is fast (nanoseconds), much faster than access to a local hard disk (milliseconds). When the RAM is fully occupied, the CPU starts communicating with the hard disk. This explains why increasing the RAM of a slow computer can markedly upgrade its performance. In a PACS system, the disk storage is typically done on a 'redundant array of inexpensive disks' (RAID), where many disks in parallel prevent loss of data in case of failure of a component.

The speed of the network should be able to accommodate the network traffic. Typically the workstation is part of a local area network (LAN). Today gigabit/second speeds are attained over wired networks, wireless is slower (30–100 Mbit/s) but convenient for laptops and 'personal digital assistants' (PDAs). Many PACS installations can be serviced remotely through LAN connections to the supplier, anywhere.

Networks are so fast nowadays that 3D volume rendering can be distributed from a central powerful computer to simple (and thus low cost) viewing stations, called 'thin clients' (a.o. Terarecon Aquarius, Fig. 9.2). A powerful dedicated graphics board (in this case the VolumePro 1000) with dedicated hardware runs several 3D viewing applications simultaneously, and is remotely controlled by the users of the thin clients. Advantage is the capability to handle huge datasets (e.g. > 3000 slices) easily, but scalability (to e.g. dozens of users) is limited.

Interestingly, the power of 'graphical processing units' (GPU, the processor on the video card (or graphics accelerator card) in the system) has increased even faster than CPU power, mainly due to the fact that GPUs form the core of the computer game industry. The millions of systems needed for this lucrative market and the high competition between the market leaders NVIDIA and ATI have created a

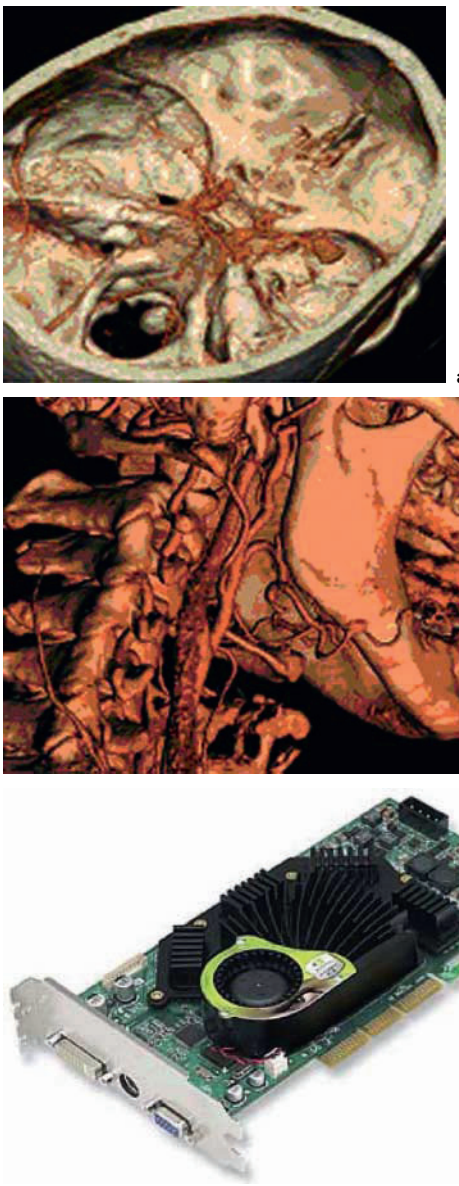

Fig. 9.1a–c. Brain aneurysm (**a**) and carotids (**b**): examples of volume renderings with a computer game graphics card (3Mensio Inc) (**c**)

huge performance/price ratio. A GPU has a 50 times faster communication speed of the data internally between memory and processor, and has dedicated hardware for rendering artificial environments, such as texture mapping, pixel shaders and an intrinsic parallel design with pixel pipelines. They have finally become fully programmable (and can be instructed by languages as DirectX and OpenGL) and are equipped with up to gigabytes of local memory. These 'games' hardware boards are now increasingly used in 3D medical visualization applications (among others 3Mensio Medical Systems). See Figure 9.1. There is also a community exploring the use of GPUs for general processing (GPGPU 2007).

The viewing screens of diagnostic workstations have to be of special diagnostic quality. Excellent reviews of the important parameters (resolution, contrast, brightness, 8, 10 or 12 bit intensity range, homogeneity, stability, viewing angle, speed, etc. are available in the so-called white papers by a variety of vendors (a.o. Barco – Barco 2007, Eizo – Eizo 2007).

9.3 Software

The revolution in PACS (and teleradiology) viewing stations was fired by the standard "Digital Imaging and Communications in Medicine" (DICOM) standard (DICOM 2007a), 4000 pages). In the 1990s the ACR (American College of Radiology) and NEMA (National Electrical Manufacturers Association) formed a joint committee to develop this standard. The standard is developed in liaison with other standardization organizations including CEN TC251 in Europe and JIRA in Japan, with review also by other organizations including IEEE, HL7 and (Health Level 7 2007) ANSI in the USA. It is now widely accepted. Convenient short tutorials are available (Whitby 2006). As the scanners and viewing software continue to develop, new features have to be added to the standard continuously. Vendors are required to make available their so-called conformity statements (see for example DICOM 2007b), i.e. a specified list of what conforms to the current version of the standard.

The second revolution was the standardization of the internal procedural organization of medical data handling in the 'Health Level 7' standard (HL7) (DICOM 2007a).

The basic function of a viewing station is the convenient viewing of the data, with a patient selection section. The functions are grouped in a so-called 'graphical user interface' (GUI). Versatile PC based viewing packages are now widely available (see RSNA 2006 for an extensive list), many also offering 'extended ASCI' character sets for the Chinese, Japanese and Korean markets.

Basic functions of the GUI include administrative functions as patient and study selection, report viewing and generation, and visualization functions as cine loop, 'maximum intensity projection' (MIP), 'multi-planar reformatting' (MPR) including oblique and curved reconstructions, cut planes, measurement tools for distances and angles, magnifying glass, annotations, etc.

The development of computer vision algorithms often follows a hierarchical pathway. The design process (rapid prototyping) is done in high-level software (examples are Mathematica, Maple, Matlab), where very powerful statements and algebraic functionality make up for very short code, but his is difficult to extent to the huge multi-dimensional medical images. When the formulas are understood and stable, the implementation is made into lower languages, like C, C++, Java. When ultimate speed (and limited variability) is required, the code can be implemented in hardware (GPU, field programmable gate array's (FPGA), dedicated chips, etc.). Many packages offer software development kits for joint development (e.g. MevisLab by MEVIS, 'Insight Segmentation and Registration Toolkit' (ITK) by NLM, etc.).

9.4 3D Visualization

The first breakthrough in the use of workstations has been by the invention of generating realistic 3D views from tomographic volume data in the 1980s. Now 3D volume rendering is fully interactive, at high resolution and real-time speed, and with a wide variety of options, making it a non-trivial matter to use it.

Many dedicated companies are now established (such as Vital Images with Vitrea, Mercury Computer Systems with Amira, Barco with Voxar, 3Mensio with 3Vision, Terarecon with Aquarius, etc.). Often a third party 3D viewing application is integrated

in the PACS viewing application, and supplied as a complete system by such an 'original equipment manufacturer' (OEM).

The principle of ray tracing ('rendering') (SIGGRAPH 2007) is actually based on mimicking the physics of light reflection with the computer: the value of a pixel in a 2D image of a 3D view (also called a 2.5D view) is calculated from the reflected amount of light from a virtual light source, either bouncing on the surface of the 3D data (this process is called 'surface rendering'), or as the summation of all contributions from the inside of the 3D dataset along the line of the ray in question, composed with a formula that takes into account the transparency (or the inverse: the opacity) of the voxels. This process is called 'volume rendering'. The user can change the opacity settings by manipulating the so-called 'transfer function', this function giving the relation between the measured pixel value from the scanner and the opacity (SEREDA et al. 2006). As there is an infinite number of settings possible, users often get confused, and a standard set of settings is supplied, e.g. for lung vessels, skull, abdominal vascular, etc., or a set of thumbnails is given with examples of presets, from which the user can choose. Attempts are underway to extract the optimal settings from the statistics of the data itself (SEREDA et al. 2006).

In virtual endoscopy (e.g. colonoscopy) the camera is positioned inside the 3D dataset. Challenges for the computer vision application are the automatic calculation of the optimal path for the fly-through through the center of the winding colon, bronchus or vessel. Clever new visualizations have been designed to screen the foldings in the colon for polyps at both the forward as backward pass simultaneously: unfolding (VILANOVA et al. 2003) (see Fig. 9.3) and viewing an unfolded cube (VOS et al. 2003) (see Fig. 9.4).

Segmentation is the process of dividing the 3D dataset in meaningful entities, which are then visualized separately. It is essential for 3D viewing by, e.g. cut-away views, and also, unfortunately, one of the most difficult issues in computer vision. It is discussed in more detail in Section 9.5. When clear contrasts are available, such as in contrast enhanced CT or MR angiography and bone structures in CT, the simple techniques of thresholding and region growing can be employed, up to now the most often used segmentation technique for 3D volume visualization.

This also explains the popularity of maximum intensity projection, where pixels in the 2.5D view are determined from the maximum along each ray from the viewing eye through the dataset (such a diverging set of rays leads to a so-called 'perspective rendering'). As this may easily lead to depth ambiguities, often the more appealing 'closest vessel projection' (CVP) is applied, where the local maximum values closest to the viewer is taken. The sampled points of the (oblique) rays through the dataset are mostly located in between the regular pixels, and are calculated by means of interpolation.

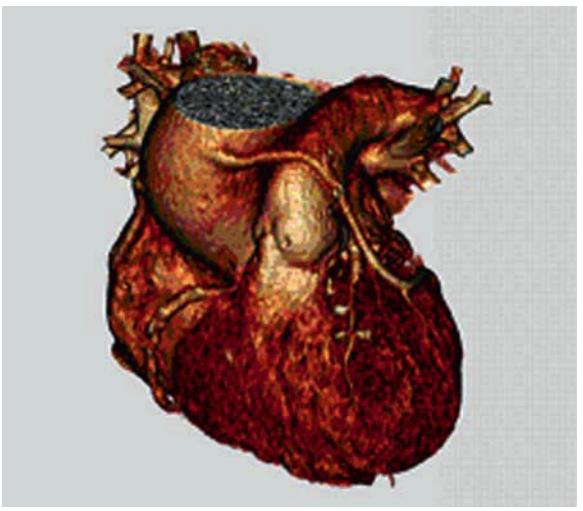

Fig. 9.2. Volume rendering of the heart and coronaries (Terarecon Inc)

Fig. 9.3. Virtual colonoscopy with unfolding enables inspection of folds from all sides. From VILANOVA et al. (2003)

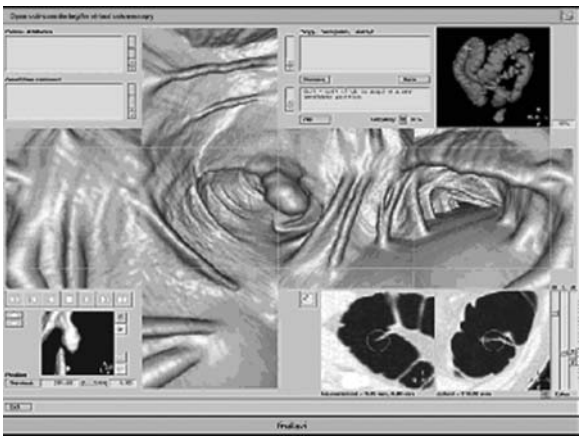

Fig. 9.4. Unfolded cube projection in virtual colonoscopy. From Vos et al. (2003)

9.5 Computer Aided Detection (CAD)

One of the primary challenges of intelligent software in modern workstations is to assist the human expert in recognition and classification of disease processes by clever computer vision algorithms. The often used term 'computer-aided diagnosis' may be an overstatement (better: 'computer-aided detection'), as the final judgement will remain with the radiologist. Typically, the computer program marks a region on a medical image with an annotation, as an attention sign to inspect the location or area in further detail. The task for the software developer is to translate the detection strategy of the expert into an efficient, effective and robust computer vision algorithm. Modern techniques are also based on (supervised and unsupervised) 'data mining'[ঌ] of huge imaging databases, to collect statistical appearances. E.g. learning the shape and texture properties of a lung nodule from 1500 or more patients in a PACS database is now within reach. Excellent reviews exist on current CAD techniques and the perspectives for CAD (Doi 2006; Gilbert and Lemke 2005). The field has just begun, and some first successes have been achieved. However, there is a huge amount of development still to be done in years to come.

Some advances in CAD techniques that have brought good progress are in the following application areas.

Mammography: this has been the first field where commercial applications found ground, in particular due to the volume production of the associated screening, the high resolution of the modality and the specific search tasks. Typical search tasks involve the automated detection of masses, microcalcifications, stellate or spiculated tumors, and the location of the nipple.

How do such algorithms work? Let us look in some detail to one example: stellate tumor detection (Karssemeijer 1995). As breast tissue consists of tubular structures from the milk-glands to the nipple, tumor extensions may preferably follow these tubular pathways. In a projection radiograph this leads to a spiculated or star-shaped pattern. The computer will inspect the contextual environment of each pixel (say 50 × 50 pixels) on the presence of lines with an orientation pointing towards the relevant pixel. In this way a total of 2500 'votes' are collected for each pixel. The pixels with a voting probability exceeding some threshold are possible candidates for further inspection.

The location of the nipple is important as a general coordinate origin for localization references with, e.g. previous recordings. The general statistical 'flow' of line structures points towards the nipple; the location can reasonably well be found by modeling the apparent statistical line structure with physical flow models.

The role of MRI in breast screening is rising. As in regular anatomical scans, too many false negative detections are found, and current attention now focuses on dynamic contrast enhanced MRI. The rationale is the high vascularity of the neoplasm, leading to a faster uptake and outwash over time of the contrast medium compared to normal tissue. Current research focuses on the understanding of this vascular flow pattern (e.g. by two-compartment modeling) and the optimal timing of the image sequence.

Polyp detection in virtual colonography: polyps are characterized by a mushroom-like extrusion of the colon wall, and can be detected by their shape: they exhibit higher local 3D curvature[ঌ] ('Gaussian curvature'[ঌ]) properties. These can be detected with methods from 'differential geometry'[ঌ] (the theory of shapes and how to measure and characterize them), and highlighted as, e.g. colored areas as attention foci for further inspection.

Methods have been developed to carry out an electronic cleansing[ঌ] of the colon wall when contrast medium is still present. An interesting current target is to reduce strongly the radiation dose of the CT scan, and still be able to detect the polyp struc-

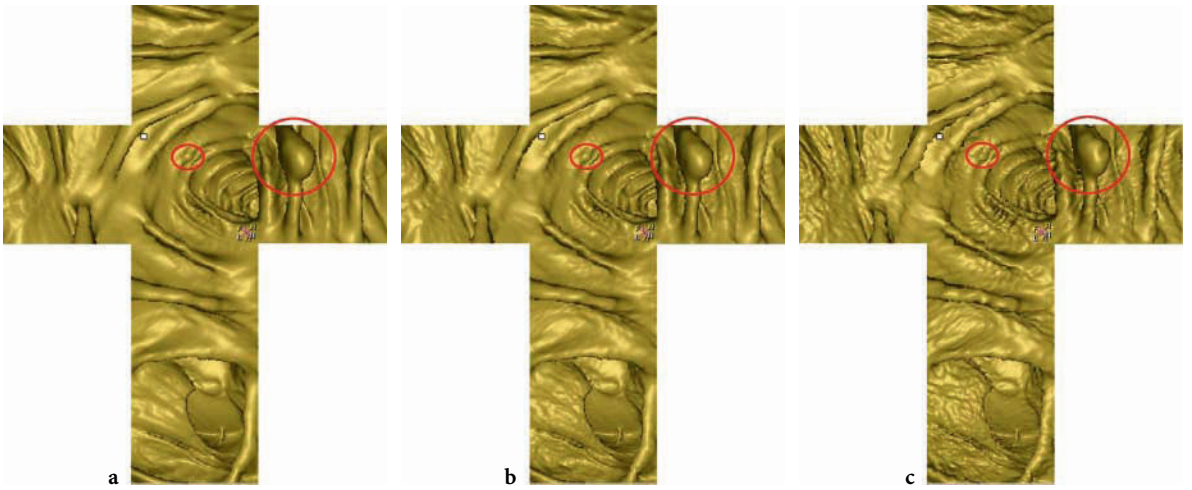

Fig. 9.5a–c. Virtual colonoscopy with surface smoothing. **a** Original dose (64 mAs); **b** 6.25 mAs; **c** 1.6 mAs. From Peters (200)

tures, despite the deterioration of the detected colon wall structures (Fig. 9.5). Clever shape smoothing techniques and edge-preserving smoothing of the colon surface have indeed enabled a substantial dose reduction.

Thorax CAD: here the focus is on the automated detection of nodules in the high resolution multi-slice CT (MSCT) data, on the detection of pulmonary emboli (Schaefer-Prokop et al. 2006, and of textural analysis by classification of pixels, e.g. for the quantification of the extent of sarcoidosis. See Sluimer et al. (2006) for a review.

Other CAD applications include *calcium scoring*, used to detect and quantify calcified coronary and aorta plaques, analysis of *retinal fundus images* for leaking blood vessels as an early indicator for diabetes, and the inspection of skin spots for melanoma (of particular attention in Australia), Burroni 2004.

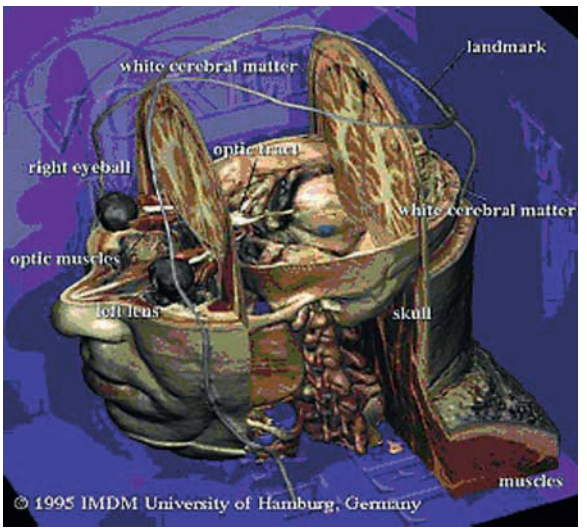

Fig. 9.6. The famous Voxel-Man atlas explored many types of optimal educational visualization. From Höhne (2004)

9.6 Atlases

The use of interactive 3D atlases on medical workstations is primarily focused on education and surgery. As an example, K.-H. Höhne's pioneering Voxel-Man series of atlases (Höhne 2004) was initiated by the 'visible human project' (Fig. 9.6). Atlases for brain surgery (e.g. the Cerefy Brain atlas family; Nowinski et al. 2005) now become probabilistic, based on a large number of patient studies.

9.7 CAD/CAM Design

Workstations can also assist in the creation of implants from the 3D scans of the patients. This is a highly active area in ENT, dental surgery, orthopedic surgery and cranio-maxillofacial surgery. Many design techniques have been developed to create the new shapes of the implants, e.g. by mirroring the healthy parts of the patient of the opposite side of the body, 3D region growing of triangulated 'finite ele-

ment models' in the assigned space, etc. The 'standard tesselation language' (STL) is a common format to describe surfaces for 3D milling equipment for rapid prototyping, such as stereolithography systems, plastic droplets ditherers, five-axes computerized milling machines, laser powder sintering systems, etc. Many dedicated rapid prototyping companies exist (e.g. Materialize Inc., see also www.cc.utah.edu/~asn8200/rapid.html). In the medical arena several large research institutes are active in this area (Caesar, Berlin; Co-Me, Zürich).

9.8 Diffusion Tensor Imaging (DTI) – Tractography

Three-dimensional (3D) visualization of fiber tracts in axonal bundles in the brain and muscle fiber bundles in heart and skeletal muscles can now be done interactively. The images are no longer composed of scalar (single) values in the voxels, but a complete diffusion tensor (a 3×3 symmetric matrix) is measured in each voxel.

The three so-called eigenvectors can be calculated with methods from linear algebra; they span the ellipsoid of the Brownian motion that the water molecules make at the location of the voxels due to thermal diffusion. Complex mathematical methods are being investigated to group the fibers in meaningful bundles, to segment and register the DTI data with anatomical data, and find fiber crossings and endings automatically. An interesting development is the photorealistic rendering of the tiny bundle structures (with specularities and shadows), based on the physics of the rendering of hair, see Figure 9.7 (Peeters et al. 2006 b).

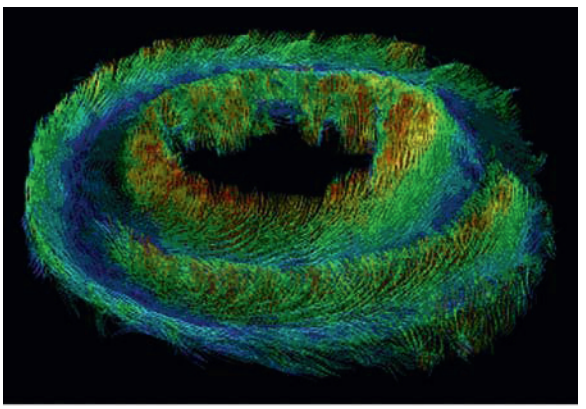

Fig. 9.7. Muscle fibers tracked in a high-resolution DTI MRI of a healthy mouse heart. Lighting and shadowing of lines combined with color coding of helix angle (α_h). From Peeters et al. (2006a)

9.9 Registration

Registration, or matching, is a classical technique in image analysis (Hajnal et al. 2001). It is employed to register anatomical to anatomical, or anatomical to functional data, in any dimension. Examples are MRI-CT, PET-CT, etc. The construction of a PET and a CT gantry in a single system effectively solves the registration problem for this modality.

The matching can be global (only translation, orientation and zooming of the image as a whole) or local (with local deformation, also called warping). Registration can be done by finding correspondence between (automatically detected) landmarks, or on the intensity landscape itself, e.g. by correlation. There is always an entity (a so-called functional) that has to be minimized for the best match: e.g. the mean squared distance between the landmarks, a Pierson correlation coefficient, or others. In particular, for multi-modality matching, the mutual information (MI) has been found to be an effective minimizer. As an example, in MRI bone voxels are black and in CT white; they show as a cluster in the joint probability histogram of the MR vs CT intensities. The MI is a measure of entropy (disorder) of this histogram.

9.10 RT Dose Planning

The accuracy of radiotherapy dose calculations, based on the attenuation values of the CT scan of the patient, needs to be very high to prevent underexposure of the tumor and overexposure of the healthy tissue. Typically the isodose surfaces are calculated and viewed in 3D in the context of the local anatomy. Increasingly the images made in the linear accellerator with the electronic portal imaging device (EPID) are used for precise localization of the beam and repeat positioning of the patient,

by precise registration techniques. The low contrast images (due to the high voltage of the imaging beam) can be enhanced by such techniques as (adaptive) histogram equalization.

9.11 Quantitative Image Analysis

This is the fastest growing application area of medical workstations. The number of applications is vast, every major vendor has research activities in this area, and many research institutes are active. To quote from the scope of 'Medical Image Analysis', one of the most influential scientific journals in the field:

"The journal is interested in approaches that utilize biomedical image datasets at all spatial scales, ranging from molecular/cellular imaging to tissue / organ imaging. While not limited to these alone, the typical biomedical image datasets of interest include those acquired from: magnetic resonance, ultrasound, computed tomography, nuclear medicine, X-ray, optical and confocal microscopy, video and range data images.

The types of papers accepted include those that cover the development and implementation of algorithms and strategies based on the use of various models (geometrical, statistical, physical, functional, etc.) to solve the following types of problems, using biomedical image datasets: representation of pictorial data, visualization, feature extraction, segmentation, inter-study and inter-subject registration, longitudinal / temporal studies, image-guided surgery and intervention, texture, shape and motion measurements, spectral analysis, digital anatomical atlases, statistical shape analysis, computational anatomy (modeling normal anatomy and its variations), computational physiology (modeling organs and living systems for image analysis, simulation and training), virtual and augmented reality for therapy planning and guidance, telemedicine with medical images, telepresence in medicine, telesurgery and image-guided medical robots, etc."

See also the huge amount of toolkits for computer vision: http://www.cs.cmu.edu/~cil/v-source.html. Important conferences in the field are MICCAI, CARS, IPMI, ISBI and SPIE MI. In the following some often-used techniques are shortly discussed. There are excellent tutorial books (Sonka et al. 2000, Bovik 2000; Yoo 2004) and review papers for the field.

Segmentation is a basic necessity for many subsequent viewing or analysis applications. Mostly thresholding and 2D/3D region growing are applied, but these often do not give the required result. Proper segmentation is notoriously difficult. There are dozens of techniques, such as model-based segmentation, methods based on statistical shape variations ('active shape models'), clustering methods in a high-dimensional feature space (e.g. for textures), histogram-based methods, physical models of contours ('snakes', level sets), region-growing methods, graph partitioning methods, and multi-scale segmentation.

The current feeling is that fully automated segmentation is a long way off, and a mix should be made between some (limited, initial) user-interaction (semi-automatic segmentation).

Feature detection is the finding of specific landmarks in the image, such as edges, corners, T-junctions, highest curvature points, etc. The most often used mathematical technique is multi-scale differential geometry (Ter Haar Romeny 2004). It is interesting that the early stages of the human visual perception system seem to employ this strategy.

Image enhancement is done by calculating specific properties which then stand out relative to the (often noisy) background. Examples are the likeness of voxels to a cylindrical structure by curvature relations ('vesselness'), edge preserving smoothing, coherence enhancing, tensor voting, etc. Commercial applications are, e.g. MUSICA ('Multi-Scale Image Contrast Amplification', by Agfa), and the Swedish ContextVision (http://www.contextvision.se/). Enhancement is often used to cancel the noise-increasing effects of substantially lowering the X-ray dose, such as in fluoroscopy and CT screening for virtual colonoscopy.

Quantitative MRI is possible by calculating the real T1 and T2 figures from the T1 and T2 weighted acquisitions, using the Bloch equation of MRI physics. Multi-modal MRI scans can be exploited for tissue classification: when different MRI techniques are applied to the same volume, each voxel is measured with a different physical property, and a feature space can be constructed with the physical units along the dimensional axes: e.g. in the characterization of tissue types in atherosclerotic lesions with T1, T2 and proton density weighted acquisitions, fat pixels tend to cluster, as do blood voxels, muscle voxels, calcified voxels, etc., see Figure 9.8.

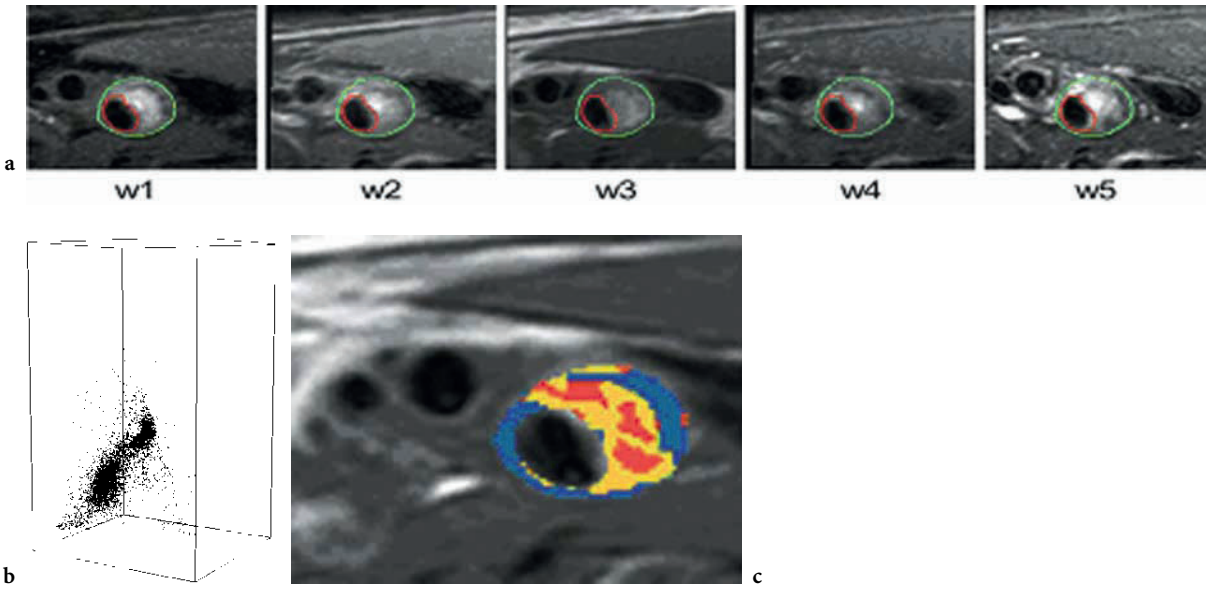

Fig. 9.8. a Multimodality MRI of atherosclerotic plaque in the human carotid artery: (w1) T1-weighted 2D TSE, (w2) ECG-gated proton density-weighted TSE, (w3) T1-weighted 3D TFE, (w4) ECG-gated partial T2-weighted TSE, (w5) ECG-gated T2-weighted TSE. **b** Feature space for cluster analysis. **c** Classification result. From HOFMAN et al. (2006)

Pattern recognition techniques like neural networks and Bayesian statistics may find the proper cluster boundaries.

Shape can be measured with differential geometric properties, such as curvature, saddle points, etc. It is often applied when, e.g. in the automated search for (almost) occluded lung vessels in pulmonary emboli, polyps on the colon vessel wall, measuring the stenotic index, spiculated lesions in mammography, etc. A popular method is based on 'active shape models', where the shape variation is established as so-called shape eigenmodes by analyzing a large set of variable shapes and performing a 'principal component analysis', a well known mathematical technique. The first eigenmode gives the main variation, the second the one but largest, etc. Fitting an atlas or model-based shape on a patient's organ or segmented structure becomes by this means much more computationally efficient.

Temporal analysis is used for bolus tracking (time-density quantification), functional maps of local perfusion parameters (of heart and brain), contrast-enhanced MRI of the breast, cardiac output calculations by measuring the volume of the left ventricle over time, multiple sclerosis lesion growth / shrinkage over time, regional cardiac wall thickness variations and local stress/strain calculations, and in fluoroscopy, e.g. the freezing of the stent in the video by cancellation of the motion of the coronary vessel.

9.12 Workstations for Life Sciences

In life sciences research a huge variety of (high dimensional) images is generated, with many new types of microscopy (confocal, two-photon, cryogenic transmission electron microscopy, etc.) and dedicated (bio-) medical small animal scanners (micro-CT, mini PET, mouse-MRI, etc.). The research on molecular imaging and molecular medicine is still primarily done in small animal models.

There is great need for quantitative image analysis. An example is, e.g. the measurement of quantitative parameters that determine the strength of newly engineered heart valve tissue of the patient's own cell line, such as collagen fiber thickness, local orientation variation and tortuosity. The source images are from two-photon microscopy, where the collagen is specifically colored with a collagen specific molecular imaging marker (Fig. 9.9).

Another example is the detailed study of the micro-vascular structure in the goat heart from ultra-thin slices of a cryogenic microtome (degree of branching, vessel diameter, diffusion and perfusion distances, etc.). Typical resolution is 25–50 micron in all directions, with datasets of 2000^3 (Fig. 9.10).

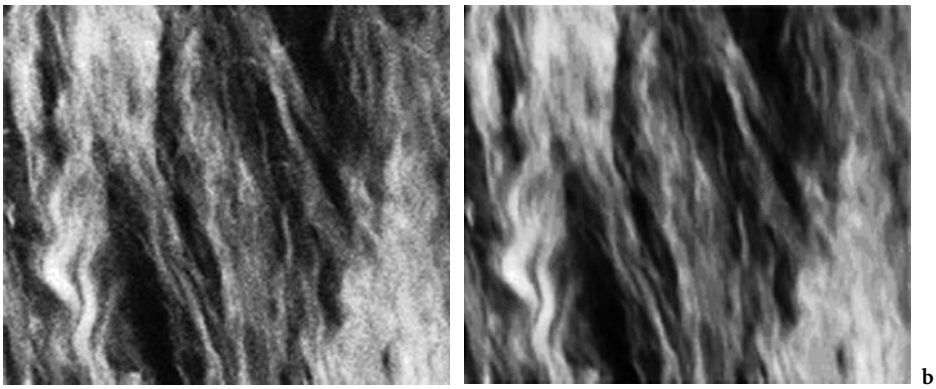

Fig. 9.9. a Two-photon florescence microscopy of collagen fibers of tissue-engineered heart-valve tissue. **b** Result of structure preserving denoising. From Daniels et al. 2006

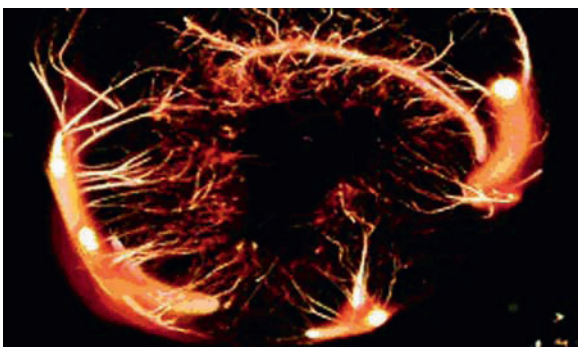

Fig. 9.10. A 3D visualization of a microtome stack (40 × 40 × 40 μm) of the micro-vasculature of a goat heart (van Bavel et al. 2006) [Bennink 2006]

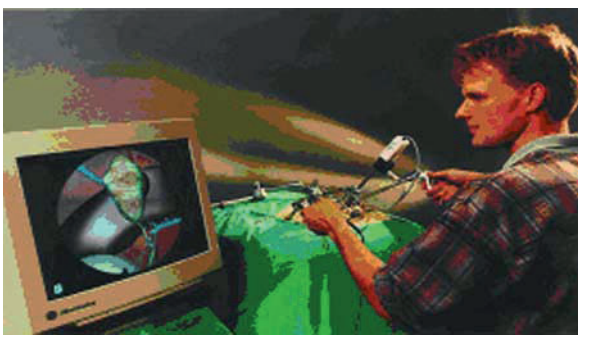

Fig. 9.11. Virtual laparoscopy trainer (Origin: Forschungszentrum Karlsruhe KISMET)

This research arena will benefit greatly in the near future from the spectacular developments in the diagnostic image analysis and visualization workstations.

9.13 Computer-Aided Surgery (CAS)

In the world of CAS some very advanced simulation and training systems (KISMET, Voxel-Man) have been created (Voxel Man surgical workstations 2007). Especially in dental implants, craniofacial surgery and laparoscopic surgery there are many and highly advanced systems today (Fig. 9.11). Surgical navigation workstations are routinely displaying the combination of the anatomy and the position and orientation of the instruments in the operating theatre.

An interesting development is the use of complex fluid dynamics modeling, which enables the prediction of rupture chances in abdominal aorta surgery, and selecting optimal therapeutic procedures with bypass surgery in the lower aorta (Fig. 9.12).

In neurosurgery workstations can be employed in the calculation of an optimal (safest) insert path for electrodes for deep brain stimulation (DBS), based on a minimal costs path avoiding blood vessels and ventricles, and starting in a gyrus. Workstations assist in inter-operative visualization by warping the pre-operative imagery to the real situation in the patient during the operation, by intra-operative MRI, or ultrasound.

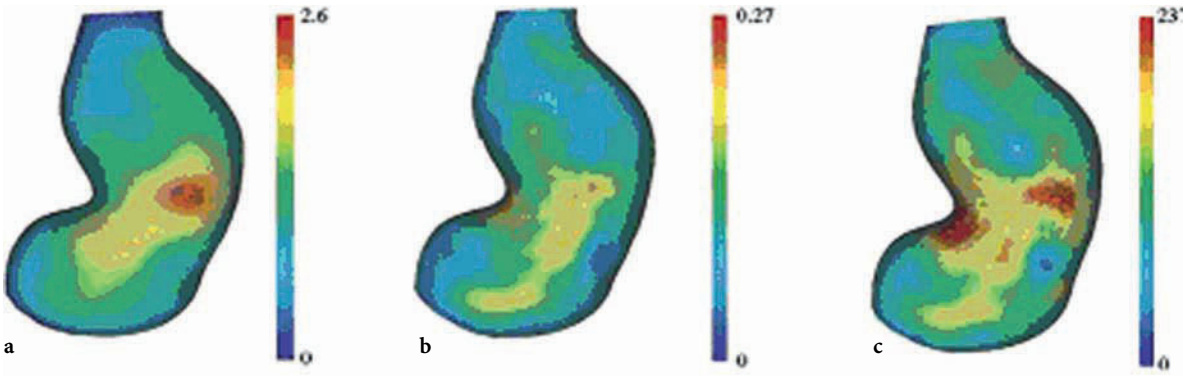

Fig. 9.12a–c. Abdominal aorta aneurysm: **a** color coding of displacement (mm); **b** Von Mises strain; **c** Von Mises stress (kPa). From DE PUTTER et al. (2005)

9.14 New Developments

The visual perception of depth (when viewing 3D) data is helped enormously if the viewer can move the data himself. There are many depth cues (stereo, depth from motion, depth from perspective), but depth from motion is the strongest. That is why maximum intensity projections (MIP) are preferably viewed dynamically. By self-tracking also the muscle's proprioceptors are giving feedback to the brain, adding to the visual sensation. The combination with human's superb eye-hand coordination has led to the concept of the Dextroscope (www.dextroscope.com), where a (computer generated) view or object can be manipulated under a half-transparent mirror, through which the viewer sees the display. Displays can also be equipped with haptic (tactile) feedback systems, which are now commercially available (Fig. 9.13).

Super-large screens, and touch screens are becoming popular; a new trend is the multi-touch screen (http://cs.nyu.edu/~jhan/ftirtouch/ with movie), where multiple positions to interact simultaneously make more complex transformations possible, such as zooming, multiple simultaneous objects interactions, etc.

Fig. 9.13. Stereo viewing and manipulation with haptic feedback

9.15 Outlook

We have actually just started with exploiting the huge power these super assistants can add, in any of the fields discussed above – hardware, software and integration. Image processing plays an essential role, be it for visualization, segmentation, computer-aided detection, navigation, registration, or quantitative analysis. There will be an ever greater need for clever and robust algorithms: it is the conviction of the author that the study of human brain mechanism for the inspiration for such algorithms has a bright future to come (TER HAAR ROMENY 2004). The radiologists will benefit from these super-assistants, and finally: the patient has the best benefit of all.

References

Barco (2007) White Papers Barco (screens, DICOM): http://www.barco.com/medical/en/downloads/whitepapers.asp?dltype=15

Bovik AC (ed) (2000) Handbook of image and video processing (communications, networking and multimedia). Academic Press

Burroni M, Corona R, Dell Eva G et al. (2004) Melanoma computer-aided diagnosis: reliability and feasibility study. Clin Cancer Res 10:1881–1886

Daniels F, ter Haar Romeny BM, Rubbens MP, van Assen HC (2006) Quantification of collagen orientation in 3D engineered tissue. In: Ibrahim F (ed) Proc Int Conf on Biomedical Engineering BioMed 2006, Kuala Lumpur, Malaysia, pp 344–348

de Putter S, Breeuwer M, Kosea U, Laffarguec F, Rouet J, Hoogeveen R, van den Bosch H, Buthe J, van de Vosse F, Gerritsen FA (2005) Automatic determination of the dynamic geometry of abdominal aortic aneurysm from MR with application to wall stress simulations. Proc CARS, International Congress Series 1281, pp 339– 344

DICOM (2007a) DICOM standard: http://medical.nema.org/

DICOM (2007b) conformance statement (example): https://www.merge.com/RESOURCES/pdf/dcs/dcs_efilm21.pdf

Doi K (2006) Diagnostic imaging over the last 50 years: research and development in medical imaging science and technology. Phys Med Biol 51:R5–R27

Eizo (2007) White Papers Eizo (screens): http://www.eizo.com/support/wp/index.asp

Gilbert FJ, Lemke H (eds) (2005) Computer-aided diagnosis. Special issue of British Journal of Radiology, vol. 78, British Institute of Radiology

GPGPU (2007) General-purpose computation using graphics hardware, http://www.gpgpu.org/

Hajnal JV, Hill DLG, Hawkes DJ (eds) (2001) Medical image registration. CRC

Health Level 7 (undated) Health Level 7, http://www.hl7.org/. See also regional sites (Australia http://www.hl7.org.au/, UK http://www.hl7.org.uk/, Canada http://www.cihi.ca/hl7, etc.)

Hofman JMA, Branderhorst WJ, ten Eikelder HMM, Cappendijk VC, Heeneman S, Kooi ME, Hilbers PAJ, ter Haar Romeny BM (2006) Quantification of atherosclerotic plaque components using in-vivo MRI and supervised classifiers", Magn Reson Med 55:790–799

Höhne K-H (2004) VOXEL-MAN 3D-Navigator" (CD-ROM). Springer, Berlin Heidelberg New York

Karssemeijer N (1995) Detection of stellate distortions in mammograms using scale-space operators. Proc. Information Processing in Medical Imaging, pp 335–346

Kaufman A, Müller K (2005) Overview of volume rendering. The visualization handbook. Elsevier

Nowinski W, Thirunavuukarasuu S, Benabid G (2005) The Cerefy clinical brain atlas. Enhanced edition with surgical planning and intraoperative support (CD-ROM). Thieme

Peeters THJM, Vilanova A, Strijkers GJ, ter Haar Romeny RBM (2006b) Visualization of the fibrous structure of the heart. Proc. 11th workshop on Vision, Modeling and Visualization. Aachen, Germany

Peeters THJM, Vilanova A, ter Haar Romeny RBM (2006a) Visualization of DTI fibers using hair-rendering techniques. In: Lelieveldt BPF, Haverkort B, de Laat CTAM, Heijnsdijk JWJ (eds) Proc ASCI 2006. Lommel, Belgium, pp 66–73

Peters JF, Grigorescu SE, Truyen R, Gerritsen FA, de Vries AH, van Gelder RE, Rogella P (2005) Robust automasted polyp detection for low-dose and normal-dise virtual colonoscopy. Proc CARS 2005, International Congress Series 1281, Berlin, Germany, pp 1146–1150

RSNA 2006 Exhibitor list: http://rsna2006.rsna.org/rsna2006/V2006/exhibitor_list/home.cfm

Schaefer-Prokop CM, van Delden OM, Bouma H, Sonnemans JJ, Gerritsen FA, Lameris JS (2006) To assess the added value of a prototype computer-aided detection (CAD) system for pulmonary embolism (PE) in contrast-enhanced multi-detector computed tomography (CT) images. Proc Eur Conf of Radiology, Vienna, Austria, EPOS Poster

Sereda P, Vilanova A, Gerritsen FA (2006) Automating transfer function design for volume rendering using hierarchical clustering of material boundaries. In: Sousa Santos B, Ertl T, Joy K (eds) Eurographics/IEEE VGTC Symposium on Visualization (EuroVis),Lisboa, Portugal, pp 243–250

Siggraph (2007) Ray tracing tutorial (SIGGRAPH): http://www.siggraph.org/education/materials/HyperGraph/raytrace/rtrace0.htm

Sluimer IC, Schilham AMR, Prokop M, van Ginneken B (2006) Computer analysis of computed tomography scans of the lung: a survey. IEEE Transactions on Medical Imaging, vol. 25, pp. 385–405

Sonka M, Michael Fitzpatrick J (eds) (2000) Handbook of medical imaging – vol. 2. Medical image processing and analysis. SPIE, Belligham, WA

ter Haar Romeny BM (2004) Front-end vision and multi-scale image analysis. Springer, Berlin Heidelberg New York

van Bavel E, Bakker EN, Pistea A, Sorop O, Spaan JA (2006) Mechanics of microvascular remodeling. A review. Clin Hemorheol Microcirc 34(1/2):35–41

Vilanova A, Gröller E (2003) Geometric modelling for virtual colon unfolding. In: Brunnett G, Hamann B, Müller H, Linsen L (eds) Geometric modeling for scientific visualization. Springer, Berlin Heidelberg New York, pp 453–468

Vos FM, van Gelder RE, Serlie IWO, Florie J, Nio CY, Glas AS, Post FH, Truyen R, Gerritsen FA, Stoker J (2003) Three-dimensional display modes for CT colonography: conventional 3D virtual colonoscopy versus unfolded cube projection. Radiology 228:878–885

Voxel Man surgical workstation (2007): http://www.uke.uni-hamburg.de/medizinische-fakultaet/voxel-man/index_ENG.php

Whitby J (2006) The DICOM Standard", White paper Barco Inc, 2006. URL: http://www.barco.com/barcoview/downloads/WhitePaper_DICOM.pdf

Yoo TS (2004) Insight into images: principles and practice for segmentation, registration, and image analysis. AK Peters

Image Processing: Clinical Applications

Temporal Bone

10

Paola Vagli, Francesca Turini Francesca Cerri, and Emanuele Neri

CONTENTS

10.1 The Middle Ear

10.1.1 Image Acquisition

As well as other anatomical districts, to generate three-dimensional (3D) reconstructions of the middle ear structures, a volumetric acquisition is required. In the case of the tympanic cavity, high-resolution computed tomography is the imaging modality of choice; although the term "high-resolution" traditionally means acquisitions performed with millimetric or sub-millimetric collimation (even with conventional CT), volumetric study is more properly used when a single or multi-row spiral CT is used. CT is generally introduced in the diagnostic workup of middle ear pathologies when external otoendoscopy is unsuccessful to demonstrate the cause of the disease. Volumetric acquisitions allow evaluating most of the components of the tympanic cavity, such as walls and ossicular chain, but fail to demonstrate the mucosal layer and ligaments.

Recently, interest in the CT study of the middle ear has been renewed by detailed endoscopic studies of this region performed during interventions with dedicated devices; this technique has been called transtympanic endoscopy, since it requires the perforation of the tympanic membrane.

Our spiral CT protocol includes axial and coronal acquisitions (beam collimation, 1 mm; pitch, 1; table incremental speed, 1 mm/s; tube rotation, 1 s; tube current, 160 mA with 120 KVp; field of view, 16 cm). Axial and coronal images are obtained at 0.5 mm of reconstruction interval with bone algorithm (Neri et al. 2000a).

A recent major advance has been the introduction of multi-row CT protocols including a single axial acquisition (along the standard axial plane, parallel to the hard palate and inferior to the orbit, thus avoiding the cornea in the primary X-ray beam of the CT scanner).

Multi-row technology allows sub-millimetric spatial resolution, which is extremely important in the z-axis, thus providing additional information when compared with single-slice CT. The visualization of thin structures such as the stapedial crura and the ossicular ligaments results in being improved by means of multi-row CT; also the ability to obtain volumetric data with isotropic voxels permits reliable image reformations in any plane of a section.

Moreover, multi-row CT shows the additional value in eliminating double examination when

P. Vagli, MD; F. Turini, MD; F. Cerri, MD; E. Neri, MD
Diagnostic and Interventional Radiology, Department of Oncology, Transplants, and Advanced Technologies in Medicine, University of Pisa, Via Roma 67, 56100, Pisa, Italy

transverse and coronal acquisitions are required in order to obtain diagnosis such as in patients with tumors or inflammation of the inner ear or affected by labyrinth fistulas.

This is extremely important in immobilized trauma patients where coronal acquisition is not achievable or in pediatric patients where a double scan should be avoided in order to reduce the radiation dose.

Jäger et al. (2005), equipped with a four-slice scanner, report the following acquisition protocol in the axial plane (0.5 mm section thickness; 0.5 mm collimation with two detector rows; 0.2 reconstruction increment; 1 mm table feed and rotation; 1 s rotation time; tube current 180 mAs with 120 kVp; field of view, 9 cm), and all images (native and reformatted) displayed at a window center of 800 HU and a window width of 4,000 HU. Despite the advent of more powerful scanners (32–64 slices) that allow a further improvement in speed and resolution along the z-axis, acquisition protocols reported in the literature remain substantially unchanged in terms of section thickness in respect to those proposed for four-slice scanners (Lane et al. 2006).

10.1.2 3D Image Processing: Value of Multiplanar Reconstructions

The near isotropic imaging obtained by spiral CT allows not only the accurate evaluation of anatomic details on native images, but even the reconstruction of oblique planes (MPR, multiplanar reconstructions) (Ali et al. 1993; Hermans et al. 1995). MPRs are well known since the introduction of CT in the clinical practice. Initial applications of MPR to the study of the middle ear were carried out with conventional CT (Haas and Kahle 1988; Grevers et al. 1989), and such experiences addressed to MPR an effective integrative role in CT imaging of the middle ear. With the advent of spiral CT, MPRs have been made available for most users, and the frequency of their application in the clinical routine has increased.

An interesting application of reformatted planes in the study of the middle ear is represented by the imaging of recurrent postoperative cholesteatoma. In this case, the combined use of axial native images, coronal and sagittal reformations allows to evaluate the shape of the tissue filling the middle ear, which in case of recurrent cholesteatoma can be identified by the prevalent scalloped limits (Veillon 1993, 1997).

Watanabe et al. (2000) evaluated MPR of the facial nerve canal in 628 CTs of the temporal bone. MPRs were created along the labyrinthine and tympanic segment, and along the tympanic and mastoid segment of the facial nerve. Further MPR along the facial nerve canal and bone fracture lines were created as well. In all cases, MPR delineated the labyrinthine and tympanic segment in one image, and the tympanic and mastoid segment in another image. In two patients with traumatic facial nerve palsy, the MPR images revealed a relationship between the facial nerve canal and the bone fracture. The authors concluded that MPR of the facial nerve canal were useful in detecting facial nerve schwannoma, traumatic facial nerve palsy and congenital facial nerve palsy.

Again, the application of MPR is variable since any case that requires integration of axial images with additional planes is valuable. One example is the postoperative evaluation of cochlear implants, where the path of the electrode within the cochlea turn is not easy to assess by native images; in such cases the creation of MPRs that allow displaying the entire electrode in a unique plane permits the precise assessment of the number of electrodes introduced.

Diederichs et al. (1996) applied a variant of MPR, called multiplanar volume reconstruction (MPVR), to the study of the middle ear after high-resolution computed tomography performed with a reduced dose. The aim of the study was to reduce image noise and at the same time increase the partial volume averaging to balance this effect; the tentative attempt failed for visualization of little bony structures, and, for example, the stapes was not visualized.

MPRs are also proposed as an alternative to direct coronal acquisitions in order to reduce the examination time and of course the patient's dose. Caldemeyer et al. (1999) demonstrated that a submillimetric and isotropic imaging of the middle ear can be obtained with spiral CT, with 0.5 mm of collimation, single volumetric scan in the axial plane, 0.2 mm of reconstruction spacing and coronal images created with MPR. Although this approach could be questionable using a single-slice scanner, the limitation of MPR seems to be overcome by multi-row CT (Fujii 2000; Gotwaldt 2001).

Recent literature (Lane et al. 2006) reports the opportunity, offered by multi-row CT scanners, to replace direct coronal scanning with reliable coronal reconstructions of image data from axial scanning. Reconstructions in any plane are thus possible

without a significant loss in resolution thanks to the acquisition of sub-millimetric section thickness and the isotropic voxels. This new approach overcomes the limitations imposed by restrictions in gantry angle and patient positioning and may help improve diagnostic accuracy of thin structures (ossicular ligaments, facial and semicircular canals dehiscence, bony nerves canals) (Jäger et al. 2005). The capability of reconstructing in any plane should lead to a reassessment of the optimal imaging plane for the depiction of normal anatomy and pathologic conditions of the temporal bone. Therefore, each reconstruction is tailored to depict a structure of common clinical interest.

In the last decade some authors (Mafee et al. 1992) advocated the use of sagittal imaging because it approximates the surgical plane of exposure; now it is possible with MPR, and with slightly different degrees of axial and coronal obliquity, para-sagittal reconstructions are useful for evaluating most of the relevant structures of the middle and inner ear, except the oval window.

Reconstructions in the plane parallel to the long axis of the petrous bone are useful for obtaining short-axis views of the cochlea, vestibular aqueduct, facial nerve canal, round window and incudomalleolar joint. Reconstructions in the plane parallel to the short axis of the petrous pyramid are valuable to optimally depict the superior semicircular canal and the long axis of the cochlea. Moreover, it is important to keep in mind that optimal depiction of a given structure often requires an oblique orientation with regard to more than one reference plane (Lane et al. 2006).

10.1.3 3D Image Processing: Segmentation, Surface and Volume Rendering

3D image processing in the study of the middle ear finds optimal conditions for image segmentation and visualization in the normal subject, making it easy to differentiate bone from the air content of the tympanic cavity. However, the presence of abundant fluid or tissue, resulting from a pathological process, makes this separation difficult.

The reconstruction of the bone is quite simple for any image processing software, surface rendering (SR) or volume rendering (VR) based. In the first case the boundary between bone and other tissues is identified at a Hounsfield density threshold of 160–200; just below this value enhancing parenchyma after iv contrast can be represented (but this is quite rare in the case of the middle ear). Again, below this value, the mucosal layer of the tympanic cavity can be found and represented if the threshold value is reduced dramatically to identify the passage between mucosa and air, as –500 HU (Pozzi Mucelli et al. 1997). It is clear that any software working with CT data sets can reconstruct in 3D the morphology of the mucosal layer, but it cannot represent colorimetric alterations in the course of edema, bleeding or dysplasia.

The knowledge of these segmentation values is extremely important to determine whether or not the reconstructed images correspond to reality. To this end a comparison between real anatomy and 3D reconstructed endoluminal views from seven formalin fixed anatomical specimens was performed by our group (Neri et al. 2000b). We found a 100% agreement between the observations for endoluminal views and anatomical sections, even if in two cases the complete visualization of the middle ear cavity could not initially be obtained for the presence of tissue remnants within the external auditory meatus. However, careful electronic removal of this tissue allowed visualizing the middle ear, while in the case of anatomical specimens, the tissue remnants were manually removed.

VR offers an alternative approach to segmentation; although it is still dependent on thresholds, the modulation of opacity values (see Chaps. 4 and 6) allows a wider range of tissue combination and display (Rubin et al. 1996; Johnson et al. 1996). With VR it is possible to visualize in the same view different tissue (having different Hounsfield density) or combine the visualization of tissue and metallic components, i.e., cochlear implants (Fig. 10.1) (Neri 2001a).

One interesting feature of SR or VR is to provide a global visualization of the aerated cavities of the middle ear. The reconstruction of the air content permits to estimate the grade of pneumatization of the tympanic cavity and mastoid cells that could change in the case of malformation and inflammation.

In contrast to the reconstruction of the air, SR and VR also provide a global view of the petrous bone. Such a perspective can be useful in many situations to estimate bony alterations: the malformation of the temporal bone that occurs in hemifacial mycrosomia, the surgical resection of bone performed in mastoidectomies, and the presence and extent of fractures.

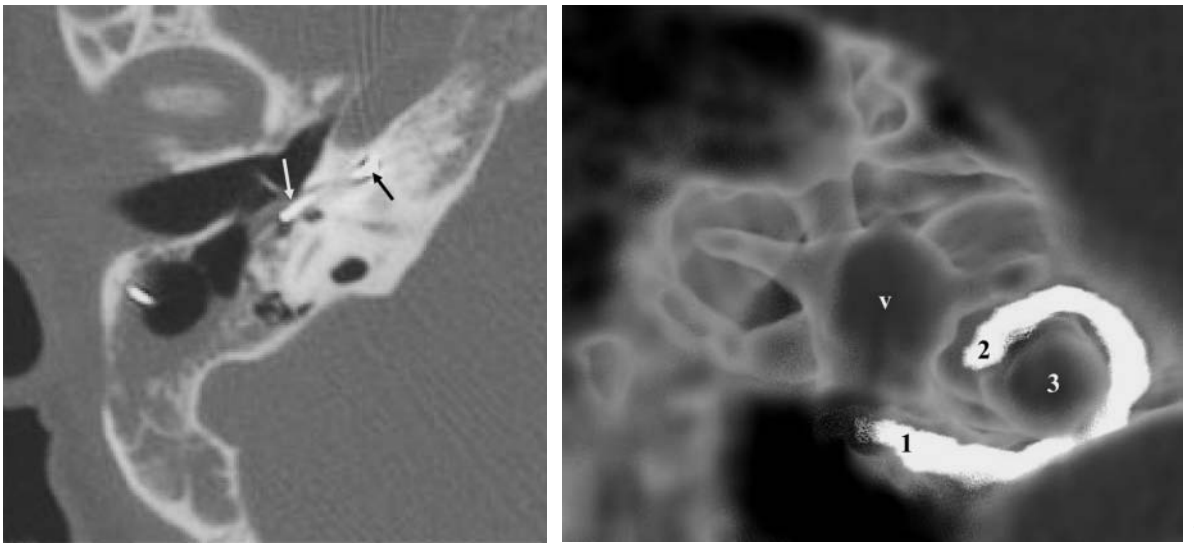

a b

Fig. 10.1a,b. Spiral CT follow-up in a patient who underwent cochlear implantation of the right ear for hearing loss. **a** Axial image crossing through the basal turn of the cochlea shows the initial (*white arrow*) and final (*black arrow*) portions of the electrode. This latter reaches the middle turn of the cochlea, but the precise location is not measurable. **b** Volume rendering of the bone labyrinth demonstrates the entire path of the electrode within the cochlea. Electrode path from basal turn (*1*) to the middle turn (*2*) is clearly visible. The apical turn (*3*) is not reached by the elecrode tip. *v*=vestibule

10.1.4 Endoluminal Views of the Middle Ear: Virtual Endoscopy (Technique)

The technical aspects of virtual endoscopy (VE) have been introduced in Chapter 7, to which the reader should refer. The application of VE to the study of the middle ear is quite simple, but requires, as for the other image processing methods, the availability of volumetric and high-resolution data. The optimal CT acquisition protocols have already been discussed.

VE of the middle ear is obtained by creating a virtual empty space within the tympanic cavity, which is really an empty space, but not accessible by direct human vision. The creation of the virtual space is generated in SR by the application of a binary segmentation in which a specific threshold level identifies the boundary between the air and the mucosal layer of the middle ear, as discussed in the previous paragraph. In VR the threshold is almost the same, and the use of a high opacity level allows enhancing the mucosal surface. In both cases the inner walls of the tympanic cavity are displayed. The majority of commercially available software allows one to point with the computer mouse within the air space (using an axial or coronal image as reference) and to generate an endoscopic view of the cavity. The virtual eye can be positioned in any space of the middle ear and directed to look towards specific structures or anatomical regions. The aim of VE of the middle ear is to obtain 3D perspectives of the tympanic cavity walls and of the ossicular chain simulating traditional endoscopy. However, before describing the application of VE in the middle ear, we report a digression toward the history of real endoscopy, and an explanation of how real endoscopy is obtained. At the end of this chapter limitations of traditional diagnostic tools and the potential benefits of VE and 3D imaging for diagnostic and surgical purposes in this field will be reported.

10.1.5 The Real Endoscopy: Transtympanic Endoscopy

The history of real endoscopy of the middle ear was started in 1967 by Zini when he tried to visualize the middle ear using a system of micromirrors, which allowed the exploration of the retrotympanum. This method, called indirect microtympanoscopy, is still used in clinical practice. Mer et al. (1967) introduced the fiberoptic endoscope into the tympanic cavity through a perforation of the tympanic membrane. Marquet and Boedts D (1975) described an endoscopic technique based on the use of a 1.7-mm

endoscope that allowed observing the attic, the ipotympanum, the protympanum and the retrotympanum. In 1982 the middle ear cavity was visualized with a needle, rigid otoscope by Nomura (1982). Subsequently, many authors started to use endoscopy for the diagnosis and post-surgical follow-up.

Modern endoscopes are based on Hopkin's optic system with variable diameter (minimum 1 mm in diameter), and length and angle variable on the basis of the region to explore. In the majority of cases the endoscopes are based on a rigid system, but in difficult cases, such as a strong curvature of the external auditory canal, the presence of stenosis or fibrotic tissue, the use of flexible endoscopes is preferred despite the lower spatial resolution and image quality.

Transtympanic endoscopy can be used as a diagnostic tool or as guidance for otosurgical interventions. In the first case the easy access of the external auditory canal allows the visualization of the tympanic membrane, a barrier between the endoscope and the middle ear; only the presence of a pathologic or surgical (miringotomy) perforation permits a limited exploration of the tympanic cavity.

The use of transtympanic endoscopy in otosurgery is aimed at providing real-time video assistance to the surgical procedure.

10.1.6 Virtual Endoscopy (Clinical Applications): The Study of the Tympanic Cavity

In a study carried out by our group (Neri et al. 2001b), a virtual endoscopic analysis of the tympanic cavity was performed by following the traditional imaging proper of transtympanic endoscopy. As radiologists we are confident with the traditional axial or coronal imaging, but we hereby describe the anatomy of the tympanic cavity from the point of view of the otologist. It means that we have a further instrument to understand this complex region and that we are now closer to the surgical views than we were before.

Creating an endoscopic perspective from the external auditory canal to look toward the middle ear, the tympanic cavity can be divided into four regions on the basis of endoscopic and surgical studies: retrotympanum (posterior), epitympanum (superior), protympanum (anterior) and ipotympanum (inferior).

The anatomy of the middle ear, as it is displayed by VE, is hereby described according to this anatomical partition. A typical VE perspective obtained from the external auditory canal allows the accurate identification of the anatomical landmarks that define these regions (Fig. 10.2a).

The retrotympanum represents more than one half of the posterior part of the tympanic cavity and includes the oval and round windows (Parlier-Cuau et al. 1998). VE allows displaying all the components of the retrotympanum (Fig. 10.2b) showing eminence and depressions, represented by: pyramidal and styloid eminence, pyramidal ridge, ponticulus, subiculum, and eminence of the mastoid portion of the facial nerve (Pickett et al. 1995; Espinoza 1989).

VE displays the pyramidal and styloid eminence as smoothed elevations of the medial wall of the tympanic cavity. The styloid or Politzer eminence, which represents the base of the styloid process, divides the retrotympanum from the ipotympanum. The pyramidal ridge is shown by VE as an elevation of the medial wall connecting both the pyramidal and styloid eminences. Turning the virtual endsocope toward the stapes, the eminence of the mastoid portion of the facial nerve appears just above the oval window niche (Thomassin et al. 1996). VE allows recognizing other two little osseous crests, represented by the ponticulus and subiculum. On the basis of these ridges, eminences and depressions of the medial wall of the tympanic cavity, the retrotympanum can be divided into four regions: the superomedial or posterior sinus tympani (or tympanic sinus of Proctor), the inferomedial or sinus tympani, the superolateral or facial sinus, and the inferolateral or fossula of Grivot (Guerrier and Guerrier 1976).

At VE the posterior sinus tympani can be seen under the eminence of the facial nerve canal and posterior to the oval window. The sinus tympani appears as a parietal depression whose landmarks are given by the ponticulus (superior), the subiculum (inferior-anterior), the pyramidal crest and eminence (posterior-lateral), and the promontory (anterior). Thomassin (1994) describes three types of sinus tympani on the basis of the feasibility of trans-tympanic endoscopy, but their morphology can be easily recognized also at VE: sinus tympani of easy exploration, characterized by a simple depression of the tympanic wall; sinus tympani of difficult exploration, represented by a depression of the wall that continues into a deep canal through the tympanic wall and opens into the retrotympanum with a little orifice; intermediate sinus tympani, with deep canal and large orifice.

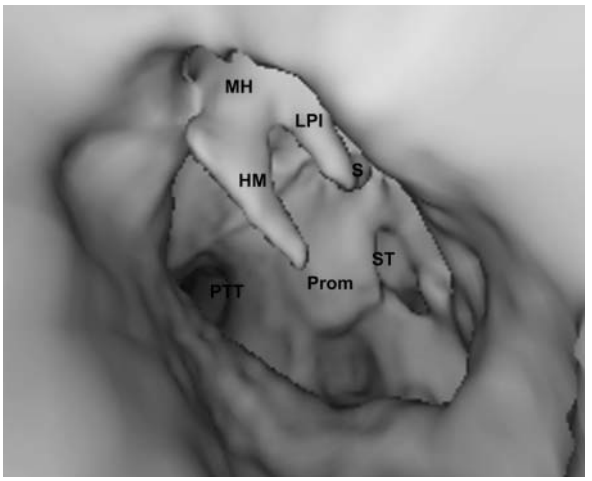

a

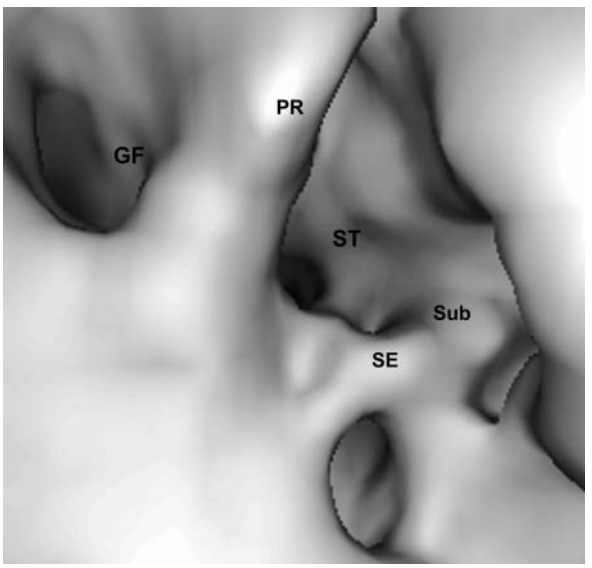

b

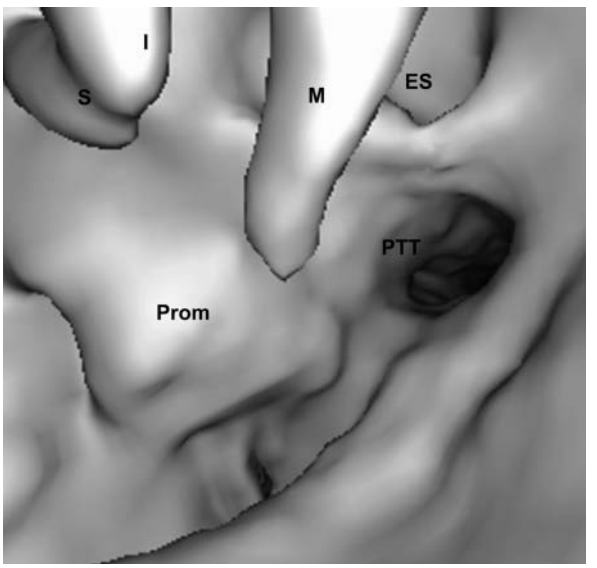

c

Fig. 10.2a–c. Virtual endoscopy of the middle ear. **a** The endoscopic view is created positioning the virtual endoscope within the external auditory canal, looking toward the middle ear cavity. The virtual perspective allows recognizing most of the structures composing this region: malleus head (*MH*) and handle (*HM*), long process of incus (*LPI*), sinus tympani (*ST*), promontory (*Prom*) and pharyngo-tympanic tube (*PTT*). **b** Detailed perspective of the *ST* and fossula of Grivot *(GF)*, divided by the pyramidal ridge (*PR*). In the inferior border of the ST, the styloid eminence (*SE*)and subiculum (*Sub*) are recognized. **c** Detailed perspective of the protympanum where the initial portion of the pharyngo-tympanic tube (*PTT*) opens. Superiorly the epytimpanic sinus (*ES*) is visible. *M*, malleus; *I*, incus; *S*, stapes

The promontory appears at VE as an eminence with a smooth surface that covers the round window. This opens from the tympanic cavity into the scala tympani of the cochlea.

Other depressions of the retrotympanic wall are the facial sinus and the fossula of Grivot. Their visualization is obtained at VE by positioning the virtual endoscope in the retrotympanum and looking posteriorly. These depressions become important landmarks during surgical interventions with a retrofacial approach.

The protympanum represents the anterior part of the tympanic cavity that includes the pharyngo-tympanic tube. The superior border of the tube divides the protympanum from the sinus epitympani. The inferior border separates the tube from the internal carotid artery. The protympanum is easy to explore with either transtympanic endoscopy or VE (Fig. 10.2c).

The ipotympanum represents the floor of the tympanic cavity, separated from the mesotympanum by a horizontal plane crossing through the inferior border of the external meatus. VEs display the floor, characterized by many osseous crests whose development is related with the dimensions of the subjacent labyrinthic cells.

The epitympanum (attic or epitympanic recess) represents the superior part of the tympanic cavity whose posterior landmark is given by the aditus ad antrum, the anterior by the supratubal recess, the lateral by the scutum and the medial by the wall of the labyrinth at the level of the second portion of the facial nerve. The superior landmark is represented by the tegmen tympani, a thin osseous lamina, with 1 mm thick. By considering a sagittal plane crossing through the superior ligaments of the incus and malleus, the epytimpanum can be

divided into a medial and lateral part. The lateral part includes the Prussak's space. The superior ligament of the malleus divides also the epitympanum into the anterior and posterior part. In the posterior part of the epytimpanum, the eminence of the lateral semicircular canal can be easily detected either by transtympanic endoscopy or VE. A significant advantage of VE in the exploration of the epitympanum is the demonstration of the entire incudomalleolar joint obtained after the electronic removal of ligaments and soft tissues.

10.1.7 Virtual Endoscopy (Clinical Applications): The Study of the Ossicular Chain

VE allows visualizing the entire ossicular chain potentially from any point of view. Positioning the virtual endoscope within the external auditory canal, VE displays the long process of incus, the stapes, and the handle of the malleus. Meanwhile, from a point of view located within the ipotympanum VE can easily display the stapes, the lenticular process of incus

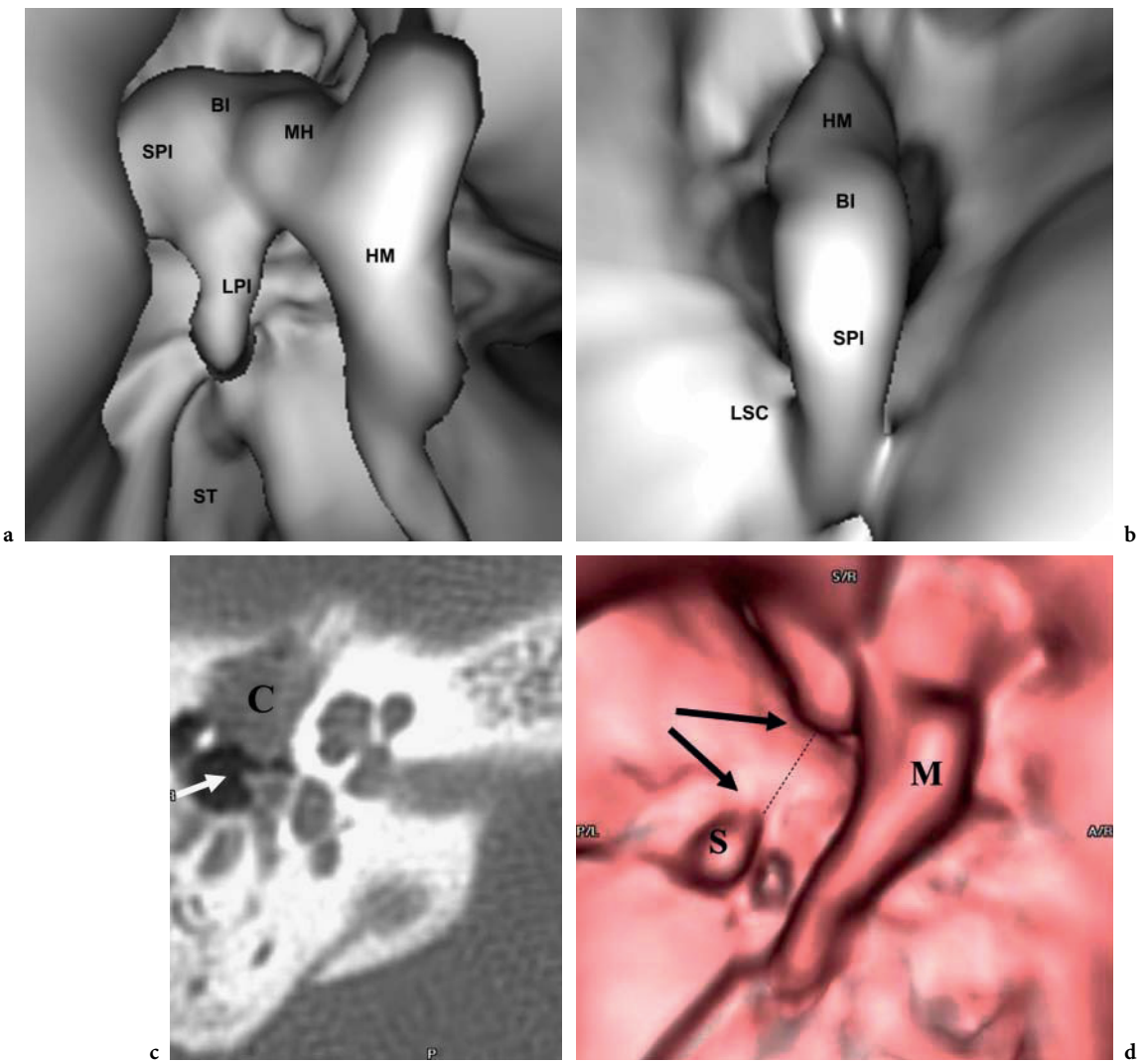

Fig. 10.3a–d. Virtual endoscopy of the ossicular chain. **a** *Lateral view* including almost the entire ossicular chain: *HM*, handle of malleus; *MH*, malleus head; *BI*, body of incus; *SPI*, short process of incus; *LPI*, long process of incus, *ST*, sinus tympani. **b** Superior view of the incudomalleolar joint. The eminence of the lateral semicircular canal (*LSC*) represents an important surgical landmark for mastoidectomy. **c** Axial CT study in a patient with right colesteatoma (*C*), that shows the absence of the lenticular process of the incus. **d** Endoluminal view of the middle ear demonstrates the absence of the lenticular process of the incus. *M*, malleus; *S*, stapes

(incudostapedial joint) and the long process of incus. However, the visualization of stapes' superstructure, with clear representation of the anterior and posterior crus, is difficult to obtain for the partial volume effects of CT acquisition. From a point of view located within the epitympanum, VE can easily display the incudo-malleolar joint; this perspective is quite important in surgery of the temporal bone when mastoidectomy is performed to access the middle ear from the aditus ad antrum. The surgical field is nicely represented, and VE even allows the recognition of the eminence of the lateral semicircular canal, whose position has to be detected before drilling the bony part of the tympanic cavity (Fig. 10.3).

10.2 The Study of the Labyrinth

The labyrinth is a small organ with a complex structure. The interpretation of anatomy by axial or coronal imaging is not very difficult for experienced radiologists. However, the increased amount of information obtained by high-resolution spiral CT with single and moreover multi-row technology, and by high-resolution MR with dedicated surface coils and sequences, has changed the traditional approach. More frequently, the data sets are analyzed with 3D reconstruction programs to better understand some anatomical details and clarify the suspicion of pathological changes. The following paragraphs will review separately the application of 3D imaging in the study of bone and membranous labyrinths.

10.2.1 Bone Labyrinth

The study of the bone labyrinth requires data sets obtained with CT. The use of spiral CT has to be preferred since data interpolation can increase image quality. The imaging protocol is the same used for middle ear imaging, since the study is commonly performed for both of these anatomical regions.

As well as in case of the middle ear, MPR can be used to study the components of the inner ear. These allow one to follow the different planes through which the cochlea, semicircular canals, vestibule, first portion of the facial nerve, internal auditory canal and vestibular duct are oriented. Even if the study of the bone labyrinth includes both axial and coronal acquisitions with a single-slice CT in adult and collaborative patients, this protocol is not always applicable in pediatric patients, or seems to be superfluous when the acquisition is performed with multirow CT (Fujii 2000; Gotwaldt 2001). In pediatric unsedated patients Luker et al. (1993) showed the utility of MPR in generating coronal views that could not be obtained during image acquisition.

Frankenthaler et al. (1998) used SR methods to generate 3D representation of ossicles, bone labyrinth and even vessels, with excellent results, but the entire image processing framework, which required a phase of segmentation and a phase of generation of the geometric model, was extremely time consuming. An alternative to this time-consuming method is direct VR, proposed by Tomandl et al. (2000). The method takes into account all of the information inherent in the CT data sets and provides a semitransparent representation of the bone labyrinth. VR, performed with a powerful workstation (available in many clinical environments), is done in real-time and seems to be compatible for the clinical routine. The selective visualization of the cochlea, vestibule and semicircular canals requires the application of different cut planes to the 3D data sets to reduce the superimposition of other bony structures, i.e., the medial wall of the tympanic cavity (Fig. 10.4). Tomandl et al. (2000) used a small volume of interest including the labyrinthine structures; this allowed avoiding the influence of other structures and reducing rendering time.

Our group (Neri 2001a) has experienced the use of CT VR in the follow-up of patients that underwent cochlear implantation. VR was helpful to display the path of the cochlear electrode and to establish the length of the portion inserted in the cochlea (Fig. 10.1).

10.2.2 Membranous Labyrinth

The membranous labyrinth is relatively easier to represent in three dimensions than the bone labyrinth since data are directly acquired by MR. The initial method applied to MR for 3D display of the labyrinth was the MIP (maximum intensity projection). The final image that is obtained represents a projectional roadmap of the labyrinthine components. The simplicity of using MIP has made it the most widely used algorithm for 3D imaging even in this case; but since MIP results from summed inten-

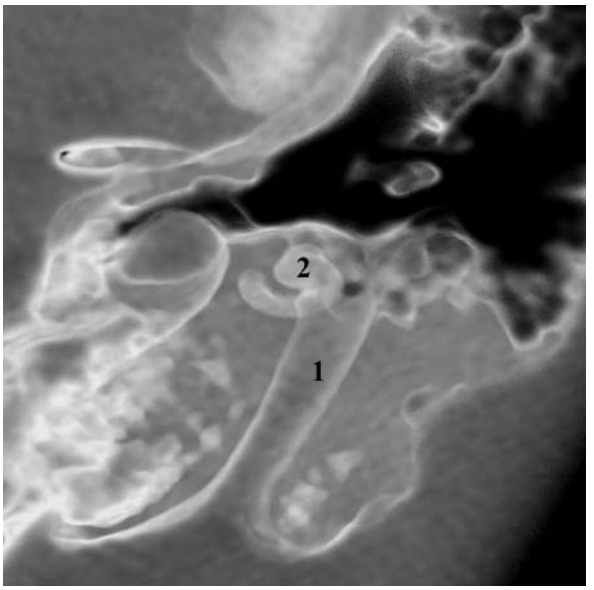

a

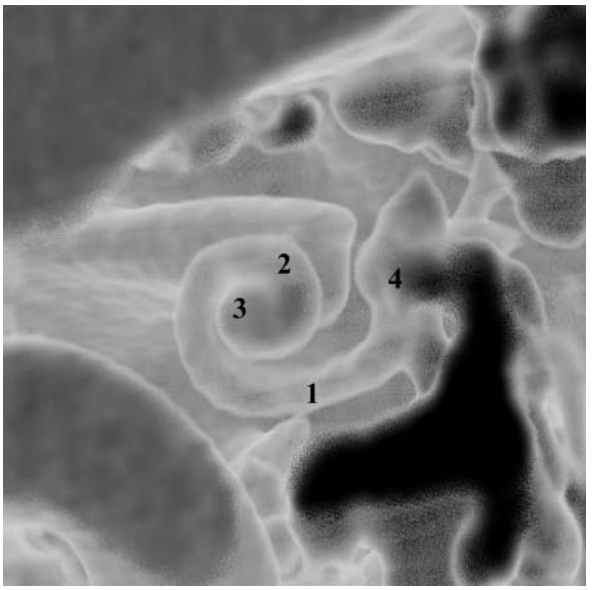

b

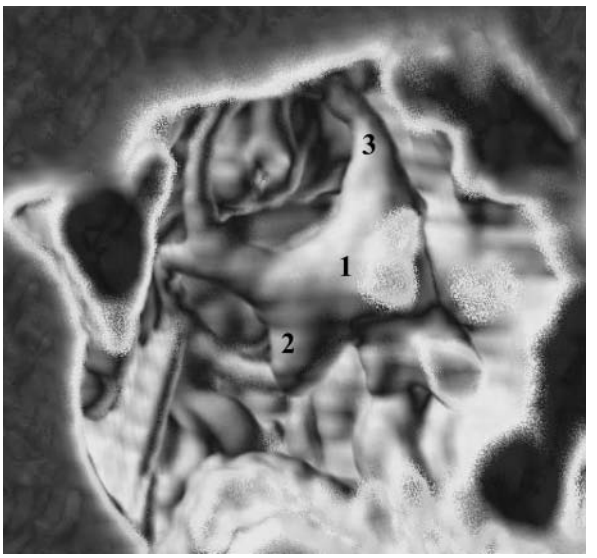

c

Fig. 10.4a–c. Volume rendering of the left labyrinth from CT data set. **a** The inferior view of the labyrinth shows the bony part of the internal auditory canal (*1*) and the apical turn of the cochlea (*2*). **b** The lateral view from the same data set allows the visualization of the entire cochlea with basal (*1*), middle (*2*) and apical (*3*) turns, and of the vestibule (*4*). **c** From the medial view the vestibule (*1*) and ampullae of posterior (*2*) and superior (*3*) semicircular canals are displayed

sity values projected onto a bi-dimensional plane, it is affected by the signal intensity of the tissue being visualized, the number of pixels of that tissue occurring along the projection, and the dynamic range of the data set. This means that small structures in an MIP may be poorly seen because they are consigned to the lower end of the display range.

A concrete solution to the limitations of MIP is VR. In our experience the 3D study of the membranous labyrinth was carried out with a 1.5-T MR unit, using a 3-inch circular surface coil for signal reception. The imaging sequence included a 3D, T2-weighted, fast spin-echo in the axial plane (Neri et al. 2000b). For 3D image processing MR data sets were processed with the software Advantage Windows 3.1 (GE/Medical Systems, Milwaukee, Wis.) for generating VR of the membranous labyrinth. Tomandl et al. (2000) as well for CT data sets, performed a preliminary segmentation of the MR data set, which was done in order to select a volume of interest. This was selected by interactive placement of cut planes through volume, perpendicular to the plane of acquisition, in order to isolate the inner ear from the surrounding anatomical structures. VR then required the determination of the optimal signal intensity interval including the signal of the labyrinth and the proper selection of opacity levels for optimal display of all its components (Fig. 10.5). In some difficult cases, VR failed to entirely demonstrate the superior and lateral semicircular canals,

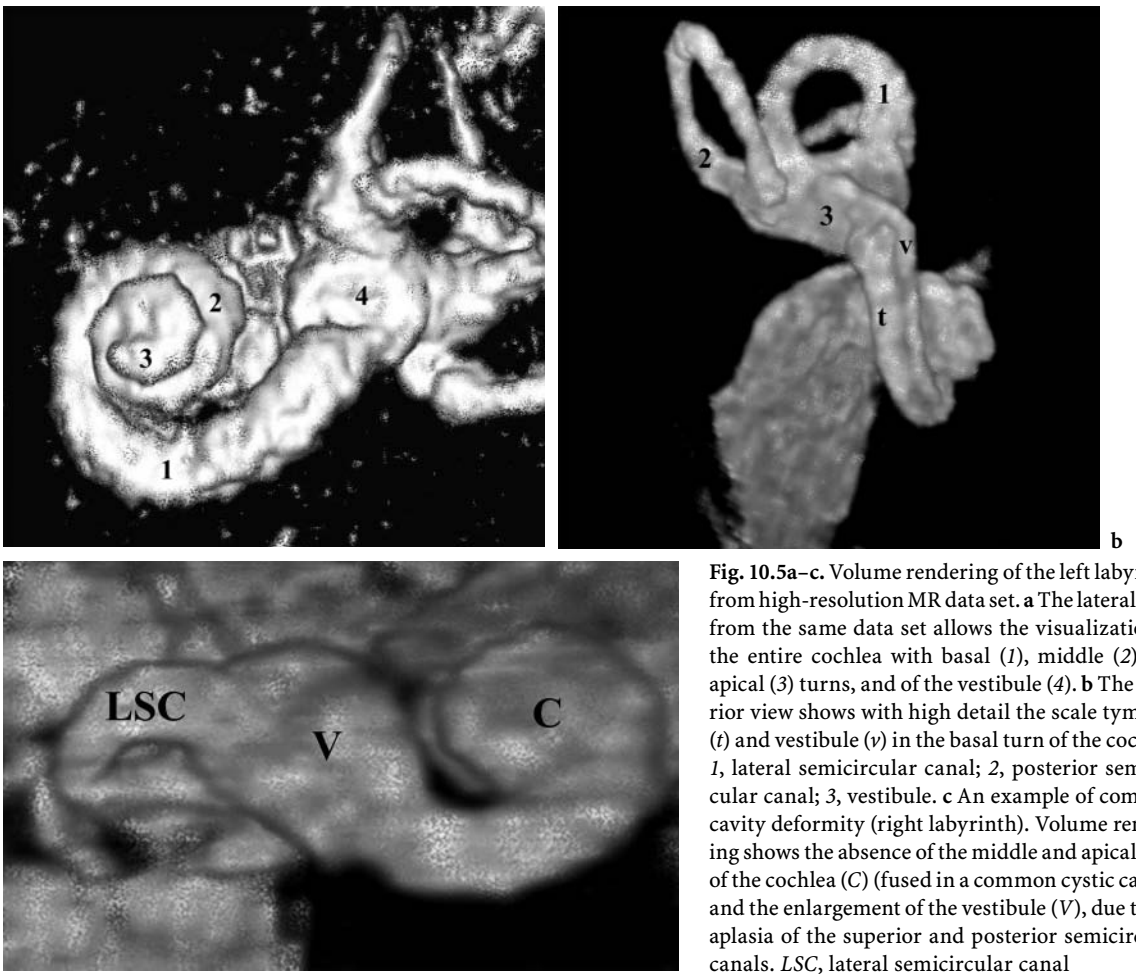

Fig. 10.5a–c. Volume rendering of the left labyrinth from high-resolution MR data set. **a** The lateral view from the same data set allows the visualization of the entire cochlea with basal (*1*), middle (*2*) and apical (*3*) turns, and of the vestibule (*4*). **b** The inferior view shows with high detail the scale tympani (*t*) and vestibule (*v*) in the basal turn of the cochlea. *1*, lateral semicircular canal; *2*, posterior semicircular canal; *3*, vestibule. **c** An example of common cavity deformity (right labyrinth). Volume rendering shows the absence of the middle and apical turn of the cochlea (*C*) (fused in a common cystic cavity) and the enlargement of the vestibule (*V*), due to the aplasia of the superior and posterior semicircular canals. *LSC*, lateral semicircular canal

probably due to partial volume effects in image acquisition. Krombach et al. (2000) compared MIP and VR in displaying the labyrinthine components and observed that VR was the unique method able to demonstrate the ampullae of semicircular canals; in the same experience, the 2.5 windings of the cochlea were best depicted with MIP.

10.3 Current Issues and Future Developments in 3D Image Processing of the Temporal Bone: Computer-Assisted Otosurgery and CT-MR Image Fusion

A restricted operative visual field prevents the surgeon's ability to visualize important structures beyond and through the exposed layers and makes it difficult to plan a trajectory to the target area. The surgeon is often aware of the presence of important structures such as vessels and nerves only after the removal of the preceding layers. To overcome these limitations the use of transtympanic endoscopy in otosurgery is aimed at providing real-time video assistance to the surgical procedure. But transtympanic endoscopy, which is minimally invasive but limited to the exploration to the full extent of the ear, only provides information on the surface anatomy of the lumen and actually no information about the anatomy within or beyond the wall. This limitation prevents the evaluation of the transmural extent of tumors and limits identifying concomitant localizations of contiguous structures. Non-invasive imaging techniques such as CT and MR allow surgeons to visualize volume tissues beyond an exposed surface, enabling identification of anatomical structures and their relationships in a bi-dimensional, cross-sectional view. As a result, surgeons have to mentally

integrate a series of images into a 3D structure, which is particularly challenging for the complex anatomic entities of the temporal bone.

VE shows added values combining a concomitant display of the endoscopical perspective to the planar, bi-dimensional, representations of native images, thus providing non-invasively a global view of this complex anatomy helpful for traditional endoscopy in localizing and analyzing tissues. Also the virtual camera overcame traditional limitations of maneuverability and space occupation allowing an endoscopic procedure without risk of perforation. The ability to perform a 360 degree examination at any given location provides a powerful examination tool, and the zooming feature permits close examination of desired areas in a way that traditional examination could not.

This could enable surgeons to better anticipate areas that may present a challenge during operation and help plan the best trajectory to target tissue.

Recent experiences in computer-aided otosurgery based on VR display of the middle and inner ear have shown promising results for the simulation of surgical procedures such as the implantation of medical devices. Damman et al. (2001) published the first experience about the feasibility of using a combination of 3D imaging-based computer systems for preoperative evaluation of the fit and mountability of an implantable hearing aid by simulating the surgical procedure.

This experience was based on the merging of the CT data of the temporal bone and those obtained by the computer-aided design files of the medical devices, both transferred to a VR environment to achieve a simulation of the surgical implantation procedure.

We have published (Neri et al. 2006) our experience in this field generating a virtual and interactive surgical field of the temporal bone with 3D images from multi-row CT data as the experience carried out in the IERAPSI project, in simulating a canal wall-up mastoidectomy (Fig. 10.6). A 3D model is required in order to overcome limitations of bi-dimensional images both from CT and MR, which do not always supply the necessary information to the surgeon for the planning of the intervention. This surgical simulation, differently from previous experiences carried on cadavers (Wiet et al. 2002; Bernardo et al. 2003), was obtained directly on patients who were candidates for surgery of the temporal bone. In such a way the surgical planning or training for students and inexpert surgeons could be done on the patient-specific 3D model, which reproduced as realistically as possible the real surgical environment. The 3D data preparation was performed with a volume-rendering software developed at CRS4. Through manual and automatic segmentation techniques, the bone, the sigmoid sinus, the jugular bulb, the internal carotid artery, and the aerated space of the tympanic cavity were identified and introduced as distinct objects in the virtual operating field. Virtual surgical instruments were introduced in the surgical field by adding a second computer and controlled by the surgeon with the right hand by a haptic Phantom device, which allowed the movement of the drill burr with six degrees of freedom and generated a force feedback with three degrees of freedom. The surgeon could control the sucker with the left hand by a haptic Phantom Desktop device with six degrees of freedom and received a force feedback with three degrees of freedom. The major limitations of this approach are related to the impossibility to represent by means of CT data soft tissues such as nerves, vessels and fluids, while the future is the simulation of specific surgical interventions, like the positioning of cochlear implants or the removal of acoustic neuroma.

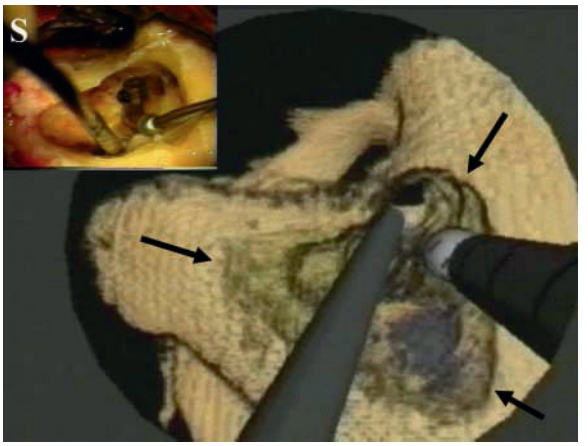

Fig. 10.6. Virtual surgery of the petrous bone. Example of simulated mastoidectomy. 3D volume rendered datasets are used in the simulation. During surgery (*S*) a triangular cavity is created in the mastoid process of the petrous bone in order to reach the middle ear. The surgical field can be generated even by the simulation (*arrows*). These images were obtained in the framework of the EU project IERAPSI, Integrated Environment for the Rehearsal and Planning of Surgical Interventions (Ist-1999-12175)

To overcome limitations in displaying alternatively soft tissues and fluids by means of MR data and air, bone or metallic devices by means of CT

recent studies (Nemec et al. 2007) have proposed the fusion of CT-MR data for computer-assisted neurosurgery of temporal bone tumors. Multi-row CT was performed in the high-resolution bone window level setting in the axial plane (slice thickness 0.8 mm), while MR protocol included axial and coronal T2-weighted FSE sequences, coronal T1-weighted SE sequences with fat suppression, unenhanced and contrast-enhanced T1-weighted SE sequences, and 3D T1-weighted GRE contrast-enhanced sequences (slice thickness of 1 mm) in the axial plane. Image data sets of CT and 3D T1-weighted GRE sequences were merged utilizing a workstation to create CT-MR fusion images. Multi-row CT and MR images were separately used to depict and characterize lesions. The fusion images were utilized for interventional planning and intraoperative image guidance. The CT-MR fusion images supported the surgeon in preoperative planning and improved surgical performance.

We also performed a study (Neri et al. 2005) on 3D CT and MR co-registration in the assessment of cochlear implantation (Fig. 10.7). The main advantage of CT-MR fusion is the matching of the electrode and its natural location, which is the membranous labyrinth along the scale tympani. We tried to imagine a visualization method that was able to display not only the electrode itself, but was also capable of showing the real anatomical boundaries of the electrode within the surrounding structures of the bony and membranous labyrinth. In our experience, MR could not differentiate scale tympani from scale vestibuli, and the electrode could therefore not be located in its real path, but the true advantage of this method is that the tip of the electrode can be precisely displayed and located in the portion of the cochlea reached. This information could reflect the clinical expectations after implantation, since different frequencies are transmitted to the organ of Corti at different levels along the cochlea turns.

Fig. 10.7. Volume rendering of CT and MR datasets in a patient with cochlear implant. The preoperative MR obtained before surgery, and CT obtained after implantation are co-registered. CT-MR fusion allow to display the electrode (*blue*) of the cochlear implant inside fluid filled labyrinth cochlea (*red*) (well represented by MR data)

References

Ali QM, Ulrich C, Becker H (1993) Three-dimensional CT of the middle ear and adjacent structures. Neuroradiology 35:238–241

Bernardo A, Preul MC, Zabramski JM, Spetzler RF (2003) A three-dimensional interactive virtual dissection model to simulate transpetrous surgical avenues. Neurosurgery 52:499–505

Caldemeyer KS, Sandrasegaran K, Shinaver CN, Mathews VP, Smith RR, Kopecky KK (1999) Temporal bone: comparison of isotropic helical CT and conventional direct axial and coronal CT. AJR 172:1675–1682

Dammann F, Bode A, Schwaderer E, Schaich M, Heuschmid M, Maassen MM (2001) Computer-aided surgical planning for implantation of hearing aids based on CT data in a VR environment. Radiographics 21:183–191

Diederichs CG, Bruhn H, Funke M, Grabbe E (1996) Spiral CT with reduced radiation dosage. Rofo 164:183–188

Espinoza J (1989) Surgical anatomy of the retrotympanum: on 25 temporal bones. Rev Laryngol Otol Rhinol 110:507–515

Frankenthaler RP, Moharir V, Kikinis R, van Kipshagen P, Jolesz F, Umans C, Fried MP (1998) Virtual otoscopy. Otolaryngol Clin North Am 31:383–392

Fujii N (2000) Imaging of the middle ear: high resolution multiplanar reconstruction and three-dimensional CT by 0.5 mm multislice helical CT. Radiology 217 (S1):673

Gotwaldt TF (2001) Multidetector CT scanning of the temporal bone in patients with cholesteatoma. Eur Radiol 11(S1):256

Grevers G, Wittmann A, Vogl T, Wiechell R (1989) Multiplanar imaging of the temporal bone. Initial results. Laryngorhinootologie 68:392–395

Guerrier Y, Guerrier B (1976) Topographic and surgical anatomy of the petrous bone. Acta Otorhinolaryngol Belg 30:22–50

Haas JP, Kahle G (1988) How best to present the radiological picture of the temporal bone today? HNO 36:89–101

Hermans R, Marchal G, Feenstra L, Baert AL (1995) Spiral CT of the temporal bone: value of imaging reconstruction at submillimetric table increments. Neuroradiology 37:150–154

Jäger L, Bonell H, Liebl M, Srivastav S, Arbusow V, Hempel M, Reiser M (2005) CT of the normal temporal bone: comparison of multi- and single-detector row CT. Radiology 235:133–141

Johnson PT, Heath DG, Bliss DF, Cabral B, Fishman EK (1996) Three-dimensional CT: real-time interactive volume rendering. AJR 167:581–583

Krombach GA, Schmitz-Rode T, Tacke J, Glowinski A, Nolte-Ernsting CC, Günther RW (2000) MRI of the inner ear: comparison of axial T2-weighted, three-dimensional turbo spin-echo images, maximum-intensity projections, and volume rendering. Invest Radiol 35:337–342

Lane JI, Lindell EP, Witte RJ, DeLone DR, Driscol CLW (2006) Middle and inner ear: improved depiction with multiplanar reconstruction of volumetric CT data. Radiographics 26:115–124

Luker GD, Lee BC, Erickson KK (1993) Spiral CT of the temporal bone in unsedated pediatric patients. AJNR Am J Neuroradiol 14:1145–1150

Mafee MF, Charletta D, Kumar A, Belmont H (1992) Large vestibular acqueduct and congenital sensorineural hearing loss. AJNR Am J Neuroradiol 13:805–819

Mer SB (1967) Fiberoptic endoscope for examining the middle ear. Arch Otolaryngol 85:387–393

Marquet J, Boedts D (1975) Otology. Acta Otorhinolaryngol Belg 29:299–316

Nemec SF, Donat MA, Mehrain S, Friedrich K, Krestan C, Matula C, Imhof H, Czerny C (2007) CT-MR image data fusion for computer assisted navigated neurosurgery of temporal bone tumors. Eur J Radiol 62:192–198

Neri E, Caramella D, Battolla L, Cosottini M, Scasso CA, Bruschini P, Pingitore R, Bartolozzi C (2000a)Virtual endoscopy of the middle and inner ear with spiral computed tomography. Am J Otol 21:799–803

Neri E, Caramella D, Cosottini M, Zampa V, Jackson A, Berrettini S, Sellari-Franceschini S, Bartolozzi C (2000b)High-resolution magnetic resonance and volume rendering of the labyrinth. Eur Radiol 10:114–118

Neri E (2001a) Outcome of cochlear implantation: assessment by volume rendered spiral CT. Eur Radiol 11(2 S1):256

Neri E, Caramella D, Panconi M, Berrettini S, Sellari Franceschini S, Forli F, Bartolozzi C (2001b) Virtual endoscopy of the middle ear. Eur Radiol 11:41–49

Neri E, Berrettini S, Salvatori L, Forli F, Franceschini SS, Bartolozzi C (2005) 3-D CT and MRI co-registration in the assessment of cochlear implantation. Med Sci Monit 11:MT63–7; (Epub 2005 Sep 26)

Neri E, Sellari Franceschini S, Berrettini S, Caramella D, Bartolozzi C (2006) IERAPSI project: simulation of a canal wall-up mastoidectomy. Comput Aided Surg 11:99–102

Nomura YA (1982) Needle otoscope (an instrument of oto-endoscopy of the middle ear). Acta Otolaryngol (Stockh) 93:73–79

Parlier-Cuau C, Champsaur P, Perrin E, Rabischong P, Lassau JP (1998) High-resolution computed tomographic study of the retrotympanum. Anatomic correlations. Surg Radiol Anat 20:215–220

Pickett BP, Cail WS, Lambert PR (1995) Sinus tympani: anatomic considerations, computed tomography, and a discussion of the retrofacial approach for removal of disease. Am J Otol 16:741–750

Pozzi Mucelli RS, Morra A, Calgaro A, Cova M, Cioffi V (1997) Virtual endoscopy of the middle ear with computed tomography. Radiol Med 94:440–446

Rubin GD, Beaulieu CF, Argiro V, Ringl H, Norbash AM, Feller JF, Dake MD, Jeffrey RB, Napel S (1996) Perspective volume rendering of CT and MR images: applications for endoscopic imaging. Radiology 199:321–330

Thomassin JM (1994) La chirurgie sous guidage endoscopique des cavitée de l'oreille moyenne. Springer, Paris

Thomassin JM, Candela FA, Decat M, Gersdorff M, Portmann D, Strunski V, Triglia JM (1996) Surgery under oto-endoscopic control. Rev Laryngol Otol Rhinol 117:409–415

Tomandl BF, Hastreiter P, Eberhardt KE, Rezk-Salama C, Naraghi R, Greess H, Nissen U, Huk WJ (2000) Virtual labyrinthoscopy: visualization of the inner ear with interactive direct volume rendering. Radiographics 20:547–558

Veillon F (1993) CT and MR imaging versus surgery of recurrent cholesteatoma in the post-operative middle ear: a 72 case study. Radiology 185 (S):248

Veillon F (1997) Imaging of recurrent postoperative cholesteatoma. International Congress of Head and Neck Radiology. Strasbourg, France, p 170

Watanabe Y, Sugai Y, Hosoya T, Yamaguchi K, Aoyagi M (2000) High-resolution computed tomography using multiplanar reconstruction for the facial nerve canal. Acta Otolaryngol 542:44–48

Wiet GJ, Stredney D, Sessanna D, Bryan JA, Welling DB, Schmalbrock P (2002) Virtual temporal bone dissection: an interactive surgical simulator. Otolaryngol Head Neck Surg 127:79–83

Zini C (1967) La microtympanoscopie indirecte. Rev Laryngol Otol Rhinol 88:736–738

Virtual Endoscopy of the Paranasal Sinuses

11

Joachim Kettenbach, Wolfgang Birkfellner, and Patrik Rogalla

CONTENTS

J. Kettenbach, MD
Associate Professor, Division of Cardiovascular and Interventional Radiology, Department of Radiology, Medical University Vienna, General Hospital, Waehringer Guertel 18–20, 1090 Vienna, Austria
W. Birkfellner, PhD
Associate Professor, Department of Biomedical Engineering and Physics, University of Vienna, General Hospital Vienna, Waehringer Guertel 18–20, 1090 Vienna/Austria
P. Rogalla, MD
Associate Professor, Department of Radiology, Charité Hospital, Humboldt-Universität Berlin, Schumannstrasse 20/21, 10098 Berlin, Germany

11.1 Introduction

The concept of functional endoscopic sinus surgery, developed by Messerklinger in the early 1970s revolutionized and radically altered the techniques used for the diagnosis and treatment of patients with sinus disease (Messerklinger 1994; Stammberger and Posawetz 1990). Messerklingers initial work, however, was conducted with information derived from plain films and conventional polytomography. This technique has been replaced by computed tomography (CT) for many years, which is now considered an essential component to identify anatomic variants that may compromise the ventilation of the sinuses and can demonstrate areas of diseased mucosa that are responsible for recurrent disease. The CT scan further provides valuable information about the presence of potential hazards such as septations of the frontal or sphenoid sinuses, the proximity and location of the orbit, the internal carotid artery and optic nerve to areas of disease. Furthermore, CT is the ideal method for the demonstration of the delicate bony structures of the ethmoid labyrinth. Even with careful diagnostic endoscopic assessment the majority of these latter abnormalities may not be evident. The ability to radiologically identify those abnormalities that may increase surgical morbidity prior to surgery is important for both the surgeon and the patient. The surgeon however, must combine high-quality axial imaging sets and to reformat them mentally, which requires extensive experience. Therefore, a transformation of the perspective-free CT images into a perspective view of the endoscope is necessary for successful surgical exploration. Advances in computer technology have led to the development of hardware and software imaging techniques that have been successfully utilized by the entertainment industry. These techniques have been adopted by the medical field, which have resulted in numerous imaging advances (Bisdas et al. 2004; Di Rienzo et al. 2003; Gilani

et al. 1997; Morra et al. 1998). This has led to even more robust three-dimensional imaging, allowing newer generation display techniques (Bisdas et al. 2004; Keller et al. 1989; Kim HJ et al. 2003; Leong et al. 2006; Rubin et al. 1993; Wolfsberger et al. 2006). When advances in CT and MRI technologies resulted in greater resolution of small structures, virtual endoscopy could clearly demonstrate anatomic structures in the nasal cavity, septal deviation, stenosis and obstruction of the middle meatus, turbinate hyperplasia, and pathological masses larger than 3 mm in diameter (Bisdas et al. 2004; Han et al. 2000; Rogalla et al. 1998; Yamashita et al. 1999). To overcome the limited view beyond the surface, either intraoperative image-guidance (Fried et al. 1998a) or navigational imaging tools may provide image-guidance during a procedure and may complement the surgeons view (Citardi and Batra 2007; Grevers et al. 2002; Nakasato et al. 2000; Neumann et al. 1999; Shahidi et al. 2002). Although not widely used in the past, clinical experiences have grown considerably, and applications, such as fusion of computed tomography (CT) with magnetic resonance tomography (MRT) have been introduced. All these tools may assist in surgical planning when approaching sinonasal disease, medical education and training. In this chapter we will provide an overview on key historical developments of virtual sinuscopy, clinical applications using CT and MR-imaging for image-guided sinus surgery and applications using a navigational system to enhance the surgeons skills during sinus surgery.

11.2 Imaging Data Acquisition

11.2.1 Computed Tomography

Pre-operative CT scanning of the paranasal sinuses is presently a standard imaging procedure (Beus et al. 1995; Bisdas et al. 2004; Branstetter and Weissman 2005; Hahnel et al. 1999; Hein et al. 2002; Hojreh et al. 2005; Rogalla et al. 1998; Zinreich 1998) although some authors prefer the axial image acquisition and coronal reconstruction (Hosemann 1996; Suojanen and Regan 1995). For some patients, axial CT acquisition is advantageous, since extended positioning of the head during image acquisition in the coronal plane can be avoided. The disadvantage, however is a more limited spatial resolution. However, spiral CT- and multislice-CT (MSCT) techniques overcome this limitation by using thin collimation and overlapping reconstruction algorithms (Hosemann 1996), even using a low-dose protocol (Rogalla et al. 1998). Furthermore, reformatted axial images obtained from diagnostic scans can be used to generate high-quality virtual endoscopic reconstructions (Branstetter and Weissman 2005). For multiplanar visualization, sagittal and coronal multiplanar reconstructions (MPR) images can be obtained with a 0.5 mm slice thickness and a 2–3 mm interval. Typical helical CT and multislice CT data acquisition parameters for paranasal sinuses are presented in Table 11.1. The bone reconstruction algorithm is routinely used in CT scanners and heightens the depiction of edges. In addition, a higher kernel hardness provides greater edge sharpness. Normal-dose sinus CT images have a pixel noise of 50–70 HU, and if an edge-enhancing reconstruction algorithm is used they are suitable for the preoperative planning and postoperative control of endoscopic sinus surgery (ESS) (Hojreh et al. 2005). Low-dose sinus CT using an edge-enhancing reconstruction algorithm produces an image quality characterized by a pixel noise of 70–90 HU. This image quality is still suitable for indications such as chronic sinusitis, septum deviation, or sinonasal polyposis and has been a recommend method for children in general. However, Rogalla et al. successfully used a low-dose protocol also to generate VR images of the paranasal sinuses (Rogalla et al. 1998). Optional nonionic contrast media can be applied to differentiate between vascular and less vascular structures.

11.2.2 Magnetic Resonance Imaging

Compared to CT, MR has the advantage of no radiation and superior tissue characterization (Branstetter and Weissman 2005; Eggesbo 2006; Hahnel et al. 1999; Howells and Ramadan 2001; Scharpf et al. 2005; Weiss et al. 2001). MR may be useful when CT has shown advanced opacification that can be due to a pyocele, fungal sinusitis or neoplastic disease and to display lesions involving the orbit or cranial compartment (Eggesbo 2006). Of particular note is the minimal artifact caused by dental fillings and the capability of multiplanar imaging (Fig. 11.1) (Hahnel et al. 1999). Coronal

Table 11.1. Typical CT acquisition parameters for the paranasal sinuses

	Coronal acquisition (Helical CT)	Axial acquisition (Helical CT)	Axial acquisition (MSCT)
	120–140 kV, 140 mAs	120–140 kV, 50–130 mAs	140 kV, 50 mAs[a]
Scan time	1.0 rev/s	0.75–1.0 rev/s	0.75 rev/s
Collimation	3.0 mm	1.5–3.0 mm	64 × 0,625 mm
Table feed	1.5–3.0 mm/s	1.5–3.0 mm/s	30 mm/s
Pitch	1	1–2	0.641
Patient position	Supine or prone; head hyperextended	Supine	
Gantry orientation	Tilted to approximate a plane perpendicular to orbitomeatal line	Parallel to hard palate	
Imaging range:	Nose to sphenoid sinus	Maxillary alveolar ridge to the superior aspect of the frontal sinus	
Field-of-View (FOV)		120–270 mm	
Contrast	Optional; 90–100 ml nonionic contrast i.v. (2 ml/s, delay 50 s) if solid tumors or encephaloceles must be excluded		
Window setting			
Soft tissue	100–400 HU		
Bone	900–4000		
Reconstruction algorithm	Bone; sharp to extrasharp edges		
Reconstruction kernel	Sharp to extrasharp edges		
Reconstruction thickness	2–3 mm	1–2.0 mm	

MSCT = Multislice Computed Tomography
[a] 120 kV, 50 mAs for low-dose CT

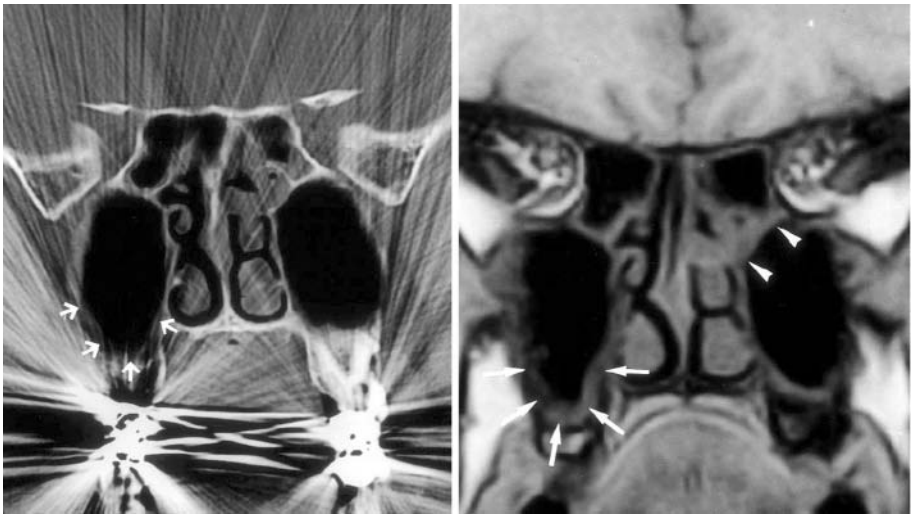

Fig. 11.1. Images obtained in a 38-year-old man suspected of having chronic inflammatory disease of the maxillary sinus. (*Left*) CT scan shows extreme artifacts from dental work. Mucosal thickening (*arrows*) in the right maxillary sinus can easily be missed. Evaluation of the frontal lobe and the orbital tissues is almost impossible, even if a soft-tissue window were used. Partial opacification of the ethmoid cells is present. (*Right*) MR image (60/12; flip angle, 40°) depicts mucosal thickening (*arrows*) in the right maxillary sinus without artifact. The frontal lobe and orbits can be evaluated very well. Soft-tissue signal intensity in the ethmoid cells (*arrowheads*) is present. Reprinted with permission from Hahnel S, Ertl-Wagner B, Tasman AJ, Forsting M, Jansen O. Relative value of MR imaging as compared with CT in the diagnosis of inflammatory paranasal sinus disease. Radiology 1999; 210:171–176

imaging with T1- and T2- weighted sequences may be sufficient in "simple sinusitis". In order to differentiate mucosal thickening and regions of pus-filled sinuses, fast short inversion time recovery (STIR) images instead of T2-weighted images have been shown to be valuable (Eggesbo 2006). If inflammatory processes, neoplasm or complications are to be ruled out, additional imaging planes and intravenous gadolinium are mandatory (Lloyd et al. 2000). Furthermore, variation in MRI signals within the sinuses has been shown to be related to many properties of the sinonasal secretions such as the viscosity, protein concentration, fat, temperature and paramagnetic properties of fungal infections or hemorrhage (Zinreich et al. 1988). MRI also has the capacity to show hemorrhage in its different stages of resolution; thus, MRI gives temporal information and thus may serve as diagnostic means for occult intracranial complications that result from unrecognized skull base violation during sinus surgery (Scharpf et al. 2005) (Table 11.2). MR imaging could also be used as a primary diagnostic tool in screening for inflammatory paranasal sinus disease under dedicated circumstances (Hahnel et al. 1999. For the paranasal and nasopharyngeal area, 4 or 5 mm slices are used. For the detailed analysis of smaller areas such as the cribriform plate thinner (≤) 3 mm slices are preferable. Fast T1-weighted volumetric gradient-echo-scans provide isotropic voxels, thus improved detail with thin 1 mm adjacent sections or with a 3D volume (Ling and Kountakis 2006; Rosahl et al. 2006) applicable for 3D rendering. For vessel visualization, three-dimensional time-of-flight (TOF) MR angiography (MRA) is preferred over phase contrast angiograms because of the better delineation of vessel walls. The actual pulse sequence for T1- and T2 images depends on the magnetic field strength. For a 1.5-Tesla scanner, a 220 × 256 matrix and double-weighted Turbo-Spin Echo (TSE) sequences (TR/TE 3500/16;96) had been used (Weiss et al. 2001). A head coil is commonly used; however best details are obtained with specially designed surface coils. Orientation of imaging plane is axial and coronal except in special circumstances when a sagittal plane may be preferable (Fahlbusch et al. 2001). To our knowledge MR data was not used to generate virtual endoscopy for nasal sinuses, however it has been demonstrated for preoperative sialoendoscopic exploratory (Su et al. 2006), for various anatomic locations including brain and vessels (Rusinek et al. 1989) and for virtual MR endoscopy of the ventricles prior neurosurgery (Lemke et al. 2004). Lemke concluded, that volume rendering of T2-weighted thin sections is preferable to surface rendering.

Table 11.2. Advantages of CT and MR imaging of sinonasal region

Advantage MR	Advantage CT
No radiation	Availability
Superior detail of soft tissues and better identifying perineural spread	Superior in delineation of fine bone structures and of fibro-osseous lesions
Better delineation of neoplasm from entrapped secretions	High-resolution CT less complex and more flexible for post-hoc analysis
Multiplanar imaging and various pulse sequences to interrogate different tissue aspects	
No hardening artifact on patients with dental implants	

11.2.3 Plain Films

In sinonasal imaging plain films have a limited role, but can depict the size of the sinuses, septal deviation and opacification (Eggesbo 2006). In acute rhinosinusitis, the demonstration of air-fluid levels can be diagnostic. However, in a pediatric population plain films were shown to be inaccurate in 75% of cases of inflammatory sinonasal disease (Lusk et al. 1989). Further, plain films are insufficient in the preoperative evaluation for planning ESS and practically useless to generate virtual endoscopic data sets.

11.3 Postprocessing

Understanding the complex anatomy of the paranasal sinuses and adjacent structures proves difficult by looking at cross-sectional CT images alone (Rodt et al. 2002). With increasing number of slices, when reconstruction is performed, the process of integrating them into a conceptual three-dimensional

(3D) model of the whole volume becomes even more difficult. However, 3D visualization has been shown to facilitate the process of mentally stacking up the numerous 2D images and to visualize them with different shading and artificial lightening. So far, several research groups have developed visualization techniques dedicated for 3D visualization of medical imaging data (Cline et al. 1987; Davis et al. 1991; DePuey et al. 1989; Dessl et al. 1997; Fried et al. 1999; Gilani et al. 1997; Kim HJ et al. 2003; Rodt et al. 2002; Rogalla et al. 1998; Wolfsberger et al. 2004). Currently, three techniques are commonly used for displaying volumetric data regardless of the modality used to obtain them (Gilani et al. 1997). The first is a "flat" depiction of the data set that shows the 3D set by highlighting selected threshold limits, also called maximum intensity projection (MIP).

11.3.1 Surface Rendering

The second technique, surface rendering (SR) provides a more realistic 3D depiction in which the data set is manipulated so that surface structures are shown, further highlighted by shading techniques, and called surface shaded display (SSD). For SSD threshold ranges from about –520 to –200 HU are recommended to eliminate voxels denser than –500 HU. Surface rendering techniques use an intermediate step, called segmentation, to transform the volume data into a mesh of polygons (Cline et al. 1987; Lee et al. 1999; Lemke et al. 2004; Rubin et al. 1993; Seemann et al. 1999). Due to the large amount of voxels to be processed and the complexity of the presentation, most segmentation techniques are semiautomatic. Approximately 9 min were required to scan the sinuses, transfer the images to a postprocessing workstation, and generate 3D high-quality images similar to those of conventional endoscopy (Bisdas et al. 2004). In healthy subjects and patients with sinonasal disease, two thresholds, –250 and –400 HU were optimal to view the different anatomic structures in this region. Furthermore, the attenuation value of an anatomic structure is slightly altered between individuals, and problems can occur when pathologic structures have to be accessed with a standardized protocol that was evaluated in healthy subjects; therefore, a threshold depicting all structures optimally does not exist. Thus, changing the threshold within certain values may ensure complete visualization of the relevant structures. The resulting mesh of polygons can be rendered using standard graphics hardware support. The drawback is often a time-consuming preparation phase and reduced accuracy, since information about the inner areas of the objects can be lost (Geiger and Kikinis 1994; Shin et al. 2000).

11.3.2 Volume Rendering

The third technique, volume rendering (VR), provides dimensional views generated by casting rays from an observation point either outside the imaging volume or from inside through the remaining part of the volume. VR can show a greater spectrum of 3D information by concentrating not only on chosen "surface" features, but also by displaying structures as if they were partially transparent (Davis et al. 1991; Gilani et al. 1997; Lee et al. 1999; Lemke et al. 2004; Levoy 1991; Rogalla et al. 1998; Seemann et al. 1999; Wiet et al. 1997). When a perspective view, chosen by the operator is added, this mode is called perspective volume rendering (PVR), a refinement of volume rendering (Kersten et al. 2006; Magnusson et al. 1991; Rusinek et al. 1989). The VR technique, however requires significantly more calculations; thus requires advanced software technology. Despite the high performance of computers today, it is recommended that the data set be reduced according to reconstruction needs. For example, since bony details are less important than mucosal surface visualization the upper 4 bits of the 12-bit data set contains much unnecessary bone information that can be discarded (Gilani et al. 1997). Processing will then take place with the 8-bit range, which contains all the information relevant to the examination and slow information processing and manipulation can be reduced. Not surprisingly, the quality of volume rendered images is a function of the quality of the input data (Lee et al. 1999). Thus, slice thickness (less than 1 mm) and pixel image matrix (usually 512 × 512) are recommended. Increasing the frequency of data sampling will also improve the quality of volume renderings (Lee et al. 1999). Different colours for each anatomical structure in models and segmented 2D images improve understanding of the anatomic structures (Rodt et al. 2002; Seemann et al. 1999). By changing the opacity, the percentage of a light ray being held up by a voxel, a structure could be made transparent. Changes in surface reflexiv-

ity, lighting direction, and lighting coordinates, the surface appearance of the imaged tissues can be manipulated to achieve the appearance of mucosal membranes. Stereoscopic views could be created where they enhanced 3D perception.

11.3.3 Artifacts

Virtual endoscopy techniques are not free of artifacts and pitfalls. Bidas et al. (2004) summarized which parameters are most important to consider. First, scanning parameters mostly cause the observed spiral patterns and unevenness of the cavity. An effort to find an optimal combination of pitch, collimation, and increment (1.25 mm collimation, table speed of 3.75 mm/s at 0.8 revolution/s) as well as the use of a postprocessing smoothing mode based on an interpolation algorithm minimize these kinds of artifacts. A postprocessing reconstruction level of 1 mm enhances the image quality; whereas a thinner beam collimation (0.5 mm) proved not to be essential, unlike recommended by others (Rogalla et al. 1998). The presence of the major artifacts (pseudoforamina) however, is highly dependent on each patient. These small defects (pseudoforamina) can appear as irregular and sharply emarginated triangles or squares in 3D images especially in the lateral and posterior walls of the maxillary sinus and in the anterior wall of the sphenoidal sinus. Choosing a threshold of –400 HU reduced the impact of these artifacts without influencing the diagnostic value of the images. Another pitfall of the VE images is false "thickening" of the mucus and thus the appearance of false-positive adhesions especially in the hiatus semilunaris and middle nasal concha region (Bisdas et al. 2004). In this case, VE cannot differentiate from the neighboring normal structures usually result from increased mucous secretions (Fig. 11.2). Finally, Moiré artifacts can be avoided using a matrix of 512 × 512. Also, a viewing angle of 60° in comparison to high-perspective angles (e.g., 120°) allow the user to locate his or her position and easily observe the structures without distortion of their size and form.

11.4 Path Generation

The following techniques can be used to guide a virtual camera through the virtual endoscopy models.

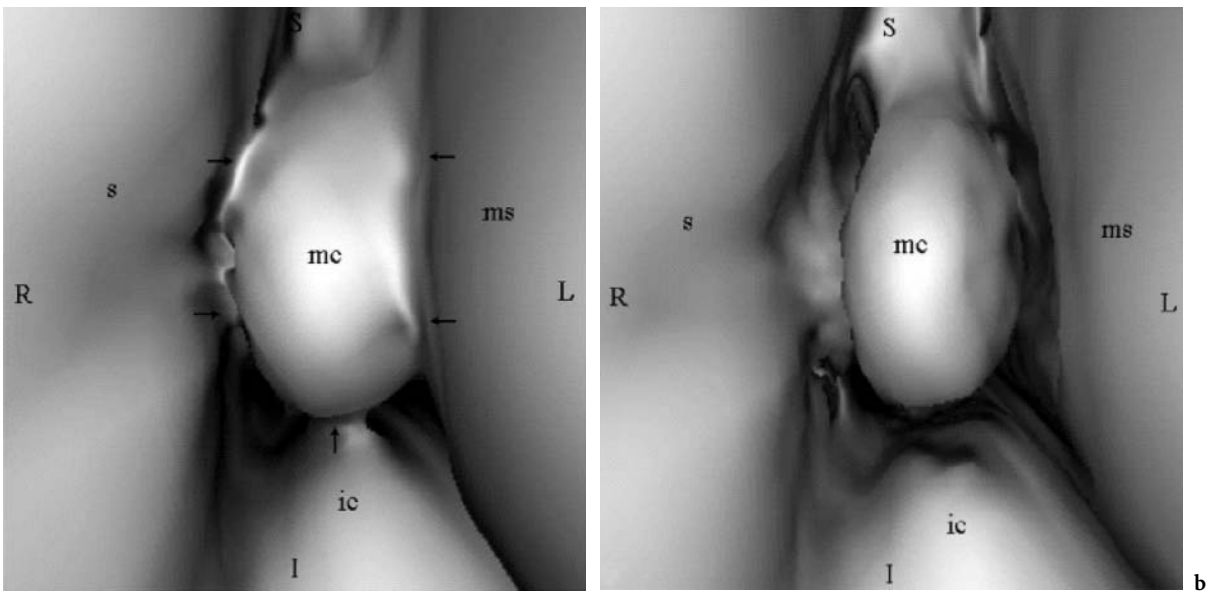

Fig. 11.2a,b. The middle nasal concha in virtual endoscopy. **a** Note the hyperplastic appearance of the middle concha as well as the false adhesions (*arrows*) between the septum, medial wall of the maxillary sinus, and inferior nasal concha. **b** The application of a higher threshold value radically removes these artifacts. *ic* indicates inferior concha; *mc*, middle concha; *ms*, maxillary sinus; *s*, septum. From: Bisdas S, J Comput Assist Tomogr 2004; 28:661–669

11.4.1 Manual Camera Movement

Using an input interface, such as a mouse or joystick the camera position, the field of view of the camera, and the focal point are interactively changed. The software may provide collision detection for the camera and anatomic surfaces, thus applying a force model to keep the camera inside the sinonasal structures (Jolesz et al. 1997). These approaches, however, require user training and the introduction of positional constraints via software to hinder the "perforation" of the imaged structure by the virtual endoscope (Carvalho 2003).

11.4.2 Semi-Automatic Path Planning

Semi-automatic path generation is also referred to as keyframing; in this technique the user specifies key path points through out the volume that are connected, usually by cubic splines, to form the final path. The user needs to have a very good understanding of complex tree-dimensional structures in order to provide good key points. The connection of the points by curves has also to take into account the boundaries of the examined structure to avoid making contact with its walls (Carvalho 2003; Kochanek and Bartels 1984). Key frames can be used easily to generate motion through open interior and exterior environments. An operator selects "key" locations in the patient's sinuses that must be viewed and the order in which these designated "key" images are to be viewed. Each key image has a unique spatial coordinate, a directional coordinate defining viewer placement in space, and a field of view defining how wide a perspective is included in the view (Gilani et al. 1997). For most images, a 60–80° field of view is appropriate to simulate the endoscopic perspective. Rogalla used a viewing angle of 120° to create an overlap of 30° on all four sides with adjacent views (Rogalla et al. 1998). The computer then connects these key views (around 150 for the sinuses) as an interpolated continuous film along a desired route. This route is also known as flight path. This interconnecting technique is also known as a spline path, generated at a rate of 25–30 frames/s. Using this technique, Rubin et al. (1993) reported that several person-hours were required to generate an elaborate flight path . For path definition through each of the nasal passages Rogalla et al. (1998) required a mean time for path definition and movie calculation of 8 (± 2) min and 3 (± 1) min, respectively .

11.4.3 Automatic Path Planning

Initial and one or more end points are specified by the user and the navigation path(s) is (are) automatically computed by software, usually by computing the centerline of the imaged structure (Carvalho 2003; Paik et al. 1998). Since most of the tubular organs such as the paranasal sinuses present a challenge for both manual camera movement and keyframing, a robot path-planning algorithm can be adapted to guide a virtual endoscope (Jolesz et al. 1997; Lengyel et al. 1990; Nain et al. 2001; Zhang et al. 2005). The camera is treated as a point robot and the walls of the organs as obstacles. These obstacles are identified as ranges of threshold values or tissue labels. The path planner labels all voxels within the 3D data set with a specified distance to a particular goal, normally defined as the terminus of the organ to be explored. Then, given a starting point, the path-planning algorithm finds the shortest path to the goal. The voxel coordinates for each point in the path are recorded and the path smoothed using the found points as key points. Thus, a flight path can be choreographed by exploring the nostrils and then the internal surfaces of the paranasal sinuses on both sides, entering them through their native ostia. Entering the maxillary sinus through the hiatus semilunaris, all aspects of the sinus can be explored and a mucosal web can be easily identified. The same can be done by entering the frontal sinuses through the frontal recess. A nasopharyngeal reconnaissance with the camera panning around the nasopharynx may be included as well. In addition, the variables could be changed to make the soft tissue become transparent so that the underlying bony anatomy becomes visible. Therefore, variations of the optic chiasm or the carotid siphon can be viewed while still demonstrating the partially transparent nasopharyngeal margin. Using variations in opacity structures the surgeon either may wish to avoid or may want to target for a minimally invasive procedure (i.e. biopsy, drainage) can be discriminated and selectively visualized. A nasopharyngeal reconnaissance with the camera panning around the nasopharynx may included as well. Showing the backside of the nasal septum and conchae, the tur-

binates and nares are viewed in much greater detail and with a larger field of view than is allowed with indirect mirror examination (Fig. 11.4). Another advantage is that structures not accessible by conventional endoscopy can be entered or views can be obtained that are not easily achievable with conventional techniques (Table 11.3). However, manual path definition is needed if mucosal swelling precludes entering a sinus. An algorithm that is more effective than key-framing and topological thinning method in terms of automated features and computing time was developed by Kim DY et al. (2006) to visualize inside of carotid artery using MR angiography images. Nevertheless, automated path definition although desirable, appears to be more difficult due to the complex anatomy and the definition of an automatic pathway does not seem practical in the complex and interindividual varying anatomy of the sinonasal region (Bisdas et al. 2004). In this case coronal MPRs are valuable to control the path definition.

Table 11.3. Advantages of virtual endoscopy of the paranasal sinuses

Highly interactive, remarkable sharp and detailed pictures of the nasal and paranasal sinuses
Visualization of complex anatomic relationships beyond obstruction by bone and soft tissue
Examination by unusal perspectives (backside of the nasal septum and conchae)
Visualization of turbinates and nares in much greater detail and with a larger field of view than allowed with indirect mirror examination
Dataset obtained as part of a routine diagnostic examination. No additional morbidity beyond that of a routine CT or MRI
Complementary visualization of overlapping pathological processes
Provides coordinates for navigational system to localize a safe surgical entrance point or of anatomical landmarks
Non-invasive

11.5 Clinical Applications

Recently developed rendering techniques including a perspective mode result in highly interactive, remarkably sharp and detailed pictures of the nasal and paranasal sinuses. These images including virtual endoscopy are easy to reconstruct using a widely available workstation equipped with advanced software (Kim HJ et al. 2003). De Nicola et al. (1997) evaluated the ability to perform a CT-based VE of the paranasal sinuses using surface rendering . However, these authors used a 3 mm slice thickness and no reconstruction overlap. Thus, the reconstruction algorithm and surface rendering yielded low quality images. A known limitation of surface rendering is that structures may have a more or less dense value than the chosen threshold value. This causes a discontinuity or continuity of the rebuild nasal-sinus surfaces that do not always correspond to reality. In addition, overlapping of different structures such as mucosa-purulent secretions are visualized only as shape modification. Thus, the arbitrary choice of the threshold value and the homogenization of different tissue densities further reduces the contrast resolution. Rogalla evaluated the applicability of VE in the sinonasal region based on volume-rendered spiral CT data in 45 patients (Rogalla et al. 1998). Using a low-dose spiral CT of the paranasal sinuses the imaging data was transferred to a workstation running software for volume rendering (EasyVision, Philips Medical Systems, Eindhoven, The Netherlands). Six orthogonal views of the maxillary sinuses and the nasopharynx and a fly-through movie of the nose were obtained. Coronal reconstructions and virtual endoscopy were compared with respect to detectability of pathology, and surgeons were asked to rank the degree of assistance of the preoperative virtual endoscopy, as compared to subsequent endoscopic surgery. Overall, anatomical details were depicted more often with coronal reconstruction's than with VE; however, a high degree of similarity between virtual endoscopy and the intraoperative endoscopic view was reported by the surgeons. The authors concluded that virtual endoscopy of the nose and paranasal sinuses may develop into a standard means to guide surgeons during endoscopic interventions (Rogalla et al. 1998) (Figs. 11.2–11.6). Hopper et al. (1999) evaluated the feasibility of highlighting surgical sites using CT-based virtual reality of the paranasal sinuses before sinus surgery in patients with significant paranasal sinus disease. For all 25 planned surgeries, the virtual images showed the entire surgical site marked on the 2D coronal images as well as the orientation of the planned surgical site to adjacent normal anatomy. For surgery of the maxillary sinuses, tag-

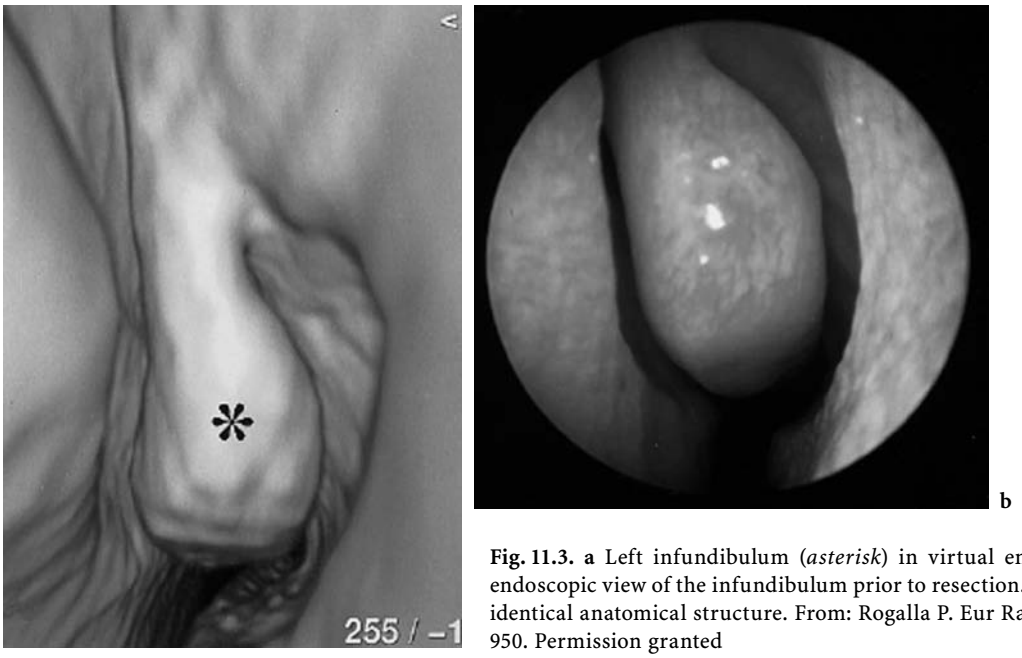

a b

Fig. 11.3. **a** Left infundibulum (*asterisk*) in virtual endoscopy. **b** True endoscopic view of the infundibulum prior to resection. Note the almost identical anatomical structure. From: Rogalla P. Eur Radiol 1998;8:946–950. Permission granted

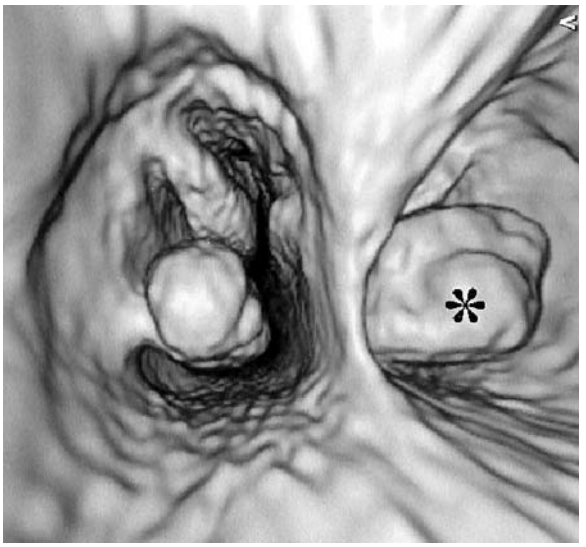

Fig. 11.4. View from nasopharynx through the conchae nasales. Polypous swelling of the dorsal aspect of the inferior right conchae (*asterisk*). Swelling less outstanding on the left side. From: Rogalla P. Eur Radiol 1998;8:946–950. Permission granted

ging and electronic removal of the middle turbinate and uncinate processes mimicked the actual surgery and allowed complete visualization of the infundibulum and the planned surgical site. Therefore, planned endoscopic paranasal sinus surgical sites could be easily and reliably highlighted using CT virtual reality techniques with respect to the patient's normal endoscopic anatomy (Hopper et al. 1999). This is particularly true in complex surgical access to the frontal and sphenoid sinuses. Displaying the superficial anatomy with the planned surgical window highlighted and with the actual surgical window opened, which demonstrated the bony depth, proved to be very useful (Fig. 11.5). To specify a safe surgical entrance point for paranasal mucoceles the value of MPRs and virtual CT sinuscopy was evaluated and compared to results confirmed by surgical endoscopy (Nakasato et al. 2000). The combination of both, MPRs and virtual sinuscopy was important in depicting safe puncture sites through an endonasal approach to treat simple mucoceles (Fig. 11.6). Since it was difficult to approach deeper lesions, VE was applicable only for the most superficial lesions and the authors concluded that a navigational system might overcome this limitation. If mucosal swelling causes occlusion of the natural ostia, VE cannot access the sinus and a manual path definition will be necessary, provided the access can be defined on coronal reconstruction's. However, VE is advantageous for viewing the entry site of the tuba auditiva, a region not well depicted on coronal reconstructions (Pandolfo et al. 2004) (Fig. 11.7). On the other hand, septal deviations are easier to define on coronal slices, whereas decisions about the septum can be impossible using VE because slight curves may escape detection due to the perspective distortion of

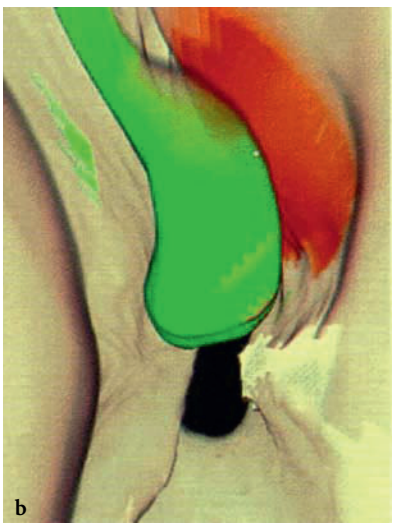

Fig. 11.5a–d. With use of volumetric rendering, it is a simple and rapid process to tag a variety of structures and pathological processes. In this normal patient, the middle and inferior turbinates and uncinate processes have been tagged in green, blue, and red, respectively (**a**). The color rendition of this image is shown in the primary viewport of Figure 11.1. Once tagged, a simple click-on command removes the tagged structures. Sequentially, the inferior turbinate (**b**), the uncinate process (**c**), and middle turbinate (**d**) have been removed, allowing full exposure of the infundibulum. The *whitish areas* represent cut-away bone. From: Hopper: J Comput Assist Tomogr 1999; 23(4):529–533. Permission granted

the images. Further, normal bone variations can be delineated on cross-sectional slices only, if they are hidden behind the surface structure (Wolfsberger et al. 2006). Thus, correlation with cross-sectional images is still recommended, to confirm precise localization and definition of structures behind a surface. This is particularly true if a sinus is completely blocked or closed and a VE is impossible. Of 600 hundred virtual endoscopies (VEs) performed, the VE views allowed a realistic illustration of the various pathologic findings, except from cases with highly obstructive sinonasal disease (Bisdas et al. 2004). The correlation between the preoperative 3D VE findings and the intraoperative findings was significant ($r = 0.83$, $p = 0.001$). Anatomic structures like the septum nasi, inferior and middle turbinates, processus uncinatus, and ductus nasolacrimalis could be better displayed at a –250 HU threshold, whereas the rest of the structures were better displayed at –400 HU. The superiority of 3D images in comparison with axial source images was noted for polyps and mucous swelling of even 1 mm in diameter, which otherwise could only be identified by the simultaneous viewing of all axial and multiplanar reconstructed images (Bisdas et al. 2004). Additionally, VE contributed significantly

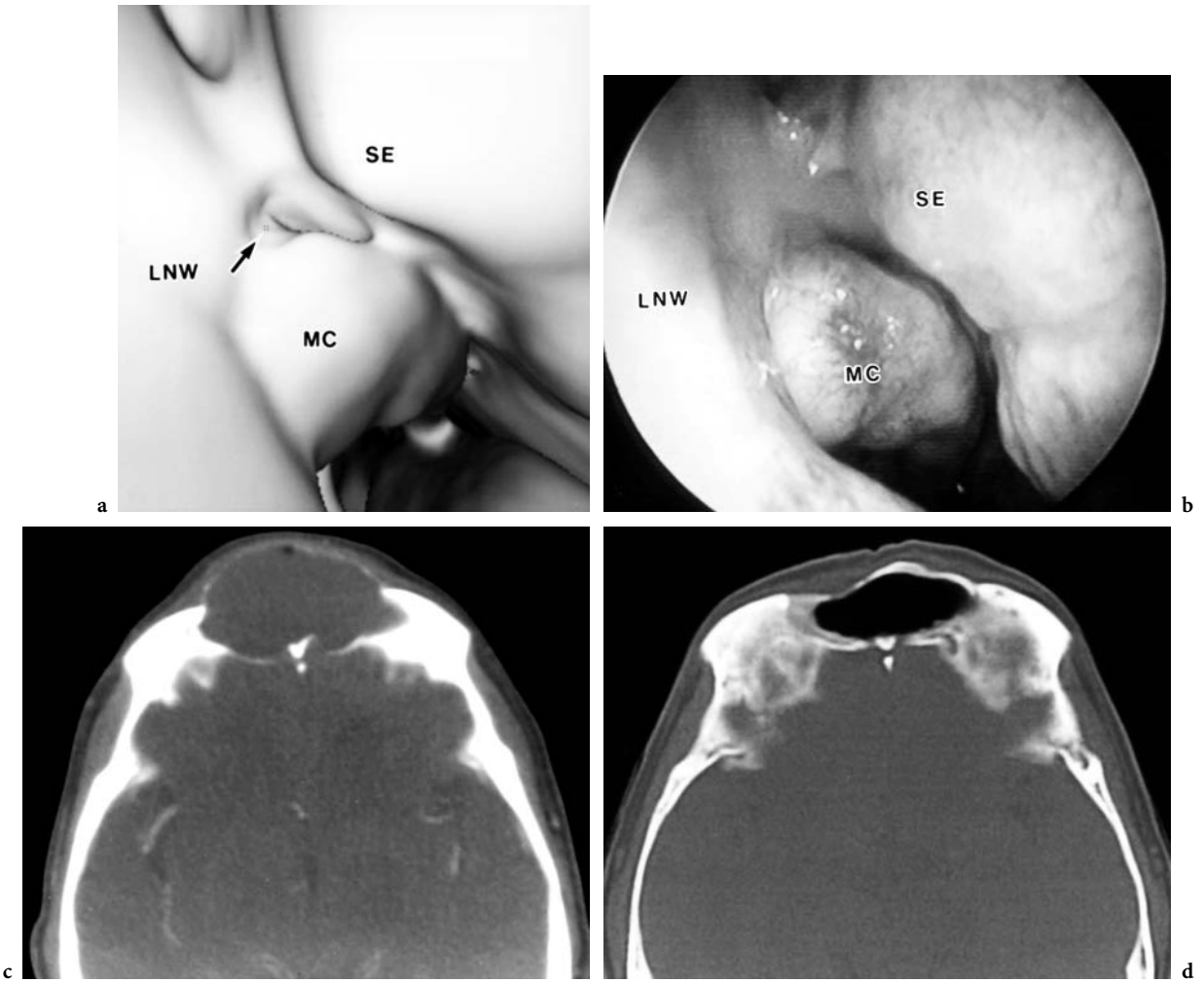

Fig. 11.6a–d. Frontal mucocele in a 52-year-old man. Virtual endoscopic (**a**) and surgical endoscopic (**b**) images of anterior portion of the right nasal cavity are shown. Also presented are preoperative (**c**) and postoperative (**d**) CT findings. The cross-cursor (*arrow*) indicates a suggested puncture site for endoscopic sinus surgery. The wall of the frontal mucocele is shown behind the nasal bone. The mucocele was successfully removed by the endonasal surgery. *SE*, nasal septum; *MC*, mucocele; *LNW*, lateral nasal wall. From: Nakasato: J Comput Assist Tomogr 2000; 24(3):486–492

in the imaging of the ostiomeatal complex of the paranasal sinuses by depicting clearly the intricate local anatomy, which is difficult to recognize even in coronal reconstructions. In cases of congenital malformations, such as choanal atresia, 3D images were useful to define the extended disease and assisted significantly in preoperative planning (Bisdas et al. 2004). However, as stated by Bisdas et al. (2004) common anatomic variants, like Haller, Onodi, and extramural Agger nasi cells; sphenomaxillary plate dehiscences in the lamina papyracea; bony lamella covering the internal carotid artery; level of differences between the cribriform plate and ethmoid roof, and sinonasal providence of the optic nerve deteriorate the power of VE and highlight the value of cross-sectional images and, especially, coronal reconstructions. Additionally, the inability of VE to distinguish between fibrotic tissue and relapses in postsurgery patients has been reported (Meloni et al. 1992). The insufficiency of VE in diagnostic differentiation owes its existence to the imperfect assessment of paranasal sinuses through CT imaging. Therefore, the authors consider VE a complementary imaging modality to cross-sectional radiographs and functional endoscopic sinus surgery (Bisdas et al. 2004).

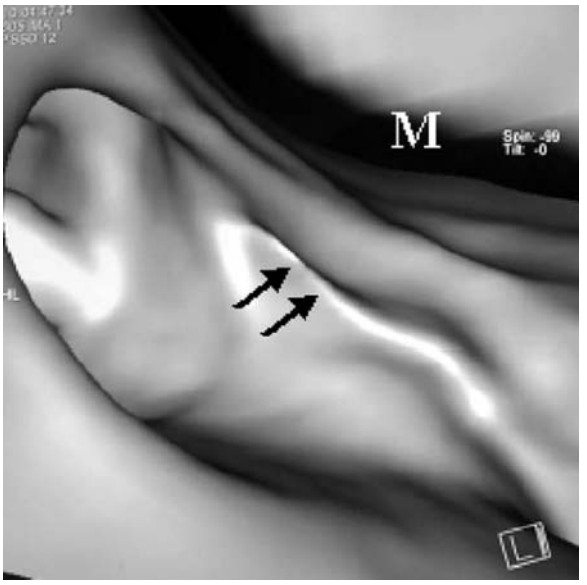

Fig. 11.7. Lateral view. Voluminous lymphatic swelling of the superior wall of the nasopharynx (*M*). The tubaric ostium is compressed (*arrows*). From: Pandolfo I. Virtual endoscopy of the nasopharynx in the evaluation of its normal anatomy and alterations due to lymphoid hyperplasia: preliminary report. Eur Radiol 2004; 14(10):1882–1888

11.6 Endoscopic Sinus Surgery Training

Besides its diagnostic value, VE can play a significant role as a teaching tool for students and trainees because it allows the real portrayal of the paranasal sinuses and therefore strengthens the possibility of these individuals becoming familiar with not only regional but endoscopic and operative assessment (Bisdas et al. 2004). Endonasal sinus surgery requires extensive training before it can be performed adequately. The near-field endoscopic anatomy is very different from the typical anatomic presentation seen in cross-sectional images or in an anatomy atlas. Even the experienced endoscopist can easily become disoriented or lost due to the complex and variable anatomy and the proximity of important structures (Hosemann 1996; May et al. 1994; Weber et al. 1998). Therefore intensive training is necessary to avoid severe complications and this is even more evident considering the fact that medical malpractice in endoscopic surgery has become a predominant concern of physicians in Japan as well as in Western countries (Anon et al. 1994; Hiyama et al. 2006). Ecke et al. (1998) combined computer graphics and virtual reality (VR) techniques to create an interactive nasal endoscopy simulator (NES) for nasal endoscopy and endonasal sinus surgery. The system consisted of a graphics workstation, a tracking system for measuring the position of the endoscope and surgical instruments in space, a head model, image data sets of the nasal cavity and paranasal sinus area, and complementary software. The current NES is comprised of a visual and auditory VR system that provides both educational and planning options for sinus surgery. However, the usual resistance, when touching relevant anatomical structures, is not provided by this system. Thus, a "force feedback system" was implemented that allows for such a response (Rudman et al. 1998). The use of virtual endoscopy for training can familiarize the operator with endoscopic anatomic appearance and can provide anatomic landmarks to assist with orientation. The information gained from such training can provide confidence, and preoperative virtual endoscopy may lead to more effective and safer endoscopic procedures (Satava and Fried 2002). Edmond (2002) demonstrated that an endoscopic sinus surgical simulator is as a valid training device and appears to positively impact operating room performance among junior otolaryngology residents. In his study differences between simulation-trained residents and others approached statistical significance for two items: anterior ethmoidectomy ($p < .0602$) and surgical confidence ($p < .0909$). Uribe et al. (2004) found that medical students displayed a steep learning curve within three to five trials on an endoscopic sinus surgery simulator and that they reached a plateau in their learning curves to within 90% of that of experienced sinus surgeons after an additional four to five trials (Glaser et al. 2006).

11.7 Image-Guided Sinus Surgery

Although the endoscopes provide bright illumination and brilliant images, the view provided is only a two-dimensional representation of a complex three-dimensional space. Endoscopes provide a wide-angle perspective, which intrinsically introduce a fish-eye effect (analogous to spherical aberration) and the potential for perceptual distortion and secondary surgical error during these procedures is

considerable (Citardi and Batra 2007). Furthermore, the view is easily obstructed by blood, mucus, or pus when the endoscope tip gently touches the mucosa (Scharpf et al. 2005). Thus, disorientation may occur for several reasons:

- The position of the endoscope tip inside the patient is not directly visible and therefore surgeons usually guess at the location based on the inserted length, orientation and monitor screen view.
- The viewing direction varies from 0° (straight forward) to 120° (backward viewing) and may rotate on its axis. Thus, when the viewing direction exceeds 0°, disorientation may occur.
- The endoscopic view is limited to the mucous surface and landmarks used to position the endoscope within the patient may become indistinguishable because of damage from disease or due to injuries from previous surgery.
- Thus, surgical rhinologists were very interested in intraoperative surgical navigation, as it was felt that this technology should reduce surgical complications and fit well with endoscopic techniques (Citardi and Batra 2007; Fried et al. 1998a; Knott et al. 2006b; Truppe et al. 1996; Wolfsberger et al. 2006; Yamashita et al. 1999).

11.7.1 Image-Guided Sinus Surgery Using MR Imaging

The first image-guided endoscopic surgeries using intraoperative MRI were reported by Fried et al. (1996, 1998b) and Hsu et al. (1998). The procedures were experimental and intended to test the unusual working environment of a unique new "open-configuration" MRI unit for head and neck surgery using near real-time image guidance. All surgeries in twelve patients were performed without complications and both the endoscopic view and the MRI scans were available at the surgical field. The image plane was surgeon controlled, and the MR scanner updated images in as little as 14 s. MRI provided adequate visualization of both the disease and the related anatomy and allowed the surgeon to navigate during the procedure (Fig. 11.8). Intraoperative MR imaging has several advantages over CT-based guidance systems. MR imaging provides multiplanar capability and has a better soft-tissue differentiation than CT. The intraoperative data reflects tissue changes during surgery and provides optimum feedback for surgical guidance. The operating environment however poses some challenges; in particular instruments including the endoscope must be made from MR-compatible materials. Also, preparation of the intraoperative MRI for ESS requires significantly more time than conventional ESS or using a navigational system during paranasal surgery (Seno et al. 2005).

11.7.2 Image-Guided Sinus Surgery Using a Navigational System

Intuitively, a navigational system should improve surgical outcomes and several reports have presented case series in which image-guided surgery (IGS) were used (Anon 1998; Cartellieri et al. 2001; Citardi and Batra 2007; Grevers et al. 2002; Strauss et al. 2006; Truppe et al. 1996). However, only Fried et al. (2002) showed a statistically significant benefit for IGS and confirmed a lower major complication rate for sinus surgery incorporating IGS. Strauss et al. (2006) quantified the clinical impact of IGS during surgery and developed a level of quality index that compared the available information before and after IGS application . In their study, information provided by the IGS system was deemed 'detrimental' in only three out of 792 IGS applications, and even in these instances, no adverse outcomes were noted. In addition, 47.9% of IGS applications yielded a change of surgical strategy. Less experienced surgeons adjusted their strategies more frequently as a result of IGS, and IGS was more commonly associated with adjustments in surgical strategy among endoscopic biopsies and tumor resection cases (Strauss et al. 2006). Metson (2003) reported on the first 1000 image-guided sinus surgery cases performed by 42 surgeons at an academic medical center. Interestingly, the initial enthusiasm for the use of a IGS system was not sustained by all physicians, and after 2 years the frequency with which image-guidance was used for sinonasal surgery reached a plateau. Nevertheless, the majority of surgeons continued to use it for selected sinus procedures over the 5-year study period. Based on their experience a knowledge base had been proposed as summarized in Table 11.4. The introduction of complex, new technology into the operating room setting can be a frustrating experience for physicians and other operating room personnel. It is therefore best if a surgeon schedules relatively simple cases

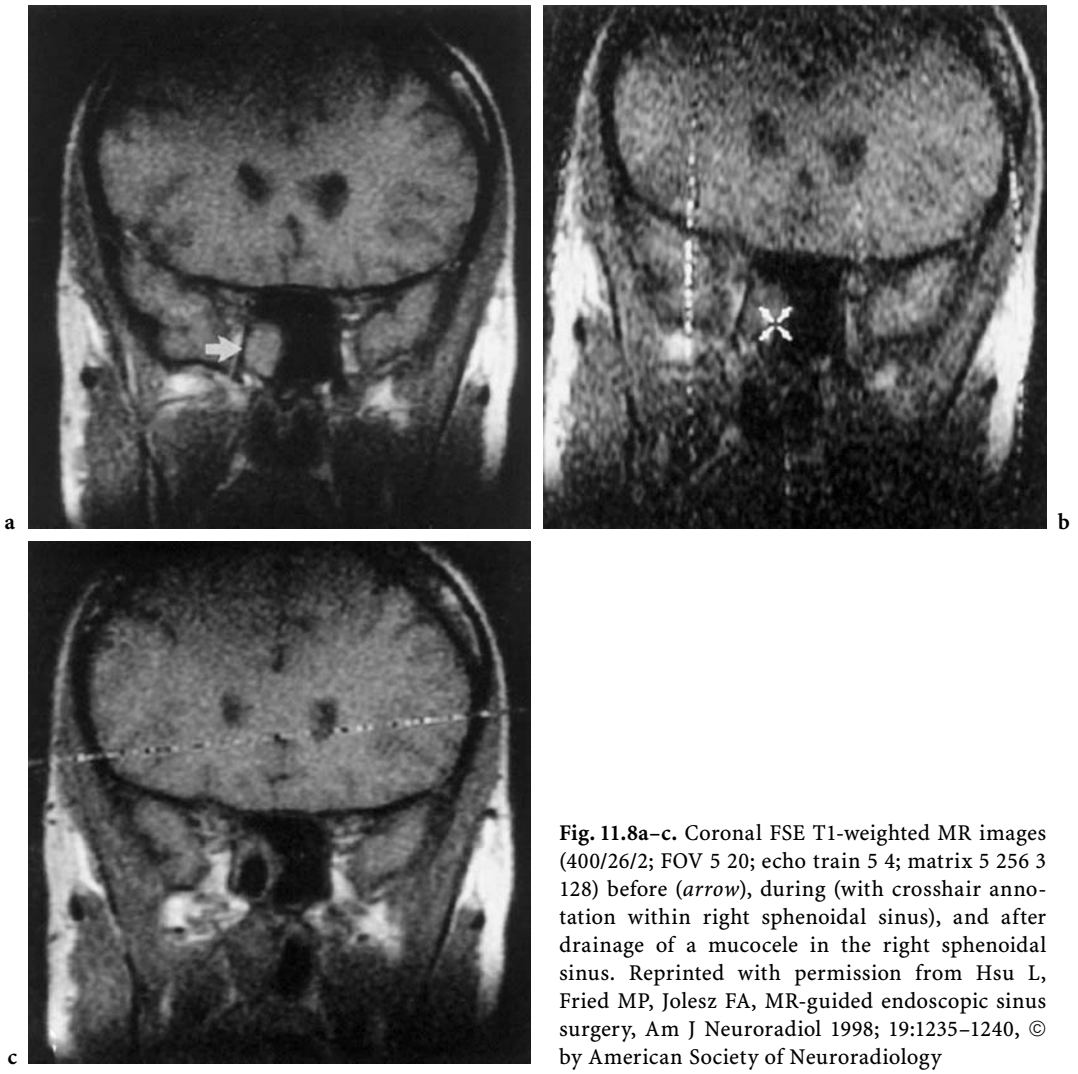

Fig. 11.8a–c. Coronal FSE T1-weighted MR images (400/26/2; FOV 5 20; echo train 5 4; matrix 5 256 3 128) before (*arrow*), during (with crosshair annotation within right sphenoidal sinus), and after drainage of a mucocele in the right sphenoidal sinus. Reprinted with permission from Hsu L, Fried MP, Jolesz FA, MR-guided endoscopic sinus surgery, Am J Neuroradiol 1998; 19:1235–1240, © by American Society of Neuroradiology

Table 11.4. Lessons learned from image-guided sinus surgery over a 5 year period.

Start with relatively easy cases when first learning to use an image-guidance system
Image-guidance systems are relatively accurate and reliable
Using an image-guidance system is associated with increased operative time and expense
Image-guidance systems enhance surgeon confidence
Image-guidance systems should not be used to make millimeter decisions about how to proceed during surgery
Trust your judgment when information from the image-guidance system conflicts with own clinical judgment
Technology is no substitute for technique

Modified from Metson (2003)

when first learning to use the image-guidance system and reserves the more challenging cases until after familiarity with the equipment has been achieved. Initial cases should be easy enough that the surgeon would feel comfortable completing the surgery without an image-guidance system, in the event that the system does not work properly or the surgeon does not find it helpful (Metson 2003). Studies have demonstrated the ability of image-guidance systems to provide anatomic localization to within 2 mm of accuracy during routine clinical use (Anon 1998; Fried et al. 1997; Metson et al. 1998). The surgeon, however, should routinely verify system accuracy against a known anatomic landmark before using it to navigate during surgery, since anatomic drift may occur during surgery, usually from movement of the headset. The initial use

of IGS has been found to increase operative time by 15–30 min per case (Metson 2003). Once a surgeon becomes familiar with the equipment, this time typically is reduced to 5–15 min per case. A cost analysis of IGS demonstrated an increased expense of more than $500 per case when such systems were used for sinus surgery (Metson 2003). The use of any disposable headsets or handpieces further increases this expense. Despite the increased time and expense associated with IGS, this technology is still widely used for sinus surgery because of the increased confidence it provides to surgeons during these procedures (Metson et al. 2000). In particular, when faced with uncertain surgical landmarks and possible disorientation, the presence of an image-guidance system to confirm the surgeon's impression of the clinical anatomy can be very reassuring. For instance, image-guidance systems are excellent to inform the surgeon whether the air space just opened is a large posterior ethmoid cell or a small sphenoid sinus. Similarly, the system can readily inform the surgeon whether the bony lamella in view is the ethmoid roof or whether there is still an additional centimeter of opacified air cells that must be opened. During image-guided sinus surgery however, the system might indicate that the tip of the surgical instrument or probe is in a location that differs from that suspected by the surgeon. In some cases this discrepancy is easy to reconcile and when anatomic drift from slippage of the headset is likely, the system needs only be re-registered to confirm this impression. In other clinical situations, however, the reasons for such discrepancy are not so clear and the surgeon must make a decision on how to proceed. In such cases, the clinical judgment of the surgeon is usually correct. Nevertheless, it is always prudent to follow the safer route and leave the final piece of bone or unopened air cell alone (Metson 2003). An even more clear statement was issued by Metson, saying that enhanced anatomic localization may increase a surgeon's confidence; however, surgeons who "push the envelope" by performing surgery they would not ordinarily do risk finding themselves "outside of the envelope", which in the case of sinus surgery could be the orbit or intracranial cavity (Metson 2003). Melroy et al. (2006) evaluated IGS for a more accurate delineation of the frontal osteoplastic flap, allowing for safer entry into the frontal sinus. They noted that, IGS generated the smallest difference between measurements and actual values and was statistically superior to Caldwell films and transillumination. However, Tabaee et al. (2005) compared patients undergoing CSF leak repair with and without IGS and did not confirm a statistically significant difference in the success rates. Based on expert consensus opinion and literature evidence base, the American Academy of Otolaryngology – Head and Neck Surgery (AAO-HNS 2006) has published an official policy statement of the appropriate use of IGS. Examples of indications in which use of computer-aided surgery may be deemed appropriate include: (1) revision sinus surgery, (2) distorted sinus anatomy of development, postoperative, or traumatic origin, (3) extensive sino-nasal polyposis, (4) pathology involving the frontal, posterior ethmoid and sphenoid sinuses, (5) disease abutting the skull base, orbit, optic nerve or carotid artery, (6) CSF rhinorrhea or conditions where there is a skull base defect, (7) benign and malignant sino-nasal neoplasms. A significant refinement was introduced by Leong et al. (2006) exploring CT-MR fusion techniques in patients with anterior skull base lesions using the InstaTrak 3500 Plus system for navigation (GE Healthcare Navigation and Visualization, Lawrence, MA) and the CBYON Suite Doctor Station (version 2.8, Med-Surgical Services, Inc., Mountain View, CA) for image fusion (Fig. 11.9). The CBYON Suite was only used for preoperative image review, whereas the InstaTrak was used both for preoperative image review and intraoperative navigation. The fused scans were excellent in defining the pathology itself and the surrounding soft and bony tissue involvement. With just the CT alone, the depth of the soft tissue involvement could not be fully appreciated beyond the boundary of the bony defects. For tumor cases, the information provided by CT-MR fusion images in this regard was crucial in determining the extent of surgery. Similarly, CT scans do not give much information about potential loculations within a mucocele; but MR images provide excellent detail about mucocele contents, but little info about the surrounding bone (or lack thereof). Furthermore, CT-MR fusion studies provide better understanding about the origin of encephaloceles at the skull base (Fig. 11.10). However, software interfaces for CT-MR fusion at least somewhat complicated, and it takes significant efforts to successfully apply this technology. Additionally, time for scan preparation, and availability of the fusion images may reduce operative time (Leong et al. 2006). While the ultimate role of CT-MR fusion has yet to be determined, this technology is not intended for routine sinus surgery, but rather

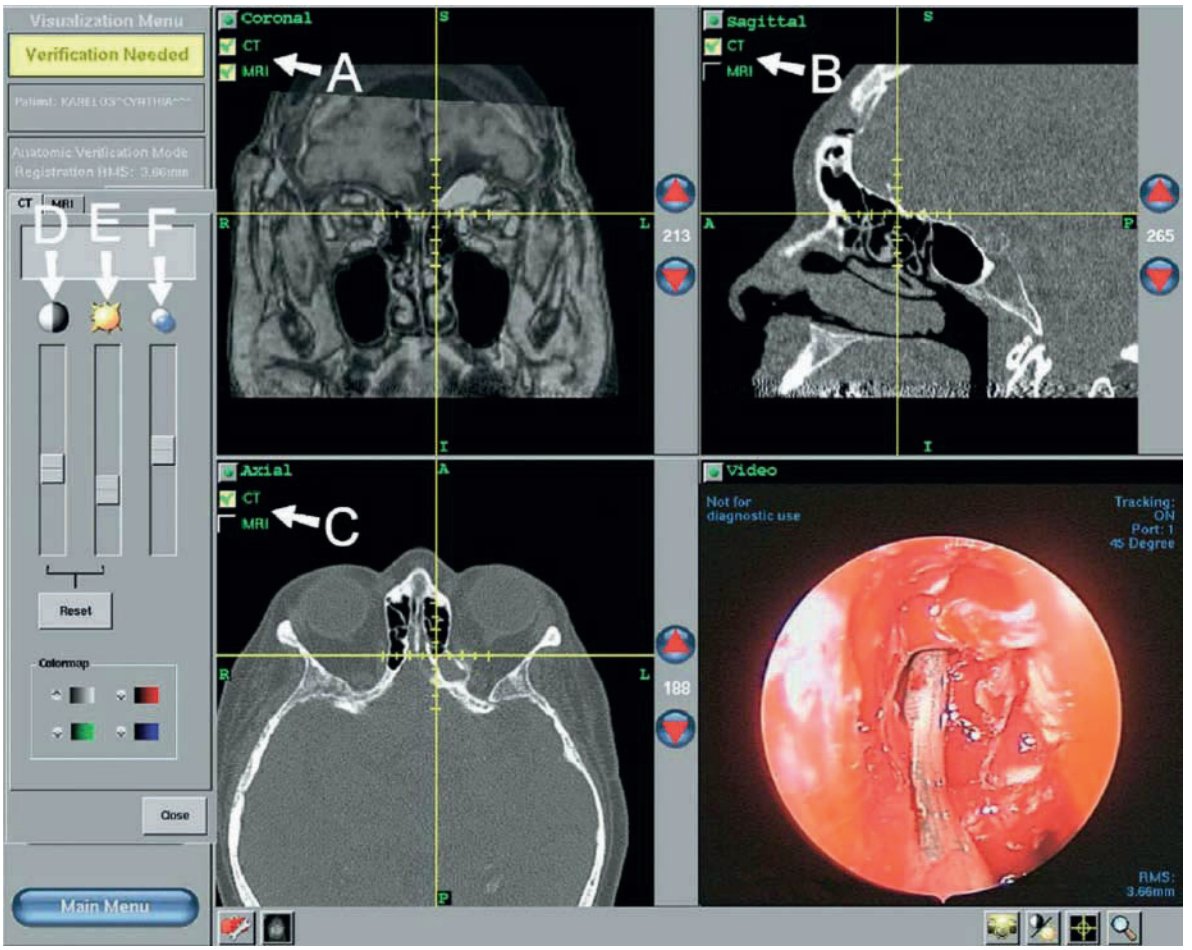

Fig. 11.9. This intraoperative image capture demonstrates the typical screen view. *Top left panel*: fused CT-MR image. *Top right, bottom left panels*: pure CT images. It is possible to select CT, MR, CT-MR fusion images directly (through toggle-type switches), or one may 'morph' between CT and MR images (through a slider-type control). *A–C*) Toggles for choosing between CT, MR and CT-MR fusion images. (*D*) Slider for image contrast. (*E*) Slider for image brightness. (*F*) Slider for CT-MR fusion control. From: Leong JL, Otolaryngol Head Neck Surg 2006; 134:868–876

during intraoperative navigation for sinonasal neoplasms, complex mucoceles, encephaloceles, and any lesion impinging on the internal carotid artery.

11.7.3 Comparison of Tracking Systems

IGS systems for sinus surgery often utilize either electromagnetic (radiofrequency) or optical (infrared) signals to localize instruments within the surgical field. An extensive overview of various concepts and applications in rhinology has been provided by Knott et al. (2006a). Metson et al. (1998) compared the use of these two different image guidance technologies for sinus surgery. Both the electromagnetic and optical systems provided anatomic localization to within 2 mm during surgery and intraoperative reregistration was effective in correcting for any anatomic drift (Table 11.5). Although the mean operative times were different (156.3 ± 8.9 min for the electromagnetic and 139.2 ± 17.7 min for the optical system ($p < 0.05$), the average intraoperative blood loss did not differ significantly between groups (electromagnetic, 190.6 ± 28.7 mL; optical, 172.4 ± 23.0 mL). Each system however, was noted to have limitations. The presence of metallic objects in the operative field interfered with functioning of the electromagnetic system, whereas the optical system required a clear line of sight to be maintained between the infrared camera and surgical handpiece. Both systems

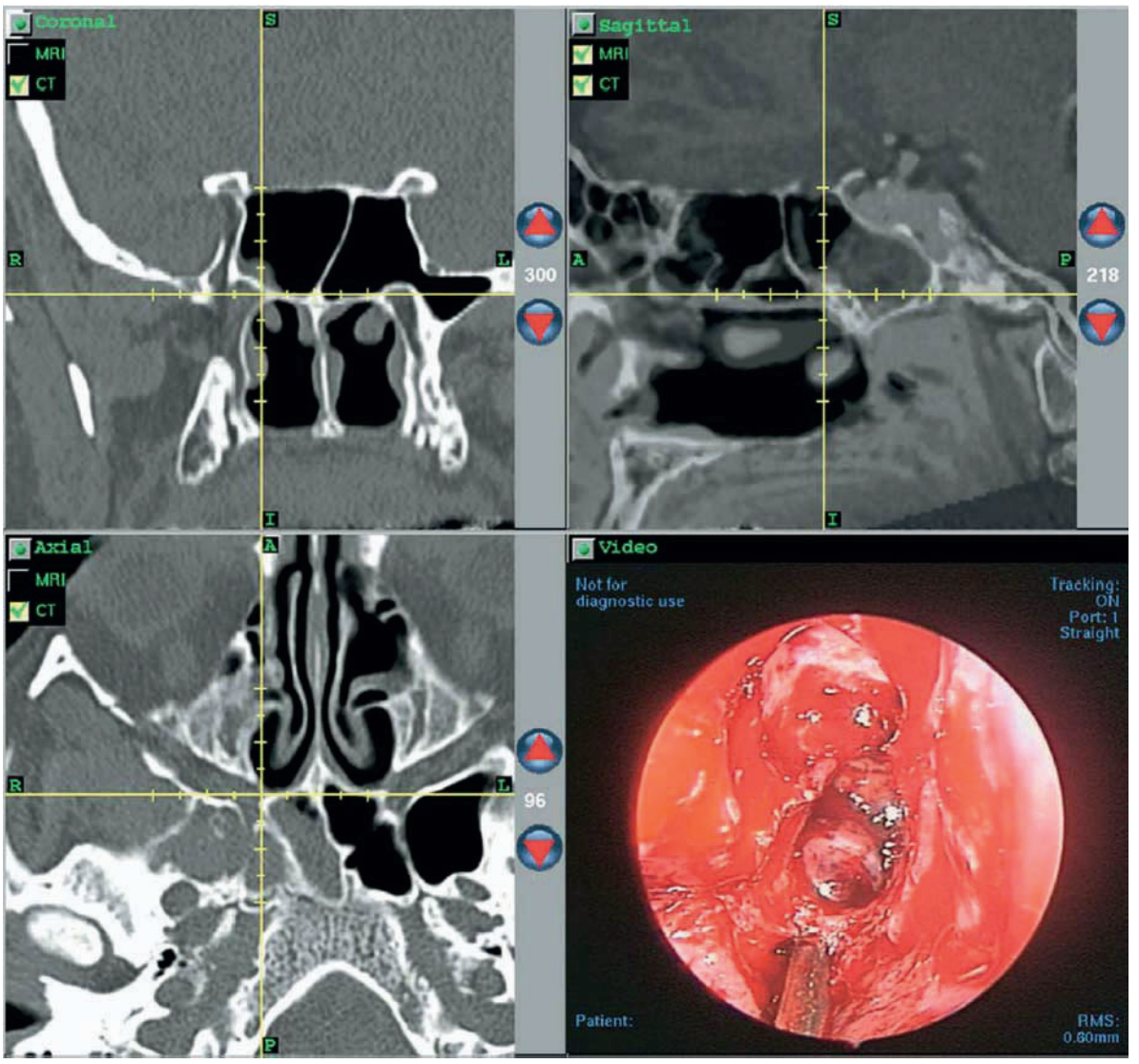

Fig. 11.10. This intraoperative image capture was obtained during computer-aided endoscopic repair of large sphenoid encephalocele. *Left panels*: conventional CT images. *Upper right panel*: fused CT-MR image. The sagittal image shows the encephalocele filling much of the sphenoid sinus. Intraoperatively, navigation with the CT-MR fusion images facilitated complete resection of the encephalocele as well as complete definition of the skull base defect. From: Leong JL, Otolaryngol Head Neck Surg 2006; 134:868–876

required specialized headsets to be worn by patients during surgery to monitor head position. The electromagnetic system also required these headsets to be worn during the preoperative computed tomography scan. Seno et al. (2005) used the Signa SP/i Intraoperative navigation system (General Electric Co., Intraoperative NS) that acquires both real time and high-resolution images during surgery, and a conventional image-guided navigation (Stealth Station TREON, Medtronic Inc., IGNS) and compared them to controls undergoing endoscopic sinus surgery without any image guidance. Preparation of the intraoperative NS required an additional 52 min and IGNS required 17 min compared to the control group. Since surgical instruments must not be attracted by the magnetic field in the operating room, intraoperative NS has some limitations. Instruments used within the NS group, were thoroughly examined and some remanufactured using MR safe materials, whereas all instruments in ESS could also be used in surgical guidance during surgery in the IGNS. Since the average distant error in both systems was

Table 11.5. Commercially available navigational systems for image-guided surgery and their reported target registration error

System (vendor)	Tracking system	Registration type	Reported accuracy
InstaTrak, (GE Navigation and Visualization, Lawrence, MA)	Electromagnetic	Automatic PPR CBR with touch	2.28 mm (95% CI 2.02–2.53) (Fried et al. 1997) 1.97 mm (95% CI 1.75–2.23) (Fried et al. 1997) 1.5 ± 0.3 mm (laboratory model) (Knott et al. 2006b)
LandMarx, (Medtronic Xomed, Jacksonville, FL)	Optical	Automatic PPR CBR	N/A 1.69 ± 0.38 mm (Metson et al. 2000) No report
Stryker Navigation System, (Stryker-Leibinger, Kalamazoo, MI)	Optical	Automatic PPR CBR ('Mask')	N/A 1.6 mm (range 0.6–3.7) (Snyderman et al. 2004) No report
VectorVision, (BrainLAB, Hemstetten, Germany)	Optical	Automatic PPR CBR with laser	No report 1.57 ± 1.1 mm (Cartellieri et al. 2001) 2.4 ± 1.7 mm (Raabe et al. 2002); Grevers et al. 2002)

Adapted from Knott et al. (2006b). CBR, contour-based registration; N/A, registration protocol not available for the specific system; PPR, paired-point registration

between 1 mm and 2.5 mm, Seno et al. concluded, that accuracy obtained with both navigation system was suitable for ESS.

11.8 Conclusion

VE obtained from CT or MRI allows evaluation of the highly variable anatomy of the nasal cavity, nasopharynx, and paranasal sinuses in a fast, reliable, and noninvasive way with no additional morbidity. Anatomical and pathological details can be visualized using unconventional angles, perspectives and overcomes the anatomic barriers of the sinuses, which are inaccessible with conventional endoscopy. Although, the accuracy of this method was confirmed by fiberoptic examination and surgery, VE of the paranasal sinuses today has found only limited clinical applications. VE demands high-resolution imaging data obtained with MSCT, but moderate hardware and postprocessing software, which may be used with every CT scanner and is fairly widely available. Rather than reading large amounts of single images, a VE operator today could use a virtual endoscopic reconstruction to review a clinical case. However, VE of the paranasal sinuses is still more a preoperative tool for assisting surgeons in education and training. Highly developed visualization software might even allow virtual surgery based on CT data for training purposes. In the case of a decreased field of view during ESS, a navigational system may aid in determining a safe surgical entrance point or in allowing the localization of anatomical landmarks. CT-guidance for procedures in the regular OR has gained wide acceptance for a variety of endoscopic procedures of the paranasal sinuses, including primary and revision endoscopic sinus surgery, osteoplastic frontal sinusotomy, transsphenoidal hypophysectomy, endoscopic CSF leak repair and endoscopic pterygomaxillary fossa biopsy. Intraoperative imaging based on MR-guidance is helpful but still in a phase of development. However, the benefits of a standardized application of VE as a complementary diagnostic and preoperative planning tool needs to be underlined, which radiologists and otorhinolaryngologists are still aware of it.

References

AAO-HNS (2006) Surgery. AAO-HNS policy on intra-operative use of computer-aided surgery. http://www.entlink.net/practice/rules/image-guiding.cfm

Anon JB (1998) Computer-aided endoscopic sinus surgery. Laryngoscope 108:949–961

Anon JB, Lipman SP, Oppenheim D, Halt RA (1994) Computer-assisted endoscopic sinus surgery. Laryngoscope 104:901–905

Beus J, Kauczor HU, Schwikkert HC, Mohr W, Mildenberger P (1995) Coronal paranasal sinus CT: using the spiral technique. Aktuelle Radiol 5:189–191

Bisdas S, Verink M, Burmeister HP, Stieve M, Becker H (2004)

Three-dimensional visualization of the nasal cavity and paranasal sinuses. Clinical results of a standardized approach using multislice helical computed tomography. J Comput Assist Tomogr 28:661–669
Branstetter BFT, Weissman JL (2005) Role of MR and CT in the paranasal sinuses. Otolaryngol Clin North Am 38:1279–1299, x
Cartellieri M, Kremser J, Vorbeck F (2001) Comparison of different 3D navigation systems by a clinical "user". Eur Arch Otorhinolaryngol 258:38–41
Carvalho BM (2003) Cone-beam helical CT virtual endoscopy: reconstruction, segmentation and automatic navigation. University of Pennsylvania, pp 201
Citardi MJ, Batra PS (2007) Intraoperative surgical navigation for endoscopic sinus surgery: rationale and indications. Curr Opin Otolaryngol Head Neck Surg 15:23–27
Cline HE, Dumoulin CL, Hart HR Jr, Lorensen WE, Ludke S (1987) 3D reconstruction of the brain from magnetic resonance images using a connectivity algorithm. Magn Reson Imaging 5:345–352
Davis RE, Levoy M, Rosenman JG et al (1991) Three-dimensional high-resolution volume rendering (HRVR) of computed tomography data: applications to otolaryngology-head and neck surgery. Laryngoscope 101:573–582
De Nicola M, Salvolini L, Salvolini U (1997) Virtual endoscopy of nasal cavity and paranasal sinuses. Eur J Radiol 24:175–180
DePuey EG, Garcia EV, Ezquerra NF (1989) Three-dimensional techniques and artificial intelligence in thallium-201 cardiac imaging. AJR Am J Roentgenol 152:1161–1168
Dessl A, Giacomuzzi SM, Springer P et al (1997) Virtual endoscopy with post-processing helical CT data sets. Aktuelle Radiol 7:216–221
Di Rienzo L, Coen Tirelli G, Turchio P, Garaci F, Guazzaroni M (2003) Comparison of virtual and conventional endoscopy of nose and paranasal sinuses. Ann Otol Rhinol Laryngol 112:139–142
Ecke U, Klimek L, Muller W, Ziegler R, Mann W (1998) Virtual reality: preparation and execution of sinus surgery. Comput Aided Surg 3:45–50
Edmond CV Jr (2002) Impact of the endoscopic sinus surgical simulator on operating room performance. Laryngoscope 112:1148–1158
Eggesbo HB (2006) Radiological imaging of inflammatory lesions in the nasal cavity and paranasal sinuses. Eur Radiol 16:872–888
Fahlbusch R, Ganslandt O, Buchfelder M, Schott W, Nimsky C (2001) Intraoperative magnetic resonance imaging during transsphenoidal surgery. J Neurosurg 95:381–390
Fried MP, Hsu L, Topulos GP, Jolesz FA (1996) Image-guided surgery in a new magnetic resonance suite: preclinical considerations. Laryngoscope 106:411–417
Fried MP, Kleefield J, Gopal H, Reardon E, Ho BT, Kuhn FA (1997) Image-guided endoscopic surgery: results of accuracy and performance in a multicenter clinical study using an electromagnetic tracking system. Laryngoscope 107:594–601
Fried MP, Kleefield J, Taylor R (1998a) New armless image-guidance system for endoscopic sinus surgery. Otolaryngol Head Neck Surg 119:528–532
Fried MP, Topulos G, Hsu L et al (1998b) Endoscopic sinus surgery with magnetic resonance imaging guidance: initial patient experience. Otolaryngol Head Neck Surg 119:374–380
Fried MP, Moharir VM, Shinmoto H et al (1999) Virtual laryngoscopy. Ann Otol Rhinol Laryngol 108:221–226
Fried MP, Moharir VM, Shin J, Taylor-Becker M, Morrison P (2002) Comparison of endoscopic sinus surgery with and without image guidance. Am J Rhinol;16:193–197
Geiger R, Kikinis R (1994) Simulation of endoscopy. Proceedings of the AAAI Spring Symposium Series: applications of computer vision in medical image processing, pp 138–140
Gilani S, Norbash AM, Ringl H, Rubin GD, Napel S, Terris DJ (1997) Virtual endoscopy of the paranasal sinuses using perspective volume rendered helical sinus computed tomography. Laryngoscope 107:25–29
Glaser AY, Hall CB, Uribe SJ, Fried MP (2006) Medical students' attitudes toward the use of an endoscopic sinus surgery simulator as a training tool. Am J Rhinol 20:177–179
Grevers G, Leunig A, Klemens A, Hagedorn H (2002) CAS of the paranasal sinuses-technology and clinical experience with the Vector-Vision-Compact-System in 102 patients. Laryngorhinootologie 81:476–483
Hahnel S, Ertl-Wagner B, Tasman AJ, Forsting M, Jansen O (1999) Relative value of MR imaging as compared with CT in the diagnosis of inflammatory paranasal sinus disease. Radiology 210:171–176
Han P, Pirsig W, Ilgen F, Gorich J, Sokiranski R (2000) Virtual endoscopy of the nasal cavity in comparison with fiberoptic endoscopy. Eur Arch Otorhinolaryngol 257:578–583
Hein E, Rogalla P, Klingebiel R, Hamm B (2002) Low-dose CT of the paranasal sinuses with eye lens protection: effect on image quality and radiation dose. Eur Radiol 12:1693–1696
Hiyama T, Tanaka S, Yoshihara M, Fukuhara T, Mukai S, Chayama K (2006) Medical malpractice litigation related to gastrointestinal endoscopy in Japan: a two-decade review of civil court cases. World J Gastroenterol 12:6857–6860
Hojreh A, Czerny C, Kainberger F (2005) Dose classification scheme for computed tomography of the paranasal sinuses. Eur J Radiol 56:31–37
Hopper KD, Iyriboz AT, Wise SW, Fornadley JA (1999) The feasibility of surgical site tagging with CT virtual reality of the paranasal sinuses. J Comput Assist Tomogr 23:529–533
Hosemann W (1996) Endonasal surgery of the paranasal sinuses-concepts, techniques, results, complications and revision interventions. Eur Arch Otorhinolaryngol Suppl 1:155–269
Howells RC, Ramadan HH (2001) Usefulness of computed tomography and magnetic resonance in fulminant invasive fungal rhinosinusitis. Am J Rhinol 15:255–261
Hsu L, Fried MP, Jolesz FA (1998) MR-guided endoscopic sinus surgery. AJNR Am J Neuroradiol 19:1235–1240
Jolesz FA, Lorensen WE, Shinmoto H et al (1997) Interactive virtual endoscopy. AJR Am J Roentgenol 169:1229–1235
Keller PJ, Drayer BP, Fram EK, Williams KD, Dumoulin CL, Souza SP (1989) MR angiography with two-dimensional acquisition and three-dimensional display. Work in progress. Radiology 173:527–532
Kersten MA, Stewart AJ, Troje N, Ellis R (2006) Enhancing

depth perception in translucent volumes. IEEE Trans Vis Comput Graph 12:1117–1123
Kim DY, Chung SM, Park JW (2006) Automatic navigation path generation based on two-phase adaptive region-growing algorithm for virtual angioscopy. Med Eng Phys 28:339–347
Kim HJ, Yoon HR, Kim KD et al (2003) Personal-computer-based three-dimensional reconstruction and simulation of maxillary sinus. Surg Radiol Anat 24:393–399
Knott PD, Batra PS, Citardi MJ (2006a) Computer aided surgery: concepts and applications in rhinology. Otolaryngol Clin North Am 39:503–522, ix
Knott PD, Batra PS, Butler RS, Citardi MJ (2006b) Contour and paired-point registration in a model for image-guided surgery. Laryngoscope 116:1877–1881
Kochanek D, Bartels R (1984) Interpolating splines with local tension, continuity, and bias control. Comput Graph 18:33–41
Lee JS, Jani AB, Pelizzari CA et al (1999) Volumetric visualization of head and neck CT data for treatment planning. Int J Radiat Oncol Biol Phys 44:693–703
Lemke AJ, Schurig-Urbaniak AM, Liebig T et al (2004) Virtual MR endoscopy of the ventricles prior to neurosurgical interventional endoscopy – evaluation of different presentation techniques. Rofo 176:1106–1113
Lengyel J, Reichert M, Donald RB (1990) Real-time robot motion planning using rasterizing. Comput Graph 24:327–335
Leong JL, Batra PS, Citardi MJ (2006) CT-MR image fusion for the management of skull base lesions. Otolaryngol Head Neck Surg 134:868–876
Levoy M (1991) Methods for improving the efficiency and versatility of volume rendering. Prog Clin Biol Res 363:473–488
Ling FT, Kountakis SE (2006) Advances in imaging of the paranasal sinuses. Curr Allergy Asthma Rep 6:502–507
Lloyd G, Lund VJ, Howard D, Savy L (2000) Optimum imaging for sinonasal malignancy. J Laryngol Otol 114:557–562
Lusk RP, Lazar RH, Muntz HR (1989) The diagnosis and treatment of recurrent and chronic sinusitis in children. Pediatr Clin North Am 36:1411–1421
Magnusson M, Lenz R, Danielsson PE (1991) Evaluation of methods for shaded surface display of CT volumes. Comput Med Imaging Graph 15:247–256
May M, Levine HL, Mester SJ, Schaitkin B (1994) Complications of endoscopic sinus surgery: analysis of 2108 patients-incidence and prevention. Laryngoscope 104:1080–1083
Meloni F, Mini R, Rovasio S, Stomeo F, Teatini GP (1992) Anatomic variations of surgical importance in ethmoid labyrinth and sphenoid sinus. A study of radiological anatomy. Surg Radiol Anat 14:65–70
Melroy CT, Dubin MG, Hardy SM, Senior BA (2006) Analysis of methods to assess frontal sinus extent in osteoplastic flap surgery: transillumination versus 6-ft Caldwell versus image guidance. Am J Rhinol 20:77–83
Messerklinger W (1994) Background and evolution of endoscopic sinus surgery. Ear Nose Throat J 73:449–450
Metson R (2003) Image-guided sinus surgery: lessons learned from the first 1000 cases. Otolaryngol Head Neck Surg 128:8–13
Metson R, Gliklich RE, Cosenza M (1998) A comparison of image guidance systems for sinus surgery. Laryngoscope 108:1164–1170
Metson RB, Cosenza MJ, Cunningham MJ, Randolph GW (2000) Physician experience with an optical image guidance system for sinus surgery. Laryngoscope 110:972–976
Morra A, Calgaro A, Cioffi V, Pravato M, Cova M, Pozzi Mucelli R (1998) Virtual endoscopy of the nasal cavity and the paranasal sinuses with computerized tomography. Anatomical study. Radiol Med (Torino) 96:29–34
Nain D, Haker R, Kikinis R, Grimson E (2001) An interactive virtual endoscopy tool. MICCAI, September 2001. http://www.ai.mit.edu/projects/medical-vision/virtual-endoscopy
Nakasato T, Katoh K, Ehara S et al (2000) Virtual CT endoscopy in determining safe surgical entrance points for paranasal mucoceles. J Comput Assist Tomogr 24:486–492
Neumann AM Jr, Pasquale-Niebles K, Bhuta T, Sillers MJ (1999) Image-guided transnasal endoscopic surgery of the paranasal sinuses and anterior skull base. Am J Rhinol 13:449–454
Paik DS, Beaulieu CF, Jeffrey RB, Rubin GD, Napel S (1998) Automated flight path planning for virtual endoscopy. Med Phys 25:629–637
Pandolfo I, Mazziotti S, Ascenti G et al (2004) Virtual endoscopy of the nasopharynx in the evaluation of its normal anatomy and alterations due to lymphoid hyperplasia: preliminary report. Eur Radiol 14:1882–1888
Raabe A, Krishnan R, Wolff R, Hermann E, Zimmermann M, Seifert V (2002) Laser surface scanning for patient registration in intracranial image-guided surgery. Neurosurgery 50:797–801; discussion 802–793
Rodt T, Ratiu P, Becker H et al (2002) 3D visualisation of the middle ear and adjacent structures using reconstructed multi-slice CT datasets, correlating 3D images and virtual endoscopy to the 2D cross-sectional images. Neuroradiology 44:783–790
Rogalla P, Nischwitz A, Gottschalk S, Huitema A, Kaschke O, Hamm B (1998) Virtual endoscopy of the nose and paranasal sinuses. Eur Radiol 8:946–950
Rosahl SK, Gharabaghi A, Hubbe U, Shahidi R, Samii M (2006) Virtual reality augmentation in skull base surgery. Skull Base 16:59–66
Rubin GD, Dake MD, Napel SA, McDonnell CH, Jeffrey RB Jr (1993) Three-dimensional spiral CT angiography of the abdomen: initial clinical experience. Radiology 186:147–152
Rudman DT, Stredney D, Sessanna D, Yagel R, Crawfis R, Heskamp D, Edmond CV Jr, Wiet GJ (1998) Functional endoscopic sinus surgery training simulator. Laryngoscope 108:1643–1647
Rusinek H, Mourino MR, Firooznia H, Weinreb JC, Chase NE (1989) Volumetric rendering of MR images. Radiology 171:269–272
Satava RM, Fried MP (2002) A methodology for objective assessment of errors: an example using an endoscopic sinus surgery simulator. Otolaryngol Clin North Am 35:1289–1301
Scharpf J, Dean R, Stultz T, Citardi MJ (2005) The magnetic resonance imaging profile of occult intracranial violations as a result of sinus surgery. Am J Otolaryngol 26:411–414

Seemann MD, Seemann O, Bonel H et al (1999) Evaluation of the middle and inner ear structures: comparison of hybrid rendering, virtual endoscopy and axial 2D source images. Eur Radiol 9:1851–1858

Seno S, Suzuki M, Sakurai H et al (2005) Image-guided endoscopic sinus surgery: a comparison of two navigation systems. Nippon Jibiinkoka Gakkai Kaiho 108:1101–1109

Shahidi R, Bax MR, Maurer CR Jr et al (2002) Implementation, calibration and accuracy testing of an image-enhanced endoscopy system. IEEE Trans Med Imaging 21:1524–1535

Shin H, Stamm G, Hogemann D, Galanski M (2000) Basic principles of data acquisition and data processing for construction of high quality virtual models. Radiologe 40:304–312

Snyderman C, Zimmer LA, Kassam A (2004) Sources of registration error with image guidance systems during endoscopic anterior cranial base surgery. Otolaryngol Head Neck Surg 131:145–149

Stammberger H, Posawetz W (1990) Functional endoscopic sinus surgery. Concept, indications and results of the Messerklinger technique. Eur Arch Otorhinolaryngol 247:63–76

Strauss G, Koulechov K, Rottger S et al (2006) Evaluation of a navigation system for ENT with surgical efficiency criteria. Laryngoscope 116:564–572

Su YX, Liao GQ, Kang Z, Zou Y (2006) Application of magnetic resonance virtual endoscopy as a presurgical procedure before sialoendoscopy. Laryngoscope 116:1899–1906

Suojanen JN, Regan F (1995) Spiral CT scanning of the paranasal sinuses. AJNR Am J Neuroradiol 16:787–789

Tabaee A, Kassenoff TL, Kacker A, Anand VK (2005) The efficacy of computer assisted surgery in the endoscopic management of cerebrospinal fluid rhinorrhea. Otolaryngol Head Neck Surg 133:936–943

Truppe MJ, Freysinger W, Gunkel AR, Thumfart WF (1996) Remote-guided surgical navigation in ENT surgery. Stud Health Technol Inform 29:280–282

Uribe JI, Ralph WM Jr, Glaser AY, Fried MP (2004) Learning curves, acquisition, and retention of skills trained with the endoscopic sinus surgery simulator. Am J Rhinol 18:87–92

Weber R, Keerl R, Hosemann W, Schauss F, Leuwer R, Draf W (1998) Complications with permanent damage in endonasal paranasal sinus operations--more frequent in experienced surgeons?. Laryngorhinootologie 77:398–401

Weiss F, Habermann CR, Welger J et al (2001) MRI in the preoperative diagnosis of chronic sinusitis: comparison with CT. Rofo;173:319–324

Wiet GJ, Yagel R, Stredney D et al (1997) A volumetric approach to virtual simulation of functional endoscopic sinus surgery. Stud Health Technol Inform 39:167–179

Wolfsberger S, Forster MT, Donat M et al (2004) Virtual endoscopy is a useful device for training and preoperative planning of transsphenoidal endoscopic pituitary surgery. Minim Invasive Neurosurg 47:214–220

Wolfsberger S, Neubauer A, Buhler K et al (2006) Advanced virtual endoscopy for endoscopic transsphenoidal pituitary surgery. Neurosurgery 59:1001–1009; discussion 1009–1010

Yamashita J, Yamauchi Y, Mochimaru M, Fukui Y, Yokoyama K (1999) Real-time 3-D model-based navigation system for endoscopic paranasal sinus surgery. IEEE Trans Biomed Eng 46:107–116

Zhang L, Chapman BE, Parker DL et al (2005) Automatic detection of three-dimensional vascular tree centerlines and bifurcations in high-resolution magnetic resonance angiography. Invest Radiol 40:661–671

Zinreich SJ (1998) Functional anatomy and computed tomography imaging of the paranasal sinuses. Am J Med Sci 316:2–12

Zinreich SJ, Kennedy DW, Malat J et al (1988) Fungal sinusitis: diagnosis with CT and MR imaging. Radiology 169:439–444

Dental and Maxillofacial Applications

12

Stephen J. Golding and Stephen R. Watt-Smith

CONTENTS

12.1 Introduction

Facial imaging is one of the areas that has been most influenced over the last two decades by the dramatic move of image processing from simple reformatting programmes to a wide range of complex post-processing methods designed to extract further information from image data. This development has been aided by significant falls in both processing times and cost of technology. The result in facial imaging is that some of these techniques are, or should be, regarded as routine in the clinical management of disease.

S. J. Golding, MD
Professor, Radiology Research Group, Nuffield Department of Surgery, University of Oxford, Oxford OX3 9DU,UK
S. R. Watt-Smith
Department of Maxillofacial Surgery, Oxford Radcliffe Hospital, Oxford, UK

This is now such a disparate field, including virtual reality and simulation of surgical procedures, that a general review cannot comprise a complete account. This chapter concentrates on the major applications which have been found to be of benefit in clinical practice. Dental and maxillary applications are not the most common in overall imaging practice but they represent areas where image processing has contributed significantly to the advancement of diagnostic and therapeutic capability.

The technical basis of image processing has been reviewed in preceding chapters. These principles are only referred to in the present chapter where there is a particular point of relevance to practice in this clinical speciality.

The applications of image processing in this area are almost entirely surgical, either in terms of diagnosis and planning surgical treatment, or monitoring its effects. The application of data processing to delivering radiation treatment is beyond the scope of this chapter.

Although most images processing techniques are now rapid and convenient, the time devoted to them still represents a resource. It is a golden rule of investigational medicine that this work should only be carried out if it is justified by change in clinical management (Golding and Watt-Smith 1999). This chapter describes those situations in which clinical management effect may be expected.

12.1.1 Technical Image Requirements

In dental and maxillofacial applications, Computed Tomography (CT) is the most frequently used imaging technique and 3D display the main objective. The development of these applications has been greatly facilitated by the growth of multislice CT (MSCT) acquisition. These developments have been described above in Chapters 3 and 6. Although technical factors vary according to the application, in

the great majority of uses the principal objective is to demonstrate differences between bone and soft tissues and therefore high resolution images, using thin section acquisition (1 mm or less) and high resolution reconstruction algorithms should be the norm.

It is now common for manufacturers of CT systems to include a range of post-processing options as standard in the workstations supplied with scanners. In the majority of instances these are suitable for common clinical applications. However more sophisticated applications may be expected from dedicated stand-alone or purpose-built systems (Chap. 9). For the purposes of 3D imaging in facial surgery the minimum requirement is high resolution 3D image processing with near real-time image rotation, accurate measure of dimensions in 3D, and computer scalpel facility (Golding and Watt-Smith 1999).

The recent introduction of cone-beam CT for facial and dental applications is an interesting development in this field. The technology is at an early stage of assessment but preliminary studies indicate that within this area of application its performance, both generally and in facial trauma, may be comparable to conventional MSCT in use (Heiland et al. 2004; Scarfe et al. 2006; Shi et al. 2006), with the attraction of dose efficiency (Tsiklakis et al. 2005; Ludlow et al. 2006).

12.1.2 Constraining Radiation Exposure

There is international concern about the rising contribution of CT to the cumulative radiation dose to the population (Golding and Shrimpton 2002; Golding 2005). CT delivers significant radiation exposure compared to other forms of imaging and care should always be exercised in its use in the face, where radiation of the optic lens and the thyroid gland are of particular concern. Many of the applications in this area are benign lesions in young patients, in whom radiation exposure constraint should be a matter of good practice. This is more important in the case of children, whose life expectancy allows more time for potential harmful effects of radiation to develop. Examinations should therefore be carefully contained to the essential area of the face and exposure factors should be manipulated to ensure that the radiation dose to the patient is kept to the minimum necessary to deliver an image quality that satisfies the diagnostic needs.

In high resolution CT of the face there is considerable exposure latitude and many post-processing programmes have a smoothing effect or otherwise highlight criteria, so that exposure can often be reduced to a fraction of that required for other diagnostic purposes. Our own exploration of the possibilities (publication forthcoming) has indicated that in routine diagnostic situations exposure may be reduced by up to two thirds and the work of ourselves and other work has indicated that in selected circumstances a 90% reduction is possible (Gholkar 1998). The replacement of CT by ultrasound and MRI is also a desirable objective where possible (Golding and Watt-Smith 1999), but as the routine requirement in this anatomical area is demonstration of bone with high spatial resolutions, reliance on CT appears probable for the foreseeable future.

12.2 Value of 3D Imaging in Maxillofacial Disease

Very soon after the introduction of 3D reformatting techniques it became clear that the face would be an important area of application. Vannier et al. (1984) drew attention to the value of 3D CT is displaying abnormal morphology of facial bone and soft tissues, predicting that this would facilitate surgical planning and provide quantitative post operative evaluation. The techniques were then primitive but the clinical indications were clear and this was supported by other researchers (Tessier and Hemmy 1986; Fishman et al. 1991; Hemmy et al. 1994; Zonneveld and Fukuta 1994). The principal applications were quickly established as trauma and the management of congenital or acquired facial deformity (Ray et al. 1993).

Initially there was some controversy as to whether 3D imaging added further diagnostic information. It was variously claimed that facial fractures were more likely to be found by 3D CT (Hunter et al. 1987) or that these were obscured by partial volume averaging and the smoothing inherent in most reformatting software (Burk et al. 1985). However it was generally felt that the principal value of 3D imaging was to communicate better the three dimensional

concepts of lesions between radiologists, who were accustomed to building such concepts from axial information and surgeons, who were not familiar with this (Golding 1989). Although diagnosis is rarely made by 3D imaging alone, overall evaluation is improved by this spatial information (Ray et al. 1993; Fox et al. 1995). Experience has now confirmed the intuitive nature of 3D anatomical imaging as it presents data envisaged by the surgeon both physically and mentally in a familiar format.

It is important, when surgical techniques are to be based on three-dimensional display, that spatial dimensions lie within surgical tolerance. It is now established that reliable reformatting programmes generate linear and volume measurements that accurately reflect physical craniometric dimensions (Cavalcanti et al. 1999a, 2004a; Jung et al. 2003). When introducing a service to the surgeon based on 3D imaging, quality assurance of this aspect is mandatory (Golding and Watt-Smith 1999).

A wide range of photorealistic display methods exist, ranging from mesh depiction through anatomically discrete methods such as surface rendering (SR) and volume rendering (VR) to holography (Ayoub et al. 1996). However in practice most applications will depend upon SR images in perspective display, or VR in transparency display. In our experience, appreciation of the information in 3D imaging is enhanced by employing visual cues evoked by image rotation; these give a greater perception of depth and of the spatial relationships of structures (Hamilton et al. 2001). Rotating display in which the image can be set to rotate automatically around an axis through approximately 180°, or by interactive control, in our experience increases the surgical utility of the technique.

There is particular value to importing three-dimensional information into the operating environment. When the facial soft tissues are retracted during surgery the surgeon loses some of the landmarks essential to natural positioning of the facial structures. We have found it valuable to include in the operating theatre monitors showing 3D images in rotating display to assist the surgeon in maintaining the view of these reference points (Golding and Watt-Smith 1999).

Although the value of 3D imaging to the surgeon is generally assumed, there have been relatively few studies attempting an objective evaluation. Experimental assessment has shown 3D to be superior to multiplanar reformatting in facial trauma with faster diagnostic assessment (Fox et al. 1995). In our own study surgeons performed more accurate readings on radiographs and 3D compared to axial CT, supporting the view that surgeons value 3D imaging as a front-line tool (Reuben et al. 2005). These studies have implications to surgical training.

A further clinical value of 3D imaging is in demonstrating and documenting postoperative result. 3D images may be helpful to demonstrate healing or position of bone grafts and for evaluating cosmetic result (Ray et al. 1993).

Facial surgery, particularly reparative and reconstructive approaches, often requires microvascular surgery to provide appropriate vascularisation to grafts. 3D CT – or MRI – angiography is beyond the scope of this chapter but in our experience provides an alternative to conventional angiography in preoperative evaluation.

12.2.1 Value of Physical Display in 3D Imaging

Although three-dimensional display was a major advance in evaluation of facial lesions and treatment planning, physical models may be key to achieving full three-dimensional simulation of the face (Ayoub et al. 1996; Cheung et al. 2002). Physical models provide a means of greater appreciation of the spatial characteristics of lesions, a significant advance for surgeons who deal with these physical characteristics in vivo.

Two major methods of producing models exist – stereolithography or lathe milling. The technical details for each are beyond the scope of this chapter but in essence stereolithography produces models by laser coagulation of light curing acrylic that grows sequentially as the laser traverses the shape. Milling cuts the model from a larger block of material (such as Dacron foam) from a number of axes and a number of projections. Although three axis mills are common, in practice five axis milling is more applicable to facial work in view of the complexity of the anatomy and the ability to create undercuts on the models (Shapiro 1996).

Physical models also offer a means of assisting facial reconstruction by acting as a template on which splints or prostheses can be modelled. This is particularly so where reconstruction of one side of the face is required following resection or other form of tissue loss. In these circumstances data from the controlateral healthy side may be superimposed on the image of the diseased side and used as a

reconstruction template after constructing a model from the combined data. Although faces are rarely symmetrical this is more likely to achieve closer to the patient's anatomy than a proprietary prosthesis. Pre-operative templates and bone plates have the added benefit not only of accuracy but saving significant time during long surgical procedures.

Fuhrmann et al. (1996) investigated the value of incorporating 3D models by milling or stereolithography into orthodontic and surgical diagnosis. They found this of value in replacing imprecise dental arches by dental casts and showed that 3D model surgery permitted verification of the feasibility of most suitable mobilisation and replacement techniques (Worrall and Christensen 2006).

An advanced approach to this use of 3D information is the construction from the patient's data of a customised prosthesis (Ray et al. 1993). This allows a replacement prosthesis to be adapted perfectly to the patient's own anatomy and has been developed for replacement of the temporomandibular joint in particular (Worrall and Christensen 2006).

12.2.2 Facial Trauma

The principal objectives of investigating the traumatised face are to establish the site of fracture lines and the spatial relationship between fragments and the bone of origin and adjacent structures. Although radiographs represent a valuable means of achieving both, in practice anything other than simple fractures such as those involving the nasal bones, are likely to require further investigation. Axial CT is unrivalled in demonstrating cortical fractures and the prime reason for carrying out 3D processing is to establish spatial distributions of fracture fragments in relation to the facial skeleton. This is well achieved by surface rendered 3D CT; it is unlikely that volume rendering has any added value (Fox et al. 1995; Rodt et al. 2006).

One of the two major uses of 3D CT of the face is trauma to the maxilla, orbit or mandible (Ray et al. 1993). In view of the objectives of surgical management, 3D imaging has its greatest impact where correction of fracture displacement is essential to obtaining a good functional and cosmetic result. This is most common in complex mid-facial fractures such as those of the zygomaticomaxillary complex, nasofrontal or nasoethmoid fractures and transfacial fractures and those of the mandible (Salvolini 2002). Gentry and Smoker (1985) have recommended that a classification of fractures based on the architectural struts of the face provides a good basis for an approach to management. Fractures may be classified as involving single or multiple struts; multiple strut fractures are further subdivided into transfacial separation or localised fractures. The spatial localisation of fragments in transfacial fractures is particularly important in restoring the shape of the face and also maintaining a normal bite but in all types of complex fracture 3D CT gives a good basis for planning symmetrical correction, including placing implants (Ray et al. 1993). The technique has been recommended for computer-assisted surgical correction (Kokoska and Citardi 2000).

Studies of the relative value of radiographs, axial CT and 3D have confirmed the crucial importance of 3D visualisation to comminuted and displaced mid facial fractures and also for comminuted mandibular fractures (Klenk and Kovacs 2004; Reuben et al. 2005; Saigal et al. 2005). A structured approach combining all techniques is likely to give the highest diagnostic yield and should be considered as routine (Remmler et al. 2001). Surgeons not only find 3D images more easy to assimilate but their diagnostic planning performance is superior when 3D CT is combined in imaging strategies (Reuben et al. 2005). 3D CT has additionally been recommended in forensic post mortem work (Salvolini 2002).

12.2.3 Facial Anomalies and Asymmetry

Planning surgery for a good functional and cosmetic result is an important use of 3D CT and there was early prediction of its value in evaluating craniofacial clefts, synostoses and other forms of asymmetry. The technique was recommended as the basis for a precise classification of anomalies and has the advantage of providing a permanent record for monitoring and documenting treatment (Hemmy et al. 1983).

In craniosynostosis 3D CT is an accurate technique for identifying normal and abnormal sutures (Altobelli et al. 1993; Tartaro et al. 1998; Medina 2000). The technique is likely to reveal subtleties of asymmetry which are not appreciated radiologically or on axial sections (Ray et al. 1993) and provides a valuable means of simulating the surgery of the anomaly by producing an operative plan for cor-

rection, with the ability to evaluate likely outcomes. It may also decrease operative time, and improve results, particularly by the facility to plan sites of osteotomy with accuracy (Ray et al. 1993). This facility extends to mathematical accuracy; Katsumata et al. (2005) have developed a coordinate point evaluation system to quantify facial asymmetry on 3D CT. In a recent report the use of a 3D Malformation Analysis, a three-dimensional methodology for planning craniofacial operative procedures was presented (Pelo et al. 2006). This helped provide additional surgical accuracy intra-operatively.

A new technique for generating bone specially in the mandible initially but later in the face followed the lead by a Ilizarov. Reports highlighted the difficulties in planning specifically related to the vectors produced by the existing distraction devices. Three-dimensional computer scans were used as a basis of planning and the difference between actual position and predicted position was attempted (Gateno et al. 2000). As the technique of distraction osteogenesis became more widespread on the face involving deformed face complexes and even the alveolar ridges ingenious methods of creating templates that aid exact positioning and vector control became popular (Gateno et al. 2003a,b; Poukens et al. 2003). Later three-dimensional virtual planning of orthognathic surgery became common place and this required 3D splints to produce accurate and anatomic 3D virtual augmented model of the skull with detail of the dental surfaces (Swennen et al. 2007). Greater sophistication with improved computer analysis and processing time has enabled software to become sufficient for three-dimensional computer aided surgical simulation (CASS) (Gateno et al. 2007; Zia et al. 2007). This may prove to be of greater clinical value as treatment by facial distraction becomes more established, even though distraction devices produce artefact which is likely to degrade the images (Molina 1999).

As this work frequently involves children in whom radiation exposure is a concern, there is a need to explore using other techniques such as MRI as a basis for planning treatment (Kleinheinz et al. 2000).

12.2.4 Maxillofacial Neoplasms

In patients presenting with facial neoplasms, either benign or malignant, diagnosis is likely to be established by clinical investigation, supplemented by radiographs and axial CT or MRI, and biopsy. The role of 3D imaging is more important in staging disease, particularly in neoplasms where surgery is the treatment of choice (Cavalcanti et al. 1999b).

The greatest use of the technique is in demonstrating areas of bony destruction where neoplasms involve the skeleton (Ray et al. 1993). Franca et al. (2000) have demonstrated the value of 3D display when staging head and neck cancer. They compared surface rendered CT with surface shading display (SSD), multiplanar reformatting (MPR), maximum intensity projection (MIP) and volume rendering (VR). MIP was useful for showing the patency of vessels and excluding compression by lesions. SSD and MPR together were felt valuable for demonstrating lymph node enlargement, whereas VR was superior at demonstrating soft tissue relationships of the primary tumour. The value of VR 3D CT has been confirmed by Cavalcanti and Antunes (2002), who showed that VR 3D CT was more reproducible and more sensitive than SR and that this extended to lesions with osseous involvement. 3D imaging may be an also valuable source of information concerning the volume of tumour, when localising lesions and monitoring the response to treatment (Cavalcanti et al. 2004b).

The difficulty inherent to visualisation of squamous cell carcinoma of the head and neck by current imaging is that invariably there are soft tissue and hard tissue components of the disease. MRI is undoubtedly superior for imaging soft tissues and CT for bone. The introduction of FDG PET has helped clinicians to identify the inherent problem of the unknown primary. However it wasn't until co-registration with CT that more accurate analysis of the position was obtained. Analyses of PET/CT vs contrast-enhanced CT (Chen AY et al. 2006), the use of PET/CT to improve accuracy of initial cervical nodal staging (Jeong et al. 2007) and the use of PET/CT for staging as well as surveillance of difficult areas such as skull base tumours have all been recently reported (Gil et al. 2007).

The use of PET/CT for post treatment assessment of the primary modality of either radiation or surgery or combination has aided the clinician's ability to make informative predictions on the possibility of early and late recurrence of the disease (Yao et al. 2005). Certainly PET CT has a higher specificity and overall diagnostic performance than CT alone in this case (Andrade et al. 2006).

Lymphoscintigraphy and sentinel node biopsy is a minimally invasive technique that samples first echelon lymph nodes and predicts the need of more extensive neck dissection. The accuracy has been assessed on oral cancers undergoing preoperative PET/CT followed by sentinel node biopsy (Civantos et al. 2003). Gross tumour replacement of lymph nodes and redirection of lymphatic flow represented a significant technical issue in oral carcinomas (Civantos et al. 2006).

12.2.5 Temporomandibular Joint Disease

Internal derangement of the temporomandibular joint is conventionally investigated by MRI, with the objective of demonstrating abnormalities of the meniscus and its relationship to the joint surfaces. 3D imaging has a contribution to make in more severe stages of joint disorganisation and degeneration, and in trauma.

In degenerative lesions this technique may be used to demonstrate bony ankylosis, and destructional deformity of the mandibular head or the joint fossa (Ray et al. 1993).

Fractures of the mandible head or neck carry a particular risk of cosmetic deformity and abnormal bite if not corrected into acceptable anatomical position. 3D CT is used, as in other examples of facial trauma, to display the spatial distribution of the fragments and their relation to the joint (Salvolini 2002). Mal-alignment of the mandibular condyle is particularly important to demonstrate or exclude, as are those fractures classed as "unfavourable" for stabilisation because of opposing muscle pull; these fractures require operative fixation. Post operative imaging may be helpful to confirm satisfactory positioning, or placement of bone grafts, and healing (Ray et al. 1993).

New techniques in imaging the temporomandibular joints have involved comparisons between single and multislice CT and the comparison of panoramic radiography and panoramic digital subtraction radiography in an attempt to detect osteophytic lesions. All CT imaging protocols were considered accurate for mandibular condyle lesion assessment and multiplanar reconstructions (MPR) using the multislice CT demonstrated the highest accuracy (Cara et al. 2007). Digital subtraction radiography improved detection accuracy of simulated and actual osteophytes (Masood et al. 2002).

12.3 Image Processing in Dental Implant Therapy

Surgical implant treatment has been a major advance in restorative dentistry and has produced software programmes designed to assist the surgeon in accurate placement of implants.

This technique is based on high resolution axial CT sections through the maxillary or mandibular alveolus and body. In essence the technique is a modified form of multiplanar reformatting, designed to create oblique sagittal sections of the teeth-bearing bone in the plane perpendicular to the curve of the alveolus. The line of the alveolus is defined manually and the software programme reconstructs the oblique sagittal sections. Good display can be obtained at low exposure (Abrahams 2001; Gahleitner et al. 2003) and cone-beam CT dedicated to dental work offers an alternative at lower cost and reduced radiation exposure (Scarfe et al. 2006; Shi et al. 2006; Tantanopornkul et al. 2007).

The software allows oblique sagittal sections which may be only 1 or 2 mm apart and enables accurate positioning of implants in edentulous areas. Images permit the assessment of the bone stock, both width and depth, the position of the neurovascular canal and the quality of the supporting bone. Cortical bone, which affects primary stability, and cancellous bone, which is important for long term stability, can be evaluated by a grading system (Cawood and Howell 2003; Lekholm and Zarb 2003). An important facility of this technique is the ability to produce life-sized images by choosing imaging parameters appropriately; these permit direct measurements to be made from printed images.

The software provides axial section localisation for the oblique sagittal images for planning the position of implants. In addition programmes can create panoramic views which are in essence sectional images analogous to orthopantomograms. These can usually be supplied several millimetres apart through the width of the mandible and maxillary alveolus and these also assist in evaluating bone stock for implantation.

Technological advances have made use of CT scans and sterolithographic model-making to provide surgical templates for the placement of dental implants in complicated cases (Sarment et al. 2003). The accuracy of such implant placement using such

techniques has been assessed to be a useful tool (Sarment et al. 2003; Widmann et al. 2006). Such computerized tomography imaging assesses both height, density and width of bone and such valuable clinical information as axis of orientation of the implant and prosthetic replacement (Almog et al. 2006).

Images produced from dental implant processing have been found clinically valuable in other applications. In dental inflammatory disease the images provide detailed evaluation of the dental root and periodontal bone, so that detection and staging of root abscess becomes more accurate (Abrahams 2001) and the technique compares favourably with orthopantomography and orthodental panoramic tomography (Murray and Whyte 2002). Oroantral fistulas are more readily demonstrated and this technique has lead to greater appreciation of the frequency of such lesions (Abrahams 2001).

Au-Yeung et al. (2001) have demonstrated the value of these images in assessing the penetration of squamous carcinoma of the mouth along the periodontal membrane and the approach has also been recommended for evaluating endodontal disease (Abrahams 2001). The technique may be regarded as a more sensitive alternative to conventional dental radiography in evaluating neoplasms, dentally- related cysts, impacted teeth and root fractures (Gahleitner et al. 2003).

12.4 Maxillofacial Image Fusion

As image processing and multi-modality investigation became established in maxillofacial disease the value of fusing or co-registering different imaging modalities, especially for the purpose of combining displays of bone and soft tissue, became clear (Levin et al. 1998; Woods et al. 1993; Ray et al. 1993). This is a fertile area for research and the general principles have been described in Chapter 8. In dental and maxillofacial work the approach is most likely to be used in the investigation of neoplasms and other forms of primary soft tissue disease.

Although 3D CT has proved to be of considerable value in facial surgery, its principal drawback is that it provides relatively poor resolution of soft tissues. In these circumstances, the facility to co-register demonstration of bone by CT with a technique of superior resolution of soft tissues, such as MRI, appears to have clear value in providing a comprehensive display of disease, combining the advantages of image processing in both techniques (Kleinheinz et al. 2000). The possibility of using combined image data to guide surgery stereoscopically appears particularly promising (Hernes et al. 2003).

Strumas et al. (2003) investigated multimodality image registration in craniofacial osteomyelitis, using SPECT and high resolution CT, concluding that this approach provided a valuable method of relating skeletal anatomy and physiology and was valuable in planning and monitoring treatment in conditions where bone turnover was abnormal.

Positron emission tomography (PET) is becoming established as a valuable means of demonstrating neoplasm and metastases in the face and neck (Ng et al. 2005). The technique is highly sensitive to metabolism in neoplasms but suffers from poor anatomical localisation. For these reasons the combination of PET and CT as a combined investigation, with co-registering of the data, appears likely to make a major impact in the evaluation of craniofacial neoplasms in the future (Goerres et al. 2006; Schoder et al. 2006).

12.5 Future Trends and Developments

In general, most of the imaging techniques described in this chapter have been shown to be accurate and reliable in clinical practice. However, research and development in this area is active and techniques continue to develop rapidly. In these circumstances it is important that quality assurance programmes are established for any technique that is incorporated into clinical practice as a routine (Golding and Watt-Smith 1999).

An interesting issue is who should be responsible for conducting the image processing. In other forms of image processing the radiologist who has generated the source examination carries out the processing in order to elucidate their examination. In maxillofacial work processed images may relate more closely to the practice of the surgeon, who may therefore be better informed to explore them, especially if this requires interaction with the software programme or simulation of the proposed surgery

or its cosmetic result. Image data can now be readily transferred by imaging networks, facilitating this approach. There are clear implications to quality assurance and surgical training, as this work must be carried out reliably and there must be no loss of information in the data transfer.

The potential of computer aided surgery appears particularly promising, as has been demonstrated in neurosurgery (Giorgi et al. 1990; Xia et al. 2000; Hayashi et al. 2001). Quality assurance is clearly a key factor in establishing the adjunct to conventional surgery (Vannier 2000).

In general, the role of these applications of imaging processing does not appear to have been explored significantly in teaching. 3D imaging techniques in particular offer advantages in communicating both normal and pathological anatomy, particularly important in areas of anatomical complexity and where the range of potential lesions is wide, as is so in the face. Facial image processing has also been used in archaeology to mould facial characteristics around skeletal remains, and in forensic medicine in attempts to develop a likeness of an individual from their skeleton (Claes et al. 2006; Vandermeulen et al. 2006). This approach may have an impact on the principle of informed consent in facial surgery; when technology has the ability to demonstrate to a patient the likely appearance of their features following surgery, it arguably becomes unacceptable to carry out significant operative intervention without first giving the patient simulation of the result (Chen and Chen 1999).

Overall, maxillofacial image processing has made significant impact in practice. However its development has clearly not yet reached a peak and further clinical benefits are to be anticipated in the future.

References

Abrahams J (2001) Dental CT imaging a look at the jaw. Radiology 334–345

Altobelli DE, Kikinis R, Mulliken JB, Cline H, Lorensen W, Jolesz F (1993) Computer-assisted three-dimensional planning in craniofacial surgery. Plast Reconstr Surg 92:576–585

Andrade RS, Heron DE, Degirmenci B, Filho PA, Branstetter BF, Seethala RR, Ferris RL, Avril N (2006) Post treatment assessment of response using FDG-PET/CT for patients treated with definiteive radiation therapy for head and neck cancers. Int J Radiat Oncol Biol Phys 65:1315–1322

Au Yeung KM, Ahuja AT, Ching ASC, Metreweli C (2001) Dentascan in oral imaging. Clin Radiol 700–713

Ayoub AF, Wray D, Moos K, Siebert P, Jin J, Niblett TB, Urquhart C, Mowforth P (1996)Three dimensional modelling for modern diagnosis and planning in maxillofacial surgery. Int J Adult Orthod Orthognath Surg 11:225–233

Burk DL et al. (1985) Three-dimensional computed tomography of acetabular fractures. Radiology 183–186

Cara AC, Gaia BF, Perrella A, Oliveira JX, Lopes PM, Cavalcanti MG (2007) Validity of single and multislice CT for assessment of mandibular condyle lesions. Dentomaxillofac Radiol 36:24–27

Cavalcanti MG, Antunes JL (2002) 3D-CT imaging processing for qualitative and quantitative analysis of maxillofacial cyst and tumours. Pesqui Odontal Bras 16:198–194

Cavalcanti MG, Haller JW, Vannier MW (1999a) Three-dimensional computed tomography landmark measurement in craniofacial surgical planning: experimental validation in vitro. J Oral Maxillofac Surg 57:690–694

Cavalcanti MG, Ruprecht A, Quets J (1999b) Progression of maxillofacial squamous cell carcinoma evaluated using computer graphics with spiral computed tomography. Dentomaxillofac Radiol 28:238–244

Cavalcanti MG, Rocha SS, Vannier MW (2004a) Craniofacial measurements based on 3D-CT volume rendering: implications for clinical applications. Dentomaxillofac Radiol 33:170–176

Cavalcanti MG, Santos DT, Perrella A, Vannier MW (2004b) CT-based analysis of malignant tumour volume and localisation. A preliminary study. Odontal Bras 18:338–344

Cawood JI, Howell RA (2003) A classification if the edentulous jaws. Intl J Oral Maxillofac Surg 232–236

Chen AY, Vilaseca I, Hudgins PA, Schuster D, Halkar R (2006) PET-CT vs contrast enhanced CT: what is the role for each after chemoradiation for advanced oropharyngeal cancer? Head Neck 28:487–495

Chen LH, Chen WH (1999) Three-dimensional computer-assisted simulation combining facial skeleton with facial morphology for orthognathic surgery. Int J Adult Orthodon Orthognath Surg 14:140–145

Cheung LK, Wong MC, Wong LL (2002) Refinement of facial reconstructive surgery by stereo-model planning. Ann R Australas Coll Dent Surg 16:129–132

Civantos FJ, Gomez C, Duque C, Pedrosos F, Goodwin WJ, Weed DT, Arnold D, Moffat F (2003) Sentinel node biopsy in oral cavity cancer: correlation with PET scan and immunohistochemistry. Head Neck 25:1–9

Civantos FJ, Moffat FL, Goodwin WJ (2006) Lymphatic mapping and sentinel lymphadenectomy for 106 head and neck lesions: contrasts between oral cavity and cutaneous malignancy. Larynoscope 112:1–15

Claes P, Vandermeulen D, De Greef S, Willems G (2006) Craniofacial reconstruction using a combined statistical model of face shape and soft tissue depths: methodology and validation. Forensic Sci Int 15:159

Fishman EK, Magid D, Neys D, Chaney E, Pizer S, Rosenman J, Levin D, Vannier M, Kuhlman J, Robertson D (1991) Three-dimensional imaging. Radiology 321–337

Fox LA, Vannier MW, West OC, Wilson AJ, Baran GA, Pilgram TK (1995) Diagnostic performance of CT, MPR and 3DCT imaging in maxillofacial trauma. Comput Med Imaging Graph 19:385–395

Franca C, Levin-Plotnik D, Sehgal V, Chen GT, Ramsey RG (2000) Use of three-dimensional spiral computed tomography imaging for staging and surgical planning of head and neck cancer. J Digital Imag 13:24–32

Fuhrmann R, Feifel H, Schnappauf A, Diedrich P (1996) Integration of three-dimensional cephalometry and 3D-skull models in combined orthodontic/surgical treatment planning. J Orofac Orthop 57:32–45

Gahleitner A, Watzek G, Imhof H (2003) Dental CT: imaging technique, anatomy, and pathological conditions of the jaws. Eur Radiol 366–376

Gateno J, Allen ME, Teichgraeber JF, Messersmith ML (2000) An in vitro study of the accuracy of a new protocol for planning distraction osteogenesis of the mandible. J Oral Maxillofac Surg 58:985–990

Gateno J, Xia J, Teichgraeber JF, Rosen A (2003a) A new technique for the creation of a computerized composite skull model. J Oral Maxillofac Surg 61:222–227

Gateno J, Xia J, Teichgraeber JF, Rosen A, Hultgren B, Vadnais T (2003b) The precision of computer-generated surgical splints. J Oral Maxillofac Surg 61:814–817

Gateno J, Xia JJ, Teichgraeber JF, Christensen AM, Lemoine JJ, Liebschner MA, Giddon MJ, Briggs ME (2007) Clinical feasibility of computer-aided surgical simulation (CASS) in the treatment of complex cranio-maxillofacial deformities. J Oral Maxillofac Surg 65:728–734

Gentry LR, Smoker WRK (1985) Computed tomography of facial trauma. Semin Ultrasound CT MR 6:129–145

Gholkar A (1988) Dynamic low-dose three-dimensional computed tomography: a preliminary study. Br J Radiol 1095–1099

Gil Z, Even-Sapir E, Margalit N, Fliss DM (2007) Integrated PET/CT system for staging and surveillance of skull base tumours. Head Neck 29:537–545

Giorgi C, Casolino DS, Ongania E, Franzini A, Broggi G, Pluchino F (1990) Guided microsurgery by computer-assisted three-dimensional analysis of neuroanatomical data stereotactically acquired. Stereotact Funct Neurosurg 54:482–487

Goerres GW, Schmid DT, Schuknecht B, Eyrich GK (2006) Bone invasion in patients with oral cavity cancer: comparison of conventional CT with PET/CT and SPECT/CT. Radiology

Golding SJ (1989) (Unnattrib) Three dimensional computed tomography. Lancet 1080

Golding SJ.(2005) Multislice Computed Tomography (MSCT): the dose challenge of the new revolution. Radiat Protect Dosim 114:303–307

Golding SJ, Shrimpton PC (2002) Radiation dose in CT; are we meeting the challenge? Br J Radiol 75:1–4

Golding SJ, Watt-Smith SR (1999) Issues in the 3D imaging-clinical surgery interface. In: Lemke H, Vannaier M, Inamura K, Farman AG (eds). Computed assisted radiology and surgery. Elsevier, Amsterdam, pp 321–325

Hamilton G et al (2001) Evaluation of the role of image rotation in visual analysis of 3D images. UKRC 2001, Programme and Abstracts. British Institute of Radiology

Hardy JE, Dodds SR, Roberts AD (1996) An objective evaluation of the effectiveness of different methods of displaying three-dimensional information with medical X-ray images. Investigative Radiology 31:433–445

Hayashi N, Kurimoto M, Hirashima Y, Ikeda H, Shibata T, Tomita T, Endo S (2001) Efficacy of navigation in skull base surgery using composite computer graphics of magnetic resonance and computer tomography images. Neurol Med Chir 41:335–339

Heiland M, Schmelzle R, Hebecker A, Schulze D (2004) Intraoperative 3D imaging of the facial skeleton using the SIRE-MOBIL Iso-C3D. Dentomaxillofac Radiol 33:130–132

Hemmy DC, David DJ, Herman G (1983) Three-dimensional reconstruction of craniofacial deformity using computed tomography. Neurosurgery 534–541

Hemmy DC, Zonneveld F, Lobregt S, Fukuta K (1994) A decade of clinical three-dimensional imaging: a review. Investig Radiol 489–495

Hernes TA, Ommedal S, Lie T, Lindseth F, Lango T, Unsgaard G (2003) Steroscopic navigation-controlled display of preoperative MRI and intraoperative 3D ultrasound in planning and guidance of neurosurgery: new technology for minimally invasive image-guided surgery approaches. Minim Invasive Neurosurg 46:129–137

Hunter JC et al. (1987) Three dimensional CT imaging of the lumbar spine. Genant HK (ed). Spine update

Jeong HS, Baek CH, Son YI, Chung M, Kyung LD, Young CJ, Kim BT, Kim HJ (2007) Use of integrated 18F-FDG PET/CT to improve the accuracy of initial cervical nodal evaluation in patients with head and neck squamous cell carcinoma. Head Neck 29:203–210

Jung H, Kim D, Hong S, Kang W, Lee S, Kim K, Kim H (2003) Quantitative evaluation of 3D volume-rendered image of human skull using multidetector CT in the assessment of distance measurements. Eur Radiol 13(suppl):547

Katsumata A, Fujishita M, Maeda M, Ariji E, Langlais RP (2005) 3D-CT evaluation of facial asymmetry. Oral Surg Oral Med Oral Pathol Oral Radiol Endod 99(2):212–220

Kleinheinz J, Stamm T, Meier N, Wiesmann HP, Ehmer U, Joos U (2000) Three-dimensional magnetic resonance imaging of the orbit in craniofacial malformations and trauma. Int J Adult Orthodon Orthognath Surg 15:64–68

Klenk G, Kovacs A (2004) Do we need three-dimensional computed tomography in maxillofacial surgery? J Craniofac Surg 15:842–850

Kokoska M S, Citardi MJ (2000) Computer-aided surgical reduction of facial fractures. Fac Plast Surg 16:169–179

Lekholm U, Zarb GA (2003) Patient selection and preparation. Osseointegration Clin Dentistry 199–209

Levin DN, Pelizzari C, Chen G, Chen C, Cooper M (1998) Retrospective geometric correlation of MR, CT and PET images. Radiology 817–823

Ludlow JB, Davies-Ludlow LE, Brooks SL, Howerton WB (2006) Dosimetry of 3 CBCT devices for oral and maxillofacial radiology: CB Mercuray, NewTom 3G and i-CAT. Dentomaxillofac Radiol 35:219–226

Masood F, Katz JO, Hardman PK, Glaros AG, Spencer P (2002) Comparison of panoramic radiography and panoramic digital subtraction radiography in the detection of simulated osteophytic lesions of the mandibular condyle. Oral Surg Oral Med Oral Pathol Oral Radiol Endod 93:626–631

Medina LS (2000) Three-dimensional CT maximum intensity projections of the calvaria: a new approach for diagnosis of craniosynostosis and fractures. Am J Neuroradiol 21:1951–1954

Molina F (1999) Combined maxillary and mandibular distraction osteogenesis. Semin Orthod 5:41–45

Murray D, Whyte A (2002) Dental panoramic tomography: what the general radiologist needs to know. Clin Radiol 1–7

Ng SH, Yen TC, Liao CT, Chang JT, Chan SC, Ko SF, Wang HM, Wong HF (2005) 18F-FDG PET and CT/MRI in oral cavity squamous cell carcinoma: a prospective study of 124 patients with histologic correlation. J Nucl Med. 46:1136–1143

Pelo S, Tassiello S, Boniello R, Gasparini G, Longobardi G (2006) A new method for assessment of craniofacial malformations. J Craniofac Surg 17:1035–1039

Poukens J, Haex J, Riediger D (2003) The use of rapid prototyping in the preoperative planning of distraction osteogenesis of the cranio-maxillofacial skeleton. Comput Aided Surg 8:146–154

Ray CE, Mahmood F, Friedman M, Tahmoressa C (1993) Applications of three-dimensional CT imaging in head and neck pathology. Radiol Clin North Am 181–194

Remmler D, Denny A, Gosain A, Sibichin S (2001) Role of three-dimensional computed tomography in the assessment of naso-orbitoethmoidal fractures. Ann Plast Surg 46:191

Reuben A, Watt-Smith SR, Dobson D, Golding SJ (2005) A comparative study of evaluation of radiographs, CT and 3D reformatted CT in facial trauma: what is the role of 3D? Br J Radiol 78:198–201

Rodt T, Bartling SO, Zajaczek JE, Vafa MA, Kapapa T, Majdani O, Krauss JK, Zumkeller M, Matties H, Becker H, Kaminsky J (2006) Evaluation of surface and volume rendering in 3D-CT of facial fractures. Dentomaxillofac Radiol 35:227–231

Saigal K, Winokur RS, Finden S, Taub D, Pribitkin E (2005) Use of three-dimensional computerized tomography reconstruction in complex facial trauma. Fac Plast Surg 21:214–220

Salvolini U (2002) Traumatic injuries: imaging of facial injuries. Eur Radiol 1253–1261

Sarment DP, Al-Shammari K, Kazor CE (2003) Stereolithographic surgical templates for placement of dental implants in complex cases. Int J Periodontics Restorative Dent 23:287–295

Scarfe WC, Farmen AG, Sukovic P (2006) Clinical applications of cone-beam computed tomography in dental practice. J Can Dent Assoc 72:75–80

Schoder H, Carlson DL, Kraus DH, Stambuk HE, Gonen M, Erdi YE, Yeung HW, Huvos AG, Shah JP, Larson SM, Wong RJ (2006) PET/CT for detecting nodal metastases in patients with oral cancer staged N0 by clinical examination and CT/MRI. Nucl Med 47:755–762

Shapiro LB (1996) Three dimensional processing and display of MRI and CT image data: applications in surgery and radiology. Doctor of Philosophy thesis, University of Oxford

Shi H, Scarfe W, Farman A (2006) Maxillary sinus 3D segmentation of reconstruction from cone beam CT data sheets. Intl J CARS 83–89

Strumas N, Antonyshyn O, Caldwell CB, Mainprize J (2003) Multimodality imaging for precise localization of craniofacial osteomyelitis. J Craniofacial Surg 14:215–219

Swennen GR, Barth EL, Eulzer C, Schutyser F (2007) The use of a new 3D splint and double CT scan procedure to obtain an accurate anatomic virtual augmented model of the skull. Int J Oral Maxillofac Surg 36:146–152

Tantanapornkul W, Okouchi K, Fujiwara Y, Yamashiro M, Maruoka Y, Ohbayashi N, Kurabayashi T (2007) A comparative study of cone-beam computed tomography and conventional panoramic radiography in assessing the topographic relationship between the mandibular canal and impacted third molars. Oral Surg Oral Med Oral Pathol Oral Radiol Endod 103:253–259

Tartaro A, Larici AR, Antonucci D, Merlino B, Colosimo C, Bonomo L (1998) Optimisation and diagnostic accuracy of computerised tomography with tridimensional spiral technique in the study of craniostenosis. Radiol Med (Torino) 96:10–17

Tsiklakis K, Donta C, Gavala S, Karayianna K, Kamenopoulou V, Hourdakis CJ (2005) Dose reduction in maxillofacial imaging using low dose cone beam CT. Eur J Radiol 56:413–417

Tessier P, Hemmy D (1986) Three dimensional imaging in medicine. Scand J Plast Reconstr Surg 3–11

Vandermeulen D, Claes P, Loeckx D, Suetens P (2006) Computerized craniofacial reconstruction using CT-derived implicit surface presentations. Foren Sci Int 15:159

Vannier MW (2000) Evaluation of 3D imaging. Crit Rev Diagn Imaging 41:315–378

Vannier MW, Marsh JL, Warren JO (1984) Three dimensional CT reconstruction images for craniofacial surgical planning and evaluation. Radiology 179–184

Woods RP, Mazziotta J, Cherry S (1993) MRI-PET Registration with automated algorithm. J Comput Assist Tomogr 17:536–546

Worrall SF, Christensen RW (2006) Alloplastic reconstruction of the temporomandibular joint in treatment of craniofacial developmental or congenital anomalies: a surgical case report. Surg Technol Int 15:291–301

Xia J, Samman N, Yeung RW, Wang D, Shen SG, Ip HH, Tideman H (2000) Computer-assisted three-dimensional surgical planning and simulation. 3D soft tissue planning and prediction. Int J Oral Maxillofac Surg 29:250–258

Yao M, Smith RB, Graham MM, Hoffman HT, Tan H, Funk GF, Graham SM, Chang K, Dornfield KJ, Menda Y, Buatti JM (2005) The role of FDG PET in management of neck metastasis from head-and-neck cancer after definitive radiation treatment. Int J Radiat Oncol Biol Phys 65:991–999

Zonneveld FW, Fukuta K (1994) A decade of clinical three-dimensional imaging: a review. Investig Radiol 574–589

Virtual Laryngoscopy

13

Joachim Kettenbach, Wolfgang Birkfellner, Erich Sorantin, and Andrik J. Aschoff

CONTENTS

J. Kettenbach, MD
Associate Professor, Division of Cardiovascular and Interventional Radiology, Department of Radiology, Medical University of Vienna, Waehringer Guertel 18–20, 1090 Vienna, Austria
W. Birkfellner, PhD
Associate Professor, Department of Biomedical Engineering and Physics, University of Vienna, General Hospital Vienna, Waehringer Guertel 18–20, 1090 Vienna, Austria
E. Sorantin, MD
Associate Professor, Department of Radiology, Medical University Graz, Auenbruggerplatz 9, 8036 Graz, Austria
A. J. Aschoff, MD
Full Professor, Department of Diagnostic and Interventional Radiology, University Clinic of Ulm, Steinhövelstrasse 9, 89075 Ulm, Germany

13.1 Introduction

Conventional endoscopy is currently the gold standard for evaluation of the upper airways, such as the larynx or the tracheal lumen. Rigid endoscopes, however, require general anesthesia, which may limit clinical application in high-risk patients, whereas flexible endoscopy depends on a cooperative patient and on a very experienced endoscopist. Furthermore, congenital anomalies or acquired stenoses may inhibit passage of the endoscope. In addition, viewing is limited strictly to the lumen, which limits the transmural evaluation of lesions. Cross-sectional imaging, using spiral computed-tomography (CT) or magnetic resonance imaging (MRI) and postprocessing of imaging data sets, may offer an additional evaluation tool for those difficult clinical situations and provide additional information about the larynx that cannot be obtained with laryngoscopy. Multiplanar reformations (MPRs), shaded surface displays (SSDs), or three-dimensional (3D) reconstructions have been the subject of research in otolaryngology-head and neck surgery (Altobelli et al. 1993; Cline et al. 1987; Eisele et al. 1994; Girod et al. 1995; Kerberle et al. 2003; Korves et al. 1995; Marsh and Vannier 1983; Schubert et al. 1996; Vannier and Marsh 1996). With these techniques, the radiologist can identify pathological findings for the clinician using several essential images without having to display all axial slices. The specific advantages of MPRs, SSDs, and 3D reconstructions are summarized in Table 13.1. Advances in imaging technology and improvements in computer technology now provide a new 3D display and visualization tool: virtual endoscopy (VE) (Eisele et al. 1994; Frankenthaler et al. 1998; Fried et al. 1997; Jolesz et al. 1997; Magnusson et al. 1991; Rodenwaldt et al. 1997; Rosenberg et al. 1994; Rubin et al. 1996; Schenck et al. 1995; Valvassori 1994; Vining 1996). Virtual laryngoscopy (VL), in particular, describes a visualization technique that

Table 13.1. Specific advantages of multiplanar reformation, shaded surface display, and color-coded 3D reformations

Multiplanar reformation (MPR)	Delineates structures that may be overlooked with axial slices (often due to partial volume effects) Coronal MPRs ideal to show whether a tumor crosses the midline
Shaded surface display (SSD)	Well-suited for visualizing dense tissue, such as bones or bone transplants, but not for soft tissue or tumors of the hypopharynx or larynx Helpful if there is extensive bony destruction of the skull, spine, hyoid, or larynx skeleton
Color-coded 3D reformations	Good depiction of spatial relation between extensive tumors and great vessels, bone, and lymph nodes, etc. Advantageous in extensive tumors that invade the surrounding structures (very useful for developing a cooperative surgical strategy or treatment plan

uses computer processing of imaging data sets, such as from spiral CT, multi-slice detector CT (MSCT) scans, or MRI. This provides an interactive visualization of the individual laryngeal anatomy similar or equivalent to that produced with standard endoscopic procedures (Robb 2000). To date, the colon, bronchi, ear, and other organs (Aquino and Vining 1999; Assimos and Vining 2001; Frankenthaler et al. 1998; Jolesz et al. 1997) have been evaluated with virtual endoscopy. When the progression of the endoscope is limited, as in the case of a difficult airway (stenosis), VL is advantageous. This is particularly true in high-risk patients with non-passable stenoses or in postoperative examinations if no biopsies are required (Table 13.2). Furthermore, VL should be particularly helpful during assessment of the difficult airway, when neoplasm, infection, inflammation, and congenital defects compromise the lumen. In addition, VL generated from a patient's anatomy, and based on the individual's CT and MRI data, allows navigation through the reconstruction, simulating a traditional endoscopic technique. A concomitant display of the global view, and a view of the related CT or MR slice, may provide information beyond traditional endoscopy in localizing and analyzing tissue. In this chapter, we will provide an overview of the key historical developments of virtual laryngoscopy, clinical applications using CT and MR imaging, and applications using a navigational system to enhance the physician's skills.

Table 13.2. Specific features of conventional and virtual laryngoscopy

Conventional laryngoscopy	Virtual laryngoscopy
No assessment beyond passage of endoscope if lumen is compromised	Assessment of regions inaccessible with standard endoscopic procedures, especially in high-risk patients
Invasive, requires sedation, risk of perforation.	Noninvasive, does not require sedation. Can be repeated as often as needed
High-resolution visualization strictly limited to the laryngeal lumen and mucous surface	Three-dimensional (3D) information on anatomical structures and pathologic processes beyond the mucosal surface demonstrates the extent of disease, as well as the involvement of surrounding vessels
Only frontal viewing angle	Variable angulation and viewing angle
Interactive	Provides more degrees of freedom regarding motion than conventional endoscope (e.g., backward views)
Enables intervention (biopsy, lavage)	Image-guided intervention if combined with a tracking system
Good differentiation between tumor and mucous impact; color and mucous appearance depicted	VE most accurate in evaluation of subglottic and nasopharyngeal anatomy
No radiation	Quantitative measurements in all viewing projections

13.2 Image Acquisition

All CT or MRI techniques that provide high-resolution, cross-sectional images, or volumetric data acquisition, can be post-processed to obtain 3D reconstructions and VL.

13.2.1 Computer Tomography (CT)

In early studies, a CT dataset with a 3-mm collimation and a pitch of 1:1 or larger was commonly used to cover larger imaging volumes, such as the entire tracheobronchial tree (Aschoff et al. 1998; Ferretti et al. 1996; Greess et al. 2000). This protocol limited the delineation of structures smaller than the slice thickness. However, spiral CT is now standard for imaging the larynx and optimum-quality axial slices can be obtained with a collimation of 1 mm and a pitch of 1 (Rodenwaldt et al. 1997). Spiral CT using a single-slice detector, however, limits the total length of the imaging volume within a single breathhold. The greatest advantages of MSCT are speed, improved detector efficiency, and the heat capacity of the X-ray tubes, which overcome the limitation of single-slice CT. Using a „conventional" single-slice spiral CT, a reasonable longitudinal coverage of the anatomical structures can be obtained with a collimation ≤ 3 mm, a pitch ≥ 1.5, and an overlapping reconstruction increment (2–3 mm). This allows a good correlation between virtual endoscopy and anatomical findings (Baum et al. 2000). Rodenwaldt et al. (1997) found that adequate quality was obtained with a collimation of 3 mm with a pitch up to 2 or a collimation of 5 mm with a pitch of 1 (Table 13.3). Any combination with larger parameters caused poor-quality axial slices . Using a collimation of 1 mm, a decreased pitch under 3, and overlapping reconstructions of 80%, expansive helical artifacts by the inner surface-rendering were documented. These "stairstep" artifacts may have resulted from the interpolation geometry associated with high contrast interfaces (Rodenwaldt et al. 1997). The authors also stated that the upper limit for the generation of a 3D model for VL was a collimation of 7 mm and a pitch of 0.5. The progressive partial volume effect did not allow increasing the product of collimation and pitch without losing adequate quality. The quality of the inner surface visualization also increased up to an overlap of 80% on the retrospectively generated overlapping reconstructions. However, a higher amount of overlap had no effect, and wasted time and computer capacity as well. For optimum tissue contrast, a volume of 150 mL contrast medium, a flow of 2.5 mL/s, and a start delay of 70–80 s are necessary. To visualize the carotid artery, a start delay of 20 s is recommended. Dynamic enhanced CT is only necessary in certain special cases, such as when a glomus tumor is suspected. Patients are advised not to swallow, instructed to hyperventilate slightly, which is then followed by continuous shallow expiration, to keep the vocal cords in an expiratory position (Aschoff et al. 1998). Other investigators recommend imaging data acquisition during a single breath-hold, which reduces motion artifacts caused by swallowing or respiration. In addition, the intensity of vascular enhancement is significantly heightened during breath-hold, which improves lymph node detection and lessens the amount of contrast medium required (Curtin et al. 1998). Additional functional CT imaging during E-phonation and/or a Valsalva maneuver (VM) are of great importance to confirm vocal cord mobility. Patients were instructed to say "E" constantly for about 10 s and, for VM, the patients were instructed to blow through closed lips (Kerberle et al. 2003).

Table 13.3. Recommended parameters to obtain a VL using a single-slice spiral CT scanner

Collimation (mm)	Pitch	Reconstruction index (mm)	Tube current (mAs)	Effective mAs (mAs/pitch)	Author
3	4–5	2	80	< 20	
2	4	1	120	30	
1	3	0.8	200	67	
4 × 2(1)	1.375 (5.5/4)	1(0.5)	120		Hoppe et al. (2002)
3	2.2		50		Choi et al. (2002)

Shorter acquisition times reduce motion artifacts (especially in the z-direction) even further, which advances the new MSCT (Berland and Smith 1998; Bode et al. 2001). Since MSCT allows almost isotropic imaging of the larynx, the image quality is as good as direct coronal scanning with no risk of amalgam artifacts (Baum et al. 2000). The achieved volumetric data sets consist of stacked slices, the number of which can be chosen even retrospectively to match the resolution requirements of the task at hand (usually around 1 mm or less). To cover the entire larynx within a single breath-hold, the protocols summarized in Table 13.4 could be used. Even with a low-dose spiral CT protocol (tube current 50 mA), the airways could be reconstructed without appreciable loss of image quality (Choi et al. 2002). For diagnostic purposes, the selected threshold CT values can be −600 HU (Hounsfield units) to −100 HU for the mucous membranes, and + 250 HU for bone. Under these conditions, almost all structures remain distinct, and scanning of the larynx provides an excellent contrast between air-containing spaces, such as the larynx, and soft tissue surfaces (Sakakura et al. 1998).

13.2.2 Magnetic Resonance Imaging (MRI)

Generally, MRI seems to be the optimum method of examination in cooperative patients, especially for evaluation of the larynx before an attempted partial laryngectomy. MRI is more sensitive than CT in the detection of neoplastic cartilage invasion, but has a somewhat lower specificity, particularly if there is thyroid cartilage involvement (Castelijns et al. 1998; Curtin et al. 1998). For MR imaging, T1-weighted, 3D volumetric, gradient-echo sequences are advantageous since they provide isotropic voxels, as well as good delineation of tumor tissue, vessels, and other soft tissue structures. The choice between CT and MRI is determined by the clinician's experience with these modalities. Both CT and MR imaging are highly sensitive for the detection of neoplastic invasion of the pre-epiglottic and paraglottic space, subglottic region, and cartilage. The high negative predictive value of both CT and MRI allows exclusion of neoplastic cartilage invasion quite reliably. Because of reactive inflammation, MRI tends to overestimate neoplastic cartilage invasion, which may, possibly,

Table 13.4. Multi-slice CT protocol for laryngeal tumor imaging

Scanner Type	Philips, Brilliance 64	Siemens, Somatom Volume Zoom	Toshiba, Astein MS	Siemens, Somatom Sensation 16		General Electric, Lightspeed-QXI
Collimation (mm)	64 × 0.625	4 × 1	4 × 1	0.75	1.5	2.5
kV	120	120	120	80[a]	120	
mAs	200	165	120	60	120	
Rotation time (sec)	0.75	0.5	0.75	0.75	0.5	
Table speed mm/rotation		6				
Pitch	0.891	1.5	1.375 (5.5/4)	7.5		
Contrast material	100 mL	120 mL	80	1.5 mL/kg		
Flow mL/sec	1.0–3.0	2.5+50 mL saline flush	3.0	2.0–3.0		
Delay	100 s–45 s	80 s	60 s	15 s[b]; 20 s[c]; 25 s[d]		
Recon.	3 mm soft tissue 2 mm bone					1–1.25 mm
Author		Keberle et al. (2003)	Hoppe et al. (2002)	Heyer et al. (2007)		Sorantin et al. (2003)

[a] Patient age < 5 years or weight < 20 kg
[b] Patient age < 1 year or < 10 kg
[c] Patient age 1–5 years or 10–20 kg
[d] Patient age > 5 years or > 20 kg

result in overtreatment, while CT tends to underestimate neoplastic cartilage invasion that could lead to inadequate therapeutic decisions (Becker 2000; Zbaren et al. 1996). The specificity of both CT and MRI is, however, limited and both methods may, therefore, overestimate the extent of tumor spread (Becker 1998). However, the overall accuracy for CT and MR imaging in detecting neoplastic invasion of cartilage is 80% vs 82% (Zbaren et al. 1996), and CT and MRI show equal staging accuracy (Zbaren et al. 1997a,b). Both, CT and MRI show tissue volume beyond the airway lumen and usually do not require sedation (Jolesz et al. 1997).

13.3. Postprocessing

CT and MR images are usually transferred to a computer workstation using internal network communication. Depending on computer hardware, images may undergo filtering for a reduction of unwanted signal (Gerig et al. 1992); (Blank and Kalender 2000; Frankenthaler et al. 1998). The next step, a so-called "segmentation," consists of a manual or automatic technique for isolating and outlining anatomic structures stacked into individual 3D objects. Usually, the construction of a trajectory is left to the clinician, who must define some points on the path manually using three orthogonal views. To overcome the drawbacks of manual path definition, an automatic path tracking method was developed by several authors (Deschamps and Cohen 2001; Sorantin et al. 2003) to build a centered path in tubular anatomical structures with minimum interactivity, given only one or two end points and the 3D image as inputs. A brief selection of hard- and software used in the past are listed in Table 13.5, and specific aspects of VL are summarized in Table 13.6. Although each technique may be used separately, multiple techniques are often used in conjunction to solve different segmentation problems (Blank and Kalender 2000; Pham et al. 2000). In some techniques, interactive exploration of the datasets is provided in near real-time, whereas earlier postprocessing techniques required

Table 13.5. Soft- and hardware used for virtual endoscopy

Software (vendor)	Hardware (vendor)	Author
Iris Explorer (Silicon Graphics, Mountain View, USA)	Indigo2 Maximum IMPACT (Silicon Graphics)	Aschoff et al. (1998)
Navigator 2.03 (GE Medical Systems, Milwaukee, Wisconsin, USA)	Sparc-10 workstation (Sun Microsystems, Mountain View, CA)	Gluecker et al. (2001)
Vitrea and Voxel View (Vital Images, Minnetonka, Minnesota, USA	O_2-workstation (Silicon Graphics)	Greess et al. (2000)
Xtension (Toshiba Corporation, Tokyo, Japan)	Ultra 1 Creator 3D (Sun Microsystems, Mountain View, CA)	Byrne et al. (2005)
V-Works version 1.0 software (CyberMed Lab, Seoul, Korea)		
virtual reality modeling language (VRML) 2.0 format		
Netscape Navigator (Netscape Communications Corp., Santa Clara, CA, USA)		
Cosmo Player version 2.1 VRML plug-in (Computer Associates International, Islandia, NY, USA)	400 MHz Pentium II processor (Intel, Santa Clara, CA, USA)	Choi et al. (2002)
Syngo, Somaris/5 (Siemens, Inc., Forchheim, Germany)	Volume Wizard (Siemens Inc.)	Joshi et al. (2003)
Integrated Data Language 5.4 (Creaso Research Systems Inc., Boulder, USA)	400 MHz Pentium III processor (Intel, Santa Clara, CA, USA)	Sorantin et al. (2003)[a]

[a] Used only for quantitative analysis of laryngeal stenosis

Table 13.6. Specific aspects of virtual laryngoscopy

Advantage	Disadvantage
• More accurate assessment of laryngeal stenosis compared to axial images or MPR • Virtual endoscopy is quick to perform and shows anatomical detail similar to conventional endoscopy • Ability to manipulate data on the post-processing station useful for education and surgical planning • Useful for obtaining views from below an obstructing lesion or stenosis, or in the occasional patient who cannot tolerate examination • No sedation or preparation is required • Possible motion artifacts due to swallowing, phonation, breathing • Noninvasive technique • No lens angle distortion • Visualization and quantification of luminal irregularities	• Radiation exposure, although the air/soft tissue interface allows reduction of exposure factors • Color, flat mucosal or submucosal irregularities, and vascularity are not depicted. No differentiation between mucous impact and tumor • Does not allow biopsy • Anatomic variability in image quality • Impaired imaging quality in apposition of two mucosal surfaces at the pyriform sinus, tongue base, epiglottis, soft palate, and pooling of secretions

predefined landmarks or visualization paths. Most commonly, surface rendering (Aschoff et al. 1998; Cline et al. 1988, 1990; Hoppe et al. 2002) or volume rendering (Cline et al. 1991; Rubin et al. 1996) was used to generate a *VE*. For surface rendering, a lower and upper threshold of –1000 HU and 500 HU, respectively, were recommended to reconstruct the airways (black-on-white mode). If segmented entities include only the mucous surfaces, this reduces significantly the amount of imaging data to be processed by more than 90%, which allows real-time navigation through the laryngeal airspace (Hoppe et al. 2002). Selecting appropriate threshold values is crucial so as not to create false-positive stenosis and mucous swelling (Aschoff et al. 1998) (Fig. 13.1). Without further manual segmentation, volume rendering also allows easy differentiation between extra- or intraluminal compression of the larynx when rendering the mucous surface semitransparent (Seemann et al. 2001). Finally, a special computer program combines all the 3D objects into a complete model, which is used for virtual laryngoscopy. Depending on the technique applied, postprocessing may take between several minutes (Rodenwaldt et al. 1996; Sorantin et al. 2003) and several hours. Virtual camera elements and free-defined virtual light, as well as variable viewing angles, are valuable features of user interfaces for VL. The camera and global views can be enlarged or reduced, rotated 360 degrees in any axis, and translocated in the vertical or horizontal plane. The camera lens may face any direction and provide a viewing angle from 1–180°. Reconstructed 3D images contain no more information than do the corresponding series of axial single scans. There is some consensus that the viewer can better appreciate spatial relationships in a 3D display than in a series of single scans (Remy-Jardin et al. 1998). By eliminating redundant details, the information can be reduced to the essentials. Advanced interfaces provide a display of multiple images: a camera view; a global or external view; and a view of the related CT or MR slice.

13.4 Clinical Applications

Conventional endoscopy does not allow a sufficient diagnostic examination below an impassable stenosis and misses evaluation of the extraluminal structures. However, there are some indications where a virtual laryngoscopy may be advantageous, with encouraging clinical results (Aschoff et al. 1998; Byrne et al. 2005; Eliashar et al. 2000; Gallivan et al. 1999; Giudice et al. 2003; Hoppe et al. 2002; Magnano et al. 2005; Men et al. 2006a,b; Moharir et al. 1998; Rodel et al. 2000; Rottgen et al. 2005; Sichel et al. 2003; Silvermann et al. 1995; Walshe et al. 2002; Wang et al. 2001) (Fig. 13.2). In their survey, Rodenwaldt et al. (1996) reconstructed the inner surface of the upper airway from spiral CT-facilitating VL and compared it to conventional endoscopy in more than 80 patients. As observed by

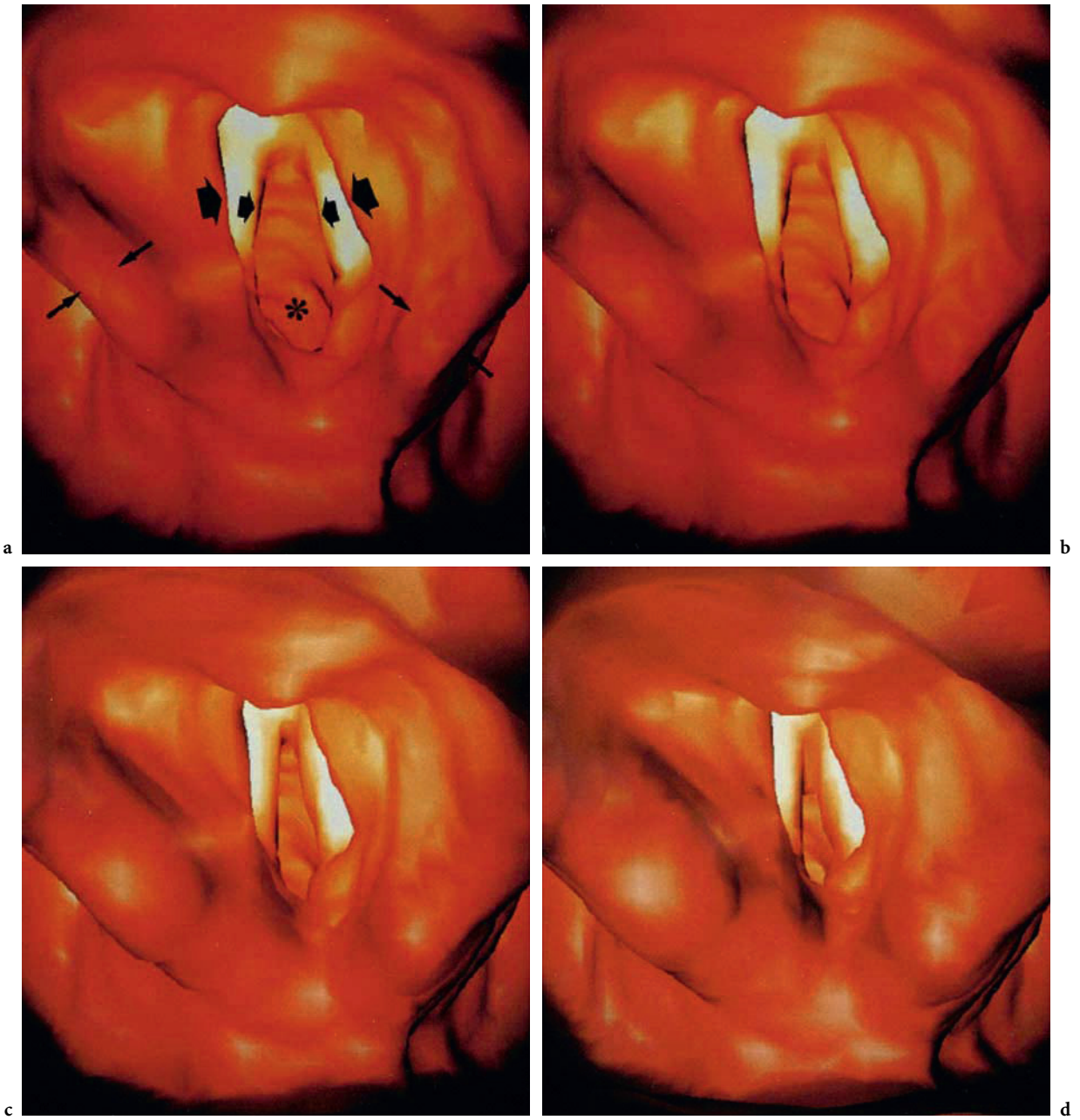

Fig. 13.1a–d. Virtual laryngoscopy of the larynx, reconstructed with different threshold levels. **a** Normal findings; the vocal cords (*short thick arrows*), the laryngeal folds (*long thick arrows*), the aryepiglottic folds (*small thin arrows*), and the trachea (*asterix*) can be seen. **b–d** With increasing threshold values, there is false-positive swelling of the mucous surface and a false-positive stenosis of the laryngeal space. Reprint with permission granted by Aschoff AJ et al. High-resolution virtual laryngoscopy based on spiral CT data. Radiologe 1998; 38:810–815

others subsequently, VL allowed precise identification of the anatomical structures and suspected pathological endoluminal findings, such as tracheal stenoses, particularly in high-risk patients or in patients with impassable stenoses. Aschoff et al. (1998) investigated the feasibility and clinical value of a high-resolution, virtual laryngoscopy based on spiral CT data sets (collimation 1 mm, pitch 1.5) in 12 patients with laryngeal pathology compared to conventional endoscopy. VL provided the correct diagnosis in 8 of 12 cases (laryngeal tumors, subglottic stenoses) and was capable of simulating the

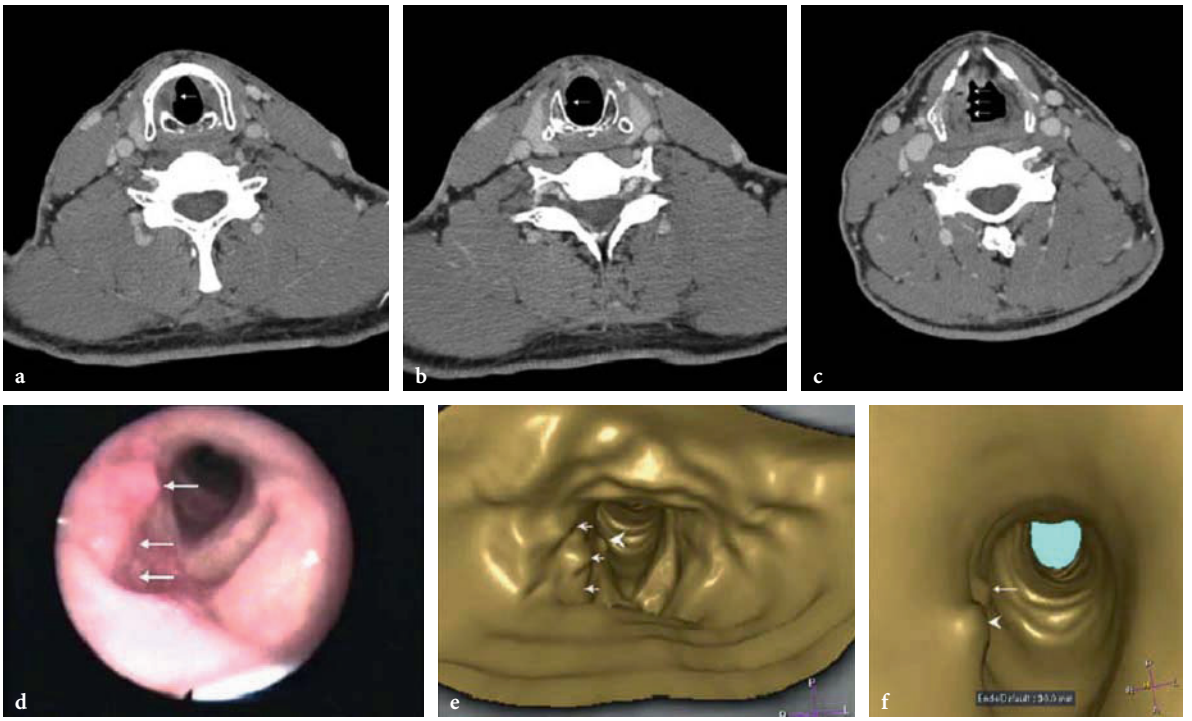

Fig. 13.2a–f. Transverse CT images (**a–c**) show multifocal carcinoma (*arrows*) involving the right vocal cord (**a**), and the right side of the subglottic (**b**) and supraglottic space (**c**). OE image (**d**) showing the right glottic-supraglottic tumor (*arrows*). VL images showing the right vocal cord lesion (*arrowhead* in **e**,**f**), the right supraglottic lesion (**e**, *arrows*), and the right subglottic lesion (**f**, *arrow*). Reprint with permission granted by Men S et al. Diagnostic contribution of virtual endoscopy in diseases of the upper airways. In: J Digit Imaging, Springer, Berlin Heidelberg New York, 2006:1–5

visual findings of endoscopy in cases of laryngeal tumors and subglottic stenoses. Small tumors (T1-stage) of the vocal cords, however, were not adequately visualized in cross-sectional CT images; thus, none of the carcinomas of the vocal cords was recognized at VL. This might be due to small vibrations of the vocal cord during E-phonation. Because of swallowing artifacts, however, reconstruction of VL failed in 2 of 12 patients. It might be worthwhile to repeat CT imaging immediately in case of involuntary swallowing. This limitation, however, can be overcome using MSCT data sets (Kerberle et al. 2003). Fried et al.(1998, 1999) developed a VL using two-dimensional (2D) CT or MRI data (Moharir et al. 1998) in patients with a normal airway, a posterior glottic stenosis, and a squamous cell carcinoma of the glottic fold. The resulting models included extraluminal anatomy that was not typical of current virtual endoscopic techniques, and these models were imported into an experimental virtual endoscopy program for airway lumen generation and interactive viewing. Their VL program allowed for display of multiple images: a camera view; a global or external view; and a view of the related CT or MR data as an orthogonal display (Fig. 13.3). The camera and global views could be enlarged or reduced, rotated 360° in any axis, and translocated in the vertical or horizontal plane. The camera lens could face any direction and provide a viewing angle of 1–180°. Any segmented individual anatomic structure could be added or deleted, and rendered transparent, and color and light intensity could be controlled. In one patient, an interarytenoid web limited the lateral excursion of the vocal cord. Subglottic structures, however, could not be visualized on the laryngeal videostroboscopic exam. Using the VL, one could see that the stenosis did not extend into the subglottic area. Using the 3D color-coded view, the segmented structures were made transparent and the transmural extent of disease was visualized. A posterior global view, with the web removed, demonstrated a non-compromised airway distal to the stenosis (Fig. 13.4). Gallivan et al. (1999) evaluated the use of CT and VL for head and neck tumors

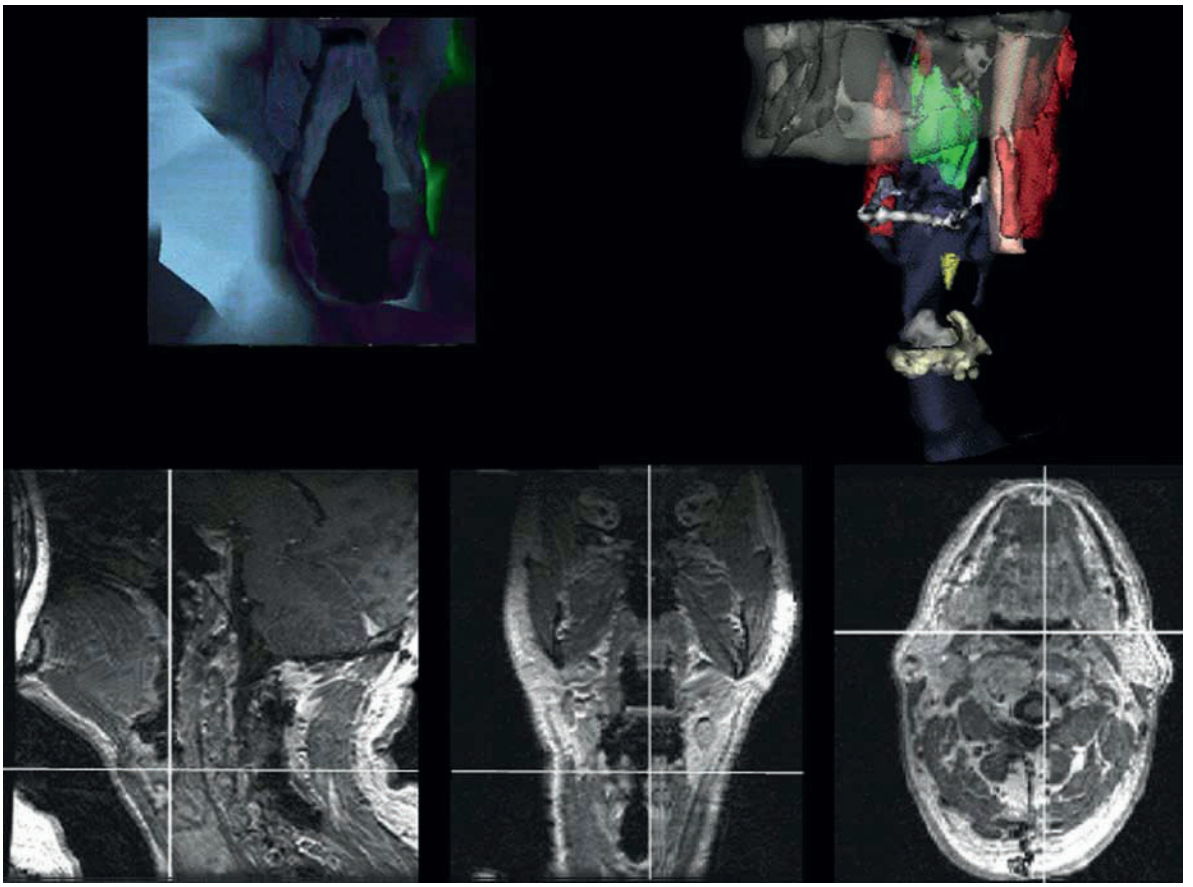

Fig. 13.3. A 55-year-old man with a retropharyngeal tumor that required endoscopy-guided intubation. A flexible endoscope and miniature (1.2 mm diameter) electromagnetic sensor (Biosense, Seatauket, NY) were introduced together in an endotracheal tube. Multiple MR images, their three-dimensional (3D) rendering, and virtual endoscopy views were displayed during intubation, showing the progress of the endotracheal tube. MR images, 3D rendering, and virtual endoscopy images were registered to the patient before the procedure. *Upper left image*: virtual endoscopy image from the viewing point of the endoscope, showing the vocal cords. *Upper right image*: 3D rendering of head and neck region, showing the actual position of the endoscope's tip (*yellow arrowhead*). *Lower images*: multiplanar MR images displaying actual tip position (*crosshairs*). From: Jolesz FA et al. Am J Roentgenol 1997; 169:1229–1235. Permission granted

distributed throughout the upper aerodigestive tract in 21 patients. Patients underwent flexible laryngoscopy, axial CT with contrast, VL, and, in most cases, operative endoscopy. VL accurately demonstrated abnormalities caused by intraluminal tumor, and a very good correlation between virtual images and flexible and rigid laryngoscopic and intraoperative findings was observed. However, appositions of normal tissue against tumor caused inaccurate depictions of the surface contour. The authors concluded that VL appeared to be most accurate in the evaluation of subglottic and nasopharyngeal anatomy. In patients with a tight tracheal stenosis, the risk of occlusion of the airway during examination excludes flexible bronchoscopy as a diagnostic technique (Carretta et al. 2006). Because rigid bronchoscopy is performed with ventilating instrumentation, it is the procedure of choice when operative procedures, such as dilation of the stenosis, have to be performed. Rigid bronchoscopy also proved to have the best accuracy in the evaluation of involvement of the subglottic larynx, which is extremely important because specific surgical techniques must be used in such patients to avoid recurrent laryngeal nerve lesions. Since post-intubation stenosis remains the most frequent indication for tracheal surgery (Carretta et al. 2006; Drosnes and Zwillenberg 1990) it might be worthwhile to follow those patients

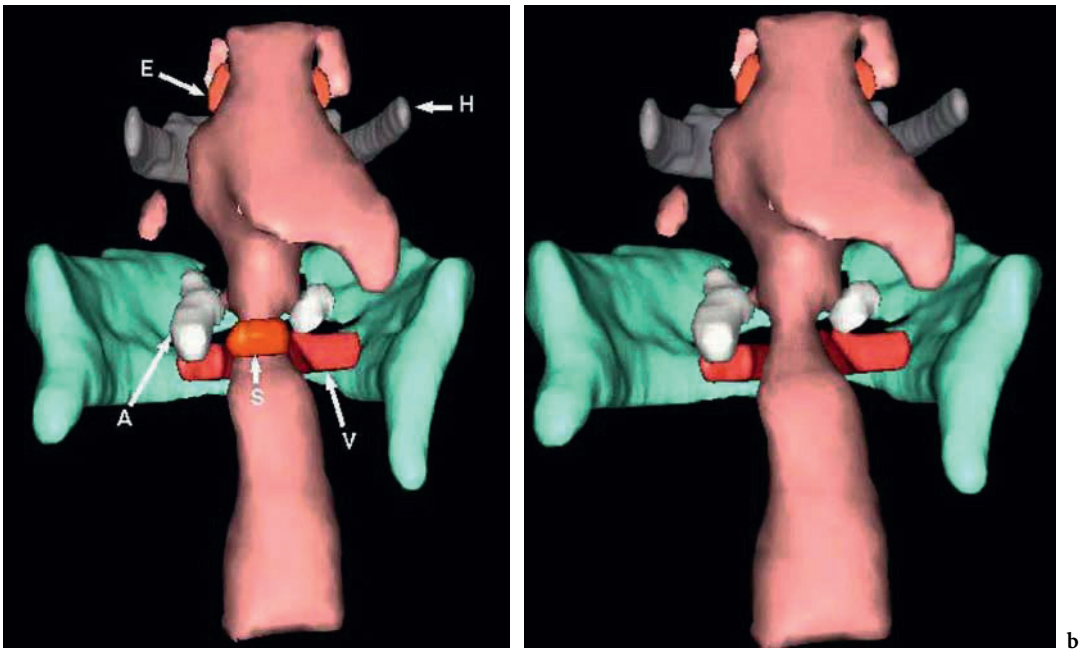

a b

Fig. 13.4. a Patient 3. A posterior global view during the virtual laryngoscopy. The airway lumen is in peach and the thyroid cartilage is rendered light blue. *A* = left arytenoid cartilage; *S* = stenotic intra-arytenoid web; *V* = right vocal fold; *H* = hyoid bone; *E* = epiglottis. From Fried MP et al. Ann Otol Rhinol Laryngol (1999);108:221–226. Permission granted. **b** Patient 3. Another posterior global view during virtual laryngoscopy. The key difference between this figure and Fig. 13.6 is that the intra-arytenoid web is rendered invisible here. The airway lumen narrowing between the arytenoid cartilages (*white*) and vocal folds (*orange*) is evident. Below the vocal folds, the diameter of the airway lumen expands, giving no further evidence of stenosis. From Fried MP et al. Ann Otol Rhinol Laryngol (1999); 108:221–226. Permission granted

using a noninvasive method, such as CT or VE, to confirm the formation of laryngeal granulomata or other post-intubation laryngeal lesions. Giovanni et al. (1998) used VL and compared it to intraoperative endoscopy of the larynx and trachea in children with dyspnea related to either subglottic angioma or laryngotracheal stenosis. Virtual endoscopy allowed accurate assessment and measurement of the stenosis of the airway in all cases (Triglia et al. 2002), despite the fact that a high-grade stenosis prevented complete operative endoscopy in 9 of 18 cases. The findings were concordant in those cases where both intraoperative and virtual endoscopy were feasible. The ability to assess extraluminal anatomy also provided a clearer picture of overall disease involvement. Hoppe et al. (2002) compared MSCT (axial, coronal and sagittal reformats) and VL with endoscopic laryngoscopy of 111 upper airway sections (supraglottis, glottis, subglottis, trachea) in 29 patients with upper airway stenosis. All CT-based methods accurately detected upper airway stenosis (accuracy was 96% for virtual laryngoscopy and MPR and 94% for axial CT slices). Correlation of fiberoptic and virtual laryngoscopy ($r = 0.94$) for grading of stenosis was closer than with sagittal reformats ($r = 0.80$), coronal reformats ($r = 0.72$), and axial CT slices ($r = 0.57$). Again, as observed by others, even high-grade stenoses that were impassable for fiberoptic laryngoscopy could be traversed with VL. To achieve a quantitative, fast, and precise assessment of laryngo-tracheal caliber changes, Sorantin et al. (2003) developed an automated segmentation algorithm. Within a mean of just 2.78 (2.1–3.9) min, the cross-sectional profile was computed and the degree and length of stenosis were presented as line charts. In a phantom test, an excellent correlation between the true and computed 3D cross-sectional profile was found ($p < 0.005$). In symptomatic patients, the average degree and length of tracheal stenoses were found to be 60.5% and 4.32 cm (Fig. 13.5). Furthermore, in addition to the glottic stenosis that prevented further endoscopic

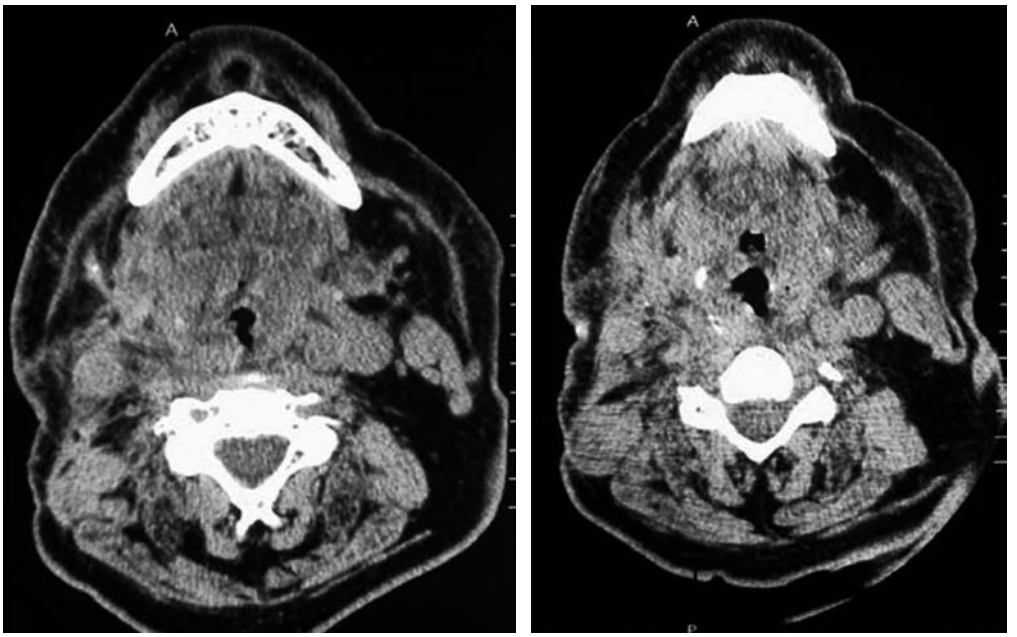

a b

c

Fig. 13.5. a,b Axial views of the vocal cords, which are stenotic post-radiotherapy, viewed from above and below; difficult to assess recurrence of tumour. **c** Virtual laryngoscopy of stenotic cords viewed from below shows no recurrence of tumour. From: Byrne AT et al. Eur J Radiol 2005; 56:38–42

inspection, automated segmentation detected subglottic and tracheal stenosis in three patients. Notably, minor caliber changes (about 8.8% stenosis, mean length of 2.31 cm), not detected on axial CT scans, were found in normal controls; however, they could also be regarded as partial volume or pulsation artifacts. Although this algorithm was not used for VL, it could be easily adapted for this task. Using multiplanar reconstructions of MSCT without further VL rendering, the correlation of multiplanar reconstructions of MSCT scans with bronchoscopy was not significant ($p = 0.08$) (Carretta et al. 2006). This emphasizes the fact that VL might have been advantageous for the evaluation of candidates for tracheal resection and reconstruction for stenosis following radiotherapy or long-term intubation (Fig. 13.6). To date, summarizing the clinical experience, VL plays an important role in evaluating the larynx while searching for stenosis, particularly following long-term intubation. The lack of detailed information about the mucous surface or motion artifacts limit the value of VL and prohibit the detection of small tumors within the mucous surface or the vocal cord (Gluecker et al. 2001).

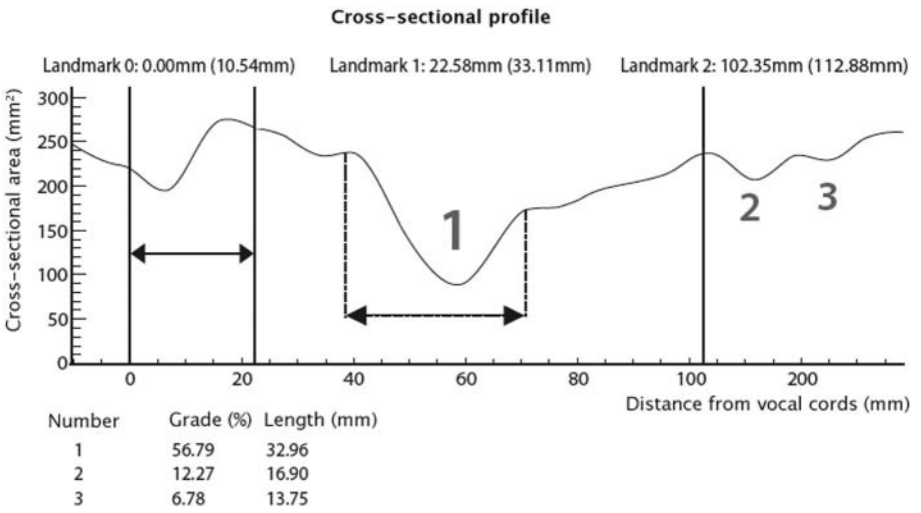

Fig. 13.6. 3D cross-sectional profile of a patient with tracheal stenosis. The cross-sectional profile (*thin black line*) shows the actual area in mm^2 at a dedicated distance from the vocal cords, as measured in mm. There is one relevant stenosis (position 1), whereas 2 subsequent stenoses (position 2 and 3) are irrelevant. Quantitative analysis of the degree and length of the stenoses are provided at the lower left margin of the graph. Modified from: Sorantin E et al. 3D cross section of the laryngotracheal tract. A new method for visualization and quantification of tracheal stenoses. Radiologe 2003; 43:1056–1068

13.5 Multi-Modality Information Integration

In many minimally invasive procedures, the physician has a limited view of the operating field and cannot visualize structures beyond the exposed surfaces. Particularly during endoscopic procedures, the endoscopist is confronted with difficult hand-eye coordination problems since he or she is looking at a camera's view of the surgical field with a totally different reference frame. In other cases, endoscopies are complicated by the similarity in visual appearance of different tissues (such as tumor and healthy tissue), although such tissues have high contrast in some medical images. The best examples of this are breast cancer and brain glioma, which can be difficult to distinguish from normal tissue (Jolesz et al. 1997). Better use of 3D imaging can improve visualization and help the physician overcome the limitations of existing procedures. Enhanced reality visualization, in particular, in which the physician's field of view is augmented with additional structural information, can provide useful guidance in planning and executing a minimally invasive procedure. To date, current methods of virtual endoscopy are limited in their 3D display of extraluminal anatomy. For example, during virtual bronchoscopy, blood vessels and the lung parenchyma are often not seen. The lack of a global context and physical clues during viewing may lead to confusion of the patient's anatomy (Summers 1997). Three-dimensional anatomical reconstruction has been reported to complement the understanding of laryngeal anatomy, especially in the subglottic area, which cannot be seen clearly by endoscopy or conventional axial CT. This is particularly advantageous in the detection of subglottic cancers, or the invasion of glottic or supraglottic cancers into the subglottic area (Sakakura et al. 1998). Greess et al. (2000) demonstrated that, in the head and neck region, MPRs were useful as additional planes to VE. Surface-shaded displays (SSDs) were valuable when there was extensive bony destruction (skull, spine, skeleton, and larynx). Color-coded 3D reformations enhance the visualization of extensive tumors and before multi-specialty surgery. Although perspective volume-rendering has been touted as a new and promising method for the future, MPRs or SSDs are more useful for visualizing pathological findings in their topographic relation to anatomical structures (Greess et al. 2000). Image fusion of different imaging modalities further enhances visualization. Information about blood vessels may be used from angiograms, about soft tissue structures from MRI, about bones from CT, or about metabolic activity

from SPECT or PET (Geets et al. 2006). Therefore, various tissue types and different physiological functions can be highlighted. This problem was addressed by incorporating a method of 3D anatomical reconstruction into a virtual endoscopic technique that can use merged CT and MR images (Fried et al. 1997; Moharir et al. 1998). Using this technique, the transparent airway lumen and the global view allowed for appreciation of the transmural extent of the tumor and the patency of blood vessels (Fig. 13.4). Moharir et al. (1998) combined MR and CT data to generate a VE that included a 3D anatomical reconstruction that allowed for visualization of soft tissue, cartilage, and bone (Fig. 13.3). This should be particularly helpful when evaluating tumors and their surrounding viscera, such as the jugular veins, carotid arteries, and others. A simultaneous display of the global view, and the related CT or MR slice, further improves the understanding of the location of the virtual camera in relation to its extraluminal spatial context.

13.6 Instrument Tracking

Correct localization and orientation relative to the surrounding anatomy is an important feature of virtual endoscopy. Complementing actual endoscopy with virtual images, however, requires knowledge of the endoscope's location within the patient. Various tracking devices or sensors (mechanical, optical, or electromagnetic) can be attached to rigid endoscopes, or smaller sensors can be introduced into the working channels of flexible endoscopes (Birkfellner et al. 1998a). By tracking the 3D position of the instruments, their position can be shown/overlaid on scans of the patient, such as MRI or CT scans (Fried et al. 1997). Several technologies are available to achieve this goal. The most widely used technology currently is optical tracking (Khadem et al. 2000; Shahidi et al. 2002). Optical tracking systems determine the position of several optical beacons in space, which provides excellent technical accuracy of typically less than 1 mm (also referred to as Fiducial Localization Error (FLE)). These systems carry a severe drawback for surgical navigation applications in ENT surgery: the system cannot operate when the line-of-sight between beacon and camera is obstructed (Fitzpatrick et al. 1998). Therefore, the beacons must be mounted outside the patient, which makes the use of an optical tracker together with a flexible endoscope impossible. Thus, electromagnetic tracking seems to provide a more successful approach to track the position of a flexible endoscope. In these systems, the position of a small sensor to measure magnetic flux or magnetic induction is determined relative to a reference field emitter. The electromagnetic field passes without significant distortion through body tissue; thus, it is possible to attach a small sensor to the tip of a flexible instrument, such as a catheter (Solomon et al.1999, 2000, 2003). Tracking of electromagnetic trackers, however, can be severely distorted when conductive or ferromagnetic materials (such as instruments made of surgical steel) are within the vicinity of the field emitter or the sensor (Birkfellner et al. 1998b). Therefore, electromagnetic digitizers are not as widespread as optical trackers in the field of surgical navigation, in general. In an experimental case study, Jolesz et al. (1997) used an electromagnetic tracking system (Magelan, Biosense, Inc. NY, now called Biosense CARTO Nonfluoroscopic Mapping and Navigation System (CARTO System)) to combine virtual laryngoscopy with conventional laryngoscopy. This technique was used during an image-guided intubation of a 55-year-old male patient with a large endolaryngeal bulging of a retropharyngeal tumor. Since the tumor compromised the larynx, the augmented endoscopy-guided intubation was performed just before the patient underwent surgery (Fig. 13.3). A virtual laryngoscopy was created from prior (two days earlier) cross-sectional MR imaging data from the patient, designed to simulate an intubation. A miniature electromagnetic sensor (1.2 mm diameter) of the tracking system was then integrated within a catheter-like sensor probe. The patient's position was then registered on the MR scan by choosing five landmarks on the patient's MR and pointing the probe to the corresponding landmarks on the patient. The flexible endoscope and the probe were both introduced into the endotracheal tube. Thus, the endoscope's position was registered in real-time on the imaging data set and visualized on a split-screen display, presenting five views simultaneously. These views were updated at about 1–2 frames per second, demonstrating the progress of the endotracheal intubation, which was completed successfully with no complications. This experiment demonstrated that an augmented endoscopy of the larynx is feasible and safe, with the added benefits of the ability to assess the transmural extent of disease and view the airway distal

to areas of luminal compromise. In the future, the most promising technologies for flexible instrument tracking are either combined magneto-optical tracking systems, which allow for reducing errors from the environment in electromagnetic trackers (Birkfellner et al. 1998a), or flexible optical fibers that measure torsion and bend. Such systems are, however, not yet available on the market.

13.7 Conclusion

An endoscopic examination of the upper airway by an otorhinolaryngologist is still the common diagnostic approach to differentiate between a space-occupying tumor and a stenosis after intubation, inflammation, or trauma. Endoscopy, as the gold standard of the endoluminal evaluation, is a fairly invasive technique with a few limitations in certain cases, does not allow a sufficient diagnostic examination below an impassable stenosis, and misses evaluation of the extraluminal structures. The developments of spiral CT and postprocessing reconstruction algorithms to generate a 3D virtual laryngoscopy have opened new possibilities, and have substantially improved speed as well as isotropic spatial resolution. With current imaging techniques, exophytic lesions, tumors, and stenoses of the larynx, even a few millimeters in size, can be detected easily. Furthermore, the ability to assess the transmural extent of disease and the view of the airway, distal to areas of luminal compromise, are advantageous. Thus, VL complements the findings of actual endoscopy, or, in some applications, might replace these findings, thus reducing the costs of hospital admission and the risks inherent in this procedure. VL has proven to be advantageous in subglottic stenoses, especially in high-risk patients or in patients with impassable stenoses. The lack of detailed information about the mucous surface, the small size, movement during expiration, and possible artifacts may prohibit the detection of tumors less than 2 mm. Therefore, the value of VL, at least for T1-stage tumors within the mucous surface or the vocal cord, is limited and it remains problematic whether surface-flattening algorithms (Haker et al. 2000) will overcome this challenge. Clinical acceptance of VL will increase when information can be generated from diagnostic scan data without the necessity to repeat the scan with a modified protocol. Though VL cannot be used for biopsy, VL has the potential to improve preoperative planning and staging, as well as intra-procedural guidance for head and neck pathology. Combined with positional sensor techniques, actual endoscopy and VL might well provide clinical benefits in guiding the correct placement of biopsy needles or laparoscopes and mote-cutting tools, which is problematic if these tools are outside the visual field. This could allow the margins of lesions to be biopsied, improving delineation of the extent of pathology. However, prior to expanded implementation, applicability and the time effort necessary to generate virtual laryngoscopy are currently prohibitive and need to be reduced in the future.

References

Altobelli DE, Kikinis R, Mulliken JB, Cline H, Lorensen W, Jolesz F (1993) Computer-assisted three-dimensional planning in craniofacial surgery. Plast Reconstr Surg 92:576–585; discussion 586–577

Aquino SL, Vining DJ (1999) Virtual bronchoscopy. Clin Chest Med 20:725–730, vii–viii

Aschoff AJ, Seifarth H, Fleiter T et al. (1998) High-resolution virtual laryngoscopy based on spiral CT data. Radiologe 38:810–815

Assimos DG, Vining DJ (2001) Virtual endoscopy. J Endourol 15:47–51

Baum U, Greess H, Lell M, Nomayr A, Lenz M (2000) Imaging of head and neck tumors-methods: CT, spiral-CT, multislice-spiral-CT. Eur J Radiol 33:153–160

Becker M (1998) Diagnosis and staging of laryngeal tumors with CT and MRI. Radiologe 38:93–100

Becker M (2000) Neoplastic invasion of laryngeal cartilage: radiologic diagnosis and therapeutic implications. Eur J Radiol 33:216–229

Berland LL, Smith JK (1998) Multidetector-array CT: once again, technology creates new opportunities. Radiology 209:327–329

Birkfellner W, Watzinger F, Wanschitz F, Ewers R, Bergmann H (1998a) Calibration of tracking systems in a surgical environment. IEEE Trans Med Imaging 17:737–742

Birkfellner W, Watzinger F, Wanschitz F et al (1998b) Systematic distortions in magnetic position digitizers. Med Phys 25:2242–2248

Blank M, Kalender WA (2000) Medical volume exploration: gaining insights virtually. Eur J Radiol 33:161–169

Bode A, Dammann F, Pelikan EH et al (2001) Analysis of artefacts by virtual endoscopy visualization of spiral CT data. Rofo 173:245–252

Byrne AT, Walshe P, McShane D, Hamilton S (2005) Virtual laryngoscopy-preliminary experience. Eur J Radiol 56:38–42

Carretta A, Melloni G, Ciriaco P et al (2006) Preoperative assessment in patients with postintubation tracheal ste-

nosis: rigid and flexible bronchoscopy versus spiral CT scan with multiplanar reconstructions. Surg Endosc 20:905–908
Castelijns JA, Hermans R, van den Brekel MW, Mukherji SK (1998) Imaging of laryngeal cancer. Semin Ultrasound CT MR 19:492–504
Choi YW, McAdams HP, Jeon SC et al (2002) Low-dose spiral CT: application to surface-rendered three-dimensional imaging of central airways. J Comput Assist Tomogr 26:335–341
Cline HE, Dumoulin CL, Hart HR Jr, Lorensen WE, Ludke S (1987) 3D reconstruction of the brain from magnetic resonance images using a connectivity algorithm. Magn Reson Imaging 5:345–352
Cline HE, Lorensen WE, Ludke S, Crawford CR, Teeter BC (1988) Two algorithms for the three-dimensional reconstruction of tomograms. Med Phys 15:320–327
Cline HE, Lorensen WE, Kikinis R, Jolesz F (1990) Three-dimensional segmentation of MR images of the head using probability and connectivity. J Comput Assist Tomogr 14:1037–1045
Cline HE, Dumoulin CL, Lorensen WE, Souza SP, Adams WJ (1991) Volume rendering and connectivity algorithms for MR angiography. Magn Reson Med 18:384–394
Curtin HD, Ishwaran H, Mancuso AA, Dalley RW, Caudry DJ, McNeil BJ (1998) Comparison of CT and MR imaging in staging of neck metastases. Radiology 207:123–130
Deschamps T, Cohen LD (2001) Fast extraction of minimal paths in 3D images and applications to virtual endoscopy. Med Image Anal 5:281–299
Drosnes DL, Zwillenberg DA (1990) Laryngeal granulomatous polyp after short-term intubation of a child. Ann Otol Rhinol Laryngol 99:183–186
Eisele DW, Richtsmeier WJ, Graybeal JC, Koch WM, Zinreich SJ (1994) Three-dimensional models for head and neck tumor treatment planning. Laryngoscope 104:433–439
Eliashar R, Davros W, Eliachar I (2000) Virtual endoscopy of the upper airway – a diagnostic tool. Postgrad Med J 76:187–188
Ferretti GR, Vining DJ, Knoplioch J, Coulomb M (1996) Tracheobronchial tree: three-dimensional spiral CT with bronchoscopic perspective. J Comput Assist Tomogr 20:777–781
Fitzpatrick JM, West JB, Maurer CR Jr (1998) Predicting error in rigid-body point-based registration. IEEE Trans Med Imaging;17:694–702
Frankenthaler RP, Moharir V, Kikinis R et al (1998) Virtual otoscopy. Otolaryngol Clin North Am 31:383–392
Fried MP, Kleefield J, Gopal H, Reardon E, Ho BT, Kuhn FA (1997) Image-guided endoscopic surgery: results of accuracy and performance in a multicenter clinical study using an electromagnetic tracking system. Laryngoscope 107:594–601
Fried MP, Topulos G, Hsu L et al (1998) Endoscopic sinus surgery with magnetic resonance imaging guidance: initial patient experience. Otolaryngol Head Neck Surg 119:374–380
Fried MP, Moharir VM, Shinmoto H et al (1999) Virtual laryngoscopy. Ann Otol Rhinol Laryngol 108:221–226
Gallivan RP, Nguyen TH, Armstrong WB (1999) Head and neck computed tomography virtual endoscopy: evaluation of a new imaging technique. Laryngoscope 109:1570–1579
Geets X, Daisne JF, Tomsej M, Duprez T, Lonneux M, Gregoire V (2006) Impact of the type of imaging modality on target volumes delineation and dose distribution in pharyngo-laryngeal squamous cell carcinoma: comparison between pre- and per-treatment studies. Radiother Oncol 78:291–297
Gerig G, Kubler O, Kikinis R, Jolesz FA (1992) Nonlinear Anisotropic Filtering of MRI Data. IEEE Trans Med Imaging 11/2:221–232
Giovanni A, Nazarian B, Sudre-Levillain I et al (1998) Geometric modeling and virtual endoscopy of the laryngotracheal lumen from computerized tomography images: initial applications to laryngo-tracheal pathology in the child. Rev Laryngol Otol Rhinol (Bord) 119:341–346
Girod S, Keeve E, Girod B (1995) Advances in interactive craniofacial surgery planning by 3D simulation and visualization. Int J Oral Maxillofac Surg 24:120–125
Giudice M, Piazza C, Foccoli P, Toninelli C, Cavaliere S, Peretti G (2003) Idiopathic subglottic stenosis: management by endoscopic and open-neck surgery in a series of 30 patients. Eur Arch Otorhinolaryngol 260:235–238
Gluecker T, Lang F, Bessler S et al (2001) 2D and 3D CT imaging correlated to rigid endoscopy in complex laryngo-tracheal stenoses. Eur Radiol 11:50–54
Greess H, Nomayr A, Tomandl B et al (2000) 2D and 3D visualisation of head and neck tumours from spiral-CT data. Eur J Radiol 33:170–177
Haker S, Angenent S, Tannenbaum A, Kikinis R (2000) Nondistorting flattening maps and the 3-D visualization of colon CT images. IEEE Trans Med Imaging 19:665–670
Heyer CM, Nuesslein TG, Jung D et al (2007) Tracheobronchial anomalies and stenoses: detection with low-dose multidetector CT with virtual tracheobronchoscopy – comparison with flexible tracheobronchoscopy. Radiology 242:542–549
Hoppe H, Thoeny HC, Dinkel HP, Zbaren P, Vock P (2002) Virtual laryngoscopy and multiplanar reformats with multirow detector CT for detection and grading of upper airway stenosis. Rofo 174:1003–1008
Jolesz FA, Lorensen WE, Shinmoto H et al (1997) Interactive virtual endoscopy. AJR Am J Roentgenol 169:1229–1235
Joshi AR, Khanna PC, Merchant SA, Khandelwal A, Agrawal N, Karnik ND (2003) Role of multidetector CT virtual bronchoscopy in the evaluation of post-tracheostomy tracheal stenosis – a preliminary study. J Assoc Physicians India 51:871–876
Keberle M, Sandstede J, Hoppe F, Fischer M, Hahn D (2003) Diagnostic impact of multiplanar reformations in multislice CT of laryngeal and hypopharyngeal carcinomas. Rofo 175:1079–1085
Khadem R, Yeh CC, Sadeghi-Tehrani M et al (2000) Comparative tracking error analysis of five different optical tracking systems. Comput Aided Surg 5:98–107
Korves B, Klimek L, Klein HM, Mosges R (1995) Image- and model-based surgical planning in otolaryngology. J Otolaryngol 24:265–270
Magnano M, Bongioannini G, Cirillo S et al (2005) Virtual endoscopy of laryngeal carcinoma: is it useful? Otolaryngol Head Neck Surg 132:776–782
Magnusson M, Lenz R, Danielsson PE (1991) Evaluation of methods for shaded surface display of CT volumes. Comput Med Imaging Graph 15:247–256

Marsh JL, Vannier MW (1983) The "third" dimension in craniofacial surgery. Plast Reconstr Surg 71:759–767

Men S, Ikiz AO, Topcu I, Cakmakci H, Ecevit C (2006a) CT and virtual endoscopy findings in congenital laryngeal web. Int J Pediatr Otorhinolaryngol 70:1125–1127

Men S, Ecevit MC, Topcu I, Kabakci N, Erdag TK, Sutay S (2006b) Diagnostic contribution of virtual endoscopy in diseases of the upper airways. J Digit Imaging, Springer, Berlin Heidelberg New York, pp 1–5

Moharir VM, Fried MP, Vernick DM et al (1998) Computer-assisted three-dimensional reconstruction of head and neck tumors. Laryngoscope 108:1592–1598

Pham DL, Xu C, Prince JL (2000) Current methods in medical image segmentation. Annu Rev Biomed Eng 2:315–337

Remy-Jardin M, Remy J, Artaud D, Fribourg M, Duhamel A (1998) Volume rendering of the tracheobronchial tree: clinical evaluation of bronchographic images. Radiology 208:761–770

Robb RA (2000) Virtual endoscopy: development and evaluation using the visible human datasets. Comput Med Imaging Graph 24:133–151

Rodel R, Rodenwaldt J, Hommerich CP (2000) Inner surface imaging of laryngeal and tracheal stenosis by spiral-CT: role of a new diagnostic procedure. Laryngorhinootologie 79:584–590

Rodenwaldt J, Kopka L, Roedel R, Grabbe E (1996) Three-dimensional surface imaging of the larynx and trachea by spiral CT: virtual endoscopy. Rofo 165:80–83

Rodenwaldt J, Kopka L, Roedel R, Margas A, Grabbe E (1997) 3D virtual endoscopy of the upper airway: optimization of the scan parameters in a cadaver phantom and clinical assessment. J Comput Assist Tomogr 21:405–411

Rosenberg SI, Silverstein H, Willcox TO, Gordon MA (1994) Endoscopy in otology and neurotology. Am J Otol 15:168–172

Rottgen R, Schurmann D, Pinkernelle J et al (2005) Detection of airways stenoses: comparison of virtual and flexible bronchoscopy. Rofo 177:338–343

Rubin GD, Beaulieu CF, Argiro V et al (1996) Perspective volume rendering of CT and MR images: applications for endoscopic imaging. Radiology 199:321–330

Sakakura A, Yamamoto Y, Uesugi Y, Nakai K, Takenaka H, Narabayashi I (1998) Three-dimensional imaging of laryngeal cancers using high-speed helical CT scanning. ORL J Otorhinolaryngol Relat Spec 60:103–107

Schenck JF, Jolesz FA, Roemer PB et al (1995) Superconducting open-configuration MR imaging system for image-guided therapy. Radiology 195:805–814

Schubert O, Sartor K, Forsting M, Reisser C (1996) Three-dimensional computed display of otosurgical operation sites by spiral CT. Neuroradiology 38:663–668

Seemann MD, Gebicke K, Luboldt W et al (2001) Hybrid 3-D rendering of the thorax and surface-based virtual bronchoscopy in surgical and interventional therapy control. Rofo 173:650–657

Shahidi R, Bax MR, Maurer CR Jr et al (2002) Implementation, calibration and accuracy testing of an image-enhanced endoscopy system. IEEE Trans Med Imaging 21:1524–1535

Sichel JY, Attal P, Dano I, Eliashar R (2003) Custom-made tracheotomy cannula designed by the assistance of virtual bronchoscopy. Laryngoscope 113:760–762

Silverman PM, Zeiberg AS, Sessions RB, Troost TR, Davros WJ, Zeman RK (1995) Helical CT of the upper airway: normal and abnormal findings on three-dimensional reconstructed images. AJR Am J Roentgenol 165:541–546

Solomon SB, Magee C, Acker DE, Venbrux AC (1999) TIPS placement in swine, guided by electromagnetic real-time needle tip localization displayed on previously acquired 3-D CT. Cardiovasc Intervent Radiol 22:411–414

Solomon SB, White P Jr, Wiener CM, Orens JB, Wang KP (2000) Three-dimensional CT-guided bronchoscopy with a real-time electromagnetic position sensor: a comparison of two image registration methods. Chest 118:1783–1787

Solomon SB, Dickfeld T, Calkins H (2003) Real-time cardiac catheter navigation on three-dimensional CT images. J Interv Card Electrophysiol 8:27–36

Sorantin E, Halmai C, Erdohelyi B et al (2003) 3D cross section of the laryngotracheal tract. A new method for visualization and quantification of tracheal stenoses. Radiologe 43:1056–1068

Summers RM (1997) Navigational aids for real-time virtual bronchoscopy. AJR Am J Roentgenol 168:1165–1170

Triglia JM, Nazarian B, Sudre-Levillain I, Marciano S, Moulin G, Giovanni A (2002) Virtual laryngotracheal endoscopy based on geometric surface modeling using spiral computed tomography data. Ann Otol Rhinol Laryngol 111:36–43

Valvassori GE (1994) Update of computed tomography and magnetic resonance in otology. Am J Otol 15:203–206

Vannier MW, Marsh JL (1996) Three-dimensional imaging, surgical planning, and image-guided therapy. Radiol Clin North Am 34:545–563

Vining DJ (1996) Virtual endoscopy: is it reality? Radiology 200:30–31

Walshe P, Hamilton S, McShane D, McConn Walsh R, Walsh MA, Timon C (2002) The potential of virtual laryngoscopy in the assessment of vocal cord lesions. Clin Otolaryngol Allied Sci 27:98–100

Wang D, Zhang W, Xiong M, Xu J (2001) Laryngeal and hypopharyngeal carcinoma: comparison of helical CT multiplanar reformation, three-dimensional reconstruction and virtual laryngoscopy. Chin Med J (Engl) 114:54–58

Zbaren P, Becker M, Lang H (1996) Pretherapeutic staging of laryngeal carcinoma. Clinical findings, computed tomography, and magnetic resonance imaging compared with histopathology. Cancer 77:1263–1273

Zbaren P, Becker M, Lang H (1997a) Staging of laryngeal cancer: endoscopy, computed tomography and magnetic resonance versus histopathology. Eur Arch Otorhinolaryngol 254 Suppl 1:S117–122

Zbaren P, Becker M, Lang H (1997b) Pretherapeutic staging of hypopharyngeal carcinoma. Clinical findings, computed tomography, and magnetic resonance imaging compared with histopathologic evaluation. Arch Otolaryngol Head Neck Surg 123:908–913

Thorax

14

Henning Meyer and Patrik Rogalla

CONTENTS

14.1 Introduction

Today computed tomography (CT) represents the standard examination technique for the chest region when there is still no diagnosis after conventional radiography. The thorax with its mainly air-filled lungs contains less X-ray-absorbing tissue than other regions such as the abdomen, for example. Therefore, lower radiation exposure suffices to yield reasonably good images. Furthermore, the high contrast between air and vessels or pathologic structures in the lungs provides very good natural contrast. Nonetheless, the evaluation of the mediastinum can be difficult in the presence of high image noise. Modern multislice CT scanners allow for an entire chest scan in about 10–15 s with a slice thickness of 1 mm and below, which is crucial to yield good results in subsequent post processing. CT is a widely available, fast, robust and relatively simple to use modality, which gives high-resolution three-dimensional images with a reasonable amount of radiation exposure.

H. Meyer, MD
P. Rogalla, MD, Associate Professor
Department of Radiology, Charité Hospital, Humboldt-University Berlin, Schumannstrasse 20/21, 10098 Berlin, Germany

14.1.1 Acquisition Parameters

In order to get good images, some basic requirements should be met. With today's fast multislice CT scanners, motion artifacts due to breathing can be largely avoided. The examination should be performed in a single breathhold starting from the lung base going up to the apices of the lungs. This way, when a patient cannot hold his/her breath for the entire scan, breathing will most likely take place when the scan has reached to the upper part of the chest. In this region, motion artifacts are not as disturbing as in the lower, much more mobile parts of the lungs.

For an evaluation of the pulmonary parenchyma, a native scan without contrast media is sufficient due to the good natural contrast between air and soft tissue structures. But for evaluating mediastinal structures such as lymph nodes, the heart or the pulmonary vessels, i.v. contrast medium should be administered in order to enhance the contrast of the soft tissue structures.

Nowadays, most scanners offer tube current modulation, which should be used to reduce the radiation exposure without reducing the image quality. The tube current should be in the range of 20 to 200 mAs depending on the chosen pitch factor.

14.2 Postprocessing Techniques

14.2.1 Postprocessing During Image Reconstruction

Postprocessing of all computed tomography (CT) source data sets already begins with the reconstruction of axial slices from the raw data. Careful parameter selection for this step is important because it affects the diagnostic quality of the resulting images. For example, both lung and soft-tissue reconstructions should be performed for chest scans to improve visualization of the respective structures, which shows an axial slice reconstructed using a soft-tissue kernel. This reconstruction is characterized by very good depiction of mediastinal soft tissue structures, while the lung contour appears blurred in the lung window. Figure 14.1 shows a reconstruction of the same slice using a harder reconstruction kernel that emphasises edges.

There is much better depiction of the lung structure in the images from the harder reconstruction kernel (Figs. 14.2 and 14.3). But it is also obvious that the soft tissue window of this reconstruction

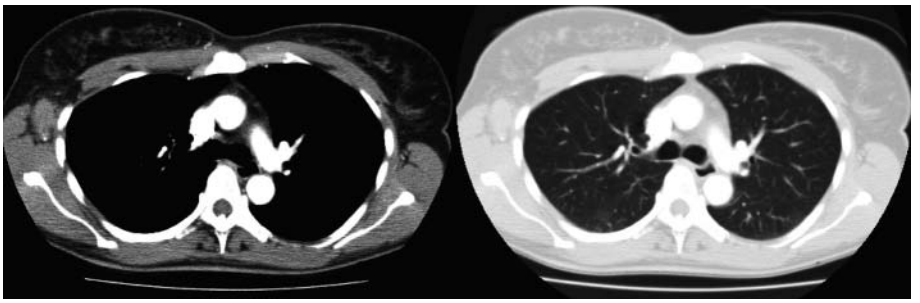

Fig. 14.1. Reconstruction using a soft tissue reconstruction kernel

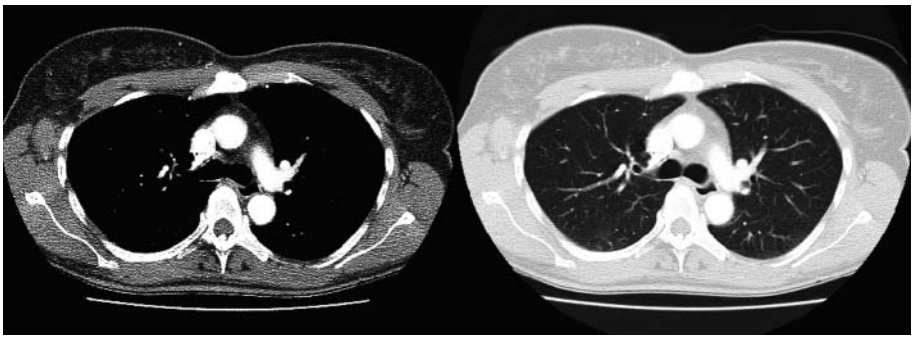

Fig. 14.2. Reconstruction using an edge-enhancing lung reconstruction kernel

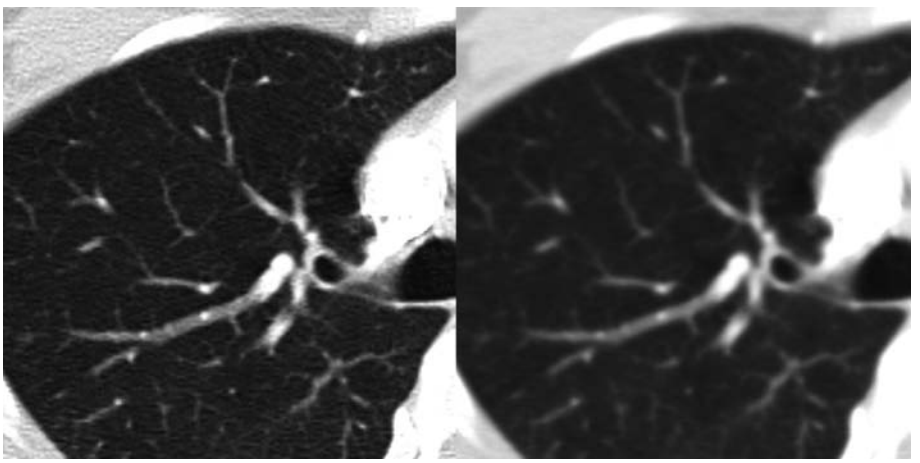

Fig. 14.3. More lung details are visible in the harder reconstruction kernel image

is unsuitable for evaluation of the mediastinal soft tissue structures due to high noise.

For routine evaluation, it is generally sufficient to reconstruct 5 mm-thick slices with 4 mm increment, resulting in 20% overlap. Overlapping reconstruction is mandatory for adequate depiction of smaller structures (e.g., pulmonary nodules) between slices. Without overlapping reconstruction, smaller structures at the edge of a slice might be obscured by partial volume effects (see Figs. 14.4, 14.5 and 14.6).

High-resolution reconstruction has been available since the advent of incremental CT and consists in reconstructing individual thin slices of all lung regions for more detailed evaluation. For MSCT, high-resolution reconstruction can be performed with 0.5 mm slice thickness and 20 mm increment.

For some diagnostic tasks such as the search for small pulmonary artery embolism, it is necessary to reconstruct continuous thin slices to enable more sophisticated postprocessing.

MSCT data sets allow reconstruction of a continuous slab of 0.5-mm slices with 20% overlap. In such a slab, resolution along the z-axis (or slice-to-slice resolution) is about twice as high as in-plane resolution of axial images. For most applications, 1 mm slices with 0.8 mm increment are sufficient. The latter has two advantages: the amount of data to be stored and transferred is reduced by half, and image noise is also reduced because more raw data are averaged. For those reconstructions a softer reconstruction kernel, e.g., body filter should be used to limit the image noise.

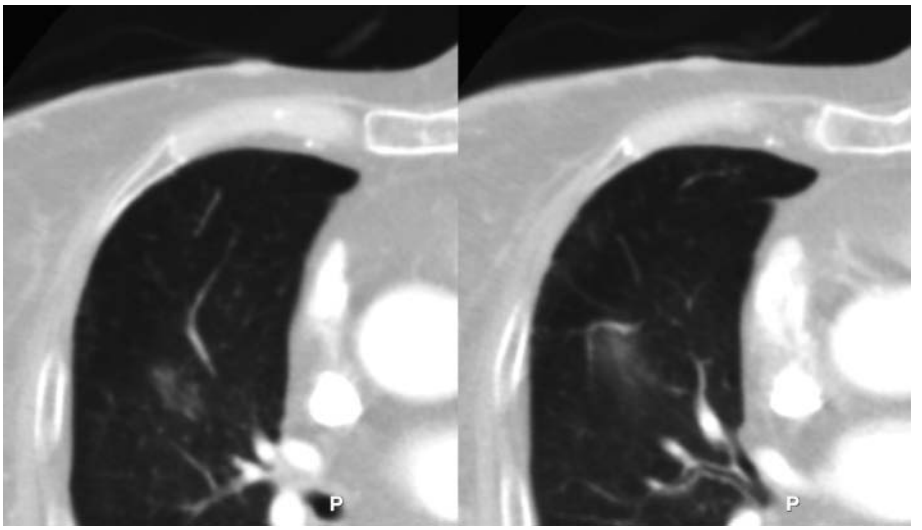

Fig. 14.4. Two adjacent slices with 5-mm-slice thickness, 0% overlap– no pulmonary nodules are visible

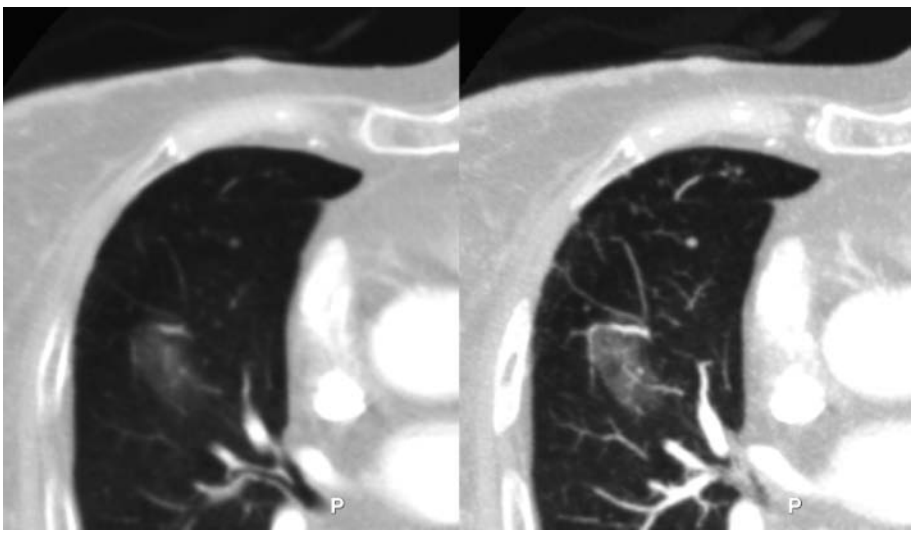

Fig. 14.5. The left image shows the image following the left image of Figure 14.4 if 20% overlap is used; in the MIP reconstruction (right) the nodule is visible even more clearly

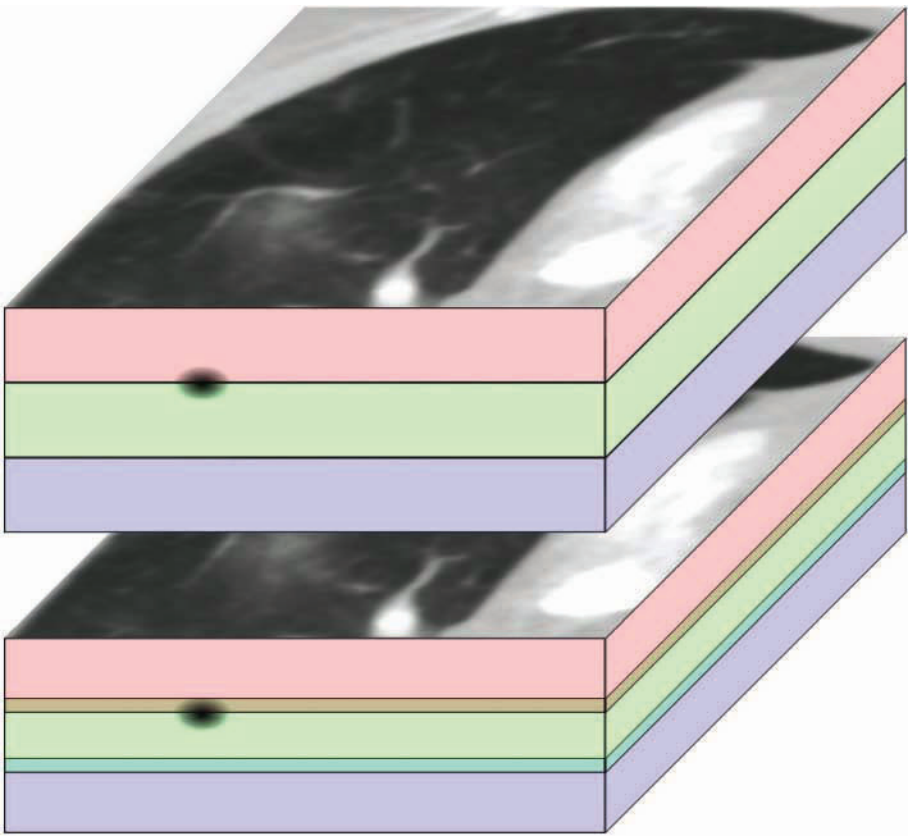

Fig. 14.6. Top: three slices without overlap–the small is located half in the red, half in the green slice and may vanish due to partial volume effect. Bottom: the entire nodule is now in the green slice–so chances are higher that the nodule will be seen

A higher in-plane resolution may be beneficial for specific diagnostic indications, e.g., reconstruction of the two pulmonary lobes with separate, smaller fields of view. A reconstruction matrix with twice the resolution, i.e., 1,024 × 1,024 pixels, will probably be available from scanner manufacturers in the future. However, one must not overestimate the expected benefit because the image information available is limited by the physical limitations of the detector, and a higher resolution of reconstructed slices does not necessarily result in a gain in information.

14.2.2 MPR, MIP and Other Reconstruction Algorithms

Axial slices are sufficient for many diagnostic purposes, while slices in the coronal, sagittal or any other plane may be useful for specific diagnostic tasks. Figure 14.7 shows an example illustrating that sagittal views allow excellent assessment of the relationship of pulmonary nodules to lobe boundaries. Such multiplanar reformations (MPR) can only be generated from thin slices because they also require high resolution along the z-axis (head-to-toe axis). Again, the reformations–just as the initial reconstructions–can be generated with different slice thicknesses. A single pixel in the reformatted image can represent a stack of voxels from the thin slices. If the pixel represents the mean value of these voxels, the projection is a so-called average projection. An average projection suppresses image noise, but edge sharpness is also degraded. An average projection with a slice thickness comprising the entire chest is an approximation to conventional radiography. Alternatively, the brightest voxel of each stack becomes the pixel of the resulting image, which is known as the maximum intensity projection (MIP). MIP images are well suited to depict bright structures with higher signal intensity than surrounding structures. Hence, MIP allows excellent evaluation of both bones and pulmonary vascular anatomy (Fig. 14.8). However, MIP images have a major drawback in evaluating vascular pathology of the lungs: embolism may be obscured because the MIP shows only the high-signal-intensity areas, which, in the case of the pulmonary arteries, are the opacified portions. Mainly thrombi completely surrounded by contrast medium are prone to be overlooked (Fig. 14.8).

A postprocessing algorithm very closely related to MIP is the minimum intensity projection (MinMIP or mIP), which selects the darkest voxel along the viewing ray to generate the image. As a result, MinMIP is well suited to depict structures with low signal relative to surrounding structures such as the respiratory tract. However, as with MIP, airway constrictions may be obscured on MinMIP images (Figs. 14.9, 14.10).

A CT scan always contains image noise and may result in either too high or too low HU values of the voxels. Since the MIP algorithm uses the brightest voxels from a stack, it tends to select voxels that are too bright and have high noise, thereby amplifying image noise. An alternative is the softMip algorithm.

Similar to MIP and average, the softMip algorithm generates one pixel from the HU values along a corresponding viewing ray. These values constitute a profile P of this ray, and the values are sorted according to their HU. After sorting of the profile, the resulting value is computed as a weighted sum of all values of the sorted profile Ps using a weighting function fw (see Fig. 14.11).

The shape of the weighting function determines the characteristics of the resulting images. Figure 14.12 shows different weighting functions and the resulting softMip images. While a constant function will result in average projection images, an impulse shaped function with the impulse at the maximum HU will result in MIP images. Intermediate functions generate images with characteristics of both average and MIP in that noise is suppressed, but edges are not blurred.

Reformations need not necessarily be performed along a single geometrical plane. It is also possible to generate curved reformations along a path. For complete visualization of the thoracic aorta, the user first has to define a path through the aorta, then a curved MPR can be generated along the defined path. Curved reformations can be generated for different slice thicknesses and using different projection algorithms.

Fig. 14.7. In sagittal views the pulmonary fissures are clearly visible. In this case it is obvious that the suspected malignoma is located in the upper lobe, pulmonary segment 1

Fig. 14.8. MIP renderings show a nice overview of the vascular and bone structures

14.2.3 Segmentation

More sophisticated reformation techniques typically require generating a subvolume from a complete data set, e.g., a slab in MPR. Specialized tools are available that allow one to select a target anatomy of interest as a subvolume. This can be done by means of various mathematical operations. A general mathematical function used for this purpose is selection according to a predefined threshold. Using this function, one may either select all voxels above the threshold while discarding those below

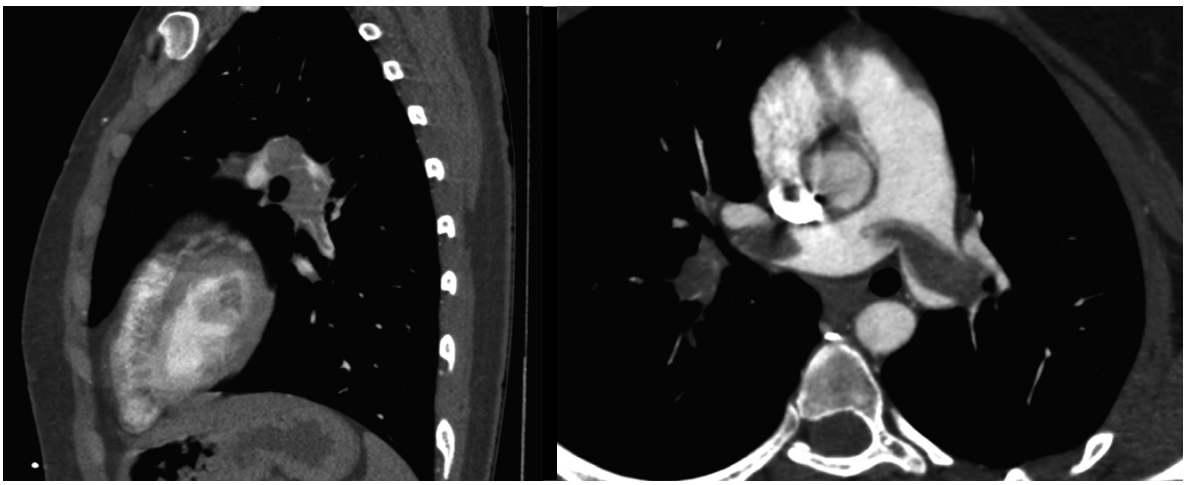

Fig. 14.9. Same patient as Figure 14.4–thin slices reveal the fulminant pulmonary embolism, which was hidden in the MIP

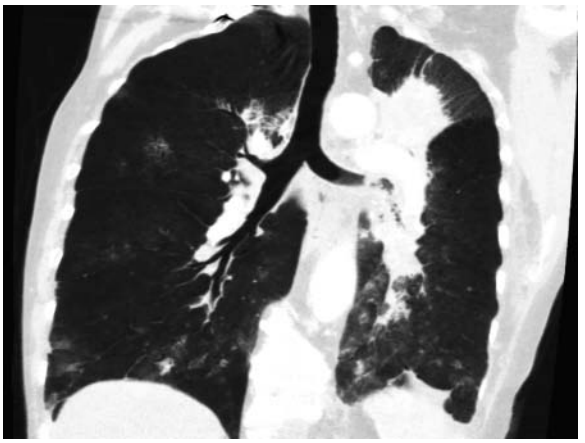

Fig. 14.10. While airways are nicely visualized in minMip, the obstruction of the left main bronchus is only visible partly

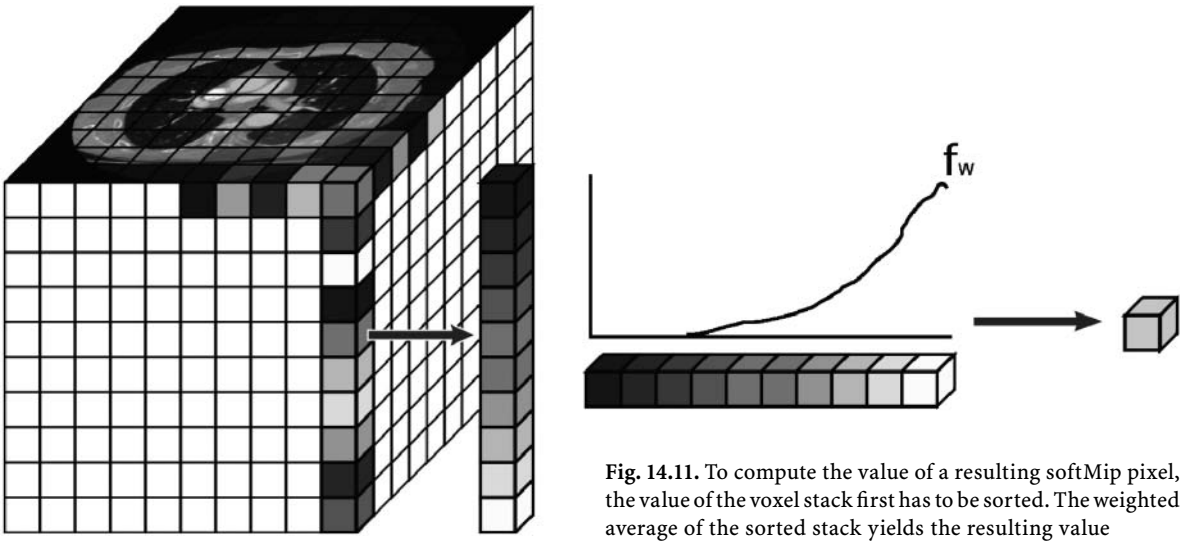

Fig. 14.11. To compute the value of a resulting softMip pixel, the value of the voxel stack first has to be sorted. The weighted average of the sorted stack yields the resulting value

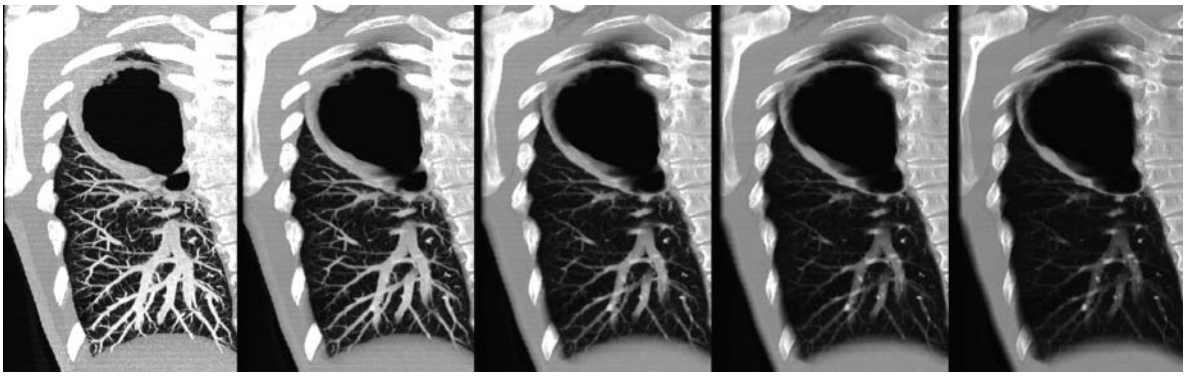

Fig. 14.12. SoftMip with different weighting functions yields images with MIP or average projection characteristics; if the weighting function is chosen carefully, one can yield images with lower noise than MIP, but higher edge sharpness than average projection

the threshold or vice versa. This operation yields a binary volume data whose voxels are either 1 or 0. This simple tool can be used, for example, to select the bones from an unenhanced chest data set. If several segments result, the user can choose the one to be taken into account by a simple mouse click. Other basic operations are morphological operations such as erosion or dilation, which serve to uniformly magnify or reduce a binary volume (see Fig. 14.13).

Using a combination of these operations, one can easily and quickly segment the lungs from a data set. This approach can be used, for instance, to generate a MIP of both lungs without interfering ribs (Fig. 14.14).

However, these simple operations alone are often not sufficient to segment the structure of interest. For instance, the aorta often coursing very close to the spine is difficult to separate because these two structures constitute a single segment. This is where so-called watershed segmentation comes in, which can be used to separate contiguous structures and yields good results in tricky cases. A detailed description of the function of this segmentation algorithm would go beyond the scope of this book.

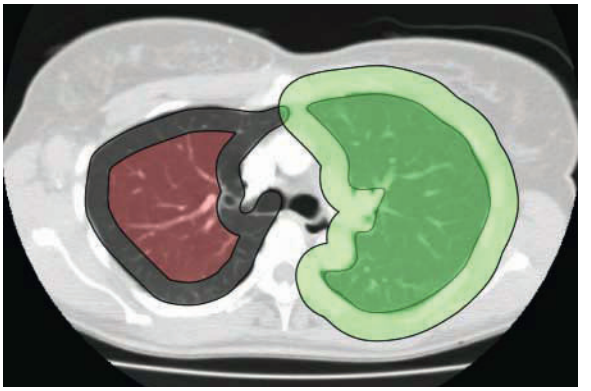

Fig. 14.13. The red shape illustrates the eroded right lung, while the green shape represents the dilated left lung

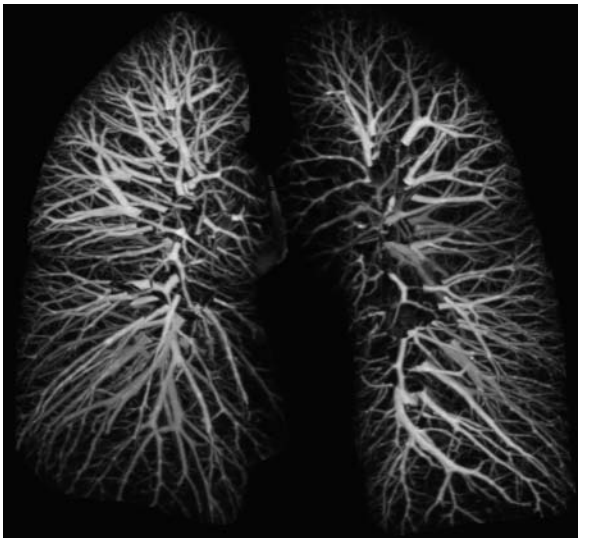

Fig. 14.14. MIP of the complete lungs without any interfering bones or mediastinal structures–generated by segmentation and erosion of the lungs

14.2.4 Shaded Surface Display

Segmentation is used not only to select specific structures for projection. Moreover, binary volumes can also be directly rendered as objects. A shaded surface display (SSD) is a depiction of the surface of such a volume. The user can select surface properties such as colors and reflection. A realistic impression is created

by directing an imaginary light source at the object. Since only the surface is displayed, this technique is especially useful for depicting the bones, which are also easy to segment as outlined above. Figure 14.15 shows an SSD of the bony chest in a patient with several rib and a sternal fractures after reanimation.

14.2.5 Volume Rendering

Volume rendering is used to depict internal structures of parenchymal organs. The technique assigns not only a color and reflection properties to each voxel, but also a transparency value, typically on the basis of the HU value. In general, a graphically displayed table lists a selection of HU values to which color and transparency values are assigned. Intermediate values are then interpolated for the remaining HU values, resulting in a transfer function for volume rendering. A volume rendering of a chest scan is presented in Figures 14.15, 14.16. To obtain an image, each voxel in the volume is individually colored and illuminated by the virtual light source, making volume rendering a time-consuming and relatively slow technique. However, more and more workstations are equipped with special rendering hardware or a 3D consumer graphic card for hardware-accelerated display. In this way, interactive volume rendering becomes possible on state-of-the-art systems.

Volume rendering can also be combined with segmentation for selected display of specific target structures. Nevertheless, the clinical value of volume rendering is usually limited to the generation of easy-to-understand overviews for clinical presentations.

Fig. 14.15. Shaded surface display of the rib cage–notice the bilateral serial rib and sternum fractures

14.2.6 Virtual Endoscopy

Virtual endoscopy is another clinical application of volume rendering and SSD and, in chest applications, allows very effective diagnostic evaluation of the respiratory tract. Good views of the air-filled trachea and bronchi can be obtained by choosing suitable segmentation parameters for SSD or a suit-

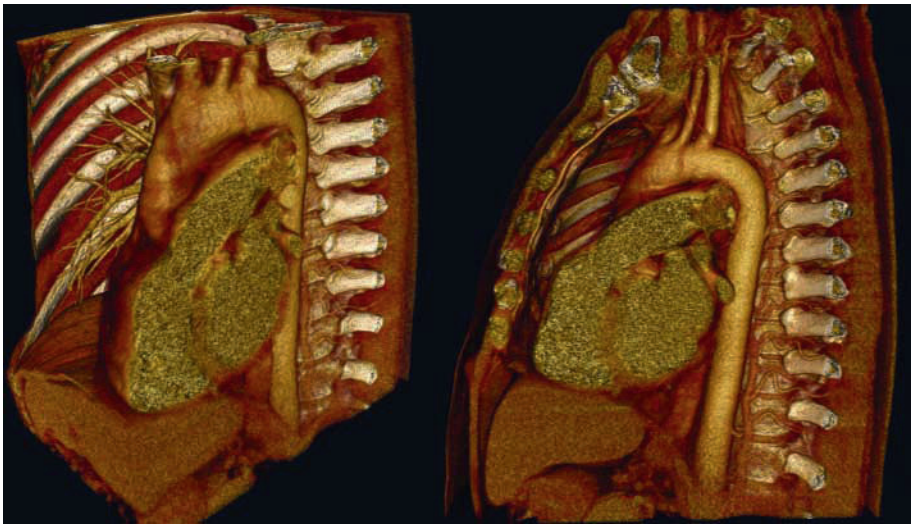

Fig. 14.16. Volume rendering of a patient with an angiosarcoma of the pulmonary artery

able transfer function for volume rendering. The airways can then be inspected by manually guiding a virtual camera through the passages or by moving the camera along a predefined path. An endoluminal view of the tracheal bifurcation is presented in Figure 14.17. With the interactive camera, the airways can be examined in a way similar to optical bronchoscopy. However, fine details of surface morphology are lost. An advantage of virtual endoscopy is that the radiologist can call up the corresponding cross-sectional images for clarification whenever he or she encounters a suspected lesion or mass by simply clicking on the structure. Figure 14.18 shows an obstruction of two smaller bronchi and the corresponding cross sections revealing the mucoid obstruction.

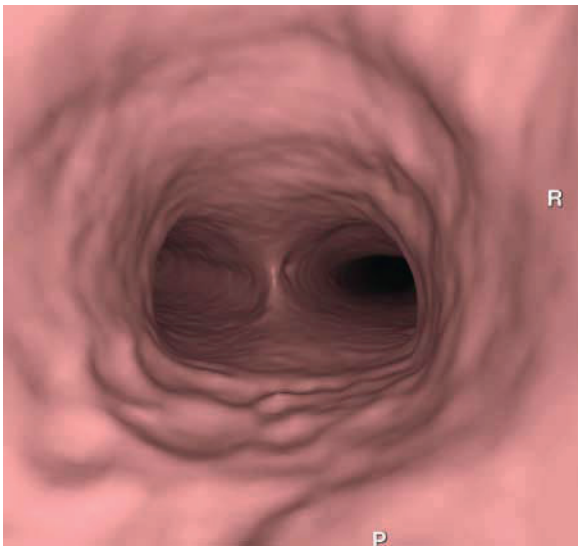

Fig. 14.17. Virtual bronchoscopic view of the tracheal bifurcation

14.3 Summary

Today's modern multislice CT scanners allow for an easy and fast examination of the entire thoracic region during a single breathhold. For sophisticated postprocessing techniques, thin overlapping slices should be reconstructed. Although many different post-processing techniques exist on modern visualization workstations, primary axial reading remains the most important step in solving a case. Projection-based techniques like MIP can visualize the pulmonary vessels nicely. Nonetheless, they should be used carefully as they might mask pathologies like pulmonary embolisms. After segmenting, the dataset reconstructions like shaded surface display can be used to clearly visualize bones or contrasted vessels. Volume rendering yields high quality aesthetic visualizations for clinical presentations. Both SSD and volume rendering allow endoscopic views of the bronchial tree.

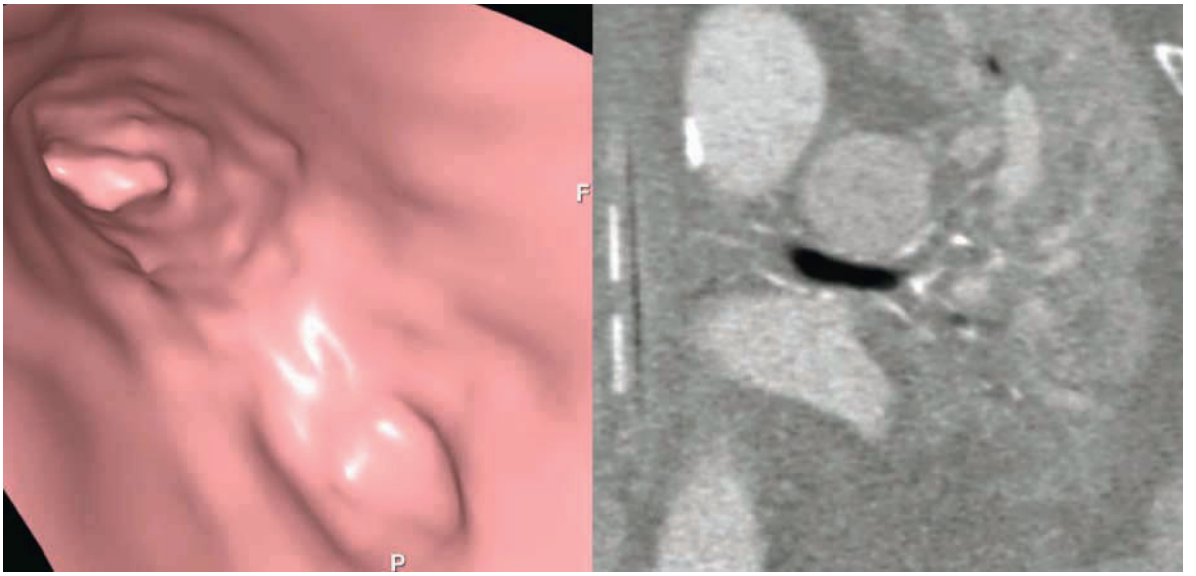

Fig. 14.18. Endoluminal view and cross-sectional correlation of a mucoid obstruction

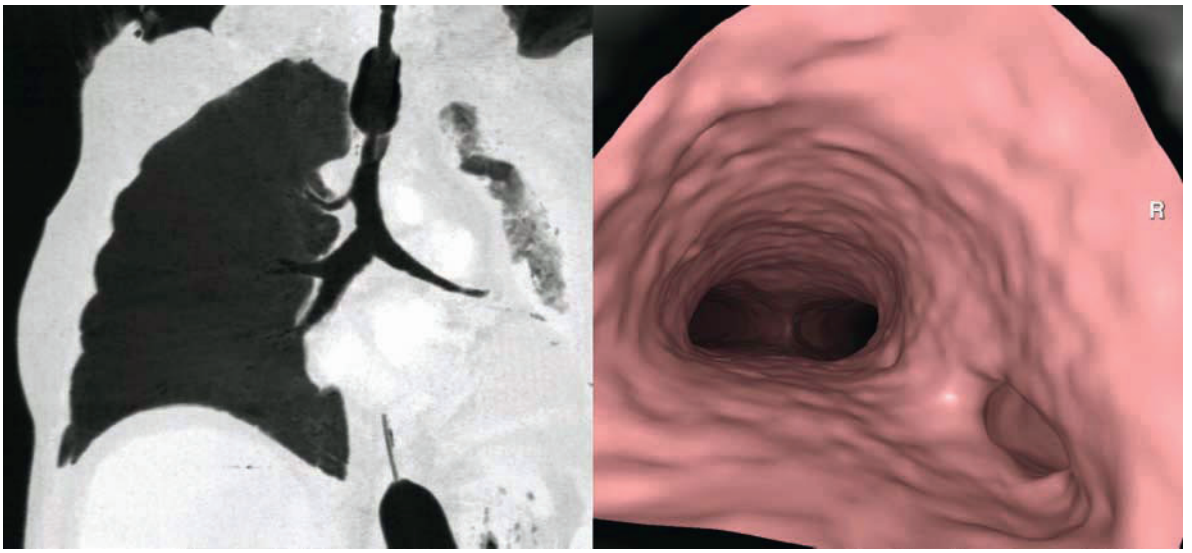

Fig. 14.19. MinMip visualization and endoluminal correlation of an accessory right upper lobe bronchus

Further Reading

Alkadhi H, Wildermuth S, Marincek B, Boehm T (2004) Accuracy and time efficiency for the detection of thoracic cage fractures: volume rendering compared with transverse computed tomography images. J Comput Assist Tomogr 28(3):378–385

Beigelman-Aubry C, Hill C, Guibal A, Savatovsky J, Grenier PA (2005) Multi-detector row CT and postprocessing techniques in the assessment of diffuse lung disease. Radiographics 25(6):1639–1652

Eibel R, Bruning R, Schopf UJ, Leimeister P, Stadie A, Reiser MF (1999) Bildanalyse bei der Mehrschicht-Spiral-CT der Lunge mit MPR- und MIP-Rekonstruktionen. Radiologe 39(11):952–957

Marten K, Funke M, Obenauer S, Baum F, Grabbe E (2003) The contribution of different postprocessing methods for multislice spiral CT in acute pulmonary embolism. Rofo 175(5):635–639

Napel S, Bergin C, Paranjpe D, Rubin GD (1992) Maximum and minimum intensity projection of spiral CT data for simultaneous 3D imaging of the pulmonary vasculature and airways (abstract). 78th 52 Scientific Sessions Radiological Society of North America Bd. 185(p). Chicago: Radiology 126

Napel S, Rubin GD, Jeffrey J (1993) STS-MIP: a new reconstruction technique for CT of the chest. J Comput Assist Tomogr 17(5):832–838

Rubin GD (2000) Data explosion: the challenge of multidetector-row CT. Eur J Radiol 36(2):74–80

Seemann MD, Heuschmid M, Vollmar J, Kuttner A, Schober W, Schafer JF, Bitzer M, Claussen CD (2003) Virtual bronchoscopy: comparison of different surface rendering models. Technol Cancer Res Treat 2(3):273–279

Zou Y, Sidky EY, Pan X (2004) Partial volume and aliasing artefacts in helical cone-beam CT. Phys Med Biol 49:2365–2375

Cardiovascular Applications

15

Christoph R. Becker

CONTENTS

15.1 Introduction

Almost every year, new CT scanners are introduced, allowing investigation of any part of the body with the highest spatial and temporal resolution within the shortest scan time. CT angiography performed with multi-detector-row CT (MDCT) and dedicated contrast protocols visualize even the smallest of vessels in the periphery of any vascular tree. Coronary arteries are of particular challenge for imaging by CT because of their small size and their continuous rapid movement. With the newest MDCT scanners, however, any vascular territory, including the coronary arteries, is now assessable with detailed anatomic (Achenbach et al. 2006).

CT, as a cross-sectional imaging modality, primarily is only able to display small parts of any artery curving within the three-dimensional space in the body. Therefore, three-dimensional visualization and post-processing tools are mandatory to display the anatomical situation and to support diagnosis and therapy. The primary post-processing tools for this purpose are volume-rendering technique (VRT), multi-planar reformatting (MPR) and maximum intensity projection (MIP). Most modern workstations provide these tools simultaneously in a split monitor mode. These workstations also support measurements for the degree of vascular stenoses, and further provide more dedicated tools for quantitative coronary assessment (QCA) of lumen stenoses and plaque analysis (Schroeder et al. 2001).

15.2 Cerebral and Supra-aortic Vessels

CT angiography (CTA) has become an important tool to detect intra-cerebral aneurysms in patients with sub-arachnoidal hemorrhage. CTA and digital subtraction angiography (DSA) are comparable in terms of assessing sub-clinical aneurysms. Nonetheless, it is difficult to detect aneurysms at the base of the skull because of bone overlay. "Digital subtraction" CTA methods require acquisition of the head and neck with two consecutive CT scans, one prior to and one after the administration of contrast media. Former methods for subtracting both datasets were of limited success due to mismatch caused by even minor patient or table movement inconsistencies between the two scans. Newer post-processing toolsm such as "matched mask bone elimination," has helped to overcome this limitation and is feasible for producing reliable selective CTA results for the diagnosis of cerebral aneurysms (Tomandl et al. 2006).

Atherosclerosis of the carotid artery represents an important risk for ischemic strokes. Therapeu-

C. R. Becker, MD
Institute of Clinical Radiology, Ludwig-Maximilians University, Grosshadern Hospital, Marchioninistrasse 15, 81377 Munich, Germany

tic decisions are based on large multi-center studies such as the North American Symptomatic Carotid Endarterectomy Trail (NASCET) and the European Carotid Surgery Trial (ECST), which proved that patients with ≥ 70% diameter stenosis of the internal carotid artery may benefit from a surgical intervention. Since the common and internal carotid arteries both run through the CT plane, most of the time it is easiest to measure the diameters necessary for the assessment of the degree of stenosis directly in the axial slices. However, in elongated vessels, e.g., sagittal or curved, planar reformatting may help to define the appropriate measurement locations (Hacklander et al. 2006).

15.3 Coronary Calcium Screening

Coronary calcium screening is a common tool for detecting sub-clinical coronary artery disease and for estimating the risk of a sudden cardiac event. Coronary calcium screening is performed with 3 mm slices, no contrast medium and with as little radiation as possible. Retrospective ECG gating is superior to prospective ECG triggering, another technique that acquires a slice every other heartbeat in order to scan the entire volume without any gaps and to reconstruct the images with overlapping slice increments. Overlapping slice reconstruction improves reproducibility of the coronary calcium quantification (Ohnesorge et al. 2002).

Even the tiniest calcification will become visible by the reconstruction with a no-edge-enhancing soft tissue kernel. The reconstructed images need to be analyzed and post-processed by a dedicated workstation. After identification of the specific calcified lesions in the coronary arteries, the workstation may automatically display different kinds of quantities of coronary calcium, such as the "Agatston score", "volume equivalent" and absolute mass (Fig. 15.1). The underlying algorithm of the Agatston score, for instance, is based on the calculation of any dense structure in the CT image with a density of more than 130 HU. The area of this lesion is then multiplied by a factor that depends on its peak density. An integer number between 1 and 4 is used for a peak density of 130–199 HU, 200–299 HU, 300–399 HU and > 400 HU, respectively. The sum of all lesions in all four coronary vessels (left main, left anterior descending, circumflex and right coronary artery) then corresponds then to the total Agatston score (Agatston et al. 1990). This algorithm requires more or less exactly the image quality known from electron beam CT (EBCT), a former dedicated but no longer available cardiac CT scanner type. As it is quite problematic to constantly reproduce the image quality from this former EBCT system with a modern MDCT scanner, the commonly reported Agatston score may only be of limited value for use with any MDCT.

Originally, coronary calcium investigation with the first EBCT scanners allowed only for acquisition of half of the heart because not more than 20 slices could be acquired at once. The limited reproducibility with this approach was therefore obvious (Hernigou et al. 1996), and a number of authors suggested algorithms to help improve the reproducibility. Finally, it turned out that the only way to improve the reproducibility of the coronary calcium measurement was to introduce a new quantification unit, the calcium "volume equivalent" (Callister et al. 1998). To determine a better reproducible volume equivalent value, isotropic interpolation is required, which can be equated to calculation of interpolated slices between two consecutive slices. However, real overlapping slice acquisition is always superior to isotropic interpolation (Ohnesorge et al. 2002), and should be used in MDCT. Nevertheless, the volume equivalent, as well as the Agatston score, both suffer from the fact that the quantities of coronary calcium derived from any CT still depends on the image quality, and therefore any values obtained, for instance from the EBCT, can hardly be compared with values obtained from MDCT systems (Becker et al. 1999).

In general, it is possible to quantify the absolute amount of coronary calcium by using a standard calibration phantom with any CT system (Ulzheimer and Kalender 2003). For this standardization the calibration phantom must be scanned with those parameters, which will also later be used in the patient investigation. As the masses of the different calcium hydroxyapatite particles in a dedicated anthropomorphic coronary calcium phantom become known, it is possible to measure the volume and the density of the corresponding spots in the CT image and then to calculate a calibration or conversion factor for deriving absolute values of these spots in milligrams.

However, in patient investigations the accuracy of the measurement may be influenced by the diameter of the chest. The X-ray absorption is different in obese as compared to slim patients, in whom radia-

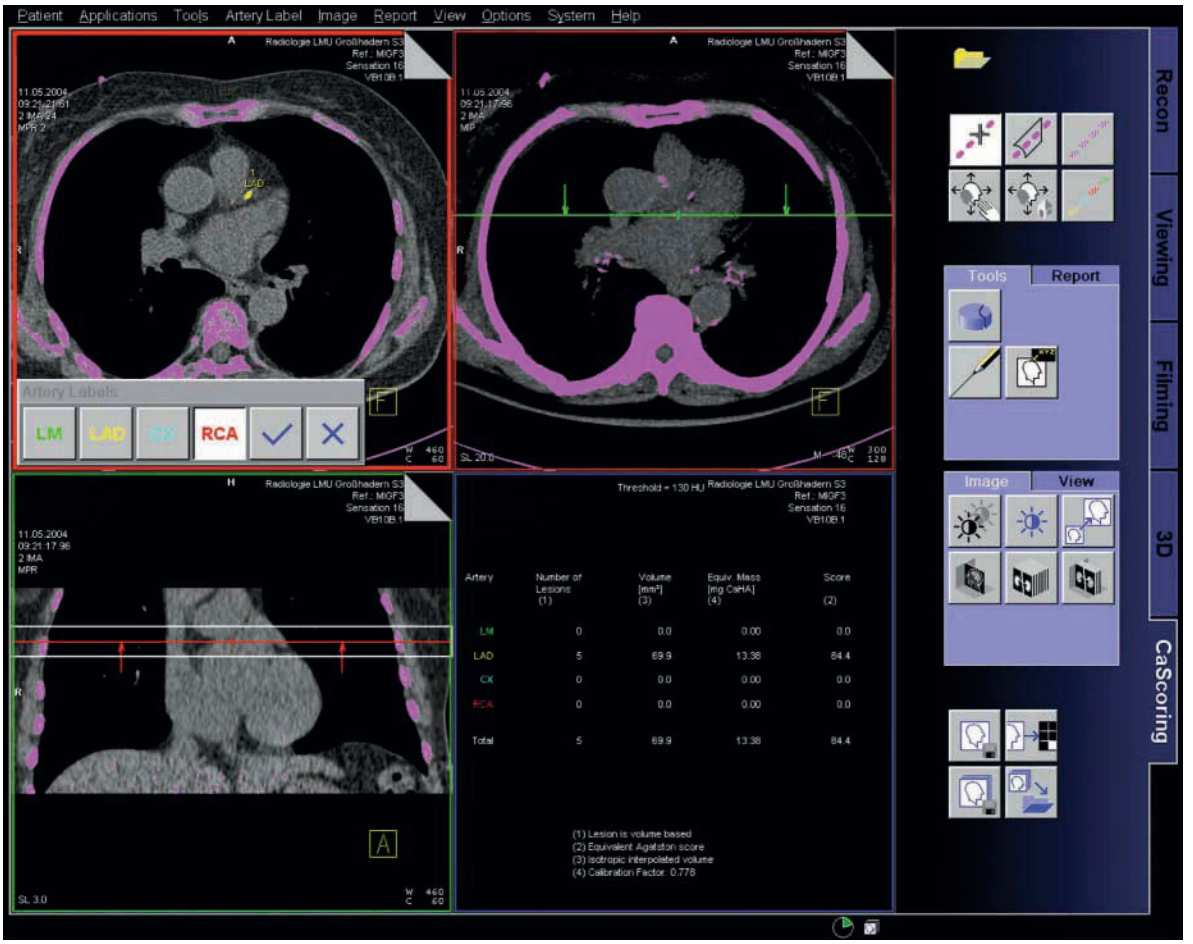

Fig. 15.1. For quantification of coronary calcium, non-enhanced low radiation dose CT scans with 3 mm slice thickness are loaded into a post-processing workstation. After semi-automated identification of the calcified lesion in the coronary arteries, these workstations automatically provide quantitative data as the Agatston score, volume equivalent and mass

tion exposure will lead to a beam hardening, resulting in lower densities of the equivalent amount of calcium. Therefore, the calibration phantom needs to be scanned with "fat rings" simulating different patient sizes that will deliver different calibration factors. In patient investigation, the topogram (scout view) will then be used to determine the diameters of the chest for the selection of the appropriate calibration factor. In practice, the calibration phantom will be measured without, with one and with two fat rings. The corresponding calibration factor will then be used for a chest diameter of < 30, 30–38 and > 38 cm, respectively.

Recently, the International Consortium on Standardization in Cardiac CT has tried to establish the standardized algorithm for coronary calcium measurements for different CT vendors. This consortium also tries to build up a database collecting data obtained in a standardized fashion to provide reference values for the absolute mass of coronary calcium (McCollough et al. 2003).

15.4 Coronary CT Angiography

For coronary CTA, the highest possible temporal and spatial resolution is mandatory to image the continuously moving small coronary arteries. The image reconstruction interval is best placed between the T- and P-wave of the ECG corresponding to either the end systolic or mid-diastole interval.

For morphological assessment of the coronary arteries, reasonably good image quality with a temporal resolution of ~80 ms can now be achieved in almost all patients regardless of heart rate (Johnson et al. 2006).

A timely, accurate and homogenous vascular lumen enhancement is essential for full diagnostic capability of coronary MDCT angiography studies. Higher contrast enhancement is superior to identify small vessels in MDCT and help automated software to segment them out of the acquired volume. The administration of nitroglycerin furthermore improves visibility of coronary arteries by inducing arterial dilation.

Image analysis begins with the identification of the coronary artery segments in the axial CT slices. Coronary segments can be numbered according to the model suggested by the American Heart Association (Austen et al. 1975). The primary axial slices are best suited to rule out coronary artery disease. However, the detection of coronary artery stenoses in axial CT images may be problematic since every slice displays only a small fragment of the entire coronary artery tree. Multi-planar reformatting, volume-rendering, virtual coronary endoscopy and shaded surface display have been tested for reconstruction of CTA images to detect coronary artery stenoses. In the beginning, none of these post-processing tools proved to be superior to axial slices for this task (Vogl et al. 2002). Maximum intensity projection (MIP) post-processing of CTA images were found to be helpful to follow the course of the coronary arteries and to create angiographic-like projections that may allow for better detection of coronary artery stenoses.

Standardized thin slab MIP reconstruction may be performed with 5 mm slab thickness and 2.5 mm increment in three different planes similar to standard cardiac catheter projections (Johnson 1996). MIP along the inter- and atria-ventricular groove creates images in similar planes as the right anterior oblique (RAO) and left anterior oblique (LAO) angiographic projections, respectively. The RAO projection is suited to demonstrate the course of the left anterior descending coronary artery, whereas the LAO projection best displays the course of the RCA and LCX. In addition, similar to coronary angiography an oblique projection can be reconstructed following the long axis of the heart. This projection plane spreads the branches of the LAD and is therefore called the "spider view". The spider view is designed to demonstrate the proximal part of all three major coronary arteries. Similar projections may also be created with the volume-rendering technique if the coronary arteries have been semi-automatically segmented out of the volume (Fig. 15.2).

For the first run, MIP images may help to identify coronary artery stenoses. Volume rendering was found to be helpful in demonstrating the course in cases of coiling and kinking of the coronary arteries, i.e., in hypertensive heart disease, in coronary fistula or in case of suspicion of any other coronary anomaly. However, every finding from post-processed images has to be confirmed in the original axial CT slices.

Initial experiences revealed a number of limitations already known from coronary CTA studies performed with the electron beam CT. Schmermund et al. (1998) reported that small vessel diameter may lead to false-positive findings. They also reported that extensive calcifications might interfere with the detection of coronary artery stenoses, resulting in false-negative results compared to selective coronary angiography. A reason for this observation may be that standard CT soft tissue reconstruction kernels are leading to a "blooming" of dense material such as coronary stents or calcifications that obscure the vessel lumen and wall changes.

It should also be considered when interpreting coronary CTA that details like collateral vessels, contrast run-off and direction of filling of coronary arteries are not visualized by CTA. Finally, the hemo-dynamic relevance of coronary artery stenoses may not only be determined by its degree but also requires motion analysis of the myocardium or myocardium perfusion data under rest and exercise. However, more and more post-processing tools are under development trying to provide quantitative measurements for the degree of stenoses in the coronary arteries. These measurements correspond to the quantitative coronary assessment (QCA) known from cardiac catheter (Fig. 15.3). The reliability of these measurements has not yet been determined.

15.5 Plaque Imaging and Analysis

More than merely displaying the lumen of the coronary arteries, MDCT by its cross-sectional nature is well-suited to demonstrating changes of the coronary artery wall. Coronary calcifications can easily

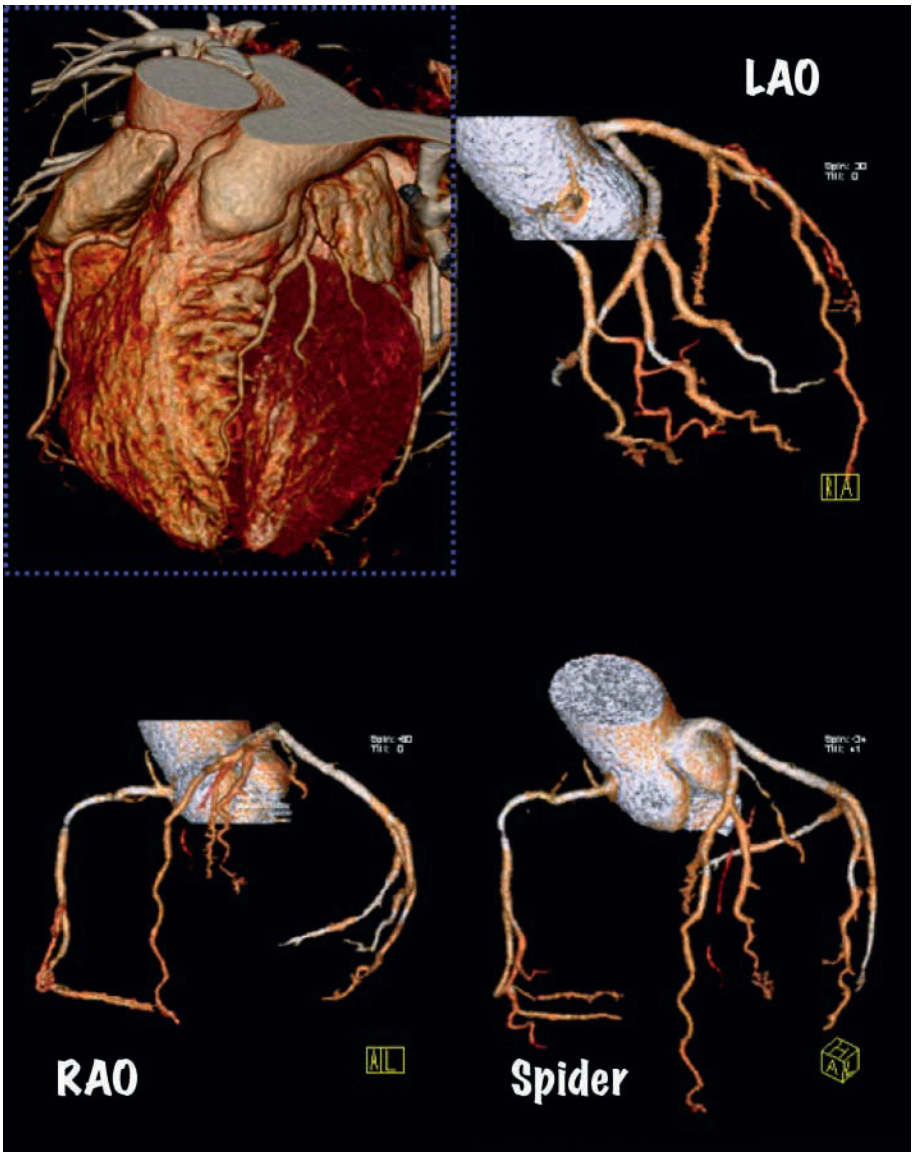

Fig. 15.2. Volume rendering is helpful in cardiac CTA datasets to display the anatomy of coronary arteries. After semi-automated segmentation of the coronary arteries out of the entire scan volume, standard-viewing projections may be created such as the LAO, RAO and spider view

be assessed even without contrast media, and represent an advanced stage of atherosclerosis. However, as different stages of coronary atherosclerosis may be present simultaneously, calcifications may also be associated with more early stages of coronary atherosclerosis. Therefore, the entire extent of coronary atherosclerosis will be underestimated by assessing coronary calcifications alone (Wexler et al. 1996). With contrast enhancement, calcified as well as non-calcified lesions can completely be assessed by MDCT simultaneously.

In patients with an acute coronary syndrome we have observed non-calcified plaques with low CT density values (20–40 HU) (Becker et al. 2000). These soft plaques in the coronary arteries may either correspond to unstable lipid-rich soft plaques or an intra-coronary thrombus formation. In asymptomatic patients and patients with chronic and stable coronary artery disease, frequently non-calcified and calcified plaques were found. The CT density of these plaques may be in the range of 90 HU and may correspond to stable fibrous rich or fibro-calcified plaques, respectively (Becker et al. 2003).

Commonly, spotty calcified lesions may be found in MDCT angiography studies that may be associated with minor wall changes in conventional coronary angiography only (Kajinami et al. 1997). However, it is known that such calcified nodules may also

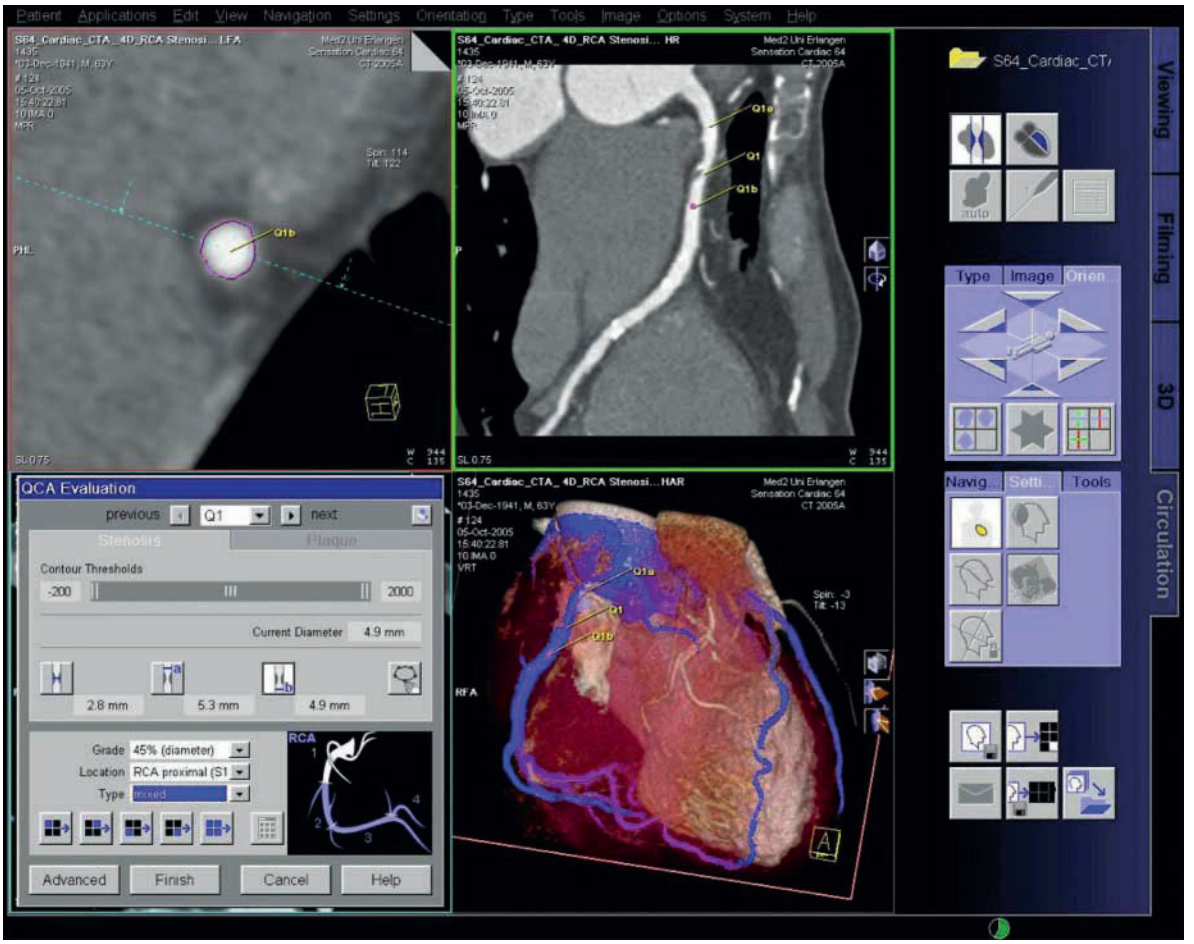

Fig. 15.3. After segmentation of the coronary arteries, dedicated software allows for quantifying the degree of coronary artery stenosis. The reliability of this measurement as compared to quantitative coronary assessment (QCA) by cardiac catheter has not yet been determined

be the source of unheralded plaque rupture and consecutive thrombosis, and may lead to sudden coronary death in very rare cases (Virmani et al. 2000). In patients with chronic and stable angina, calcified and non-calcified plaques are commonly found next to each other (Leber et al. 2003).

Even in contrast-enhanced studies, coronary calcifications can easily be detected and quantified because the density of calcium (> 350 HU) is beyond the density of contrast media in the coronary artery lumen (250–300 HU) (Hong et al. 2002). However, because of partial volume effects, it is much more difficult to quantify non-calcified rather than calcified plaques. The optimal quantification algorithm for the different presentation of coronary atherosclerosis as seen in MDCT is still under development (Fig. 15.4).

15.6 Cardiac Function by CT

By assessing the myocardium in patients with known history of coronary artery disease, sub-endocardial or trans-mural myocardial infarction scars may frequently be identified as hypodense areas. With further organization and healing of a sub-endocardial or trans-mural myocardial infarction, a thinning of the myocardial wall or myocardial aneurysm may take place. Due to myocardial dysfunction, or in atrial fibrillation, thrombus formation is likely to develop in the cardiac chambers and can be detected by CTA in the axial slices even more than by trans-thoracic ultrasound (Masuda et al. 1984).

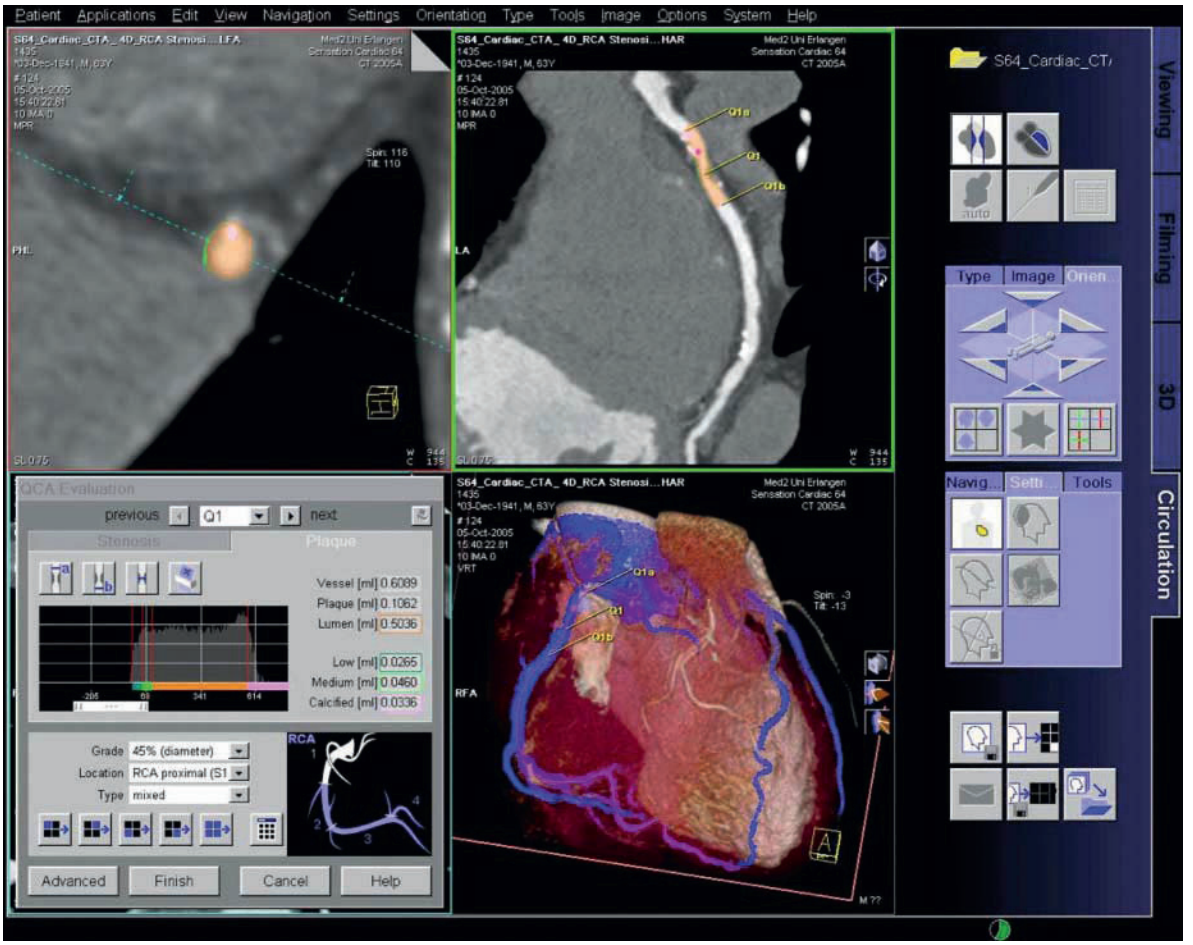

Fig. 15.4. The same software also may provide information about the composition of atherosclerotic plaque. The final way of quantifying these lesions in the coronary artery wall has not yet been determined and remains problematic, since the display of these lesions is very much influenced by partial volume effects

A late uptake of contrast media after first pass in the myocardium of patients after infarction has already been observed in CT similar to MRI about 20 years ago (Masuda et al. 1984). It is rather likely that this kind of myocardial enhancement may correspond to interstitial uptake of contrast media within necrotic myocytes, 6 weeks to 3 months after onset. The optimal point of time for scanning may be in between 5 and 10 min after first pass of the contrast media (Huber et al. 1981).

In addition, retrospective ECG gating allows for reconstruction of images at any time within the cardiac cycle. Setting the images together that are reconstructed every 50 ms after the R wave in the ECG allows visualization of the cardiac function in real time with a temporal resolution of 20 frames per second. The functional CT data can be evaluated by software in a similar fashion as MRI images, and global as well as regional wall motion may be determined (Halliburton et al. 2003). Currently, software is developed that determines the global functional parameters directly by contour recognition of the ventricle and myocardial wall from the original axial slices. This approach is much more time-efficient, and may be even more reliable than the reconstruction and evaluation of short axis images (Fig. 15.5).

However, it is also mandatory to refer to the axial slices in order to report the para-cardial findings that may frequently be observed in CTA studies. These findings may include lymph node enlargement, pulmonary nodules and tumors (Horton et al. 2002), or even quite commonly esophageal hernias. These incidental findings should trigger an

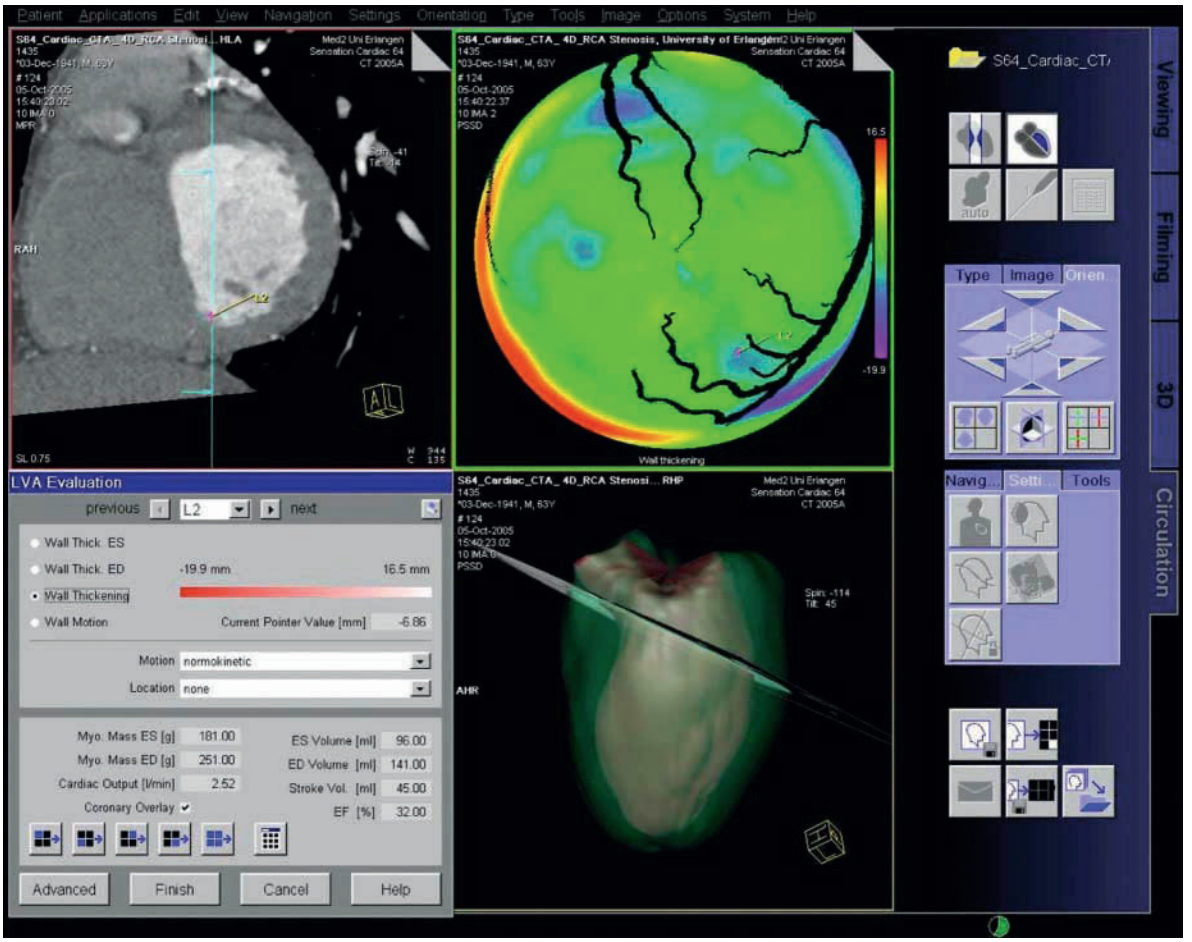

Fig. 15.5. Retrospectively gated image acquisition by CT does not only contain information about the coronary arteries but also about the function of the myocardium. Newer post-processing is under development, and tries to determine the axial CT slices reconstructed at different time points of the cardiac cycle. These workstations may provide data about the global functional parameter, as well as regional wall motion abnormalities

additional reconstruction with a larger field of view, or a more dedicated CT investigation should be recommended.

In patients with paroxysmal atrial fibrillation, ablation of ectopic foci is a common interventional procedure. CT data from the heart may serve for displaying the anatomy, detecting the anomalous course of pulmonary veins, intervention planning and guided navigation. Volume rendering in this respect is an ideal modality to display the anatomy of the pulmonary veins and the left atrium. As a possible complication of this intervention, stenoses of the pulmonary veins leading to pulmonary congestion have been reported. The presence and morphology of these stenoses can easily be assessed by CT (Purerfellner et al. 2003) in the axial slices as well in the three-dimensional post-processing (Fig. 15.6).

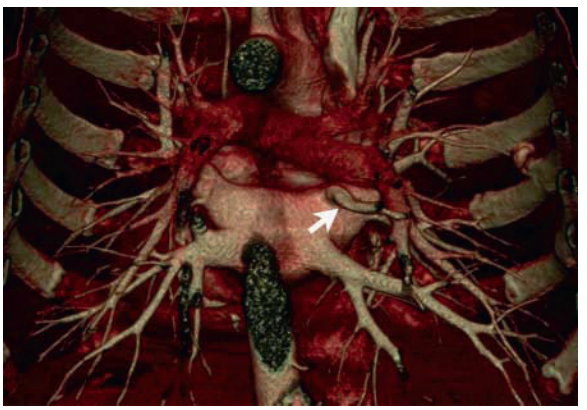

Fig. 15.6. Volume-rendered dataset of the pulmonary veins after removing the vertebral column. The image displays nicely the anatomy, such as the main left and right, upper, low and lower pulmonary veins, as well as the accessory vein in the left upper field (*arrow*)

15.7 Thoracic and Abdominal Aorta

The thoracic aorta may be affected by several different diseases, such as aortic dissection, intramural hematoma, penetrating atherosclerotic ulcer, aneurysms and traumatic injury. Any of these diseases may well be displayed in the axial slices, as well with post-processing (Takahashi and Stanford 2005). Volume rendering in particular is helpful in displaying the anatomical situation of the thoracic aorta after stent graft placement (Fig. 15.7).

The same holds true for the visualization of the abdominal aorta and for stent graft planning and for post-operative control for endo-leakage (Bartolozzi et al. 1998). Prior to surgery, CTA may be able to display the origin of the renal arteries and the distance from the abdominal aneurysm, as well as the course of the iliac arteries.

In living transplant donors, it is essential to display the vascular anatomy prior to surgery. Scanning, e.g. of the liver, by CT requires acquisition of different well-defined contrast phases for the detection of the overlaying different vascular structures. Newer workstations provide for three-dimensional display of the vascular anatomy and automatic virtual segmentation and operation planning of the different liver segments (Frericks et al. 2004).

Renal arteries are more commonly investigated by MRI rather than by CT. However, CTA in combination with oblique MIP or VRT is helpful in the detection of different pathologies of the renal arteries, such as atherosclerotic stenosis, fibromuscular dysplasia or Takayasu arteritis. Post-processing of the renal arteries also allows measurement of the degree of stenosis prior to intervention, or as follow-up control (Sabharwal et al. 2006).

In emergency situations CTA often is the first line option for the diagnosis of mesenteric ischemia or bleeding (Fleischmann 2003). Coronal MIP reconstructions often supports this diagnosis.

15.8 Peripheral Run Off

Imaging of lower extremity arteries becomes an increasingly important clinical tool for the rapid diagnosis of the vascular situation, e.g. in patients

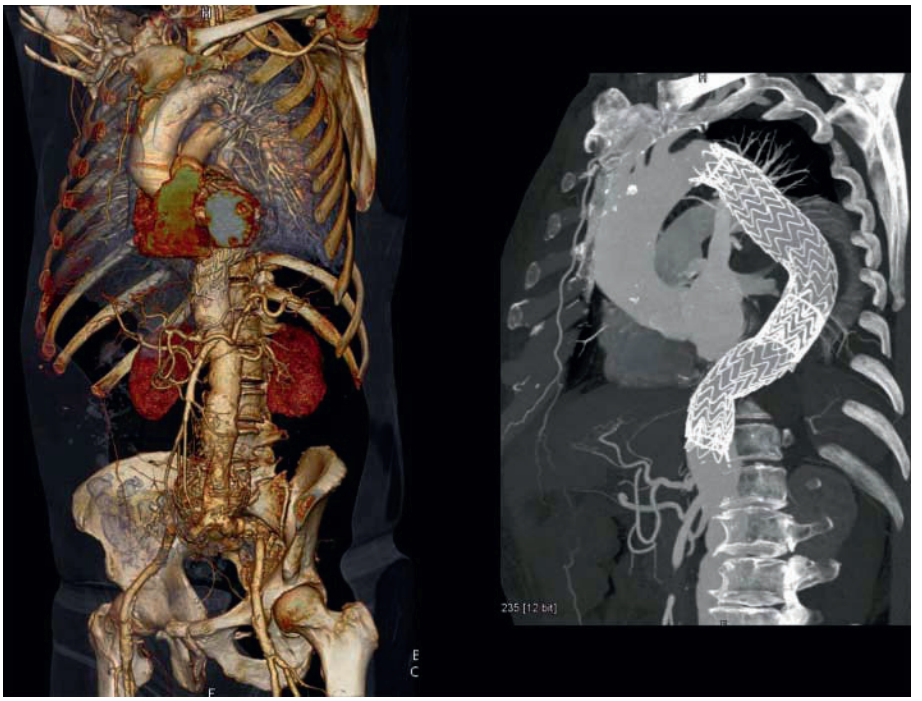

Fig. 15.7. Volume-rendered image and maximum intensity projection of a CTA dataset of a patient with two overlapping thoracic stents in the thoracic aorta. CTA also displays normal abdominal aorta and ectatic iliac arteries

with intermittent claudication, chronic limb-threatening ischemia, aneurysms, acute ischemia, follow-up, and surveillance after surgical or per-cutaneous revascularization (Fleischmann et al. 2006). For diagnostic purposes, the vascular tree as acquired by CT needs to be displayed in an angiographic-like fashion. MIP is well-suited in particular if only minor calcifications are present. However, MIP reconstruction requires segmentation and removal of bone structure. Even with advanced workstations this is still a time-consuming process that is difficult to implement in daily clinical routine.

Volume rendering is helpful in displaying the anatomical situation, e.g. the length of stenoses in the superficial femoral artery, and is able to provide information about the therapeutic options. The upper part of the abdominal aorta, iliac and femoral arteries is displayed in VRT AP and oblique views. The popliteal and lower limb arteries are best displayed in VRT PA views. Because VRT provides three-dimensional information, it is not necessary to segment the bones from the arteries. A complete set of images can be produced within a short period of time and can be delivered shortly after scanning (Fig. 15.8).

However, in the case of severe calcifications and stents, significant stenosis may easily be overseen when using VRT and MIP. Therefore, MPR and curved planar reformation may be an alternative for displaying diseased vessel segments. To improve the rapid availability of these post-processing alternatives, automated segmentation and vessel centerlining would be required, which is still a topic for further debate.

15.9 Future Aspects

The most recent development in CT scanners is dual-source technology. Two separate X-ray sources and two detector systems are arranged perpendicular to each other, and rotate around the body. Initially, the design was chosen to improve the temporal resolution for cardiac imaging. However, if these two tubes run at different kV levels, elements with different order numbers such as calcium and iodine may be separated by their different dual energy indices. As

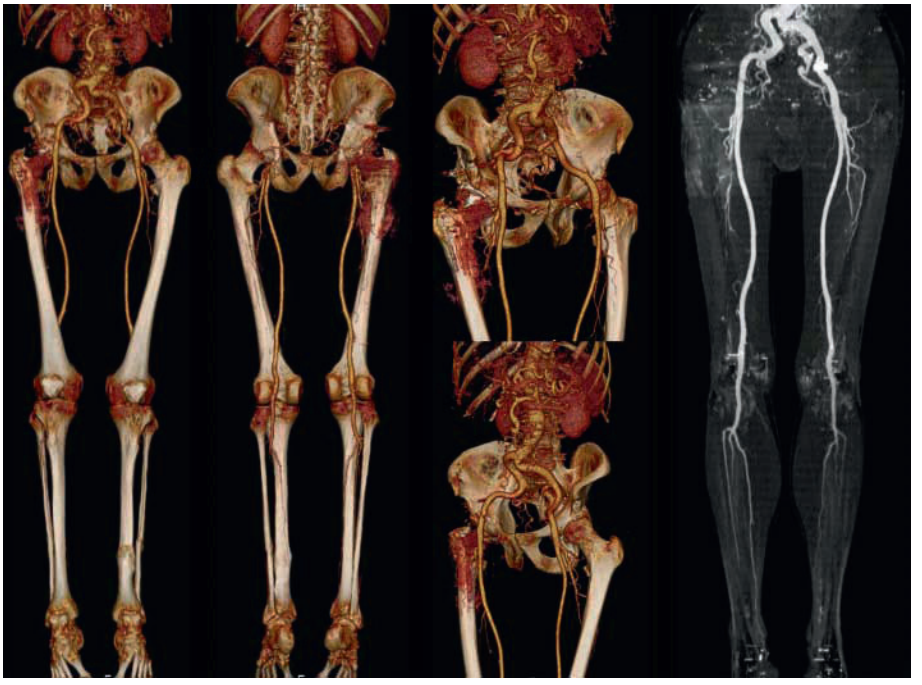

Fig. 15.8. Volume-rendering technique of peripheral run-off study post-processed in standardized fashion with AP, PA, LAO and RAO views. The arteries are always well-displayed in their superficial course. Maximum intensity projections are well-suited for demonstrating the course of the arteries after segmentation of the bones. However, this technique is time-consuming and does not always deliver consistently high image quality

a result, immediate selective angiography may be feasible by dual energy CT imaging, requiring less post-processing for displaying the results (Johnson et al. 2006). Furthermore, the "blooming artifact" of arterial calcifications that hinders the detection of stenoses may be reduced substantially. These systems are still under development, and the technical and financial effort is rather high. Therefore, the conventional method of CT scanning will most likely determine the workflow for three-dimensional post-processing in the next decade.

At most institutions, dedicated post-processing is only available either at the CT scanner side console or with dedicated stand-alone workstations. For post-processing on stand-alone workstations it is always required to send the data to the workstation or to retrieve them from the central picture and communication archive (PACS). The demand for immediate post-processing of three-dimensional datasets from CTA slice data from anywhere, e.g. in a hospital, is rapidly increasing. New client-server concepts are under development that may provide these tools in a broadband network. A high performance central server collects and administers the data from the CT scanners, and allows any connected personal computer to serve as a terminal to immediately display the result of the post-processing and to allow interactive manipulation of the data. The advantage of this concept is that post-processing is available from any personal computer in the hospital or outside that is connected to the central server. The overall costs of such a system are low compared to the costs of numerous high-performance workstations. The effort of maintenance for a client-server network is far lower than for several different workstations at different locations.

Systems like these will help to make three-dimensional post-processing widely available, and thus more often incorporated into clinical routine reporting and demonstration.

References

Achenbach S, Ropers D, Kuettner A et al (2006) Contrast-enhanced coronary artery visualization by dual-source computed tomography – initial experience. Eur J Radiol 57:331–335

Agatston AS, Janowitz WR, Hildner FJ, Zusmer NR, Viamonte M, Detrano R (1990) Quantification of coronary artery calcium using ultrafast computed tomography. J Am Coll Cardiol 15:827–832

Austen WG, Edwards JE, Frye RL et al (1975) A reporting system on patients evaluated for coronary artery disease. Report of the Ad Hoc Committee for Grading of Coronary Artery Disease, Council on Cardiovascular Surgery, American Heart Association. Circulation 51:5–40

Bartolozzi C, Neri E, Caramella D (1998) CT in vascular pathologies. Eur Radiol 8:679–684

Becker CR, Nikolaou K, Muders M et al (2003) Ex vivo coronary atherosclerotic plaque characterization with multi-detector-row CT. Eur Radiol 13:2094–2098

Becker CR, Knez A, Ohnesorge B, Schoepf UJ, Reiser MF (2000) Imaging of noncalcified coronary plaques using helical CT with retrospective ECG gating. AJR Am J Roentgenol 175:423–424

Becker CR, Knez A, Jakobs TF et al (1999) Detection and quantification of coronary artery calcification with electron-beam and conventional CT. Eur Radiol 9:620–624

Callister TQ, Cooil B, Raya SP, Lippolis NJ, Russo DJ, Raggi P (1998) Coronary artery disease: improved reproducibility of calcium scoring with an electron-beam CT volumetric method. Radiology 208:807–814

Fleischmann D, Hallett RL, Rubin GD (2006) CT angiography of peripheral arterial disease. J Vasc Interv Radiol 17:3–26

Fleischmann D (2003) MDCT of renal and mesenteric vessels. Eur Radiol 13:M94–101

Frericks BB, Caldarone FC, Nashan B et al (2004) 3D CT modeling of hepatic vessel architecture and volume calculation in living donated liver transplantation. Eur Radiol 14:326–333

Hacklander T, Wegner H, Hoppe S et al (2006) Agreement of multislice CT angiography and MR angiography in assessing the degree of carotid artery stenosis in consideration of different methods of postprocessing. J Comput Assist Tomogr 30:433–442

Halliburton SS, Petersilka M, Schvartzman PR, Obuchowski N, White RD (2003) Evaluation of left ventricular dysfunction using multiphasic reconstructions of coronary multi-slice computed tomography data in patients with chronic ischemic heart disease: validation against cine magnetic resonance imaging. Int J Cardiovasc Imaging 19:73–83

Hernigou A, Challande P, Boudeville JC, Sene V, Grataloup C, Plainfosse MC (1996) Reproducibility of coronary calcification detection with electron-beam computed tomography. Eur Radiol 6:210–216

Hong C, Becker C, Schoepf UJ, Ohnesorge B, Bruening R, Reiser M (2002) Absolute quantification of coronary artery calcium in non-enhanced and contrast enhanced multidetector-row CT studies. Radiology 223:474–480

Horton KM, Post WS, Blumenthal RS, Fishman EK (2002) Prevalence of significant noncardiac findings on electron-beam computed tomography coronary artery calcium screening examinations. Circulation 106:532–534

Huber D, Lapray J, Hessel S (1981) In vivo evaluation of experimental myocardial infarcts by ungated computed tomography. AJR Am J Roentgenol136:469–473

Johnson TR, Krauss B, Sedlmair M et al (2006) Material differentiation by dual energy CT: initial experience. Eur Radiol, in press

Johnson T, Nikolaou K, Wintersperger B et al (2006) Dual-source CT cardiac imaging: initial expericence. Eur Radiol, in press

Johnson M (1996) Principles and practice of coronary angiography. In: Skorton D, Schelbert H, Wolf G, Brundage B (eds) Marcus cardiac imaging: a companion to Braunwald´s heart disease, 2nd edn. WB Sanders Company, Philadelphia,pp 220–250

Kajinami K, Seki H, Takekoshi N, Mabuchi H (1997) Coronary calcification and coronary atherosclerosis: site by site comparative morphologic study of electron beam computed tomography and coronary angiography. J Am Coll Cardiol 29:1549–1556

Leber AW, Knez A, White CW et al (2003) Composition of coronary atherosclerotic plaques in patients with acute myocardial infarction and stable angina pectoris determined by contrast-enhanced multislice computed tomography. Am J Cardiol 91:714–718

Masuda Y, Yoshida H, Morooka N, Watanabe S, Inagaki Y (1984) The usefulness of X-ray computed tomography for the diagnosis of myocardial infarction. Circulation 70:217–225

McCollough CH, Ulzheimer S, Halliburton SS, White RD, Kalender WA (2003) A multi-scanner, multi-manufacturer, international standard for the quantification of coronary artery calcium using cardiac CT. Radiology 229:630

Ohnesorge B, Flohr T, Fischbach R et al (2002) Reproducibility of coronary calcium quantification in repeat examinations with retrospectively ECG-gated multisection spiral CT. Eur Radiol 12:1532–1540

Purerfellner H, Cihal R, Aichinger J, Martinek M, Nesser HJ (2003) Pulmonary vein stenosis by ostial irrigated-tip ablation: incidence, time course, and prediction. J Cardiovasc Electrophysiol 14:158–164

Sabharwal R, Vladica P, Coleman P (2006) Multidetector spiral CT renal angiography in the diagnosis of renal artery fibromuscular dysplasia. Eur J Radiol 61:520–527

Schmermund A, Rensing BJ, Sheedy PF, Bell MR, Rumberger JA (1998) Intravenous electron-beam computed tomographic coronary angiography for segmental analysis of coronary artery stenosis. Am J Cardiol 31:1547–1554

Schroeder S, Kopp AF, Ohnesorge B et al (2001) Accuracy and reliability of quantitative measurements in coronary arteries by multi-slice computed tomography: experimental and initial clinical results. Clin Radiol 56:466–474

Takahashi K, Stanford W (2005) Multidetector CT of the thoracic aorta. Int J Cardiovasc Imaging 21:141–153

Tomandl BF, Hammen T, Klotz E, Ditt H, Stemper B, Lell M (2006) Bone-subtraction CT angiography for the evaluation of intracranial aneurysms. AJNR Am J Neuroradiol 27:55–59

Ulzheimer S, Kalender WA (2003) Assessment of calcium scoring performance in cardiac computed tomography. Eur Radiol 13:484–497

Virmani R, Kolodgie FD, Burke AP, Frab A, Schwartz SM (2000) Lessons from sudden coronary death. A comprehensive morphological classification scheme for atherosclerotic lesions. Arterioscler Thromb Vasc Biol 20:1262–1275

Vogl TJ, Abolmaali ND, Diebold T et al (2002) Techniques for the detection of coronary atherosclerosis: multi-detector row CT coronary angiography. Radiology 223:212–220

Wexler L, Brundage B, Crouse J et al (1996) Coronary artery calcification: pathophysiology, epidemiology, imaging methods, and clinical implications. A statement for health professionals from the American Heart Association. Circulation 94:1175–1192

From the Esophagus to the Small Bowel

16

Franco Iafrate, Pasquale Paolantonio, Carlo Nicola De Cecco, Riccardo Ferrari, Valeria Panebianco, and Andrea Laghi

CONTENTS

F. Iafrate, MD; V. Panebianco, MD
Department of Radiological Sciences, University of Rome "La Sapienza", Policlinico Umberto I, Viale Regina Elena 324, 00161 Rome, Italy
P. Paolantonio, MD; C. N. De Cecco, MD; R. Ferrari, MD; A. Laghi, MD
Department of Radiological Sciences, University of Rome "La Sapienza", Polo Pontino I.C.O.T. Latina, Via Franco Faggiana 34, 04100 Latina, Italy

16.1 Introduction

Although the introduction of double-contrast radiographic techniques has reduced the comparative advantage of endoscopy over barium studies, most papers suggest that upper gastrointestinal endoscopy is more accurate, particularly regarding the evaluation of inflammatory mucosal abnormalities, bleeding lesions, (Thoeni and Cello 1980) and the post-operative stomach (Ominsky and Moss 1979).

Upper gastrointestinal endoscopy is a safe and effective technique, with not only diagnostic advantages, but also because it provides the opportunity to perform interventional procedures (biopsy, sclerotherapy, etc.). A very important limitation is that upper gastrointestinal endoscopy displays only the inner surface of hollow organs, thus preventing evaluation of the transmural extent of tumors as well as involvement of abdominal lymph nodes and peritoneal fat. Furthermore, disease extension to surrounding anatomical structures cannot be detected.

These limitations are the major impetus of the search for an inexpensive technique that would provide both endoscopic and exoscopic information simultaneously (Gonvers and Burnand 1996; Schmid et al.1999).

Both CT and MRI have proven to be valuable adjuncts to barium studies and endoscopy in the evaluation of gastric, esophageal and small bowel diseases because of their ability to delineate the primary pathologic condition and demonstrate how far the disease has extended to adjacent or distant organs.

The advent of multidetector CT (MDCT) and its further technological development (i.e. new 64-slice detector arrays, faster gantry rotation time, improved tube heat capacity) has completely changed the strategies of CT data acquisition as well as data reviewing and processing. This has a great impact not only on cardiac and vascular studies, where the new technology is mostly focused, but also in abdominal imaging.

The introduction of 64-slice MDCT scanners opens a new phase for CT imaging, thanks to the improved spatial resolution on the longitudinal axis as well as the increase speed of acquisition. Since new acquisition protocols make routinely use of sub-millimeter collimation and sub-millimeter image reconstruction, a real "volumetric" approach to abdominal imaging is made possible.

At the same time, a whole-body study may be acquired also in less than 10 s with a superb image quality. It turns into the two major advantages of MDCT in abdominal imaging, represented by multiplanar and multiphasic capabilities. Multiplanarity, due to acquisition of three-dimensional data sets with isotropic voxels, results in the ability to analyse CT images on multiple planes (i.e. sagittal, coronal and oblique) making diagnosis of lesions in critical anatomic location easier. Dedicated software are able to reconstruct MDCT data volumes and to generate three-dimensional images. These new software, more user-friendly, faster and powerful may generate high quality 3D reconstructions, ranging from surface views to 3D vascular and parenchymatous organ models. In abdominal imaging, 3D reconstructions play a very important role in therapy planning, helping in the decisional process among conventional surgery, laparoscopic surgery and non surgical, interventional approach.

Moreover in stomach and esophagus, 3D imaging offers endoluminal projections (the so called "virtual endoscopy") able to generate images simulating a conventional endoscopy, moreover providing a complete evaluation of surrounding anatomical structures.

In the case of MRI, the availability of high performance gradient systems, together with fast scanning techniques, has allowed acquisition of complex 3D data sets within the confines of a comfortable breath-hold (Leung and McKinnon 1996). The further advantage of MRI is the ability to perform multiplanar acquisition, which is particularly useful when evaluating the esophagus, the stomach and the small bowel to detect the longitudinal extension of a lesion.

Thus, currently, both spiral CT and MRI are able to provide volumetric datasets suitable for 3D reconstructions using dedicated software. The utility of 3D images provides improved evaluation of the anatomical relationships between different organs, especially when extra-mural invasion is suspected. Moreover, conventional slice-to slice presentation of data sets precludes contiguous viewing of the inner wall, forcing radiologists to create a mental picture of anatomic continuity, which can be faulty. The most recent development in volumetric analysis is virtual reality imaging, a form of interactive 3D imaging that provides computer-rendered intraluminal views of any hollow viscera, comparable to fiberoptic viewing. Virtual endoscopy enables the operator to virtually navigate inside the organs using datasets extracted from CT scans or MRI images (Jolesz and Lorensen 1997).

In this chapter we will review the specific technical requirements necessary to obtain adequate studies of the upper gastrointestinal tract from esophagus to small bowel passing through the stomach and the clinical applications of 3D imaging techniques.

16.2 Study Techniques

Specific techniques are necessary to acquire datasets suitable for three-dimensional reconstructions. Concerning stomach, esophagus, and small bowel together with the optimization of acquisition parameters, luminal distention of hollow viscera is also mandatory if evaluation of the parietal wall and virtual endoscopy images are required. Different techniques for optimizing both CT and MRI studies have been proposed, all of which aim to minimize patient discomfort and increase the quality of image datasets. Following the acquisition of the dataset, images must be reconstructed using either Multiplanar Reformatted Images (MPR) or dedicated software, which use different algorithms to generate three-dimensional reconstructions.

16.2.1 Computed Tomography

Optimal 3D image rendering requires high resolution data acquisition, both in-plane (x- and y-axis) and through-plane (z-axis). For this reason, voxels should be isotropic, i.e. have the same size along the three axes, and be as small as possible, in order to increase spatial resolution. Using a single slice spiral CT, however, the effective slice thickness is greater than the collimation width, and this is directly proportional to the pitch value, thereby reducing the longitudinal spatial resolution along the z-axis. On

the other hand, a high pitch value is also necessary to increase the volume coverage. Thus, a compromise between volume to be acquired and longitudinal spatial resolution is necessary, with the primary goal being the acquisition of the entire volumetric dataset within a single breath-hold to remove respiratory misregistration artifacts.

Scan protocols should be optimized in conjunction with the specific technical features of different spiral CT scanners, especially in terms of gantry rotation time and volume coverage with a single spiral scan. However, a routine scan protocol, achievable on several types of equipment, should be based on at least 3 mm collimation thickness, 2 mm image reconstruction, and a pitch less than 2, with the value depending strictly on gantry rotation time. Such a protocol should allow coverage of the entire anatomical region under evaluation, either the esophagus, the stomach or the small bowel with a longitudinal resolution compatible with good quality 3D reconstructions.

Using 4-slices multidetector spiral CT, the scan time can be reduced dramatically compared to conventional spiral CT, with consequent radiation dose reduction, or the volume to be investigated can be extended.

With the advent of newer 16- to 64-slice MDCT scanners, no technical compromise is now needed since these systems are capable of using sub-millimeter collimation and sub-millimeter image reconstruction, with a subsequent shorter scan duration and longer scan ranges.

The use of the newer multidetector systems, produces high-resolution 3-dimensional images of whole body including upper gastrointestinal tract, thus providing information not available from conventional radiographic exams. Furthermore data from a single MDCT scan simultaneously provide information on the condition of small bowel, gastric and esophageal wall, vasculature and surrounding anatomic structures such lymph nodes and peritoneal fat, rapidly investigating important causes of abdominal pain. Because MDCT may eventually provide important benefits for surgeons, gastroenterologists and their patients, it is important that this kind of doctors be aware of recent advances in this technology. In the next sections we will discuss MDCT and MRI strengths, limitations and approaches to optimizing image quality, which include distention of hollow organs using air or contrast agents, appropriate use of intravenous and oral contrast media and technical parameters.

16.2.1.1 Esophagus

The esophagus is a hollow organ and may appear collapsed on routine CT. Its non-distended wall, even if normal, may appear thickened, nodular and irregular, thus simulating a tumor. Furthermore, it is difficult to judge the superior and inferior extent of esophageal tumors on standard CT exams (Lyang and Chan 1996).

When the esophagus is adequately distended prior to examination, 3D image reconstruction of the esophageal lumen is possible.

In the evaluation of esophageal diseases, the use of an anti-peristaltic drug suppresses normal peristalsis, which may simulate tumor thickening of the esophageal wall. Realistic 3D reconstruction of esophageal tumors is dependent on good gaseous distention of the esophagus above and below the tumor, which can be obtained by oral administration of effervescent granules prior to examination.

Griffith and Kew (1999) evaluated 70 patients with known esophageal cancer. The study technique included the oral administration of a capsule of effervescent granules mixed with water immediately prior to scanning, together with an intravenous injection of an antispasmodic drug; intravenous injection of iodinated contrast medium was also performed to evaluate the liver parenchyma. The imaging protocol included a scan of the thorax and upper abdomen with the patient in the prone position during a single breathhold with beam collimation of 10 mm and a pitch of 1.5. However, the scan time of 20–25 s was sometimes too long for frail esophageal tumor patients and insertion of a breath interval was necessary; the location of this breath interval was chosen away from the esophageal tumor. Alternatively, the pitch was increased to 2, thus reducing the scan time by one-quarter. Using MDCT obviously the scan time is dramatically reduced from 25 s of 4-rows MDCT to 6 s of 64-rows MDCT, thus minimizing problems for frail esophageal tumors patients.

In our experience using a 64-rows multidetector CT, shortly before scanning – approximately 35 s, judged by us as optimum delay necessary for a good distention to take place – the patient ingests 7 g of a mixture of effervescent granules that generate CO_2 with a small amount of water (Panebianco et al. 2006a).

After obtaining esophageal luminal distention, we perform the first acquisition with the patient in the supine position acquiring images with a collimation

thickness of 0.625 mm, a pitch of 0.984, and image reconstruction of 0.625 mm to maximize mucosal detail and to proceed with a realistic detailed view of lesions; the second acquisition is performed beginning 60 s after i.v. administration of iodinated contrast media with a slice thickness of 1.25 mm and image reconstruction of 1 mm in order to visualize extraluminal extension of the disease.

16.2.1.2 Stomach

For the stomach as well as for the esophagus, luminal distention, reduction of peristaltic motion and an optimal distribution of residual fluids are mandatory in order to obtain high quality 3D datasets (Lee and Ko 1996a, 1999; Kim SH 2005). The required contrast difference between the gastric wall and its lumen can be enhanced by ingestion of positive or negative contrast materials.

Positive oral contrast materials are diluted water-soluble contrast materials or barium sulfate, and they are not suitable for performing virtual navigation.

Negative contrast media include either tap water, a low Hounsfield value barium suspension (VoLumen, E-Z-Em) or air. Compared to air, on 2D axial images, water and VoLumen have the advantage of generating no beam-hardening effects, but with virtual CT gastroscopy, negative contrast agents may show artifacts that can mimic polyps, erosions, or flat ulcers.

Concerning Virtual CT gastroscopy best results are obtained by the oral administration of effervescent powders. In any case, attention must be given to the fact that extensive gastric fluid may produce an air-fluid level that prevents the reconstruction of the underlying mucosa. Consequently, the patient should be properly prepared with a 12-h fast and ingestion of a very small amount of water with the effervescent powder, and two spiral acquisitions, with the patient in both the supine and prone, or better in the left posterior oblique position, should be acquired (Kim AY et al. 2005; Bielen et al. 2001). To maximize mucosal detail and to proceed with a realistic detailed intraluminal view of lesions, a narrow beam collimation is the most crucial factor. Typical parameters are strictly dependent on different used system and are reported in Table 16.1. Depending on the parameters, artifacts such as smoothing, stair step, longitudinal blurring, and distortion may be minimized. During the second spiral acquisition, to assess the stage of gastric carcinoma, if present, intravenous administration of iodinated contrast medium is required with acquisition of images during the portovenous phase (Kim AY et al. 2005).

16.2.1.3 Small Bowel

Owing to its length, caliber, and overlap of loops, small bowel remains one the most challenging segment of gastrointestinal tract to be evaluated.

The technique of enteroclysis is considered the gold standard for the radiological investigation of small bowel disorders (Maglinte et al. 1996a; Bender et al. 1999; Schmidt et al. 2005), since only volume challenges results in homogenous luminal distention, which is mandatory for the detection of intestinal diseases.

The additional inherent advantage of cross-sectional imaging such as CT and MR enteroclysis is the simultaneous depiction of intraluminal, mural and extraintestinal pathologies.

Due to the ability of multidetector CT scanners to scan large volumes at faster speed with the ability to perform reconstruction following the examination, CT enteroclysis has become a more feasible extension of the conventional enteroclysis and CT methods of examining the small intestine. Using this technique, adequate luminal distention is mandatory because poorly distended loops can simulate disease or hide pathologic processes (Bender et al. 1999). In the past, inadequate small bowel luminal distention has necessitated nasojejunal intubation to infuse contrast material (Gore et al. 1996).

Table 16.1.

	Oral contrast media	kV	MAs	Collimation	PITCH	Reconstruction
Springer	Eff. granules	120	220	5 mm	1	1 mm
Lee	Eff. granules	120	233	3 mm	1.3–2	1 mm
Ogata	Eff. granules	120	180–220	3 mm	1.2	1 mm
Laghi	VoLumen	120	Smart mA	64 × 0.625 mm	0.984	0.625

Nowadays adequate distention can usually be achieved with oral hyperhydration with either positive and negative contrast agents resulting in a new examination, so-called CT enterography, making this technique a useful, well tolerated study for the evaluation of diseases affecting the mucosa and bowel wall.

With the advent of multidetector CT (MDCT) scanners with 16, 32 and 64 rows of detectors there has been renewed interest in assessing the small bowel with CT. These studies, often referred as CT enterography, bring new challenges even to new oral contrast agents administration.

In attempt to improve small bowel distention during CT enterography, multiple oral contrast agents have been tested.

The use of positive contrast agents, such as dilute barium solution, is problematic in creating 3D images if CT angiography is simultaneously being performed – for example in the assessment of gastrointestinal blood loss. Moreover, the presence of a positive contrast agent often obscures evaluation of the bowel wall and mucosa which are key features of a CT enterography examination especially in Crohn disease, where pathologic mural enhancement is obscured by intraluminal positive contrast agents, since enhancement of the small bowel wall with intravenous contrast material decrease the attenuation difference between the lumen and the wall of the small bowel.

Neutral contrast agents have been shown to be valuable in the diagnosis of small-bowel disorders, including ischemia, neoplasms, and Crohn disease.

Most clinical experience is with water as a contrast agent. Water is considered an excellent contrast agent when used during upper abdominal CT scanning, but because water is rapidly absorbed through the intestinal wall, the use of this contrast agent in the jejunum and ileum is limited. Nasoenteric tubes have been proposed as a method to deliver contrast agents in a rapid bolus that would allow scanning prior to substantial absorption at CT enteroclysis. Patient acceptance, however, is markedly reduced because of the need for intubation and because of the increased time and materials associated with the procedure.

Water and water-methylcellulose solution have been replaced by polyethylene glycol (PEG) electrolyte solution or low Hounsfield value barium suspension, 0.1% ultra-low-dose barium with sorbitol, a nonadsorbable sugar alcohol that promotes luminal distention and limits resorption of water across the length of the small bowel (Megibow et al. 2006).

In their study Megibow et al. prospectively evaluated bowel wall distention and bowel wall appearance after an orally administered 0.1% barium suspension, VoLumen (E-Z-Em, USA) as a bowel marking agent for MDCT and they concluded that this oral contrast agent provides an excellent distention and visualization of mural features in the gastrointestinal tract.

Like the others hollow organs a narrow beam collimation is crucial to achieve an high detailed mucosa and enhance lesions. Typical imaging protocols are reported in Table 16.2.

In our experience using MDCT , after distending gastrointestinal tract using 1.2 L of VoLumen (E-Z-Em, USA) as oral contrast agent, consumed within 50 min before the exam , we scan patients only in

Table 16.2.

	Oral contrast media	kV	MAs	Collimation	PITCH	Reconstruction
Schmidt	Methyl-cellulose	120	200–240	4 × 2.5 mm	1.5	2–2.5 mm
Boudiaf	Water	120	165	4 × 2.5 mm	-	3 mm
Romano	Methyl-cellulose	120	300	1 mm	-	3–4 mm
Doerfler	Mucofalka	-	-	5 mm	1.5	1.4 mm
Wold	Water	120	270	-	-	2.5 mm
Zhang	Iso-osmotic mannitole	120	130	-	-	-
Megibow	Low Hounsfield barium suspension(VoLumen)	-	-	16 × 1.75	-	3–4 mm
Iafrate	Low Hounsfield barium suspension (VoLumen)	120	Smart MA	64 × 0.625	0.984	3 mm

[a]Mucofalk consists of granules containing epidermal particles and the collapsed adjacent layers removed from the dried ripe seeds of Plantago ovata Forssk (Ispaghula husk)

supine positions using a collimation thickness of 64 × 0.625 mm or 64 × 1.25 mm, a pitch of 0.625 mm and image reconstruction of 3 mm (Iafrate et al. 2006).

The study technique also included intravenous administration of iodinated contrast medium which permits excellent assessment of hypervascular lesions and hyperenhancing segment (Paulsen et al. 2006).

The administration of glucagon can be useful to induce relaxation of small bowel and reduction of peristalsis; the administration of meteclopramide is also suggested to prevent nausea and vomiting.

16.2.2 Magnetic Resonance Imaging

The availability of high performance gradient systems has allowed the acquisition of three-dimensional MR data sets in a single breath-hold. MRI offers several chances for the non-invasive diagnosis of upper GI tract and for small bowel disease.

On the basis of this MR data, virtual angioscopy has been performed in the aorta as well as the pulmonary artery. This technique also has been applied to the endoluminal evaluation of colonic disorders, and was recently adapted to obtain endoscopic and extraluminal views of the stomach. MR evaluation of esophageal lesions is relatively limited and, at the moment, no experience exists concerning the acquisition of 3D MRI datasets.

For the evaluation of the stomach prior to examination, an antiperistaltic drug is injected to reduce motion artifacts. Adequate gastric distention can be obtained by oral administration of water. Moreover the availability of 3D GRE fast sequence enable optimal capabilities for post-processing technique in terms of endoluminal 3D reconstructions and multiplanar reconstruction due to near-isotropic voxel properties. A three-dimensional study is based on the acquisition of a T1-weighted 3D gradient echo sequence with short TR and short TE, which provides an almost isotropic voxel. Three-dimensional (3D) Fourier transform GRE imaging has potential advantages over 2D imaging. Compared to traditional 2D GRE sequences, properly structured 3D GRE sequences have the capacity to provide thinner sections, no gaps, fat saturation, higher SNR, and comparable image contrast in the same breath-hold time frame. Furthermore, with appropriately thin sections and accurate timing, the same data set could be used to generate high quality MR angiograms and thus provide added value. Therefore, 3D GRE imaging has the potential to yield a comprehensive evaluation of the upper abdomen. The recent advancement in terms of parallel imaging acquisition enhance MR capabilities in terms of spatial and temporal resolution.

Recently MRI was tested in the evaluation of esophageal disorders with interesting results especially in the evaluation of motility disorders (Panebianco et al. 2006b).

Thanks to the advancement of cardiac MRI, ultra-fast sequences with high temporal resolution are available on state of the art MR scanners. These sequences are represented by cine GRE sequence and cine-truFISP sequences that enables the evaluation of both esophageal motility and gastric-empty.

Due to high temporal resolution these sequences are known as fluoro-MRI sequences enabling a real time evaluation of dynamic processes.

Concerning the small bowel, MRI offers optimal diagnostic chances owing to its multiplanar and 3D capabilities that are very useful in the investigation of small bowel loops that have unpredictable orientation. MR studies of the bowel requires intestinal distention that may be easily obtained with oral administration of contrast agents.

16.2.3 Data Processing and Viewing

After data acquisition, images are transferred to a dedicated workstation over an Ethernet or an Intranet network to be post-processed.

Three-dimensional data sets can be examined using different 2D and 3D reconstruction techniques, starting with multiplanar reformations along three orthogonal axes and in oblique planes.

Three-dimensional reconstructions can be obtained by using both surface rendering and volume rendering algorithms.

Using an adequate threshold value, all pixels other than those of this value are automatically removed. Contiguous pixels at the boundary of a predefined threshold value are modeled as surfaces. In SSD, only the first voxel encountered along the projection ray that is above a user-defined threshold is selected as an inner surface of the gastric lumen. Computer-produced imaginary sources of illumination depict surface reflections that are encoded in the image gray scale.

With volume rendering, more flexible management of the 3D dataset is possible, with generation of surface views (similar to surface rendering), 3D models, and tissue transition projection images, which resemble a "double contrast" barium study (Fig. 16.1). The major advantage of volume rendering is the entire dataset is preserved, with either no or very limited data segmentation, and tissue reconstruction using different opacity levels.

Using both surface and volume rendering algorithms, virtual endoscopic images resembling conventional endoscopic views are rendered. Color can be assigned to simulate expected normal tissue color in vivo. In addition, "fly through" sequences within the lumen can be produced by creating a "flight path". The camera position along the endoscopic path must be defined by an interactive display of correlated two-dimensional and three-dimensional data sets in a multiwindow format, thus assisting the virtual endoscopist in establishing the relation of anatomic structures located outside the surfaces.

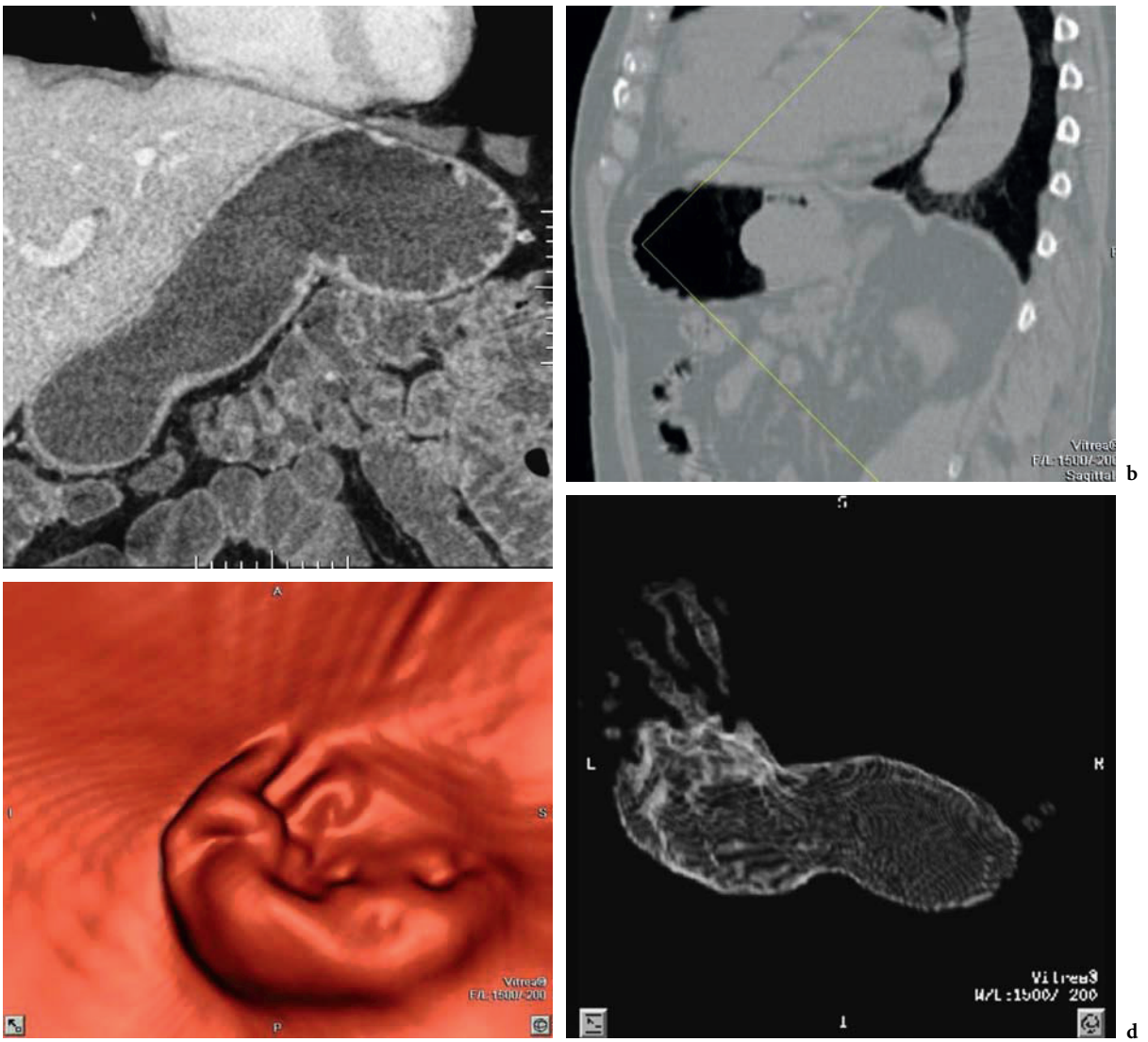

Fig. 16.1a–d. Volume-rendered images of the stomach. **a** 2D coronal oblique vision of the entire stomach reformatted image showing the gastric lumen distended by low Hounsfield value barium suspension. **b** 2D sagittal image with reference lines showing the position of the virtual camera. **c** Endoscopic view of the internal surface of the stomach with evidence of gastric polypoid lesion. **d** Tissue transition projection image ("virtual double contrast" evaluation of the stomach) showing a well-distended gastric lumen with clear evidence of the mucosal surface of the gastric antrum

16.3 Clinical Applications

16.3.1 Esophagus

Most esophageal tumors are diagnosed by endoscopy, with thoraco-abdominal axial CT used to stage tumor spread; acquisition of 3D data set permits acquisition of three-dimensional modeling, virtual endoscopic images, and conventional axial CT information within a single examination.

Realistic 3D reconstructions of the esophageal lumen are strictly dependent on good gaseous distension of the esophagus above and below the tumor. Three-dimensional display of the esophagus provides a readily recognizable image depicting tumor length and location with respect to other mediastinal structures and the gastro-oesophageal junction, and provides an estimation of longitudinal tumor extension (Fig. 16.2); this is useful additional information, particularly for stenosing tumors that do not allow passage of an endoscope.

The analysis of multiplanar images permits a highly reliable definition of the degree of perivisceral extension and metastatic involvement, yielding improved locoregional staging capabilities.

The disadvantages of 3D CT of esophageal tumors are related to suboptimal distention of the lumen, which leads to unsatisfactory reconstructions and an inability to differentiate between a non-distended normal lumen and a malignant stricture.

Although not the examination of choice, volumetric CT might show esophageal diverticula, with images comparable to conventional barium studies.

16.3.2 Stomach

Virtual endoscopy is a valuable technique to detect gastric lesions and, when malignancy is suspected, to establish locoregional and distant involvement within a single examination.

When compared to axial 2D CT, virtual endoscopy has the advantage of displaying gastric lesions as they are seen with conventional gastroscopy, thus allowing an accurate categorization according to the Borrmann classification. Moreover, with the ability to display virtual endoscopic images, there is an increased rate in the detection of early gastric cancer (EGC), as reported by Lee and Ko 1998b.

When compared to conventional endoscopy, virtual gastroscopy presents several advantages.

Because of its larger field-of-view, virtual endoscopy enables a more accurate evaluation of lesion size; simultaneous availability of endoscopic, multiplanar, and axial 2D images permits, at the same time, local staging of gastric lesions, including the depth of parietal and perivisceral extension and the detection of lymph node and distant metastasis.

It should also be noted that three-dimensional CT is a noninvasive technique, with minimum patient discomfort related to gastric distention; consequently, it is associated with higher patient compli-

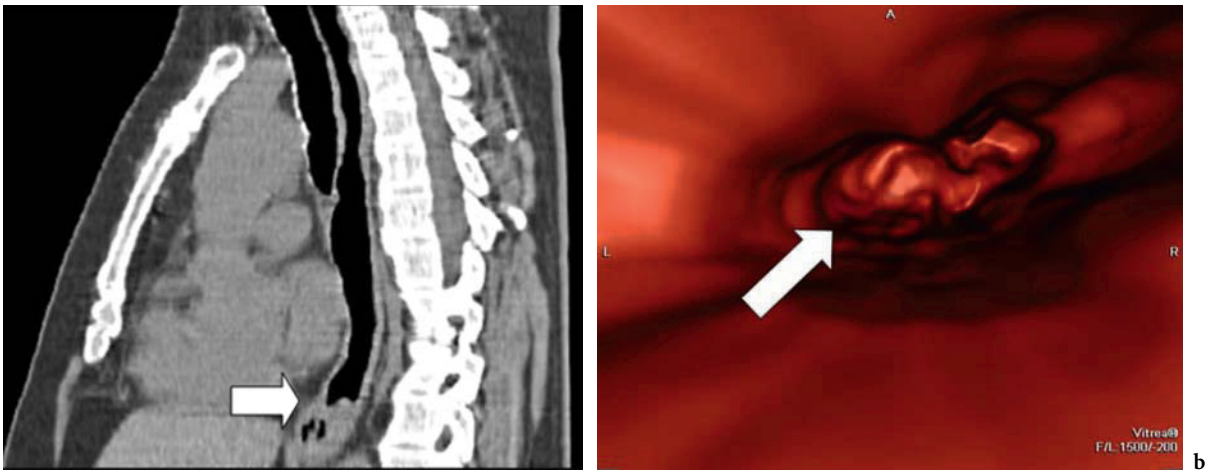

a b

Fig. 16.2. a Sagittal multiplanar reformation of the esophagus showing a neoplastic stricture (*arrow*) located at the lower third of the esophagus. **b** Virtual endoscopy view showing endoluminal appearance of the lesion (*arrow*) within esophageal lumen

ance. However, compared to colonoscopy, fiberoptic gastroscopy is easier to perform and this is one of the reasons MR or CT imaging of the stomach are not considered ideal methods for detecting primary tumors. In addition, when a neoplastic lesion is detected during fiberoptic endoscopy, the lesion is biopsied and the patient could be scheduled for surgical treatment without the need for other diagnostic examinations.

Virtual endoscopy has several limitations, primarily concerning the inability to detect flat or small lesions or to obtain histologic results. An additional limitation is related to ionizing radiation if CT is used, but because acquisition time is short and so much more useful information is obtained, this disadvantage is negligible.

In any case, virtual gastroscopy should be considered a natural complement to a CT or MR study of the upper abdomen when a gastric disease is suspected or when a known neoplastic lesion must be staged. At the moment, mainly due to the fact that conventional gastroscopy is not invasive as colonoscopy, there is no indication to use this imaging technique as a primary method for evaluation of the gastric lumen.

In the next sections, different clinical results for gastric pathologies will be reviewed.

16.3.2.1 Gastric Carcinoma

The role of CT in advanced gastric cancer (AGC) is to detect the primary lesion and to stage the tumor accurately. However, assessment of endoluminal morphology is limited when using axial images alone.

3D images depict gastric wall surfaces in continuity and allow interactive, operator-initiated exploration, navigation, and maneuvering within the inner space of the organ, thus demonstrating the tumor mass as seen with gastroscopy.

At the same time, the relation to anatomic structures located outside the surfaces is continuously maintained and displayed with reference to the position of the viewed segment. The use of 3D or 2D pointers assists the operator to locate the lesion precisely, which could also be useful for mapping the tumor before a surgical resection.

In addition, this technique makes it possible to record accurately the maximum volume of the mass without magnification and the resulting image distortion; as a consequence, virtual endoscopy may be more accurate for measuring gastric lesions than conventional endoscopy because of its wider field-of-view (Kim AY et al. 2005; Lee and Ko 1999c–d).

When virtual endoscopy reconstructions are performed, it is also possible to define tumor morphology according to the Borrmann classification (Tables 16.3 and 16.4).

Table 16.3. Bormann classification of advanced gastric cancer

I	Intraluminal protruding mass
II	Central ulcer within the tumor mass
III	Infiltrative tumor surrounding the ulcer
IV	Luminal narrowing

Table 16.4. Bormann classification of Early Gastric Cancer

I	Polypoid
II	Superficial
	II a Elevated
	II b Flat
	II c Depressed
III	Excavated

Displaying multiplanar and three-dimensional reconstructions allows an accurate evaluation of perigastric tumor involvement; likewise, the simultaneous availability of axial 2D images is mandatory for detecting lymphatic involvement as well as distant metastasis (Fig. 16.3).

The detection of early gastric cancer (EGC) on axial CT is generally low With the use of 3D CT, not only is the detection rate of EGC over 90%, but it is also possible to obtain accurate categorization according to the Borrmann classification (Table 16.5) (Figs. 16.4–16.6).

In general, 3D CT images of EGC I and II a are excellent but those of EGC II b and II c are poor as reported by Lee (1998).

Table 16.5. Parameters evaluated by virtual gastroscopy

- Location
- Dimensions and size
- Morphology (according to Borrmann classification)
- Extraparietal involvement
- Lymphadenopathy
- Metastasis

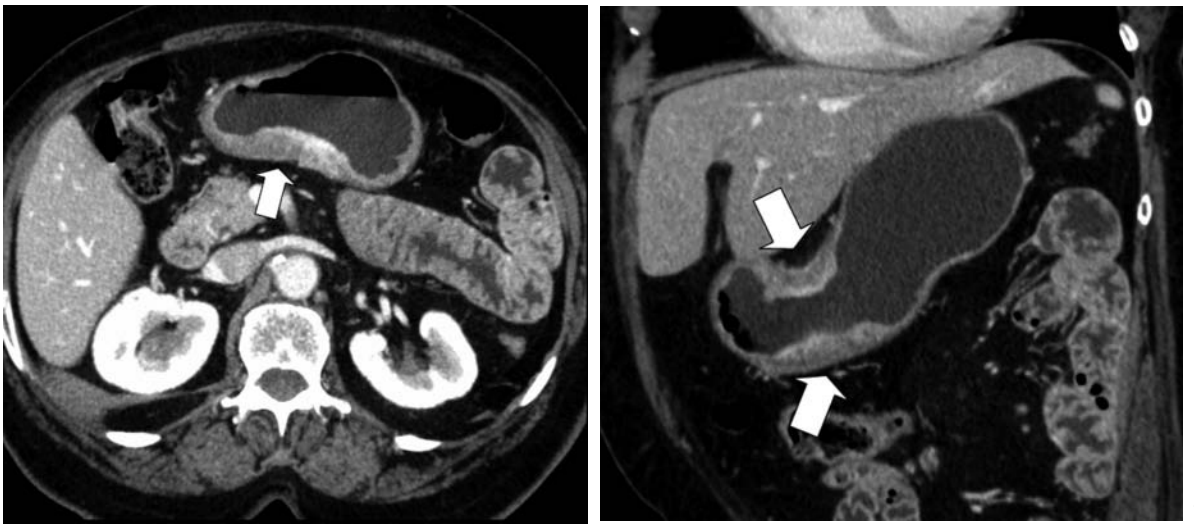

Fig. 16.3. a Enhanced axial CT using water as oral contrast material shows markedly distended stomach with a circumferential mass (*arrow*) located at gastric angulus. **b** Coronal oblique view clearly demonstrate the overall length of the neoplastic lesion (*arrows*) and its relationship with gastric wall and perigastric fat tissue not involved by the tumor

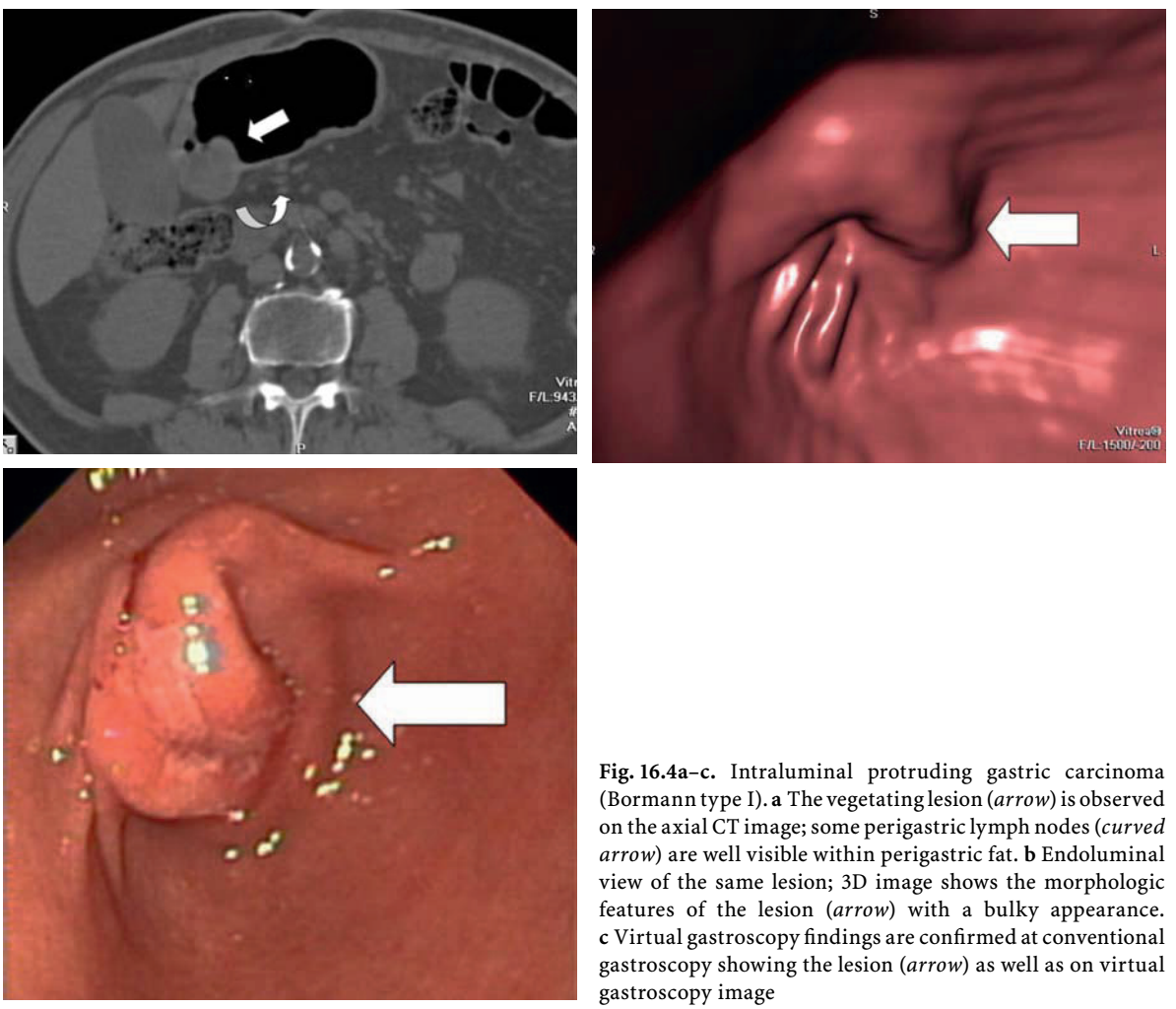

Fig. 16.4a–c. Intraluminal protruding gastric carcinoma (Bormann type I). **a** The vegetating lesion (*arrow*) is observed on the axial CT image; some perigastric lymph nodes (*curved arrow*) are well visible within perigastric fat. **b** Endoluminal view of the same lesion; 3D image shows the morphologic features of the lesion (*arrow*) with a bulky appearance. **c** Virtual gastroscopy findings are confirmed at conventional gastroscopy showing the lesion (*arrow*) as well as on virtual gastroscopy image

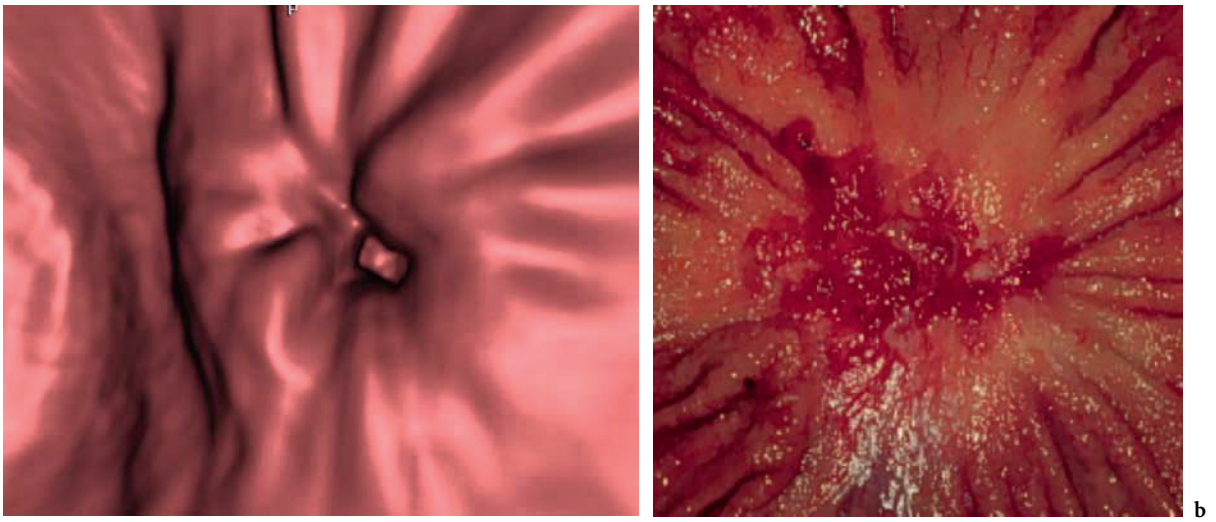

Fig. 16.5. a Ulcerative lesion (Bormann type II) demonstrated on a virtual endoscopy image; radiated folds are clearly evident. **b** Pathologic specimen shows similar findings for the gastric ulcer

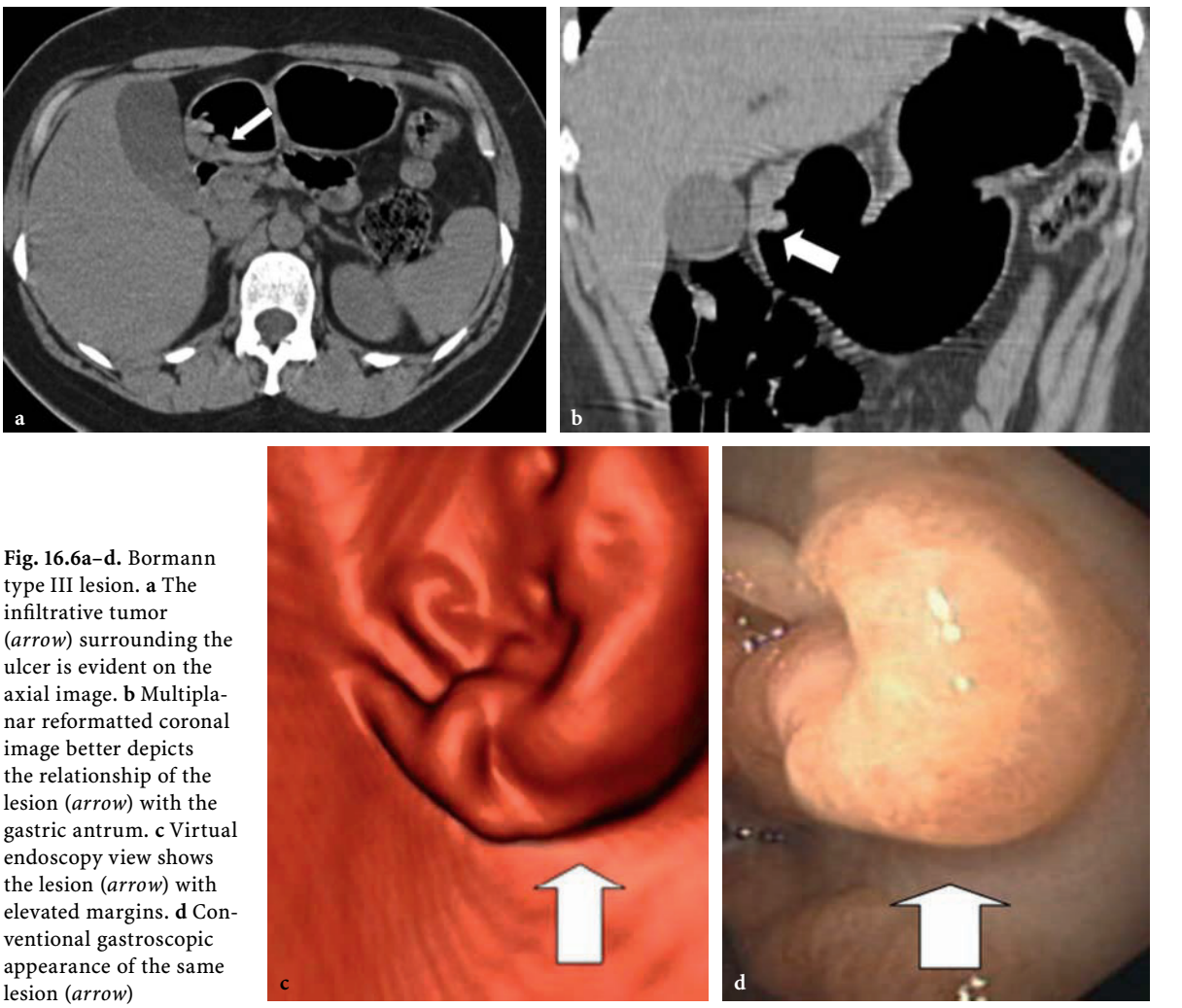

Fig. 16.6a–d. Bormann type III lesion. **a** The infiltrative tumor (*arrow*) surrounding the ulcer is evident on the axial image. **b** Multiplanar reformatted coronal image better depicts the relationship of the lesion (*arrow*) with the gastric antrum. **c** Virtual endoscopy view shows the lesion (*arrow*) with elevated margins. **d** Conventional gastroscopic appearance of the same lesion (*arrow*)

16.3.2.2 Other Gastric Lesions

Spiral CT of gastric leiomyoma discloses a well-demarcated, smooth, round, uniformly attenuated endogastric mass. The characteristic indication of submucosal tumor on an upper gastrointestinal series or gastroscopy is the presence of bridging folds over the tumor mass. This sign is not detected on the tumor surface with axial CT scanning. On virtual endoscopy, bridging folds may be detected around the protruding mass. 3D CT produces excellent images of gastric leiomyoma.

Spiral CT of gastric lymphoma discloses a less enhanced and a markedly thickened wall or discrete masses. Three-dimensional reconstructions also provide an accurate depiction of these features.

Finally, a controversial application for virtual endoscopy is the benign gastric ulcer, as reported by Lee and Ko (1998b) and more recently by Horton and Fishman (2003a). In this case, spiral CT is not used to detect merely the ulcer crater but also may be performed in cases of suspected perforation or in cases of difficult differentiation from malignant ulcers by gastroscopy or barium study. Indeed, three-dimensional imaging of the benign ulcer provides good quality images, and often ulcer craters are well visualized, even indicating a surrounding condition of gastritis.

16.3.3 MRI of the Esophagus and Stomach

Nevertheless, there are several experiences in the evaluation of organic lesion of esophagus and stomach using tru-FISP and VIBE sequences, the use of MRI is limited in the daily practice respect to MDCT.

However, recently interesting experiences were performed using cine GRE sequences and Tru-FISP sequences in the evaluation of esophageal and gastric motility.

MRI is proposed in the evaluation of patient with suspected achalasia and diffuse esophageal spasmus (Fig. 16.7). In this field there are less chances for the post-processing approach. The unique advantage of Fluoro-MRI with respect to conventional fluoroscopy is represented by the lack of ionizing radiation delivered to patients.

Fig. 16.7. Fluoro MRI of the esophagus. Cine-Turbo-FLASH T1 weighted sequence acquired on coronal plane during ingestion of a solution of GD-DTPA (1%) mixed with water showing esophageal achalasia. The lack of relaxation of low esophageal sphincter (*arrow*) as well as low third esophageal dilatation during ingestion of oral contrast agent is well visible

16.3.4 Small Bowel

The small bowel has historically been a difficult portion of the gastrointestinal tract to examine because of the lack of access via endoscopic methods that forces the clinician to rely on clinical impression and radiological studies for diagnosis of small bowel pathology. Multidetector Computed Tomographic Enteroclysis (MDCT-E) and CT Enterography add cross-sectional imaging, three-dimensional modeling and virtual endoscopic images to identify small bowel pathology to include masses, inflammatory disease, gastrointestinal bleeding of unknown origin, and partial obstruction. Compared with the traditional small bowel follow-through examination, CT enterography has several advantages: (1) it displays the entire thickness of the bowel wall, (2) it allows examination of deep ileal loops in the pelvis without superimposition, and (3) it permits evaluation of the surrounding mesentery and perienteric fat. CT enterography also allows assessment of solid organs and provides a global overview of the abdomen.

16.3.4.1 Crohn

Conventional abdominopelvic CT has traditionally been used to guide the management of extraenteric complications of Crohn disease such as abscesses, fistulas, phlegmon, obstruction, and other extraenteric sequelae but has played a minimal role in identifying small bowel inflammatory disease per se. CT enterography identifies active Crohn disease and its complications because of its higher spatial resolution and its superior capacity in defining the full extent of bowel wall thickening and the mesenteric extent of the disease process. In a single examination, the full extent of disease can be determined in a rapid, noninvasive fashion. The accuracy and non-invasive nature of CT enterography make it a primary tool in the setting of suspected Crohn disease (Horton and Fishman 2003b).

Our experience showed that using a 64 row multidetector CT and multiplanar projections improve the anatomic presentation of the bowel and produces fewer images that have orientations similar to those of conventional examinations. The axial images were always diagnostic, but MPR images were helpful for the observer's confidence and especially useful for demonstration of disease and changes who were not accustomed to axial scans.

A well-distended small bowel is mandatory to prevent diagnostic error due to empty loops, poorly distended bowel segments may mimic mucosal hyperenhancement or bowel wall thickening and falsely suggest Crohn disease (Zhang et al. 2005; Doerfler et al. 2003). The use of intravenous contrast medium is indicated because it allows better definition of the internal surface of the intestinal wall (Winter et al. 1996), especially when evaluating the degree of enhancement better identification of small vessels, increases anatomic details and relationships, and provides better differentiation among adjacent structures and definition of bowel wall thickness and contour (Fig. 16.8). In our institution, we scanned the patient during peak arterial enhancement as suggested by Rollandi et al. (1999) who found that this phase is the most appropriate for analyzing the inflamed bowel wall and 35 s after we perform a portovenous phase where mural stratification appears more clear.

CT is very useful clinically in defining and differentiating the abnormalities that occur in active mucosal and mural inflammation: mural stratification mucosal, mural hyperenhancement, edema in the perienteric mesenteric fat, and engorged vasa recta (Meyers and McGuire 1995; Mako et al. 2000). Submucosal fat deposition and mural thickening without enhancement or mural stratification typically correlate with fibrotic or quiescent disease. One limitation of the CT enterography technique is that it may fail to depict very mild inflammation. Additionally, CT enterography is more sensitive than fluoroscopic examination in the detection of extraenteric findings such as abscesses and fistulas.

That CT enterography helps detect both active Crohn disease and small bowel strictures is particularly important now that early reports have shown that endoscopic patency capsules may themselves precipitate small bowel obstruction (Gay et al. 2005; Boivin et al. 2004). In many institutions, capsule endoscopic assessment is reserved for patients with negative CT examinations in whom clinical suspicion remains.

Radiologists should also know the possible pitfalls in Crohn diagnosis. Segmental mural hyperenhancement can be present in diseases other than active Crohn disease, like portal or mesenteric vein clot, luminal collapse, backwash ileitis, and short gut syndrome. Mural wall thickening is also a nonspecific finding when seen in isolation and should be seen in conjunction with segmental mural hyperenhancement (Paulsen et al. 2006). Spasm or collapse of small bowel loops can be especially problematic because spasm is an early finding in Crohn disease and collapse is associated with thickening and increased attenuation of the small bowel wall. In this setting, repeat scanning through the region of interest and reliance on extraenteric findings of inflammation such as dilated vasa recta, fistulas, and perienteric inflammatory changes can be helpful (Mazzeo et al. 2001).

16.3.4.2 Small Bowel Obstruction

The diagnosis of partial small bowel obstructions has typically been based on clinical examinations and often confirmed with radiological studies. Conventional enteroclysis has been proven to be an effective diagnostic tool for partial small bowel obstructions (pSBOs) with sensitivity/specificity of 89%/100% (Shrake et al. 1991; Maglinte et al. 1996a). The results for distal pSBO are not as good, especially in the pelvis, where loops of bowel and the bladder often obscure potential pSBOs, making diagnosis difficult. Computed tomography has also

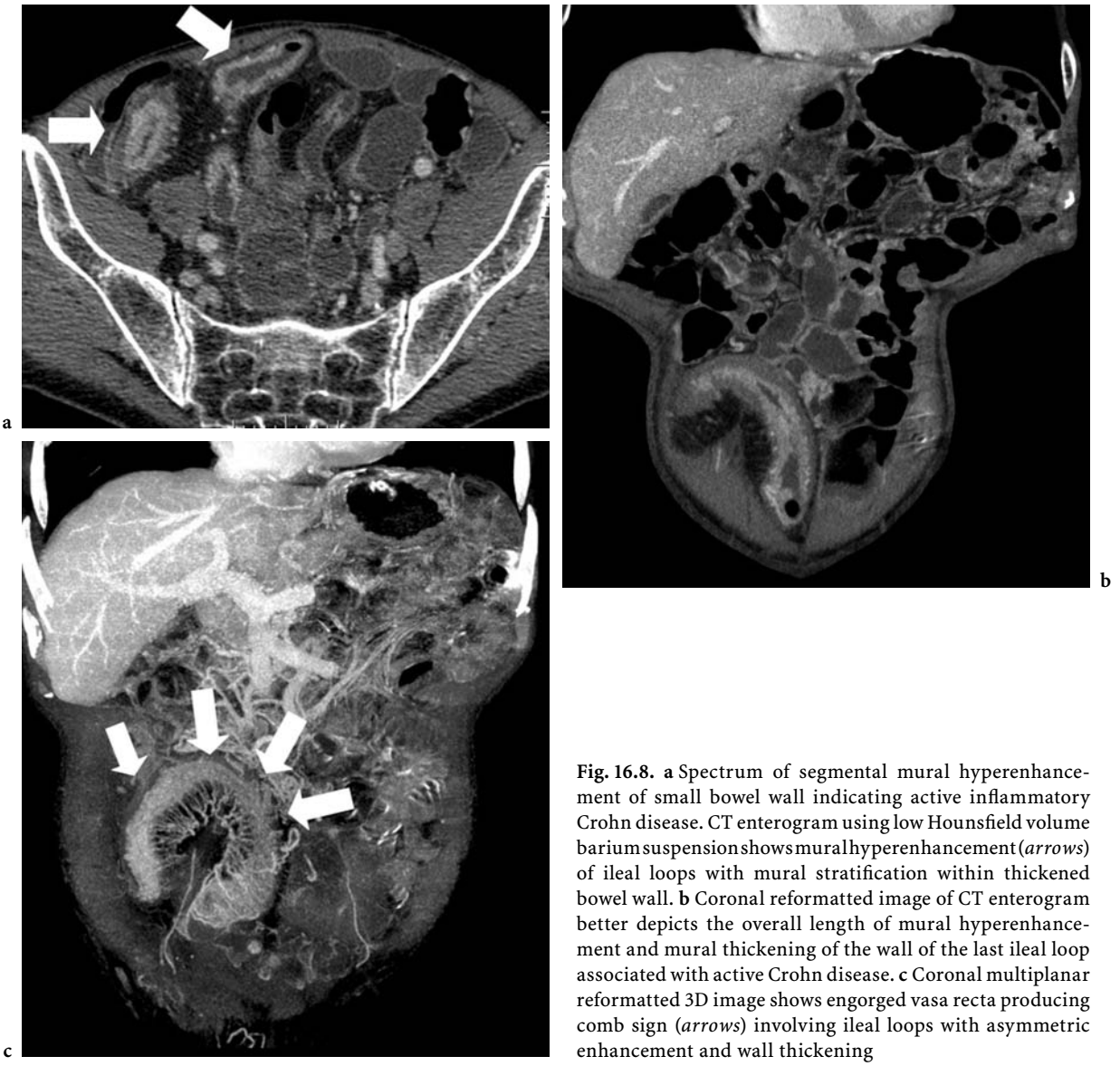

Fig. 16.8. **a** Spectrum of segmental mural hyperenhancement of small bowel wall indicating active inflammatory Crohn disease. CT enterogram using low Hounsfield volume barium suspension shows mural hyperenhancement (*arrows*) of ileal loops with mural stratification within thickened bowel wall. **b** Coronal reformatted image of CT enterogram better depicts the overall length of mural hyperenhancement and mural thickening of the wall of the last ileal loop associated with active Crohn disease. **c** Coronal multiplanar reformatted 3D image shows engorged vasa recta producing comb sign (*arrows*) involving ileal loops with asymmetric enhancement and wall thickening

shown excellent results for high-grade pSBO with sensitivity of 89%, but the sensitivity drops to less than 50% for distal, low-grade pSBO (Maglinte et al. 1996b). Computed tomography-enteroclysis (CT-E) has proven results with sensitivity/specificity 89%/100%, matching the success of conventional enteroclysis (Bender et al. 1996).

The theoretic advantage of CT-enterography is the potential to provide a unique perspective on the location and relations of the various causes of small bowel obstruction not previously available, it also has the added benefit of high-resolution anatomic relationship; this not only helps to define the nature of the partial obstruction, but it can also serve to guide the surgeon to execute more limited and better localized surgical incisions for adhesiolysis as well as for estimating the length and adequacy of unobstructed bowel available for bypass using virtual enteroscopy.

16.3.4.3 Small Bowel Tumors

Small bowel neoplasms are rare; it is estimated that they represent 3%–6% of all primary malignancies of the gastrointestinal tract and less than 2% of all malignant tumors (Gourtsoyannis and Makò 1997). Diagnosis is often delayed because of pau-

city and non-specificity of clinical symptoms and the small dimensions of the tumor during the early stage make diagnosis with conventional barium examinations difficult. MDCT-E has turned out to be a feasibility technique in the diagnosis of intestinal masses, leading to a more confident diagnosis of malignancy. The analysis of multiplanar images permits a highly reliable definition of the degree of perivisceral extension and metastatic involvement, yielding improved locoregional staging capabilities; likewise, the simultaneous availability of axial 2D images is mandatory for detecting lymphatic involvement as well as distant metastasis. The disadvantages of 3D CT of small bowel tumors are related to suboptimal distention of the lumen, which leads to unsatisfactory reconstructions.

The most common small bowel tumors (in decreasing order of frequency of occurrence) are adenocarcinoma, carcinoid tumor, lymphoma, and gastrointestinal stromal tumor. Usually these tumors may appear at CT enterography as focal intraluminal masses, focal areas of bowel wall thickening, or areas of increased mural enhancement, certain appearances suggest particular tumors. A pedunculated or predominantly exoenteric mass suggests a gastrointestinal stromal tumor. An exoenteric mass combined with adjacent lymphadenopathy or aneurysmal ulceration suggests lymphoma as the primary consideration (North and Pack 2000). Carcinoid tumors arise from neuroendocrine precursors in the mucosa or small bowel wall and may manifest as avidly enhancing polyps (often in the ileum) or as enhancing carpet lesions, mimicking the wall thickening of Crohn disease. Mesenteric carcinoid metastases demonstrate a desmoplastic reaction, may contain eccentric calcification, or may be clustered near the mesenteric root, whereas hepatic carcinoid metastases are hypervascular and necrotic. Adenocarcinomas assume a variety of shapes but are generally located in the proximal small bowel (Yang et al. 2003).

16.3.4.4 Others Findings

Studies have shown that MDCT-enterography may demonstrate characteristic findings of celiac disease, including small bowel dilatation, fold separation, non-obstructing small bowel intussusception, and extraintestinal diseases such as adenopathy and celiac-associated T-cell lymphoma (Strobl and Warshauer 1995). Reversal of the jejunoileal fold pattern with villous atrophy in the proximal small bowel can be visualized at CT enterography. Jejunization of the ileum may be particularly noticeable on coronal reformatted images.

MDCT-E is not used for the diagnosis or staging of ulcerative colitis. Even when radiologic findings are present, they are often non-specific (Horton et al. 2000). Because of the sensitivity of CT enterography for Crohn disease, the principal role of this modality in patients with suspected ulcerative colitis is to help exclude findings of Crohn disease such as small bowel inflammation.

Another area of interest for CT-enteroclysis is small bowel bleeding. Conventional enteroclysis has been reported to have a 10% diagnostic yield for gastrointestinal bleeds of unknown origin. Computed tomography has been reported to be an accurate diagnostic tool for bowel arteriovenous malformations, but it requires bowel distention for an adequate study. The combination of intravenous contrast and small bowel distention with methylcellulose/ neutral contrast will give CT-E an advantage over either study.

16.3.5 MRI of the Small Bowel

An adequate small bowel distension is mandatory for an accurate study and it is obtained by using either oral contrast agent ("MR follow-through") or naso-jejuneal catheter ("MR enteroclysis").

Major clinical indication is represented by the evaluation of patients with suspected Inflammatory Bowel Disease (IBD), in particular in the diagnosis and follow-up of patients with Crohn's disease. MR of the small bowel allows an optimal evaluation of parietal inflammatory changes represented by wall thickening and contrast enhancement.

The absence of ionising radiation, considering the young age of most of the patients as well as the frequency of the examinations, is an important advantage over other techniques (X-ray and CT enteroclysis).

In patients with proved or suspected Crohn's disease, cross-sectional images should be analyzed specifically for identification and characterization of pathologically altered bowel segment.

The core of small bowel evaluation in case of suspected Crohn's disease is represented by the individuation of inflammatory changes of small bowel wall.

Inflammatory changes of small bowel wall are represented by bowel wall thickening and increased contrast enhancement.

The normal wall thickness of the small intestine is between 1 mm and 3 mm, when the lumen is distended. Any portion of the bowel wall exceeding 4–5 mm is considered abnormal. An adequate intestinal distension is mandatory because collapsed loops or spastic intestinal segments may mimic wall thickening. Small bowel wall thickening is a very sensitive, but not pathognomonic sign of Crohn's disease, since it is observed in several other intestinal diseases, like infections, ischemic disorders and graft-versus-host disease.

Although superficial mucosal lesions are easily missed due to inadequate spatial resolution, MR imaging is able to detect early inflammatory changes of the bowel wall, based on enhancement following intravenous injection of contrast medium.

Two are the patterns of enhancement of a pathologic bowel segment: "homogeneous" and "stratified". Homogeneous enhancement is a diffuse transmural enhancement with no recognition of different bowel layers. A stratification of the bowel wall (the so called "target" or "double halo" appearance) is related to mucosal enhancement with hypoenhancing outer layer.

If T2-weighted and contrast-enhanced T1-weighted images are simultaneously considered, two different patterns can be recognized: stratification on T2-weighted images (slightly hyperintense mucosa and sub-mucosa and hypointense muscular layer) associated with transmural enhancement (no stratification) on T1-weighted images. This pattern is more frequently associated with early stages of Crohn's disease and it is very common in paediatric and young adults (Fig. 16.9). Absence of stratification on T2-weighted images, where the bowel wall is diffusely hypointense, due to fibrosis, associated with stratified enhancement pattern on T1-weighted images. This is typical of long-standing Crohn's disease, with fibrosis, or of patients following intense medical treatment.

The recognition of a stricture is easy, if considering that the normal lumen of the small intestine is around 2.5 cm in diameter. The presence of a pre-stenotic dilatation may help in the diagnosis. Extramural abnormalities include fibro-fatty proliferation, vascular engorgement on the mesenteric side of the bowel and mesenteric lymphadenopathy. Crohn's disease from a pathological point of view is a chronic granoulomatous inflammation affecting the bowel wall and extending to the perivisceral mesenteric fatty tissue.

16.4 Conclusions

In conclusion, 3D imaging of the esophagus, stomach and small bowel represents a valuable adjunct to conventional cross-sectional imaging, which can

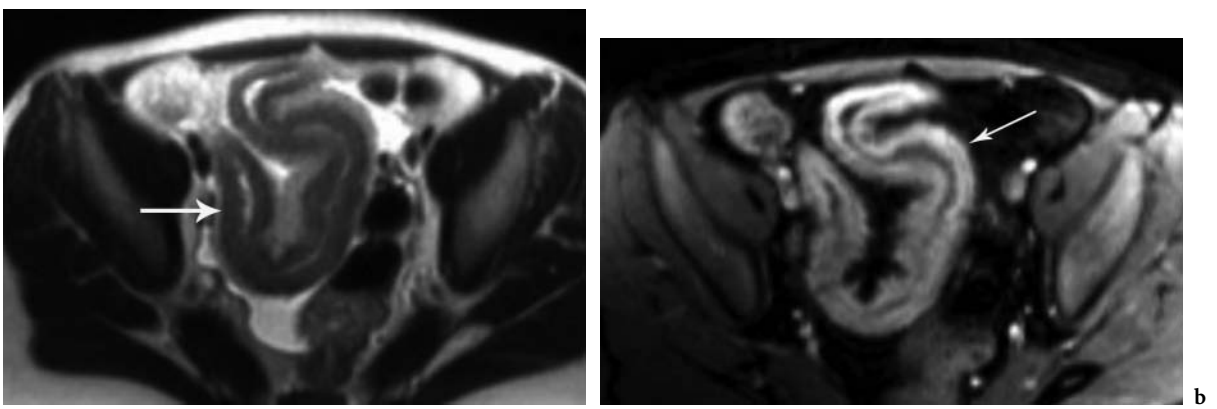

a b

Fig. 16.9. a Patient with Crohn disease MRI T2 weighted sequences clearly evaluates typical enhancement of bowel wall (*arrow*) **b** The use of T1 weighted sequence after intravenous administration of contrast agent is mandatory to depict enhancement of bowel wall. Using biphasic contrast agents, on T2 weighted images, bowel wall has low signal intensity, included between intraluminal contrast agent signal intensity and fat tissue signal intensity. On T1 weighted images, acquired after intravenous administration of , GD-DTPA, hyperintensity of bowel wall is better evaluated between hypointensity of fat tissue (using fat-suppressed sequence) and hypointensity of intraluminal contrast agent characterised by low signal intensity

be easily obtained from both CT and MR datasets using dedicated workstations and commercially available software. Virtual endoscopy images offer a more comprehensive evaluation of the disease process from an inner perspective representing a potentially interesting compliment to conventional endoscopy. From the other hand the use of multiplanar projections improve the anatomic presentation of the abdominal organs (esophagus, stomach and small bowel) and produces fewer images that have orientations similar to those of conventional examinations.

References

Bender GN, Timmons JH, Willard WC et al (1996) Computed tomographic enteroclysis: one methodology. Invest Radiol 31:43–49

Bender GN, Maglinte DD, Klöppel R et al (1999) CT-enteroclysis: a superflous diagnostic procedure or valuable when investigating small bowel disease? AJR Am J Roentgenol 172:373–378

Bielen D, Vanbeckevoort D, Thomeer M et al (2001) Virtual endoscopy, in Multislice CT: a practical guide, Proceedings of the 5th International SOMATOM CT Scientific User Conference, Zurich, June 2000, pp 204–215

Boivin ML, Voderholzer W, Lochs H (2004) M2A patency capsule: the Berlin experience (abstr). Gastroenterology 126(suppl 2):459

Doerfler OC, Ruppert-Kohlmayr AJ, Reittner P et al (2003) Helical CT of the small bowel with an alternative oral contrast material in patients with Crohn disease. Abdom Imaging 28:313–318

Gay G, Delvaux M, Laurent V et al (2005) Temporary intestinal occlusion induced by a "patency capsule" in a patient with Crohn's disease. Endoscopy 37:174–177

Gonvers J, Burnand B (1996) Appropriateness and diagnostic yield of upper gastrointestinal endoscopy in an open-access endoscopy unit. Endoscopy 28:661–666

Gore RM, Balthazar EJ, Ghahremani GG et al (1996) CT features of ulcerative colitis and Crohn's disease. AJR Am J Roentgenol 169:3–15

Gourtsoyannis N, Makò E (1997) Imaging of primary small intestinal tumors by enteroclysis and CT with pathological correlations. Eur Radiol 7:625–642

Griffith JF, Kew J (1999) 3D CT imaging of oesophageal carcinoma. Eur J Radiol 32:216–220

Horton KM, Fishman EK (2003a) Current role of CT in imaging of the stomach. Radiographics 23(1):75–87. Review

Horton KM, Fishman EK (2003b) The current status of multidetector row CT and three-dimensional imaging of the small bowel. Radiol Clin North Am 41:199–212

Horton KM, Corl FM, Fishman EK (2000) CT evaluation of the colon: inflammatory disease. RadioGraphics 20:399–418

Iafrate F, Paolantonio P, Ferrari R et al (2006) 64 MDCT and low Hounsfield value barium suspension (Volumen): an "explosive combination" for the evaluation of the small bowel and the upper GI tract: comparison with a positive contrast agent and water. Eur Radiol 16(Suppl 3):51

Jolesz F, Lorensen W (1997) Interactive virtual endoscopy. AJR Am J Roentgenol 169:1229–1235

Kim AY, Kim HJ, Ha HK (2005) Gastric cancer by multidetector row CT: preoperative staging. Abdom Imaging 30(4):465–472. Review

Kim SH, Lee JM, Han JK et al (2005) Effect of adjusted positioning on gastric distention and fluid distribution during CT gastrography. AJR Am J Roentgenol 185(5):1180–1184

Lee DH (1998) Three dimensional imaging of the stomach by spiral CT. J Comput Assist Tomogr 22:52–58

Lee DH, Ko YT (1996a) The findings and the role of axial CT imaging and 3D imaging of gastric lesion by spiral CT. J Korean Radiol Soc 35:731–738

Lee DH, Ko YT (1998b) The role of 3D spiral CT in early gastric carcinoma. J Comput Assist Tomogr 22:709–713

Lee DH, Ko YT (1999c) Advanced gastric carcinoma: the role of three-dimensional and axial imaging by spiral CT. Abdominal Imaging 24:111–116

Lee DH, Ko YT (1999d) The role of three-dimensional and axial imaging in advanced gastric carcinoma by spiral CT. Abdom Imaging 24:111–116

Leung DA, McKinnon GC (1996) Breath hold, contrast-enhanced, three dimensional MR angiography. Radiology 201:569–571

Lyang EY, Chan A (1996) Short communication: oesophageal tumour volume measurement using spiral CT. Br J Radiol 69:344–347

Maglinte DDT, Reyes BL, Harmon BH et al (1996a) Reliability and role of plain film radiography and CT in the diagnosis of small bowel obstruction. AJR Am J Roentgenol 167:1451–1455

Maglinte DD, Kelvin F, O'Connor K (1996b) Current status of small bowel radiography. Abdom Imaging 2:247–257

Mako EK, Mester AR, Tarjan A et al (2000) Enteroclysis and spiral CT examination in diagnosis and evaluation of small bowel Crohn disease. Eur J Radiol 35:168–175

Mazzeo S, Caramella D, Battolla L et al (2001) Crohn disease of the small bowel: spiral CT evaluation after oral hyperidratation with isotonic solution. J Comput Assist Tomogr 24:612–616

Megibow AJ, Babb J, Hecht E et al (2006) Evaluation of bowel distention and bowel wall appearance by using neutral oral contrast agent for multidetector row CT. Radiology 238:87–95

Meyers MA, McGuire PV (1995) Spiral CT demonstration of hypervascularity in Crohn disease: "vascular jejunization of the ileum" or the "comb sign". Abdom Imaging 20:327–332

North JH, Pack MS (2000) Malignant tumors of the small intestine: a review of 144 cases. Am Surg 66:46–51

Ominsky SH, Moss AA (1979) The postoperative stomach: a comparative study of double-contrast barium examinations and endoscopy. Gastrointest Radiol 4:17–21

Orjollet-Lecoanet C, Menard Y, Martins A et al (2000) CT enteroclysis for detection of small bowel tumors. J Radiol 81:618–627

Panebianco V, Grazhdani H, Iafrate F et al (2006a) 3D CT protocol in the assessment of the esophageal neoplastic lesions: can it improve TNM staging? Eur Radiol 16(2):414–421

Panebianco V, Habib FI, Tomei E (2006b) Initial experience with magnetic resonance fluoroscopy in the evaluation of esophageal motility disorders. Comparison with manometry and barium fluoroscopy. Eur Radiol 16(9):1926–1933

Paulsen SR, Huprich JE, Fletcher JG et al (2006) CT enterography as a diagnostic tool in evaluating small bowel disorders: review of clinical experience with over 700 cases. RadioGraphics 26:641–662

Rollandi GA, Curone PF, Biscaldi E et al (1999) Spiral CT of the abdomen after distention of small bowel loops with transparent enema in patients with Crohn's disease. Abdom Imaging 24:544–549

Schmid MR, Hany TF, Debatin JF (1999) 3D MR gastrography: exoscopic and endoscopic analysis of the stomach. Eur Radiol 9:73–77

Shmidt S, Chevallier P, Chalaron et al (2005) Eur. Radiol 15:238–246

Shrake PD, Rex DK, Lappas JC et al (1991) Radiographic evaluation of suspected small bowel obstruction. Am J Gastroenterol 86:175–178

Strobl PW, Warshauer DM (1995) CT diagnosis of celiac disease. J Comput Assist Tomogr 19:319–320

Thoeni RF, Cello JP (1980) A critical look at the accuracy of endoscopy and double-contrast radiography of the upper gastrointestinal (UGI) tract in patients with substantial UGI hemorrhage. Radiology 135:305–308

Winter TC, Ager JD, Nghiem HV et al (1996) Upper gastrointestinal tract and abdomen: water as an orally administered contrast agent for helical CT. Radiology 201(2):365–370

Yang YS, Huang QY, Wang WF et al (2003) Primary jejunoileal neoplasmas: a review of 60 cases. World J Gastroenterol 9(4):862–864

Zhang LH, Zhang S, Hu HJ (2005) Multi-detector CT enterography with iso-osmotic mannitol as oral contrast for detecting small bowel disease. World J Gastroenterol 11(15):2324–2329

CT and MR Colonography

17

Daniele Regge, Teresa Maria Gallo, Cristiana Laudi, Giovanni Galatola, and Vincenzo Tartaglia

CONTENTS

D. Regge, MD; T. M. Gallo, MD; V. Tartaglia, MD
Radiology Unit, Institute for Research and Treatment of Cancer (IRCC), Str. Provinciale 142, Candiolo, 10060 Torino, Italy
C. Laudi, MD; G. Galatola, MD
Gastroenterology Unit, Institute for Research and Treatment of Cancer (IRCC), Str. Provinciale 142, Candiolo, 10060 Torino, Italy

17.1 Definitions

CT or MR colonography, first described as virtual colonoscopy by Vining in 1994, is a non-invasive imaging method that uses CT or MR data sets combined with specialised imaging software to examine the colon. Various names have been given to virtual colonoscopy, including CT pneumocolon and CT or MR colonography. Since 2002, CT colonography (CTC) and MR colonography (MRC) have been definitively included as standard reference terms in medical databases.

17.2 CT Colonography

17.2.1 Diet and Bowel Preparation

Adequate bowel preparation is essential for an accurate CTC examination. Individuals undergoing CTC should consume a low residue diet, avoiding high-fibre food such as fruit and vegetables that produce faecal residues. Residual fluid and solid residues may reduce sensitivity and specificity of CTC. Endoluminal fluid can obscure polyps; solid stool can mimic a true polyp and, if present in large quantities, obscure polyps.

Despite the large amount of published studies on CTC, there is no consensus about the optimum regimen for bowel preparation. Two commonly used bowel-cleansing regimens are polyethylene glycol electrolyte (PEG) lavage solution and saline cathartics such as phospho-soda and magnesium citrate, both of which are available in commercial preparations. Table 17.1 details the most common preparation schemes.

Table 17.1. Standard preparations for CTC

"WET PREP" (lavage solution)	"DRY PREP" (saline cathartics)
Low residue diet starting three days before the examination (no flavoured cheese, condiments, whole-grain bread, crackers, cereals, popcorn, raw fruit, mustard…)	
The day before the examination: • 4 L of polyethylene glycol electrolyte solution between 3:00 and 7:00 PM • Liquid diet	The day before the examination: • 45 ml of sodium phosphate diluted in 200 cc of water at 8.00 AM and 8:00 PM • Liquid diet
On the day of examination: nil by mouth.	
A bisacodyl rectal suppository is given to the patient immediately before CTC	

Several studies have evaluated the effect of these two bowel preparations on the amount of residual fluid present within the colon at the time of CTC. The standard PEG solution usually leaves a large quantity of residual fluid within the colon that may hamper visibility for the radiologist, but it poses no problems to the endoscopist, since fluid may be easily aspirated by the endoscope. Radiologists prefer a "dry" colon, such as that produced by phospho-soda and/or magnesium citrate, as this generally results in a smaller amount of residual fluid compared to the electrolyte lavage solutions (Macari et al. 2001). Furthermore, patients usually tolerate saline cathartics better than they do PEG (Kolts et al. 1993; Oliveira et al. 1997).

Complications resulting from the administration of sodium phosphate cathartics are uncommon, but they have been reported in the literature (Fass et al. 1993; Ehrenpreis et al. 1996; Vukasin et al. 1997). Saline cathartics are contraindicated in patients with renal failure and pre-existing electrolyte abnormalities, congestive heart failure and ascites.

The use of cathartic or laxative is, however, an unwelcomed discomfort for patients, and rarely achieves an optimal cleansing of the colon. Thus, some endoscopists have attempted ways to "tag" the faecal content of the colon with orally administered iodinated contrast media and/or barium (Table 17.2) so that solid and liquid residues can be "subtracted" during the post-processing phase, which results in a potentially optimal virtual cleansing of the colon. (Lefere et al. 2002; Pickhardt and Choi 2003; Lefere et al. 2005). Faecal tagging improves specificity through better differentiation between faecal residues and tumoural lesions (Fig. 17.1). Faecal tagging without cathartic cleansing (Table 17.2) has recently been used on a routine basis and shown to significantly improve patient compliance (Bielen et al. 2003; Iannacone et al. 2004).

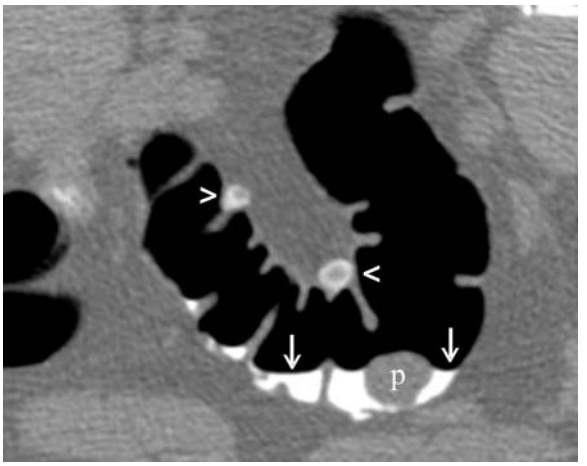

Fig. 17.1. Axial CT scan through the sigmoid colon. Image shows high-density fluid tagged with iodine (*arrows*) and a 15 mm polyp (*p*) clearly depicted due to its soft-tissue attenuation. Two fluid-filled diverticula can be observed on the opposite wall (*arrow-points*)

17.2.2 Spasmolytic Agents

The use of spasmolytic agents is controversial. Glucagon does not improve colonic distension; compared to Glucagon and placebo, Buscopan® leads to better colon distension, especially for the rectosigmoid, but about 5% of patients complain of side effects (Goei et al. 1995; Yee et al. 1999; Morrin et al. 2002; Taylor et al. 2003; Bruzzi et al. 2003). Furthermore, contraindications exist for Buscopan®, such as glaucoma, prostatic hypertrophy and heart diseases. Another considerable disadvantage is the need for obtaining venous access, even when unenhanced CT is performed. For such reasons, spasmolytic agents are not routinely recommended for CT colonography; they

Table 17.2. Preparations for faecal tagging CTC

Faecal Tagging and Cathartic Preparation (Pickhardt et al. 2003)	Faecal Tagging with Reduced Cathartic Preparation (Lefere et al. 2002)	Faecal Tagging without Cathartic Preparation (Mod. from Iannaccone et al. 2004)
Low residue diet starting three days before the examination (no flavoured cheese, condiments, whole-grain bread, crackers, cereals, popcorn, raw fruit, mustard…).		
Two days before the examination: • 250 ml of barium diluted at 2.1% by weight after dinner	----	Two days before the examination: • 20 ml of diatrizoate meglumine and diatrizoate sodium (Gastrografin®) in a glass of water at each of the three meals
The day before the examination: • 250 ml of barium diluted at 2.1% by weight at each of the three meals • 45 ml of sodium phosphate (Phospholax®) diluted in 200 cc of water at 8:00 AM and 8:00 PM • 60 ml of Gastrografin® diluted in water after dinner	The day before the examination: • 250 ml of barium diluted at 2.1% by weight at each of the three meals • 16.4 g of magnesium citrate solution at 6:00 PM • Four bisacodyl tablets orally at 6.00 PM	The day before the examination: • 20 ml of Gastrografin® diluted in a glass of water at each of the three meals
On the day of examination: • 60 ml of Gastrografin® diluted in water 2 h before the test • nil by mouth	On the day of examination: • nil by mouth	On the day of examination: • nil by mouth
A bisacodyl rectal suppository is given to the patient immediately before CTC		

may be considered when pain is elicited during rectal administration of room air or CO_2 and when there is insufficient colon distension, as may occur with diverticular disease.

17.2.3 Mechanical Bowel Distension

Adequate colonic distension is crucial for high quality imaging, and is just as important as a proper bowel cleansing. In a collapsed colon, polyps cannot be visualised and the narrowed lumen can mimic colon carcinomas. Before the patient is placed onto the CT table, he is asked to void his bowel. A short rectal tube (Fig. 17.2) is introduced in the rectum with the patient in right lateral decubitus, and room air or CO_2 is gently insufflated. Room air is used most commonly because it is readily available and provides reliable colonic distension. Room air is an inert gas in equilibrium with the body tissues, thus there is no diffusion gradient across the colonic wall, and the patient may develop pain due to colonic and small bowel over-distension until the air is eventually expelled by peristalsis. CO_2 has been proposed as a valid alternative, as it is

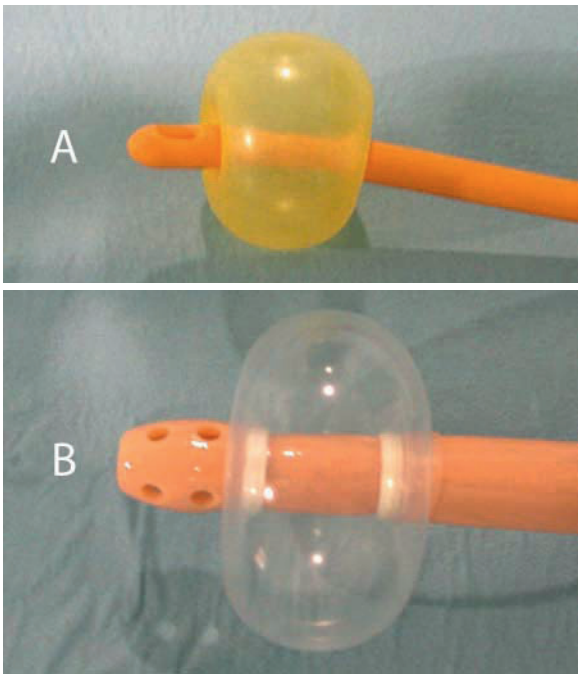

Fig. 17.2. Two balloon rectal tubes commonly used to insufflate air in the bowel. Type *A*) is a 24 French flexible rubber Foley catheter, normally used for bladder catheterization; type *B*) is a large bore rigid plastic tube with multiple lateral holes preferred in incontinent patients

passively absorbed by the intestinal mucosa via the lipid phase of the membranes and should therefore be promptly eliminated through exhalation, which result in better colonic distension (Rogalla et al. 2000).

Recent studies have confirmed that automated CO_2 insufflation significantly improves colonic distension compared to manual insufflation; the benefit is greatest in the left colon, particularly in the supine position. However, patient acceptance is similar for manual and automatic CO_2 insufflation (Burling et al. 2006).

17.2.4 Scanning and Image Acquisition

Before proceeding to image acquisition, the degree of colon distension is assessed on frontal and lateral CT scout views; the colon can thus be re-inflated if necessary (Fig. 17.3). CT scanning is performed in the prone and supine positions while the patient holds his breath, as dual acquisition has been shown to significantly improve CTC sensitivity (Fig. 17.4) and specificity (Fig. 17.5) (Fletcher et al. 2000; Morrin et al. 2002).

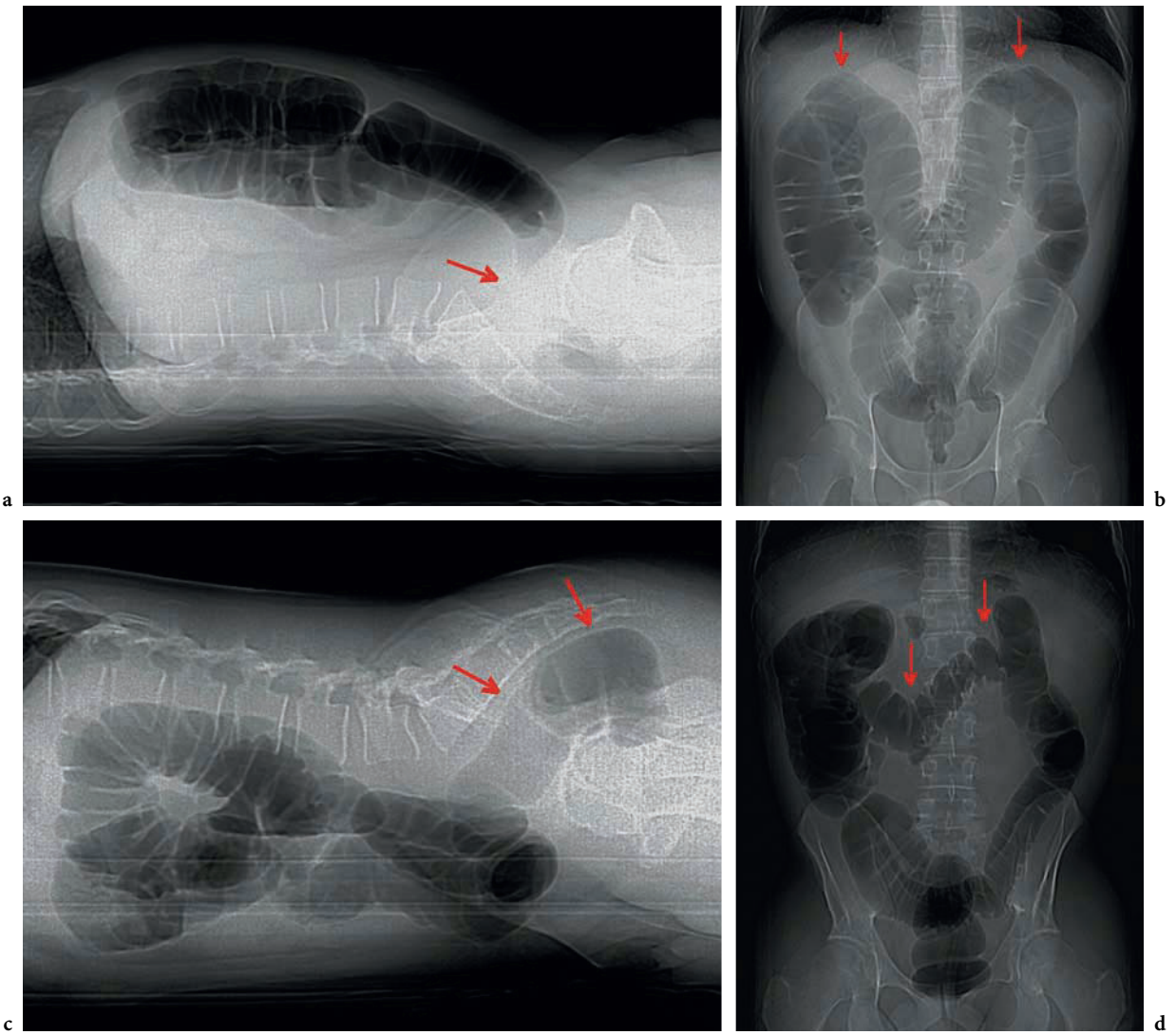

Fig. 17.3a–d. Scouts in the lateral and AP views show how gas distributes within the large bowel in the supine (**a**,**b**) and prone (**c**,**d**) positions. All images are from the same patient. In the supine position gas is displaced anteriorly, and images show poor distension of the rectum (**a**, *arrow*) and good distension of the transverse colon (**b**, *arrows*). Conversely, in the prone position gas prevails in those colon segments that are located posteriorly, and images show a distended rectum (**c**, *arrows*) and a sub-optimally distended transverse colon (**d**, *arrows*)

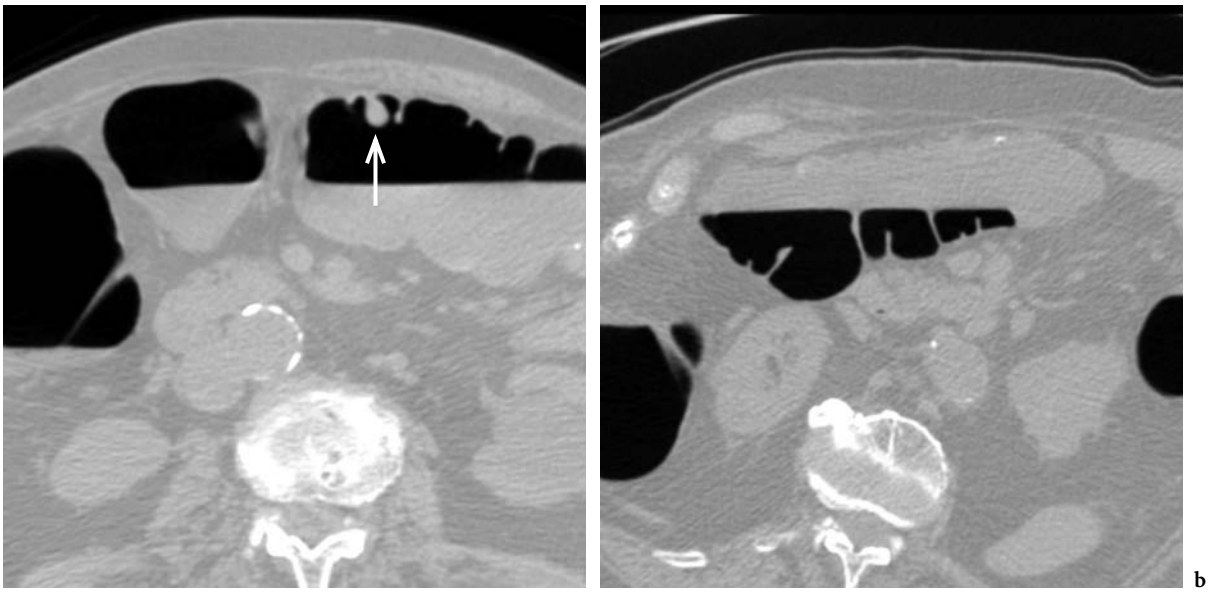

Fig. 17.4a,b. Axial scans thorough the transverse colon in the supine (**a**) and prone (**b**) positions with a lung window setting. **a** An 8 mm peduncolated polyp is visible on the anterior bowel wall (*arrow*); **b** in the prone position the polyp is covered by fluid. If only prone scans had been performed the polyp would not have been detected

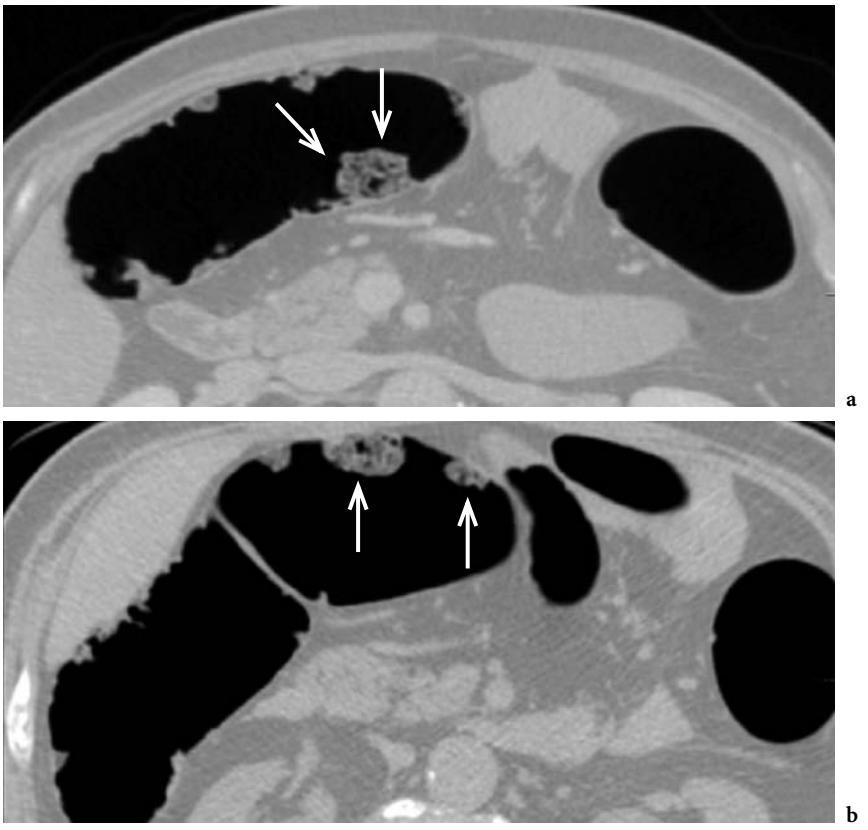

Fig. 17.5a,b. Axial scans through the transverse colon in the supine (**a**) and prone (**b**) positions with a lung window setting. Both images show multiple filling defects protruding within the bowel lumen, with markedly inhomogeneous patterns alternating soft tissue values and air density. Some of the defects are in different gravity favoured positions in the supine (**a**, *arrows*) and prone scans (**b**, *arrows*). The structural characteristics and the mobility of the objects are typical of faecal residues

Multidetector CT scanners are recommended for CTC because they allow faster volume coverage and thinner collimation, thus reducing motion artefacts and increasing resolution on the z-axis. The scanning protocol must be adapted according to the clinical context. If colorectal cancer (CRC) is known at the time of scanning or detected during the first acquisition, CTC must be performed as a regular abdominal scan, with intravenous contrast media administration and appropriate tube current values. In all the other cases a low dose protocol should be considered, as higher doses do not provide any better diagnostic accuracy (Van Gelder et al. 2002; Van Gelder et al. 2004; Zalis et al. 2005). Accordingly, in our routine clinical practice tube currents inferior to 50 mAs are now used.

A reasonable balance between slice collimation and the smallest size lesion that one wants to detect should be considered when planning scan protocols. Since there is general consensus that polyp lesions smaller than 6 mm are not clinically relevant and should therefore not be reported, excessively thin slices are probably not necessary. For this reason, most protocols suggest a slice collimation of 2–3 mm, with a 50–70% overlap (Macari et al. 2002; Power et al. 2002; Laghi et al. 2003). Very thin slicing does not add information on the z-axis, increases the noise-to-signal ratio and, from a clinical point of view, may reduce specificity due to higher probability of false-positive findings (Embleton et al. 2003).

17.2.5 Post-processing and Exam Evaluation

Different multipurpose and specialised software is now available for colon evaluation by CT or MR data sets.

A simple direct way to examine the colon is by panning through 2D images. The 2D interpretation technique, advocated by many CTC experts, should be performed on a workstation suitable for permitting comparison of supine and prone data sets of axial images in both lung and soft tissue settings, adding 2D multiplanar reformation if necessary. The advantage of this reading technique is that it does not require dedicated software and is therefore available on most general-purpose workstations. Some workstations allow 3D visualisation of regions of interest, identified on the 2D multiplanar images, by a simple command such as a mouse click; observing objects in 3D may aid in the differential diagnosis; for example, between a thickened fold and a polyp (Fig. 17.6).

A second group of software programs extract images of the air-filled colon, generate an automated centreline for luminal navigation and electronically remove from the images the opacified residual fluid in a routine processing scheme. The diagnostic interface permits a virtual "fly-through" tour of the 3D image, and a rapid correlation with the 2D images for any suspected abnormality.

When using a primary 3D interpretation technique, navigation should be performed in both directions to maximise polyp detection unless the image is represented in such a way that the eye can observe behind obstacles (e.g. folds) as is the case with the virtual dissection or unfolded cube techniques that will be discussed in the next Chapters 19 and 20. The 3D method may be more accurate than 2D interpretation, especially for smaller lesions, but it is more time-consuming (Dachman et al. 1998; Macari et al. 2000; Rex et al. 1999).

Although debate continues regarding which rendering technique should be used for primary evaluation, the two techniques are complementary, and their combined use increases the CT accuracy.

17.2.6 Reporting CTC

The first section of a CTC report should contain information on patient preparation and exam technique, including whether intravenous contrast material and/or spasmolytic agents have been administered. A description of exam quality should follow, and possible causes of incomplete bowel wall visualisation should be reported.

Relevant CT findings should be classified according to their morphology, size and location. A polyp is a structure with soft-tissue attenuation values, is attached to the bowel wall and protrudes from within the colon lumen (Zalis et al. 2005). Polyps may be classified according to their shape as peduncolated, sessile or flat. Peduncolated polyps have a stalk (Fig. 17.4), sessile lesions are broad-based, and flat lesions have a vertical elevation from the mucosal surface that does not exceed 3 mm. Lesions should be positioned in one of the following six colon segments: rectum, sigmoid colon, descending colon, transverse colon, ascending colon and cecum.

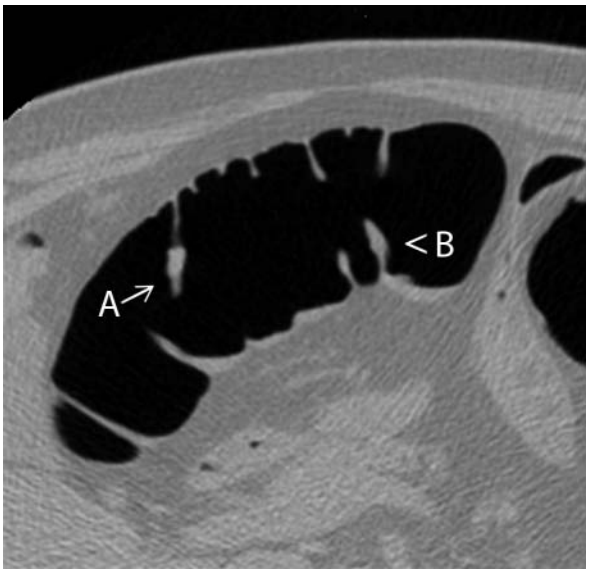

a

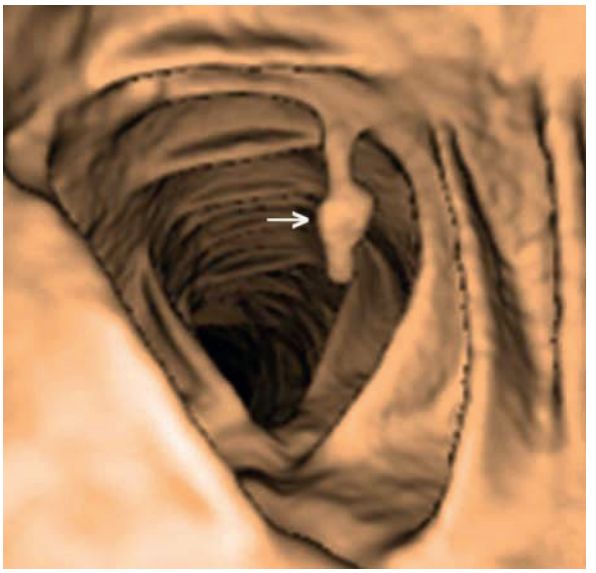

b

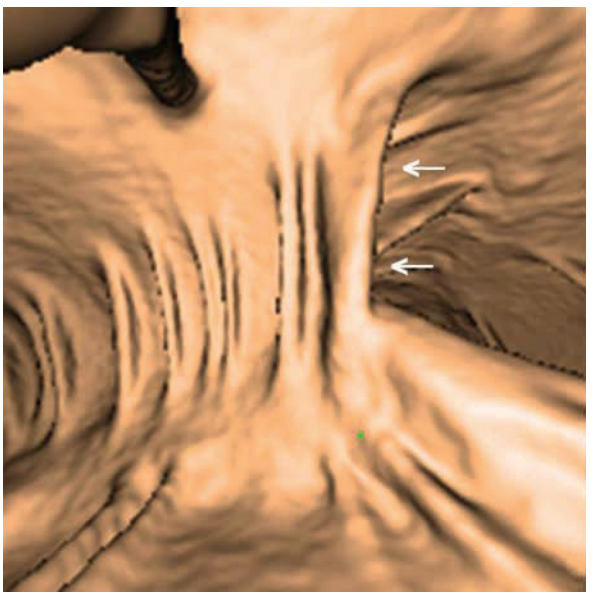

c

Fig. 17.6a–c. Axial scan through the transverse colon in the supine position (**a**) and 3D endoscopic rendering mode (**b**,**c**). **a** Two identical filling defects on the anterior (*arrow*-object *A*) and posterior wall (*arrow point*-object *B*). 3D images show that object *A* is a polyp (**b**, *arrow*) and that object *B* is a fold (**c**, *arrows*)

The rectum and sigmoid together define the proximal colon, the remaining four segments the distal colon.

Lesion size is defined by the single largest diameter measured using a lung tissue setting (1500 HU window width; -200 HU window level). Measurement should be performed on the 2D supine or prone multiplanar view.

Polyps with a diameter of 5 mm or less are defined as diminutive lesions. In the majority of cases these lesions are hyperplastic and therefore have no malignant potential. In addition, adenomas 5 mm or less in diameter have a very low risk of evolution towards malignancy, and their growth is very slow. As a result, the tendency is to not report diminutive lesions, in part because doing so may lead to a high rate of false-positive findings (Zalis et al. 2005).

Polyps between 6 and 9 mm are defined as intermediate lesions. Most of them are eventually found to be low-grade dysplasia adenomas, less than 1% are found to be harbour invasive carcinomas and 30% are found to be hyperplastic lesions. Thus, surveillance either with conventional or virtual colonoscopy may be a reasonable option in these cases

unless multiple lesions or a family or personal history for cancer are present, any one of which suggests referral for colonoscopy.

Lesions 1 cm or larger are defined as large and should be referred for colonoscopy. Lesions larger than 3 cm are defined as masses and may be referred directly to the surgeon whenever their aspect is obviously malignant and endoscopy biopsies cannot be safely performed (Fig. 17.7).

In the final part of the report the radiologist should communicate clinically relevant extracolonic findings and suggest follow-up examinations, if necessary. Further issues related to extracolonic assessment are reported in the specific section.

17.2.7 Indications and Results

17.2.7.1 Clinical Practice

Table 17.3 reports the results of the most relevant studies on CTC accuracy using conventional colonoscopy (CC) as the reference standard. Results show that the sensitivity and specificity of CTC in the detection of polyps and cancer is still lower than that of CC and that the accuracy of CTC increases with size and is highest for polyps 1 cm or larger. Therefore, CTC should not be used as a first approach

a

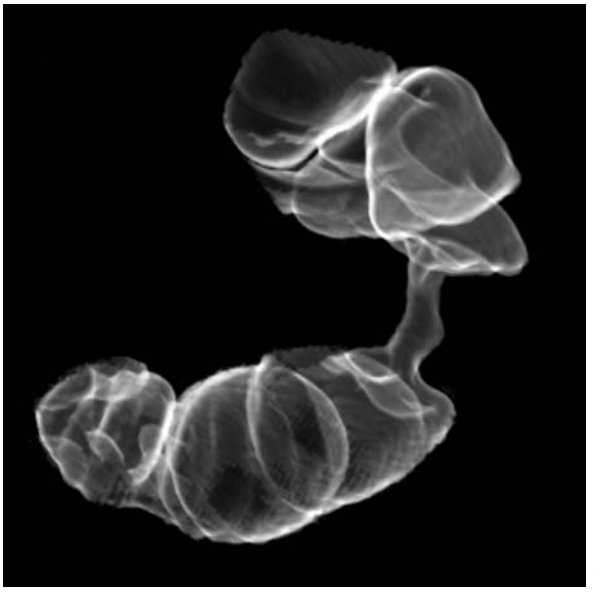

b

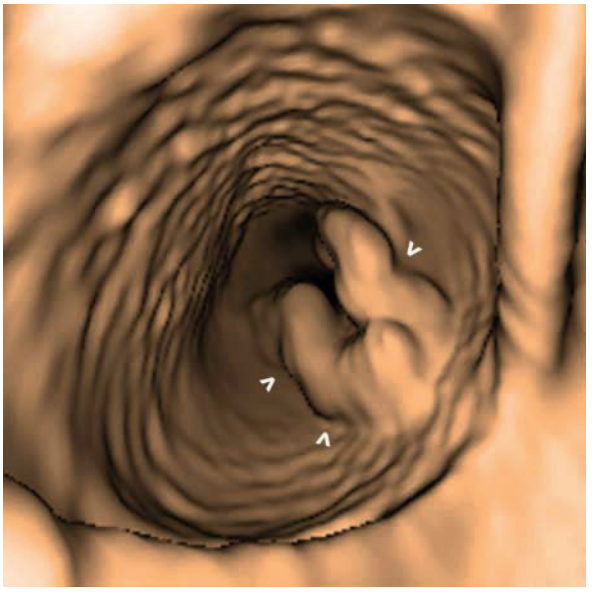

c

Fig. 17.7a–c. Forty-seven year old female with rectal bleeding submitted to CTC. **a** Axial CTC scan shows circumferential irregular thickening of a 4 cm segment of the sigmoid colon bowel wall (*arrow points*). **b,c** Barium enema-like and 3D endoluminal views show severe stenosis of the involved segment and annular vegetations at the proximal and distal margins (*arrow points*). CTC signs were suggestive of CRC and the patient was sent directly to surgery, which confirmed the imaging findings

Table 17.3. Sensitivity and Specificity of CTC: Results of Major Clinical Series

Authors	N Pts	Inclusion criteria	Overall Per-patient SE (%)	Overall Per-patient SP (%)	Per-patient SE for lesions more than 10 mm (%)	Per-Polyp SE for lesions more than 10 mm (%)
Fenlon et al. 1999	100	3	82	84	96.0	91
Fletcher et al. 2000	180	1,3	-	-	85.4	75.2
Hara et al. 2001	283	1,3	-	-	78	80
Yee et al. 2001	300	1,2,3	90.1	72	100	90
Laghi et al. 2002	165	1,3	93	-	-	-
Lefere et al. 2002	100	1,2,3	85	88	100	100
Ginnerup et al. 2003	148	1,3	-	-	95.7	92.3
Pineau et al. 2003	205	1,2,3	61.8	70.7	90	77.8
Johnson et al. 2003	703	1,3	-	-	64	63
Pickhardt et al. 2003	1233	2	-	-	93.8	92.2
Van Gelder et al. 2004	249	1,3	62	31	84	76
Cotton et al. 2004	600	1,3	20.5	90.5	54.8	52
Rockey et al. 2005	614	1,3	-	-	59	64

Inclusion criteria: 1, symptomatic patients; 2, asymptomatic patients with average risk for CRC; 3, asymptomatic patients with increased risk for CRC (family history, previous polypectomy, etc.); N, number; SE, sensitivity; SP,specificity

alternative to CC, but should rather be considered a complementary technique. For symptomatic patients with rectal bleeding, anaemia, weight loss or positive faecal occult blood test (FOBT), CC remains the test of choice, as it allows biopsies or polypectomies to be performed at the time of the examination.

CTC in symptomatic patients is to be considered when colonoscopy can not be completed or carried out; this may occur due to mechanical hindrance such as pelvic adhesions, in cases of high risk of perforation as in complicated diverticular disease, when there is an obstruction due to cancer or extracolonic diseases, when the cecum cannot be reached in extreme dolicocolon conditions, or in patients with poor tolerance to colonoscopy in whom heavy sedation may be dangerous (elderly patients or patients with severe co-morbidity). Such indications are similar to those of double contrast barium enema (DCBE); however, CTC has been shown to be both more accurate and better tolerated than DCBE, and should be used preferentially whenever available (Rockey et al. 2005; Taylor et al. 2005; Taylor et al. 2006). Furthermore, in cases of obstructing colonic cancer, CTC is a valuable tool, as it can be conveniently performed at the time of a contrast-enhanced abdominal CT scan for staging purposes to detect synchronous colorectal carcinomas, metastases, and extracolonic lesions, thus avoiding the use of another examination because it occurs generally by using the less accurate DCBE. In patients on oral anti-coagulant therapy, CTC is an option as a first-approach test to select those patients with an indication to CC in whom switching to low-molecular weight heparin is necessary to proceed with operative colonoscopy, thus reducing the inherent risk of doing so unnecessarily in patients without colonic lesions. (Dunn and Turpie 2003).

CTC is also a valid alternative option in elderly patients, in whom first-approach CC may result in a higher percentage of incomplete examinations due to poor bowel cleansing, poor tolerance and increased risk of complications.

In symptomatic patients with a clinical suspect of diverticular disease, CTC may be preferred to CC as it has a lower risk of perforation. Although a plain CT abdominal scan may be sufficient to diagnose diverticular disease, it may not be adequate for evaluating synchronous polyps or other colonic lesions, which are expected in a higher percentage considering the old age of most patients; obtaining a diagnosis of diverticular disease may be a prelude to surgery, and it would be appropriate for the surgeon to know about other possible synchronous colonic lesions (Lefere et al. 2003; Gollub et al. 2005).

17.2.7.2 Screening

CRC is the second most common cause of cancer-related death and is a major public health concern (Bray et al. 2002). CRC develops in more than 90% of cases via the adenoma-carcinoma sequence, entailing the progressive transformation of normal to malignant cells in a series of stepwise genetic mutations (Jass 2002). As this is a slow process taking about 10 years to complete, the vast majority of colorectal cancers can be prevented by colonoscopic removal of the precursor adenoma (Stryker 1987; Winawer et al. 1996). Currently, diagnostic tests for colorectal cancer screening are FOBT, DCBE, sigmoidoscopy and CC.

In the average-risk general population, yearly FOBT starting from the age of 50 years is cost-effective in reducing colorectal cancer mortality between 18 and 33% (Mandel et al. 1993; Mandel et al. 1999; Mandel et al. 2000; Kronborg et al. 1996; Hardcastle et al. 1996). However, FOBT has a low sensitivity (20% for adenomas, 40% for cancers) and compliance is low if the test is proposed on a yearly basis.

DCBE is a viable option but there is concern about its low detection rate (48% for adenomas larger or equal to 1 cm) and the likelihood that it may even miss gross cancerous lesions (Winawer et al. 2000). Sigmoidoscopy is less invasive and more acceptable than CC, but it does not explore the proximal colon, and therefore its "protective" effect is limited (Selby et al. 1992; Newcomb et al. 1992; Lieberman et al. 2001; Segnan et al. 2005).

CC could be the ideal screening test, with a hypothetical preventive effect lasting at least 10 years (Lieberman et al. 2000; Winawer et al. 2003; Schoenfled 2005). However, it carries significant discomfort and is not free from complications, thus lowering patient compliance with screening programs entailing CC (Ioannou et al. 2003).

CTC is less invasive and more accepted than CC, and has been proposed as an alternative test for screening purposes. At the present time, the studies comparing CTC and CC have shown a wide variability of results, with "per patient" sensitivities for detection of clinically significant lesions (e.g. lesions larger than or equal to 1 cm) ranging from 47–100% (see Table 17.3). Technology (single/multislice CT, collimation, type of software, etc.), operator experience and relative risk of the target population may account for these differences.

As a result, the guidelines issued by most scientific societies still underline that before CTC can be proposed for population-based screening programs, further research needs to be performed (Winawer et al. 2003; Smith et al. 2004). Multicentre studies are in progress to assess whether CTC is an effective procedure in screening asymptomatic subjects using double check CC as the reference standard.

17.2.8 Complications

CTC is considered the safest procedure for imaging of the whole colon. Despite this, a few cases of colonic perforation have been described in the literature. The initial two cases have been reported in patients with ulcerative colitis and an obstructive lesion of the recto-sigmoid junction (Coady-Fariborzian et al. 2004; Kamar et al. 2004); recently, perforation following CTC has been reported in a subject without known colonic disease (Young et al. 2006).

A retrospective multicentre evaluation has been carried out in 11 medical centres in Israel to assess the incidence of colonic perforation at CTC (Sosna et al. 2006). Seven cases of colonic perforation were identified out of a total of 11,870 examinations, equivalent to a risk rate of 0.0059%. This value compares favourably with those of DCBE (0.04%) and CC (diagnostic 0.06%; therapeutic 0.19%; Williams and Harned 1991; de Zwart et al. 2001; Tran et al. 2001; Dafnis et al. 2001). Six perforations occurred in symptomatic subjects and only one in an individual undergoing CTC for screening. The mean age of the patients was 78 years and in all cases there were increased risk factors for colonic perforation: left inguinal hernia containing colon, severe diverticulitis, or obstructive carcinoma. Surgical treatment was required in four patients, whereas in the remaining three conservative treatment was effective. A comparable perforation rate (0.005%) has been reported in a second retrospective analysis of 17,067 English patients (Burling et al. 2006b); additionally, three self-limiting vasovagal episodes and one attack of cardiac angina have been reported. No deaths related to CTC have been reported in the literature at the present time.

In conclusion, CTC is a very safe procedure, but colonic perforation may occur, especially in symptomatic and elderly patients, particularly if they carry a risk condition known to hinder the free passage of air towards the proximal colon segments.

17.2.9 Tolerance

Several investigators have evaluated patient preference to different colon examinations. While there is no doubt that patients accept CTC better than DCBE (Taylor et al. 2005; Taylor et al. 2006), results comparing CTC and CC acceptability are controversial because they mainly depend on how the procedures were conducted. In some studies patients preferred CTC (Svensson et al. 2002; Thomeer et al. 2002; Gluecker et al. 2003; Ristvedt et al. 2003). The differing acceptability rates also depend on whether or not deep sedation is used. In studies where patients preferred CC, spasmolytic agents were rarely administered during CTC, whereas most patients undergoing CC received sedation (Forbes and Mendelson 2000; Akerkar et al. 2001; Ristvedt et al. 2003). In reports where patients favoured CTC, bowel relaxants were routinely administered during CTC, while sedation or analgesics were less frequently employed for CC (Svensson et al. 2002; Thomeer et al. 2002; Gluecker et al. 2003; Van Gelder et al. 2004).

Pain during CTC is caused by over-distension of the colon. There is evidence in the literature that manual or automatic insufflation of CO_2 reduces patient discomfort due to the rapid absorption of the gas by the bowel wall, thus increasing exam tolerance (Burling et al. 2006; Shinners et al. 2006).

17.2.10 Extracolonic Findings

CTC entails an unenhanced scan of all the abdominal and pelvic organs. Thus, finding extracolonic abnormalities during CTC examinations occurs in 35–85% of cases (Hara et al. 2000; Edwards et al. 2001; Ginnerup Pedersen et al. 2003; Gluecker et al. 2003; Hellstrom et al. 2004; Rajapaksa et al. 2004; Pickhardt and Taylor 2006). Extracolonic findings are usually classified according to their clinical relevance as being of either major, moderate or minor importance. Findings of major importance include those requiring some form of treatment and/or further investigations; those of moderate importance do not require immediate treatment but probably necessitate further investigations; findings of minor importance are considered benign and do not require further action. (Sosna et al. 2005). Clinically relevant extracolonic findings of major to moderate importance are reported in 10–23% of CTC examinations (Pickhardt and Taylor 2006). Unsuspected extracolonic malignancies, such as ovarian cancer, renal cell carcinoma, lymphomas, lung cancers, ileal carcinoid tumour, and tumours of the small bowel may be detected at an early stage and result in a benefit for the patients.

Extracolonic findings represent an important controversy with regard to low dose CTC, especially if the examination is proposed for screening of asymptomatic individuals. Detection of important abdominal and pelvic extracolonic abnormalities may benefit individuals undergoing CTC, but due to the high level of image noise, the definition of such lesions requires additional studies, thus increasing both patient anxiety and cost (Sosna et al. 2005).

17.3 MRI Colonography

The work-up for patients undergoing MRC is similar to that proposed for CTC. Nevertheless, some differences must be taken into account. As for any other MRI examination, patients should be screened for contraindications to the exam, such as severe claustrophobia, presence of cardiac pacemakers or metallic implants in critical regions (e.g. brain and spinal chord). The presence of hip prostheses, which normally is not regarded as a contraindication to MRI, may prevent a complete analysis of the rectum and sigmoid colon. Therefore, these patients should be considered for alternative tests such as CTC.

17.3.1 Diet and Bowel Preparation

Bowel preparation is necessary prior to MRC; bowel cleansing similar to CC can be used, as reported in Table 17.1, or "faecal tagging" can be an alternative. Tagging is obtained by adding a contrast agent (usually highly concentrated barium sulphate) to the diet in order to modify the signal intensity of the faecal material, adapting it to the signal properties of the rectal enema. By adopting this preparation the faecal material becomes "virtually invisible" (Lauenstein 2006). "Faecal tagging" eliminates the need for bowel cleansing and makes MRC more acceptable to patients (Elwood et al. 1995).

17.3.2 Spasmolytic Agents

The administration of spasmolytic agents (e.g. Buscopan® or Glucagon), which is controversial for CTC, has instead been proven of benefit for MRC: bowel spasms are limited and motion artefacts are significantly reduced (Luboldt et al. 2002).

17.3.3 Imaging Acquisition

Patients should be examined on a 1.5-T MR scanner equipped with strong gradient systems. In this way, data acquisition can be confined to one breath-hold. The examination itself is performed with the patient either in the prone or supine position. A combination of at least two surface coils should be used for signal reception to permit coverage of the entire colon. Two techniques, "bright lumen" and "dark lumen" MRC, have been proposed based on the types of signal within the colonic lumen. The latter is generally preferred, as it offers several advantages.

17.3.3.1 Bright Lumen

Bright lumen MRC, first described in 1997 (Luboldt et al. 1997), is based on the rectal administration of water mixed with paramagnetic contrast medium (Luboldt et al. 2000). Using the gadolinium enema with T1-weighted 3D gradient echo (GRE) sequences, the colonic lumen is rendered bright, whereas the colonic walls, as well as any disease arising from it, remain dark. Once the enema has reached the cecum, a 3D dataset of the abdomen encompassing the entire colon is collected. To allow for the presence of residual air exhibiting "filling defects" similar to polyps within the colonic lumen, the exam is performed both in the prone and supine position. The main limit of this technique is the differentiation between colorectal masses and residual faecal material, which can be difficult, and in some cases impossible.

17.3.3.2 Dark Lumen

In the "dark lumen" technique the colon is filled with 2,000–2,500 ml of warm tap water using hydrostatic pressure after placement of a rectal enema tube or a thin flexible catheter (Lauenstein et al. 2001; Ajaj et al. 2003; Schreyer et al. 2005; Scheibl et al. 2005). The filling process can be monitored by the acquisition of non-slice select sequences providing an update image every two to three seconds.

The acquisition is obtained either with T2-weighted fat suppressed single-shot sequences (e.g. HASTE) or with steady state precession sequences (TrueFISP, balanced fast field echo or FIESTA) in the axial and/or coronal plane. With these sequences the water-filled colonic lumen has a high intensity signal, whereas the colonic wall and lesions arising from it show up as dark filling defects (Fig. 17.8a). Subsequently, a T1-weighted 3D gradient-echo sequence is performed in the coronal plane both prior to and 75 seconds after intravenous administration of gadolinium (Fig. 17.8b,c) (Lauenstein 2006). The examination can be completed with a T1-weighted 2D FLASH sequence in the axial plane, which permits assessment of the adjacent abdominal organs with high image quality.

Dark lumen MRC provides considerable advantages over the bright lumen approach. First, patients do not have to be scanned in both the prone and supine position because residual air in the colon is hypointense on T1-weighted scans and therefore poses no differential diagnosis issues with respect to organic lesions that are also hyperintense. Second, direct analysis of the bowel wall enhancement and of parenchymal organs contained within the field of view is possible due to the intravenous administration of paramagnetic contrast material. Finally, the cost of the rectal enema, consisting only of tap water, is reduced.

17.3.4 Image Processing

Initially MRC should be read in the multiplanar reformation mode, scrolling through the contrast-enhanced 3D data set in all three orthogonal planes. Whenever a mass protruding from the colonic wall is detected, the identical part of the colon should be analysed on the pre-contrast scan. Increase in signal intensity within the mass can aid in differentiating between residual stool particles and colorectal lesions: while colorectal lesions always show strong enhancement, residual stools never show any contrast uptake (Fig. 17.8b,c).

Evaluation of the T2-weighted scans provides helpful information regarding inflammation processes;

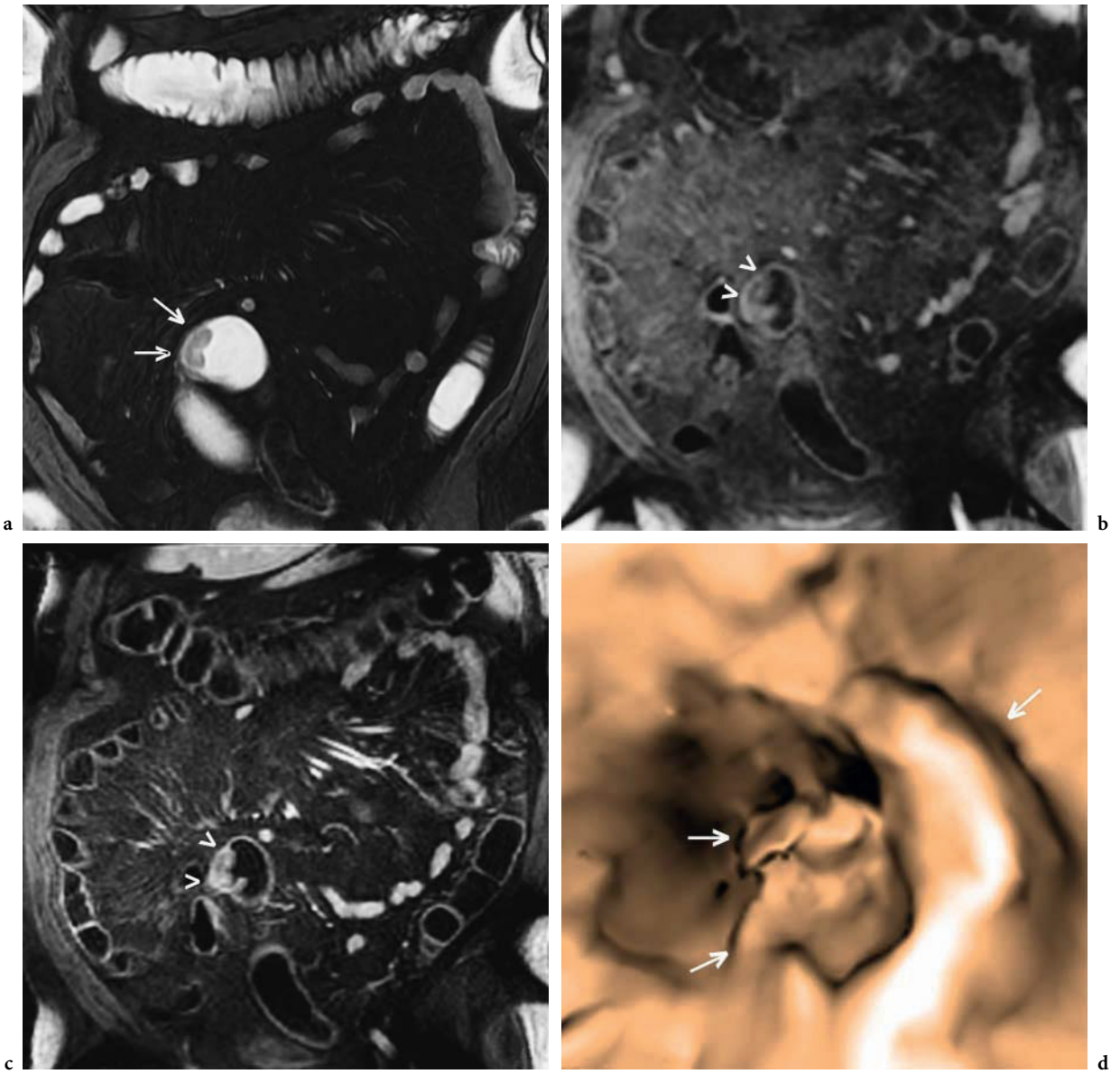

Fig. 18.8a–d. Fifty-five year old male with positive FOBT submitted to MRC after conventional bowel prep and water enema. **a** A single-shot fat suppressed breath-hold T2-weighted sequence on the coronal plain shows a 3 cm plaque-like hypointense lesion protruding within the bowel wall lumen at the sigmoid colon level (*arrows*). **b**,**c** The T1-weighted 3D gradient-echo coronal fat suppressed sequence performed both before and 75 seconds after intravenous administration of paramagnetic contrast material shows marked enhancement of the lesion, confirming its neoplastic nature (*arrow points*). **d** The 3D endoluminal view, obtained from processing of the gradient-echo sequence, allows visualisation of the vegetating component of the lesion (*arrows*). Histology on the biopsy performed during CC showed well-differentiated CRC

visceral oedema is clearly depicted on fat suppressed images while pericolic stranding is visible on non-suppressed images. Virtual endoscopic rendering, described in detail in section 17.2, can be applied to MRC (Fig. 17.8d) and may improve identification of small protruding lesions (Schoenenberger et al. 1997).

17.3.5 Indications and Results

The main indication to MRC is inflammatory bowel disease (IBD) (Koh et al. 2001; Ajaj et al. 2005; Schreyer et al. 2005; Rottgen et al. 2006). High contrast resolution, obtained by comparing T1-

weighted scans during intravenous administration of paramagnetic contrast material with pre-contrast scans, allows clear depiction of inflammatory changes.

Ajaj et al. correctly identified active IBD in 90% of colonic segments (Ajaj et al. 2005). Other studies have attempted to correlate the severity of inflammation on MRC with CC findings on a per segment basis, yielding sensitivity and specificity values ranging from 53–91% and 71–100% respectively (Koh et al. 2001; Schreyer et al. 2005; Rottgen et al. 2006). The main limitation of MRC seems to be in the identification of subtle inflammatory changes. This is probably due to the insufficient spatial resolution of the technique when inflammation is limited to the mucosal layer (Ajaj et al. 2005). In conclusion, CC remains the primary test for diagnosing IBD, as biopsies of the intestinal wall need to be performed in such cases. For its low invasiveness, MRC can be proposed as a way to monitor treatment.

Another indication for MRC is the early diagnosis of colorectal neoplasia. MRC is an appealing alternative to CTC due to its excellent soft tissue contrast and lack of ionising radiation exposure. The per-patient sensitivities and specificities are reported for most important clinical series in Table 17.4. These preliminary results show good specificity but a wide range of sensitivity, due at least in part to the technical differences between studies. While these results are encouraging, MRC still has several disadvantages, such as its limited spatial resolution, long acquisition times and susceptibility to motion artefacts, which still needs to be addressed before it can be proposed in a routine clinical setting or for secondary prevention.

MRC has also been used to assess diverticular disease. In a preliminary study performed by Schreyer et al., sigmoid diverticula were always correctly diagnosed at MRC (Schreyer et al. 2004). Similarly Ajaj et al. reported sensitivity and specificity values in detecting sigmoid diverticulitis of 86 and 92%, respectively (Ajaj et al. 2003). In this clinical setting MRC can also depict signs of extracolonic involvement (fistulae, conglomerate tumours and abscesses) thus representing a valid alternative to CTC.

17.4 Future Perspectives

The main challenge of colonography techniques relates to their potential use in mass screening programs. To increase its appeal, CTC, and in the long run possibly also MRC, will have to improve acceptance so that sufficiently high compliance rates can be reached. To do this it will be necessary to reduce the burden of preparation, using gentler schemes that do not require laxatives and which involve less preparation, with better-tasting oral contrast material for faecal and fluid tagging. The widespread use of CO_2 instead of air may reduce pain from colon distension, and low dose protocols should be implemented in order to reduce radiation hazards.

Further prospective multicentre studies with sufficient statistical power need to be performed to assess sensitivity and specificity in average risk or higher risk individuals before CTC can be proposed for screening, as no definitive information has yet

Table 17.4. Sensitivity and Specificity of MRC: Review of Major Clinical Series

Authors	N Pts	Inclusion criteria	Overall Per-patient SE (%)	Overall Per-patient SP (%)	Per-patient SE for lesions more than 10 mm (%)	Per-polyp SE for lesions more than 10 mm (%)
Luboldt et al. 2000	117	1	47	81	93	-
Lauenstein et al. 2002	24	1	91.7	100	-	-
Ajaj et al. 2003	120	1,3	84.6	100	-	-
Leung et al. 2004	156	1,2,3	86	97	40	28.6
Ajaj et al. 2004	55	1,3	88.9	100	-	-
Hartmann et al. 2005	92	1,2	89	96	100	100
Goehde et al. 2005	42	1,3	29.4	92	50	-

Inclusion criteria: 1, symptomatic patients; 2, asymptomatic patients with average risk for CRC; 3, asymptomatic patients with increased risk for CRC (family history, previous polypectomy, etc.); N, number; SE, sensitivity; SP, specificity

emerged from the available literature. If ongoing and new studies yield controversial or unsatisfactory CTC performances, then another possibility must be explored. Computer aided diagnosis (CAD) has recently been tested on a large series of patients from a screening population, giving sensitivity values similar to those of double check CC (Summers et al. 2005). This tool has also been evaluated as a second reader: adding polyps detected by CAD to those detected by the radiologist results in significantly higher sensitivity values compared to separate readings (Summers et al. 2002; Taylor et al. 2006). Therefore, interestingly, CAD apparently may recognise polyps not observed by the radiologist and vice-versa.

In the long run, if adequate mathematical algorithms are implemented for automatic segmentation, candidate selection and digital subtraction of tagged fluid, and if artificial neural networks will effectively improve training and near 100% sensitivity, CAD schedules could be proposed as first readers. In this way, the reading time may be reduced and perception errors – more likely to occur in screening populations due to the high rate of negative tests – may be avoided, thus increasing the cost-effectiveness of CTC and making it an attractive test for secondary prevention programs.

References

Ajaj W, Pelster G, Treichel U et al (2003) Dark lumen magnetic resonance colonography: comparison with conventional colonoscopy for the detection of colorectal pathology. Gut 52:1738–1743

Ajaj W, Lauenstein TC, Pelster G et al (2004) MR Colonography: how does air compare to water for colonic distension? J Magn Reson Imaging 19:216–221

Ajaj W, Lauenstein TC, Pelster G et al (2005) Magnetic resonance colonography for the detection of inflammatory disease of the large bowel: quantifying the inflammatory activity. Gut 54:257–263

Ajaj W, Ruehm SG, Lauenstein T et al (2005) Dark lumen magnetic resonance colonography in patients with suspected sigmoid diverticulitis: a feasibility study. Eur Radiol 15:2316–2322

Akerkar GA, Yee J, Hung R et al (2001) Patient experience and preferences toward colon cancer screening: a comparison of virtual colonoscopy and conventional colonoscopy. Gastrointest Endosc 54:310–315

Bielen D, Thomeer M, Vanbeckevoort D et al (2003) Dry preparation for virtual CT colonography with fecal tagging using water-soluble contrast medium: initial results. Eur Radiol 13:453–458

Bray F, Sankila R, Ferlay J et al (2002) Estimates of cancer incidence and mortality in Europe in 1995. Eur J Cancer 38:99–166

Bruzzi JF, Moss AC, Brennan DD et al (2003) Efficacy of IV Buscopan as a muscle relaxant in CT colonography. Eur Radiol 13:2264–70

Burling D, Halligan S, Slater A et al (2006a) Potentially serious adverse events at CT colonography in symptomatic patients: national survey of the United Kingdom. Radiology 239:464–471

Burling D, Taylor SA, Halligan S et al (2006b) Automated insufflation of carbon dioxide for MDCT colonography: distension and patient experience compared with manual insufflation. AJR Am J Roentgenol 186:96–103

Coady-Fariborzian L, Angel LP, Procaccino JA (2004) Perforated colon secondary to virtual colonoscopy: report of a case. Dis Colon Rectum 47:1247–1249

Cotton PB, Durkalski VL, Pineau BC et al (2004) Computed tomographic colonography (virtual colonoscopy): a multicenter comparison with standard colonoscopy for detection of colorectal neoplasia. JAMA 14; 291:1713–1719

Dachman AH, Kuniyoshi JK, Boyle CM et al (1998) CT colonography with three-dimensional problem solving for detection of colonic polyps. AJR Am J Roentgenol 171:989–995

Dafnis G, Ekbom A, Pahlman L et al (2001) Complications of diagnostic and therapeutic colonoscopy within a defined population in Sweden. Gastrointest Endosc 2001 54:302–309

de Zwart IM, Griffioen G, Shaw MP et al (2001) Barium enema and endoscopy for the detection of colorectal neoplasia: sensitivity, specificity, complications and its determinants. Clin Radiol 56:401–409

Dunn AS, Turpie AG (2003) Perioperative management of patients receiving oral anticoagulants: a systematic review. Arch Intern Med 28;163:901–908

Edwards JT, Wood CJ, Mendelson RM et al (2001) Extracolonic findings at virtual colonoscopy: implications for screening programs. Am J Gastroenterol 96:3009–3012

Ehrenpreis ED, Nogueras JJ, Botoman VA et al (1996) Serum electrolyte abnormalities secondary to Fleet's Phospho-Soda colonoscopy prep. A review of three cases. Surg Endosc 10:1022–1024

Elwood MJ, Ali G, Schlup MT et al (1995) Flexible sigmoidoscopy or colonoscopy for colorectal screening: a randomized trial of performance and acceptability. Cancer Detec Prev 19:337–347

Embleton KV, Nicholson DA, Hufton AP et al (2003) Optimization of scanning parameters for multi-slice CT colonography: experiments with synthetic and animal phantoms. Clin Radiol 58:955–963

Fass R, Do S, Hixson LJ (1993) Fatal hyperphosphatemia following Fleet Phospo-Soda in a patient with colonic ileus. Am J Gastroenterol 88:929–932

Fenlon HM, Nunes DP, Schroy PC 3rd et al (1999) A comparison of virtual and conventional colonoscopy for the detection of colorectal polyps. N Engl J Med 341:1496–1503

Fletcher JG, Johnson CD, Welch TJ et al (2000) Optimization of CT colonography technique: prospective trial in 180 patients. Radiology 216:704–711

Forbes GM, Mendelson RM (2000) Patient acceptance of virtual colonoscopy. Endoscopy 32:274–275

Ginnerup Pedersen B, Christiansen TE, Bjerregaard NC et al (2003a) Colonoscopy and multidetector-array computed-tomographic colonography: detection rates and feasibility. Endoscopy 35:736–742
Ginnerup Pedersen B, Rosenkilde M, Christiansen TE et al (2003b) Extracolonic findings at computed tomography colonography are a challenge. Gut 52:1744–1747
Gluecker TM, Johnson CD, Harmsen WS et al (2003a) Colorectal cancer screening with CT colonography, colonoscopy, and double contrast barium enema examination: prospective assessment of patient perceptions and preferences. Radiology 227:378–384
Gluecker TM, Johnson CD, Wilson LA et al (2003b) Extracolonic findings at CT colonography: evaluation of prevalence and cost in a screening population. Gastroenterology 124:911–916
Goehde SC, Descher E, Boekstegers A et al (2005) Dark lumen MR colonography based on fecal tagging for detection of colorectal masses: accuracy and patient acceptance. Abdom Imaging 30:576–583
Goei R, Nix M, Kessels AH et al (1995) Use of antispasmodic drugs in double contrast barium enema examination: glucagon or buscopan? Clin Radiol 50:553–557
Gollub MJ, Jhaveri S, Schwartz E et al (2005) CT colonography features of sigmoid diverticular disease. Clin Imaging 29:200–206
Hara AK, Johnson CD, MacCarty RL et al (2000) Incidental extracolonic findings at CT colonography. Radiology 215:353–357
Hara AK, Johnson CD, MacCarty RL et al (2001) Welch TJ, McCollough CH, Harmsen WS. CT colonography: single- versus multi-detector row imaging. Radiology 219:461–465
Hardcastle JD, Chamberlain JO, Robinson MH et al (1996) Randomised controlled trial of faecal-occult-blood screening for colorectal cancer. Lancet 348:1472–1477
Hartmann D, Bassler B, Schilling D et al (2005) Colorectal polyps: detection with dark-lumen MR colonography versus conventional colonoscopy. Radiology 238:143–149
Hellstrom M, Svensson MH, Lasson A (2004) Extracolonic and incidental findings on CT colonography (virtual colonoscopy) AJR 182:631–638
Iannaccone R, Laghi A, Catalano C et al (2004) Computed tomographic colonography without cathartic preparation for the detection of colorectal polyps. Gastroenterology 127:1300–1311
Ioannou GN, Chapko MK, Dominitz JA (2003) Predictors of colorectal cancer screening participation in the United States. Am J Gastroenterol 98:2082–2091
Jass JR (2002) Pathogenesis of colorectal cancer Surg Clin North Am 82:891–904
Johnson CD, Harmsen WS, Wilson LA et al (2003) Prospective blinded evaluation of computed tomographic colonography for screen detection of colorectal polyps. Gastroenterology 125:311–319
Kamar M, Portnoy O, Bar-Dayan A et al (2004) Actual colonic perforation in virtual colonoscopy: report of a case. Dis Colon Rectum 47:1490–1491
Koh DM, Miao Y, Chinn RJ et al (2001) MR imaging evaluation of the activity of Crohn's disease. AJR 177:1325–1332
Kolts BE, Lyles WE, Achem SR et al (1993) A comparison of the effectiveness and patient tolerance of oral sodium phosphate, castor oil, and standard electrolyte lavage for colonoscopy or sigmoidoscopy preparation. Am J Gastroenterol 88:1218–1223
Kronborg O, Fenger C, Olsen J et al (1996) Randomised study of screening for colorectal cancer with faecal-occult-blood test. Lancet 348:1467–1471
Laghi A, Iannacone R, Carbone I et al (2002) Detection of colorectal lesions with virtual computed tomographic colonography. Am J Surg 183:124–131
Laghi A, Iannaccone R, Mangiapane F (2003) Experimental colonic phantom for the evaluation of the optimal scanning technique for CT colonography using a multidetector spiral CT equipment. Eur Radiol 13:459–466
Lauenstein TC, Herborn CU, Vogt FM et al (2001) Dark lumen MR-colonography: initial experience. Rofo 173:785–789
Lauenstein TC, Goehde SC, Ruehm SG et al (2002) MR Colonography with barium-based fecal tagging: initial clinical experience. Radiology 223:248–254
Lauenstein TC (2006) MR colonography: current status. Eur Radiol 16:1519–1526
Lefere PA, Gryspeerdt SS, Dewyspelaere J et al (2002) Dietary fecal tagging as a cleansing method before CT colonography: initial results polyp detection and patient acceptance. Radiology 224:393–403
Lefere P, Gryspeerdt S, Baekelandt M et al (2003) Diverticular disease in CT colonography. Eur Radiol. 13 Suppl 4: L62–74
Lefere P, Gryspeerdt S, Marrannes J et al (2005) CT colonography after fecal tagging with a reduced cathartic cleansing and a reduced volume of barium. AJR Am J Roentgenol 184:1836–1842
Leung WK, Lam WW, Wu JC et al (2004) Magnetic resonance colonography in the detection of colonic neoplasm in high-risk and average-risk individuals. Am J Gastroenterol 99:102–108
Lieberman D, Weiss D, Bond W et al (2000) Use of colonoscopy to screen asymptomatic adults for colorectal cancer. N Eng J Med 343:162–168
Lieberman D, Weiss D et al (2001) One-time screening for colorectal cancer with combined fecal occult-blood testing and examination of the distal colon. N Eng J Med 345:555–560
Luboldt W, Bauerfeind P, Steiner P et al (1997) Preliminary assessment of three dimensional magnetic resonance imaging for various colonic disorders. Lancet 349:1288–1291
Luboldt W, Bauerfeind P, Wildermuth S et al (2000) Colonic masses: detection with MR colonography. Radiology 216:383–388
Luboldt W, Fletcher JG, Vogl TJ (2002) Colonography: current status, research directions and challenges: update 2002. Eur Radiol 12:502–524
Macari M, Milano A, Lavelle M et al (2000) Comparison of time-efficient CT colonography with two- and three-dimensional colonic evaluation for detecting colorectal polyps. AJR Am J Roentgenol 174:1543–1549
Macari M, Lavelle M, Pedrosa I et al (2001) Effect of different bowel preparations on residual fluid at CT colonography. Radiology 218:274–277
Macari M, Bini EJ, Xue X et al (2002) Colorectal neoplasms: prospective comparison of thin-section low-dose multidetector row CT colonography and conventional colonoscopy for detection. Radiology 224:383–392

Mandel JS, Bond JH, Chuech TR et al (1993) Reducing mortality from colorectal cancer by screening for fecal occult blood. Minnesota Colon Cancer Control Study. N Eng J Med 328:1365–1371

Mandel JS, Church TR, Ederer F et al (1999) Colorectal cancer mortality: effectiveness of biennial screening for fecal occult blood. J Natl Cancer Inst 91:434–437

Mandel JS, Church TR, Bond JH et al (2000) The effect of fecal occult-blood screening on the incidence of colorectal cancer. N Engl J Med 343:1603–1607

Morrin MM, Farrell RJ, Keogan Mt et al (2002) CT colonography: colonic distention improved by dual positioning but not intravenous glucagon. Eur Radiol 12:525–530

Newcomb PA, Norfleet RG, Storer BE et al (1992) Screening sigmoidoscopy and colorectal cancer mortality. J Nat Cancer Inst 84:1572–1575

Oliveira L, Wexner SD, Daniel N et al (1997) Mechanical bowel preparation for elective colorectal surgery. A prospective, randomized, surgeon-blinded trial comparing sodium phosphate and polyethylene glycol-based oral lavage solutions. Dis Colon Rectum 40:585–591

Pickhardt PJ, Choi JR, Hwang I et al (2003) Computer tomographic virtual colonoscopy to screen for colorectal neoplasia in asymptomatic adults. N Engl J Med 349:2191–2200

Pickhardt PJ, Choi JH (2003) Electronic cleansing and stool tagging in CT colonography: advantages and pitfalls with primary three-dimensional evaluation. AJR Am J Roentgenol 181:799–805

Pickhardt PJ, Taylor AJ (2006) Extracolonic findings identified in asymptomatic adults at screening CT colonography. AJR Am J Roentgenol 186:718–728

Pineau BC, Paskett ED, Chen GJ et al (2003) Virtual colonoscopy using oral contrast compared with colonoscopy for the detection of patients with colorectal polyps. Gastroenterology 125:304–310

Power NP, Pryor MD, Martin A et al (2002) Optimization of scanning parameters for CT colonography. Br J Radiol 75:401–408

Rajapaksa RC, Macari M, Bini EJ (2004) Prevalence and impact of extracolonic findings in patients undergoing CT colonography. Clin Gastroenterol 38:767–771

Rex DK, Vining D, Kopecky KK (1999) An initial experience with screening for colon polyps using spiral CT with and without CT colography (virtual colonoscopy) Gastrointest Endosc 50:309–313

Ristvedt SL, McFarland EG, Weinstock LB et al (2003) Patient preferences for CT colonography, conventional colonoscopy, and bowel preparation. Am J Gastroenterol 98:578–585

Rockey DC, Paulson E, Niedzwiecki D et al (2005) Analysis of air contrast barium enema, computed tomographic colonography, and colonoscopy: prospective comparison. Lancet 365:305–311

Rogalla P, Meiri N and Bartram CI (2000) Virtual Endoscopy of Colon. In Virtual Endoscopy and related 3D Techniques. Ed. P. Rogalla, J. Terwisscha van Scheltinga and B. Hamm

Rottgen R, Herzog H, Lopez-Haninnen E et al (2006) Bowel wall enhancement in magnetic resonance colonography for assessing activity in Crohn's disease. Clin Imaging 30:27–31

Scheibl K, Schreyer AG, Kullmann F et al (2005) Magnetic resonance imaging gastrography: evaluation of the dark lumen technique compared with conventional gastroscopy in patients with malignant gastric disease. Invest Radiol 40:164–172

Schoenenberger AW, Bauerfeind P, Krestin GP et al (1997) Virtual colonoscopy with magnetic resonance imaging: in vitro evaluation of a new concept. Gastroenterology 112:1863–1870

Schoenfled P, Cash B, Flood A et al (2005) Colonoscopy screening of average-risk women for colorectal neoplasia. N Eng J Med 352:2061–2068

Schreyer AG, Furst A, Agha A et al (2004) Magnetic resonance imaging based colonography for diagnosis and assessment of diverticulosis and diverticulitis. Int J Colorectal Dis 19:474–480

Schreyer AG, Goelder S, Scheibl K et al (2005a) Dark lumen magnetic resonance enteroclysis in combination with MRI colonography for whole bowel assessment in patients with Chron's disease: first clinical experience. Inflamm Bowel Dis 11:388–394

Schreyer AG, Rath HC, Kikinis R et al (2005b) Comparison of magnetic resonance imaging colonography with conventional colonoscopy for the assessment of intestinal inflammation in patients with inflammatory bowel disease: a feasibility study. Gut 54:250–256

Segnan N, Senore C, Andreoni B et al (2005) Randomized trial of different screening strategies for colorectal cancer: patient response and detection rate. J Nat Canc Inst 97:347–357

Selby JV, Friedman GD, Quesenberry CP Jr et al (1992) A case-control study of screening sigmoidoscopy and mortality from colorectal cancer. N Eng J Med 326:653–657

Shinners TJ, Pickhardt PJ, Taylor AJ et al (2006) Patient-controlled room air insufflation versus automated carbon dioxide delivery for CT colonography. AJR Am J Roentgenol 186:1491–1496

Smith RA, Cokkines W, Harmon JE (2004) American Cancer Society guidelines for Early detection of Cancer. CA Cancer J Clin 54:41–52

Sosna J, Krskal JB, Bar-Ziv J et al (2005) Extracolonic findings at CT colonography Abdom Imaging; 30:709–713

Sosna J, Blachar A, Amitai M et al (2006) Colonic perforation at CT colonography: assessment of risk in a multicenter large cohort. Radiology 239:457–463

Stryker SJ (1987) Natural history of untreated colonic polyps. Gastroenterology 93:1009–1013

Summers RM, Jerebko AK, Franaszek M et al (2002) Colonic polyps: complementary role of computer-aided detection in CT colonography. Radiology 225:391–399

Summers RM, Yao J, Pickhardt PJ et al (2005) Computed tomographic virtual colonoscopy computer-aided polyp detection in a screening population. Gatroenterology 129:1832–1844

Svensson MH, Svensson E, Lasson A et al (2002) Patient acceptance of CT colonography and conventional colonoscopy: prospective comparative study in patients with or suspected of having colorectal disease. Radiology 222:337–345

Taylor SA, Halligan S, Goh V et al (2003) Optimizing colonic distention for multi-detector row CT colonography: effect of hyoscine butylbromide and rectal balloon catheter. Radiology 229:99–108

Taylor SA, Halligan S, Burling D et al (2005) Intra-individual comparison of patient acceptability of multidetector-row

CT colonography and double-contrast barium enema. Clin Radiol 60:207–214
Taylor SA, Halligan S, Burling D et al (2006a) Computer-Assisted Reader Software Versus Expert Reviewers for Polyp Detection on CT Colonography. AJR Am J Roentgenol 186:696–702
Taylor SA, Halligan S, Slater A et al (2006b) Comparison of radiologists' confidence in excluding significant colorectal neoplasia with multidetector-row CT colonography compared with double contrast barium enema. Br J Radiol 79:208–215
Thomeer M, Bielen D, Vanbeckevoort D et al (2002) Patient acceptance for CT colonography: what is the real issue? Eur Radiol 12:1410–1415
Tran DQ, Rosen L, Kim R et al (2001) Actual colonoscopy: what are the risks of perforation? Am Surg 67:845–847
Van Gelder RE, Venema HW, Serlie IW et al (2002) CT colonography at different radiation dose levels: feasibility of dose reduction. Radiology 224:25–33
Van Gelder E, Birnie E, Florie J et al (2004a) CT colonography and colonoscopy: assessment of patient preference in a 5-week follow up study. Radiology 233:328–337
Van Gelder RE, Nio CY, Florie J et al (2004b) Computed tomographic colonography compared with colonoscopy in patients at increased risk for colorectal cancer. Gastroenterology 127:41–48
Van Gelder RE, Venema HW, Florie J et al (2004c) CT colonography: feasibility of substantial dose reduction - comparison of medium to very low doses in identical patients. Radiology 232:611–620
Vora P, Chapman A (2004) Complications from radiographer-performed double contrast barium enemas. Clin Radiol 59:364–368
Vukasin P, Weston LA, Beart RW (1997) Oral Fleet Phospho-Soda laxative-induced hyperphosphatemia and hypocalcemic tetany in an adult: report of a case. Dis Colon Rectum 40:497–499
Williams SM, Harned RK (1991) Recognition and prevention of barium enema complications. Curr Probl Diagn Radiol 20:123–151
Winawer SJ, Zauber AG, Gerdes H et al (1996) Prevention of colorectal cancer by colonoscopic polypectomy. N Eng J Med 329:1997–1981
Winawer SJ, Stewart ET, Zauber AG et al (2000) A comparison of colonoscopy and double-contrast barium enema for surveillance after polypectomy. National Polyp Study Work Group. N Engl J Med 15; 342:1766–1772
Winawer SJ, Fletcher RH, Rex D et al (2003) Colorectal screening and surveillance: clinical guidelines rationale-update based on new evidence Gastroenterology 124:544–560
Yee J, Hung RK, Akerkar GA et al (1999) The usefulness of glucagon hydrochloride for colonic distention in CT colonography. AJR Am J Roentgenol 173:169–172
Yee J, Akerkar GA, Hung RK et al (2001) Colorectal neoplasia: performance characteristics of CT colonography for detection in 300 patients. Radiology 219:685–692
Yee J, Kumar NN, Hung RK et al (2003) Comparison of supine and prone scanning separately and in combination at CT colonography. Radiology 226:653–661
Young BM, Fletcher JG, Earnest F et al (2006) Colonic perforation at CT colonography in a patient without known colonic disease. AJR Am J Roentgenol 186:119–121
Zalis ME, Barish MA, Choi JR, Working Group on Virtual Colonoscopy (2005a) CT colonography reporting and data system: a consensus proposal. Radiology 236:3–9
Zalis ME, Perumpillichira JJ, Kim JY et al (2005b) Polyp size at CT colonography after electronic subtraction cleansing in an anthropomorphic colon phantom. Radiology 236:118–124

Techniques of Virtual Dissection of the Colon Based on Spiral CT Data

18

Erich Sorantin, Emese Balogh, Anna Vilanova i Bartrolí, Kálmán Palágyi, László G. Nyúl, Franz Lindbichler, and Andrea Ruppert

CONTENTS

18.1 Introduction and Medical Background

Colorectal cancer represents the third most commonly diagnosed cancer and is the second leading cause of cancer deaths in the United States (Gazelle et al. 2000). In addition, colorectal cancer is responsible for about 11% of all new cancer cases per year (Gazelle et al. 2000). Five-year prognosis is about 90% for patients with localized disease compared to 60% if there is a regional spread and a drop to 10% in patients with distant metastasis (Gazelle et al. 2000). In the field of medicine there is a widely accepted opinion that most colorectal cancers arise from pre-existent adenomatous polyps (Johnson 2000). Therefore, different societies, such as the American Cancer Society, have proposed screening for colorectal cancer (Byers et al. 1997; Winawer et al. 1997). Today, different options exist for detection of colorectal cancer, including digital rectal examination, fecal occult blood testing, flexible and rigid sigmoidoscopy, barium enema and its variants, colonoscopy and recently computed tomography or magnetic resonance-based virtual colonography (Gazelle et al. 2000). All have inherent advantages and disadvantages. Colonoscopy is regarded as the gold standard for colonic investigations, but unfortunately it can only be completed in about 85–95% of patients. But with colonoscopy only the retrograde viewing direction is possible, thus making detection of small polyps on the aboral side of colonic folds difficult. In addition, the anatomic distribution of colorectal cancer has changed over the years. In the 1940s cancer of the rectum and sigmoid colon accounted for 65–80% of all colorectal cancers, compared to 52–61% within the last 30 years. Consecutively, the number of cancers in the proximal colon has increased, which is possibly related to the increasing number of cholecystectomies (Gazelle et al. 2000).

If screening for colorectal cancer is considered, the chosen investigation should allow assess to the whole colon in all patients, and the whole colonic surface should be possible to inspect. Cross-sectional imaging modalities like helical computed tomography or magnetic resonance tomography, together with appropriate image post-processing, could represent a perfect screening tool, fulfilling all the above-mentioned conditions. In 1994 Vining and Gelfand reported their experience of apply-

E. Sorantin, MD; F. Lindbichler, MD; A. Ruppert, MD
Department of Radiology, University Hospital Graz, Auenbruggerplatz 34, 8036 Graz, Austria
E. Balogh, MS; K. Palágyi, PhD; L. G. Nyúl, PhD
Department of Applied Informatics, University of Szeged, Árpád tér 2, 6720 Szeged, Hungary
A. Vilanova i Bartrolí, PhD
Institute of Computer Graphics and Algorithms, Vienna University of Technology, Karlsplatz 13/186/2, 1040 Vienna, Austria

ing methods of virtual reality to helical computed tomography in order to produce endoluminal views similar to colonoscopy (Johnson 2000). Today, CT colonography refers to a helical computed tomography investigation, where the colon is fully prepared and distended by room air or carbon dioxide (Johnson 2000). Afterwards, offline post-processing of the axial computed tomography is done by generating 2D and 3D reconstructions, including virtual endoluminal views of the colonic surface (Johnson 2000). To overcome the problem of missed polyps on the oral side of the colonic folds, ante and retrograde views are generated (Lefere et al. 2006; Pickhardt et al. 2006). Alias names like virtual colonoscopy, virtual endoscopy, 3D endoscopy and CT colonography have been abandoned in favor of CT colonography or MR colonography (Johnson 1998).

Since the generation of all these views is a time-consuming task, new and faster image processing algorithms, as well as alternative display techniques like virtual pathology, Mercator map projection and panoramic projections, were developed and are under evaluation (Johnson 2000). Today it is not clear which type of 3D reconstruction is preferable (Pickhardt 2003; Burling et al. 2006; Rottgen et al. 2005).

The technical background and image reconstruction for another display technique called virtual dissection will be described within this chapter. Using this technique the colonic surface will be automatically extracted from CT data, stretched, then flattened. Example images, derived from both an artificial phantom and a cadaverous one, will be shown. All image reconstructions were computed from multirow detector computed tomography (MRDCT) data. The individual steps are described in the following section. Two different image processing approaches will be presented, as well as the preliminary results and conclusions.

18.2 Methods

18.2.1 Workflow

Different steps have to be undertaken to obtain a virtual dissection of the colon. After MRDCT scanning, the reconstructed, overlapping slices were transferred by the hospitals network to graphical laboratory computers. At the segmentation step (Sect. 18.2.2.1) the interesting structure within the abdomen, e.g., the colon, was defined. The following skeletonization (Sect. 18.2.2.2) enabled the extraction of the colonic central path. Using the central path, two different approaches were used to perform a virtual dissection: 2D flattening (Sect. 18.2.2.3) and a 3D local flattening approach (Sect. 18.2.2.4). A workflow schema can be seen in Figure 18.1.

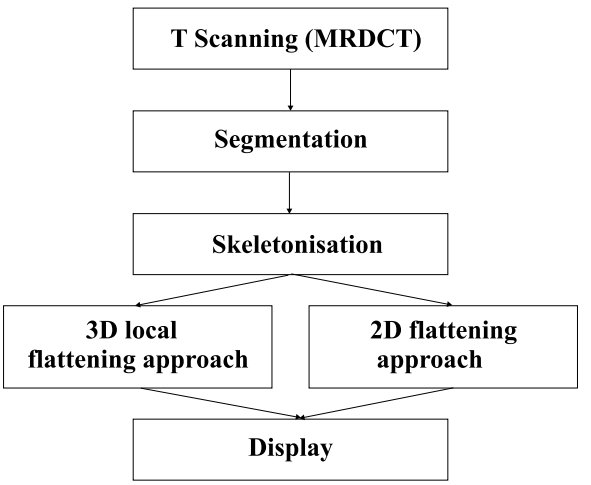

Fig. 18.1. Workflow scheme

18.2.2 Image Processing

18.2.2.1 Segmentation – Fuzzy Connectedness

A vast amount of literature exists on image segmentation techniques. Many different approaches were investigated for segmenting images of different body regions from different imaging modalities. Their accuracy and reproducibility in some applications is not satisfactory or may not even be known. These are, however, very important factors that need to be taken into account when devising a method for actual practical use.

After some quick experiments with "simple" techniques (a 3D generalization of region growing and manual drawing augmented by splines) it was found that, although the object of the study (i.e. the colon) is clearly defined in the CT images, the results produced by these techniques were not well reproducible and the processes were inefficient (regarding

the amount of the necessary human interaction and the way human input is required). Since this is the very first step in the post-processing operation line of our project, everything depends on the segmentation results. Therefore, a validated, accurate and highly reproducible method should be used to avoid problems later in the process. This is what made us decide to utilize the segmentation method using fuzzy connectedness (Udupa and Samarasekera 1996; Udupa et al. 1994).

Images are inherently fuzzy. Their inhomogeneity is partially due to the graded composition of the material being imaged and to the imaging process itself (e.g. blurring, partial volume effects). Fuzzy connectedness captures this fuzziness, as well as the spatial coherence of the voxels in a well-defined manner. It has a mathematically formulated theory proving its robustness. This framework and the algorithms have now been successfully applied extensively on thousands of 3D volumes in several routine clinical applications (Udupa et al. 2000).

The fuzzy connectedness method has a proven to have a high rate of reproducibility and is very efficient regarding user intervention and computational requirements. In our case (i.e. segmenting the colon from a 3D CT image volume) air has a well-defined range of Hounsfield units, so the parameters for fuzzy affinities required by the method may be set once and then used for all studies without per-study training. The user specifies the rectangular volume of interest (VOI) using a GUI, as well as one (or a few, if necessary) "seed points" within the colon for seeding the fuzzy connected objects. The VOI operation is to reduce the data volume to be processed by the fuzzy connectedness method, as well as to exclude unwanted regions from the processing volume that would otherwise make several additional post-processing steps necessary. The seed points are specified by clicking on voxels "deep" inside the colon in order to avoid the uncertain regions near the boundary. Generally, a single seed point is sufficient; however, several points may be specified if necessary.

Fuzzy connectedness is a very robust segmentation technique that effectively handles inhomogeneity (coming from both tissue properties and the imaging procedure). It is also robust against the selection of seed points (if boundaries are avoided). Since the only user input (apart from the VOI selection) is the seed specification, and all other parameters are fixed, our segmentation inherits the reproducibility and efficiency of the fuzzy connectedness method.

Since an absolute fuzzy connectedness is used and a single object is segmented, the uncertain boundary regions (due to partial volume effects) are not captured by the fuzzy objects; therefore, the segmentation was too tight (uniformly along the entire object) according to the physician's opinion. A 3D dilation using a $3 \times 3 \times 3$ structuring element is applied to the segmented fuzzy connected object, thus making it better fit the observer's expectations. Finally, the segmented binary 3D volume is transformed into cubic voxels by linear interpolation because some of the successive steps (e.g. skeletonization) require isotropic data.

18.2.2.2 Skeletonization

The notion of skeletonization was introduced by Blum (1964) as a region-based shape feature/descriptor that summarizes the general form of objects/shapes. An illustrative definition of the skeleton is given using the prairie-fire analogy: the object boundary is set on fire and the skeleton is formed by the loci where the fire fronts meet and quench each other. This definition can be naturally extended to any dimension.

During the last two decades, skeletonization (i.e. extracting skeleton from digital binary images) has become a challenging research field. Three major skeletonization techniques have been proposed: the distance transform method, the method based on Voronoi diagrams and the iterative object reduction method, also called "thinning".

Thinning is preferred, since it is fairly fast and capable of producing a good approximation to the skeleton in a topology-preserving way (Kong and Rosenfeld 1989). It is based on digital simulation of the fire front propagation: border points (i.e. 1's that are adjacent to 0's) of a binary object that satisfy certain topological and geometrical constraints are deleted in iteration steps. The entire process is repeated until only the "skeleton" is left. In 3D, there are two major types of thinning: surface thinning produces the medial surface of an object (by preserving surface end-points) while curve thinning can extract the medial lines of an object (by preserving line end-points) (Palágyi and Kuba 1999). It is easy to see that the skeleton of a 3D object may contain surface patches; therefore, surface thinning produces a better approximation to the skeleton than curve thinning does. Despite this, in cases of "near tubular" 3D objects (e.g. airway, blood vessel

and gastro-intestinal tract) medial lines provide more reasonable shape features.

An already published sequential 3D thinning algorithm (Palágyi et al. 2001) is applied to extract the medial lines from the segmented colon.

18.2.2.3 2D Flattening Approach

As a first approach for colonic virtual dissection, a transformation of the problem from 3D to 2D was done in the following way. After obtaining the central path by skeletonization (as described in Sect. 18.2.2.2) the 3D cross-sectional profile orthogonal to the central path was calculated. Care is taken to sample enough cross-sections along the central path; in our experience 1.0 mm is sufficient. Because of the structure of the colon, nearby cross-sections may conflict and, as a result, polyps may be missed or counted multiple times. Wang et al. tried to solve this problem by using electrical field lines generated by a locally charged path (Wang et al. 1999; Wang et al. 1998). To avoid this conflict, the angle between two inter-sectioning cross-sectionals was interpolated and recalculated iteratively until the no intersection occurred. Then, the segmented colon was remapped into a new gray-level 3D data volume. Data at every degree of the cross-section were put into a new 3D volume (constant angle sampling).

The result is a virtually stretched and flattened colon. Figure 18.2a shows an orthogonal cross-section of the colon before flattening, and Figure 18.2b shows the same cross-section after flattening. The flattening process is also illustrated in the figures. The obtained 3D data volume contains the virtually stretched and flattened colon. For visualization of the colonic surface after stretching and flattening, both volume and surface rendering techniques were implemented.

18.2.2.4 3D Local Flattening Approach

The method presented in this section (Vilanova Bartolí et al. 2001) does not generate a flat model of the whole colon, but allows the inspection of locally flattened regions in such a way that double counting of polyps does not occur.

The presented method involves moving a camera along the central path of the colon. The central path is calculated using a thinning algorithm. Afterwards, the path is approximated by a B-spline curve.

For each camera position, a small cylinder tangent to the path is defined. The middle point of the cylinder axis corresponds to the camera position. Rays starting at the cylinder axis and orthogonal to the cylinder surface are traced (see Fig. 18.3). For each ray, direct volume rendering compositing is used to calculate the color that corresponds to the cylinder point where the ray was projected. Finally, the colored cylinder with the sampled rays is mapped onto a 2D image by simply unfolding the cylinder. The cylinder axis must be short enough that it does not penetrate the surface of the colon. This can be done by taking the distance of the path to the organ surface into account.

The result is a video where each frame shows the projection of a small part of the inner surface of the organ onto the cylinder. If the camera is moved slowly enough the coherence between frames will be high and the observer will be able to follow the movement of the surface.

In the presented method, possible double sampling of polyps emerges between frames. However, it does not cause a double counting of polyps because the human brain is able to track the polyp movement due to the coherence between frames. Moving along the central path in such a high curvature area, a polyp might move up and down (due to

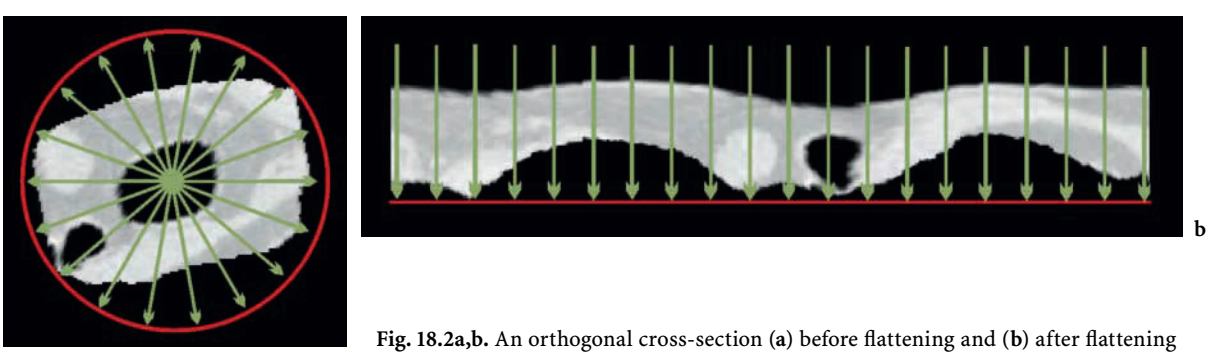

a b

Fig. 18.2a,b. An orthogonal cross-section (**a**) before flattening and (**b**) after flattening

double sampling) but is clearly identified as a single object.

The proposed projection is illustrated in Figure 18.3. A cylinder $C(h, \alpha)$ is defined for each camera position. This cylinder is colored by tracing rays orthogonal to the cylinder surface (i.e., projecting a region of the surface onto the cylinder). Then the cylinder is mapped to the final image $I(u, v)$ by a simple mapping function $f: (h, \alpha) \rightarrow (u, v)$.

18.2.2.4.1 Constant Angle Sampling

The sampling distance (i.e., the distance between two consecutive rays) in the h-direction is constant, and it must be at most half of the size of a voxel (see Fig. 18.3). In this way the Nyquist frequency in the h-direction is preserved.

For each h-value the rays are traced in radial directions with respect to the cylinder axis. The rays are diverging from each other, so the volume data is not sampled uniformly if the incremental angle is constant. Furthermore, features can be missed.

18.2.2.4.2 Perimeter Sampling

Perimeter sampling represents another way to sample the surface uniformly. In this method, a constant sample length (l) is defined. l must be half the size (at most) of a voxel in order to maintain the Nyquist frequency and therefore to not miss any important feature. l should have the same value as the sampling distance in the h-direction to preserve the ratio, or proportion, in the final mapping.

The algorithm incrementally calculates the ray directions that are in the plane defined by a certain value of h. The angle between the current ray and the next one is computed such that the length of the surface sample that the current ray represents equals l in the α-direction. The first ray is traced along an arbitrary angle, α_0, which must be the same for all camera positions. r_i is defined as the distance from the cylinder axis to the surface point hit by the ray. The surface sample length in the α-direction that a ray represents is approximated by the arc with radius r_i.

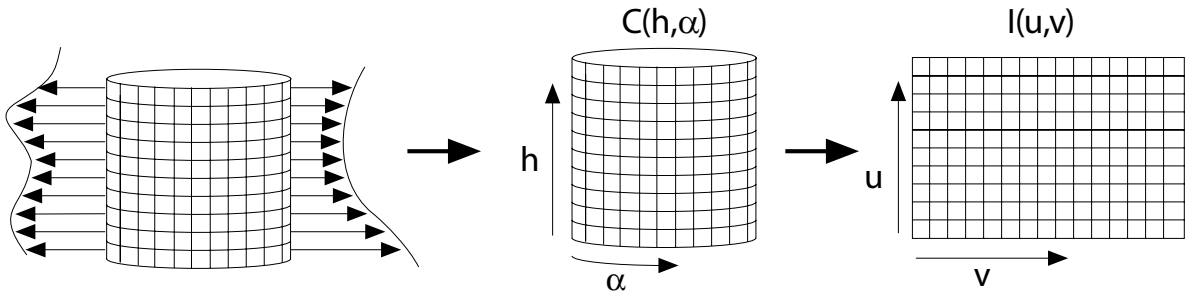

Fig. 18.3. The projection procedure. A region of the surface is projected to the cylinder $C(h, \alpha)$. Then the cylinder is mapped to the image $I(u, v)$

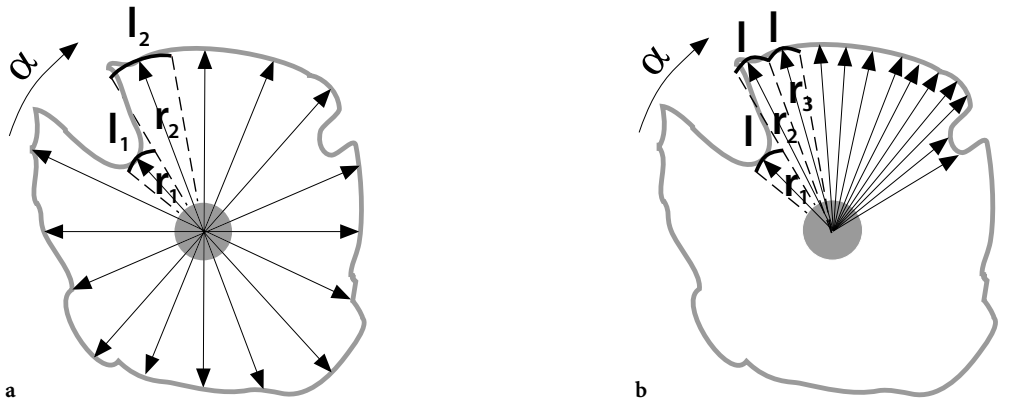

Fig. 18.4. a Constant angle sampling. Different surface lengths are represented by the same length in the cylinder. **b** Perimeter sampling: same length but different angle

Therefore, the value of the angle increment for the next ray is estimated as l/r_i radians.

In this case, the mapping function maps the contours and also the surface of the generalized cylinder uniformly. Moving along the central path, contours of varying length are represented by varying numbers of rays. This results in the fact that in the v-direction (horizontal scanlines) typically only part of the pixels are covered by an unfolded contour in the mapping to the image plane. The projected points that correspond to the rays at angle α_0 are positioned on a vertical line in the center of the image. Then, from left to right the ray values are mapped to the image until the perimeter length is reached.

This projection has the area preservation property, i.e. the relative sizes of surface elements are preserved in the image plane and do not depend on the proximity of the cylinder axis to the surface. On the other hand, a distortion is introduced with respect to the h and α-direction, so the angles are not preserved anymore. There is no distortion at the vertical center line of the image, but the distortion increases progressively when moved to the left and right.

18.2.2.4.3 Image Enhancement

Using the distance of the hit surface point to the cylinder axis r_i, a depth image can be generated. This depth image, together with the shaded image, represents a height field, similar to a landscape in topography. A good way to visualize landscapes in topographical maps is by showing level lines, where each line corresponds to a level of depth. The level lines improve the perception of depth and surface changes of the map. The level lines are also drawn as an enhancement of the shaded flattened image. They are generated based on the technique described by Saito and Takahashi (1990).

18.2.3 Phantoms

To test the algorithm, both an artificial and cadaverous phantom were created. Each phantom was scanned using a multirow detector CT (GE Lightspeed QXI, GE Medical Systems). A collimation of 2.5 mm and a high quality pitch were selected. Scans were reconstructed using the manufacturer's standard reconstruction program with a slice thickness of 1.25 mm, an increment of 0.5 mm and a matrix of 512 × 512. Thus, the resulting in-plane pixel size was 0.585 mm.

18.2.3.1 Artificial Phantom

An artificial phantom was created by putting small plasticine beads into a plastic tube. In that way, six polyps were created. A photograph of one of the ends of the tube is shown in Figure 18.5.

18.2.3.2 Cadaverous Phantom

The second phantom consisted of a 50 cm-long part of a normal, cadaverous colon. The bowel was cleansed and 13 artificial polyps were created using fat tissue. After room air inflation, the specimen was placed in a 5-l water bath containing 5 ml Gastrografin® (Schering, Austria) solution. In this way the attenuation of the human abdomen was simulated. A photograph of the phantom can be seen in Figure 18.6. After CT scanning, a real dissection was performed and compared visually to the computed virtual dissection. Moreover, the real size of the polyps were measured using a sliding calliper. Details can be found in Table 18.1.

Fig. 18.5a,b. Parts of the tube phantom with inbedded plasticine beads

Fig. 18.6. Photograph of the cadaverous phantom

Table 18.1. Real size of created polyps

Polyp number	Size (mm)
1	8.6 × 5.5
2	3.9 × 5.0
3	3.5 × 2.5
4	5.7 × 7.0
5	4.6 × 3.8
6	6.01 × 7.7
7	2.6 × 2.6
8	3.4 × 3.4
9	5.8 × 4.1
10	8.6 × 5.2
11	11.8 × 9.0
12	6.9 × 4.9
13	11.2 × 7.5

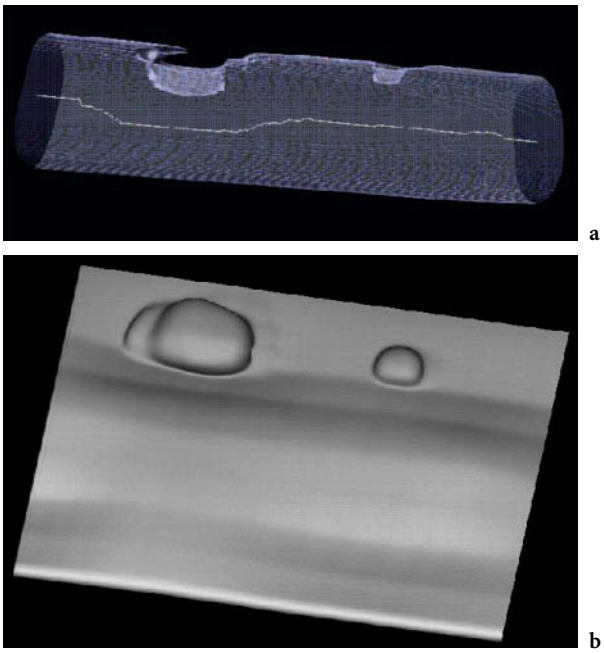

Fig. 18.7. a Transparent 3D model with the cental path. **b** The inner surface after virtual dissection using the 2D flattening approach

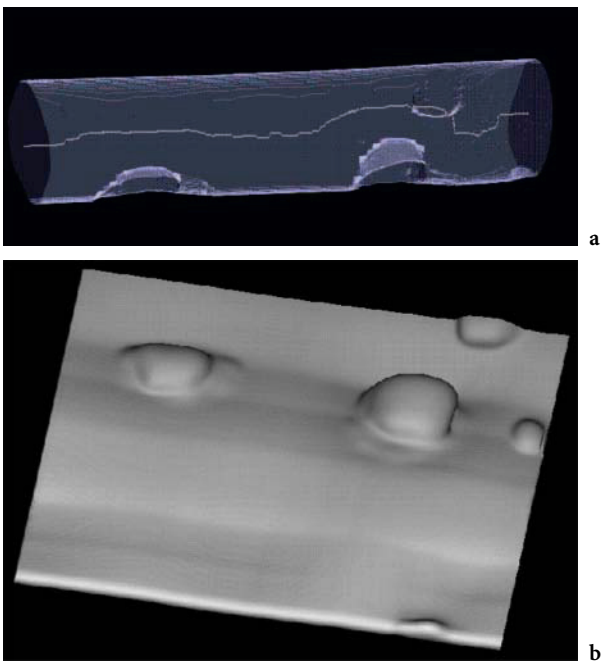

Fig. 18.8a,b. The other end of the artificial phantom. **a** Transparent 3D model with the cental path. **b** The inner surface after virtual dissection using the 2D flattening approach

18.3 Results

18.3.1 Artificial Phantom

The artificial phantom contains six simulated polyps placed in the two ends of the plastic tube. The result after segmentation with its central path is shown in Figure 18.7a. Figure 18.7b depicts the computed virtual dissection using the 2D flattening approach. The two polyps can be clearly seen. The other parts of the phantom is presented in a similar way. The four polyps are placed in this end of the tube can be seen clearly on the reconstructions (see Figs. 18.5b

and 18.8). All the polyps can be clearly detected on the images after virtual dissection (see Figs. 18.7b and 18.8b). The polyps appeared on virtual dissection as bumps.

18.3.2 Cadaverous Phantom

In the case of cadaverous phantoms, a total of 13 artificial polyps were created using fat tissues. Figure 18.9a exhibits the surface-rendered 3D reconstruction of the segmented colon, and Figure 18.9b presents the same binary object with its central path as a transparent 3D model. In Figure 18.10 the appearance of the created polyps on axial and virtual endoscopic views can be seen.

After scanning, a real dissection of the colon was performed, and the polyps were marked with small *white arrows* (see Fig. 18.11). Figure 18.12 presents the inner surface of the cadaverous colon after virtual dissection is performed using the 2D flattening approach. Figure 18.13 shows a frame obtained by the 3D local flattening approach using the two presented sampling techniques. An example of image enhancements achieved by the level lines method is shown in Figure 18.14.

With both techniques – the 2D flattening approach and the 3D local flattening approach – all 13 artificially created polyps appeared as folds or bumps and could be identified by visual inspection. In our preliminary experience on surface-rendered views the polyps could be seen more easily. The time

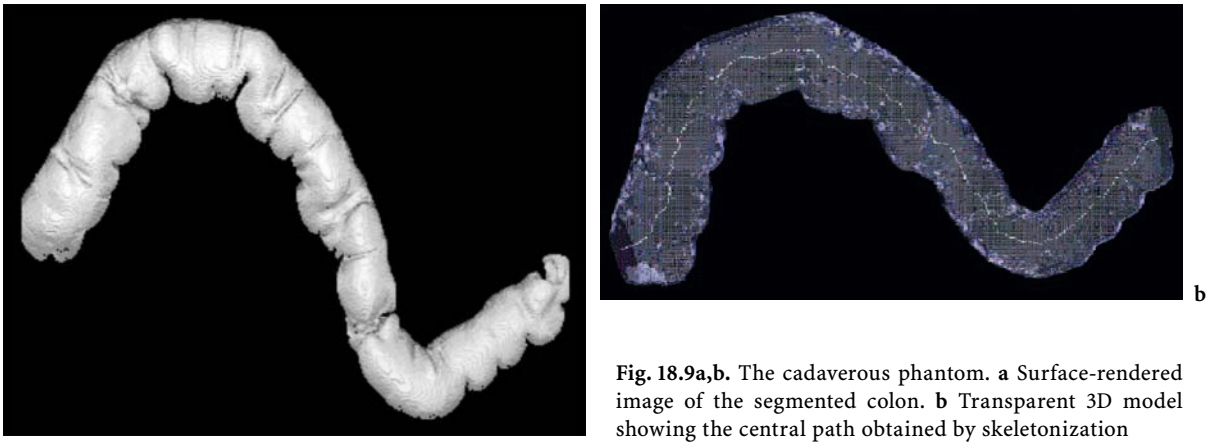

Fig. 18.9a,b. The cadaverous phantom. **a** Surface-rendered image of the segmented colon. **b** Transparent 3D model showing the central path obtained by skeletonization

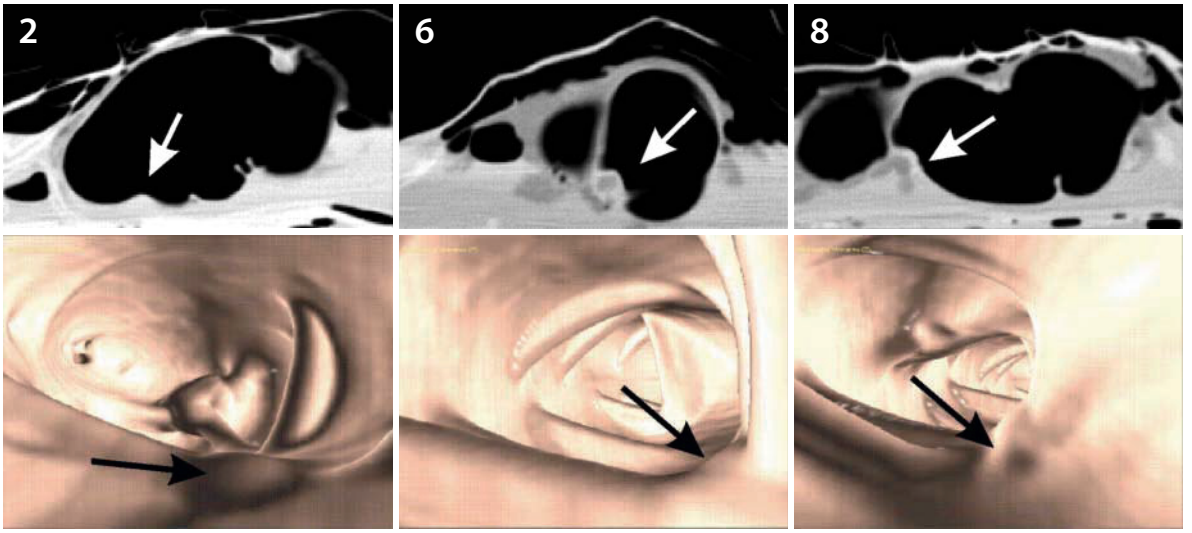

Fig. 18.10. Three representative polyps shown on axial CT scans (*upper row*) and the same polyps presented on virtual endoscopic views (*lower row*)

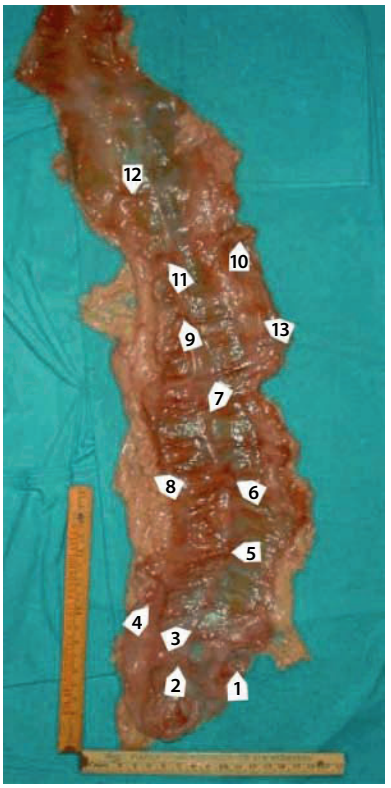

Fig. 18.11. Dissection of the cadaverous colon phantom

Fig. 18.12. Virtual dissection of the cadaverous colon phantom using the 2D flattening approach

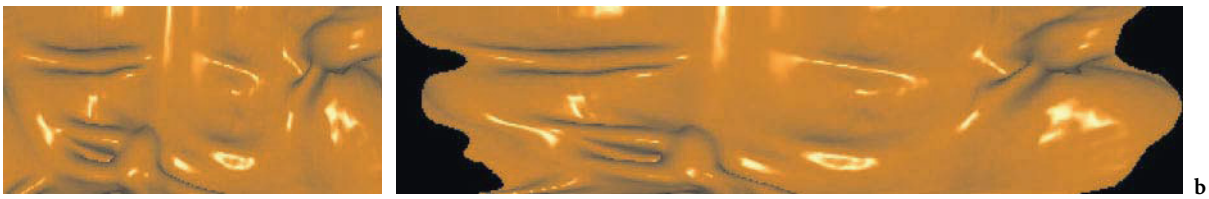

a b

Fig. 18.13a,b. A frame derived from the 3D local flattening approach: **a** Resulting image of the projection technique using constant angle sampling. **b** Same camera position as **a**, but with a perimeter sampling

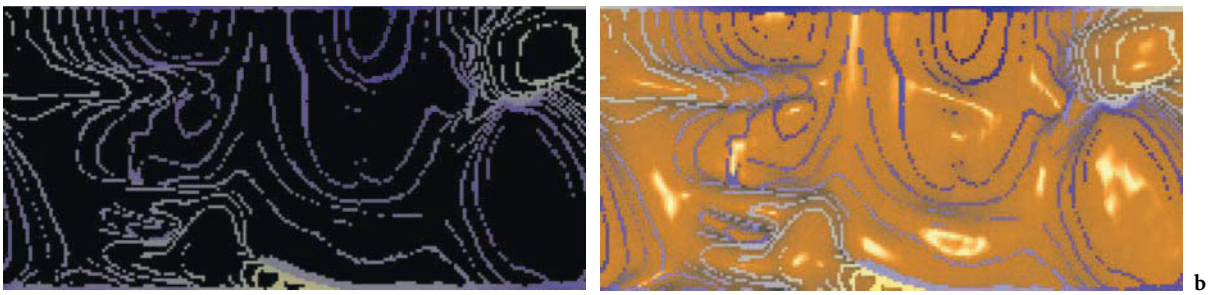

a b

Fig. 18.14a,b. Image enhancement for the 3D local flattening approach. **a** Level lines with color codes indicating the depth. **b** Combination of the level lines and shaded image

needed for generation of the virtual dissection views was 10 min. for the operator and about 2 h of offline computing for the workstation.

In addition, an application has been developed for the 3D local flattening approach as presented in Section 18.2.2.4. The result of the method is a video where each frame corresponds to a flattened area of the colon. The application allows the physician to easily associate the frames of the video with its corresponding region in the original volume data. The application consists of different visualization techniques shown in separated windows whose interaction is connected to one another.

One window shows the consecutive flattened frames of the video. The current camera position corresponds with the frame shown at the moment. An overview

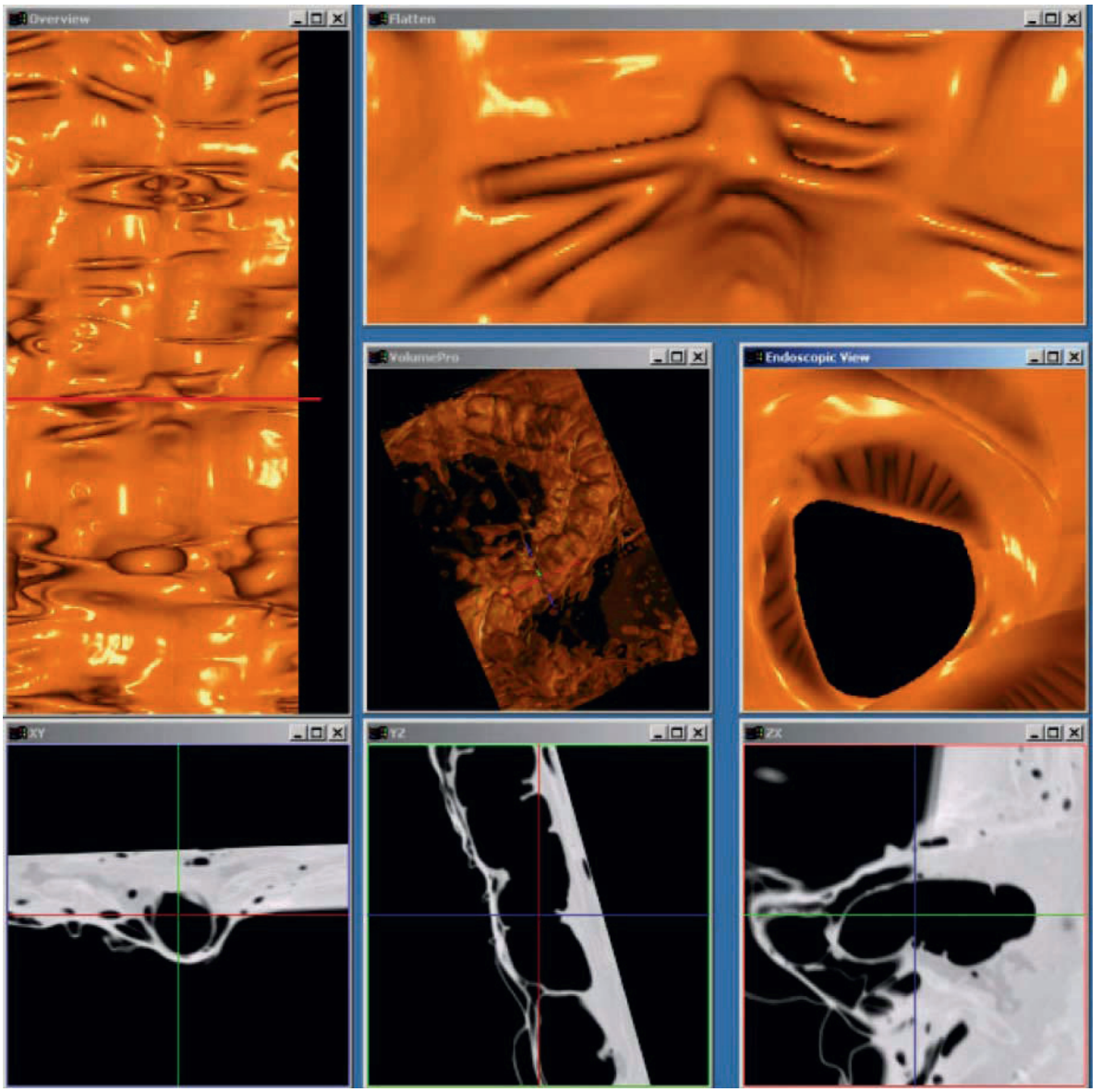

Fig. 18.15. Interactive application for evaluation of virtual dissection using the 3D local flattening approach. Seven different windows are shown on the computer screen: left upper corner: virtual dissection of the colon using the 3D local flattening approach (constant angle sampling). The *red vertical line* depicts the position of the virtual camera, which is used for anatomic cross-referencing on the ohter views. Upper right corner: magnified view from the left. Middle row, center: view from above. Middle row, right: virtual endoscopic view. Lower row: axial CT slice and multiplanar reconstructions (coronal, sagittal) at the position of the virtual camera. Whenever the position of the virtual camera is moved upwards or downwards with the cursor keys, all windows are updated automatically

image is generated using the horizontal center lines of each frame. In the overview image, the current camera position is indicated by highlighting its corresponding horizontal center line. The overview image is incorrect since the cross-sections that correspond to each line intersect each other, but the image gives enough context information to orient the user. Furthermore, there are three windows that show the three orthogonal planes corresponding to the three coordinate planes of the current camera frame. These planes are generated using multiplanar reconstruction.

A window showing a common perspective view of the data set is also present. This window is updated with the current camera frame each time the frame changes. If the user clicks in an area of the flattened frame, the perspective camera view is updated. The camera of the perspective view points to the same area that has been clicked in the flattened frame.

The relationship between windows and different visualization techniques provides an applicable tool for inspection of the data set. An example screenshot can be seen in Figure 18.15.

18.4 Preliminary Medical Evaluation

On the virtual dissection view, three experienced radiologists rated the 13 polyps of the cadaverous phantom. Altogether three polyps were missed – details can be found in Table 18.2. All missed polyps exhibited a size of less than or equal to 5.0 mm, and can be regarded as clinically insignificant. All raters agreed on 11 polyps (10 correctly identified, 1 false negative polyp), thus indicating an interobserver agreement of 84.6%.

Table 18.2. Size of missed polyps

Rater	Polyp number	Size (mm)
I	3	3.5 × 2.5
I	8	3.4 × 3.4
II	2	3.9 × 5.0
II	8	3.4 × 3.4
III	8	3.4 × 3.4

18.5 Conclusion

In both fiber-optic colonoscopy and CT colonography, polyps behind colonic folds may be not seen at standard oral views due to the structure of the colon. Further endoscopic views visualize only a small part of the inner colonic surface. The technique of virtual dissection avoids these problems and presents the colonic surface in the same manner as on the pathologist's table. Theoretically, due to the view from „above", all polyps should be displayed – and not hidden by the colonic folds.

Navigation through the colon in oral and aboral is a time-consuming and labor-intensive task. The presented two methods for obtaining a virtual dissection are mainly automated. Basic operator interaction is only needed for starting the segmentation procedure. In case of unwanted side branches of the central path, produced by the skeletonization procedure, a further editing step is necessary. This can be done quickly by using a point-and-click technique on a 3D reconstruction of the object, the central path and the unwanted side branches. All other steps are automated and need no operator interaction. A total time of about 2 h, with an operator attendance of minutes, seems acceptable. Therefore, virtual dissection seems to be a promising display technique for CT colonography, especially if a mass screening for polyp detection is considered. Up to now it cannot be decided if the 2D flattening approach or the 3D local flattening approach will be the better choice for clinical routine. This has to be worked out in future prospective clinical trials. In our preliminary evaluation there was a reasonable interobserver agreement that the missed polyps can be regarded as having no clinical significance.

An inherited disadvantage of virtual dissection is the deformation introduced by the individual steps of image processing. Therefore, high-resolution source images are important, thus making it necessary to use MRDCT. A slice thickness of 1.0–1.5 mm at an overlap of 0.5–1.0 mm seems appropriate. A higher slice thickness will result in less resolution, higher deformation and therefore less image quality.

References

Blum H (1964) A transformation for extracting new descriptors of shape. In Proc. Symposiun on Models for the perception of Speech and Visual Form, pages 362–380

Burling D, Halligan S, Taylor S, Brennand DJ, Altman DG, Bassett P, Atkin W, Bartram CI (2006) Polyp measurement using CT colonography: agreement with colonoscopy and effect of viewing conditions on interobserver and intraobserver agreement. AJR Am J Roentgenol 186:1597–604

Byers T, Levin B, Rothenberger D et al (1997) American cancer society guidelines for screening and surveillance for early detection of colorectal polyps and cancer: update 1997. Cancer J Clin 47:154–160

Gazelle G, McPhanon P, Schol F (2000) Screening for colorectal cancer. Radiology 215:327–335

Johnson C (1998) Virtual endoscopy: what's in a name? Am J Roentgenol 171:1201–1202

Johnson C (2000) Ct colonography: The next colon screening examination? Radiology 216:331–341

Kong T, Rosenfeld A (1989) Digital topology: Introduction and survey. Computer Vision, Graphics, and Image Processing 48:357–393

Lefere P, Gryspeerdt S, Schotte K (2006) Virtual colonoscopy–an overview. Onkologie 29(6):281–286

Palágyi K, Kuba A (1999) A parallel 3D 12–subiteration thinning algorithm. Graphical Models and Image Processing 61:199–221

Palágyi K, Sorantin E, Balogh E, Kuba A, Halmai C, Erdohelyi B, Hausegger K (2001). A sequential 3D thinning algorithm and its medical applications. In Proc. 17th Int. Conf. Information Processing in Medical imaging, IPMI 2001, Lecture Notes in Computer Sciences, Springer

Pickhardt PJ (2003) Three-dimensional endoluminal CT colonography (virtual colonoscopy): comparison of three commercially available systems. AJR Am J Roentgenol 181:1599–1606

Pickhardt PJ, Taylor AJ, Gopal DV (2006) Surface visualization at 3D endoluminal CT colonography: degree of coverage and implications for polyp detection. Gastroenterology 130:1582–1587

Rottgen R, Fischbach F, Plotkin M, Lorenz M, Freund T, Schroder RJ, Felix RR (2005) CT colonography using different reconstruction modi. Clin Imaging 29:195–199

Saito T, Takahashi T (1990) Comprehensible rendering of 3-D shapes. In SIGGRAPH'90 Conference Proceedings, Annual Conference Series, p. 197–206

Udupa JK, Grossman RI, Nyúl LG, Ge Y, Wei L (2000) Multiprotocol MR image segmentation in multiple sclerosis: Experience with over 1000 studies. In SPIE Proceedings, vol. 3979, p. 1017–1027

Udupa JK, Odhner D, Samarasekera S, Goncalves RJ, Iyer K, Venugopal K, Furuie S (1994) 3DVIEWNIX: An open, transportable, multidimensional, multimodality, multiparametric imaging software system. In SPIE Proceedings, vol. 2164, p. 58–73

Udupa JK, Samarasekera S (1996) Fuzzy connectedness and object definition: Theory, algorithms, and applications in image segmentation. Graphical Models and Image Processing, 58:246–261

Vilanova Bartrolí A, Wegenkittl R, König A, Gröller E, Sorantin E (2001) Virtual colon flattening. In VisSym '01 Joint Eurographics – IEEE TCVG Symposium on Visualization, p. 127–136

Wang G, Dave SB, Brown BP, Zhang Z, McFarland EG, Haller JW (1999) Colon unraveling based on electrical field: Recent progress and further work. In Proceedings SPIE, vol. 3660, p. 125–132

Wang G, McFarland EG, Brown BP, Vanier MW (1998) GI tract unraveling with curved cross-sections. IEEE Transaction on Medical Imaging 17:318–322

Winawer S, Fletcher R, Miller L (1997) Colorectal cancer screening: clinical guidelines and rationale. Gastroenterology 112:594–642

Unfolded Cube Projection of the Colon

19

Ayso H. de Vries, Frans M. Vos, Iwo W. O. Serlie, and Jaap Stoker

CONTENTS

19.1 Introduction

In the evaluation of computed tomography (CT) colonography examinations generally two different approaches exist:

In a primary two-dimensional (2D) approach, axial helical CT images are used for the detection of colorectal polyps or colorectal cancer. If these images are not conclusive at a certain location, either multiplanar reformatted (MPR) images (coronal, sagittal or oblique) or 3D rendered images can be used for problem solving (i.e. differentiating between abnormalities and normal anatomy).

Alternatively, in a primary three-dimensional (3D) approach 3D rendered images are primarily used for the detection of abnormalities. A complementary 2D method is then used for problem solving.

A. H. de Vries, MD; J. Stoker, MD, PhD, Professor
Department of Radiology, Academic Medical Center, University of Amsterdam, Meibergdreef 9, 1105 AZ Amsterdam, The Netherlands
F. M. Vos, MSc, PhD; I. W. O. Serlie, MSc
Quantitative Imaging Group, Faculty of Applied Sciences, Delft University of Technology, Lorentzweg 1, 2628 CJ, Delft, The Netherlands

Thus, Although 2D images and 3D images are complementary, one method of display is generally used for primary investigation of the CT data while the other method is used for problem solving. In a primary 2D approach, 3D images serve to differentiate polyps from complex folds. On the other hand, in a primary 3D approach 2D images are used to evaluate colonic surface submerged by fecal fluid or residue or to assess the density or heterogeneity of a suspected lesion. This information can be used to differentiate polyps from fecal material.

A significant difference in accuracy between the two principles of reviewing has not been demonstrated yet. In comparative studies of primary 2D and various different 3D review methods, significant differences in detection of polyps have not been demonstrated (McFarland et al. 2001; Hoppe et al. 2004; van Gelder et al. 2006; Johnson et al. 2007; Kim et al. 2007).

Though, several multicenter studies that used substantial numbers of patients in comparing CT colonography to colonoscopy (Pickhardt et al. 2003; Cotton et al. 2004; Rockey et al. 2005) have reported controversial results. These controversial results have led to speculations about their cause: the bowel preparation (with or without oral contrast), the scanning parameters (5 mm vs. thinner), the role of the experience of the reviewer, the review method (primary 2D or primary 3D), etc. It is striking, though, that the comparative study that reported the highest sensitivity had used a primary 3D review approach (Pickhardt et al. 2003), whereas two studies with the lower sensitivity used a primary 2D review method.

In a systematic review of 33 comparative CT colonography studies Mulhall et al. mentioned the mode of reviewing as an explanation for the varying results between the studies (Mulhall et al. 2005) as well. The per-patient sensitivity was higher in studies that used a primary 3D display mode compared to those that used a primary 2D display mode. This explanation must be interpreted with caution, though, since it was based on the data of only two primary 3D studies (Pickhardt et al. 2003; Yee et al. 2001).

19.2 Advantages and Disadvantages of a 3D Approach

The potential advantage of a 3D review method is most likely based on the more intuitive presentation of the colonic surface (Fig. 19.1) and the longer exposure time of polyps to the observer (Lee and Pickhardt 2004).

The more intuitive 3D presentation of the colon wall and lesions facilitates the communication of the CT colonography findings to a clinician or a patient.

The longer exposure time of abnormalities may result in less perceptive errors made by the reviewer. Lee and Pickhardt compared the exposure time of 20 polyps in both an axial 2D method and a conventional endoluminal 3D method. They concluded that the opportunity of polyp detection, including both exposure time and distance of polyp visualization, is significantly greater for the 3D endoluminal display.

Apart from these advantages, the conventional primary 3D display has two important drawbacks.

The first drawback is its inability to display areas behind haustral folds (discussed below). The second drawback is its time-consuming nature (Macari et al. 2000; McFarland et al. 2001). This is caused by the fact that a single fly-through often does not cover the complete surface of the colon. Therefore a time-consuming two-directional fly-through is requisite. In addition, in contrast to a primary 2D method, a 3D rendered image cannot display submerged parts of colonic wall. Therefore an additional 2D assessment of submerged parts of the colon may be needed.

The inability to display areas behind folds is caused by the limited viewing angle of the virtual camera during a fly-through. Although hypotonic agents and adequate distension are known to decrease the problem (Rogalla et al. 2005), haustral folds may still occlude the colonic wall and thereby reduce sensitivity (Fig. 19.2). In order to cover as much colonic surface as possible, evaluation in both antegrade and retrograde direction is mandatory. A two-directional fly-through reduces these unseen colonic areas by approximately 20% (Paik et al. 2000, Vos et al. 2003). However, substantial parts of the colonic wall that potentially harbor polyps remain unseen. Interactive evaluation can overcome this problem at the expense of an additional, and often substantial, increase in reading time.

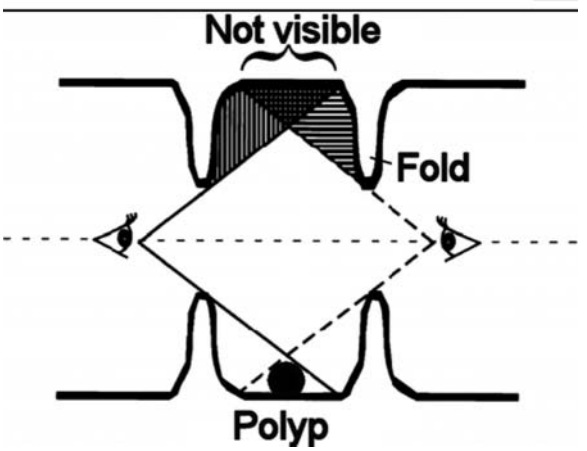

Fig. 19.2. Areas in black are areas that are missed when using a conventional 3D method

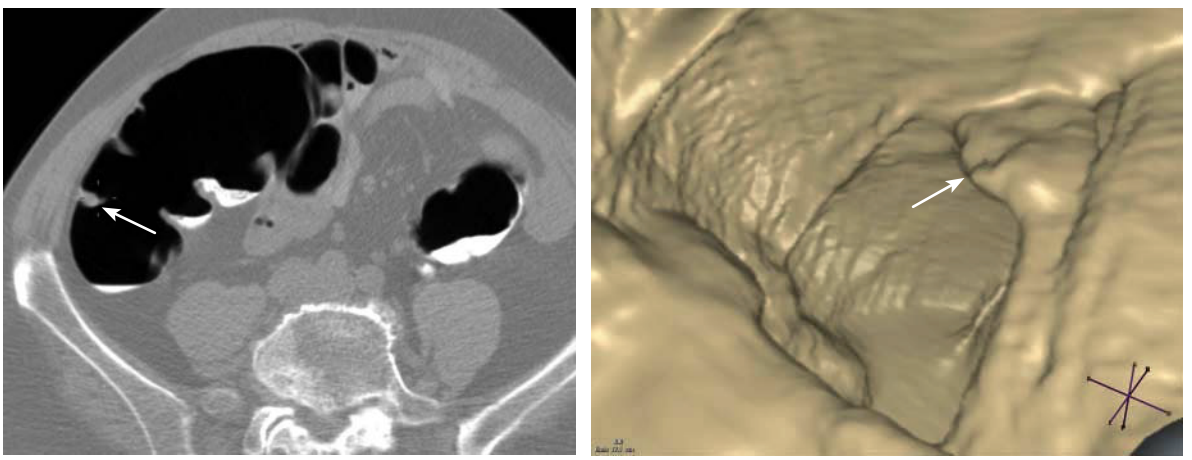

a **b**

Fig. 19.1a,b. Polyp (*white arrow*) that was initially missed in a primary 2D review method (**a**), but which can easily be seen in a 3D setting (**b**)

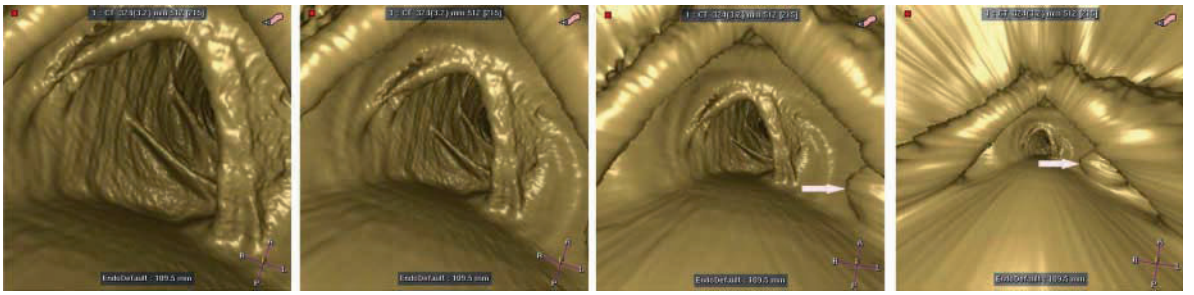

Fig. 19.3. The respective images are made with a viewing angle of 60°, 90°, 120° and 160°. The increase of colonic surface is illustrated by a polyp behind a fold (*arrow*) that can only be detected from this direction with endoluminal views of 120° and 160°, and would otherwise be missed

To overcome the problem of unseen areas, various alternatives have been suggested. An obvious solution would be to increase the viewing angle of the virtual camera. A major drawback is the resulting distortion, especially at the edges, which limits the use of large viewing angles (Fig. 19.3).

Another solution to the problem of unseen areas is a computer tool that identifies and displays the areas that were not visualized during two-directional fly-through. These areas can be indicated by color on an overview image. For practical purposes, the areas can be presented in descending order of size.

So a ideal 3D display mode shows the complete colonic surface without image distortion (so polyps can be recognized as such) in a time efficient way. A techniques that satisfy these three requirements has a less "colonoscopy"-like representation than the conventional 3D fly-through: the unfolded cube display.

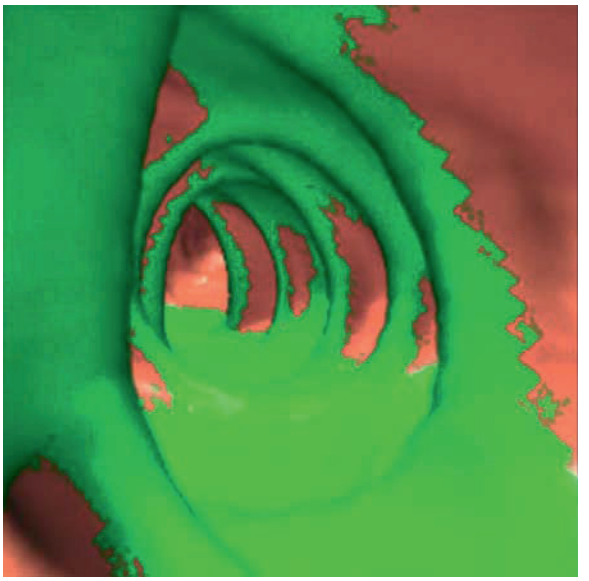

Fig. 19.4. Endoluminal view showing uninvestigated areas (indicated *pink*) that were not previously viewed during conventional fly-through

19.3 The Principle of the Unfolded Cube Display

In an endoluminal 3D display method, cine loop images are generated for both prone and supine position. The images are generated by means of sampling volume-rendered images with a certain interval along a predefined track through the colon (i.e. central path). The principle of volume rendering comes down to placing a virtual camera in the CT volume and making voxels below a pre-determined threshold translucent (air) and those above the threshold opaque (soft tissue). By successively displaying the volume rendered images the illusion of fly-through is realized.

Several automated methods for the generation of a central path through the colon are available (Franaszek et al. 2006; Truyen et al. 2000). This central path is not only a prerequisite for the conventional 3D method but for the 3D unfolded cube display method and the method of 3D virtual dissection as well. Due to the use of the central path therer is no need to manually navigate the virtual camera.

By placing virtual cubes on the central path of the colon with a predetermined interval, the unfolded cubes display method generates a cine view. On each cube face a 90° view of the rendered colonic surface is projected (Fig. 19.5). By folding out the six images onto a single plane (unfolded cube display), a 360° field of view is rendered. As a consequence

the reader may not only observe the colonic surface in antegrade and retrograde direction, but also on the lateral sides.

The unfolded cube display method is commercially available (ViewForum, Philips Medical Systems, Best, The Netherlands). The user interface of this workstation is illustrated in Figure 19.6. In this primary 3D method the unfolded cube display is combined with an axial and MPR 2D display mode for problem solving.

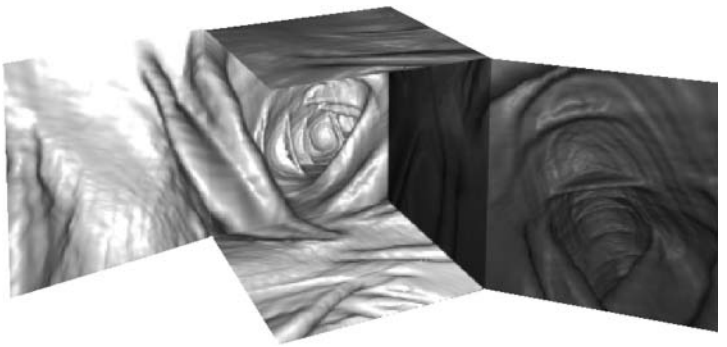

Fig. 19.5. The principle of the unfolded cube display is shown by unfolding the faces of the cube. On each of the six faces a 90° viewing angle from the center of the cube is projected

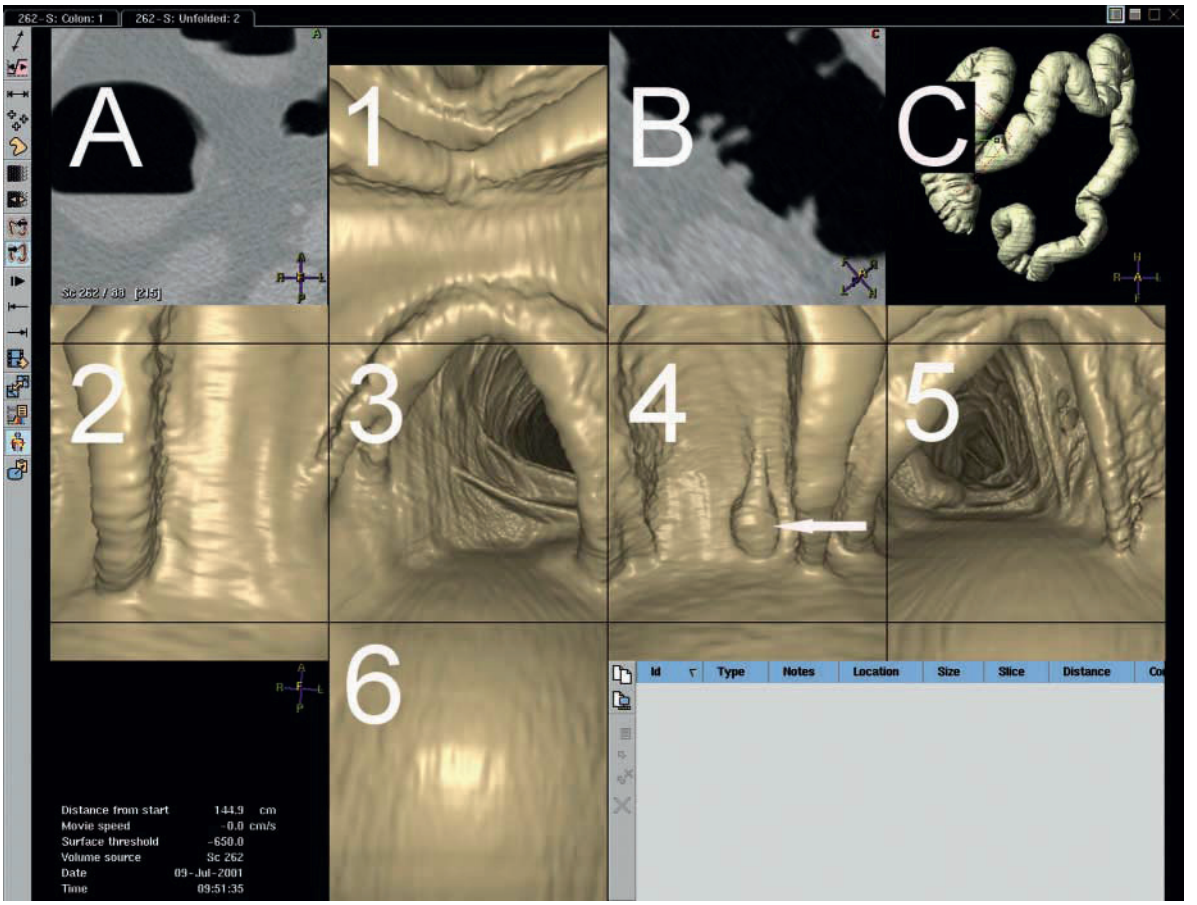

Fig. 19.6. Unfolded cube user interface in supine position showing the sessile adenomatous polyp (*white arrow*) that is displayed in Figure 19.2. In contrast to the (60° and 90°) conventional 3D display mode, the polyp is well detectable. Faces 2 and 4 represent a 90° view on the lateral sides of the colon; face 1 represents the top side and face 6 the bottom side. In face 3 the frontal direction of view is displayed, and in face 5 the backward direction of view is displayed

19.4 Evaluation of the Unfolded Cube Display

In a study conducted by Vos et al. (2003) the unfolded cube display method was compared to a conventional 3D (two-directional) review approach. Two blinded trained observers reviewed a selected population of 30 patients twice, with a median interval of more than 11 weeks between the reviews. The observers first used the unfolded cube display method for polyp detection, and then, in random order, the conventional 3D method. The viewing angle in the conventional review method was set to 120° to compromise between image distortion and surface visibility. Surface visibility, evaluation time per patient, as well as sensitivity and specificity, were compared between both approach.

Findings in the study showed that the unfolded cube display method depicted an extra 5% of the colonic surface compared to the conventional 3D method (99.5% vs. 93.8%). Note that for the unfolded cube display a single fly-through was required in contrast to the conventional 3D method, which required both an ante- and retrograde fly-through. When a single fly-through was performed in the conventional 3D method, only 73% of the colonic surface was depicted on average. It is self-evident that when colonic surface is not depicted it can hamper sensitivity of CT colonography.

Based on the recorded evaluation times, Vos et al. concluded that CT colonography with the unfolded cube display mode enables time-efficient inspection; the average evaluation time per patient was nearly 20 minutes vs. approximately 35 minutes with a (two-directional) conventional 3D display method. This review time is slightly longer than the primary 2D review time in other studies. (Macari et al. 2000; Neri et al. 2006)

The time-consuming nature of conventional 3D CT colonography can be explained by the fact that both an ante- and retrograde fly-through is required. Second, image distortion near the edge of the conventional 3D display (Fig. 19.3) often requires interactive adjustment for closer observation of these areas.

Sensitivity on a per patient basis for medium and large polyps was not significantly different between the two methods for each observer. Note that the probability that a polyp resides in an invisible area is only 6.2% with a conventional 3D display because 93.8% of the surface area is visible (the probability is 0.5% with the unfolded cube display). Consequently, a much larger population is needed to demonstrate a significant difference in sensitivity. Although a significant difference in accuracy was not demonstrated, the sample size sufficed to demonstrate significant differences in time efficiency and surface visibility.

The unfolded cube display method was also used in a cohort study of 249 patients of increased risk for colorectal cancer (Van Gelder et al. 2004). Using the unfolded cube display method, 84% of patients with polyps larger than 10 mm were correctly identified, the specificity was 92%. These results are in the same range as the findings of the aforementioned large multicenter screening study that also used a primary 3D evaluation.

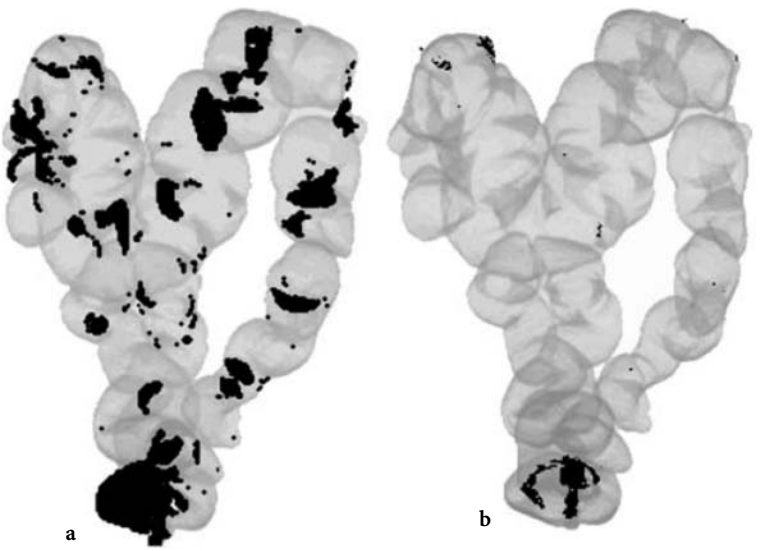

Fig. 19.7. a Unvisualized areas (*black*) of the conventional 3D display. **b** Unvisualized areas of the unfolded cube display. This image shows a substantial reduction of missed areas with the unfolded cube display

19.5 Virtual Dissection

Like the unfolded cube display, the virtual dissection method has been developed to display the colonic surface in a time-efficient way. All versions have in common that the entire lumen of the colon is opened and straightened along the longitudinal axis. An example is depicted in Figure 19.8. The potential advantages of this method include the easy overview over a substantial part of the colonic surface and complete visualization of the entire mucosal surface. In theory, this may lead to decreased interpretation time and high accuracy. A drawback of the method is that straightening of a curved structure like the colon results in distortion of the colonic surface, especially at locations where the colon is strongly curved (such as the flexures). Compared to the unfolded cube display, the forward and backward viewing directions are omitted. Consequently, the frontal site and back site of structures may not be as well visualized as they would be with the unfolded cube display method. This problem can be reduced by the possibility of changing the perspective from perpendicular to the colonic wall, to a more oblique view on the colonic surface.

To our knowledge, no comparative studies of the unfolded cube display method and the virtual dissection method have been performed. However, in two recent comparative studies 3D virtual dissection was compared to a primary 2D method (Kim et al. 2007; Johnson et al 2007). In both studies a similar accuracy was reported for the detection of polyps, though the review time was significantly reduced; both studies reported approximately14 minutes for primary 2D evaluation and about 10 minutes for 3D virtual dissection.

19.6 Conclusion

The unfolded cube display is an alternative 3D method for evaluating CT colonography data. The method is more time-efficient and yields better surface visibility than a conventional 3D technique. The unfolded cube display is not hampered by distortion at flexures or decreased visualization of folds, as is the case with the virtual dissection method. Further studies should evaluate the role of the unfolded cube display.

References

Cotton PB, Durkalski VL, Benoit PC, Palesch YY, Mauldin PD, Hoffman B et al (2004) Computed tomographic colonography (virtual colonoscopy) – A multicenter comparison with standard colonoscopy for detection of colorectal neoplasia. JAMA 291:1713–1719

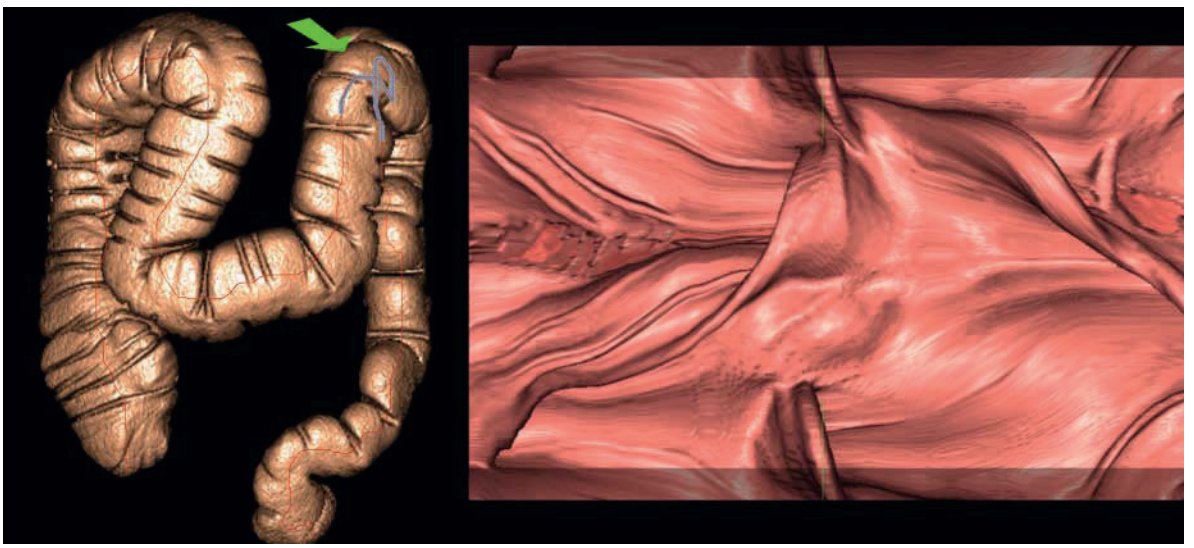

Fig. 19.8. Virtual dissection method displaying the splenic flexure. Although a large surface can be inspected at a glance, distortions (especially in curved segments) are present

Franaszek M, Summers RM, Pickhardt PJ, Choi JR (2006) Hybrid segmentation of colon filled with air and opacified fluid for CT colonography. IEEE Trans Med Imaging 25:358–368

Hoppe H, Quattropani C, Spreng A, Mattich J, Netzer P, Dinkel HP (2004) Virtual colon dissection with CT colonography compared with axial interpretation and conventional colonoscopy: preliminary results. AJR Am J Roentgenol 182:1151–1158

Johnson CD, Fletcher JG, MacCarty RL, Mandrekar JN, Harmsen WS, Limburg PJ et al (2007) Effect of slice thickness and primary 2D versus 3D virtual dissection on colorectal lesion detection at CT colonography in 452 asymptomatic adults.AJR Am J Roentgenol. 189:672–80

Kim SH, Lee JM, Eun HW, Lee MW, Han JK, Lee JY et al (2007) Two- versus three-dimensional colon evaluation with recently developed virtual dissection software for CT colonography. Radiology 244:852–64

Lee A, Pickhardt P (2004) Polyp visualization at CT colonography: comparison of 2D axial and 3D endoluminal displays. Proc 90th Scientific Assembly and Annual Meeting of the Radiological Society of North America, Chicago

Macari M, Milano A, Lavelle M, Berman P, Megibow AJ (2000) Comparison of time-efficient CT colonography with two- and three-dimensional colonic evaluation for detecting colorectal polyps. AJR Am J Roentgenol 174:1543–1549

McFarland EG, Brink JA, Pilgram TK, Heiken JP, Balfe DM, Hirselj DA et al (2001) Spiral CT colonography: Reader agreement and diagnostic performance with two- and three-dimensional image-display techniques. Radiology 218:375–383

Mulhall BP, Veerappan GR, Jackson JL (2005) Meta-analysis: computed tomographic colonography. Ann Intern Med 142:635–650

Neri E, Vannozzi F, Vagli P, Bardine A, Bartolozzi C (2006) Time efficiency of CT colonography: 2D vs 3D visualization. Computerized Medical Imaging and Graphics 30:175–180

Paik DS, Beaulieu CF, Jeffrey RB, Karadi CA, Napel S (2000) Visualization modes for CT colonography using cylindrical and planar map projections. J Comput Assist Tomogr 24:179–188

Pickhardt PJ, Choi JR, Hwang I, Butler JA, Puckett ML, Hildebrandt HA et al (2003) Computed tomographic virtual colonoscopy to screen for colorectal neoplasia in asymptomatic adults. N Engl J Med 349:2191–2200

Rockey DC, Poulson E, Niedzwiecki D, Davis W, Bosworth HB, Sanders L et al. (2005) Analysis of air contrast barium enema, computed tomographic colonography, and colonoscopy: prospective comparison. Lancet 365:305–311

Rogalla P, Lembcke A, Ruckert JC, Hein E, Bollow M, Rogalla NE et al. (2005) Spasmolysis at CT colonography: butyl scopolamine versus glucagon. Radiology 236:184–188

Truyen R, Lefere P, Gryspeerdt S, Deschamps T (2000) Speed and robustness of (semi-) automatic path tracking (abstr). Second International Symposium on Virtual Colonoscopy. p. 102

Van Gelder RE, Nio CY, Florie J, Bartelsman JF, Snel P, De Jager SW et al (2004) Computed tomographic colonography compared with colonoscopy in patients at increased risk for colorectal cancer. Gastroenterology 127:41–48

Van Gelder RE, Florie J, Nio CY, Jensch S, de Jager SW, Vos FM et al (2006) A comparison of primary two- and three-dimensional methods to review CT colonography. Eur Radiol. 17:1181–92

Vos FM, Van Gelder RE, Serlie IWO, Florie J, Nio CY, Glas AS et al (2003) Three-dimensional display modes for CT colonography: Conventional 3D virtual colonoscopy versus unfolded cube projection. Radiology 228:878–885

Yee J, Akerkar GA, Hung RK, Steinauer-Gebauer AM, Wall SD, McQuaid KR (2001) Colorectal neoplasia: performance characteristics of CT colonography fordetection in 300 patients. Radiology 219:685–692

Liver

20

Laura Crocetti, Elena Bozzi, Clotilde Della Pina, Riccardo Lencioni, and C. Bartolozzi

CONTENTS

20.1 Introduction

Image processing is a very important tool in improving the quantity and quality of information given by ultrasound (US), computed tomography (CT), and magnetic resonance imaging (MRI) of the liver. The liver is the largest organ in the body, has a very complex anatomy and can be affected by many different diseases, including diffuse and focal diseases. Among diffuse diseases, cirrhosis has the highest prevalence and can be associated with portal hypertension and hepatocellular carcinoma (HCC) (Bartolozzi and Lencioni 1999). Cirrhotic patients are even more often candidates for orthotopic liver transplantation (OLT), and need an accurate evaluation of the liver itself and of its vascularization. Post-processing with three-dimensional (3D) evaluation of surfaces, volumes and vessels is of crucial importance in surgical planning.

L. Crocetti, MD; E. Bozzi, MD; C. Della Pina, MD; R. Lencioni, MD; C. Bartolozzi, MD
Division of Diagnostic and Interventional Radiology, Department of Oncology, Transplants and New Technologies in Medicine, University of Pisa, Via Roma 67, 56125 Pisa, Italy

Many benign and malignant neoplasms (the latter being divided into primary and secondary tumors) can be located within the liver parenchyma. Diagnostic assessment of these neoplasms can be achieved by traditional examination techniques implemented by 3D reconstructions (Bartolozzi and Lencioni 1999).

Malignant tumors can be treated either with surgery or interventional treatments (Bartolozzi and Lencioni 1999). Three-dimensional images allow a precise evaluation of the segmental location of the lesion, and of its relationship with vessels and other surrounding organs. More information about treatment outcome is also available with this technique.

This chapter will deal with 3D image processing of the liver in the evaluation of candidates for either surgery or other interventional treatments.

20.2 Lobar and Segmental Anatomy of the Liver

Three-dimensional image processing plays a crucial role in pre-treatment evaluation of patients who need to be added to the waiting list for either living donor or OLT, or who have to undergo surgery or other therapeutic procedures for hepatic tumors (Bartolozzi and Lencioni 1999; Togo et al. 1998). In all of these patients, conventional imaging implemented by 3D image processing is useful in assessing hepatic morphology and vascular anatomy, detecting focal liver lesions, calculating liver volume, and evaluating portal hypertension (Heath et al. 1995; Nghiem et al. 1999; van Leeuwen et al. 1995).

As far as surface anatomy of the liver is concerned, it can be shown by means of CT and MR surface shaded display (SSD) that allow one to identify the classical lobar anatomy of the liver (van Leeuwen et al. 1994a,b). A correlation between external landmarks (i.e., fissures) and internal landmarks

(i.e., vessels) is possible with an overview on anatomical variations and a different course of internal and external landmarks. This information is very important for the surgeon because what he sees on the surface may not correspond to what he will find in the liver parenchyma. The H-shaped indentations on the visceral faces of the liver divide it into four externally defined lobes: the right, left, quadrate and caudate. The right-hand limb of the H is formed by the fossa for gallbladder anteriorly and by a deep sulcus for the inferior vena cava posteriorly. The gallbladder fossa separates the anterior part of the externally defined right lobe from the quadrate lobe. The sulcus for the inferior vena cava separates the posterior portion of the right lobe from the caudate lobe. Between the gallbladder fossa and the sulcus for the inferior vena cava the right limb of the H is deficient where a caudate process connects the caudate lobe to the right lobe. The left limb of the H is formed by two deep fissures that contain true ligaments in their depths. Anteriorly it is formed by the deep fissure for the ligamentum teres, which separates the anterior part of the externally defined left lobe from the quadrate lobe. Posteriorly it is formed by the fissure for the ligamentum venosum, which separates the posterior part of the left lobe (Friedman and Dachman 1994).

Segmental anatomy is crucial in order to precisely localize a focal lesion, evaluate the possibility of a resection, find the adequate technique for resection, and to estimate the ease or difficulty of a biopsy or any other percutaneous maneuver. Segmental anatomy is the basis of modern hepatic surgery (Togo et al. 1999). Planes of resection in liver surgery, and the correct positioning of devices for interventional treatment, are largely determined by the precise position of the tumor relative to the individual segmental anatomy. Consequently, localization of liver lesions, and pre-operative evaluation of resection planes, require consideration of the significant anatomic variations in the segmental anatomy of the liver (Crocetti et al. 2005).

Each segment is supplied by a sheath containing branches of the hepatic artery and portal vein, as well as a draining bile duct, which enters the middle of the segment. The venous drainage is by hepatic vein, which tends to run between segmental divisions (Couinaud 1957; Healy and Schroy 1953; Healy 1970; Michels 1996; Goldsmith and Woodburne 1957; Bismuth et al. 1988).

The left portal vein divides into three branches: lateral posterior, lateral anterior and medial. The lateral posterior feeds segment 2. The lateral anterior feeds segment 3. The medial branch feeds segment 4.

The right portal vein divides into two branches, one anterior and one posterior. The anterior branch divides into a superior branch for segment 8, and inferior branch for segment 5. Segment 8 is localized between the middle hepatic vein (left), the right hepatic vein (right), and the inferior vena cava (superior and posterior). It lies over segment 5. Segment 5 is localized between the middle hepatic vein and the gallbladder fossa (left), the right hepatic vein (right), and the surface of the liver (inferior and anterior). It lies under segment 8. Segment 5 does not reach the inferior vena cava. The posterior branch divides into a superior branch for segment 7, and inferior branch for segment 6. Segment 7 is localized behind the right hepatic vein (right), and the inferior vena cava medial. It lies over segment 6, and is hidden by segment 8 when looking at the liver from the front. Segment 6 is localized behind the right hepatic vein and the surface of the liver (inferior and anterior). It lies under segment 7. Segment 6 does not reach the inferior vena cava, but is usually located in front of the right kidney.

Segment 1 is not fed by a single portal vein, and drains through multiple short hepatic veins into the inferior vena cava. Segment 1 is located between the portal trunk (anterior), the inferior vena cava (posterior), and the liver surface (left), and is in complete continuity with segment 7 on its right side (Fig. 20.1).

Spiral CT allows the acquisition of consistent volumetric data of the entire liver during the peak of vascular enhancement. From these volumetric data,

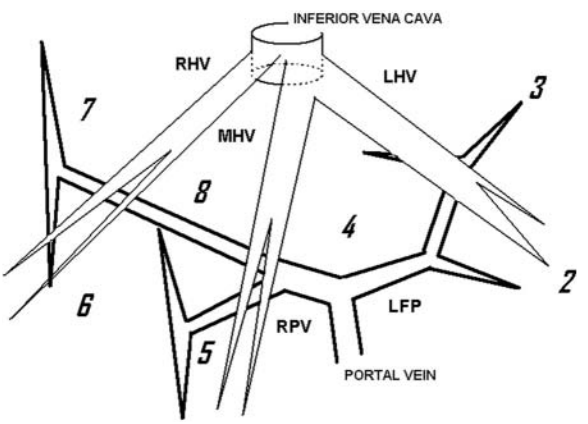

Fig. 20.1. Hepatic segmental anatomy. *RHP:* right hepatic vein; *MHP*: middle hepatic vein; *LHV*: left hepatic vein; *RPV*: right portal vein; *LPV*: left portal vein

detailed 3D renderings can be created representing the intrahepatic portal branches, hepatic venous system, and hepatic contour. By studying the portal branches from different angles and projections, in relation to the hepatic veins and hepatic contour, it is possible to assess the individual segmentation pattern of the liver in vivo and to represent it by means of surface renderings (van Leeuwen et al. 1994a,b). When a resection is planned, it is of crucial importance for the surgeon to know where the avascular planes between the different portal territories are located. Because these avascular planes often are not discernible on the outside of the liver, it can be very helpful to the surgeon if the location of these planes is demonstrated pre-operatively. Three-dimensional renderings are far closer to the surgical reality as perceived during liver resection than are the transverse slices, and can help to plan a resection tailored to the individual segmental anatomy (van Leeuwen et al. 1994a,b, 1995).

Cirrhotic changes within the liver in patients who are candidates for OLT or interventional treatment for HCC can be demonstrated by means of 3D-CT and MR angiography: liver atrophy, nodularity, reduced size of right hepatic lobe and enlargement of the left hepatic lobe or caudate lobe (Smith et al. 1998).

The ability to measure liver volume before surgery can be useful in determining the extent and nature of hepatic resection, especially in the case of atypical resections. Accurate assessment of liver volume and an estimate of liver function may also allow prediction of post-operative liver failure in patients undergoing resection, and can assist in embolization procedures, help with the planning of staged hepatic resection for bilobar disease, and aid in selection and surgical planning of living-related liver donors (Glombitza et al. 1999; Wigmore et al. 2001; Lang et al. 2005; Meier et al. 2004; Laghi 2006). In this setting in particular, the calculation of the volume of living donor liver transplantation. Hepatic volumes can be determined by manually tracing the contours of both the entire liver and the graft (segments 5–8). The volume of the donor's liver can be calculated together with the volume of the remnant liver after right or left hepatectomy (Fig. 20.2).

An insufficient remnant liver volume, calculated pre-operatively, might lead to the performance of iatrogenic occlusion of the right or left portal vein in order to determine a lobar liver hypertrophy, making the resection feasible. Software for calculation of liver volume is under continuous improvement. From completely manual software – where

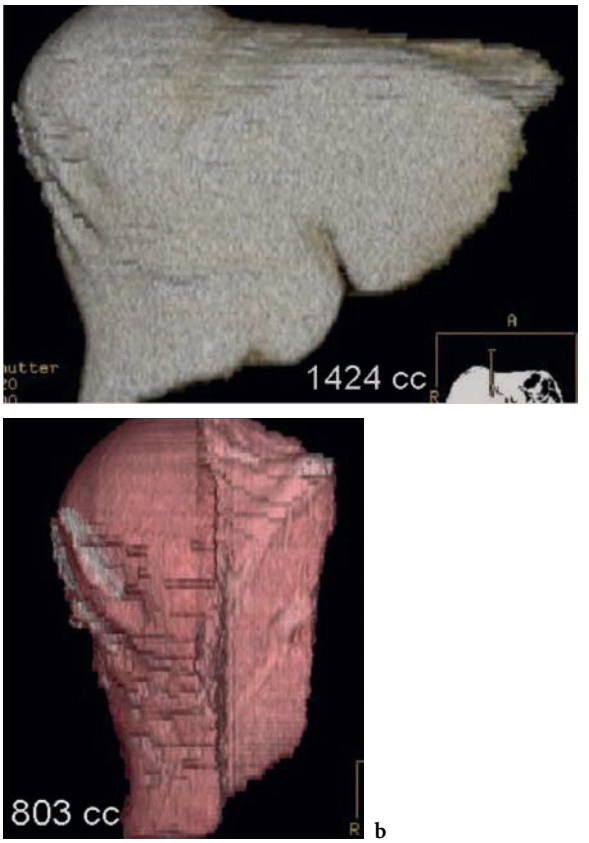

Fig. 20.2a,b. Assessment of hepatic volumetry in a living liver donor. Hepatic volumes are determined by manually tracing the contours of both the entire liver and the graft (segments 5–8) in the venous phase. **a** The volume of the donor's liver is calculated together with **(b)** the volume of the remnant liver, deemed sufficient, after left hepatectomy. The virtual hepatectomy plane followed the middle hepatic vein, corresponding to the plane of the performed surgery

it was necessary to manually outline liver contour slice by slice – there are now semi-automatic and completely automatic programs (Meier et al. 2004; Castillo et al. 2005). Computer-based 3D virtual operation planning systems are available. Virtual liver resection was shown to be a useful tool especially in complicated operations, but also in minor resections in patients with deteriorated liver function. Significant vessels crossing the resection line are readily visible, and bleeding is minimized. The technique may diminish need of temporary clamping of the liver hilum (Pringle's maneuver), which is widely used in liver tumor surgery. It improves the surgeon's knowledge of liver anatomy and can also be used in practicing and providing training on liver surgery (Wigmore et al. 2001; Numminen et al.

2005). Information can be displayed using colored maps or 3D movies. Automated techniques are also extremely time-efficient, with a mean segmentation time of 7 min, compared to the 40 min usually necessary for manual segmentation (Meier et al. 2004; Castillo et al. 2005). The exact prediction of postoperative liver function can be provided by means of measures of the total and resected volume of liver parenchyma (Glombitza et al. 1999; Wigmore et al. 2001; Lang et al. 2005; Meier et al. 2004; Laghi 2006).

Three-dimensional imaging can provide precise anatomical delineation of damaged areas after hepatic injuries, particularly in relation to major vessels. The 3D reconstruction can facilitate decisions regarding intraoperative, re-operative and non-operative management (Goodman et al. 1995).

20.3 Hepatic Vessels

20.3.1 Arterial Vessels

Knowledge of hepatic vascular abnormalities can be crucial for surgical planning in many situations, particularly in the workup of patients who are candidates for liver transplantation or liver resections, or in the evaluation of potential adult donors prior to transplantation (Kamel et al. 2001; Lee 2001; Guiney 2003; Lang 2005; Almusa and Federle 2006). Three-dimensional CT and MR imaging evaluation, by means of maximum intensity projection (MIP), SSD and volume rendering (VR) projection, allow the visualization of many vascular findings. The entire spiral CT data set is used to create a 3D CT angiogram. The resultant 3D angiogram displays depth, surface relationships and relative CT attenuation values (Johnson et al. 1996a,b; Kuszyk et al. 1995).

Michels' classic autopsy series of 200 dissections, published in 1966, defined the basic anatomic variations in hepatic arterial supply, and has served as the benchmark for all subsequent contributions in this area (Table 20.1). Variant patterns occurred in 45% of cases, and the commonest arterial variant has been shown to be an aberrant right hepatic supply, which is seen in 13%–18% of patients (Coinaud 1986). Michels' motivation was to maximize the database of the surgeon performing procedures in and around the porta hepatis, so as to avoid injury to vascular and ductal structures. A modification of the Michels' classification was developed to reflect the presence of vessels that were either accessory or replaced, so that Michels' original ten groups could be reduced to five major types and a most rare sixth variant (Hiatt et al. 1994) (Table 20.2) (Fig. 20.3).

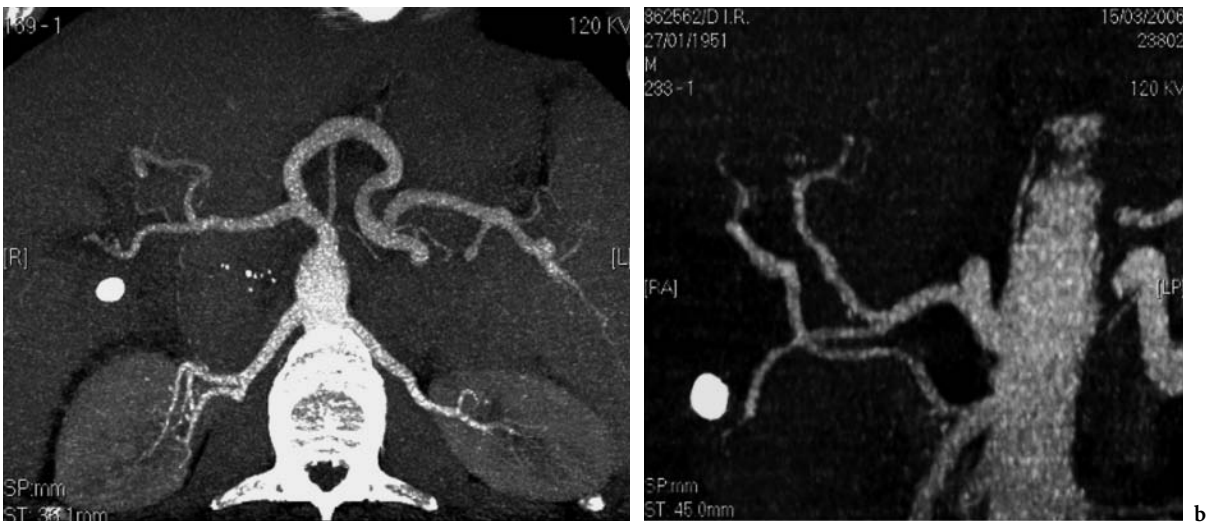

a b

Fig. 20.3a,b. Hepatic arterial anatomy according to Hiatt. **a** MIP reconstruction of Hiatt's type 1 anatomy; i.e., conventional anatomy with the common hepatic artery arising from the celiac axis to the gastroduodenal and proper hepatic arteries. The proper hepatic artery divides distally into right and left branches. **b** MIP reconstruction of Hiatt's type 3 anatomy; i.e., a replaced right hepatic artery originating from the superior mesenteric artery

Table 20.1. The anatomy of arterial supply to the liver categorized according to the standard classification system proposed by Michels (1966)

Type I: conventional anatomy. Proper HA arising from common HA and then giving rise to right and left HAs as the sole supply of arterial blood to liver
Type II: replaced left HA arising from left gastric artery
Type III: replaced right HA arising from SMA
Type IV: both replaced right and left HAs as described for types II and III
Type V: accessory left HA arising from left gastric artery
Type VI: accessory right HA arising from SMA
Type VII: accessory right HA arising from SMA, and accessory left HA arising from left gastric artery
Type VIII: replaced right HA and accessory left HA, or replaced left HA and accessory right HA
Type IX: entire hepatic trunk arising from SMA
Type X: entire hepatic trunk arising from the left gastric artery

HA, hepatic artery; SMA, superior mesenteric artery.

Table 20.2. Arterial variations classified according to Hiatt et al. (1994)

Type 1: the common HA arising from the celiac axis to form the gastroduodenal and proper hepatic arteries; the proper HA dividing distally into right and left branches
Type 2: a replaced or accessory left HA arising from the left gastric artery
Type 3: a replaced or accessory right HA originating from the SMA
Type 4: double-replaced pattern with the right HA arising from the SMA, and the left HA being a branch of the left gastric artery
Type 5: the entire common HA originating as a branch of the SMA
Type 6: common HA arising directly from the aorta

HA, hepatic artery; SMA, superior mesenteric artery.

Among various patterns, Michels' type IX anatomy or Hiatt's type 5 can potentially change the surgical approach during liver transplantation. In this anatomic variant, there is complete replacement of the hepatic trunk to the superior mesenteric artery. The aberrant course of this artery deep to the portal vein may necessitate altering the sequence of the vascular anastomoses so that the hepatic arterial reconstruction is performed prior to portal vein anastomoses (Nghiem et al. 1999).

Recently, a modified classification of hepatic artery variations in two types of hepatic arterial perfusion was proposed. In the first, the whole hepatic arterial supply comes from the common hepatic artery, while in the second the arterial blood reaches the liver, partially or completely, by other arteries rather than by the common hepatic artery. Accordingly, variations can be divided into two groups: Group 1 includes the variations of the common hepatic artery and its branches. Group 2 includes anomalies of the hepatic artery when a left hepatic artery and/or a right hepatic artery are present (Abdullah et al. 2006). This classification seems to be more useful for application in liver transplantation. The presence of accessory or replaced arteries (group 2 anomalies) means that other arteries supply a part or the totality of the liver (rather than the common hepatic artery). When they irrigate a substantial part of the liver, these replaced and accessory arteries have to be preserved by possibly performing arterial reconstruction. Furthermore, when one of these variant arteries supplies all or most of the liver, the arterial anastomosis during liver transplantation has to be performed on this variant artery. In this instance, the size of hepatic arteries appears to be the most important factor in identifying the dominant artery and the voluminous variants of the hepatic artery that had to be imperatively preserved in order to avoid liver parenchyma and/or biliary tree ischemia, which may cause graft waste (Fig. 20.4).

Additionally, group 1 of this classification takes into account the proper variations of the common hepatic artery, and reminds the surgeons to take care of the small branches that originate directly from the proper hepatic artery, such as the segment IV artery, which is so important to preserve during split liver transplantation (Chaib et al. 2005; Saylisoy et al. 2005) (Fig. 20.5).

Pre-operative radiological examinations are of major importance in order to detect hepatic artery variations in the transplant recipient or in the donor when living-related liver transplantation is considered. The current sensitivity of contrast-enhanced angio-CT or MR angiography for identification of hepatic artery variations has been recently estimated to be 91%–94% and 91%–100%, respectively (Winter et al. 1995; Carr et al. 2003; Coskun et al. 2005; Lee et al. 2003; Schroeder et al. 2006; Smith et al. 1998).

Multidetector CT permits high-speed, high-resolution helical images of the entire liver volume during a single breath-hold. Rapid helical data acquisition has resulted in increased body coverage, decreased motion artifacts, and better use of

a

b

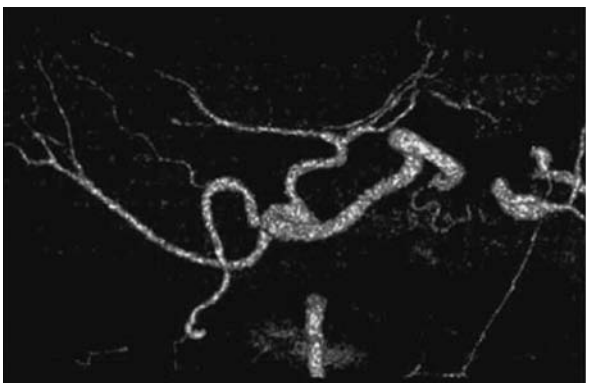

c

Fig. 20.4a–c. Variations of the hepatic artery when a left hepatic artery is present. **a** MIP image of a thin left hepatic artery arising from the left gastric artery in the presence of a dominant right hepatic artery. **b** MIP and **(c)** VR images show a dominant left hepatic artery arising from the left gastric artery, and a thin right hepatic artery originating from the proper hepatic artery

Fig. 20.5. Variation of the common hepatic artery. 3D-CT angiogram with MIP reconstruction shows the trifurcation of the common hepatic artery

the contrast bolus. The combination of fast helical scanning and image processing in 3D, multiplanar reconstructions has resulted in improved image quality and the ability to depict fine anatomic vascular details (Kamel 2001). In the study of Lee et al. (2003), the overall accuracy of CT angiography for assessment of hepatic arterial anatomy was 81%. CT angiography accurately depicted 25 (93%) anatomic variations in 20 donors (91%). However, a few of the limitations of CT angiography were identified. First, respiratory motion artifacts compromised detailed hepatic artery analysis in six donors (10%). Second, the origins of the arteries supplying segment 4 were not demonstrated or were misinterpreted in 11 donors (18%). Third, CT angiography failed to depict the second-order branches of the right hepatic artery in four donors (6%) and the second-order branches of the left hepatic artery in 11 donors (18%) (Lee et al. 2003). In CT angiography techniques using multidetector-row CT, MIP is superior to VR for the depicting hepatic artery anatomic variations and post-processing time (Bjun et al. 2003).

Hepatic MR angiography has been described for the evaluation of transplant recipients (Kopka et al. 1999; Lavelle 2001; Lee et al. 2000; Glockner et al. 2001) and, more recently, in potential right lobe liver donors (Fulcher et al. 2001; Lee et al. 2001). Evaluation of the hepatic circulation with contrast-enhanced MR angiography, however, has remained a challenge. Whereas the main hepatic artery with its right and left branches can usually be depicted with most MR angiography techniques, it has proven more difficult to routinely demonstrate the smaller arterial segmental branch vessels, which are important to identify in living liver donors before surgery (Fig. 20.6). With the advent of more powerful gradient subsystems, much shorter repetition times are achievable. This improvement in speed of acquisition can be used to implement MR angiography with higher degrees of spatial resolution than were previously achievable in a comfortable breath-hold. With repetition times of the order of 3 ms or less, and with use of a 512-matrix size, it is possible to achieve pixel sizes smaller than 1 mm. This is sufficient to identify the smaller segmental hepatic arterial branches and therefore has the potential to completely avoid the need for invasive conventional angiography (Carr et al. 2003).

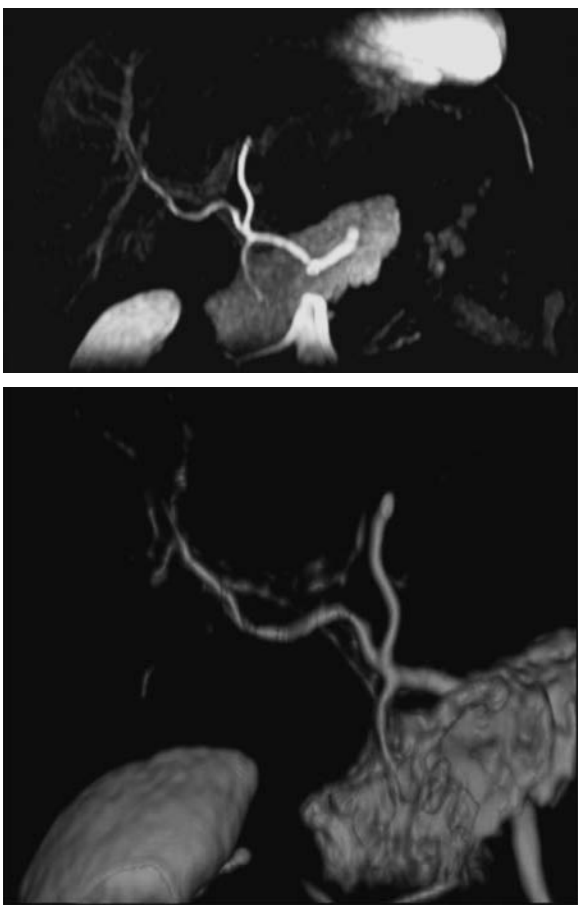

Fig. 20.6a,b. MR angiography. **a** MIP and (**b**) VR reconstructions show the trifurcation of the common hepatic artery

Recent studies have shown that MR angiography is accurate for detecting anatomic variants of the hepatic vasculature in potential living liver donor candidates (Fulcher et al. 2001; Lee et al. 2001; Boeve et al. 2001). These studies used either contrast-enhanced 3D spoiled gradient-echo pulse sequences (Lee et al. 2001; Boeve et al. 2001) or time-of-flight techniques (Fulcher et al. 2001). The study by Carr et al. (2003) implemented contrast-enhanced MR angiography by use of a 3D FLASH pulse sequence with asymmetric k space sampling, short TR (<3 ms), and 512-pixel matrix size. This resulted in much shorter acquisition times, allowing higher spatial resolution to be achieved with voxel sizes on the order of 1.4 mm × 0.7 mm × 1.5 mm. This degree of resolution is essential to consistently depict the segmental arterial branches in the liver, particularly the supply to segment 4. In this study, the hepatic arterial system was visualized to the segmental level in the majority of cases. In particular, the segment 4 branch was visualized in nearly all donors (96%). Although most anomalous vessels are detected with this technique, smaller, less common accessory arteries may potentially be missed (Carr et al. 2003).

Multidetector CT has been compared to MR in the evaluation of potential living liver donors (Schroeder et al. 2005). In several studies, both MR angiography and CT angiography proved to have a diagnostic accuracy comparable to catheter angiography in evaluating hepatic arterial anatomy, with an excellent intraoperative correlation (Schroeder et al. 2006; Carr et al. 2003; Coskun et al. 2005). However, in the study by Schroeder et al. (2005) the display of the hepatic arterial system was deemed more accurate and reliable on the CT images, which was mirrored both by a higher number of detected variants and by a higher rated image quality. This was considered an effect of the higher spatial resolution achievable by multidetector CT.

In the setting of cadaveric liver transplantation it is more important to identify vascular anomalies of the celiac axis than hepatic artery variations. Indeed, celiac axis anomalies, such as atheromatous celiac-trunk stenosis or diaphragmatic arcuate ligament, could necessitate celiac axis revasculariza-

tion or aorto-hepatic reconstruction, leading also to retrieval of the arterial iliac allograft in the cadaver donor if necessary (Ducerf et al. 1998) (Fig. 20.7).

Patients with cirrhosis and portal hypertension are at increased risk for developing splenic artery aneurysms. The major pathogenic factor seems to be the high flow rate in the splenic artery, which causes dilatation, elongation and tortuosity of the main splenic artery in cirrhotic patients. The pre-operative diagnosis of splenic artery aneurysms is crucial because this area is not routinely explored during transplantation surgery, and the patients may be at higher risk of a splenic artery aneurysm rupture in the post-transplant period. The decreased portal venous pressure and the increase in splenic arterial flow may cause the splenic artery aneurysms to expand and rupture. 3D-CT and MR provide a non-invasive means to evaluate the presence of splenic artery aneurysms, which have to be ligated before liver transplantation (Nghiem et al. 1999) (Fig. 20.8).

20.3.2 Hepatic Veins

Anatomical variants can also be found in portal and hepatic vein trees. A large right inferior hepatic vein, draining segment 6, is found in 15%–20% of normal subjects. When a right inferior hepatic vein

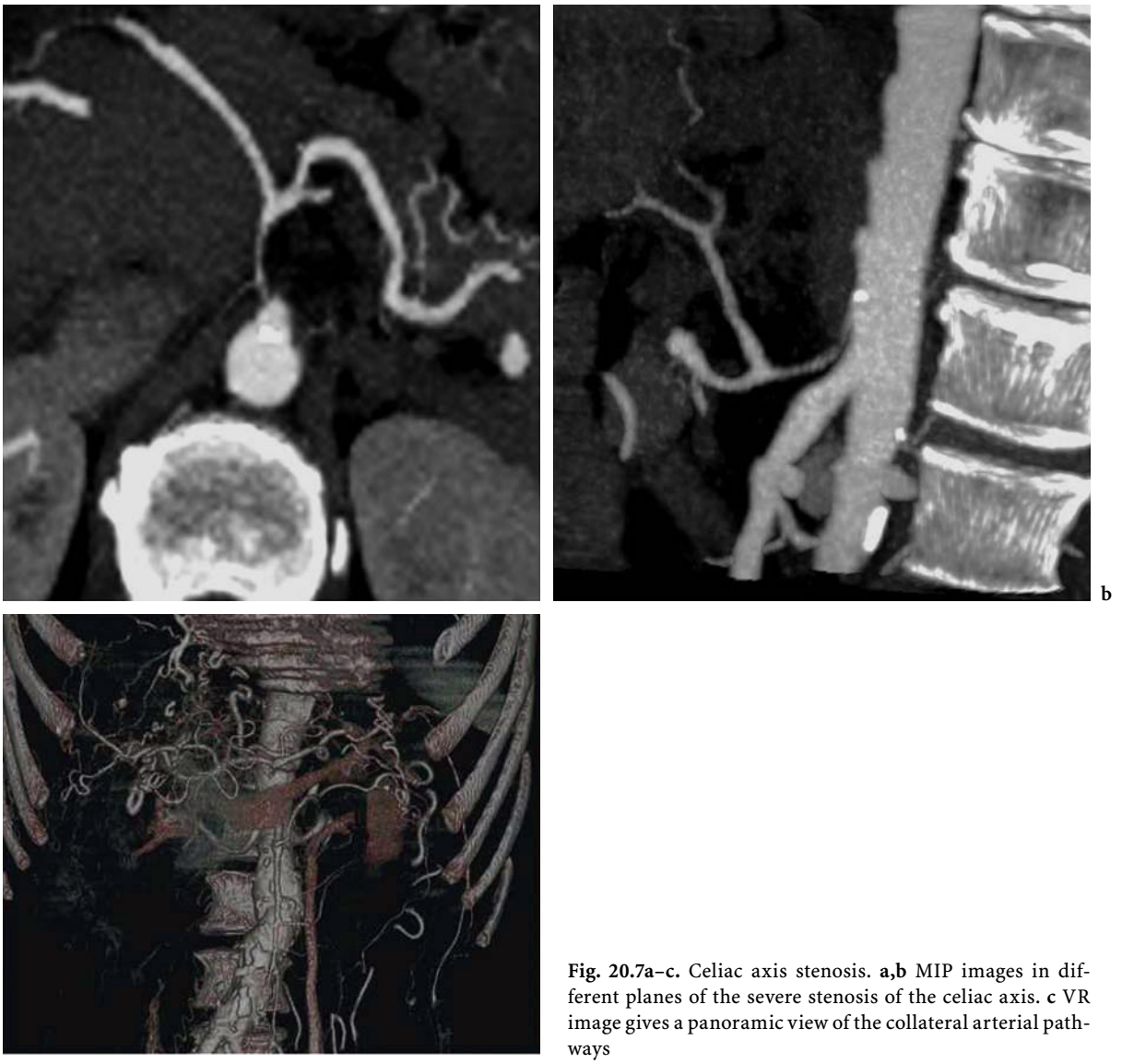

Fig. 20.7a–c. Celiac axis stenosis. **a,b** MIP images in different planes of the severe stenosis of the celiac axis. **c** VR image gives a panoramic view of the collateral arterial pathways

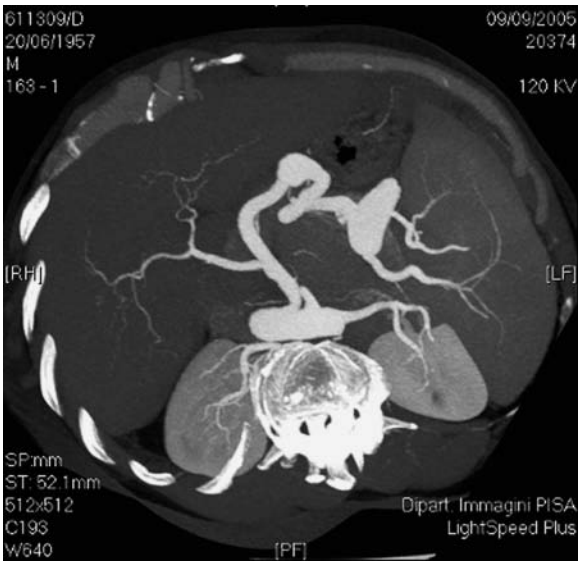

Fig. 20.8. 3D-CT angiogram. MIP image shows double splenic aneurism

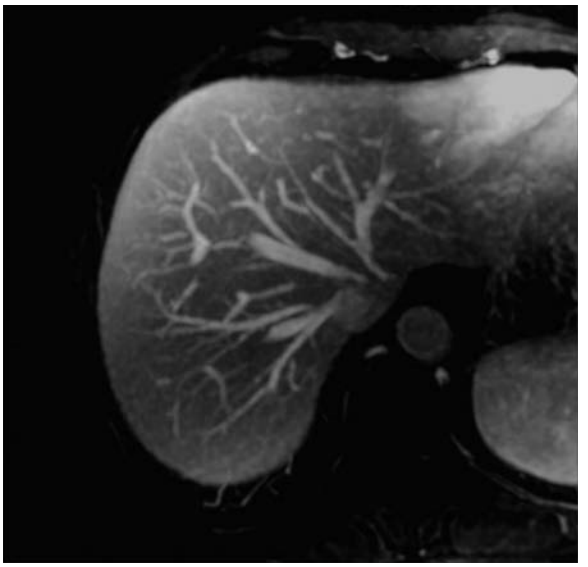

Fig. 20.9. Hepatic veins. MR angiography MIP image shows hepatic veins and their main branches

is present, the right hepatic vein is usually smaller, as it does not drain segment 6. In some cases, the right hepatic vein is absent, or limited to a very small vessel, when a large inferior right hepatic vein is associated with a predominant middle hepatic vein. There is a balance in territories drained by each hepatic vein. For surgical purposes, evaluation of the approximate territory drained by each hepatic vein is interesting, especially in order to prevent intraoperative bleeding, but also to preserve hepatic tissue. For example, an accessory inferior hepatic vein can allow preservation of the posteroinferior area of the right lobe despite transection of the right hepatic vein in partial hepatectomy (Makuuchi et al. 1987). In the study by Erbay et al. (2003) intraoperative assessment confirmed the hepatic venous assessment was performed by means of multidetector CT in 56 (90%) of the 62 donors who underwent surgery. The hepatic veins can be demonstrated also with MR angiography, whereas this is almost impossible with angiography (Fig. 20.9). CT and MR imaging have comparable results in identifying variants of the hepatic venous system in the study by Schroeder et al. (2005). True fast imaging with steady-state precession (FISP) is a recently developed two-dimensional technique that has the advantage of producing high signal-to-noise ratios from blood without the need for contrast injection (Barkhausen et al. 2001). As a result, large vascular structures such as veins are well seen. By combining true FISP with contrast-enhanced MR angiography, it is possible to consistently and accurately depict hepatic venous and portal venous anatomy in addition to arterial structures without relying completely on MR angiography (Carr et al. 2003).

20.3.3 Portal Veins

Portal vein variants occur in 20% of cases. In most instances, the portal bifurcation is located higher than usual, and may be strictly intrahepatic, which may represent a surgical problem when ligation of the right or left portal vein is required. The most usual abnormality is the left portal vein arising from the right portal vein or from the anterior branch or the right portal vein. Rarely, the right portal vein arises from the intrahepatic left portal vein; usually, the anterior branch of the right portal vein arises from the segment 4 branch of the left portal vein. The large number of variations in portal branching patterns determine variation in segmental anatomy. Three-dimensional CT and contrast-enhanced MR angiography allow a precise evaluation of splenic, superior mesenteric and portal veins, and of significant anatomic variation in the segmental anatomy of the liver (Lee et al. 2000; Ito et al. 2000; Saddik et al. 1999; Soyer et al. 1996c; van Leeuwen et al. 1994a,b). Even though the anatomical information

is similar, the display of the portal venous is more convenient with MR imaging (Fig. 20.10). Combined with 3D renderings, the enhanced contrast conspicuity represents an important contributing factor to greater diagnostic confidence, even when compared with digital subtraction angiography (Yamashita et al. 1996; Schroeder et al. 2005).

The evaluation of the portal venous system has been reported to be sufficient with time-of-flight and phase contrast techniques (Kopka et al. 1999).

Many candidates for liver transplantation and interventional treatments for HCC are cirrhotic patients. It is very important to have an overview on the portal system of these patients, who are likely to have portal hypertension (Okuda and Benhamou 1991).

Performance of an acquisition during the portal phase of enhancement of a CT enables evaluation of portal and variceal anatomy and of portosystemic shunts without the need for an additional injection of contrast material. Three-dimensional reconstruction of portal-phase CT angiograms enhances the perception of the courses and anatomic relationships of varices and shunts, and the presence and extension of portal thrombosis (Henseler et al. 2001). SSD can be very useful for displaying variceal anatomy during the portal phase. Also, 3D-MR angiography can detect the presence and the extension of collateral vessel pathways. Patients with portal hypertension benefit from the use of MR angiography, probably because of the increased contrast material sensitivity of the technique (Soyer et al. 1997; Kopka et al. 1999). In particular, the region of the confluence of the portal vein can be evaluated with higher diagnostic confidence on MR angiograms than on DSA images, due to the inflow of unenhanced blood from the splenic vein (at splenoportography) or the superior mesenteric vein (at mesentericoportography) (Okumura et al. 1999; Ono et al. 1996; Kopka et al. 1999).

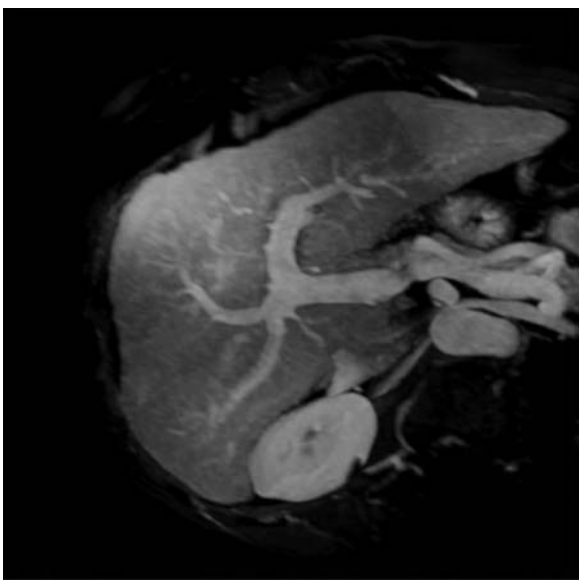

Fig. 20.10. Portal vein. MR angiography MIP image shows portal vein trifurcation

The demonstration of variceal anatomy provides important information to the surgeon or the interventional radiologist, anticipating difficult procedures in patients who often are already in a clinically tenuous condition. This knowledge is important not only for major operations such as liver transplantation but also for more common procedures in which an unexpected varix can result in significant bleeding.

The most common and most clinically important portosystemic shunt is through gastroesophageal varices, fed mainly by the left gastric vein. Bleeding from esophageal varices is a major cause of death in patients with portal hypertension. It is very important to identify all the vessels shunting blood to the gastroesophageal varices and to occlude them, thus preventing bleeding and, eventually, the significant loss of blood from the portal vein after transplantation (Henseler et al. 2001; Ono et al. 1997) (Fig. 20.11).

Other collateral vessels include recanalized paraumbilical veins, which are of special clinical concern to the surgeon considering a large abdominal incision. Paraumbilical veins are small veins that run in the falciform ligament, with the atrophied umbilical vein (ligamentum teres), and which may hypertrophy in the presence of elevated portal venous pressure. The recanalized paraumbilical vein originates from the left portal vein, courses along the falciform ligament and usually extends toward the umbilicus, behind the anterior abdominal wall (Horton and Fishman 1998).

Collateral vessels originating from the splenic hilar region may communicate directly with the renal vein or travel a great distance before communicating with the systemic circulation. Other retroperitoneal shunts that can be identified my means of CT or better visualized by 3D-CTA are the iliolumbar, intercostal and phrenic vein shunts. These can be difficult to identify intraoperatively, and pre-operative knowledge of their presence and course is valuable, since it is advantageous to ligate these varices to prevent loss of blood from the portal vein.

a b

Fig. 20.11a,b. Porto-systemic shunts. **a** Spleno-renal portosystemic shunt and **(b)** collateral vessels arising form left gastric vein communicating with left splenic vein as demonstrated by MIP images

Intrahepatic collateral pathways can develop in cirrhotic patients with portal hypertension. Park et al. (1990) classified them in 4 types: type 1 when there is a vessel of large diameter that connects the right portal branch with the inferior vena cava; type 2 when there are one or more communications between the portal vein and hepatic veins in one hepatic segment; type 3 when there is an aneurysmatic shunt between peripheral branches of the portal vein and hepatic veins; type 4 when there are multiple communications between portal peripheral branches and hepatic vein branches in both hepatic lobes.

Abnormalities of hemodynamics in the portal system, or the presence of HCC, may lead to portal thrombosis – the latter being a neoplastic thrombosis. Portal vein thrombosis significantly affects treatment choice in patients with HCC, and was once considered a relative contraindication to OLT. Patients with complete portal thrombosis and multinodular or large HCC cannot undergo transcatheter arterial chemoembolization, and thus only palliative treatments can be performed. The use of increasingly sophisticated techniques to treat splanchnic venous thrombosis has eliminated the contraindication for OLT represented by portal thrombosis, but knowledge of the extent of the thrombosis is crucial for planning a successful portal vein reconstruction. 3D-CT angiograms and 3D-MRI provide important information about the presence and extension of portal thrombosis, therefore allowing correct treatment planning (Nghiem et al. 1999; Smith et al. 1998) (Fig. 20.12).

20.4 Liver Tumors

Three-dimensional rendering techniques provide a variety of methods for visualization of liver lesions in relation to the vessels and hepatic parenchyma, and therefore can give important information to the surgeon and the interventional radiologist about lesion location and relations with surrounding vessels and organs (Soyer et al. 1991, 1996a) (Fig. 20.13). These techniques can also improve, as shown in recent studies, the morphologic detection and characterization of benign and malignant lesions located in liver parenchyma (Taupitz et al. 1995; Bennett et al. 1991; Bjerner et al. 1998).

Among different 3D-imaging techniques, Uchida et al. (1999) found that VR 3D-CT images during intravenous injection without the MIP technique produced 3D images of high quality with excellent visualization of tumors and their relationship to vital structures. MIP technique, in fact, cannot

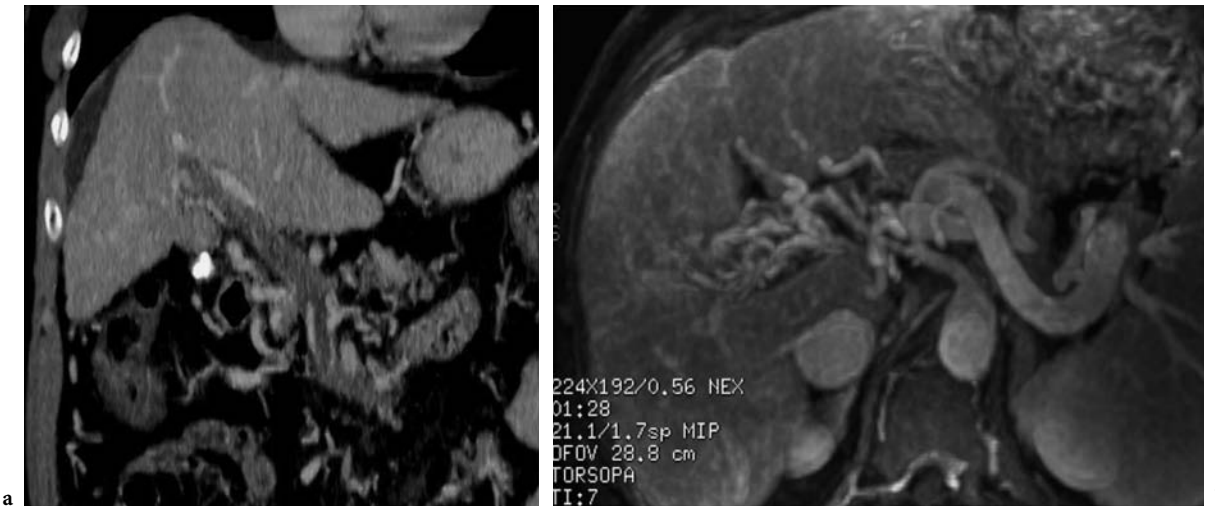

a b

Fig. 20.12a,b. Portal vein pathologies. **a** MIP image reconstruction from a CT dataset shows complete thrombosis of the portal vein and of its right branch, and partial thrombosis of the superior mesenteric vein. **b** MIP image reconstruction from a MR dataset shows a portal cavernoma

a b c d

Fig. 20.13a–d. Focal nodular hyperplasia (FNH) at multidetector CT. **a** Axial image, acquired during arterial phase, shows a large FNH of the right lobe. MIP images show **(b)** enlarged hepatic artery with intranodular branches, **c** The relationship of the FNH with the hepatic veins, which are displaced by the mass, and **(d)** the presence of additional hepatic veins

simultaneously depict internal structures such as liver lesion and vessels. VR technique is conversely capable of depicting multiobject displays, including the surface of the liver tumors and vessels. Different threshold values can be established to separately reconstruct liver surface, tumor, portal vein and hepatic veins; then, the VR technique image can be contracted with all four reconstructed objects simultaneously displayed (simultaneous display). This multiobject display gives stereotactic understanding of hepatic mass lesions, and VR technique has proven effective in the assessment of tumor invasion of the portal and intrahepatic venous structures. VR technique images can be displayed in color following Hounsfield unit values (Uchida et al. 1999).

Multidetector CT with advanced image processing is also useful in delineating uncommon hypervascular hepatic lesions that can simulate tumors on arterial phase imaging. Many of these lesions can be recognized by their characteristic appearance, which can reduce the need for additional imaging, follow-up and histologic correlation (Kamel et al. 2006). The volume of each tumor can be calculated with high accuracy by using dedicated semi-automatic and automatic programs; an optimal correlation between the automatically and the manually calculated tumor volumes was observed in 96.8% of the lesions in a study including three independent radiologists (Meier et al. 2004).

Hawighorst et al. (1999) underlined that each hepatic lesion can be identified and characterized on 3D gadolinium-enhanced MR angiographic images by analyzing the spatial variations and evolution of contrast enhancement in each lesion. The functional information derived from this additional information at all three MR angiographic phases significantly improved lesion characterization of all lesions, as compared to the characterization of the conventional sequences. A complete 3D volume set offers the opportunity to reformat hepatic lesions with multiple views. This allows liver anatomy and vascular structures to be assessed with multiplanar reconstructions. Furthermore, maximum intensity projections improve the assessment of lesion volume. MIP and multiplanar reconstructions can also improve lesion delineation, and potentially enable the detection of the feeding and draining vessels (Hawighorst et al. 1999; Bennett et al. 1991; Bjerner et al. 1998; Blasbalg et al. 2000; Kim et al. 2001).

Gadolinium chelate-enhanced 3D spoiled GRE source images, for example, seem to be superior to MIP reformatted images for the assessment of morphologic features of FNH. MIP reformatted images are superior to the corresponding source imaging for showing the main branches of the hepatic artery, an arterial branch going to the FNH, and a small artery within the FNH radiating to peripheral areas. The combination of 3D spoiled GRE source images and MIP allows the analysis of morphologic, hemodynamic and angioarchitectural patterns of FNH (Soyer et al. 1996).

For the diagnosis of hepatocellular carcinoma, 3D-FISP dynamic MRI is potentially useful in the detection of HCCs, regardless of their vascularity and histological grade, because of its high contrast and spatial resolution. This indicates the usefulness of 3D-FISP in the demonstration of hypovascular as well as hypervascular lesions (Shinozaki et al. 2002).

A recent study demonstrated that dynamic study performed with transverse 3D fat-suppressed T1-weighted spoiled gradient-echo acquisition can be used as a stand-alone sequence for the diagnosis of HCC in patients with cirrhosis prior to liver transplantation, and that the addition of 2D T2-weighted MR imaging did not improve the accuracy or confidence in diagnosis of HCCs or dysplastic nodules (Hecht et al. 2006).

If, in assessing liver anatomy and vasculature, 3D US has not yet gained an established role, its capability for guiding interventional procedures and for providing more accurate localization and size estimation of tumors has been demonstrated (Downey et al. 1995; State et al. 1996; Cesarani et al. 1999; Downey et al. 2000; Nelson and Pretorius 1998). A study showed that 3D US is able to accurately locate the device tip within or near the tumor and to readily display configurational information when multiple devices are used. In fact, 3D US provided additional helpful information that resulted in confident placement of the ablative devices because of the capability of understanding exact 3D relationships of anatomic structures and ablative devices by studying the simultaneous display of three orthogonal imaging planes (Rose et al. 2001).

Volume measurement with 3D US is more accurate than measurement with conventional sonography, and comparable or even better than those made using CT investigations (Liess et al. 1994; Wolf et al. 1998; Gilja et al. 1999; Linney and Deng 1999). Moreover, changes in size can be more readily identified on serial studies, and 3D US may be applied complementarily to CT and MR imaging as an economical procedure for the follow up of tumor disease (Liess et al. 1994; Wolf et al. 1998; Cesarani et al. 1999).

Three-dimensional images can be reconstructed from a power US study, with or without administration of contrast media, and visualized as a cine loop. The intratumoral blood-flow of focal liver lesions can thus be visualized and can be useful for the differential diagnosis of hepatic tumors, especially HCC and FNH. In fact, these tumors have distinctly different intratumoral vascular structures (Hirai et al. 1998; Cesarani et al. 1999; Campani et al. 1998). Three-dimensional power Doppler US can effectively depict the associated arteries of HCCs, and there is a good correlation with angiographic study (Liang et al. 2003).

Three-dimensional reconstructions can also be useful in cases of follow-up of lesions after local therapies (percutaneous ethanol injection, trans-arterial chemo-embolization and radiofrequency thermal ablation). A comparison between the pre- and post-treatment imaging of the lesions is able to demonstrate the reduction of the viable tumor tissue in case of a successful treatment. The lesion can be isolated from the surrounding liver parenchyma and characterized by color-coding and volume rendering. In this way, 3D imaging contributes to the precise estimation of tumor necrosis, and permits one to indicate whether or not the treatment has been successful (Lencioni et al. 2000). A recent pilot study that assessed the diagnostic performance of a computer-aided 3D-CT analytic tool for evaluating local recurrences of liver metastases after the first month following RF ablation by quantifying shape changes in ablated tumors, showed that the 3D analytic tool proved helpful in quantifying ablated tumor shape variations, and allowed recurrences to be detected even in the absence of abnormal enhancement (Bricault et al. 2006).

References

Almusa O, Federle MP (2006) Abdominal imaging and intervention in liver transplantation. Liver Transpl. 12:184–193

Barkhausen J, Ruehm S, Goyen M et al (2001) MR evaluation of ventricular function: true fast imaging with steady-state precession versus fast low-angle shot cine MR imaging. Feasibility study. Radiology 219:264–269

Bartolozzi C, Lencioni R (1999) Liver malignancies. Springer, Berlin

Bennett WF, Bova JG, Petty L, Martin EW Jr (1991) Preoperative 3D rendering of MR imaging in liver metastases. JCAT 15:979–984

Bismuth H, Castaing D, Garden OJ (1988) Segmental surgery of the liver. Surg Ann 20:291–310

Bjerner T, Johansson L, Haglund U, Ahlstrom H (1998) 3D surface rendering of images from multiple MR pulse sequences in the pre-operative evaluation of hepatic lesions. Acta Radiol 39:698–700

Blasbalg R, Mitchell DG, Outwater EK, Ito K, Gabata T, Chiowanich P (2000) Free MRA of the abdomen: postprocessing dynamic gadolinium-enhanced 3D axial images. Abdom Imaging 25:62–66

Boeve WJ, Kok T, Haagsma EB et al (2001) Superior diagnostic strength of combined contrast-enhanced MR angiography and MR imaging compared to intra-arterial DSA in liver transplant candidates. Magn Reson Imaging 19:609–622

Bricault I, Kikinis R, Morrison PR et al (2006) Liver metastases: 3D shape–based analysis of CT scans for detection of local recurrence after radiofrequency ablation. Radiology 241:243–250

Byun JH, Kim TK, Lee SS et al (2003) Evaluation of the hepatic artery in potential donors for living donor liver transplantation by computed tomography angiography using multidetector-row computed tomography: comparison of volume rendering and maximum intensity projection techniques. J Comput Assist Tomogr 27:125–131

Carr JC, Nemcek AA Jr, Abecassis M et al (2003) Preoperative evaluation of the entire hepatic vasculature in living liver donors with use of contrast-enhanced MR angiography and true fast imaging with steady-state precession. J Vasc Interv Radiol 14:441–449

Chaib E, Ribeiro MAF Jr, Saad WA, Gama-Rodrigues J (2005) The main hepatic anatomic variations for the purpose of split-liver transplantation. Transplant Proc 37:1063–1066

Campani R, Bottinelli O, Calliada F, Coscia D (1998) The latest in ultrasound: three dimensional imaging. Part II. Eur J Radiol 27:S183–S187

Castillo OA, Keriakos K, Stinchon JF, Jara H, Soto JA (2005) Automated liver segmentation and volume calculation from MDCT data sets using a dual-clustering technique: comparison with planimetry. Radiology (p) 509 abstract

Cesarani F, Isolato G, Capello S, Bianchi SD (1999) Tridimensional ultrasonography. First clinical experience with dedicated devices and review of the literature. Radiol Med 97:256–264

Coskun M, Kayahan EM, Ozbek O, Cakir B, Dalgic A, Haberal M (2005) Imaging of hepatic arterial anatomy for depicting vascular variations in living related liver transplant donor candidates with multidetector computed tomography: comparison with conventional angiography. Transplant Proc 37:1070–1073

Couinaud C (1957) Le foie: etudes anatomiques et chirurgicales. Masson, Paris

Couinaud C (1986) Anatomie chirurgicale du foie: quelques aspects nouveaux. Chirurgie 112:337–342

Couinaud C (1998) The dorsal sector of the liver. Chirurgie 123:8–15

Crocetti L, Della Pina C, Rocchi E, Montagnani S, Lera J, Bartolozzi C (2005) Imaging landarks for segmental lesion localization. In: Lencioni R, Cioni D, Bartolozzi C (eds.) Focal liver lesions. Springer, Berlin, pp 63–72

Downey DB, Chin JL, Fenster A (1995) Three-dimensional US-guided cryosurgery. Radiology 197(P):539

Downey DB, Fenster A, Williams JC (2000) Clinical utility of three-dimensional US. RadioGraphics 20:559–571

Ducerf C, Rode A, De La Roche E et al (1998) Compression of the celiac trunk by the diaphragmatic arcuate ligament during supramesocolonic surgery. Ann Chir 52:495–502
Erbay N, Raptopoulos V, Pomfret EA, Kamel IR, Kruskal JB (2003) Living donor liver transplantation in adults: vascular variants important in surgical planning for donors and recipients. AJR Am J Roentgenol 181:109–114
Friedman AC, Dachman AH (1994) Radiology of the liver, biliary tract, and pancreas. Mosby, St. Louis
Fulcher A, Szucs R, Bassignani M et al (2001) Right lobe living donor liver transplantation: preoperative evaluation of the donor with MR imaging. AJR Am J Roentgenol 176:1483–1491
Gilja OH, Hausken T, Bersted A, Odegaard S (1999) Measurements of organ volume by ultrasonography. Proc Inst Mech Eng 213:247–259
Glockner JF (2001) Three-dimensional gadolinium enhanced MR angiography: applications for abdominal imaging. RadioGraphics 21:357–370
Glombitza G, Lamade W, Demiris AM et al (1999) Virtual planning of liver resections: image processing, visualization and volumetric evaluation. Int J Med Inf 53:225–237
Goldsmith NA, Woodburne RT (1957) The surgical anatomy pertaining to liver resection. Surg Gynecol Obstet 195:310–318
Goodman DA, Tiruchelvan V, Tabb DR, Agarwal N, Rhoads JE Jr (1995) 3D CT reconstruction in the surgical management of hepatic injuries. Ann R Coll Surg Engl 77:7–11
Guiney MJ, Kruskal JB, Sosna J, Hanto DW, Goldberg SN, Raptopoulos V (2003) Multi-detector row CT of relevant vascular anatomy of the surgical plane in split-liver transplantation. Radiology 229:401–407
Hawighorst H, Schoenberg SO, Knopp MV, Essig M, Miltner P, van Kaick G (1999) Hepatic lesions: morphologic and functional characterization with multpiphase breathhold 3D gadolinium-enhanced MR angiography - initial results. Radiology 210:89–96
Healy JE (1970) Vascular anatomy of the liver. Ann NY Acad Sci 170:8–17
Healy JE, Schroy PC (1953) Anatomy of the biliary ducts within the human liver: analysis of prevailing pattern of branchings and major variations of the biliary ducts. Arch Surg 66:599–619
Heath DG, Soyer PA, Kuszyk BS et al (1995) Three-dimensional spiral CT during arterial portography: comparison of three rendering techniques. RadioGraphics 15:1001–1011
Hecht EM, Holland AE, Israel GM et al (2006) Hepatocellular carcinoma in the cirrhotic liver: gadolinium enhanced 3D T1-weighted MR imaging as a stand-alone sequence for diagnosis. Radiology 239:438–447
Henseler KP, Pozniak MA, Lee FT, Winter TC III (2001) Three-dimensional CT angiography of spontaneous portosystemic shunts. RadioGraphics 21:691–704
Hiatt JR, Gabbay J, Busuttil RW (1994) Durgical anatomy of hepatic arteries in 1000 cases. Ann Surg 220:50–52
Hirai T, Ohishi H, Yamada R et al (1998) Three-dimensional power Doppler sonography of tumor vascularity. Radiat Med 16:353–357
Horton KM, Fishman EK (1998) Paraumbilical vein in the cirrhotic patient: imaging with 3D CT angiography. Abdom Imaging 23:404–408
Ito K, Blasbalg R, Hussain SM, Mitchell DG (2000) Portal vein and its tributaries: evaluation with thin section three-dimensional contrast-enhanced dynamic fat-suppressed MR imaging. Radiology 215:381–386
Johnson PT, Heath DG, Bliss DF, Cabral B, Fishman EK (1996a) Three dimensional CT: real-time interactive volume rendering. AJR Am J Roentgenol 167:581–583
Johnson PT, Heath DG, Kuszyk BS, Fishman EK (1996b) CT angiography with volume-rendering: advantages and applications in splanchnic vascular imaging. Radiology 200:564–568
Kamel IR, Kruskal JB, Pomfret EA, Keogan MT, Warmbrand G, Raptopoulos V (2001) Impact of multidetector CT on donor selection and surgical planning before living adult right lobe liver transplantation. AJR Am J Roentgenol 176:193–200
Kamel IR, Liapi E, Fishman EK et al (2006) Incidental nonneoplastic hypervascular lesions in the noncirrhotic liver: diagnosis with 16-MDCT and 3D CT angiography AJR Am J Roentgenol 287:682–687
Kopka L, Rodenwaldt J, Vosshenrich R et al (1999) Hepatic blood supply: comparison of optimized dual phase contrast-enhanced three-dimensional MR angiography and digital subtraction angiography. Radiology 211:51–58
Kuszyk BS, Heath DG, Ney DR et al (1995) CT angiography with volume rendering: image findings. AJR Am J Roentgenol 165:445–448
Laghi A (2006) Multidetector CT (64 Slices) of the liver: examination techniques. Eur Radiol Sep 29 (Epub ahead of print)
Lang H, Radtke A, Hindennach M et al (2005) Impact of virtual tumor resection and computer-assisted risk analysis on operation planning and intraoperative strategy in major hepatic resection. Arch Surg 140:629–638
Lavelle MT, Lee VS, Rofsky NM, Krinsky GA, Weinreb JC (2001) Dynamic contrast-enhanced three-dimensional MR imaging of liver parenchyma: souce images and angiographic reconstructions to define hepatic arterial anatomy. Radiology 218:389–394
Lee SS, Kim TK, Byun JH et al (2003) Hepatic arteries in potential donors for living related liver transplantation: evaluation with multi-detector row CT angiography. Radiology 227:391–399
Lee VS, Lavelle MT, Rofsky NM et al (2000) Hepatic MR imaging with a dynamic contrast-enhanced isotropic volumetric interpolated breath-hold examination: feasibility, reproducibility, and technical quality. Radiology 215:365:372
Lee VS, Morgan GR, Teperman LW et al (2001) MR imaging as the sole preoperative imaging modality for right hepatectomy: a prospective study of living adult-to-adult liver donor candidates. AJR Am J Roentgenol 176:1475–1482
Lencioni RA, Neri E, Caramella D, Cioni D, Vagli P, Bartolozzi C (2000) Radiofrequency thermal ablation of liver malignancies: assessment of treatment outcome by volume-rendered spiral CT. Radiology 217(P):228
Liang JD, Yang PM, Liang PC (2003) Three-dimensional power Doppler ultrasonography for demonstrating associated arteries of hepatocellular carcinoma. J Formos Med Assoc 102:367–374
Linney AD, Deng J (1999) Three-dimensional morphometry in ultrasound. Proc Inst Mech Eng 213:235–245
Liess H, Roth C, Umgelter A, Zoller WG (1994) Improvements in volumetric quantificatrion of circumscribed hepatic lesions by three-dimensional sonography. Z Gastroenterol 32:488–492

Makuuchi M, Hasegawa H, Yamazaki S, Takayasu K (1987) Four new hepatectomy procedures for resection of the right hepatic vein and preservation of the inferior right hepatic vein. Surg Gynecol Ostet 164:68–72

Meier S, Schenk A, Mildenberger P, Bourquain H, Pitton M, Thelen M (2004) Evaluation of a new software tool for the automatic volume calculation of hepatic tumors. First results. Rofo Fortschr Geb Rontgenstr Neuen Bildgeb Verfahr 176:234–238

Michels N (1966) Newer anatomy of the liver and its variant blood supply and collateral circulation. Am J Surg 112:337–347

Nelson TR, Pretorius DH (1998) Three-dimensional ultrasound imaging. Ultrasound in Med & Biol 24:1243–1270

Nghiem HV, Dimas CT, Mc Vicar JP et al (1999) Impact of double helical CT and three-dimensional CT arteriography on surgical planning for hepatic transplantation. Abdom Imaging 24:278–284

Numminen K, Sipila O, Makisalo H (2005) Preoperative hepatic 3D models: virtual liver resection using three-dimensional imaging technique. Eur J Radiol 56:179–184

Okuda K, Benhamou JP (1991) Portal hypertension: clinical and physiological aspects. Springer-Verlag, Tokyo

Okumura A, Watanabe Y, Dohke M et al (1999) Contrast-enhanced three-dimensional MR portography. RadioGraphics 19:973–987

Ono N, Toyonaga A, Nishimura H, Hayabuchi N, Tanikawa K (1997) Evaluation of magnetic resonance angiography on portosystemic collaterals in cirrhotic patients. Am J Gastroenterol 92:1515–1519

Park JH, Cha SH, Han JK, Han MC (1990) Intrahepatic portosystemic venous shunt. AJR Am J Roentgenol 155:527

Rose SC, Hassanein TI, Easter DW et al (2001) Value of three-dimensional US for optimizing guidance for ablating focal liver tumors. J Vasc Interv Radiol 12:507–515

Saddik D, Frazer C, Robins P, Reed W, Davis S (1999) Gadolinium-enhanced three-dimensional MR portal venography. AJR Am J Roentgenol 19:973–987

Saylisoy S, Atasoy C, Ersoz S, Karayalcin K, Akyar S (2005) Multislice CT angiography in the evaluation of hepatic vascular anatomy in potential right lobe donors. Diagn Interv Radiol 11:51–59

Shinozaki K, Honda H, Yoshimitsu K et al (2002) Optimal multi-phase three-dimensional fast imaging with steady-state free precession dynamic MRI and its clinical application to the diagnosis of hepatocellular carcinoma. Radiat Med. 20:111–119

Schroeder T, Radtke A, Kuehl H, Debatin JF, Malago M, Ruehm SG (2006) Evaluation of living liver donors with an all-inclusive 3D multi-detector row CT protocol. Radiology 238:900–910

Smith PA, Klein AS, Heath DG, Chavin K, Fishman EK (1998) Dual-phase spiral CT angiography with volumetric 3D rendering for preoperative liver transplant evaluation: preliminary observations. JCAT 22:868–874

Soyer P, Roche A, Gad M et al (1991) Preoperative segmental localization of hepatic metastases: utility of three-dimensional CT during arterial portography. Radiology 180:653–658

Soyer P, de Givry SC Gueye C, Lenormand S, Somveille E, Scherre A (1996a) Detection of focal hepatic lesions with MR imaging: prospective comparison of T2-weighted fast spin-echo with and without fat suppression, T2-weighted breath-hold fast spin-echo, and gadolinium chelate enhanced 3D gradient-recalled imaging. AJR Am J Roentgenol 166:1115–1121

Soyer P, Dufresne AC, Somveille E, Scherrer A (1996b) Focal nodular hyperplasia of the liver: assessment of hemodynamic and angioarchitectural patterns with gadolinium chelate-enhanced 3D spoiled gradient-recalled MRI and maximum intensity projection reformatted images. JCAT 20:898–904

Soyer P, Heath D, Bluemke DA et al (1996c) Three-dimensional helical CT of intrahepatic venous structures: comparison of three rendering techniques. JCAT 20:122–127

Soyer P, Dufresne AC, Somveille E, Scherrer A (1997) MR imaging of the liver: effect of portal hypertension on hepatic parenchymal enhancement using a gadolinium chelate. JMRI 7:142–146

State A, Livengston MA, Garrett WF et al (1996) Technologies for augmented reality systems: realizing ultrasound-guided needle biopsies. Proceedings of SIGGRAPH '96. Comput Graph 13:439–446

Taupitz M, Speidel A, Hamm B et al (1995) T2-weighted breath-hold MR imaging of the liver at 1.5 T: results with a three-dimensional steady-state free precession sequence in 87 patients. Radiology 194:439–446

Togo S, Shimada H, Kanemura E et al (1998) Usefulness of three-dimensional computed tomography for anatomic liver resection: sub-subsegmentectomy. Surgery 123:73–78

Uchida M, Ishibashi M, Abe T, Nishimura H, Hayabuchi N (1999) Three-dimensional imaging of liver tumors using helical CT during intravenous injection of contrast medium. JCAT 23:435–440

van Leeuwen MS, Fernandez MA, van Es HW, Stokking R, Dillon EH, Feldberg MAM (1994a) Variations in venous and segmental anatomy of the liver: two- and three-dimensional MR imaging in healthy volunteers. AJR Am J Roentgenol 162:1337–1345

van Leeuwen MS, Noordzij J, Fernandez MA, Hennipman A, Feldberg MAM, Dillon EH (1994b) Portal venous and segmental anatomy of the right hemiliver: observations based on three-dimensional spiral CT renderings. AJR Am J Roentgenol 163:1395–1404

van Leween MS, Noordzij J, Hennipman A, Feldberg MA (1995) Planning for liver surgery using three dimensional imaging techniques. Eur J Cancer 31:1212–1215

Wigmore SJ, Redhead DN, Yan XJ et al (2001) Virtual hepatic resection using three-dimensional reconstruction of helical computed tomography angioportograms. Ann Surg 233:221–226

Winter TC Jr, Freeny PC, Nghiem HV et al (1995) Hepatic arterial anatomy in transplantation candidates: evaluation with three-dimensional CT arteriography. Radiology 195:363–370

Wolf GK, Lang H, Prokop M, Schreiber M, Zoller W (1998) Volume measurements of localized hepatic lesions using three-dimensional sonography in comparison with three-dimensional computed tomography. Eur J Med Res 23:157–164

Yamashita Y, Mitsuzaki K, Miyazaki T et al (1996) Gadolinium-enhanced breath-hold three-dimensional MR angiography of the portal vein: value of the magnetization-prepared rapid acquisition gradient-echo sequence. Radiology 201: 283–288

Pancreas

21

Salvatore Mazzeo, Valentina Battaglia, and Carla Cappelli

CONTENTS

21.1 Introduction

Pancreatic evaluation obtained by diagnostic imaging techniques has strongly improved in these last few years, especially after the advent of multidetector CT (MDCT) (Sata et al. 2006); this new type of CT has, in fact, permitted to obtain a finer image resolution and an increased velocity on the z-axis, allowing to acquire a larger amount of row data per exam and to avoid breath and motion artefacts (Hu et al. 2000); last but not least, the faster imaging acquisition has allowed the improvement of intravenous contrast medium administration and the achievement of the optimisation of post-contrastographic scans.

Mainly, faster imaging acquisition on the z-axis and the optimisation of contrast administration, allowed by multidetector technology, have determined the improvement of CT study of the pancreas, permitting to formulate a gland study protocol, as reported in many works (McNulty et al. 2001; Nino-Murcia et al. 2000), that consists of an unenhanced, an arterial (pancreatic phase–generally at 40") and a venous phase (at 70"); all these scans are generally acquired with thin slice thickness (<3 mm) and a reconstruction interval that can vary from 0.5–1.5 mm.

In cases of suspected neuroendocrine pancreatic tumours, also a praecox arterial pancreatic (at 20–25") phase (Horton et al. 2006) can be performed, in order to visualize the immediate lesion wash-in and the tumour behaviour in following successive scans; a delayed (180") scan can be moreover performed in patients with ductal adenocarcinoma, which sometimes can show a late enhancement.

The importance of acquiring successive post-contrastographic scans, at standardized delay of acquisition, has revealed fundamental not only in characterizing lesions, basing on their enhancement behaviour, but also to obtain a digital dataset to post process, which is especially useful when staging neoplasms (Nino-Murcia et al. 2000).

The strong increase of the number of data acquired and the finer image quality (mainly due to the very thin slice thickness) than that previously obtained with conventional CT reverberated in fact on the improvement of the post-processing image quality that has so markedly been raised in these last years, resulting in new exciting applications for CT (Calhoun et al. 1999).

21.2 Post-Processing Techniques

Post-processing imaging could not have been developed without advances in computer hardware, software and display technologies, not only because of the previous image quality, but also because image processing and display were very time consuming.

S. Mazzeo, MD; V. Battaglia, MD; C. Cappelli, MD
Diagnostic and Interventional Radiology, Department of Oncology, Transplants and Advanced Technologies in Medicine, University of Pisa, Via Roma 67, 56125 Pisa, Italy

It happened for other viscera examinations, bi- (2D) and three-dimensional (3D) reconstructed images have gained importance also in the study of pancreatic diseases.

The two most used bi-dimensional reformatting techniques in order to study pancreatic pathologies are, as reported in many works, average intensity multiplanar reformatted (MPR) and its variant, curved planar (CPR) reformatted imaging (Baek et al. 2001; Nino-Murcia et al. 2003).

MPR and CPR, obtained in different sectional planes, have revealed to be fundamental in or-der to evaluate the relationships between pancreatic disease and peri-pancreatic structures, especially in the preoperative CT assessment of pancreatic carcinoma and mainly in the evaluation of loco-regional spreading, furnishing fine details in the visualisation of the relationship between tumour and blood vessels (Nino-Murcia et al. 2003) (Fig. 21.1).

These techniques also play an important role in evaluating the peri-lesional soft tissue and, particularly, the tumoral involvement of lymph nodes and retroperitoneal fat, corresponding to the retroportal pancreatic margin (Baek et al. 2001; Brugel et al. 2004).

CPRs are, moreover, frequently applied in tumoral staging evaluation, especially in the depiction of the main pancreatic duct and, as reported by Prokesch (2002), they have been shown to be equivalent to transverse images in the detection of pancreatic tumours and determination of resectability.

It is also mandatory to report that several investigators have found MRP to be nonetheless very much accurate (Rieker et al. 1997) in evaluating pancreatic pathologies and especially pancreatic tumour, avoiding then the use of 3D reconstructed images.

Anyway, even when using the most recent imaging technologies, pancreas location does not always allow to obtain the entire organ and the narrow structure images to be displayed on the same plane in one slice (Jing-Shan et al. 2004).

For these reasons, nowadays, 3D imaging has strongly improved, thanks to the possibility to elaborate the large volumetric data set acquired by spiral CT, permitting the adoption of peculiar windows of visualization (MIP: minimum intensity projections–MinIP) (Rubin et al. 1995; Achenbach et al. 1998; Nino-Murcia et al. 2001) and the performance of volume-rendering (VR) imaging of anal-

a

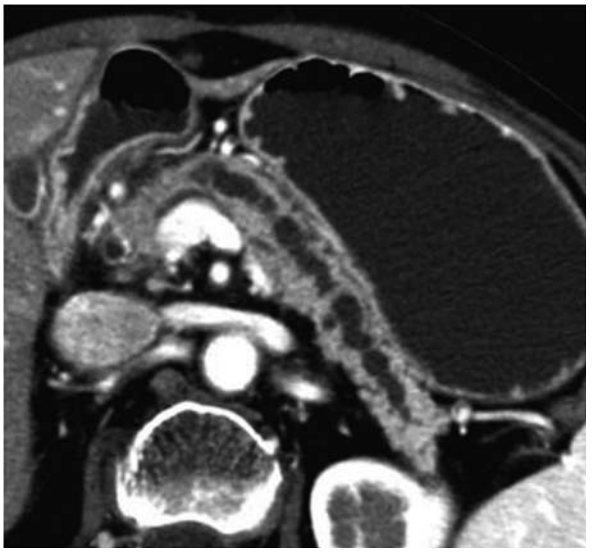

b

Fig. 21.1a,b. MPR coronal oblique image (**a**) of the pancreatic gland in the venous phase: it is possible to appreciate the normal pancreatic and peripancreatic anatomy; (**b**) CPR axial oblique image showing a dilation of the main pancreatic duct in a patient with ductal adenocarcinoma of the inferior part of the pancreatic head

ysed structures (Fishman et al. 2006). Surely, in the study of the pancreas, VR and MIP represent a very important tool of investigation.

MIP algorithm permits in fact to represent the highest attenuation voxel comprised in the explored volume and it has revealed useful in the vessels evaluation; its limitations, especially when studying peripancreatic vessels in patients with ductal adenocarcinoma, are due to the lack of spatiality of represented images, differently from VR (Horton et al. 2002) (Fig. 21.2).

Anyway, MIP can be applied in many pancreatic studies, but mainly in vascular evaluation, and also in acute and chronic pancreatitis and its complications.

Previously not often used because very time consuming, nowadays VR, thanks to recent advances in computer hardware, has become a practical and interactive technique that allows processing and display to occur in real time (minimum 5–10 frames/s) at relatively inexpensive workstations.

About 3D imaging, given up the static surface-rendered (SSD) images, mainly because of its inability to show under (sub)-surface details, VR images have been preferred in the study of pancreatic pathologies, mainly in the evaluation of peri-pancreatic vessels in the pre-operative study of patients affected by carcinoma as well as in the evaluation of the arterial vasculature of patients candidates for pancreas transplantation.

VR is in fact a 3D technique that permits to maintain the spatial relationships among different critical structures, such as those located in the retroperitoneum, permitting to obtain a very accurate evaluation of the real loco-regional tumoral spread; moreover, differently from SSD, VR allows the representation of all different values of attenuation of the pixel contained in the volume of study, representing thus the most advanced technique in clinical/diagnostic routine (Calhoun et al. 1999) (Fig. 21.3).

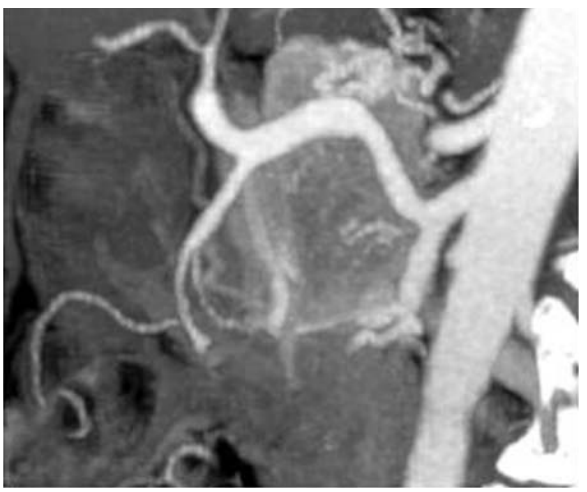

Fig. 21.2. Sagittal oblique MIP image showing the celiac trunk and the vessels around a neuroendocrine pancreatic neoplasm: the spatial relationship of the vessel is not maintained

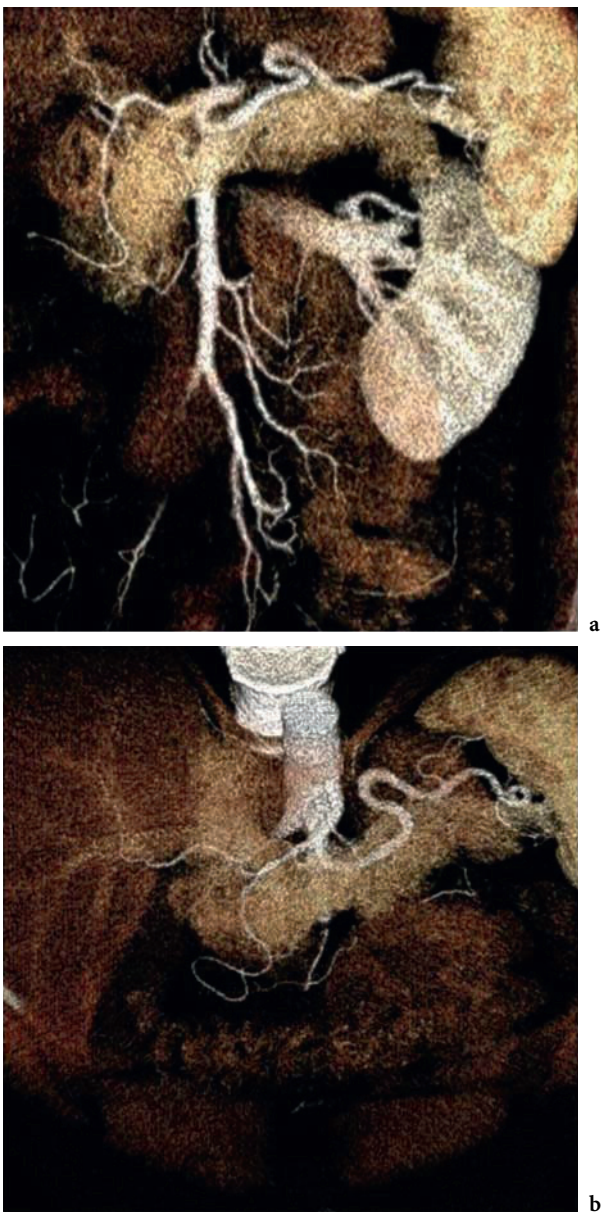

Fig. 21.3a,b. VR 3D images (**a,b**). VR allows to mainatin the spatial relationships among different critical structures, such as those located in the retroperitoneum and permits the representation of all the different values of attenuation of the pixel contained in the volume of study

Recently, in concomitance to these virtual bi- and three-dimensional imaging studies, also the pancreatic evaluation by virtual imaging has stronlgy improved by performing the CT virtual pancreatoscopy (Sata et al. 2006).

21.3 CT Pancreatoscopy and Virtual Pancreatography

Not routinely performed, CT virtual pancreatoscopy, first reported in 1998 by Prassopoulos et al. and Nakagohri et al., is a new tool for diagnosis of pancreatic pathologies (Tanizawa et al. 2003).

This technique consists in the acquisition of a MDCT scan, previously preceded by the introduction of 5–15 ml of iodine non-ionic contrast medium administration in the main pancreatic duct [performing a nasopancreatic drainage during a routine endoscopic retrograde pancreatoscopy (ERP)]. The CT data acquired are then post-processed to obtain 3D images of the pancreatic duct (3D-CT pancreatography) and virtual pancreatoscopy (CT-VP).

CT pancreatography is, in substance, the application of virtual endoscopy to the pancreatic gland, allowing the study the inner surface of the gland ducts and resulting useful in evaluating many ductal diseases and, overall, in case of cystic pancreatic neoplasms, especially intraductal papillary mucinous neoplasms (IPMN).

Some studies have reported a high accuracy in detecting duct anomalies and tumours (Prassopoulos et al. 1998; Nakagohri et al. 1998) of both VP and CT pancreatography a these two techniques show, in some cases, finer details than ERP or intra-operative retrograde pancreatoscopy (IORP) (Sata et al. 2006); the main limitation in applying them consists in the risk of pancreatitis, related to the necessary pre-CT ERP (Sata et al. 2006).

21.4 Ductal Adenocarcinoma

Despite the poor prognosis and the often late diagnosis, nowadays surgery still represents the only possible curative therapy of ductal pancreatic adenocarcinoma (Fortner et al. 1996).

Because of the improvement of more aggressive surgical techniques and the necessity to obtain the most accurate pre-operative staging, imaging post-processing has become a fundamental part of pre-operative radiological evaluation of patients with pancreatic cancers, especially for the correct analysis of the loco-regional neoplastic infiltration (Prokesch et al. 2002), which strongly influences the prognosis and so the eventual resectability.

One of the most important and difficult steps in pancreatic neoplasm staging is to evaluate the relationship between the neoplasm and the surrounding major peripancreatic vessels; a number of studies have been conducted in order to establish a correct grading in neoplastic vessel infiltration (Lu et al. 1997; Mazzeo et al. 2007), being this one of the most important key points in determining patient resectablity (Allema et al. 1995).

Thanks to the availability of high-resolution CT data sets, a large variety of 2D and 3D reformations can be produced; moreover, one of the main advantages of MDCT is to obtain isotropic data sets, thus allowing obtaining high quality images (Brugel et al. 2004) and thus permitting a very accurate pre-operative evaluation.

If in the past patients underwent pre-operative angiography in order to correctly define the eventual vascular encasement, nowadays, MPR, MIP and VR have completely substituted it (Horton 2002).

MPR, even if not furnishing a 3D point of view of pancreatic and peripancreatic structures, is probably one of the most used methods to evaluate loco-regional tumoral spreading (Prokesch et al. 2002) (Fig. 21.4); thanks to the elaboration of images on different planes, it is in fact possible to correctly determine the neoplasm's dimensions, the contiguity to the main duct and the eventual relationship with the surrounding vessels, especially in doubtful cases.

Moreover, MPR can furnish an accurate analysis of the infiltration of the retroperitoneal fat, corresponding to the retroportal resection margin, this another key point of pre-surgical planning, due to the relationship between fat micro/macro invasion and patient survival (Luttges et al. 1998) (Fig. 21.5).

Even if very useful in loco-regional tumoral staging, MPR obviously cannot give volumetric evaluation of structures; generally, MIP and VR are the preferred algorithms to create vascular maps, and especially VR has shown the potential for replacing angiography.

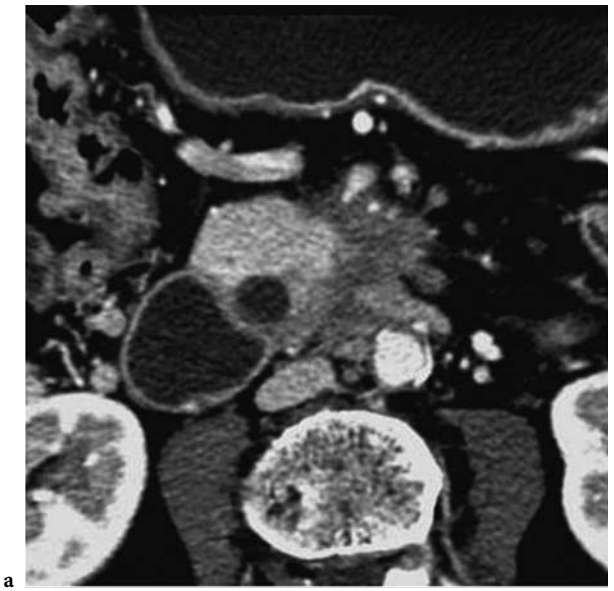

a

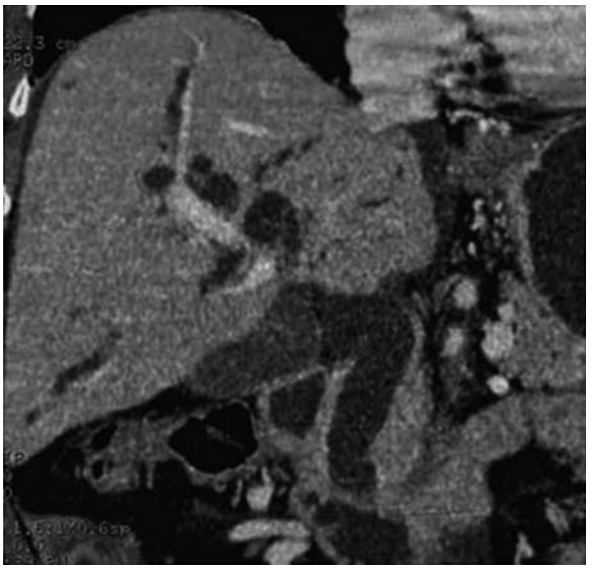

b

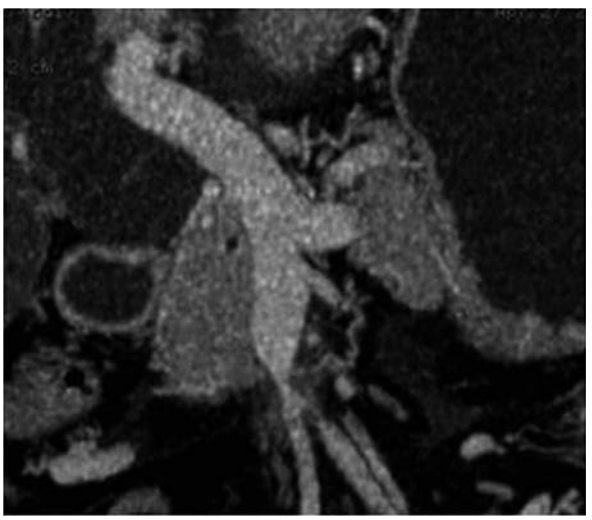

c

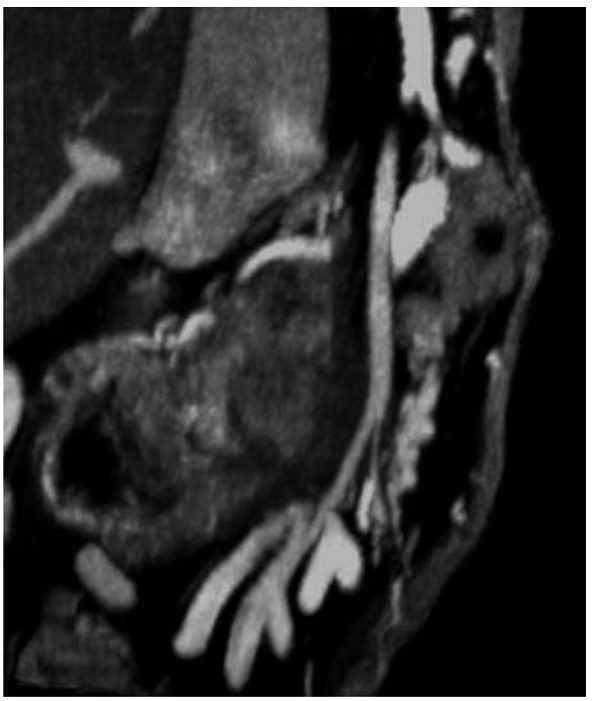

d

e

Fig. 21.4a–e. Axial oblique MPR image (**a**) showing a ductal adenocarcinoma of the pancreas infiltrating the mesenteric root and the retroperitoneum; on the coronal oblique MPR (**b**) it is also possible to appreciate the dilation of the common biliary duct due to the tumoral infiltration. MIP (**c,d**) coronal oblique images show instead the vascular encasement of the mesenteric vein (**c**) and artery (**d**) due to the loco-regional tumour spreading. VRs (**e**) furnish instead a global view of the pancreatic and peripancreatic structures (the *red arrow* shows the pancreatic neoplasm)

Fig. 21.5a–c. Axial oblique MPR (**a**) showing normal retroperitoneal fat, corresponding to the retroperitoneal pancreatic margin, next to the superior mesenteric artery; in the coronal oblique MIP image (**b**) it is instead possible to appreciate an abnormal density of the fat tissue, suspected for microinfiltration; the VR 3D image (**c**) shows the tumoral invasion of the retroperitoneum

VR, in fact, unlike MIP, maintains spatial relationship and depth and it has shown to be superior to MIP in the evaluation of peri-pancreatic vessels (Hong et al. 1999); VR may also be used to show the presence of normal vascular variants (Fig. 21.6).

21.5 Cystic Pancreatic Neoplasms

Even if cystic pancreatic neoplasms account for a very small percentage of the gland tumours, the possibility of some of them to change into malignant lesions determines the necessity to study and stage accurately them and especially mucinous neoplasms and intraductal papillary mucinous neoplasms (IPMN) in both its variants (main and branch duct type) (Itay et al. 2001).

Radiological differentiation between benign and malignant lesions is moreover important in order to determine the appropriate treatment, especially in cases of suspected IPMN, due to the mucin overproduction with the consequent dilation of the main duct and compromission in correct visualization of the precise lesion site (Sahani et al. 2006).

In these last few years, even if ERCP and MRCP still represent an important diagnostic step in diagnosis and characterisation of cystic neoplasm, MDCT has strongly contributed to the depiction and the evaluation of these tumours. Particularly, the introduction and the use of very small detector size and the possibility of acquiring data from quite isotropic voxels have permitted the improvement of the reformatted imaging quality.

The dilation of the MPD, the location and size of the neoplasms are in fact accurately assessed by performing a MDCT study, even in patients with obstruction of the main duct, in whom ERP can be difficult to perform because of the mucinous obstruction of the lumen of the duct. In evaluating cystic pancreatic neoplasms, CPR and MPR play a fundamental role, while MIP and VR are less used, mainly because of the less frequent vascular invasion.

Two-dimensional imaging allows in fact the depiction of communication between the lesion and the main/branch pancreatic ducts, permitting first of all to determine the lesion nature (IPMN versus other cystic pancreatic adenomas/carcinomas) (Nino-Murcia M et al. 2003) (Fig. 21.7).

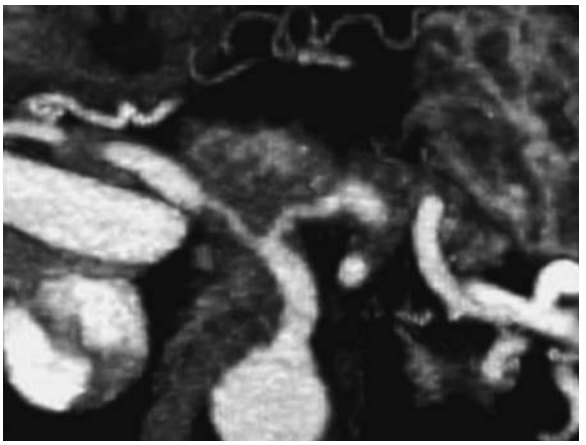

Fig. 21.6. Axial MIP image clearly depicts the stenosis of the hepatic and the splenic arteries involved in the neoplasm

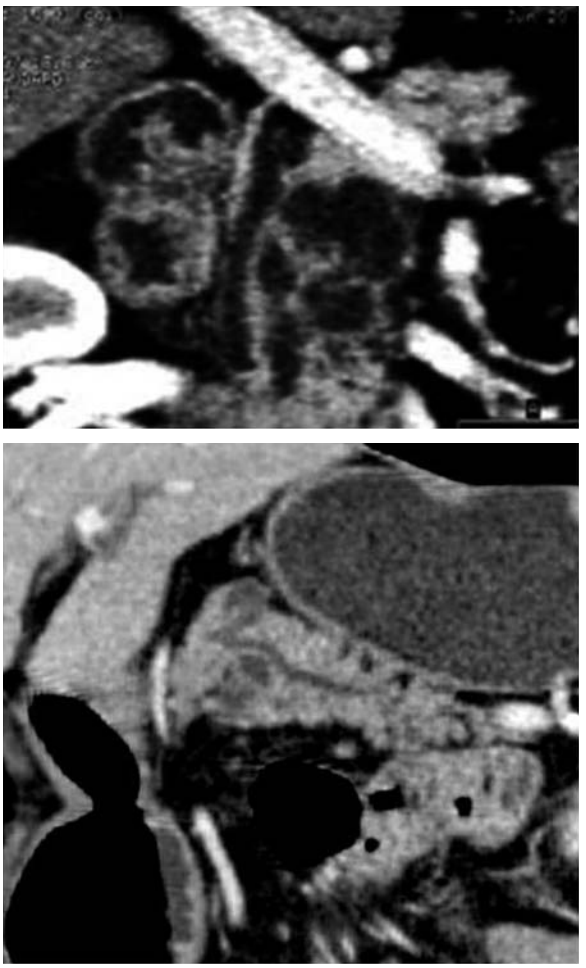

a

b

Fig. 21.7a,b. Coronal oblique MPR image (**a**) showing the dilation of the main pancreatic duct due to the adjacent cystic lesion (IPMN) of the pancreatic head; in the MinIP (**b**) image it is possible to highlight the communication between the lesion and the main pancreatic duct as well as the tumour multifocality

Mainly CPR, because of the natural ductal curvature, permits to display on a two-dimensional image the course of the main pancreatic duct, to visualise its contents and to clearly measure its dimensions; moreover, CPR allows to highlight the dilation, stenosis and possible calcification; reformatted bi-dimensional imaging also allows the clear analysis of lesion morphological characteristics (thin/thick septa, presence of calcification and their location inside the lesion), providing additional imaging details (Sahani et al. 2006).

Regarding 3D imaging, the most frequently applied technique when analysing cystic pancreatic neoplasms is certainly MinIP, usually obtained using multi-projection volume reconstruction (MPVR) software by selecting an oblique slab that contained the entire lesion/anatomical structure to be evaluated; MinIP permits to highlight hypodense tumours in order to increase the conspicuity of the lesion, the common bile duct and pancreatic dilated ducts (Nino-Murcia et al. 2003), thus furnishing a better visualisation of small lesions and finest ductal details (Fig. 21.8).

21.6 Pancreatitis

CT of the abdomen is the standard imaging modality for evaluating acute and chronic pancreatitis and their complications. In addition, CT can be used as a prognostic indicator of the severity of acute pancreatitis, mainly because it allows a complete visualization of the pancreas and retroperitoneum. As well as in the study of other pancreatic disease, imaging reformation is useful and often applied in the evaluation of acute and chronic pancreatitis, not only for diagnosis, but also for the study of possible complications.

As in the study of pancreatic neoplasms, also in the post-processing imaging evaluation of pancreatitis, bi-dimensional techniques (MPR and CPR) are often applied. The diagnosis of acute pancreatitis performed by MDCT is in fact based mainly on some peculiar imaging characteristics, quite well defined by axial images only, such as periglandular edema, focal or diffuse enlargement of the pancreas, with inhomogeneous enhancement, irregular contour of the pancreatic margins, thickening of peripancreatic fat planes, thickening of fascial planes and the presence of intraperitoneal or retroperitoneal fluid collections,

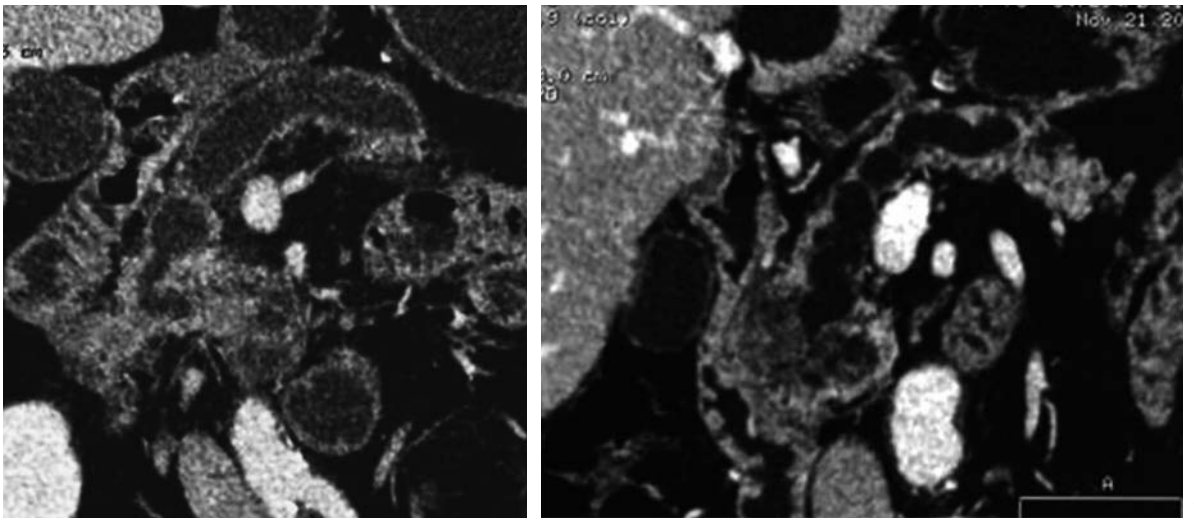

Fig. 21.8a,b. Coronal oblique MinIP images show the dilation of all the main pancreatic duct (**a**) and the mucinous cistoadenocarcinoma of the pancreas causing the stenosis (**b**)

most commonly found in the peripancreatic and anterior pararenal spaces (Balthazar et al. 1985, 2002).

The evaluation of complications, instead, often requires image post-processing: the presence of fluid collections, abscesses or haemorrhage can in fact be well defined by applying MPR on sagittal, coronal or oblique planes, in order to evaluate the relationships between the pancreas and omental recesses; also in the evaluation of pseudocysts, in order to obtain a differential diagnosis with cystic neoplasms, it is correct to apply a 3D technique such as MinIP that can emphasize the absence of communications between the lesion and the pancreatic duct (for differential diagnosis with IMPN) and that highlights the psuedocystic wall and internal lesion characteristics, in order to pose the differential diagnosis with serous/mucinous cistoadenoma (Cohen-Scali et al. 2003). MIP and VR can, in any event, be useful in the evaluation of suspected vascular complications, such as venous thrombosis and pseudoaneurysm formation.

Bi- and three-dimensional imaging can, moreover, constitute a diagnostic tool of evaluation also of chronic pancreatitis; CPR can in fact display on a single plane the entire gland, emphasising the parechymal atrophy with or without fatty replacement as well as focal enlargement found in association with ductal dilation, calcifications and irregularity. MPR, associated with MinIP or not, can finally be applied in the evaluation of pseudocysts and overall biliary duct stenosis and dilations, frequently due to intraductal calcifications or post-inflammatory stenosis (Fig. 21.9).

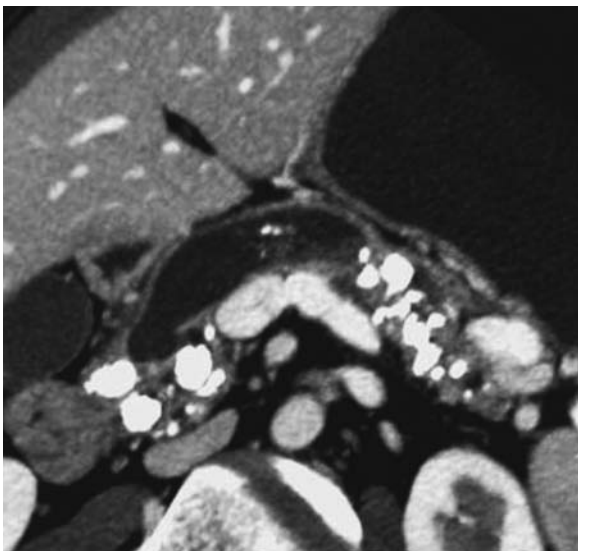

Fig. 21.9. Patient with chronic pancreatitis. Axial oblique MPR showing the dilation of the Wirsung and the multiple coarse calcifications located all over the gland

Conclusions

In conclusion, thanks to the advent of multidetector technology, CT has allowed the performance of very accurate studies of the pancreatic gland, permitting to obtain a high quality resolution of post-processing techniques, permitting then a precise definition of the entire peri-pancreatic anatomy and thus the

finest pre-operative evaluation in case of pancreatic diseases.

The recent development of virtual CT pancreatic evaluation, moreover, opens new exciting fields of application, showing better results than previous techniques and resulting particularly useful, especially for surgical planning.

References

Achenbach S, Moshage W, Ropers D, Bachmann K (1998) Curved multiplanar reconstructions for the evaluation of contrast enhanced electron beam CT the coronary arteries. Am J Roentgenol 170:895–899

Allema JH, Reinders ME, van Gulk TM et al (1995) Prognostic factors for survival after pancreaticoduodenectomy for patients with carcinoma of the head region. Cancer 75:2069–2076

Baek SY, Sheafor DH, Keogan MT et al (2001) Two-dimensional multiplanar and three-dimensional volume-rendered vascular CT in pancreatic carcinoma: interobserver agreement and comparison with standard helical techniques. Am J Roentgenol 176:1467–1473

Balthazar EJ, Ranson JH, Naidich DP et al (1985) Acute pancreatitis: prognostic value of CT. Radiology 156: 767–772

Balthazar EJ (2002) Acute pancreatitis: assessment of severity with clinical and CT evaluation. Radiology 223:603–613

Brugel M, Link TM, Rummeny EJ et al (2004) Assessment of vascular invasion in pancreatic head cancers with multislice CT: value of multiplanar reconstructions. Eur Radiol 14:1188–1195

Calhoun PS, Kuszyk BS, Heath GG et al (1999) Three-dimensional volume rendering of spiral CT data: theory and method. RadioGraphics 19:745–764

Cohen-Scali F, Vilgrain V, Brancatelli G et al (2003) Discrimination of unilocular macrocystic serous cystoadenoma from pancreatic pseudocysts and mucinous cystadenoma with CT: initial obsrevations. Radiology 228:727–733

Fishman EK, Horton KM, Urban BA (2000) Multidetector CT angiography in the evaluation of pancreatic carcinoma: preliminary observation. J Comput Assist Tomogr 24:849–853

Fishman EK, Ney DR, Heath DG et al (2006) Volume rendering versus maximum intensity projection in CT angiography: what works best, when and why. RadioGraphics 26:905–922

Fortner JG, Klimstra DS, Senie RT et al (1996) Tumor size is the primary prognosticator for pancreatic cancer after regional panceatectomy. Ann Surg 223:147–153

Hong KC, Freeny PC (1999) Pancreatioduodenal arcades and dorsal pancreatic artery: comparison of CT angiography with three-dimensional volume rendering, maximum intensity projection and shaded-surface display. AJR AM J Roentgenol 211:337–343

Horton KM, Fishman EK (2002) Volume-rendered 3D CT of the mesenteric Vasculature: Normal Anatomy, Anatomic Variants and pathologic conditions. RadioGraphics 22:161–172

Horton KM, Hruban RH, Yeo C et al (2006) Multi-detector row CT of pancreatic islet cell tumors. RadioGraphics 26:453–464

Hu H, He D, Foley D et al (2000) Four multidetector-row helical CT: image quality and volume coverage speed. Radiology 215:55–62

Itay Y, Minami M (2001) Intraductal papillary mucinous tumor and mucinous cystic neoplasm: CT and MRI findings. Int J Gastrointest Cancer 30:47–63

Lu DSK, Reber HA, Krasny RM et al (1997) Local staging of pancreatic cancer: criteria for unresectability of major vessels as revealed by pancreatic phase, thin section helical CT. Am J Roentgenol 168:1439–1443

Mazzeo S, Cappelli C, Caramella D et al (2007) Evaluation of vascular infiltration in resected patients for pancreatic cancer: comparison among multidetector CT, intraoperative findings and histopathology. Abdom Imaging Mar 27 (Epub ahead of print)

Mc Nulty NJ, Francis IR, Platt JF et al (2001) Multi-detector row helical CT of the pancreas: effect of contrast enhanced multiphasic imaging on enhancement of the pancreas, peripancreatic vasculature and pancreatic adenocarcinoma. Radiology 220:97–102

Nakagohri T, Jolesz FA, Okuda S et al (1998) Virtual pancreatoscopy of mucin producting pancreatic tumors. Computed Aid Surg 3:264–268

Nino-Murcia M, Jeffrey RB Jr, Beaulieu CF et al (2001) Multidetector CT of the pancreas and bile duct system: value of curved planar reformations. Am J Roentgenol 176:689–693

Nino-Murcia M, Jeffrey RB et al (2002) Multidetector-row CT and volumetric imaging of pancreatic neoplasms. Gastroenterol Clin North Am 31:881–896

Jing-Shan Gong, Jin-Min Xu (2004) Role of curved planar reformations using multidetector spiral CT in diagnosis of pancreatic and peri-pancreatic diseases. World J Gastroenterol 10:1943–1947

Prassopoulos P, Raptopulos V, Chuttani R et al (1998) Development of virtual CT cholangiopancreatoscopy. Radiology 209:570–574

Prokesch RW, Chow LC, Beaulieu CF et al (2002) Local staging of pancreatic carcinoma with multidetector-row CT: use of curved planar reformations–initial experience. Radiology 225:759–765

Rieker O, Duber C, Neufang A et al (1997) CT angiography versus intra-arterial digital subtraction angiography for assessment of aortoiliac occlusive disease. AJR 169:1133–1138

Rubin GD, Dake MD, Semba CP et al (1995) Current status of three dimensional spiral CT scanning for imaging the vasculature. Radiol Clin North Am 33:51–70

Sahani DV, Kadavigere R, Blake M et al (2006) Intraductal papillary mucinous neoplasms of pancreas: multi detector row CT with 2D curved reformations–Correlations with MRCP. Radiology 238:560–569

Sata N, Kurihara K et al (2006) CT virtual pancreatoscopy: a new method for diagnosing intraductal papillary mucinous neoplasm (IPMN) of the pancreas. Abdom Imaging 31:326–331

Tanizawa Y, Nakagohri T, Konishi M et al (2003) Virtual pancreatoscopy of pancreatic cancer. Hepatogastroenterology 50:559–562

Further Reading

Irie H, Honda H, Albie H et al (2000) MR cholangiopancreatographic differentiation of benign and malignant intraductal mucin-producing tumors of the pancreas. AJR Am J Roentgenol 174:1403–1408

Lüttges J, Vogel I et al (1998) The retroperitoneal resection margin and vessel involvement are important factors determining survival after pancreaticoduodenectomy for ductal adenocarcinoma of the head of the pancreas. Virchows Arch 433:237–242

Maeshiro K, Nakayama Y, Yasunami Y et al (1998) Diagnosis of mucin-producing tumor of the pancreas by balloon-catheter endoscopic retrograde pancreatography: compression study. Hepatogastroenterology 45:1986–1995

Mehmet ES, Ichikawa T, Sou H et al (2006) Pancreatic adenocarcinoma: MDCT versus MRI in the detection and assessment of loco-regional extension. J Comput Assist Tomogr 30:583–590

Procacci C, Graziani R, Bicego E et al (1996) Intraductal mucin-producing tumors of the pancreas: imaging findings. Radiology 198:249–257

Tamm E, Charnsangavej C, Szklaruk J et al (2001) Advanced 3-D imaging for the evaluation of pancreatic cancer with multidetector CT. Int J Gastrointest Cancer 30:65–71

Biliary Tract

22

Piero Boraschi and Francescamaria Donati

CONTENTS

22.1 Introduction

In recent years, the advent of endoscopic biliary surgery and the introduction of MR cholangiopancreatography (Barish et al. 1995; Becker et al. 1997; Guibaud et al. 1994; Hall-Craggs et al. 1993; Ishizaki et al. 1993; Macaulay et al. 1995; Morimoto et al. 1992; Reinhold et al. 1995; Reinhold and Bret 1996; Soto et al. 1995) have renewed an interest in the techniques of pancreatobiliary tract imaging.

Among the imaging techniques currently advocated for evaluating the biliary tract, sonography and computed tomography (CT) are frequently used in the initial noninvasive approach in patients with symptoms and signs referable to the pancreaticobiliary system. In many instances, particularly in cases of malignant bile duct obstruction, sonography and CT may provide the necessary information for planning further treatment.

P. Boraschi, MD; F. Donati, MD
2nd Department of Radiology, Pisa University Hospital, Via Paradisa 2, 56124 Pisa, Italy

Although these modalities are sensitive in the detection of biliary obstruction, direct colangiography [including endoscopic retrograde cholangiopancreatography (ERCP)] and, to a lesser extent, percutaneous transhepatic cholangiography (PTC), often remain the standard of reference for visualizing the presence and level of the biliary obstruction, as well as suggesting its etiology. Significant advantages of ERCP include the unparalleled resolution obtained and the ability to perform therapeutic measures at the time of initial diagnosis. Nevertheless, ERCP is operator-dependent and is limited by considerable morbidity (1%–7%) and mortality (0.2%–1%). Complications, including pancreatitis, sepsis, hemobilia, and bowel perforation can be life-threatening, and delay or even diminish the chance of managing the primary disease.

This situation has changed since the advent of MR cholangiopancreatography, which was introduced in 1991 by Wallner et al. (1991). This technique is an absolutely noninvasive imaging modality that combines the benefits of both projectional and cross-sectional imaging techniques, and provides an overview of the entire biliary and pancreatic ductal system by means of data acquisition and image reconstruction rendered on the coronal plane in a conventional cholangiography fashion. A major challenge of MRCP is to achieve accuracy comparable to that of ERCP for most clinical indications requiring direct opacification of the pancreaticobiliary ductal system.

22.2 MR Cholangiography and CT Cholangiography

MR cholangiography (MRC) has become a reliable diagnostic method of investigating the biliary tree since it is a completely noninvasive examination, is

performed rapidly and does not expose the patient to ionizing radiation or iodinated contrast material. Technical refinements such as advances in MR hardware and software have improved image quality of MRC and shortened examination times. It should be noted, however, that the performance of MRC is operator-dependent and radiologist-intensive. The major disadvantage of MRC is that it is entirely diagnostic, as opposed to ERCP, which provides diagnostic information as well as access for therapeutic interventions.

This technique has shown high diagnostic potentialities and has been effectively introduced in clinical practice for the evaluation of many pancreatobiliary diseases (Becker et al. 1997; Reinhold and Bret 1996). The clinical applications of MRC include diagnosis of common bile duct stones (Boraschi et al. 1999b; Guibaud et al. 1994); malignancies of the biliary tract; congenital anomalies such as aberrant bile ducts, choledochal cysts and Caroli disease; primary sclerosing cholangitis (PSC); and gallbladder disease such as stones and carcinoma. In addition, MR cholangiography plays a crucial role in the evaluation of patients who have experienced an incomplete or failed ERCP attempt, as well as in the evaluation of post-surgical biliary tract disorders such as in liver recipients (Boraschi et al. 2001; Boraschi and Donati 2004) or in patients for whom ERCP is difficult or impossible to perform due to surgical alterations of the gastrointestinal tract. As a result of these expanding clinical applications, MRC has replaced diagnostic ERCP in some institutions as a means of identifying biliary diseases. Once disease has been detected with MRC, patients may then be triaged appropriately for therapy with ERCP, surgery or radiologic intervention.

The MRC technique is based on heavily T2-weighted images obtained with different pulse sequences. As a result, stationary fluids, including bile and pancreatic secretions, have a high signal intensity, while solid organs have a low signal intensity. This combination of imaging characteristics means that MRC provides optimal contrast between the hyperintense signal of bile and the hypointense signal of the background.

T2-weighted gradient-echo sequences with the steady-state free precession (SSFP) technique were initially used by Wallner et al. (1991), Morimoto et al. (1992), Hall-Craggs et al. (1993), and Ishizaki et al. (1993). Subsequently, other investigators have utilized two-dimensional (2D) and three-dimensional (3D) heavily T2-weighted fast spin-echo sequences to generate MRCs (Barish et al. 1995; Boraschi et al. 1999a; Boraschi et al. 1999b; Reinhold et al. 1995; Reinhold and Bret 1996; Soto et al. 1995). In a study comparing 2D fast spin-echo and 3D SSFP pulse sequences, Reinhold et al. (1995) reported that fast spin-echo sequences are significantly better for the visualization of both biliary tree and pancreatic ducts. More recent studies have described the clinical usefulness of MRC performed with a new heavily T2-weighted sequence, the half-Fourier rapid acquisition with relaxation enhancement (RARE) sequence with or without image reconstruction for the evaluation of the biliary system. This technique has a very fast acquisition time and shows slow-flowing fluids such as bile as being very bright (Miyazaki et al. 1996; Regan et al. 1996). Actually, the most common T2-weighted MRC technique is the single-shot fast spin-echo sequence (SSFSE, GE Healthcare) or half-Fourier acquisition single-shot turbo spin-echo (HASTE, Siemens). In general, the first step in performing MRC is to localize the biliary tract by acquiring a scout MRC obtained at a section thickness of 40–70 mm (thick-slab or single-shot projection MRC). Although this technique permits depiction of the majority of the biliary tract on a single image, it does not allow for assessment of the subtle details of the ductal system in many instances. To depict the finer details of the ducts, a multi-slice, thin-slab MRC technique is often employed. Multiple, thin-slab images of the biliary tract are acquired at section thickness ranging from 2 to 5 mm in the coronal plane and at a variety of angles that optimally depict the ductal system. Although many diagnostic decisions are made on the basis of 2D or 3D thin-slab images, these images may be manipulated with post-processing algorithms in order to generate 3D reconstruction of the biliary ductal system. Other new pulse sequences may have potential in MRC, such as steady-state free precession sequences (fast imaging using steady-state acquisition, FIESTA, GE Healthcare; fast imaging with steady-state precession, TrueFISP, Siemens) or a 3D fast recovery fast spin echo pulse sequence (3D-FRFSE, GE Healthcare), which provides high-resolution heavily T2-weighted images with shorter acquisition time compared to conventional 3D FSE imaging (Sodickson et al. 2006). The use of recently introduced technical advancements such as parallel imaging and prospective acquisition correction may further increase the diagnostic value of MRC. In fact, the section thickness can be decreased to less than 1 mm with use of these technical improve-

ments. Additional information may be obtained when conventional T1- and T2-weighted techniques are performed in the axial and/or coronal plane in conjunction with MRC (Boraschi et al. 1999a). In the setting of a suspected malignancy, MR angiography may also yield important information in determining the respectability of neoplasms.

More recently, functional MR cholangiography (fMRC) has been proposed as an alternative or complementary technique to conventional T2-weighted MRC. This emerging technique has the potential to provide a comprehensive evaluation for the anatomical and functional assessment of the gallbladder and biliary tree (Fayad et al. 2005). fMRC is performed after preliminary intravenous administration of a hepatobiliary contrast agent such as mangafodipir trisodium (Mn-DPDP, Teslascan; GE Healthcare) or gadobenate dimeglumine (Gd-BOPTA, MultiHance, Bracco), which is excreted via the biliary system. These hepatobiliary contrast agents are administered intravenously, taken up by the liver, and transported to bile, where they cause T1 shortening as a result of paramagnetic effects. Because they are excreted primarily via the biliary tract, Mn-DPDP-enhanced and Gd-BOPTA MRI are suitable as MR cholangiogram to provide the assessment of the hepatobiliary system. Hence, fMRC images of the biliary system are obtained as follows: approximately 30 min after the injection of mangafodipir, or between 1 and 2 h after Gd-BOPTA administration, high resolution T1-weighted 3D gradient-recalled echo (GRE) sequences are obtained in coronal, coronal oblique, and axial planes. If initial images do not show contrast material in the biliary tree, this sequence can be repeated as needed at longer intervals to obtain additional delayed imaging.

The most important advantage of fMRC is its ability to depict functional information. Partial and complete obstruction may be distinguished along with the inciting anatomic abnormality, a feature particularly useful for treatment planning. In addition, variant bile duct anatomy (Figs. 22.1, 22.2), complex biliary-enteric anastomoses (Fig. 22.3), biliary stent patency (particularly non-metal stents), and suspected biliary extravasation can be thoroughly evaluated with fMRC (Fayad et al. 2005).

CT is commonly indicated for the evaluation of suspected hepatic and biliary pathology. The recent introduction of multidetector CT (MDCT) provides unique capabilities that are valuable especially in hepatic volume acquisitions, combining short scan times, narrow collimation and the ability to obtain multiphase data. Such technical improvement allows thinner slices to be obtained in shorter scan times, with good patient compliance and less motion artifacts. As a noninvasive technique, MDCT dedicated to the biliary tract represents a good alternative to MRC.

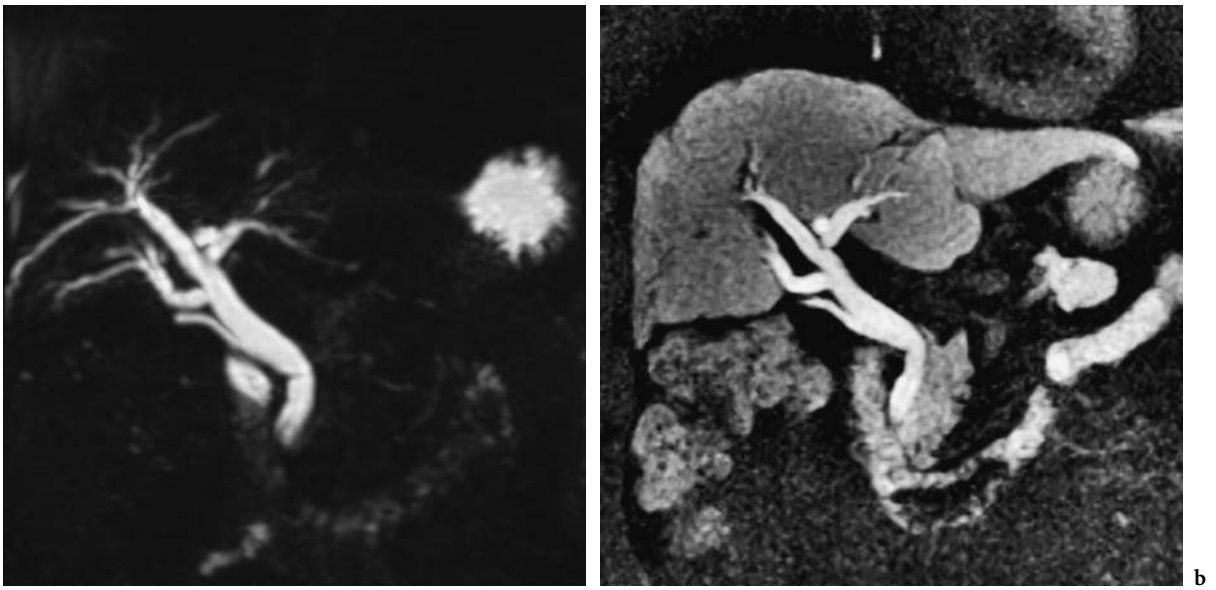

a b

Fig. 22.1a,b. Aberrant bile duct. Both coronal oblique MIP 3D heavily T2-weighted (**a**) and mangafodipir-trisodium-enhanced T1-weighted (**b**) MR cholangiograms show the aberrant drainage of the right posterior duct into the common hepatic duct; in this patient with a history of recurrent choledocholithiasis after cholecystectomy, a residual cystic duct is also appreciable

Fig. 22.2a–e. Choledochal cyst. Coronal oblique (**a**) and curved planar (**b**) reformations of multidetector CT cholangiography without contrast agent well exhibit a choledochal cyst with concomitant dilation of common, right and left hepatic ducts. MR cholangiography, obtained in the same patient with both conventional T2-weighted images (**c**,**d**) and MIP 3D mangafodipir-trisodium-enhanced T1-weighted sequence (**e**), confirms these findings

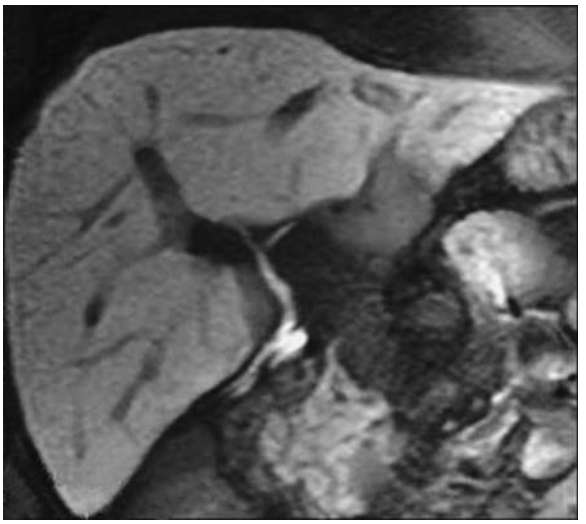

Fig. 22.3. Bilio-enteric anastomosis in liver transplant patient. Coronal MIP 3D mangafodipir-trisodium-enhanced T1-weighted MR cholangiogram permits both morphological and functional evaluation of the bilio-enteric anastomosis. No complication is present in this case

CT cholangiographic procedures can be divide into two groups: those in which the biliary system is accentuated as a low-attenuating structure on minimum intensity projection or multiplanar reformatted images (no cholangiographic contrast agent is needed) and those in which the bile duct is highlighted as a high-attenuating structure with use of oral cholangiographic contrast medium, intravenous cholangiographic contrast agent, or direct cholangiography (Ahmetoglu et al. 2004; Alibrahim et al. 2006; Cabada Giadàs et al. 2002; Kim et al. 2004; Zandrino et al. 2002).

CT techniques are especially useful when MRI is unavailable or contraindicated, or when the quality of MRC images is suboptimal (CT cholangiography, in fact, has a better spatial resolution, hence its clearer depiction of small ducts) but to date the use of radiation, the low availability of biliary contrast media and the possible adverse reactions to iodinated contrast agents all have had a negative impact on a large-scale diffusion. However, some studies have reported promising results of 3D multidetector row CT cholangiography after intravenous injection of iodipamide meglumine for defining the extent of ductal invasion by hilar cholangiocarcinoma (Kim et al. 2006) and for assessing biliary anatomy of potential living liver donors (Wang et al. 2005). In the right lobe, living transplantation assessment of the biliary anatomy and identification of normal variants are challenging points in the donor selection process and in surgical planning. Relevant preoperative surgical information includes an assessment of donor hepatic segmental volume, exclusion of focal or diffuse donor hepatic abnormalities (such as incidental liver masses, steatosis) and depiction of vascular and biliary anatomy to estimate the number of vascular and biliary anastomoses in the recipient.

22.3 Image Processing Techniques

Biliary tract examinations using rapid 3D volumetric techniques can be performed with both multidetector CT and MR cholangiography. Integration between volumetric acquisition and 3D surface and volume-rendering techniques permits the study of the biliary tract in a noninvasive way.

Knowledge of segmental anatomy and intersegmental biliary connections is an essential prerequisite to the effective management of patients with complex bile duct anatomy (e.g., congenital abnormalities, bilio-enteric anastomoses). Three-dimensional imaging techniques are also very useful for an accurate anatomical assessment before surgery.

Preliminary experiences on 3D reconstructions of the biliary system have been carried out by some investigators with surface and volume rendering of CT cholangiography data sets for preoperative evaluation before laparoscopic cholecystectomy (Kinami et al. 1999). Three-dimensional CT cholangiography (Fleishmann et al. 1996; Kinami et al. 1999; Klein et al. 1993; Sajjad et al. 1999) has been reported as a 3D shaded surface display image of the biliary tract obtained by using helical CT after intravenous administration of biliary contrast medium (meglumine iotroxate). This technique can also be performed by means of a percutaneous transhepatic cholangio-drainage tube. Slice thickness of 3 mm with a pitch of up to 1.7 in a single breath-hold acquisition has been considered essential for an optimal scanning protocol. A 3D helical CT study of the biliary tract without cholangiographic contrast material has also been proposed by others (Zandrino et al. 2002; Zeman et al. 1995).

Optimization of CT cholangiography using multidetector scanners has improved the potentialities of this technique, which has been recently rehabili-

tated (Ahmetoglu et al. 2004; Kim et al. 2004; Kim et al. 2006; Nino-Murcia et al. 2001; Wang et al. 2005). Utilizing a 16-detector row CT scanner, 16 helical scans are captured in a single 0.5-s gantry rotation, and this increase in speed allows routine use of a very thin collimation (the 1-mm transverse sections can be reconstructed at 0.7-mm intervals). The advent of MDCT – owing to rapid scanning, thinner (1 mm) sections and the parallel escalation in the capabilities of the workstations – has enabled the evolution from section-based to volume-based techniques. Therefore, we assumed that high axial resolution of MDCT allows one to obtain higher quality multiplanar reformations and 3D reconstructions of the biliary tree.

However, with CT cholangiography performed with oral or intravenous contrast agents, reliable biliary excretion of contrast material cannot be guaranteed in patients with high-grade biliary obstruction, and CT cholangiography performed without biliary contrast agent does not enable detailed 3D evaluation of the biliary tree in the absence of significant distention.

The diagnostic approach to biliary tract pathology has undergone a major change due to the introduction of MRC. Actually, this noninvasive imaging technique for the visualization of the biliary ducts with images similar to those obtained with ERCP, PTC or even CT cholangiography, can be performed with both high-resolution heavily T2-weighted sequences and T1-weighted 3D GRE sequences after preliminary intravenous administration of a hepatobiliary contrast agent.

Various post-processing techniques have been shown to be effective in displaying the biliary tract. Multiplanar reformatted images in the coronal, oblique coronal or oblique axial plane help to define the location and extent of the disease shown on native images (Fig. 22.4). However, since most structures of interest do not lie within a single plane, this technique is limited to the visualization of the entire biliary tract, and particularly of the entire common bile duct, unless curved planar reformation is used (Nino-Murcia et al. 2001).

CT and MR source images may be processed to generate 3D reconstructions, which can be obtained with both external and endoluminal points of view of the organ anatomy. The maximum intensity projection (MIP), the minimum intensity projection (MinIP), the shaded surface display (SSD), the perspective volume rendering (VR), and the multiplanar volume reconstruction (MPVR) algorithms provide external views of the biliary tract. Endoluminal points of view of the biliary tree can be obtained with virtual endoscopy (VE) by using either MRC or CT cholangiography data sets.

22.3.1 Shaded Surface Display (SSD), Maximum Intensity Projection (MIP), and Minimum Intensity Projection (MinIP)

Shaded surface display (SSD) is a technique that was in use a few years ago. With this algorithm a threshold value in the Hounsfield density/intensity scale is set so that only tissues with voxel values equal or superior to the threshold are rendered. Then a virtual light source creates light and shading effects simulating a 3D perspective. The result resembles a cast, as only external overlapping surfaces can be appreciated, while all the information beyond this interface is lost. After lengthy pre-processing, a 3D model of the biliary tract can be constructed and manipulated. However, anything not related to the selected surface was discarded, resulting in the loss of vital information.

In the MIP algorithm a parallel ray beam is projected through a 3D matrix of interpolated data to create, without information loss, an image where any pixel is assigned the maximum value encountered by the ray along its axis. Alternatively, an analogue algorithm can assign the minimum value to the pixels, generating a minimum intensity projection (MinIP) image (Rao et al. 2005; Raptopoulos et al. 1998).

MIP and SSD can provide a global map of the biliary tree anatomy that can be helpful in the interpretation of native MRC and CT cholangiography images (particularly post-surgical anatomy, anatomic variants of the pancreatico-biliary ductal system and large biliary neoplasms). In fact, in patients with cholangiocarcinomas and bilioenteric anastomoses, 3D reconstructed images are helpful in identifying the infiltration of common bile duct and intrahepatic ducts, and in correctly assessing post-surgical anatomy of the biliary system (Figs. 22.5, 22.6).

However, some have stressed the limitations of such algorithms in the depiction of small intraductal pathology, particularly in the detection of small calculi in the common bile duct using MRC (Boraschi et al. 1999a; Regan et al. 1996; Reinhold and Bret 1996). Therefore, meticulous

a

b

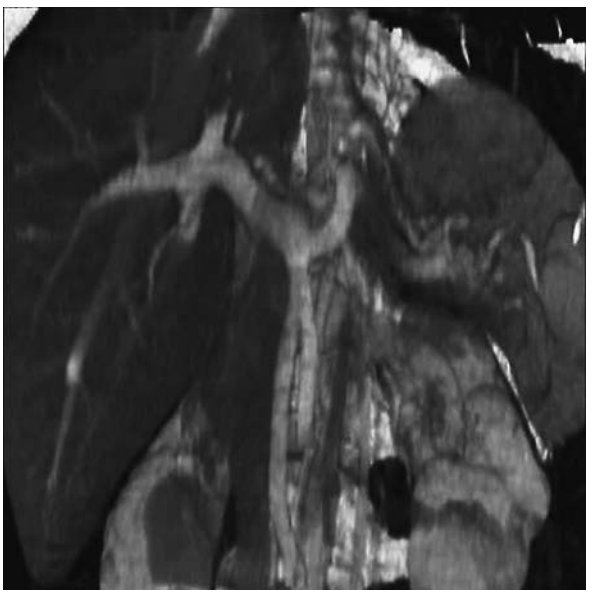

c

Fig. 22.4a–c. Hilar cholangiocarcinoma. Axial oblique reformatted CT image (**a**) reveals atrophy of the left lateral hepatic segments and dilation of the intrahepatic bile ducts and right and left hepatic ducts. MPVR CT image (**b**), obtained in a coronal oblique plane, demonstrates extension of the neoplastic lesion involving the proximal common hepatic duct and right and left hepatic duct. VR 3D image (**c**), obtained in the portal venous phase, exhibits neoplastic infiltration of left portal vein

review of coronal and axial images is extremely important to allow the identification of small endoluminal pathologies. In fact, if fluid completely surrounds the intraluminal filling defect, the latter is missed on the reconstructed MIP and SSD images because it is obscured by the higher signal intensity of surrounding bile.

Three-dimensional CT cholangiography using MinIP is a relatively new technique in which routine iodinated intravenous contrast agent is given to enhance the hepatic parenchyma (Rao et al. 2005). The minimum intensity pixels within the liver (of fluid density as contained in the bile ducts) are picked up from the volumetric information available from the venous phase data sets using dedicated software, and are projected as a MinIP. In this manner, the high-density structures, such as the contrast-enhanced vessels and hepatic parenchyma, do not interfere in the final image, thus resulting in a 3D display of a low density biliary system. To date, there has been little reported work on 3D CT cholangiography using MinIP.

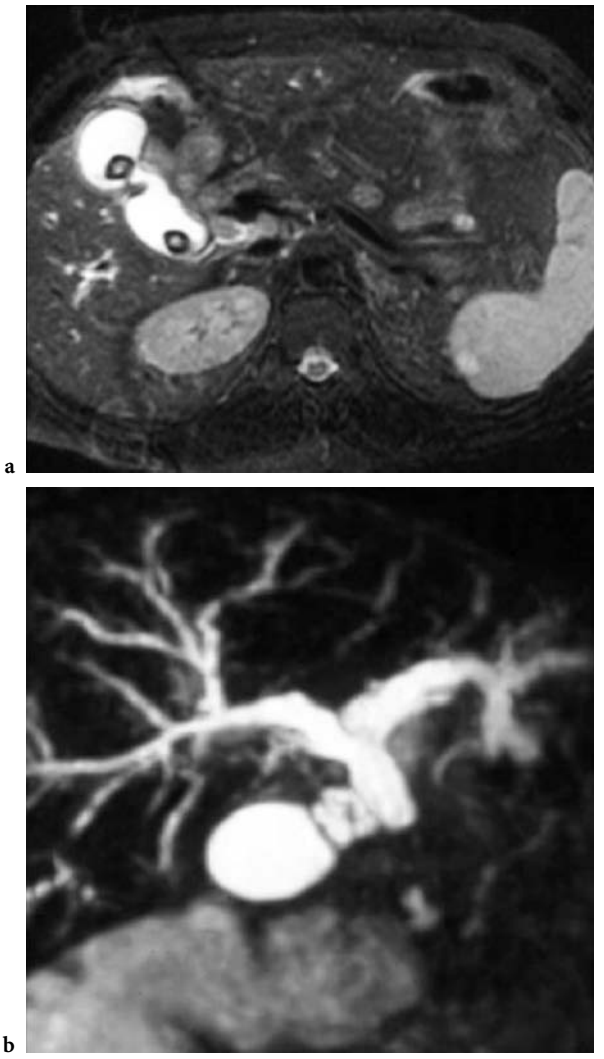

Fig. 22.5a,b. Gallbladder carcinoma. Axial heavily T2-weighted SSFSE image (**a**) exhibits multiple gallstones and a neoplastic thickness of the gallbladder wall, involving the adjacent liver parenchyma and the extrahepatic biliary tree. Coronal oblique MIP 3D heavily T2-weighted MR cholangiogram (**b**) shows marked dilation of intrahepatic bile ducts, right and left hepatic ducts, and common hepatic duct with signs of abrupt obstruction at this level

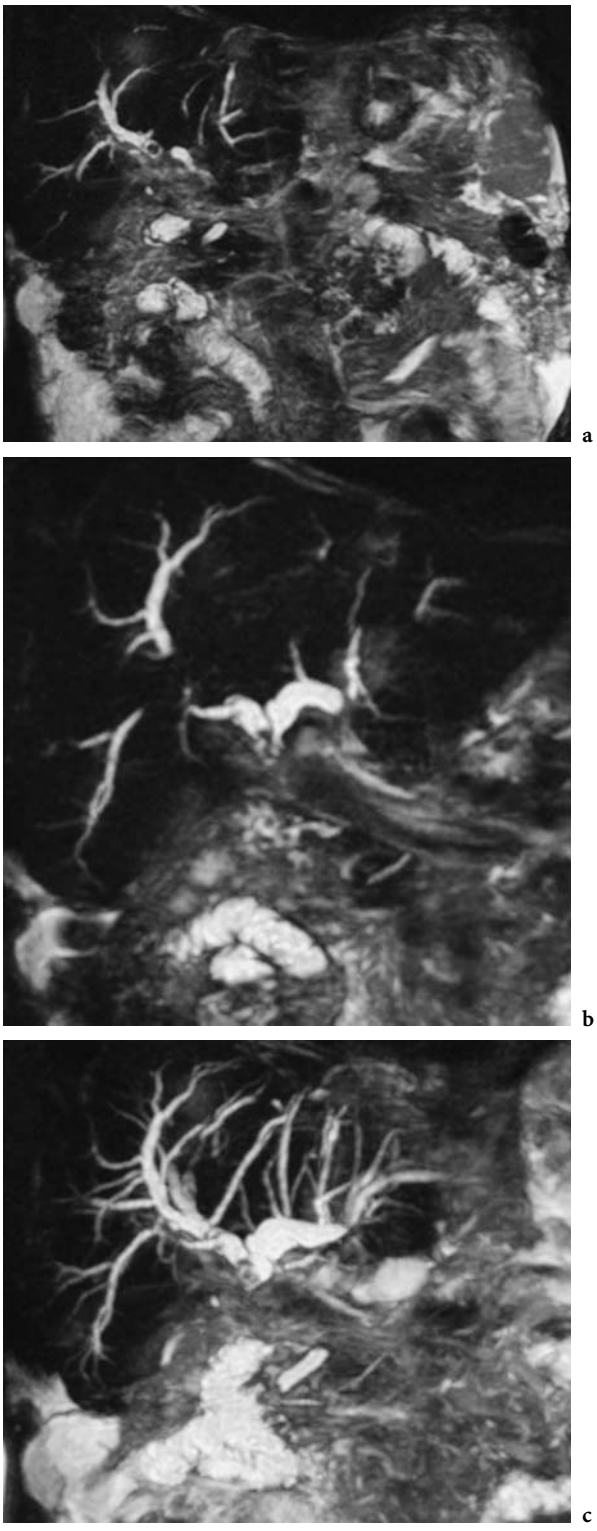

Fig. 22.6a–c. Biliary lithiasis in a patient with hepaticojejunostomy. Coronal thin MIP 3D heavily T2-weighted MR cholangiograms (**a**,**b**) show the presence of multiple stones into both the right hepatic duct and the pre-anastomotic common hepatic duct. Coronal thick MIP 3D heavily T2-weighted MR cholangiogram (**c**) better shows the dilation of the intrahepatic biliary system, the right and left hepatic ducts and the common hepatic duct

22.3.2 Volume Rendering (VR)

Rendering is the process of taking a collection of images in one form (for example, a stack of CT or MR slices) and applying an image processing technique in order to generate a single output image. Typically, the image output is interactive, with new images being calculated dynamically in response to operator input. With the advancement of processing power, the newer level of rendering, called perspective volume rendering, became practical.

In fact, VR is the latest development for 3D visualization of the anatomy of the biliary tree (Kondo et al. 2001; Neri et al. 2000; Wielopolski et al. 1999). This method allows one to simultaneously display different anatomical structures imaged within a single volume. It provides an image created by simulated rays of light, arising from a virtual source (i.e., the eye of the user look-

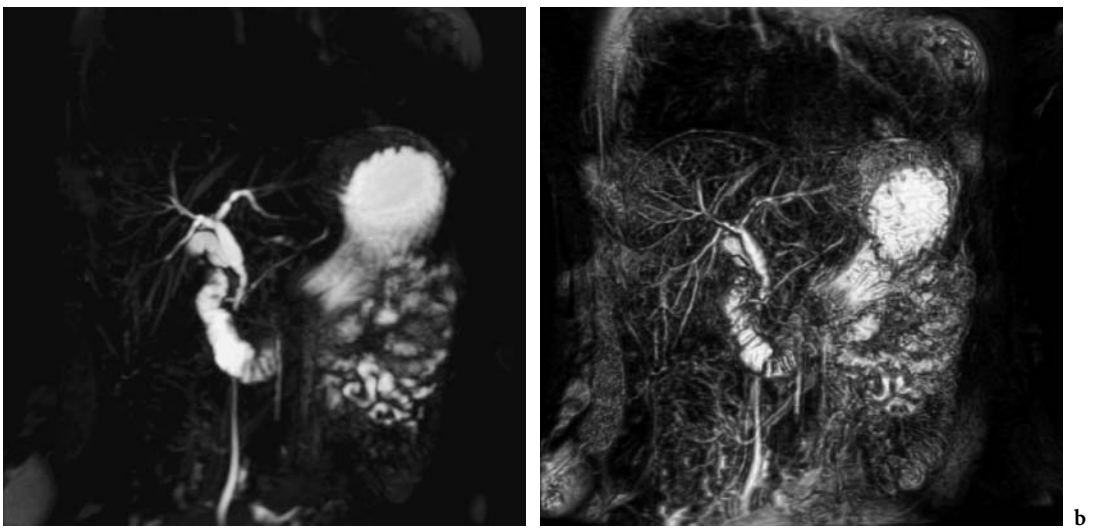

a b

Fig. 22.7a,b. Primary sclerosing cholangitis. Coronal MIP 3D heavily T2-weighted MR cholangiogram (**a**) demonstrates diffuse focal strictures of both the intrahepatic and particularly the extrahepatic bile ducts. MR VR with a large threshold (**b**) better visualizes the entire biliary system and characterizes the strictures showing thickening and irregularities of the ductal wall

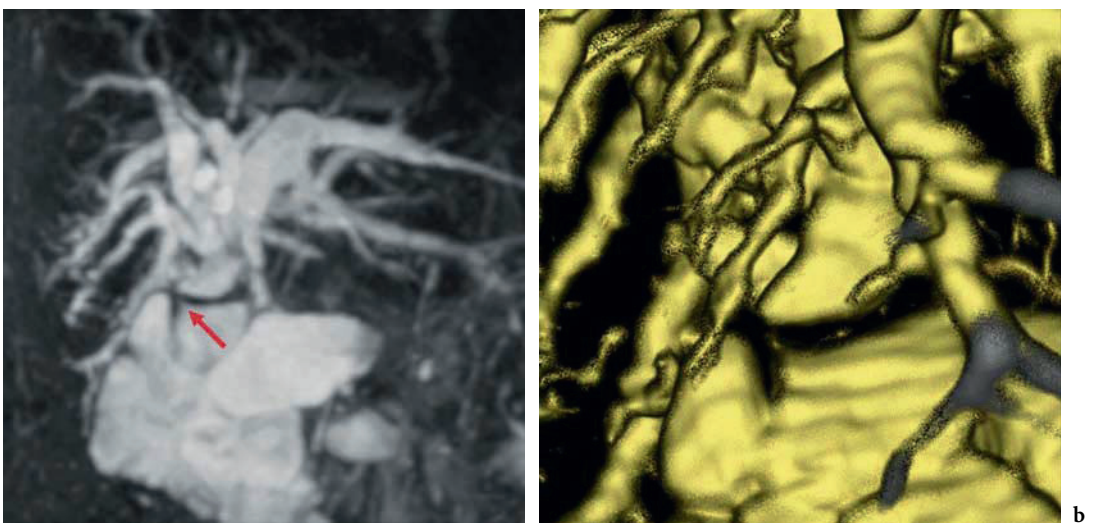

a b

Fig. 22.8a,b. Stenosis of hepaticojejunostomy. Coronal oblique MIP 3D heavily T2-weighted MR cholangiogram (**a**) and MR VR enlargement (**b**) accurately depict an anastomotic stricture (*arrow*) with marked dilation of the pre-anastomotic extra and intrahepatic biliary systems

ing through the computer display), traversing the imaging volume that has been attenuated by its contents, and assigns certain characteristics such as opacity, color, light and shininess to specific voxel values. In its purest form, this method does not use pre-processing, and no information is lost in the original data sets.

VR has the advantage of providing a clear roadmap of the entire biliary tree, but its real role in demonstrating pathological changes deserves further clinical evaluation (Fig. 22.7). We have identified possible applications of this image processing method in a follow-up of patients who previously underwent bilio-enteric anastomoses (Boraschi et al. 2000) (Fig. 22.8), whereas Kondo et al. (2001) suggest the use of volume rendering as an alternative to MIP reconstructions of MRC for evaluating choledocholithiasis (Fig. 22.9).

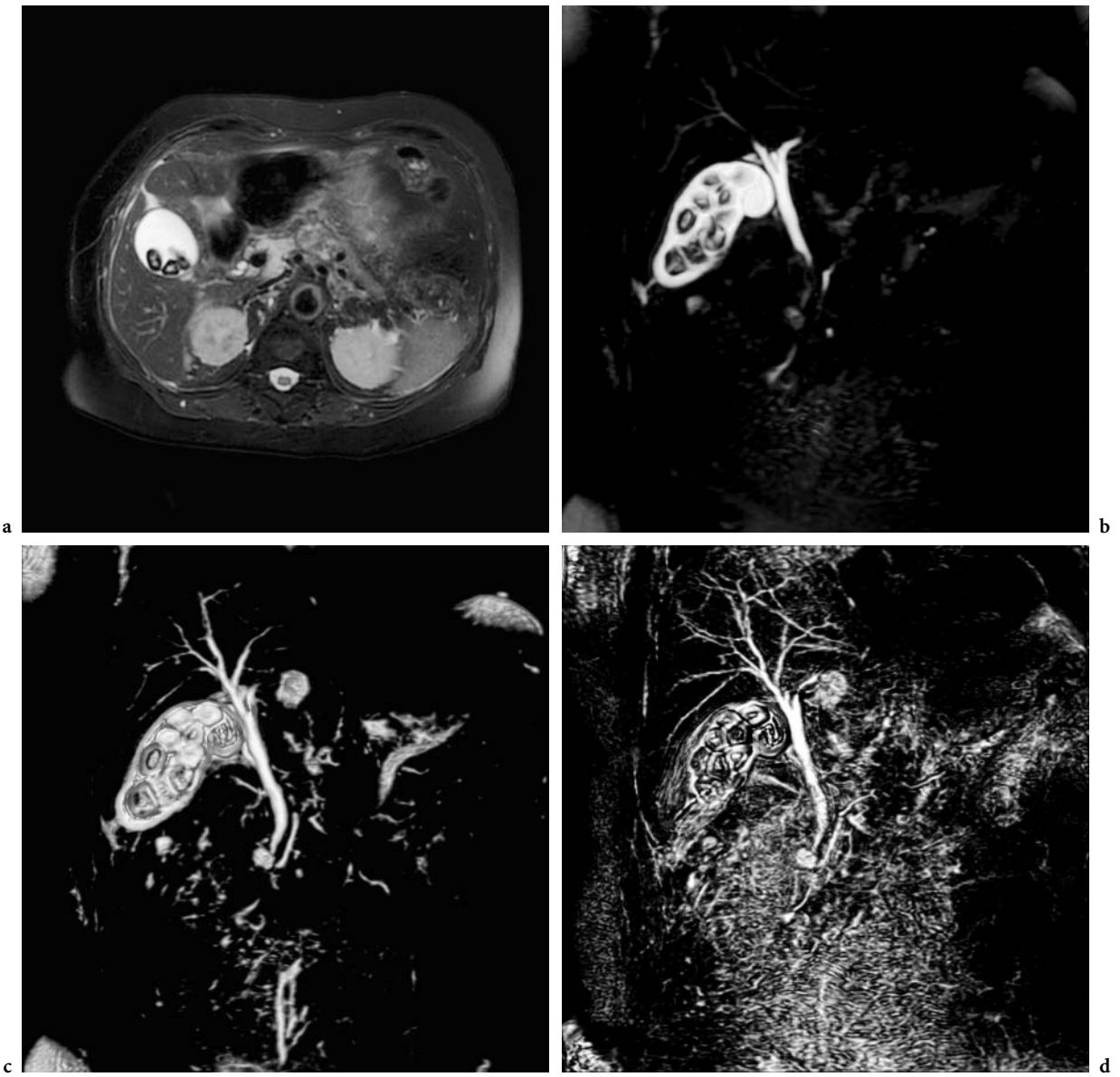

Fig. 22.9a–d. Gallstones. Axial T2-weighted FSE image (**a**) shows multiple stones in the gallbladder. Coronal thin MIP 3D heavily T2-weighted MR cholangiogram (**b**) depicts gallbladder lithiasis and shows a normal caliber of hepatic ducts and the common bile duct. MR VR images better demonstrate these findings; in particular, VR using a small threshold (**c**) permits the visualization of the subtle details, such as the calculi, while VR with a large threshold (**d**) permits an easier visualization of the entire biliary system

22.3.3 MR and CT Virtual Cholangioscopy

Virtual endoscopy (VE) permits intraluminal structures within the body to be visualized from inside in three dimensions. With either computed tomography or magnetic resonance imaging data sets, the approach has been successfully applied in the investigation of the colon, vessels, bronchial tree, middle and inner ear, cerebrospinal fluid spaces, urinary tract and biliary tract.

The exploration of the biliary tract with fiber optic cholangioscopy is a relatively new and well established procedure that has provided interesting applications in the diagnostic approach and therapeutic management of biliary stones, in the differential diagnosis between benign and malignant lesions, and in the staging of ductal malignancies (Picus 1995). However, this technique is operator-dependent, expensive, time-consuming, but most of all invasive and affected by many complications related to the use of the cholangioscope, such as hemorrhage into the biliary ducts (with a percentage ranging between 4.1% and 12%), laceration of the bile duct (2%), bacteriemia, vagal reactions, nausea, fever and diarrhea. Moreover, the large number of failed acquisitions has to be taken into consideration (Picus 1995).

Virtual simulation of fiber optic endoscopy can be obtained with a new software tool based on surface or volume rendering techniques, called "virtual cholangioscopy" when specifically applied to the study of the biliary system (Dubno et al. 1998; Neri et al. 1999a–c Prassopoulos et al. 1998).

Endoluminal views of the pancreatic and bile ducts can be obtained by rendering CT or MR data sets.

Virtual CT cholangiopancreatoscopy (Prassopoulos et al. 1998; Koito et al. 2001) is a relatively new technique that permits exploration of the common bile duct (CBD) and the pancreatic duct (PD) from an endoluminal point of view. The application of the VE surface algorithm to helical CT data sets with proper setting of the thresholds allows the rendering of only interface pixels, which is to say those pixels on the border between endoluminal fluid (bile, pancreatic secretions) and surrounding soft tissue (CBD/PD wall).

The use of MR data sets for virtual endoscopy was first reported in a study of the aorta and its branches with MR angiography (Davis et al. 1996). Due to the high signal intensity of blood generated by this acquisition technique, the voxels representing the aorta correspond to the brightest gray level. In this approach the voxels of the vascular structures can be easily segmented to be used for VE.

Since MRCP images have comparable characteristics with respect to the images provided by MR angiography, segmentation and generation of endoscopic views is potentially feasible (Dubno et al. 1998; Neri et al. 1999a,b; Prassopoulos et al. 2002).

Segmentation of MRCP data sets has been made feasible by the high contrast difference between the bile ducts (brightest voxels) and the surrounding tissue (darkest voxels). Therefore, MRVE has clearly shown internal views of the biliary tract, although in some cases (i.e., in normal patients with no bile duct dilatation) signal intensity is not enough to provide the necessary number of voxels for segmentation.

Navigation sequences can be simulated through the common bile duct (CBD), hepatic duct (HD), left (LHD) and right (RHD) hepatic ducts and intrahepatic branches, pancreatic duct (PD), cystic duct (CD) and gallbladder. All these anatomical details appear as tubular structures, with a smooth internal surface.

The endoluminal patterns of pathological findings showed by MRCP images were depicted by Neri et al. (1999b). Three groups of endoluminal patterns were identified: endoluminal "polyp-like" mass (Fig. 22.10), luminal stenosis (Fig. 22.11) and luminal occlusion. "Hole artifacts" through the internal wall were also observed and interpreted as mistakes of segmentation due to incorrect threshold selection. According to this study, biliary stones were depicted mainly as polyp-like endoluminal masses (85% of cases). Thus, it is supposed that the polyp-like pattern is their most probable appearance inside the lumen, but in a few cases, when the stones determined an important degree of stenosis of the lumen, they were identified as luminal stenosis (10%) and occlusion (5%). In these cases, the polyp-like morphology of the stone was not recognized because the lumen did not provide sufficient voxels for virtual navigation. In the remaining cases, the pathological conditions of the bile ducts were variably interpreted as stenoses or occlusions, but the morphology of the endoluminal changes was never detected by the observers. This means that MR virtual endoscopy does not show the cause of luminal involvement but rather only provides information about the effects of this involvement (high sensitivity, low specificity).

To evaluate the applications of MR cholangioscopy in a clinical setting, Neri et al. (1999c) set out to

Fig. 22.10a–c. Choledocholithiasis. Coronal thin-slab SSFSE T2-weighted MR cholangiogram (**a**) shows two stones in the distal tract of the common bile duct. Coronal oblique MIP T2-weighted MR cholangiogram (**b**) confirms these findings and demonstrates dilation of the biliary tract. The MRVE view (**c**), simulated to look toward the ampulla, shows the endoluminal "polyp-like" mass pattern of the common bile duct from the inside

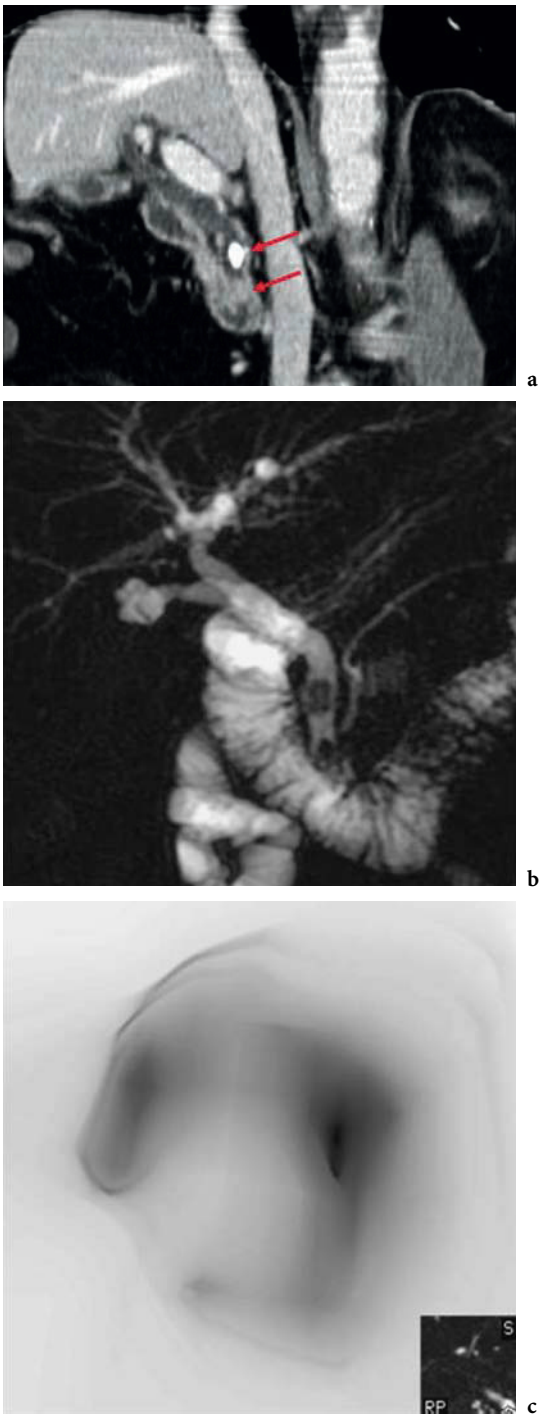

Fig. 22.11a–c. Choledocholithiasis. MPVR CT image (**a**), obtained in a coronal oblique plane, shows dilation of the biliary tract for the presence of two calculi (*arrows*) in the distal portion of the common bile duct. Coronal thick-slab SSFSE T2-weighted MR cholangiogram (**b**) confirms these findings. The MRVE view (**c**), simulated to look toward the ampulla, shows the luminal stenosis pattern of the common bile duct from the inside

establish if MRCP, together with virtual endoscopy, could improve the noninvasive detection of CBD stones. When applied to MRC as a complementary technique, it improved the detection sensitivity for CBD calculi; on its own, however, it cannot provide any useful information, as it never allows characterization of incidental lesions. This limitation can be overcome by the use of cursors that allow observers to point at the surface of interest and obtain, interactively, in real time, the corresponding multiplanar MR images or surface shaded 3D reconstructions crossing through the indicated point. In this way each abnormal finding can be characterized with the T2-signal of the lesion. This novel combined approach permits lesions to be identified more easily using virtual endoscopy and then characterized on the basis of standard MR signal characteristics allowing, for example, CBD stones (signal void) to be precisely identified, as reported also by Simone et al. (2004).

22.4 Conclusions

Although much of imaging information can be visualized on conventional CT and MR images, 3D reconstructions, multiplanar and curved planar reformatted images of the biliary tract provide quick and clear visualization of the complex relationships of anatomy and pathology, increase our confidence in diagnosis and contribute to our understanding of the disease process. In fact, in most cases 3D imaging does not add quantitative information to CT and MR cholangiography, but the main advantage with respect to cross-sectional anatomy is represented by a different rendering of data, more familiar to the human eye. It is also our experience that these additions to the standard armamentarium of imaging techniques have a strong resonance with both the referring clinician and surgical staff, who find them to be both informative and significant adjuncts in patient management and surgical planning of biliary disease.

The constant integration between CT/MR source images and image processing techniques, both with external and endoluminal points of view, can improve the diagnostic potentialities of volumetric acquisition with multidetector CT and MR cholangiography in the evaluation of biliary tract diseases.

References

Ahmetoglu A, Kosucu P, Kul S et al (2004) MDCT cholangiography with volume rendering for the assessment of patients with biliary obstruction. AJR Am J Roentgenol 183:1327–1332

Alibrahim E, Gibson RN, Vincent J et al (2006) Spiral computed tomography-intravenous cholangiography with three-dimensional reconstructions for imaging the biliary tree. Australas Radiol 50:136–142

Barish MA, Yucel EK, Soto JA et al (1995) MR cholangiopancreatography: efficacy of three-dimensional turbo spin-echo technique. AJR Am J Roentgenol 165:295–300

Becker CD, Grossholz M, Mentha G et al (1997) MR cholangiopancreatography: technique, potential indications and diagnostic features of benign, postoperative and malignant conditions. Eur Radiol 7:865–874

Boraschi P, Braccini G, Gigoni R et al (1999a) MR cholangiopancreatography: value of axial and coronal fast spin-echo fat-suppressed T2-weighted sequences. Eur J Radiol 32:171–181

Boraschi P, Neri E, Braccini G et al (1999b) Choledocolithiasis: diagnostic accuracy of MR colangiopancreatography. Three-year experience. Magn Reson Imaging 17:1245–1253

Boraschi P, Neri E, Gigoni R et al (2000) MR volume-rendering of bilio-enteric anastomoses. Radiology 217(P):667

Boraschi P, Braccini G, Gigoni R et al (2001) Detection of biliary complications after orthotopic liver transplantation with MR cholangiography. Magn Reson Imaging 19:1097–1105

Boraschi P, Donati F (2004) Complications of orthotopic liver transplantation: imaging findings. Abdom Imaging 29:189–202

Cabada Giadàs T, Sarrìa Octavio de Toledo L, Martinez-Berganza Asensio MT et al (2002) Helical CT cholangiography in the evaluation of the biliary tract: application to the diagnosis of choledocolithiasis. Abdom Imaging 27:61–70

Davis CP, Ladd ME, Romanowski BJ et al (1996) Human aorta: preliminary results with virtual endoscopy based on three-dimensional MR imaging data sets. Radiology 199:37–40

Dubno B, Debatin JF, Luboldt W et al (1998) Virtual MR cholangiography. AJR Am J Roentgenol 171:1547–1550

Fayad LM, Kamel IR, Mitchell DG et al (2005) Functional MR cholangiography: diagnosis of functional abnormalities of the gallbladder and biliary tree. AJR Am J Roentgenol 184:1563–1571

Fleischmann D, Ringl H, Schofl R et al (1996) Three-dimensional spiral CT cholangiography in patients with suspected obstructive biliary disease: comparison with endoscopic retrograde cholangiography. Radiology 198:861–868

Guibaud L, Bret PM, Reinhold C et al (1994) Diagnosis of choledocholithiasis: value of MR cholangiography. AJR Am J Roentgenol 163:847–850

Hall-Craggs MA, Allen CM, Owens CM et al (1993) MR cholangiography: clinical evaluation in 40 cases. Radiology 189:423–427

Ishizaki Y, Wakayama T, Okada Y et al (1993) Magnetic resonance cholangiography for evaluation of obstructive jaundice. Am J Gastroenterol 88:2072–2077

Kim HC, Park SH, Park SI et al (2004) Three-dimensional reconstructed images using multidetector computed

tomography in evaluation of the biliary tract. Abdom Imaging 29:472–478
Kim HJ, Kim AY, Hong SS et al (2006) Biliary ductal evaluation of hilar cholangiocarcinoma: three-dimensional direct multi-detector row CT cholangiographic findings versus surgical and pathologic results – Feasibility study. Radiology 238:300–308
Kinami S, Yao T, Kurachi M et al (1999) Clinical evaluation of 3D-CT cholangiography for preoperative examination in laparoscopic cholecystectomy. J Gastroenterol 34:111–118
Klein HM, Wein B, Truong S et al (1993) Computed tomographic cholangiography using spiral CT scanning and 3D image processing. Br J Radiol 66:762–767
Koito K, Namieno T, Hirokawa N et al (2001) Virtual CT cholangioscopy: comparison with fiberoptic cholangioscopy. Endoscopy 33:676–681
Kondo H, Kanematsu M, Stiratori Y et al (2001) MR cholangiography with volume rendering: receiver operating characteristics curve analysis in patients with choledocholithiasis. AJR Am J Roentgenol 176:1183–1189
Macaulay SE, Schulte SJ, Sekijma JH et al (1995) Evaluation of a non-breath-hold MR cholangiography technique. Radiology 196:227–232
Miyazaki T, Yamashita Y, Tsuchigame T et al (1996) MR cholangiopancreatography using HASTE (half-Fourier acquisition single-shot turbo spin-echo) sequences. AJR Am J Roentgenol 166:1297–1303
Morimoto K, Shimoi M, Shirakawa T et al (1992) Biliary obstruction: evaluation with three-dimensional MR cholangiography. Radiology 183:578–580
Neri E, Boraschi P, Braccini G et al (1999a) MR virtual endoscopy of the pancreaticobiliary tract: a feasible technique? Abdom Imaging 24:289–291
Neri E, Boraschi P, Braccini G et al (1999b) MR virtual endoscopy of the pancreaticobiliary tract. Magn Reson Imaging 17:59–67
Neri E, Caramella D, Boraschi P et al (1999c) Magnetic resonance virtual endoscopy of the common bile duct stones. Surg Endosc 13:632–633
Neri E, Boraschi P, Caramella D et al (2000) Real-time volume rendering of MRCP: clinical applications. MAGMA 10:35–42
Nino-Murcia M, Jeffrey RB, Beaulieu CF et al (2001) Multidetector CT of the pancreas and bile duct system: value of curved planar reformations. AJR Am J Roentgenol 176:689–693
Picus D (1995) Percutaneous biliary endoscopy. J Vasc Interv Radiol 6:303–310
Prassopoulos P, Raptopoulos V, Chuttani R et al (1998) Development of virtual CT cholangiopancreatoscopy. Radiology 209:570–574
Prassopoulos P, Papanikolaou N, Maris T et al (2002) Development of contrast-enhanced virtual MR cholangioscopy: a feasibility study. Eur Radiol 12:1438–1441
Rao ND, Gulati MS, Paul SB et al (2005) Three-dimensional helical computed tomography cholangiography with minimum intensity projection in gallbladder carcinoma patients with obstructive jaundice: comparison with magnetic resonance cholangiography and percutaneous transhepatic cholangiography. J Gastroenterol Hepatol 20:304–308
Raptopoulos V, Prassopoulos P, Chuttani R et al (1998) Multiplanar CT pancreatography and distal cholangiography with minimum intensity projections. Radiology 207:317–324
Regan F, Smith D, Khazan R et al (1996) MR cholangiography in biliary obstruction using half-Fourier acquisition. J Comput Assist Tomogr 20:627–632
Reinhold C, Guibaud L, Genin G et al (1995) MR cholangiopancreatography: comparison between two-dimensional fast spin-echo and three-dimensional gradient-echo pulse sequences. J Magn Reson Imaging 4:379–384
Reinhold C, Bret PM (1996) Current status of MR cholangiopancreatography. AJR Am J Roentgenol 166:1285–1295
Sajjad Z, Oxtoby J, West D et al (1999) Biliary imaging by spiral CT cholangiography – a retrospective analysis. Br J Radiol 72:149–152
Simone M, Mutter D, Rubino F et al (2004) Three-dimensional virtual cholangioscopy: a reliable tool for the diagnosis of common bile duct stones. Ann Surg 240:82–88
Sodickson A, Mortele KJ, Barish MA et al (2006) Three-dimensional fast-recovery fast spin-echo MRCP: comparison with two-dimensional single-shot fast spin-echo techniques. Radiology 238:549–559
Soto JA, Barish MA, Yucel EK et al (1995) MR cholangiopancreatography: findings on 3D fast spin-echo imaging. AJR Am J Roentgenol 165:1397–1401
Wallner BK, Schumacher KA, Weidenmaier W et al (1991) Dilated biliary tract: evaluation with MR cholangiography with a T2-weighted contrast-enhanced fast sequence. Radiology 181:805–808
Wang ZJ, Yeh BM, Roberts JP et al (2005) Living donor candidates for right hepatic lobe transplantation: evaluation at CT cholangiography – initial experience. Radiology 235:899–904
Wielopolski PA, Gaa J, Wielopolski DR et al (1999) Breath-hold MR cholangiopancreatography with three-dimensional, segmented, echo-planar imaging and volume rendering. Radiology 210:247–252
Zandrino F, Benzi L, Ferretti ML et al (2002) Multislice CT cholangiography without biliary contrast agents: technique and initial clinical results in the assessment of patients with biliary obstruction. Eur Radiol 12:1055–1061
Zeman RK, Berman PM, Silverman PM et al (1995) Biliary tract: three-dimensional helical CT without cholangiographic contrast material. Radiology 196:865–867

Urinary Tract

23

Piero Boraschi, Francescamaria Donati, and Simonetta Salemi

CONTENTS

23.1 Introduction

The radiological evaluation of patients with common and complex urologic disease is changing rapidly. Historically, intravenous urography has been recommended as the initial imaging test in the evaluation of upper urinary tract disease in patients with flank pain, hematuria and other suspected urologic disease. Recent improvements in image processing and three-dimensional (3D) visualization increased the potential of current imaging techniques for the study of the urinary tract. In this setting, computed tomography and magnetic resonance imaging – improved by post-processing displays – have become crucial techniques for the accurate evaluation of anatomy and pathology.

P. Boraschi, MD; F. Donati, MD
2nd Department of Radiology, Pisa University Hospital, Via Paradisa 2, 56124 Pisa, Italy
S. Salemi, MD
Diagnostic and Interventional Radiology, Department of Oncology, Transplants and Advanced Technologies in Medicine, University of Pisa, Via Roma 67, 56125 Pisa, Italy

23.2 CT and MR Urography

In recent years, concepts and techniques pertaining to CT urography (CTU) and MR urography (MRU) have been evolving. As the technology continues to improve, CTU and MRU will combine CT and MRI with the ultimate diagnostic capabilities of intravenous urography.

Recently, several investigators have suggested that CT urography, with its ability to acquire thinly collimated data sets that can be used to create excellent quality 3D images of the urinary tract, can replace or even improve on excretory urography in identifying urothelial abnormalities and disorders (McTavish 2002; Kawashima et al. 2004; Caoili et al. 2005b; Korobkin 2005).

CT has evolved from single-detector row scanners into multi-detector row helical volumetric acquisition techniques, and these advances have had a significant impact on imaging of the urinary tract. With the introduction of multi-detector row CT, the abdomen and pelvis can be imaged in a single breath hold with thinly collimated images. As a result, the urinary tract can be imaged with high spatial resolution in both transverse and non-transverse planes. Multi-detector row CT has been used to perform urography in an examination that includes unenhanced and enhanced images of the urinary tract and provides intravenous urography-like coronal images during the excretory phase. As with conventional intravenous urography, visualization of the intrarenal collecting system and ureter at multi-detector row CTU depends on opacification and distension. A fundamental problem with multi-detector row CTU (and with any imaging technique that attempts to image the entire urinary collecting system) is that, because of peristalsis, it is difficult to obtain a single image in which all urinary tract segments are opacified and distended. It has been shown that supplementing the contrast material used at multi-detector row CTU with intrave-

nous saline improves opacification of the collecting system and ureters (Silverman et al. 2006), but doing so requires specific protocols for dedicated imaging.

Before the examination, some suggest orally administering about 1L of water (Sheth and Fishman 2004). The four-detector row CTU protocol is as follows: The initial phase is unenhanced (2.5 mm collimation with a pitch of 1.00–1.25, 120 kVp, and 155–200 mA) in order to localize the kidneys and eventual suspected masses, and to reveal incidental calcifications (or calculi) and even fatty lesions. After administering intravenous contrast medium (130–160 ml at a rate of 3–5 ml/s) an arterial phase and a nephrographic phase can be obtained with the same parameters as the baseline scan. The first enhanced phase (subject to calculation of the delay time to maximum vascular enhancement) combines the enhancement of the renal arterial vasculature and cortical parenchyma, generally obtained 25–30 s after injection. Then the second enhanced phase is obtained about 80–100 s after injection and provides information about the whole renal parenchyma and incidental focal lesions. An additional, delayed acquisition (about 5–6 min after injection) captures the contrast within the collecting system, the ureters and the bladder in a urographic fashion by using 1.0-mm collimation, a pitch of 0.65–1.00, 120 kVp, and 165–185 mA. The mean effective dose for patients examined with the four-detector row CT scanner has been reported to be 14.8 mSv ± 3.1.

The 16-detector row CTU protocol is as follows: for the unenhanced scan, the abdomen and pelvis are imaged by using 1.5-mm collimation with a pitch of 0.875, 120 kVp, and 160–280 mA. The kidneys are scanned 30 and 90–100 s after intravenous administration of 130–160 ml of contrast medium at a rate of at least 3 ml/s by using the same parameters. The entire abdomen is scanned during the excretory phase, 5–6 min after the contrast medium is injected, by using 0.75-mm collimation, a pitch of 0.82–1.00, 120 kVp, and 160–280 mA.

However, despite these findings, some patients' ureters may still not be fully opacified or distended. The intravenous administration of furosemide (10 mg over 1 min, 2–3 min before the contrast medium injection) either alone or in addition to intravenous saline (250 ml of saline) improved the depiction of the normal urinary collecting system at multi-detector row CTU (Silverman et al. 2006).

Actually, MRU serves as an alternative imaging technique for the study of the urinary tract.

MRU is currently performed by pursuing two different imaging strategies. On the one hand, heavily T2-weighted pulse sequences are employed for obtaining static-water images of the urinary tract. On the other hand, the T1-weighted MRU technique imitates conventional intravenous urography and is, therefore, referred to as gadolinium-enhanced excretory MRU. With this technique, the contrast-enhanced urine can be visualized with fast T1-weighted pulse sequences obtained after renal excretion of an intravenously injected Gd-chelate. The feasibility of excretory MRU depends on renal excretory function; consequently, T1-weighted MRU provides morphologic and at least gross functional information (Nolte-Ernsting et al. 1998; El-Diasty et al. 2003; Garcia-Valtuille et al. 2006).

In static-fluid MRU, the fundamental concept is that simple fluids, such as urine, have very long T2 relaxation times. Heavily T2-weighted pulse sequences generate images with high signal intensity from static fluid in the collecting systems, whereas the signal intensity from parenchymal tissues with shorter T2 relaxation times is suppressed. The use of a heavily T2-weighted rapid acquisition with relaxation enhancement (RARE) sequence was the first approach to visualize the urinary tract by means of MR imaging (Roy et al. 1994; Hagspiel et al. 2005). Actually, the most common T2-weighted technique is the single-shot fast spin-echo sequence (SSFSE, GE Healthcare) or half-Fourier acquisition single-shot turbo spin-echo (HASTE, Siemens). Other new pulse sequences may have potential in MRU, such as steady-state free precession sequences (fast imaging using steady-state acquisition, FIESTA, GE Healthcare; fast imaging with steady-state precession, TrueFISP, Siemens) or a three-dimensional fast recovery fast spin echo pulse sequence (3D-FRFSE, GE Healthcare), which provides high-resolution heavily T2-weighted images with shorter acquisition time compared to conventional 3D FSE imaging (O'Malley et al. 1997; Kawashima et al. 2003; Nolte-Ernsting et al. 2003).

There are two approaches to obtaining static-fluid MR urographic views. One approach is to acquire a single thick slab projection MR image (SSFSE or HASTE) with a section thickness of up to 80 mm during a short breath-hold of approximately 2–3 s. It provides a quick coronal or oblique coronal urographic overview without requiring any post-processing. The second approach is based on the acquisition of multiple, overlapping thin sec-

tions of the urinary tract obtained mostly in the same plane and which have to be post-processed. The multislice method is more time-consuming, but the acquisition of thin single slices reduces partial-volume averaging and offers a better opportunity to detect small intraluminal filling defects, which may be obscured by surrounding urine, particularly in the dilated system on a single thick slab. In a multislice sequence, each section can be obtained within a short breath-hold, or the data can also be acquired by respiratory triggering. Static-fluid T2-weighted MRU is especially suited for imaging the dilated urinary tract, in which the large amount of water generates a good signal-to-noise ratio. The urographic effect is independent of the renal excretory function, so T2-weighted MRU can even be used to visualize the markedly obstructed urinary tract of a quiescent kidney. Static-fluid MRU can be performed in children, and is suitable for the visualization of urinary tract disorders in women during pregnancy and in patients with contraindications to iodinated contrast media, whereas this technique proved less useful in patients with non-dilated urinary tracts. To achieve sufficient visualization of the unobstructed urinary tract on T2-weighted MR urograms, substantial hydration is necessary, which necessitates the supplementation of intravenous furosemide (Catalano et al. 1999; Kawashima et al. 2003; Nolte-Ernsting et al. 2001, 2003).

Gadolinium-enhanced T1-weighted MRU imitates conventional intravenous urography in that an intravenously injected gadolinium contrast agent is excreted by the kidneys and the gadolinium-enhanced urine is imaged with the use of T1-weighted three-dimensional spoiled gradient-echo sequences. To optimize the endoluminal T1-enhancing properties of gadolinium agents after renal excretion, the combination of gadolinium with a low-dose furosemide injection has proved to be highly effective in excretory MRU. 3D-GRE T1-weighted sequences (LAVA, GE Healthcare; VIBE, Siemens) have proved to be well suited for use in gadolinium excretory MR urography. The 3D sequence dataset is usually acquired in the coronal or oblique coronal plane 5–8 min after intravenous administration of gadolinium contrast agents (Nolte-Ernsting et al. 2001, 2003; Kawashima et al. 2003). The technical success of gadolinium-enhanced MRU depends substantially on the excretory function of the kidneys. Therefore, excretory MRU provides morphologic and at least gross functional information about the urinary tract.

T1- and T2-weighted MRU techniques are complementary tools that offer several first-choice applications and diverse combinations with other MR imaging methods. Another promising aspect is that MRU can be performed easily in conjunction with standard pulse sequences, functional MR imaging, or MR angiography. An integrative uroradiologic examination protocol may obviate multiple separate diagnostic tests, which are costly, time-consuming, and sometimes invasive. Static-fluid and excretory MRU already are important imaging modalities in pediatric uroradiology. In a growing number of departments, urography in children is performed almost exclusively with MR imaging (Nolte-Ernsting et al. 2003).

23.3 3D Image Processing Techniques

Integration between volumetric acquisition and 3D surface and volume rendering techniques permits the study of the urinary tract in a noninvasive manner.

Some investigators have carried out preliminary studies on 3D reconstructions of the collecting system with surface rendering of MRU data sets (Nolte-Ernsting et al. 1999; Neri et al. 2000). Experiences with 3D volume-rendered CT of the kidney donors (Dachman et al. 1998) have also been reported, which aimed to provide an accurate anatomical assessment before surgery.

As a rule, the radiologist interactively reviews the volumetric data sets of CTU or MRU in a dedicated workstation, and generates appropriate images that are similar in appearance to conventional film urograms. Initial urologist acceptance of these techniques may be enhanced by display of the reformatted images of the urinary tract (Sheth and Fishman 2004). The length of time required to generate relevant images varies with the experience of the radiologist and the complexity of the case, but it is generally less than 10 min once the radiologist is familiar with the technique.

Several image processing techniques have been shown to be effective in displaying the urinary tract.

Multiplanar reformatted images in coronal or oblique coronal planes help to define the location and extent of the lesions shown on axial source images.

However, since most structures of interest do not lie within a single plane, this technique is limited to the visualization of the entire urinary tract and particularly the entire ureter unless curved planar reformation is used.

Three-dimensional reconstructions can be obtained with both external and endoluminal points of view of the organ anatomy (Rubin et al. 1996; Rubin 2003). Maximum intensity projection (MIP), average intensity projection (AIP), shaded surface display (SSD), perspective volume rendering (VR) and multiplanar volume reconstruction (MPVR) algorithms provide external views of the kidney and urinary tract (Dalrymple et al. 2005). Endoluminal points of view of the urinary tract can be obtained with virtual endoscopy (VE) by using either MRU or the urographic phase of CT.

With MIP, the maximum voxel intensity along a line of viewer projection in a given volume is displayed. High attenuation structures such as the collecting system are nicely displayed in images resembling conventional urograms. Thin-slab reformatted MIP images have the advantage of covering a considerably longer range than standard multiplanar reformation, and have the ability to demonstrate small filling defects and thickened urothelial walls, which may be obscured by adjacent contrast material in the collecting system and periureteral soft tissues with thick-slab reformation.

AIP describes one type of algorithm used to thicken multiplanar reconstructions. The image represents the average of each component attenuation value encountered by a ray cast through an object toward the viewer's eye. Thickening the multiplanar slab by using AIP, it is possible to produce a smoother image with less noise and improved contrast resolution. The image quality is similar to that used in axial evaluation of the abdomen.

SSD, also called surface rendering, provides a 3D view of the surface of an object that must first be separated from other structures (a process called segmentation that may require meticulous editing).

Volume rendering (now preferable to SSD for most, if not all applications) is the most versatile reconstruction technique, as it uses the information provided in the entire data set by assigning a specific degree of opacity to each attenuation value within the volume of interest. It also allows the viewer to interact with the data sets in real time, obviating complex editing. Thus, anatomic structures with varying degrees of opacities (e.g., blood vessels, renal parenchyma, urinary tract) can be displayed simultaneously. The main drawback of VR is the need for a more powerful computer and expensive workstation.

23.3.1 Virtual Endoscopy of the Upper Urinary Tract

The simulation of a fiber optic perspective can be obtained trough dedicated software that reconstructs CT and MR images in three dimensions by creating surface or volume-rendered endoscopic images (Rubin et al. 1996).

The dilatation of the urinary tract is prerequisite for generating virtual endoscopy of static-fluid MRU data sets, since the dilatation of the ureter or renal pelvis increases the availability of bright image pixels and, consequently, the voxels that VE can use to reconstruct the lumen in three dimensions and to create the virtual space for endoscopic navigation. The feasibility of virtual endoscopy with MRU has been proposed both with and without gadolinium (Nolte-Ernsting et al. 1999; Neri et al. 2000).

In a previous experience by Neri et al. (2000), a series of 26 patients with neoplastic lesions, calculi, stenosis of the ureteropelvic junction and postoperative fibrotic strictures of the ureter were studied with MRU that was performed with a fat-suppressed, respiratory-triggered, two-dimensional, heavily T2-weighted fast spin echo sequence in the coronal plane. VE views were displayed in a combined fashion with MR source images, and VE findings could be correlated with the coronal views. VE of the renal pelvis and calices was feasible in all cases at the site of urinary obstruction. VE of the ureter, from the ureteropelvic junction to the site of obstruction, was obtained with acceptable quality when its caliber was at least 5 mm. The controlateral side could be partially explored in 11 cases (43%), and navigation was feasible in the calices, renal pelvis and proximal tract of the ureter. The dilatation of the urinary tract was a prerequisite for generating endoscopic views, and the majority of pathological patterns were described as occlusion of the lumen. Neoplastic lesions appeared as endoluminal masses, and VE demonstrated the endoluminal appearance of the lesions, their morphology, position with respect to calices, and extent.

23.4 Role of Imaging in the Study of Pathological Findings

Technical developments in CT and MR imaging currently allow excellent diagnostic capabilities for disorders of the urinary tract. Post-processing techniques can offer added value in solving anatomical dilemmas. Current potential applications of 3D imaging include the noninvasive study of congenital anomalies, preoperative evaluation in kidney donors, detection of lithiasis and preoperative planning of surgery for neoplasms.

23.4.1 Congenital Anomalies/Kidney Donors

The importance of accurate knowledge of the renal anatomy, especially in a kidney to be transplanted, is of fundamental relevance in the preoperative assessment of these patients. Native CT/MR images and post-processing techniques are the best way to examine in a noninvasive manner kidney dimensions, morphology and parenchyma condition before and after contrast enhancement; to evaluate size, number and course of the renal arteries and veins; to detect anomalies of the collecting system (anomalous ureteropelvic junction, complete duplication of the renal collecting system, and so on) (Farres et al. 1998; Sheth and Fishman 2004; El-Diasty et al. 2005) (Figs. 23.1–23.3). Multiplanar and 3D reformatted images rarely add information that may result in a different therapeutic approach, but help to provide an alternative point of view of patient anatomy that may be useful in surgical planning (Fig. 23.4).

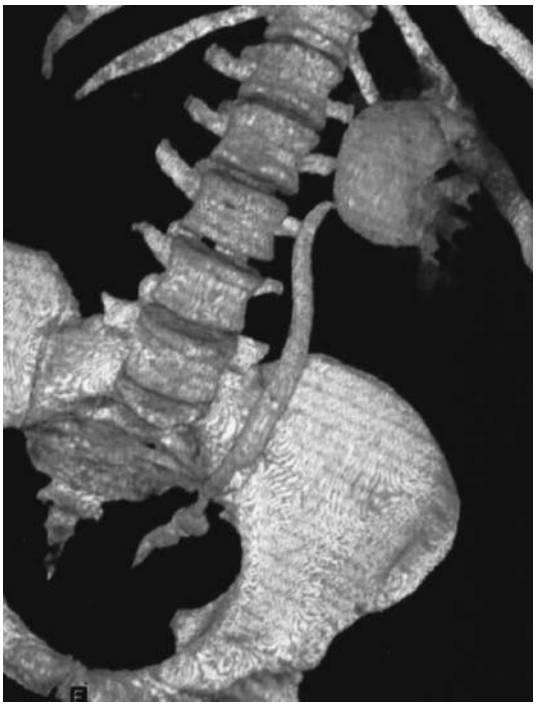

Fig. 23.1. SSD coronal oblique image in the excretory phase of multidetector CT demonstrates dilation of calices and pelvis in the left kidney due to a stenosis of the ureteropelvic junction

23.4.2 Lithiasis

CT imaging is progressively gaining an important role in the management of patients with suspected lithiasis of the urinary tract. An unenhanced scan of the entire abdomen performed in a single breathhold, at high resolution, allows the depiction of calcifications in the urinary tract (Tublin et al. 2002). In difficult cases where the position of calcification cannot be precisely defined, the use of intravenous contrast helps in delineating the entire urinary map (Fig. 23.5) and also allows calculi located in the renal

Fig. 23.2. VR CT-urographic coronal image shows anomalous ureteropelvic junction with dilation of calices and pelvis of both kidneys

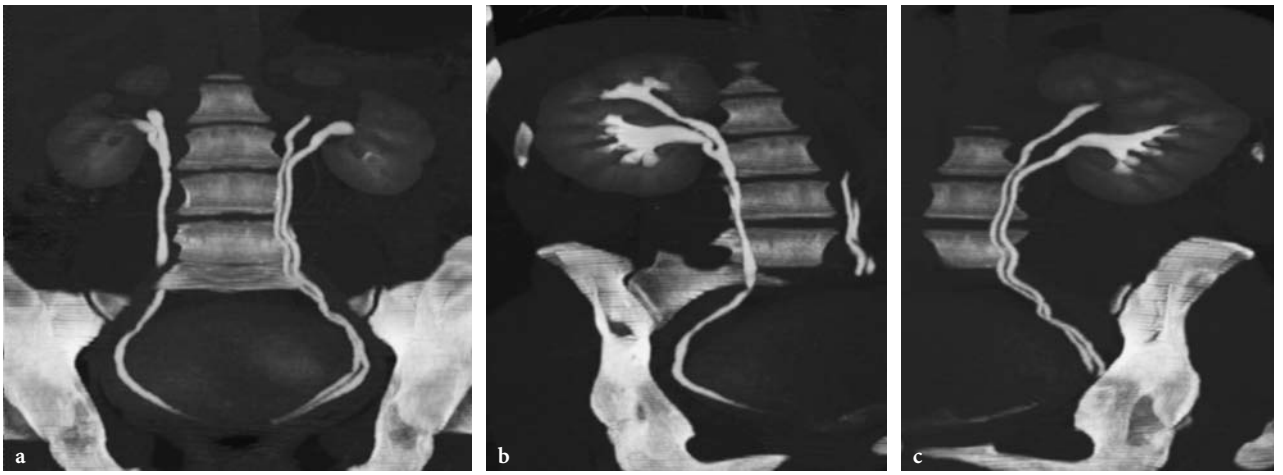

Fig. 23.3a–c. Coronal MIP (**a**) and coronal oblique MIP (**b**,**c**) images in the excretory phase of CTU show a partially duplicated right renal collecting system and a completely duplicated left collecting system

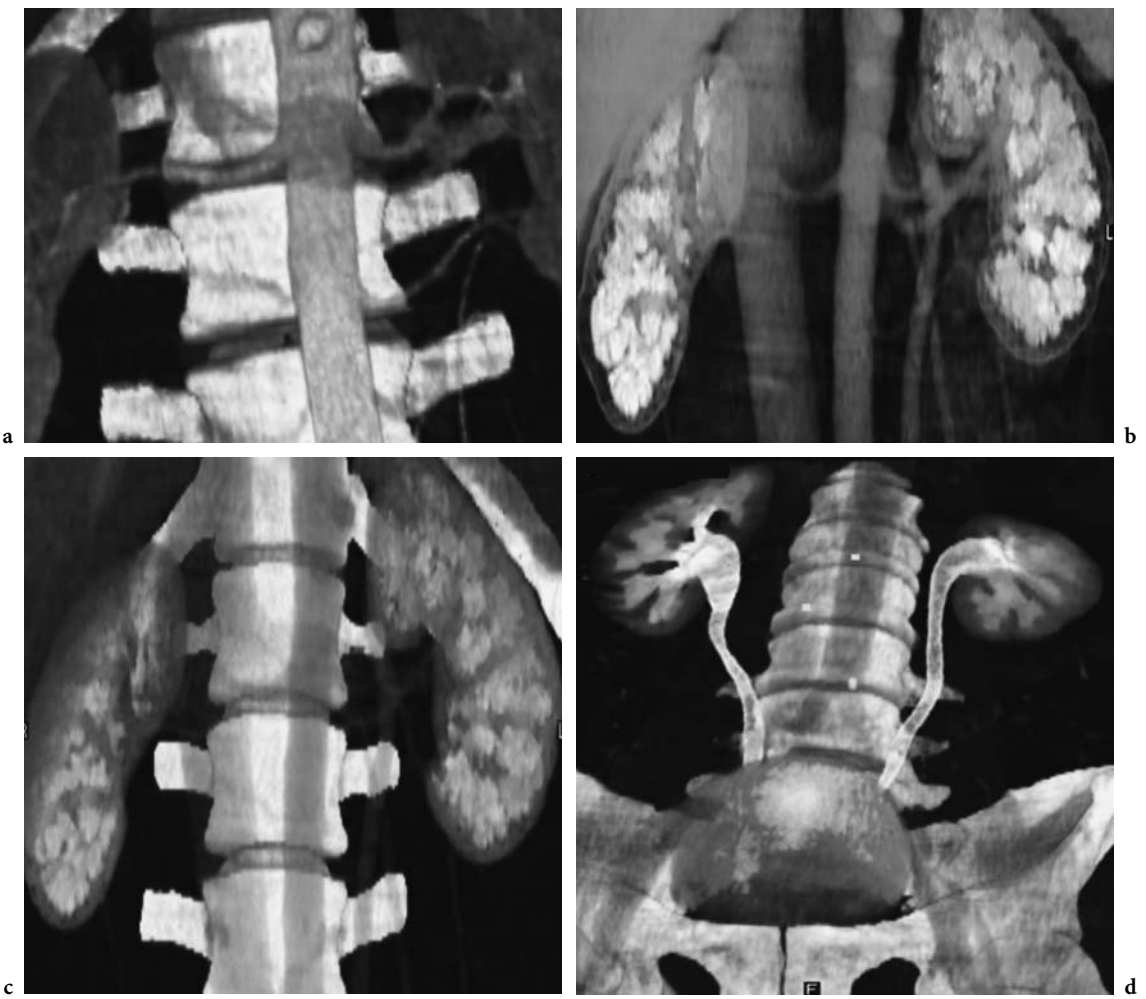

Fig. 23.4a–d. Multidetector CT evaluation in a potential renal donor. VR 3D images, obtained in the multiple phases of renal enhancement, perfectly demonstrate (**a**) normal renal arteries with left accessory artery, (**b**) normal renal veins, (**c**) regular renal dimensions, morphology and parenchyma condition, and (**d**) normal collecting systems

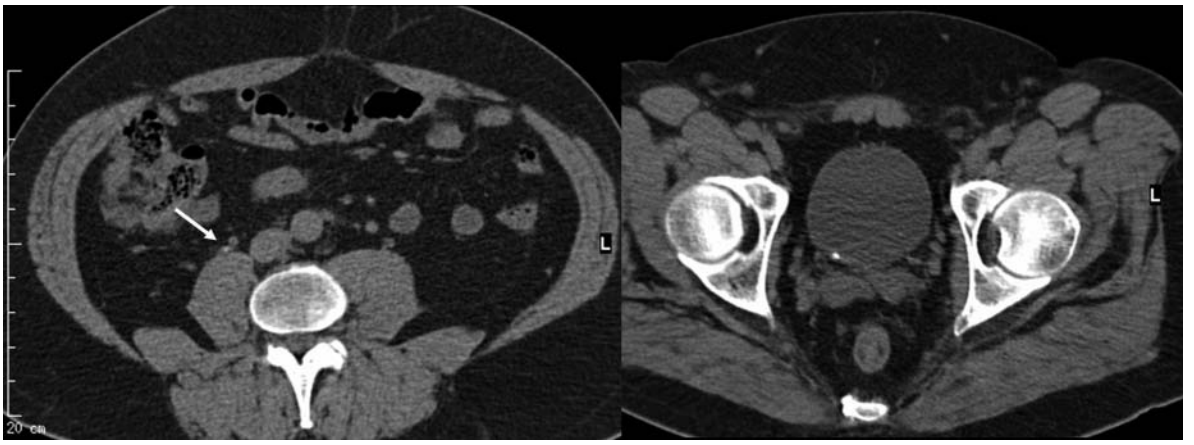

a

b

c

d

Fig. 23.5a–d. Multidetector CT evaluation in a patient with severe right flank pain and history of right renal colics. Unenhanced CT (**a**) shows two stones, respectively, in the right middle ureter (*arrow*) and in the right ureterovesicle junction. Coronal oblique MIP images in the excretory phase (**b**,**c**) demonstrate moderate right hydronephrosis and slight dilation of the proximal ipsilateral ureter with partial obstruction at the level of the middle ureteral stone; in addition, the presence of the right ureterovesicle junction stone is confirmed, with non-dilated distal ureter. The left normal ureter is seen along its entire course. VR CT urography (**d**) better depicts the entire collecting system of both kidneys, showing right pyelocaliectasis with reduction of renal cortical thickness

pelvis to be distinguished from calcified plaques of the arterial system (Kenney 2003). If surgery of lithiasis is planned, the CT study should include evaluation of the renal parenchyma and renal arteries, as well as malformations of the kidneys. Some investigators have suggested the use of MR imaging, which can easily detect urinary dilation and is especially sensitive, to identify signs secondary to the obstruction (hydronephrosis, ureteral dilation, perinephric stranding and periureteral edema) (Nolte-Ernsting et al. 2001, 2003; Kawashima et al. 2003) (Fig. 23.6). In order to study the upper urinary tract, 3D data reconstructions with MIP, multiplanar reconstructions and volume rendering are used to generate images simulating intravenous urography. However, the classic MIP provides a projectional roadmap of the collecting system but is limited by the poor perception of depth and relationship with contiguous anatomical structures. This limitation can be overcome by volume rendering and multiplanar reconstructions that can display in the same reconstruction the urinary tract, the renal parenchyma and the vessels (Kawashima et al. 2004). Since volume rendering is fast in generating 3D displays, it could be suitable even in emergency conditions (renal colic for example). Virtual endoscopy of the renal pelvis and calices utilizing MR data sets can be used for evaluating urinary obstruction due to lithiasis or neoplasm. As mentioned previously, the dilatation of the urinary tract is a prerequisite for generating endoscopic views, and the majority of pathological patterns were described as occlusion of the lumen or mass protruding into the lumen (Fig. 23.7) (Neri 2000).

23.4.3 Neoplasms

The detection of renal tumors (renal cell carcinoma and transitional cell carcinoma) has substantially progressed in recent years because of improved CT and MR imaging. Besides, imaging evaluation is particularly important when planning complex surgical treatments. In this setting, both multidetector CT urography and MR urography can integrate all of

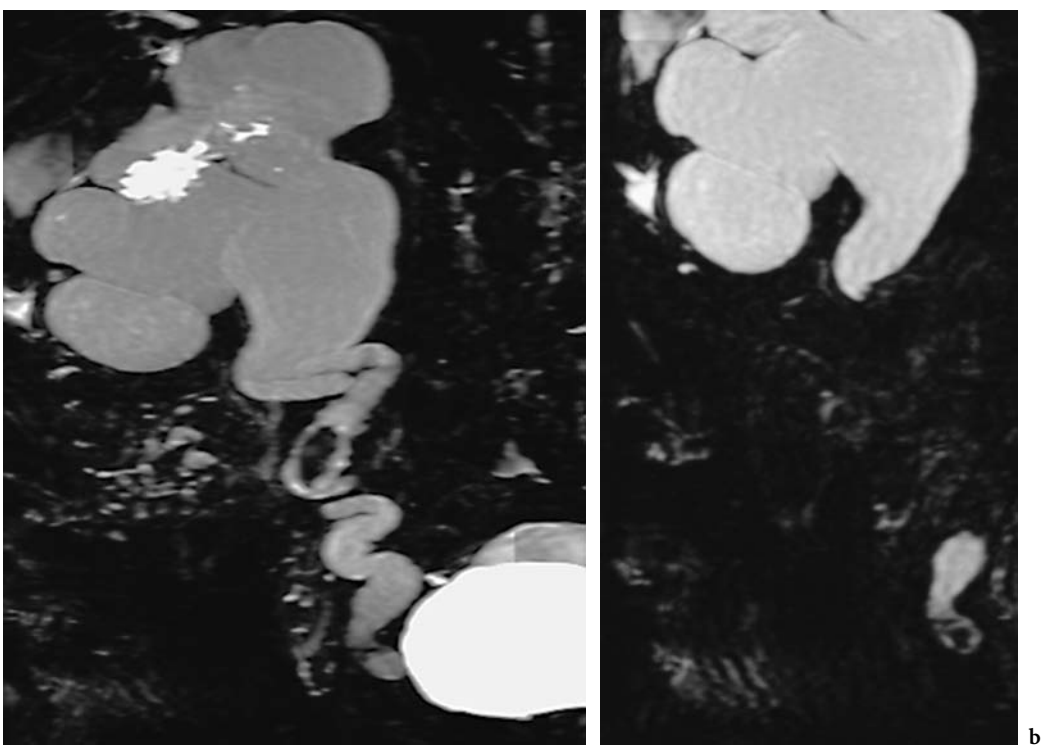

Fig. 23.6a,b. Coronal oblique thin MIP 3D heavily T2-weighted MR urogram (**a**) shows marked pyelocaliectasis and ureterectasis with multiple ureteral kinking of the right urinary tract; a stone in the proximal ureter is clearly identified. Oblique thin MIP 3D heavily T2-weighted image (**b**) reveals another small stone in the distal right ureter

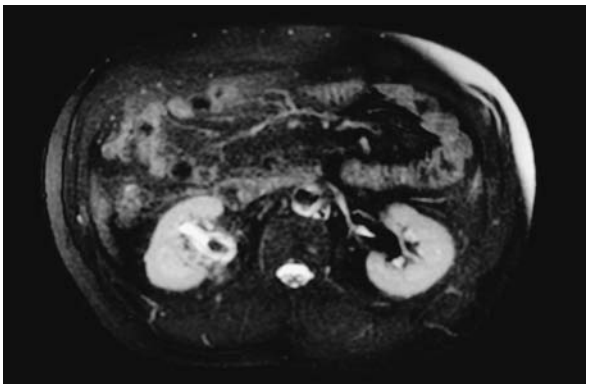

a

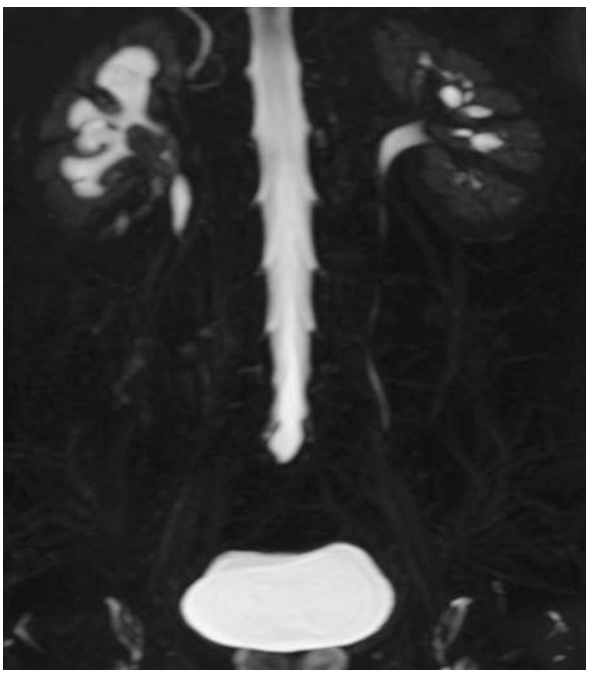

b

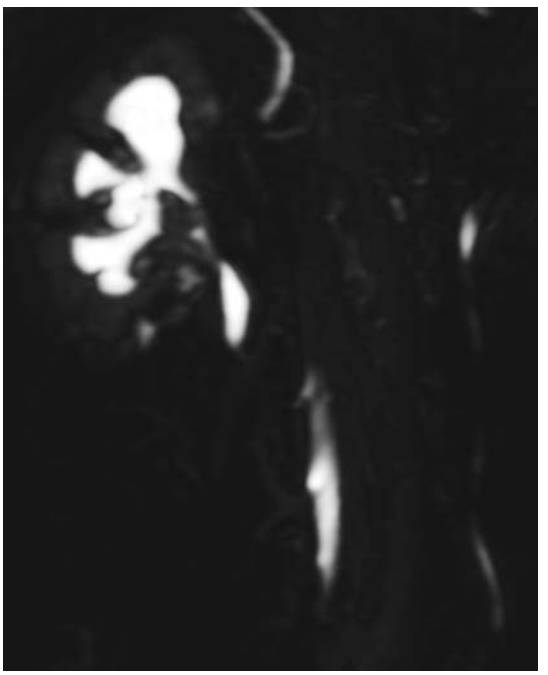

c

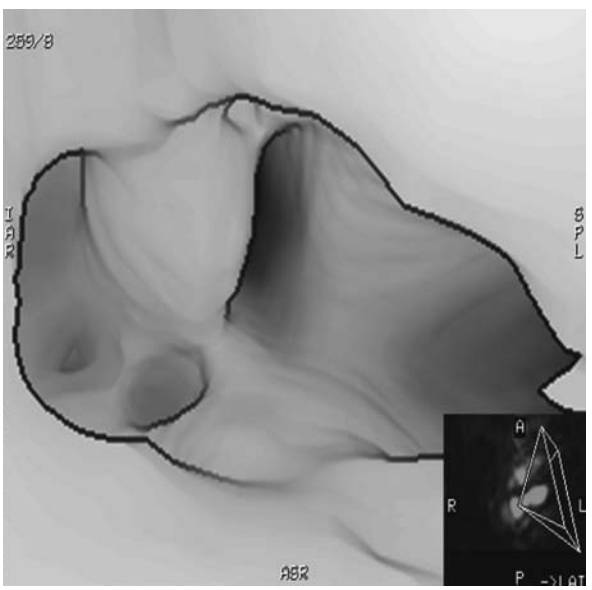

d

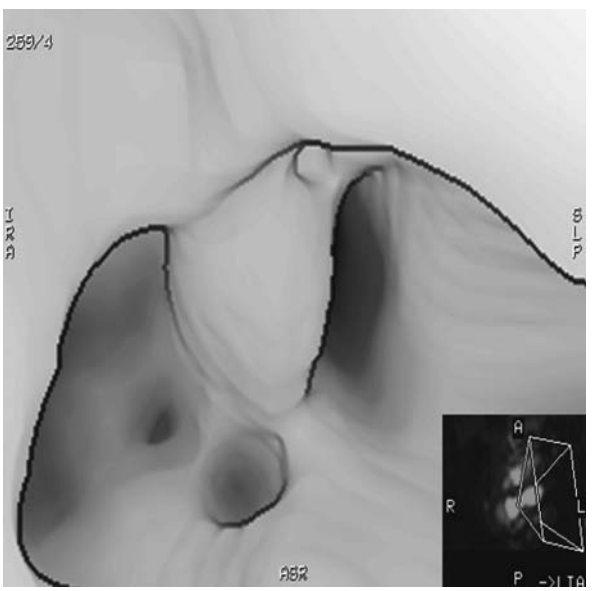

e

Fig. 23.7a–e. Axial heavily T2-weighted SSFSE image (**a**) shows a stone in the right renal pelvis. Coronal (**b**) and coronal oblique thin MIP 3D heavily T2-weighted MR (**c**) urograms show right-sided pyelocaliectasis, and better demonstrate a voluminous stone in the renal pelvis. Virtual endoscopy of the renal pelvis (**d**,**e**), performed using heavily T2-weighted MR urography data sets, shows the endoluminal appearance of both the dilated calices and the stone, and better depicts its morphology, position with respect to calices, and extension

the necessary information into a single noninvasive preoperative examination (Kawashima et al. 2003; Joffe et al. 2003; Nolte-Ernsting et al. 2003).

The renal parenchyma is evaluated with axial scans, and then the intrarenal collecting systems and ureters are visualized by multiplanar reformation and 3D volume rendering of the excretory phase (Fig. 23.8). These techniques applied to multiple phases of CT and MR imaging represent a useful tool for delineating neoplasms (site, extension) and global anatomy (relationship with adjacent vascular structures and collecting system) before surgery, with an eye to save the maximum amount of renal parenchyma (nephron-sparing surgery) and minimize complications such as ischemic injury or intraoperative bleeding (Coll et al. 1999; Sheth et al. 2001; Urban et al. 2001; Caoili et al. 2005a).

23.5 Conclusion

In conclusion, CT and MR urography post-processing techniques are able to offer a precise, noninvasive anatomical definition of the entire urinary tract with both external and endoluminal points of view, and also help to extract the most relevant and useful diagnostic information, particularly in surgical planning.

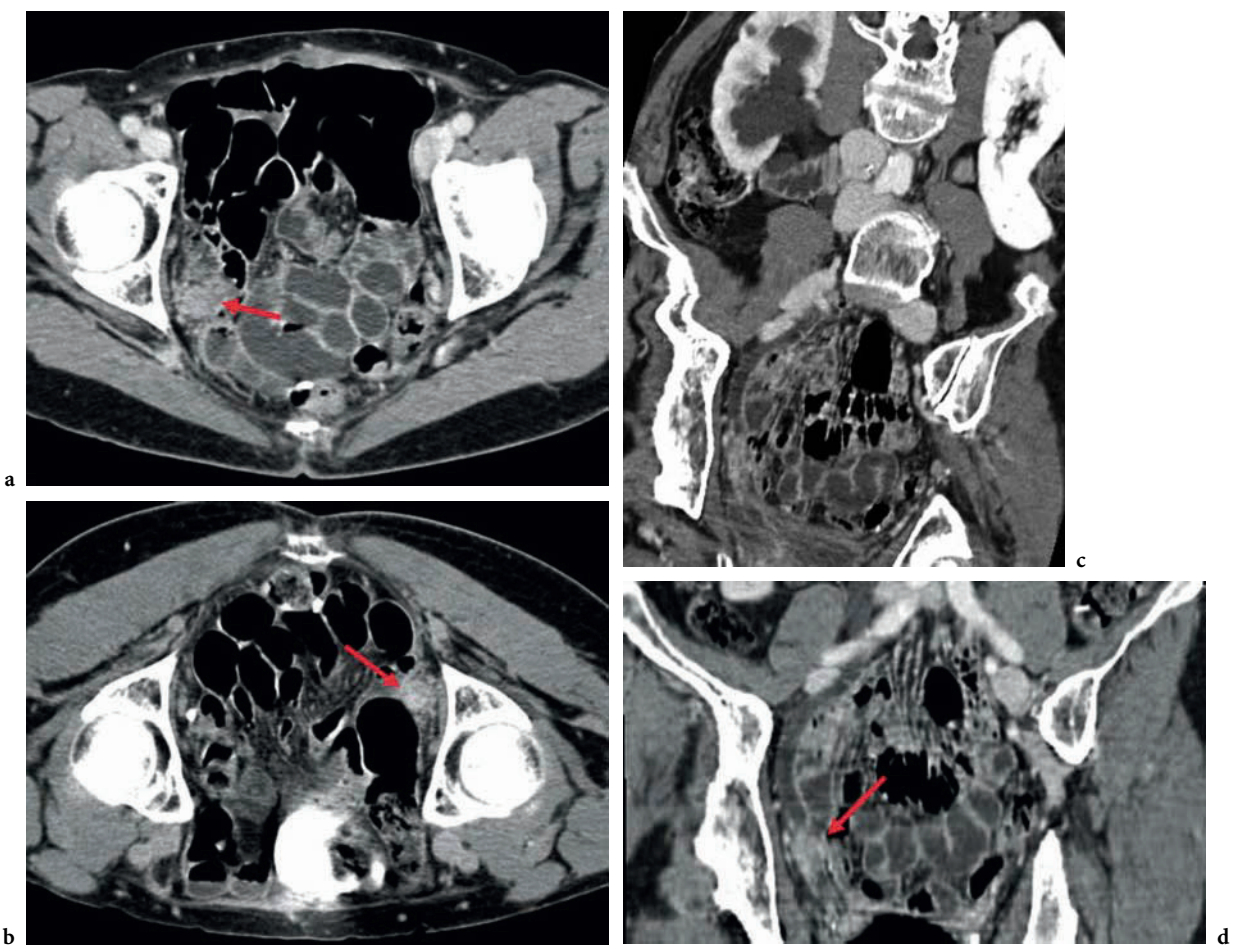

Fig. 24.8a–d. Supine (**a**) and prone (**b**) axial post-contrast CT images reveal a soft tissue mass of the right pelvic ureter (*arrows*). Coronal oblique reformatted images (**c**,**d**) show right-sided pyelocaliectasis and ureterectasis, and demonstrate the site and extension of the right ureteral mass (*arrow*). The patient underwent surgery, and the final histopathological diagnosis was papillary urothelial carcinoma

References

Caoili EM, Cohan RH, Inampudi P et al (2005a) MDCT urography of upper tract: urothelial neoplasms. AJR Am J Roentgenol 184:1873–1881

Caoili EM, Inampudi P, Cohan RH et al (2005b) Optimization of multi–detector row CT urography: effect of compression, saline administration, and prolongation of acquisition delay. Radiology 235:116–123

Catalano C, Pavone P, Laghi A et al (1999) MR pyelography and conventional MR imaging in urinary tract obstruction. Acta Radiol 40:198–202

Coll DM, Uzzo RG, Herts BR et al (1999) Three-dimensional volume rendered computerized tomography for preoperative evaluation and intraoperative treatment of patients undergoing nephron sparing surgery. J Urol 161:1097–1102

Dachman AH, Newmark GM, Mitchell MT et al (1998) Helical CT examination of potential kidney donors. AJR Am J Roentgenol 171:193–200

Dalrymple NC, Srinivasa RP, Freckleton MW et al (2005) Informatics in radiology (infoRAD): introduction to the language of three-dimensional imaging with multidetector CT. RadioGraphics 25:1409–1428

El-Diasty T, Mansour O, Farouk A (2003) Diuretic contrast-enhanced magnetic resonance urography versus intravenous urography for depiction of non dilated urinary tract. Abdom Imaging 28:135–145

El-Diasty TA, El-Ghar ME, Shokeir AA et al (2005) Magnetic resonance imaging as a sole method for the morphological and functional evaluation of live kidney donors. BJU Int 96:111–116

Farres MT, Pedron P, Gattengo B et al (1998) Helical CT of the ureteropelvic junction obstruction: accuracy in detection of crossing vessels. J Comput assist Tomogr 22:300–303

Garcia-Valtuille R, Garcia-Valtuille AI, Abascal F et al (2006) Magnetic resonance urography: a pictorial overview. Br J Radiol 79:614–626

Hagspiel KD , Butty S, Nandalur KR et al (2005) Magnetic resonance urography for the assessment of potential renal donors: comparison of the RARE technique with a low-dose gadolinium-enhanced magnetic resonance urography technique in the absence of pharmacological and mechanical intervention. Eur Radiol 15:2230–2237

Joffe SA, Servaes S, Okon S et al (2003) Multi-detector row CT urography in the evaluation of hematuria. RadioGraphics 23:1441–1456

Kawashima A, Glockner JF, King BF Jr (2003) CT urography and MR urography. Radiol Clin North Am 41:945–961

Kawashima K, Vrtiska TJ, LeRoy AJ et al (2004) CT urography. RadioGraphics 24:S35–58

Kenney PJ (2003) CT evaluation of urinary lithiasis. Radiol Clin North Am 41:979–999

Korobkin M (2005) CT urography. Eur Radiol 15 (Suppl 4): D82–84

McTavish JD, Jinzaki M, Zou KH et al (2002) Multidetector row CT urography: comparison of strategies for depicting the normal urinary collecting system. Radiology 225:783–790

Neri E, Boraschi P, Caramella D et al (2000) MR virtual endoscopy of the upper urinary tract. AJR Am J Roentgenol 175:1697–1702

Nolte-Ernsting CC, Adam GB, Gunther RW (2001) MR urography: examination techniques and clinical applications. Eur Radiol 11:355–372

Nolte-Ernsting CC, Bucker A, Adam GB et al (1998) Gadolinium-enhanced excretory MR urography after low-dose diuretic injection: comparison with conventional excretory urography. Radiology 209:147–157

Nolte-Ernsting CC, Krombach G, Staatz G et al (1999) Virtual endoscopy of the upper urinary tract based on contrast-enhanced MR urography data sets. Rofo 170:550–556

Nolte-Ernsting CC, Staatz G, Tacke J et al (2003) MR urography today. Abdom Imaging 28:191–209

O'Malley ME, Soto JA, Yucel EK et al (1997) MR urography: evaluation of a three-dimensional fast spin-echo technique in patients with hydronephrosis. AJR Am J Roentgenol 168:387–392

Roy C, Saussine C, Jahn C et al (1994) Evaluation of RARE-MR urography in the assessment of ureterohydronephrosis. J Comput Assist Tomogr 18:601–608

Rubin GD (2003) 3-D imaging with MDCT. Eur J Radiol 45[Suppl 1]:S37–S41

Rubin GD, Beaulieu CF, Argiro V et al (1996) Perspective volume rendering of CT and MR images: applications for endoscopic imaging. Radiology 199:321–330

Sheth S, Fishman EK (2004) Multi-detector row CT of the kidneys and urinary tract: techniques and applications in the diagnosis of benign diseases. RadioGraphics 24: e20

Sheth S, Scatarige JC, Horton KM et al (2001) Current concepts in the diagnosis and management of renal cell carcinoma: role of multidetector CT and three-dimensional CT. RadioGraphics 21:S237–S254

Silverman SG, Akabar SA, Mortele KJ et al (2006) Multidetector row CT urography of normal urinary collecting system: furosemide versus saline as adjunct to contrast medium. Radiology 240:749–755

Tublin ME, Murphy ME, Delong DM et al (2002) Conspicuity of renal calculi at unenhanced CT: effects of calculus composition and size and CT technique. Radiology 225:91–96

Urban BA, Ratner LE, Fishman EK (2001) Three-dimensional volume-rendered CT angiography of the renal arteries and veins: normal anatomy, variants, and clinical applications. RadioGraphics 21:373–386

Musculoskeletal System

24

Anne Cotten, Benoît Sauer, and Alain Blum-Moyse

CONTENTS

A. Cotten, MD
Professor, Service de Radiologie Ostéo-Articulaire, Hôpital Roger Salengro - CHRU de Lille, Boulevard du Pr. J. Leclercq, 59037 Lille Cédex, France
B. Sauer, MD
A. Blum-Moyse, MD
Service de Radiologie, Hôpital Central, 29 Avenue Maréchal de Lattre de Tassigny, 54035 Nancy Cédex, France

24.1 Introduction

Musculoskeletal applications of three-dimensional (3D) imaging were among the first to be developed and remain its most common clinical application, as this noninvasive method offers a unique tool to characterize the bone morphology and to understand the architecture and kinematics of normal and pathologic joints in vivo. Indeed, accurate evaluation of complex anatomy or complex spatial relationships between the lesions and adjacent anatomic structures plays a major role in clinical applications of 3D imaging, as it represents a dramatic improvement over the use of planar cross-sectional imaging alone. This imaging has been shown to have an impact on diagnosis and surgical management in a number of skeletal applications including trauma, malformations and tumors. Moreover, 3D images frequently integrate hundreds of sections in a form that is often easier to interpret than the sections themselves (Calhoun et al. 1999).

Three-dimensional imaging has been developed from images obtained with multiple modalities, but computed tomography and magnetic resonance imaging represent the most common data sets in the musculoskeletal applications of 3D imaging. However, a recent X-ray imaging system (EOS) has also developed and may have potential useful indications in future.

24.2 EOS System

The EOS system is new X-ray imaging system unique in that it combines the advantages of 3D imaging, very low irradiation doses, and weight bearing full-body scanning of simultaneous face and profile. This result is the combination of two major innovations:

- A digital dual radiography scanning system using microstrip gas detectors, developed through research carried out by the Nobel Prize Georges Charpak and Biospace. This system makes it possible to take very low-dose irradiation X-rays (5–10 times less than conventional X-rays), with high quality images. In the EOS system, two sets of these detectors are placed at an angle of 90.
- A new modelling technique using software capable of making a precise 3D reconstruction of the external envelop of an osteoarticular structure from a simple pair of X-rays (front and side) unlike the 500 or more CT-scan slices necessary to reconstruct a spine or a pelvis. This system requires a hundred to thousand times less radiation. Moreover, the EOS 3D image is available for patients in the upright position, thereby reflecting their weight-bearing condition.

This combination of large format digital X-ray imaging with 3D bone imaging in the upright position make this system potentially useful for the diagnosis, planning and follow-up of orthopaedic and surgical treatment, particularly those of scoliosis (Le Bras et al. 2003; Pomero et al. 2004; Mitton et al. 2006) (Figs. 24.1 and 24.2).

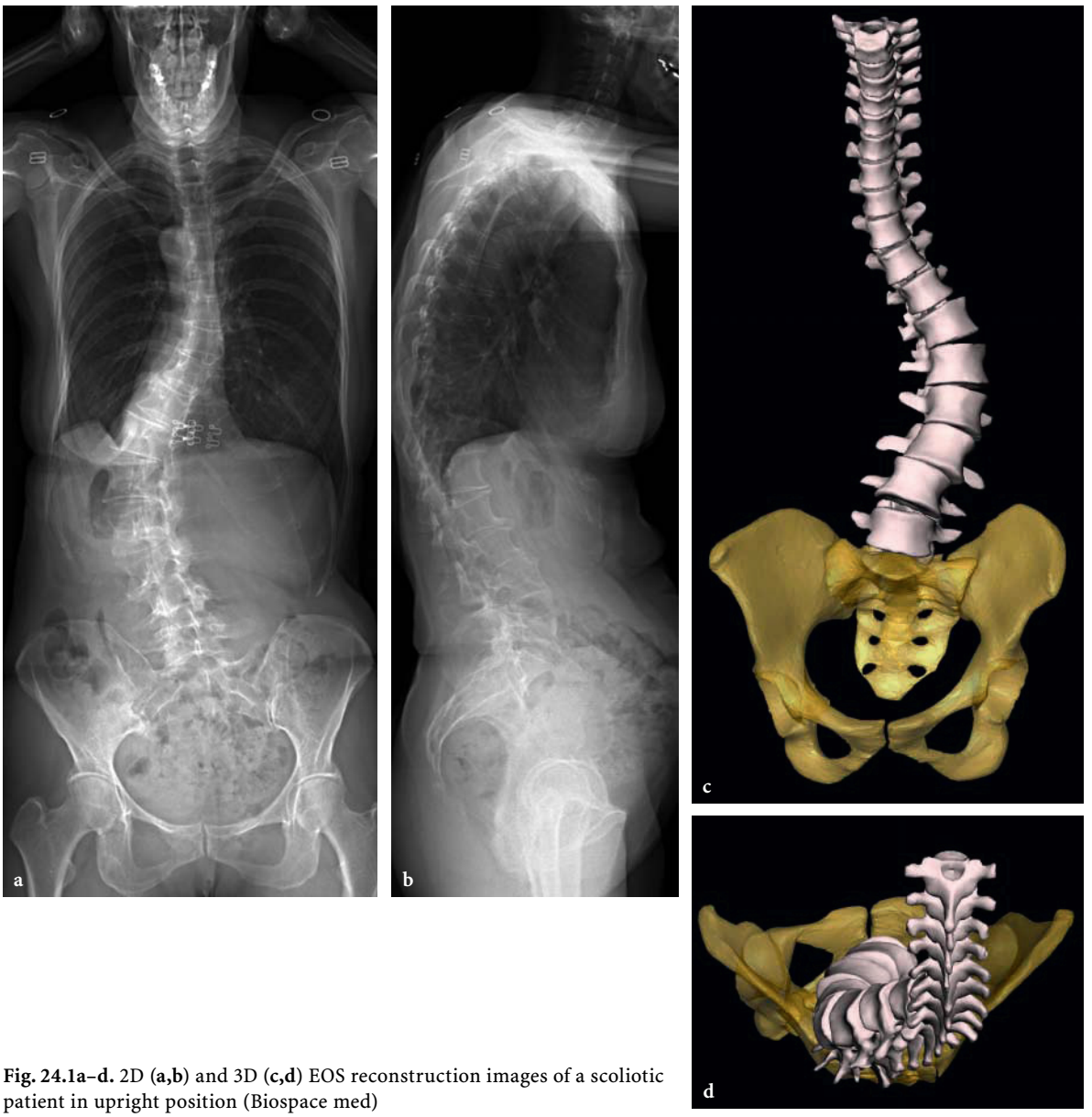

Fig. 24.1a–d. 2D (**a,b**) and 3D (**c,d**) EOS reconstruction images of a scoliotic patient in upright position (Biospace med)

24.3 3D CT and MR Imaging

Three-dimensional medical images of CT and MR data sets can be generated with a variety of computer algorithms. The three most commonly used techniques are shaded surface display (SSD), maximum intensity projection (MIP) and 3D volume rendering (Calhoun et al. 1999).

24.4 Computer Algorithms

24.4.1 Shaded Surface Display (SDD)

SSD is a process in which apparent surfaces are determined within the volume of data and an image representing the derived surfaces is displayed (Calhoun et al. 1999). Because this process reduces the original data volume down to a compact surface model, surface rendering algorithms can operate very rapidly, with flexibility in image rendering (Kuszyk et al. 1996). In general, surface rendered images have the clearest volume depth cues of all 3D images, producing skeletal images that appear more three-dimensional than those created using volume rendering (Calhoun et al. 1999). Applications in surgical planning take advantage of this capability that allows surface models to be interactively repositioned and manipulated.

However, their clinical utility in skeletal pathology is compromised by an inability to show subcortical detail (Calhoun et al. 1999) (Fig. 24.3). Indeed, surface rendering depicts only the bone surface. Most of the available data is not incorporated into the 3D image. In cases where the pathology of interest is subcortical or obscured by overlying bone, surface rendering does not display the lesion. Another drawback is poor image fidelity. Surface rendering simplifies the data into a binary form, classifying each pixel as either 100% bone or 0% bone. This finite voxel size in medical data produces many voxels that are only fractionally composed of bone, and classifying them as all or none introduces stair-step artefacts into the image (Drebin et al. 1989; Wang and Vannier 1994). By varying the threshold minimally, a fracture gap can open or close, bony processes lengthen and shorten, and "holes" in the cortex are created and fused (Kuszyk et al. 1996). The last drawback is that surface rendering is not adequate for the visualization of structures that do not have naturally well differentiated surfaces (Calhoun et al. 1999).

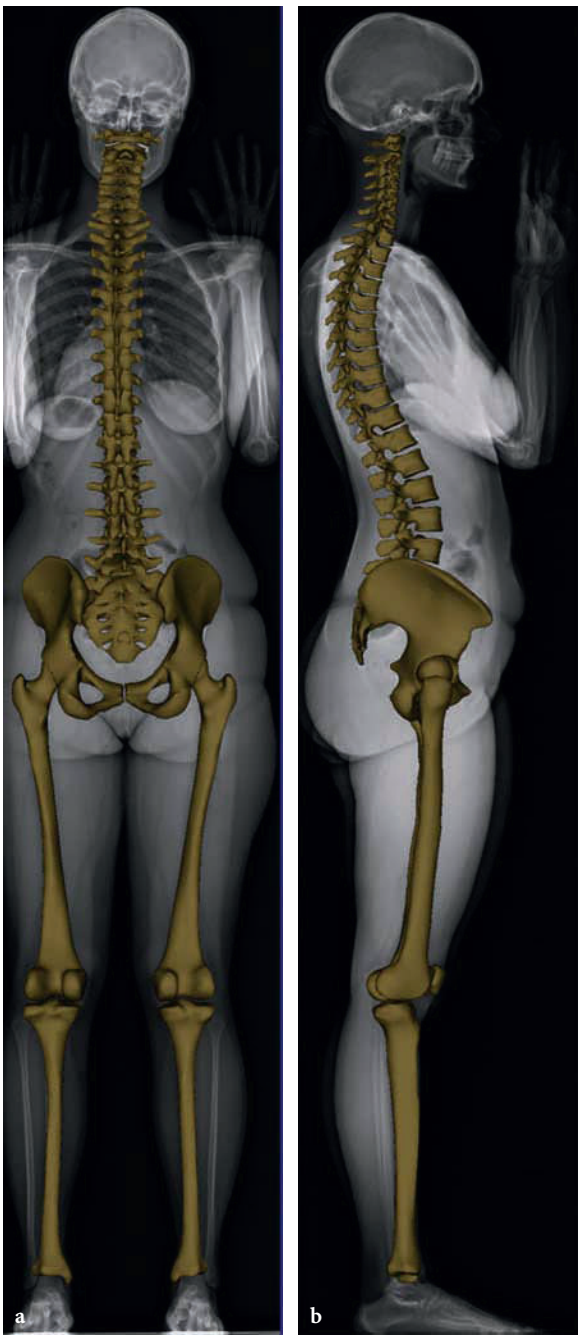

Fig. 24.2a,b. Superposition of the 3D EOS reconstruction on the 2D images in a patient in upright position (Biospace med). Analysis of spine and legs deformities is made possible

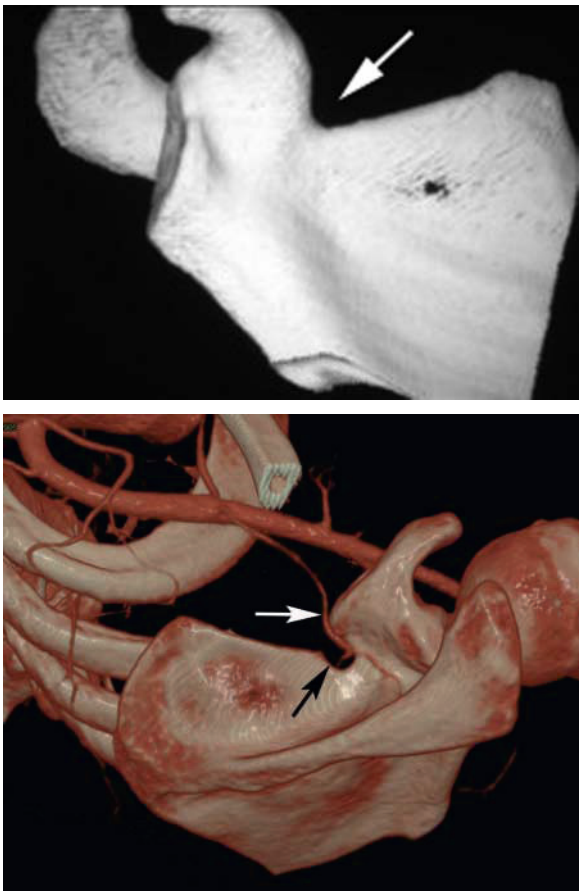

Fig. 24.3a,b. Suprascapular notch analysed by SDD (**a**) and VRT performed after contrast administration (**b**). The suprascapular artery (*white arrow*) and its relationship with the suprascapular notch is well demonstrated on the VRT image

24.4.2 Maximum Intensity Projection (MIP)

MIP is the simplest of all 3D rendering techniques. In MIP, the intensity assigned to a pixel in the rendition is simply the maximum scene intensity encountered along the projection line. It is most effective when the objects of interest are the brightest in the scene and have a simple 3D morphology and a minims gradation of intensity values. One limitation of this technique that must be taken into account to interpret the rendered images properly is that MIP image misrepresents anatomic spatial relationships because the planar projected data do not take spatial location into account (Calhoun et al. 1999). The anterior anatomic structures cannot be differentiated from the posterior ones.

The sliding thin slab maximum intensity projection (STS-MIP) and multiplanar volume reconstruction (MPVR) represent alternatives to MIP in which the volume is restricted to a thin slab that is only few voxel widths in depth (Napel et al. 1993). Pre processing is no longer required and the resulting images have a high contrast resolution.

Contrast material enhanced CT angiography and MR angiography are ideal applications for MIP (Udupa 1999) (Fig. 24.4). They both offer more rapid examination than conventional angiography and lower or no radiation dose. In addition, the 3D nature of the acquired data makes them amenable to post processing and reprojection from any angle (Napel et al. 1992).

Another application of MIP for the diagnosis of craniostenosis and fracture of the calvaria has recently been reported (Medina 2000).

24.4.3 Volume Rendering

Unlike surface rendering, volume rendering uses a percentage classification that provides a realistic depiction of voxels that are only fractionally composed of bone (Kuszyk et al. 1996). Moreover, the algorithm incorporates all the data contained in the volume into the displayed image, leading to greater fidelity in the data. This algorithm has the advantage of showing multiple overlying and internal features with a displayed intensity related to the amount of bone encountered along a line extending through the volume. The main drawback associated with volume rendering is the difficulty in appreciating 3D relationships in very transparent volume rendered images.

Three volume rendering techniques (unshaded bone, shaded bone and shaded opaque bone) can help reveal both surface and internal detail and can be used for a better understanding of the volume rendered images:

- The unshaded bone algorithm creates images that appear similar to plain radiographs. The lack of surface shading and enhancement makes these images the simplest, most artefact-free of the three volume rendering techniques. For some authors (Kuszyk et al. 1996), the ability to depict multiple overlying structures with few artefacts has made this algorithm the most useful volume rendering technique for most skeletal applications. Video loop rotation greatly enhances 3D understanding when viewing these images.

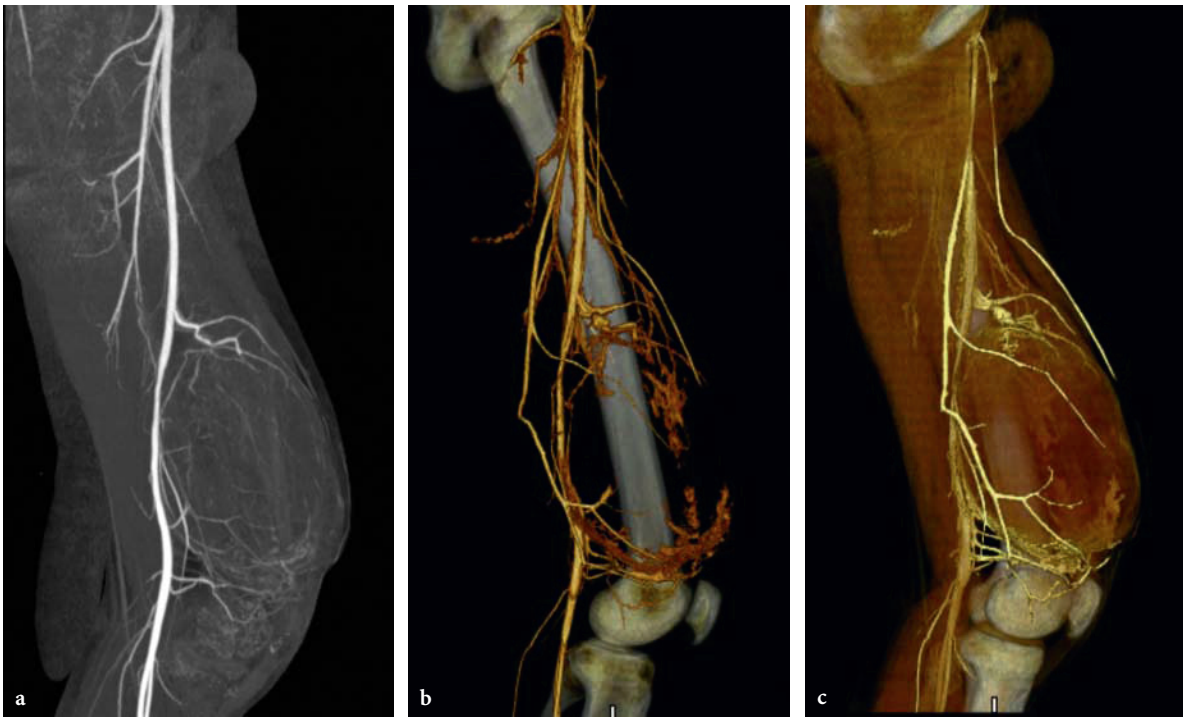

Fig. 24.4a–c. Sarcoma of the thigh. The visibility of the relationship between the soft tissue tumour and the adjacent vessels on MIP (**a**) and VRT (**b,c**) images may be useful for surgical planing, especially when this precise relationship in the space is provided (VRT images). Color can be used for differentiation between anatomic structures of different densities, and soft tissue can be deleted (**b**) to highlight vascular structures, or not (**c**)

- The shaded bone algorithm incorporates surface shading and enhancement at interfaces of tissues with different CT numbers. This can be useful for accentuating lytic or sclerotic lesions, or clearly defining the medullary canal. However, this technique increases computer rendering time and can serve as a source of artefact which can make these images difficult to interpret. Kuszyk et al. (1996) have found the shaded bone to be the least helpful of the three volume rendering algorithms.
- The opaque bone algorithm may be useful in applications in which detail and 3D understanding are of importance. Indeed, opacity dramatically improves 3D anatomic relationships with a degree of clarity similar to that of surface rendering. In the extreme case where the opacity is 100%, no internal detail is visible and the resulting image is effectively a surface model (Kuszyk et al. 1996). However, the decreased transparency in these images can make it more difficult to appreciate multiple overlying structures and subcortical lesions.

Color can be used for differentiation between anatomic structures of different densities. For example, it may be helpful in displaying the tendons or vessels. However, it must be determined whether the use of color provides additional information.

As volume rendering is now possible on inexpensive desktop computers, it seems to be the most valuable algorithm for most skeletal applications as it has the advantages of both MIP (good contrast and good differentiation between tissues) and SSD (precise location of the lesion in the space) (Fig. 24.4). Moreover, with this algorithm it is easy to select different volumes, to delete some tissues, to highlight others, to isolate bones or to present them with their adjacent soft tissues or vessels (Figs. 24.4–24.6). Bones and vessels may appear more or less transparent, depending on the necessity to analyze the anatomic structures located behind them (Iochum et al. 2001). It is also easy to obtain different projections of the anatomic area and to turn around it.

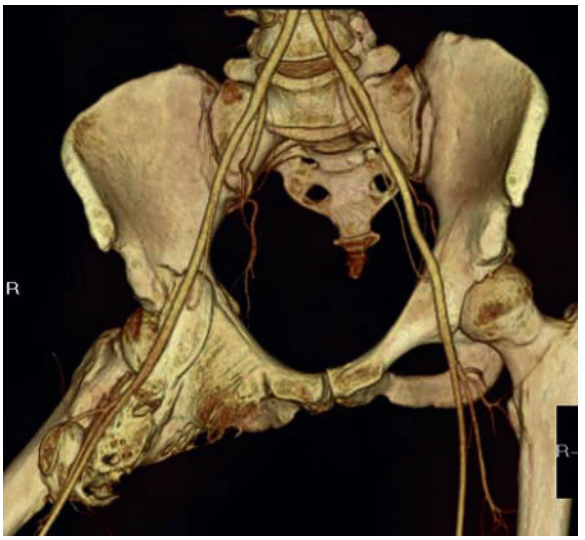

Fig. 24.5. Hip paraosteoarthropathy. The relationship between the right paraarticular ossification and the adjacent iliac artery is well demonstrated on this VRT image

Fig. 24.6. Acetabulum fracture. VRT allows the clear and precise visualization of this nondisplaced fracture after deletion of the femur

24.5 Clinical Applications

24.5.1 Trauma

The first applications of 3D imaging were in the evaluation of skeletal fractures and planning for orthopedic surgery. Indeed, a precise classification and an optimal understanding of fractures are the basis of conservative treatment or adequate surgery. Three-dimensional images are particularly useful for planning surgery, especially in determining the surgical approach and screw placement. This is especially the case for acetabular fractures, where 3D evaluation is of the utmost importance for precise definition of the direction and magnitude of displacement of the bone (Figs. 24.6 and 24.7). The hip joint space and its relationship to the fracture must be accurately analyzed. In selected cases, the femur can be disarticulated from the acetabulum (Fig. 24.6). Preoperative planning of fractures in anatomically complex areas such as the scapula, the spine, the foot and the wrist can also be improved by 3D imaging.

Fractures analysis is frequently based on the axial sections as well as on multiplanar reconstructions (MPRs) and 3D surface shaded rendering. However, although MPR allows precise quantification of the displacement of the fragments, it does not display a global

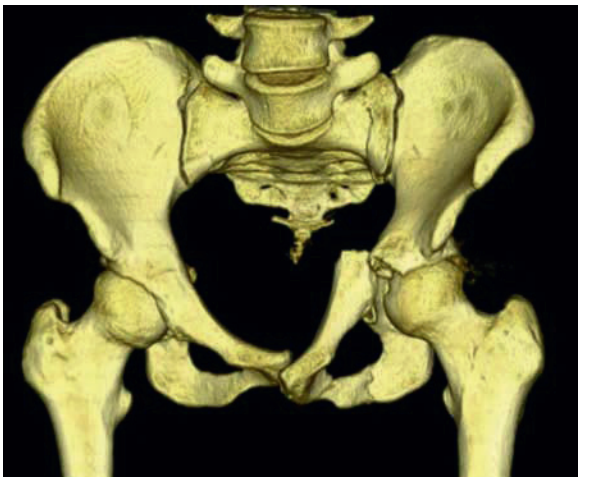

Fig. 24.7. Acetabulum fracture. VRT allows an accurate analysis of the displacement of the fracture

and comprehensible view of the lesions (Fig. 24.8). This explains why surgeons usually prefer 3D images for surgical planning (Pretorius and Fishman 1999a). Three-dimensional surface shaded rendering greatly facilitates the evaluation of complex fractures, but can fail to recognize minimally displaced fractures and lesions beneath the bony surface. Moreover, the images can demonstrate stair-step artefacts.

Volume rendering has been found highly superior to shaded surface rendering for the accurate demonstration of subtle fractures, particularly those ori-

ented in the axial plane (Pretorius and Fishman 1999b). It also clearly demonstrates complex injuries and complicated spatial information about the relative positions of fracture fragments (Figs. 24.9 and 24.10). The use of intravenously administered contrast material allows simultaneous evaluation of osseous and vascular structures within the affected area. Associated vascular injuries can be identified

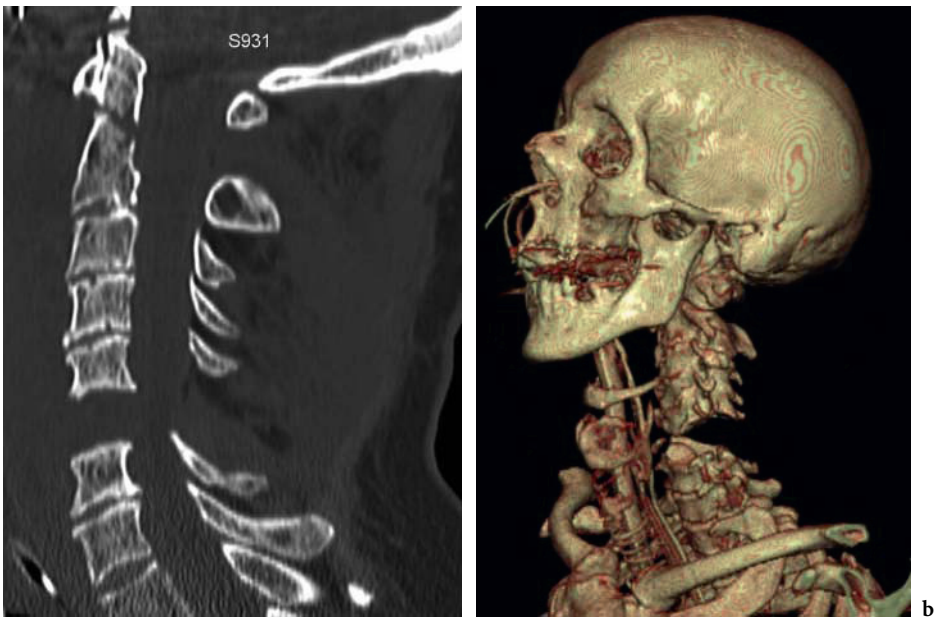

a b

Fig. 24.8a,b. C5–C6 dislocation with associated C2 fracture. Fracture and bone displacement are well analyzed on the MPR image (**a**), but the VRT image (**b**) allows a more global and comprehensible view of the lesions

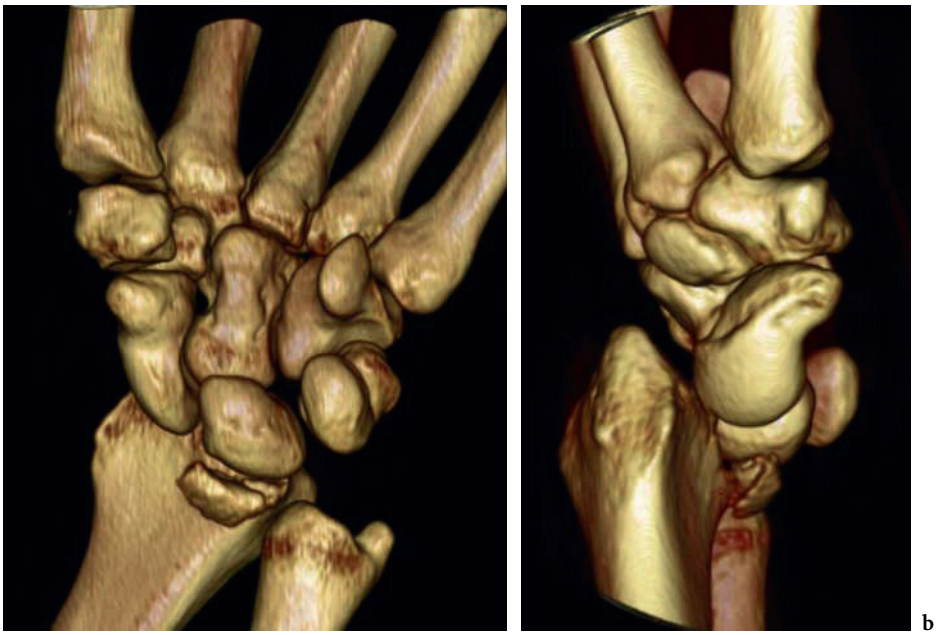

a b

Fig. 24.9a,b. Palmar radiocarpal dislocation with fracture of the volar aspect of the distal radius. Bones displacement and fracture are well depicted on these VRT images

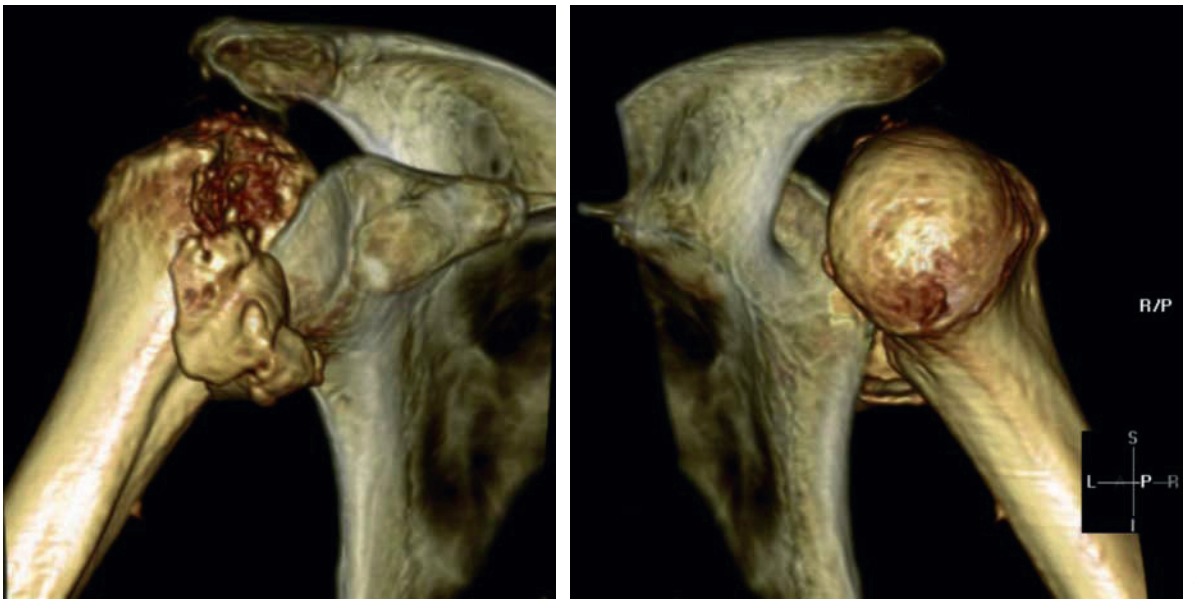

a b

Fig. 24.10a,b. Posterior dislocation of the shoulder. VRT images are useful for the analysis of the displaced humeral bone fragment and for the relationship between the humeral head and the glenoid

or excluded (Fig. 24.11). Moreover, reconstructions can be optimized to achieve high spatial or density resolution. Finally the images do not demonstrate stair-step artefacts.

24.5.2 Tumors

Three-dimensional imaging is also valuable in the evaluation of tumor extent and helps confirm the initial decision regarding tumor resectability and preoperative planning for the most appropriate type of tumor resection. Both CT and MR imaging can provide precise vascular cartography. However, CT volume rendering is the only 3D modality that allows, on the same image, clear visibility of the tumoral bone, soft tissue and vessels (Fig. 24.4). Two or three CT acquisitions must be performed. The first must be obtained at the peak of the contrast bolus in the artery and the second at the venous time. Sometimes it may be interesting to perform a third acquisition at a distance from the first contrast administration, and consequently to wait for the enhancement of the tumor. A second intravenous administration of contrast medium can then be performed to reveal the precise relationship between the enhanced tumor and the adjacent vessels (Blum and Regent 1995). Neovascularity is seen well with either the volume rendering technique or maximum intensity projection (MIP) imaging. Soft tissue vascular malformations are also especially well demonstrated and it is possible to map out the relationship of the lesion to arterial feeders (Fig. 24.12).

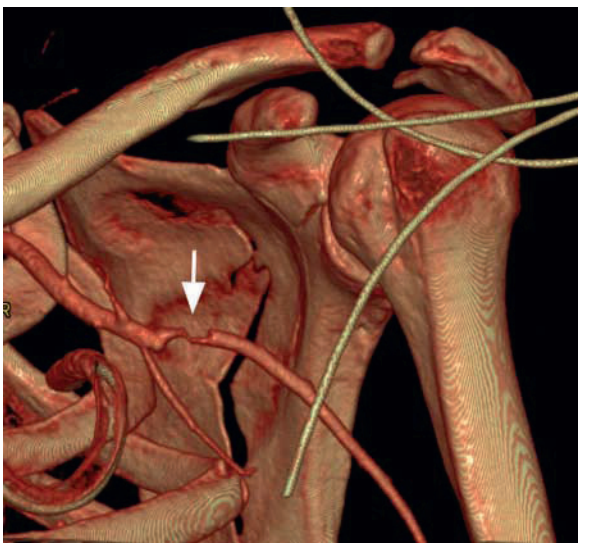

Fig. 24.11. Dissection of the axillary artery associated with a fracture of the body of the scapula. The simultaneous evaluation of osseous and vascular structures within the affected area is especially helpful in trauma (VRT image)

24.5.3 Malformations and Complex Osteoarticular Relationships

Three-dimensional images represent an efficient and comprehensive way to understand preoperatively the complexity of anatomic and pathologic relationships in the case of bone and joint malformations. For example, 3D CT can be a useful tool in the assessment of patients with congenital scoliosis, in that the 3D images provide easier comprehension of the anomalous segments and their relationship with other vertebrae (Fig. 24.13). Indeed, the complex 3D nature of the vertebral malformations makes their characterization by planar cross-sectional imaging methods difficult. Even if curved sagittal reconstructions can be helpful for the analysis of the relationship between the spine and the cord, MPR images do not display the global morphology of the anomalous segments and their interrelationships

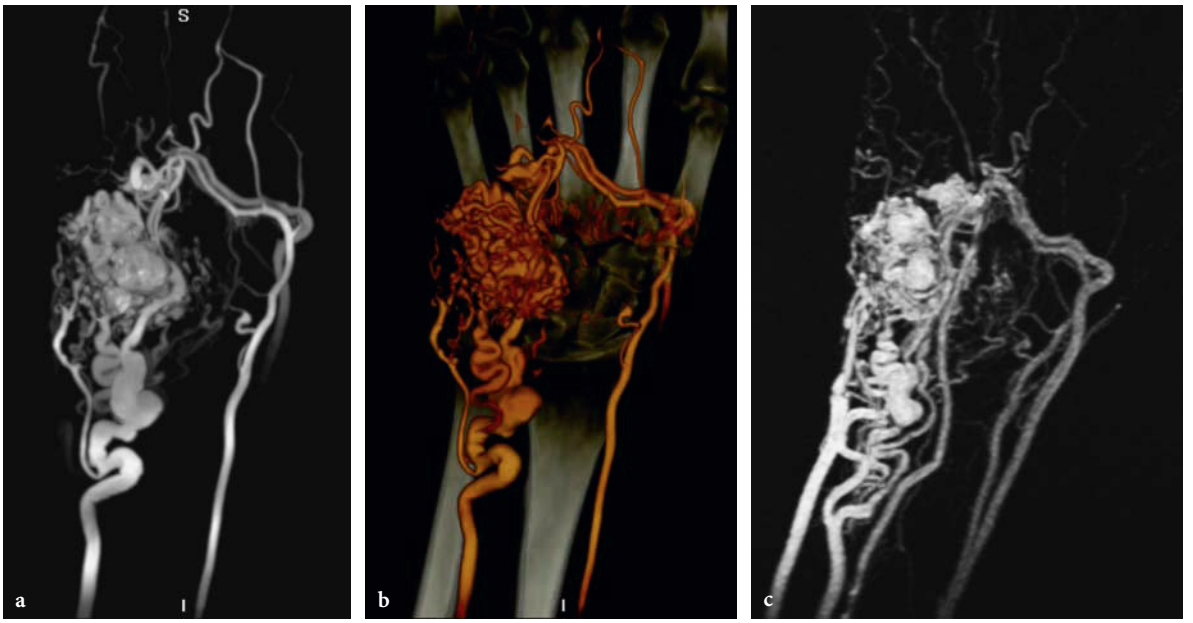

Fig. 24.12a–c. Vascular malformation of the wrist. The MIP (**a**) and VRT (**b**) images from multidetector CT angiography and MR angiography (**c**) show a dilated serpentine ulnar artery that, along with the medial palmar branch and the superficial palmar arch, feeds a high-flow vascular malformation (**a,b** reprinted with permission from Blum et al. 2006)

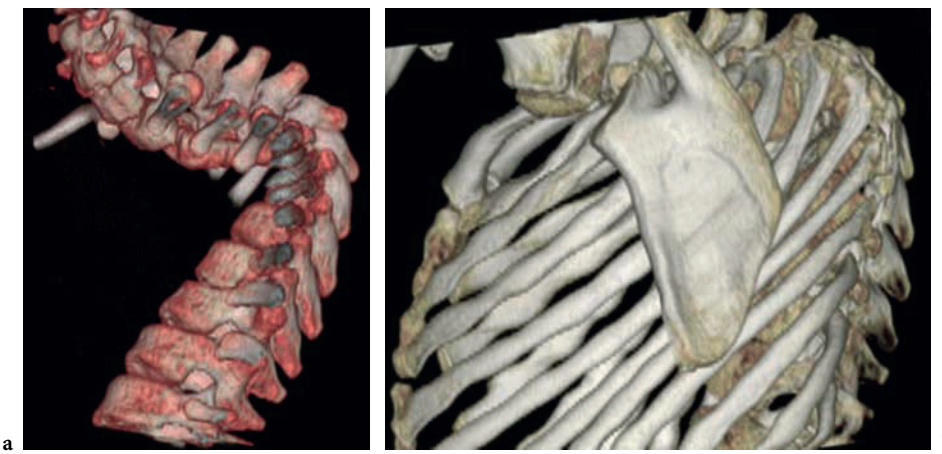

Fig. 24.13a,b. Scoliosis. VRT may be especially helpful in the comprehension of the complex 3D morphology of the anomalous spinal segment

in an easily perceived manner. Bush and Kalen (1999) have reported that, in 4 of their 12 cases of congenital scoliosis, 3D CT was markedly superior to CT with MPR in displaying the pathology, in that the pathology revealed by the 3D images was difficult to comprehend on both axial CT sections and the reformatted images, even in retrospect.

Three-dimensional display of CT data is also extremely valuable for planning reorientation osteotomies for the treatment of residual dysplasia of the hip. Three-dimensional reconstructions also greatly facilitate the diagnosis of rare pathologies such as snapping scapula (Mozes et al. 1999), related to mechanical impingement between the scapula and the rib cage, by demonstrating the bony component of this entity. Three-dimensional CT has also been found helpful in delineating Sprengel deformity in detail, and in planning scapuloplasty (Cho et al. 2000).

24.5.4 Paediatric Patients

The introduction of multidetector CT allowing true isotropic high-resolution volume data sets is especially valuable in the paediatric patient on a number of levels. First, this technique nearly eliminates the need for sedation and enables the successful completion of most studies in less than 10 s, which helps minimize the need for sedation and patient cooperation (Fayad et al. 2005). Second, the ability to retrospectively reconstruct multiple high-resolution image sets from the original raw data is possible, thereby requiring only one acquisition for production of three-dimensional (3D) CT images in numerous planes (Fayad et al. 2005). Finally, when used correctly, 3D CT volume imaging can help minimize the radiation dose to the paediatric patient.

24.5.5 Control of Orthopedic Hardware

Due to significant susceptibility artifact created by surgical hardware, MRI is not the study of choice for postoperative evaluations, especially for the assessment of healing of treated fractures and complications such as osteomyelitis or recurrence of a skeletal tumor (Fayad et al. 2005). When hardware is present, postoperative review of patients can be effectively accomplished by 3D volume rendering as this technique eliminates the vast majority of streak artefact (Fig. 24.14) and clearly delineates the relationship between hardware, bones and bone fragments (Calhoun et al. 1999; Pretorius and Fishman 1999b). CT of orthopedic hardware results in severe X-ray attenuation, which can lead to "missing" data on reconstructed axial images. With 3D imaging, data reformation from the axial plane into other planes will weight the true signal over the randomly distributed artifact when integrating two adjacent axial images. In this way, the true signal will be enhanced and artifact related to metal will be reduced on volume-rendered 3D CT images (Fayad et al. 2005).

24.5.6 Functional Anatomy of the Musculoskeletal System

Three-dimensional reconstructions of CT and MR images can delineate precisely the spatial relationship between bones and musculotendinous structures and produce a good 3D visual presentation of biodynamic events of human joints. Rotational motion of a shoulder, knee flexion, other complex musculoskeletal motions and muscle contraction (Fig. 24.15) can be assessed, as well as the effect of muscle dysfunction and its relevance to the mechanics of joints (Totterman et al. 1998). This method is of great interest because many biomechanical studies are based on dramatically simplified anatomic models.

Assessment of the dynamic compression of the subclavian artery when it crosses one of the tunnels of the thoracic outlet has been performed with both CT and MR imaging (Fig. 24.16). With CT, the arterial compression seems better depicted with volume rendered reconstructions than with the 3D shaded surface images and with sagittal reformations (Remy-Jardin et al. 2000). With MR imaging, MIP or volume rendering can be performed (Demondion 2007).

24.5.7 Cartilage

The emergence of new therapeutic concepts for treating cartilage disorders explains the increasing demand for accurate and objective evaluation of cartilage morphology in vivo (Hyhlik-Dürr et al.

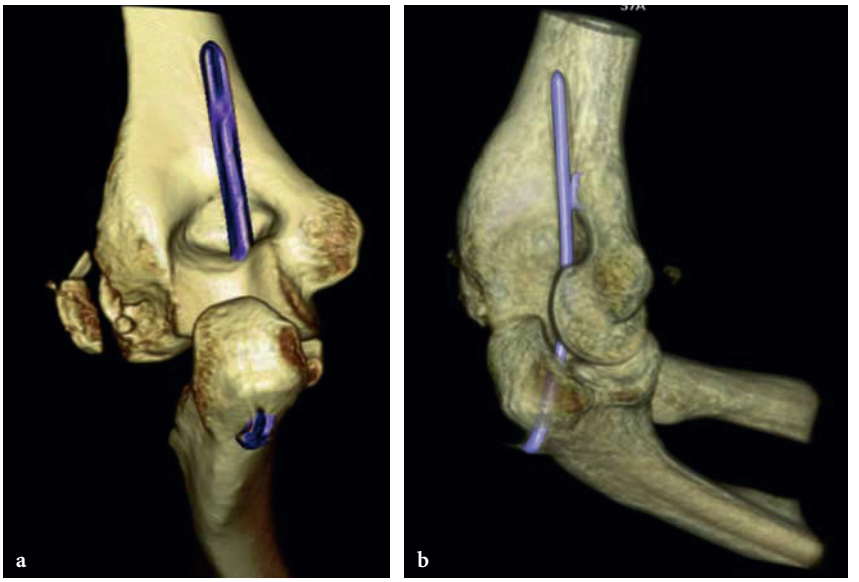

Fig. 24.14a,b. Dislocation of the elbow with lateral epicondyle fracture, treated by a humero-olecranial pin. The orthopedic hardware may be well analyzed on these VRT images with different degrees of opacity

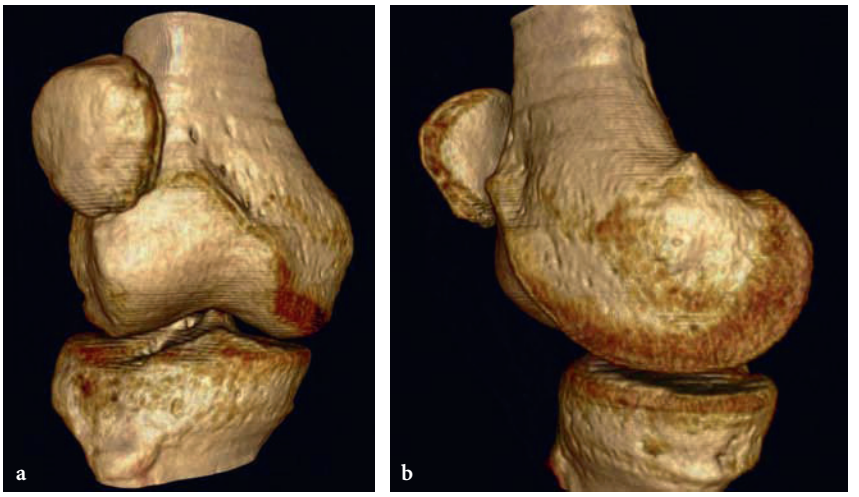

Fig. 24.15a,b. VRT images of the knee performed during quadriceps muscle contraction. Note the subluxation and rotation of the patella, and the trochlear dysplasia

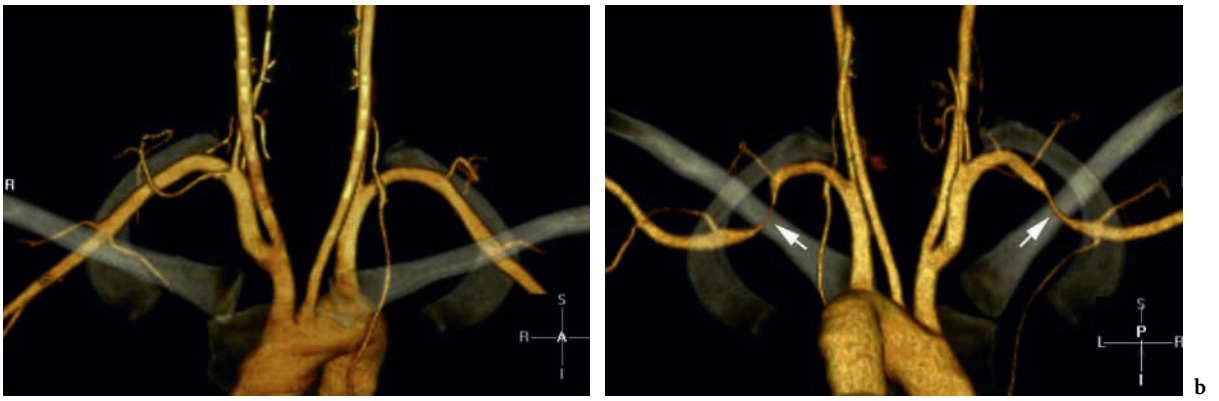

Fig. 24.16a,b. Bilateral thoracic outlet syndrome explored with CT imaging with the arms alongside the body (**a**) and after elevation of the arms (**b**). Compression of the subclavian artery in the entrance of the costoclavicular space (*arrows*) is well demonstrated after elevation of the arms

2000), especially with MR imaging due to its noninvasive nature. Because sectional images cannot be identically reproduced in longitudinal studies, 3D reconstruction postprocessing methods have been developed to quantify cartilage morphology (volume and thickness) independent of the respective section position and orientation (Hyhlik-Dürr et al. 2000). Several studies suggest the interest of quantitative MR-based cartilage morphometry as a tool to diagnose, stage and follow cartilage loss in the knee.

Sequences must be optimized to achieve a high spatial resolution and a fast acquisition time. As sequences must allow analysis of the cartilage with high contrast to the surrounding tissue, thin sliced 3D spoiled gradient echo sequences with spectral fat suppression (Eckstein et al. 1998) or with selective water excitation (Hyhlik-Dürr et al. 2000) are usually performed. The water excitation protocol allows the water-bound protons in the cartilage to be excited selectively and directly. Therefore, no prepulse is required as in conventional fat-suppressed imaging protocols.

Segmentation of the cartilage is then performed semiautomatically on a section by section basis by using a gray value oriented region-growing algorithm. An isotropic voxel size can be obtained with a shape-based interpolation method, and the cartilage is reconstructed in three dimensions with an optimized surface reconstructing algorithm (Eckstein et al. 1998; Hyhlik-Dürr et al. 2000). The cartilage volume is then computed from these reconstructions. The cartilage thickness can be determined by using a 3D minimal distance algorithm (Losch et al. 1997; Eckstein et al. 1998).

24.5.8 Navigation in Diagnosis and Therapy

Software systems simulating surgery and image-guided navigation for surgery and other therapeutic interventions have grown in importance in recent years. Key elements in image navigation systems are preoperative 3D imaging, a graphical display and interactive input devices. CT and MR imaging are commonplace today and 3D images are useful in complex interventions. Osteotomy and setting of pedicle screws in orthopedic surgery profit greatly from the high targeting precision of this technique (Laine et al. 2000). The term computer-aided surgery is now mainly used for intraoperative navigation within the body combining a 3D digitizer with preoperative CT/MR imaging.

Other navigation systems may also use intraoperative acquisition of images (Woodard et al. 2001; Haberland et al. 2000). These systems are consequently able to reflect the intraoperative changes.

24.6 3D Ultrasound

Three-dimensional ultrasound (3D US) is in the early stages of clinical assessment but seems to offer several advantages over conventional US, including 3D US image reconstruction with a single pass of the US beam, virtually unlimited viewing perspectives, and repeatable evaluation of anatomic structures and diseases entities (Downey et al. 2000). Image acquisition must be performed very cautiously, as unplanned transducer movement or involuntary patient motion (e.g., cardiac motion, respiratory motion) may produce artefacts severely degrading the quality of the images.

Three-dimensional US data acquisition systems can be tracked freehand systems (in which devices are attached to the transducer), untracked freehand systems (in which the images are digitized as the operator moves the transducer with a smooth, steady motion), mechanical assemblies (in which the transducer is propelled or rotated mechanically) or two-dimensional arrays (in which a square-faced or circular-faced transducer obtains true 3D data from an array of detectors) (Downey et al. 2000). Three-dimensional reconstruction techniques use a 3D surface model or a voxel-based volume model. Three different rendering modes can be selected: surface rendering for photorealistic images of objects, transparent rendering as either a maximum mode to enhance hyperechoic structures (e.g., bones) a minimum mode to accentuate hypoechoic structures (e.g., blood vessels and cysts) or color mode rendering for spatial reconstructions of volumes including Doppler or angiographic information (Brandl et al. 1999). MPR can also be performed.

If 3D US seems promising in fetal, gynecologic, prostate, breast and power Doppler imaging, the clinical applications of this technique in musculoskeletal diseases are still uncertain. Leotta and Martin (2000) have reported a technique for measuring the thickness of the rotator cuff from the 3D

compound volumes. To the best of our knowledge, only two papers have reported the usefulness of 3D US in the assessment of the rotator cuff lesions. For these authors, 3D US appears to facilitate diagnosis of partial-thickness rotator cuff tears both in patients and in artificial rotator cuff lesions of cadaveric shoulder joints (Wallny et al. 2000). However, further studies are required to confirm these results. Indeed if this modality may appear to be a powerful adjunctive tool to 2D US in providing a more comprehensive visualization of lesions, it must be determined whether the use of 3D US provides additional information and has an effect on patient management.

Three-dimensional high-resolution US has also proved to be useful for in vitro assessment of cartilage remodeling of rat patella in osteoarthritis (Lefebvre et al. 1998). Another application of 3D US could be in performing biopsy. Indeed, it has been suggested that 3D US can help facilitate needle localization and guidance during biopsy.

Finally, although it may appear time-consuming to measure the volume of lesions using 3D US, this technique of volume calculation allowing images of multiple areas to be obtained simultaneously in uniform conditions must be assessed, as it may have valuable applications in tumors and in the assessment of synovial disorders (Strunk et al. 2006).

References

Blum A, Regent D (1995) Scanner hélicoidal. Principes et modalités pratiques d'utilisation. Collection d'Imagerie Radiologique. Masson, Paris

Blum AG, Zabel JP, Kohlmann R et al (2006) Pathologic conditions of the hypothenar eminence: evaluation with multidetector CT and MR imaging. Radiographics 26:1021–1044

Brandl H, Gritzky A, Haizinger M (1999) 3D ultrasound: a dedicated system. Eur Radiol 9:S331–S333

Bush CH, Kalen V (1999) Three-dimensional computed tomography in the assessment of congenital scoliosis. Skeletal Radiol 28:632–637

Calhoun PS, Kuszyk BS, Heath DG et al (1999) Three-dimensional volume rendering of spiral CT data: theory and method. Radiographics 19:745–764

Cho TJ, Choi IH, Chung CY et al (2000) The Sprengel deformity: morphometric analysis using 3D CT and its clinical relevance. J Bone Joint Surg Br 82:711–718

Demondion X, Herbinet P, Van Sin Jan S, Boutry N, Chantelot CH, Cotten A (2007) Imaging assessment of a thoracic outlet syndrome. RadioGraphics (ahead of print)

Downey DB, Fenster A, Williams JC (2000) Clinical utility of three-dimensional US. Radiographics 20:559–571

Drebin RA, Magid D, Robertson DD et al (1989) Fidelity of three-dimensional CT imaging for detecting fractures gaps. J Comput Assist Tomogr 13:487–489

Eckstein F, Tieschky M, Faber SC et al (1998) Effect of physical exercise on cartilage volume and thickness in vivo: MR imaging study. Radiology 207:243–248

Fayad LM, Bluemke DA, Fishman EK (2005a) Musculoskeletal imaging with computed tomography and magnetic resonance imaging: when is computed tomography the study of choice? Curr Probl Diagn Radiol 34:220–237

Fayad LM, Johnson P, Fishman EK (2005b) Multidetector CT of musculoskeletal disease in the pediatric patient: principles, techniques, and clinical applications. RadioGraphics 25:603–618

Haberland N, Ebmeier K, Grunewald JP et al (2000) Incorporation of intraoperative computerized tomography in a newly developed spinal navigation technique. Comput Aided Surg 5:18–27

Hyhlik-Dürr A, Faber S, Burgkart R et al (2000) Precision of tibial cartilage morphometry with a coronal water-excitation MR sequence. Eur Radiol 10:297–300

Iochum S, Ludig T, Walter F, Fuchs A, Henrot P, Blum A (2001) Value of volume rendering in musculo-skeletal disorders. J Radiol 82:221–230

Kuszyk BS, Heath DG, Bliss DF et al (1996) Skeletal 3D CT: advantages of volume rendering over surface rendering. Skeletal Radiol 25:207–214

Laine T, Lund T, Ylikoski M et al (2000) Accuracy of pedicle screw insertion with and without computer assistance: a randomised controlled clinical study in 100 consecutive patients. Eur Spine J 9:235–240

Le Bras A, Laporte S, Mitton D, de Guise JA, Skalli W (2003) Three-dimensional (3D) detailed reconstruction of human vertebrae from low-dose digital stereoradiography. Eur J Orthop Surg Traumatol 13:57–62

Lefebvre F, Graillat N, Cherin E et al (1998) Automatic three-dimensional reconstruction and characterization of articular cartilage from high-resolution ultrasound acquisitions. Ultrasound Med Biol 24:1369–1381

Leotta DF, Martin RW (2000) Three-dimensional spatial compounding of ultrasound scans with weighting by incidence angle. Ultrason Imaging 22:1–19

Losch A, Eckstein F, Haubner M, Englmeier KH (1997) A non-invasive technique for 3-dimensional assessment of articular cartilage thickness based on MRI. I. Development of a computational method. Magn Reson Imaging 15:785–804

Medina LS (2000) Three-dimensional CT maximum intensity projections of the calvaria: a new approach for diagnosis of craniosynostosis and fractures. AJNR Am J Neuroradiol 21:1951–1954

Mitton D, Deschenes S, Laporte S, Godbout B, Bertrand S, de Guise JA, Skalli W (2006) 3D Reconstruction of the pelvis from bi-planar radiography. Comput Methods Biomech Biomed Eng 9:1–5

Mozes G, Bickels J, Ovadia D et al (1999) The use of three-dimensional computed tomography in evaluating snapping scapula syndrome. Orthopedics 22:1029–1033

Napel S, Marks MP, Rubin GD et al (1992) CT angiography of spiral CT and maximum intensity projection. Radiology 185:607–610

Napel S, Rubin GD, Jeffrey RB et al (1993) STS-MIP: a new reconstruction technique for CT of the chest. J Comput Assist Tomogr 17:832–838

Pomero V, Mitton D, Laporte S, de Guise JA, Skalli W (2004). Fast accurate stereoradiographic 3D-reconstruction of the spine using a combined geometric and statistic model. Clin Biomech 19:240–247

Pretorius ES, Fishman EK (1999a) Spiral CT and three-dimensional CT of musculoskeletal pathology. Radiol Clin North Am 37:953–974

Pretorius ES, Fishman EK (1999b) Volume-rendered three-dimensional spiral CT: musculoskeletal applications. Radiographics 19:1143–1160

Remy-Jardin M, Remy J, Masson P et al (2000) CT angiography of thoracic outlet syndrome: evaluation of imaging protocols for the detection of arterial stenosis. J Comput Assist Tomogr 24:349–361

Strunk J, Klingenberger P, Strube K, Bachmann G, Muller-Ladner U, Kluge A (2006) Three-dimensional Doppler sonographic vascular imaging in regions with increased MR enhancement in inflamed wrists of patients with rheumatoid arthritis. Joint Bone Spine 73:518–522

Totterman S, Tamez-Pena J, Kwok E et al (1998) 3D visual presentation of shoulder joint motion. Stud Health Technol Inform 50:27–33

Udupa JK (1999) Three-dimensional visualization and analysis methodologies: a current perspective. Radiographics 19:783–806

Wallny TA, Theuerkauf I, Schild RL et al (2000) The three-dimensional ultrasound evaluation of the rotator cuff an experimental study. Eur J Ultrasound 11:135–141

Wang GE, Vannier MW (1994) Stair-step artifacts in three-dimensional helical CT: an experimental study. Radiology 191:79–83

Woodard EJ, Leon SP, Moriarty TM et al (2001) Initial experience with intraoperative magnetic resonance imaging in spine surgery. Spine 26:410–417

Special Topics

Clinical Applications of 3D Imaging in Emergencies

25

Michael Rieger

CONTENTS

25.1 Introduction

After the introduction of multislice CT in 1992 with the advent of dual-slice scanners, this technology was improved in 1998 by the implementation of 4-slice, in 2000 with 8-slice, in 2002 with 16-slice, and in 2004 with 64-slice scanners. Development continues and at the turn of 2006 the first 64-slice dual-source devices with a very high temporal and spatial resolution were installed; thus one seems to observe a 2-year cycle for the launch of new CT devices. The technical enhancement that CT devices have experienced in recent years resulted in a considerable improvement of image quality and clinical applications. Scanning can be performed much faster, resulting in improved temporal resolution and reduced motion artifacts. The spectrum of indications has extended, and the algorithm of examinations changed, resulting in major advantages of multislice CT in traumatic and emergency imaging. On the one hand, the new scanners allow rapid and detailed examinations of the musculoskeletal system in submillimeter slices without limitation of scan volume; on the other hand, the high-resolution source images are the basis for high quality 2D and 3D reconstructions. The combination of both has proved valuable in the diagnosis of subtle abnormalities and in planning therapy.

M. Rieger, MD
Medizinische Universität Innsbruck, Universitätsklinik für Radiodiagnostik 1, Anichstrasse 35, 6020 Innsbruck, Austria

25.2 Computer Tomography

In comparison to single-slice CT, multislice CT fulfilled a fundamental step from a cross-sectional towards a true three-dimensional imaging modality that enables arbitrary cut planes as well as excellent 3D displays of the data volume. The basis for high quality 2D and 3D reconstructions is appropriate image acquisition with appropriate acquisition protocols. Single-slice CT suffered from a disproportion between the resolution in the axial plane (x- and y-axis), which is mostly a function of geometry and detector design, and the longitudinal resolution (z-axis), which is a function of the slice thickness. To generate an isotropic volume in the case of non-isotropic raw-data, interpolation steps are necessary. This disadvantage has been overcome with multislice CT which enables acquisition of near-isotropic voxels, a prerequisite for depiction of highly detailed 2- and

3D images Philipp et al. (2003). In order to produce homogenous reconstructions, the primary source images with a slice thickness of 0.5 mm–1.25 mm, depending on the CT device used, are reconstructed in overlapping steps of 50%, and the scan and display filter of view is adapted to the size of the scanned object. To take full advantage of these capabilities, production of 2D and 3D reconstructions has become an integral part of musculoskeletal and vascular examinations. Sections in the same image quality as the source date can be obtained in any plane. Positioning of the body part to be examined in the gantry becomes less important because any plane can be reformatted from the acquired volume. This capability simplifies examination of traumatized patients in particular. Imaging data from joints within casts can be reformatted retrospectively into orthogonal planes (Rydberg et al. 2000).

25.3 Three-Dimensional Rendering Techniques

Different 3D rendering techniques have proved a valuable tool in the diagnosis of various pathologic findings and for therapy planning in musculoskeletal disorders. For 3D post-processing, three different algorithms are commonly used. The surface shaded display (SSD) algorithm takes the first voxel encountered along a projection ray that exceeds a user-defined threshold value and defines the position and attenuation value of that voxel as the surface of the object. No additional information along the projection ray contributes to the viewed image; the surface is derived from only a small percentage (less than 10%) of the available CT data. All structures are shown in the same color, and information about the attenuation of a structure is lost completely. Therefore, SSD images are only capable of demonstrating gross 3D relationships but fail to display lesions hidden beneath the bone surface. It is not adequate for the visualization of structures that do not have naturally well-differentiated surfaces. As a result of this technical disadvantage some, especially undislocated, fractures may be under-diagnosed. In addition, SSD also tends to demonstrate stair-step artifacts. An advantage of this technique is that many of today's graphics computers are optimized for the display of surface models. Applications in surgical planning (e.g., for virtual planning in corrective osteotomy, for maxillofacial reconstruction) take advantage of this capability that allows surface models to be interactively repositioned and manipulated.

The maximum intensity projection (MIP) technique evaluates each voxel along a line from the viewer's eye through the volume of data and selects the maximum voxel value, which is then used as the displayed value. MIP has proved to be particularly useful in creating angiographic images from CT and magnetic resonance (MR) imaging data. MIP has some shortcomings that must be taken into account to interpret the rendered images properly: the displayed voxel intensity will represent only the material with the highest intensity along the projected ray. A high-intensity material such as calcification will obscure information from intravascular contrast material. MIP usually has superior accuracy compared with SSD in CT angiography.

The third 3D rendering technique, volume rendering (VR), makes use of the entire data set and thus conveys more information than SSD and MIP. In VR, the contributions of each voxel along a line of sight from the viewer's eye through the data set are summed. This process is repeated many times to determine each pixel value in the displayed image. VR can show multiple internal and overlying features, and the displayed intensity is related to the amount of bone encountered along a line extending through the volume (Fig. 25.1). Additionally, the flexibility of the VR algorithm allows the radiologist to tailor the degree of surface shading and bone opacity to the actual clinical problem. These advantages have made VR the superior method as compared with SSD for a variety of multislice CT applications. For the performance of 3D rendering techniques it is important to calculate the source data in a standard reconstruction kernel instead of a bone algorithm. This is explained by the much higher image noise of the transverse images when reconstructed with the bone algorithm. As a result of that image noise, certain randomly distributed soft tissue pixels gain equally high attenuation values as bone. They may then appear in the VR images, reduce the image quality, and possibly render the coherence of the displayed structures difficult (Pretorius and Fishman 1999; Kuszyk et al. 1996; Alkadhi et al. 2004; Calhoun et al. 1999).

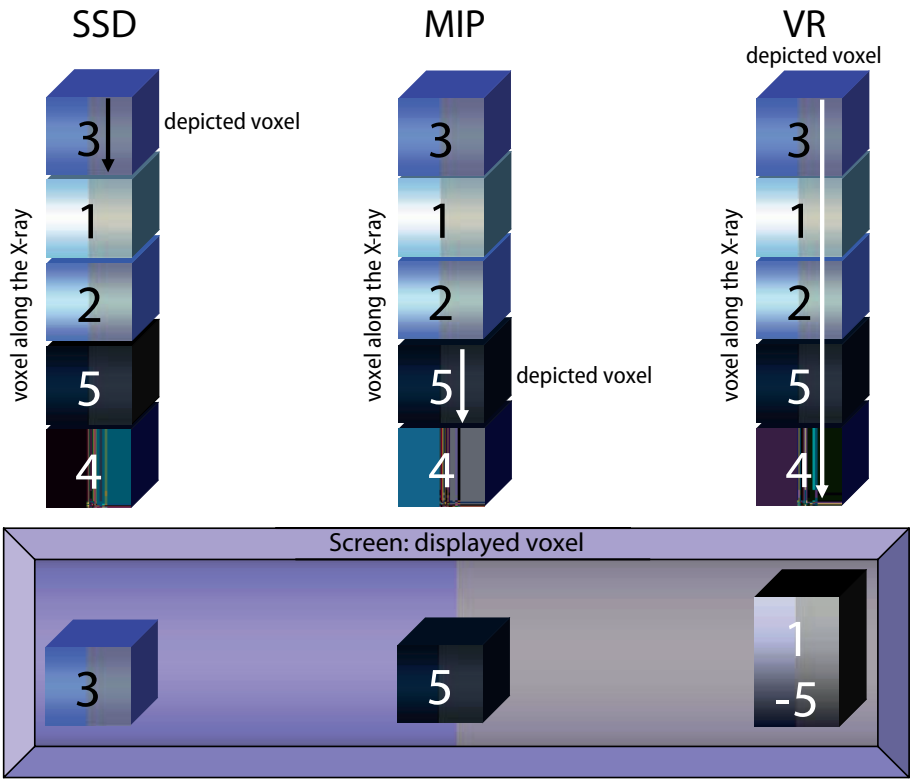

Fig. 25.1. The surface shaded display (SSD), maximum intensity projection (MIP) and volume-rendering (VR) techiques. The SSD algorithm takes the first voxel encountered along a projection ray that exceeds a user-defined threshold value and defines the position and attenuation value of that voxel as the surface of the object. MIP technique evaluates each voxel along a line from the viewer's eye through the volume of data and selects the maximum voxel value, which is then used as the displayed value. In VR, the contributions of each voxel along a line of sight from the viewer's eye through the data set are summed

25.4 Vascular Emergencies

25.4.1 Acute Subarachnoidal Hemorrhage

Recent studies found detection rates of intracranial aneurysms with multislice CT angiography up to 97%, and some authors already solely rely on findings of CT angiography (CTA) in patients with SAH. In our experience, as well as in some reports in the literature, there have already been cases where CTA showed aneurysms that were not seen on standard DSA. For the increasing number of aneurysms treated by using an endovascular approach, CTA may be used as a tool for therapeutic decision making and therapy planning; a major advantage of CTA compared with DSA is the non-invasive work-up, which can be performed immediately following the confirmation of SAH with non-enhanced CT and the generation of high resolution 3D information on the exact anatomy of the intracranial arteries within a few minutes (Fig. 25.2). These 3D models can also be very helpful for therapy planning. When intravascular

Fig. 25.2. Oblique transversal reformatted volume-rendered multi-detector row CT angiogram with a superior cut of a patient suffering from a subarachnoidal hemorrhage. Image shows a giant aneurysm of the right median cerebral artery (*black asterisk*) with a small daughter aneurysm (*long arrow*). There are two other small aneurysms, one in the posterior branch of the median cerebral artery (*short arrow*) and the other in the anterior communicating cerebral artery (*arrowhead*)

coiling is the therapy chosen on the basis of CTA findings, additional pre-therapeutic DSA is not necessary, as it is part of the coiling procedure. In addition, CTA can help predict the ideal angle for the endovascular approach. Information on the exact dimensions of an aneurysm provided by CTA can be used to determine the diameter of the first coil. For the neurosurgeon, information about adjacent vascular structures and the possibility of simulating the intraoperative view prior to surgery are often helpful (Tomandl et al. 2004). In our hospital, cases of subarachnoid hemorrhage with a negative CTA are additionally examined by means of DSA to exclude non-aneurysmal lesions such as arteriovenous fistulas or small angiomas.

25.4.2 Aortic Aneurysm, Dissection and Intramural Hematoma

Acute aortic dissection is a cardiovascular emergency that requires prompt diagnosis and treatment. CTA is a useful tool for diagnosing aortic aneurysms, dissections and intramural hematomas, determing their extent and predicting appropriate management. While the diagnosis of aneurysms, dissections and intramural hematomas is readily made from transverse sections, an assessment of the extent of the lesion, particularly when arterial branches are involved, is facilitated by the performance of 2D and 3D reconstructions. Together with reconstructions, CTA is more accurate than DSA for predicting aortic aneurysm size and is superior to DSA in its ability to demonstrate mural thrombus within an aneurysm, inflammatory aneurysms, and peri-aneurysmal blood due to contained rupture (Rubin 2003).

For Stanford type A aortic dissection or type A intramural hematoma, accurate diagnosis is urgently needed because in such cases early surgical repair should be considered, whereas the majority of patients with uncomplicated type B aortic dissection or intramural hematoma can be treated succsessfully with medical therapy. For acute type A aortic dissection time is very important for diagnosis and treatment because it is difficult to predict when it will rupture. (Yoshida et al. 2003). Multislice CT will not only detect aortic dissections and intramural hematomas, but will also assess the extent of its involvement. Devices with 16 rows or more will nearly overcome aortic motion artefacts, also in an ungated emergency examination, and therefore depict the pathology in a very high quality. MIP and VR can enable visualization that is equal or superior to that obtained with catheter angiography and demonstrate the relationship of the dissection and intramural hematoma to aortic branches (Fig. 25.3).

MSCT with MIP and VR may diagnose a traumatic or non-traumatic ruptured thoracic and abdominal aortic aneurysm on the basis of a contrast-enhanced CT scan that shows an aortic aneurysm with adjacent periaortic hemorrhage (Fig. 25.4) and may depict active bleeding, the extension of the aneurysm, the presence and extent of mural thrombosis and the stenosis or occlusion of vessels. For interventional stent repair, most of the measurements for determination of the optimal dimension and type of stent-graft are obtained with MSCT and 3D reconstructions.

Fig. 25.3. Oblique sagital volume-rendered multi-detector row CT angiogram of segmented thoracic aorta in a patient with an acute dissection Stanford A. The reconstruction shows the involvement of the supra-aortic braches (*arrows*). The dissection membrane is depicted as sharply bounded line (*arrowheads*)

Fig. 25.4. Oblique coronal volume-rendered multi-detector row CT angiogram of a ruptured aneurysm (*white asterisk*) of the abdominal aorta in a patient suffering from acute abdomen. Demonstration of the extensive retroperitoneal hemorrhage (*arrows*)

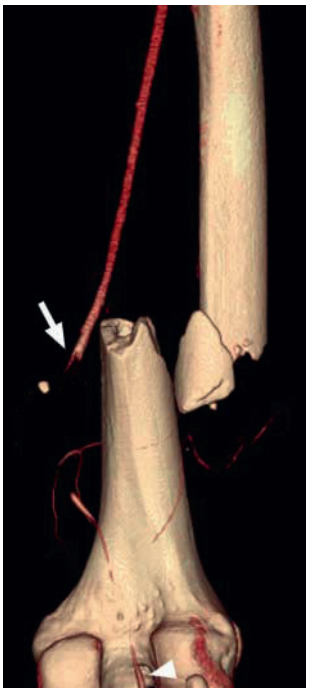

Fig. 25.5. Volume-rendered multi-detector row CT angiogram in a patient with blunt trauma to the left upper leg. Volume-rendered view shows an abrupt contrast material stop with irregular edge at the distal segment of the superficial femoral artery, which is laterally deviated, indicating arterial rupture (*arrow*). Image shows also a severely dislocated fracture of the femur shaft at the level of arterial interruption

25.4.3 Arterial Injuries of the Extremities

For the planning of surgical strategy after traumatic injuries of the upper or lower extremities, rapid investigation and accurate determination of the presence and location of an possibly accompanying vascular involvement is essential. The rapid acquisition and high-quality 3D perspectives of MSCT angiography enable reliable and reproducible detection of traumatic arterial injuries. Multiplanar reformations and volume-rendered views of the examined extremity facilitates the evaluation of the vascular structures and their relationship to bony structures, and have the potential to reduce image interpretation time when compared to the numerous axial source scans (Fig. 25.5). Furthermore, the rendered views were more appreciated by the surgeons. In summary, in our study we could demonstrate that MSCT angiography with 3D reconstructions enabled a significant and reproducible detectability and characterization of extremity arterial injuries with high image quality and vascular delineation. Therefore, MSCT angiography has substantial potential as the initial diagnostic method in patients with upper or lower extremity trauma (Rieger et al. 2006).

25.5 Skeletal Emergencies

The two major roles of MSCT in patients with musculoskeletal trauma are to define or exclude a fracture, and in the case of a fracture to determine its characterization and classification so as to provide guidance for therapy. In addition, MSCT will give information about soft-tissue pathologies and demonstrate osseous anatomy, especially in anatomically complex areas – for example pelvis, scapula, spine, foot and joint fractures. In comparison with trauma radiography, the results of which are often of poor quality, volume-rendered MSCT represents a significant advance in trauma imaging and significant saving in terms of patient time spent in the radiology department. In patients with pelvic fractures seen on axial CT images, treatment decisions have been shown to be altered in up to 30% of cases

because of findings on multiplanar or volume-rendered images. In general, these changes in treatment result when multiplanar or volume-rendered images reveal a more severe injury than was clinically suspected or than was seen on axial images (Pretorius and Fishman 1999).

25.5.1 Scull and Facial Fractures

Facial fractures are a common consequence of direct trauma, for example in a traffic accident. The complex anatomy of the facial structures requires superposition-free, detailed imaging. Therefore, helical CT in general is considered the standard imaging modality of facial fractures for characterization and classification. CT in at least two orthogonal planes, axial and coronal, is the standard examination to make a reliable and precise diagnosis for treatment planning (Philipp et al. 2003; Rosenthal et al. 2000). Narrow-collimation (0.6 mm–1.2 mm) axial acquisition yields a volume that allows creation of 2D and 3D reconstructions with very high spatial resolution (Fig. 25.6). Sections can be obtained in any plane.

25.5.2 Spinal Trauma

Radiologists and trauma surgeons are constantly trying to find ways to reduce the amount of time it takes to adequately image victims of trauma and simultaneously to improve the diagnostic quality. Considering the devastating consequences, especially for patients in whom a spine injury has been missed at examination, all casualties who have sustained trauma must be assessed for possible spine fractures. Ideally, the spine should be cleared within minutes after the admission of a trauma patient to the emergency room. In many cases, however, patients who have sustained severe trauma are uncooperative or unstable, and are thus difficult to examine clinically. Thus, a rapid and simultaneously accurate diagnostic of the suspected injured spine must be performed. The diagnostic work-up must detect the full extent of the injury, including the characterization and classification of the fracture, and must respond to the question whether a fracture is stable or not (Fig. 25.7). In cases with possible spinal cord damage caused by the spinal canal narrowing, bone fragments, hematoma or intervertebral disc material should be rapidly detected. In choosing the best

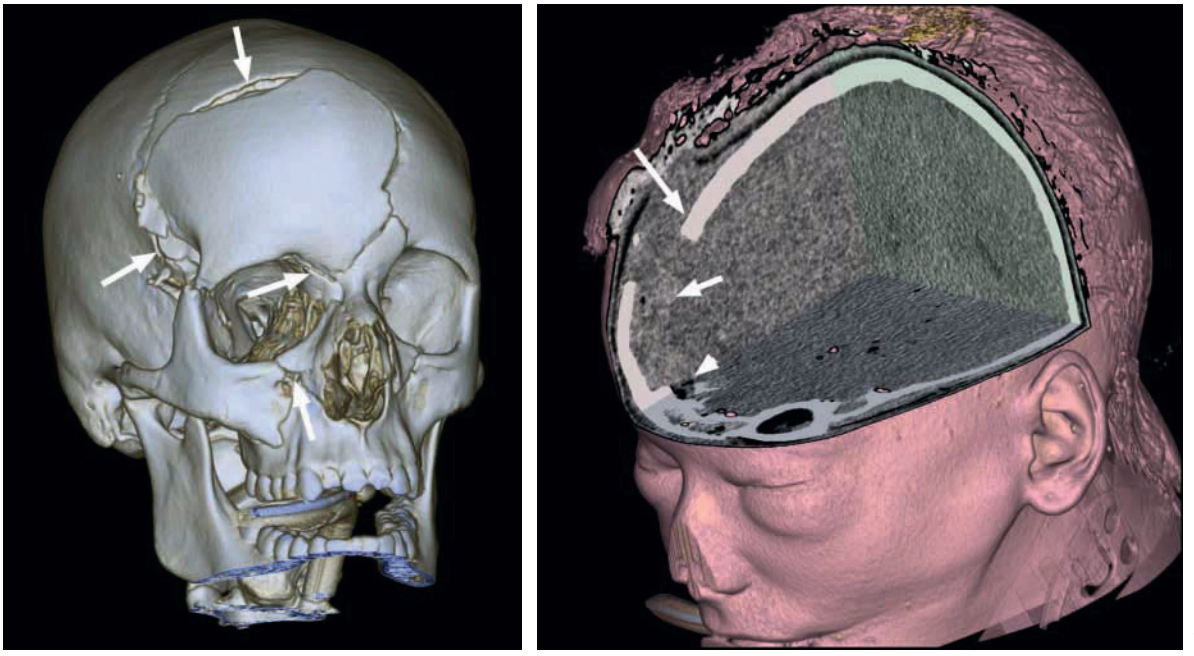

Fig. 25.6a,b. Volume-rendered multi-detector row CT images in a patient with a blunt high velocity trauma to the head. **a** Volume-rendering reconstruction with a high threshold for osseous depiction shows a depressed fracture of the skull accompanied by facial fractures (*arrows*). **b** Volume-rendering reconstruction with a low soft tissue threshold and a cut through the brain demonstrates a bleeding into the frontal lobe and some air bubbles indicating an open fracture

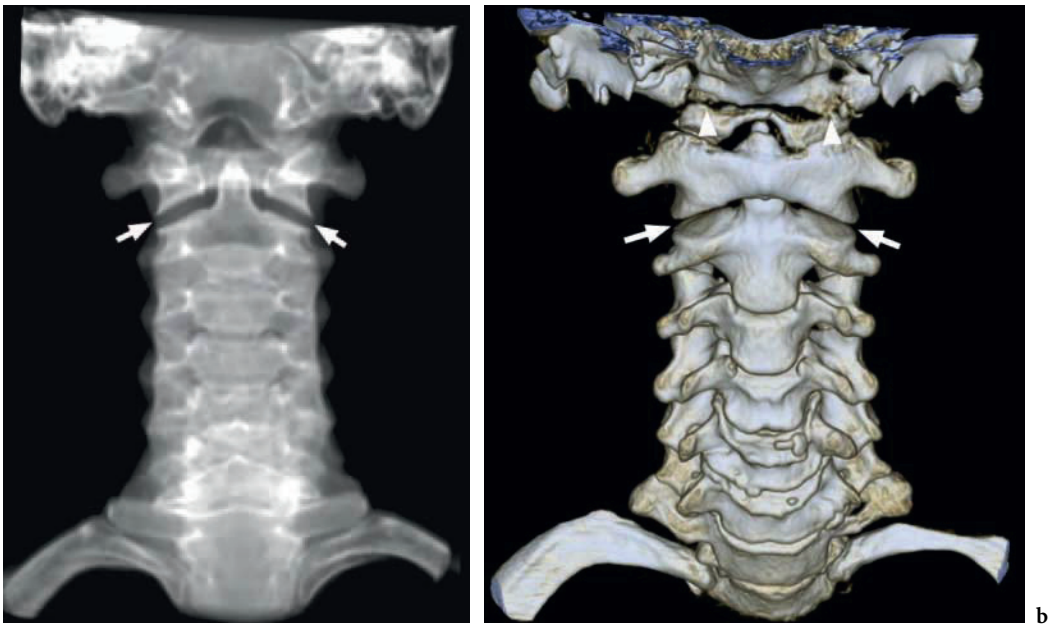

Fig. 25.7a,b. Coronal volume-rendered multi-detector row CT images in a patient with a high speed motorcycle accident to the upper cervical spine and the occipito-cervical junction. **a** Volume-rendering reconstruction with a low bone opacity shows a widening of the atlanto-axial junction as defined by a subluxation (*arrows*), which could not be detected in the axial source images. **b** Oblique coronal reformatted volume-rendering reconstruction shows an additional fracture of the occipital condyles (*arrowheads*)

imaging algorithm for evaluation of spine fractures, the radiologist is often hampered by time limitations, lack of patient cooperation and hard-pushed due to the hemodynamic instability or coexistent traumatic lesion (Daffner 2001; Wintermark et al. 2003). Radiologic standards are constantly in a state of development and it appears that there may be a shifting of the standard of care relating not so much to whether radiologic imaging ought to be performed for patients who sustained spine trauma, but rather to what kind of imaging should be performed. The event of helical CT and especially of multislice CT, with its intrinsic possibility to perform highest quality reconstructions, has accelerated this shift (Berlin 2003; Rieger 2006). For the optimal work-up of patients with severe spinal trauma, Imhof and Fuchsjager (2002) concludes that multislice CT with reconstructions rules out or proves any bone abnormalities (e.g., fractures or dislocations) with highest precision. Conventional radiographs are diagnostically insufficient and, in the cervical spine in up to 57% of cases, false-negative Research into the diagnostics of spinal fractures showed the superiority of MSCT with reconstructions over conventional radiographs (Rieger 2002). Schroder et al. (2003) demonstrated the advantage of 3D reconstructions of spinal fractures, especially with rotational instability over 2D reformations in regard to the fracture perceptibility, the anatomical clarity and the percentage of correct classification.

25.5.3 Thoracic Cage and Shoulder Girdle Fractures

Fractures of the ribs and sternum are the most common of all major chest injuries, occurring in almost 40% of patients who sustain a severe blunt trauma, but the sensitivity of conventional radiographs for the detection of rib and sternal fractures is especially low in polytraumatized patients. Fractures of the scapula are often very subtle on conventional X-rays. Therefore, conventional chest radiographs are not ideal for the diagnosis of thoracic cage fractures. Our own results, as well as results published in other publications, indicate the advantage of MSCT over conventional X-rays concerning thoracic cage fractures and, in addition, MSCT simultaneously discloses associated pulmonary and mediastinal injuries. Alkadhi et al. (2004) demonstrated that VR is a very useful and time-saving tool with a

high diagnostic accuracy because of the oblique course of the ribs, which, in contrast to VR, cannot be depicted in its entirety on a single transverse image. Volume-rendered MSCT is also very sensitive in the detection and characterization of fractures of the scapula, sternum and sternoclavicular joint (Alkadhi et al. 2004; Rieger et al. 2002; Pretorius and Fishman 1999).

25.5.4 Fractures of the Extremities

Many examinations are requested after conventional radiographs since: (a) a recognized fracture needs further evaluation to classify and characterize a fracture for therapy planning; (b) conventional X-rays show a questionable fracture; and (c) conventional radiographs are inconspicuous in a patient with clinical signs of a fracture (Novelline et al. 1999). In comparison with conventional radiographs, MSCT with 2D and 3D reconstructions clearly displays fractures and the degree of fragment displacement without superimposition. In addition, information about the displacement of fragments, impaction, comminution and sub-luxation can be demonstrated in arbitrary perspective. Especially in complex fractures involving articular joints, VR reconstruction with segmentation allows displaying the extent of dislocation of fragments, which are often not detectable in conventional radiographs, and enables exact fracture characterization and classification. Different studies demonstrated that the inter- and intra-individual reproducibility of the AO/OTA classification on the basis of conventional radiographs resulted in only moderate congruence. For example, different investigators identically classified only 38% of fractures of the proximal humerus. Similar results provided studies concerning fractures of the distal radius and distal tibia. Due to these results, it does not seem reasonable to classify complex intra-articular fractures only by means of conventional radiographs. Also, axial CT can be challenging when trying to interpret regions of complex anatomy such as ankle and hindfoot (Fig. 25.8). For example, the precise localization of the articular facets of the subtalar joints may be difficult to appreciate on routine axial scans. High-resolution reconstructions created from the CT data provide an additional perspective that can improve depiction of the subtalar joint anatomy.

Fig. 25.8. Volume-rendered multi-detector row CT image of the ankle and hindfoot in a patient following a fall from a height. VR view shows a calcaneal comminuted fracture (*arrows*) with an involvement of the talo-calcaneal facet (*arrowhead*).The tendons are well depicted because they are surrounded by fat

Multislice CT is extremely sensitive in the detection of fractures, and source images together with rendered reconstructions can display the spatial relationship of fracture fragments in complex anatomic regions. Complementary CT examination of intra-articular fractures of the distal tibia caused in 64% of subjects a change in the surgical treatment, and in 82% additional information concerning the fracture characterization and classification (Burkhardt et al. 2003).

25.5.5 Pelvic Fractures

Injuries of the pelvis occur in the majority of cases as a result of accidents with high kinetic energy, and are correlated with significant morbidity and mortality caused by associated complications like severe hemorrhage. Rapid diagnostic workup for accurate fracture characterization and classification, as well as demonstration of a hemorrhage, is essential. MSCT with reconstructions should be the first imaging tool in suspected pelvic fractures resulting from a high-energy accident. In patients with an additionally suspected hemorrhage, intravenous contrast medium should be applied to predict its source. Although most of fractures and possible bleedings can be detected reading only

source images, reconstructions are advantageous in the visualization of subtle fractures, especially those orientated in the axial plane. Multislice CT combined with multiplanar 2D or 3D reconstructions has become an outstanding and effective tool for understanding complex fracture patterns (Fig. 25.9) (Wedegartner et al. 2003; Stambaugh and Blackmore 2003).

25.5.6 Polytrauma

After stabilization of life-threatening conditions, polytraumatized patients require a fast, reliable, and comprehensive diagnostic work-up for specifying a therapy plan. The most common error in the first phase after admission of polytraumatized patients to the emergency room is the delayed and insufficient diagnostic, which impairs the prognosis of these patients. Therefore, the polytrauma patient in particular has benefited from the introduction of multislice CT, whose whole potential can be used in these patients. The speed of this technique permits a whole body evaluation within a few seconds in thin slices during the application of one bolus of intra-venous contrast medium. Using these source images, transverse, sagital and coronal reformations in 5 mm, for example, can be performed for diagnosing injuries of the brain, neck, thorax, abdomen and pelvis, as well as thin-slab reformations of the skeletal system in any plane. There is no more need for using different diagnostic modalities for evaluating injuries of polytraumatized patients (Knollmann and Coakley 2006).

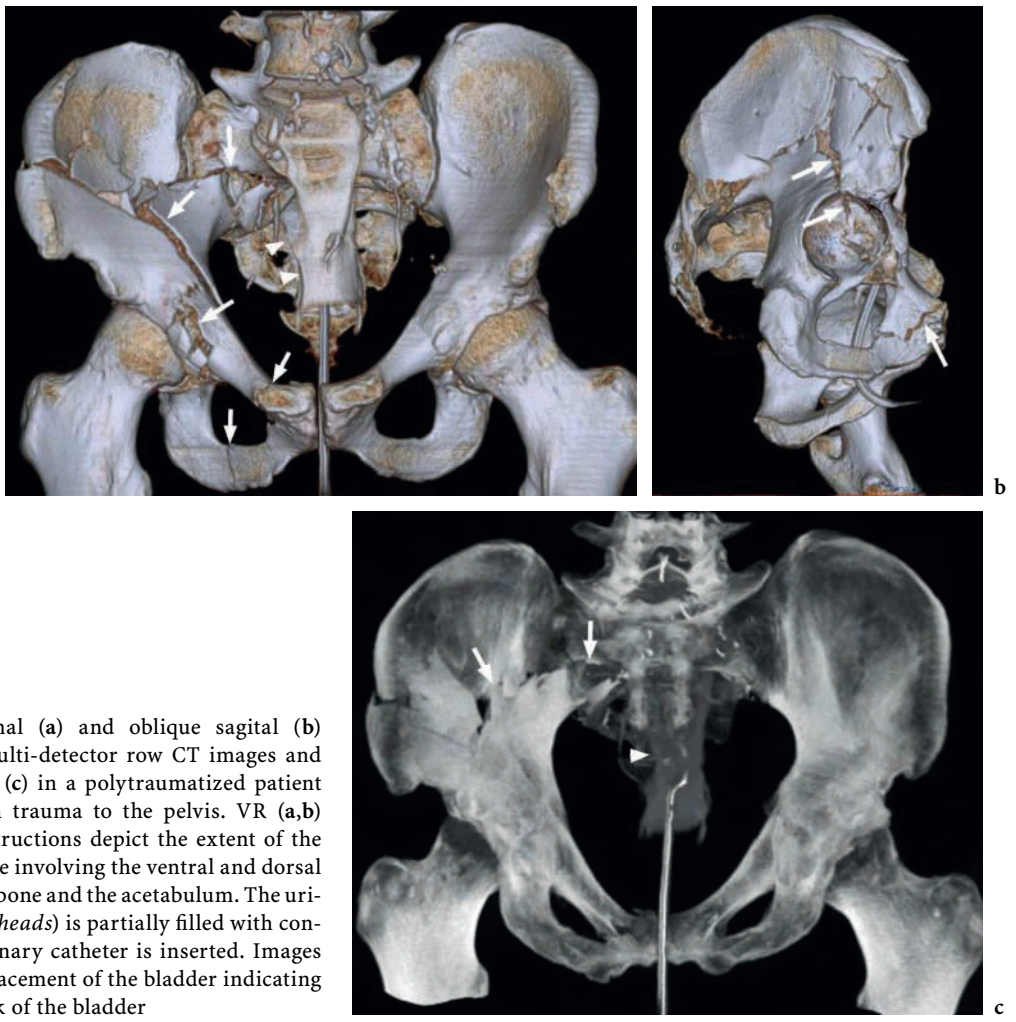

Fig. 25.9a–c. Coronal (**a**) and oblique sagital (**b**) volume-rendered multi-detector row CT images and MIP reconstruction (**c**) in a polytraumatized patient with a severe crush trauma to the pelvis. VR (**a**,**b**) and MIP (**c**) reconstructions depict the extent of the comminuted fracture involving the ventral and dorsal pelvic ring, the iliac bone and the acetabulum. The urinary bladder (*arrowheads*) is partially filled with contrast medium, a urinary catheter is inserted. Images show a cranial displacement of the bladder indicating an injury of the neck of the bladder

25.5.7 Infection and Tumor

An increasing number of examinations are being performed for the evaluation of known or suspected musculoskeletal infection. Multislice CT with 2D and 3D reconstructions are useful tools for detecting infections and abscesses, determining which compartments are involved and for describing the extent of an infection. For this question it is necessary to apply intravenous contrast medium. Multislice CT is also used to evaluate cortical bone and associated soft-tissue masses in suspected osteomyelitis. The presence of sequester can be verified and the response to therapy monitored (Knollmann and Coakley 2006).

Multislice CT is useful in defining the full extent of primary and metastatic bone tumors. Although MR imaging has become the leading modality for evaluating the extent of bone and soft-tissue neoplasms, CT is nearly as efficacious, and remains superior to MR imaging in the detection of cortical destruction and lesion calcification (Buckwalter et al. 2001).

References

Alkadhi H, Wildermuth S, Marincek B, Boehm T (2004) Accuracy and time efficiency for the detection of thoracic cage fractures: volume rendering compared with transverse computed tomography images. J Comput Assist Tomogr 28:378–385

Berlin L (2003) CT versus radiography for initial evaluation of cervical spine trauma: what is the standard of care? AJR Am J Roentgenol 180:911–915

Buckwalter KA, Rydberg J, Kopecky KK, Crow K, Yang EL (2001) Musculoskeletal imaging with multislice CT. AJR Am J Roentgenol 176:979–986

Burkhardt M, Gansslen A, Uder M, Pohlemann T (2003) New possibilities in fracture visualization by means of CT: reconstructions, 3D plannings – difficult joint fractures – modern management – improved visualization and operative planning in joint fractures. Zentralbl Chir 128:34–39

Calhoun PS, Kuszyk BS, Heath DG, Carley JC, Fishman EK (1999) Three-dimensional volume rendering of spiral CT data: theory and method. Radiographics 19:745–764

Daffner RH (2001) Helical CT of the cervical spine for trauma patients: a time study. AJR Am J Roentgenol 177:677–679

Imhof H, Fuchsjager M (2002) Traumatic injuries: imaging of spinal injuries. Eur Radiol 12:1262–1272

Knollmann F, Coakley FV (2006) Multislice CT – principles and protocols. Saunder, Philadelphia Michael Rieger. Muskuloskeletal MSCT ELSEVIER. Ref Type: Generic

Kuszyk BS, Heath DG, Bliss DF, Fishman EK (1996) Skeletal 3-D CT: advantages of volume rendering over surface rendering. Skeletal Radiol 25:207–214

Novelline RA, Rhea JT, Rao PM, Stuk JL (1999) Helical CT in emergency radiology. Radiology 213:321–339

Philipp MO, Kubin K, Mang T, Hormann M, Metz VM (2003) Three-dimensional volume rendering of multidetector-row CT data: applicable for emergency radiology. Eur J Radiol 48:33–38

Pretorius ES, Fishman EK (1999) Volume-rendered three-dimensional spiral CT: musculoskeletal applications. Radiographics 19:1143–1160

Rieger M, Sparr H, Esterhammer R, Fink C, Bale R, Czermak B, Jaschke W (2002) Modern CT diagnosis of acute thoracic and abdominal trauma. Radiologe 42:556–563

Rieger M, Mallouhi A, El Attal R, Kathrein A, Knop C, Blauth M, Jaschke W (2006) Acute diagnosis of spinal trauma. Radiologe

Rieger M, Mallouhi A, Tauscher T, Lutz M, Jaschke WR (2006) Traumatic arterial injuries of the extremities: initial evaluation with MDCT angiography. AJR Am J Roentgenol 186:656–664

Rosenthal E, Quint DJ, Johns M, Peterson B, Hoeffner E (2000) Diagnostic maxillofacial coronal images reformatted from helically acquired thin-section axial CT data. AJR Am J Roentgenol 175:1177–1181

Rubin GD (2003) MDCT imaging of the aorta and peripheral vessels. Eur J Radiol 45[Suppl 1]:S42–S49

Rydberg J, Buckwalter KA, Caldemeyer KS, Phillips MD, Conces DJ Jr, Aisen AM, Persohn SA, Kopecky KK (2000) Multisection CT: scanning techniques and clinical applications. Radiographics 20:1787–1806

Schroder RJ, Albus M, Kandziora F, Herzog H, Rottgen R, Maurer J, Felix R (2003) Diagnostic value of three-dimensional reconstruction in CT of traumatic spinal fractures. Rofo 175:1500–1507

Stambaugh LE 3rd, Blackmore CC (2003) Pelvic ring disruptions in emergency radiology. Eur J Radiol 48:71–87

Tomandl BF, Kostner NC, Schempershofe M, Huk WJ, Strauss C, Anker L, Hastreiter P (2004) CT angiography of intracranial aneurysms: a focus on postprocessing. Radiographics 24:637–655

Wedegartner U, Gatzka C, Rueger JM, Adam G (2003) Multislice CT (MSCT) in the detection and classification of pelvic and acetabular fractures. Rofo 175:105–111

Wintermark M, Mouhsine E, Theumann N, Mordasini P, van Melle G, Leyvraz PF, Schnyder P (2003) Thoracolumbar spine fractures in patients who have sustained severe trauma: depiction with multi-detector row CT. Radiology 227:681–689

Yoshida S, Akiba H, Tamakawa M, Yama N, Hareyama M, Morishita K, Abe T (2003) Thoracic involvement of type A aortic dissection and intramural hematoma: diagnostic accuracy–comparison of emergency helical CT and surgical findings. Radiology 228:430–435

Computer-Aided Diagnosis: Clinical Applications in the Breast

26

Toni W. Vomweg

CONTENTS

T. W. Vomweg, MD
Radiological Centre Dr. van Essen, Emil-Schüller-Strasse 31–33, 56068 Koblenz, Germany

26.1 Introduction

26.1.1 Diseases of the Female Breast

The breast consists of two main types of tissues – glandular tissues and supporting (stromal) tissues. The glandular part is responsible for milk production during lactation and mainly consists of lobules and ducts. The support tissue of the breast includes fatty tissue and fibrous connective tissue, which consist of ligaments that support the shape of the breast.

Any of these areas of the breast can undergo changes that cause findings in radiological imaging. There are two main groups of breast changes: benign breast conditions and breast cancers (malignant conditions). The most common benign breast conditions are fibrocystic changes, benign breast tumors and breast inflammation (Santen and Mansel 2005). The most common malignant condition is breast cancer, which may be classified further by histopathology into invasive subtypes: ductal, tubular, lobular, medullar, and mucinous carcinoma, and noninvasive subtypes: DCIS (ductal carcinoma in situ) as well as several more highly specialized subclasses Brenton et al. 2005; Charafe-Jauffret et al. 2005).

With slight differences between all Western industrialized nations, breast cancer is the second leading cause of cancer deaths among women today (following lung cancer) and is the most common cancer among women (excluding nonmelanoma skin cancers). According to the World Health Organization WHO 2002), more than 1.2 million people worldwide will be diagnosed with breast cancer in 2005. It is estimated that in 2006 about 212,920 new cases of invasive breast cancer, and about 61,980 new cases of DCIS, will be diagnosed among women in the United States of America, the nation with the highest rate of breast cancer diagnoses in the world.

The situation is similar to the one in Europe, where about one out of every nine women develops breast cancer during her lifetime.

Radiological imaging of the female breast plays a major role in the detection of breast cancer, as mammography screening is the only available tool proven to reduce mortality of breast cancer by early tumor detection.

26.1.2 Breast Cancer Appearance in Radiological Imaging

The two main imaging methods for breast cancer diagnosis are the mammogram and the ultrasound.

A mammogram is an X-ray image of the compressed breast. A normal investigation consists of two projections of each breast: a cranial-caudal projection that is accomplished by a medial-lateral-oblique projection at 45° (often) or a medial-lateral projection (seldom). Conventional film-based mammography systems are now accompanied by digital mammography systems, using full field digital detector arrays (FFDM) or storage phosphor radiography (Pisano and Yaffe 2005). Mammography has proven to be an effective tool for the early detection of breast cancer. Therefore, it is approved as an X-ray investigation method for healthy women older than 49 years as a screening method. The larger portion of mammograms carried out today are screening mammograms. In case of any suspicious clinical finding (e.g. a palpable lump), a diagnostic mammography is carried out.

The two main types of abnormalities found on mammograms are calcifications and masses. Calcifications are tiny mineral deposits within the breast tissue. Caused by their much higher absorption of X-rays, they appear as small white spots on the films. They are divided into macrocalcifications and microcalcifications depending on their maximum diameter. Macrocalcifications are large calcium deposits caused by old injuries, inflammations or regressive changes of benign masses. Therefore, the deposits are associated with benign conditions and do not require a biopsy. Macrocalcifications are found in about half the women over age 50, and in 1 of every 10 women under age 50 WHO 2002) (Fig. 26.1).

Microcalcifications are tiny specks of calcium in the breast. They may appear alone or in clusters. Asymmetric distribution into one or a few clusters, as well as the shape and layout of microcalcifications, can be correlated to likelihoods of malignancy (Nishimura et al. 2004).

Masses can be a result of a cancer or a benign condition. Masses absorb X-rays at a slightly higher rate than does normal glandular tissue, and therefore become visible on the mammogram. Morphological features can be obtained (e.g. shape, smoothness of boundary, the presence of spicules and many others) to estimate the likelihood of malignancy.

All breast lesions are described and reported according to the breast imaging reporting and data system (BI-RADS). BI-RADS is a mammography, ultrasound and MRI lexicon developed by the American College of Radiology American College of Radiology 2003) for the description of breast lesions. The BI-RADS lexicon includes briefly described features such as the margin of a mass and the distribution of calcifications. Furthermore, it provides definitions of final assessment categories designed to describe the radiologist's level of suspicion about the mammographic abnormality. If a mammographic mass cannot be determined to be benign with sufficient certainty, an ultrasound or even a biopsy will be recommended. In the case of findings that appear most likely to be benign, a follow-up investigation should confirm the absence of growth.

Breast ultrasound is often used to evaluate ambiguous findings in a mammogram or a physical exam. It is widely available and less expensive than other options, such as MRI. Usually, breast ultrasound is used to target a specific area of concern indicated by the mammogram. It is useful for detecting breast masses and is the easiest way to determine whether or not a fluid-filled cyst is present without doing a needle biopsy. Furthermore, ultrasound helps to distinguish between benign and cancerous tumors, especially among younger women with a high breast density. In these cases mammography's sensitivity and specificity is lower than ultrasound, which gives ultrasound imaging the potential to be used as the first step in the diagnostic chain.

As in mammography, many features can be assessed by ultrasound correlating to the likelihood of malignancy. Figure 26.2 shows a simple, well-defined structure with a brighter area located below. The structure itself does not contain any reflecting structures. Many "solid" tumors detected by a screening mammography end up here with the diagnosis of a simple cyst after ultrasound. Benign tumors, such as the highly widespread fibroadeno-

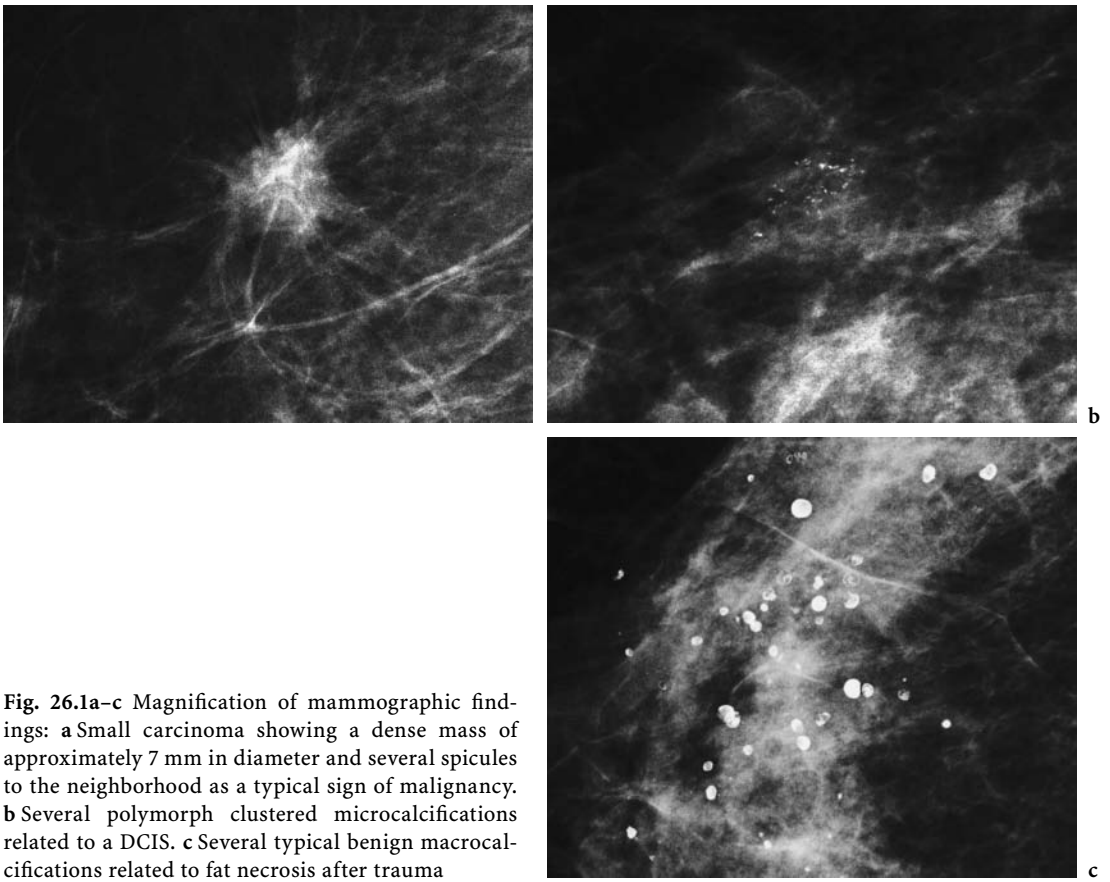

Fig. 26.1a–c Magnification of mammographic findings: **a** Small carcinoma showing a dense mass of approximately 7 mm in diameter and several spicules to the neighborhood as a typical sign of malignancy. **b** Several polymorph clustered microcalcifications related to a DCIS. **c** Several typical benign macrocalcifications related to fat necrosis after trauma

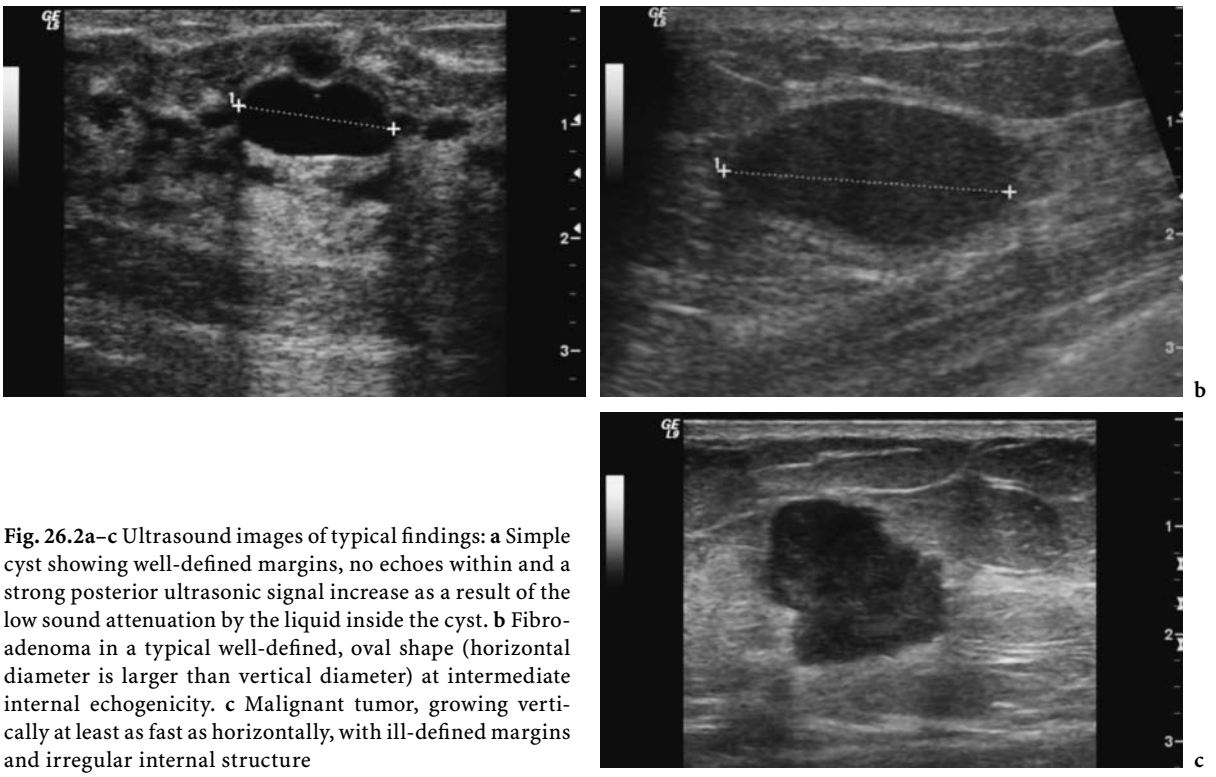

Fig. 26.2a–c Ultrasound images of typical findings: **a** Simple cyst showing well-defined margins, no echoes within and a strong posterior ultrasonic signal increase as a result of the low sound attenuation by the liquid inside the cyst. **b** Fibroadenoma in a typical well-defined, oval shape (horizontal diameter is larger than vertical diameter) at intermediate internal echogenicity. **c** Malignant tumor, growing vertically at least as fast as horizontally, with ill-defined margins and irregular internal structure

mas, often show well-defined margins, iso-intense internal texture and no relevant sound amplification or absorption Skaane and Engedal 1998). Malignant tumors often have ill-defined margins, hypo-intense internal texture and sound attenuation phenomena behind the tumor Baker and Soo 2000).

Contrast-enhanced (CE) MR imaging of the breast, also called MR mammography, provides the highest quantity of information in the form of a cross-sectional 3D image enlarged by the dimension of time (signal intensity/time curve by the intravenous application of contrast medium). It is already applied as a routine procedure in the assessment of silicone implants Lalonde et al. 2005), monitoring of neoadjuvant chemotherapy (Wasser et al. 2003; Weatherall et al. 2001) and screening of high-risk patients for hereditary breast cancer Berg 2001; Kriege et al. 2006; Kuhl 2002; Morris 2001; Podo et al. 2002; Topping et al. 2003). It is furthermore helpful in the differentiation of scars and tumor-relapse (Aichinger et al. 2002; Lalonde et al. 2005; Pediconi et al. 2005) and preoperative tumor assessment Fischer et al. 2004; Sardanelli et al. 2004). In the course of an MR investigation of the breast, a 3D block that surrounds one or both breasts (deter-

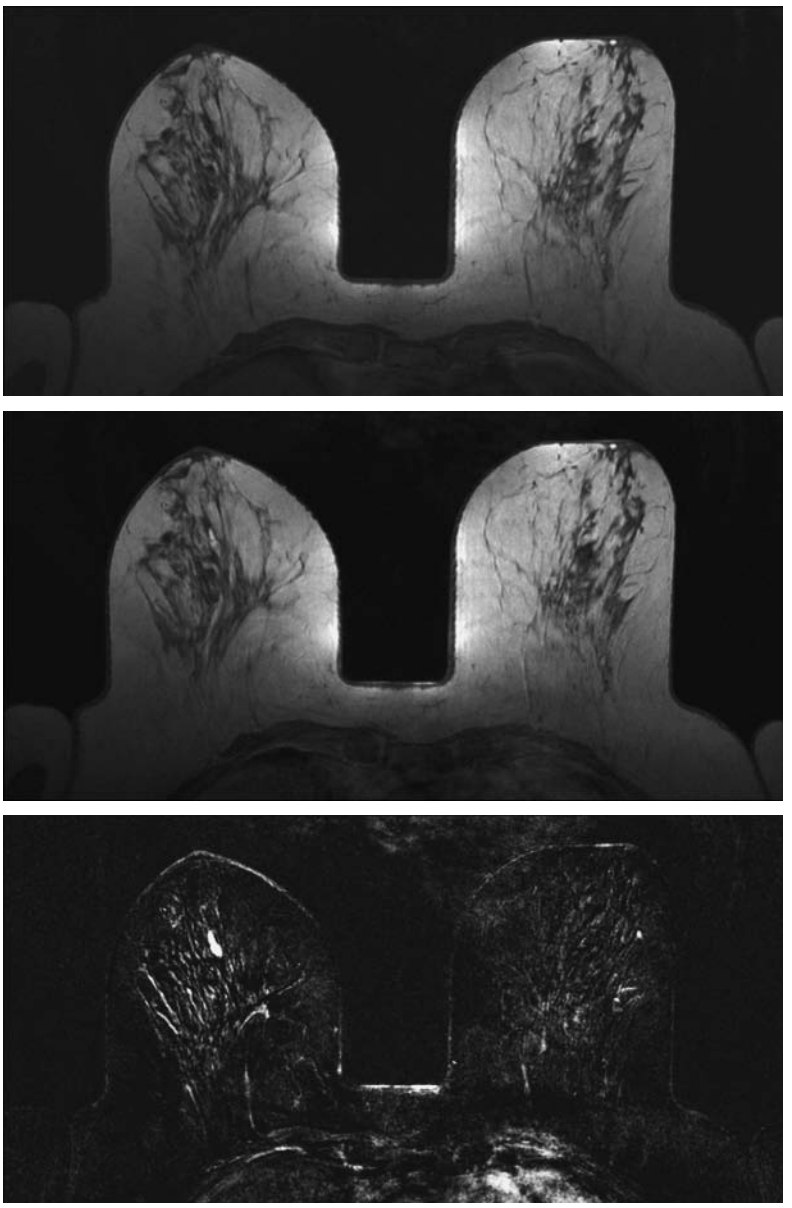

Fig. 26.3a–c. The same section of a transversal MRI of the breast (FLASH 3D, Siemens Magnetom Sonata, 512 × 256 pixel matrix, Magnevist, Schering) **a** before contrast media (CM) application, **b** 5 min after CM application, and **c** subtraction image c = b – a. The subtraction series reveals a small oval tumor in one breast arranged according to a duct. Histology revealed a ductal carcinoma

mined by the use of a dedicated single or double breast coil) is investigated by a T1-weighted MR series. After the injection of a paramagnetic contrast agent, the measurement of the same 3D block is repeated several times without changing the imaging parameters (block position, slice thickness, echo time, repetition time, flip angle). Any contrast enhancement uptake within the breast tissue can be visualized by voxel-based subtraction of the first image series from the considered series. The subtraction can be replaced by using fat-suppressed sequences. Due to increased vascularization and an increased endothelial permeability, solid tumors do normally show a strong signal intensity increase Carriero et al. 2002; Leach 2001; Sardanelli et al. 2005; Teifke et al. 2006). Figure 26.3 shows the appearance of a ductal carcinoma at a dynamic MRI.

Any appearing contrast-enhanced lesion is assessed in a two-step process: (1) architectural features are studied and, as in mammography, ill-defined margins, spicules and various other morphological features are correlated to the presence of a malignant tumor Furman-Haran et al. 2001; Heywang-Koebrunner et al. 2001; Morris 2001; Obenauer et al. 2002; Vomweg et al. 2004; Wedegartner et al. 2001). (2) In addition, signal intensities of contrast-enhanced lesions are measured over time by each following repeated series. This results in individual signal intensity/time curves that can be assessed by means of curve analysis or certain kinetic models Kuhl and Schild 2000; Liney et al. 1999).

26.1.3 Rationale of CAD Usage in Breast Imaging

By using mammography as a screening examination according to international guidelines, breast cancers are able to be located at the earliest possible stage when they are most treatable Cady and Michaelson 2001; Tabar et al. 2001; WHO 2002). The overall results of several randomized controlled trials indicate that mammographic screening of women over age 50 could possibly reduce breast cancer mortality by at least 25% Jatoi 1999). For this reason, the number of breast exams worldwide is steadily rising. However, it is important to know that a huge number of unspecific findings and benign changes appear in breast imaging and are often not easily distinguished from malignant or semi-malignant tumors by any modality.

Although mammography screening has proved its efficiency as a screening method, its sensitivity and positive predictive value are lower compared to other screening tools WHO 2002). In dense breasts, which have a larger amount of fibro-glandular tissue, sensitivity and specificity of mammography may decrease due to the natural limitation of X-ray mammography as a summarized plain film image Sardanelli et al. 2004). Furthermore, the assessment of mammography, ultrasound and MRI of the breast shows high inter-observer variability Mussurakis et al. 1996; Skaane et al. 1997).

This is in part compensated for through the procedure of double reading in breast mammography, a technique that has become standard in most countries known for having a "screening tradition" such as in Europe.

The procedure of double reading connotes that each mammogram is assessed independently by two physicians. In case of a consensus of diagnosis a clear statement can be given. In case of a disagreement, a third reader or a consensus conference of the two readers is needed. Although the assessment of a mammography is not very time-consuming, the tremendous cost is currently under investigation by health ministries and economists (Stout et al. 2006). The use of CAD systems has several abilities to show a benefit: (a) increased efficiency of the time needed for an investigation by adding CAD as an additional aid or reader; (b) decreased costs by replacing a human reader by a CAD system, and (c) availability as a second automatic opinion or additional aid in the breast imaging modalities that do not currently use double reading (ultrasound, MRI) in order to increase efficiency of these modalities.

26.1.4 Information Referred to in this Chapter

The author collected available publications by means of Internet-based research at Medline, Current Contents and CiteSeer to produce a broad overview in the field of clinical applications of computer-aided diagnosis in the breast. The literature cited was chosen in order to give the reader the most convenient access to further details of the work of the related author or group. Printed publications (journal articles or books) have been preferred. Conference proceedings or electronic sources were chosen for citation when no printed publication was available. The list

of authors and groups named, as well as the list of literature cited, do not claim to be complete.

26.2 Computer-Aided Detection and Diagnosis in Mammograms

Most of the currently available systems are designed to aid the human reader in the detection of lesions in mammography. CAD systems for computer-aided decision or even computer diagnosis are still under development. X-ray mammograms may typically show two different types of findings, namely calcifications and masses. Due to the fact that different procedures of image processing have partly been used to detect them, the following chapters are divided into categories describing the detection of calcifications and of masses.

26.2.1 Detection of Calcifications

The radiologist may miss small calcifications because they are typically only subtle changes that can be almost totally hidden by overlapping breast parenchyma, especially in dense breasts. However, from an image processing point of view, calcifications are the only structures in mammography that show very high signal intensities (very bright spots on the X-ray film) and therefore have a good contrast compared to the surrounding breast parenchyma. Their size, shape, morphology, number and distribution vary.

Several groups start by using image pre-processing algorithms to reduce image noise, e.g. median filters (Clarke et al. 1994; Qian et al. 1998; Yu and Guan 2000), Gaussian band-pass filters (Zheng et al. 1995c), high-boost filter (Wallet et al. 1997) or other mechanisms for contrast enhancement (McLoughlin et al. 2004; Nunes et al. 2006).

Detection of microcalcifications is often done by filters such as tree-structured wavelet transforms (Boccignone et al. 2000; Lemaur et al. 2003; Mata Campos et al. 2000; Mini et al. 2004; Qian et al. 1998; Yu and Guan 2000), filter banks Nakayama et al. 2006; Qian et al. 1994), edge detector algorithms (Ema et al. 1995; Pettazzoni et al. 2001) or spatial filters (Lee and Lithgow 2000).

In addition, classical segmentation algorithms such as adaptive threshold based systems (Gavrielides et al. 2000; Netsch and Peitgen 1999; Wallet et al. 1997), region growing algorithms (Paquerault et al. 2004), active contour models (Bankman et al. 1997) and watershed segmentation (Paquerault et al. 2004) have been used directly for detection of microcalcifications. Segmentation on the basis of signal classification by fuzzy-logic-based detectors (Cheng et al. 1998; Gavrielides et al. 2000), support vector machines (SVM) Bazzani et al. 2001), as well as ANNs (Mini et al. 2004; Schmidt et al. 1999) have been utilized.

All reported mechanisms give good detection results. A direct comparison of detection results is not possible due to large differences in origin, quality (analog, digital) and number of mammograms used. However, fibro-glandular and microcystic degenerative processes within the breast tissue often lead to subtle microcalcifications that are normally distributed among one or both breasts. Occasionally, detected microcalcifications cause false-positive findings. Of course, a CAD system should detect and reveal to a human reader only clustered and polymorph calcifications that probably are indicative of malignancy. Several authors have described quantitative and qualitative features of clustering to achieve a quantitative analysis of the number of particles per cluster, area of clusters, maximum distance to nearest neighbor, geometric mean distance to nearest neighbor and a so called "distribution pattern index" (Ng et al. 1996). Through gradual discriminant analysis, sets of features were selected and rules were applied to acquire rule-based discrimination for benign and malignant tumors (Leichter et al. 2000). Sklansky et al. (2000) developed software to help the radiologist by offering ROIs showing similar clusters of microcalcifications with known histology to the prospective human reader, significantly reducing the number of benign biopsies and misdiagnosed cancers. Leichter et al. (2004) showed that the cluster geometry was more effective in differentiating benign from malignant clusters than was the shape of individual microcalcification.

Jiang et al. (2001) demonstrated that the detection of a high number of false-positive computer-detected microcalcifications degrades classification performance of the global CAD system for clustered microcalcifications substantially (Jiang et al. 2001). Therefore, the aim of the following research activities was to differentiate between clustered and non-

clustered microcalcifications in order to reduce the number of wrongly detected clusters.

As early as in 1992, Wu et al. (1992) reported the application of a multilayered feed forward artificial neural network to distinguish clustered microcalcifications from normal non-clustered areas in the frequency domain. Working with the ROC curve, it was possible to eliminate approximately 50% of false-positive marks while preserving 95% of the positive clusters. The performance was improved by using a shift-invariant neural network instead of the standard type (elimination of 55% false-positive ROIs without loosing any true positive ROI) (Zhang et al. 1994) and by improved methods for region grouping (Qian et al. 2002). Ema et al. (1995) used a combination of a set of linear gradient templates oriented in 16 different directions and a local edge gradient analysis to eliminate 80% of the false-positive clusters with a loss of 3% of true positive clusters on an independent sample set.

In 1995, Zheng et al. (1995c) reported a multistage CAD scheme using a Gaussian band-pass filter and nonlinear threshold operation followed by a multilayer ANN to reduce the number of false-positively detected clusters.

Jiang et al. (1996) reported using a three-layered feed-forward ANN for the differentiation of malignant from benign clustered microcalcifications. In this semi-automatic approach, a human reader initiated the identification of regions containing microcalcifications, followed by the automatic segmentation and computation of eight computer-extracted features used as ANN input. In a test set ($n = 53$) the system identified 100% (82) of the malignant (benign) clusters and outperformed five radiologists in differentiation of benign and malignant clusters.

Chan et al. (1998) worked on similar ROIs by calculating spatial gray level dependence (SGLD) matrices at ten different pixel distances in both the axial and diagonal directions. While using a genetic algorithm to "breed" the right feature selection out of texture and morphological features, they reached an Az value of 0.89 in the differentiation between benign and malignant calcification clusters ($n = 145$ clusters). This performance was further improved by averaging the score of different views of the same cluster of calcifications up to a sensitivity of 93.3% at a rate of 0.7 false-positive findings per image (Gurcan et al. 2002) by the use of an optimized convolution neural network.

Schmidt et al. (1999) implemented two-layer feed-forward artificial neural networks for both detection and evaluation of clustered microcalcifications. The measured sensitivity for the detection of grouped microcalcifications was 0.98. For the task of differentiation between typical and atypical clusters an Az value of 0.87 was computed, while for the diagnosis an Az value of 0.87 (sensitivity 97%, specificity 47%) was obtained.

Papadopoulos et al. (2002) constructed a hybrid system using pre-processing, automatic extraction of 22 features and classification by neural network to achieve Az values of 0.91 and 0.92 on Nijmegen and MIAS datasets, respectively, at 1.8 (1.15) false-positive clusters per image.

El-Naqa et al. (2002) reported a sensitivity of 94% at one false-positive cluster per image by using a support vector machine for detection of clustered microcalcifications. Halkiotis and Mantas (2002) combined topographic representation of pixel intensities, various filters and a feed-forward neural network to detect clustered microcalcifications at 90% sensitivity and only 0.11 false-positive clusters per image. Recently, Kallergi (2004) reported a combined approach for computer diagnosis of clustered microcalcifications, taking into account the factor of patient age, and showed 100% sensitivity for a specificity of 85% (Az = 0.98).

Brem et al. (2005) showed that computer-aided detection of clustered microcalcifications is pretty robust also in dense breasts, while detection of masses is impacted by increased breast density. Although clustered microcalcifications can be detected very easily, several other kinds of microcalcifications, e.g. groups of amorphous calcifications, still require some research and development. The automatic matching of microcalcification projections viewed on two mammograms of the same breast is also of scientific and practical interest (Tiedeu et al. 2005). This would possibly improve confidence of CAD systems, as well as aid stereotactic biopsies (Arodz et al. 2006).

26.2.2 Detection of Masses

Detection of masses in digitized mammograms started around 1967 using an approach inspired by a human reader: each woman has her own unique structure and distribution of glandular tissue within the breast that is normally considered to be symmetric between both sides. Therefore, a radiologist compares the right and left breasts during visual

assessment of mammograms to remark architectural asymmetries that may indicate the presence of a mass. By subtracting mammograms of both sides from each other, asymmetries could be revealed (Hand et al. 1979; Kimme et al. 1975; Winsberg et al. 1967). This approach was improved around 1990 by automatic breast segmentation and registration of digitized mammograms of the left and right side that made the approach more robust (Yin et al. 1991, 1993). Using this approach to identify masses, a subsequent analysis of features of each mass allowed for the reduction of the number of false-positive findings (Lau and Bischof 1991; Yin et al. 1994a,b).

Shortly after these early reports, mass detection in mammograms turned out to be a multi-stage task similar to the detection of microcalcifications. It became obvious that a well-designed and multi-level pre-processing was needed to achieve robust mass detection. Qian et al. (1999) compared the performance of adaptive and nonadaptive pre-processing methods for breast mass detection. The authors programmed algorithms for noise suppression, artifact removal, wavelet transform decomposition, multiresolution enhancement and image smoothing. The so-called "adaptive" process analyzed some statistical image features at the beginning, before it started each preprocessing algorithm by individually adapted parameters. A "non-adaptive" process always used the same settings. They compared the results of the CAD system with and without the adaptive algorithms. The adaptive CAD method showed a sensitivity of 96% (1.71 false-positive results per image) compared with 89% (1.91 false-positive results per image) for the non adaptive CAD method at 100 mammograms. This was confirmed in conjunction with various other groups that also used combined pre-processing steps for background correction in order to improve contrast of masses (Li et al. 2001).

The principle approach of mass detection in mammograms was to use some kind of detection algorithm (e.g. filter-based, region-growing, discrete contour-based) in combination with calculated features (texture-based, morphology-based). This approach is used by various groups: Zheng et al. (1995b) took Gaussian bandpass filtering and calculated different features, such as the global minima of optical density in a smoothed image, the original image and a filtered image (Zheng et al. 1995a, 1996) reaching high sensitivity values at around two false-positive findings per image (Chang et al. 1996).

Petrick et al. (1996) used a density-weighted contrast enhancement segmentation to detect masses in combination to wavelet filters and texture feature evaluation by LDA. This approach was later improved by region-growing algorithms towards malignant masses detection in 87% (135 of 156) at rate of 1.5 CAD markers per mammogram (Petrick et al. 1999, 2002).

Kobatake et al. (1999) used an adaptive filter called the "iris filter" to detect regions with low contrast to their background. Multiresolution and multiorientation wavelet transforms have been used for image pre-processing (Li et al. 1997), as well as mass detection (Li et al. 1997) earlier.

Timp and Karssemeijer (2004) proposed an automatic segmentation method based on dynamic programming for lesion segmentation, and achieved valuable results in comparison to discrete contour model and region growing.

Over the last 10 years, feature extraction of previously detected masses have gained increasing importance in order to reduce the number of false-positive detected masses, as well as to assess the likelihood of malignancy of the masses (Catarious et al. 2004). At an early date, several other groups addressed the relevance of stellate morphology of masses in mammograms (Giger et al. 1994; Huo et al. 1995; Karssemeijer and te Brake 1996; Kegelmeyer Jr. et al. 1994). Vyborny et al. (2000) pointed out that 55% of masses detected in a screening population presented spicules. Kovalerchuk et al. (1997) developed a fuzzy logic approach to identify and characterize lobulated and microlobulated masses. Sahiner et al. (2001) combined spiculation measures and other morphological features. Rymon et al. (1998) used a set of 24 features as input data for a hybrid classifier of a set enumeration, and an artificial neural network for identification of masses on mammograms, yielding an Az value of 0.94. Several other groups also used neural networks as classifiers at the end of the detection process that have often performed better than linear discriminant classifier (LDA) in this task (Fogel et al. 1998; Hadjiiski et al. 1999; Li et al. 2002; Sajda et al. 2002). Chang et al. (2001) tried to retrospectively reduce the number of detected masses by a CAD scheme, calculating the likelihood of a suspicious region to be a mass in comparison to a set of previously learned "known masses". Several groups also used a database of mass templates to be compared with any detected mass by using mutual information (Tourassi et al. 2003) or other methods (Baydush et al. 2003; Floyd

et al. 2000; Ozekes et al. 2005; Taylor et al. 1999) as a similarity metric. Numerous groups have trained artificial adaptive systems to differentiate between normal tissue and real masses (Hadjiiski et al. 2001; Sahiner et al. 1996; Varela et al. 2006) resulting in a further significant decrease of false-positive detected masses in mammograms, and improved robustness of the overall CAD system (Chang et al. 1996). Another way to reduce the number of false-positive detected masses is the fusion of two-view information (Kita et al. 2002; Paquerault et al. 2002; Zhou et al. 2004). This follows the radiological principle that a "real" mass should be visible on two imaging planes in contrast to structures with enhanced absorbance, which are only visible in one plane. These structures are then called "architectural distortion".

Hadjinski et al. (2001, 2006) enlarged computer-aided mass detection in mammography by the dimension of time. Masses on both the current and the prior mammograms were automatically segmented using an active contour method. A total of 20 run length statistics texture features, three speculation features, and 12 morphological features were extracted from each mass and complemented by other calculated features. Gradual feature selection and linear discriminant analysis classification reduced the input data to 10 features used for differentiation of malignant and benign masses, yielding an Az value of 0.88 on the test dataset (Hadjiiski et al. 2001, 2006). It has significantly improved a radiologist's accuracy in classifying masses on digitized screen-film mammograms as either malignant or benign (Hadjiiski et al. 2006).

26.2.3 Current Research in the Field of CAD in Mammography

Meanwhile, algorithms and routines for computer-aided detection and diagnosis in mammography have been thoroughly reviewed by different authors (Karssemeijer and Hendriks 1997; Sampat et al. 2005). Larger parts of the research are now concentrated within and performed by companies, which have successfully introduced to the market products for CAD in mammography. Many of the researchers responsible for initial steps towards CAD in mammography are now involved with, or have even founded, these companies. Therefore, it may be assumed that the current status of research in computer-aided detection and diagnosis is not reflected in total by the currently available scientific literature. Nowadays, due to patenting and marketing requirements, scientific publication may be delayed or even discarded in total. Any interested reader may compensate for this at least in part by studying the text of patents available online at the homepages of US, European and Asian patent offices.

Table 26.1 lists the names and products of vendors for CAD in mammograms.

Table 26.1. List of vendors and products related to computer-aided detection in mammography (status as of Jan 2007 to the best of our knowledge)

Vendor	URL	Product name	FDA approval (status as of 2006-08-01)
R2 Technology	www.r2tech.com	Image Checker	Yes
ICAD	www.icadmed.com	Second Look MammoReader	Yes
VuCOMP	www.vucomp.com	M-Vu	510(k)
Eastman Kodak Company	www.kodak.com/go/mammo	Mammography CAD Engine	Yes
Image diagnost International GmbH	www.imagediagnost.de/english/	CAD server	No
SIEMENS Medical Solutions, formerly CADVision Medical Technologies Ltd.	www.medical.siemens.com (Currently Image Checker software by R2 Technology is used and sold as Mammography CAD-system by Siemens Medical Solutions)	CADVision	No

26.3 Computer-Aided Detection and Diagnosis in Ultrasound

Ultrasound of the breast is normally performed in B-mode and results in scans that show grayscale section images. CAD systems may be designed to aid in two ways: (1) as a real-time system that interprets information of the scanner during the course of the investigation, e.g. in order to assist the user with regard to the detection of breast lesions; and (2) as an off-line system that interprets previously exported images of an optimized view of a single lesion selected by a human observer (normally obtained at the largest diameter of a lesion). Research described in older publications primarily worked on digitized or even filmed ultrasound images. Today's systems work on digitally transferred images following the DICOM standard.

In 1992, Goldberg et al. (1992) published a very early report on the study of lesions in 200 patients who had undergone ultrasonographic examination and biopsy by means of computer vision techniques aimed to improve the specificity of the ultrasonographic diagnosis. For this purpose, he made use of a camera to digitize film prints of B-scans and did manual lesion segmentation. Run-length and Markovian features, representing the texture of each lesion, were first calculated and then classified by a three-layer feed-forward artificial neural network trained by back propagation. The network classified the malignant cases with 100% sensitivity in a leave-one-out experiment (41.5% specificity).

In Taiwan, a group of researchers are working with D.R. Chen, R.F. Chang and Y.L. Huang on the automated processing of sonographic images of the breast by texture based features.

Out of a database of 255 histologically confirmed tumors, each sonographic lesion was imaged in two planes (longitudinal and transversal). In addition, two ROIs were placed within each grabbed ultrasound image: the first ROI surrounded the lesion, including normal tissue, and the second ROI was placed inside the lesion. This was done for both planes, resulting in four ROIs. Then the textures of these ROIs were analyzed by 24 autocorrelation texture features. Subsequently, a hierarchical model of five component neural networks was used to assess these features. It achieved an Az value of 0.98 through the differentiation of 36 malignant and 219 benign tumors of the sample set (k-fold cross validation) (Chen DR et al. 1999, 2000a).

Afterwards, the group also used learning vector quantization models on slightly different sample sets (sensitivity 96.7%, specificity 86.7%) (Chang et al. 2000; Chen DR et al. 2000a), self-organizing maps (sensitivity 97.6%, specificity 79.5%) (Chen DR et al. 2000b), support vector machines (sensitivity 95.45%, specificity 91.43%) (Chang et al. 2003), as well as bootstrap techniques (sensitivity 95.35%, specificity 79.10%) (Chen DR et al. 2002). The results of these studies show that the CAD system was able to outperform radiologists who assessed the same datasets. Moreover, various other groups have published similar results that could be achieved by using textural features only for mass differentiation (Kim et al. 2001; Shankar et al. 2005).

Although the great potential of texture analysis for the differentiation of malignant and benign tumors had been demonstrated notably by the group in Taiwan, it later stated and emphasized that sonographic texture analysis varies by the employed ultrasound system. Therefore, CAD systems that make use of texture features normally only work well on one specific ultrasound system, but not automatically on another one (Chang et al. 2005; Chen DR et al. 2005). However, this problem may be solved through the adjustment of parameters of the ultrasound device or the texture recognition algorithms. Kuo et al. (2002b) modeled an automatic system by using intelligent selection algorithms.

Koyama et al. (1997) stepped closer to the point of view of a radiologist and worked on visually assessed features rated on a five-point scale, describing clinically well-known morphological findings such as shape, border, halo (boundary echoes) and internal/posterior/edge shadows of the tumor. Through the application of a fuzzy inference system as classifier, they were able to reach up to 95% sensitivity at 76% specificity in differentiating benign and malignant lesions (Koyama et al. 1997; Sawaki et al. 1999). Therefore, in order to overcome the restrictions of textures, lesion segmentation and calculation of morphological features (and additional textural features if needed) were investigated and turned out to be promising techniques. Segmentation can be carried out manually (Chen CM et al. 2003; Kuo et al. 2002a), but is also possible through automatic functions (Chang et al. 2005; Huang and Chen W 2004; Madabhushi and Metaxas 2003; Mogatadakala et al. 2006; Sahiner et al. 2004; Xiao et al. 2002). After vari-

ous authors had addressed single morphological features, such as tumor contour features and the amount of features raised (Chou et al. 2001; Huang et al. 2004), the number of features increased: Horsch et al. (2002, 2004) investigated the combination of four features related to the lesion shape, margin, texture, and posterior acoustic behavior. Joo et al. (2004) worked on five morphological features that represented shape as well as edge characteristics, and darkness of a nodule. Chang et al. (2005) used six morphological features after automatic mass segmentation, and a support vector machine to yield a sensitivity of 88.9% and a specificity of 92.5%; Gefen et al. (2003) enlarged ultrasound features by patient age and clinical findings; and Song et al. (2005) analyzed margin sharpness, margin echoes, angular variation in margins and patient age once by means of logistic regression (Az = 0.853) and once through an artificial neural network (Az = 0.856).

CEDARA Software Corp distributes B-CAD as a commercially available product (http://www.cedara.com; originally developed by Medipattern Corporation, Toronto) that is designed to aid radiologists by automatic segmentation and feature extraction (shape and orientation), as well as annotation and report generation of sonographic findings according to the ACR BI-RADS Ultrasound Lexicon (American College of Radiology 2003). The software received US Food and Drug Administration 510(k) clearance in May 2005.

Beyond the information of one or more B-scan images of a tumor, new techniques in ultrasound may provide additional information per investigation. For instance, in "elastography," ultrasonic waveforms before and after a light-tissue compression can be compared by means of image registration to calculate characteristic values out of the registration vectors. Further analysis may then be conducted by a support vector machine to classify solid breast lesions with an Az value of 0.9358 (Chen CJ et al. 2006; Moon et al. 2005).

In addition to B-scans, 3D-ultrasonography promises to increase the amount of data of this investigative modality. Initial investigations show a potentially significant advantage (Chen DR et al. 2003; Sahiner et al. 2004).

Next to differentiating malignant and benign lesions, ANNs have also been used on sonographic findings to detect or exclude breast implant ruptures. Venta et al. (1998) demonstrated that ANNs in tandem with the unaided radiological diagnosis can improve the accuracy rate in the detection of implant rupture based on sonographic findings.

26.4 Computer-Aided Detection and Diagnosis in Contrast-Enhanced MRI of the Breast

26.4.1 Dynamic Versus Morphological Features

Contrast-enhanced MRI often reveals incidental contrast-enhancing findings that have to be differentiated between benign and malignant – in addition to the area or tumor the investigation was originally intended for (Teifke et al. 2003). Reported specificity values assessing these findings range from 30% to 85% depending on the way the image is evaluated (Harms and Flamig 1993; Heywang-Koebrunner et al. 2001; Kaiser 1993, 1994). Therefore, the high proportion of false-positive results is still the main limitation of MRM, a limitation which becomes increasingly evident when using parallel image acquisition on high-field strength MRI scanners which enables radiologists to provide high resolution images. The higher the resolution of modern imaging protocols, the more additional small foci will be detected and will need to be evaluated, leading to an increased number of false positives.

The diagnostic relevance of dynamic studies in differentiating primary breast tumors by using currently available extracellular small molecular gadolinium chelates has been proven in several investigations, and also in a multi-center trial (Heywang-Koebrunner et al. 2001). The initial phase of CM uptake, maximum relative enhancement and washout in the late post-contrast phase turned out to be the most valuable criteria by which to assess the likelihood of the malignancy of a lesion among other parameters. This enabled the describing of different dynamic curve types (Kuhl et al. 1999). However, a group of lesions with intermediate signal-time-curves will always remain unclear because enhancement rates show broad overlap between benign and malignant lesions (Kuhl et al. (2005).

In addition to dynamic features, and comparable to the evaluation of mammographic findings, architectural features of contrast-enhancing lesions are analyzed (Degani et al. 1997; Furman-Haran et al. 2001; Nunes et al. 1997; Obenauer et al. 2002). Now-

adays, higher spatial resolution improves the detection of typical signs of malignancy such as irregular margins, spiculation or central necrosis. Reports of single center trials using the latest scanner technology indicate that due to rising technical possibilities the analysis of morphological features will soon turn out to be more important than the analysis of contrast media kinetics (Kuhl et al. 2005; Vomweg et al. 2004). Due to these technical improvements the amount and quality of information, the need of time for assessment, and the potential benefit of using CAD systems in contrast-enhanced breast MRI are currently still rising.

26.4.2 Computer-Aided Detection and Diagnosis of Contrast-Enhancing Lesions

MR investigations of the breast do often show movement artifacts caused by subtle breast movements due to breathing, trembling, heart beat or muscle relaxation during the investigation. In particular, voxel-based approaches analyzing signal intensity/time curves of single voxels or small ROIs depend on the exact tissue localization, and will provide wrong results if motion correction is not applied. Therefore, a non-rigid mono-modal registration for motion correction is the most important pre-processing tool in breast MRI computer-aided diagnosis.

Soon after the invention of contrast-enhanced breast MRI, computer-aided diagnosis started by calculating color-coded maps. This method superimposes the gray scaled 3D image block with colors indicating the kinetic behavior after contrast media application on a voxel-by-voxel basis. It enables the radiologist reviewing the superimposed 3D image block to analyze morphology as well as the dynamic behavior within one turn. Without superimposing dynamic signal intensity/time curve information into one 3D series, the radiologist would have to investigate all subsequent series thoroughly. The colors are normally assigned to scaled dynamic indices (e.g. maximum slope, time to peak, percent of signal intensity increase) (Setti et al. 2001) (Fig. 26.4). In several studies, an underlying set of prototype signal intensity/time curves (Kuhl et al. 1996) or even a pharmacokinetic model (Hess et al. 1994) was used for color coding.

Color-coded DICOM overlays were the preferred output of breast MRI computer-aided diagnosis software until recently, but are now also used to visualize more complex processing results: authors successfully clustered series of similar temporal behavior by self organizing maps (Fischer and Hennig 1999; Nattkemper and Wismuller 2005; Vomweg et al. 2005). Lucht et al. (2001) went one step further by testing the performance of artificial neural networks for the classification of signal intensity/time curves on ROIs containing structures with known histology (105 parenchyma, 162 malignant, and 102 benign tissue regions). They also investigated different temporal resolutions of the signal intensity/time-curves (28 measurements, 23 s each, down to just three measurements taken 1.8, 3, and 10 min after contrast medium administration) and showed that discrimination of malignant and benign lesions using dynamic information alone is best if 28 measurement points – and therefore the highest temporal resolution of the imaging protocol – were used (sensitivity: 84%, specificity: 81%). Using standard imaging protocols that normally consist of two to six repetitions of a 3D MR sequence within a maximum measurement time of 6–8 min after contrast media application, other groups applied various types of neural networks with nearly similar results (Abdolmaleki et al. 2001; Kelcz et al. 2002; Twellmann et al. 2005; Vergnaghi et al. 2001).

To work on an object or lesion level (not on single voxels) manual or (semi-) automatic ROI placement followed by lesion segmentation is needed. Most groups work on subtraction series or fat-suppressed post-contrast series for lesion detection. Used algorithms do vary: el-Kwae et al. (1998) trained a Boolean neural network (BNN) by a set of malignant, benign and false-positive patterns extracted by experts from selected MR studies. Marti-Bonmati et al. (2004) tried out three pattern-recognition methods (artificial neural networks, support vector machine, k-nearest neighbor) and found that a back-propagation network performed best in lesion detection. Chen W et al. (2006) segmented lesions within a previously manually chosen rough ROI by fuzzy c-means, clustering correctly in 97% of 121 masses. Alterson and Plewes (2003) used bilateral symmetry analysis to detect abnormal regions of the breast.

After successful lesion detection, morphological and dynamic features have to be assessed manually or automatically. These features may then be analyzed to come to a probability of malignancy. By 1997 Abdolmaleki et al. (1997) had already assessed six manually obtained features by a three-layer feed-forward neural network, and showed that methods of artificial intelligence are capable of dif-

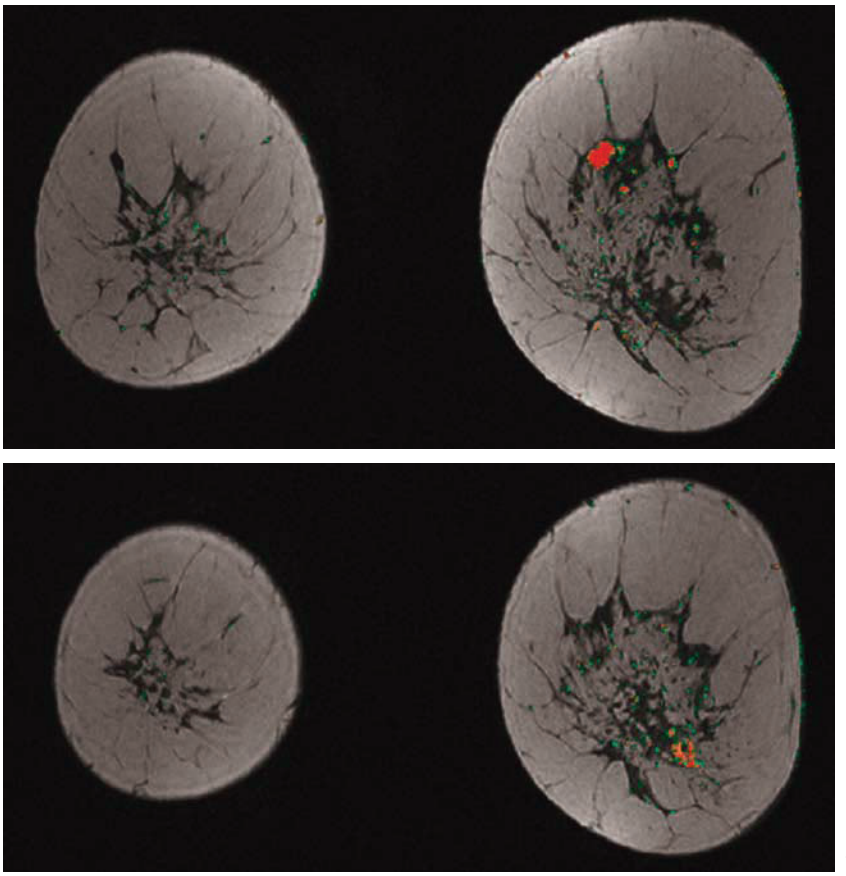

Fig. 26.4a,b. Two sections of a color-coded dynamic MRI of the breast. The colors indicate the percentage of signal intensity increase on a voxel-by-voxel basis. *Red* indicates a strong initial signal intensity increase that may be related to the presence of malignant tumors. In addition to one malignant tumor in (**a**) many other regions (**b**) of the exams may be colored by this simple dynamic-based approach

ferentiating malignant and benign tumors by these features. Recently, Szabo et al. (2004a,b) used morphological features in combination with dynamic features and reported an ANN considering margin, time to peak and washout features only to work best. Nattkemper et al. (2005) found that contour and wash-out type features determined the best Az value of 0.88 using a support vector machine as classifier. Vomweg et al. (2003) used up to 29 manually obtained features containing patient history information as input for a variety of different network topologies and reached a maximum sensitivity of 94.6% and a specificity of 91.9% with a validation sample set of 131 histological proven lesions. Chen W et al. (2004) achieved an Az value of 0.86 using automatic volume growing for lesion segmentation followed by automatic assessment of six morphological and dynamic features.

Many of the research reports enumerated above also compared the performance of the CAD system and a human expert reader or statistical means: most of the CAD systems proved to be equivalent and sometimes even better than their competitors. Caused by the steadily rising number of images and thus rising a number of findings and time-need, CAD software soon helped radiologists regain efficiency assessing breast MR exams. This has led to a quick distribution of CAD products especially in the US (Wood 2005). But commercialized MRI CAD systems have received FDA approval as image processing or MRI data manipulation tools only. Comprehensive clinical trials to prove their efficacy as diagnostic aids or even as full-automatic second opinion is outstanding.

Table 26.2 gives a list of software products currently available.

Table 26.2. List of vendors and products related to computer-aided diagnosis in contrast-enhanced (CE) breast MRI (status as of January 2007 to the best of our knowledge)

Vendor	URL	Product name	Registration	FDA approval (status as of Januar 2007)
CAD SCIENCES (3TP)	www.cadsciences.com	Streamline	yes	510(k)
Confirma	www.confirma.com	CADstream / SureLoc	2D/3D	510(k)
Invivo (MeVis Diagnostics)	www.igc.com/invivo	DynaCAD	2D/3D	510(k)
PENN Diagnostics	www.oncad.com/	ONCAD Formerly: "CADimas"	n.a.	510(k) CADimas

26.5 Computer Diagnosis in Breast Imaging

Most of the software discussed in previous chapters performs different measurements internally to calculate the likelihood of malignancy or suspicion. This value is needed to decide by threshold whether or not a finding should be pointed out to the user. Normally, the value itself is not given to the user. In some programs, the color or size of a marker indicates the level of suspicion.

At this level the software all belongs to the categories "computer-aided detection" and/or "computer-aided diagnosis". The status of "computer diagnosis," meaning computer software working on the images without relevant user interaction and delivering a diagnosis like a human observer, is difficult to reach. Such software needs much effort not only in detection and diagnosis algorithms but also in the surrounding software framework, which has to be robust and also has to cope with different variants of images from different providers. Considering the CAD software products available for mammography, it appears that vendors have already solved these issues, at least in part.

But the biggest problem to be solved while producing a computer diagnosis software is that of regulation: before it is introduced to the market, software claiming to deliver a diagnosis has to prove that it works at least as well as a radiologist reading. A study would been needed to compare the performance of the software and the radiologist in an independent setting compared to a gold-standard. In breast imaging such a setting is hardly constructible. Without very convincing data, authorities in the US and Europe will not license software claiming to provide a computer diagnosis, and will therefore not authorize any usage in human patients.

From a financial point of view a computer-only generated second opinion would be very valuable. Computer diagnosis could replace a second reader in mammography screening or in the assessment of MR studies. Considering the costs of a radiologist doing second reading, the potential of such software to be sold at a high price is very interesting and will push the manufacturers in that direction. Once the computer does the same work in parallel to a human observer its performance will be comparable directly.

Acknowledgements

The author would like to thank Andrea Teifke and Dirk Mayer for their contribution of mammography, MRI and ultrasound images, as well as Adam Maciak and Sarah Hilbert for their critical reviews.

References

Abdolmaleki P, Buadu LD, Murayama S et al (1997) Neural network analysis of breast cancer from MRI findings. Radiat Med 15:283–293

Abdolmaleki P, Buadu LD, Naderimansh H et al (2001) Feature extraction and classification of breast cancer on dynamic magnetic resonance imaging using artificial neural network. Cancer Lett 171:183–191

Aichinger U, Schulz-Wendtland R, Kramer S et al (2002) Scar or recurrence – comparison of MRI and color-coded ultrasound with echo signal amplifiers. Rofo 174:1395–1401

Alterson R, Plewes DB (2003) Bilateral symmetry analysis of breast MRI. Phys Med Biol 48:3431–3443

American College of Radiology (2003) ACR BI-RADS – Mammography, Ultrasound & Magnetic Resonance Imaging, 4th edn. Reston, VA
Arodz T, Kurdziel M, Popiela TJ et al (2006) Detection of clustered microcalcifications in small field digital mammography. Comput Methods Programs Biomed 81:56–65
Baker JA, Soo MS (2000) The evolving role of sonography in evaluating solid breast masses. Semin Ultrasound CT MR 21:286–296
Bankman IN, Nizialek T, Simon I et al (1997) Segmentation algorithms for detecting microcalcifications in mammograms. IEEE Trans Inf Technol Biomed 1:141–149
Baydush AH, Catarious DM, Abbey CK et al (2003) Computer aided detection of masses in mammography using subregion Hotelling observers. Med Phys. 30:1781–1787
Bazzani A, Bevilacqua A, Bollini D et al (2001) An SVM classifier to separate false signals from microcalcifications in digital mammograms. Phys Med Biol 46:1651–1663
Berg WA (2001) Overview of breast imaging. Semin Roentgenol 36:180–186
Boccignone G, Chianese A, Picariello A et al (2000) Computer aided detection of microcalcifications in digital mammograms. Comput Biol Med 30:267–286
Brem RF, Hoffmeister JW, Rapelyea JA et al (2005) Impact of breast density on computer-aided detection for breast cancer. AJR Am J Roentgenol 184:439–444
Brenton JD, Carey LA, Ahmed AA et al (2005) Molecular classification and molecular forecasting of breast cancer: ready for clinical application? J Clin Oncol 23:7350–7360
Cady B, Michaelson JS (2001) The life-sparing potential of mammographic screening. Cancer 91:1699–1703
Carriero A, Ambrossini R, Mattei PA et al (2002) Magnetic resonance of the breast: correlation between enhancement patterns and microvessel density in malignant tumors. J Exp Clin Cancer Res 21:83–87
Catarious DMJ, Baydush AH, Floyd CEJ et al (2004) Incorporation of an iterative, linear segmentation routine into a mammographic mass CAD system. Med Phys 31:1512–1520
Chan HP, Sahiner B, Lam KL et al (1998) Computerized analysis of mammographic microcalcifications in morphological and texture feature spaces. Med Phys 25:2007–2019
Chang RF, Kuo WJ, Chen DR, et al. (2000) Computer-aided diagnosis for surgical office-based breast ultrasound. Arch Surg 135:696–699
Chang RF, Wu WJ, Moon WK et al (2003) Improvement in breast tumor discrimination by support vector machines and speckle-emphasis texture analysis. Ultrasound Med Biol 29:679–686
Chang RF, Wu WJ, Moon WK et al (2005) Automatic ultrasound segmentation and morphology based diagnosis of solid breast tumors. Breast Cancer Res Treat 89:179–185
Chang YH, Hardesty LA, Hakim CM et al (2001) Knowledge-based computer-aided detection of masses on digitized mammograms: a preliminary assessment. Med Phys 28:455–461
Chang YH, Zheng B, Gur D et al (1996) Robustness of computerized identification of masses in digitized mammograms. A preliminary assessment. Invest Radiol 31:563–568
Charafe-Jauffret E, Ginestier C, Monville F et al (2005) How to best classify breast cancer: conventional and novel classifications (review). Int J Oncol 27:1307–1313
Chen CJ, Chang RF, Moon WK et al (2006) 2-D ultrasound strain images for breast cancer diagnosis using nonrigid subregion registration. Ultrasound Med Biol 32:837–846
Chen CM, Chou YH, Han KC et al (2003) Breast lesions on sonograms: computer-aided diagnosis with nearly setting-independent features and artificial neural networks. Radiology 226:504–514
Chen DR, Chang RF, Huang YL et al (1999) Computer-aided diagnosis applied to US of solid breast nodules by using neural networks. Radiology 213:407–412
Chen DR, Chang RF, Huang YL et al (2000a) Texture analysis of breast tumors on sonograms. Semin Ultrasound CT MR 21:308–316
Chen DR, Chang RF, Huang YL et al (2000b) Breast cancer diagnosis using self-organizing map for sonography. Ultrasound Med Biol 26:405–411
Chen DR, Kuo WJ, Chang RF et al (2002) Use of the bootstrap technique with small training sets for computer-aided diagnosis in breast ultrasound. Ultrasound Med Biol 28:897–902
Chen DR, Chang RF, Chen WM et al (2003) Computer-aided diagnosis for 3-dimensional breast ultrasonography. Arch Surg 138:296–302
Chen DR, Chang RF, Chen CJ et al (2005) Classification of breast ultrasound images using fractal feature. Clin Imaging 29:235–245
Chen W, Giger ML, Bick U et al (2006) A fuzzy c-means (FCM)-based approach for computerized segmentation of breast lesions in dynamic contrast-enhanced MR images. Acad Radiol 13:63–72
Chen W, Giger ML, Lan L et al (2004) Computerized interpretation of breast MRI: investigation of enhancement-variance dynamics. Med Phys 31:1076–1082
Cheng HD, Lui YM, Freimanis RI et al (1998) A novel approach to microcalcification detection using fuzzy logic technique. IEEE Trans Med Imaging 17:442–450
Chou YH, Tiu CM, Hung GS et al (2001) Stepwise logistic regression analysis of tumor contour features for breast ultrasound diagnosis. Ultrasound Med Biol 27:1493–1498
Clarke LP, Kallergi M, Qian W et al (1994) Tree-structured non-linear filter and wavelet transform for microcalcification segmentation in digital mammography. Cancer Lett 77:173–181
Degani H, Gusis V, Weinstein D et al (1997) Mapping pathophysiological features of breast tumors by MRI at high spatial resolution. Nat Med 3:780–782
el-Kwae EA, Fishman JE, Bianchi MJ et al (1998) Detection of suspected malignant patterns in three-dimensional magnetic resonance breast images. J Digit Imaging 11:83–93
El-Naqa I, Yang Y, Wernick MN et al (2002) A support vector machine approach for detection of microcalcifications. IEEE Trans Med Imaging 21:1552–1563
Ema T, Doi K, Nishikawa RM et al (1995) Image feature analysis and computer-aided diagnosis in mammography: reduction of false-positive clustered microcalcifications using local edge-gradient analysis. Med Phys 22:161–169
Fischer H, Hennig J (1999) Neural network-based analysis of MR time series. Magn Reson Med 41:124–131
Fischer U, Zachariae O, Baum F et al (2004) The influence of preoperative MRI of the breasts on recurrence rate in patients with breast cancer. Eur Radiol 14:1725–1731

Floyd C, Lo JY, Tourassi GD et al (2000) Case-based reasoning computer algorithm that uses mammographic findings for breast biopsy decisions. AJR Am J Roentgenol 175:1347–1352
Fogel DB, Wasson EC, Boughton EM et al (1998) Linear and neural models for classifying breast masses. IEEE Trans Med Imaging 17:485–488
Furman-Haran E, Grobgeld D, Kelcz F et al (2001) Critical role of spatial resolution in dynamic contrast-enhanced breast MRI. J Magn Reson Imaging 13:862–867
Gavrielides MA, Lo JY, Vargas-Voracek R et al (2000) Segmentation of suspicious clustered microcalcifications in mammograms. Med Phys 27:13–22
Gefen S, Tretiak OJ, Piccoli CW et al (2003) ROC analysis of ultrasound tissue characterization classifiers for breast cancer diagnosis. IEEE Trans Med Imaging 22:170–177
Giger ML, Vyborny CJ, Schmidt RA et al (1994) Computerized characterization of mammographic masses: analysis of spiculation. Cancer Lett 77:201–211
Goldberg V, Manduca A, Ewert DL et al (1992) Improvement in specificity of ultrasonography for diagnosis of breast tumors by means of artificial intelligence. Med Phys 19:1475–1481
Gurcan MN, Chan HP, Sahiner B et al (2002) Optimal neural network architecture selection: improvement in computerized detection of microcalcifications. Acad Radiol 9:420–429
Hadjiiski L, Sahiner B, Chan HP et al (1999) Classification of malignant and benign masses based on hybrid ART2LDA approach. IEEE Trans Med Imaging 18:1178–1187
Hadjiiski L, Sahiner B, Chan HP et al (2001) Analysis of temporal changes of mammographic features: computer-aided classification of malignant and benign breast masses. Med Phys 28:2309–2317
Hadjiiski L, Sahiner B, Helvie MA et al (2006) Breast masses: computer-aided diagnosis with serial mammograms. Radiology 240:343–356
Halkiotis S, Mantas J (2002) Automatic detection of clustered microcalcifications in digital mammograms. Stud Health Technol Inform 90:24–29
Hand W, Semmlow JL, Ackerman LV et al (1979) Computer screening of xeromammograms: a technique for defining suspicious areas of the breast. Comput Biomed Res 12:445–460
Harms SE, Flamig DP (1993) MR imaging of the breast. J Magn Reson Imaging 3:277–283
Hess T, Knopp MV, Hoffmann U et al (1994) A pharmacokinetic analysis of Gd-DTPA enhancement in MRT in breast carcinoma. Rofo 160:518–523
Heywang-Koebrunner S, Bick U, Bradley WG Jr et al (2001) International investigation of breast MRI: results of a multicenter study (11 sites) concerning diagnostic parameters for contrast-enhanced MRI based on 519 histopathologically correlated lesions. Eur Radiol 11:531–546
Horsch K, Giger ML, Venta LA et al (2002) Computerized diagnosis of breast lesions on ultrasound. Med Phys 29:157–164
Horsch K, Giger ML, Vyborny CJ et al (2004) Performance of computer-aided diagnosis in the interpretation of lesions on breast sonography. Acad Radiol 11:272–280
Huang SF, Chang RF, Chen DR et al (2004) Characterization of spiculation on ultrasound lesions. IEEE Trans Med Imaging 23:111–121
Huang YL, Chen DR (2004) Watershed segmentation for breast tumor in 2-D sonography. Ultrasound Med Biol 30:625–632
Huo Z, Giger ML, Vyborny CJ et al (1995) Analysis of spiculation in the computerized classification of mammographic masses. Med Phys 22:1569–1579
Jatoi I (1999) Breast cancer screening. Am J Surg 177:518–524
Jiang Y, Nishikawa RM, Wolverton DE et al (1996) Malignant and benign clustered microcalcifications: automated feature analysis and classification. Radiology 198:671–678
Jiang Y, Nishikawa RM, Papaioannou J et al (2001) Dependence of computer classification of clustered microcalcifications on the correct detection of microcalcifications. Med Phys 28:1949–1957
Joo S, Yang YS, Moon WK et al (2004) Computer-aided diagnosis of solid breast nodules: use of an artificial neural network based on multiple sonographic features. IEEE Trans Med Imaging 23:1292–1300
Kaiser WA (1993) MR Mammographie. Radiologe 33:292–299
Kaiser WA (1994) False-positive results in dynamic MR mammography. Causes, frequency, and methods to avoid. Magn Reson Imaging Clin N Am 2:539–555
Kallergi M (2004) Computer-aided diagnosis of mammographic microcalcification clusters. Med Phys 31:314–326
Karssemeijer N, te Brake G (1996) Detection of stellate distortions in mammograms. IEEE Trans Med Imaging 15:611–619
Karssemeijer N, Hendriks JH (1997) Computer-assisted reading of mammograms. Eur Radiol 7:743–748
Kegelmeyer Jr W, Pruneda JM, Bourland PD et al (1994) Computer-aided mammographic screening for spiculated lesions. Radiology 191:331–337
Kelcz F, Furman-Haran E, Grobgeld D et al (2002) Clinical testing of high-spatial-resolution parametric contrast-enhanced MR imaging of the breast. AJR Am J Roentgenol 179:1485–1492
Kim KG, Kim JH, Min BG et al (2001) Comparative analysis of texture characteristics of malignant and benign tumors in breast ultrasonograms. J Digit Imaging 14:208–210
Kimme C, O'Loughlin B, Sklansky J (1975) Automatic detection of suspicious abnormalities in breast radiographs. In: Klinger A, Fu S, Kunii T (eds) Data structures, computer graphics and pattern recognition. Academic, New York, pp 427–447
Kita Y, Tohno E, Highnam R et al (2002) A CAD system for the 3D location of lesions in mammograms. Med Image Anal 6:267–273
Kobatake H, Murakami M, Takeo H et al (1999) Computerized detection of malignant tumors on digital mammograms. IEEE Trans Med Imaging 18:369–378
Kovalerchuk B, Triantaphyllou E, Ruiz JF et al (1997) Fuzzy logic in computer-aided breast cancer diagnosis: analysis of lobulation. Artif Intell Med 11:75–85
Koyama S, Obata Y, Shimamoto K, et al. (1997) Breast ultrasonography: computer-aided diagnosis using fuzzy inference. J Ultrasound Med 16:665–672
Kriege M, Brekelmans CT, Obdeijn IM et al (2006) Factors affecting sensitivity and specificity of screening mammography and MRI in women with an inherited risk for breast cancer. Breast Cancer Res Treat [Epub ahead of print]

Kuhl CK (2002) High-risk screening: multi-modality surveillance of women at high risk for breast cancer (proven or suspected carriers of a breast cancer susceptibility gene). J Exp Clin Cancer Res 21:103–106
Kuhl CK, Schild HH (2000) Dynamic image interpretation of MRI of the breast. J Magn Reson Imaging 12:965–974
Kuhl CK, Bieling HB, Lutterbey G et al (1996) Standardization and acceleration of quantitative analysis of dynamic MR mammographies via parametric images and automatized ROI definition. Rofo 164:475–482
Kuhl CK, Mielcareck P, Klaschik S et al (1999) Dynamic breast MR imaging: are signal intensity time course data useful for differential diagnosis of enhancing lesions? Radiology 211:101–110
Kuhl CK, Schild HH, Morakkabati N et al (2005) Dynamic bilateral contrast-enhanced MR imaging of the breast: trade-off between spatial and temporal resolution. Radiology 236:789–800
Kuo WJ, Chang RF, Lee CC et al (2002a) Retrieval technique for the diagnosis of solid breast tumors on sonogram. Ultrasound Med Biol 28:903–909
Kuo WJ, Chang RF, Moon WK et al (2002b) Computer-aided diagnosis of breast tumors with different US systems. Acad Radiol 9:793–799
Lalonde L, David J, Trop I et al (2005) Magnetic resonance imaging of the breast: current indications. Can Assoc Radiol J 56:301–308
Lau TK, Bischof WF (1991) Automated detection of breast tumors using the asymmetry approach. Comput Biomed Res 24:273–295
Leach MO (2001) Application of magnetic resonance imaging to angiogenesis in breast cancer. Breast Cancer Res 3:22–27
Lee KL, Lithgow B (2000) Detection of microcalcifications using spatial filtering. Australas Phys Eng Sci Med 23:62–65
Leichter I, Lederman R, Buchbinder S et al (2000) Optimizing parameters for computer-aided diagnosis of microcalcifications at mammography. Acad Radiol 7:406–412
Leichter I, Lederman R, Buchbinder SS et al (2004) Computerized evaluation of mammographic lesions: what diagnostic role does the shape of the individual microcalcifications play compared with the geometry of the cluster? AJR Am J Roentgenol 182:705–712
Lemaur G, Drouiche K, DeConinck J et al (2003) Highly regular wavelets for the detection of clustered microcalcifications in mammograms. IEEE Trans Med Imaging 22:393–401
Li H, Wang Y, Liu KJ et al (2001) Computerized radiographic mass detection - part I: Lesion site selection by morphological enhancement and contextual segmentation. IEEE Trans Med Imaging 20:289–301
Li L, Qian W, Clarke LP et al (1997) Digital mammography: computer-assisted diagnosis method for mass detection with multiorientation and multiresolution wavelet transforms. Acad Radiol 4:724–731
Li L, Clark RA, Thomas JA et al (2002) Computer-aided diagnosis of masses with full-field digital mammography. Acad Radiol 9:4–12
Liney GP, Gibbs P, Hayes C et al (1999) Dynamic contrast-enhanced MRI in the differentiation of breast tumors: user-defined versus semi-automated region-of-interest analysis. J Magn Reson Imaging 10:945–949
Lucht RE, Knopp MV, Brix G et al (2001) Classification of signal-time-curves from dynamic MR mammography by neural networks. Magn Reson Imaging 19:51–57
Madabhushi A, Metaxas DN (2003) Combining low-, high-level and empirical domain knowledge for automated segmentation of ultrasonic breast lesions. IEEE Trans Med Imaging 22:155–169
Garcia-Gomez JM, Vidal C, Marti-Bonmati L, Galant J, Sans N, Robles M, Casacuberta F (2004) Benign/malignant classifier of soft tissue tumors using MR imaging. MAGMA 14:194–201
Mata Campos R, Vidal EM, Nava E et al (2000) Detection of microcalcifications by means of multiscale methods and statistical techniques. J Digit Imaging 13:221–225
McLoughlin KJ, Bones PJ, Karssemeijer N et al (2004) Noise equalization for detection of microcalcification clusters in direct digital mammogram images. IEEE Trans Med Imaging 23:313–320
Mini MG, Devassia VP, Thomas T et al (2004) Multiplexed wavelet transform technique for detection of microcalcification in digitized mammograms. J Digit Imaging 17:285–291
Mogatadakala KV, Donohue KD, Piccoli CW et al (2006) Detection of breast lesion regions in ultrasound images using wavelets and order statistics. Med Phys 33:840–849
Moon WK, Chang RF, Chen CJ et al (2005) Solid breast masses: classification with computer-aided analysis of continuous US images obtained with probe compression. Radiology 236:458–464
Morris EA (2001) Illustrated breast MR lexicon. Semin Roentgenol 36:238–429
Morris EA (2001) Review of breast MRI: indications and limitations. Semin Roentgenol 36:226–237
Mussurakis S, Buckley DL, Coady AM et al (1996) Observer variability in the interpretation of contrast enhanced MRI of the breast. Br J Radiol 69:1009–1016
Nakayama R, Uchiyama Y, Yamamoto K et al (2006) Computer-aided diagnosis scheme using a filter bank for detection of microcalcification clusters in mammograms. IEEE Trans Biomed Eng 53:273–283
Nattkemper TW, Wismuller A (2005) Tumor feature visualization with unsupervised learning. Med Image Anal 9:344–351
Nattkemper TW, Arnrich B, Lichte O et al (2005) Evaluation of radiological features for breast tumor classification in clinical screening with machine learning methods. Artif Intell Med 34:129–139
Netsch T, Peitgen HO (1999) Scale-space signatures for the detection of clustered microcalculations in digital mammograms. IEEE Trans Med Imaging 18:774–786
Ng KH, Looi LM, Bradley DA et al (1996) Microcalcification clustering parameters in breast disease: a morphometric analysis of radiographs of excision specimens. Br J Radiol 69:326–334
Nishimura S, Takahashi K, Gomi N et al (2004) What is the predictor for invasion in non-palpable breast cancer with microcalcifications? Breast Cancer 11:49–54
Nunes LW, Schnall MD, Orel SG et al (1997) Breast MR imaging: interpretation model. Radiology 202:833–841
Nunes FL, Schiabel H, Goes CE (2007) Contrast enhancement in dense breast images to aid clustered microcalcifications detection. J Digit Imaging 20:53–66 [Epub ahead of print]

Obenauer S, Schorn C, Stelter B et al (2002) Contrast-enhanced high in-plane resolution dynamic MRI of the breast. Are there advantages in comparison to standard dynamic MRI? Clin Imaging 26:161–165

Ozekes S, Osman O, Camurcu AY et al (2005) Mammographic mass detection using a mass template. Korean J Radiol 6:221–228

Papadopoulos A, Fotiadis DI, Likas A et al (2002) An automatic microcalcification detection system based on a hybrid neural network classifier. Artif Intell Med 25:149–167

Paquerault S, Petrick N, Chan HP et al (2002) Improvement of computerized mass detection on mammograms: fusion of two-view information. Med Phys 29:238–247

Paquerault S, Yarusso LM, Papaioannou J et al (2004) Radial gradient-based segmentation of mammographic microcalcifications: observer evaluation and effect on CAD performance. Med Phys 31:2648–2657

Pediconi F, Occhiato R, Venditti F et al (2005) Radial scars of the breast: contrast-enhanced magnetic resonance mammography appearance. Breast J 11:23–28

Petrick N, Chan HP, Wei D et al (1996) Automated detection of breast masses on mammograms using adaptive contrast enhancement and texture classification. Med Phys 23:1685–1696

Petrick N, Chan HP, Sahiner B et al (1999) Combined adaptive enhancement and region-growing segmentation of breast masses on digitized mammograms. Med Phys 26:1642–1654

Petrick N, Sahiner B, Chan HP et al (2002) Breast cancer detection: evaluation of a mass-detection algorithm for computer-aided diagnosis - experience in 263 patients. Radiology 224:217–224

Pettazzoni P, Pallotti G, Mattina M et al (2001) Computerized detection of clustered microcalcifications: a modular approach with non-linear filters. Med Hypotheses 56:442–447

Pisano ED, Yaffe MJ (2005) Digital mammography. Radiology 234:353–362

Podo F, Sardanelli F, Canese R et al (2002) The Italian multicenter project on evaluation of MRI and other imaging modalities in early detection of breast cancer in subjects at high genetic risk. J Exp Clin Cancer Res 21:115–124

Qian W, Clarke LP, Li HD et al (1994) Digital mammography: M-channel quadrature mirror filters (QMFs) for microcalcification extraction. Comput Med Imaging Graph JT - Computerized medical imaging and graphics: the official journal of the Computerized Medical Imaging Society. 18:301–314

Qian W, Clarke LP, Song D et al (1998) Digital mammography: hybrid four-channel wavelet transform for microcalcification segmentation. Acad Radiol 5:354–364

Qian W, Li L, Clarke L et al (1999) Digital mammography: comparison of adaptive and nonadaptive CAD methods for mass detection. Acad Radiol 6:471–480

Qian W, Mao F, Sun X et al (2002) An improved method of region grouping for microcalcification detection in digital mammograms. Comput Med Imaging Graph 26:361–368

Rymon R, Zheng B, Chang YH et al (1998) Incorporation of a set enumeration trees-based classifier into a hybrid computer-assisted diagnosis scheme for mass detection. Acad Radiol 5:181–187

Sahiner B, Chan HP, Wei D et al (1996) Image feature selection by a genetic algorithm: application to classification of mass and normal breast tissue. Med Phys 23:1671–1684

Sahiner B, Chan HP, Petrick N et al (2001) Improvement of mammographic mass characterization using spiculation meausures and morphological features. Med Phys 28:1455–1465

Sahiner B, Chan HP, Roubidoux MA et al (2004) Computerized characterization of breast masses on three-dimensional ultrasound volumes. Med Phys 31:744–754

Sajda P, Spence C, Pearson J et al (2002) Learning contextual relationships in mammograms using a hierarchical pyramid neural network. IEEE Trans Med Imaging 21:239–250

Sampat MP, Markey M, Bovik AC (2005) Computer-aided detection and diagnosis in mammography. In: Bovik A (ed) Handbook of image and video processing, 2nd edn. Elsevier Academic Press, Burlington, pp 1195–1218

Santen RJ, Mansel R (2005) Benign breast disorders. N Engl J Med 353:275–285

Sardanelli F, Giuseppetti GM, Panizza P et al (2004) Sensitivity of MRI versus mammography for detecting foci of multifocal, multicentric breast cancer in Fatty and dense breasts using the whole-breast pathologic examination as a gold standard. AJR Am J Roentgenol 183:1149–1157

Sardanelli F, Iozzelli A, Fausto A et al (2005) Gadobenate dimeglumine-enhanced MR imaging breast vascular maps: Association between invasive cancer and ipsilateral increased vascularity. Radiology 235:791-797

Sawaki A, Shimamoto K, Satake H et al (1999) Breast ultrasonography: diagnostic efficacy of a computer-aided diagnostic system using fuzzy inference. Radiat Med 17:41–45

Schmidt F, Sorantin E, Szepesvari C et al (1999) An automatic method for the identification and interpretation of clustered microcalcifications in mammograms. Phys Med Biol 44:1231–1243

Setti E, Trecate G, Ferrari M et al (2001) Breast magnetic resonance imaging: a computer-based analysis of enhancement curves. J Digit Imaging 14:226–228

Shankar PM, Piccoli CW, Reid JM et al (2005) Application of the compound probability density function for characterization of breast masses in ultrasound B scans. Phys Med Biol 50:2241–2248

Skaane P, Engedal K (1998) Analysis of sonographic features in the differentiation of fibroadenoma and invasive ductal carcinoma. AJR Am J Roentgenol 170:109–114

Skaane P, Engedal K, Skjennald A et al (1997) Interobserver variation in the interpretation of breast imaging. Comparison of mammography, ultrasonography, and both combined in the interpretation of palpable noncalcified breast masses. Acta Radiol 38:497–502

Sklansky J, Tao EY, Bazargan M et al (2000) Computer-aided, case-based diagnosis of mammographic regions of interest containing microcalcifications. Acad Radiol 7:395–405

Song JH, Venkatesh SS, Conant EA et al (2005) Comparative analysis of logistic regression and artificial neural network for computer-aided diagnosis of breast masses. Acad Radiol 12:487–495

Soo MS, Rosen EL, Xia JQ et al (2005) Computer-aided detection of amorphous calcifications. AJR Am J Roentgenol 184:887–892

Stout NK, Rosenberg MA, Trentham-Dietz A et al (2006) Retrospective cost-effectiveness analysis of screening mammography. J Natl Cancer Inst 98:774–782
Szabo BK, Aspelin P, Wiberg MK et al (2004a) Neural network approach to the segmentation and classification of dynamic magnetic resonance images of the breast: comparison with empiric and quantitative kinetic parameters. Acad Radiol 11:1344–1354
Szabo BK, Wiberg MK, Bone B et al (2004b) Application of artificial neural networks to the analysis of dynamic MR imaging features of the breast. Eur Radiol 14:1217–1225
Tabar L, Vitak B, Tony HH et al (2001) Beyond randomized controlled trials: organized mammographic screening substantially reduces breast carcinoma mortality. Cancer 91:1724–1731
Taylor P, Fox J, Pokropek AT, et al. (1999) The development and evaluation of CADMIUM: a prototype system to assist in the interpretation of mammograms. Med Image Anal 3:321–337
Teifke A, Lehr HA, Vomweg TW et al (2003) Outcome analysis and rational management of enhancing lesions incidentally detected on contrast-enhanced MRI of the breast. AJR Am J Roentgenol 181:655–662
Teifke A, Behr O, Schmidt M et al (2006) Dynamic MR imaging of breast lesions: correlation with microvessel distribution pattern and histologic characteristics of prognosis. Radiology 239:351–360
Tiedeu A, Daul C, Graebling P et al (2005) Correspondences between microcalcification projections on two mammographic views acquired with digital systems. Comput Med Imaging Graph 29:543–553
Timp S, Karssemeijer N (2004) A new 2D segmentation method based on dynamic programming applied to computer-aided detection in mammography. Med Phys 31:958–971
Topping A, George C, Wilson G et al (2003) Appropriateness of MRI scanning in the detection of ruptured implants used for breast reconstruction. Br J Plast Surg 56:186–189
Tourassi GD, Vargas-Voracek R, Catarious DM et al (2003) Computer-assisted detection of mammographic masses: a template matching scheme based on mutual information. Med Phys 30:2123–2130
Twellmann T, Lichte O, Nattkemper TW et al (2005) An adaptive tissue characterization network for model-free visualization of dynamic contrast-enhanced magnetic resonance image data. IEEE Trans Med Imaging 24:1256–1266
Varela C, Tahoces PG, Mendez AJ et al (2006) Computerized detection of breast masses in digitized mammograms. Comput Biol Med 37:2142-26
Venta LA, Salchenberger LM, Venta ER et al (1998) Improved diagnosis of breast implant rupture with sonographic findings and artificial neural networks. Acad Radiol 5:238–244
Vergnaghi D, Monti A, Setti E et al (2001) A use of a neural network to evaluate contrast enhancement curves in breast magnetic resonance images. J Digit Imaging 14:58–59
Vomweg TW, Buscema M, Kauczor HU et al (2003) Improved artificial neural networks in prediction of malignancy of lesions in contrast-enhanced MR-mammography. Med Phys 30:2350–2359
Vomweg TW, Teifke A, Kunz RP et al (2004) Combination of low and high resolution sequences in two orientations for dynamic contrast-enhanced MRI of the breast: more than a compromise. Eur Radiol 14:1732–1742
Vomweg TW, Teifke A, Kauczor HU et al (2005) Self-organizing neural networks for automatic detection and classification of contrast-enhancing lesions in dynamic MR-mammography. Rofo 177:703–713
Vyborny CJ, Doi T, O'Shaughnessy KF et al (2000) Breast cancer: importance of spiculation in computer-aided detection. Radiology 215:703–707
Wallet BC, Solka JL, Priebe CE et al (1997) A method for detecting microcalcifications in digital mammograms. J Digit Imaging 10:136–139
Wasser K, Klein SK, Fink C et al (2003) Evaluation of neoadjuvant chemotherapeutic response of breast cancer using dynamic MRI with high temporal resolution. Eur Radiol 13:80–87
Weatherall PT, Evans GF, Metzger GJ et al (2001) MRI vs. histologic measurement of breast cancer following chemotherapy: comparison with X-ray mammography and palpation. J Magn Reson Imaging 13:868–75
Wedegartner U, Bick U, Wortler K et al (2001) Differentiation between benign and malignant findings on MR-mammography: usefulness of morphological criteria. Eur Radiol 11:1645–50
WHO (2002) Breast Cancer Screening, 1st IARC Press, World Health Organization, Lyon
Winsberg F, Elkin M, Macy J et al (1967) Detection of radiographic abnormalities in mammograms by means of optical scanning and computer analysis. Radiology 89:211–215
Wood C (2005) Computer-Aided Detection (CAD) for breast MRI. Technol Cancer Res Treat 4:49–53
Wu Y, Doi K, Giger ML et al (1992) Computerized detection of clustered microcalcifications in digital mammograms: applications of artificial neural networks. Med Phys 19:555–560
Xiao G, Brady M, Noble JA et al (2002) Segmentation of ultrasound B-mode images with intensity inhomogeneity correction. IEEE Trans Med Imaging 21:48–57
Yin FF, Giger ML, Doi K et al (1991) Computerized detection of masses in digital mammograms: analysis of bilateral subtraction images. Med Phys 18:955–963
Yin FF, Giger ML, Vyborny CJ et al (1993) Comparison of bilateral-subtraction and single-image processing techniques in the computerized detection of mammographic masses. Invest Radiol 28:473–481
Yin FF, Giger ML, Doi K et al (1994a) Computerized detection of masses in digital mammograms: automated alignment of breast images and its effect on bilateral-subtraction technique. Med Phys 21:445–52
Yin FF, Giger ML, Doi K et al (1994b) Computerized detection of masses in digital mammograms: investigation of feature-analysis techniques. J Digit Imaging JT – Journal of digital imaging: the official journal of the Society for Computer Applications in Radiology. 7:18–26
Yu S, Guan L (2000) A CAD system for the automatic detection of clustered microcalcifications in digitized mammogram films. IEEE Trans Med Imaging 19:115–126
Zhang W, Doi K, Giger ML et al (1994) Computerized detection of clustered microcalcifications in digital mammo-

grams using a shift-invariant artificial neural network. Med Phys 21:517–524
Zheng B, Chang YH, Gur D et al (1995a) Computerized detection of masses in digitized mammograms using single-image segmentation and a multilayer topographic feature analysis. Acad Radiol 2:959–966
Zheng B, Chang YH, Gur D et al (1995b) Computerized detection of masses from digitized mammograms: comparison of single-image segmentation and bilateral-image subtraction. Acad Radiol 2:1056–1061
Zheng B, Chang YH, Staiger M et al (1995c) Computer-aided detection of clustered microcalcifications in digitized mammograms. Acad Radiol 2:655–662
Zheng B, Chang YH, Gur D et al (1996) Mass detection in digitized mammograms using two independent computer-assisted diagnosis schemes. AJR Am J Roentgenol 167:1421–1424
Zhou C, Chan HP, Paramagul C et al (2004) Computerized nipple identification for multiple image analysis in computer-aided diagnosis. Med Phys 31:2871–2882

Computer Aided Diagnosis: Clinical Applications in CT Colonography

27

Hiroyuki Yoshida and Abraham H. Dachman

CONTENTS

27.1 Introduction

During the past decade, numerous attempts have been made to develop computerized methods that process, analyze, and display multidimensional medical images in radiology. A typical example is the three-dimensional (3D) visualization of semi-automatically segmented organs (e.g. segmentation of the liver, endoluminal visualization of the colon and bronchus), or image processing of a part of an organ for the generation of an image that is more easily interpreted by human readers (e.g. peripheral equalization of the breast in mammograms, digital subtraction bowel cleansing in virtual colonoscopy). These computerized methods often automate only one of the image-processing tasks and depend on user interaction for the remaining tasks.

Computer-aided diagnosis (CAD) goes beyond these semi-automated image-processing applications and steps into the area of medical image understanding or interpretation. In its most general form, CAD can be defined as a diagnosis made by a radiologist who uses the output of a computerized scheme for automated image analysis as a diagnostic aid. The concept of CAD is universal across different modalities and disease types. However, CAD is expected to be most beneficial for those examinations that became feasible only recently due to the advancement of digital imaging technologies, in which very many high-resolution images need to be interpreted rapidly to find a lesion with low incidence.

CT colonography (CTC), also known as virtual colonoscopy, is a promising alternative technique for screening of colon cancers (Levin et al. 2003; Macari and Bini 2005; Morrin and LaMont 2003). CTC typically uses a multi-detector CT scanner to obtain a series of cross-sectional images of the abdomen for detection of polyps and masses in the colon. The transverse CT images can be reformatted into multiplanar reconstruction (MPR) view for examination of the colon (2D reading), or they can be reformatted to a simulated 3D "endoluminal view" of the entire colon that is comparable to that seen with optical colonoscopy (3D reading). In this visualization mode, radiologists can "fly through" the virtual colon, from the rectum to the cecum and back, searching for polyps and masses. In any reading mode, radiologists can non-invasively examine the interior of the colon without physically invading it; thus, it is a safer procedure than optical colonoscopy.

H. Yoshida, PhD; A. H. Dachman, PhD
Department of Radiology, Massachusetts General Hospital and Harvard Medical School, 25 New Chardon Street, Suite 400C, Boston, MA 02114, USA

CAD for CTC typically refers to a computerized scheme for automated detection of polyps and masses in CTC data, whether they are 2D images or 3D volume (Yoshida et al. 2005a; Yoshida et al. 200b). It reveals the locations of suspicious polyps and masses to radiologists. This offers a second opinion that has the potential of improving radiologists' detection performance, and of reducing variability of the diagnostic accuracy among radiologists, without significantly increasing the reading time.

During the last several years, rapid technical developments have established the fundamental CAD scheme for the detection of polyps, and commercial systems that implement the full CAD scheme or a part of it are becoming widely available (Yoshida et al. 2007). The latest CAD systems yield clinically acceptable high sensitivity and low false-positive rates, and thus CAD is becoming a major diagnosis aid for CTC. In the following sections of this chapter, we will describe the clinical benefits, principles, display modes, reader paradigms, known clinical performance of CAD and that of radiologists aided by CAD, and pitfalls of CAD.

27.2 Clinical Benefit of CAD

One of the major obstacles preventing CTC from becoming an effective means for polyp detection is that reader expertise is required for interpreting the CTC images – in particular, for detection of small polyps (Bodily et al. 2005; Burling et al. 2006; Fletcher et al. 2005; Slater et al. 2006). In particular, the detection performance among readers can be quite variable, which may be one of the factors for the large variation in the results of reported large-scale clinical trials (Fletcher et al. 2005). This problem is becoming substantial as CTC becomes a more accepted non-invasive examination of the colon, due to the steep learning curve of this new diagnosis method as well as the lack of formal training for the interpretation of CTC.

CAD is attractive because it has the potential to overcome this difficulty; that is, CAD has the potential to improve detection performance and reduce variability of detection accuracy among readers.

An improvement in the detection performance can be achieved because CAD can reduce perceptual errors during the detection of polyps. These perceptual errors may be caused by the presence of normal structures that mimic polyps, by fecal residuals or by variable conspicuity of polyps, depending on the display method. The absence of visual cues that normally exist with colonoscopy, such as mucosal color changes and a large number of images for each patient, also makes image interpretation tedious and susceptible to perceptual error (Bodily et al. 2005; Burling et al. 2006; Fletcher et al. 2005; Slater et al. 2006). Endoluminal 3D interpretation is also subject to observer error since 20% of the mucosa is not seen with a unidirectional fly-through (Pickhardt et al. 206)

A reduction of variability can be achieved because CAD can provide objective and consistent results, while the performance of a radiologist may be influenced by his or her skill and experience. Moreover, a variety of circumstances, including distraction and fatigue, as well as time constraints in a busy clinical practice, influence the diagnostic performance. Although radiologists may detect a certain type of polyp in the majority of cases, the same people may miss the same type of polyp under different reading conditions. Use of CAD can potentially overcome this lack of consistency by radiologists, and thus it can be useful for reducing variability among readers in identifying polyps in CTC.

The current status of CAD on the above two issues will be described in sections 27.5 and 27.6.

27.3 Principles of CAD for CT Colonography

Majority of the CAD systems available today consist of the following processing units: a) digital imaging and communications in medicine (DICOM) image reader for reading CTC images from a picture archiving system (PACS) in a CAD system over a network, b) extraction of the colonic wall from the CTC images, c) detection of polyp candidates in the extracted colon, d) discrimination of false-positives from polyps among polyp candidates, and e) display of the detected polyps on the screen of a 3D workstation.

Understanding each of the processing units is essential for understanding the types of CAD pitfalls in clinical CTC cases. A summary of the key techniques for each of these units, except for the first, is provided below.

27.3.1 Extraction of the Colon

Any system designed to detect colonic polyps may potentially detect polypoid objects that have soft-tissue CT density and protrude into the lumen. Therefore, any polypoid soft-tissue structure in the small bowel, stomach, or even the lungs can be erroneously detected as a polyp. Thus, the first step of CAD after reading in the CTC images is the extraction of the colonic wall while removing other luminal organs with soft-tissue density, such as the small bowel, stomach and lung bases.

Several methods for extraction of the colon have been developed. Some of them are fully automated (Frimmel et al. 2005; Li and Santago 2005; Masutani et al. 2001; Näppi et al. 2002a; Wyatt et al. 2006) whereas others are semi-automated (Chen et al. 2000; Franaszek et al. 2006; Iordanescu et al. 2005) and thus require user interaction for identification of the colonic wall on which polyps are searched. Most of these methods use the CT values characteristic of the colonic wall and the contrast between the colonic wall (soft-tissue density) and the air (or an oral contrast agent if it is used for opacifying residual stool and fluid) in the colonic lumen as a means of extracting the colon from a 3D volume.

One of the approaches (Näppi et al. 2002a) extracted the visible colonic wall by removing the normal structures that were not connected to the colon, based on thresholding of the 3D volume with the CT values characteristic of these structures. In the second step, they removed extracolonic components that were in contact with the outer surface of the colonic wall, such as the stomach and small bowel, by applying a self-adjusting volume-growing technique to the colonic lumen. On average, the regions extracted by this method covered approximately 98% of the visible surface region of the colonic wall (Fig. 27.1).

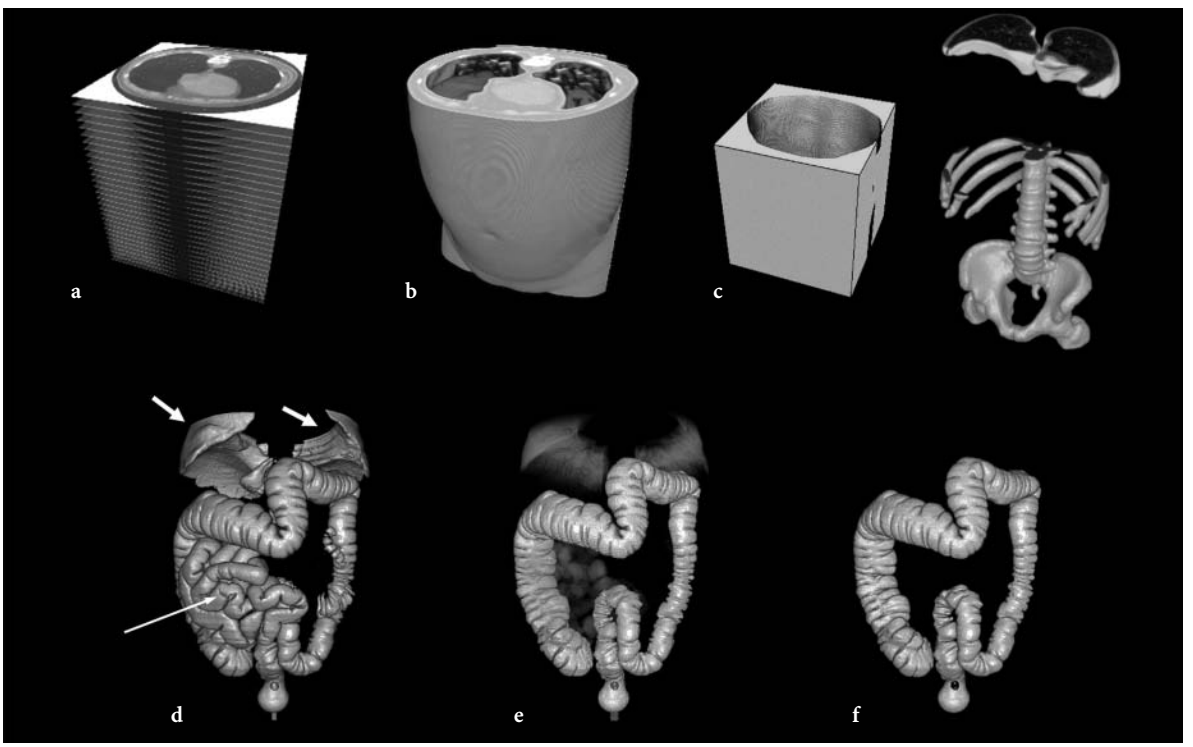

Fig. 27.1a–f. The KGS segmentation process. **a** Axial CT images from a VC examination. **b** 3D isotropic volume of the abdomen generated from the CT image in (**a**). **c** Extracolonic structures removed in the anatomy-based extraction process. The process first eliminates the region outside the body (*left*), the lung bases (*upper right*), and the osseous structures (*lower right*). **d** Result of the anatomy-based extraction. This process extracts the entire colon; however, a portion of the lung bases (*thick arrows*) and small bowel (*thin arrow*) remain unremoved. **e** Segmentation of the colon by use of colon-based analysis. This process identifies the air-filled colonic lumen by use of volume growing. The identified colonic lumen is highlighted, whereas the extracolonic structures are dimmed. **f** Final segmented colon obtained by intersection of (**d**) and (**e**). Note that the extracolonic structures, which are included in (**d**), are not present in the final segmentation

Generally, there is a trade-off between the amount of extracted colon (colon coverage) and that of extracolonic structures. Therefore, the main technical challenge in colon extraction is to extract collapsed regions while minimally extracting such extracolonic structures as noted above. Some of the colon extraction methods avoid this problem simply by assuming that the colons are well-cleansed and distended (Franaszek et al. 2006; Iordanescu et al. 2005). Therefore, users need to be careful when they subject real clinical CTC images in which colons contain collapsed regions to a CAD system that uses such a limited colon extraction process, because it may generate false-negatives (see Section 27.7.2). Many visualization software packages make this potential error easy to notice by providing simultaneous barium enema-like or volume rendered overview of the colon and by providing a semi-automated means of adding/removing colonic segments.

27.3.2 Detection of Suspicious Polyps

Polyps tend to appear as bulbous, cap-like structures adhering to the extracted colonic wall and protruding to the lumen, whereas folds appear as elongated, ridge-like structures, and the colonic wall itself appears as a large, nearly flat, cup-like structure (Fig. 27.2b,c). Therefore, shape analyses that differentiate among these distinct types of shapes and scales are effective in the detection of polyps. To this end, various methods have been developed, including use of a volumetric shape index and curvedness (Yoshida and Näppi 2001) (Fig. 27.3), surface curvature with a rule-based filter (Summers et al. 2000; Summers et al. 2005a), sphere fitting (Kiss et al. 2002), and overlapping surface normal method (Paik et al. 2004).

In the approach that employs the volumetric shape index and curvedness (Yoshida and Näppi 2001), the shape index is used to analyze the vicinity of a voxel and determines to which of the following five topologic classes a voxel belongs: cup, rut, saddle, ridge, or cap. A region representing the highest shape index values corresponds to a cap-like shape, and thus the region is detected as a polyp candidate. Color coding of the anatomic structures in the colonic lumen based on the shape index can thus differentiate among polyps, folds, and colonic walls effectively (Fig. 27.2d). The volumetric curvedness represents how gently curved a surface is, and thus it provides scale information about an object: a very small value implies a very gentle change, whereas a large positive value implies a very sharp, knife-like edge. Generally, points on a large sphere-like object have small curvedness values, and thus the colonic wall, polyps and folds have small, medium and large curvedness values, respectively. Therefore, a combination approach using the shape index and curvedness can differentiate effectively among polyps, folds and the colonic wall.

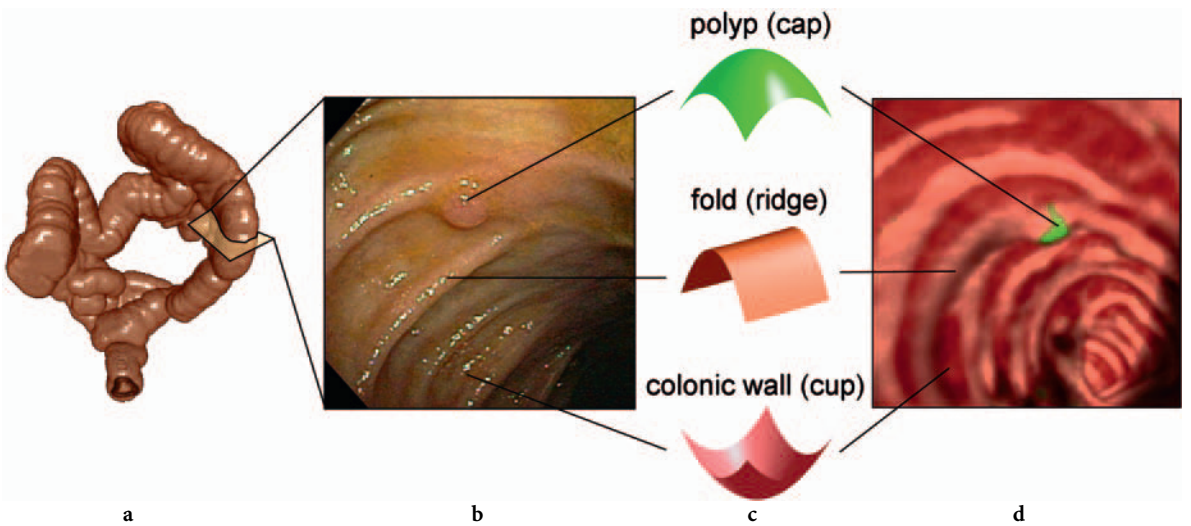

Fig. 27.2a–d. The geometric modeling of the structures in the colonic lumen. **a** Colon extracted from the VC data. **b** Colonoscopy image of a 6-mm polyp in the sigmoid colon. **c** Geometric models of the structures in the colonic lumen. **d** Pseudocoloring of the colonic lumen based on the shape index values corresponding to the geometric models (see Fig. 27.3). The polyp (*green*) is clearly differentiated from the folds (*pink*) and the colonic wall (*brown*)

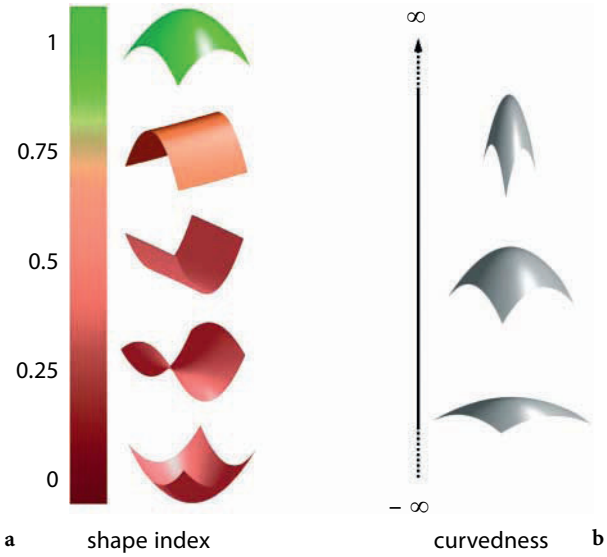

Fig. 27.3a,b. The volumetric shape index and curvedness. **a** The shape index maps the topological shape of a surface patch into a numerical value. The figure shows five sample shapes with their shape index values: cup, rut, saddle, ridge, and cap. Color coding of these different types of shapes can differentiate among the structures on the colonic wall (see Fig. 27.4). **b** The curvedness represents the size and scale of the shape. For example, a gentle cap-like shape and a sharp cap-like shape have the same shape index value, but have a different curvedness values

The polyp candidates thus found are often used as a "seed" region for extraction of the entire region of the polyp candidate. Methods such as a fuzzy clustering and a deformable model (Yao et al. 2004) and conditional morphological dilation (Näppi and Yoshida 2003) are used for this purpose. The latter approach extracts the entire region by iteratively adding a layer of voxels to the surface of the seed region. Examples of extracted polyp regions are shown in Figure 27.4. The extracted region of the polyp are often used for measuring the volume and diameter of the polyp, which has the potential to provide more consistent and reproducible size measurement of polyps (Blake et al. 2005; Burling et al. 2005 ; Pickhardt et al. 2005).

27.3.3 Removal of False-Positive Findings

The polyp candidates thus detected include a large number of false-positive findings. Studies have shown that prominent folds and stool are major sources of false-positives in CAD (Yoshida et al. 2002a; Yoshida et al. 2002b). Various methods characterising false-positives have been developed

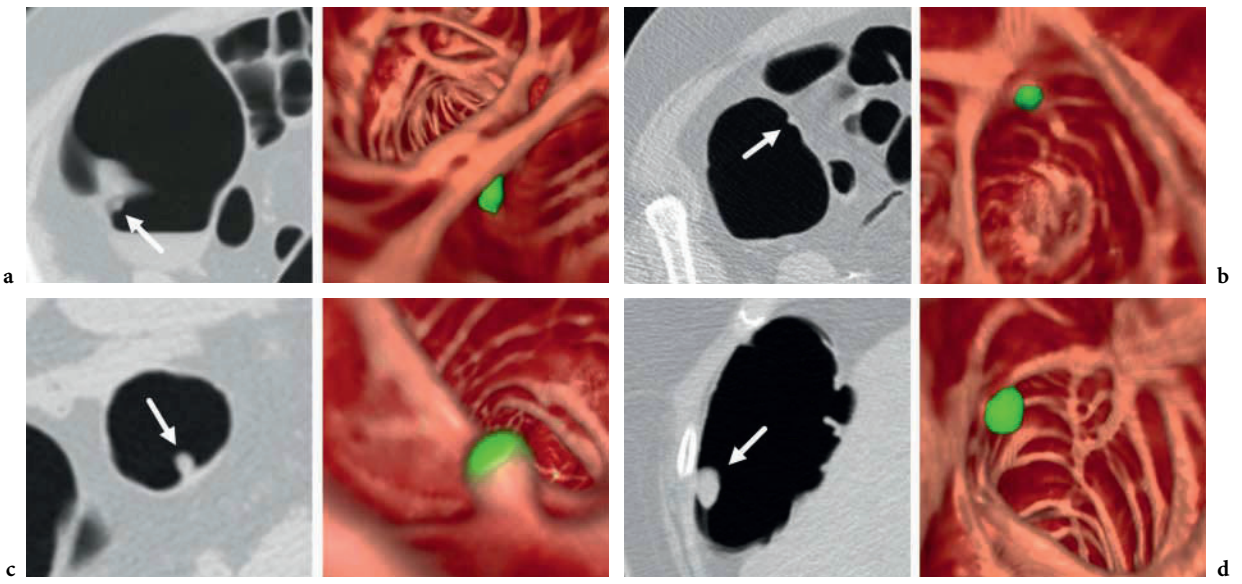

Fig. 27.4a–d. Example of polyps detected by CAD. For each pair, the left image shows an axial CT image containing a polyp, indicated by an *arrow*, and the right image shows its 3D endoluminal view by perspective volume rendering. The color coding is based on the shape index values (see Fig. 27.3, 27.4) (Näppi et al. 2005a), in which polyps, folds and the colonic wall are shown in green, pink and brown, respectively. **a** A 6-mm sessile polyp in the cecum and (**b**) a 5.3-mm polyp in the cecum. These polyps were missed by a radiologist at first reading. **c** A 7-mm polyp in the transverse colon, and (**d**) an 11-mm sessile polyp in the hepatic flexure. Polyps are clearly differentiated from folds and the colonic wall. Reprinted, with permission, from (Yoshida and Dachman 2005)

for reduction of their number, including volumetric texture analysis (Näppi and Yoshida 2002), CT attenuation (Summers et al. 2001), random orthogonal shape section (Gokturk et al. 2001), optical flow (Acar et al. 2002), and various internal features of polyps (Wang et al. 2005).

Stool differentiation is often based on the difference in the internal density variations between polyps and stool. These density variations are caused by the tendency of stool to contain air bubbles that can be recognized in CT images as an inhomogeneous textural pattern, or a mottled pattern. In contrast, polyps tend to have a homogeneous textural pattern, or solid pattern, without intratumoral air. Thus, the use of volumetric texture analysis that characterizes the homogeneity of the CT density within a polyp, such as the variance of CT values (Näppi and Yoshida 2002), is effective for differentiating stool from polyps.

Differentiation of the prominent folds from polyps is often based on the difference in appearance between them because, generally, prominent folds appear to be more elongated objects than do polyps. A technique called gradient concentration (Näppi and Yoshida 2002) measures the degree of concentration of the gradient orientations of the CT values within a polyp candidate. The gradient vectors in a polyp tend to converge to a point deep in the center of the polyp, whereas in a fold they converge to a line. Because of this difference, the distribution of the gradient concentration can be an effective means for differentiating folds from polyps.

Once image features characteristic to false-positives are extracted from polyp candidates, they are subjected to a statistical classifier for differentiation of false-positives from true polyps based on these features. In principle, any combination of features and classifiers that provides a high classification performance should be sufficient for the differentiation task. To this end, investigators use parametric classifiers such as discriminant analysis (Yoshida and Näppi 2001), as well as non-parametric classifiers such as neural networks (Jerebko et al. 2003b; Kiss et al. 2002; Näppi et al. 2004b), a committee of neural networks (Jerebko et al. 2003a) and a support vector machine (Jerebko et al. 2005). These classifiers generate a decision boundary that optimally partitions the feature space into a polyp class and a false-positive class based on supervised learning (Duda et al. 2001). Those candidates that belong to the polyp class are reported as detected polyps by CAD.

27.4 Display Modes and Reader Paradigms

For CAD to be useful in clinical practice, it must be integrated into the clinical work flow. Workstations specialising in, or which have a function of visualization of, CTC data are now widely available. Such workstations are capable of displaying 2D multiplanar reconstruction views and a real-time 3D endoluminal perspective view with a fly-through mode. Thus, CAD is typically integrated with these visualization workstations in the form of either a plug-in module or a stand-alone CAD workstation, and the detection results are displayed as "CAD marks" that indicate the locations of the detected lesions in a form of arrows or painted regions (Näppi et al. 2005a) (Fig. 27.5). Some CAD workstations have an option that displays a list of detected polyps and allows users to visit the CAD detections sequentially by mouse clicks; others have an option to display the characteristics of the detected polyps, such as the volume, diameter and the likelihood of polyps when a user clicks on one of the detections (Burling et al. 2005; Taylor et al. 2006a; Taylor et al. 2006b).

In clinical practice, how and with what timing the CAD output is shown to the reader for the subsequent interpretation differentiate the CAD reader paradigms. Three CAD reader paradigms have been proposed so far: 1) the first reader paradigm, in which the computer reads CTC images first, and a human reader reads the images by examining CAD marks; 2) the second reader paradigm, in which a human reader first interprets CTC images without CAD marks, then the CAD marks are displayed as a "second opinion" to the reader for review so as to make the final decision; and 3) the computer-assisted reader (CAR) paradigm, in which a human reader reviews the CAD markings, which are superimposed on the CTC images, at the time when the reader reviews the CTC images.

The first paradigm, CAD as a first reader, is attractive because it allows readers to focus only on a small number of polyp candidates indicated by CAD for successive identification of the true polyps; thus this paradigm can drastically reduce interpretation time. This paradigm can possibly be used for separating out negative CTC cases even before radiologists read the cases (Evancho 2002). However, such a separation is likely to come with an increased number of missed abnormalities, because there is always a trade-off between sensitivity and specificity

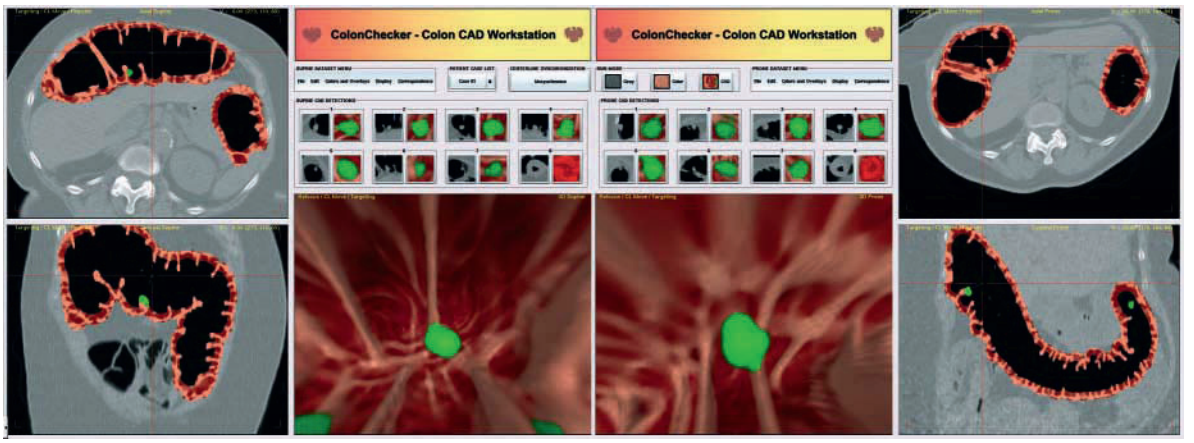

Fig. 27.5 User interface of a colon CAD workstation (Yoshida et al. 2004b). The left and right images show the 2D multiplanar reconstruction (MPR) views of the supine and prone scans of a patient, respectively, with the computer-extracted colonic wall superimposed. The lower middle two images show the 3D endoluminal views of the colon. The CAD output is integrated into the 2D MPR and 3D endoluminal views by use of the coloring scheme that delineates the detected polyps and the normal structures in the colonic lumen. Polyps detected by CAD are shown as a list of icons in the middle rows in the figure. By clicking on one of these icons, one can jump to the corresponding polyp on a 3D endoluminal view and/or an MPR view. The polyp (*green*) is displayed in both supine and prone views if it is found in the corresponding regions in these two views

in CAD (D'Orsi 2001). Moreover, thus far no study has convincingly shown that CAD can shorten the interpretation time of CTC examinations. Therefore, no CAD system, including commercial or non-commercial prototypes, can currently claim it provides the first reader paradigm as a default.

The second paradigm, CAD as a second reader, is the most conventional usage of CAD systems. In this paradigm, CAD provides a reader with the opportunity to find polyps that might otherwise have been missed at the first review. However, this paradigm may increase the interpretation time because additional time is needed for examining the possible lesions found by CAD but not by the reader. However, such an increase in time is expected to be small, or the total reading time may be unchanged, as demonstrated by an observer study (Mani et al. 2004). Currently, most of the CAD systems, commercial or academic, assume this paradigm as their default mode.

The last paradigm, computer-assisted reader (CAR), is a recently proposed paradigm (Taylor et al. 2006a; Taylor et al. 2006b) in which CAD highlights polyp candidates for a reader at the time of the primary interpretation. Here, the CAD markings are indented to direct a reader's attention to the corresponding regions of adjacent unfiltered data (Taylor et al. 2006a); thus, obvious false-positives are not expected to substantially interfere with interpretation, and the time of interpretation does not increase substantially. Moreover, when combined with 2D primary reading, this paradigm has the potential to allow a rapid interpretation of CTC images;that is, 2D primary reading with a computer-assisted reader has the potential to substantially reduce the interpretation time compared to 3D primary reading by use the of the fly-through mode with endoluminal view (Taylor et al. 2006b).

Currently available commercial CAD systems or academic prototypes employ either the second or the third paradigm. The choice of a reader paradigm depends on the user's preference, clinical requirements, and the availability of a CAD system that implements a preferred reader paradigm. It should be noted that, at the moment, only insufficient data are available for deciding which reader paradigm is optimal for rapid and accurate detection of polyps on CTC images. Further comparative studies need to be conducted for evaluation of the effect of different types of CAD paradigms.

27.5 Accuracy of CAD in Polyp Detection

Several retrospective clinical trials were conducted to demonstrate the performance of CAD schemes (Kiss et al. 2002; Näppi et al. 2004b; Näppi and Yoshida 2003; Paik et al. 2004; Summers et al. 2001;

Summers et al. 2005b; Taylor et al. 2006a; Yoshida et al. 2002a; Yoshida and Näppi 2001; Yoshida et al. 2002b).

Among the full CAD schemes published in peer-reviewed journals, the one developed at the University of Chicago yielded a 95% by-polyp sensitivity, with an average of 1.5 false-positives per patient (0.7 false-positives per data set), based on 72 patients (144 data sets), including a total of 21 polyps ≥5 mm in 14 patients. In a by-patient analysis, the sensitivity was 100%, with 1.3 false-positives per patient (Näppi and Yoshida 2003). The same group also reported a 90.5% by-polyp sensitivity with 2.4 false-positives per patient (1.4 false-positives per data set) based on a larger CTC database of 121 patients (242 data sets), including a total of 42 polyps ≥5 mm in 28 patients (Näppi et al. 2005b). The University Hospital Gasthuisberg group achieved an 80% by-polyp sensitivity, with 8.2 false-positives per patient (4.1 false-positives per data set), based on 18 patients, with 15 polyps ≥5 mm in 9 patients (Kiss et al. 2002). In this study, fecal tagging was used for most of the cases.

A group at Stanford University reported a 100% sensitivity with 7.0 false-positives per data set (only the supine data set of each patient was used) based on 8 patients that included a total of 7 polyps >10 mm in 4 patients (Paik et al. 2004). The sensitivity was less than 50% at the same false-positive rate for 11 polyps 5–9 mm that were found in 3 of the above 8 patients. A group at the National Institutes of Health reported a 90% sensitivity with 15.7 false-positives per data set, based on 40 patients (80 data sets) that included a total of 39 polyps ≥3 mm in 20 patients (Jerebko et al. 2003b). In a separate study, they reported 98% sensitivity with 2.1 false-positives per case (1.0 per data set) for polyps ≥10 mm, and 61% with 8 false-positives per case (4 false-positives per data set) for polyps ≥6 mm, based on 792 patients (1,584 data sets), which were a subset of the cases from the multicenter clinical trial (Pickhardt et al. 2003) and included a total of 119 ≥6 mm polyps (of which 28 were 10 mm or larger) (Summers et al. 2005b).

A group at the University College Hospital reported the performance of a commercial CAR system (ColonCAR version 1.2, MedicSight PLC, London, UK), which showed a sensitivity of 81% with 13 false-positives per patient, based on 25 patients (50 data sets), including a total of 21 polyps ≥5 mm in 14 patients (Taylor et al. 2006a).

In these studies, the performance of CAD was evaluated on CTC cases that were retrospectively collected from independent clinical trials or from routine clinical practice. Therefore, populations from which the CTC cases were selected, CTC protocol, and CT parameter settings were diversely different among these studies. No prospective clinical trial has yet been conducted on the evaluation of the performance of CAD. Moreover, conducting a rigorous meta-analysis of the performance of the above CAD schemes is difficult because the detection algorithms, the methods for evaluation of the detection performance, and the CTC databases used for the evaluation differ greatly among studies.

Nevertheless, the above studies appear to indicate that CAD is likely to succeed in detecting polyps with high sensitivity and a low false-positive rate – it appears that the performance of CAD schemes ranges between 70 and 100% by-patient sensitivity for polyps ≥6 mm, with 2–8 false-positives per patient, and the performance can reach up to 100% by-patient sensitivity with 1.3 false-positives per patient for polyps ≥5 mm (Näppi and Yoshida 2003). Reported performance of CTC showed that, for human readers, the pooled by-patient sensitivity for polyps ≥10 mm and for those 6–9 mm was 85% and 70%, respectively (Mulhall et al. 2005). Comparing this performance with that of CAD, it appears that the performance, especially the sensitivity, of CAD is comparable or even superior to that of human readers.

27.6 Improvement of Reader Performance

The ultimate goal of CAD is to improve the performance of radiologists in the detection of polyps and masses. Thus, establishing the sensitivity and specificity of CAD is only the first step in the evaluation of the benefit of CAD; CAD must be shown to improve the performance of radiologists.

It should be noted that CAD does not have to be as accurate as expert radiologists in order to improve the detection performance of human readers. Computers make detection errors, as do human beings. However, together they can improve the diagnostic performance.

Such a tendency can be found in early clinical studies (Summers et al. 2002; Okamura et al. 2004 Mani et al. 2004). One of these studies (Okamura et al. 2004) evaluated the effect of CAD on radiologists

in an environment that closely resembles a clinical interpretation environment of CTC, and showed that CAD could substantially improve a radiologist's detection performance (Okamura et al. 2004). Four observers with different levels of reading skill (two experienced radiologists, a gastroenterologist, and a radiology resident) participated in the study, in which an observer read 20 CTC data sets (including 11 polyps 5–12 mm in size), first without and then with CAD. The observer rated the confidence level regarding the presence of at least one polyp ≥ 5 mm in the colon. As shown in Figure 27.6, the detection performance, measured by the area under the receiver-operating characteristic curve (A_z) (Metz 2000), increased for all of the observers when they used CAD, regardless of the different levels of their reading skill. The average A_z values without and with CAD were 0.70 and 0.85, respectively, and the difference was statistically significant ($p = 0.025$). Among the four observers, the increase in the A_z value was the highest for the gastroenterologist (0.21).

Another observer study was conducted by Mani et al. (2004) based on 41 CTC cases, in which the average by-polyp and by-patient detection performance for three observers increased from 63 to 74% and from 73 to 90%, respectively, for 12 polyps ≥ 10 mm in 10 subjects, although the differences were not statistically significant.

Similar small-scale studies are reported at conferences, all of which indicate the potential of CAD in increasing a radiologist's detection performance, especially for those with less experience, as indicated by the second study. A larger scale study needs to be conducted to show convincingly the benefits of CAD in improving the detection performance, in reducing the variability of the detection accuracy among readers, and in bringing the detection accuracy of inexperienced readers up to that of experienced readers.

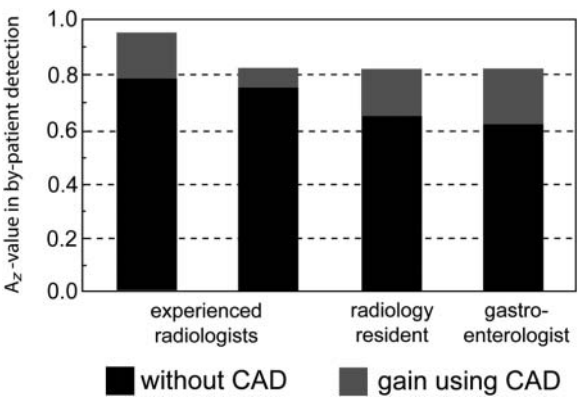

Fig. 27.6. Example of the gain in the human reader performance obtained by use of CAD (Okamura et al. 2004). Regardless of the different levels of reading skill, the detection performance, measured by the area under the ROC curve (vertical axis), increased for all of the readers when they used CAD. Among the four observers, the increase in performance was the largest for the gastroenterologist

27.7 Pitfalls

Knowing the typical patterns of pitfalls, for example types of false-positives and negatives that frequently occur in CAD, is important for the efficient use of CAD as a detection aid in a clinical setting. The following subsections explain common sources of false-positives and negatives in CAD.

27.7.1 False-Positives in CAD

One of the common, noticeable problems with CAD is that it tends to generate a much large number of false-positives than does human readers (Roehrig 2005). False-positives may lead to unnecessary further workups such as polypectomy by colonoscopy. Therefore, knowledge about the pattern of the CAD false-positives is important for dismissing them and for reducing the unnecessary false-positives.

Studies have shown that most of the false-positives detected by CAD tend to exhibit polyp-like shapes, and the major causes of CAD false-positives are thickened haustral folds and retained stool (Pickhardt 2004; Yoshida et al. 2002a; Yoshida et al. 2002b), which is similar to the cause of false-positives by human readers (Pickhardt 2004). An example of the breakdown of the false-positive sources is the following: Approximately half (45%) of the false-positives are caused by folds or flexural pseudotumors. They consist of sharp folds at the sigmoid colon, folds prominent on the colonic wall, two converging folds, ends of folds in the tortuous colon, and folds in the not-well-distended colon. One fifth (20%) are caused by solid stool, which is often a major source of error for radiologists as well. Approximately 15% are caused by residual materials inside the small bowel and stomach, and 10% are

caused by the ileocecal valve. Among other causes of false-positives are rectal tubes, elevation of the anorectal junction by the rectal tube, and motion artifacts, each amounting to less than 3%.

Representative examples of CAD false-positives are shown in Figure 27.8. Figure 27.7a shows a prominent fold (*arrow*). The tip of the fold appeared to be a cap-like structure, and thus it was incorrectly identified by CAD as a polyp. Figure 27.7b shows a piece of solid stool (*arrow*). This polyp-mimicking stool has a cap-like appearance and a solid internal texture pattern, and thus it was detected incorrectly as a polyp. Figure 27.7c shows an ileocecal valve (*arrow*). The tip of the ileocecal valve often has the cap-like appearance of a polyp and thus can be a cause of false-positives in CAD. Figure 27.7d shows the residual materials (*arrow*) inside the small bowel and stomach. Although a majority of the small bowel and stomach is removed in the colon extraction step, a small piece of them may be extracted along with the colon, and thus residual materials in the small bowel and stomach can cause false-positive detections.

Fortunately, the majority of the CAD false-positives – approximately 80–90% of them – can be dismissed relatively easily based on their characteristic locations and appearance, and thus they are not a productivity hindrance (Okamura et al. 2004; Taylor et al. 2003). For example, a false-positive detection on a thickened fold can be easily dismissed in a 3D endoluminal view, in which the reader can see the global structure of a fold on which a small bump that CAD points to is located. False-positives due to ileocecal valves and the rectal tube can easily be dismissed based on their anatomic location and shape; a semi-automated recognition of ileocecal valves (Summers et al. 2004) and rectal tubes (Iordanescu and Summers 2004; Suzuki et al. 2006) may make this already easy task even easier (Summers et al. 2004). Solid stool can be difficult false-positives to dismiss; however, one may distinguish them from polyps by visual correspondence analysis between prone and supine views; this relatively elaborate task can also be facilitated by a computerized correspondence between supine and prone data sets (Näppi et al. 2004c).

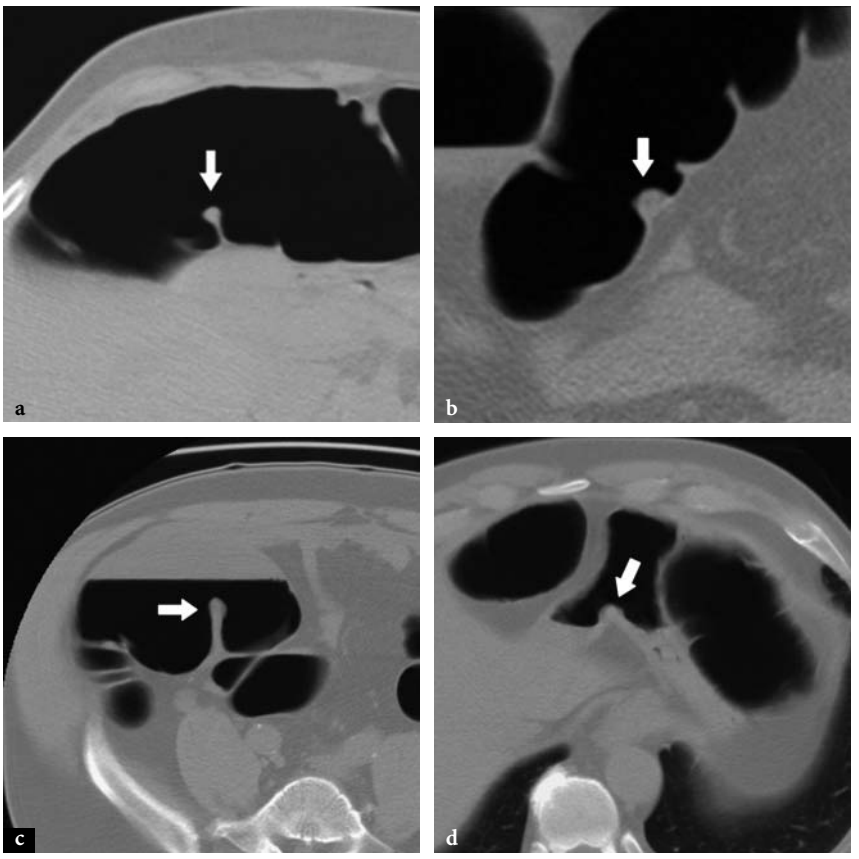

Fig. 27.7.a–d Example of CAD false-positives. **a** Prominent fold. The tip of the fold in the figure (*arrow*) appears to be a cap-like structure, and thus it was incorrectly identified by CAD as a polyp. **b** Solid stool. This polyp-mimicking stool has a cap-like appearance and a solid internal texture pattern, and thus it was detected incorrectly as a polyp. **c** Ileocecal valve. The tip of the ileocecal valve often has the cap-like appearance of a polyp and thus can be a cause of false-positives in CAD. **d** Residual materials inside the small bowel and stomach. Although a majority of the small bowel and stomach is removed in the colon extraction step, a small piece of them may be extracted along with the colon, and thus residual materials in the small bowel and stomach can cause false-positives. (Reprint, with permission, from (Yoshida and Dachman 2005)

However, there are types of false-positives, such as solid stool that mimics the shape of polyps and adheres to the colonic wall, which are difficult to differentiate from polyps even for an experienced radiologist. One study has shown that approximately one false-positive per case required more detailed problem solving (Taylor et al. 2003); another study showed that, on average, 23% of the CAD false-positives were erroneously interpreted as polyps by a reader (Okamura et al. 2004). Moreover, the pattern of the false-positives may differ across different CAD systems. More research is required for establishing how radiologists can remove these false-positives to make a correct final diagnosis more reliably.

27.7.2 False-Negatives in CAD

The types of false-negatives included in CAD results are similar to those encountered by radiologists (Yoshida et al. 2002a; Yoshida et al. 2002b). Most CAD techniques depend on a shape analysis that assumes that polyps appear to have a cap-like shape, i.e. they appear as polypoid lesions, and they protrude sufficiently into the lumen. Therefore, flat lesions and diminutive polyps < 5 mm in size, small (5–9 mm) polyps that lose a portion due to the partial volume effect, and large lesions whose shape deviates significantly from polypoid (e.g. infiltrating carcinoma) can often be false-negatives. Moreover, polyps that are located in a collapsed region of the colon or those that are submerged in (untagged) fluid may also be missed by CAD. Improvement of CAD techniques for reliable detection of these types of polyps remains for future investigation.

Representative examples of CAD false-negatives are shown in Figure 27.8. Figure 27.8a shows a magnified view of a 6-mm polyp at the proximal transverse colon (*white arrow*), and Figure 27.8b shows its 3D endoscopic view (*white arrow*). This polyp was located in a narrow valley where two folds merge, and thus the shape of the polyp was distorted. Moreover, a motion artifact made the polyp appear blurred, and thus it was a false-negative polyp. The neighboring polyp (*black arrow*), located below the

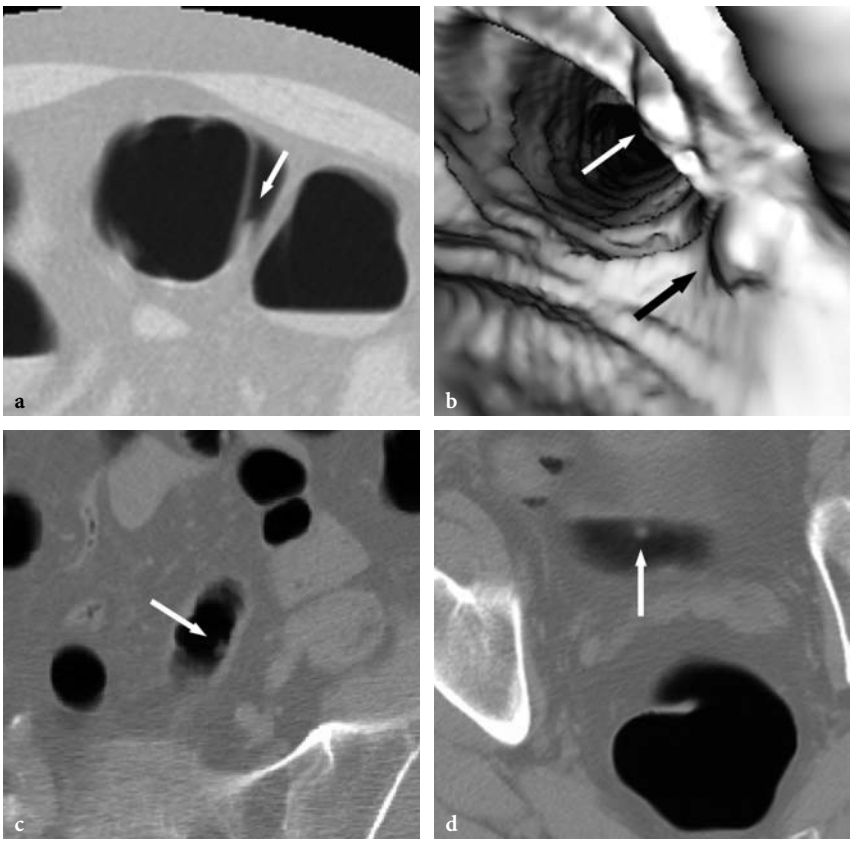

Fig. 27.8a–d. Example of CAD false-negatives. **a** Magnified view of a 6-mm polyp at the proximal transverse colon (*white arrow*). **b** 3D endoluminal view of the polyp (*white arrow*). This polyp was located in a narrow valley where two folds merge, and thus the shape of the polyp was distorted; moreover, a motion artifact made the polyp appear blurred, and thus it was a false-negative polyp. The neighboring polyp (*black arrow*), located below the convergence of the two folds, was detected by CAD because it was less distorted than the above polyp. **c** 7-mm polyp in the sigmoid colon. **d** 8-mm polyp in the sigmoid colon. The polyps in (**c**) and (**d**) appear smaller than expected from their size, mainly because of the partial volume effect; thus these polyps were false-negative polyps for CAD. (Reprint, with permission, from Yoshida and Dachman 2005)

convergence of the two folds, was detected by CAD because it was less distorted than the above polyp. Figure 27.8c shows a 7-mm polyp in the sigmoid colon, and Figure 27.8d shows an 8-mm polyp in the sigmoid colon. These polyps appear smaller than expected from their size, mainly because they lost a portion due to the partial volume effect, and thus these polyps were false-negative polyps in CAD.

27.8 CAD for Colorectal Masses

Despite the importance of accurately detecting cancers, only a very small number of CAD schemes have been developed for detection of colorectal masses that are likely to be cancers. This is probably because colorectal masses are generally considered to be easily seen by radiologists due to their size and invasiveness. On the contrary, it is not easy for CAD to detect and accurately delineate entire mass regions; instead, CAD tends erroneously to report local surface bumps of a mass as several polyps.

The detection of both polyps and masses by CAD would be a more efficient computer aid in the interpretation of CTC examinations than is the detection of polyps alone. If masses are not detected by CAD, radiologists need to perform a careful and complete review of all CTC cases for the presence of masses, which may increase the reading time. Moreover, accurate detection of masses may depend on a radiologist's experience and on how rapidly he reads the cases (Morrin et al. 2003). Therefore, the application of CAD to the detection of masses could improve the diagnostic accuracy of CTC by reducing potential reading errors due to reader fatigue, inexperience, or a too rapid reading. Furthermore, without explicit mass detection, CAD could also confuse radiologists by presenting portions of masses as several polyps.

Automated detection of masses poses challenges for CAD because they may appear as intraluminal types (lobulated, polypoid, or circumferential) or non-intraluminal types (mucosal wall-thickening type of growth pattern or masses that block the colon), both of which have a wide variation in shape characteristics. Only a few CAD schemes for the detection of colorectal cancers have addressed this challenge (Näppi et al. 2002b; Näppi et al. 2004a). One of these studies (Näppi et al. 2004a) used a fuzzy merging method and wall-thickening analysis for delineation of intraluminal and non-intraluminal masses, respectively. The CAD scheme detected 93% of masses (13 of the 14 masses) in 82 patients and extracted their regions, with 0.21 false-positives per patient on average. Figure 27.9a shows a 50-mm intraluminal circumferential mass with apple-core morphology, and Figure 27.9b shows its endoscopic view. The entire mass region was extracted by the mass detection method, as indicated by the white regions in Figure 27.9c,d.

Preliminary results indicate that CAD has the potential to detect colorectal masses in CTC with high accuracy. However, further research and a large-scale evaluation are needed for development of a CAD scheme that can detect and delineate various types of masses reliably.

27.9 CAD for Reduced Bowel Preparation and Electronic Cleansing

Fecal tagging is a means of tagging of feces, especially fluid, by an oral contrast agent such as a barium suspension or water-soluble iodinated contrast material. The orally administered contrast agent is opaque to X-rays because of its high molecular density, and thus it opacifies residual solid stool and fluid in the colon in CTC while maintaining other soft-tissue structures such as polyps and folds untagged. Fecal tagging is a promising method for differentiating residual feces from polyps, thus improving accuracy in the detection of polyps (Bielen et al. 2003; Pickhardt et al. 2003; Thomeer et al. 2003). Studies also showed that a combination of fecal tagging and reduced bowel cleansing – a well-tolerated preparation for patients – could be a viable alternative to full cathartic colon cleansing, which is one of the major sources of poor patient compliance in colon cancer screening (Lefere et al. 2004a; Lefere et al. 2004b; Lefere et al. 2002).

Because residual solid stool and fluid are opacified by fecal tagging, an image processing approach can be applied to segment the tagged fecal material, effectively removing it from the CTC images. Such an approach, called electronic cleansing, is an emerging technology for removing the stool and fluid in the colon; thus, it is useful for implementa-

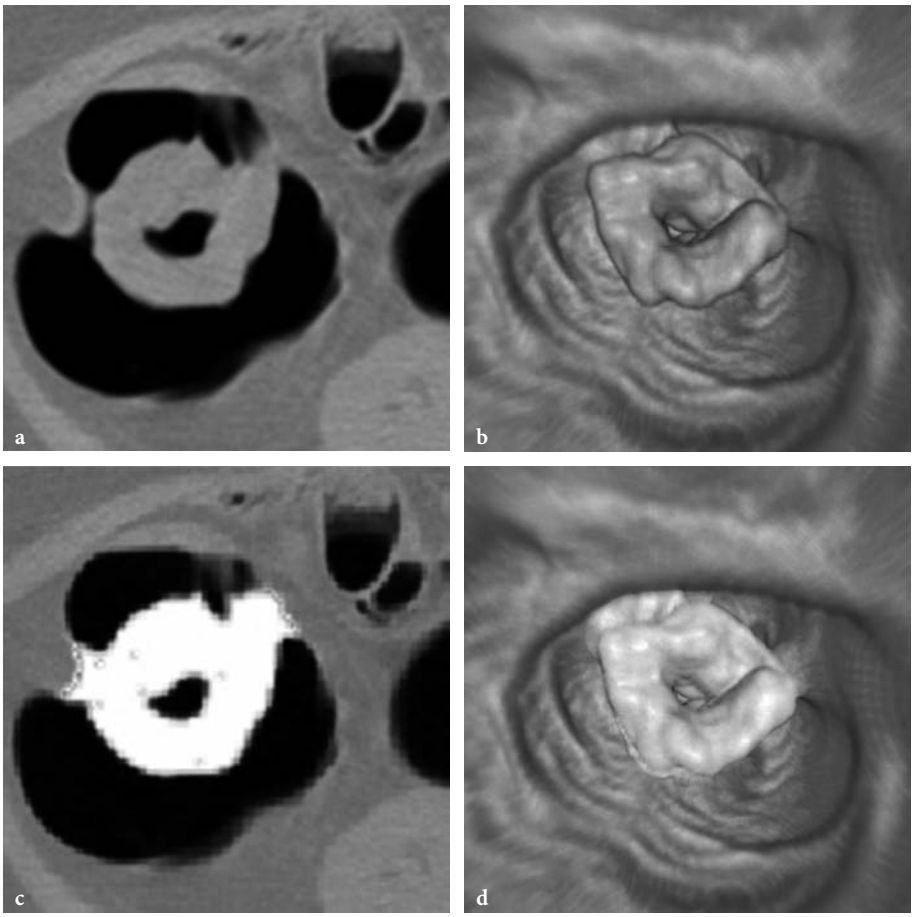

Fig. 27.9.a–d Detection of masses: **a** 50-mm intraluminal circumferential mass with apple-core morphology, and (**b**) its CTC endoluminal view. **c** The entire mass region was extracted in a mass detection method in CAD, as indicated by the white region in the MPR view, and (**d**) its CTC endoluminal view

tion of reduced or laxative-free bowel cleansing in CTC examinations, while maintaining the accuracy of human readers in detecting polyps (Zalis and Hahn 2001; Zalis et al. 2003; Zalis et al. 2004b).

Reduced bowel cleansing introduces an additional challenge to CAD because it tends to introduce a large amount of fecal residue, some of which may be tagged well, whereas some may not be tagged completely. Such a mixture of tagged and untagged stool can be a cause of false-positives in CAD (Yoshida et al. 2004a) (Fig. 27.10a). Electronic cleansing may also introduce artifacts because of the partial volume effect and a suboptimal mucosal reconstruction method, especially at the interface of air and tagged fluid along the colonic wall or at the interface of air, fluid, and a fold (Zalis et al. 2004a). Moreover, electronic cleansing may create 3D artifacts that simulate polyps because incomplete cleansing due to suboptimal opacification of luminal fluid can result in artifacts that may have the appearance of polyposis (Pickhardt and Choi 2003), which can be a cause of false-positives in CAD. These tendencies are particularly noticeable when reduced or laxative-free bowel preparation is used.

Current investigations of CAD for fecal-tagging CTC with reduced or minimum preparation (Yoshida et al. 2004a; Zalis et al. 2004a) are encouraging in that CAD showed the potential to detect polyps not only in the dry region of the colon, but also those submerged in the tagged fluid (Fig. 27.10b). However, the results of these studies are very limited and are not conclusive; therefore, CAD for fecal-tagging CTC remains a subject for future research.

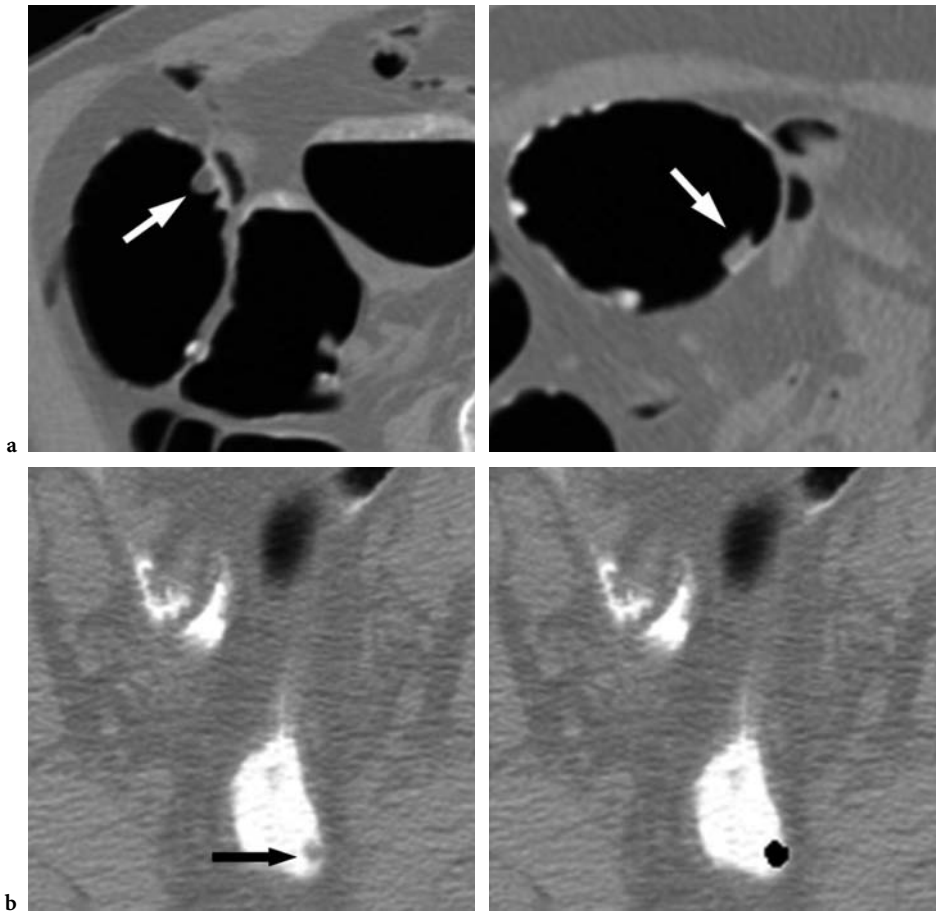

Fig. 27.10a,b. Examples of true and false-positives in CAD for fecal-tagging CTC. **a** The pieces of stool (*arrows*) adhering to the colonic wall were not tagged by the barium-based tagging regimen. Because they mimic the shape of a polyp, they were erroneously detected as polyps by CAD (Courtesy of P. Lefere, M.D., Stedelijk Ziekenhuis, Roeselare, Belgium). **b** The polyp (*black arrow*) in the left image was submerged in the tagged fluid; however, it was correctly detected and segmented by CAD, as indicated by the black region in the right image. (Courtesy of Michael E. Zalis, M.D., Massachusetts General Hospital, Boston, MA.)

27.10 Conclusions

CAD techniques for CTC have advanced substantially during the last several years. As a result, a fundamental CAD scheme for the detection of polyps has been established, and commercial products are now available. Thus far, CAD shows the potential for detecting polyps and cancers with high sensitivity and with a clinically acceptable low false-positive rate. However, CAD for CTC needs to be improved further for more accurate and reliable detection of polyps and cancers. There are a number of technical challenges that CAD must overcome, and the resulting CAD systems should be evaluated based on large-scale, multicenter, prospective clinical trials. If the assistance in interpretation offered by CAD is shown to improve the diagnostic performance substantially, CAD is likely to make CTC a cost-effective clinical procedure, especially in the screening setting.

In the future, no matter what types of visualization method (endoscopic, virtual dissection view, etc.) and reading method (2D primary or 3D primary reading) are widely used, it is expected that the detection of polyps by CTC will make use of some form of CAD. As the benefits of CAD are established, it will become more difficult to justify not using it, just as it would be difficult for a radiologist to justify not using a magnifying glass for reading mammographic films. CAD will be a powerful diagnostic tool that will provide radiologists with an opportunity to expand their sphere of influence by placing these CAD systems under their control, rather than losing procedures irretrievably to other specialists.

References

Acar B, Beaulieu CF, Gokturk SB et al (2002) Edge displacement field-based classification for improved detection of polyps in CT colonography. IEEE Trans Med Imaging 21:1461–1467

Bielen D, Thomeer M, Vanbeckevoort D et al (2003) Dry preparation for virtual CT colonography with fecal tagging using water-soluble contrast medium: initial results. Eur Radiol 13:453–458

Blake ME, Soto JA, Hayes RA et al (2005) Automated volumetry at CT colonography: a phantom study. Acad Radiol 12:608–613

Bodily KD, Fletcher JG, Engelby T et al (2005) Nonradiologists as second readers for intraluminal findings at CT colonography. Acad Radiol 12:67–73

Burling D, Halligan S, Altman DG et al (2006) CT colonography interpretation times: effect of reader experience, fatigue, and scan findings in a multi-centre setting. Eur Radiol 16:1745–1749

Burling D, Halligan S, Roddie ME et al (2005) Computed tomography colonography: automated diameter and volume measurement of colonic polyps compared with a manual technique-in vitro study. J Comput Assist Tomogr 29:387–393

Chen D, Liang Z, Wax MR et al (2000) A novel approach to extract colon lumen from CT images for virtual colonoscopy. IEEE Trans Med Imaging 19:1220–1226

D'Orsi CJ (2001) Computer-aided detection: there is no free lunch. Radiology 221:585–586

Duda RO, Hart PE, Stork DG (2001) Pattern Recognition. John Wiley & Sons, Hoboken, NJ

Evancho AM (2002) Computer-aided diagnosis: blessing or curse? Radiology 225:606; author reply 606–607

Fletcher JG, Booya F, Johnson CD et al (2005) CT colonography: unraveling the twists and turns. Curr Opin Gastroenterol 21:90–98

Franaszek M, Summers RM, Pickhardt PJ et al (2006) Hybrid segmentation of colon filled with air and opacified fluid for CT colonography. IEEE Trans Med Imaging 25:358–368

Frimmel H, Nappi J, Yoshida H (2005) Centerline-based colon segmentation for CT colonography. Med Phys 32:2665–2672

Gokturk SB, Tomasi C, Acar B et al (2001) A statistical 3-D pattern processing method for computer-aided detection of polyps in CT colonography. IEEE Trans Med Imaging 20:1251–1260

Iordanescu G, Pickhardt PJ, Choi JR et al (2005) Automated seed placement for colon segmentation in computed tomography colonography. Acad Radiol 12:182–190

Iordanescu G, Summers RM (2004) Reduction of false-positives on the rectal tube in computer-aided detection for CT colonography. Medical Physics 31:2855–2862

Jerebko AK, Malley JD, Franaszek M et al (2003a) Multiple neural network classification scheme for detection of colonic polyps in CT colonography data sets. Acad Radiol 10:154–160

Jerebko AK, Malley JD, Franaszek M et al (2005) Support vector machines committee classification method for computer-aided polyp detection in CT colonography. Acad Radiol 12:479–486

Jerebko AK, Summers RM, Malley JD et al (2003b) Computer-assisted detection of colonic polyps with CT colonography using neural networks and binary classification trees. Med Phys 30:52–60

Kiss G, Van Cleynenbreugel J, Thomeer M et al (2002) Computer-aided diagnosis in virtual colonography via combination of surface normal and sphere fitting methods. Eur Radiol 12:77–81

Lefere P, Gryspeerdt S, Baekelandt M et al (2004a) Laxative-free CT colonography. AJR Am J Roentgenol 183:945–948

Lefere PA, Gryspeerdt SS, Baekelandt M et al (2004b) CT colonography after fecal tagging with a reduced cathartic cleansing and a small volume of barium. AJR Am J Roentgenol 182:75–76

Lefere PA, Gryspeerdt SS, Dewyspelaere J et al (2002) Dietary fecal tagging as a cleansing method before CT colonography: initial results – polyp detection and patient acceptance. Radiology 224:393–403

Levin B, Brooks D, Smith RA et al (2003) Emerging technologies in screening for colorectal cancer: CT colonography, immunochemical fecal occult blood tests, and stool screening using molecular markers. CA Cancer J Clin 53:44–55

Li H, Santago P (2005) Automatic Colon Segmentation with Dual Scan CT Colonography. J Digit Imaging 18:42–54

Macari M, Bini EJ (2005) CT colonography: where have we been and where are we going? Radiology 237:819–833

Mani A, Napel S, Paik DS et al (2004) Computed tomography colonography: feasibility of computer-aided polyp detection in a „first reader" paradigm. J Comput Assist Tomogr 28:318–326

Masutani Y, Yoshida H, MacEneaney PM et al (2001) Automated segmentation of colonic walls for computerized detection of polyps in CT colonography. J Comput Assist Tomogr 25:629–638

Metz CE (2000) Fundamental ROC analysis. pp. 751–770. In: J Beutel, HL Kundel, and RLV Metter (eds) Handbook of Medical Imaging. SPIE Press, Bellingham, WA, USA

Morrin M, Sosna J, Kruskal J et al (2003) Diagnostic performance of radiologists with differing levels of expertise in the evaluation of CT colonography. Radiology 226(P):365

Morrin MM, LaMont JT (2003) Screening virtual colonoscopy – ready for prime time? N Engl J Med 349:2261–2264

Mulhall BP, Veerappan GR, Jackson JL (2005) Meta-analysis: computed tomographic colonography. Ann Intern Med 142:635–650

Näppi J, Dachman AH, MacEneaney P et al (2002a) Automated knowledge-guided segmentation of colonic walls for computerized detection of polyps in CT colonography. J Comput Assist Tomogr 26:493–504

Näppi J, Frimmel H, Dachman AH et al (2002b) Computer aided detection of masses in CT colonography: techniques and evaluation. Radiology 225(P):406

Näppi J, Frimmel H, Dachman AH et al (2004a) Computerized detection of colorectal masses in CT colonography based on fuzzy merging and wall-thickening analysis. Med Phys 31:860–872

Näppi J, Frimmel H, Dachman AH et al (2004b) A new high-performance CAD scheme for the detection of polyps in CT colonography. pp. 839–848. In: M Sonka, and JM Fitzpatrick (eds) Medical Imaging 2004: Image Processing. SPIE

Näppi J, Frimmel H, Okamura A et al (2004c) Region-based supine-prone correspondence for reduction of false-pos-

itives in CAD of CT colonography. pp. 993–998. CARS – Computer Assisted Radiology and Surgery. Elsevier, Chicago, IL, USA
Näppi J, Frimmel H, Yoshida H (2005a) Virtual endoscopic visualization of the colon by shape-scale signatures. IEEE Trans Inf Technol Biomed 9:120–131
Näppi J, Okamura A, Frimmel H et al (2005b) Region-based supine-prone correspondence for the reduction of false-positive CAD polyp candidates in CT colonography. Acad Radiol 12:695–707
Näppi J, Yoshida H (2002) Automated detection of polyps with CT colonography: evaluation of volumetric features for reduction of false-positive findings. Acad Radiol 9:386–397
Näppi J, Yoshida H (2003) Feature-guided analysis for reduction of false-positives in CAD of polyps for computed tomographic colonography. Med Phys 30:1592–1601
Okamura A, Dachman AH, Parsad N et al (2004) Evaluation of the Effect of CAD on observers' performance in detection of polyps in CT colonography. pp. 989–992. In: HU Lemke, MW Vannier, K Inamura, AG Farman, K Doi, and JHC Reiber (eds) CARS – Computer Assisted Radiology and Surgery. Elsevier, Chicago, IL, USA
Paik DS, Beaulieu CF, Rubin GD et al (2004) Surface normal overlap: a computer-aided detection algorithm with application to colonic polyps and lung nodules in helical CT. IEEE Trans Med Imaging 23:661–675
Pickhardt PJ (2004) Differential diagnosis of polypoid lesions seen at CT colonography (virtual colonoscopy). Radiographics 24:1535–1556; discussion 1557–1559
Pickhardt PJ, Choi JH (2003) Electronic cleansing and stool tagging in CT colonography: advantages and pitfalls with primary three-dimensional evaluation. AJR Am J Roentgenol 181:799–805
Pickhardt PJ, Choi JR, Hwang I et al (2003) Computed tomographic virtual colonoscopy to screen for colorectal neoplasia in asymptomatic adults. N Engl J Med 349:2191–2200
Pickhardt PJ, Lee AD, McFarland EG et al (2005) Linear polyp measurement at CT colonography: in vitro and in vivo comparison of two-dimensional and three-dimensional displays. Radiology 236:872–878
Pickhardt PJ, Taylor AJ, Gopal DV (2006) Surface visualization at 3D endoluminal CT colonography: degree of coverage and implications for polyp detection. Gastroenterology 130:1582–1587
Roehrig J (2005) The manufacturer's perspective. Br J Radiol 78 Spec No 1:S41–45
Slater A, Taylor SA, Tam E et al (2006) Reader error during CT colonography: causes and implications for training. Eur Radiol 16:2275–2283
Summers RM, Beaulieu CF, Pusanik LM et al (2000) Automated polyp detector for CT colonography: feasibility study. Radiology 216:284–290
Summers RM, Franaszek M, Miller MT et al (2005a) Computer-aided detection of polyps on oral contrast-enhanced CT colonography. AJR Am J Roentgenol 184:105–108
Summers RM, Jerebko AK, Franaszek M et al (2002) Colonic polyps: complementary role of computer-aided detection in CT colonography. Radiology 225:391–399
Summers RM, Johnson CD, Pusanik LM et al (2001) Automated polyp detection at CT colonography: feasibility assessment in a human population. Radiology 219:51–59
Summers RM, Yao J, Johnson CD (2004) CT colonography with computer-aided detection: automated recognition of ileocecal valve to reduce number of false-positive detections. Radiology 233:266–272
Summers RM, Yao J, Pickhardt PJ et al (2005b) Computed tomographic virtual colonoscopy computer-aided polyp detection in a screening population. Gastroenterology 129:1832–1844
Suzuki K, Yoshida H, Näppi J et al (2006) Massive-training artificial neural network (MTANN) for reduction of false-positives in computer-aided detection of polyps: suppression of rectal tubes. Medical Physics 10:3814–3824
Taylor SA, Halligan S, Burling D et al (2006a) Computer-assisted reader software versus expert reviewers for polyp detection on CT colonography. AJR Am J Roentgenol 186:696–702
Taylor SA, Halligan S, Saunders BP et al (2003) Acceptance by patients of multidetector CT colonography compared with barium enema examinations, flexible sigmoidoscopy, and colonoscopy. AJR Am J Roentgenol 181:913–921
Taylor SA, Halligan S, Slater A et al (2006b) Polyp detection with CT colonography: primary 3D endoluminal analysis versus primary 2D transverse analysis with computer-assisted reader software. Radiology 239:759–767
Thomeer M, Carbone I, Bosmans H et al (2003) Stool tagging applied in thin-slice multidetector computed tomography colonography. J Comput Assist Tomogr 27:132–139
Wang Z, Liang Z, Li L et al (2005) Reduction of false-positives by internal features for polyp detection in CT-based virtual colonoscopy. Med Phys 32:3602–3616
Wyatt CL, Ge Y, Vining DJ (2006) Segmentation in virtual colonoscopy using a geometric deformable model. Comput Med Imaging Graph 30:17–30
Yao J, Miller M, Franaszek M et al (2004) Colonic polyp segmentation in CT colonography based on fuzzy clustering and deformable models. IEEE Trans Med Imaging 23:1344–1352
Yoshida H, Dachman AH (2005) CAD techniques, challenges, and controversies in computed tomographic colonography. Abdom Imaging 30:26–41
Yoshida H, Lefere P, Näppi J et al (2004a) Computer-aided detection of polyps in CT colonography with dietary fecal tagging: pilot assessment of performance. Radiology 227(P):577
Yoshida H, Masutani Y, MacEneaney P et al (2002a) Computerized detection of colonic polyps at CT colonography on the basis of volumetric features: pilot study. Radiology 222:327–336
Yoshida H, Näppi J (2001) Three-dimensional computer-aided diagnosis scheme for detection of colonic polyps. IEEE Trans Med Imaging 20:1261–1274
Yoshida H, Näppi J, MacEneaney P et al (2002b) Computer-aided diagnosis scheme for detection of polyps at CT colonography. Radiographics 22:963–979
Yoshida H, Näppi J, Parsad N et al (2004b) ColonChecker: a state-of-the-art CAD workstation for detection of polyps in CT colonography. Radiology 227(P):809
Yoshida H, Dachman AH (2005a) CAD techniques, challenges, and controversies in computed tomographic colonography. Abdom Imaging 30:26–41
Yoshida H (2005b) Three-dimensional computer-aided diagnosis in CT colonography. In: Armato S, Brown M, eds.

Diagnostic Radiology Physics: Multidimensional Image Processing, Analysis, and Display. Oak Brook, IL: Radiological Society of North America 237–251

Yoshida H, Nappi J (2007) CAD in CT colonography without and with oral contrast agents: Progress and challenges. Comput Med Imaging Graph 31:267–284

Zalis M, Yoshida H, Näppi J et al (2004a) Evaluation of false-positive detections in combined computer-aided polyp detection and minimal preparation/digital subtraction CT colonography (CTC). Radiology 227(P):578

Zalis ME, Hahn PF (2001) Digital subtraction bowel cleansing in CT colonography. AJR Am J Roentgenol 176:646–648

Zalis ME, Perumpillichira J, Del Frate C et al (2003) CT colonography: digital subtraction bowel cleansing with mucosal reconstruction: initial observations. Radiology 226:911–917

Zalis ME, Perumpillichira J, Hahn PF (2004b) Digital subtraction bowel cleansing for CT colonography using morphological and linear filtration methods. IEEE Trans Med Imaging 23:1335–1343

Ultrasound-, CT- and MR-Guided Robot-Assisted Interventions

28

Joachim Kettenbach, Gernot Kronreif, Andreas Melzer, Gabor Fichtinger, Dan Stoianovici, and Kevin Cleary

CONTENTS

J. Kettenbach, MD
Associate Professor, Department of Radiology, Division of Cardiovascular and Interventional Radiology, Medical University Vienna, General Hospital, Waehringer Guertel 18–20, 1090 Vienna, Austria
G. Kronreif, PhD
Advanced Service Robotics, PROFACTOR Research and Solutions GmbH, 2444 Seibersdorf, Austria
A. Melzer, MD
Professor, Institute for Medical Science & Technology, Universities Dundee & St. Andrews Ninewells Hospital and Medical School University Campus Ewing Building, Dundee, DD1 4HN, UK
G. Fichtinger, PhD
Engineering Research Center, The Johns Hopkins University, Baltimore, MD 21218-2682, USA
D. Stoianovici, PhD
URobotics Laboratory, JHBMC-D0300, 5200 Eastern Avenue, Baltimore, MD 21224, USA
K. Cleary, PhD
Department of Radiology, Imaging Science and Information Systems (ISIS) Center, Georgetown University Medical Center, Washington, DC, USA

28.1 Introduction

The economic advantages and increased precision persistently demonstrated by industrial robots have stimulated the application of robots in the medical arena (Fichtinger et al. 2001; Cleary and Nguyen 2001; Nathoo et al. 2005). The main advantages of medical robotic systems include accurate needle guidance and stable access, leading to increased precision, accuracy and reproducible sampling of different parts of a lesion. Robotic-assisted procedures also involve the insertion of tubular therapy devices (ablation probes, catheters, bone drills, screws, tissue ablating devices, etc.) into the body, with the guidance of intra-operative imaging devices, such as CT, MRI, ultrasound or fluoroscopy (Cleary and Nguyen 2001; Cleary et al. 2006; Davies 2000; Fichtinger et al. 2001; Howe and Matsuoka 1999; Pott et al. 2005). The potential advantages are well known in the technical community (Fichtinger et al. 2001) and a variety of medical robots have been developed in recent years, including robotics

for rehabilitation, or miniature robots that might be placed inside the body (Fichtinger et al. 2001; Kassim et al. 2005; Masamune et al. 2001; Nathoo et al. 2001; Satava 2003; Yanof et al. 2001). This chapter is not intended to be comprehensive, but rather, to provide an overview on robotic systems that play an active role during a percutaneous image-guided intervention, such as biopsy, tumor ablation, or placement of spinal blocks, with a focus on key historical developments.

28.2 Definition of a Robot

At its most basic level, a robot consists of nearly rigid mechanical links that are connected with joints that allow relative motion from one link to another (Cleary and Nguyen 2001). The engines that power the sections between the joints to their desired positions are either powered by hydraulics, air and/or electricity (Fichtinger et al. 2002; Kettenbach et al. 2005c; Melzer et al. 2003; Nathoo et al. 2005). Each joint having one degree of freedom (DOF) implies that a simple robotic arm with three joints (3-DOF) may move in three ways: left and right, forward and backward, and up and down (Nathoo et al. 2005). Most working robots have a 6-DOF robotic arm that may resemble human arms, with components such as shoulders, elbows, wrists, and even fingers. Designed in various shapes and sizes, this type of robot is adequate to perform basic tasks through arbitrary positioning and orientation of the end-effector, which may be a tool, such as a biopsy needle, a probe endoscope, or a retractor. Medical robots can be classified into three broad categories: (1) In supervisory-controlled systems, the surgeon plans the operation off-line and specifies the motions the robot must follow to perform the operation (Fig. 28.1a). The robot then performs the specified motions autonomously under the supervision of the surgeon (Nathoo et al. 2005). (2) In telesurgical systems, the robot is under direct control of the surgeon, typically using a force feedback joystick (Fig. 28.1b) (Bodner et al. 2003; Nathoo et al. 2005; Stoianovici 2000). (3) In shared-control systems, the robot provides steady-hand manipulation of the instrument while the surgeon remains in control of the procedure (Fig. 28.1c) (Taylor et al. 1999). By the use of a shared control system, for instance, the surgeon's physiological tremor of ~40 µm can be reduced to ~4 µm (Apuzzo 1997). A shared-control mode could also limit a physician to moving an ablative instrument (drill) into a critical anatomical region.

To further understand the potential impact of robotics in surgical or interventional procedures, it is important to understand the relevant key differences between human and machine capabilities (Table 28.1). The main advantages of robots come from their ability to use abundant, detailed, quantitative information to perform accurate, repetitive motions and to operate in environments inhospitable or inaccessible to humans (especially through telesurgery and supervisory control) (Nathoo et al. 2005). However, robots have very limited decision-making and qualitative judgment ability. Conversely, humans are superior at integrating diverse sources of information, using qualitative data, and exercising judgment. Humans also have superior dexterity and robust hand-eye coordination, although on a limited scale, and, most importantly, an exquisite

Table 28.1. Differences between humans and robots [adapted from Howe and Matsuoka (1999)]

Humans	Robots
Strengths	
Strong hand-eye coordination	Good geometric accuracy
Dexterous (at human scale)	Stable and untiring with repeatability
Flexible and adaptable	Designed for wide range of scales, motion scaling with potential future applications for micro- and nanosurgery
Able to use qualitative information	Integrates extensive and diverse information
Good judgment	Uses diverse sensors (chemical, force, acoustic, etc.) in control
Limitations	
Limited dexterity outside natural state	Limited dexterity and hand-eye coordination
Prone to tremor and fatigue	Poor qualitative decision-making ability
Limited ability to use quantitative information	Limited to relatively simple tasks
Limited sterility and prone to error	Large operating room space requirement, expensive, technology in flux

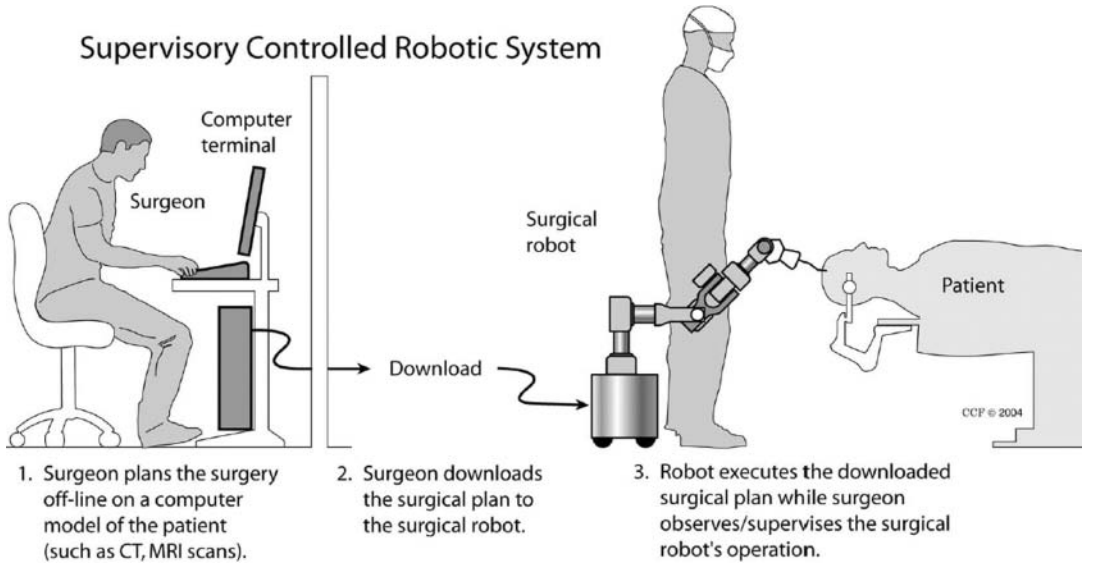

a

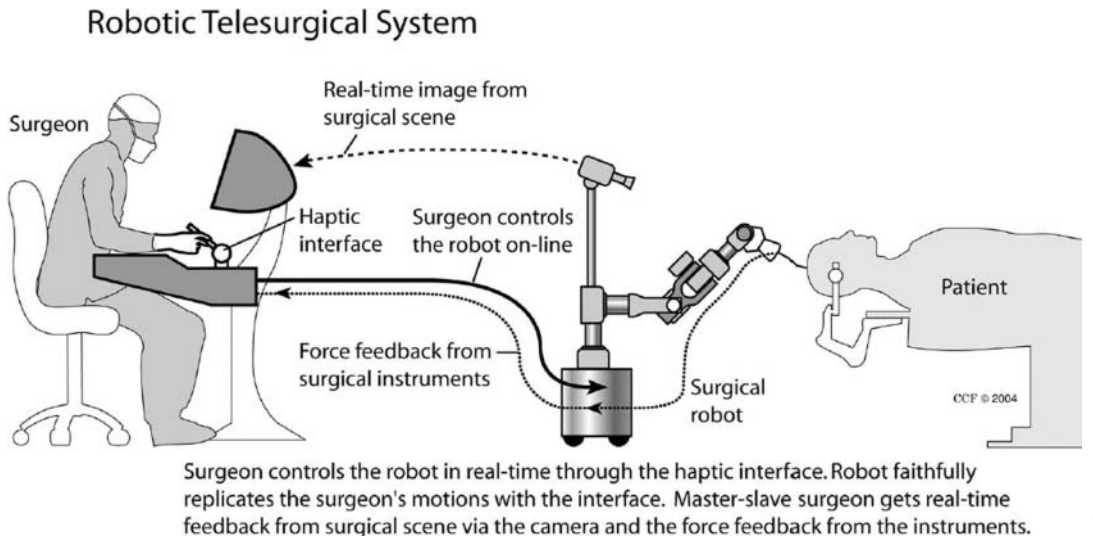

b

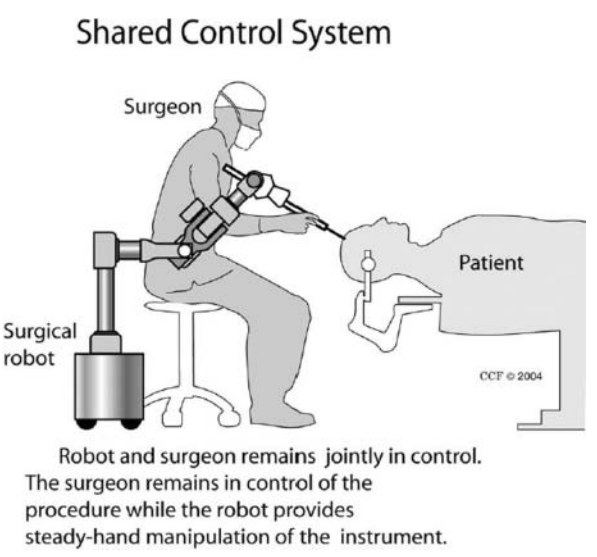

c

Fig. 28.1a–c. Technical classification of robotic systems: **a** Supervisory controlled system, in which the surgeon plans the operation off line and the robot performs the specified motions autonomously under the supervision of the surgeon. **b** Telesurgical system, in which the robot is under direct control of the surgeon with an on-line input device, which is typically a force feedback joystick (master). **c** Shared control system, in which the robot and surgeon share control of the surgical instrument. [Modified from Nathoo et al. (2005) with permission]

sense of touch. These crucial differences in capabilities imply that current surgical robotic systems are restricted to basic tasks, such as biopsy or stereotactic placement of instruments, or to performing surgery through very limited access.

28.3 Basic Considerations

28.3.1 Registration

A typical robotic-assisted procedure consists of an initial image acquisition step, followed by data transfer to the control computer, path planning using a specially developed software program and then the procedure itself (Cleary and Nguyen 2001). The images can be in digital form (fluoroscopy, CT or MRI images) or can be digitized (radiographs, or US, for example) using a digitizing table, scanner, or frame-grabbing. Once the path is planned, the images are transferred directly from the planning workstation to the control workstation in the operating room over an Ethernet link (Kettenbach et al. 2005b; Melzer et al. 2003). To carry out the procedure, the coordinate system of the robot must be registered to the coordinate system of the patient's anatomy, as displayed on the imaging system. If the robot is permanently attached to the patient table of the imaging device, this registration can be done once through the calibration procedure by a rigid calibration cage attached to the end-effector of the robot around the patient's target (Cleary and Nguyen 2001; Fichtinger et al. 2002). If the robot is designed to be moved from one imaging device to another, or to be placed on the table for certain procedures, fast and accurate registration techniques are required (Cleary et al. 2006).

28.3.2 Patient Movement and Respiration

Interventional procedures can be affected by patient motion or organ movement due to respiration (Xu et al. 2005). Thus, target movement must be recognized and accurately tracked, in addition to the constant calculation of the actual trajectory of a needle guide, based on the internal sensor systems of the robot. This may allow either automatic compensation of the trajectory (Clifford et al. 2002; Hong et al. 2004; Xu et al. 2005) by the robot or manual correction using a robot input device. Small movements of the patient could be registered with a tracker tool mounted on the surface of a patient, or by using a laser ranger scanner (Cash et al. 2003). An immobilization device (BodyFix immobilization device, Medical Intelligence, Schwabmünchen, Germany) has also been proven to be useful in reducing patient movement during computer-aided surgery (Bale et al. 2002). Further developments may include the use of motion filters, similar to those used with cardiac robots (Bale et al. 2002; Cuvillon et al. 2006; Nakamura and Kishi 2001).

28.3.3 Safety Issues

Safety with robot-assisted surgery requires rigorous, mandatory preclinical testing before clinical application, since potential hazards to the patient and the surgical team as a result of failure and unintended actions by the robot are major concerns (Korb et al. 2005; Nathoo et al. 2005). To achieve a high level of hardware safety, the following general approaches have been recommended (Howe and Matsuoka 1999; Korb et al. 2005): redundancy in kinematics and sensors, limited size of the workspace of the robot to avoid potential unintended damage to areas outside the point of operation, the use of less powerful actuators, and the combination of active and passive mechanisms in the robot design and sterilization (Bargar et al. 1998; Nathoo et al. 2005). Redundancy, however, also increases hardware and software complexity, which increases the fragility of the system overall and makes the design more costly (Korb et al. 2005).

28.4 Robotic-Assisted Applications

28.4.1 Historical Review

Derived mainly from experience in the industrial sector, the large technology base that exists in robotic research facilitated the transformation of industrial

robots into medical robots. Intracranial neurosurgical procedures were then the focus of the first robotic systems since a high degree of spatial accuracy and precision targeting is required to reach the anatomy of interest while minimizing collateral damage. The cranial anatomy also provided relatively fixed landmarks (Fankhauser et al. 1994; Glauser et al. 1995; Hefti et al. 1998; Kall et al. 1985; Li et al. 2002; Nathoo et al. 2005; Young 1987). The first robot-assisted surgical intervention was performed in 1985, when Kwoh et al. (1988) used a modified Puma 560 industrial robot (Advance Research & Robotics, Oxford, CT) to define the trajectory of a frame-based brain biopsy. Drake et al. (1991) used a modified industrial robot to resect deep benign astrocytomas in a small series of patients. However, many questions about the effectiveness, safety, and cost remained open and their work was discontinued. The use of medical robots, however, continued to expand, not only in neurosurgery (Goto et al. 2003; Hongo et al. 2002; Nathoo et al. 2005; Zimmermann et al. 2002), but also in other fields, and has also been applied in several other surgical disciplines (Carpentier et al. 1999; Gutmann et al. 2002; Kelly 2000; Le Roux et al. 2001; Ruurda et al. 2003), including soft tissue surgery (Bale et al. 2002; Bowersox et al. 1996; Chapman et al. 2001, 2002; Davies 2000; Geis et al. 1996; Harris et al. 1997; Katz et al. 2006; Mendez-Torres et al. 2005), heart surgery (Autschbach et al. 2000; Boyd et al. 2000; Cadeddu et al. 1997; Kiaii et al. 2000; Kodera et al. 2001; Mohr et al. 2001; Reichenspurner et al. 1999), orthopedics (Bargar et al. 1998; Honl et al. 2003; Nogler et al. 2004; Stoianovici 2000; Taylor et al. 1999), and radiosurgery (Adler et al. 1997). A list of several clinical areas where robotics has been applied for percutaneous procedures is shown in Table 28.2.

28.4.2 Ultrasound-Guided Robotic Systems

Percutaneous procedures, such as biopsy, involve free-hand percutaneous ultrasound (US) in con-

Table 28.2. Interventional robotic systems as described in this chapter

System (reference)	Institution	Status	Imaging modality
Robotized system for remote US (Arbeille et al. 2004)	Medecine, Physiologie Spatiales, CHU Trousseau, Tours, France	Clinical tests	US
Needle-insertion robot for percutaneous cholecystostomy (Hong et al. 2004)	Department of Mechano-Informatics, Graduate School of Information Science and Technology, The University of Tokyo, Tokyo, Japan	Phantom and animal experiments	US
B-Rob I and II (Kettenbach et al. 2005)	Austrian Research Centers GmbH (Seibersdorf, Austria)	Phantom studies	Ultrasound and CT
Robot-assisted hepatic tumor ablation (Boctor et al. 2004)	Johns Hopkins University (Baltimore, MD, USA)	Phantom studies	Ultrasound
Robot-assisted prostate brachytherapy system (Taylor et al. 1995)	Johns Hopkins University (Baltimore, MD, USA)	Phantom and cadaver studies	Ultrasound
NeuroMate (Varma et al. 2003)	Integrated Surgical Systems (Davis, CA, USA)	More than 1600 neurosurgical procedures	CT
AcuBot (Cleary et al. 2006)	Johns Hopkins University/ Georgetown University (DC, USA)	Cadaver studies Animal studies Clinical trial done	Fluoroscopy and CT
Robot for percutaneous vertebroplasty (Onogi et al. 2005)	Graduate School of Frontier Sciences, The University of Tokyo (Tokyo, Japan)	Phantom experiments	CT, fluoroscopy
INNOMOTION (Cleary et al. 2006)	Innomedic/FZK/ FH Ge (Germany)	Animal studies Clinical use started	CT and MRI
MRBot (Muntener et al. 2006)	Johns Hopkins University (Baltimore, MD, USA)	Phantom and animal studies	MRI (CT)
Robot for MR-guided transrectal prostate intervention (Krieger et al. 2005)	Johns Hopkins University (Baltimore, MD, USA)	Clinical studies	MRI

junction with manual tool positioning. Free-hand handling and aligning of a surgical tool to follow a planned trajectory is also a challenging task. This task requires manipulation of the tool, while at the same time observing the motion on a monitor. Even for the experienced physician, performance and reliability are not guaranteed. Therefore, among several groups, there has been recent interest in US-guided, robotically assisted needle placement (Boctor et al. 2004; Fichtinger et al. 2006; Hong et al. 2004; Kettenbach et al. 2005b). To improve the accessibility of lesions, even in cases of limited space at the skin entry site or a difficult angulated access, a guiding system, such as a robot, might provide stable and precise access.

28.4.2.1 Remote Ultrasonography

For diagnostic purposes, a master-slave robotized system was developed to enable a remote echographic diagnosis (Vilchis et al. 2003). While the expert moves a virtual probe placed on a haptic device, the real probe is placed on a lightweight and user-friendly slave robot and moved by it on the body of the patient located remotely. The contact force between the probe and the patient is fed back to the operator, allowing him/her to have a haptic virtual environment and to preserve the medical expert proprioception in order to facilitate the hand-eye coordination necessary for echographic examination (Arbeille et al. 2003, 2004; Vilchis et al. 2003). While this robot is not intended for intervention, the basic concept is important and might be adapted for remotely guided biopsy.

28.4.2.2 Robot for Percutaneous Cholecystostomy

Hong et al. (2004) developed a real-time, ultrasound-guided, needle insertion robot for percutaneous cholecystostomy. To overcome organ or target displacement due to involuntary patient motion, their prototype robot used intraoperative US images and modified the needle path automatically in real-time by using a novel ultrasonic image segmentation technique. In phantom and volunteer experiments, the needle path updating time was 130 and 301 ms per cycle, respectively, and animal experiments confirmed accurate needle placement within the target.

28.4.2.3 B-Rob I System

A 7-DOF prototype stand-alone robotic system (B-Rob I) for both US- and CT-guided biopsy was developed by Austrian Research Centers (ARC) (Seibersdorf, Austria) (Kettenbach et al. 2005b). A 4-DOF robotic arm with three linear and one rotational axis was used for gross positioning (Fig. 28.2a,b). Mounted at the end of the robotic arm, the 3-DOF needle positioning unit (NPU) was used for fine positioning, including a linear DOF drive with a limited stroke of 50 mm, which served to move the NPU to the patient's skin (Fig. 28.2c). A remote center of motion ("pivot point") for angulation of the needle was maintained by the kinematic structure of the NPU as another safety measure during the intervention. The robot system is controlled by two industrial PCs. One PC provides high-level control of the robot system, and a second PC handles the interface to the optical tracker system (Polaris, Northern Digital, Bakersfield, CA), as well as the planning and monitoring software. This PC also includes a video capture card (WinTV-PCI-FM 718, Hauppauge, NY, USA) for grabbing images from an ultrasound probe or the CT monitor to support planning of an intervention. After acquisition of images of the target region, the physician selects the desired skin entry point as well as the target point. With that information, the relevant data (angulation, distance to the target lesion) were calculated and automatically sent to the robot controller via a TCP/IP socket connection. Using the graphical user interface (GUI) of the planning software, the virtual trajectory of the biopsy can be viewed to verify the intervention path. After planning the intervention, the robot can be moved toward its final position by a coordinated motion of the axes. The performance of the complete system has been extensively evaluated in a series of in vitro tests using a needle-penetrable phantom (Kettenbach et al. 2005b,c). Peas (mean diameter 59.4 ± 0.7 mm) were embedded as targets within a custom-made gel phantom. The mean duration of a robot-assisted in vitro biopsy procedure, including targeting, planning, biopsy, and retrieval of specimens, was 2.6 ± 1.0 min (range, 1.5–6.0). The system showed sufficient operational stability and accuracy for the procedures under consideration. The measured targeting accuracy (1.48 mm ± 0.62 mm) was better, compared to traditional techniques, by combining the advantages of needle guidance and the free-hand technique (Kettenbach et al. 2005a).

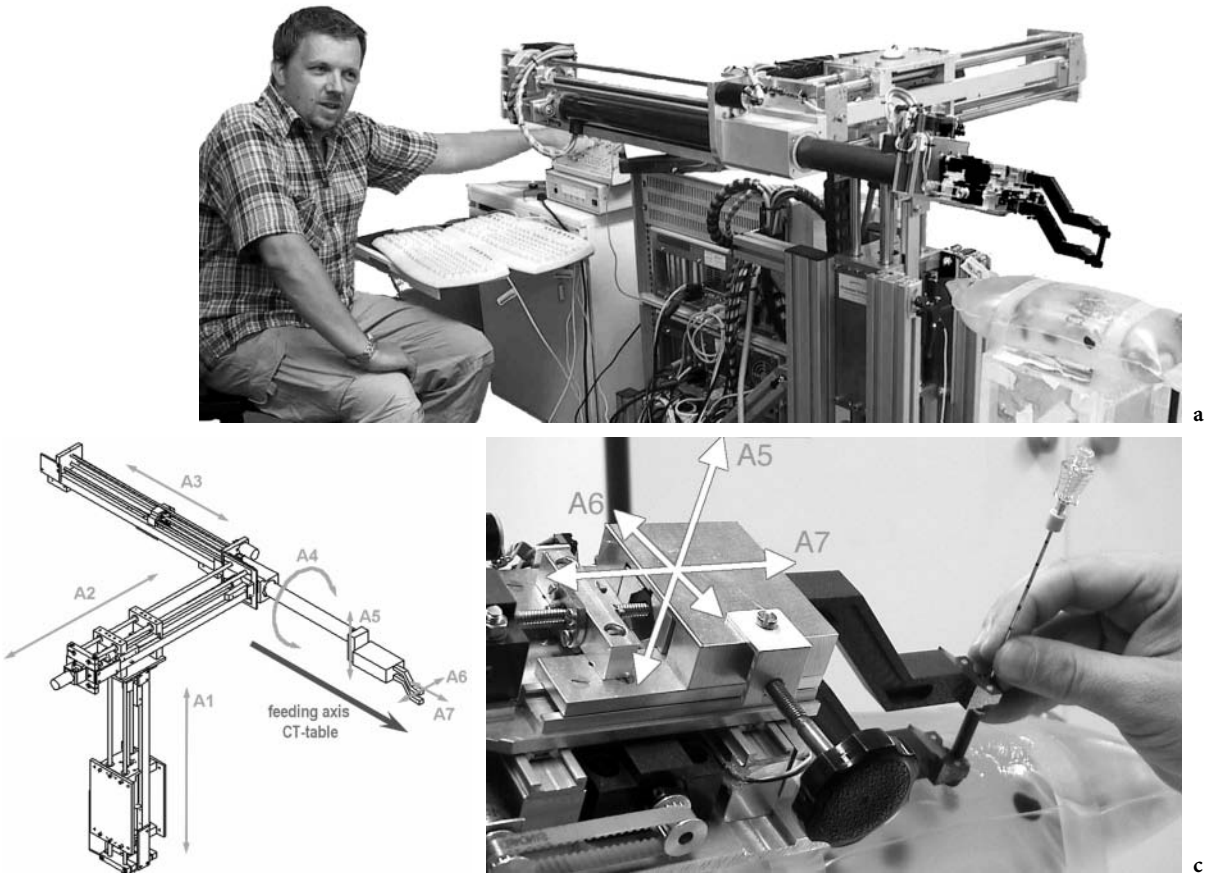

Fig. 28.2a–c. The 7-DOF prototype, B-Rob I system for both US- and CT-guided biopsy as developed by Austrian Research Centers (Seibersdorf, Austria). **a** A 4-DOF robotic arm with three linear and one rotational axis is used for gross positioning. **b** The schematic drawing demonstrates the different axes. **c** At the end of the robotic arm the kinematic structure of the 3-DOF needle positioning unit maintains a remote center of motion ("pivot point") for angulation of the needle instrument

Integration of the complete system on a mobile rack allows short set-up time and easy installation of the system at different sites. On the other hand, the chosen approach leads to a very bulky system and to a very high grade of automation (Cleary et al. 2006).

28.4.2.4 Robotic System for Intraoperative US-Guided Hepatic Tumor Ablation

Free-hand US also may result in undefined gap distribution, anatomic deformation due to variable pressure from the sonographer's hand, and severe difficulty in maintaining an optimal scanning position. In response to this limitation, Boctor and his group (2004) developed a dual-armed robotic system for intraoperative US-guided hepatic tumor ablation. Their system is based on a laparoscopic assistance robotic system (LARS) developed previously (Taylor et al. 1995), a commercial ultrasound scanner, a pulsed magnetic field position and orientation measurement system (Kuszyk et al. 2000) and an radiofrequency (RF) ablation probe (Fig. 28.3). The system managed both ultrasound manipulation and 5-DOF needle guidance to assist the surgeon in device manipulation and hand-eye coordination, so that more effort could be concentrated on planning and monitoring the procedure. Using the electro-magnetic tracking system rather than robot encoders, this approach permits quick reconfiguration of the set-up and simplifies modular replacement of end-effectors. By this means, tool tips (US and needle) must be calibrated only to the tracker, and the motion of both robots is based entirely on the sensed tool location. Boctor et al.

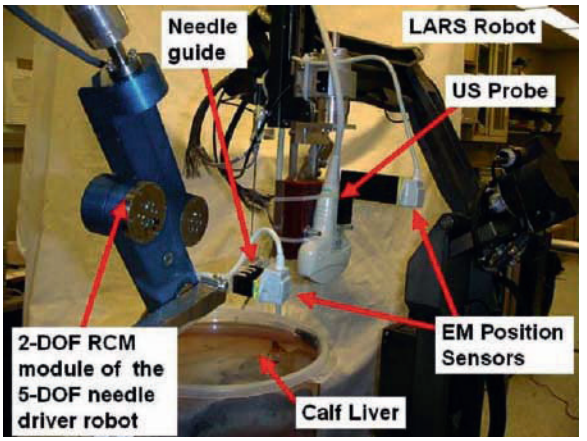

Fig. 28.3. Close-up of biopsy experiment; a robot (the IBM/JHU LARS) holds the ultrasound probe and a second robot is used for positioning a needle guide. On both, an electromagnetic (EM) tracking system (Flock of Birds, model 6D FOB, Ascension Technology, Inc.) interfaces with the robot workstation. [Reprinted with permission from Boctor et al. (2004)]

(2004). Thus, the robot does not need to be pre-calibrated to tracker space. Furthermore, real-time tracking of the tool tip also allows for mimicking a remote center of motion (RCM) without actually using a precisely manufactured RCM mechanism. In Boctor et al. (2004), the authors used a 5-DOF robot in which the motion stages were not pre-calibrated relative to one another. The robot became self-calibrated through readings from the real-time tracker. The robot was able to perform a quasi-RCM motion from just 12 tracker readings. Unlike other robot systems (Hong et al. 2004; Stoianovici et al. 2003), the 5-DOF needle-insertion module is not powered and serves as a passive needle guide. The needle is driven manually to the predetermined depth, and monitored by the depth marker and in the real-time computer display. The reason for this choice was to retain the surgeon's natural haptic feeling and thereby increase safety of the system. The average mismatch between real and planned insertion depths of the needle was about 3.0 mm. Using robotic needle insertion with robotic US data, the success rate in hitting an artificial target was 7 of 7 (100%) trials. Using robotic insertion with free-hand US data, the success rate was only 3 of 4 (75 %) trials. This could be attributed to: (1) the presence of gaps that degrade the planning accuracy; and/or (2) the synchronization inaccuracy due to the dynamic tracking of the free-hand system.

28.4.2.5 Robot-Assisted, Ultrasound-Guided Prostate Brachytherapy System

Preliminary experimental results of a phantom study obtained with a robot-assisted transrectal ultrasound (TRUS)-guided prostate brachytherapy system were published recently (Fichtinger et al. 2006). The spatially co-registered needle-insertion robot received each entry/target coordinate pair of the implant plan, inserted a preloaded needle, and then the seeds were deposited (Fig. 28.4). The needles/sources were tracked in TRUS, thus allowing the plan to be updated as the procedure progressed. Based on TRUS, the average transverse placement error was 2 mm (worst case, 2.5 mm; 80% less than 2 mm), and the average sagittal error was 2.5 mm (worst case, 5.0 mm; 70% less than 2.5 mm). Although the concept and technical viability of robot-assisted brachytherapy were demonstrated, and the overall performance was promising, the AcuBot (discussed in more depth later) system was bulky to mount and cumbersome to calibrate in a quick outpatient procedure. The previously described B-Rob II device, however, appears to be an excellent needle positioning mechanism to replace the conventional needle guiding template on the transrectal ultra-

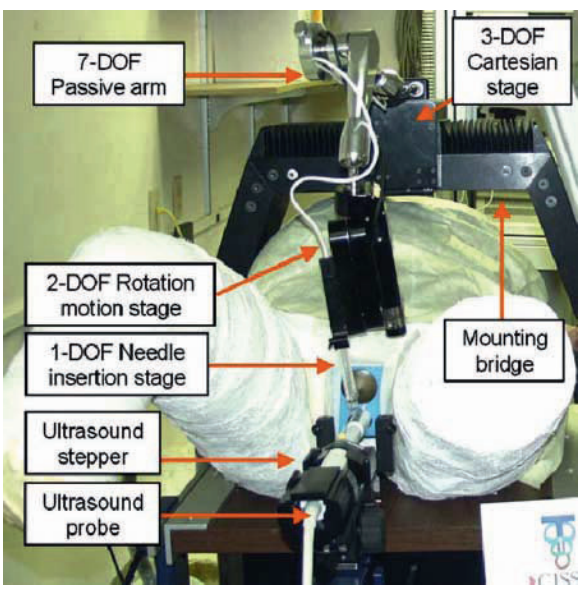

Fig. 28.4. Close view of the robot for transurethral prostate biopsy. The principal components and motion stages (with indication to their degrees of freedom, or DOF) are labeled individually [Reproduced from Fichtinger et al. (2006) with permission]

sound stepper (see Fig. 28.7b,c), thereby creating a brachytherapy robot system without imparting major changes in the current clinical install base and workflow (Kennedy et al. 2006). Interestingly, the needle is inserted manually, in order to preserve natural haptic sensing in penetrating heterogeneous perineal tissues. Further optimization and studies are currently underway to confirm the possibility of improved dosimetry.

28.4.3 Computed Tomography-Guided Robotic Systems

CT fluoroscopy offers many advantages for performance of interventional procedures. With CT fluoroscopy, the trajectory of a needle can be tracked in real-time, which allows the physician to make adjustments as necessary. This advantage has made procedures significantly faster, with equivalent or better success rates than those with standard intermittent CT imaging (Gianfelice et al. 2000; Silverman et al. 1999; Solomon et al. 2002). The major limitation of CT fluoroscopy is the relatively high radiation exposure to patient and physician (Nawfel et al. 2000). Operating a robot remotely may be used to limit radiation exposure in CT fluoroscopy-guided interventional procedures (Solomon et al. 2002). The one limitation of using the robot is the extra preparation time of at least 15 min needed to attach the robot to the CT table and for registration (Kettenbach et al. 2005c; Solomon et al. 2002). However, in the future, the robot could be mounted on the CT table and registration could be performed during installation and would not have to be repeated with each additional patient. Needle advancement, however, should still be done by the physician in order to avoid the need for complex haptic interfaces for force feedback (Barnes et al. 1997).

28.4.3.1 Minerva

One of the earliest robotic systems developed for precise CT-guided stereotactic brain biopsy was the neurosurgical robot Minerva (Glauser et al. 1995). A 5-DOF robot with two linear axes (vertical and lateral), two rotary axes (moving in a horizontal and vertical plane), and a linear axis (to move the tool to and from the patient's head) was designed to work within the CT scanner so that the surgeon could follow the position of the instruments on successive CT scans. The system was used for two operations on patients in 1993, but the project has since been discontinued.

28.4.3.2 NeuroMate

The NeuroMate, a six-axis robot for neurosurgical applications, was the first commercially available, image-guided, robotic-assisted system used for neurosurgery, which evolved from the work of Benabid et al. (1987) at Grenoble University. Particular attention was paid to safety issues and the current version is a commercial, FDA-approved product that has been licensed by Integrated Surgical Systems (Davis, California, USA). Since 1989, the system has been used in more than 1600 procedures that include neurosurgical tumor biopsies, stereoelectroencephalographic investigations of patients with epilepsy and stereotactic and functional neurosurgery (Li et al. 2002; Varma et al. 2003).

28.4.3.3 PAKY Robotic System

The PAKY system, a robot for percutaneous needle puncture, incorporates a 1-DOF PAKY (percutaneous access of the kidney) radiolucent needle driver, a 2-DOF RCM (remote center of motion) module capable of needle orientation, a 3-DOF XYZ Cartesian stage for translational positioning of the needle tip, and a passive 7-DOF positioning arm (S-arm) (Fichtinger et al. 2002; Su et al. 2002). The lower joints are positioned and locked manually, while the upper stages are motorized (Fig. 28.5).

28.4.3.3.1 Clinical Trial for Percutaneous Biopsy and Tumor Ablation

Solomon et al. (2002) used the PAKY robotic system in 16 patients during CT-guided procedures. The accuracy in the phantom calibration test was 0.6° angular and 1.65 mm linear. All 23 procedures (RF ablation, core needle biopsy, nephrostomy, and neobladder access) were performed successfully without complication. However, in four cases, the target was not met adequately, and fine-tuning adjustment with joystick control was required to ultimately reach the target. In all cases, however, the study showed that the use of the robot reduced radiation exposure for the patient and medical personnel.

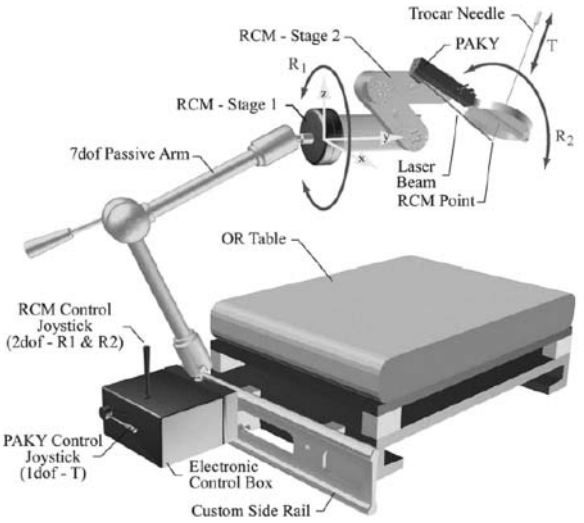

Fig. 28.5. Robot for percutaneous needle puncture procedures (PAKY-RCM system). The lower joints are positioned and locked manually, while the upper stages are motorized. The needle positioner at the tip is transparent to X-rays to enable radiographic guidance. [Reproduced from Stoianovici et al. (1998) with permission]

28.4.3.3.2
Clinical Trial for Nerve Blocks under Fluoroscopy

After cadaver studies were successfully completed using the PAKY robot to precisely position a needle in the lumbar spine (Cleary et al. 2002), a randomized clinical trial of 20 patients undergoing nerve and facet blocks was performed. Using A/P fluoroscopy to position and orient the needle, and lateral fluoroscopy to monitor the depth of insertion, the results to date show that it is feasible to use a joystick-controlled robot for nerve and facet blocks (Cleary et al. 2006). The mean accuracy in the robot (1.105 mm) and manual needle application mode (1.238 mm) is about the same. Therefore, the robot can be used for accurate needle placement in this application. While not enough data was gathered for statistical significance in this study, some general trends could be observed. As expected, the pain score post-treatment was significantly less than the pain score pre-treatment in both the robot and manual arms. While this study was done under fluoroscopy, the authors adapted the system using motion compensation for CT-guided robotic spinal needle placement (Xu et al. 2004). In this study, the average position error of targeting a moving organ was less than 1 mm (Xu et al. 2005, 2006).

28.4.3.3.3
Preclinical Trial for Prostate Brachytherapy

Fichtinger et al. (2002) used a modified 7-DOF PAKY-RCM robot for accurate and consistent placement of transperineal needles into the prostate with intraoperative image guidance inside the gantry of a CT scanner. The robot was registered to the image space with a stereotactic adapter, thus did not need further calibration. In open air, the average accuracy was better than 1 mm at a 5–8 cm depth. In various phantoms, the average orientation error was 1.3°, and the average distance between the needle tip and the target was 2 mm.

28.4.3.3.4
Clinical Trial for Nephrostomy

When comparing PAKY-RCM with standard manual nephrostomy techniques, the mean number of attempts was 2.2 ± 1.6 vs. 3.2 ± 2.5 ($p = 0.14$), time to access was 10.4 ± 6.5 min vs. 15.1 ± 8.8 min ($p = 0.06$), and the estimated blood loss score was 1.3 ± 0.49 vs. 1.7 ± 0.66 ($p = 0.14$) (Su et al. 2002). The PAKY-RCM was successful in obtaining access in 87% (20 of 23) of cases. The other three patients (13%) required conversion to manual techniques.

28.4.3.4
AcuBot Robot

The AcuBot robot is a modular robotic system that has been developed over the past 5 years in the URobotics Laboratory at Johns Hopkins Medical Institutions (Baltimore, MD, USA) (Cleary et al. 2006; Stoianovici et al. 2003). The AcuBot incorporates the original 1-DOF PAKY radiolucent needle driver, a 2-DOF RCM module capable of needle orientation, a 3-DOF XYZ Cartesian stage for translational positioning of the needle tip, and a passive 7-DOF positioning arm mounted onto a bridge frame mounted over the CT table (Fig. 28.6) (Cadeddu et al. 1997; Cleary et al. 2001, 2006; Howe and Matsuoka 1999). The arm can be positioned and rigidly locked from a single lever. The base of the arm is mounted in a 3-DOF Cartesian stage, the XYZ module (Tx, Ty, and Tz translations). The user interface consists of a 15" resistive touch screen, a two-axis joystick, a switch panel, and an emergency Stop button (Stoianovici et al. 2003). The robot system was used for needle registration studies, and showed an experimental accuracy of < 1 mm in-slice targets, and 1.5 mm for out-of-slice targets (Cleary et al. 2006).

28.4.3.4.1 Clinical Trials for CT-Fluoroscopy-Guided Biopsy and Tumor Ablation

Xu et al. (2004) used CT fluoroscopy for robotically-assisted lung biopsy in a phantom and animal model using motion compensation. A non-invasive algorithm tracked the 3D position of the target lesion using 2D CT fluoroscopy image sequences. A small region of the CT fluoroscopy image is registered to a corresponding region in a pre-operative CT volume to infer the position of the target lesion with respect to the imaging plane. The registration is implemented in a coarse to fine fashion. The true transformation of each frame of the CT fluoroscopy image is then incorporated into a Kalman filter to predict the lesion's position for the next frame. In this study, the average positioning error for targeting a moving organ using the AcuBot system was under 1 mm (Xu et al. 2005, 2006) (Fig. 28.6). Clinical cases of kidney and spine biopsy, RF ablation, and nephrostomy tube placement were successfully performed with no complications (Patriciu et al. 2005; Solomon et al. 2006; Su et al. 2002).

28.4.3.5 Robot for Percutaneous Vertebroplasty

Percutaneous vertebroplasty is quite difficult because a narrow arcus vertebra is punctured with accuracy, and an operator's hand is exposed to X-ray continuously. Onogi et al. (2005) developed a 5-DOF needle insertion robot for percutaneous vertebroplasty that is compact in size (350 mm × D 400 mm × H270 mm, weight: 15 kg) so that it can be inserted in the space between the C-arm and the patient on the operating table. The robot system is controlled by a dedicated surgical navigation system where the appropriate needle trajectory is planned based on pre-operative three-dimensional CT images. The needle holding part of the robot is X-ray lucent so that the needle insertion process can be monitored by fluoroscopy. A safety mechanism called mechanical fuse released the needle-holding disk properly when excessive force was applied to the needle. In vitro evaluation of the system showed that average position and orientation errors were less than 1.0 mm and 1.0°, respectively.

Fig. 28.6. The AcuBot robot system, used for needle placement in respiratory lung phantom during CT-fluoroscopy

28.4.3.6 B-Rob II System

The first in vitro trials of the aforementioned B-Rob I system, using a penetrable gel phantom (Fig. 28.2), showed that the chosen robot concept allows one to achieve a high accuracy for percutaneous needle placement, with a mean deviation of the needle tip from the center of the target of 1.2 ± 0.9 mm and 0.6 ± 0.4 mm in the x- and z-axes, respectively (Kettenbach et al. 2005c), at the cost of a very complex mechanical and control setup. The main goal for a new design was to slim down the very bulky B-Rob I system and to transfer the concepts demonstrated from the B-Rob I prototype into a practical clinical set-up (Cleary et al. 2006). The major goals for the new development carried out by PROFACTOR Research and Solutions GmbH (Seibersdorf, Austria) were: a modular set-up for a broad variety of clinical applications; a significant reduction of technical complexity (compared to the previous prototype) to reach an acceptable cost/benefit ratio for the entire system; and a "plug and play" philosophy (Kronreif et al. 2003, 2005). The mechanical architecture for the new design was based on the parallelogram mechanism already in use for the NPU of the B-Rob I prototype (Fig. 28.7) (Kettenbach et al. 2005c). Planning of the intervention is based on US or CT imaging data sets acquired immediately before an intervention (Fichtinger et al 2007). The spatial relation between the imaging space and the targeting device is either established by means of a tracker system (optical or mechanical) or via robot registration based on a CT data set. The system is easy to use and does not appreciably interfere with the clinical workflow. A risk analysis of the complete system did not report any major risks (Korb et al. 2005).

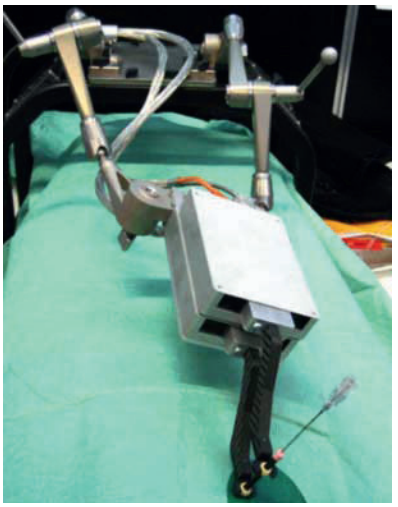

a

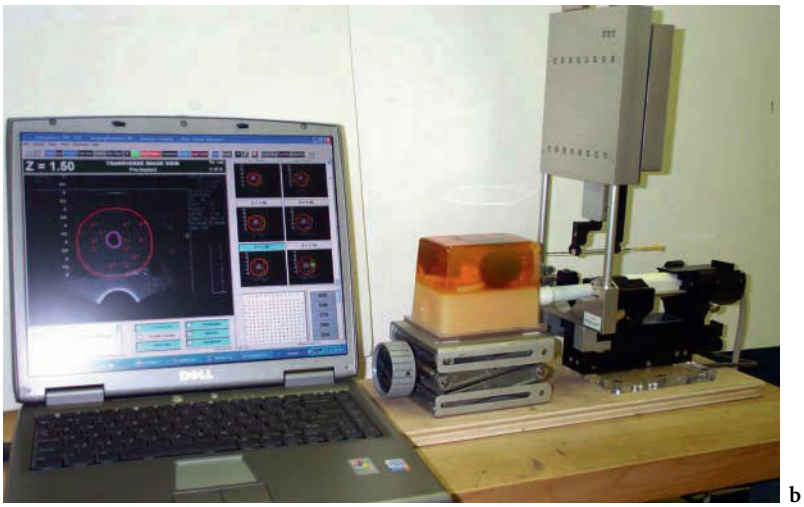

b

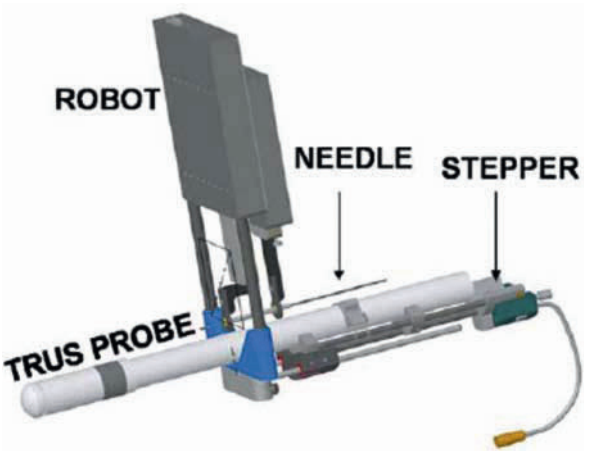

c

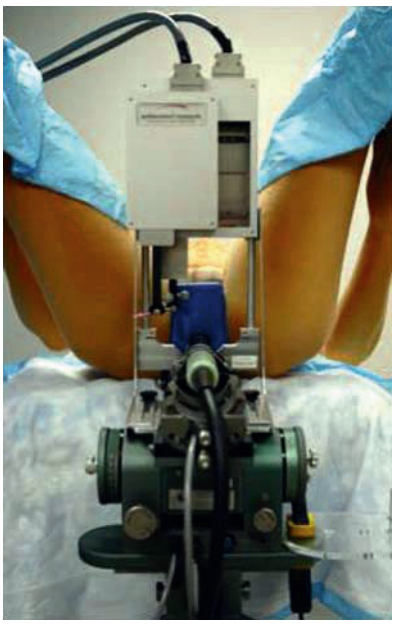

Fig. 30.7a–c. A detailed view of the needle positioning system of B-Rob II. **a** Two positioning modules provide 4-DOF and angulation of the two parallel fingers, which are connected to each other by means of spherical joints. The fingers, the polymer bearings and the needle guide can be disconnected from the needle positioning units by means of a rapid-change bayonet connection (e.g. for easy sterilization or in case of an emergency). If the two modules are moved simultaneously (parallel mode) the needle is moved in xy-direction. For angulation both have to be moved differently (angulation mode). If the bottom module is fixed and the top module moves, a pivoting movement at the level of the skin entry can be easily realized. **b,c** The B-Rob II robot mounted over the ultrasound probe in brachytherapy setup on in phantom experiment at the Johns Hopkins University. During the clinical procedure, the B-Rob II robot is situated over the abdomen

28.4.3.7 CT- and MR-compatible, Instrument-Guiding Robotic INNOMOTION

MR-guided percutaneous interventions have been clinically established, in particular, with open, low-field MR systems (Koenig et al. 2001; Lewin et al. 1998; Silverman et al. 1995). However, the imaging quality of closed-bore scanners is superior to open-field systems. Because the access to the patient is limited in a closed MR system, a fully MR-compatible pneumatic assistance system, INNOMOTION (Innomedic, Herxheim & FZK, Karlsruhe Germany & TH Gelsenkirchen), was developed to provide precise and reproducible instrument positioning inside the magnet (Fig. 28.8) (Hempel et al. 2003; Melzer et al. 2003). The kinematics of the device, however, have been carefully optimized for use in both closed-

bore MRI scanners and the CT gantry. Pneumatic cylinders, using slow-motion control, drive a 6-DOF robotic arm, attached to a 180° arch that is mounted to the patient table of the scanner, which can be passively pre-positioned on either side of the arch at 0°, ± 35°, and ± 67° to the vertical, according to the region of interest (e.g., spine, liver, kidney, breast). The robot is referenced to the coordinate system of the MR scanner using a contrast-filled marker and the CT version comprises air-filled marker for automated registration. Suitable slices from CT or MRI are selected and sent via the network in DICOM format to the computer of the robotic-assisted system. The insertion site and a target point are selected on the graphic user interface, and the corresponding coordinates are sent to the control unit. The drives are activated and the application module is moved with the tool center point at the insertion site on the skin. The cannula can then be inserted through a guiding sleeve or along an open angle. As determined with in vitro and in animal experiments, targeting precision of the insertion site in the axial plane was ± 1 mm (minimum of 0.5 mm and maximum of 3 mm). The angular deviation in the transverse plane of the cannulae was ± 1°, with a minimum of 0.5° and a maximum of 3° (Cleary et al. 2006). In phantom tests, Zangos et al. (2006) reported a mean deviation of the needle tip to the target of 0.35 mm and further demonstrated the feasibility of transgluteal puncture of the prostate gland in a cadaver study.

28.4.3.8 MrBot: A Fully MRI- and CT-Compatible Robot for Prostate Image-Guided Interventions

A new robot, MrBot (http://urology.jhu.edu/urobotics/projects/MrBot/), has been recently developed at Hopkins for fully automated, image-guided access to the prostate gland (Muntener et al. 2006). The robot is customized for transperineal needle insertion and designed to be compatible with all known types of medical imaging equipment (Fig. 28.9). This includes uncompromised compatibility with MRI scanners (tested up to 7T) up to 7 T, size accessibility within closed-bore tunnel-shaped scanners, and clinical intervention safety. Precision tests in tissue mock-ups yielded a mean seed placement error of 0.72 ± 0.36 mm (Stoianovici et al. 2007). The robot is electricity free, being operated with air pressure and light for feedback. A new type of motor, PneuStep, was developed for full MRI compatibility, high precision of motion, and medical safety.

28.4.3.9 MRI-Guided Transrectal Prostate Intervention Robot

Conventionally, robots like the previously described MrBot or INNOMOTION, depend on powered actuators, joint encoders, and some form of registration of the device with regard to the MRI scanner. A pow-

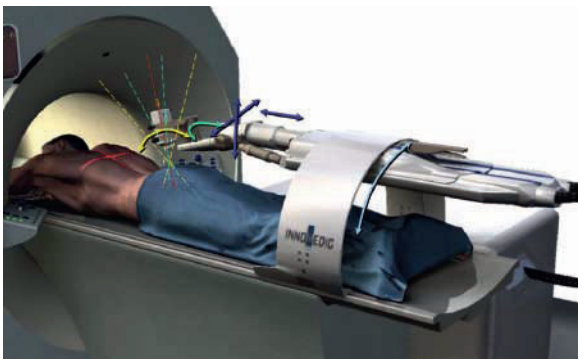

Fig. 28.8. The CT- and MR-compatible pneumatic robotic instrument guiding system (Innomotion) provides 6-DOF guidance and optional remote biopsy needle insertion

Fig. 28.9. The MR compatible robot (MrBot) developed for prostate brachytherapy at Johns Hopkins tested in an animal study

Fig. 28.10. The MR-compatible robot device, developed for transrectal prostate interventions, as assembled on the MRI table

erful alternative to this conventional approach was introduced at the Engineering Research Center of the Johns Hopkins University for robotic manipulation during transrectal prostate interventions in closed high-field MRI scanners (Krieger et al. 2005), shown in Figure 28.10. The 3-DOF decoupled device is inserted into the rectum and then maps the workspace in oblique cylindrical coordinates. The end-effector contains three real-time active tracking coils that provide full 6-DOF positional feedback in MRI scanner coordinates with 20-Hz frequency (Derbyshire et al. 1998). At the same time, the desired speed of motion is slow and the required accuracy is in the millimeter range (the smallest size of clinically significant tumors). Considering these favorable constraints and the powerful real-time tracking, the device can be visually moved toward the target by manually powered torsion cables from outside the MRI scanner. The resulting system is simple, inexpensive, robust, and safe. Its development progressed rapidly from concept to multiple clinical trials within less than 2 years. To date, 37 patients have been treated in prostate cancer biopsy and seed placement procedures (Krieger et al. 2005; Menard et al. 2005; Susil et al. 2006).

28.5 Conclusions

As percutaneous, minimally invasive procedures under image guidance continue to increase in number and importance, there will be more demand for technological assistance. It is our belief that robotic systems will be an important part of future interventions, but this role needs to be further demonstrated in randomized clinical trials. Robotic systems can enhance surgical and interventional procedures through improved precision, stability, and dexterity. Furthermore, a robot is resistant to radiation and infection. Thus, a robot-assisted procedure will be of great clinical value for several reasons: (1) it provides very stable instrument guidance, even for angulated approaches; (2) it allows access to a target when the presence of an imaging device (e.g., an US transducer) would limit the access for a biopsy needle (intercostal approach); (3) it assists the physician during the coaxial biopsy or during a US check from a different approach while advancing the needle; and (4) the integration of quantitative information from US, CT, or MRI, in particular, allows robots to actively compensate for motion, such as respiration. By compensating for patient motion, the target can be made to appear static. Robot-assisted biopsy may further expand the time window during which a lesion can be explored when using contrast agents, since more time can be spent to target a lesion (Nilsson and Krause 2003). Thereafter, a robot may guide the needle into the most promising region of the lesion without the need for a second contrast injection. To be accepted in clinical practice, however, the set-up of a robot must be easy and intuitive and should require only minimal operator training. A robot-assisted procedure must be cost-effective and should not significantly increase the length of a procedure. Robotic systems, however, are not meant to replace the physician, but rather to augment the capabilities of the physician. This will also facilitate the development of new procedures that could not previously be performed without the aid of robots. We hope that, in the future, this will improve the quality of patient care and that combining the general abilities of a robot and a surgeon will generate great synergy. In any case, this will require considerable interaction between multiple disciplines, including medicine, engineering, computer science, and physics.

References

Adler JR Jr, Chang SD, Murphy MJ, Doty J, Geis P, Hancock SL (1997) The cyberknife: a frameless robotic system for radiosurgery. Stereotact Funct Neurosurg 69:124–128

Apuzzo ML (1997) In the realm of ideas: the advent of advanced surgery of the human cerebrum and neurosurgical education. Acta Neurochir Suppl 69:145–150

Arbeille P, Poisson G, Vieyres P, Ayoub J, Porcher M, Boulay JL (2003) Echographic examination in isolated sites controlled from an expert center using a 2-D echograph guided by a teleoperated robotic arm. Ultrasound Med Biol 29:993–1000

Arbeille P, Ruiz J, Ayoub J et al (2004) The robot and the satellite for tele-operating echographic examination in Earth isolated sites, or onboard ISS. J Gravit Physiol 11:233–234

Autschbach R, Onnasch JF, Falk V et al (2000) The Leipzig experience with robotic valve surgery. J Card Surg 15:82–87

Bale RJ, Lottersberger C, Vogele M et al (2002) A novel vacuum device for extremity immobilisation during digital angiography: preliminary clinical experiences. Eur Radiol 12:2890–2894

Bargar WL, Bauer A, Borner M (1998) Primary and revision total hip replacement using the Robodoc system. Clin Orthop (354):82–91

Barnes SZ, Morr DR, Oggero E, Pagnacco G, Berme N (1997) The realization of a haptic (force feedback) interface device for the purpose of angioplasty surgery simulation. Biomed Sci Instrum 33:19–24

Benabid AL, Cinquin P, Lavalle S, Le Bas JF, Demongeot J, de Rougemont J (1987) Computer-driven robot for stereotactic surgery connected to CT scan and magnetic resonance imaging. Technological design and preliminary results. Appl Neurophysiol 50:153–154

Boctor EM, Fischer G, Choti MA, Fichtinger G, Taylor RH (2004) A dual-armed robotic system for intraoperative ultrasound guided hepatic ablative therapy: a prospective study. In: Proceedings of the 2004 IEEE International Conference on Robotics & Automation. IEEE, New York, NY, 3:2517–2522

Boctor EM, Webster RJ 3rd, Mathieu H, Okamura AM, Fichtinger G (2004) Virtual remote center of motion control for needle placement robots. Comput Aided Surg 9:175–183

Bale RJ, Lottersberger C, Vogele M et al (2002) First experiences with the da Vinci operating robot in thoracic surgery. Eur J Cardiothorac Surg 25:844–851

Bowersox JC, Shah A, Jensen J, Hill J, Cordts PR, Green PS (1996) Vascular applications of telepresence surgery: initial feasibility studies in swine. J Vasc Surg 23:281–287

Boyd WD, Rayman R, Desai ND et al (2000) Closed-chest coronary artery bypass grafting on the beating heart with the use of a computer-enhanced surgical robotic system. J Thorac Cardiovasc Surg 120:807–809

Cadeddu JA, Bzostek A, Schreiner S et al (1997) A robotic system for percutaneous renal access. J Urol 158:1589–1593

Carpentier A, Loulmet D, Aupecle B, Berrebi A, Relland J (1999) Computer-assisted cardiac surgery. Lancet 353:379–380

Cash DM, Sinha TK, Chapman WC et al (2003) Incorporation of a laser range scanner into image-guided liver surgery: surface acquisition, registration, and tracking. Med Phys 30:1671–1682

Chapman WH, Young JA, Albrecht RJ, Kim VB, Nifong LW, Chitwood WR Jr (2001) Robotic Nissen fundoplication: alternative surgical technique for the treatment of gastroesophageal reflux disease. J Laparoendosc Adv Surg Tech A 11:27–30

Chapman WH, 3rd, Albrecht RJ, Kim VB, Young JA, Chitwood WR Jr (2002) Computer-assisted laparoscopic splenectomy with the da Vinci surgical robot. J Laparoendosc Adv Surg Tech A 12:155–159

Cleary K, Nguyen C (2001) State of the art in surgical robotics: clinical applications and technology challenges. Comput Aided Surg 6:312–328

Cleary K, Freedman M, Clifford M, Lindisch D, Onda S, Jiang L (2001) Image-guided robotic delivery system for precise placement of therapeutic agents. J Control Release 74:363–368

Cleary K, Stoianovici D, Patriciu A, Mazilu D, Lindisch D, Watson V (2002) Robotically assisted nerve and facet blocks: a cadaveric study. Acad Radiol 9:821–825

Cleary K, Melzer A, Watson V, Kronreif G, Stoianovici D (2006) Interventional robotic systems: applications and technology state-of-the-art. Minim Invasive Ther Allied Technol 15:101–113

Clifford MA, Banovac F, Levy E, Cleary K (2002) Assessment of hepatic motion secondary to respiration for computer assisted interventions. Comput Aided Surg 7:291–299

Cuvillon L, Gangloff J, De Mathelin M, Forgione A (2006) Towards robotized beating heart TECABG: assessment of the heart dynamics using high-speed vision. Comput Aided Surg 11:267–277

Davies B (2000) A review of robotics in surgery. Proc Inst Mech Eng [H] 214:129–140

Derbyshire JA, Wright GA, Henkelman RM, Hinks RS (1998) Dynamic scan-plane tracking using MR position monitoring. J Magn Reson Imaging 8:924–932

Drake JM, Joy M, Goldenberg A, Kreindler D (1991) Computer- and robot-assisted resection of thalamic astrocytomas in children. Neurosurgery 29:27–33

Fankhauser H, Glauser D, Flury P et al (1994) Robot for CT-guided stereotactic neurosurgery. Stereotact Funct Neurosurg 63:93–98

Fichtinger G, Stoianovici D, Taylor KS (2001) The surgical CAD/CAM paradigm and an implementation for robotically-assisted percutaneous local therapy. In: Cohen CS (ed) 30th Annual Applied Imagery Pattern Recognition Workshop (AIPR 2001). IEEE Computer Soc, Los Alamitos, CA, pp 3–8

Fichtinger G, Burdette EC, Tanacs A et al (2006) Robotically assisted prostate brachytherapy with transrectal ultrasound guidance – phantom experiments. Brachytherapy 5:14–26

Fichtinger G, Fiene J, Kennedy C, Iordachita I, Kronreif G, Song DY, Burdette EC, Kazanzides P, Robotic Assistance for Ultrasound Guided Prostate Brachytherapy, Tenth International Conference on Medical Image Computing and Computer-Assisted Intervention, Brisbane 2007; Ayache N, Ourselin S, Maeder A (Eds. 2007): MICCAI 2007, Part I, LNCS 4791, pp 119–127

Fichtinger G, DeWeese TL, Patriciu A et al (2002) System for robotically assisted prostate biopsy and therapy with intraoperative CT guidance. Acad Radiol 9:60–74

Geis WP, Kim HC, Brennan EJ Jr, McAfee PC, Wang Y (1996) Robotic arm enhancement to accommodate improved efficiency and decreased resource utilization in complex minimally invasive surgical procedures. Stud Health Technol Inform 29:471–481

Gianfelice D, Lepanto L, Perreault P, Chartrand-Lefebvre C, Milette PC (2000) Value of CT fluoroscopy for percutaneous biopsy procedures. J Vasc Interv Radiol 11:879–884

Glauser D, Fankhauser H, Epitaux M, Hefti JL, Jaccottet A (1995) Neurosurgical robot Minerva: first results and current developments. J Image Guid Surg 1:266–272

Goto T, Hongo K, Kakizawa Y et al (2003) Clinical application of robotic telemanipulation system in neurosurgery. Case report. J Neurosurg 99:1082–1084

Gutmann B, Fischer H, Gumb L, Melzer A, Remmele T, Voges U (2002) Principles of MR/CT compatible robotics for image guided procedures. RSNA 2002

Harris SJ, Arambula-Cosio F, Mei Q et al (1997) The Probot – an active robot for prostate resection. Proc Inst Mech Eng 211:317–325

Hefti JL, Epitaux M, Glauser D, Fankhauser H (1998) Robotic three-dimensional positioning of a stimulation electrode in the brain. Comput Aided Surg 3:1–10

Hempel E, Fischer H, Gumb L et al (2003) An MRI-compatible surgical robot for precise radiological interventions. Comput Aided Surg 8:180–191

Hong J, Dohi T, Hashizume M, Konishi K, Hata N (2004) An ultrasound-driven needle-insertion robot for percutaneous cholecystostomy. Phys Med Biol 49:441–455

Hongo K, Kobayashi S, Kakizawa Y et al (2002) NeuRobot: telecontrolled micromanipulator system for minimally invasive microneurosurgery-preliminary results. Neurosurgery 51:985–988; discussion 988

Honl M, Dierk O, Gauck C et al (2003) Comparison of robotic-assisted and manual implantation of a primary total hip replacement. A prospective study. J Bone Joint Surg Am 85-A:1470–1478

Howe RD, Matsuoka Y (1999) Robotics for surgery. Annu Rev Biomed Eng 1:211–240

Kall BA, Kelly PJ, Goerss S, Frieder G (1985) Methodology and clinical experience with computed tomography and a computer-resident stereotactic atlas. Neurosurgery 17:400–407

Kassim I, Phee L, Ng WS, Gong F, Dario P, Mosse CA (2006) Locomotion techniques for robotic colonoscopy. IEEE Eng Med Biol Mag 25:49–56

Katz RD, Taylor JA, Rosson GD, Brown PR, Singh NK (2006) Robotics in plastic and reconstructive surgery: use of a telemanipulator slave robot to perform microvascular anastomoses. J Reconstr Microsurg 22:53–57

Kelly PJ (2000) Stereotactic surgery: what is past is prologue. Neurosurgery 46:16–27

Kennedy CW, Iordachita I, Burdette EC et al (2006) Robotically assisted needle placement for prostate brachytherapy. In: (eds) Conference of American Association of Physicists in Medicine. J Med Phys 33:2208

Kettenbach J, Kronreif G, Birkfellner W, Figl M, Bergmann H, Lammer J (2005a) Roboter-assisted biopsy vs. free-hand-technique using ultrasound guidance: first in-vitro results. Radiological Society of North America (RSNA)

Kettenbach J, Kronreif G, Figl M et al (2005b) Robot-assisted biopsy using ultrasound guidance: initial results from in vitro tests. Eur Radiol 15:765–771

Kettenbach J, Kronreif G, Figl M et al (2005c) Robot-assisted biopsy using CT-guidance: initial results from in vitro tests. Invest Radiol 40:219–228

Kiaii B, Boyd WD, Rayman R et al (2000) Robot-assisted computer enhanced closed-chest coronary surgery: preliminary experience using a Harmonic Scalpel and ZEUS. Heart Surg Forum 3:194–197

Kodera K, Kiaii B, Rayman R, Novick RJ, Boyd WD (2001) Closed chest CABG on the beating heart with a computer-enhanced articulating system: case report. Heart Surg Forum 4:305–306

Koenig CW, Duda SH, Truebenbach J et al (2001) MR-guided biopsy of musculoskeletal lesions in a low-field system. J Magn Reson Imaging 13:761–768

Korb W, Kornfeld M, Birkfellner W et al (2005) Risk analysis and safety assessment in surgical robotics: a case study on a biopsy robot. Minim Invasive Ther Allied Technol 14:23–31

Krieger A, Susil RC, Menard C et al (2005) Design of a novel MRI compatible manipulator for image guided prostate interventions. IEEE Trans Biomed Eng 52:306–313

Kronreif G, Fürst M, J, Figl M, Hanel R (2003) Robotic guidance for percutaneous interventions. Advanced Robotics 17:541–560

Kronreif G, Figl M, Kettenbach J et al (2005) IntraROB – A programmable targeting device for interventional radiology. In: Lemke HU (ed) CARS. Elsevier B.V., ICS 1281:407–411

Kuszyk BS, Boitnott JK, Choti MA et al (2000) Local tumor recurrence following hepatic cryoablation: radiologic-histopathologic correlation in a rabbit model. Radiology 217:477–486

Kwoh YS, Hou J, Jonckheere EA, Hayati S (1988) A robot with improved absolute positioning accuracy for CT guided stereotactic brain surgery. IEEE Trans Biomed Eng 35:153–160

Le Roux PD, Das H, Esquenazi S, Kelly PJ (2001) Robot-assisted microsurgery: a feasibility study in the rat. Neurosurgery 48:584–589

Lewin JS, Petersilge CA, Hatem SF et al (1998) Interactive MR imaging-guided biopsy and aspiration with a modified clinical C-arm system. AJR Am J Roentgenol 170:1593–1601

Li QH, Zamorano L, Pandya A, Perez R, Gong J, Diaz F (2002) The application accuracy of the NeuroMate robot – a quantitative comparison with frameless and frame-based surgical localization systems. Comput Aided Surg 7:90–98

Masamune K, Fichtinger G, Patriciu A et al (2001) System for robotically assisted percutaneous procedures with computed tomography guidance. Comput Aided Surg 6:370–383

Melzer A, Gutmann B, Lukoschek A et al (2003) Experimental evaluation of an MRI compatible telerobotic system for CT MRI guided interventions. Radiological Society of North America (RSNA). Radiology Suppl

Menard C, Susil RC, Choyke P et al (2005) An interventional magnetic resonance imaging technique for the molecular characterization of intraprostatic dynamic contrast enhancement. Mol Imaging 4:63–66

Mendez-Torres F, Woods M, Thomas R (2005) Technical modifications for robot-assisted laparoscopic pyeloplasty. J Endourol 19:393–396

Mohr FW, Falk V, Diegeler A et al (2001) Computer-enhanced "robotic" cardiac surgery: experience in 148 patients. J Thorac Cardiovasc Surg 121:842–853

Muntener M, Patriciu A, Petrisor D, Mazilu D, Kavoussi L, Cleary K, Stoianovici D: Magnetic Resonance Imaging Compatible Robotic System for Fully Automated Brachytherapy Seed Placement. Urology. Dec 2006; Vol.68(6) pp.1313–1317. http://urology.jhu.edu/urobotics/pub/2006-muntener-urology.pdf

Nakamura Y, Kishi K (2001) Robotic stabilization that assists cardiac surgery on beating hearts. Stud Health Technol Inform 81:355–361

Nathoo N, Cavusoglu MC, Vogelbaum MA, Barnett GH (2005) In touch with robotics: neurosurgery for the future. Neurosurgery 56:421–433; discussion 421–433

Nawfel RD, Judy PF, Silverman SG, Hooton S, Tuncali K, Adams DF (2000) Patient and personnel exposure during CT fluoroscopy-guided interventional procedures. Radiology 216:180–184

Nilsson A, Krause J (2003) Targeted tumour biopsy under contrast-enhanced ultrasound guidance. Eur Radiol 13 Suppl 4:L239–240

Nogler M, Polikeit A, Wimmer C, Bruckner A, Ferguson SJ, Krismer M (2004) Primary stability of a robodoc implanted anatomical stem versus manual implantation. Clin Biomech (Bristol, Avon) 19:123–129

Onogi S, Morimoto K, Sakuma I et al (2005) Development of the needle insertion robot for percutaneous vertebro-

plasty. Med Image Comput Comput Assist Interv Int Conf Med Image Comput Comput Assist Interv 8:105–113
Patriciu A, Awad M, Solomon SB et al (2005) Robotic assisted radio-frequency ablation of liver tumors-randomized patient study. In: Duncan JS, Gerig G (eds) Med Image Comput Comput Assist Interv Int Conf. Springer Verlag, Berlin, Germany, PT 2 3750:526–533
Patriciu A, Petrisor D, Muntener M, Mazilu D, Schar M, Stoianovici D. (2007) Automatic Brachytherapy Seed Placement under MRI Guidance. IEEE Transactions on Biomedical Engineering 54(8): 1499–1506. http://urology.jhu.edu/urobotics/pub/2007-patriciu-tbme.pdf
Pott PP, Scharf HP, Schwarz ML (2005) Today's state of the art in surgical robotics. Comput Aided Surg 10:101–132
Reichenspurner H, Damiano RJ, Mack M et al (1999) Use of the voice-controlled and computer-assisted surgical system ZEUS for endoscopic coronary artery bypass grafting. J Thorac Cardiovasc Surg 118:11–16
Ruurda JP, Hanlo PW, Hennipman A, Broeders IA (2003) Robot-assisted thoracoscopic resection of a benign mediastinal neurogenic tumor: technical note. Neurosurgery 52:462–464; discussion 464
Satava RM (2003) Robotic surgery: from past to future – a personal journey. Surg Clin North Am 83:1491–1500, xii
Silverman SG, Tuncali K, Adams DF, Nawfel RD, Zou KH, Judy PF (1999) CT fluoroscopy-guided abdominal interventions: techniques, results, and radiation exposure. Radiology 212:673–681
Silverman SG, Collick BD, Figueira MR et al (1995) Interactive MR-guided biopsy in an open-configuration MR imaging system. Radiology 197:175–181
Solomon SB, Bohlman ME, Choti MA (2002) Percutaneous gadolinium injection under MR guidance to mark target for CT-guided radiofrequency ablation. J Vasc Interv Radiol 13:419–421
Solomon SB, Patriciu A, Stoianovici DS (2006) Tumor ablation treatment planning coupled to robotic implementation: a feasibility study. J Vasc Interv Radiol 17:903–907
Solomon SB, Patriciu A, Bohlman ME, Kavoussi LR, Stoianovici D (2002) Robotically driven interventions: a method of using CT fluoroscopy without radiation exposure to the physician. Radiology 225:277–282
Stoianovici D (2000) Robotic surgery. World J Urol 18:289–295
Stoianovici D, Cleary K, Patriciu A, Mazilu D et al (2003) AcuBot: a robot for radiological interventions. IEEE Transactions on Robotics and Automation 19:926–930
Stoianovici D, Patriciu A, Mazilu D, Petrisor D, Kavoussi L (2007) A New Type of Motor: Pneumatic Step Motor. IEEE/ASME Transactions on Mechatronics 12: 98–106. http://urology.jhu.edu/urobotics/pub/2007-stoianovici-tmech.pdf
Su LM, Stoianovici D, Jarrett TW et al (2002) Robotic percutaneous access to the kidney: comparison with standard manual access. J Endourol 16:471–475
Susil RC, Menard C, Krieger A et al (2006) Transrectal prostate biopsy and fiducial marker placement in a standard 1.5 T magnetic resonance imaging scanner. J Urol 175:113–120
Taylor RH, Funda J, Elridge B et al (1995) A telerobotic assistant for laparosocopic surgery. IEEE Eng Med Biol Mag 14:279–288
Taylor RH, Jenson P, Whitcomb LL et al (1999) A steady-hand robotic system for microsurgical augmentation. Int J Robotics Res 18:1201–1210
Varma TR, Eldridge PR, Forster A et al (2003) Use of the NeuroMate stereotactic robot in a frameless mode for movement disorder surgery. Stereotact Funct Neurosurg 80:132–135
Vilchis A, Masuda K, Troccaz J, Cinquin P (2003) Robot-based tele-echography: the TER system. Stud Health Technol Inform 95:212–217
Xu S, Fichtinger G, Taylor RH, Cleary K (2004) 3D motion tracking of pulmonary lesions using CT fluoroscopy images for robotically assisted lung biopsy. In: Galloway RL (ed) Medical Imaging 2004. SPIE-INT Society Optical Engineering, Bellingham, WA, USA 5367:394–402
Xu S, Cleary K, Stoianovici D, Fichtinger G (2005) Registration and motion compensation CT-guided spinal of a needle placement robot for procedures. In: Galloway RL, Cleary KR (eds) Medical Imaging 2005 Conference. SPIE-INT Society Optical Engineering, Bellingham, WA, USA, 1–2:661–669
Xu S, Fichtinger G, Taylor RH, Banovac F, Cleary K (2006) CT fluoroscopy-guided robotically-assisted lung biopsy. In: Cleary KR, Galloway RL (eds) Medical Imaging 2006 Conference. SPIE-INT Society Optical Engineering, Bellingham, WA, USA, 6141:L1411–L1411
Yanof J, Haaga J, Klahr P et al (2001) CT-integrated robot for interventional procedures: preliminary experiment and computer-human interfaces. Comput Aided Surg 6:352–359
Young RF (1987) Application of robotics to stereotactic neurosurgery. Neurol Res 9:123–128
Zangos S, Herzog C, Eichler K et al (2006) MR-compatible assistance system for punction in a high-field system: device and feasibility of transgluteal biopsies of the prostate gland. Eur Radiol 17:1118-1124
Zimmermann M, Krishnan R, Raabe A, Seifert V (2002) Robot-assisted navigated neuroendoscopy. Neurosurgery 51:1446–1451; discussion 1451–1452

Virtual Liver Surgery Planning

29

Erich Sorantin, Georg Werkgartner, Reinhard Beichel, Alexander Bornik, Bernhard Reitinger, Nikolaus Popovic, and Milan Sonka

CONTENTS

29.1 Introduction

Liver tumors account for a considerable number of deaths every year (World Health Organization, 2004). One of type of primary liver tumors is hepatocellular carcinoma, which arises frequently as a complication of liver cirrhosis. Additionally, almost any tumor can seed metastasis within the liver, colorectal cancer being at the top of the list.

For many patients suffering from liver tumors, surgery may represent the only curative approach; for others only palliative, interventional techniques are available for local tumor control (e.g., cryotherapy, chemoembolization, ethanol injection, and radio frequency ablation).

Individual treatment plans are based on laboratory results and imaging modalities such as ultrasound, spiral computed tomography (SCT), magnetic resonance imaging (MRI) and nuclear medicine studies. Meticulous interpretation of the available imaging modalities is necessary in order to assess all aspects of the disease. Unfortunately, liver tumors exhibit complex patho-anatomical relationships to surrounding vessels and bile ducts. Additionally, the involved Couinead segments are mandatory to know, but the correct identification represents a difficult task (Fischer et al. 2002; Rieker et al. 2000; Strunk et al. 2003). Three-dimensional (3D) reconstructions can help in this situation but hardly exhibit quantitative information. It has to be considered that whenever surgery is not deemed a suitable therapeutic approach, there will be no other curative treatment option available.

Therefore, an interdisciplinary team of radiologists, surgeons and engineers started the development of a system that should enhance and augment the therapeutic decision process. Moreover, the system should not only allow one to use new visualization technologies like augmented reality, but should also deliver quantitative data like the number of involved segments, total liver volume and tumor volume. This marked the advent of the Virtual Liver Surgery Planning System (VLSPS).

The goal of this chapter is to demonstrate the properties of the VLSPS and how the system can be used for clinical workup in liver cancer patients.

E. Sorantin, MD; N. Popovic, MD
Department of Radiology, Medical University Graz, Auenbruggerplatz 9, 8036 Graz, Austria
G. Werkgartner, MD
Department of Surgery, Medical University Graz, Auenbruggerplatz 9, 8036 Graz, Austria
R. Beichel ; A. Bornik; B. Reitinger
Institute for Computer Graphics and Vision, University of Technology, Inffeldgasse 16, 8010 Graz, Austria
M. Sonka
Department of Electrical and Computer Engineering, The University of Iowa, Iowa City, IA 52242, USA

29.2 System Description

29.2.1 Workflow

Several steps are necessary to run the VLSPS: patient data acquisition, medical image analysis, 3D dis-

play using an augmented reality system and interdisciplinary team decision-making as to the best therapeutic approach. Figure 29.1 demonstrates the workflow in more detail.

Patient data acquisition is based on spiral CT and the whole data processing part is optimized for it. MRI could be used instead of spiral CT, but is not implemented yet. For spiral CT, scanning multirow detector computed tomography is used; in the past the detector used was a GE Lightspeed QXI Scanner (GE Systems, Milwaukee, WI, USA), but recently there was an opportunity to use a Siemens Somatom Sensation (Siemens Medical System Inc., Forchheim, Germany).

After data acquisition, images are transferred to the hospital's PACS system as well as to a DICOM server, which is not part of the PACS system. Images are stored temporarily on the machine's hard disk. At regular intervals a script checks if there are new data and, if so, the DICOM header information will be sent to a database, the images will be converted to the more common Analyze image format, made anonymous and finally transferred to the medical image analysis system (analyzedirect.com). All data transfers adher to current Austrian legal requirements.

The medical image analysis system performs the segmentation task (e.g. the liver surface, the portal venous system and the liver veins are segmented). Due to recently developed algorithms this task is mostly automated (Fig. 29.2) (Beichel et al. 2001; Beichel et al. 2002). Based on these calculations the boundaries of the individual liver segments, as well as their volume, can be estimated (Fig. 29.3) (Bornik et al. 2004). Moreover, tools were developed for easy 3D editing of the image data when the automated segmentation process fails (Fig. 29.4) (Reitinger et al. 2004).

For visualization, an augmented reality system is used. Details and components are given in Figure 29.5. The head-mounted display consists of two "see through" monitors (800×600 pixels each). Both monitors act as part of the graphic system, which is fed by the corresponding computer with two stereoscopic images. These monitors are fixed on a helmet that also contains the tracking tar-

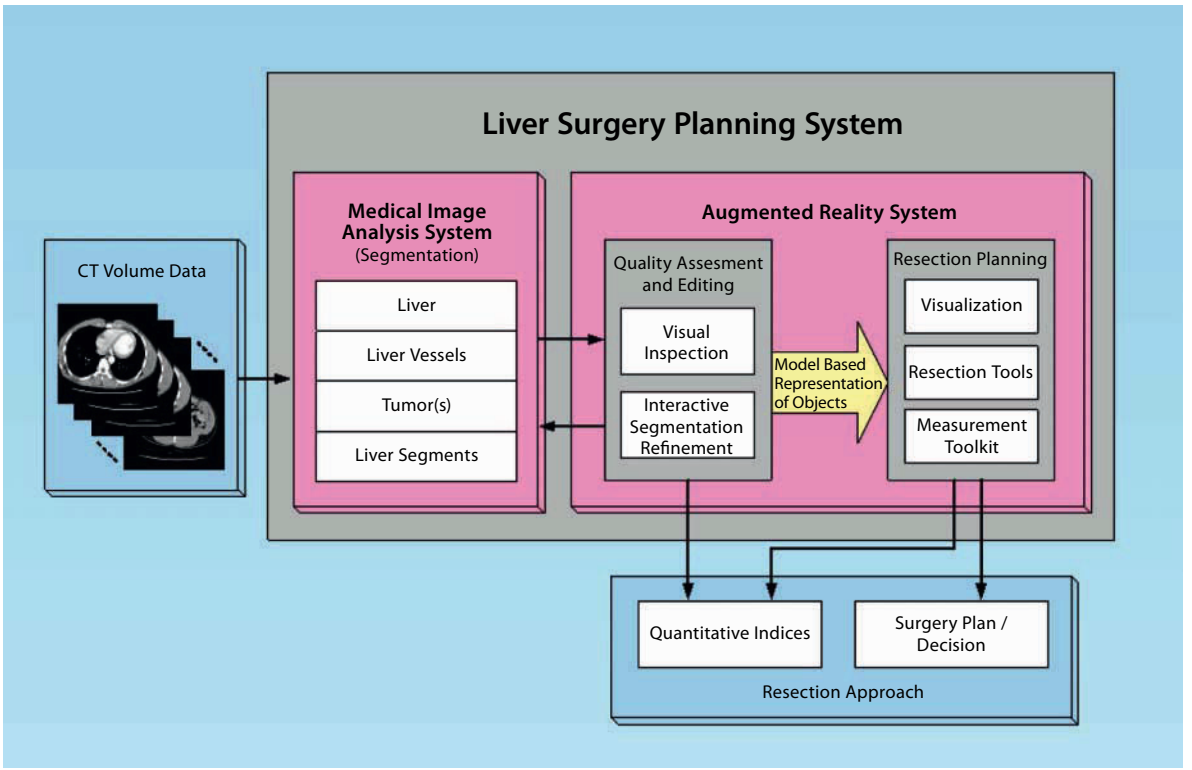

Fig. 29.1. VLSPS workflow. The lefthand stack of spiral CT images represent data acquisition; the *pink* part in the center of the figure outlines the different data processing steps. The *blue* part on lower right corner symbolizes the quantitative results generated by the VLSPS, and all parts together lead to a decision regarding the best-suited therapeutic approach

gets. The cameras emit infrared flashes, which are reflected by the tracking targets. Based on the shape of the tracking targets, as well as the time needed for reflection of the infrared flashes, the system calculates the operator's position within the 3D space. These calculations are performed in real time, and after every change of the operator's position the stereoscopic images are updated and sent to the see through monitors. For system interaction the operator uses the so-called personal interaction panel (PIP). Depending which side of the panel is up, the

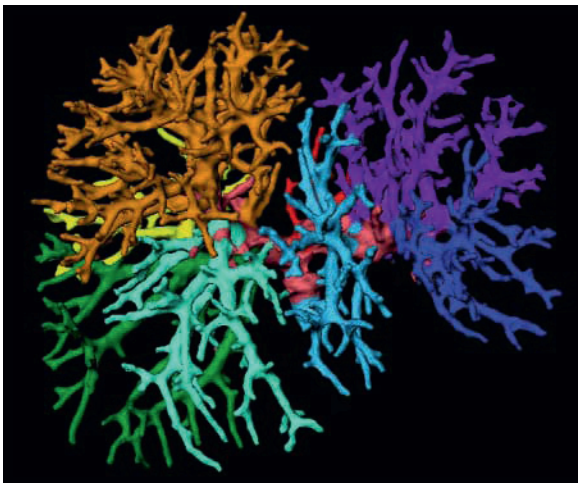

Fig. 29.2. 3D representation of the automated segmented portal venous system. Different colors mark the portal branches belonging to different liver segments

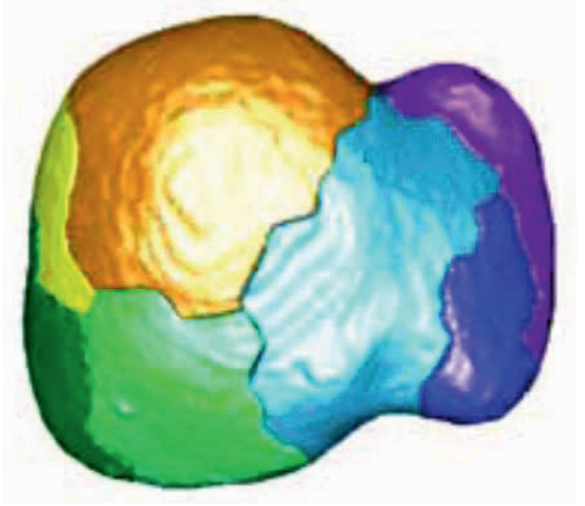

Fig. 29.3. 3D reconstruction of the computer-calculated and generated liver segments

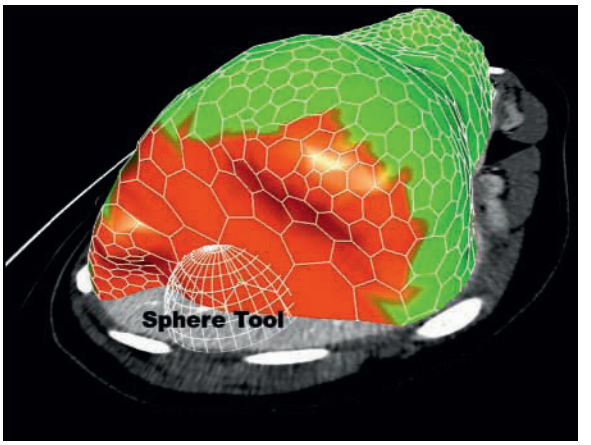

Fig. 29.4. Snapshot obtained during 3D editing displaying the sphere tool. In this particular example the complete liver contour was not detected automatically, therefore manual editing is necessary. The sphere tool represents a device that allows a person to select a particular area of the liver surface (marked in *red*) and afterwards to "push" or "pull" the selected liver contour as long as it fits the desired one. This procedure allows fast and easy 3D editing

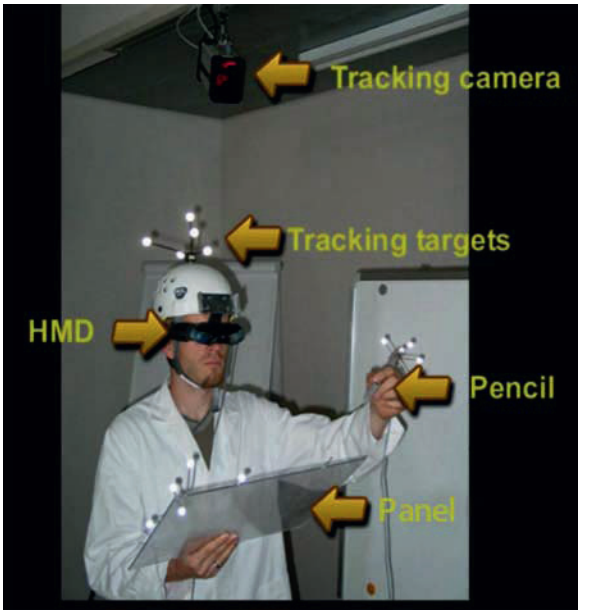

Fig. 29.5. Components of the augmented reality system. Operator wears a head-mounted display (HMD). Tracking targets are fixed to the top of the HMD. The tracking cameras (usually four) send infrared flashes, which are reflected by the tracking targets. This information forms the basis for calculating the operator's position within the 3D space. The panel represents the interface to the system and covers two tasks, depending on its position (more details in Figs. 29.6, 29.7). On one side it displays action buttons and sliders for the operator; if flipped it acts as a cutting device for display of surrounding spiral CT data. All actions are carried out using a virtual pencil

action behavior is changed: a) action buttons and sliders, which are activated by the touch of a virtual pencil, allow the scene to change (e.g., opacity of objects, performing measurements and much more) (Fig. 29.6); and b) if the panel is flipped, it acts as a cutting plane in order to display the source image data (Fig. 29.7).

The therapeutic decision process is supported and augmented in several ways. First, precise 3D display of the underlying patho-anatomy is achieved by visualization using the augmented reality system. Second, the resection of a lesion can be simulated by displaying the onco-surgical safety margin (Fig. 29.8). Third, individual distance measurements can be made in 3D; a "snap in" mechanism helps the operator choose the right distance between two objects, such as a tumor and surrounding vessels. Fourth, various surgical scenarios can be simulated and evaluated (Fig. 29.9). Quantitative results are displayed by clicking with the virtual pencil on the corresponding action button (Table 29.1).

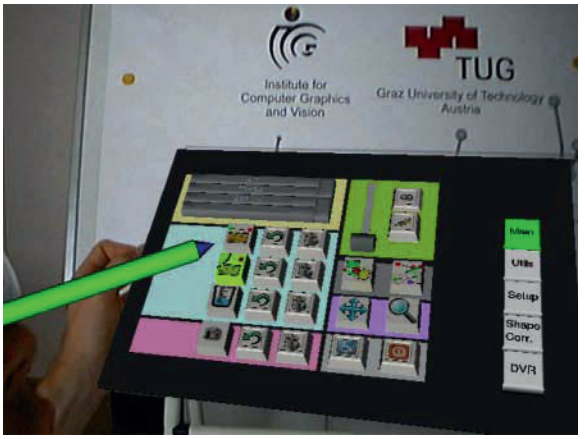

Fig. 29.6. The action button side of the PIP is shown; the pencil is used to activate the different functions

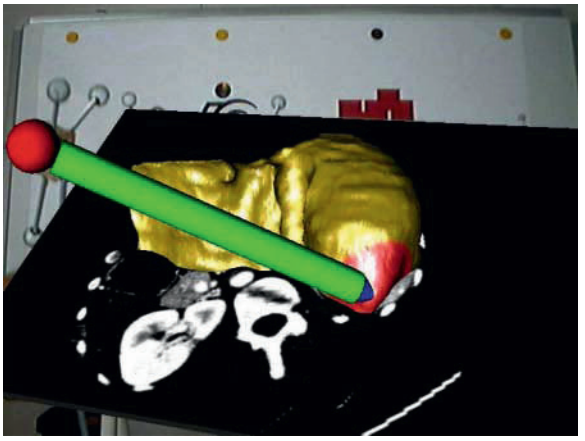

Fig. 29.7. A 3D reconstruction of a liver, as well as the pencil, which has activated a part of the liver surface for editing, is shown. The source CT data are displayed as selected by the PIP cutting plane

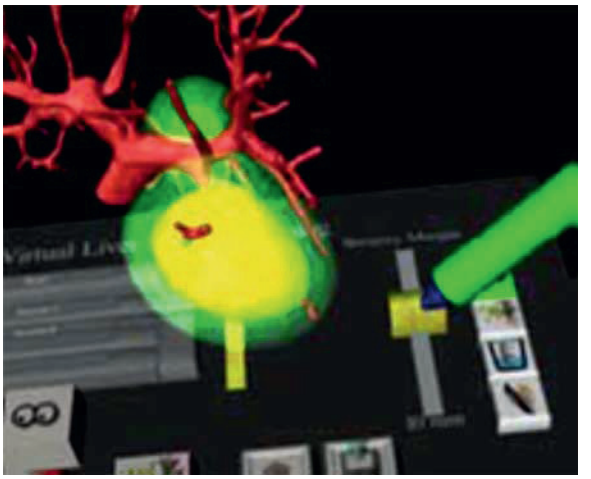

Fig. 29.8. Snapshot of the simulation step. The portal venous vessels are displayed in *red*; the tumor in *yellow* and the the *green* structure represents the onco-surgical safety margin. Moreover, the PIP with action buttons and sliders, as well as the virtual pencil, is displayed

Table 29.1. Quantitative results of the simulation process in another patient. All relevant results are listed

Information about case xxx	
# of tumors	1
Liver volume	1,376.00 ml
Tumor volume	177.00 ml
Proposed resected segments	II
Type of resection	atypical
Volume of resected tissue	atypical resection: 325.00 ml
	anatomic resection: 397.00 ml
Volume of remaining liver tissue	atypical resection: 1,051.00 ml
	anatomic resection: 979.00 ml
Relative volume of the resected tissue	atypical resection: 29%
	anatomic resection: 23%
Time required for planning	15 min

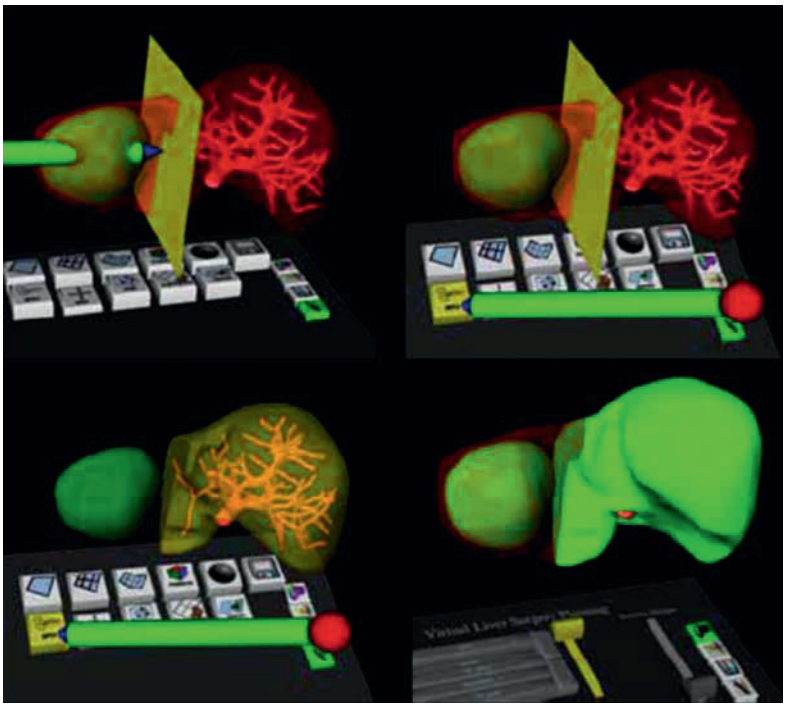

Fig. 29.9. Another scene from the simulation process. The different steps of a hemihepatectomy are depicted (liver, tumor, virtual pencil, PIP)

29.2.2 Hardware and Software Setup

For image transfer from the spiral CT machine to a DICOM server, a hospital's intranet is used. A Silicon Graphics Workstation Octane serves as the DICOM server (Silicon Graphics Inc., MountView, CA, USA; http://www.sgi.com) using the free available DICOM server software from the Electronic Radiology Laboratory Mallinckrodt Institute of Radiology (http://www.erl.wustl.edu/DICOM/ctn.html).

For data processing and display operations Linux-based workstations (Debian GNU/Linux; http://www.debian.org/) are used, which are equipped with AMD™ 64-bit Opteron processors (Advanced Micro Devices Inc., Sunnyvale, CA, USA; http://www.amd.com) and up to 64 GB of RAM. To run the augmented reality system, two workstations are necessary: one is responsible for collecting and processing the data of the infrared cameras used for determining the operator's position, whereas the other uses these data for recomputing the stereoscopic views of the new position and updating the HMD. All parts are connected by a segmented local 100,00 MBit TCP/IP network. Software for all steps of data processing, as well the augmented reality system, was developed at the Institute for Computer Graphics and Vision, University of Technology Graz, Austria. The augmented reality system is based on an Austrian collaborative research project between the Universities of Technology, Graz and Vienna, called "Studierstube" (http://studierstube.icg.tu-graz.ac.at). The A.R.T. Dtrack 1 system was used for infrared and tracking cameras (http://www.ar-tracking.de).

29.3 System Evaluation

The VLSPS system has already been evaluated in different ways. First, there was interest as to whether there was any advantage of the 3D editing tools, such as the above-mentioned sphere tool. Therefore, from seven spiral CT scenes the liver surface was segmented and a local deformation produced artificially. The original liver volume, as well as the volume of the deformed liver, were known. Therefore, the volume error, as produced by the deformation, was known (Table 29.2). Afterward, three observers edited these seven scenes with the help of 3D tools, and the relative volume deviation of the edited liver volume from the original one was

Table 29.2. Volume error produced artificially for evaluation of 3D editing tools

Scene #	Induced Error
1	15.2%
2	6.7%
3	9.2%
4	4.1%
5	64.2%
6	8.4%
7	38.9%

calculated again (Figs. 29.4, 29.10). As depicted in Figure 29.11, after an average of only 10.8 min. the final deviation was well below 4%.

Another setting of scenes was targeted to the assessment of the accuracy of the augmented reality system. Thirteen scenes were prepared in the following way: a patient's liver surface was segmented from a spiral CT scan, and different shaped and sized geometrical bodies "transplanted" (one or more). These bodies should simulate tumors (Fig. 29.12). Since these "transplanted" tumors were inserted artificially, their volume, as well as the liver volume, was known.

These scenes were transformed to slices again and saved in the DICOM format (nema.org). A group of ten senior physicians (five radiologists, four surgeons, one internist – grouped as radiologists and non-radiologists) had to evaluate these scenes at three different display settings: a) 2D: slices and multiplanar reconstructions; b) 3D: shaded surface display; and c) using the VLSPS. For a) and b) the Tiani J-Vision 3.3.13 Software (Tiani Inc., Vienna, Austria; http://www.tiani.com) was used. All physicians had to estimate the ratio between the transplanted tumors and the whole liver separately in 2D, 3D and using the VLSPS. The time needed for each task was recorded. Afterward, an analysis of variance was calculated using the SAS statistical software package (Statistical Analysis System, Cary, NC, USA).

As can be seem in Figure 29.13, there were considerable differences between the used display systems. As it can expected, the error for ratio estimation decreases if transplanted tumors get bigger. Moreover, as can be seen from Figure 29.14, the relative error of ratio estimations, as well as the time needed, declines from 2D to 3D to the VLSPS. It is worth noting that by switching from 2D to 3D radiologists gain less performance than non-radiologists. This finding may be explained by the fact that radiologists are trained to interpret cross-sectional slices, and the added 3D display is less important than it is for a non-radiologist. But both groups, radiologists and non-radiologists, improved their accuracy using the VLSPS. At ANOVA for ratio estimations this trend can be confirmed, since a statistically significant effect for the type of display ($p < 0.001$) and a nested effect for the type of display and user ($p = 0.0001$) as well as a borderline effect for the size of the transplanted tumors ($p = 0.0455$). Details can be found in Table 29.3. Furthermore, similar results can be found for time requirements (Table 29.4).

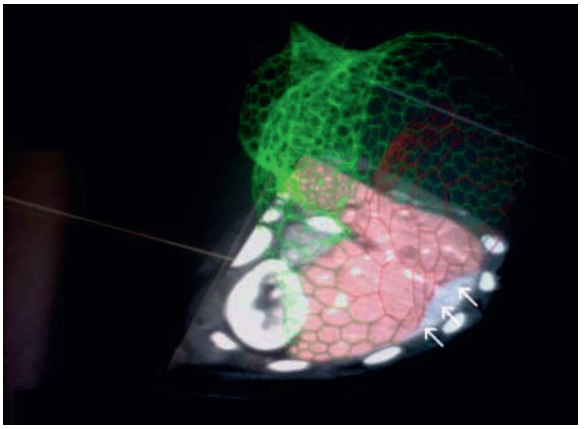

Fig. 29.10. Working view at 3D editing. Segmented liver surface is represented by a mesh graft; additionally, the spiral CT source data, as well as the liver contour on the spiral CT data, can be seen. *White arrows* mark the area where the automated segmentation process failed to detect the liver contour

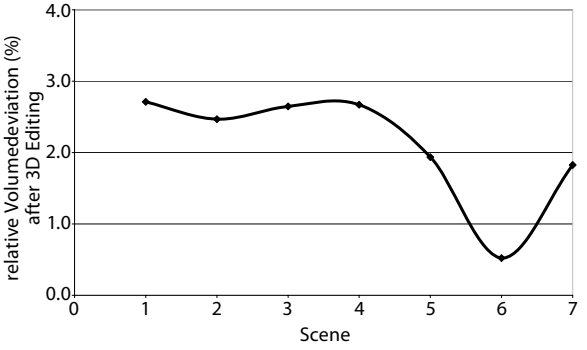

Fig. 29.11. Chart displaying the final volume deviation after 3D editing of seven scenes. As can be seen, the final deviation is well below 4%. An average time of only 10.8 min for 3D editing was necessary

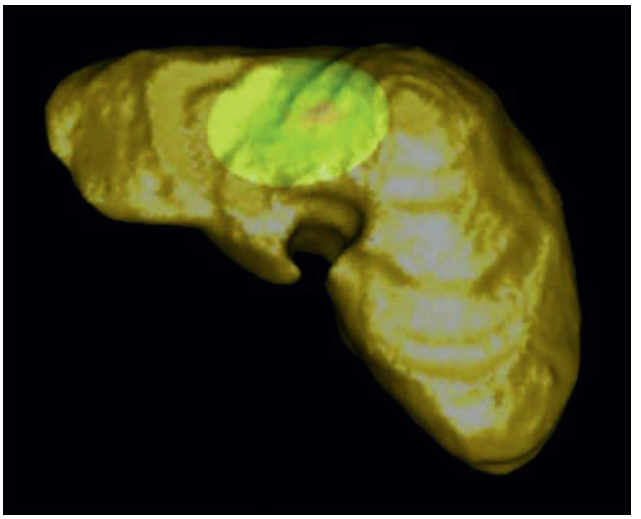

Fig. 29.12. A 3D reconstruction (using shaded surface display) of an extracted liver surface with an transplanted tumor

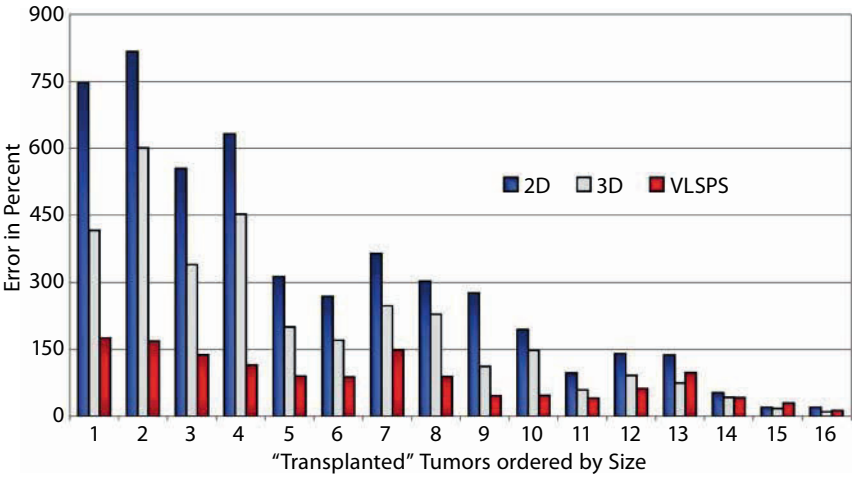

Fig. 29.13. Performance as achieved by the different display systems. The transplanted tumors are ordered by size. As can be expected, the performance increases if the ratio between the transplanted tumor and the liver decreases. But for all sizes the VLSPS performs best

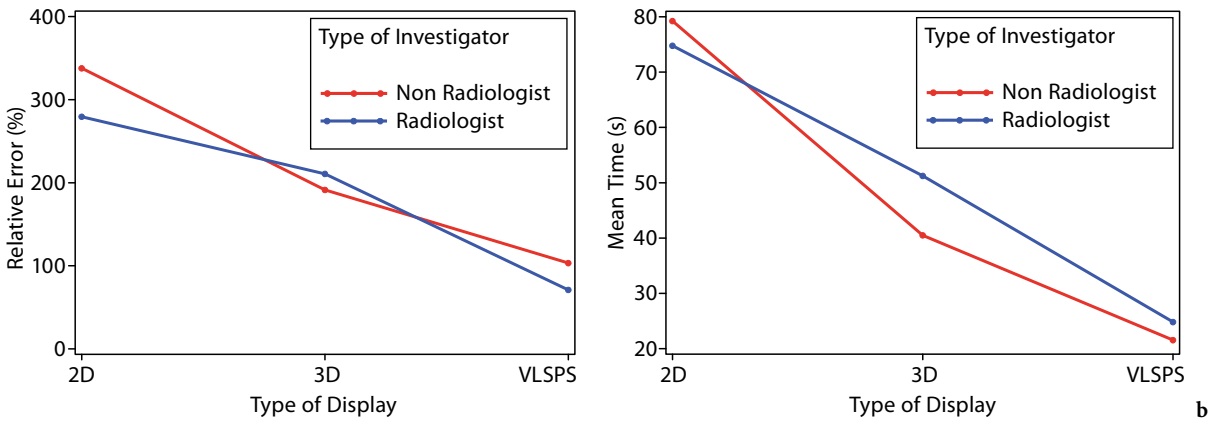

Fig. 29.14a,b. Achieved evaluation performance regarding ratio estimation in dependence of display system for different users (**a**) as well as the needed operator's time (**b**)

Table 29.3. ANOVA results for ratio (transplanted tumors / total liver volume) estimates

Effect	F-value	p
Type of display	58.22	**<.0001 ***
User (radiologist/non-radiologist)	1.98	0.1596
Tumor size	4.82	**0.0455 ***
Display*user	1.57	0.2100
Tumor size*display	569.13	**0.0001 ***
Tumor size*user	0.29	0.5881

bold face and * marks those effects that are statistically significant

Table 29.4. ANOVA results for time requirement

Effect	F-value	p
Type of display	95.92	**<.0001 ***
User (radiologist/non-radiologist)	1.24	0.2663
Display*user	1.86	0.1579
User*scene	1.58	**0.033 ***
Tumor size*user	0.29	0.5881

bold face and * marks those effects that are statistically significant

In the past, the whole team was engaged in development and in implementing improvements. Nevertheless, the system was already applied to two patients, in whom surgical therapy was regarded to be borderline suitable. Both patients were evaluated using the VLSPS, and a surgical approach was chosen. Intra-operative findings correlated well with the pre-operative VLSPS evaluation.

29.4 Conclusion

Technical progress regarding imaging modalities, computer hardware and the availability of open source operation systems like Linux enables challenging new applications (linux.org). The speed of computing as well as the tracking hardware for augmented reality systems allows us to generate real time systems, which can be used interactively. Besides pioneering work (Fishman et al. 1996), only a few institutions have already faced these new possibilities (Sonka et al.). First, evaluation of the VLSPS was targeted to prove if there was any advantage to using such a display. Our results indicate that the VLSPS augments the therapeutic decision making. Moreover, it is worth noting that the improved visualization of VLSPS narrows the gap between radiologists and clinical colleagues, thus indicating a better understanding between different medical specialties. Until recently clinical experience has been limited, but the system is now ready to run. Before using the VLSPS in the clinical routine a retrospective study will be carried out, and after successful completion of that study, and with permission of the ethics board, the VLSPS will be introduced into the daily routine.

References

http://www.analyzedirect.com, last accessed September 14, 2006
http://www.linux.org, last accessed September 14, 2006
http://medical.nema.org, last accessed September 14, 2006
Beichel R, Mitchell S et al (2001) Shape-and appearance-based segmentation of volumetric medical images. In: ICIP'01, vol. 2, pp. 589–592
Beichel R, Gotschuli G et al (2002) Diaphragm dome surface segmentation in CT data sets: A 3D active appearance model approach. In: Milan Sonka and J. Michael Fitzpatrick (eds) SPIE: Medical Imaging: Image Processing, vol. 4684, pp. 475–484
Bornik A, Pock T et al (2004) Liver segment approximation in CT data for surgical resection planning. In: Proceedings of the SPIE Medical Imaging 2004: Visualization, Image-Guided Procedures, and Display, San Diego, pp. 1435–1446
Fischer L, Cardenas C, Thorn M et al (2002) Limits of Couinaud's liver segment classification: a quantitative computer-based three-dimensional analysis. J Comput Assist Tomogr 26:962–967
Fishman EK, Kuszyk BS et al (1996) Surgical planning for liver resection. Computer 29:64–72
Reitinger B, Bornik A et al (2004) Tools for augmented reality based liver resection planning. In: Proceedings of the SPIE Medical Imaging 2004: Visualization, Image-Guided Procedures, and Display, San Diego, pp. 88–99
Rieker O, Mildenberger P, Hintze C et al (2000) Segmental anatomy of the liver in computed tomography: do we localize the lesion accurately? Rofo Fortschr Geb Rontgenstr Neuen Bildgeb Verfahr 172:147–152
Sonka M, Beichel R et al Computer-aided liver surgery planning. http://www.engineering.uiowa.edu/
Strunk H, Stuckmann G et al (2003) Limitations and pitfalls of Couinaud's segmentation of the liver in transaxial Imaging. Eur Radiol 13:2472–2482
World Health Organization (2004) World health report, http://www.who.int/whr/2004/en. Technical report, World Health Organization

List of Acronyms

2D	two-dimensional
2DFT	two-dimensional Fourier transformation
3D	three-dimensional
3D MR	three-dimensional magnetic resonance
3DFT	three-dimensional Fourier transformation
AAM	active appearance model
AIP	average intensity projection
AR	augmented reality
ASM	active shape model
BI-RADS	breast imaging reporting and data system
CAD	computer-aided detection
CAS	computed-aided surgery
CASS	computer-aided surgical simulation
CBD	common bile duct
CCA	connected component analysis
CE-MRA	contrast enhancement magnetic resonance angiography
CISS	constructive interference steady state
CPR	curved planar reconstructions
CRC	colorectal cancer
CSF	cerebral spinal fluid
CTA	CT angiography
CTC	CT colonography
CTDI	computed tomography dose index
CTE	CT enterography
CTU	CT urography
CTVP	CT virtual pancreatoscopy
DCBE	double contrast barium enema
DCIS	ductal carcinoma in situ
DESS	double echo steady state
DOF	degrees-of-freedom
DSA	digital subtraction angiography
DTI	diffusion tensor imaging
DWI	diffusion weighted imaging
EBCT	electron beam CT
EGC	early gastric cancer
EM	expectation-maximisation
EPI	echo planar imaging
ERCP	endoscopic retrograde cholangiopancreatography
ERP	endoscopic retrograde pancreatography
FESS	functional endoscopic sinus surgery
FFDM	full field digital detector arrays
FFE	fast field echo
FID	free induction decay
FIESTA	fast imaging employing steady state acquisition
FISP	fast imaging with steady state processing
FLASH	fast low angle shot sequence
fMR	functional magnetic resonance
FNH	focal nodular hyperplasia
FOBT	faecal occult blood testing
FOV	field of view
GRASS	gradient refocused acquisition in a steady state
GRE	gradient recalled echo
GUI	graphical user interface
GVF	gradient vector flow
HA	hepatic artery
HASTE	half-Fourier acquisition single-shot turbo spin echo
HCC	hepatocellular carcinoma
HD	hepatic duct
HMD	head-mounted display
ICP	iterative closest point
IORP	intraoperative retrograde pancreatoscopy
IPMN	intraductal papillary mucinous neoplasm
LARS	laparoscopic assistance robotic systems
LAVA	liver acquisition volume acceleration
LDA	linear discriminating classifier
LED	light emitting diodes
LHD	left hepatic duct
LI	linear interpolation
LUT	look up table
MDCT	multi-detector row computed tomography
MinIp	minimum intensity projection
MIP	maximum intensity projection
MPR	multi planar reconstruction
MP-RAGE	magnetization prepared rapid gradient echo
MPVR	multi planar volume reconstruction
MRA	MR angiography
MRC	MR cholangiography
MRCP	magnetic resonance cholangiopancreatography
MRDCT	multi-row detector computed tomography
MRU	MR urography
MSD	mean standard deviation
NES	nasal endoscopy simulator
NPU	needle positioning unit
PACS	picture archiving communication systems
PC	phase contrast
PD	pancreatic duct
PET	positron emission tomography
PIP	personal interaction panel
PSC	primary sclerosing cholangitis

PSIF	FISP sequence reversed in time
PTC	percutaneous transhepatic cholangiography
PVR	perspective volume rendering
QCA	quantitative coronary assessment
RAM	random accessible memory
RARE	rapid aquisition relaxation enhancement
RCM	remote center of motion
RF	radiofrequency
RHD	right hepatic duct
ROI	region of interest
SCT	spiral computed tomography
SE	spin echo
SGLD	spatial grey level dependance
SNR	signal-to-noise ratio
SPECT	single photon emission tomography
SPGR	spoiled gradient recalled
SR	surface rendering
SSD	shaded surface display
SSFP	steady-state free precession
SSFSE	single-shot fast spin echo
STM	statistical trained models
STS-MIP	sliding thin slab maximum intensity projection
TOF	time-of-flight
TR	repetition time
TRUS	transrectal ultrasound
TSE	turbo spin echo
VB	virtual bronchoscopy
VE	virtual endoscopy
VIBE	volumetric interpolated breath hold examination
VLSPS	virtual liver surgery planning system
VOI	volume of interest
VR	volume rendering
VRML	virtual reality modelling language

Subject Index

D

E

F

G

H

I

K

L

M

N

O

P

Q

R

S

T

U

V

W

List of Contributors

Andrik J. Aschoff, MD
Full Professor, Department of Diagnostic and Interventional Radiology
University Clinic of Ulm
Steinhövelstrasse 9
89075 Ulm
Germany

Emese Balogh, MS
Department of Applied Informatics
University of Szeged
Árpád tér 2
6720 Szeged
Hungary

Carlo Bartolozzi, MD
Professor, Division of Diagnostic and Interventional Radiology
Department of Oncology, Transplants, and New Technologies in Medicine
University of Pisa
Via Roma 67
56100 Pisa
Italy

Alex Bardine, MD
Diagnostic and Interventional Radiology
Department of Oncology, Transplants, and Advanced Technologies in Medicine
University of Pisa
Via Roma 67
56100 Pisa
Italy

Valentina Battaglia, MD
Diagnostic and Interventional Radiology
Department of Oncology, Transplants, and Advanced Technologies in Medicine
University of Pisa
Via Roma 67
56100 Pisa
Italy

Christoph R. Becker, MD
Institute of Clinical Radiology
Ludwig-Maximilians University
Großhadern Hospital
Marchioninistrasse 15
81377 Munich
Germany

Reinhard Beichel, PhD
Institute for Computer Graphics and Vision
University of Technology
Inffeldgasse 16
8010 Graz
Austria

Wolfgang Birkfellner, PhD
Associate Professor, Department of Biomedical Engineering and Physics
University of Vienna
General Hospital Vienna
Waehringer Guertel 18–20
1090 Vienna
Austria

Alain Blum-Moyse, MD
Service de Radiologie
Hôpital Central
29 Avenue Maréchal de Lattre de Tassigny
54035 Nancy Cédex
France

Piero Boraschi, MD
2nd Department of Radiology
Pisa University Hospital
Via Paradisa 2
56124 Pisa
Italy

Alexander Bornik
Institute for Computer Graphics and Vision
University of Technology
Inffeldgasse 16
8010 Graz
Austria

Elena Bozzi, MD
Division of Diagnostic and Interventional Radiology
Department of Oncology, Transplants and
New Technologies in Medicine
University of Pisa
Via Roma 67
56100 Pisa
Italy

Carla Capelli, MD
Diagnostic and Interventional Radiology
Department of Oncology, Transplants and
Advanced Technologies in Medicine
University of Pisa
Via Roma 67
56100 Pisa
Italy

Davide Caramella, MD
Professor, Diagnostic and Interventional Radiology
Department of Oncology, Transplants, and
Advanced Technologies in Medicine
University of Pisa
Via Roma 67
56100 Pisa
Italy

Claudia Cecchi, MD
Diagnostic and Interventional Radiology
Department of Oncology, Transplants, and
Advanced Technologies in Medicine
University of Pisa
Via Roma 67
56100 Pisa
Italy

Francesca Cerri, MD
Diagnostic and Interventional Radiology
Department of Oncology, Transplants, and
Advanced Technologies in Medicine
University of Pisa
Via Roma 67
56100 Pisa
Italy

Kevin Cleary, PhD
Department of Radiology
Imaging Science and Information Systems (ISIS) Center
Georgetown University Medical Center
Washington, DC
USA

Anne Cotten, MD
Professor, Service de Radiologie Ostéo-Articulaire
Hôpital Roger Salengro
CHRU de Lille – Universitaire de Lille
Boulevard du Pr. J. Leclercq
59037 Lille Cédex
France

Laura Crocetti, MD
Assistant Professor, Division of Diagnostic and
Interventional Radiology
Department of Oncology, Transplants, and
New Technologies in Medicine
University of Pisa
Via Roma 67
56125 Pisa
Italy

Abraham H. Dachman, PhD
Department of Radiology
Massachusetts General Hospital
Harvard Medical School
75 Blossom Court, Suite 220
Boston, Massachusetts 02114
USA

Carlo Nicola De Cecco, MD
Department of Radiological Sciences
University of Rome "La Sapienza"
Polo Pontino – I.C.O.T. Latina
Via di Villa Emiliani 4
00197 Rome
Italy

Clotilde Della Pina, MD
Research Fellow, Division of Diagnostic and
Interventional Radiology
Department of Oncology, Transplants, and
New Technologies in Medicine
University of Pisa
Via Roma 67
56100 Pisa
Italy

Ayso H. de Vries, MD
Department of Radiology
Academic Medical Center
University of Amsterdam
Meibergdreef 9
1100 AZ, Amsterdam
The Netherlands

Francescamaria Donati, MD
2nd Department of Radiology
Pisa University Hospital
Via Paradisa 2
56124 Pisa
Italy

Riccardo Ferrari, MD
Department of Radiological Sciences
University of Rome "La Sapienza"
Polo Pontino – I.C.O.T. Latina
Via di Villa Emiliani 4
00197 Rome
Italy

Gabor Fichtinger, PhD
Engineering Research Center
The Johns Hopkins University
Baltimore, MD 21218–2682
USA

Giovanni Galatola, MD
Gastroenterology Unit
Institute for Research and Treatment of Cancer (IRCC)
Str. Provinciale 142, Km 3,95, Candiolo
10060 Torino
Italy

Teresa Maria Gallo, MD
Radiology Unit
Institute for Research and Treatment of Cancer (IRCC)
Str. Provinciale 142, Km 3,95, Candiolo
10060 Torino
Italy

Stephen J. Golding, MD
Professor, Radiology Research Group
Nuffield Department of Surgery
University of Oxford
Oxford OX3 9DU
UK

Franco Iafrate, MD
Department of Radiological Sciences
University of Rome "La Sapienza"
Policlinico Umberto I
Viale Regina Elena 324
00161 Rome
Italy

Alan Jackson, PhD, FRCR, FRCP
Professor, Imaging Science
and Biomedical Engineering
The Medical School
University of Manchester
Stopford Building
Oxford Road
Manchester M13 9PT
UK

Nigel W. John, PhD
Professor of Computing
School of Computer Science
Bangor University
Dean Street
Bangor LL57 1UT
UK

Spyros Karampekios, MD
Department of Radiology
University Hospital of Heraklion
University of Crete, Faculty of Medicine
P.O. Box 2208
71003 Iraklion Crete
Greece

Joachim Kettenbach, MD
Associate Professor, Department of Radiology
Division of Cardiovascular and Interventional Radiology
Medical University of Vienna
General Hospital
Währinger Gürtel 18-20
1090 Wien
Austria

Gernot Kronreif, PhD
Advances Service Robotics
PROFACTOR Research and Solutions GmbH
2444 Seibersdorf
Austria

Andrea Laghi, MD
Department of Radiological Sciences
University of Rome "La Sapienza"
Polo Pontio – I.C.O.T. Latina
Via di Villa Emiliani 4
00197 Rome
Italy

Luigi Landini, MD
Professor, Department of Information Engineering
University of Pisa
Via Diotisalvi, 2
56126 Pisa
Italy

Cristiana Laudi, MD
Gastroenterology Unit
Institute for Research and Treatment of Cancer (IRCC)
Str. Provinciale 142, Km 3,95, Candiolo
10060 Torino
Italy

Riccardo Lencioni, MD
Associate Professor, Division of Diagnostic and
Interventional Radiology
Department of Oncology, Transplants, and
New Technologies in Medicine
University of Pisa
Via Roma 67
56125 Pisa
Italy

Franz Lindbichler, MD
Department of Radiology
University Hospital Graz
Auenbruggerplatz 34
8036 Graz
Austria

Michael Macari, MD
Associate Professor, Department of Radiology
Sectin Chief, Abdominal Imaging
New York University Medical Center, Tisch Hospital
560 First Ave, Suite HW 202
New York, NY 10016
USA

Paolo Marcheschi, MSc
Istituto di Fisiologia Clinica, CNR
Via Moruzzi, 1
56124 Pisa
Italy

Salvatore Mazzeo, MD
Diagnostic and Interventional Radiology
Department of Oncology, Transplants, and
Advanced Technologies in Medicine
University of Pisa
Via Roma 67
56100 Pisa
Italy

Bernard Meyer, MD
Department of Radiology
Charité Hospital
Humboldt-University Berlin
Schumannstrasse 20/21
10098 Berlin
Germany

Andreas Melzer, MD
Institute for Medical Science & Technology
Universities Dundee & St. Andrews Ninewells Hospital
and Medical School University Campus Ewing Building
Dundee, DD1 4HN
UK

Emanuele Neri, MD
Diagnostic and Interventional Radiology
Department of Oncology, Transplants, and
Advanced Technologies in Medicine
University of Pisa
Via Roma 67
56100 Pisa
Italy

LászlóG. Nyúl, PhD
Department of Applied Informatics
University of Szeged
Árpád tér 2
6720 Szeged
Hungary

Kálmán Palágyi, PhD
Department of Applied Informatics
University of Szeged
Árpád tér 2
6720 Szeged
Hungary

Valeria Panebianco, MD
Department of Radiological Sciences
University of Rome "La Sapienza"
Policlinico Umberto I
Viale Regina Elena 324
00161 Rome
Italy

Pasquale Paolantonio, MD
Department of Radiological Sciences
University of Rome "La Sapienza"
Polo Pontino – I.C.O.T. Latina
Via Franco Faggiana 34
04100 Latina
Italy

Nickolas Papanikolaou, PhD
Biomedical Engineer, Department of Radiology
University Hospital of Heraklion
University of Crete, Faculty of Medicine
P.O. Box 2208
71003 Iraklion Crete
Greece

Nikolaus Popovic, MD
Department of Radiology
Medical University Graz
Auenbruggerplatz 9
8036 Graz
Austria

Vincenzo Positano, Professor
CNR – Institute of Clinical Physiology
Via Moruzzi, 1
56124 Pisa
Italy

Daniele Regge, MD
Radiology Unit
Institute for Research and Treatment of Cancer (IRCC)
Str. Provinciale 142, Km 3,95, Candiolo
10060 Torino
Italy

Bernhard Reitinger, Dipl-Ing., Dr. techn.
Institute for Computer Graphics and Vision
University of Technology
Inffeldgasse 16
8010 Graz
Austria

Michael Rieger, MD
Medizinische Universität Innsbruck
Universitäts-Klinik für Radiodiagnostik 1
Anichstrasse 35
6020 Innsbruck
Austria

Patrik Rogalla, MD
AssociateProfessor, Department of Radiology
Charité Hospital
Humboldt-University Berlin
Schumannstrasse 20/21
10098 Berlin
Germany

Andrea Ruppert, MD
Department of Radiology
University Hospital Graz
Auenbruggerplatz 34
8036 Graz
Austria

Simonetta Salemi, MD
Diagnostic and Interventional Radiology
Department of Oncology
Transplants and Advanced Technologies in Medicine
University of Pisa
Via Roma 67
56125 Pisa
Italy

Maria Filomena Santarelli, PhD
CNR – Institute of Clinical Physiology
Via Moruzzi, 1
56124 Pisa
Italy

Benoît Sauer, MD
Service de Radiologie
Hôpital Central
29 Avenue Maréchal de Lattre de Tassigny
54035 Nancy Cédex
France

Iwo W. O. Serlie, MSc
Quantitative Imaging Group
Faculty of Applied Sciences
Delft University of Technology
Lorentzweg 1
2628 CJ, Delft
The Netherlands

Milan Sonka, Professor
Department of Electrical and Computer Engineering
The University of Iowa
Iowa City
IA 52242
USA

Erich Sorantin, MD
Associate Professor, Department of Radiology
University Hospital Graz
Auenbruggerplatz 34
8036 Graz
Austria

Stavros M Stivaros, MD
Imaging Science and Biomedical Engineering
The Medical School
University of Manchester
Stopford Building
Oxford Road
Manchester M13 9PT
UK

Don Stoianovici, PhD
URobotics Laboratory
JHBMC-D0300
5200 Eastern Avenue
Baltimore, MD 21224
USA

Jaap Stoker, MD, PhD
Professor, Department of Radiology
Academic Medical Center
University of Amsterdam
Meibergdreef 9
1105 AZ, Amsterdam
The Netherlands

Vincenzo Tartaglia, MD
Radiology Unit
Institute for Research and Treatment of Cancer (IRCC)
Str. Provinciale 142, Km 3,95, Candiolo
10060 Torino
Italy

Bart M. ter Haar Romeny, PhD
Professor, Eindhoven University of Technology
Department of Biomedical Engineering
Image Analysis and Interpretation
PO Box 513, WH 2.106
5600 MB Eindhoven
The Netherlands

Neil A Thacker, MD
Imaging Science and Biomedical Engineering
The Medical School
University of Manchester
Stopford Building
Oxford Road
Manchester M13 9PT
UK

Francesca Turini, MD
Diagnostic and Interventional Radiology
Department of Oncology, Transplants, and
Advanced Technologies in Medicine
University of Pisa
Via Roma 67
56100 Pisa
Italy

Paola Vagli, MD
Diagnostic and Interventional Radiology
Department of Oncology, Transplants, and
Advanced Technologies in Medicine
University of Pisa
Via Roma 67
56100 Pisa
Italy

Anna Vilanova i Bartrolí, PhD
Institute of Computer Graphics and Algorithms
Vienna University of Technology
Karlsplatz 13/186/2
1040 Vienna
Austria

Toni W. Vomweg, MD
Radiological Centre Dr. van Essen
Emil-Schüller-Strasse 31–33
56068 Koblenz
Germany

Frans M. Vos, MSc, PhD
Quantitative Imaging Group
Faculty of Applied Sciences
Delft University of Technology
Lorentzweg 1
2628 CJ, Delft
The Netherlands

Stephen R. Watt-Smith, MB BS, BDS, FDSRCS, MD
Department of Maxillofacial Surgery
Oxford Radcliffe Hospital
University of Oxford
Oxford OX3 9DU
UK

Georg Werkgartner, MD
Department of Surgery
Medical University Graz
Auenbruggerplatz 9
8036 Graz
Austria

Hiroyuki Yoshida, PhD
Associate Professor
Department of Radiology
Massachusetts General Hospital
Harvard Medical School
75 Blossom Court, Suite 220
Boston, Massachusetts 02114
USA

Medical Radiology Diagnostic Imaging and Radiation Oncology

Titles in the series already published

Diagnostic Imaging

Innovations in Diagnostic Imaging
Edited by J. H. Anderson

Radiology of the Upper Urinary Tract
Edited by E. K. Lang

The Thymus - Diagnostic Imaging, Functions, and Pathologic Anatomy
Edited by E. Walter, E. Willich, and W. R. Webb

Interventional Neuroradiology
Edited by A. Valavanis

Radiology of the Pancreas
Edited by A. L. Baert, co-edited by G. Delorme

Radiology of the Lower Urinary Tract
Edited by E. K. Lang

Magnetic Resonance Angiography
Edited by I. P. Arlart, G. M. Bongartz, and G. Marchal

Contrast-Enhanced MRI of the Breast
S. Heywang-Köbrunner and R. Beck

Spiral CT of the Chest
Edited by M. Rémy-Jardin and J. Rémy

Radiological Diagnosis of Breast Diseases
Edited by M. Friedrich and E.A. Sickles

Radiology of the Trauma
Edited by M. Heller and A. Fink

Biliary Tract Radiology
Edited by P. Rossi, co-edited by M. Brezi

Radiological Imaging of Sports Injuries
Edited by C. Masciocchi

Modern Imaging of the Alimentary Tube
Edited by A. R. Margulis

Diagnosis and Therapy of Spinal Tumors
Edited by P. R. Algra, J. Valk, and J. J. Heimans

Interventional Magnetic Resonance Imaging
Edited by J. F. Debatin and G. Adam

Abdominal and Pelvic MRI
Edited by A. Heuck and M. Reiser

Orthopedic Imaging
Techniques and Applications
Edited by A. M. Davies and H. Pettersson

Radiology of the Female Pelvic Organs
Edited by E. K.Lang

Magnetic Resonance of the Heart and Great Vessels
Clinical Applications
Edited by J. Bogaert, A.J. Duerinckx, and F. E. Rademakers

Modern Head and Neck Imaging
Edited by S. K. Mukherji and J. A. Castelijns

Radiological Imaging of Endocrine Diseases
Edited by J. N. Bruneton in collaboration with B. Padovani and M.-Y. Mourou

Trends in Contrast Media
Edited by H. S. Thomsen, R. N. Muller, and R. F. Mattrey

Functional MRI
Edited by C. T. W. Moonen and P. A. Bandettini

Radiology of the Pancreas
2nd Revised Edition
Edited by A. L. Baert. Co-edited by G. Delorme and L. Van Hoe

Emergency Pediatric Radiology
Edited by H. Carty

Spiral CT of the Abdomen
Edited by F. Terrier, M. Grossholz, and C. D. Becker

Liver Malignancies
Diagnostic and Interventional Radiology
Edited by C. Bartolozzi and R. Lencioni

Medical Imaging of the Spleen
Edited by A. M. De Schepper and F. Vanhoenacker

Radiology of Peripheral Vascular Diseases
Edited by E. Zeitler

Diagnostic Nuclear Medicine
Edited by C. Schiepers

Radiology of Blunt Trauma of the Chest
P. Schnyder and M. Wintermark

Portal Hypertension
Diagnostic Imaging-Guided Therapy
Edited by P. Rossi
Co-edited by P. Ricci and L. Broglia

Recent Advances in Diagnostic Neuroradiology
Edited by Ph. Demaerel

Virtual Endoscopy and Related 3D Techniques
Edited by P. Rogalla, J. Terwisscha Van Scheltinga, and B. Hamm

Multislice CT
Edited by M. F. Reiser, M. Takahashi, M. Modic, and R. Bruening

Pediatric Uroradiology
Edited by R. Fotter

Transfontanellar Doppler Imaging in Neonates
A. Couture and C. Veyrac

Radiology of AIDS
A Practical Approach
Edited by J.W.A.J. Reeders and P.C. Goodman

CT of the Peritoneum
Armando Rossi and Giorgio Rossi

Magnetic Resonance Angiography
2nd Revised Edition
Edited by I. P. Arlart, G. M. Bongratz, and G. Marchal

Pediatric Chest Imaging
Edited by Javier Lucaya and Janet L. Strife

Applications of Sonography in Head and Neck Pathology
Edited by J. N. Bruneton in collaboration with C. Raffaelli and O. Dassonville

Imaging of the Larynx
Edited by R. Hermans

3D Image Processing
Techniques and Clinical Applications
Edited by D. Caramella and C. Bartolozzi

Imaging of Orbital and Visual Pathway Pathology
Edited by W. S. Müller-Forell

Pediatric ENT Radiology
Edited by S. J. King and A. E. Boothroyd

Radiological Imaging of the Small Intestine
Edited by N. C. Gourtsoyiannis

Imaging of the Knee
Techniques and Applications
Edited by A. M. Davies and V. N. Cassar-Pullicino

Perinatal Imaging
From Ultrasound to MR Imaging
Edited by Fred E. Avni

Radiological Imaging of the Neonatal Chest
Edited by V. Donoghue

Diagnostic and Interventional Radiology in Liver Transplantation
Edited by E. Bücheler, V. Nicolas, C. E. Broelsch, X. Rogiers, and G. Krupski

Radiology of Osteoporosis
Edited by S. Grampp

Imaging Pelvic Floor Disorders
Edited by C. I. Bartram and J. O. L. DeLancey
Associate Editors: S. Halligan, F. M. Kelvin, and J. Stoker

Imaging of the Pancreas
Cystic and Rare Tumors
Edited by C. Procacci and A. J. Megibow

High Resolution Sonography of the Peripheral Nervous System
Edited by S. Peer and G. Bodner

Imaging of the Foot and Ankle
Techniques and Applications
Edited by A. M. Davies,
R. W. Whitehouse, and J. P. R. Jenkins

Radiology Imaging of the Ureter
Edited by F. Joffre, Ph. Otal,
and M. Soulie

Imaging of the Shoulder
Techniques and Applications
Edited by A. M. Davies and J. Hodler

Radiology of the Petrous Bone
Edited by M. Lemmerling and
S. S. Kollias

Interventional Radiology in Cancer
Edited by A. Adam, R. F. Dondelinger,
and P. R. Mueller

Duplex and Color Doppler Imaging
of the Venous System
Edited by G. H. Mostbeck

Multidetector-Row CT of the Thorax
Edited by U. J. Schoepf

Functional Imaging of the Chest
Edited by H.-U. Kauczor

Radiology of the Pharynx
and the Esophagus
Edited by O. Ekberg

Radiological Imaging
in Hematological Malignancies
Edited by A. Guermazi

Imaging and Intervention in
Abdominal Trauma
Edited by R. F. Dondelinger

Multislice CT
2nd Revised Edition
Edited by M. F. Reiser, M. Takahashi,
M. Modic, and C. R. Becker

Intracranial Vascular Malformations
and Aneurysms
From Diagnostic Work-Up
to Endovascular Therapy
Edited by M. Forsting

Radiology and Imaging of the Colon
Edited by A. H. Chapman

Coronary Radiology
Edited by M. Oudkerk

Dynamic Contrast-Enhanced Magnetic
Resonance Imaging in Oncology
Edited by A. Jackson, D. L. Buckley,
and G. J. M. Parker

Imaging in Treatment Planning
for Sinonasal Diseases
Edited by R. Maroldi and P. Nicolai

Clinical Cardiac MRI
With Interactive CD-ROM
Edited by J. Bogaert, S. Dymarkowski,
and A. M. Taylor

Focal Liver Lesions
Detection, Characterization, Ablation
Edited by R. Lencioni, D. Cioni,
and C. Bartolozzi

Multidetector-Row CT Angiography
Edited by C. Catalano and
R. Passariello

Paediatric Musculoskeletal Diseases
With an Emphasis on Ultrasound
Edited by D. Wilson

Contrast Media in Ultrasonography
Basic Principles and Clinical Applications
Edited by Emilio Quaia

MR Imaging in White Matter Diseases of
the Brain and Spinal Cord
Edited by M. Filippi, N. De Stefano,
V. Dousset, and J. C. McGowan

Diagnostic Nuclear Medicine
2nd Revised Edition
Edited by C. Schiepers

Imaging of the Kidney Cancer
Edited by A. Guermazi

Magnetic Resonance Imaging in
Ischemic Stroke
Edited by R. von Kummer and T. Back

Imaging of the Hip & Bony Pelvis
Techniques and Applications
Edited by A. M. Davies, K. J. Johnson,
and R. W. Whitehouse

Imaging of Occupational and
Environmental Disorders of the Chest
Edited by P. A. Gevenois and
P. De Vuyst

Contrast Media
Safety Issues and ESUR Guidelines
Edited by H. S. Thomsen

Virtual Colonoscopy
A Practical Guide
Edited by P. Lefere and S. Gryspeerdt

Vascular Embolotherapy
A Comprehensive Approach
Volume 1: *General Principles, Chest,*
Abdomen, and Great Vessels
Edited by J. Golzarian. Co-edited by
S. Sun and M. J. Sharafuddin

Vascular Embolotherapy
A Comprehensive Approach
Volume 2: *Oncology, Trauma, Gene*
Therapy, Vascular Malformations,
and Neck
Edited by J. Golzarian. Co-edited by
S. Sun and M. J. Sharafuddin

Head and Neck Cancer Imaging
Edited by R. Hermans

Vascular Interventional Radiology
Current Evidence in
Endovascular Surgery
Edited by M. G. Cowling

Ultrasound of the Gastrointestinal Tract
Edited by G. Maconi and
G. Bianchi Porro

Imaging of Orthopedic Sports Injuries
Edited by F. M. Vanhoenacker,
M. Maas, J. L. M. A. Gielen

Parallel Imaging in
Clinical MR Applications
Edited by S. O. Schoenberg, O. Dietrich,
and M. F. Reiser

MRI and CT of the Female Pelvis
Edited by B. Hamm and R. Forstner

Ultrasound of the Musculoskeletal System
S. Bianchi and C. Martinoli

Spinal Imaging
Diagnostic Imaging of the Spine and
Spinal Cord
Edited by J. W. M. Van Goethem,
L. van den Hauwe, and P. M. Parizel

Radiation Dose from Adult and Pediatric
Multidetector Computed Tomography
Edited by D. Tack and P. A. Gevenois

Computed Tomography of the Lung
A Pattern Approach
J. A. Verschakelen and W. De Wever

Clinical Functional MRI
Presurgical Functional Neuroimaging
Edited bei C. Stippich

Imaging in Transplantation
Edited by A. A. Bankier

Radiological Imaging of the Digestive
System in Infants and Children
Edited by A. S. Devos and
J. G. Blickman

Pediatric Chest Imaging
Chest Imaging in Infants and Children
2nd Revised Edition
Edited by J. Lucaya and J. L. Strife

Radiological Imaging
of the Neonatal Chest
2nd Revised Edition
Edited by V. Donoghue

Radiology of the Stomach and Duodenum
Edited by A. H. Freeman and E. Sala

Imaging in Pediatric Skeletal Trauma
Techniques and Applications
Edited by K. J. Johnson and E. Bache

Percutaneous Tumor Ablation in
Medical Radiology
Edited by T. J. Vogl, T. K. Helmberger,
M. G. Mack, and M. F. Reiser

Screening and Preventive Diagnosis with
Radiological Imaging
Edited by M. F. Reiser, G. van Kaick,
C. Fink, and S. O. Schoenberg

Color Doppler US of the Penis
Edited by M. Bertolotto

Image Processing in Radiology
Current Applications
Edited by E. Neri, D. Caramella,
and C. Bartolozzi

Springer

Medical Radiology Diagnostic Imaging and Radiation Oncology

Titles in the series already published

Radiation Oncology

Lung Cancer
Edited by C.W. Scarantino

Innovations in Radiation Oncology
Edited by H. R. Withers
and L. J. Peters

Radiation Therapy
of Head and Neck Cancer
Edited by G. E. Laramore

Gastrointestinal Cancer –
Radiation Therapy
Edited by R.R. Dobelbower, Jr.

Radiation Exposure
and Occupational Risks
Edited by E. Scherer, C. Streffer,
and K.-R. Trott

Radiation Therapy of Benign Diseases
A Clinical Guide
S. E. Order and S. S. Donaldson

Interventional Radiation
Therapy Techniques – Brachytherapy
Edited by R. Sauer

Radiopathology of Organs and Tissues
Edited by E. Scherer, C. Streffer,
and K.-R. Trott

Concomitant Continuous Infusion
Chemotherapy and Radiation
Edited by M. Rotman
and C. J. Rosenthal

Intraoperative Radiotherapy –
Clinical Experiences and Results
Edited by F. A. Calvo, M. Santos,
and L.W. Brady

Radiotherapy of Intraocular
and Orbital Tumors
Edited by W. E. Alberti and
R. H. Sagerman

Interstitial and Intracavitary
Thermoradiotherapy
Edited by M. H. Seegenschmiedt
and R. Sauer

Non-Disseminated Breast Cancer
Controversial Issues in Management
Edited by G. H. Fletcher and S.H. Levitt

Current Topics in
Clinical Radiobiology of Tumors
Edited by H.-P. Beck-Bornholdt

Practical Approaches to
Cancer Invasion and Metastases
A Compendium of Radiation
Oncologists' Responses to 40 Histories
Edited by A. R. Kagan with the
Assistance of R. J. Steckel

Radiation Therapy in Pediatric Oncology
Edited by J. R. Cassady

Radiation Therapy Physics
Edited by A. R. Smith

Late Sequelae in Oncology
Edited by J. Dunst and R. Sauer

Mediastinal Tumors. Update 1995
Edited by D. E. Wood and
C. R. Thomas, Jr.

Thermoradiotherapy
and Thermochemotherapy
Volume 1:
Biology, Physiology, and Physics
Volume 2:
Clinical Applications
Edited by M.H. Seegenschmiedt,
P. Fessenden, and C.C. Vernon

Carcinoma of the Prostate
Innovations in Management
Edited by Z. Petrovich, L. Baert,
and L.W. Brady

Radiation Oncology
of Gynecological Cancers
Edited by H.W. Vahrson

Carcinoma of the Bladder
Innovations in Management
Edited by Z. Petrovich, L. Baert,
and L.W. Brady

Blood Perfusion and
Microenvironment of Human Tumors
Implications for
Clinical Radiooncology
Edited by M. Molls and P. Vaupel

Radiation Therapy of Benign Diseases
A Clinical Guide
2nd Revised Edition
S. E. Order and S. S. Donaldson

Carcinoma of the Kidney and Testis,
and Rare Urologic Malignancies
Innovations in Management
Edited by Z. Petrovich, L. Baert,
and L.W. Brady

Progress and Perspectives in the
Treatment of Lung Cancer
Edited by P. Van Houtte,
J. Klastersky, and P. Rocmans

Combined Modality Therapy of
Central Nervous System Tumors
Edited by Z. Petrovich, L. W. Brady,
M. L. Apuzzo, and M. Bamberg

Age-Related Macular Degeneration
Current Treatment Concepts
Edited by W. A. Alberti, G. Richard,
and R. H. Sagerman

Radiotherapy of Intraocular
and Orbital Tumors
2nd Revised Edition
Edited by R. H. Sagerman,
and W. E. Alberti

Modification of Radiation Response
Cytokines, Growth Factors,
and Other Biolgical Targets
Edited by C. Nieder, L. Milas,
and K. K. Ang

Radiation Oncology for Cure and Palliation
R. G. Parker, N. A. Janjan,
and M. T. Selch

Clinical Target Volumes in Conformal and
Intensity Modulated Radiation Therapy
A Clinical Guide to Cancer Treatment
Edited by V. Grégoire, P. Scalliet,
and K. K. Ang

Advances in Radiation Oncology
in Lung Cancer
Edited by Branislav Jeremić

New Technologies in Radiation Oncology
Edited by W. Schlegel, T. Bortfeld,
and A.-L. Grosu

Technical Basis of Radiation Therapy
4th Revised Edition
Edited by S. H. Levitt, J. A. Purdy,
C. A. Perez, and S. Vijayakumar

CURED I • LENT
Late Effects of Cancer Treatment
on Normal Tissues
Edited by P. Rubin, L. S. Constine,
L. B. Marks, and P. Okunieff

Clinical Practice of Radiation Therapy for
Benign Diseases
Contemporary Concepts and Clinical
Results
Edited by M. H. Seegenschmiedt,
H.-B. Makoski, K.-R. Trott, and
L. W. Brady

Springer